

MARINE 2019

Computational Methods in Marine Engineering VIII

13-15 May, 2019, Gothenburg, Sweden

Edited by: R. Bensow and J. Ringsberg



**VIII International Conference on
Computational Methods in
Marine Engineering
MARINE 2019**

**Gothenburg, Sweden
May 13 – 15, 2019**

A publication of:

**International Center for Numerical
Methods in Engineering (CIMNE)**
Barcelona, Spain



First Edition: May 2019

© The Authors

ISBN: 978-84-949194-3-5

Printed by: Artes Gráficas Torres S.L., Huelva 9, 08940 Cornellà de Llobregat,
Spain

TABLE OF CONTENTS

| | |
|--|-----|
| Preface | 7 |
| Acknowledgements and Supporting Organizations..... | 9 |
| Summary | 11 |
| Contents | 13 |
| Lectures..... | 21 |
| Authors Index..... | 833 |

PREFACE

This volume contains full-length papers of contributions presented at *MARINE 2019*, the *Eight International Conference on Computational Methods in Marine Engineering*, held at Chalmers Conference Center, Gothenburg, Sweden, May 13-15, 2019. The first edition of this series of conferences was held in Oslo, Norway, in June 2005, with following editions every second year, in Barcelona, Spain, June 2007, in Trondheim, Norway, June 2009, in Lisbon, Portugal, September 2011, in Hamburg, Germany, May 2013, in Rome, Italy, June 2015, and, finally in Nantes, France, May 2017.

In the spirit of previous editions, the objective of MARINE 2019 is to provide “a meeting place for researchers developing computational methods and scientists and engineers focusing on challenging applications in Marine Engineering”. The state of the art in computational approaches is addressed in sessions on, e.g. computational fluid dynamics (both fundamental and applied), propulsors, design and optimization, fluid-structure interaction with a specific focus on ship hydrodynamics, lightweight design and structures. We see further large contributions to topics related to multiphase flows, both on development of the numerical methods as to applications related to e.g. water entry problems, waves-structure interaction, and seakeeping. Further, the interest on marine renewable energy is continued large.

The conference programme includes five plenary lectures, six keynote lectures, and in total over one hundred and fifty seven contributions distributed in seventeen contributed sessions and equally seventeen invited sessions organised by recognised experts. The programme extends over three days with four parallel sessions.

MARINE 2019 is the eight international conference on this topic organized in the framework of the Thematic Conferences of the European Community on Computational Methods in Applied Sciences (ECCOMAS). Moreover, MARINE 2019 is a Special Interest Conference of the International Association for Computational Mechanics (IACM). The conference is jointly organized by Chalmers University of Technology, Department of Mechanics and Maritime Sciences and by the International Center for Numerical Methods in Engineering (CIMNE) in co-operation with the Technical University of Catalonia (UPC).

Our sincere appreciation goes to plenary lecturers, keynote lecturers, invited session organizers and all authors who have contributed to the outstanding scientific quality of the conference as reflected in the proceedings. Finally, we wish to thank Mr. Alessio Bazzanella and Ms Laia Aranda and the staff from the Congress Department of CIMNE, Barcelona, Spain, for their excellent work in the support of the conference organization and for the publication of this volume.

Gothenburg, 13th of May 2019

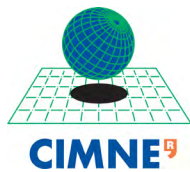
Rickard Bensow and Jonas Ringsberg, Editors

ACKNOWLEDGEMENTS

The conference organizers acknowledge the support towards the organization of the MARINE 2019 Conference to the following organizations:



Chalmers University, Sweden



International Center for Numerical Methods in Engineering (CIMNE), Spain



Universitat Politècnica de Catalunya (UPC)



European Community on Computational Methods in Applied Sciences (ECCOMAS)



International Association for Computational Mechanics (IACM)



KONGSBERG

Kongsberg Maritime



Caterpillar Propulsion



BETA CAE SYSTEM



Siemens

SUMMARY

INVITED SESSIONS

| | |
|---|-----|
| IS- Application of FSI in marine propulsion and energy converters | 23 |
| IS- Application of scale-resolving turbulence modelling techniques to ship hydrodynamics | 48 |
| IS- Biomimetics in marine technology | 71 |
| IS- Cavitation and cavitation-induced erosion..... | 83 |
| IS- Computational Environmental Mechanics for the Blue Growth | 99 |
| IS- Flow problems and control, optimisation, and uncertainty | 111 |
| IS- Marine Energy | 134 |
| IS- Multi-fidelity analysis and optimization methods in marine engineering | 169 |
| IS- Numerical Methods for Multiphase Flows | 213 |
| IS- Numerical modeling of flexible structures in offshore environment | 259 |
| IS- Numerical Modelling for Air Lubrication..... | 285 |
| IS- Optimisation & uncertainty quantification in practical hydrodynamic ship design ... | 296 |
| IS- Physics and simulation of hydrofoils | 334 |
| IS- Water Impact | 359 |

CONTRIBUTED SESSIONS

| | |
|---|-----|
| Cavitation | 371 |
| Fluid Dynamics | 393 |
| High speed vessels | 417 |
| Marine Renewables | 441 |
| Mooring and FSI | 453 |
| Numerical Modelling and CFD..... | 465 |
| Off-shore | 525 |
| Optimisation and Machine Learning | 544 |
| Propulsors | 568 |
| Ship Design..... | 615 |
| Ship Motions | 625 |
| Ship Scale Performance | 682 |
| Structures and Materials | 742 |
| Wave Modelling | 771 |
| Waves-Structure Interaction | 795 |

CONTENTS

INVITED SESSIONS

IS- Application of FSI in marine propulsion and energy converters

naoe-FOAM-SJTU Solver for Ship Flows and Ocean Engineering Flows..... 23
D. Wan

Open Water Characteristics of Three Model Scale Flexible Propellers..... 35
L. Savio and K. Koushan

IS- Application of scale-resolving turbulence modelling techniques to ship hydrodynamics

PANS Simulations: Low versus high Reynolds Number Approach 48
M. Klapwijk, T. Lloyd, G. Vaz and T. van Terwisga

VpLES- Particle Intensified Large Eddy Simulation..... 60
N. Kornev and S. Samarbakhsh

IS- Biomimetics in marine technology

Bio-inspired Propulsion in Ocean Engineering: Learning from Nature 71
G. Shi, R. Li and Q. Xiao

IS- Cavitation and cavitation-induced erosion

A Method for the Coupling of Compressible 3D Flow Simulations with a Cavitation Erosion Model for Ductile Materials and Assessment of the Incubation Time 83
F. Schreiner, S. Mottyll and R. Skoda

IS- Computational Environmental Mechanics for the Blue Growth

An Overview on the use of the Ffowcs Williams-Hawkings Equation for the Hydroacoustic Analysis of Marine Propellers..... 99
S. Ianniello and C. Testa

IS- Flow problems and control, optimisation, and uncertainty

A Complete Data-Driven Framework for the Efficient Solution of Parametric Shape Design and Optimization in Naval Engineering Problems (Keynote Lecture)111
N. Demo, M. Tezzele, A. Mola and G. Rozza

Shape Optimization through Proper Orthogonal Decomposition with Interpolation and Dynamic Mode Decomposition Enhanced by Active Subspaces122
M. Tezzele, N. Demo and G. Rozza

IS- Marine Energy

| | |
|---|------------|
| Experimental Validation of a RANS-VOF Numerical Model of the Wave Generation, Propagation and Dissipation in a 2D Wave Flume | 134 |
| <i>L. Galera, U. Izquierdo, G.A. Esteban, J.M. Blanco and I. Albaina</i> | |

| | |
|---|------------|
| On the Importance of Advanced Mesh Motion Models in CFD-based Numerical Wave Tanks for WEC Testing | 145 |
| <i>C. Windt, J. Davidson, D. Chandar and J.V. Ringwood</i> | |

| | |
|--|------------|
| Uncertainty Quantification of the Dynamics of a Wave Energy Converter.. | 157 |
| <i>G. Moura Paredes, C. Eskilsson and J. P. Kofoed</i> | |

IS- Multi-fidelity analysis and optimization methods in marine engineering

| | |
|--|------------|
| 3D Structural Design Tool for Monohull and Multihull Vessels..... | 169 |
| <i>J. Wyman, J. Knight and D. Kring</i> | |

| | |
|---|------------|
| An Adaptive N-Fidelity Metamodel for Design and Operational-Uncertainty Space Exploration of Complex Industrial Problems | 177 |
| <i>A. Serani, R. Pellegrini, R. Broglia, J. Wackers, M. Visonneau and M. Diez</i> | |

| | |
|--|------------|
| An Assessment of Multifidelity Procedures for Ship Hull Form Optimisation | 189 |
| <i>H.C. Raven and T.P. Scholcz</i> | |

| | |
|---|------------|
| Efficient Reduction in Shape Parameter Space Dimension for Ship Propeller Blade Design | 201 |
| <i>A. Mola, M. Tezzele, M. Gadalla, F. Valdenazzi, D Grassi, R. Padovan and G. Rozza</i> | |

IS- Numerical Methods for Multiphase Flows

| | |
|--|------------|
| A high-order and Mesh-free Computational Model for Non-linear Water Waves | 213 |
| <i>M. E. Nielsen, B. Fornberg and L. Damkilde</i> | |

| | |
|--|------------|
| Application of a Coupled Level Set and Volume of Fluid Method for Unsteady Simulations with an Unstructured Flow Solver | 223 |
| <i>B. E. LeBlanc, C. M. Klaij, H.-C. Chen and A. G. Gerber</i> | |

| | |
|---|------------|
| Extension of a Fast Method for 2D SteadyFree Surface Flow to Stretched Surface Grids | 235 |
| <i>T. Demeester, E.H. van Brummelen and J. Degroote</i> | |

| | |
|--|------------|
| Numerical Modeling of Contact Discontinuities in Two-phase Flow | 247 |
| <i>R. Remmerswaal and A.E.P. Veldman</i> | |

IS- Numerical modeling of flexible structures in offshore environment

| | |
|--|------------|
| Analysis of Flexible Net Structures in Marine Environment | 259 |
| <i>A.J. Berstad and L.F. Heimstad</i> | |

| | |
|--|------------|
| Application of FhSim for the Analysis of Environmental Loads on a Complete Fish-Farm System | 271 |
| <i>A. Tsarau and D. Kristiansen</i> | |

IS- Numerical Modelling for Air Lubrication

| | |
|---|------------|
| Eulerian-Lagrangian Simulation on Microbubbles in Turbulent Channel Flow | 285 |
| <i>X. Zhang and D. Wan</i> | |

IS- Optimisation & uncertainty quantification in practical hydrodynamic ship design

| | |
|--|------------|
| A Practical Tool for the Hydro-acoustic Optimization of Naval Propellers .. | 296 |
| <i>F. Valdenazzi, F. Conti, S. Gaggero, D. Grassi, C. Vaccaro and D. Villa</i> | |

| | |
|--|------------|
| Data Driven uncertainty Quantification for Computational Fluid Dynamics based Ship Design | 309 |
| <i>T.P. Scholcz</i> | |

| | |
|---|------------|
| Improved Hull Design with Potential-Flow-Based Parametric Computer Experiments | 321 |
| <i>O.F.A. van Straten, E. Celik, J.H.S. de Baar, B. Ascic and J.S. de Jong</i> | |

IS- Physics and simulation of hydrofoils

| | |
|--|------------|
| A Synergetic Design Study of a Passenger-Hydrofoil Flapped Surface: Experimental and Computational Fluid Dynamics, Optimization, and Control..... | 334 |
| <i>L. Antognoli, M. Bibuli, M. Diez, D. Durante, S. Ficini, S. Marrone, A. Odetti, I. Santic and A. Serani</i> | |

| | |
|---|------------|
| CFD Investigation of Ventilation-Cavitation Coupling on Surface-Piercing Super-Cavitating Hydrofoils | 346 |
| <i>S. Brizzolara</i> | |

IS- Water Impact

| | |
|--|------------|
| Numerical Hydrodynamic Study on the Effects of Body-Curvature during Ditching | 359 |
| <i>J.D. Mesa and K.J. Maki</i> | |

CONTRIBUTED SESSIONS

Cavitation

| | |
|---|------------|
| Experimental and Numerical Investigation of Blade Geometry Effect on Propeller Cavitation and Noise..... | 371 |
| <i>X.-Q. Dong, Q. Wang and C.-J. Yang</i> | |

| | |
|---|-----|
| Propeller Tip Vortex Cavitation Mitigation using Roughness | 383 |
|---|-----|

A. Asnaghi, U. Svennberg, R. Gustafsson and R. Bensow

Fluid Dynamics

| | |
|--|-----|
| Assessment of Computational Techniques for the Prediction of Acoustic Sources From Lifting Surfaces Using LES and DNS | 393 |
|--|-----|

T.A. Smith and Y. Ventikos

| | |
|--|-----|
| Experimental Validation of Aerodynamic Computational Results in the Aft-deck of a Simplified Frigate Shape (SFS2) | 405 |
|--|-----|

R. Bardera, J. C. Matias and A. Garcia-Magariño

High speed vessels

| | |
|---|-----|
| A Numerical and Analytical Way for Double-stepped Planing Hull in Regular Wave | 417 |
|---|-----|

R. Niazmand Bilandi, S. Mancini, A. Dashtimanesh, S. Tavakoli and M. De Carlini

| | |
|---|-----|
| Verification and Validation study of OpenFOAM on the Generic Prismatic Planing Hull Form | 428 |
|---|-----|

J. Li, L. Bonfiglio and S. Brizzolara

Marine Renewables

| | |
|--|-----|
| Design of Low Drag-to-Power Ratio Hydro-kinetic Turbine | 441 |
|--|-----|

A. Shiri, J. Hallander and B. Bergqvist

Mooring and FSI

| | |
|--|-----|
| Numerical Modelling of the Interaction between a Fish Net and Fluid using CFD | 453 |
|--|-----|

T. Martin, A. Kamath and H. Bihs

Numerical Modelling and CFD

| | |
|---|-----|
| A Sensitivity Analysis of CFD Transition Modelling in the Context of Vortex Roll-Up Prediction | 465 |
|---|-----|

R. Liebrand, M. Klapwijk, T. Lloyd, G. Vaz and R. Lopes

| | |
|---|-----|
| Analysis of the Blade Boundary Layer Flow of a Marine Propeller with RANSE | 477 |
|---|-----|

J.M. Baltazar, D.B. Melo and D.R. Rijpkema

| | |
|--|-----|
| Disequilibrium Wall Function in RANSE Computation applied to Flow Conditions around Ship's Hull | 491 |
|--|-----|

C.-U. Böttner and I. Shevchuk

Improvement of an Existing Shoreline Evolution Numerical Model.....502
M. Lima and C. Coelho

Improving the Numerical Robustness of Buoyancy modified k- ω SST Turbulence Model514
C. Liu, W. Zhao, J. Wang and D. Wan

Off-shore

Internal Flow-induced Instability Analysis of Catenary Risers525
K.N. Bakis and N. Srinil

Merits of the Maximum Entropy Meshless Method for Coupled Analysis of Offshore Problems.....537
M. Nazem and M. Cassidy

Optimisation and Machine Learning

A Data-Driven Probabilistic Learning approach for the Prediction of Controllable Pitch Propellers Performance.....544
S. Gaggero, A. Coppedè, D. Villa, G. Vernengo and L. Bonfiglio

Research on Selection of Base for Impact Assessment of Shipborne.....556
J. Chen and Z. Chi

Propulsors

Design of Open-Water and Wake-Adapted Optimum Propellers based on A Vortex Lattice Lifting-Surface Model.....568
H. Yong-sheng, W. Qi, D. Xiao-Qian and Y. Chen-Jun

Kinematics and Load Conditions at the Voith-Schneider-Propeller580
T. Rosenlöcher, B. Schlecht and M. Rösner

Numerical Investigation of Tip Geometry on the Tip-clearance Flow Features of a Pump-jet Propulsor588
X.-Q. Ji, X.-Q. Dong, W. Li, C.-J. Yang and F. Noblesse

Possibilities to determine Design Loads for Thrusters.....600
M. Kostial, F. Mieth, T. Rosenlöcher and B. Schlecht

Viscous Effects on the Hydrodynamic Performance of Semi-Active Flapping Propulsor607
N. Thaweewat, S. Phoemsaphawee and S. Jungrungruentaworn

Ship Design

Efficiency Improvement Effect and Water Noise Reduction by Energy Saving Devices615
T. Tachikawa, Y. Okada, K. Katayama, A. Okazaki, M. Okazaki, K. Fukuda, Y. Kobayashi and T. Kajino

Ship Motions

- A Linearized Free-Surface RANS Method for Ship Maneuvering**625
P. Geremia, K.J. Maki and P. Alexias
- Numerical Investigation of a large Diameter Propeller Emergence Risk for a Vessel in Waves**634
M. Irannezhad, A. Eslamdoost and R. Bensow
- Prediction of Parametric Rolling for a Container Ship in Regular and Irregular Waves using a Fully Nonlinear Time Domain Potential Flow Method**646
F. Coslovich, M. Kjellberg and C-E. Janson
- To evaluate the Influence of DOF on manoeuvring Prediction by direct CFD Zig-Zag Simulations**.....658
X. Gao and G. Deng
- Validation of a Roll Decay Test of an Offshore Installation Vessel using OpenFOAM**.....670
B. Devolder, F. Stempinski, A. Mol and P. Rauwoens

Ship Scale Performance

- Effects of Section Geometry on the Energy-saving Rate of PBCF and Model/full-scale Correlation - A CFD Study**682
H. Zhang, X.-Q. Dong, W. Li, Ch.-J. Yang and F. Noblesse
- Numerical Friction Lines for CFD Based Form Factor Determination Method**694
K.B. Korkmaz, S. Werner and R. Bensow
- Numerical Study of Roughness Model Effect at Actual Ship Scale**.....706
K. Ohashi
- Prediction of Ship Resistance with the use of Full-scale CFD Simulations**718
K. Niklas and H. Pruszko
- Ship Scale Validation of CFD Model of Self-propelled Ship**.....730
H. Mikkelsen, M. L. Steffensen, C. Ciortan and J. H. Walther

Structures and Materials

- Homogenized and Non-Classical Beam Theories in Ship Structural Design - Challenges and Opportunities**742
J. Romanoff, A. Karttunen, B. Reinaldo Goncalves and J.N. Reddy
- Structure Design of the Ship Pedestal based on Topology Optimization**754
C. Zhang, Z. Zeng and C. Ji

Wave Modelling

Efficient Time Domain Simulations of Waves.....771
O. Lundbäck

Simulation of Irregular Wave Motion using a Flap-type Wavemaker783
S. Ramezanzadeh, M. Ozbulut and M. Yildiz

Waves-Structure Interaction

A first Assessment of the Interdependency of Mesh Motion and Free Surface Models in OpenFOAM Regarding Wave-Structure Interaction795
G. Decorte, G. Lombaert and J. Monbaliu

Numerical and Experimental Investigation of Moored-Floating Structures in Regular Waves807
L.-C. Dempwolff, T. Martin, A. Kamath and H. Bihs

The ComMotion Project: Computational Methods for Moving and Deforming Objects in Extreme Waves820
A.E.P. Veldman, P. Van der Plas, H. Seubers, M. Hosseini Zahraei, X. Chang, P.R. Wellens and J. Helder

LECTURES

naoe-FOAM-SJTU SOLVER FOR SHIP FLOWS AND OCEAN ENGINEERING FLOWS

JIANHUA WANG AND DECHENG WAN*

State Key Laboratory of Ocean Engineering, School of Naval Architecture, Ocean and Civil Engineering, Collaborative Innovation Center for Advanced Ship and Deep-Sea Exploration, Shanghai Jiao Tong University, 200240 Shanghai, China

*Corresponding author: dcwan@sjtu.edu.cn

Key words: Ship hydrodynamics, ocean engineering, 6DoF motion, overset grid, naoe-FOAM-SJTU solver,

Abstract. Ship and ocean engineering flows is a very complex and highly non-linear problem. Traditional experimental methods and potential flow theory have limitations in predicting the complex flows. A CFD solver naoe-FOAM-SJTU is developed based on the open source platform OpenFOAM with the purpose of simulating various ship and ocean engineering flow problems. In the present paper, the self-developed modules, i.e., wave generation and absorption, 6 degrees of freedom (6DoF) motion, mooring system and overset grid are introduced to illustrate the development of the CFD solver. Furthermore, extensive applications to ship flows and ocean engineering flows using naoe-FOAM-SJTU solver are conducted and validated by available experimental data. It has been proved that the CFD solver naoe-FOAM-SJTU is suitable and reliable in predicting the complex viscous flows around ship and offshore structures. Future development of naoe-FOAM-SJTU solver will focus on further enhancement of accuracy and efficiency for CFD simulations of complex flows in ship and ocean engineering.

1 INTRODUCTION

Viscous flow around floating structures with free surface is one of the typical features in ship and ocean engineering. Understanding the hydrodynamic performance of ship and ocean structures can help people design safer and more productive ocean structures. With the development of scientific knowledge, many fundamental problems about the ship and ocean engineering flows have been solved. Among them, the resistance and stability of ships and platforms in calm water can be precisely predicted. However, dynamic features of real ship and ocean structures are complicated including violent sea environment, the large motion of floating structures, high Re turbulent flow, ship hull-propeller-rudder interaction, multi-scale flows, etc. In order to get better understanding of flow mechanism, researchers have focused on resolving complex viscous flow in ship and ocean engineering.

There are some typical features in ship flows and ocean engineering flows, such as multi-system interaction, nonlinear free surface, high Re turbulent flow, and so on. The potential flow and experimental test used to be the major approaches in the past researches. However, the computational fluid dynamic (CFD) approach has become a powerful tool to investigate

these complex flow problems with the development of high-performance computing (HPC). One of the advantages of CFD method is that it can obtain more detailed flow field information, which make it easier to analyze the in-depth mechanism. CFD simulation can overcome the difficulties of nonlinear phenomenon and multi-system interactions that can hardly be estimated by potential flow method. Furthermore, the cost of CFD computations is relatively lower compared with the expensive facilities of experiment. Therefore, more and more researchers apply CFD method to study the complex flow problems in the field of ship and ocean engineering.

Despite the powerful capability of CFD, it is still challenging to handle various complex viscous flows in ship and ocean engineering, such as violent free surface waves, complex motions with ship hull-propeller-rudder interaction, large amplitude platform motions with mooring lines, vortex-induced vibration (VIV) of marine risers, and so on. Therefore, it is very essential to develop a specific CFD solver to investigate the performance of ship flows and ocean engineering flows. In the present paper, emphasis is put on the development of the naoe-FOAM-SJTU solver for complex flows in ship and ocean engineering. The naoe-FOAM-SJTU solver, which is developed by the Computational Marine Hydrodynamics Lab (CMHL) in Shanghai Jiao Tong University (SJTU), can be used as a powerful tool to estimate the hydrodynamic performance of ship and offshore structures. It can also be utilized to obtain a better understanding of the complex ship flows and ocean engineering flows.

In this paper, main modules in naoe-FOAM-SJTU solver is firstly introduced, where the wave generation and absorption, 6DoF motion, mooring system, overset grid are described in detail. Then, typical applications for ship and ocean engineering flows using the developed modules are presented. Finally, a brief conclusion is drawn.

2 NAOE-FOAM-SJTU SOLVER

The present naoe-FOAM-SJTU^[1,2] solver is developed based on the open source platform OpenFOAM^[3]. Based on the supported features in OpenFOAM, the development for naoe-FOAM-SJTU solver is mainly through the implementation of specific modules. Figure 1 demonstrates the main framework of the present CFD solver naoe-FOAM-SJTU.

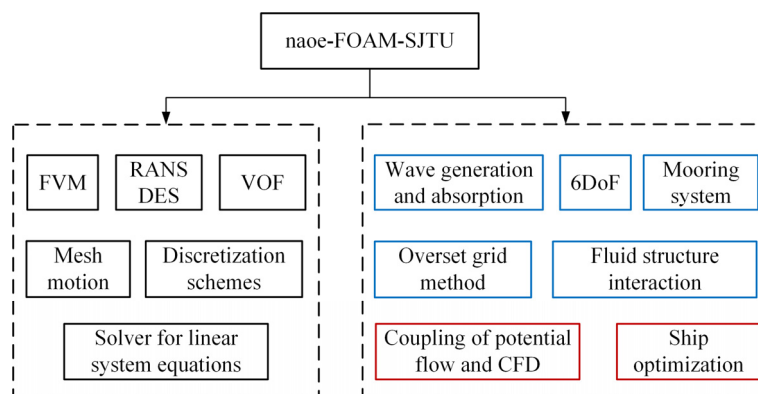


Figure 1: Main framework of naoe-FOAM-SJTU solver

The CFD solver is developed based on OpenFOAM and the built-in modules, such as finite volume method (FVM), discretization schemes, solver for linear system equations. Further

implementation of ship and ocean engineering modules in the solver is shown in the right column of Figure 1, where the blue marked modules are already developed and modules in red are the ongoing work at present. The basic modules in OpenFOAM has been explained in the OpenFOAM user guide, thus, only the specific modules are illustrated herein.

2.1 Wave generation and absorption

For ship and ocean engineering flows, wave environment is the most typical situation. Therefore, ocean wave generation should be done firstly for the development of a marine hydrodynamic CFD solver. So far, there have already been several modules developed based on OpenFOAM, such as waves2foam^[4], olaFlow^[5,6]. In the present solver, two wave generation approaches^[7-9] have been implemented, one is the modelling of a piston or flap type wavemaker, another one is the velocity-inlet boundary conditions (BC). A piston or flap type wavemaker is achieved by giving the prescribed wave profile to the movement of the wave boundary incorporated with the moving mesh technique in OpenFOAM. This procedure is usually used to generate regular waves, solitary waves, freak waves just like the wavemaker in an actual wave basin.

The inlet BC type wavemaker imposes both the velocity of water particles and the position of free surface at the incident wave boundary. Figure 2 illustrates the code structure of wave generation module based on inlet BC in naoe-FOAM-SJTU solver.

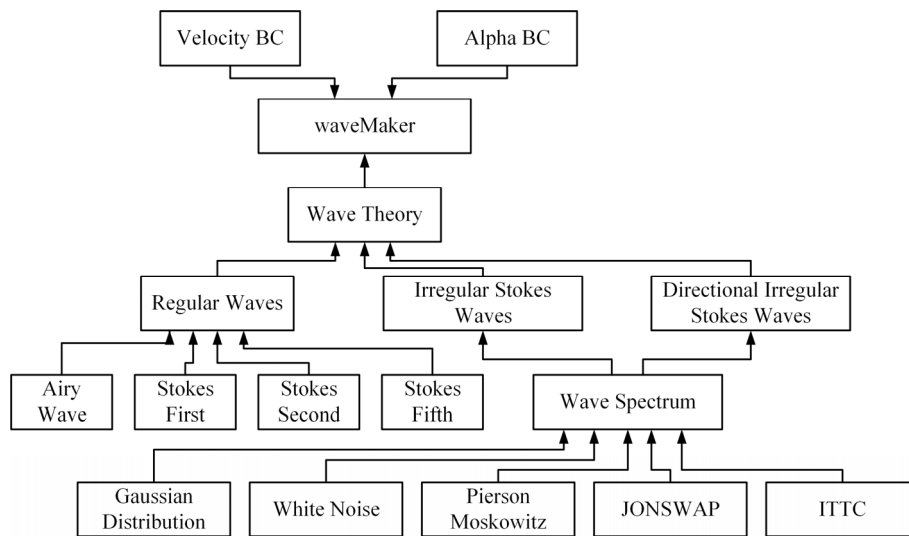


Figure 2: Code structure of wave generation module in naoe-FOAM-SJTU solver

The present wave generation module can generate both regular and irregular waves according to corresponding wave theories. Regular waves vary from the airy wave to the fifth-order Stokes waves. For the irregular waves, a wave spectrum based correction approach^[9] is used in the present wave generation module. The most frequently used spectrum, such as PM, JONSWAP, one/two parameter ITTC, are implemented to the present solver to extend the ability of generating various ocean waves. The present wave generation module has been applied to many benchmark cases and the results are validated by available experimental results^[10].

Wave absorption, also called wave damping is implemented in the solver using a sponge layer ahead the outlet boundary with a certain length. In the damping zone, the wave can be absorbed by adding a source term in momentum equation. The detailed implementation can be found in the reference^[7].

2.2 6DoF motion and overset grid module

To estimate the flow characters of floating structures in ship and ocean engineering, the motion behavior should be computed firstly. In naoe-FOAM-SJTU, a 6DoF motion solver based on Euler angle description is implemented. Two coordinate systems, i.e. earth-fixed coordinate system and ship-fixed coordinate system, are employed to calculate the rigid body motions. During the process of 6DoF computation, the forces and moments are first computed in the earth-fixed coordinate system. Then the predicted values are transformed into ship-fixed coordinate system for the calculation of accelerations. After that, the accelerations are integrated to obtain the ship velocities, which are then transformed back to earth-fixed coordinate system to get the ship displacement by integrating the velocities. Detailed implementation of 6DoF motion solver can be found in reference^[2].

The motion of ship hull and offshore platforms can be computed through the above process. However, when considering complex motions of ship hull-propeller-rudder system or floating offshore wind turbines, the 6DoF motion solver should be extended to have the ability of handling complex motion with a hierarchy of bodies. In naoe-FOAM-SJTU solver, a multi-level motion solver is implemented through the combination of dynamic overset grid technology. Figure 3 demonstrates the motion level of ship-propeller system.

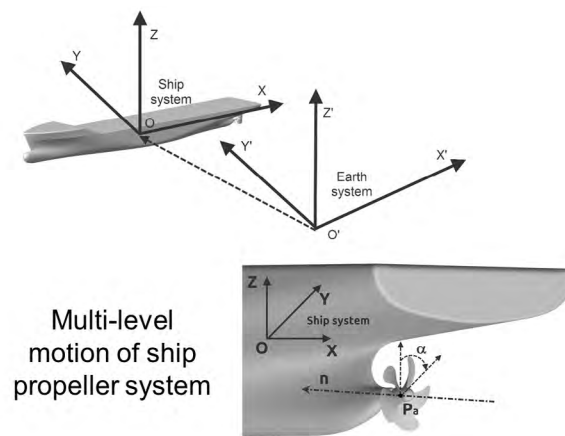


Figure 3: Multi-level motion solver for ship-propeller system

The strategies to compute the movements of propeller, rudder, turbine and other appendages depend on what problem to solve. For example, self-propulsion simulation employs a PI controller to update the rotation of propeller. The 6DoF motion module with a hierarchy of bodies can be used to simulate various complex conditions in ship and ocean engineering incorporating with the dynamic overset grid method.

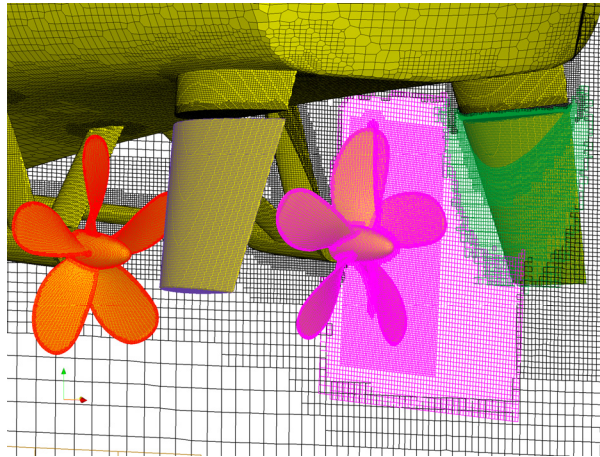


Figure 4: Overset grid arrangement around ship hull propeller and rudder

The dynamic overset grid module in naoe-FOAM-SJTU solver is implemented with the purpose of handling with large amplitude motion or multi-level motion. Figure 4 shows a typical overset grid arrangement around ship hull, propeller and rudder. The computational grids for each part have overlapping areas, in which the flow information is interpolated. In the present solver, the sugger++ program^[11] is utilized to compute the domain connectivity information.

2.3 Mooring system module

Mooring lines are widely used in ocean engineering to keep the stability of floating platforms in ocean waves. In order to resolve the ocean engineering flows, a mooring system module is required to predict the performance of offshore platforms. In naoe-FOAM-SJTU solver, a mooring system module is developed based on OpenFOAM and several types of mooring lines are implemented. The main framework of the mooring system module is shown in Figure 5.

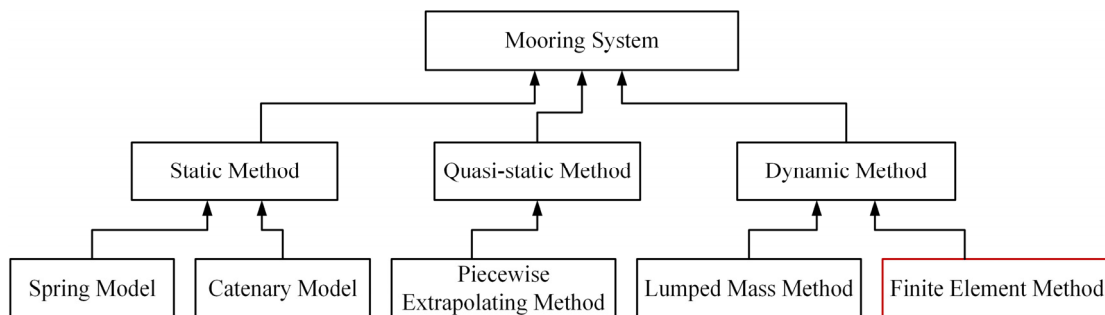


Figure 5: Main framework of mooring system module

The module is divided into three categories according to the equations, i.e. static method, quasi-static method and dynamic method. In static method, the spring model and catenary model are implemented. As for the quasi-static approach, a piecewise extrapolating method (PEM) is adopted to discretize the mooring line into several segments, where the equations of

static equilibrium for each segment is solved. In addition, the PEM approach can consider the different structural properties for mooring lines consist of different components. Both the static and quasi-static method ignore the effect of mooring line movement. Thus, a dynamic module including 3D lumped mass method (LMM) and finite element method (FEM) is also implemented. The restoring force of mooring lines computed by LMM and FEM approach is obtained by solving the dynamic equations of motion, where the inertial force related with mooring line motion can be considered. The present mooring system module has been applied to predict mooring forces of various floating structures in wave environments^[12-14].

Other developed modules as shown in Figure 1 have been described in the reference^[15], and they are not discussed here.

3 APPLICATIONS TO SHIP FLOWS AND OCEAN ENGINEERING FLOWS

3.1 Ship flows

Based on the developed modules for ship flows, the naoe-FOAM-SJTU solver has been applied to various conditions in ship engineering. Ship advancing in calm water is the most fundamental study in ship hydrodynamics and several benchmark computations have been carried out to validate the present CFD solver.

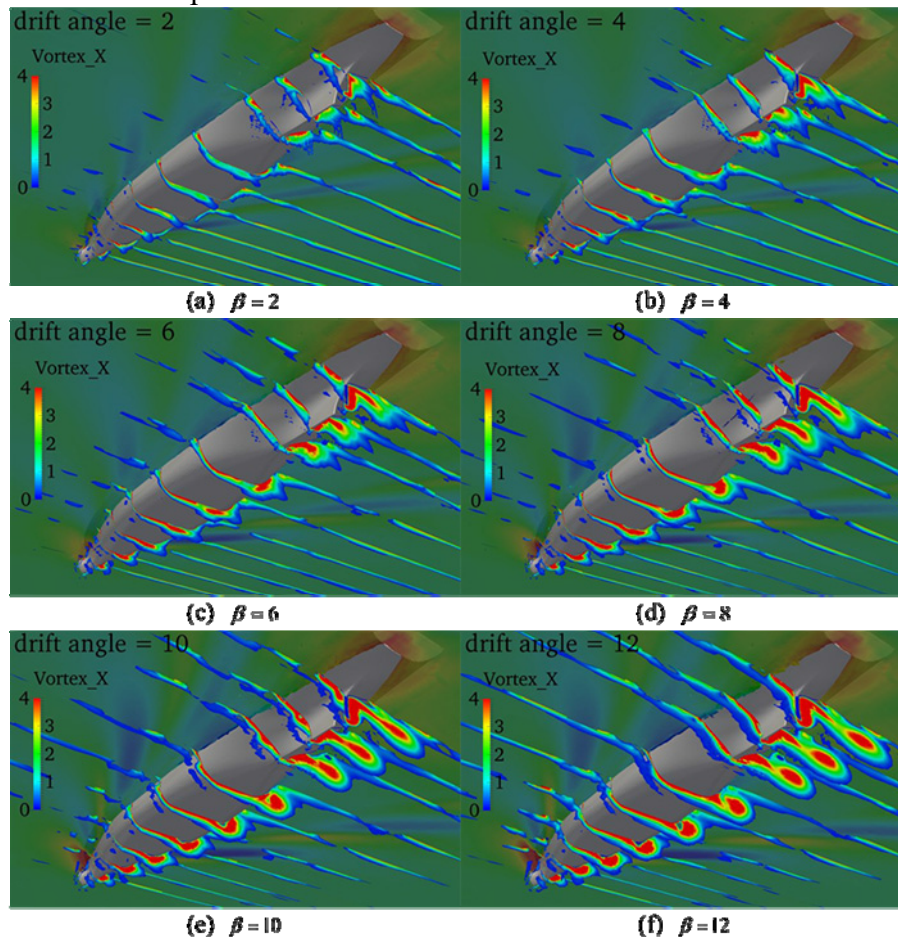


Figure 6: Vortices separated from ship hull with drift angles

Zha et al.^[16] conducted numerical predictions of ship resistance in calm water with emphasis on viscous wave-making resistance for 6 ship hulls. They also simulated high-speed catamaran in calm water^[17], where different ship speeds were considered. The numerical results agreed very well with the measurement data. Wave making and vortex field were well predicted and further analysis of the hydrodynamic performance was discussed. Wang et al.^[18] further investigated the hydrodynamic performance for a ship with different drift angles. The detailed vortices separated from the ship hull can be well resolved as shown in Figure 6. More recently, the CFD solver was applied to simulate breaking wave phenomena of high-speed surface ships^[19]. The grid density and turbulence model effect on the breaking bow waves were analyzed in detail.

Ship in waves, also called seakeeping, is another key performance of ship. Based on the developed wave generation and absorption module, various ocean waves can be generated. Incorporating with the 6DoF motion module, ship motions in waves can be estimated by the developed CFD solver. Shen et al.^[20] and Ye et al.^[21] conducted the numerical simulations of ship motion in head waves using RANS approach. Different wave steepness and wave lengths were considered in the simulations and the predicted wave added resistance was validated by the available experimental data. More recently, Liu et al.^[22] used naoe-FOAM-SJTU solver to predict more violent wave conditions for DTC ship model. The computations were carried out for the benchmark case, where the ship model was free to heave, pitch and roll, in oblique waves. Dynamic overset grid was adopted to handle with the large ship motions. Strong wave slamming and large ship motions can be observed as shown in Figure 7. In addition, mean drift forces and moments on the ship hull can be well predicted compared with the available experimental data.

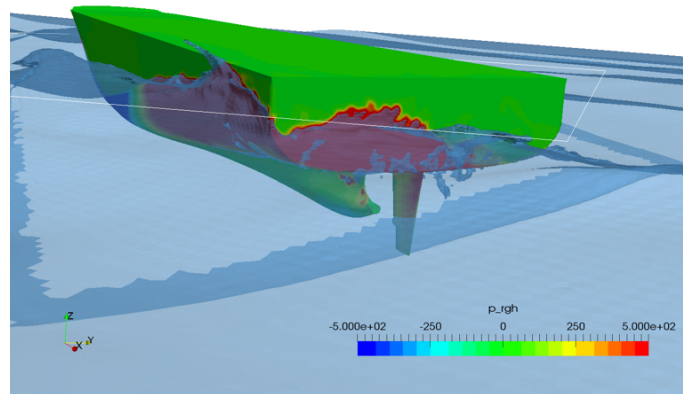


Figure 7: Slamming on ship hull in rough sea states

Despite the simulations of ship flows with bare hull model, free running ship with complex ship hull-propeller-rudder interaction has also been investigated based on the developed overset grid module associated with full 6DoF motion with a hierarchy of bodies. Shen et al.^[2] performed numerical computations of ship self-propulsion and zigzag maneuver of KCS ship in calm water, and the predicted self-propulsion parameters as well as maneuvering parameters were validated by the available experimental results. Wang et al.^[23] carried out the self-propulsion simulation of a twin-screw fully appended ship model and extends to the

simulation of turning circle maneuver. Wang et al.^[24,25] further extended the present naoe-FOAM-SJTU solver to simulate ship maneuvering in waves (shown in Figure 8) and the numerical results showed that the solver is suitable and reliable in predicting the performance of ship maneuvering in waves.

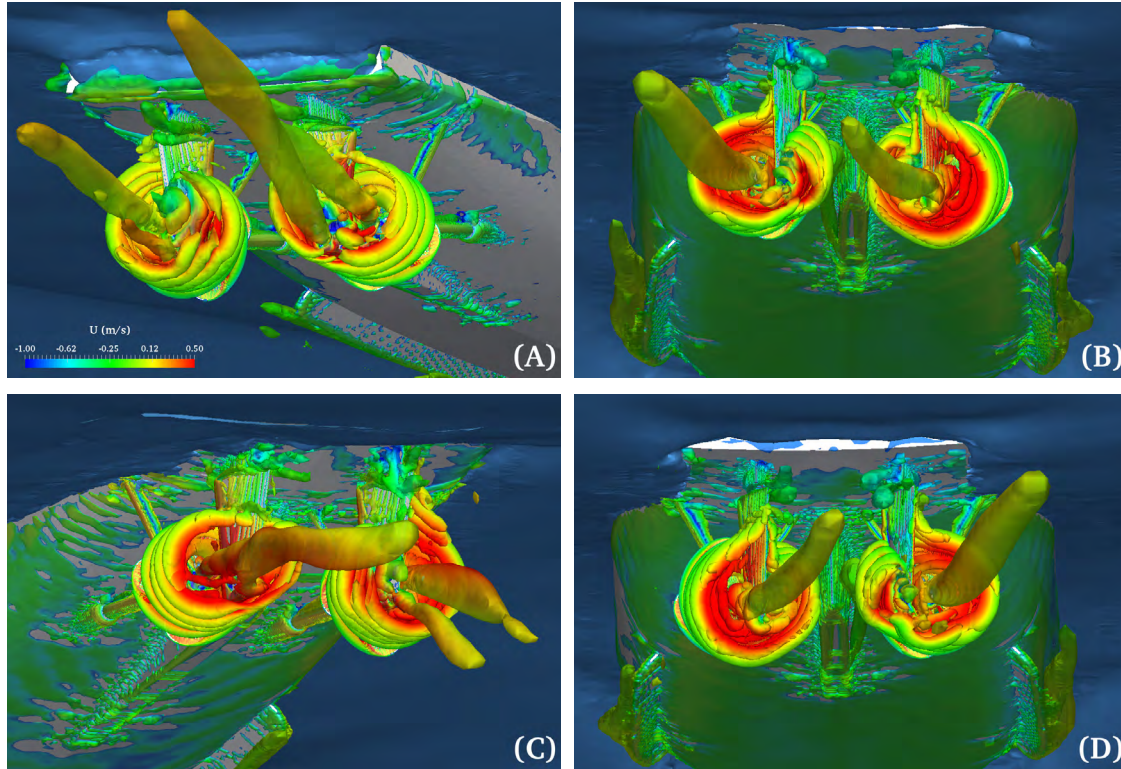


Figure 8: Iso-surfaces of $Q=100$ colored with axial velocity for the zigzag maneuver in waves

Apart from the investigations of ship advancing in calm water, seakeeping, propulsion and maneuvering, naoe-FOAM-SJTU solver has also been applied to estimate the performance of energy save device (ESD), cavitation, multi-ship interactions, and so on. With the upgrade of the present solver, more and more complex ship flows can be numerically studied.

3.2 Ocean engineering flows

Ocean engineering flows includes various engineering problems for offshore platforms both fixed and floating. The developed naoe-FOAM-SJTU solver has also been applied to the simulation of various ocean engineering flows. Based on the wave generation and absorption module, wave-structure interaction can be simulated. For fixed structures, wave run-up is very important for the safe deck design. Cao and Wan^[10] presented benchmark simulations of wave run-up on single cylinder and four cylinders using the current solver as shown in Figure 9. Different wave periods and wave heights were studied and wave run-up heights around the cylinders were recorded with virtual wave probes and compared with experimental data. They concluded that naoe-FOAM-SJTU is capable of dealing with wave run-up problems with good accuracy. Incorporating with the 6DoF motion module, naoe-FOAM-SJTU solver can

predict wave-induced motions of floating platforms. Liu and Wan^[12] conducted numerical investigations of the motion response of a triple-hulled offshore observation platform with different incident waves. Time histories of motions and loads under different wave conditions were compared and analyzed.

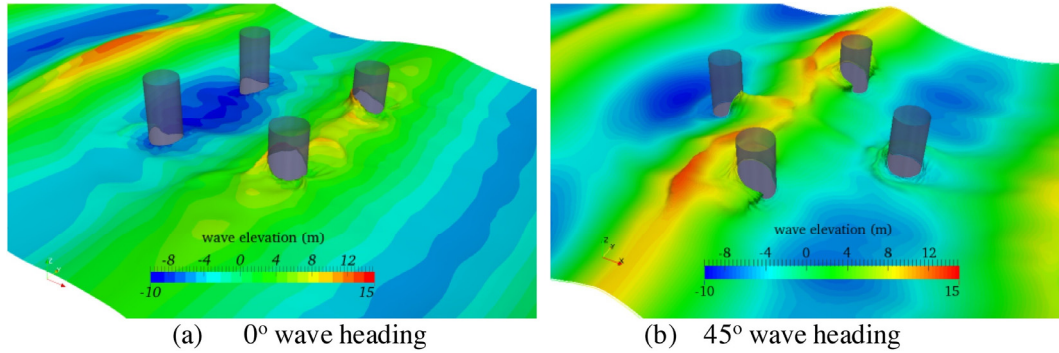


Figure 9: Wave run-up simulation of multi-cylinders

Based on mooring system module, coupled analysis of floating platform and mooring lines can be performed. Wang and Wan^[26] carried out coupled analysis of a floating pier and its mooring system in regular waves. The multicomponent mooring lines were modelled by dynamic analysis Lumped Mass method (LMM). Motion response were compared with that obtained by the static analysis method. The results showed that dynamic analysis is necessary for coupling analysis between floating platform and mooring lines.

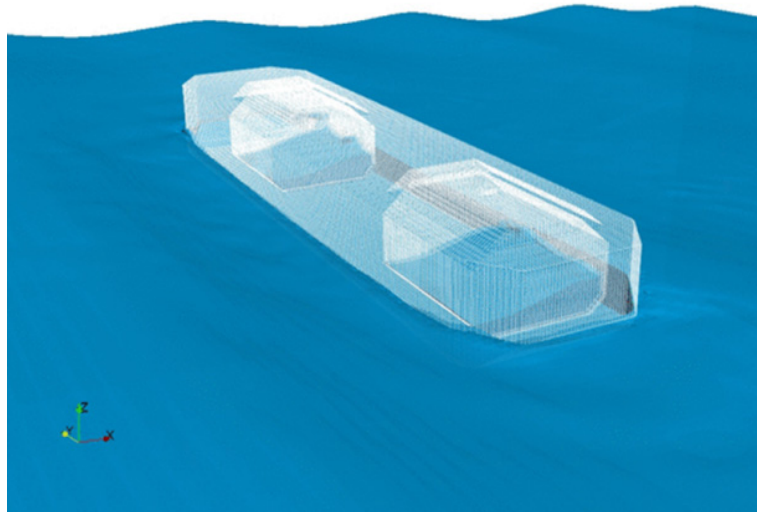


Figure 10: Instantaneous wave profile of FPSO with sloshing tanks

Zhuang and Wan^[27] studied the motion response of a single-mooring FPSO using overset grid and mooring system module. The predicted natural periods for heave decay test were in good agreement with experiment. Motions and mooring forces were further analyzed. Xia and Wan^[28] investigated the wave evolution and hydrodynamic characteristics of a floating

platform in shallow water with submerged terrain near island. The Response Amplitude Operators (RAOs) of the platform in regular waves were in good agreement with experimental data. Further wave evolution and breaking process over the submerged terrain were also depicted and analyzed. The naoe-FOAM-SJTU solver can also perform coupled analysis of motion response of an FPSO with sloshing LNG tanks in waves. Zhuang and Wan^[13] performed such simulations in which the external wave flow and internal tank sloshing were solved simultaneously. Figure 10 presents the complex flows inside the tank and the wave profile around the FPSO.

The present solver has also been applied to simulate the vortex-induced motions (VIM) of submersible platforms and Spar type platforms under sea currents. By using the mooring system module, 6DoF motion module and the high Re turbulence model, the complex viscous flows around floating platforms can be solved. The Detached-Eddy Simulation (DES) can predict massively separated flow at relatively low cost and was adopted by naoe-FOAM-SJTU to predict VIM. Zhao et al.^[14] simulated the VIM of a paired-column semi-submersible by using the naoe-FOAM-SJTU solver. The “lock-in” phenomena were captured. Synchronization vortex shedding patterns between upstream columns are observed in the “lock-in” range. The transverse motion response and zero crossing period are in good agreement with experiment. Figure 11 illustrates the 3D vortical structures of the semi-submersible platform under sea currents.

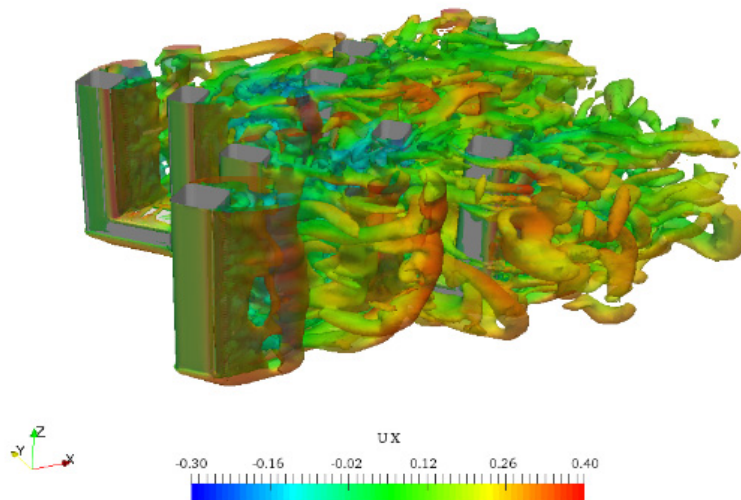


Figure 11: Vortical structure around semi-submersible platform

Other typical ocean engineering flows, such as vortex-induced vibration (VIV) of marine risers, multi floating body interactions, can also be simulated using naoe-FOAM-SJTU. Due to the length limitation, they are not presented here.

4 CONCLUSIONS

In the present paper, the development of main modules in naoe-FOAM-SJTU solver including wave generation and absorption, mooring system, 6DoF motion and overset grid are introduced in detail. The developed modules are used to simulate complex ship flows and ocean engineering flows. Then, extensive applications are discussed focusing on complex flows in ship and ocean engineering. It is concluded that with the development of specified modules in OpenFOAM, the present naoe-FOAM-SJTU solver can well resolve the complex ship and ocean engineering flows.

Future development of naoe-FOAM-SJTU solver will focus on two parts, one is the improvement of existing modules and another one is the adding more modules for ship and ocean engineering flows. Efficiency and accuracy will be the two key issues for the improvement of the present modules. More modules, including coupling strategy between potential flow and viscous flow, ship optimization design, are considered to extend the ability of naoe-FOAM-SJTU in engineering applications.

ACKNOWLEDGEMENTS

This work is supported by the National Natural Science Foundation of China (51879159, 51490675, 11432009, 51579145), Chang Jiang Scholars Program (T2014099), Shanghai Excellent Academic Leaders Program (17XD1402300), Program for Professor of Special Appointment (Eastern Scholar) at Shanghai Institutions of Higher Learning (2013022), Innovative Special Project of Numerical Tank of Ministry of Industry and Information Technology of China (2016-23/09) and Lloyd's Register Foundation for doctoral student, to which the authors are most grateful.

REFERENCES

- [1] Shen, Z., Cao, H., Ye, H., Wan, D.C. *The manual of CFD solver for ship and ocean engineering flows: naoe-FOAM-SJTU*, Shanghai Jiao Tong University, (2012).
- [2] Shen, Z., Wan, D.C., Carrica, P.M. Dynamic overset grids in OpenFOAM with application to KCS self-propulsion and maneuvering. *Ocean Eng.* **108**:287–306, (2015),.
- [3] Jasak, H. OpenFOAM: Open source CFD in research and industry. *Int. J. Nav. Archit. Ocean Eng.*, **1**:89–94, (2009).
- [4] Jacobsen, N.G., Fuhrman, D.R., Fredsøe, J. A wave generation toolbox for the open-source CFD library: OpenFoam®. *Int. J. Numer. Methods Fluids*, **70**:1073–1088, (2012).
- [5] Higuera, P., Lara, J.L., Losada, I.J. Realistic wave generation and active wave absorption for Navier–Stokes models: Application to OpenFOAM®. *Coast. Eng.* **71**:102–118, (2013).
- [6] Higuera, P., Lara, J.L., Losada, I.J. Simulating coastal engineering processes with OpenFOAM®. *Coast. Eng.* **71**:119–134, (2013).
- [7] Cao, H., Wan, D.C. Development of Multidirectional Nonlinear Numerical Wave Tank by naoe-FOAM-SJTU Solver. *Int. J. Ocean Syst. Eng.* **4**:52–59, (2014).
- [8] Cao, H., Wan, D. C. RANS-VOF solver for solitary wave run-up on a circular cylinder. *China Ocean Eng.* **29**:183–196, (2015).

- [9] Shen, Z., Wan, D.C. An irregular wave generating approach based on naoe-FOAM-SJTU solver. *China Ocean Eng.* **30**:177–192, (2016).
- [10] Cao, H., Wan, D.C. Benchmark computations of wave run-up on single cylinder and four cylinders by naoe-FOAM-SJTU solver. *Appl. Ocean Res.* **65**:327–337, (2017).
- [11] Noack, R.W., Boger, D.A., Kunz, R.F., Carrica, P.M. Suggar++: An improved general overset grid assembly capability. In Proceedings of the Proceedings of the 19th AIAA Computational Fluid Dynamics Conference, San Antonio TX, pp. 22–25, (2009).
- [12] Liu, Y., Wan, D.C. Numerical simulation of motion response of an offshore observation platform in waves. *J. Mar. Sci. Appl.* **12**:89–97, (2013).
- [13] Zhuang, Y., Wan, D.C. Numerical Study on Ship Motion Fully Coupled with LNG Tank Sloshing in CFD Method. *Int. J. Comput. Methods*, 1840022, (2017).
- [14] Zhao, W., Zou, L., Wan, D.C., Hu, Z. Numerical investigation of vortex-induced motions of a paired-column semi-submersible in currents. *Ocean Eng.* **164**:272–283, (2018).
- [15] Wang, J., Zhao, W., Wan, D.C. Development of naoe-FOAM-SJTU solver based on OpenFOAM for marine hydrodynamics. *J. Hydrodyn.* **31**:1–20, (2019).
- [16] Zha, R., Ye, H., Shen, Z., Wan, D.C. Numerical study of viscous wave-making resistance of ship navigation in still water. *J. Mar. Sci. Appl.*, **13**:158–166, (2014).
- [17] Zha, R., Ye, H., Shen, Z., Wan, D.C. Numerical computations of resistance of high speed catamaran in calm water. *J. Hydrodyn.*, **26**:930–938, (2015).
- [18] Wang, J., Liu, X., Wan, D.C. Numerical Simulation of an Oblique Towed Ship by naoe-FOAM-SJTU Solver. In Proceedings of the 25th International Offshore and Polar Engineering Conference, Big Island, Hawaii, USA, (2015).
- [19] Wang, J., Ren, Z., Wan, D.C. RANS and DDES Computations of High Speed KRISO Container Ship. In Proceedings of the 32nd Symposium on Naval Hydrodynamics, Hamburg, Germany, (2018).
- [20] Shen, Z., Wan, D.C. RANS computations of added resistance and motions of a ship in head waves. *Int. J. Offshore Polar Eng.*, **23**:264–271, (2013).
- [21] Ye, H., Shen, Z., Wan, D.C. Numerical prediction of added resistance and vertical ship motions in regular head waves. *J. Mar. Sci. Appl.*, **11**:410–416, (2012).
- [22] Liu, C., Wang, J., Wan, D.C. CFD Computation of Wave Forces and Motions of DTC Ship in Oblique Waves. *Int. J. Offshore Polar Eng.* **28**: 154–163, (2018).
- [23] Wang, J., Zhao, W., Wan, D.C. Free Maneuvering Simulation of ONR Tumblehome Using Overset Grid Method in naoe-FOAM-SJTU Solver. In Proceedings of the 31th Symposium on Naval Hydrodynamics, Monterey, USA, (2016).
- [24] Wang, J., Zou, L., Wan, D.C. CFD simulations of free running ship under course keeping control. *Ocean Eng.*, **141**:450–464, (2017).
- [25] Wang, J., Zou, L., Wan, D.C. Numerical simulations of zigzag maneuver of free running ship in waves by RANS-Overset grid method. *Ocean Eng.*, **162**:55–79, (2018).
- [26] Wang, J., Wan, D.C. Dynamic coupling analysis of the mooring system and floating pier in the South China Sea. *Chin. J. Hydrodyn.*, **30**:180–186, (2015).
- [27] Zhuang, Y., Wan, D.C. Numerical study of single point mooring system FPSO based on overset grids. *J. Jiangsu Univ. Sci. Technol. Nat. Sci. Ed.*, **31**:574–578, (2017).
- [28] Xia, K., Wan, D.C. Numerical investigation of motion response of floating platform near submerged terrain. *The Ocean Eng.*, **36**:10–17, (2018).

OPEN WATER CHARACTERISTICS OF THREE MODEL SCALE FLEXIBLE PROPELLERS

Luca Savio ^{*†} and Kouros Koushan^{*†}

^{*} Department of Ship and Ocean Structures
SINTEF Ocean
Trondheim, Norway
e-mail: Luca.Savio@sintef.no , web page: <https://www.sintef.no/ocean/>

[†] Department of Marine Technology
Norges teknisk-naturvitenskapelige universitet (NTNU)
Trondheim, Norway
e-mail: kontakt@marin.ntnu.no - Web page: <https://www.ntnu.edu/imt>

Key words: Experimental Hydrodynamics, Marine Propellers, Static Hydroelasticity

Abstract. In this paper the experimental setup, the data analysis procedure and some results of a series of tests on 3 propeller blade designs that aimed to provide validation data for static hydroelastic computations are discussed. The propellers were produced both in a rigid and in a flexible variant so that the effect of elasticity of the material could be studied.

1 INTRODUCTION

The hydroelastic behavior of propellers has been a recurring topic in ship propulsion; seen at time as a possible cause for failures of propulsive systems and some other times as an opportunity for improving the performances of propellers as a noise and vibration sources, it often suffered from a lack of experimental material to validate design and analysis codes. There are, as a matter of facts, very stringent limitations on what can be done in experiments on propeller models in hydrodynamic facilities. These limitations arise both from the scaling laws the experiments abide to and from the difficulties in producing flexible, with controlled mechanical properties, propeller blades. However, the progresses in computer simulations of fluids and structures allow for another strategy to be sought. In fact, it is possible to use the numerical simulations as a link between the model scale experiments, where the test conditions can be accurately controlled, and the full scale products, which is where hydroelasticity ultimately matters. The strategy, that is often used in hydrodynamics, is to validate the codes in model scale, in this way ensuring that can be used to simulate full scale phenomena.

In this paper we present the results from a series of tests carried out on three homogeneous and isotropic flexible propeller blade sets. The three propellers are variations of the same geometry, where the original blade skew distribution was altered. The blades were produced both in

aluminum and in a epoxy-like resin, through the technique of resin casting. The aluminum blades served to make the form for the resin blades, and as a reference as rigid blades since their elasticity can be neglected in model scale. The tests were carried out in SINTEF Ocean's large towing tank in open water condition, i.e the inflow to the propeller was uniformly distributed. The tests were performed at different propeller rotational speeds and at different pitch settings. In order to establish a reference condition for the flexible propellers, all the tested conditions were also run with the rigid blades; in this way, it was possible to quantify the significance of the different Reynolds number at which the blades were tested. It is worth pointing out that the terms rigid and flexible are used here to refer to the blades made of aluminum and resin respectively; in fact, even-though also the aluminum blades are strictly speaking flexible, their stiffness in model scale makes any deformations under the effect of hydrodynamic loads too small to be observable; on the contrary, the resin blades clearly show deformation when loaded that can be measured by the laboratory equipment.

Care was taken not to excite any resonance in the blades. Furthermore, since the inflow was homogeneous, the response of the blades was static. Because of the lack of any dynamics, the tests presented here fall under the category of static hydroelasticity.

1.1 Symbols used in the paper

The following non dimensional numbers will be used in the paper.

$$J = \frac{V}{nD} \quad (1)$$

$$K_T = \frac{T}{\rho n^2 D^4} \quad (2)$$

$$K_Q = \frac{Q}{\rho n^2 D^5} \quad (3)$$

$$\eta_O = \frac{J}{2\pi} \frac{K_T}{K_Q} \quad (4)$$

where J is the advance number, K_T the thrust coefficient, K_Q the torque coefficient and η_O the propeller efficient. Further, V [m/s] is the advance speed, n [rps] is the rotational speed or shaft speed, D [m] is the diameter and P [m] the pitch of the propeller; T [N] is the thrust delivered by the propeller and Q [Nm] the torque absorbed by the propeller. The suffixes A and R indicate the data relative to the aluminum and resin propeller respectively.

2 GEOMETRY DEFINITION AND MODEL PRODUCTION

When referring to hydro-elasticity of propellers it is common to think of the so called bend-twist coupling of composite blades. Bend twist-coupling is phenomenon by which a structure that is bent in spanwise direction shows also some twist of the sections perpendicular to the direction of bending. In marine propellers, one typical application of bend-twist coupling is to create a blade structure that reduces the pitch by structural response when subjected to a load increase. The most common way of obtaining such a de-pitching effect under increased load is to use composites materials with an ad-hoc ply orientation sequence. However, bend-twist coupling

exists also for isotropic and homogeneous lifting surfaces when the center of pressure is away from the elastic axis of the structure. In principle it is possible to control bend-twist coupling of isotropic blades by changing the relative location of the blade elastic axis and the center of pressure, for example by acting on the skew distribution. However, it has to be remarked that the blade skew distribution is determined by considerations regarding cavitation and hence it is very unlikely that the skew distribution can be used for controlling the hydroelastic behavior of marine propellers. Nevertheless, for research purposes, using the skew distribution is a straightforward strategy to generate blades that have a different elastic behavior starting from the same parent geometry. The propeller geometries that will be presented in the next paragraph were designed within the framework of the project PROPSALE for studying numerically the effects of Reynolds number on the open water curves of marine propellers. The three geometries are identical a part from the skew distribution; for this reason they were perfect candidates for the purpose of generating flexible model scale propellers that show different hydroelastic behaviors.

2.1 Geometrical definition of the propellers

The parent propeller geometry from which the other geometries were derived is P1374 whose geometry is public and a large amount of numerical and experimental data is available. Propeller P1374 was designed by SINTEF Ocean using the design code AKPD/AKPA as a propeller to be used for research purposes; it was, therefore, straightforward to generate variations of the original geometry.

Propeller P1374 has a total skew of 23 degrees distributed in a balanced way. The first variation, P1565, was obtained by removing the skew completely and the second, P1566, by abandoning the balanced skew design for an almost linear distribution. The skew distribution of the 3 geometries is shown in Figure 1; the skew is given in mm, according to the geometry definitions used by AKPD/AKPA.

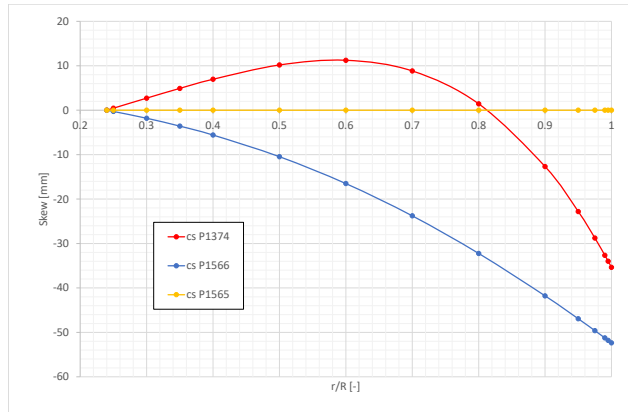


Figure 1: Comparison of the skew distribution for the 3 geometries

The silhouette of the blades depicted in Figure 2 offers a visual impression of the differences between the three designs.

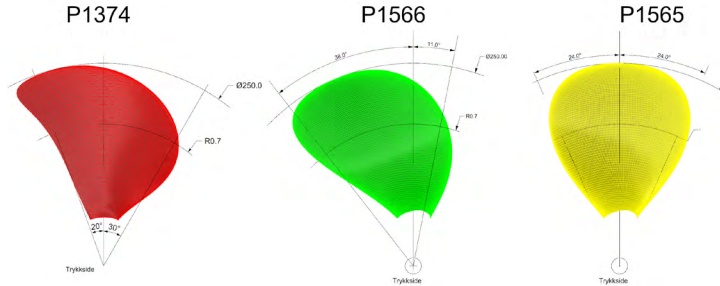


Figure 2: Silhouette of the blades of propellers P1374, P1565 and P1566

2.2 Production method for the flexible propellers

The propeller blades that are used in model testing are often produced in a metallic material, such as aluminum or bronze, with the latter being the most common, in order to limit the deformations during testing. It is not often that the blades need to show a measurable deformation in model scale, and hence there is no standard practice on how to produce them. Several techniques may be employed, as for example, 3D printing, milling and resin casting. After some considerations on the advantages and disadvantages of the different options, it was chosen to use the resin casting technique

At first glance 3D printing may appear the most appealing technique because it is fast and relatively inexpensive. Almost any geometry, even hollow geometries, can be produced with no added complexity to the production process. However, the homogeneity and isotropy of the material properties of the printed object are a matter of discussion in the scientific community, and have not been addressed until recently when 3D printing was no longer only adopted in prototyping but also in production. Test performed in the HyDynPro project showed that, at least for the printer that was used in that case, the printing material was rather homogeneous, unless the printing process completely failed. Nevertheless, given the lack of certainty on whether the material could be considered isotropic or not, it was decided to abandon this option.

Propeller models may also be milled out of a block of raw material that has the desired mechanical properties, ensuring that the material is homogeneous and isotropic. The list of

materials that can be used is much larger than that can be used with any of the other proposed techniques. Milling, in addition, is the process that is used for metal propellers and hence it may be foreseen that most of the same production technique can be utilized. However, some aspects have to be pointed out; first, milling plastic materials is rather different from milling metal, it requires experience and some rethinking of the manufacturing process; second, the production process through milling requires some manual work since some parts cannot be reached by the cutting tool, the result of hand work on plastic may be rather different from the one obtained with on the metal propeller. Since milling turned out to be not as straightforward as it may have looked at first glance, it was abandoned.

Resin casting was the last technology to be evaluated, but was in the end selected because, at least in this specific case, it is rather cheap and has reasonably short production times. The resin casting process starts with the production of a plastic mold, made of silicon, that is obtained from a template; the mold is, therefore, a negative copy of the template which is therefrom called a positive. In the silicon mold it is then cast a specific resin that is left to cure in a vacuum chamber, where the temperature is kept constant. There are two main restriction to resin casting: the selection of materials and the need of a positive template. As far as the selection of materials is concerned, the range of mechanical properties that the different resins offer is not very wide; in fact, most of the casting materials have a Young's modulus in the range 2-4 GPa. The need of the positive template may be a drawback if only the flexible object is needed; luckily, for this project also the metallic propeller was needed and hence no extra cost was incurred to make the positive template. In case just the flexible propeller blades are needed, the cost of making the positive metallic template would be significantly higher than the cost of the flexible blades.

The resin blades were manufactured by a company that specializes in rapid prototyping, PROTOTAL A.S, using a casting resin type 8051 produced by MCP HEK Tooling GmbH. The main mechanical properties of the material are reported in Table 1 . The reported data are taken from the data sheet, i.e. no independent test was carried out to confirm them. The Poisson's ratio is not specified by the producer, but given the nature of the material, can be assumed to be 0.33.

Table 1: Main mechanical parameters of the adopted resin

| | | |
|-------------------------|------|--------------------|
| Tensile E-Modulus | 2150 | MPa |
| Tensile Strength | 55.9 | MPa |
| Flexural E-Modulus | 1965 | MPa |
| Flexural Strength | 85.9 | MPa |
| Specific Gravity Part A | 1120 | kg/dm ³ |
| Specific Gravity Part B | 1190 | kg/dm ³ |

3 SETUP AND EXECUTUTION OF THE TESTS

3.1 Test setup

The tests were carried out using the standard test setup used for open propellers in the towing tank. In the standard setup the propeller is placed in front of the dynamometer that is mounted to the towing carriage. The forward motion of the propeller is that of the towing carriage, while the rotational speed is set by an electric motor that drives the propeller shaft. For any given combination of propeller speed and carriage speed the thrust generated and the torque adsorbed by the propeller are measured. The propeller is mounted on the dynamometer as Figure 3 shows; it is important to note that only the forces generated on the left side of the 1mm gap visible in the figure are measured by the dynamometer.

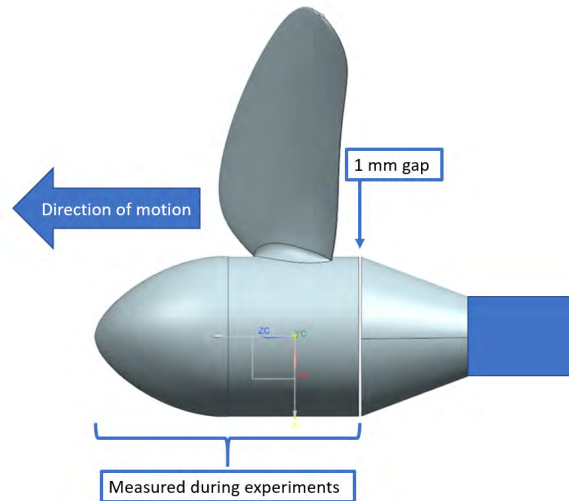


Figure 3: Propeller setup on the dynamometer

Traditionally, when the tests are carried in the configuration described in this paragraph, a test at various advance and rotational speeds with a dummy hub (instead of the propeller) and the propeller cap is carried out to measure the resistance of the hub and cap. The measured resistance is then subtracted from the measurement carried out with the propeller to constitute what is traditionally reported as the propeller open water. Also in this case the correction test was carried out and the data are available both with and without the correction. The uncorrected data should be used anytime it is possible to integrate the force on the entire surface the is on left side of the 1mm gap; this is always the case for CFD codes, for example, and therefrom the double presentation of the data.

3.2 Test conditions and execution

The same set of tests were carried out on all propellers, rigid and flexible, and comprised variations in pitch setting (P/D), rotational speed and advance coefficient. In addition to the design pitch ratio (1.1) a reduced pitch (0.9) and an increased pitch (1.2) were tested. The

propellers were tested at the rotational speeds 7, 9 and 11. The advance coefficient was varied in steps that were defined based on the pitch settings as Table 2 lists.

Table 2: Advance coefficients as a function of the pitch setting

| P/D 0.9 | P/D 1.1 | P/D 1.2 |
|---------|------------|---------|
| 0.15 | 0.2 | 0.225 |
| 0.3 | 0.4 | 0.45 |
| 0.45 | 0.6 | 0.675 |
| 0.6 | 0.8 | 0.9 |
| 0.75 | 1 | 1.125 |
| 0.9 | 1.2 | 1.35 |
| 1.05 | | |

In total 905 measurements were performed during the experimental campaign. In order to limit viscoelastic effects in the material, the test conditions were chosen so that the material would not be loaded more than 1/3 on its tensile strength limit. Finite element computation were carried out to check the stress levels in the material.

The tests were conducted in the following way. First, the propeller revolutions (rps) were adjusted to the desired value while the carriage was standing still. Then, the carriage speed was varied in steps until the maximum J value for the given condition was reached. The recording time between the steps was 10 seconds.

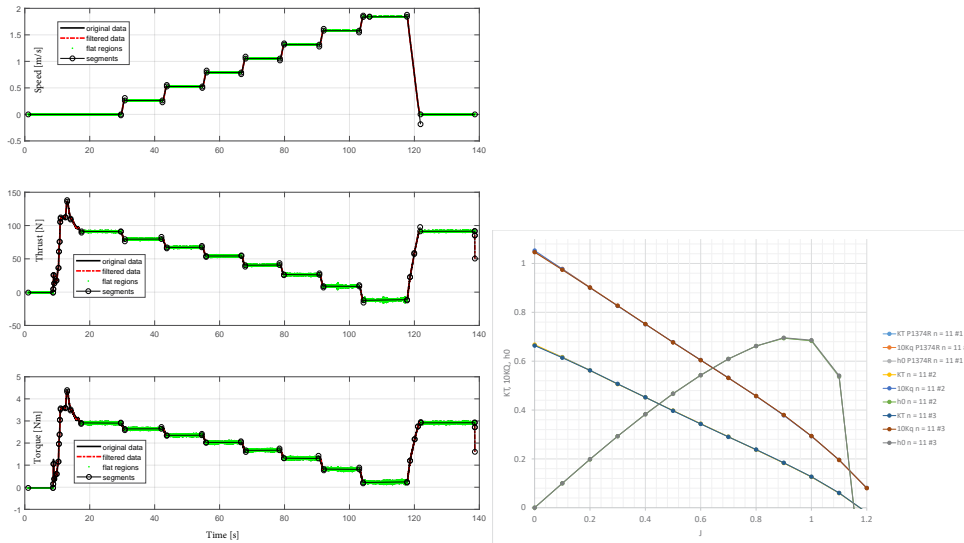


Figure 4: Example of a time series from the tests (left) and of the results from repeated runs (right)

Figure 4 left shows a typical test where the carriage speed was stepped through the different

advance coefficients from zero speed (bollard pull) to the maximum speed, that coincided to negative propeller thrust. The figure shows as green segments the parts of the signals that have been identified as stable and flat regions of the signal over which the average values are computed. A region of signal is considered to be stable and flat if it can be approximated as a segment that has the absolute value of the slope (rate of variation) lower than a given threshold. The threshold for the slope of the carriage speed was set to $0.01m/s$, for thrust to $0.1N/s$ and to $0.01Nm/s$ for torque. Compared to the values that are normally accepted, the threshold for thrust was higher than usual. The higher value for the threshold of propeller thrust may indicate that some visco-elastic creep in the material was present. In order to check whether the blades underwent significant visco-elastic deformations, at the end of every run a bollard pull run is recorded to be compared to the one at the beginning of the run. With reference again to Figure 4 left, it can be seen that the propeller thrust and torque at the end of the run match those at the beginning of the run. In addition, for the flexible blades, the each condition was repeated three times. In Figure 4 right, the three repetitions for the same propeller are shown on the same graph; the high repeatability of the tests, witnessed by the fact that the curves are indistinguishable, is a good indication that the blades were not temporarily nor permanently deformed.

4 DATA ANALYSIS AND EXPERIMENTAL UNCERTAINTY

4.1 Data Analysis

From the data recorded during the experiments, the average values over the flat regions were extracted as shown in Figure 4. When more than one run was available for the same propeller configuration and J value, which we will call from now on a condition, the average of the average values was computed. Once a single value per condition was obtained, the values were interpolated by fifth order polynomials. An example of the data fitting is shown in Figure 5 where the dots are the measured data and the lines the fitted polynomials.

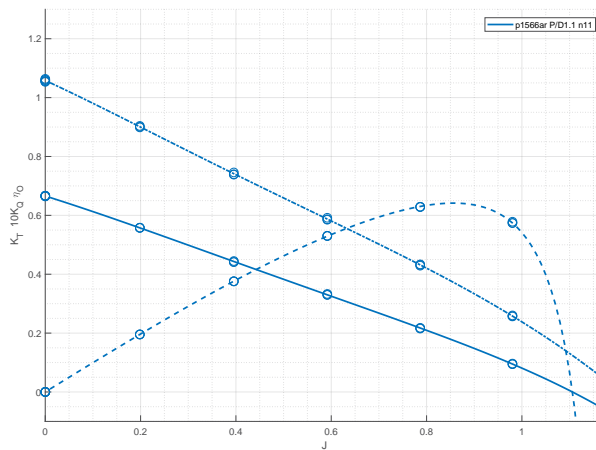


Figure 5: Curve fitting to the data

4.2 Evaluation of experimental uncertainty

The uncertainty of the experiments has been evaluated according to the type B evaluation as described by the GUM [1] standard. In the evaluation the sources of uncertainty that were considered are relative both to the measurement chain and to the propeller geometrical conformity. The relative experimental uncertainty has been found to be in the order of magnitude of 3% and increasing for high J values.

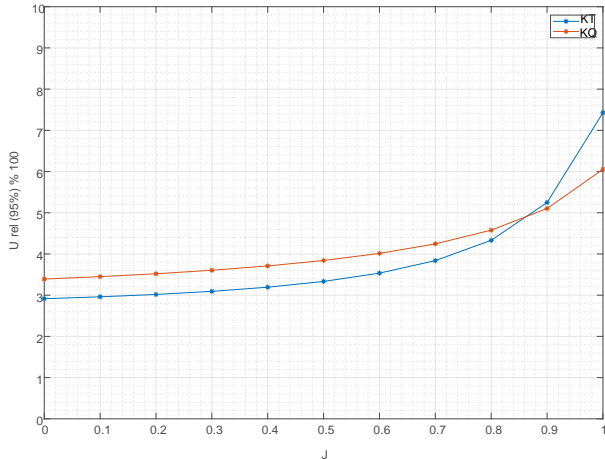


Figure 6: Relative uncertainty for $n=7$ rps

Figure 6 reports a typical relative uncertainty plot for $n = 7$ rps; this rotational speed is considered the worst case scenario as the measured forces are the lowest of the three speeds tested.

5 DATA PRESENTATION

It is not possible to present here all the data that were collected in the tests, but they can be made available upon request, both as raw measured data or as interpolating polynomials. In both cases the data are presented both with and without correction for the hub and cap resistance.

Several of expected features that have been observed in the data will be briefly described here in order to show how rich is the data set in terms of validation material.

The tests were performed for each propeller at different rotational speed also for the metallic version. It is expected that the efficiency of the propeller increases with the increasing Reynolds number; this well-known Reynolds effect can be seen in Figure 7 for one of the metallic propellers.

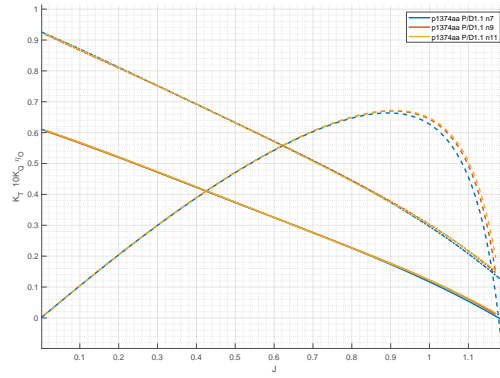


Figure 7: Reynolds effect of the open water curves

The effect of the different skew distributions of the three propeller designs can be seen in Figure 8 where the open-water curves of the three aluminium propellers are compared at the same pitch and shaft speed.

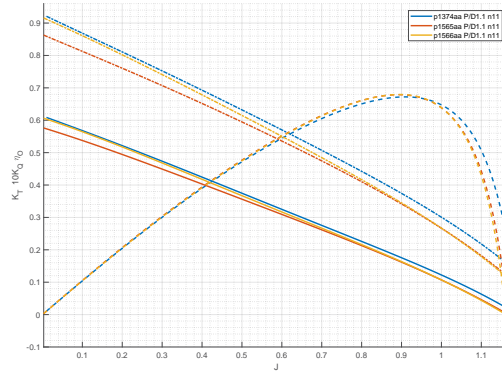


Figure 8: Effect of skew distribution

Because the inflow to the propellers was homogeneous, the resin blades showed a static response to the hydrodynamic load. Albeit the deformations were not measured, the increase of the thrust and torque coefficients of the resin blades compared to their metallic variant indicates that the blades were surely twisted in radial direction as Figure 9 shows.

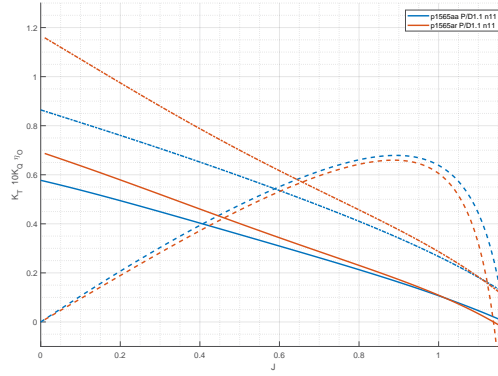


Figure 9: Comparison of open-water curves for the same propeller in metal and resin

The effect of the shaft speed, that translates into propeller load, on the blade twist can be clearly seen in Figure 10 where left to right the difference between the flexible and the rigid thrust coefficient $\delta K_T = K_{TR} - K_{TA}$ at the different shaft speeds is presented for the geometries P1374, P1565 and P1566, respectively.

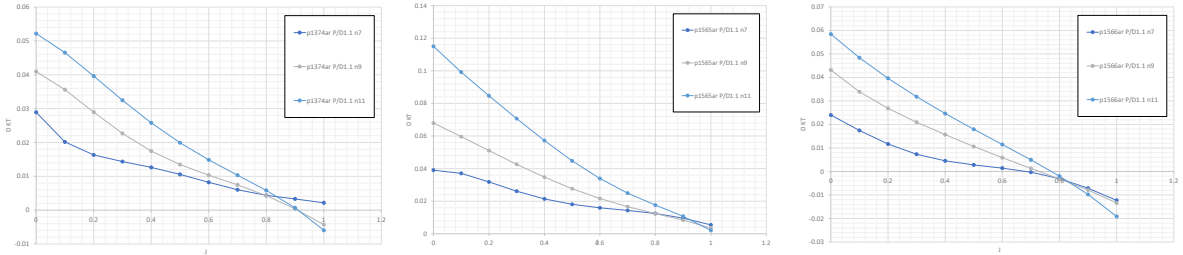


Figure 10: Effect on the propeller loading on the twist of the blades

The difference in thrust coefficient δK_T increases for J values lower than the J of maximum efficiency, while it decreases for higher values of J . Propellers are designed to operate with optimal angles of attack around the J of maximum efficiency. For J values lower than the design one, the angles of attack are increasing with decreasing J values, while the opposite happens for J values that are higher than the design one. In both cases the relative position of the pressure and section shear centers changes, resulting in a varying twist of the blade in radial direction dependent on the J value. From Figure 10 it can be seen that the all three geometries tend to show little twist in the J range from 0.8 to 0.9, i.e. close to the design point. The blade twist results in a global pitch increase for advance coefficients lower than the design point and decrease for advance coefficients higher than the design one. Furthermore, a closer look to the three graphs reveals that there are clear differences in how the different designs behave in relation to variation in load. The relation between thrust coefficient change and J value is compared for the three propellers for $n = 11$ rps in Figure 11. The reason why the three blade respond differently to changes in J values is twofold, but both reasons relate to the skew distribution.

The first reason is that the skew distribution changes quite significantly the open-water curves as already shown in Figure 8. The second reason is that, as mentioned in the second paragraph, the skew distribution changes the elastic axis of the blade.

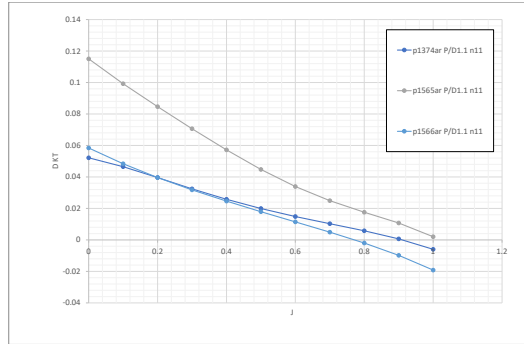


Figure 11: Comparison of the different J to relative KT for the three designs at $n=11$ rps

6 CONCLUSIONS

The measurements performed on three propeller designs that were produced both in aluminium and resin have been presented. The tests were performed at different P/D settings and propeller shaft speed in open water condition in SINTEF Ocean large towing tank. The geometries of the propellers and the data from the tests can be obtained upon request.

The tests aimed to provide validation material for numerical simulations of the static hydroelastic response of marine propellers. The test matrix is wide enough to allow validating design and simulation codes against the effect of the Reynolds number, the effect of skew distribution on the open-water curves of rigid propellers and the static hydroelastic response of the resin propellers. The tests presented here are part of the FleksProp project that intends to establish better design practices for the marine flexible propulsors, thus including not only propeller, but also thrusters. Within the scope of the project also composite propellers will be investigated and the interaction of the propeller with the thruster body will be considered too.

7 ACKNOWLEDGEMENTS

The present work has been fully supported by the FleksProp project. The FleksProp project is cooperation between SINTEF Ocean, the Norwegian University of Science and Technology NTNU and Rolls Royce Marine with the economic support of the Research Council of Norway (RCN) and Rolls Royce Marine. The economic support of the Research Council of Norway and Rolls Royce Marine is greatly appreciated.

REFERENCES

- [1] JCGM 100:2008 GUM 1995 with minor corrections - valuation of measurement data — Guide to the expression of uncertainty in measurement

- [2] Atkinson, P. & Glover, E.J. (1988). 'Propeller hydroelastic effects'. Propellers 88 Symposium, Virginia Beach, Virginia, September 20-21, 1988.
- [3] Savio, L.(2015): Measurements of the deflection of a flexible propeller blade by means of stereo imaging. SMP2015 - The Fourth International Symposium on Marine Propulsors; 2015-05-31 - 2015-06-04
- [4] Yin L. Young, Nitin Garg, Paul A. Brandner, Bryce W. Pearce, Daniel Butler, David Clarke, Andrew W. Phillips, Load-dependent bend-twist coupling effects on the steady-state hydroelastic response of composite hydrofoils, Composite Structures, Volume 189, 2018, Pages 398-418, ISSN 0263-8223, <https://doi.org/10.1016/j.compstruct.2017.09.112>.
- [5] Achkinadze, A.S., Krasilnikov, V.I. (1999). 'A Numerical Lifting-Surface Technique for Account of Radial Velocity Component in Screw Propeller Design Problem. Proceedings of the 7th International Conference on Numerical Ship Hydrodynamic NSH7, July 19-22, Nantes, France.
- [6] Achkinadze, A.S., Krasilnikov, V.I. and Stepanov, I.E. (2000). 'A Hydrodynamic Design Procedure for Multi-Stage Blade-Row Propulsors Using Generalized Linear Model of the Vortex Wake. Proceedings of the Propellers/Shafting'2000 SNAME Symposium, Virginia Beach, VA, September 20-21.

PANS SIMULATIONS: LOW VERSUS HIGH REYNOLDS NUMBER APPROACH

MAARTEN KLAPWIJK^{*†‡}, THOMAS LLOYD[‡], GUILHERME VAZ[‡] and TOM van TERWISGA^{†‡}

[†] Faculty of Mechanical, Maritime and Material Engineering
Delft University of Technology
Mekelweg 5, 2628 CD Delft, The Netherlands
e-mail: m.d.klapwijk@tudelft.nl, web page: <http://www.tudelft.nl/>

[‡] Maritime Research Institute Netherlands (MARIN)
Haagsteeg 2, 6708 PM Wageningen, The Netherlands
e-mail: m.klapwijk@academy.marin.nl, web page: <http://www.marin.nl/>

Key words: PANS, Turbulent channel flow, ReFRESCO, CFD

Abstract. Different approaches for specifying the ratio of modelled-to-total dissipation (f_ε) in the PANS model, based on the $k - \omega$ SST model, are evaluated for different ratios of the modelled-to-total kinetic energy, f_k . Based on theoretical reasoning it is argued that applying $f_\varepsilon = a \cdot f_k$ should have little effect, and that $f_\varepsilon = f_k$ is not expected to improve the results. This is confirmed by applying the approaches to a turbulent channel flow at $Re_\tau = 395$ and 180, and comparing the results to the often used ‘high Reynolds number’ approach ($f_\varepsilon = 1.0$). Reducing f_ε leads to a reduction in range of scales in the flow; dissipation is allowed at larger scales and therefore smaller scales are suppressed.

1 INTRODUCTION

The application of high fidelity turbulence models for industrial problems, such as cavitation calculations, is mostly focused on the use of *hybrid* models such as Detached Eddy Simulation (DES) based models. These models switch between Reynolds Averaged Navier-Stokes (RANS) and Large Eddy Simulation (LES) based on the local grid size, wall distance and RANS length scale, with the aim of improving the accuracy compared to full RANS. However this approach may lead to commutation errors in the transition between the two zones, and is highly grid dependent due to the zonal formulation. In addition numerical error quantification is made difficult due to entanglement of the modelling and discretisation errors. *Bridging* models, such as Partially Averaged Navier-Stokes (PANS), are an alternative approach without these problems. The PANS model can operate at any degree of physical resolution, independent of the grid, by setting the modelled-to-total ratios of turbulence kinetic energy (f_k) and dissipation (f_ε) [1]. In literature, the model is applied almost exclusively using $f_k \ll 1$ and $f_\varepsilon = 1.0$ (known as the ‘high Reynolds number’ approach), an exception being the work of [2] and [3]. This approach assumes that the PANS cut-off is located at lower wave numbers than the dissipation range and therefore that the dissipation occurs entirely at the modelled scales. This is valid if there is a clear separation between the large energy containing scales and the small dissipative scales (identifiable by the inertial subrange, which fol-

lows Kolmogorov's law) [1, 3]. Theoretically, for low Reynolds number flows, where the scales overlap, or for high Reynolds number flows with a high physical resolution (low f_k), part of the dissipation should also be resolved. This implies that f_ε should be lower than 1.0. It is expected that the resolved structures, obtained when $f_k < 1.0$, should change due to increased dissipation.

Although most maritime applications are high Reynolds number flows, it is not unlikely that some cases require high physical resolutions, i.e. low f_k . For low Reynolds numbers, an often mentioned approach is to keep $f_k = f_\varepsilon$, whereas for moderate Reynolds numbers, $f_k < f_\varepsilon < 1.0$ has been recommended [3, 4]. Pereira et al. [5] state that if $f_k = f_\varepsilon$ the only change with respect to the underlying RANS model is an increase of the effective diffusion coefficient and cross-diffusion term; these terms go infinity when f_k goes to 0. Using this approach vortex shedding for a cylinder was underpredicted, especially with lower f_k . By contrast Lakshmipathy et al. [3] obtained satisfactory results for the same test case using a finer grid, indicating a potential grid dependency. Frendi et al. [2] simulated a backward facing step, using a fixed f_k and varying f_ε . These authors state that for wall-bounded flows viscous effects and dissipation should be taken into account by lowering f_ε . Better agreement with experiments was reported with this approach, although only the parameter f_ε was varied, with f_k kept fixed as 0.2. Their results indicated a decrease in range of scales with decreasing f_ε , due to the increased dissipation.

The current work evaluates the three aforementioned approaches for specifying f_ε ($f_\varepsilon = 1.0$, $f_\varepsilon = a \cdot f_k$ with $a = 2$ and $f_\varepsilon = f_k$) by applying them to a turbulent channel flow at both 'low' ($Re_\tau = 180$) and 'moderate' ($Re_\tau = 395$) Reynolds numbers. The results are compared to Direct Numerical Simulation (DNS) reference data by Moser et al. [6]. The results of the high Reynolds number approach were previously presented, together with LES results, in Klapwijk et al. [7]. Those results exhibited two clear regimes, based on the value of f_k . If the filter length described by f_k is smaller than the driving mechanism of the turbulent flow, proper results are obtained; if f_k is larger turbulent fluctuations are not resolved and a laminar result is obtained. In the current work only the values of f_k yielding a turbulent flow are considered, which are $f_k = 0.15, 0.10$ and 0.05 . To maintain a distinction between modelling and numerical error, a strong aspect of PANS, f_k and f_ε are kept constant in time and space.

This paper consists of a description of the PANS model, an investigation of the theoretical effects of the approaches for specifying f_ε , after which the test case and the corresponding results are described.

2 PANS MODEL

2.1 Model formulation

The Partially-Averaged Navier-Stokes equations are obtained by filtering the continuity and momentum equations, thereby decomposing all instantaneous quantities, Φ , into a resolved, $\langle \Phi \rangle$, and a modelled (unresolved) component, ϕ , according to $\Phi = \langle \Phi \rangle + \phi$ [8]. The PANS equations for incompressible, single-phase flow are

$$\frac{\partial \langle u_i \rangle}{\partial t} = 0, \quad (1)$$

$$\frac{D \langle u_i \rangle}{Dt} = \frac{\partial}{\partial x_j} \left[\nu \left(\frac{\partial \langle u_i \rangle}{\partial x_j} + \frac{\partial \langle u_j \rangle}{\partial x_i} \right) \right] + \frac{1}{\rho} \frac{\partial \tau(u_i, u_j)}{\partial x_j} - \frac{1}{\rho} \frac{\partial \langle p \rangle}{\partial x_i}. \quad (2)$$

In these equations u_i indicates the velocity components, p the pressure, ν the kinematic viscosity, ρ the density and $\tau(u_i, u_j)$ the sub-filter stress tensor which is modelled using Boussinesq's hypothesis,

$$\frac{\tau(u_i, u_j)}{\rho} = 2\nu_t \langle S_{ij} \rangle - \frac{2}{3}k\delta_{ij} \quad (3)$$

with ν_t the turbulence viscosity, $\langle S_{ij} \rangle$ the resolved strain-rate tensor, k the modelled turbulence kinetic energy, and δ_{ij} indicates the Kronecker delta. To close the set of equations a Reynolds Averaged Navier-Stokes (RANS) model is used. The PANS model in this work is based on the $k - \omega$ Shear-Stress Transport (SST) model [1, 9]. The transport equations of the SST model are reformulated including the modelled-to-total ratio of turbulence kinetic energy and dissipation rate

$$f_k = \frac{k}{K} \quad \text{and} \quad f_\omega = \frac{\omega}{\Omega} = \frac{f_\varepsilon}{f_k}. \quad (4)$$

This leads to the reformulated equations

$$\frac{Dk}{Dt} = P_k - \beta^* \omega k + \frac{\partial}{\partial x_j} \left[\left(\nu + \nu_t \sigma_k \frac{f_\omega}{f_k} \right) \frac{\partial k}{\partial x_j} \right], \quad (5)$$

$$\frac{D\omega}{Dt} = \frac{\alpha}{\nu_t} P_k - \left(P' - \frac{P'}{f_\omega} + \frac{\beta \omega}{f_\omega} \right) \omega + \frac{\partial}{\partial x_j} \left[\left(\nu + \nu_t \sigma_\omega \frac{f_\omega}{f_k} \right) \frac{\partial \omega}{\partial x_j} \right] + 2 \frac{\sigma_{\omega 2}}{\omega} \frac{f_\omega}{f_k} (1 - F_1) \frac{\partial k}{\partial x_j} \frac{\partial \omega}{\partial x_j}, \quad (6)$$

with

$$P' = \frac{\alpha \beta^* k}{\nu_t} \quad \text{and} \quad \nu_t = \frac{a_1 k}{\max(a_1 \omega; \langle S \rangle F_2)}. \quad (7)$$

For the model constants and auxiliary functions, F_1 and F_2 , see Menter et al. [9], while for more details on the implementation of the PANS model used here, the reader is referred to Pereira et al. [5].

Note that the separation into a resolved and a modelled component is very similar to the LES approach. Both approaches can be classified as variable-resolution turbulence simulations but based on a different closure paradigm; the closure of PANS is viscosity-based (sub-filter viscosity is a function of the modelled flow field (k, ω)), whereas in LES the closure is grid-based (sub-filter viscosity is a function of the cut-off length scale (Δ)) [10]. Consequently, in contrast to LES, the cut-off length scale of the resolved flow is not predetermined in PANS. The physical resolution is only determined by the settings, this leads to an overlap between the PANS resolved and modelled spectra [10], as shown in Figure 1. Since the grid remains fixed, computations with an f_k larger than what the grid allows are comparable to an explicitly filtered LES although based on a different modelling framework. Computations with a very low f_k value are effectively an Implicit LES (under-resolved DNS).

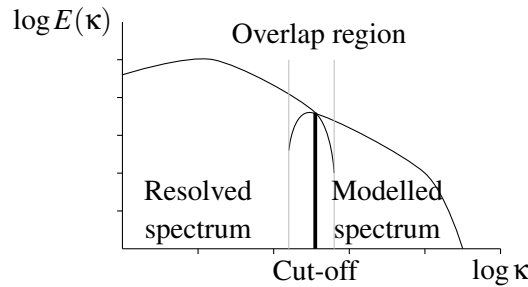


Figure 1: Schematic PANS wave-number energy spectrum, showing the overlap between resolved and modelled velocity scales. Based on Reyes et al. [10].

2.2 Specifying f_ϵ

Kinetic energy is mostly contained in the larger scales, whereas dissipation occurs in the smallest scales; this dictates $0 \leq f_k \leq f_\epsilon \leq 1$ [4]. For specifying f_ϵ , three Reynolds number regimes can be distinguished in literature, which lead to different corresponding values of f_ϵ : the ‘high’, ‘moderate’ and ‘low’ Reynolds number approaches. Generally speaking in the high Reynolds number case, there is a clear separation between the large energy-containing scales and the small dissipative scales (identifiable by the inertial subrange, which follows Kolmogorov’s law) [1, 3]. For a low Reynolds number flow these scales overlap. A moderate Reynolds number lies between these limits. In terms of scale separation, clearly this distinction is difficult to quantify. In generalised form, if f_ϵ is taken as $f_\epsilon = a \cdot f_k$, the transport equations (5 and 6) reduce to

$$\underbrace{\frac{Dk}{Dt}}_{\text{I}} = \underbrace{P_k}_{\text{II}} - \underbrace{\beta^* \omega k}_{\text{III}} + \underbrace{\frac{\partial}{\partial x_j} \left[\left(\mathbf{v} + \mathbf{v}_t \sigma_k \frac{a}{f_k} \right) \frac{\partial k}{\partial x_j} \right]}_{\text{IV}}, \quad (8)$$

$$\underbrace{\frac{D\omega}{Dt}}_{\text{V}} = \underbrace{\frac{\alpha}{v_t} P_k}_{\text{VI}} - \underbrace{\left(\left(1 - \frac{1}{a} \right) P' + \frac{\beta \omega}{a} \right) \omega}_{\text{VII}} + \underbrace{\frac{\partial}{\partial x_j} \left[\left(\mathbf{v} + \mathbf{v}_t \sigma_\omega \frac{a}{f_k} \right) \frac{\partial \omega}{\partial x_j} \right]}_{\text{VIII}} + \underbrace{2 \frac{\sigma_{\omega 2}}{\omega} \frac{a}{f_k} (1 - F_1) \frac{\partial k}{\partial x_j} \frac{\partial \omega}{\partial x_j}}_{\text{IX}}. \quad (9)$$

In the k equation (8), term (I) indicates rate of change plus convection, (II) rate of production, (III) rate of destruction and (IV) transport by molecular and turbulent diffusion. In the ω equation (9) the terms are rate of change (V), rate of production (VI), rate of destruction (VII), transport by molecular and turbulent diffusion (VIII) and cross-diffusion (IX). This last term is a result of the $\epsilon = k\omega$ transformation in the construction of the SST model [11]. The terms in red differ from the standard SST model. For these equations the effect of the three approaches for specifying f_ϵ will be discussed from a numerical perspective. It is clear that terms (I), (II), (III), (V) and (VI) are independent of f_k and a .

High Reynolds number approach In this case $f_\epsilon = 1.0$ ($a = 1/f_k$); here the transport by diffusion (IV and VIII) and cross-diffusion term (IX) increase proportionally to $1/f_k^2$ with decreasing f_k . The rate of destruction (VII) decreases proportionally to f_k . So for $f_k < 1.0$ the diffusion term in the k equation increases, spreading the modelled turbulent kinetic energy in space. At the same time, in the ω equation, the diffusion terms dominate over the destruction term. This implies that for low f_k values the dissipation is more spread out in space but the rate of destruction of ω is reduced.

Moderate Reynolds number approach In this case $f_\epsilon = a \cdot f_k$ with $1.0 < a < 1/f_k$. Consequently terms (IV), (VIII) and (IX) increase proportionally to a/f_k . Term (VII) is independent of f_k and is proportional to a . Again the diffusion terms increase, and the destruction term in the ω equation decreases. The difference between these terms is smaller than for the high Reynolds number approach, so it is expected that dissipation occurs more locally.

Low Reynolds number approach In the limit of $f_\epsilon = f_k$ ($a = 1.0$) terms (IV), (VIII) and (IX) increase proportionally to $1/f_k$. Term (VII) is now constant and reduces to $\beta\omega^2$, which is identical to the original SST model. The term containing P' disappears completely. With decreasing f_k the model remains identical to the SST model but with increased diffusion and cross-diffusion terms (IV, VIII and IX) [5].

Reyes et al. [10] derived the relationship between PANS and RANS turbulence viscosity as

$$\frac{\nu_{t,PANS}}{\nu_{t,RANS}} = \frac{f_k^2}{f_\epsilon} \quad (10)$$

and related the PANS Kolmogorov scales to the physical integral scales for length (η/L), time (t_η/T) and velocity (u_η/U) as

$$\frac{\eta}{L} \sim C_\mu^{3/4} \frac{f_k^{3/2}}{f_\epsilon}, \quad \frac{t_\eta}{T} \sim C_\mu^{1/2} \frac{f_k}{f_\epsilon}, \quad \frac{u_\eta}{U} \sim C_\mu^{1/2} f_k^{1/2}. \quad (11)$$

The effect of the different approaches on these ratios across the f_k range is shown graphically in Figure 2, with $a = 2$ used throughout as example. Note that these ratios are independent of Reynolds number. The figure is corrected for the fact that f_ϵ cannot be not higher than f_k . The point after which the viscosity and length scales for $f_\epsilon = 1.0$ and $f_\epsilon = a \cdot f_k$ deviate, and where a discontinuity for the time scale is located, lies at $f_k = \frac{1}{a}$. For the turbulence viscosity and the length scales, the high Reynolds number approach yields the lowest ratios across the entire f_k range, meaning that the turbulence viscosity is lowered, more unsteadiness and smaller length scales can be expected in the solution. The moderate Reynolds number approach yields the same if $f_k > \frac{1}{a}$; for $f_k < \frac{1}{a}$ the turbulent viscosity and length scales are larger, i.e. it is expected that the smallest structures are absent. The low Reynolds number approach yields the highest ratio for all f_k except at the limits of $f_k = 0$ or 1. The time scales however show the opposite trend, across the f_k range the lowest ratio is for the moderate Reynolds approach. The low Reynolds number approach is independent of f_k , while the high approach lies in between these limits. The velocity scales decrease with $f_k^{1/2}$ independently of f_ϵ .

Note that for the high Reynolds number approach there is little difference in terms of turbulence viscosity and length scales if f_k is small (in the range $f_k < 0.2$). This corresponds to the findings in Klapwijk et al. [7], where only a fully developed turbulent solution was found for small f_k , but then little difference was seen between the different f_k values. In contrast, in this range the time scales are strongly affected.

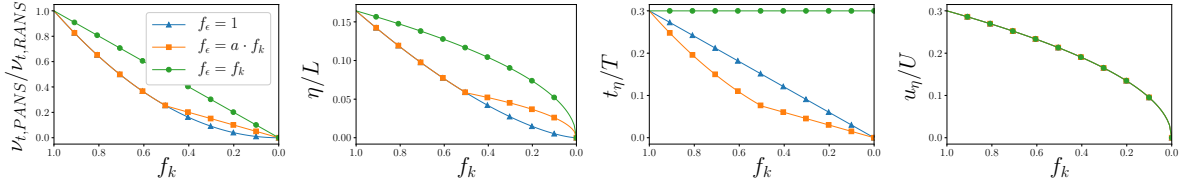


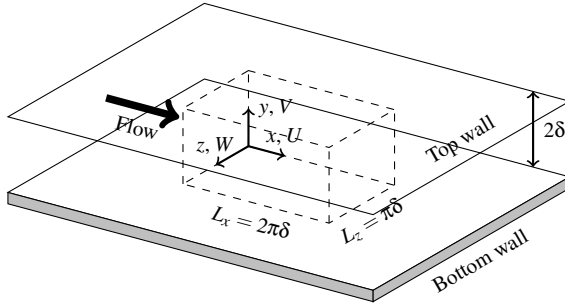
Figure 2: Relationship between PANS and RANS turbulence viscosity, ν_t , length, η_u/L , time, t_{η_u}/T , and velocity scales, u_{η_u}/U , versus f_k for different f_ϵ approaches. Here $a = 2$.

Based on these theoretical observations some questions arise concerning the use of the low Reynolds number approach. There appears to be no clear advantage; additional diffusion is added in the equations, and theoretically the the turbulent viscosity and length scales are larger than for the high Reynolds number approach, indicating that the smallest scales will be suppressed. For the moderate Reynolds number approach, small differences compared to $f_\epsilon = 1.0$ are expected, and only for low f_k . In order to check these findings in a practical case, in the remainder of the paper the three approaches are applied to a turbulent channel flow at two different Reynolds numbers ($Re_\tau = 395$ and 180).

3 NUMERICAL SETUP AND SOLVER

The numerical setup has already been reported in Klapwijk et al. [7]. Computations are made using a rectangular domain, with two no-slip walls oriented normal to the y -axis (see Figure 3). The remaining boundaries are connected using periodic boundary conditions in order to approximate an infinite channel. Comparisons between different model settings are performed on a Cartesian grid, with a density of $N_x = 127$, $N_y = 95$ and $N_z = 95$ with clustering towards the walls. For $Re_\tau = 395$ this results in $x^+ \approx 12$, $y^+ \approx 0.1$ and $z^+ \approx 10$. The non-dimensional time step $\Delta t^* = \frac{u_\tau \Delta t}{2\delta} \approx 1 \times 10^{-3}$ leads to $\Delta t^+ = \frac{u_\tau^2 \Delta t}{\nu} \approx 0.08$ (2000 time steps per flow-through time). The grid density and time step are below LES guidelines and approach DNS resolution [12]. To maintain the proper bulk and friction Reynolds numbers, $Re_b = \frac{U_b 2\delta}{\nu}$ and $Re_\tau = \frac{u_\tau \delta}{\nu}$ respectively, a body force is applied which is proportional to the pressure gradient $\frac{dp}{dx} = -\frac{\tau_w}{\delta}$, with $\tau_w = \rho u_\tau^2$ [13]. The Péclet number has a magnitude of $O(10)$. As shown in the literature, the use of scale-resolving turbulence models for a turbulent channel yields a so-called supercritical laminar solution for which many flow-through times are needed to trigger transition to the turbulent regime [14]. In order to speed up the transition, the method suggested by Schoppa and Hussain [15] is used here. For more details, see Klapwijk et al. [7].

The numerical solver used for all simulations in this work is ReFRESKO, a multiphase unsteady incompressible viscous flow solver using RANS and Scale-Resolving Simulation models such as SAS, DDES/IDDES, XLES, PANS and LES approaches, complemented with cavitation models and volume-fraction transport equations for different phases (www.refresco.org). Time integration is performed implicitly using a second-order accurate scheme, all terms in the governing equations are discretised in space using second-order accurate central differencing, except for the convection terms of the turbulence equations, which use a first-order upwind scheme.



| Symbol | Case 1 | Case 2 |
|------------------------------|------------------------|------------------------|
| Re_τ | 395 | 180 |
| Re_b | 13800 | 6300 |
| δ [m] | 0.1 | 0.1 |
| U_b [m/s] | 6.928×10^{-2} | 3.157×10^{-2} |
| u_τ [m/s] | 3.966×10^{-3} | 1.807×10^{-3} |
| τ_w [N/m ²] | 1.570×10^{-2} | 3.259×10^{-3} |
| ν [m ² /s] | 1.004×10^{-6} | 1.004×10^{-6} |
| ρ [kg/m ³] | 998 | 998 |

Figure 3: Schematic overview of the domain and physical parameters. The dashed lines indicate the computational domain. The figure is based on the drawing of de Villiers [14].

4 NUMERICAL ERROR ESTIMATION

In order to verify the results the numerical errors were investigated. A distinction can be made between input, iterative, discretisation, and, in the case of unsteady computations, statistical errors. The input error is assumed to be negligible; the effect of the other error sources is investigated here.

Iterative error The residuals, normalised by the element on the diagonal of the matrix in the system of equations, were used to check the iterative convergence. Following the approach advocated by Eça et al. [16], a computation ($f_k = 0.10$, $f_\varepsilon = 1.0$) was performed using different iterative convergence criteria ($L_2 = 10^{-3}$, 10^{-4} , 10^{-5} , 10^{-6} , 10^{-7} and 10^{-8}). Five flow-through times are computed, starting

from a fully developed solution. Due to the limited number of flow-through times these results have a larger statistical error. The effect on the mean velocity (\bar{u}/U_b), Reynolds stresses ($Re_{ij} = \overline{u'_i u'_j}/u_\tau^2$) and turbulence kinetic energy spectra ($E_u(f)$) at $y^+ \approx 20$ is shown in Figure 4. The mean velocity appears almost unaffected; for the Reynolds stresses and spectra, $L_2 = 10^{-3}$ and 10^{-4} show a large mismatch with the reference data. The magnitude of the peak value Re_{uu} and the turbulence kinetic energy spectra converge for stricter convergence criteria towards the DNS data. As a compromise between cost and accuracy, the criterium $L_2 = 10^{-6}$ is used in the remainder of this work. This yields a negligible iterative error compared to the statistical error. Applying this criterium leads to a residual of $L_\infty = 10^{-5}$ in each time step for momentum. The residuals for pressure and turbulence equations are at least one order of magnitude smaller.

Discretisation error To assess the effect of the discretisation error, four different grids (with refinement ratios $r_i = h_i/h_1 = \Delta t_i/\Delta t_1 = 1.00, 1.25, 1.57$ and 1.97) were employed. The effect is again shown in Figure 4. Both the mean velocity and Reynolds stresses appear reasonably insensitive to grid resolution, only Re_{uu} deviates slightly on the finest grid. The main differences are observed for the turbulence kinetic energy spectra. Grid refinement leads to a slightly increased cut-off frequency, since the smaller cells allow for higher frequencies to be resolved. This indicates that the employed f_k (0.10) is below the grid cut-off, i.e. the grid is not at DNS resolution. Based on the similarity between the results it is concluded that the coarsest grid has a sufficient resolution.

Statistical error To remove the start-up effects and estimate the statistical uncertainty of the results, the Transient Scanning Technique is employed [17]. In Klapwijk et al. [7] it was concluded that the first 11 flow-through times must be removed to eliminate the start-up effects. The mean values are then computed based on approximately 45 flow-through times, resulting in a statistical uncertainty for the mean axial velocity between 0.5 and 2.5%, and for the Reynolds stress components between 5 and 10%. For more details the reader is referred to Klapwijk et al. [7].

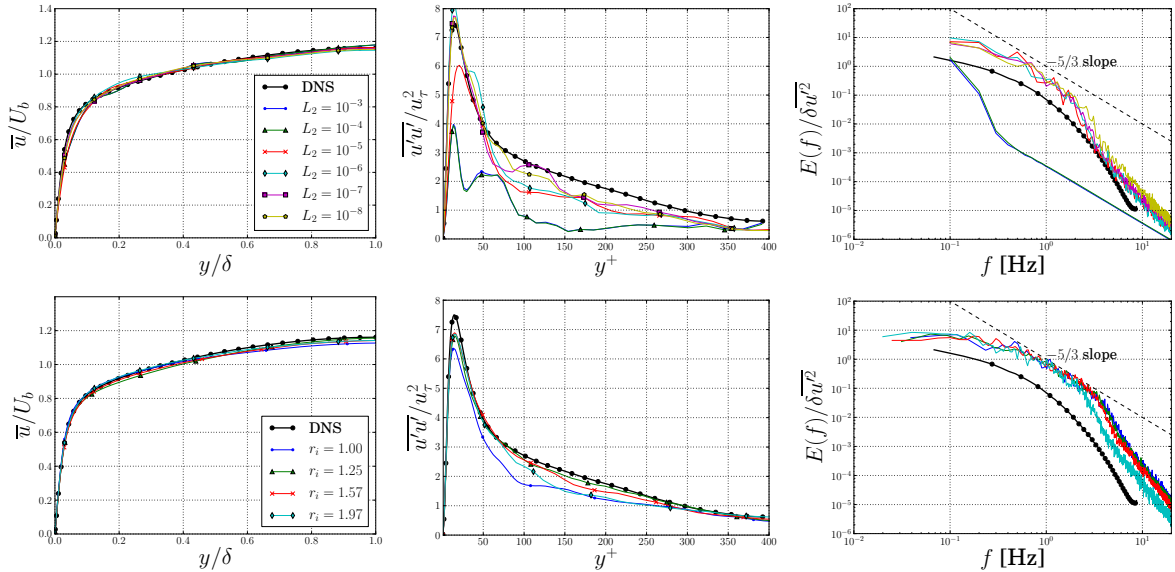


Figure 4: Mean velocity (\bar{u}) profiles, Reynolds stress (Re_{uu}) profiles and turbulence kinetic energy spectra ($E_{u,y^+\approx 20}(f)$) using different iterative convergence criteria (top row), and on different grids (bottom row).

5 RESULTS FOR DIFFERENT f_ε

For all figures in this section the three approaches ('high', 'moderate' and 'low' Reynolds number) are shown from left to right, indicated as H , M and L respectively. For M , f_ε is taken as $2 \cdot f_k$, i.e. $a = 2$. For $Re_\tau = 180$, the initialisation method (Section 3) yields a laminar flow for M and L . This is an indication of added dissipation (the initial perturbations are dampened). For comparison purposes, a second set of computations is performed where the computations are restarted from a fully turbulent H computation.

Figure 5 shows the mean velocity versus the channel height. For both Re_τ values H matches the DNS well independently of f_k . M shows slight discrepancies in the profile; especially for $Re_\tau = 180$, the velocity is underpredicted near the centre. L at $Re_\tau = 395$ and with $f_k = 0.15$ shows a more parabolic profile, which is an indication of a laminar flow. Both of the lower f_k values do show a turbulent flow profile, however the boundary layer appears to be thinner than half of the channel height. The velocity is almost constant in the region $0.5 \leq y/\delta \leq 1.0$. At the lower Re_τ , both $f_k = 0.15$ and 0.10 show a laminar profile. The profile for $f_k = 0.05$ matches the DNS data reasonably well.

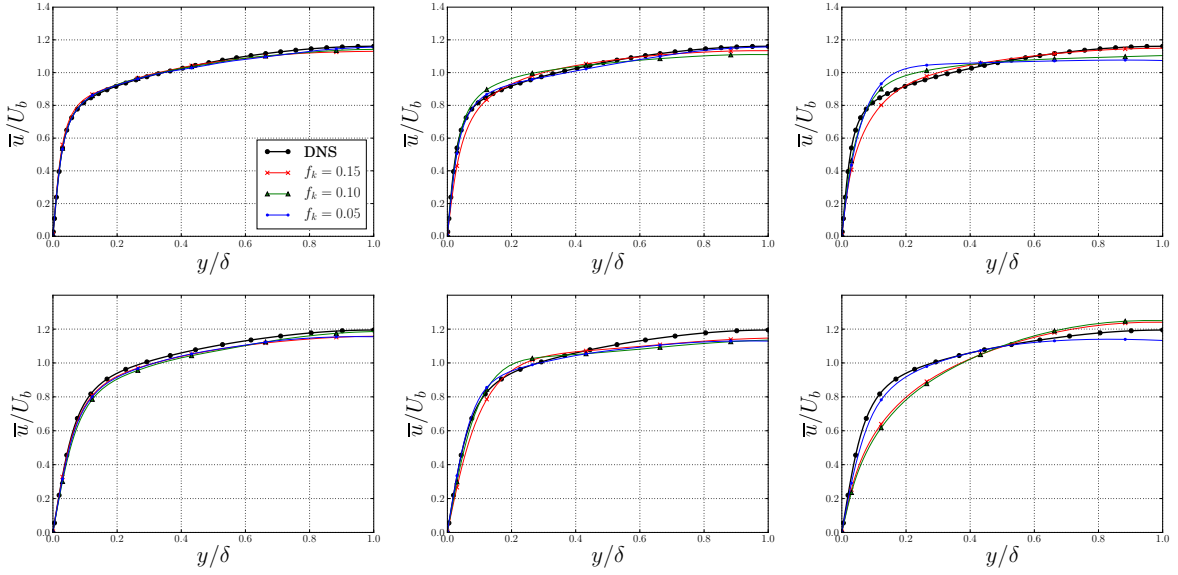


Figure 5: Velocity profiles (\bar{u}/U_b), from left to right H , M and L for $Re_\tau = 395$ (top) and 180 (bottom).

Figure 6 shows two components of the Reynolds stress profiles. The results for H and M are very similar. For both Re_τ , Re_{uu} and Re_{uv} both show the correct profile, the magnitude converges towards the DNS data with decreasing f_k . Re_{uv} is slightly underpredicted. Re_{uu} at $Re_\tau = 180$ is overpredicted near the wall for H and M . L clearly deviates from the reference data. At $Re_\tau = 395$, the Re_{uu} profiles show the correct shape, but $f_k = 0.15$ and 0.05 underpredict the magnitude. Re_{uv} is not captured by all f_k values. For $Re_\tau = 180$, the profile is correct for $f_k = 0.05$, although the magnitude is not well captured. For this Re_τ , $f_k = 0.05$ is again the only setting which captures Re_{uv} reasonably. For the other f_k settings, Re_{uv} is almost zero, indicating laminar flow, which is in agreement with the mean velocity profiles.

The turbulence kinetic energy spectra are shown in Figure 7. As expected the spectra at the lower Re_τ show less scale separation, while for the higher Re_τ , a $-5/3$ slope is observed in part of the frequency range. For H the value of f_k has little influence on the spectra, for M the effect of reducing f_k is more

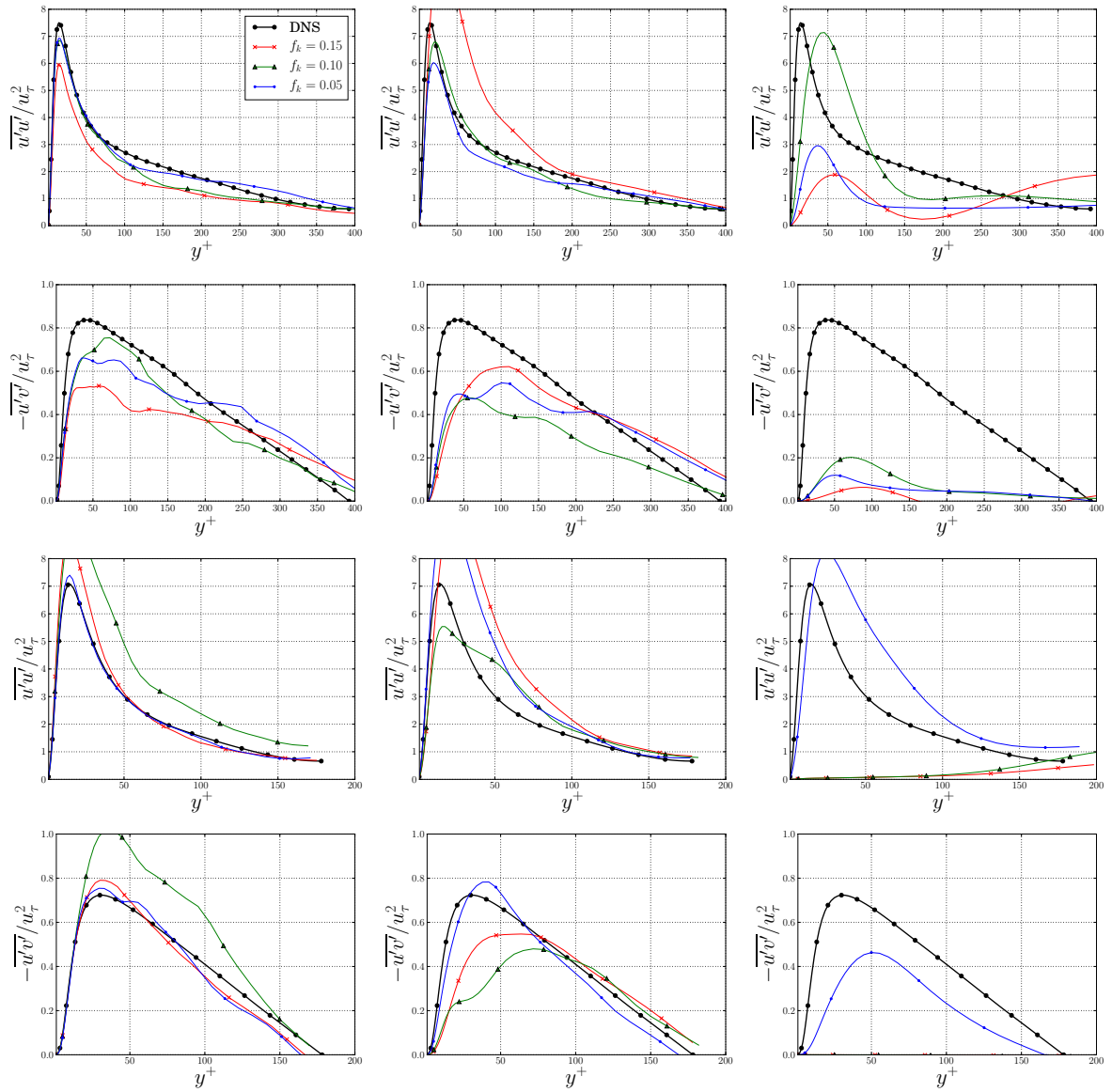


Figure 6: Normalised Reynolds stress profiles (Re_{ij}), from left to right H , M and L for $Re_\tau = 395$ (rows one and two) and $Re_\tau = 180$ (rows three and four).

visible. A lower f_k leads to more resolved turbulence, i.e. more energy in the spectrum and a higher cut-off frequency. This effect is the largest at $Re_\tau = 180$. The same influence of f_k is clear for L ; only $f_k = 0.05$ at $Re_\tau = 180$ matches the reference set, but still the energy at higher frequencies is lower than for M and H . In all other computations the energy is too low, the spectrum shows again that the flow is mostly laminar. It is clear that reducing f_ε reduces the energy in the spectrum; M contains less energy than H , again especially at higher frequencies.

Finally the effect of f_ε on the flow is visualised using structures based on the Q -criterion in Figures 8 and 9 for $Re_\tau = 395$ and 180 respectively. For both Reynolds numbers the same observations are made;

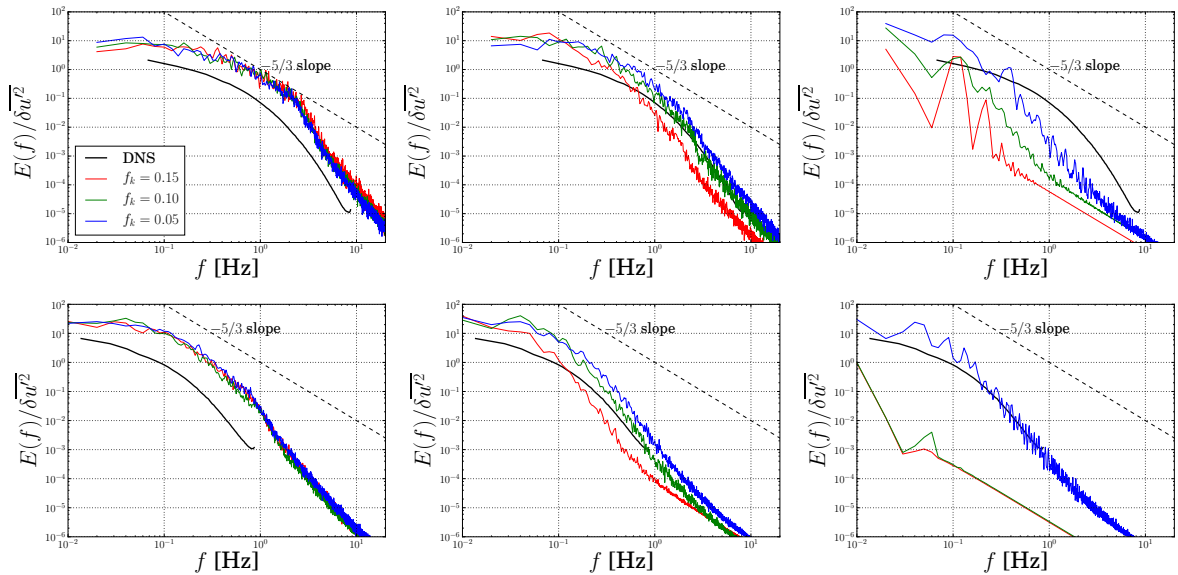


Figure 7: Turbulence kinetic energy spectra ($E_{u,y^+ \approx 20}(f)$), from left to right H , M and L . $Re_\tau = 395$ (top row) and $Re_\tau = 180$ (bottom row).

for H the structures appear independent of f_k . M shows a large dependency on f_k ; lowering f_k leads to more and smaller scales, for higher f_k only larger structures are observed away from the walls. This decrease in range of scales is in line with results by Frendi et al. [2]. The behaviour can be related to the definition of f_ε : for $f_\varepsilon = 1.0$, all dissipation occurs at the smallest scales, while if $f_\varepsilon < 1.0$, dissipation can also occur at larger scales. As a consequence the smaller scales are suppressed, since the turbulence is dissipated ‘earlier’. By reducing f_k and thereby also f_ε the range of scales increases again. For L the absence of structures for $f_k = 0.15$ for both Re_τ , and for $f_k = 0.10$ for $Re_\tau = 180$ again indicates a laminar flow. $f_k = 0.10$ at $Re_\tau = 395$ shows some large structures, but these do not resemble the turbulent structures as seen for the other approaches or for LES simulations [7]. For $f_k = 0.05$ it is observed that the smallest structures are absent, which is in line with the turbulence kinetic spectrum.

6 CONCLUSIONS

Different approaches for specifying f_ε in the PANS model were compared based on theory and turbulent channel flow simulations. Little difference between the moderate and high Reynolds number approaches was found. The moderate Reynolds number approach does have a larger dependency on f_k , since due to the smaller value of f_ε , the turbulence dissipation is no longer confined to the smallest scales. For the low Reynolds number approach, it was demonstrated that excess diffusion is added to the equations. A laminar-like solution is obtained independent of the flow initialization or Reynolds number. It is concluded that even at a low Reynolds number, $f_k = f_\varepsilon$ is an approach which should not be used due to the suppression of the smaller scales. Only when using a very low f_k (in the DNS limit) reasonable results for the mean velocity and Reynolds stress profiles can be obtained, although in that case the results obtained using $f_\varepsilon = 1.0$ also match the reference data well for the present test case, and contain more energy at the smaller scales.

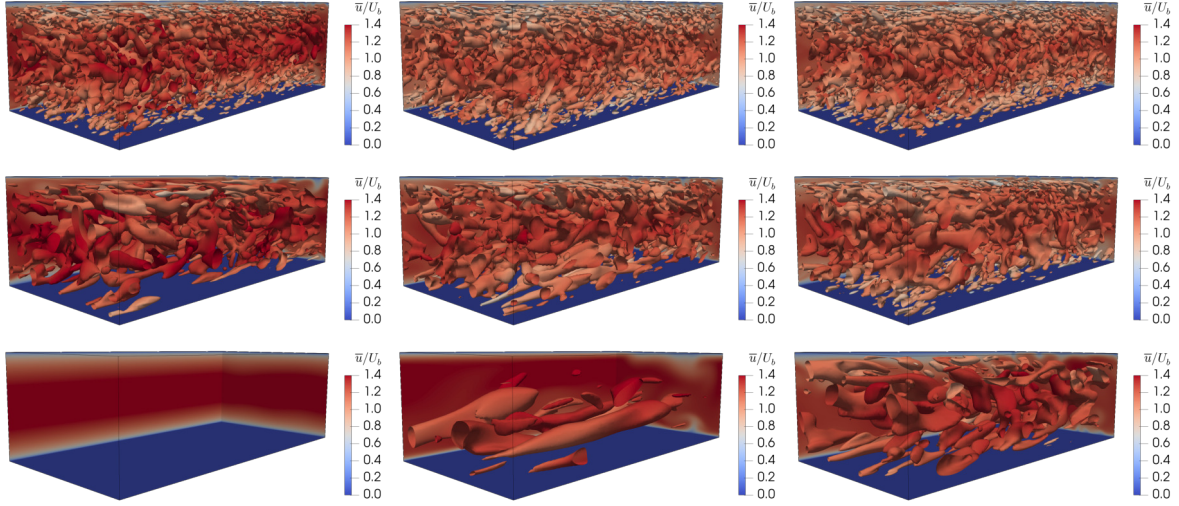


Figure 8: Instantaneous turbulent flow fields ($Q = 0.7$), coloured by $\bar{u}^* = \bar{u}/U_b$. From left to right $f_k = 0.15, 0.10$ and 0.05 , for $f_\epsilon = 1.0$ (first row), $f_\epsilon = 2 \cdot f_k$ (second row) and $f_\epsilon = f_k$ (third row). $Re_\tau = 395$.

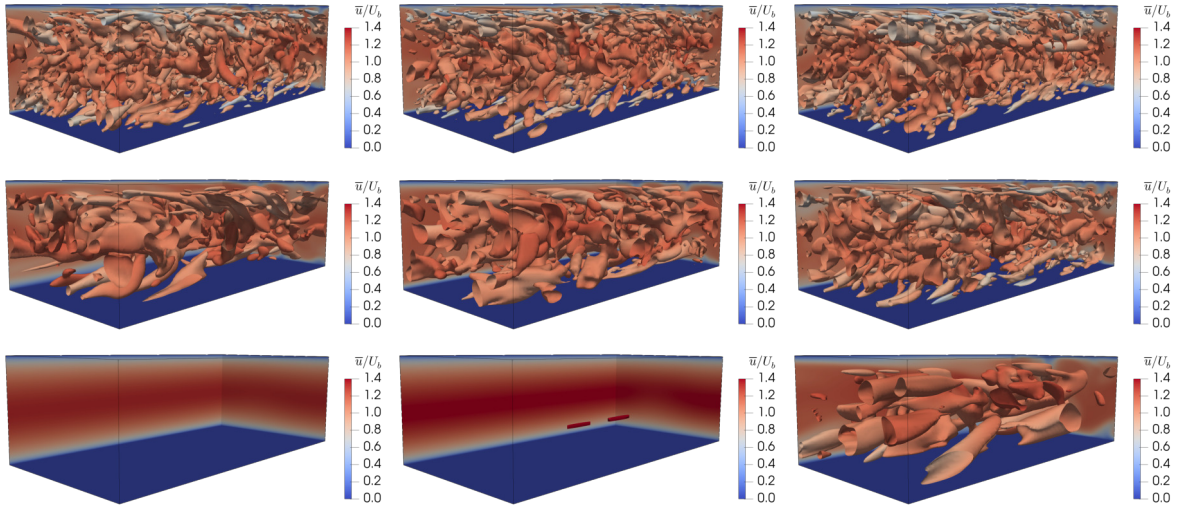


Figure 9: Instantaneous turbulent flow fields ($Q = 0.7$), coloured by $\bar{u}^* = \bar{u}/U_b$. From left to right $f_k = 0.15, 0.10$ and 0.05 , for $f_\epsilon = 1.0$ (first row), $f_\epsilon = 2 \cdot f_k$ (second row) and $f_\epsilon = f_k$ (third row). $Re_\tau = 180$.

For industrial flow cases at high Reynolds number, it is recommended to use $f_\varepsilon = 1.0$. That being said, if the reasoning is followed which leads to allowing f_k to vary in time and space, one can wonder whether the same should be applied to f_ε , i.e. f_ε depending on local flow quantities. There is currently no relationship to dynamically estimate f_ε found in the literature, while pursuing this method has the risk of re-introducing the problem of numerical and modelling error entanglement.

ACKNOWLEDGEMENTS

This research was financially supported by the Netherlands Organisation for Scientific Research, NWO, as part of the NOISOURCE project, and by the Dutch Ministry of Economic Affairs. The work was carried out on the Dutch national e-infrastructure, with the support of SURF Cooperative, on the *Reynolds* (TU Delft) and *Marclus3* (MARIN) clusters.

References

- [1] F.S. Pereira, G. Vaz, L. Eça, and S.S. Girimaji. Simulation of the Flow Around a Circular Cylinder at $Re=3900$ with Partially-Averaged Navier-Stokes Equations. *International Journal of Heat and Fluid Flow*, 69, 2018.
- [2] A. Frendi, A. Tosh, and S. Girimaji. Flow Past a Backward-Facing Step: Comparison of PANS, DES and URANS Results with Experiments. *International Journal for Computational Methods in Engineering Science and Mechanics*, 8(1):23–38, 2007.
- [3] S. Lakshmipathy, D.A. Reyes, and S. Girimaji. Partially Averaged Navier-Stokes Method: Modeling and Simulation of Low Reynolds Number Effects in Flow Past a Circular Cylinder. In *6th AIAA Theoretical Fluid Mechanics Conference*, page 3107, 2011.
- [4] S.S. Girimaji. Partially-Averaged Navier-Stokes Model for Turbulence: A Reynolds-Averaged Navier-Stokes to Direct Numerical Simulation Bridging Method. *Journal of Applied Mechanics*, 73(3):413–421, 2006.
- [5] F.S. Pereira, G. Vaz, and L. Eça. An assessment of Scale-Resolving Simulation models for the flow around a circular cylinder. *Turbulence, Heat and Mass Transfer*, 8, 2015.
- [6] R.D. Moser, J. Kim, and N.N. Mansour. Direct numerical simulation of turbulent channel flow up to $Re_\tau = 590$. *Physics of fluids*, 11(4):943–945, 1999.
- [7] M. Klapwijk, T. Lloyd, G. Vaz, and T. van Terwisga. Channel Flow at $Re_\tau = 395$: LES is more (turbulent than PANS). In *21st Numerical Towing Tank Symposium (NuTTS'18), Cortona, Italy*, 2018.
- [8] S.S. Girimaji and K.S. Abdol-Hamid. Partially averaged Navier-Stokes Model for Turbulence: Implementation and Validation. In *43rd AIAA Aerospace Sciences Meeting and Exhibit*, page 502, 2005.
- [9] F.R. Menter, M. Kuntz, and R. Langtry. Ten years of industrial experience with the SST turbulence model. *Turbulence, heat and mass transfer*, 4(1):625–632, 2003.
- [10] D.A. Reyes, J.M. Cooper, and S.S. Girimaji. Characterizing velocity fluctuations in partially resolved turbulence simulations. *Physics of Fluids*, 26(8):085106, 2014.
- [11] H.K. Versteeg and W. Malalasekera. *An Introduction to Computational Fluid Dynamics The Finite Volume Method*. Pearson Education Limited, 2007. ISBN 9780131274983.
- [12] N.J. Georgiadis, D.P. Rizzetta, and C. Fureby. Large-Eddy Simulation: Current Capabilities, Recommended Practices, and Future Research. *AIAA journal*, 48(8):1772–1784, 2010.
- [13] S.B. Pope. *Turbulent Flows*. Cambridge University Press, 2000. ISBN 9780521598866.
- [14] E. de Villiers. *The Potential of Large Eddy Simulation for the Modelling of Wall Bounded Flows*. PhD thesis, University of London, 2007.
- [15] W. Schoppa and F. Hussain. Coherent structure dynamics in near-wall turbulence. *Fluid Dynamics Research*, 26(2): 119–139, 2000.
- [16] L. Eça, G. Vaz, and M. Hoekstra. On the Role of Iterative Errors in Unsteady Flow Simulations. In *21st Numerical Towing Tank Symposium (NuTTS'18), Cortona, Italy*, 2018.
- [17] J. Brouwer, J. Tukker, and M. Van Rijsbergen. Uncertainty analysis and stationarity test of finite length time series signals. In *The 4th International Conference on Advanced Model Measurement Technology for the Maritime Industry (AMT15), Istanbul, Turkey*, 2015.

V_{π} LES- VORTEX PARTICLE INTENSIFIED LARGE EDDY SIMULATION

S. Samarbakhsh* and N. Kornev†

Chair of modeling and simulation
University of Rostock
Rostock, Germany

*e-mail: sina.samarbakhsh@uni-rostock.de

†e-mail: nikolai.kornev@uni-rostock.de

Key words: LES, subgrid model, meshless method, free jet, hybrid Eulerian/Lagrangian method

Abstract. This paper presents the progress in the development of a novel numerical technique which utilizes the combination of grid based and grid free computational methods. This novel Large Eddy Simulation approach with a direct resolution of the subgrid motion of fine concentrated vortices. The method, proposed first by [10], is based on combination of a grid based and the grid free computational vortex particle (VPM) methods. The large scale flow structures are simulated on the grid whereas the concentrated structures are modeled using VPM. Due to this combination the advantages of both methods are strengthened whereas the disadvantages are diminished. The procedure of the separation of small concentrated vortices from the large scale ones is based on LES filtering idea. The flow dynamics is governed by two coupled transport equations taking two-way interaction between large and fine structures into account. The fine structures are mapped back to the grid if their size grows due to diffusion. Algorithmic aspects specific for three dimensional flow simulations are discussed. Validity and advantages of the new approach were illustrated for a well tried benchmark test of the decaying homogeneous isotropic turbulence and turbulent free jet flow. The aim of this paper is to present some new results on the possibility of the model reduction and explanation of the anisotropy of fine scale vortices.

1 INTRODUCTION

Insufficient resolution of fine vortex structures in turbulent flows is one of the key problems in Computational Fluid Dynamics (CFD). The most advanced and popular technique to resolve multi scale flow structures is the Large Eddy Simulation (LES) which is based on the idea of scale decomposition into large and small ones. While the large eddies are directly resolved on the grid, the effect of small vortices is taken into account through a subgrid stress (SGS) model.

The subgrid motion is not resolved in LES but rather it is modelled using different functional and structural approaches. However, there are many problems which require direct representation of the subgrid motion to simulate, for instance, mixing or particle dynamics in turbulent

flows. In our previous papers (see [11, 9, 16, 10, 12]), we propose a simulation technique resembling LES with an effort to directly reproduce the subgrid motion at least in the statistical sense. It is suggested to apply a hybrid grid and particle based method, utilizing a combination of the finite volume and computational vortex particle (VPM) (see [5]) methods. The large scale field is represented on the grid like in LES, whereas the small scale one (subgrid field) is calculated using the VPM. The new method called $V\pi$ LES is a purely Lagrangian one for small structures and purely grid based one for large scale structures.

The method is based on the decomposition of the velocity \mathbf{u} and vorticity fields $\boldsymbol{\omega}$ into the distributed large scale (upper index 'g') and concentrated small scale (upper index 'v') fields:

$$\mathbf{u}(\mathbf{x}, t) = \mathbf{u}^g(\mathbf{x}, t) + \mathbf{u}^v(\mathbf{x}, t), \boldsymbol{\omega}(\mathbf{x}, t) = \boldsymbol{\omega}^g(\mathbf{x}, t) + \boldsymbol{\omega}^v(\mathbf{x}, t) \quad (1)$$

The fine vortex detection procedure utilizes the Large Eddy Simulation (LES) filtration applied to the grid based velocity field \mathbf{u}^g :

$$\bar{\mathbf{u}}^g(\mathbf{x}, t) = \int_{-\infty}^{\infty} \mathbf{u}^g(\mathbf{s}, t) F(\mathbf{x} - \mathbf{s}) d\mathbf{s} \quad (2)$$

where $F(\mathbf{x} - \mathbf{s})$ is a certain filter function. The small scale velocity field \mathbf{u}' calculated as the difference between the original and filtered fields

$$\mathbf{u}'(\mathbf{x}, t) = \mathbf{u}^g(\mathbf{x}, t) - \bar{\mathbf{u}}^g(\mathbf{x}, t) \quad (3)$$

should be approximated by vortex particles in regions of concentrated vortices which are detected using any vortex identification criteria, for instance, λ_{ci} ([1]). The cells with $\lambda_i > \lambda_{ci, min}$ contain the vortices which in principle can be converted to vortex particles. Such cells are marked as active ones using the $\lambda_{i, active}$ field:

$$\lambda_{i, active} = \begin{cases} 1, & \text{if } \lambda_{ci} > \lambda_{ci, min} \\ 0, & \text{otherwise} \end{cases} \quad (4)$$

where $\lambda_{ci, min}$ is a certain small value introduced in order to limit the number of particles.

To keep the required computational resources on an acceptable level, only small vortices with size proportional to the local cell size Δ are to be converted to single vortex particles. Neighboring cells which all have $\lambda_{i, active} = 1$ form large vortices. For them it is supposed that the larger vortices with scales of a few Δ can accurately be represented on the grid. Therefore the next task is to detect cells with fine vortices. According to our algorithm, all neighboring cells of the i -th cell are checked for the condition $\lambda_{ci} > \lambda_{ci, min}$. If all neighbors fulfill this condition, we identify a cell cluster which remains on the grid and all its cells become non-active $\lambda_{i, active} = 0$. Only vortices in cells keeping $\lambda_{i, active} = 1$ are to be replaced by vortex particles.

At each cell with $\lambda_{i, active} = 1$ the new vortex particle is introduced at the cell center if the permissible number of vortex particles per cell N_{pt} is not exceeded. Otherwise, the new vortex replaces the cell's weakest one. The number N_{pt} was introduced to keep the total number at a reasonable level. This restriction is conform with the concept that the largest contribution to the subgrid kinetic energy is made by a small fraction of the strongest vortices. The radius of

the new vortex is set as $\sigma = \beta Vol_i^{1/3}$, where β is the overlapping ratio which is taken as $\beta = 2$ and Vol_i is the volume of the i -th cell. A thorough analysis of the influence of N_{pt} and $\lambda_{ci,min}$ for the jet case is given in [12] in Sec. 4.3.5. The vortex particle strength is calculated as

$$\boldsymbol{\alpha} = Vol_i \boldsymbol{\omega}^v = Vol_i (\nabla \times \mathbf{u}') \quad (5)$$

The velocity $\mathbf{u}^v(\mathbf{x}, t)$, induced by the vortex particles, is calculated at grid points \mathbf{x} using the Biot-Savart law

$$\mathbf{u}^v(\mathbf{x}, t) = \frac{1}{4\pi} \nabla \times \int_{FlowVolume} \frac{\boldsymbol{\omega}^v(\boldsymbol{\xi}, t)}{|\mathbf{x} - \boldsymbol{\xi}|} dV(\boldsymbol{\xi})$$

and subtracted from the grid velocity $\mathbf{u}^{g,new} = \mathbf{u}^g - \mathbf{u}^v$. Thus, the total velocity at grid points $\mathbf{u}^{g,new} + \mathbf{u}^v = \mathbf{u}^g$ remains constant after the vortex particle generation procedure.

A thorough validation and verification study is performed for wall free flows including decaying isotropic turbulence (DIT) [4] (see results in [12]) and free turbulent jet [8, 2] (see results in [15]) test cases. The aim of this paper is to present some new results on the possibility of the model reduction and explanation of the anisotropy of fine scale vortices.

2 GOVERNING EQUATION

The evolution of vortex particles and large scale flow represented on the grid is described by a system of two coupled transport equations derived in [9, 10, 12] for incompressible isothermal flows:

$$\frac{\partial \mathbf{u}^g}{\partial t} + (\mathbf{u}^g \cdot \nabla) \mathbf{u}^g = -\frac{1}{\rho} \nabla p^g + \nu \Delta \mathbf{u}^g + \overline{\mathbf{u}^v \times \boldsymbol{\omega}^g} \quad (6)$$

$$\frac{d\boldsymbol{\omega}^v}{dt} = (\boldsymbol{\omega}^v \cdot \nabla)(\mathbf{u}^v + \mathbf{u}^g) + \nu \Delta \boldsymbol{\omega}^v + \nabla \times [\mathbf{u}^v \times \boldsymbol{\omega}^g - \overline{\mathbf{u}^v \times \boldsymbol{\omega}^g}], \quad (7)$$

The sum of the curl of the first equation and the second equation retrieves the original Navier Stokes equation written in the form of the vorticity transport equation. The first equation (6) is coupled with the second one (7) through the additional term $\overline{\mathbf{u}^v \times \boldsymbol{\omega}^g}$ whereas the coupling of the second equation with the first one is due to the terms $(\mathbf{u}^g \cdot \nabla) \boldsymbol{\omega}^v$, $(\boldsymbol{\omega}^v \cdot \nabla) \mathbf{u}^g$ and $\nabla \times [\mathbf{u}^v \times \boldsymbol{\omega}^g - \overline{\mathbf{u}^v \times \boldsymbol{\omega}^g}]$. The equations (6) and (7) are solved sequentially. The first equation is solved on the grid whereas the second one uses the grid free Vortex Particle Method (VPM) [5]. The physical meaning of the coupling term $\overline{\mathbf{u}^v \times \boldsymbol{\omega}^g}$ is explained in [10]. The vortex particle displacement is calculated from the trajectory equation

$$\frac{d\mathbf{r}_i}{dt} = \mathbf{u}_i^g + \mathbf{u}_i^v, \quad (8)$$

where i is the particle number. Computation of the velocity induced by vortex particles \mathbf{u}^v is performed with the direct summation of the Bio-Savart law taking into account one or two layers of neighboring cells. Only induction of the neighboring points is taken into account because the velocity \mathbf{u}^v is much less than \mathbf{u}^g and it is mostly determined by interaction of neighboring particles lying at a short distance. The justification of this simplification presented in [12] is that the correlation between neighboring small scale vortices is weak and they are well

separated. This simplification can be considered as a kind of model which results in a very fast computational procedure of a local character suitable for parallel calculations.

The velocity induced by a vortex particle can be calculated from the formula

$$\mathbf{u}_p^v = \frac{1}{4\pi} \frac{\boldsymbol{\alpha} \times \boldsymbol{\xi}}{\xi^3} (1 - e^{-\xi^3/\sigma^3}) \quad (9)$$

proposed by [14]. Here α and σ are the strength and the radius of a vortex particle, which are defined below. The velocity induced by a set of particles \mathbf{u}^v is calculated as the sum of \mathbf{u}_p^v . It should be noted that the technique presented here is independent of any specific choice of vortex particles. Particularly, a set of functions introduced in [13] can be used within the present method.

3 NUMERICAL SOLUTION OF THE EQUATIONS (7) AND (8) USING THE VPM

Instability of numerical solution of the equation (7) caused by the stretching term $(\boldsymbol{\omega} \cdot \nabla)\mathbf{u}$ is the most important problem of the VPM along with the computation of the velocity \mathbf{u}^v . In grid based methods with low and moderate order schemes, the action of the stretching is effectively counterbalanced by the numerical viscosity which is very low in Lagrangian vortex particle methods. Theoretically, a stable VPM solution can be obtained by increasing the accuracy of the stretching and diffusion simulation which can be attained by a high number of vortex particles and high temporal resolution. Both make the method impractical at least for high Reynolds numbers. After many efforts the authors settled on the algorithm which was originally proposed by [7] and modified in [12]. This algorithm consists of the following substeps:

- Calculation of the change of the vorticity strength magnitude

$$\frac{d|\boldsymbol{\omega}^v|}{dt} = \frac{d\sqrt{\boldsymbol{\omega}^v \cdot \boldsymbol{\omega}^v}}{dt} = \frac{\boldsymbol{\omega}^v}{|\boldsymbol{\omega}^v|} \cdot \frac{d\boldsymbol{\omega}^v}{dt} \quad (10)$$

where $\frac{d\boldsymbol{\omega}^v}{dt}$ is calculated from (7) without the viscous diffusion term. The term $(\boldsymbol{\omega}^v \cdot \nabla)\mathbf{u}^v$ is calculated taking into account adjacent vortex particles located only within one or two layers of neighboring cells.

- Calculation of the particle length from the equation of the elementary section dl transported in inviscid flow

$$\frac{dl}{dt} = \frac{l}{|\boldsymbol{\omega}^v|} \frac{d|\boldsymbol{\omega}^v|}{dt} \quad (11)$$

- Calculation of the particle core radius from the equation describing the transport of an elementary tube with length l and radius σ in inviscid flow

$$\frac{d\sigma}{dt} = -\frac{\sigma}{2l} \frac{dl}{dt} \quad (12)$$

- Consideration of the viscosity influence using the core spreading method (CSM) (see [5]). The particle core radius is increased by $\Delta\sigma$:

$$\Delta\sigma = \sqrt{4\nu\Delta t} \quad (13)$$

- Calculation of the new particle orientation

$$\boldsymbol{\omega}^* = \boldsymbol{\omega}^v(t) + \frac{d\boldsymbol{\omega}^v}{dt} \Delta t \quad (14)$$

- Calculation of the particle strength magnitude from [7]

$$|\boldsymbol{\alpha}(t + \Delta t)| = |\boldsymbol{\alpha}(t)| \frac{\sigma(t + \Delta t)}{\sigma(t)} \quad (15)$$

- Calculation of the new strength vector

$$\boldsymbol{\alpha}(t + \Delta t) = |\boldsymbol{\alpha}(t + \Delta t)| \frac{\boldsymbol{\omega}^*}{|\boldsymbol{\omega}^*|} \quad (16)$$

In the original version proposed by [7] the next step should be the redistribution of particles whose length has doubled. According to our experience the redistribution results in an avalanche-like increase of the vortex particles number in areas of strong stretching. To prevent this [7] proposed a special elimination procedure based on a knowledge of a threshold for the dissipation rate which is difficult to set in a general flow case. To develop a robust code, to obtain a stable solution and to keep the particle number in a reasonable range we avoid the redistribution procedure in our computations. Thus, the smallest vortices are removed. This reduces the range of scales that must be resolved in a numerical calculation. Such a reduction, as pointed out by [3], is an immanent part of every turbulence model.

There is a permanent exchange between the small vortices and large scale ones represented on the grid. Large scale vortices become small due to stretching and are converted to particles. If particles grow due to viscosity and flow stagnation and exceed some size they are mapped back to the grid. The simple Euler method is used for the integration of the differential equations. The flowchart of the whole algorithm is presented in [12].

The present method has the same error sources as every LES model [6]. Two comments should be made on the filtering errors. First, the authors understand that the models relying on the small scales comparable with cell sizes can suffer from the filter aliasing errors inherently presented in each numerical method. For instance, such errors most strongly affect dynamic type models which rely heavily on the smallest scales to determine SGS properties [6]. Second, since our algorithm does not use commutation of differencing and filtering operators which is the big difficulty in LES formalism and represents the second part of the filtering errors, the commutation error is not present.

4 RESULT AND DISCUSSION

4.1 Summary of previous results

Validation and verification performed for wall free flows including decaying isotropic turbulence and free turbulent jet test cases revealed the following facts:

- The effect of the term $\overline{\mathbf{u}^v \times \boldsymbol{\omega}^g}$ in the equation (7) is similar to that of a LES subgrid model. At coarse resolutions, it acts as a diffusive Large Eddy Simulation subgrid model resulting in a LES-like behavior of the whole method.

- The energy back scattering is captured by the present method. As mentioned in [15], the intensification of the turbulent kinetic energy due to back scattering is proved to be very important to properly reproduce the jet breakdown and transition to turbulence close to the nozzle without any artificial turbulence forcing at the nozzle.

- The term $\overline{\mathbf{u}^v \times \boldsymbol{\omega}^g}$ is automatically switched off when the resolution increases, i.e. the present method is consistent and converges to the Direct Numerical Simulation.

- In the laminar flows the vortex particle influence is automatically switched off because of reduction of vortex particles population and weakening their strengths in the smooth laminar velocity fields.

- The Reynolds stresses of the velocity field induced by particles possess the pronounced anisotropy which is space dependent.

- The model for the jet case can be sufficiently reduced by neglecting the inner interaction between particles. This results in a drastic reduction of the computational time.

Some additional results on the model reduction and anisotropy Reynolds stresses are given in this section. The results are obtained for the free jet at the Reynolds number $Re = 10^4$ based on the jet center line velocity at the nozzle $U_j = 1\text{m/s}$ and the nozzle diameter $D = 0.01\text{m}$, i.e. $Re = U_j D / \nu$. Description of the grid with $1.5 \cdot 10^5$ cells and numerical setup are thoroughly described in [15].

4.2 Model reduction

As shown in [12] the equations (7) and (8) can sufficiently be reduced by neglecting inner interaction between vortex particles without a significant loss of the simulation accuracy. The reduced equations take the form:

$$\frac{\partial \boldsymbol{\omega}^v}{\partial t} + (\mathbf{u}^g \cdot \nabla) \boldsymbol{\omega}^g = (\boldsymbol{\omega}^v \cdot \nabla) \mathbf{u}^g + \nu \Delta \boldsymbol{\omega}^v, \quad (17)$$

and the r.h.s of the trajectory equation (18) contains only the grid based velocity

$$\frac{d\mathbf{r}_i}{dt} = \mathbf{u}_i^g \quad (18)$$

As demonstrated in [12], the influence of inner interactions on spatially averaged kinetic energy and scalar dissipation rate is relatively weak and can be neglected in the calculation. Thereby the computations can be done sufficiently faster. This model is further referred to as the passive vortices model. Within the next simplification step the influence of the grid based solution on the evolution of vortex particles strengths is neglected. The equations describing the vortex particle evolution take the simplest form:

$$\frac{\partial \boldsymbol{\omega}^v}{\partial t} + (\mathbf{u}^g \cdot \nabla) \boldsymbol{\omega}^g = \nu \Delta \boldsymbol{\omega}^v, \quad (19)$$

$$\frac{d\mathbf{r}_i}{dt} = \mathbf{u}_i^g \quad (20)$$

Figure 1-a demonstrates results for the r.m.s. of the axial velocity obtained using the full model equations (7) and (8), passive vortices model equations (17) and (18) and the model

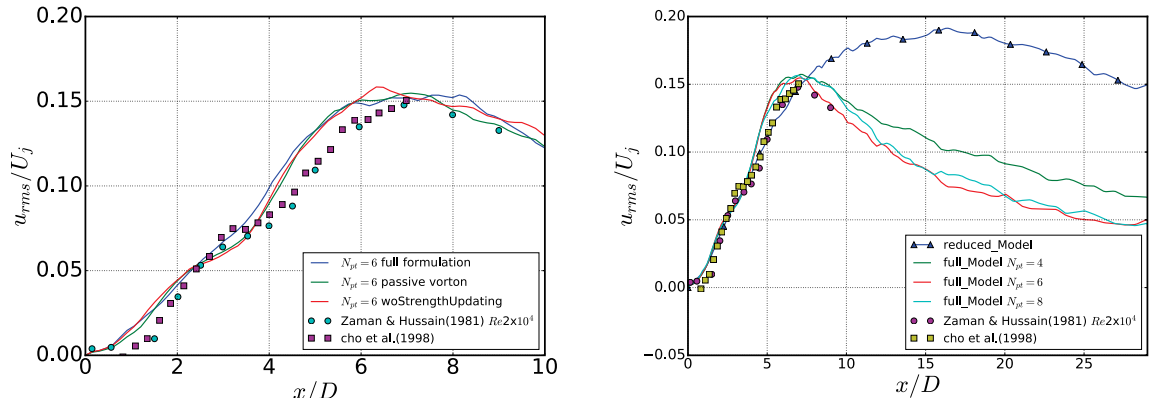


Figure 1: Influence of the model reduction on the evolution of u_{rms} along the jet centerline. Full formulation- Eqs. (7) and (8), passive vortices- Eqs. (17) and (18), woStrengthUpdating -Eqs. (19) and (20), reduced model- rudimentary model with consideration of only new generating vortices.

without influence of the grid based flow on vortex particles strengths (19) and (20). The difference between all results is negligible pointing out that vortex particles serve just as triggers or intensifiers of turbulence and their inner interaction doesn't contribute sufficiently to the flow evolution. Hence the name of the method is the LES intensified by the vortex particles or $V\pi$ LES.

In the next step of model reduction only the influence of vortex particles generated in the current time step are considered and vortex particles generated in the previous time step were mapped back to the grid. If it would work, the whole modeling approach described above can be neglected and just a small perturbation caused by new generating vortices would be enough to trigger the turbulence on a proper level. The motion and strengths change of vortices is not considered. The time of computations would be the smallest among all models since the resulting model becomes rudimentary. As can be seen in Figure 1-b the result shows that the vortex particles trigger the turbulence and have a good agreement with experiment in the near jet exit region while in the far field region decay of the kinetic energy is not proper. It can be interpreted in this way that the energy drain of fine scale motion from large scale motion is not high enough and accumulation of kinetic energy on the grid flow motion happens. Concluding, not only new generated vortices but also the whole set of vortices including those generated upstream in previous time steps have a significant influence on the turbulence development downstream. With other words, the fine scale vortices model (7) and (8) can be reduced but not neglected.

4.3 Anisotropy of fine scale structures induced by vortex particles

Since a deterministic prediction of a turbulent flow as mentioned in the definition of the turbulent motion by Lesieur (1997) is practically impossible, the task of every SGS model is to reproduce the subgrid motion only in the statistical sense. The following features of the subgrid motion should be captured by a proper subgrid model: non-equilibrium effects including laminar-turbulent zones, energy backscatter and anisotropy of fine scale motion. In this subsection the

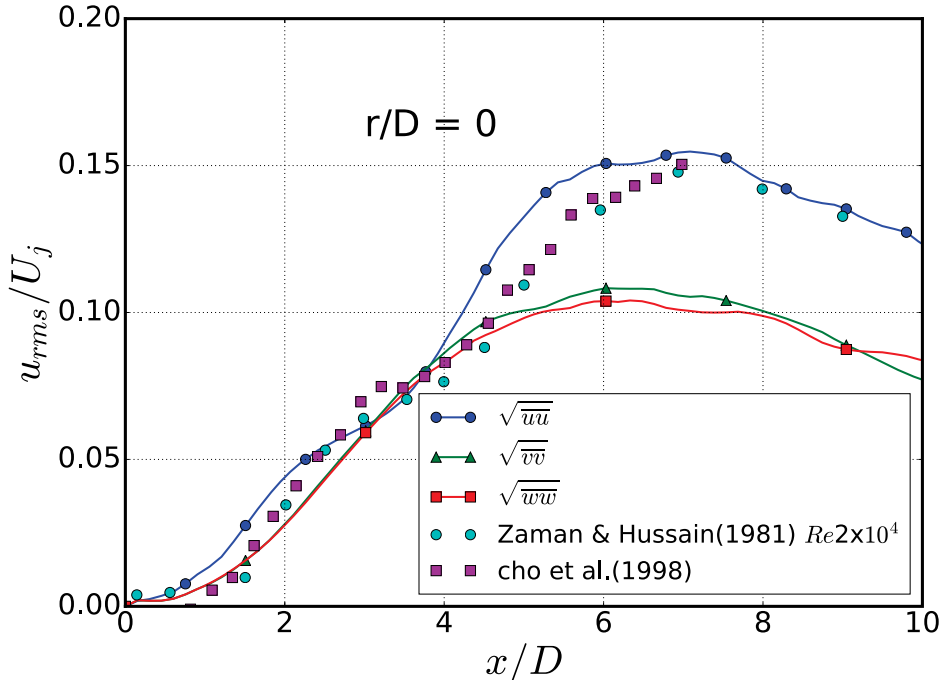


Figure 2: Distribution of the diagonal Reynolds stress components for the total velocity $\mathbf{u}^g + \mathbf{u}^v$ along the jet axis. Symbols show experimental data.

anisotropy of velocities induced by fine vortices is discussed.

The total flow shows a well pronounced anisotropy with the dominance of the axial fluctuations on the jet centerline (see Fig. 2). Reynolds stresses R_{ii}^v of the velocity field \mathbf{u}^v shows also a clear anisotropy which is space-dependent. On the center line at $x/D > 5$ two diagonal stresses are equal to each other $R_{22}^v \approx R_{33}^v$ and dominate over R_{11}^v (see Fig. 3). To explain this effect, we consider stochastic distribution of the statistically independent axis-symmetric vortex particles on the centerline with strengths aligned with the x-axis. They induce velocities $u_x^v = 0$ and $u_y^v \neq 0, u_z^v \neq 0$. Due to axis symmetrical character of each vortex the spatially averaged squares of velocities u_y^v and u_z^v are equal, i.e. $\overline{(u_y^v)^2} = \overline{(u_z^v)^2}$. Precession of vortices around their spins causes the appearance of the longitudinal velocities u_x^v which are much smaller than u_y^v and u_z^v . Thus, the jet axis area at $x/D > 5$ is populated by vortex particles with axes predominantly oriented along the jet propagation or mean flow direction. At $x/D < 5$ on the centerline and at $r/D = 0.25$ the fine scale turbulence is nearly isotropic $R_{11}^v \approx R_{22}^v \approx R_{33}^v$ in the beginning of the jet development (see Fig. 4-a), i.e. this area is populated with vortex particles with orientations uniformly distributed around a sphere. Further downstream the same anisotropy takes place as that on the jet axis. At the jet boundary the fine scale turbulence becomes anisotropic with a clear dominance of the radial fluctuations $R_{22}^v > R_{11}^v \approx R_{33}^v$ (see Fig. 4-b), i.e. the dominating fluctuations are in the direction of the dominating large scale entrainment motion.

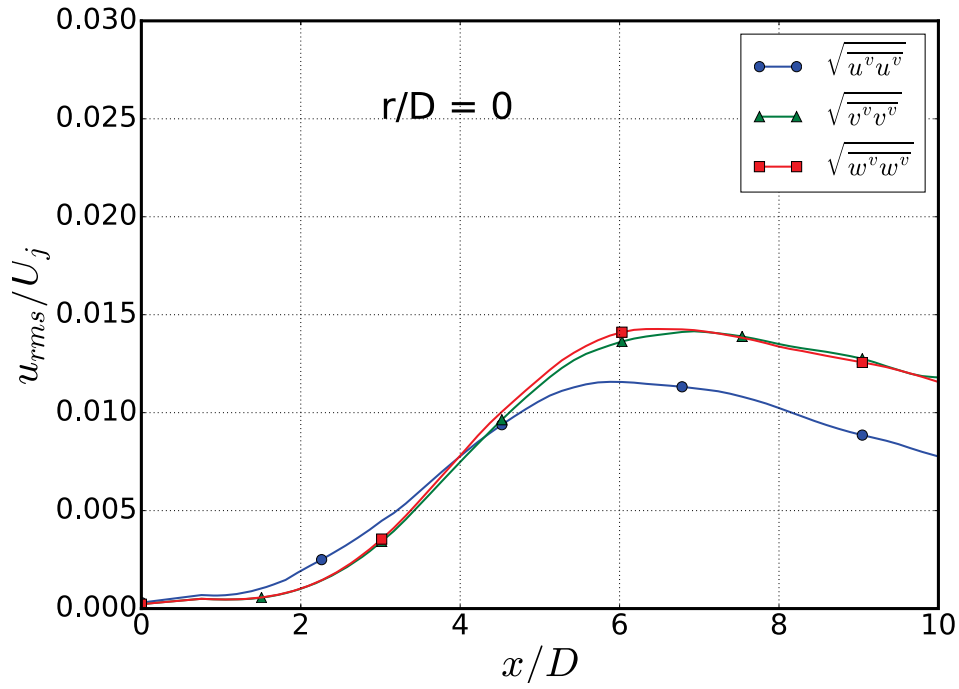


Figure 3: Distribution of the diagonal Reynolds stress components for the fine scale velocity \mathbf{u}^v along the jet axis

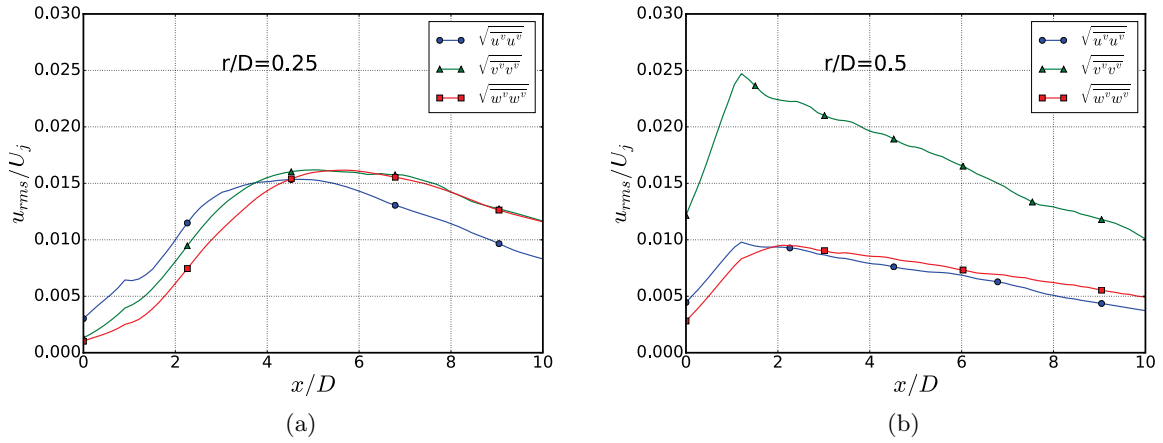


Figure 4: Distribution of the diagonal Reynolds stress components for the fine scale velocity \mathbf{u}^v along the line $r/D = 0.25$ and $r/D = 0.5$

5 CONCLUSION

The paper presents validation and verification study of a novel $V\pi$ LES method which is based on the decomposition of the flow structures in large scale ones, resolved on the grid, and small scale ones, represented by vortex particles (see also [10] and [12]). In this paper it was shown that the model can be sufficiently reduced. However, the reduction has a certain limit. The inner interaction between vortices and the influence of large scales on strengths of fine vortices can be neglected. This results in a very efficient and fast computational procedure. However, the whole fine scale vortices model (7) and (8) can not be neglected. The Reynolds stress of the velocity field induced by particles possesses a pronounced anisotropy which is space dependent. The next task is the validation of $V\pi$ LES for wall bounded flows which will be considered in future works of the authors.

REFERENCES

- [1] CHAKRABORTY, P., BALACHANDAR, S., AND ADRIAN, R. On the relationships between local vortex identification schemes. *Journal of Fluid Mechanics* 535 (2005), 189–214.
- [2] CHO, S. K., YOO, J. Y., AND CHOI, H. Vortex pairing in an axisymmetric jet using two-frequency acoustic forcing at low to moderate Strouhal numbers. *Experiments in Fluids* 25, 4 (1998), 305–315.
- [3] CHORIN, A. *Vorticity and turbulence*. Springer, 1994.
- [4] COMTE-BELLOT, G., AND CORRIN, S. Simple Eulerian time correlation of full-and narrow-band velocity signals in grid-generated, isotropic turbulence. *Journal of Fluid Mechanics* 48, 2 (1971), 273–337.
- [5] COTTET, G., AND KOUMOUTSAKOS, P. *Vortex Methods: Theory and Practice*. Cambridge University Press, 2000.
- [6] DE VILLIERS, E. *The Potential of Large Eddy Simulation for the Modeling of Wall Bounded Flows*. PhD thesis, Imperial College of Science, Technology and Medicine, 2006.
- [7] FUKUDA, K., AND KAMEMOTO, K. Application of a redistribution model incorporated in a vortex method to turbulent flow analysis. In *Proceedings of the 3rd International Conference on Vortex Flows and Vortex Models (ICVFM2005)* (Yokohama, Japan, 2005).
- [8] HUSSAIN, A. F., AND ZAMAN, K. B. M. Q. The preferred mode of the axisymmetric jet. *J. Fluid Mech.* 110 (1981), 39–71.
- [9] KORNEV, N. Improvement of vortex resolution through application of hybrid methods. In *Proceedings of the 6th International Conference on Vortex Flows and Vortex Models, Nagoya, Japan* (2014).
- [10] KORNEV, N. Hybrid method based on embedded coupled simulation of vortex particles in grid based solution. *Computational Particle Mechanics* 5, 3 (2018), 269–283.

- [11] KORNEV, N., AND JACOBI, G. Development of a hybrid approach using coupled grid-based and grid-free method. In *Proc. Int. Conf. Marine Engineering, Hamburg* (2013), p. Paper 292.
- [12] KORNEV, N., AND SAMARBAKHSHL, E. Large Eddy Simulation with direct resolution of subgrid motion using a grid free vortex particle method. *International Journal of Heat and Fluid Flow* 75 (2019), 86–102.
- [13] LEONARD, A., AND WINCKELMANS, G. Contribution to vortex particle methods for the computation of three-dimensional incompressible unsteady flows. *J. Comput. Phys.*, 109 (1993), 247–273.
- [14] MOSHER, M. A method for computing three dimensional vortex flows. *Zeitschrift für Flugwissenschaften* 9, 3 (1985), 125–133.
- [15] SAMARBAKHSH, E., AND KORNEV, N. Simulation of the free jet using the vortex particle intensified LES ($V\pi$ LES). *International Journal of Heat and Fluid Flow*, submitted (2019).
- [16] SAMARBAKHSH, S., AND KORNEV, N. Hybrid method based on embedded coupled simulation of vortex particles in grid solution. In *Proceedings of the 7th International Conference on Vortex Flows and Models, Rostock, Germany* (2016).

BIO-INSPIRED PROPULSION IN OCEAN ENGINEERING: LEARNING FROM NATURE

GUANGYU SHI[†], RUOXIN LI[†] AND QING XIAO^{†*}

[†] Department of Naval Architecture, Ocean and Marine Engineering,
University of Strathclyde, Glasgow, G4 0LZ, UK

* Corresponding author: qing.xiao@strath.ac.uk

Key words: Biomimetics, Propulsion, Locomotion, Multi-Body Dynamics, Fluid-Structure Interaction

Abstract. In this paper, the CFD technology widely used in biomimetic applications is firstly reviewed in a brief manner. We then present two types of computational models employed in studies of ray-finned fishes: single-fin model and body-fin model. The single-fin models capture some key features possessed by real fish fins, such as anisotropic property, flexible rays and actively controlled curvature. In the body-fin models, the fish motion can be either prescribed or predicted. Fish models with prescribed motions are usually employed to provide insights in the hydrodynamics while those models with predicted motions can be used to investigate the stability and maneuvering problems.

1 INTRODUCTION

With over 500 million years of evolution, fishes have diversified into a great variety of aquatic habitats and display a diversity of locomotion modes. It is not surprising that engineers seek inspirations from fish when designing autonomous underwater vehicles. Among all kinds of fishes, the ray-finned fishes distinguish themselves from others by the presence of multiple fins featured by the soft membrane embedded with bony rays. By the effective coordination of body and multiple fins, ray-finned fishes exhibit great abilities in the locomotion, maneuvering and stabilizing, which inspired a further industry development in underwater vehicles. Therefore, the study on the ray-finned fishes is attracting increasing attention due to its promising application in the design of underwater vehicles.

Generally, the study methods of ray-finned fishes can be divided into two groups: physical experiment and numerical modeling. The physical experiments can be carried out with either live fishes or robotic models (see some reviews in [1]–[6]). However, for experiments with live fishes, the effects of individual traits are difficult to be isolated and the fishes are limited to extant species. The mechanical fish models can be good alternatives to live fishes for research; however, they are constraint by the availability of practical materials. Compared with physical experiments, numerical simulations have the following advantages: 1) it is able to explore large parameter matrix; 2) it could provide holographic information of the flow field; 3) it is able to examine ‘what if’ type of questions. Therefore, numerical modeling has become an indispensable approach for the functional study of fish locomotion.

In this paper, we mainly focus on the numerical simulations of the ray-finned fish. The CFD technology (including flow models, moving mesh and coupling methods) commonly

used in simulations of biomimetic problems is briefly reviewed in Section 2. Then we present two types of computational models for the functional study of ray-finned fishes in Section 3. Conclusions are given in the final section.

2 CFD TECHNOLOGY

With the rapid advancement in high-performance computers and the availability of sophisticated numerical methods, CFD simulation is playing more important role in scientific research as well as industrial applications. The CFD simulations have the advantages in providing both spatially and temporally resolved, detailed flow field analysis [7], which may provide insights into physical problems. In this section, the various flow models, mesh manipulation approaches and coupling methods with other fields are briefly reviewed.

2.1 Flow modeling

(1) Inviscid flow

The inviscid flow simulations are computationally inexpensive and allow researchers to quickly estimate the fluid load and other flow features in a large parameter space. However, these methods possess inherent weakness due to the neglect of viscous effects. This is because the fact that most of biomimetic flows are often dominated by flow separation as well as vortex interactions, which are resulted from viscous effects. Thus, the absence of the flow viscosity may lead to inaccurate results. Examples of using these methods to study biomimetic problems can be found in [8]–[11].

(2) Viscous flow

Within the context of biomimetic flows, the dynamics of the viscous fluid is governed by Navier-Stokes equations. The inclusion of the viscosity leads to more complicated flow phenomena (e.g., boundary-layer separation, transition and turbulence) and makes the simulation of fluid dynamics much more difficult, especially the modeling of turbulence. For certain circumstances at low and intermediate Reynolds number regimes, the turbulent effect is trivial, i.e., laminar simulations are sufficient, see example in [12]–[16]. For cases where the turbulence plays an important role (e.g., Reynolds number is of order of 10^4 or greater), proper turbulence models (e.g., *RANS*, *DES*, *LES*) must be used [17]–[19].

2.2 Mesh manipulation

To numerically solve the Navier-Stokes equations, a grid system is usually needed for discretization. For biomimetic problems which usually involve large body motions and/or deformations, the grid for CFD simulations also needs to be deformed or regenerated in order to deal with the moving boundaries. Generally, three types of grid systems are often used for the simulations of biomimetic flows: body-fitted grid, overset grid and Cartesian grid.

(1) Body-fitted grid

A body-fitted grid, which conforms to the wet boundaries of the body, can be either structured or unstructured. A structured grid can only be composed of hexahedral cells and all grid cells are organized in such a way that they can be accessed via i, j, k indices in three

directions. However, generating a single structured grid for a complex geometry is challenging and even impossible. To tackle this problem, a multi-block structured grid is usually generated for complex geometries, where the computational domain is decomposed into large hexahedral blocks which are discretized using structured grid method. Nevertheless, multi-block grid generations for complex geometries still require plenty of time and user experience. On the contrary, unstructured grids which consist of cells of arbitrary shapes are more suitable for complex geometries. In unstructured grids, all cells must be arranged into a one-dimensional array and a connectivity list which provides the information of number of neighbors and their corresponding positions is also required.

For biomimetic systems which involve only small or medium body deformations, moving grid algorithms for both structured and unstructured can be adopted. However, for the problems involving large body deformations and/or multiple bodies in relative motion, the CFD grids need to be regenerated, which usually requires much additional computational efforts.

(2) Overset grid

The concept of overset grid was initially proposed to alleviate the complexity of generating structured grids over complex geometries and handle cases involving multiple bodies with relative motion [20]. It was then extended to unstructured grids [21]. In overset grids, the complex geometry is usually decomposed into several components and a body-fitted subgrid is generated for each component. To establish the connectivity and then interpolate flow variables between different subgrids, an additional piece of code is needed. The creation of the domain-connectivity could be a time-demanding process, especially for unsteady flow simulations. Besides, overset grid methods do not solve the problems associated with large body deformations due to the fact that a body-fitted grid is generated for each component. A compromise solution is to combine the overset grid method with the remesh technique, where only subgrids involving large deformations need to be regenerated. Examples using overset grid methods to study biomimetic problems can be found in [14]–[16].

(3) Cartesian grid

The immersed boundary method solves the Navier-Stokes equations on stationary Cartesian grids, which requires no mesh deformation or regeneration when dealing with moving boundaries. Therefore, this method is well suited for bio-hydrodynamic flow simulations involving complex geometries and large body deformations (see examples in [12], [13], [22], [23]).

2.3 Multi-physics coupling

Many biological systems contain flexible structures, where the fluid-structure interaction may play an important role. To simulate the problems involving elastic structures, the CFD solvers need to be coupled with structural solvers. The coupling is usually accomplished within a partitioned framework, where the flow and solid equations are discretized and solved independently. With a partitioned method, the coupling can be either explicit [24] or implicit [25]. The advantages of using explicit schemes are implementing simplicity and computational efficiency, because no sub-iteration is required within each time step. However,

the numerical stability of explicit method is strictly limited by a stability condition [26]. To remove the stability condition, the implicit coupling methods must be employed. But the implicit schemes introduce sub-interactions within one time step to achieve the equilibrium at the fluid-structure interface, which greatly increases the computational cost. For examples of biomimetic simulations involve fluid-structure interactions, please refer to [8], [9], [11], [14], [16], [23].

In some studies, researchers are more interested in self-propelled swimming, where CFD solvers need to be coupled with body-dynamics (BD) or multi-body-dynamics (MBD) codes [15], [27]. The coupling can be explicit or implicit, similar with the methods discussed above.

3 COMPUTATIONAL MODELS OF FISH LOCOMOTION

Morphologically, ray-finned fishes usually possess a flexible body with several different fins which can be categorized into two groups: median fins (dorsal, ventral and caudal) and paired fins (pectoral and pelvic). By coordinating the body undulation and fin movements, ray-finned fishes are able to generate locomotion force in various directions, thus can achieve high controllability and maneuverability to engage with the aquatic environment. Generally, the numerical studies of the ray-finned fish can be classified into two groups: (1) Single-fin model. This model focuses on the dynamics of an isolated fish fin. (2) Body-fin model. This model contains both the body and fins in order to investigate the possible body-fin and fin-fin interactions.

From the perspective of how the swimming motion is dealt with, the numerical studies of fish locomotion can also be divided into two major categories: (a) swimming with a prescribed motion; (b) self-propelled swimming, where the swimming speed and motion trajectory are treated as unknown variables predicted by the CFD simulation.

3.1 Single-fin model

The internal structures of fish fins are biologically complicated. They are composed of thin and soft membranes stiffened by bony fin rays. The bending stiffness of the membrane is negligible, thus the rigidity of a fin is primarily determined by the embedded rays. Due to the non-uniformity of bending stiffness of each ray and the difference between different rays, a ray-strengthened fin displays anisotropic structural properties [1]. Besides, each ray can be activated individually via the sophisticated musculature system attached to the rays. Moreover, a fin ray has a bio-laminar design and embedded tendons, which allow fishes to actively control the curvature and rigidity of each ray [28]. These features enable fishes to accomplish multi-degree-of-freedom (DOF) controls over the fin surfaces. However, these unique features are difficult to be modeled numerically. Traditionally, the fish fins are modeled as a rigid or elastic plate with two DOF motions (e.g., heave and pitch) [29]–[31]. But these models are considered to be oversimplified, thus may severely compromise the evaluated performance. In the present section, we present several numerical models working towards including some main characters of ray-supported fins.

Figure 1 illustrates several numerical fin models: (a) a rectangular ray-supported caudal fin; (b) a trapezoid ray-supported caudal fin; (c) a ray-supported pectoral fin; (d) a complex pectoral fin reconstructed from experimental measurement. With the rectangular caudal fin model (Figure 1 (a)), Shi et al. [16] presented a fluid-structure interaction model for the ray-

supported fish fins and studied the effects of various spanwise stiffness distributions on the propulsion performance of the caudal fin. In their study, the flow field was simulated by solving the unsteady Navier-Stokes equations while the rays were represented by nonlinear beams. The Reynolds number was fixed at $Re=1000$, thus no turbulence model was used. The fin was actuated by a sinusoidal sway motion at the front end and was deformed passively. The numerical results from their study indicated that the uniform stiffness distribution eventually led to a ‘cupping’ deformation and performed the best in terms of thrust generation and propulsion efficiency. The ‘cupping’ deformation induced by a cup stiffness distribution seemed to be over-cupped, thus experienced a rapid drop in thrust and propulsion efficiency at higher flexibility.

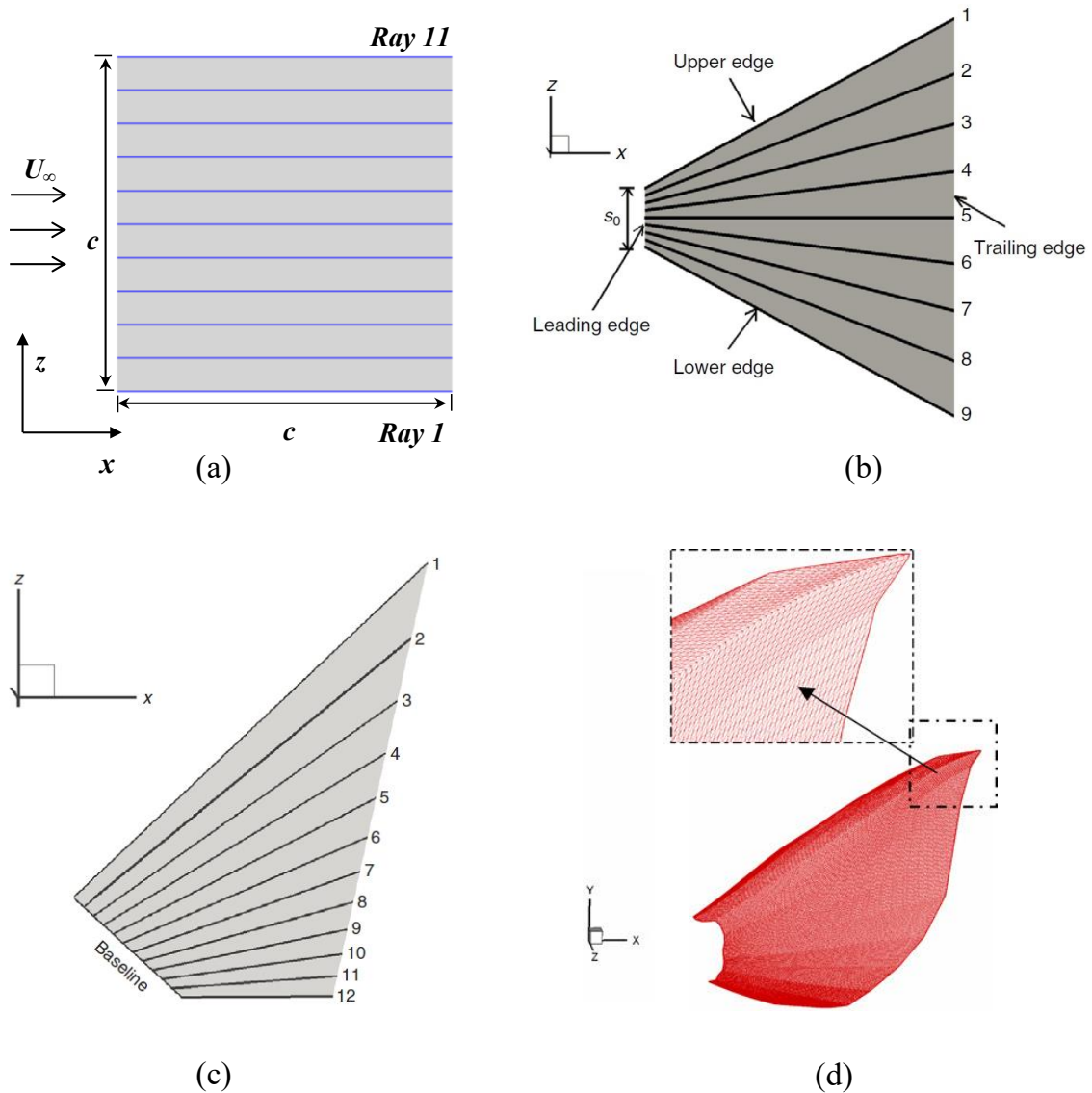


Figure 1 Various ray-fin models. (a) Caudal fin model of Shi et al. [16]. (b) Caudal fin model of Zhu and Shoele [8]. (c) Pectoral fin model of Shoele and Zhu [9]. (d) Pectoral fin model of Mittal et al. [22].

Zhu and Shoele [8] [9] developed two ray-strengthened fin models for a caudal fin with a combined sway and yaw motion (Figure 1 (b)) and a pectoral fin in labriform swimming (Figure 1 (c)). In both fin models, a potential flow solver was coupled with nonlinear beam models which structurally represented the fin rays. The general conclusions of their studies are that flexible rays are able to increase the propulsion efficiency and reduce the lateral force generation. Besides, the sensitivity of the fin performance to kinematic parameters is reduced due to the anisotropic property of the fin. In their pectoral fin case, they also found that with a reinforced leading edge, the performance of the pectoral fin was further improved. However, in their studies, the flow was assumed to be inviscid. Thus, the vortices shed in locations other than the trailing edge were not considered, which may lead to inaccurate result.

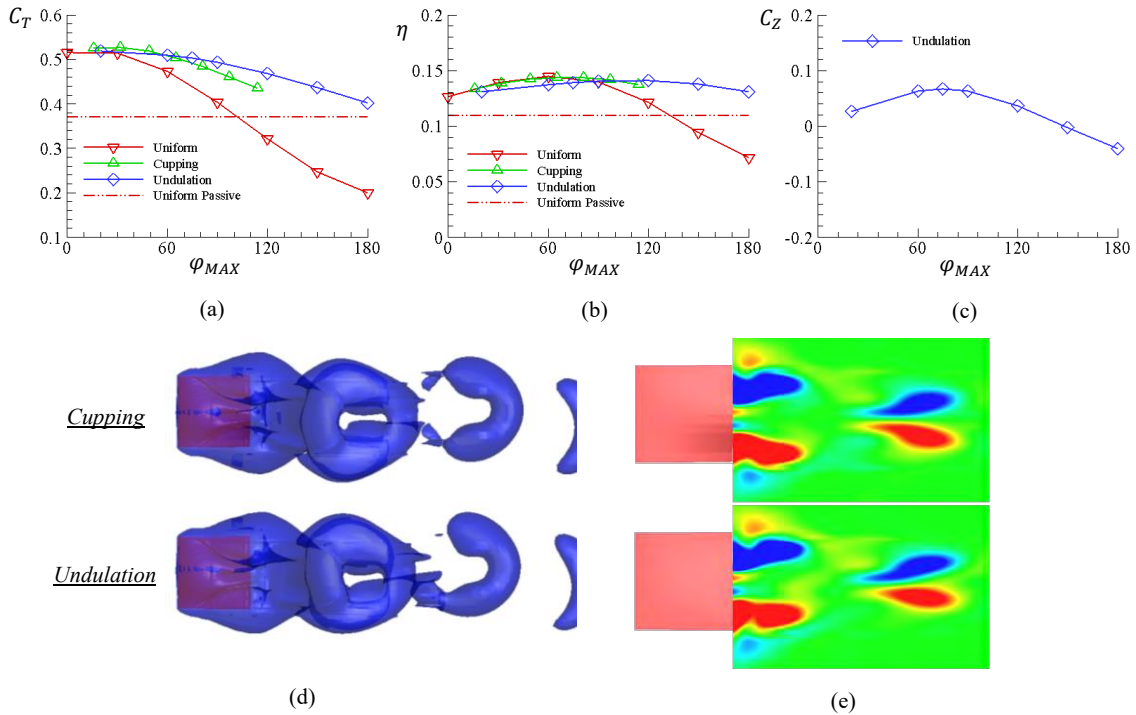


Figure 2 Time-averaged (a) thrust coefficient, (b) propulsion efficiency and (c) lift coefficient as a function of maximum phase lag φ_{MAX} in an actively controlled caudal fin. (d) Iso-surfaces of vorticity magnitude behind the fin. (e) Vorticity fields behind the fin. The contours display y -component of the vorticity within $y = y_{max}$ plane.

The fin models of Shi et al. [16], Zhu and Shoele [8], [9] captured some important features (e.g., ray-strengthened, anisotropic materials, flexible rays) of fish fins while also utilized simplified geometries and kinematics, thus they cannot reproduce some complicated fin motions of live fish. To investigate the hydrodynamics of real fish fins, Mittal et al. [22] numerically examined the hydrodynamics of a pectoral fin (Figure 1 (d)). In their model, the geometry and kinematics were reconstructed from experimental measurements and the flow field was simulated with a Cartesian-grid-based immersed-boundary solver. They found that the thrust generated by the highly deformable pectoral fin was positive in a complete motion cycle, indicating a superior capacity of thrust generation compared with traditional flapping foils.

As discussed previously, fishes are able to actively change the curvature of the rays due to the bi-laminar structure. To take this into consideration, we further developed a caudal fin model with active control based on the work of Shi et al. [16]. The fin rays are actuated by a sinusoidal swaying motion at the front ends and a distributed external force along each ray mimicking the pulling effect from tendons. All the rays have the same normalized bending stiffness ($K_b = 2.0$) and mass ratio ($m^* = 0.2$). The phase lag between the sway motion and the external force of the i^{th} ray is defined as φ_i . By designing specific distributions of φ_i , different caudal fin deforming patterns can be achieved, including the undulating motion which cannot be accomplished via solely passive deformations. Some preliminary results from our simulations are presented in the present paper.

Figure 2 (a-c) demonstrate the time-averaged thrust coefficient C_T , propulsion efficiency η and lift coefficient C_Z associated with three deforming patterns (uniform, cupping and undulating) as a function of the maximum phase lag φ_{MAX} , which is defined as $\varphi_{MAX} = \max\{\varphi_i\}$. The passive deformation case (labeled as ‘Uniform Passive’ in Figure 2) is also included for comparison. It can be observed that with active control, the propulsion performance of all types of deformations considered here is improved. The exceptions are that for actively controlled uniform deforming pattern (labeled as ‘Uniform’ in Figure 2), both C_T and η drop below the value of the passive case when φ_{MAX} are at larger values. The cupping and undulating deformations outperform the passive case within the phase lag range studied herein. Especially at high phase lags where the thrust and efficiency of the uniform deformation start to drop significantly, both cupping and undulating deformations still show promising performance. Another advantage of the undulating deformation over the others is that it can generate considerable lift force in vertical direction (see Figure 2 (c)), which is believed to play an important role in fish’s maneuver behaviors. A closer inspection of Figure 2 (c) reveals that by varying the phase lag distribution, the caudal fin can change both the magnitude and the direction of the vertical force, which means that fishes can play with the vertical force for maneuvering while maintaining a higher thrust for propulsion.

Figure 2 (d) and (e) show the vorticity fields behind the flexible caudal fin. It can be observed that for both deformations, vortex rings are generated behind the fin. The cupping deformation produces symmetrical wake while the wake generated by the undulation deformation is asymmetrical. This inclined wake is responsible for the production of net force in vertical direction.

3.2 Body-fin model

Previous experimental studies [32], [33] demonstrate that the vortices shed from the dorsal and anal fins could significantly alter the flow experienced by the caudal fin. Therefore, it is very necessary to investigate the performance of the whole fish with multiple fins, which may involve complicated body-fin and fin-fin interactions. Here, we present two typical body-fin models, as shown in Figure 3. In both models, the geometries and kinematics were reconstructed from experimental data. The major difference between the two models was the approach used to deal with the swimming motion. In the first model (Figure 3(a)), the fish was tethered swimming with a constant current speed [13] and the motion was prescribed, while in the second model (Figure 3(b)), the fish was self-propelled, where the motion was resolved using a MBD algorithm [27].

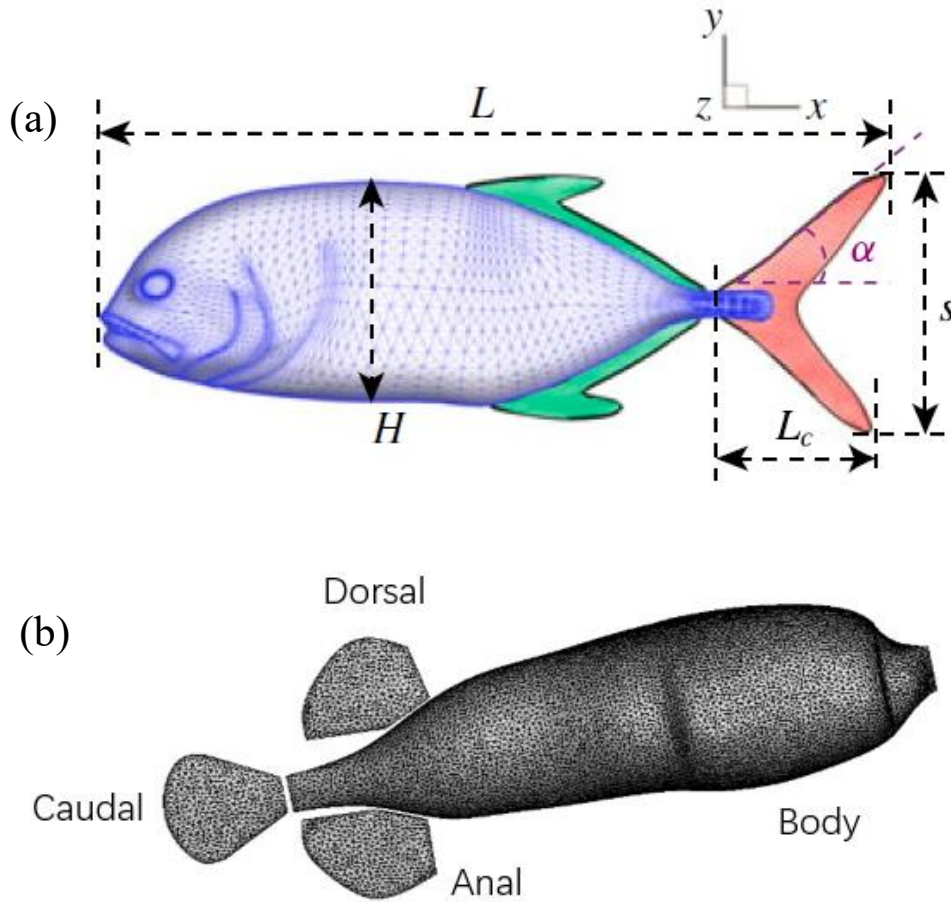


Figure 3 Computational body-fin models reconstructed from experiments. (a) Creville Jack (*Caranx hippos*) fish [13]. (b) Pufferfish [27].

With the body-fin model shown in Figure 3(b) and the MBD algorithm developed in Ref. [27], we investigated the effect of fin flexibility on the performance of a self-propelled pufferfish. We found that the fish with flexible fins is able to swim approximately twice faster than that with rigid fins, which is attributed to a higher acceleration and a longer accelerating process, as shown in Figure 4 (a). Besides, the flexible fins could reduce the power consumption, thus resulted in an increase of efficiency. Figure 4 (b) illustrates the time-averaged total force \bar{F}_T . The total force \bar{F}_T of a pufferfish with flexible fins is larger than that with rigid fins, which indicates that the fish with flexible fins has a longer acceleration process. The total force decreases to zero after some motion periods, indicating that the fish reaches its cruising stage. Figure 4 (c) demonstrates the instantaneous wake structures for rigid and flexible fin cases. It is observed that the vortices generated by the rigid fins are more scattered in lateral directions, which contributes less to thrust generation and leads to higher power consumption. For the flexible fins, the vortices are shed from the fin tips and convert quickly to the downstream, thereby producing larger thrust force.

It should be noted that the modeling tool developed in our previous work [27] is quite versatile, which is capable of solving a variety of biomimetic problems, e.g., a swimmer with

rigid undulatory body and an integrated system with both undulatory body and flexible fins. One advantage of our modeling tool based on multi-body dynamics algorithm is that it can handle self-propel swimming with multiple degrees of freedom. This feature allows us to study the stability and maneuvering problems of complex bio-inspired underwater robots. Currently, the integration of the MBD tool with a controlling strategy (e.g., PID controller) is under development at our research group. The integrated code can be used to investigate the possible body and/or fin kinematics to achieve better stability or maneuver behaviors under various flow environments. The insights shed from our single-fin model may provide valuable guidance on the design of the fin kinematics used in our more complicated body-fin model.

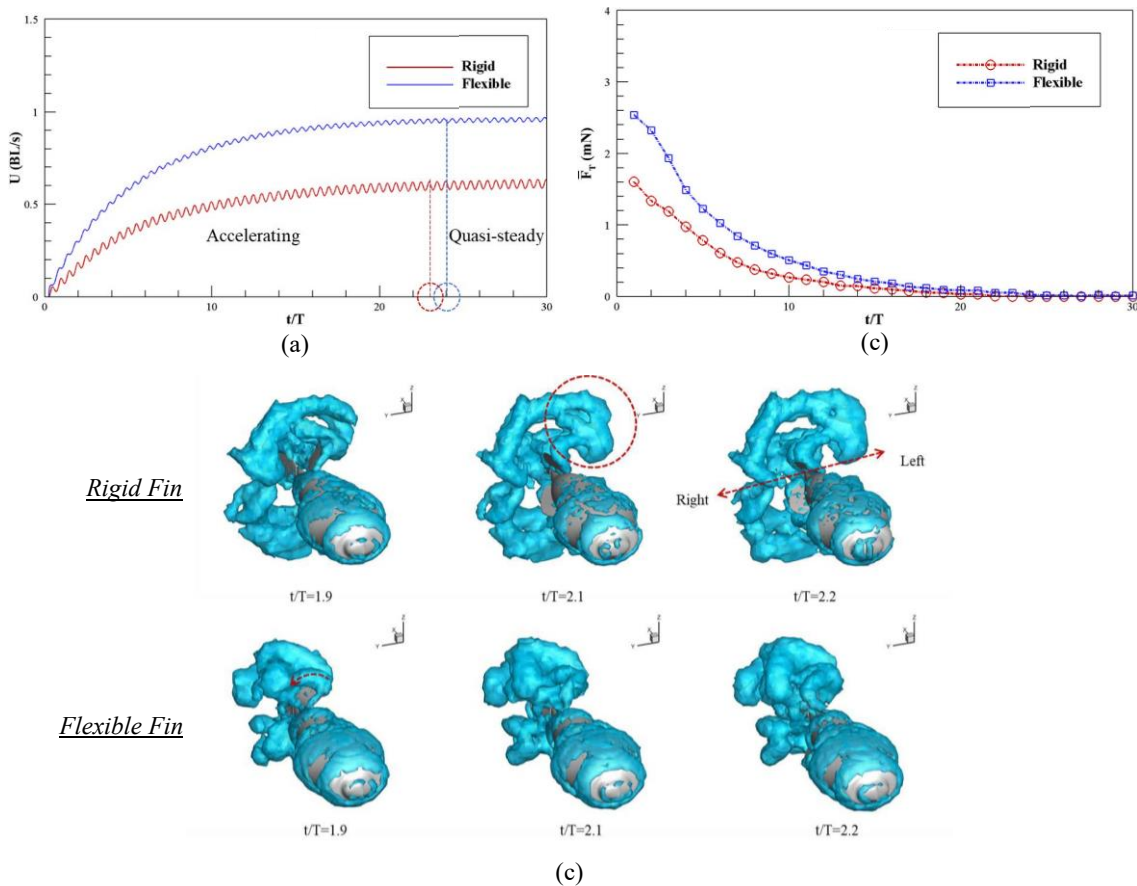


Figure 4 (a) Swimming speed evolutionary history for rigid and flexible fins. (b) Time histories of cycle-averaged total force. (c) Instantaneous vortex topology.

4 CONCLUSIONS

Fishes exhibit remarkable stability, controllability and maneuverability when swimming in aquatic environment, which inspires engineers to design fish-like underwater vehicles. Among a variety of fish swimming modes, some ray-finned fishes primarily rely on their fins for locomotion, which provide a promising prototype for underwater robot design. Generally, three study methods for ray-finned fishes are available nowadays, namely physical experiments with live fishes, physical experiments with robotic fishes and numerical modeling. Each method has its merits and drawbacks. Numerical simulations have the

advantages of providing detailed flow field data and exploring a larger parameter matrix, thus have become an indispensable approach for the study of biomimetic problems.

With different numerical tools, studies on ray-finned fishes can be categorized into two groups: single-fin model and body-fin model. The fins of ray-finned fishes possess distinctive features e.g., a thin and soft membrane strengthened by bony rays, anisotropic material property, individual actuation of each ray as well as actively controllable ray curvature and stiffness. Despite the complex design of ray-supported fish fins, there are still studies attempting to consider some of the key characters mentioned above [8], [9], [16], [22]. The important conclusions from their research are: 1) the ray flexibility may reduce the sensitivity of fin's propulsion efficiency to the kinematics such as frequency and amplitude. 2) Appropriate cupping deformations can reduce the power expenditure of a caudal fin. 3) Actively controlled undulating motion can generate a vertical force which could be used for fish maneuvering while retaining a high thrust and efficiency. These insights may provide valuable guidance for the design of underwater vehicles.

To investigate the possible body-fin or fin-fin interactions, a body-fin model needs to be used. The body-fin model can swim either with a prescribed motion or with a self-propelled motion. The former case (prescribed motion) is usually used to study the complex hydrodynamics of a whole fish under steady swimming mode or maneuver behaviors, which could enrich our understanding of fish locomotion. The later case (self-propelled), however, allows researchers to investigate the stability and controllability problems of robotic fishes. The self-propelled body-fin model can also be used to explore the possible fish kinematics to keep stability under different flow environments and accomplish various maneuver behaviors if integrated with a proper control strategy.

ACKNOWLEDGEMENTS

The first author would like to thank the China Scholarship Council (CSC) and University of Strathclyde for the financial support during his study in the UK. Results were partially obtained using the ARCHIE-WeSt High Performance Computer (www.archie-west.ac.uk) based at the University of Strathclyde.

REFERENCES

- [1] G. V. Lauder and E. G. Drucker, "Morphology and Experimental Hydrodynamics of Fish Fin Control Surfaces," *IEEE J. Ocean. Eng.*, vol. 29, no. 3, pp. 556–571, 2004.
- [2] F. E. Fish and G. V. Lauder, "Passive and Active Flow Control By Swimming Fishes and Mammals," *Annu. Rev. Fluid Mech.*, vol. 38, no. 1, pp. 193–224, 2006.
- [3] G. V. Lauder and P. G. A. Madden, "Learning from Fish: Kinematics and Experimental Hydrodynamics for Roboticists," *Int. J. Autom. Comput.*, vol. 4, pp. 325–335, 2006.
- [4] G. V. Lauder, "Fish Locomotion: Recent Advances and New Directions," *Ann. Rev. Mar. Sci.*, vol. 7, no. 1, pp. 521–545, 2015.
- [5] M. Saadat, F. E. Fish, A. G. Domel, V. Di Santo, G. V. Lauder, and H. Haj-Hariri, "On the rules for aquatic locomotion," *Phys. Rev. Fluids*, vol. 083102, pp. 1–12, 2017.
- [6] F. E. Fish and G. V. Lauder, "Control surfaces of aquatic vertebrates: active and passive design and function," *J. Exp. Biol.*, vol. 220, pp. 4351–4363, 2017.
- [7] R. Mittal, "Computational modeling in biohydrodynamics: Trends, challenges, and recent advances," *IEEE J. Ocean. Eng.*, vol. 29, no. 3, pp. 595–604, 2004.
- [8] Q. Zhu and K. Shoele, "Propulsion performance of a skeleton-strengthened fin.," *J. Exp. Biol.*, vol. 211, pp. 2087–2100, 2008.

- [9] K. Shoele and Q. Zhu, “Numerical simulation of a pectoral fin during labriform swimming,” *J. Exp. Biol.*, vol. 213, pp. 2038–2047, 2010.
- [10] K. Shoele and Q. Zhu, “Fluid-structure interactions of skeleton-reinforced fins: performance analysis of a paired fin in lift-based propulsion,” *J. Exp. Biol.*, vol. 212, pp. 2679–2690, 2009.
- [11] Q. Zhu and XB Bi, “Effects of stiffness distribution and spanwise deformation on the dynamics of a ray-supported caudal fin,” *Bioinspir. Biomim.*, vol. 12, no. 2, p. 26011, 2017.
- [12] H. Dong, M. Bozkurttas, R. Mittal, P. Madden, and G. V. Lauder, “Computational modelling and analysis of the hydrodynamics of a highly deformable fish pectoral fin,” *J. Fluid Mech.*, vol. 645, pp. 345–373, 2010.
- [13] G. Liu, Y. Ren, H. Dong, O. Akanyeti, J. C. Liao, and G. V. Lauder, “Computational analysis of vortex dynamics and performance enhancement due to body-fin and fin-fin interactions in fish-like locomotion,” *J. Fluid Mech.*, vol. 829, pp. 65–88, 2017.
- [14] T. Nakata and H. Liu, “A fluid-structure interaction model of insect flight with flexible wings,” *J. Comput. Phys.*, vol. 231, no. 4, pp. 1822–1847, 2012.
- [15] G. Li, U. K. Müller, J. L. Van Leeuwen, and H. Liu, “Body dynamics and hydrodynamics of swimming fish larvae: a computational study,” *J. Exp. Biol.*, pp. 4015–4033, 2012.
- [16] G. Shi, Q. Xiao, Q. Zhu, and W. Liao, 2019, “Fluid-structure interaction modeling on a three-dimensional ray-strengthened caudal fin,” *Bioinspir. Biomim.*, (under review).
- [17] M. Bozkurttas, H. Dong, R. Mittal, P. Madden, and G. Lauder, “Hydrodynamic Performance of Deformable Fish Fins and Flapping Foils,” *44th AIAA Aerosp. Sci. Meet. Exhib.*, no. January, pp. 1–11, 2006.
- [18] X. Chang, L. Zhang, and X. He, “Numerical study of the thunniform mode of fish swimming with different Reynolds number and caudal fin shape,” *Comput. Fluids*, vol. 68, pp. 54–70, 2012.
- [19] R. G. B. II, I. Borazjani, E. L. Blevins, and G. V. Lauder, “Hydrodynamics of swimming in stingrays: numerical simulations and the role of the leading-edge vortex,” *J. Fluid Mech.*, pp. 407–443, 2016.
- [20] J. BENEK, J. STEGER, and F. C. DOUGHERTY, “A flexible grid embedding technique with application to the Euler equations,” in *6th Computational Fluid Dynamics Conference Danvers*, American Institute of Aeronautics and Astronautics, 1983.
- [21] K. Nakahashi, F. Togashi, and D. Sharov, “Intergrid-Boundary Definition Method for Overset Unstructured Grid Approach,” *AIAA J.*, vol. 38, no. 11, pp. 2077–2084, Nov. 2000.
- [22] R. Mittal, H. Dong, M. Bozkurttas, G. V. Lauder, and P. Madden, “Locomotion with flexible propulsors: II. Computational modeling of pectoral fin swimming in sunfish,” *Bioinspiration and Biomimetics*, vol. 1, no. 4, 2006.
- [23] F.-B. Tian, H. Dai, H. Luo, J. F. Doyle, and B. Rousseau, “Fluid-structure interaction involving large deformations: 3D simulations and applications to biological systems,” *J. Comput. Phys.*, vol. 258, pp. 451–469, 2014.
- [24] C. Farhat and M. Lesoinne, “Two efficient staggered algorithms for the serial and parallel solution of three-dimensional nonlinear transient aeroelastic problems,” *Comput. Methods Appl. Mech. Eng.*, vol. 182, no. 3–4, pp. 499–515, 2000.
- [25] J. Degroote, R. Haelterman, S. Annerel, P. Bruggeman, and J. Vierendeels, “Performance of partitioned procedures in fluid-structure interaction,” *Comput. Struct.*, vol. 88, no. 7–8, pp. 446–457, 2010.
- [26] P. Causin, J. F. Gerbeau, and F. Nobile, “Added-mass effect in the design of partitioned algorithms for fluid-structure problems,” *Comput. Methods Appl. Mech. Eng.*, vol. 194, no. 42–44, pp. 4506–4527, 2005.
- [27] R. Li, Q. Xiao, Y. Liu, J. Hu, L. Li, G. Li, H. Liu, K. Hu, and L. Wen, “A multi-body dynamics based numerical modelling tool for solving aquatic biomimetic problems,” *Bioinspiration and Biomimetics*, vol. 13, no. 5, 2018.
- [28] S. Alben, P. G. Madden, and G. V. Lauder, “The mechanics of active fin-shape control in ray-finned fishes,” *J. R. Soc. Interface*, vol. 4, no. 13, pp. 243–56, 2007.
- [29] G. C. Lewin and H. Haj-Hariri, “Modelling thrust generation of a two-dimensional heaving airfoil in a viscous flow,” *J. Fluid Mech.*, vol. 492, no. 492, pp. 339–362, 2003.
- [30] H. Dai, H. Luo, P. J. S. A. F. de Sousa, and J. F. Doyle, “Thrust performance of a flexible low-aspect-ratio pitching plate,” *Phys. Fluids*, vol. 24, no. 10, pp. 1–9, 2012.

- [31] P. D. Yeh and A. Alexeev, “Free swimming of an elastic plate plunging at low Reynolds number,” *Phys. Fluids*, vol. 26, no. 5, 2014.
- [32] E. D. Tytell, “Median fin function in bluegill sunfish *Lepomis macrochirus*: streamwise vortex structure during steady swimming,” *J. Exp. Biol.*, vol. 209, pp. 1516–1534, 2006.
- [33] E. M. Standen and G. V. Lauder, “Hydrodynamic function of dorsal and anal fins in brook trout (*Salvelinus fontinalis*),” *J. Exp. Biol.*, pp. 325–339, 2007.

A METHOD FOR THE COUPLING OF COMPRESSIBLE 3D FLOW SIMULATIONS WITH A CAVITATION EROSION MODEL FOR DUCTILE MATERIALS AND ASSESSMENT OF THE INCUBATION TIME

Felix Schreiner*, Stephan Mottyll and Romuald Skoda

Chair of Hydraulic Fluid Machinery
Ruhr-University Bochum
Universitätsstraße 150, 44801 Bochum, Germany
web page: www.hsm.rub.de

* Corresponding author, e-mail: felix.schreiner@ruhr-uni-bochum.de

Key words: 3D CFD, OpenFOAM, cavitation erosion, erosion model, incubation time

Abstract. A compressible 3D in-house flow solver with temporal nanosecond resolution is coupled to a simple material erosion model for ductile materials. Due to limited spatial resolution, not all details of collapsing wall adjacent single bubbles can be resolved, and thus a collapse detection algorithm based on the mass flux divergence is applied. Load collectives are statistically evaluated by the multitude of detected collapses and serve as input for the material model. Grid dependence is carefully assessed. Since the physical simulation time is much shorter than the realistic exposure time, a method for the time extrapolation of the wall load to capture realistic time scales together with a step-by-step implementation is presented. The simulation method is applied on an impinging water jet test case as well as on an ultrasound cavitation case. A validation on temporally highly-resolved pressure measurement data is performed. Limitations of the particular material model are pointed out. The coupled CFD – material model comprises one model parameter, in terms of the cell size of a reference computational grid to handle grid dependence, that needs to be case-dependently fixed e.g. on measurement data. We conclude, that for a more predictive method, the detailed spatial resolution of single bubble collapses seems indispensable.

1 INTRODUCTION

Hydrodynamic cavitation is the development of voids in liquids by local depressurization below a critical pressure [1], e.g. induced by flow acceleration at propellers. As the ambient liquid pressure around the voids increases again further downstream, re-condensation leads to violent void collapses resulting in shock waves. In wall-adjacent flow regions, micro-jets in the collapsing bubbles act on the wall and induce high peak loads that may lead to material failure after a certain time. Besides vibration and noise it is cavitation erosion that causes serious issues in marine engineering applications and may limit the lifetime of ship propulsion units.

The damage potential of cavitation has been well recognized by both physicians and engineers, so that significant efforts have been made for the assessment of erosion sensitive wall zones by CFD methods. Besides the qualitative prediction of flow aggressiveness and erosion sensitive wall zones, it is of increasing interest for the design of propulsion units to determine the temporal evolution of erosion-induced damage and to assess the time to failure, i.e. the incubation time, what is the aim of the present study.

The cavitating flow in propulsion units can be approximated by simplified geometries, which can be better controlled in a lab environment than rotating propellers. This study focuses therefore on two standardized test cases, an axisymmetric nozzle as well as an ultrasonic horn test facility. In the axisymmetric nozzle, a jet impinges a wall and is accelerated and radially redirected, leading to cyclic shedding ring-shaped cavitation clouds and a ring-shaped erosion pattern [2–4]. Different CFD methods have been employed for the assessment of the flow aggressiveness on that test case. Mihatsch et al. [5–7] presented the assessment of erosion sensitive wall zones by a compressible CFD method and a collapse detection algorithm. Mottyll [8] has reproduced these results by our in-house implementation of essentially the same numerical scheme. Additionally, Mottyll [8] has assessed erosion sensitive wall zones by a more simple method as proposed by Skoda et al. [9]: By counting events exceeding threshold values for wall pressure and void collapse rate, erosion indicators and a map of dimensionless erosion probability are obtained. Koukouvinis et al. [10] are considering the temporal derivative of the void fraction to introduce erosion indices for the assessment of erosion sensitive wall zones. Peters et al. [11] deduced a dimensionless erosion intensity from a micro-jet model, validated it on the axisymmetric nozzle case and applied this method to a ship propeller [12].

The ultrasound cavitation test case is standardized for material erosion resistance tests according to ASTM G32 (American Society for Testing and Materials) [13]. Cavitation is generated by an oscillation horn tip at $f_{\text{drive}} \approx 20$ kHz and shows void dynamics similar to hydrodynamic cavitation [14, 15]. The ring-shaped erosion sensitive wall zones are well predicted by [15, 16], and different erosion mechanisms at horn tip and stationary specimen are revealed [15]. Besides the common incubation time measurements [17], a direct assessment of flow aggressiveness by pressure measurements has been presented by Paepenmüller et al. [18].

In these exemplary cited studies a good prediction of erosion sensitive wall zones as a qualitative measure of cavitation erosion could be obtained. However, no parameters of the solid material have been considered in these simulations. For the incubation time assessment as a quantitative measure, a model for the material response to cavitation impacts needs to be considered. For the axisymmetric nozzle test case, Mihatsch et al. [7, 19] have presented an assessment of the incubation time by a coupling of their CFD code with a simple material model [2]. We adopt that procedure in the present study and evaluate its applicability for an ultrasonic horn test case. We present a method for the time extrapolation of the wall load to capture realistic time scales. Furthermore, we provide a step-by-step implementation of the coupling of the CFD code, i.e. collapse load collectives deduced from the flow solution, with the material model. The coupled CFD method and material model is referred to as erosion model in what follows. Additionally specific limitations of the material model are pointed out.

The paper is organized as follows. In section 2, the flow solution method together with the numerical setups as well as the evaluation of single collapses and collapse load collectives are presented. In section 3, we present the flow solver validation on pressure measurement data. In

section 4, the material model and its coupling to the flow solver by collapse load collectives is illustrated. Results in terms of incubation time are discussed for the axisymmetric nozzle and ultrasonic horn test cases. Our conclusions in regard of future marine applications and model improvements are drawn in section 5.

2 METHODOLOGY

2.1 Flow Solver

For the resolution of void collapses, a compressible flow solver and a time resolution in the range of nanoseconds needs to be employed. Thus, the density-based low Mach number consistent Godunov-type numerical scheme by [20, 21] has been adopted, that was designed for resolving pressure wave dynamics and shocks in cavitating flows. We perform an explicit Runge-Kutta time integration and a finite volume discretization of the Euler equations for an inviscid fluid, coupled with an isentropic barotropic equation of state neglecting non-dissolved gas. A homogeneous mixture of liquid and vapor at thermodynamic equilibrium within each cell is assumed.

Details of the flow solver and our native in-house block-structured implementation `hydRUB` can be found in [8, 15, 22]. Results of the present study have been obtained with our unstructured OpenFOAM implementation of the solver, referred to as `hydRUBFoam` [18, 23]. For density, the MINMOD reconstruction scheme [24] is employed, while for velocity the GammaV scheme [25] is utilized to provide 2nd order accuracy. Further details on the flow solver can be found in [8, 15, 18, 22, 23].

2.2 Test Cases and Numerical Setup

The axisymmetric radial nozzle test case is sketched in Fig. 1a, together with the numerical setup. The nozzle flow strikes onto a target disc (i.e. the lower wall) and is redirected radially outward into the small gap between upper and lower wall. A ring-shaped erosive zone occurs at the target disc within a radius range of about $r \approx 19...27$ mm [26]. Measured incubation times are taken from [2, 7]. The numerical setup has been adopted from [6, 7] and is summarized in Table 1, together with the operation conditions. A grid study is performed with a refinement of the inner grid region (referred to as *analysis domain* in Fig. 1a), while the outer grid is left unchanged and connected by non-matching interfaces, i.e. hanging nodes.

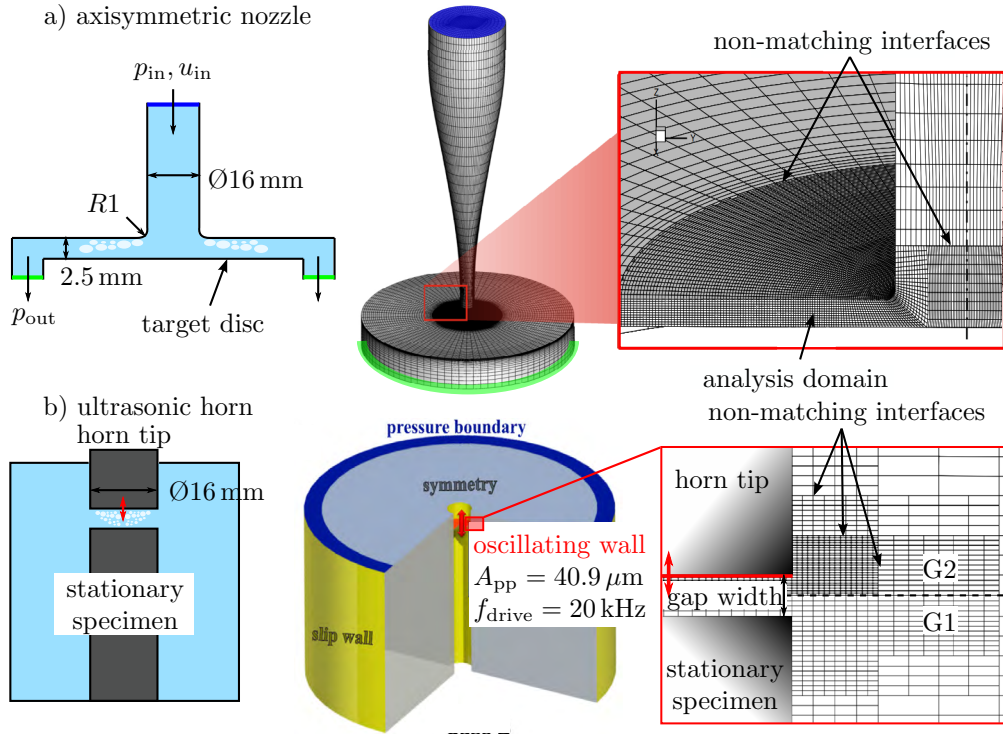


Figure 1: Illustration of the axisymmetric nozzle and the ultrasonic horn test case with the numerical setups

The ultrasonic horn test case (see Fig. 1b) is operated at 19.8 kHz horn driving frequency and $40.9\ \mu\text{m}$ peak-to-peak amplitude. The horn tip is immersed into distilled water at equilibrium air saturation, kept at 20°C by an actively controlled indirect cooling circuit. The gap width between horn tip and the stationary specimen equals 0.5 mm . The numerical setup has been adopted from [15, 18, 22] and is summarized in Table 1. Two spatial resolutions have been employed for a grid study. The computational grids G1 and G2 with hanging-node configuration are depicted in Fig. 1b.

Table 1: Operation and setup parameters of the axisymmetric nozzle and the ultrasonic horn test case

| axisymmetric nozzle | | | ultrasonic horn | | |
|--------------------------|------------------------------------|-----------|--------------------------|---------------------|-----------|
| inlet pressure | 40 bar | | peak-to-peak amplitude | $40.9\ \mu\text{m}$ | |
| outlet pressure | 18.9 bar | | frequency | 19.8 kHz | |
| inlet velocity | $1.37\ \text{m}\cdot\text{s}^{-1}$ | | gap width | 0.5 mm | |
| grid | G1 | G2 | grid | G1 | G2 |
| total numb. of cells [-] | 382 000 | 2 393 000 | total numb. of cells [-] | 105 000 | 329 000 |
| numb. cells in gap [-] | 12 | 24 | numb. cells in gap [-] | 8 | 16 |
| num. time step [ns] | 30.2 | 19.1 | num. time step [ns] | 16.8 | 8.1 |
| sim. phys. time [ms] | ~ 359 | ~ 86 | sim. phys. time [ms] | ~ 163 | ~ 85 |

2.3 Collapse Detection and Load Collectives

The flow solver (see section 2.1) has been shown to reproduce the dynamics of collapsing wall adjacent single bubbles, i.e. micro-jet formation and torus-shaped shock wave, given that the spatial resolution is sufficiently high [27, 28]. For the simulation of macroscopic test cases as the axisymmetric nozzle and the ultrasonic horn, such a bubble-resolving spatial resolution is not feasible due to tremendous computational effort. Thus, we account for collapses and peak pressures of distinct voids in a certain vicinity of the wall by a mass flux divergence criterion proposed by Mihatsch et al. [5, 6]. Albeit we may not resolve the collapse of each microscopic bubble, we resolve void collapses down to a scale that is just in the range of our spatial resolution, and we refer to that procedure as meso-scale simulation. In order to cope with the limited spatial resolution, grid dependence is treated by the projection of the collapse pressure p_{coll} to a reference grid with yet arbitrary reference cell length x_{ref} [6], and a corrected collapse pressure p_{corr} is obtained according to eq. 1.

$$p_{\text{corr}} = \frac{\sqrt[3]{V_{\text{cell}}}}{x_{\text{ref}}} p_{\text{coll}} \quad (1)$$

The occurrence of collapses in terms of the cumulated collapse rate ccr is corrected by eq. 2 and the introduction of the empirical parameter $\kappa = 3/2$ [6].

$$ccr_{\text{corr}} = \left(\frac{\sqrt[3]{V_{\text{cell}}}}{x_{\text{ref}}} \right)^{\kappa} ccr \quad (2)$$

By a statistical evaluation of a multitude of collapses, collapse load collectives are obtained in terms of the cumulated collapse rate ccr vs. collapse pressure p_{coll} . Details of this evaluation method are described in [15]. Exemplary collapse load collectives are illustrated in Fig. 2 for the erosion-prone wall region of the axisymmetric nozzle, defined as a somewhat arbitrary wall adjacent layer $dz_{\text{wall}} < 500 \mu\text{m}$ normal to the bottom wall and a ring segment of $\Delta r = 19..32 \text{ mm}$. According to Schmidt et al. [29], a void collapse that occurs within the fluid domain in a certain distance from the wall, emits a pressure wave that reaches the wall, and the resulting maximum wall pressure is essentially grid-independent. Nevertheless, according to [15], we do not perform a projection of detected collapses to the wall, since it is the collapses that occur in the immediately wall-adjacent cell layer that primary contribute to high wall loads. As this wall-adjacent cell layer on the fine computational grid is not present on the coarse grid, a significant grid dependence remains after wall projection of the collapse pressure [15]. Thus, all collapse events within the erosion-prone wall region are considered to be representative for the wall load, without projection to the wall. This procedure is equivalent to the assumption that the pressure peak of each detected collapse acts immediately on the wall, irrespective of its actual wall distance. It is noteworthy that this procedure slightly deviates from the one by [7], who introduced a wall projection of collapse pressure with the maximum value of either x_{ref} or the wall distance of a collapse occurrence. As can be seen in Fig. 2, the grid dependence of the uncorrected load collectives (no corr.) is effectively compensated by the projection to a reference grid x_{ref} (eq. 1) and by the rate correction (eq. 2). After correction, the load collectives of both grids essentially match and can be approximated by a trendline for each value of x_{ref} . An appropriate value of x_{ref} is yet undetermined, a fact that will be addressed in section 4.3.

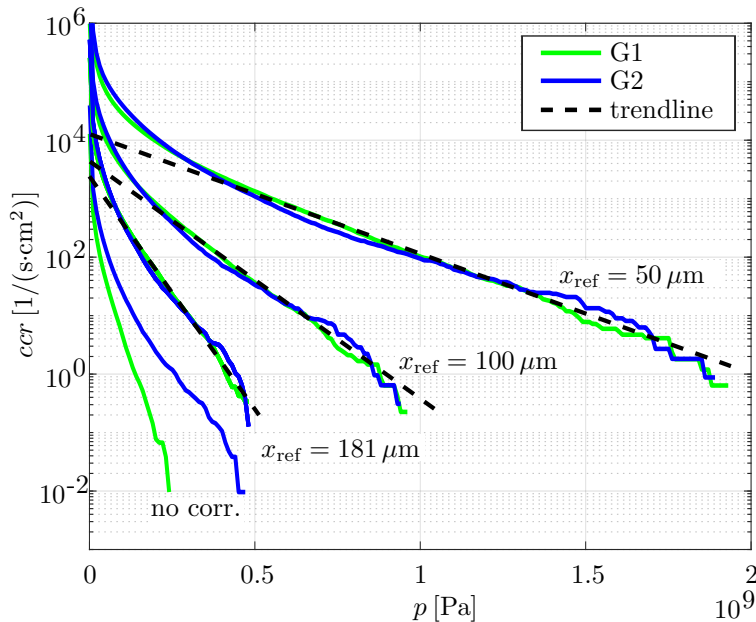


Figure 2: Exemplary collapse load collectives for the axisymmetric nozzle without correction (no corr.) and with correction according to eqs. 1 and 2 with different scaling parameters x_{ref}

3 VALIDATION BY PRESSURE MEASUREMENTS

In a proceeding study [18] we performed temporally high-resolved wall load measurements with $\text{\O}5.0$ mm polyvinylidene fluoride (PVDF) pressure sensors flush-mounted in the erosion sensitive wall region of the stationary specimen. Due to the relatively large sensor size, we label the load as *force* instead of *pressure*. We evaluated the results statistically in terms of force load collectives, i.e. cumulative force rate *cfr* vs. measured sensor force (not to be confused with collapse load collectives in terms of *ccr* vs. collapse pressure, see Fig. 2) and compared CFD results by a virtual sensor to the measurements. The force load collectives in the simulation were essentially grid-independent and matched the measured force load collectives with a very good accuracy for different gap widths [18].

Regarding the axisymmetric nozzle test case, Franc et al. [4] performed wall pressure measurements by a commercial piezoelectric sensor with $\text{\O}3.6$ mm in the erosion sensitive ring-shape zone at the target disc. In their simulations, Mihatsch et al. [6] reproduced this experiment by a virtual pressure sensor, found a significant grid dependence of the sensor force load collectives and performed an analogous projection to a reference grid as has been proposed for the collapse load collective by eq. 2. By matching their virtual sensor results to measured force load collectives, the value of x_{ref} has been fixed to a value of $181 \mu\text{m}$. This value of x_{ref} has subsequently been applied also to the collapse load collective. Thus, x_{ref} is fixed by this calibration procedure. We could reproduce the procedure by Mihatsch et al. [6] with our in-house solver implementations `hydrUB` [8] as well as `hydrUBFoam` and ended up at essentially the same value of $x_{\text{ref}} = 181 \mu\text{m}$. The corresponding collapse load collective is also depicted in Fig.2.

Obviously, the grid dependence of force load collectives at the axisymmetric nozzle test case

plays a decisive role for the fixing of x_{ref} . As stated above we did not observe an appreciable grid dependence in our ultrasonic horn simulations [18], where larger sensors $\text{Ø}5 \text{ mm}$ have been used. Therefore, we systematically vary the sensor size of the axisymmetric nozzle case by splitting a ring-shaped virtual sensor in circumferential portions as illustrated in Fig. 3a. It is noteworthy that the simplification of the sensor geometry from circular shape to a ring segment is without any significance, since in radial sensor extent direction a statistically homogeneous load is present [8]. The resulting force load collectives in Fig. 3b indicate that the grid dependence is in fact decreasing for larger sensor areas. For a sensor area of about $A_{\text{sensor}} = 18.5 \text{ mm}^2$ and larger, the force load collective is essentially grid independent. We made an equivalent observation in preliminary ultrasonic horn simulations, where we successively scaled-down the virtual sensor and observed an increasing grid dependence towards smaller virtual sensors. It can be concluded that for increasing sensor area size, the single punctual peak loads are increasingly averaged out over more cell faces, leading to an increasing grid-independence. It is also noteworthy that for their x_{ref} fixing on a $\text{Ø}3.6 \text{ mm}$ sensor, Mihatsch et al. [6] applied grid resolutions with cell face numbers that correspond to our $A_{\text{sensor}} = 10 \text{ mm}^2$, where we still observe a significant grid dependence according to Fig 3b. It will be interesting to see whether for finer grids, the grid dependence will diminish for the $\text{Ø}3.6 \text{ mm}$ sensor. That will be investigated in further studies.

The sensor size variation reveals that the grid dependence of force load collective and thus the fixing of x_{ref} are significantly affected by the sensor size. We therefore prefer to immediately determine x_{ref} by incubation time measurements as will be discussed in what follows.

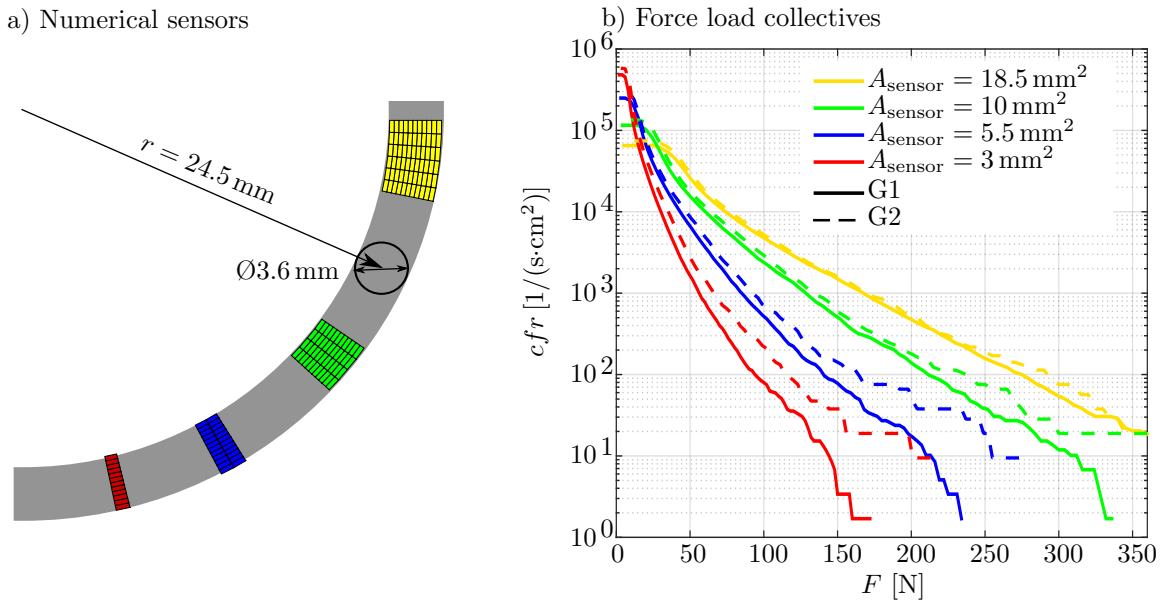


Figure 3: Size variation of exemplary virtual sensors (a) with resulting force load collectives (b)

4 ASSESSMENT OF INCUBATION TIME

4.1 Material Model

Franc et al. [2] proposed a simple one-dimensional erosion material model for ductile steels. The erosion process is based on the accumulation of plastic material deformation and successive work hardening up to material failure, determining the incubation time. The key assumption of the model involves, that the absorbed energy can be successively accumulated for each collapse impact until fracture limit at the ultimate strain is reached [30]. Strain rate effects and loads below the yield strength of the material are neglected. In the original intention of the material model [2], flow aggressiveness is evaluated by statistical analyses of experimental pitting results in terms of impact rate, mean load and mean impact area, which serve as input data for the material model. Further model approaches e.g. [31, 32] assume a ductile deterioration of the material by micro cavities and creeping. Hattori et al. [17, 33, 34] proposed a material model accounting for high cycle fatigue mechanisms. Although these exemplary cited material models comprise physically sound assumptions, we prefer in a first step to couple the ductile model by Franc et al. [2] to the CFD code due to its plainness and because the flow-induced load can be prescribed in a straightforward way, which is presented in the subsequent section.

4.2 Coupling of Load Collectives and Material Model

We start with a brief summary of the material model, details can be found in [2]. It is assumed that the material response to a specified load follows the stress-strain relationship of Ludwig-type:

$$\sigma(\varepsilon) = \sigma_Y + K \varepsilon^n \quad (3)$$

The yield stress σ_Y , strength index K and strain hardening exponent n are specific for each material and obtained by tensile tests. For successive impacts and a progressive surface hardening, the resulting one-dimensional strain profile is approximated by a one-dimensional power law:

$$\varepsilon(x) = \varepsilon_0 \left(1 - \frac{x}{l}\right)^\theta \quad (4)$$

ε_0 is the strain at the surface ($x = 0$) and x the distance to the surface. l is the thickness of the hardened layer, which progressively increases with exposure time, until it reaches a maximum thickness L . The metallurgical parameters L and the shape factor Θ are determined from micro-hardness measurements in a cross-section of an eroded sample. The energy that is absorbed for a strain ε_i can be formulated as:

$$W(\varepsilon_i) = \int_{x=0}^l \left[\int_{\varepsilon=0}^{\varepsilon(x)} \sigma d\varepsilon \right] \bar{S} dx = \varepsilon_i \bar{S} L \left(\frac{\varepsilon_i}{\varepsilon_U} \right)^{1/\theta} \frac{\sigma_Y + \beta K \varepsilon_i^n}{1 + \theta} \quad (5)$$

$$\text{with: } \beta = \frac{1 + \theta}{(1 + n)(1 + \theta + n\theta)}$$

\bar{S} is the mean impact area and has been obtained by a statistical pit analysis in the experiment [2], together with a mean load $\bar{\sigma}$ and a mean impact rate \dot{N} . In our CFD approach, no mean value of $\bar{\sigma}$, but the entire spectrum of collapses is taken into account for the evaluation of

$W(\sigma_i)$. First, $W(\sigma_i)$ is obtained from $W(\varepsilon_i)$ by inserting eq. 3 into eq. 5. $W(\sigma_i)$ is the absorbed energy given by a stress σ_i . The basic idea is, that, as soon as the accumulated energy (obtained by summing up the distinct values of $W(\sigma_i)$) exceeds the fraction energy $W(\sigma_U)$, the incubation time has been achieved. σ_U is the ultimate strength of the material and obtained from tensile tests. The spectrum of σ_i is obtained from our CFD collapse load collectives. In what follows, we provide a summarized step-by-step algorithm. The steps are illustrated in Fig. 4.

- (1) The radial direction is discretized into ring zones with radial position r_{pos} and a radial width Δr_{ring} . The distinct rings may overlap. In order to provide a radial variation of collapse load collectives, the detected collapses are filtered so that they are located within the radial ring zone. Only collapses in a certain wall vicinity $< dz_{\text{wall}}$ are taken into account. Δr_{ring} must be chosen large enough to provide a sufficient statistic of collapses. A further constraint that requires rather small values of dz_{wall} is to represent a certain wall vicinity. Values of Δr_{ring} and dz_{wall} are provided further below when the results are discussed.
- (2) The collapse load collectives are projected to a reference grid x_{ref} according to eqs. 1 and 2.
- (3) Frequent collapses with low pressure and seldom collapses with high pressure are sorted out to provide a unique trendline (step 4). A minimum pressure level p_{min} and a minimum rate $count_{\text{min}}$ are empirically prescribed. Values of p_{min} and $count_{\text{min}}$ are provided in the result section. Note that $count_{\text{min}}$ is applied to the total number of collapse occurrences in the simulation time interval and is not concerned by the projection to the reference grid x_{ref} . $count_{\text{min}}$ is applied to the rate before the rate correction in terms of eq. 2. On the other hand, p_{min} is applied to the corrected pressure p_{corr} , i.e. after evaluation of eq. 1.
- (4) By the filtered collapse load collectives according to step 3, a linear regression is obtained for each radial zone with the fitting parameters A and B:

$$ccr_{\text{corr}}(p_{\text{corr}}) [1/(\text{s} \cdot \text{cm}^2)] = [(10^A)^{p_{\text{corr}}} \cdot 10^B] \quad (6)$$

$ccr_{\text{corr}}(p_{\text{corr}})$ represents a rate of collapses per unit surface area and unit time.

- (5) Each single impact affects only a small area A_{impact} . We assume the $ccr_{\text{corr}}(p_{\text{corr}})$ occurs with the same probability within each ring zone and set $A_{\text{impact}} = \bar{S}$. According to [19], we set \bar{S} in eq. 5 equal to the surface of a reference cell x_{ref}^2 . Thus, we obtain the collapse rate for one uniform covering of a complete ring zone surface $ccr'(p_{\text{corr}})$:

$$ccr'(p_{\text{corr}}) [\text{s}^{-1}] = x_{\text{ref}}^2 \cdot ccr_{\text{corr}}(p_{\text{corr}}) \quad (7)$$

- (6) $ccr'(p_{\text{corr}})$ is temporally extrapolated to the number of collapses $ccr''(p_{\text{corr}}, T)$ for a time interval T :

$$ccr''(p_{\text{corr}}, T) [-] = ccr'(p_{\text{corr}}) [\text{s}^{-1}] \cdot T = x_{\text{ref}}^2 \cdot T \cdot ccr_{\text{corr}}(p_{\text{corr}}) [1/(\text{s} \cdot \text{cm}^2)]. \quad (8)$$

The dimensionless measure $ccr''(p_{\text{corr}}, T)$ represents the cumulative collapse rate for a specified physical time T acting on the impact area \bar{S} .

- (7) Discrete loads i.e. $p_i = p_1, p_2, \dots, p_m$ are obtained by regarding p_{corr} at integral values of $ccr'' = 1, 2, \dots, m$. Since the ductile material model accounts only for loads above the yield strength and loads that occur at least once per covering, the discrete loads are filtered with $p_i \geq \sigma_Y$ and $\min(ccr'') = 1$.

These discrete loads p_i correspond to σ_i and serve as input for the material model. The energy absorbed by the material is accumulated for all loads occurring within a time interval T :

$$W_{\text{tot}}(T) = \sum_{i=1}^m W(\sigma_i) \quad (9)$$

When $W_{\text{tot}}(T)$ approaches the fracture energy $W(\sigma_U)$, then T approaches the incubation time t_{inc} . The condition

$$W(\sigma_U) - W_{\text{tot}}(t_{\text{inc}}) = 0 \quad (10)$$

is numerically solved for t_{inc} by a bisection method.

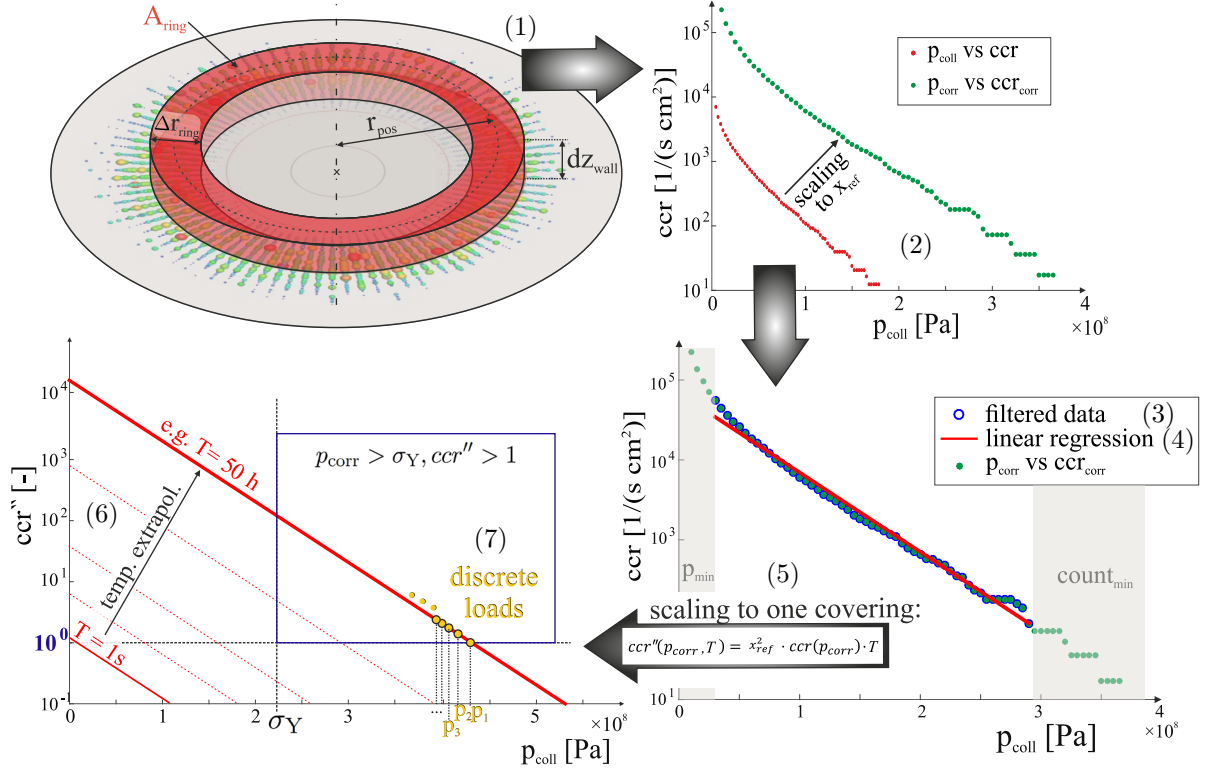


Figure 4: Schematic illustration of the load approximation from CFD results that serve as input for the material model

4.3 Results

4.3.1 Axisymmetric Nozzle

Based on preliminary studies [6–8, 19] we choose a range within $r = 20 \dots 41$ mm for the discretization of radial zones with $\Delta r_{\text{ring}} = 4$ mm and $dz_{\text{wall}} = 500 \mu\text{m}$. The resulting collapse load collectives are depicted in Fig. 5a for three exemplary radial positions. Collapse pressure and rate have been projected to a reference grid $x_{\text{ref}} = 245 \mu\text{m}$ (this value will be explained further below) according to eqs. 1 and 2. As expected, the grid dependence could be effectively

minimized, so that a unique trendline in terms of a linear regression according to eq. 6 can be introduced. Seldom occurring collapses are marked by circles in Fig. 5a and have been selected out by choosing the threshold value $count_{\min} = 6$. p_{\min} equals 50 bar. Based on these load collectives, the incubation time is assessed for the stainless steel SS-A2205 and a Nickel Aluminum Bronze alloy NAB. The material properties are summarized in Table 2.

In Fig. 5b, the radial distribution of the incubation time is depicted. The positions of the exemplary load collectives (Fig 5a) are marked by lines, so that the association between flow aggressiveness in terms of collapse load collectives and the incubation time gets obvious. Note that the load collective at $r = 26$ mm (red line) comprises a higher rate in terms of ccr_{corr} than the load collective at $r = 34$ mm (green line), but at the same time shows a slightly flatter slope. The latter might result in less violent collapses after temporal extrapolation according to eq. 8. Since the incubation time for $r = 26$ mm is lower than for $r = 34$ mm, it can be concluded that both load collectives cross only at very high loads (not shown here) close to the fracture stress and the higher rate dominates over the lower slope resulting in a more aggressive flow situation at $r = 26$ mm than at the location $r = 34$ mm. For a comparison with the measured incubation time, the radially minimum value of the simulation results is evaluated. The reference grid parameter x_{ref} is chosen in a way that it matches the measured incubation time for SS-A2205, $t_{\text{inc}} = 35$ h [7], resulting in $x_{\text{ref}} = 245 \mu\text{m}$. Thus per definition, t_{inc} matches the measured value at $r = 27$ mm for SS-A2205.

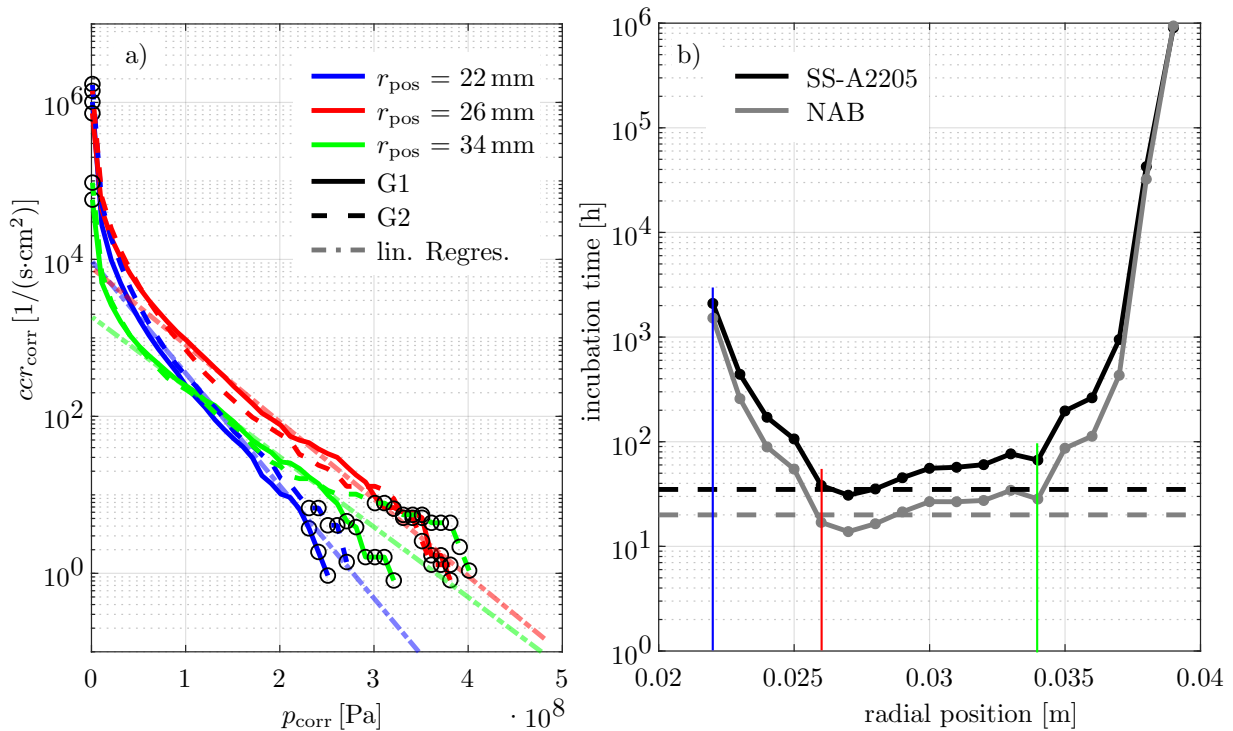


Figure 5: Collapse load collectives for exemplary radial positions for two grids G1 and G2 with regression according to eq. 6 (a) and the radial distribution of incubation time for two materials (b). The experimental incubation times are obtained from [7] and depicted as dashed lines.

According to the measurements by Chahine et al. [26], the erosion sensitive wall zones are located in a range of about $r \approx 19...27$ mm. While the minimum value of t_{inc} occurs at $r = 27$ mm and is thus located just within that range, the region of high flow aggressiveness is predicted rather in a range of about $r = 25...34$ mm and is thus shifted to higher radii. It is important to note that preliminary studies [7,8] on a different operation point ($p_{\text{in}} = 21.3$ bar) have revealed an even more pronounced shift of low incubation time to a too large radial position. Mottlyll [8] has evaluated the flow aggressiveness by erosion indicators [9] and found the same region of high flow aggressiveness $r = 21...28$ mm compared to Koukouvinis et al. [10], although the incubation has been predicted too far downstream. By applying the erosion indicator method [9] by preliminary simulations in the present study, we could also confirm for $p_{\text{in}} = 40$ bar the correct location of high flow aggressiveness. Thus, the downstream shift of low incubation time can be attributed to the erosion modelling and not to shortcomings of the flow simulation: By the temporal extrapolation of the collapse load collective regressions from short simulated physical time (less than one second) to long incubation time (several hours), seldom occurring collapses with high collapse pressure might be artificially overvalued. This overvaluing of high-pressure collapses is further increased, since solely loads that exceed the material yield strength are considered by the ductile material model and thus loads in the macroscopic elastic region are a priori neglected. High cycle fatigue, however, may also contribute significantly to material failure [17,34] and is completely neglected in our study by the use of a purely ductile material model [2].

In spite of these significant assumptions, we applied the material model to a second material in terms of NAB, also shown in Fig. 5b. Note that it is the same load collectives that enter the material model for both materials, only the material parameters according to Table 2 change. The incubation time for NAB is lower by a factor ~ 2 than for SS-A2205, which corresponds to the experimentally achieved ratio. Thus, the erosion model shows the proper qualitative answer to material properties.

Finally, it is noteworthy that a different reference grid size $x_{\text{ref}} = 181 \mu\text{m}$, that has been proposed by [6,7,19] for the operation point $p_{\text{in}} = 21.3$ bar, yields an incubation time one order of magnitude too low in our present investigation of $p_{\text{in}} = 40$ bar. This makes the universal validity of the value of x_{ref} questionable, a conclusion that will be further supported by our ultrasound test case investigations that are presented in the subsequent subsection.

Table 2: Material parameters from tensile [3] and micro-hardness tests [26]

| Material | σ_Y | σ_U | K | n | L | θ |
|----------|------------|------------|----------|--------|---------|----------|
| SS-A2205 | 230 MPa | 790 MPa | 910 MPa | 1/3.2 | 1.25 mm | 2.2 |
| NAB | 355 MPa | 683 MPa | 1210 MPa | 1/2.07 | 1.07 mm | 2.8 |
| 316L | 400 MPa | 1020 MPa | 900 MPa | 1/2 | 0.2 mm | 5 |

4.3.2 Ultrasonic Horn

The entire radial extent of the stationary specimen is discretized with $\Delta r_{\text{ring}} = 2.5$ mm and $dz_{\text{wall}} = 200 \mu\text{m}$. As for the axisymmetric nozzle, $\text{count}_{\text{min}} = 6$ and $p_{\text{min}} = 50$ bar have

been chosen. Stainless steel 316L is considered and the material parameters are summarized in Table 2. In Fig. 6, the radial distribution of the incubation time is depicted. The incubation time continuously increases towards larger radial locations and has its minimum in the specimen center, which is in agreement with radial distribution of flow aggressiveness, either evaluated by erosion indicators or a zonal evaluation of collapse load collectives [15]. The reference grid parameter x_{ref} is chosen in a way that it matches the measured incubation time $t_{\text{inc}} = 2.25$ h [18] for a zone with $\text{Ø}5$ mm in the specimen center, resulting in $x_{\text{ref}} = 60 \mu\text{m}$. Note that in Fig. 6, the ring-shape discretization with the ring width of $\Delta r_{\text{ring}} = 2.5$ mm (as exemplary shown in blue) is resulting in a $\text{Ø}5$ mm area for the radial position $r = 1.25$ mm (red), as each radial position is defining the center of inner and outer radius of the ring-segments. Summarizing, the reference grid $x_{\text{ref}} = 60 \mu\text{m}$ for the ultrasonic test case deviates significantly from the values that have been obtained for the axisymmetric nozzle, $x_{\text{ref}} = 181 \mu\text{m}$ and $x_{\text{ref}} = 245 \mu\text{m}$ and is thus case-dependent.

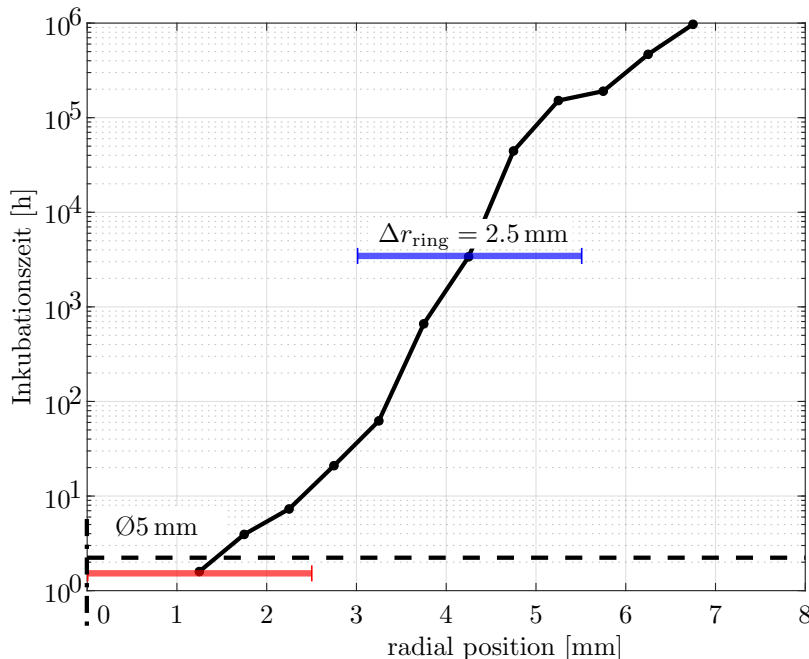


Figure 6: The radial distribution of the incubation time for the stationary specimen compared to the experimental value $t_{\text{inc}} = 2.25$ h (dashed line) measured by [18]. The exemplary ring width $\Delta r_{\text{ring}} = 2.5$ mm is shown in blue, resulting in a $\text{Ø}5$ mm area for $r = 1.25$ mm (red).

5 CONCLUSION AND OUTLOOK

A method for the coupling of CFD collapse load collectives with a simple material model was presented and applied for the assessment of incubation time on two standardized test cases. We presented a method for the time extrapolation of the wall load to capture realistic time scales together with a step-by-step implementation guideline. We also pointed out limitations of the particular material model such as the neglect of loads below the materials yield strength and

suggest to consider material models that also take into account high-cycle fatigue mechanisms as well as strain-rate dependence of the material properties in further studies.

The scaling of collapse load collectives to a referenced grid showed that the reference grid parameter x_{ref} is case-dependent. A calibration of x_{ref} as proposed by [6], by pressure measurements and the exploitation of the grid dependence of the virtual sensor results, depends on the sensor size and does not seem to be generally valid. We conclude that the erosion model, i.e. coupled CFD – material model, comprises at least one model parameter that needs to be case-dependently fixed on measurement data. Thus, we suggest to consider a wider range of operation conditions and test cases in order to further figure out the significance of the model parameter x_{ref} .

For a more predictive method, the detailed spatial resolution of the multitude of single bubble collapses seems to be indispensable.

ACKNOWLEDGEMENTS

The authors wish to gratefully acknowledge the financial support by the Federal Ministry for Economic Affairs and Energy (BMWi) (Project ID 03SX454D). The authors also gratefully acknowledge the Gauss Centre for Supercomputing e.V. (www.gausscentre.eu) for providing computing time through the John von Neumann Institute for Computing (NIC) on the GCS Supercomputer JUWELS at Jülich Supercomputing Centre (JSC).

REFERENCES

- [1] C. E. Brennen. *Cavitation and Bubble Dynamics*. Cambridge University Press, Cambridge (2013).
- [2] J.-P. Franc. Incubation Time and Cavitation Erosion Rate of Work-Hardening Materials. *Journal of Fluids Engineering*, **131**:021303 (2009).
- [3] J.-P. Franc, M. Riondet, A. Karimi, and G. L. Chahine. Material and velocity effects on cavitation erosion pitting. *Wear*, **274-275**:248–259 (2012).
- [4] J.-P. Franc, M. Riondet, A. Karimi, and G. L. Chahine. Impact Load Measurements in an Erosive Cavitating Flow. *Journal of Fluids Engineering*, **133**:121301 (2011).
- [5] M. S. Mihatsch, S. J. Schmidt, M. Thalhamer, N. A. Adams, R. Skoda, and U. Iben. Collapse detection in compressible 3-D cavitating flows and assessment of erosion criteria. *WIMRC 3rd International Cavitation Forum 2011* (2011).
- [6] M. S. Mihatsch, S. J. Schmidt, and N. A. Adams. Cavitation erosion prediction based on analysis of flow dynamics and impact load spectra. *Physics of Fluids*, **27**:103302 (2015).
- [7] M. S. Mihatsch. *Numerical Prediction of Erosion and Degassing Effects in Cavitating Flows*. Ph.D. thesis, TU München (2016).
- [8] S. Mottlyll. *Numerical 3D Flow Simulation of Cavitation at Ultrasonic Horns and Assessment of Flow Aggressiveness, Erosion Sensitive Wall Zones and Incubation Time*. Ph.D. thesis, Ruhr-Universität Bochum (2017).
- [9] R. Skoda, U. Iben, A. Morozov, M. S. Mihatsch, S. J. Schmidt, and N. A. Adams. Numerical simulation of collapse induced shock dynamics for the prediction of the geometry, pressure and temperature impact on the cavitation erosion in micro channels. *WIMRC 3rd International Cavitation Forum 2011* (2011).

-
- [10] P. Koukouvinis, G. Bergeles, and M. Gavaises. A new methodology for estimating cavitation erosion: Application on a high speed cavitation test rig. In *11th World Congress on Computational Mechanics (WCCM XI)* (2014).
- [11] A. Peters, H. Sagar, U. Lantermann, and O. el Moctar. Numerical modelling and prediction of cavitation erosion. *Wear*, **338-339**:189–201 (2015).
- [12] A. Peters, U. Lantermann, and O. el Moctar. Numerical prediction of cavitation erosion on a ship propeller in model- and full-scale. *Wear*, **408-409** (2018).
- [13] ASTM-G32. Standard test method for cavitation erosion using vibratory apparatus. *ASTM International* (2008).
- [14] A. Žnidarčič, R. Mettin, C. Cairós, and M. Dular. Attached cavitation at a small diameter ultrasonic horn tip. *Physics of Fluids*, **26**:023304 (2014).
- [15] S. Mottyll and R. Skoda. Numerical 3D flow simulation of ultrasonic horns with attached cavitation structures and assessment of flow aggressiveness and cavitation erosion sensitive wall zones. *Ultrasonics Sonochemistry*, **31**:570–589 (2016).
- [16] S. Mottyll and R. Skoda. Numerical 3D flow simulation of attached cavitation structures at ultrasonic horn tips and statistical evaluation of flow aggressiveness via load collectives. *Journal of Physics: Conference Series*, **656**:012052 (2015).
- [17] S. Hattori and E. Nakao. Cavitation erosion mechanisms and quantitative evaluation based on erosion particles. *Wear*, **249**:839–845 (2001).
- [18] S. A. Paepenmüller, J. Kuhlmann, M. Blume, and R. Skoda. Assessment of Flow Aggressiveness at an Ultrasonic Horn Cavitation Erosion Test Device by PVDF Pressure Measurements and 3D Flow Simulations. In *Proceedings of the 10th International Symposium on Cavitation (CAV2018)*, J. Katz, editor. ASME, New York, NY (2018).
- [19] M. S. Mihatsch, S. J. Schmidt, and N. A. Adams. Estimation of incubation times through numerical simulation of 3-D unsteady cavitating flows. *SHF Conference* (2013).
- [20] S. J. Schmidt, I. H. Sezal, and G. H. Schnerr. Compressible simulation of high-speed hydrodynamics with phase change. *European Conference on Computational Fluid Dynamics* (2006).
- [21] S. J. Schmidt, I. H. Sezal, G. H. Schnerr, and M. Thalhamer. Riemann Techniques for the Simulation of Compressible Liquid Flows with Phase-transition at all Mach numbers - Shock and Wave Dynamics in Cavitating 3-D Micro and Macro Systems. *46th AIAA Aerospace Sciences Meeting and Exhibit* (2008).
- [22] S. Mottyll, S. Müller, P. Niederhofer, J. Hussong, S. Huth, and R. Skoda. Analysis of the cavitating flow induced by an ultrasonic horn – Numerical 3D simulation for the analysis of vapour structures and the assessment of erosion-sensitive areas. *EPJ Web of Conferences*, **67**:02078 (2014).
- [23] C. Deimel and R. Skoda. Implementation of an explicit density-based solver for the simulation of cavitating flows in OpenFOAM. *9th OpenFOAM Workshop, Zagreb, Croatia*.
- [24] A. Harten. High resolution schemes for hyperbolic conservation laws. *Journal of Computational Physics*, **49**:357–393 (1983).
- [25] H. Jasak, H. G. Weller, and A. D. Gosman. High resolution nvd differencing scheme for arbitrarily unstructured meshes. *International Journal for Numerical Methods in Fluids*, **31**:431–449 (1999).
- [26] K.-H. Kim, G. Chahine, J.-P. Franc, and A. Karimi, editors. *Advanced Experimental and*

- Numerical Techniques for Cavitation Erosion Prediction*, volume 106 of *Fluid Mechanics and Its Applications*. Springer Netherlands, Dordrecht (2014).
- [27] C. Kaufhold, F. Pöhl, S. Mottyll, R. Skoda, and W. Theisen. Numerical simulation of the deformation behavior of metallic materials under cavitation induced load in the incubation period. *Wear*, **376-377**:1138–1146 (2017).
- [28] F. Pöhl, S. Mottyll, R. Skoda, and S. Huth. Evaluation of cavitation-induced pressure loads applied to material surfaces by finite-element-assisted pit analysis and numerical investigation of the elasto-plastic deformation of metallic materials. *Wear*, **330-331**:618–628 (2015).
- [29] S. J. Schmidt, M. S. Mihatsch, M. Thalhamer, and N. A. Adams. Assessment of the Prediction Capability of a Thermodynamic Cavitation Model for the Collapse Characteristics of a Vapor-Bubble Cloud. *WIMRC 3rd International Cavitation Forum 2011* (2011).
- [30] A. Karimi and W. R. Leo. Phenomenological model for cavitation erosion rate computation. *Materials Science and Engineering*, **95**:1–14 (1987).
- [31] A. L. Gurson. Continuum theory of ductile rupture by void nucleation and growth: Part i—yield criteria and flow rules for porous ductile media. *Transaction of ASME*, **99** (1977).
- [32] A. Needleman and V. Tvergaard. An analysis of ductile rupture in notched bars. *Journal of the Mechanics and Physics of Solids*, **32**:461 – 490 (1984).
- [33] S. Hattori, T. Hirose, and K. Sugiyama. Prediction method for cavitation erosion based on measurement of bubble collapse impact loads. *Journal of Physics: Conference Series*, **147**:012011 (2009).
- [34] S. Hattori, T. Hirose, and K. Sugiyama. Prediction method for cavitation erosion based on measurement of bubble collapse impact loads. *Wear*, **269**:507–514 (2010).

AN OVERVIEW ON THE USE OF THE FFOWCS WILLIAMS-HAWKINGS EQUATION FOR THE HYDROACOUSTIC ANALYSIS OF MARINE PROPELLERS

IANNIELLO S. AND TESTA C.

Institute of Marine Engineering (INM)
CNR - National Research Council
Via di Vallerano, 00128 Rome, Italy
e-mail: sandro.ianniello@cnr.it, claudio.testa@cnr.it

Key words: Hydroacoustics, Ffowcs Williams-Hawkings, Acoustic Analogy

Summary. Since the last 70s, the integral formulations solving the Ffowcs Williams-Hawkings equation are the standard approach for the prediction of noise generated by a body moving in a fluid flow and, in particular, propulsion and/or lifting devices based on rotating blades. This methodology represents the base of research and commercial software used by aeronautical industry and is more and more being applied to naval sector too, in the attempt of providing the shipbuilding industry with effective predictive tools, which to fulfill the stringent regulations on underwater noise emission with. The paper offers a brief overview on the use of the Acoustic Analogy for marine propeller hydroacoustics. At first, we propose a comprehensive numerical analysis which emphasizes the intrinsic, nonlinear nature of the problem. Then, some possible computational strategies to evaluate the noise induced by a *sheet* cavitation phenomenon are proposed and compared. Some numerical results are presented, by avoiding as much as possible any mathematical detail on the adopted, integral formulations and focusing the attention of the significant capabilities and the effectiveness of the methodology.

1 INTRODUCTION

The Ffowcs Williams-Hawkings (FWH) equation published in 1969 [1] represents an extension of the original work of Lighthill on the aerodynamically generated sound [2] and governs the noise generated by any body moving in a fluid flow. It may be easily derived from the fundamental conservation laws of mass and momentum, expressed in terms of generalized functions, by representing the presence of the body as a “discontinuity” in the fluid field. Under the assumption of negligible effects of viscosity on sound generation (which reduces the compressive stress tensor to the scalar pressure field) and isentropic transformations for the fluid (which allows to approximate the pressure-density relationship with the linear term of its series expansion, so that the *acoustic* pressure is expressed by $p' = c_0^2 \tilde{\rho}$, being $\tilde{\rho}$ the density perturbation and c_0 the constant speed of sound), this differential, non-homogeneous wave equation reads

$$\mathbb{D}^2 p' = \frac{\partial}{\partial t} \{[\rho_0 v_n + \rho \Delta_n^{uv}] \delta(f)\} - \frac{\partial}{\partial x_i} \{[\tilde{p} \hat{n}_j + \rho u_i \Delta_n^{uv}] \delta(f)\} + \frac{\partial^2}{\partial x_i \partial x_j} [T_{ij} H(f)] \quad (1)$$

where the D'Alembert operator is expressed by

$$\mathbb{D}^2 = \frac{1}{c_0^2} \frac{\partial^2}{\partial t^2} - \nabla^2,$$

and the function $f = 0$ (being f is the *support* of the Dirac and Heaviside functions, δ and H), represents a radiating surface D in the three-dimensional space. In equation (1), ρ_0 is the fluid density of the undisturbed medium; $\Delta_n^{uv} = u_n - v_n$, where \mathbf{u} and \mathbf{v} are the velocity of the fluid and the surface D , respectively, and the subscript n indicates the projection along the outward normal direction to D ; the same direction is identified by the j -component of the unit normal vector $\hat{\mathbf{n}}$, while $\tilde{p} = p - p_0$ is the pressure disturbance and $T_{ij} = u_i u_j + (\tilde{p} - c_0^2 \tilde{\rho}) \delta_{ij}$ the Lighthill tensor, with δ_{ij} the Kronecker symbol. The role played by the domain D is essential and strongly characterizes the solving approach. When D coincides with the surface S of the (rigid) moving body, the impermeability condition ($\Delta_n^{uv} = 0$) simplifies equation (1) and the three source terms on the right-hand side identify the well known *thickness*, *loading* and *quadrupole* noise components [3, 4]. Otherwise, the integration domain is immersed in the flow field and the solution is achieved by adding the contribution from the first two surface integrals, determined on the *porous*, radiating domain $D: f = 0$, and the third, volume term, computed in the whole flow region $V: f > 0$, affected by the body motion [5]. Theoretically speaking, the choice of a domain D embedding all possible noise sources, makes the volume term's contribution null and enables the evaluation of p' by surface integrals only. In any case, equation (1) is rewritten in an integral form through the Green method and the use of the free-space function

$$G(\mathbf{x}, t; \mathbf{y}, \tau) = \frac{\delta(g)}{4\pi r}; \quad g = \tau - t + \frac{r}{c_0}, \quad (2)$$

where \mathbf{x} and \mathbf{y} represent the observer and the source locations, t and τ are the observer and emission times and $r = |\mathbf{x}(t) - \mathbf{y}(\tau)|$ the source-observer distance.

As said, the FWH-based integral formulations represent the standard approach in Aeroacoustics and are widely used by aeronautical industry. In the last years, this methodology is catching on in the naval sector, where the stringent regulations on underwater noise emission push the shipbuilding industry to acquire and use hydroacoustic predictive tools, possibly at a design stage. Of course, equation (1) governs the sound generated by a body moving both in air and underwater; nevertheless, the deep differences of the physical characteristics of these fluids and, consequently, of the conditions at which analogous devices can operate, should lead to a careful and proper interpretation of the numerical solutions and to take nothing for granted. In this context, it has been shown that, unlike analogous aeronautical devices and regardless of the low rotational speed, the hydroacoustic field of a marine propeller is dominated by the non linear (quadrupole) term of equation (1). This behavior is related to the intrinsic features of propagation mechanisms of a rotating source and the significant destructive interference occurring in multibladed devices. A pseudo-analytic demonstration of these assertions may be found in [6]. Here, the same conclusions are carried out through a numerical simulation.

2 NON CAVITATING PROPELLER IN OPEN WATER

A FWH-based hydroacoustic analysis of a conventional marine propeller in open water (uniform, nocavitating flow) is here taken into account. The tested device is the INSEAN

E779A propeller and the analysis refers to an advance ratio $J = 0.71$, for which some complete sets of data are available, coming from both a DES (Detached Eddy Simulation) and a RANS (Reynolds Averaged Navier Stokes) hydrodynamic simulation. The rotational speed is fixed to $n = 25$ rps, corresponding to $M_R = 0.0118$. Due to the lack of underwater noise measurements and despite the incompressibility assumption characterizing both the RANS and DES data, the FWH noise predictions is somehow *validated* through a direct comparison with the pressure signatures provided by the hydrodynamic solvers (see [7]).

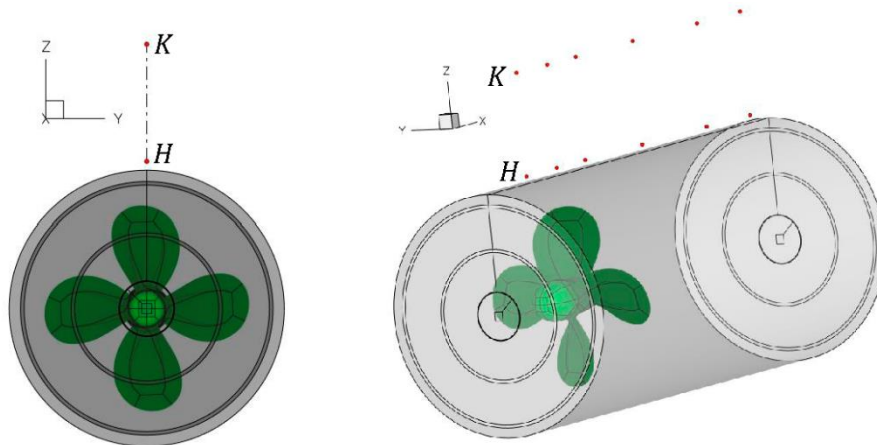


Figure 1- The E779A propeller, the porous domain S_p and hydrophones.

The prediction of noise is pursued in time domain through both the linear formulation 1A [4] and the porous approach [5] in order to identify the actual contribution of linear and nonlinear sources. The hydrodynamic mesh is constituted by several 3D blocks. In particular, the flow around the propeller is determined on subsequent, cylindrical layers which can act as porous domains S_p ; furthermore, also the noise measurement points are selected among the computational nodes located outwardly S_p , as to avoid any data-fitting procedure. Figure 1 shows one of these surfaces embedding the propeller and the numerical hydrophones, aligned to the flow and located on two horizontal lines, named H and K . These points have to fulfill two conflicting requirements: they must be positioned outside the porous domain and, then, far enough from both the body and all nonlinearities occurring in the flow; at the same time, they should be also located in a region far from the computational boundaries, where the pressure is hopefully determined with a good accuracy. The differences between the RANS and DES simulations are well known. A standard RANS approach averages the value of the velocity everywhere: the turbulent viscosity is convected in the flow by a transport equation and the modeling of the velocity turbulent component always gives rise to a significant diffusion of the numerical solution. In particular, the vorticity in the downstream region is soon smeared out. In a DES approach, on the contrary, the eddy viscosity depends on a link between the mesh spatial resolution and the distance from the rigid surfaces: the more the computational cell is small, the more the viscosity reduces moving far from the body. This means that by using a rather fine mesh, the blade detached eddies are determined in a sort of direct way and the undesirable numerical damping is notably reduced. It is important to point out that both the approaches provide the same pressure distribution upon the blade surface, as confirmed by the

very good comparison with experimental data (not shown here for brevity). Then, if the interest is focused on the propeller performances (thrust, torque, efficiency), as well as on the computation of the FWH linear terms, their effectiveness and reliability are, in essence, equivalent. On the contrary, the capability to model the vorticity in the downstream region is significantly different, as it clearly appears in figure 2 (see [8]).

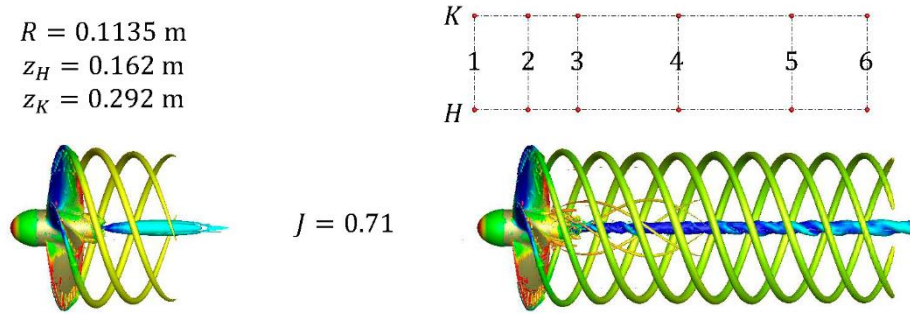


Figure 2- RANS (left) and DES (right) solutions, at $J=0.71$.

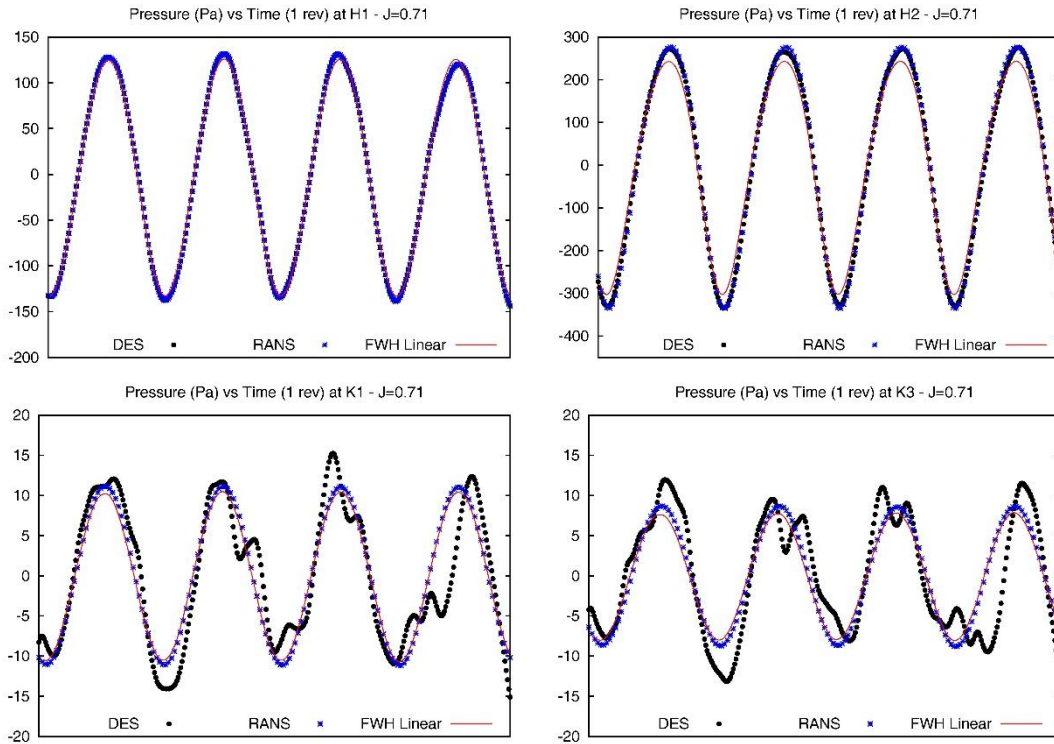


Figure 3- RANS, DES and FWH (linear) pressure signals in the proximity of the propeller.

It is worth noting that the mesh used for the two runs is exactly the same, so that the only difference stands in the aforementioned way the turbulent component of the velocity is taken into account. For additional details about the hydrodynamic solution, the reader can refer to [9, 10]. Figure 3 shows the pressure time histories determined by DES and RANS simulation and the corresponding noise prediction carried out by the FWH linear formulation 1A (using the

DES hydrodynamic data) at different points. Very close to and upstream the propeller (points H_1 and K_1 , top pictures), all the signatures are totally characterized by the BPF and the linear noise prediction matches very well the two (coincident) time histories provided by the hydrodynamic solvers. As we move from the body, however, the DES solution starts to exhibit a more irregular waveform and to differ from the other signatures. This difference immediately becomes visible at more distant points, like K_1 or K_3 , (bottom pictures). There, the DES pressure is always characterized by more pronounced fluctuations and, apparently, by a higher frequency content, while the RANS pressure still agrees well with the linear noise prediction and exhibits a much more regular shape, with four well defined peak values corresponding to the propeller blades. Such a persisting, good agreement between the RANS and the FWH-based solutions is rather self-explained. Both of them, in fact, are not able to account for the same, fundamental phenomena occurring in the field, that is the vorticity spreading in the downstream region. The RANS solution is incapable to capture this effect because of the numerical diffusion, while the linear FWH solution does not include it explicitly. Not surprisingly, the differences with the DES pressure become more and more pronounced at the furthest points from the body, where the pressure is more affected by the whole 3D vorticity field, compared to points where p is dominated by the tonal component, ruled by the blades' passage. In fact, behind points 3, both the RANS and the FWH linear solutions lose any reliability.

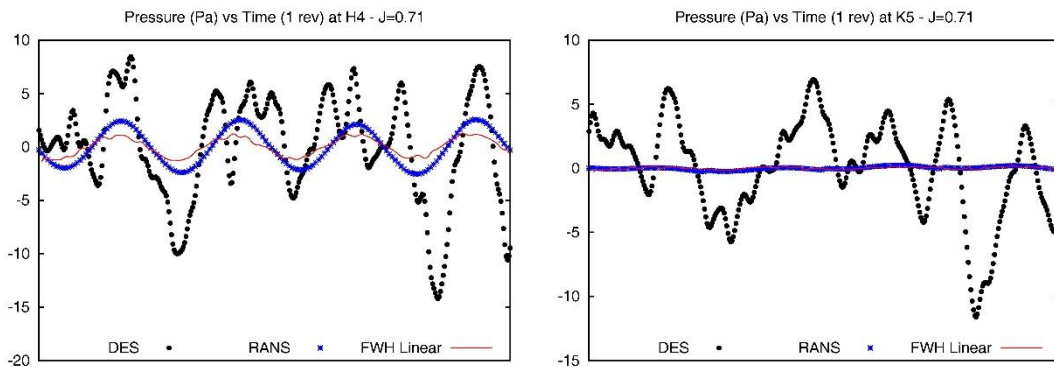


Figure 4- RANS, DES and FWH (linear) numerical solutions at points H_4 and K_5 .

Figure 4 just reports the results at point H_4 (left) and K_5 (right). While the DES pressure goes on to exhibit a more and more irregular, fluctuating waveform the RANS and the FWH solutions rapidly approach zero. Due to the closeness of the measurement points to the propeller, this annihilation of pressure is clearly unrealistic. Nonetheless, the two unreliable solutions are characterized by a significant dissimilarity. The RANS pressure is actually *wrong*, being related to the numerical diffusion (see figure 2) and the inherent inability of the computational model. The acoustic solution, on the contrary, is no doubt *correct*: the linear terms, in fact, only depend on blades' shape and hydrodynamic (DES) loads, that is the same quantities providing the very good and reliable noise predictions in the proximity of the blades' tip. Then, the vanishing of the FWH noise signature appears as an incontrovertible fact, due to the unambiguous lack of the nonlinear effects and, above all, the behavior of the linear terms for *any* propeller rotating at $M_R \sim 0.01$. Let us focus, now, our attention on the actual role played by the nonlinear noise sources, here computable through the porous formulation. Figure 5

shows the comparison between the DES hydrodynamic pressure, still the FWH linear noise prediction and the porous solution achieved by using the integration domain depicted in figure 1. Upstream the propeller (point H_1 , top-left picture) the porous and linear formulations provide the same noise signature and agree very well with the DES data; this confirms the negligible contribution of the quadrupole term in the strict proximity of the propeller .

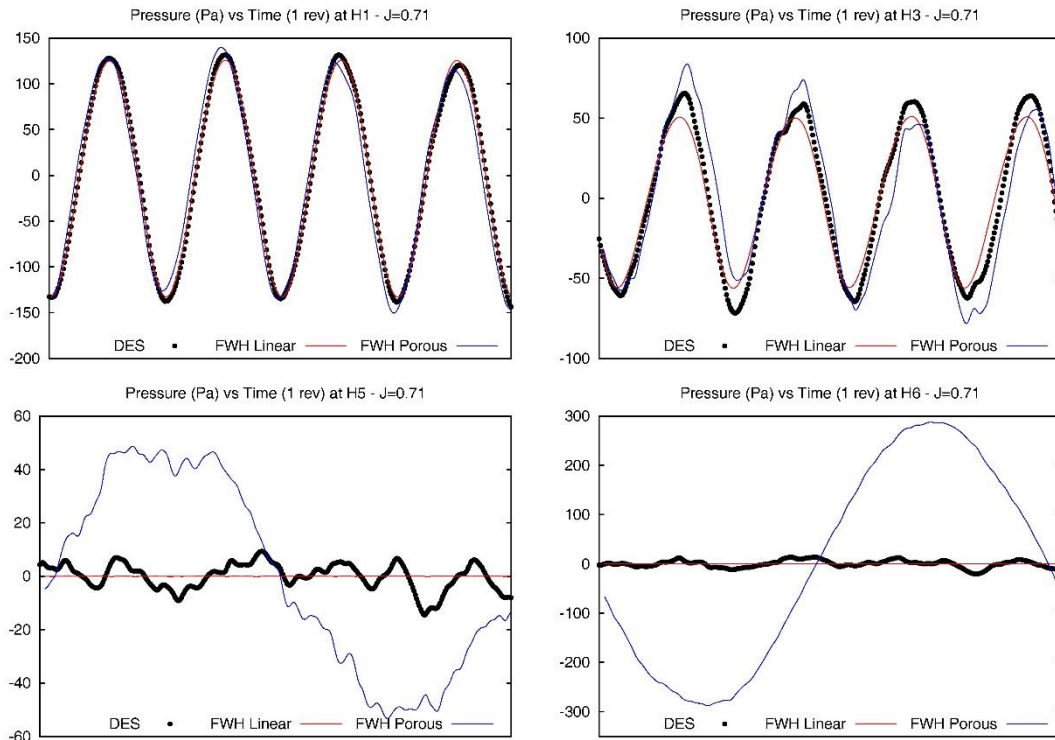


Figure 5- Comparison between DES pressure and the noise predictions achieved by the FWH linear (1A) and porous formulations, at points H_1 , H_3 , H_5 and H_6 .

Nevertheless, as we move toward the downstream region, the solution is affected by the well known *end-cap* problem and exhibits an undesired behavior. At the downstream point H_3 (top-right), for instance, the linear formulation shows a slight underestimation with respect to the DES pressure, reasonably attributable to the effects of the blade tip vortex. The accounting for the nonlinear sources, however, does not improve the solution and, actually, seems to provide a worse result. Such a worsening becomes dramatic at points H_5 and H_6 (bottom pictures), where the noise predictions appear completely unreliable. As known, the reason for such a poor quality result is the crossing of the porous domain by the tip vortex, which represents an indirect demonstration of the fundamental role played by the vorticity field. In fact, from a theoretical point of view, the porous formulation imposes two conditions on the integration domain S_p : *i*) to be a closed surface and *ii*) to embed all possible noise sources. The domain depicted in figure 1 satisfies the first condition, but, due to the unavoidable limits of the computational domain, it cannot guarantee the fulfillment of the second one. Even worse. The downstream cap of the cylindrical domain S_p not only does not embed the whole vorticity field, but it is totally immersed in the blade tip vortex spreading downstream the body, which there, presumably,

represents the dominant source of noise. Thus, the results in figure 5 simply represent some *not converged* solutions. Figure 6 shows the same noise signatures at points H_3 , H_5 (figure 5), here determined by splitting the integration domain S_p in three parts: the open cylinder, encircling the propeller and the whole blade tip vortex, and the two caps located upstream and downstream the body. As clearly shown in the left picture, the slight discrepancy occurring at point H_3 between the DES pressure and the porous formulation comes from the oscillating waveform imposed by the contribution of the downstream cap of S_p , while the signature provided by only the open cylinder perfectly overlaps the DES data.

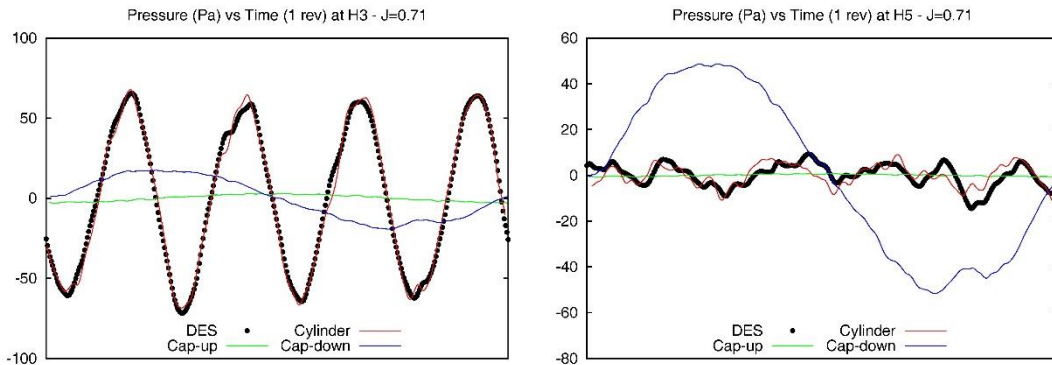


Figure 6- The FWH porous solutions at H_4 and K_5 , as splitted from different parts of S_p .

Moving toward the same downstream cap, its detrimental effects obviously increase, and at point H_5 (right picture) the overall signature is dominated by a fictitious oscillation of notable amplitude. At the same time, the contribution from the upstream cap (where the flow is very smooth) is always negligible and the noise signature provided by the open cylinder seems to match the DES pressure in a satisfactory way. The numerical effects related to the end-cap problem may be faced in different ways [11, 12, 13, 14]. Nevertheless, what we wish to point out here is that these effects do not concern the FWH linear solution at all. They point out how the tip vortex released in the field represents the main source of noise and confirm the intrinsic, nonlinear nature of the hydroacoustic field generated by a marine propeller, regardless of the low values of the rotational speed.

3 SHEET CAVITATING PROPELLERS

Another important and not standard application of the FWH equation concerns the assessment of noise induced by sheet cavitation phenomena. Acoustically speaking, cavitation is highly undesirable, as it induces an impulsive sound and deeply modifies the baseline acoustic signature of the propeller. These effects are inherently related to the spectrum of the high-energy radiated noise, that exhibits a low frequency range, governed both by tones (multiple of the blade passage frequency) and broadband hump (due to the large scale cavity dynamics), and a higher frequency broadband range due to the collapse of vapour bubbles [15, 16]. Furthermore, the occurrence of cavitation makes the detection of the sources of sound a very complicated and partially unsolved problem. In fact, the modern CFD is able to provide a satisfactory estimation of cavitation patterns [17], but a reliable simulation of important underlying phenomena (especially those related to cavities collapsing stage) is still far from being achieved.

Such a modeling uncertainty seems to be less critical in case of a sheet cavitation, which frequently occurs on conventional propellers operating in the hull wake field. It consists of a relatively *thin* vapour region which typically forms at blade leading edge, fluctuates in size in a limited azimuth range and eventually collapses, always remaining essentially attached to the blade surface (see figure 7). Under the assumption that: *i*) cavitation pockets remain attached to the blades surface and *ii*) the collapse of the cavity, due to condensation, does not imply violent implosions so that vapor bubble evolves in a smooth way (by progressively reducing its size up to disappear), a potential-flow hydrodynamics yields a reliable description of the cavity dynamics in terms of inception, growth and collapse [17].

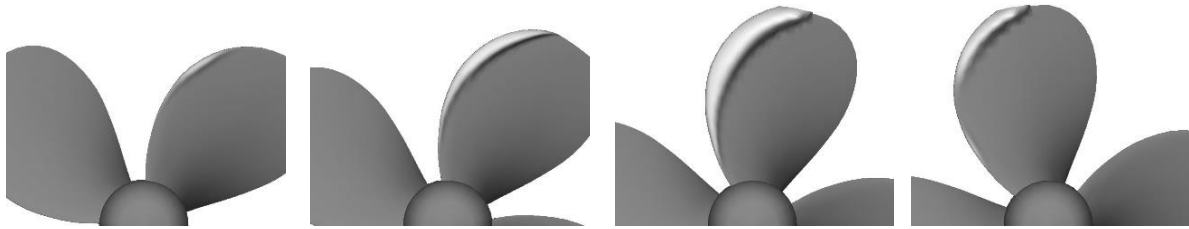


Figure 7 – Sheet cavity time evolution.

In this framework, two alternative FWH-based formulations may be applied to predict the radiated noise. The first approach, named Equivalent Blade Modeling (EBM), simply adopts the standard linear formulation 1A and uses a time-varying integration domain corresponding to blade *plus* cavity ($f = 0: S_B + S_C$). In this way, the possible presence of the cavity is essentially taken into account by the FWH thickness component, through the shape's variations of an alternative (virtual) source-body. Actually, the method violates the basic assumption of a rigid body which the FWH-based formulation is based on, but in virtue of the aforementioned approximations, the cavity time evolution may be considered as an ordered sequence of steady-states. The second approach, referred to as Transpiration Velocity Modeling (TVM), is more rigorous: it basically arises from the porous formulation and adopts a velocity/acceleration transpiration term (extracted from the hydrodynamic solution) to impose a *porous* boundary condition on the portion of the body surface affected by the cavity (S_{CB}). This condition is expressed by the relation

$$(\mathbf{u} - \mathbf{v}) \cdot \mathbf{n} = \frac{dh_C}{dt},$$

where h_C represents the time-dependent cavity thickness. Then, a 2D integral on S_{CB} adds to the classic FWH thickness and loading components and accounts for the hydroacoustic effects of the vapour cavity. The TVM approach establishes an important correlation between radiated noise and sheet cavitation pattern, yielding a mathematically-consistent description of blade-attached and fluctuating vapour pockets into an integral formulation for undeformable bodies. A schematic representation of the differences between these alternative schemes is depicted in figure 8, while the mathematical details may be found in [18, 19]. Hereafter, some numerical results concerning the analysis of the E779A propeller model, operating within the nonuniform onset flow depicted in the left picture of figure 9, are presented. The free-stream flow speed is $U_\infty = 6.24$ m/s and propeller rotational speed is $n = 30.5$ rps, corresponding to an advance

coefficient $J = 0.9$ and a cavitation number $\sigma = 4.455$. The large velocity defect in the core of the wake is expected to determine strong variations of pressure distributions on the blades and, hence, to induce a transient cavitation.

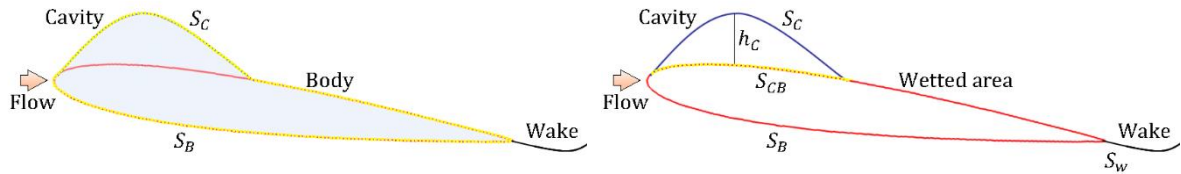


Figure 8 – Comparison between EBM (right) and TVM (left) schemes.

A fully-validated BEM (Boundary Elements Method) code, solving the Laplace equation for 3D unsteady flows around lifting bodies, working in arbitrary onset flows under unsteady sheet cavitating conditions, is used to provide the input data to the acoustic codes. The noise predictions refer to three numerical hydrophones located in the proximity of the body: point P_2 is located in the disk plane, while points H_4 and H_5 are representative for the downstream and upstream regions, respectively (right picture of the same figure 9). Once the time histories of pressure and cavity thickness distributions are determined by the BEM solver, the noise is determined through the TVM method. It is interesting to note that the hydrodynamic solution refers to the actual four-bladed propeller, while the noise is determined (and shown) just for a single blade, as to emphasize the role of cavitation on the resulting waveform.

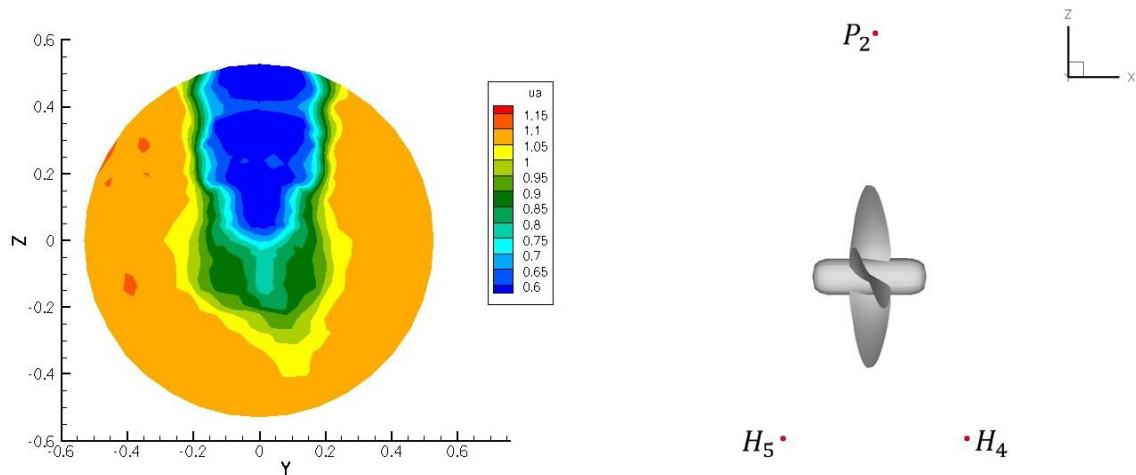


Figure 9 – The nonuniform inflow inducing a sheet cavitation on the E779A propeller model and the hydrophones used for the corresponding hydroacoustic analysis.

Left pictures in figure 10 show the comparison between the noise predictions achieved in absence of cavitation (wet condition) and in presence of a cavity (TVM scheme), at the three points of figure 7 (P_2 , H_4 and H_5 at top, center and bottom pictures, respectively). As expected, the occurrence of cavitation induces a highly impulsive waveform on pressure signatures, along with a relevant increase of the magnitude of the acoustic disturbance. This exactly happens at the azimuthal positions corresponding to cavity occurrence on the blade and it is possible to

demonstrate that the significant pressure pulses induced by cavitation are governed by the second time derivative of the cavity volume [18].

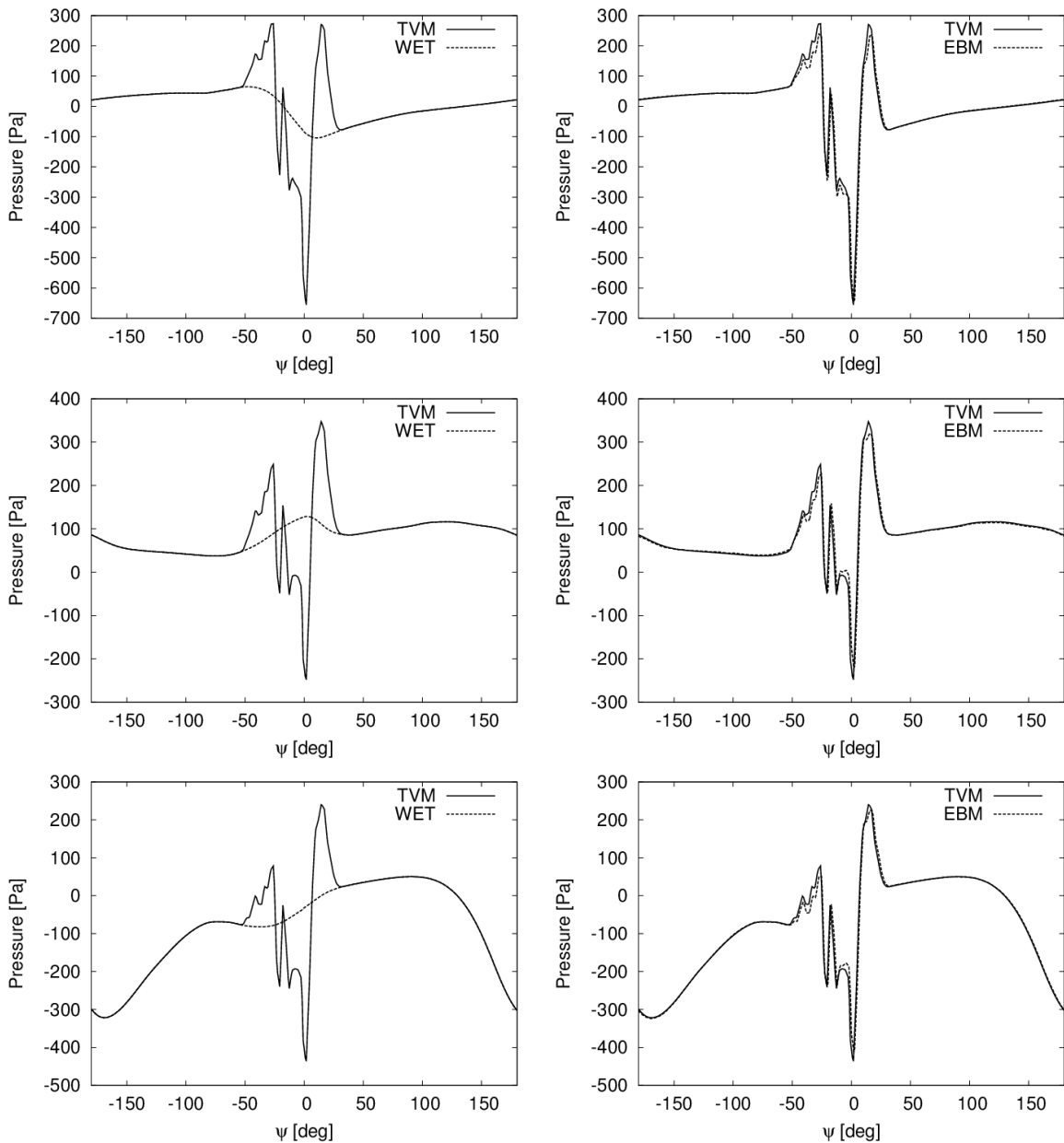


Figure 10 – On the left, the noise predictions in presence (TVM scheme) and absence (wet condition) of sheet cavitation; on the right, the comparison between the alternative approaches (TVM and EBM). Points P_2 (top pictures), H_4 (center pictures) and H_5 (bottom pictures).

Note that, due to the symmetrical location of H_4 and H_5 with respect to the disk plane, the signatures exhibit the expected sign inversion related to pressure values on face and back sides of the thrusting blade. The right pictures in the same figure 10 show the comparison between

the noise signals determined through the TVM and EBM approaches. The agreement is very good, both in terms of phase and magnitude: the waveform is practically the same, albeit subtle discrepancies, due to the different modelling of cavitation noise sources. In this context, note that the acoustic integrals of the TVM approach are affected by the presence of external time derivatives (and, then, more sensitive to fluctuations of numerical nature, induced by the accuracy of the hydrodynamic input data), while these inaccuracies do not affect the EBM method, where no derivative act on the integrals. The lack of cavitation noise measurements does not enable a definite validation of the presented results; nevertheless, the excellent agreement of the numerical solutions, here achieved by two alternative and theoretically different computing techniques, bodes well regarding their own reliability (although limited to some specific aspects of cavitation phenomena).

4 CONCLUSIONS

A brief overview on the use of the Acoustic Analogy for the hydroacoustic analysis of a marine propeller has been proposed. The FWH-based integral formulations represent very powerful and adaptive computational tools: they allow to achieve a reliable assessment of the underwater noise and, at the same time, a deep understanding of the generating noise mechanisms taking place in the flow. In the first part of the paper, through the use of hydrodynamic datasets coming from both RANS and DES simulations, we have numerically demonstrated that (unlike analogous aeronautical devices) the underwater noise generated by a marine propeller is dominated by nonlinear sources. This important feature of the hydroacoustic field is due to the occurrence and persistence of significant flow nonlinearities in the downstream region (the tip vortex) and, above all, the impressive decay of the FWH linear components, ruled by the low rotational Mach number. Then, the assessment of noise induced by a sheet cavitation has been carried out, through two alternative and rather different approaches. As expected, the occurrence of a cavity on the blade surface induces an impulsive waveform on pressure signatures and significantly alters its amplitude and frequency content.

REFERENCES

- [1] Ffowcs Williams, J.E. and Hawkings, D.L. *Sound generation by turbulence and surfaces in arbitrary motion*, Philosophical Transaction of Royal Society, 264 (A1151), 1969
- [2] Lighthill, M. J., *On sound generated aerodynamically. I General theory*, Proceedings of Royal Society, A211 (11709), 1952
- [3] Farassat, F. *Theory of Noise generation from Moving Bodies with an Application to Helicopter Rotors*, NASA, TR-R-451, 1975
- [4] Farassat, F. *Linear Acoustic Formulas for Calculation of Rotating Blade Noise*, AIAA Journal, 19 (9), 1122-1130, 1981
- [5] Di Francescantonio, P. *A new boundary integral formulation for the prediction of sound radiation*, Journal of sound & vibration, 202(4), 1997
- [6] Ianniello, S. *The Ffowcs Williams-Hawkings equation for hydroacoustic analysis of rotating blades. Part 1. The rotpole*, Journal of Fluid Mechanics, 797, 345-388, 2016

- [7] Ianniello, S., Muscari, R., Di Mascio, A. *Ship underwater noise assessment by the acoustic analogy. Part I: nonlinear analysis of a marine propeller in a uniform flow*, Journal of Marine Science and Technology, 18(4), 547-570, 2013
- [8] Jeong, J. and Hussain, F. *On the identification of a vortex*. Journal of Fluid Mechanics, 285, 69–94, 1995.
- [9] Di Mascio, A., Broglia R., Muscari, R. *On the application of the single-phase level set method to naval hydrodynamic flows*, Computer & Fluids 36, 868–886, 2007
- [10] Di Mascio, A., Broglia, R., Muscari, R. *Prediction of hydrodynamic coefficients of ship hulls by high-order Godunovtype methods*, Journal of Marine Science and Technology, 14, 19–29, 2009
- [11] Rahier, G., Huet, M., Prieur, J. *Additional terms for the use of the Ffowcs Williams and Hawkings surface integrals in turbulent flows*, Computer & Fluids, 120, 158-172, 2015
- [12] Lockard, D.P., Casper, J.H., *Permeable surface corrections for Ffowcs Williams and Hawkings integrals*, Proceedings of the 11th AIAA/CEAS Aeroacoustics Conference, Monterey, CA, 2005
- [13] Ikeda, T., Enomoto, S., Yamamoto, K. *Quadrupole effects in the Ffowcs Williams-Hawkings equation using permeable control surface*, Proceedings of the 18th AIAA/CEAS Aeroacoustics Conference, Colorado Springs, CO, 2012
- [14] Nitzkorski, Z., Mahesh, K. *A dynamic end cap technique for sound computation using the Ffowcs Williams and Hawkings equation*, Physics of Fluids, 26, 2014
- [15] Brown, N.A. *Cavitation noise problem and solutions*, International Symposium on Shipboard Acoustics, Noordwijkerhout, The Netherlands, 1976
- [16] Breslin, J.P., Andersen, P. *Hydrodynamics of ship propellers*, Cambridge University Press, Cambridge, 1994
- [17] Salvatore, F., Streckwall, H., van Terwisga, T., *Propeller cavitation modelling by CFD-results from the VIRTUE 2008 Rome Workshop*, 1st International Symposium on Marine Propulsors, Trondheim, Norway, 2009
- [18] Salvatore, F., Ianniello, S., Preliminary results on acoustic modelling of cavitating propellers, Computational Mechanics, 32(4), 291-300, 2003
- [19] Testa, C., Ianniello, S., Salvatore, F. *A Ffowcs Williams and Hawkings formulation for hydroacoustic analysis of propeller sheet cavitation*, Journal of Sound & Vibration, 413, 421-441, 2018

A COMPLETE DATA-DRIVEN FRAMEWORK FOR THE EFFICIENT SOLUTION OF PARAMETRIC SHAPE DESIGN AND OPTIMISATION IN NAVAL ENGINEERING PROBLEMS

NICOLA DEMO*, MARCO TEZZELE*, ANDREA MOLA* AND
GIANLUIGI ROZZA*

*Mathematics Area, mathLab, SISSA, International School of Advanced Studies,
via Bonomea 265, I-34136 Trieste, Italy
e-mail: nicola.demo@sissa.it, marco.tezzele@sissa.it, andrea.mola@sissa.it,
gianluigi.rozza@sissa.it

Key words: Proper Orthogonal Decomposition, Data-driven Reduced Order Modeling, Shape Parametrisation, Free Form Deformation

Abstract. In the reduced order modeling (ROM) framework, the solution of a parametric partial differential equation is approximated by combining the high-fidelity solutions of the problem at hand for several properly chosen configurations. Examples of the ROM application, in the naval field, can be found in [31, 24]. Mandatory ingredient for the ROM methods is the relation between the high-fidelity solutions and the parameters. Dealing with geometrical parameters, especially in the industrial context, this relation may be unknown and not trivial (simulations over hand morphed geometries) or very complex (high number of parameters or many nested morphing techniques). To overcome these scenarios, we propose in this contribution an efficient and complete data-driven framework involving ROM techniques for shape design and optimization, extending the pipeline presented in [7]. By applying the singular value decomposition (SVD) to the points coordinates defining the hull geometry — assuming the topology is inalterated by the deformation —, we are able to compute the optimal space which the deformed geometries belong to, hence using the modal coefficients as the new parameters we can reconstruct the parametric formulation of the domain. Finally the output of interest is approximated using the proper orthogonal decomposition with interpolation technique. To conclude, we apply this framework to a naval shape design problem where the bulbous bow is morphed to reduce the total resistance of the ship advancing in calm water.

1 Introduction

The reduced basis method (RBM) [13, 21] is a well-spread technique for reduced order modeling, both in academia and in industry [24, 23, 31, 20], and consists in two phases: an offline phase that can be carried out on high performance computing facilities, and an online one that exploits the reduced dimensionality of the system to perform the parametric computation on portable devices. In the offline stage the reduced order space is created from full order complex simulations computed for certain values of the parameters. The selection of the reduced basis functions that span this new reduced space can be carried out by different techniques. In this work we employ the proper orthogonal decomposition (POD) [19, 3], which is based on the singular value decomposition (SVD), on the set of high-fidelity snapshots. After the creation of such space, in the online phase a new parametric solution is calculated as a linear combination of the precomputed reduced basis functions. The creation of a reduced order model is crucial in the shape optimisation context where the optimiser needs to compute several high-fidelity simulations.

Novelty of this work is the creation of a reduced order space containing the manifold of admissible shapes by applying POD over the sampled geometries, in order to reduce the parameter space dimension and to enhance the order reduction of the output fields. To generate the original design space we employ the free form deformation (FFD) method, a well-known shape parametrisation technique. Another approach for reduced order modeling enhanced by parameter space reduction technique can be found in [30] where they propose a coupling between POD-Galerkin methods and active subspaces. After the creation of the reduced space for the admissible shapes, we can exploit this new parametric formulation for the construction of the reduced space for the output fields, using the non-intrusive technique called POD with interpolation (PODI) [5, 6, 10] for the online computation of the coefficients of the linear combination. We would like to cite [16] where they present the concept of a shape manifold representing all the admissible shapes, independently of the original design parameters, and thus exploiting the intrinsic dimensionality of the problem.

This work is organised as follows: after the presentation of the general setting of the problem, there is a brief overview of the FFD method, then we illustrate how the parameter space reduction is performed, and we present PODI for the reduction of the high-fidelity snapshots. Finally the numerical results are presented with the conclusions and some perspective.

2 The problem

Let $\Omega \subset \mathbb{R}^3$ be the reference hull domain. We define a parametric shape morphing function \mathcal{M} as follows

$$\mathcal{M}(\mathbf{x}; \boldsymbol{\mu}) : \mathbb{R}^3 \rightarrow \mathbb{R}^3, \quad (1)$$

which maps Ω into the deformed domain $\Omega(\boldsymbol{\mu})$ as $\Omega(\boldsymbol{\mu}) = \mathcal{M}(\Omega; \boldsymbol{\mu})$, where $\boldsymbol{\mu} \in \mathbb{D} \subset \mathbb{R}^5$ represents the vector of the geometrical parameters. \mathbb{D} will be properly defined in Section 4. Such map \mathcal{M} can represent many different morphing techniques (not necessarily affine) such as free form deformation (FFD) [26], radial basis functions (RBF) interpolation [4, 17, 15], and the inverse distance weighting (IDW) interpolation [27, 33, 11, 2], for instance. In this work we use the FFD, presented in Section 3, to morph a bulbous bow of a benchmark hull. We chose the DTMB 5415 hull thanks to the vast amount of experimental data available in the literature, see

for example [18]. In Figure 1 the domain Ω and a particular of the bulbous bow we are going to parametrize and deform.

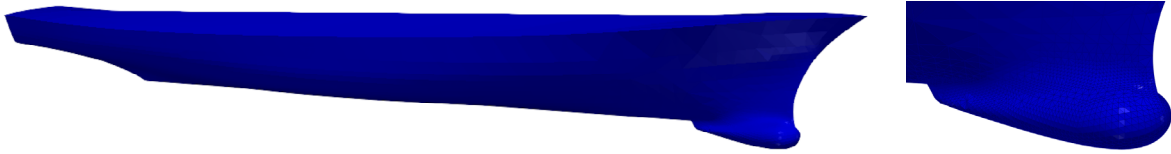


Figure 1: Complete hull domain representing the DTMB 5415 and, on the right, a zoom on the bulbous bow.

The pipeline is the following: using geometrical FFD parameters we generate several deformed hulls; then we apply the POD on the coordinates of the points describing the deformed geometries, and the new parameters will be the POD coefficients of the selected modes; after checking for possible linear dependencies between these coefficients, we sample the reduced parameter space producing new deformed hulls upon which we are going to actually perform CFD simulations. Regarding the full order model, we use the Reynolds-averaged Navier-Stokes equations to describe the incompressible and turbulent flow around the ship. The Froude number has been set to 0.2 and we chose the k - ω SST model for the turbulence since it is one of the most popular benchmark for hydrodynamic analysis for industrial naval problems. In this way we reduce the parameter space, staying on the manifold of the admissible shapes, and reducing the burden of the output reduced space construction through PODI.

3 Free form deformation of the bulbous bow

Here we are going to properly define the deformation map \mathcal{M} introduced in Eq. (1), which we employed for this work, and that corresponds to the free form deformation (FFD) technique. The original formulation of the FFD can be found in [26], for more recent works in the context of reduced basis methods for shape optimization we cite [14, 22, 28]. It has also been applied to naval engineering problems in [7, 8, 32], while for an automotive case see [25].

The FFD map is the composition of three maps described in the following, while for a visual representation we refer to Figure 2:

- the function ψ maps the physical domain to the reference one where we construct the reference lattice of points, denoted with \mathbf{P} around the object to be morphed;
- the function T performs the actual deformation since it applies the displacements defined by $\boldsymbol{\mu}_{\text{FFD}}$ to the lattice \mathbf{P} . It uses the B-splines or Bernstein polynomials tensor product to morph all the points inside the lattice of control points;
- finally we need to map back the deformed domain to the physical configuration through the map ψ^{-1} .

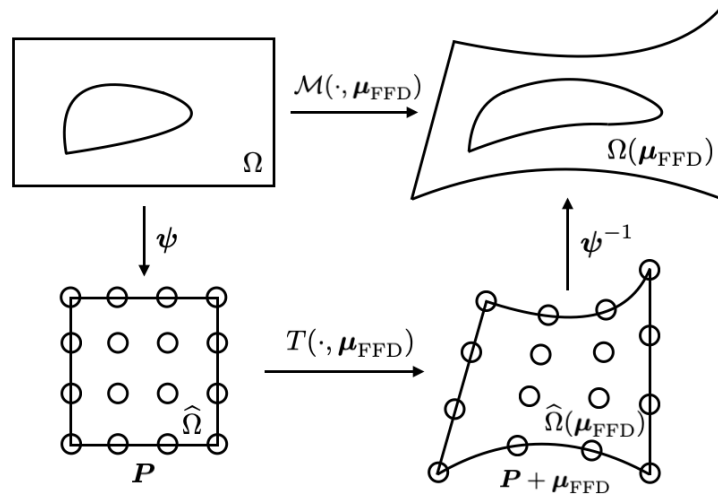


Figure 2: Sketch of the FFD map \mathcal{M} composition. The domain is mapped to a reference configuration, then the lattice of FFD control points induce the body deformation, and finally the morphed object is mapped back to the physical space.

Se we can define the FFD map \mathcal{M} through the composition of the three maps presented above as

$$\mathcal{M}(\mathbf{x}, \boldsymbol{\mu}_{\text{FFD}}) := (\psi^{-1} \circ T \circ \psi)(\mathbf{x}, \boldsymbol{\mu}_{\text{FFD}}) \quad \forall \mathbf{x} \in \Omega. \quad (2)$$

In Figure 3 it is possible to see the actual lattice of points we used, in green, for a particular choice of the FFD parameters. For an actual implementation of this method in Python, along with other possible deformation methods, we refer to the open source package called PyGeM - Python Geometrical Morphing [1].

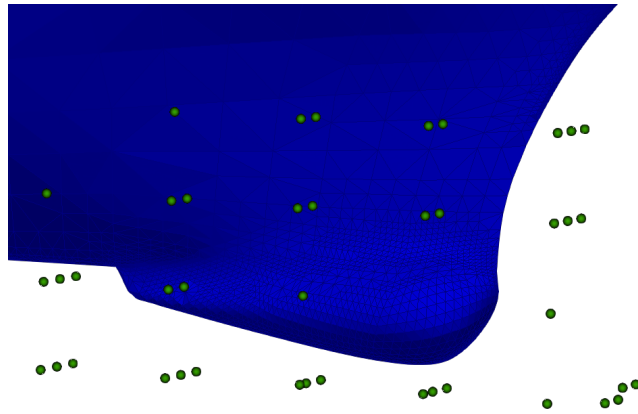


Figure 3: Example of FFD parametrisation and morphing of the DTMB 5415 hull. In green the lattice of control points that define the actual deformation.

4 Reduction of the parameter space through POD of the mesh coordinates

In order to reduce the parameter space dimension we apply the POD on a set of snapshots that depends on the FFD parameters. Each snapshot is the collection of all the coordinates of the points defining the *stl* file geometry. Since the generation of these snapshots does not depend on complex simulations but only on the particular FFD deformation, we are able to create a dataset with as many entries as we want. So we create a database of $N_{\text{train}} = 1500$ geometrical parameters $\boldsymbol{\mu}_{\text{FFD}} \in \mathbb{D} := [-0.3, 0.3]^5$ sampled with a uniform distribution. Moreover we create the corresponding database of mesh coordinates \mathbf{u} corresponding to these parameters, that is $\Theta = [\mathbf{u}(\boldsymbol{\mu}_{\text{FFD},1}) | \dots | \mathbf{u}(\boldsymbol{\mu}_{\text{FFD},N_{\text{train}}})]$. Then we perform the singular value decomposition (SVD) on Θ in order to extract the matrix of POD modes:

$$\Theta = \Psi \Sigma \Phi^T, \quad (3)$$

where with Ψ and Φ we denote the left and right singular vectors matrices of Θ respectively, and with Σ the diagonal matrix containing the singular values in decreasing order. The columns of Ψ , denoted with ψ_i , are the so-called POD modes. We can thus express the approximated reduced mesh with the first N modes as

$$\mathbf{u}^N = \sum_{i=1}^N \alpha_i \psi_i, \quad (4)$$

where α_i are the so called POD coefficients. To compute them in matrix form we just use the database we created as follows

$$\boldsymbol{\alpha} = \Psi^T \Theta, \quad (5)$$

and then we truncate to the first N modes and coefficients.

After the selection of the number of POD modes required to have an accurate approximation of each geometry, we end up with the first reduction of the parameter space, that is with 3 POD coefficients $\boldsymbol{\mu}_{\text{POD}} := \boldsymbol{\alpha} \in \mathbb{R}^3$, we are able to represent all the possible deformations for $\boldsymbol{\mu}_{\text{FFD}} \in \mathbb{D}$. So we can express every geometry with 3 modes, but the coefficients can still be linearly dependent. We can investigate this dependance by plotting every component $\boldsymbol{\mu}_{\text{POD}}^{(i)}$ against each other. As we can see from the plot on the left in Figure 4, we can approximate $\boldsymbol{\mu}_{\text{POD}}^{(2)}$ with a linear regression given $\boldsymbol{\mu}_{\text{POD}}^{(1)}$. For what concerns $\boldsymbol{\mu}_{\text{POD}}^{(3)}$, we can constraint it to be inside the quadrilateral in Figure 4, on the right. So we are able to express every possible geometry described with the original 5 FFD parameters with only 2 new independent parameters. We can thus sample the full parameter space using a new reduced space, preserving the geometrical variability, and reducing the construction cost of the reduced output field space. This, as we are going to present, results in a faster optimization procedure.

5 Non-intrusive reduced order modeling by means of PODI

Proper orthogonal decomposition with interpolation is a non-intrusive data-driven method for reduced order modeling allowing an efficient approximation of the solution of parametric partial differential equations. As well as for the geometries, we collect in a database the high-fidelity solutions of several CFD simulations corresponding to different configurations, then we

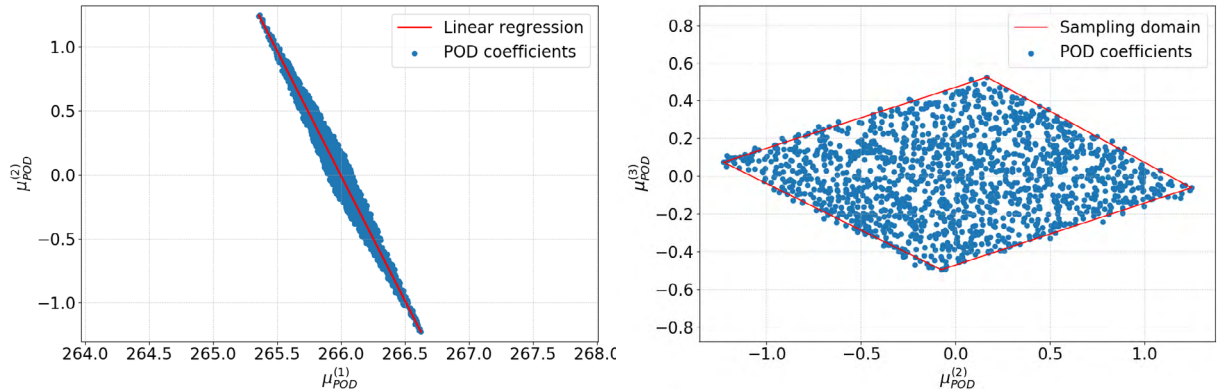


Figure 4: POD coefficients dependance. On the left we have $\mu_{\text{POD}}^{(2)}$ with respect to $\mu_{\text{POD}}^{(1)}$ in blue, and in red the linear regression to approximate one as a function of the other. On the right $\mu_{\text{POD}}^{(3)}$ against $\mu_{\text{POD}}^{(2)}$ in blue, and in red the boundaries defining the quadrilateral in which the sampling is performed.

apply the POD algorithm to the solutions matrix — the matrix whose columns are the solutions — in order to extract the POD modes that span the optimal space which the solutions belong to. Thus the solutions can be projected onto the reduced space: we represent the high-fidelity solutions as linear combination of the POD modes. Similarly to Eq. (4), the modal coefficients of the i -th solution $\mathbf{x}_i^{\text{PODI}}$ — also called the reduced solution — are obtained as:

$$\mathbf{x}_i^{\text{PODI}} = \mathbf{U}^T \mathbf{x}_i \quad \forall i \in \{1, \dots, M\} \quad (6)$$

where \mathbf{U} refers to the POD modes and M is the number of high-fidelity solutions. We call N the number of POD modes and \mathcal{N} the dimension of high-fidelity solutions then $\mathbf{x}_i^{\text{PODI}} \in V^N$ and $\mathbf{x}_i \in V^{\mathcal{N}}$. Since in complex problems we have an high number of degrees of freedom, typically we have $N \ll \mathcal{N}$. The low-rank representation of the solutions allows to easily interpolate them, exploiting the relation between the reduced solutions and the input parameters: in this way, we can compute the modal coefficients for any new parametric point and project the reduced solution onto the high dimensional space for a real-time approximation of the truth solution. This technique is defined non-intrusive, since it relies only on the solutions, without requiring information about the physical system and the equations describing it. For this reason it is particularly suited for industrial problem, thanks to its capability to be coupled also with commercial solvers. The downside is the error introduced by the interpolation, depending by the method itself, and the requirement of solutions with the same dimensionality, that can be a problem if the computational grid is built from scratch for any new configuration. Possible solutions are the projection of the solution on a reference mesh [7], or to deform the grid using the laplacian diffusion [29]. Moreover, we cite [12, 25] for other examples of PODI applications. For this work, we employed the open source Python package EZyRB [9] as software to perform the data-driven model order reduction.

6 Numerical results

In this section we present the results for the application of the complete pipeline to the problem presented in Section 2.

First, we sample the full parameter space \mathbb{D} extracting $N_{\text{POD}} = 100$ parameters to construct the reduce order model without any further reduction, and we identify this approach with the subscript ‘‘POD’’. Then, as explained in Section 4, we compute the shape manifold with 1500 different deformations, and we extract the new coefficients describing the new reduced parameter space. We sample this 2-dimensional space uniformly and we collect $N_{\text{POD}+\text{reduction}} = 80$ solution snapshots. We can compare the decay of the singular values of the snapshots matrix for the two approaches. In Figure 5 we can note how the proposed computational pipeline results in a faster decay and thus in a better approximation for a given number of POD modes.

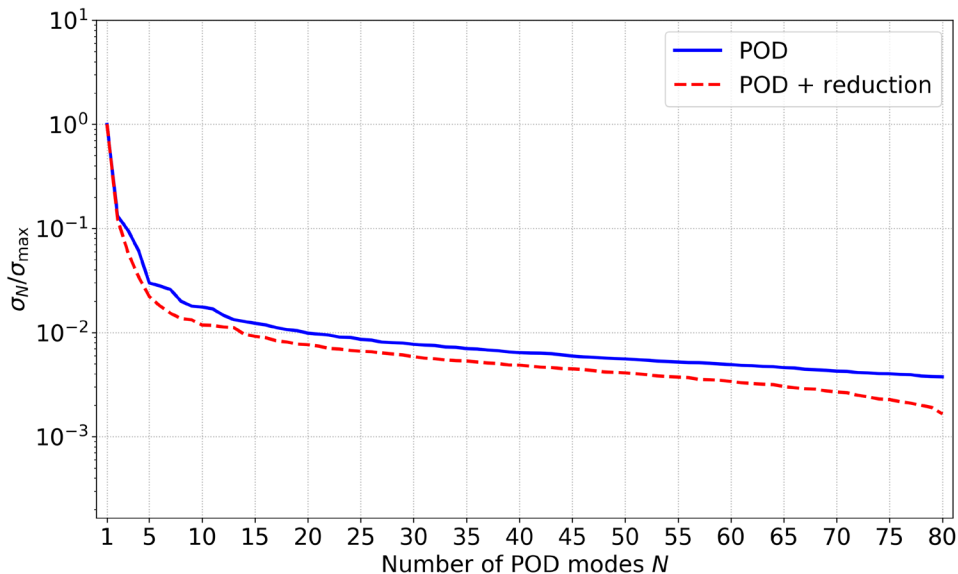


Figure 5: POD singular values decay as a function of the number of modes. The blue line corresponds to the original sampling in the full parameter space, while the red dotted line, which identifies the POD+reduction approach, corresponds to the sampling in the new reduced parameter space.

We underline that, despite the gain is not so big, the results do not involve further high-fidelity simulations. We only collected several different deformations at a negligible computational cost with respect to a single full order CFD simulation. Moreover the construction of the interpolator takes a huge advantage of the reduced parameter space since it counters the curse of dimensionality.

We can conclude that the proposed preprocessing step has sever benefits in terms of accuracy of the reduced order model at a small cost from a computational point of view.

7 Conclusions and perspectives

In this work we presented a complete data-driven numerical pipeline for shape optimization in naval engineering problems. The object was to find the optimal bulbous bow to minimize the total drag resistance of a hull advancing in calm water. First we parametrized and morphed the bulbous bow through the free form deformation method. Then we reduced the parameter space dimension approximating the shape manifold with the use of proper orthogonal decomposition and the investigation on linear dependence of the POD coefficients. We create the reduced order model sampling only the reduced two dimensional parameter space and with POD with interpolation we can compute in real time the outputs of interest for untried new parameters. Thus the optimizer can query the surrogate model and find the optimal shape.

Acknowledgements

This work was partially performed in the context of the project SOPHYA - “Seakeeping Of Planing Hull Yachts”, supported by Regione FVG, POR-FESR 2014-2020, Piano Operativo Regionale Fondo Europeo per lo Sviluppo Regionale, and partially supported by European Union Funding for Research and Innovation — Horizon 2020 Program — in the framework of European Research Council Executive Agency: H2020 ERC CoG 2015 AROMA-CFD project 681447 “Advanced Reduced Order Methods with Applications in Computational Fluid Dynamics” P.I. Gianluigi Rozza.

REFERENCES

- [1] PyGeM: Python Geometrical Morphing. Available at: <https://github.com/mathLab/PyGeM>.
- [2] F. Ballarin, A. D’Amario, S. Perotto, and G. Rozza. A POD-selective inverse distance weighting method for fast parametrized shape morphing. *International Journal for Numerical Methods in Engineering*, 117(8):860–884, 2018.
- [3] P. Benner, M. Ohlberger, A. Patera, G. Rozza, and K. Urban, editors. *Model Reduction of Parametrized Systems*, volume 17 of *MS&A – Modeling, Simulation and Applications*. Springer, 2017.
- [4] M. D. Buhmann. *Radial basis functions: theory and implementations*, volume 12. Cambridge university press, 2003.
- [5] T. Bui-Thanh, M. Damodaran, and K. Willcox. Proper orthogonal decomposition extensions for parametric applications in compressible aerodynamics. In *21st AIAA Applied Aerodynamics Conference*, page 4213, 2003.
- [6] K. Carlberg, C. Bou-Mosleh, and C. Farhat. Efficient non-linear model reduction via a least-squares Petrov-Galerkin projection and compressive tensor approximations. *International Journal for Numerical Methods in Engineering*, 86(2):155–181, oct 2010.
- [7] N. Demo, M. Tezzele, G. Gustin, G. Lavini, and G. Rozza. Shape optimization by means of proper orthogonal decomposition and dynamic mode decomposition. In *Technology and Sci-*

- ence for the Ships of the Future: Proceedings of NAV 2018: 19th International Conference on Ship & Maritime Research, pages 212–219. IOS Press, 2018.
- [8] N. Demo, M. Tezzele, A. Mola, and G. Rozza. An efficient shape parametrisation by free-form deformation enhanced by active subspace for hull hydrodynamic ship design problems in open source environment. In *The 28th International Ocean and Polar Engineering Conference*, 2018.
- [9] N. Demo, M. Tezzele, and G. Rozza. EZyRB: Easy Reduced Basis method. *The Journal of Open Source Software*, 3(24):661, 2018.
- [10] R. Everson and L. Sirovich. Karhunen–loève procedure for gappy data. *JOSA A*, 12(8):1657–1664, 1995.
- [11] D. Forti and G. Rozza. Efficient geometrical parametrisation techniques of interfaces for reduced-order modelling: application to fluid–structure interaction coupling problems. *International Journal of Computational Fluid Dynamics*, 28(3-4):158–169, 2014.
- [12] F. Garotta, N. Demo, M. Tezzele, M. Carraturo, A. Reali, and G. Rozza. Reduced Order Isogeometric Analysis Approach for PDEs in Parametrized Domains. *Submitted, QUIET special volume*, 2018.
- [13] J. S. Hesthaven, G. Rozza, and B. Stamm. *Certified Reduced Basis Methods for Parametrized Partial Differential Equations*. Springer Briefs in Mathematics. Springer, Switzerland, 1 edition, 2015.
- [14] T. Lassila and G. Rozza. Parametric free-form shape design with PDE models and reduced basis method. *Computer Methods in Applied Mechanics and Engineering*, 199(23–24):1583–1592, 2010.
- [15] A. Manzoni, A. Quarteroni, and G. Rozza. Model reduction techniques for fast blood flow simulation in parametrized geometries. *International journal for numerical methods in biomedical engineering*, 28(6-7):604–625, 2012.
- [16] L. Meng, P. Breitkopf, G. Le Quilliec, B. Raghavan, and P. Villon. Nonlinear shape-manifold learning approach: concepts, tools and applications. *Archives of Computational Methods in Engineering*, 25(1):1–21, 2018.
- [17] A. Morris, C. Allen, and T. Rendall. CFD-based optimization of aerofoils using radial basis functions for domain element parameterization and mesh deformation. *International Journal for Numerical Methods in Fluids*, 58(8):827–860, 2008.
- [18] A. Olivieri, F. Pistani, A. Avanzini, F. Stern, and R. Penna. Towing tank experiments of resistance, sinkage and trim, boundary layer, wake, and free surface flow around a naval combatant in-sean 2340 model. Technical report, DTIC Document, 2001.
- [19] A. Quarteroni and G. Rozza. *Reduced Order Methods for Modeling and Computational Reduction*, volume 9 of *MS&A – Modeling, Simulation and Applications*. Springer, 2014.

- [20] G. Rozza, M. W. Hess, G. Stabile, M. Tezzele, and F. Ballarin. Preliminaries and warming-up: Basic ideas and tools. In P. Benner, S. Grivet-Talocia, A. Quarteroni, G. Rozza, W. H. A. Schilders, and L. M. Silveira, editors, *Handbook on Model Order Reduction*, volume 1, chapter 1. De Gruyter, 2019.
- [21] G. Rozza, D. B. P. Huynh, and A. T. Patera. Reduced basis approximation and a posteriori error estimation for affinely parametrized elliptic coercive partial differential equations. *Archives of Computational Methods in Engineering*, 15(3):1, 2007.
- [22] G. Rozza, A. Koshakji, and A. Quarteroni. Free Form Deformation techniques applied to 3D shape optimization problems. *Communications in Applied and Industrial Mathematics*, 4(0):1–26, 2013.
- [23] G. Rozza, M. H. Malik, N. Demo, M. Tezzele, M. Girfoglio, G. Stabile, and A. Mola. Advances in Reduced Order Methods for Parametric Industrial Problems in Computational Fluid Dynamics. Glasgow, UK, 2018. ECCOMAS Proceedings.
- [24] F. Salmoiraghi, F. Ballarin, G. Corsi, A. Mola, M. Tezzele, and G. Rozza. Advances in geometrical parametrization and reduced order models and methods for computational fluid dynamics problems in applied sciences and engineering: Overview and perspectives. *ECCOMAS Congress 2016 - Proceedings of the 7th European Congress on Computational Methods in Applied Sciences and Engineering*, 1:1013–1031, 2016.
- [25] F. Salmoiraghi, A. Scardigli, H. Telib, and G. Rozza. Free-form deformation, mesh morphing and reduced-order methods: enablers for efficient aerodynamic shape optimisation. *International Journal of Computational Fluid Dynamics*, 0(0):1–15, 2018.
- [26] T. Sederberg and S. Parry. Free-Form Deformation of solid geometric models. In *Proceedings of SIGGRAPH - Special Interest Group on GRAPHics and Interactive Techniques*, pages 151–159. SIGGRAPH, 1986.
- [27] D. Shepard. A two-dimensional interpolation function for irregularly-spaced data. In *Proceedings-1968 ACM National Conference*, pages 517–524. ACM, 1968.
- [28] D. Sieger, S. Menzel, and M. Botsch. On shape deformation techniques for simulation-based design optimization. In *New Challenges in Grid Generation and Adaptivity for Scientific Computing*, pages 281–303. Springer, 2015.
- [29] G. Stabile and G. Rozza. Efficient geometrical parametrization for finite-volume based reduced order methods. *Submitted*, 2019.
- [30] M. Tezzele, F. Ballarin, and G. Rozza. Combined parameter and model reduction of cardiovascular problems by means of active subspaces and POD-Galerkin methods. In *Mathematical and Numerical Modeling of the Cardiovascular System and Applications*. SEMA SIMAI Springer Series 16, 2018.
- [31] M. Tezzele, N. Demo, A. Mola, and G. Rozza. An integrated data-driven computational pipeline with model order reduction for industrial and applied mathematics. *Submitted, Special Volume ECMI*, 2018.

- [32] M. Tezzele, F. Salmoiraghi, A. Mola, and G. Rozza. Dimension reduction in heterogeneous parametric spaces with application to naval engineering shape design problems. *Advanced Modeling and Simulation in Engineering Sciences*, 5(1):25, Sep 2018.
- [33] J. Witteveen and H. Bijl. Explicit mesh deformation using Inverse Distance Weighting interpolation. In *19th AIAA Computational Fluid Dynamics*. AIAA, 2009.

SHAPE OPTIMIZATION THROUGH PROPER ORTHOGONAL DECOMPOSITION WITH INTERPOLATION AND DYNAMIC MODE DECOMPOSITION ENHANCED BY ACTIVE SUBSPACES

MARCO TEZZELE*, NICOLA DEMO* AND GIANLUIGI ROZZA*

*Mathematics Area, mathLab, SISSA, International School of Advanced Studies,
via Bonomea 265, I-34136 Trieste, Italy
e-mail: marco.tezzele@sissa.it, nicola.demo@sissa.it, gianluigi.rozza@sissa.it

Key words: Nonintrusive Model Order Reduction, Active Subspaces, Free Form Deformation, POD with Interpolation, Dynamic Mode Decomposition, Parameter Space Reduction

Abstract. We propose a numerical pipeline for shape optimization in naval engineering involving two different non-intrusive reduced order method (ROM) techniques. Such methods are proper orthogonal decomposition with interpolation (PODI) and dynamic mode decomposition (DMD). The ROM proposed will be enhanced by active subspaces (AS) as a pre-processing tool that reduce the parameter space dimension and suggest better sampling of the input space.

We will focus on geometrical parameters describing the perturbation of a reference bulbous bow through the free form deformation (FFD) technique. The ROM are based on a finite volume method (FV) to simulate the multi-phase incompressible flow around the deformed hulls.

In previous works we studied the reduction of the parameter space in naval engineering through AS [38, 10] focusing on different parts of the hull. PODI and DMD have been employed for the study of fast and reliable shape optimization cycles on a bulbous bow in [9].

The novelty of this work is the simultaneous reduction of both the input parameter space and the output fields of interest. In particular AS will be trained computing the total drag resistance of a hull advancing in calm water and its gradients with respect to the input parameters. DMD will improve the performance of each simulation of the campaign using only few snapshots of the solution fields in order to predict the regime state of the system. Finally PODI will interpolate the coefficients of the POD decomposition of the output fields for a fast approximation of all the fields at new untried parameters given by the optimization algorithm. This will result in a non-intrusive data-driven numerical optimization pipeline completely independent with respect to the full order solver used and it can be easily incorporated into existing numerical pipelines, from the reference CAD to the optimal shape.

1 Introduction

In a shape optimization problem, we aim to find the shape — among all the admissible geometries — that minimizes a certain objective function. In this work we propose a novel approach to optimize the total resistance of a ship hull advancing in calm water by deforming the original hull, a common problem in the naval engineering field.

First we define the total resistance as the sum of the viscous and lift forces acting on the hull. Formally, our optimization problem can be expressed as

$$\min_{\forall \boldsymbol{\mu} \in D} f(\Omega, \boldsymbol{\mu}) = \min_{\forall \boldsymbol{\mu} \in D} \oint p \cos \theta \, d\Omega_{\boldsymbol{\mu}} + \oint \tau_x \, d\Omega_{\boldsymbol{\mu}}, \quad (1)$$

where the $D \subset \mathbb{R}^P$ is the parametric domain, P the number of parameters, $\Omega \in \mathbb{R}^3$ is the reference hull domain, and $\Omega_{\boldsymbol{\mu}} = \mathcal{M}(\Omega, \boldsymbol{\mu})$ is the deformed hull. The morphing map $\mathcal{M}(\cdot, \boldsymbol{\mu}) : \mathbb{R}^3 \rightarrow \mathbb{R}^3$ we use in this work is the free form deformation (FFD) and will be properly defined in Section 2. Examples of other deformation techniques are radial basis functions (RBF) interpolation [5, 22, 21], and inverse distance weighting (IDW) interpolation [32, 13, 2]. The unknowns p and τ_x denote respectively the pressure and the x component of the wall shear stress over the hull surface, while θ is the angle between the flow direction and the surface. The evaluation of the objective function requires a numerical simulation of the flow around the ship, which has a high computational cost. The purpose of this work is beyond an analysis of the adopted full order model for the fluid dynamics, we just provide a brief summary in order to facilitate the understanding of the pipeline. We resolve the Reynolds-averaged Navier Stokes (RANS) equations with the k - ω SST turbulence model using a finite volume approach, a typical benchmark in industrial hydrodynamics analysis. Such model deals very well with turbulent fluid, but at high computational cost. Moreover, due to the complexity of the optimization problem, we typically need many evaluations of the objective function to converge to the optimal shape.

For this work we choose to simulate the flow around the DTMB 5415 hull due to the existence of a vast amount of literature and benchmark tests. In Figure 1 the undeformed hull domain.

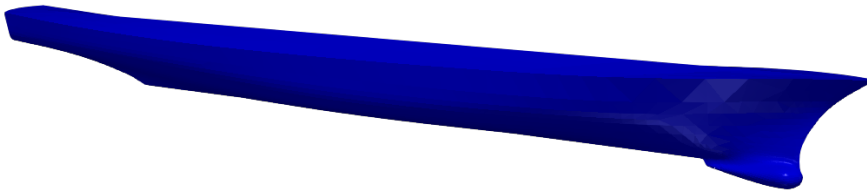


Figure 1: Complete hull domain of the DTMB 5415.

In order to reduce the computational cost, we introduce in the optimization framework two reduced order modeling (ROM) techniques. These techniques are able to represent complex systems in a low dimensional space, reducing the number of degrees of freedom used in the full order model discretization and providing an efficient and reliable approximation of the solution. The ROM methods initially collect a database of high-fidelity solutions — the solutions

computed using the full-order model — during the most computationally expensive phase, also called *offline* phase. Then, the solutions are combined to build the reduced space we query during the *online* phase to obtain the new solution. In this work, we adopt the dynamic mode decomposition (DMD) and proper orthogonal decomposition with interpolation (PODI), two emerging data-driven techniques. PODI is used to approximate, given the high-fidelity solutions computed for some deformed hulls, the solution for any new parametric point in the domain D . DMD algorithm instead provides a simplification of the dynamics of complex system: we use it in order to accelerate the single high-fidelity simulations we need for PODI method, by storing few system outputs and exploiting them to approximate the flow dynamics. For more details about equation-free ROM methods, we suggest [37], while for a complete overview — including intrusive approaches — we cite [27, 26, 24].

Moreover, additionally to these methods, we use the active subspace (AS) property as pre-processing tool in order to be able to reduce the dimension of the parameter space and obtain a better accuracy in ROM solution approximation.

In this contribution, we focus on all the components of the computational pipeline: in Section 2 we provide a brief overview of the FFD method, the Section 3 illustrates the DMD algorithm, in Section 4 the AS property is explained, while Section 5 describes the idea behind PODI technique. Finally, Sections 6 and 7 provide respectively the numerical results collected during this work and the final conclusions.

2 The free form deformation technique

Free form deformation (FFD) is a widespread deformation technique. Proposed in [31], FFD was initially employed in computer graphics, getting more popular both in academia and industry in the last decades. In this section, we provide an overview of the method: for more details about FFD, among all the works in literature, we recommend [25, 9, 14].

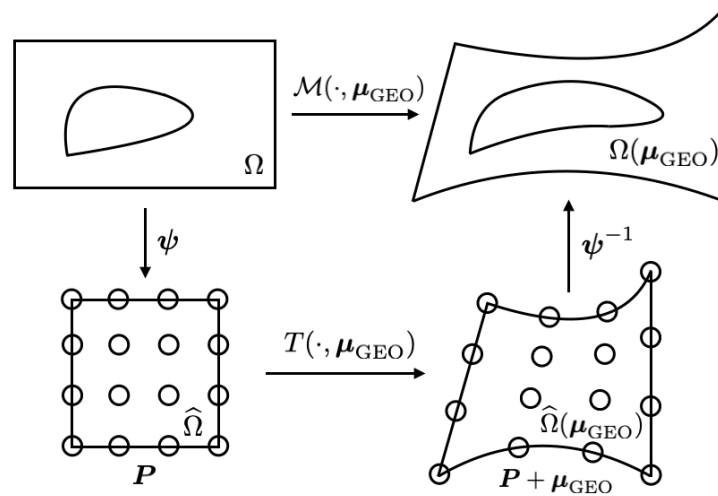


Figure 2: Graphical representation of the FFD morphing map \mathcal{M} as composition of the maps ψ , T , and ψ^{-1} . The displacements of the control points P define the morphing of the domain.

The idea of FFD is very intuitive: the domain is deformed by manipulating a lattice of points surrounding the object to morph. The displacements of these control points are the input parameters $\boldsymbol{\mu}_{\text{GEO}}$. To achieve this result 1) the physical domain Ω is mapped to the reference domain $\widehat{\Omega}$ using the function ψ , and a lattice of control points \mathbf{P} is constructed around the object to deform, then 2) through the map T the reference domain is morphed using B-splines or Bernstein polynomials tensor product and finally 3) the deformed domain is remapped to the physical one by using ψ^{-1} . In Figure 2 is shown a sketch of the free form deformation map as a composition of the three functions presented above. Formally, we can define the deformation map \mathcal{M} as

$$\mathcal{M}(\mathbf{x}, \boldsymbol{\mu}_{\text{GEO}}) := (\psi^{-1} \circ T \circ \psi)(\mathbf{x}, \boldsymbol{\mu}_{\text{GEO}}) \quad \forall \mathbf{x} \in \Omega. \quad (2)$$

This technique allows to manipulate complex geometries and also computational grids, since it is able to preserve derivatives continuity and perform global deformation using only few parameters. Figure 3 shows the position of the lattice of control points around a bulbous bow, which is the part of the hull we want to parametrize and morph. Regarding the implementation, the results in this contribution are obtained using PyGeM [1], an open source Python package implementing several deformation techniques.

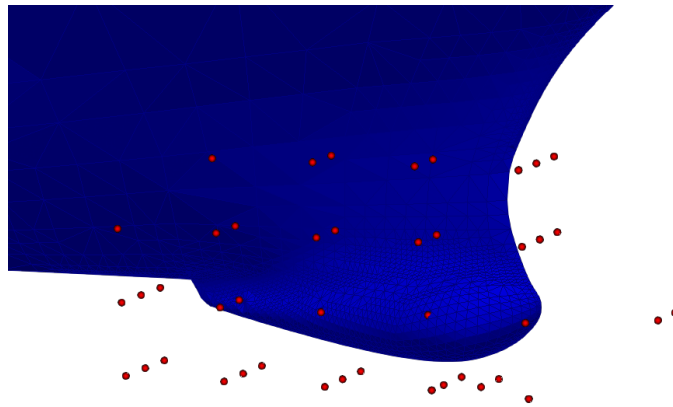


Figure 3: Example of bulbous bow deformation using the FFD method. The red dots are the FFD control points, already manipulated.

3 Dynamic mode decomposition as accelerator of the single simulations

Dynamic mode decomposition is a data-driven modal decomposition technique for analysing the dynamics of nonlinear systems [29, 30]. A comprehensive overview on DMD and its major variants is in [17]. Other nonintrusive approaches with randomized DMD can be found in [4, 3], while naval engineering applications are in [9, 10].

Here we present a brief overview of the method and how we integrate it in the computational pipeline we propose. Let us consider m snapshots representing the state of the system for a given time interval: $\{\mathbf{x}_i\}_{i=1}^m \in \mathbb{R}^n$. We seek a linear operator \mathbf{A} to approximate the nonlinear dynamics of the state variable \mathbf{x} , that is $\mathbf{x}_{k+1} = \mathbf{A}\mathbf{x}_k$. In order to find the DMD decomposition

we only need to approximate the eigenpairs of the operator \mathbf{A} , without explicitly compute it. We proceed by dividing the snapshots in two matrices \mathbf{X} and \mathbf{Y} as in the following:

$$\mathbf{X} = \begin{bmatrix} x_1^1 & x_2^1 & \cdots & x_{m-1}^1 \\ x_1^2 & x_2^2 & \cdots & x_{m-1}^2 \\ \vdots & \vdots & \ddots & \vdots \\ x_1^n & x_2^n & \cdots & x_{m-1}^n \end{bmatrix}, \quad \mathbf{Y} = \begin{bmatrix} x_2^1 & x_3^1 & \cdots & x_m^1 \\ x_2^2 & x_3^2 & \cdots & x_m^2 \\ \vdots & \vdots & \ddots & \vdots \\ x_2^n & x_3^n & \cdots & x_m^n \end{bmatrix}.$$

With this representation we seek \mathbf{A} such that $\mathbf{Y} \approx \mathbf{A}\mathbf{X}$. Using the Moore-Penrose pseudo-inverse operator, denoted by \dagger , we express the best-fit matrix as $\mathbf{A} = \mathbf{Y}\mathbf{X}^\dagger$. We can compute the POD modes of the matrix \mathbf{X} and project the data onto the subspace defined by them. We use the truncated singular value decomposition obtaining $\mathbf{X} \approx \mathbf{U}_r \mathbf{\Sigma}_r \mathbf{V}_r^*$, where the unitary matrix \mathbf{U}_r contains the first r modes. With these modes we can compute the reduced operator $\tilde{\mathbf{A}} \in \mathbb{C}^{r \times r}$ as $\tilde{\mathbf{A}} = \mathbf{U}_r^* \mathbf{A} \mathbf{U}_r = \mathbf{U}_r^* \mathbf{Y} \mathbf{X}^\dagger \mathbf{U}_r = \mathbf{U}_r^* \mathbf{Y} \mathbf{V}_r \mathbf{\Sigma}_r^{-1} \mathbf{U}_r^* \mathbf{U}_r = \mathbf{U}_r^* \mathbf{Y} \mathbf{V}_r \mathbf{\Sigma}_r^{-1}$, without the explicit computation of the full operator \mathbf{A} . The reduced operator describe the evolution of the low-rank approximated state $\tilde{\mathbf{x}}_k \in \mathbb{R}^r$ as $\tilde{\mathbf{x}}_{k+1} = \tilde{\mathbf{A}} \tilde{\mathbf{x}}_k$. We can then recover the high-dimensional state \mathbf{x}_k using the POD modes already computed: $\mathbf{x}_k = \mathbf{U}_r \tilde{\mathbf{x}}_k$.

Using the eigendecomposition of the matrix $\tilde{\mathbf{A}}$, that is $\tilde{\mathbf{A}} \mathbf{W} = \mathbf{W} \mathbf{\Lambda}$, we are able to compute the eigenpairs of the full operator \mathbf{A} . In particular the eigenvalues in $\mathbf{\Lambda}$ correspond to the nonzero eigenvalues of \mathbf{A} , while the eigenvectors $\mathbf{\Phi}$ of \mathbf{A} can be computed in two ways: by projecting the low-rank approximation \mathbf{W} on the high-dimensional space $\mathbf{\Phi} = \mathbf{U}_r \mathbf{W}$, or by computing them exactly with $\mathbf{\Phi} = \mathbf{Y} \mathbf{V}_r \mathbf{\Sigma}_r^{-1} \mathbf{W}$.

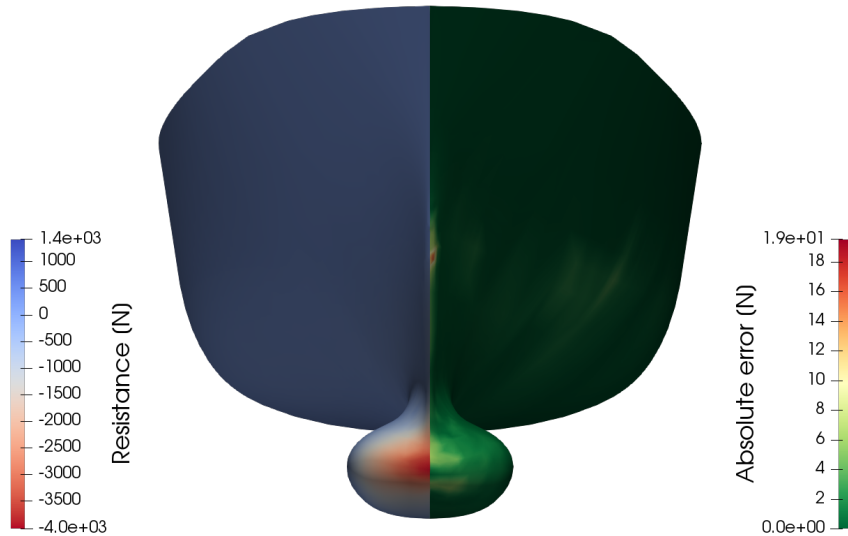


Figure 4: Example of total drag reconstructed using the DMD algorithm. On the left the reconstructed field, while on the right the absolute error with respect to the high-fidelity solution.

The actual implementation of the DMD algorithm we used and many different variants from

multiresolution DMD [18], to DMD with control [23], and higher order DMD [19], can be found in the open source Python package PyDMD [12].

In this work the DMD is used to accelerate the computation of the total drag resistance for a given deformed hull. It uses only few snapshots of the high-fidelity simulation, equispaced in time, to predict the evolution of the target output. In particular we are interested in the value of the total drag at regime. Figure 4 reports the forces field approximated using DMD and the absolute error with respect to the high-fidelity solution for a particular geometrical configuration.

4 How to reduce the parameter space dimension with active subspaces

The active subspaces (AS) property has been formalized by Constantine in [7, 8]. It is a property of a scalar function $f : \mathbb{R}^N \rightarrow \mathbb{R}$ and a probability density function $\rho : \mathbb{R}^N \rightarrow \mathbb{R}^+$, where N is the number of the input parameters. Taking linear combinations of the original parameters we can approximate f using these new parameters, thus reducing the parameter space dimension. The output of interest $f(\boldsymbol{\mu}_{\text{GEO}})$, in our case the total drag of the hull advancing in calm water, depends on the geometrical parameters introduced in Section 2, while ρ describe the uncertainty in the model inputs, i.e. how we sample the parameter space. For sake of clarity we will drop the pedix and from now on $f(\boldsymbol{\mu}) := f(\boldsymbol{\mu}_{\text{GEO}})$. The general idea is to rotate the input domain, after a proper rescale, in order to unveil a low dimensional parametrization of f , which means to find proper directions in the input space where f varies the most on average. We do so by checking the gradients of the output of interest with respect to the parameters.

To proper exploit the AS property we introduce some hypotheses: f has to be continuous and differentiable with square-integrable partial derivatives in the support of ρ . Then we introduce the uncentered covariance matrix \mathbf{C} of the gradients of the target function, which is the matrix constructed with the average products of partial derivatives of the map f as follows

$$\mathbf{C} = \mathbb{E}[\nabla_{\boldsymbol{\mu}} f \nabla_{\boldsymbol{\mu}} f^T] = \int (\nabla_{\boldsymbol{\mu}} f)(\nabla_{\boldsymbol{\mu}} f)^T \rho d\boldsymbol{\mu}, \quad (3)$$

where with \mathbb{E} we identify the expected value, and $\nabla_{\boldsymbol{\mu}} f = \nabla f(\boldsymbol{\mu}) = \left[\frac{\partial f}{\partial \mu_1}, \dots, \frac{\partial f}{\partial \mu_p} \right]^T$ is the column vector of partial derivatives of f . Since \mathbf{C} is symmetric we can express it with its real eigenvalue decomposition $\mathbf{C} = \mathbf{W}\boldsymbol{\Lambda}\mathbf{W}^T$, where \mathbf{W} is the eigenvectors matrix, and $\boldsymbol{\Lambda}$ the diagonal matrix with the eigenvalues in descending order. It can be proven that the eigenvalues express the amount of variance of the gradient along the corresponding eigenvector direction. This means that taking the first M most energetic eigenvalues and the corresponding eigenvectors, we can approximate the target function with a reduce number of input parameters. So the eigenpairs of \mathbf{C} define the active subspaces of the pair (f, ρ) . We proceed by partitioning \mathbf{W} and $\boldsymbol{\Lambda}$ as follows

$$\boldsymbol{\Lambda} = \begin{bmatrix} \boldsymbol{\Lambda}_1 & \\ & \boldsymbol{\Lambda}_2 \end{bmatrix}, \quad \mathbf{W} = [\mathbf{W}_1 \quad \mathbf{W}_2], \quad (4)$$

where the pedix 1 means the first M eigenvalues and eigenvectors respectively. Now we can use \mathbf{W}_1 to project the original parameters to the active subspace, that is the span of the first M eigenvectors. This means to align the input parameter space to \mathbf{W}_1 and retain only the directions where f varies the most on average. We call active variable $\boldsymbol{\mu}_M$ the range of \mathbf{W}_1^T ,

that is $\boldsymbol{\mu}_M = \mathbf{W}_1^T \boldsymbol{\mu} \in \mathbb{R}^M$. We can thus introduce a lower-dimension approximation $g : \mathbb{R}^M \rightarrow \mathbb{R}$ of the quantity of interest f , which is a function of $\boldsymbol{\mu}_M$ as follows

$$f(\boldsymbol{\mu}) \approx g(\mathbf{W}_1^T \boldsymbol{\mu}) = g(\boldsymbol{\mu}_M). \quad (5)$$

Active subspaces have been proven useful in naval applications in [38, 36, 10], but also coupled with POD-Galerkin model order reduction [35]. A gradient-free algorithm for the discovery of active subspaces has been proposed in [6], while an AS variant using average gradients in [20].

We are going to find the active subspace for the total drag resistance of the deformed hulls obtained by the FFD method and the application of the DMD algorithm. Then we are going to exploit this active subspace to perform a better sampling of the parameter space and thus enhancing the construction of the reduced order model.

5 Proper orthogonal decomposition with interpolation

Reduced order modeling (ROM) is a popular technique to reduce the computational cost of numerical simulations. Among all the available methods to achieve this reduction, we focus in this contribution to the reduced basis method using the proper orthogonal decomposition (POD) algorithm for the basis identification. This method allows to reduce the number of degrees of freedom of a parametric system by collecting the *snapshots* — the full order system outputs — for several different configurations and combining them in an efficient way for a real-time approximation of new solutions (for any new configuration). In the POD reduction framework, we can discern two main techniques: POD-Galerkin, which requires all the details of the full order system to generate a consistent low-dimensional representation of the physical problem, and POD with interpolation (PODI), which instead requires only the snapshots. Due to these requirements, the PODI method is particularly suited for industrial problem, since it is able to be coupled to all the numerical solvers, even commercial ones. In this contribution, we adopt PODI method. For more information about POD-Galerkin, we suggest [34, 33, 16, 15], while for other examples of PODI applications we recommend [14, 11, 28].

To calculate the POD modes we use the singular value decomposition (SVD) applied to the snapshots matrix \mathbf{X} such that $\mathbf{X} = \mathbf{U}\boldsymbol{\Sigma}\mathbf{V}^*$. The columns of the unitary matrix \mathbf{U} are the POD modes and the corresponding singular values, the elements in the diagonal matrix $\boldsymbol{\Sigma}$ in decreasing order, indicate the energy associated to each mode. Hence it is possible to select the first modes — the most energetic — to span the reduced space and project onto it the high-fidelity snapshots. In matricial form, we have:

$$\mathbf{X}^{\text{POD}} = \mathbf{U}_N^T \mathbf{X}, \quad (6)$$

where \mathbf{U}_N is the matrix containing the first N modes, and \mathbf{X}^{POD} is the matrix whose columns $\mathbf{x}_i^{\text{POD}}$ are the reduced snapshots. We note that $\mathbf{x}_i^{\text{POD}} \in V^N$ and $\mathbf{x}_i \in V^{\mathcal{N}}$ where \mathcal{N} refers to the number of degrees of freedom of the full-order system. Finally, due to the reduced dimension, we are able to interpolate the reduced snapshots in order to approximate the solution manifold. The new interpolated reduced snapshots are then mapped back to the high-dimensional space for a real-time evaluation of the solution. To perform the non-intrusive model order reduction, we use the open source package EZyRB [11].

6 Numerical results

Here we are going to present the results of the complete numerical pipeline applied to the DTMB 5415 hull. Moreover we demonstrate the improvements obtained using the proposed pipeline, called POD+AS, with respect to the POD approach on the full parameter space.

After generating $N_{\text{POD}} = 100$ deformed hulls, we perform the high-fidelity simulations accelerated via the DMD algorithm. We construct the snapshots matrix and compute the POD modes and the corresponding eigenvalues for the construction of the reduced output space. We compare this approach with the one proposed in this work that exploits a preprocessing step with the finding of the active subspace for the total drag resistance. With the N_{POD} input/output couples, we individuate an eigenvector \mathbf{W}_1 (compare Section 4) describing an active subspace of dimension 1, and we sample the full space only along the active direction described by this vector. After this second sampling we collect a new set of high-fidelity simulations formed by $N_{\text{POD+AS}} = 80$ snapshots. For this new snapshots matrix we compute again the POD modes and eigenvalues, and we compare the two approaches looking at the POD singular values decay. A faster decay means a better approximation of the output fields for a fixed number of modes. In Figure 5 the blue line shows the singular values σ_i divided by the first and greatest singular value σ_{\max} for the sampling of the full parameter space; with the dashed red line the POD singular values decay for the POD+AS approach. A faster decay is observed, especially for the first few modes. This translates in an enhanced reduced order model, which exhibits a better approximation of the solutions manifold, with respect to the classical approach.

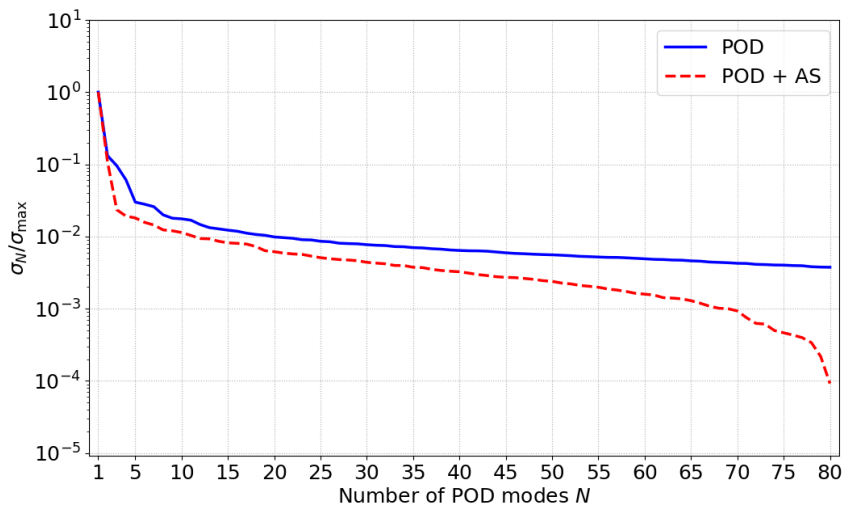


Figure 5: POD singular values decay as a function of the number of modes. The blue line corresponds to the original sampling, while the red dotted line, called POD+AS approach, corresponds to the sampling along the active direction.

Since we are relying on multidimensional interpolation to reconstruct the solutions at untried

parameters, having a new reduced parameter space improves the creation of such interpolator. In the POD+AS approach we have to interpolate a univariate function in N -dimension, where N is the number of POD modes we retain. In the POD approach on the full parameter space instead, we have the same number of modes to fit but a multivariate function depending on 5 input parameters, resulting in a difficult interpolation.

7 Conclusions and perspectives

In this work we presented a nonintrusive numerical pipeline for shape optimization of the bulbous bow of a benchmark hull. It comprises automatic geometrical parametrization and morphing through FFD, estimation of the total drag resistance via DMD using only few snapshots of the time-dependent high fidelity simulations, the reduction of the parameter space exploiting the AS property, and the construction of a surrogate model with PODI for the real-time evaluation of the many-query problem solved by an optimization algorithm. We proved that the reduction of the parameter space can further enhance the reduced order model creation. Moreover all this parts of the pipeline can be used and integrated separately into an existing computational workflow resulting in a great interest for industrial applications.

Acknowledgements

This work was partially performed in the context of the project SOPHYA - “Seakeeping Of Planing Hull Yachts” supported by Regione FVG, POR-FESR 2014-2020, Piano Operativo Regionale Fondo Europeo per lo Sviluppo Regionale, and partially supported by European Union Funding for Research and Innovation — Horizon 2020 Program — in the framework of European Research Council Executive Agency: H2020 ERC CoG 2015 AROMA-CFD project 681447 “Advanced Reduced Order Methods with Applications in Computational Fluid Dynamics” P.I. Gianluigi Rozza.

REFERENCES

- [1] PyGeM: Python Geometrical Morphing. Available at: <https://github.com/mathLab/PyGeM>.
- [2] F. Ballarin, A. D’Amario, S. Perotto, and G. Rozza. A POD-selective inverse distance weighting method for fast parametrized shape morphing. *International Journal for Numerical Methods in Engineering*, 117(8):860–884, 2018.
- [3] D. Bistrian and I. Navon. Efficiency of randomised dynamic mode decomposition for reduced order modelling. *International Journal of Computational Fluid Dynamics*, 32(2-3):88–103, 2018.
- [4] D. A. Bistrian and I. M. Navon. Randomized dynamic mode decomposition for nonintrusive reduced order modelling. *International Journal for Numerical Methods in Engineering*, 112(1):3–25, 2017.
- [5] M. D. Buhmann. *Radial basis functions: theory and implementations*, volume 12. Cambridge university press, 2003.

- [6] K. D. Coleman, A. Lewis, R. C. Smith, B. Williams, M. Morris, and B. Khuwaileh. Gradient-free construction of active subspaces for dimension reduction in complex models with applications to neutronics. *SIAM/ASA Journal on Uncertainty Quantification*, 7(1):117–142, 2019.
- [7] P. G. Constantine. *Active subspaces: Emerging ideas for dimension reduction in parameter studies*, volume 2. SIAM, 2015.
- [8] P. G. Constantine, E. Dow, and Q. Wang. Active subspace methods in theory and practice: applications to kriging surfaces. *SIAM Journal on Scientific Computing*, 36(4):A1500–A1524, 2014.
- [9] N. Demo, M. Tezzele, G. Gustin, G. Lavini, and G. Rozza. Shape optimization by means of proper orthogonal decomposition and dynamic mode decomposition. In *Technology and Science for the Ships of the Future: Proceedings of NAV 2018: 19th International Conference on Ship & Maritime Research*, pages 212–219. IOS Press, 2018.
- [10] N. Demo, M. Tezzele, A. Mola, and G. Rozza. An efficient shape parametrisation by free-form deformation enhanced by active subspace for hull hydrodynamic ship design problems in open source environment. In *The 28th International Ocean and Polar Engineering Conference*, 2018.
- [11] N. Demo, M. Tezzele, and G. Rozza. EZyRB: Easy Reduced Basis method. *The Journal of Open Source Software*, 3(24):661, 2018.
- [12] N. Demo, M. Tezzele, and G. Rozza. PyDMD: Python Dynamic Mode Decomposition. *The Journal of Open Source Software*, 3(22):530, 2018.
- [13] D. Forti and G. Rozza. Efficient geometrical parametrisation techniques of interfaces for reduced-order modelling: application to fluid–structure interaction coupling problems. *International Journal of Computational Fluid Dynamics*, 28(3-4):158–169, 2014.
- [14] F. Garotta, N. Demo, M. Tezzele, M. Carraturo, A. Reali, and G. Rozza. Reduced Order Isogeometric Analysis Approach for PDEs in Parametrized Domains. *Submitted, QUIET special volume*, 2018.
- [15] S. Georgaka, G. Stabile, G. Rozza, and M. J. Bluck. Parametric pod-galerkin model order reduction for unsteady-state heat transfer problems. *arXiv preprint arXiv:1808.05175*, 2018.
- [16] E. N. Karatzas, F. Ballarin, and G. Rozza. Projection-based reduced order models for a cut finite element method in parametrized domains. *arXiv preprint arXiv:1901.03846*, 2019.
- [17] J. N. Kutz, S. L. Brunton, B. W. Brunton, and J. L. Proctor. *Dynamic mode decomposition: data-driven modeling of complex systems*, volume 149. SIAM, 2016.
- [18] J. N. Kutz, X. Fu, and S. L. Brunton. Multiresolution dynamic mode decomposition. *SIAM Journal on Applied Dynamical Systems*, 15(2):713–735, 2016.

- [19] S. Le Clainche and J. M. Vega. Higher order dynamic mode decomposition. *SIAM Journal on Applied Dynamical Systems*, 16(2):882–925, 2017.
- [20] M. R. Lee. Modified active subspaces using the average of gradients. *SIAM/ASA Journal on Uncertainty Quantification*, 7(1):53–66, 2019.
- [21] A. Manzoni, A. Quarteroni, and G. Rozza. Model reduction techniques for fast blood flow simulation in parametrized geometries. *International journal for numerical methods in biomedical engineering*, 28(6-7):604–625, 2012.
- [22] A. Morris, C. Allen, and T. Rendall. CFD-based optimization of aerofoils using radial basis functions for domain element parameterization and mesh deformation. *International Journal for Numerical Methods in Fluids*, 58(8):827–860, 2008.
- [23] J. L. Proctor, S. L. Brunton, and J. N. Kutz. Dynamic mode decomposition with control. *SIAM Journal on Applied Dynamical Systems*, 15(1):142–161, 2016.
- [24] G. Rozza, M. W. Hess, G. Stabile, M. Tezzele, and F. Ballarin. Preliminaries and warming-up: Basic ideas and tools. In P. Benner, S. Grivet-Talocia, A. Quarteroni, G. Rozza, W. H. A. Schilders, and L. M. Silveira, editors, *Handbook on Model Order Reduction*, volume 1, chapter 1. De Gruyter, 2019.
- [25] G. Rozza, A. Koshakji, and A. Quarteroni. Free Form Deformation techniques applied to 3D shape optimization problems. *Communications in Applied and Industrial Mathematics*, 4(0):1–26, 2013.
- [26] G. Rozza, M. H. Malik, N. Demo, M. Tezzele, M. Girfoglio, G. Stabile, and A. Mola. Advances in Reduced Order Methods for Parametric Industrial Problems in Computational Fluid Dynamics. Glasgow, UK, 2018. ECCOMAS Proceedings.
- [27] F. Salmoiraghi, F. Ballarin, G. Corsi, A. Mola, M. Tezzele, and G. Rozza. Advances in geometrical parametrization and reduced order models and methods for computational fluid dynamics problems in applied sciences and engineering: Overview and perspectives. *ECCOMAS Congress 2016 - Proceedings of the 7th European Congress on Computational Methods in Applied Sciences and Engineering*, 1:1013–1031, 2016.
- [28] F. Salmoiraghi, A. Scardigli, H. Telib, and G. Rozza. Free-form deformation, mesh morphing and reduced-order methods: enablers for efficient aerodynamic shape optimisation. *International Journal of Computational Fluid Dynamics*, 0(0):1–15, 2018.
- [29] P. J. Schmid. Dynamic mode decomposition of numerical and experimental data. *Journal of fluid mechanics*, 656:5–28, 2010.
- [30] P. J. Schmid, L. Li, M. P. Juniper, and O. Pust. Applications of the dynamic mode decomposition. *Theoretical and Computational Fluid Dynamics*, 25(1-4):249–259, 2011.
- [31] T. Sederberg and S. Parry. Free-Form Deformation of solid geometric models. In *Proceedings of SIGGRAPH - Special Interest Group on GRAPHics and Interactive Techniques*, pages 151–159. SIGGRAPH, 1986.

- [32] D. Shepard. A two-dimensional interpolation function for irregularly-spaced data. In *Proceedings-1968 ACM National Conference*, pages 517–524. ACM, 1968.
- [33] G. Stabile, S. N. Hijazi, S. Lorenzi, A. Mola, and G. Rozza. Pod-galerkin reduced order methods for cfd using finite volume discretisation: Vortex shedding around a circular cylinder. *Communication in Applied Industrial Mathematics*, 8(1):210–236, dec 2017.
- [34] G. Stabile and G. Rozza. Finite volume pod-galerkin stabilised reduced order methods for the parametrised incompressible navier–stokes equations. *Computers & Fluids*, 173:273–284, 2018.
- [35] M. Tezzele, F. Ballarin, and G. Rozza. Combined parameter and model reduction of cardiovascular problems by means of active subspaces and POD-Galerkin methods. In D. Boffi, L. F. Pavarino, G. Rozza, S. Scacchi, and C. Vergara, editors, *Mathematical and Numerical Modeling of the Cardiovascular System and Applications*, pages 185–207. Springer International Publishing, 2018.
- [36] M. Tezzele, N. Demo, M. Gadalla, A. Mola, and G. Rozza. Model order reduction by means of active subspaces and dynamic mode decomposition for parametric hull shape design hydrodynamics. In *Technology and Science for the Ships of the Future: Proceedings of NAV 2018: 19th International Conference on Ship & Maritime Research*, pages 569–576. IOS Press, 2018.
- [37] M. Tezzele, N. Demo, A. Mola, and G. Rozza. An integrated data-driven computational pipeline with model order reduction for industrial and applied mathematics. *Submitted, Special Volume ECMI*, 2018.
- [38] M. Tezzele, F. Salmoiraghi, A. Mola, and G. Rozza. Dimension reduction in heterogeneous parametric spaces with application to naval engineering shape design problems. *Advanced Modeling and Simulation in Engineering Sciences*, 5(1):25, Sep 2018.

EXPERIMENTAL VALIDATION OF A RANS-VOF NUMERICAL MODEL OF THE WAVE GENERATION AND PROPAGATION IN A 2D WAVE FLUME

MARINE 2019

L. GALERA^{*}, U. IZQUIERDO, G.A. ESTEBAN, J.M. BLANCO, I. ALBAINA AND
A. ARISTONDO

School of Engineering of Bilbao, Department of Nuclear Engineering and Fluid Mechanics
University of the Basque Country (UPV/EHU)
Plaza Ingeniero Torres Quevedo 1, 48013 Bilbao, Spain
^{*}Email: galera.lander@gmail.com, Web page: www.ehu.eus

Key words: Numerical wave flume, model validation, wave characterization

Abstract. This paper focus on the study of free surface variation in a Numerical Wave Flume (NWF) due to a paddle movement. The NWF is the numerical representation of a 12.5 meters long Experimental Wave Flume (EWF) of the laboratory of the University of the Basque Country. The experiments and the numerical simulations are performed in several depths (0.3, 0.4 and 0.5 meters). Besides different velocities for the paddle movement are induced between 0.064 and 0.1 m/s. The numerical simulations are based on an Eulerian Multiphase of two fluids, air and water, more concretely the Volume of Fluid model. The surface variation in two points (6.0 and 6.3 meters from the wave flume start) is studied in both numerical and experimental wave flumes and compared its variation through the experiment time. Besides, the experiments will be analyzed in the wave maker theory. The results show the models quality in the first moments of the experiments, where the reflection does not appear, in which the results from both experimental and numerical simulations are pretty similar.

1 INTRODUCTION

The need of decrease the greenhouse gases emissions is one of the main objectives in order to fight the climate change and the global warming. The United Nations (UN) agreed to aim this decrease, among other objectives, in the Paris agreement [1]. In order to fulfill this purpose, the use of renewable energies seems to be one of the best options. Some technologies like onshore wind or solar have arisen as the most known ones, but the need of augment the number of technologies to harness energy is present [2]. Thus, offshore renewable energies ensue as one of most promising options.

The seas occupy the greater part of our planet surface and, hence, are one of the most important areas for the energy subtraction. In order to harness energy from them, different technologies have emerged as the most attractive ones. Offshore wind has shown encouraging results when fixed, although there are countries that have non-existent or small areas to install this type of technology [3]. The fast decrease in the levelized cost of electricity (LCOE) of the bottom-fixed wind turbines, especially in countries like the UK or Denmark, makes floating wind an appealing technology for those countries that have no continental shelf or those ones that have used the main part of it.

On the other hand, the wave energy, which bases on a very raw technology with promising ideas, is nowadays facing out to engineering challenges focused on the increase of the efficiency. Similar to other research fields, the technology development is carried out with numerical simulations and the corresponding experiments, at a reduced scale, to validate the models used. This procedure aims at the cost reduction in the initial steps of the design process and, once the models are validated, they can be scaled up according to the corresponding similitude laws [4].

Wave flumes allow the possibility to carry out experimental studies of wave energy converters (WEC) at a small scale. The study of the behavior of these devices must be carried out under different conditions, which are representative of the real sea states [5] (Kim et al. 2016). Therefore, the first step, prior to the test of any device, is the characterization of the swell that can be generated in an Experimental Wave Flume (EWF).

In parallel, the corresponding numerical wave flume (NWF) was designed in order to compare results and verify numerical models, following the same approach of other research groups [6]. A NWF is a computational image of an EWF [7], which helps to implement different wave conditions and modifications [8]. In order to do this, Computational Fluid Dynamics (CFD) increase in importance due to the evolution of the processors and the computational power, significantly decreasing the computational time of the simulations.

This work aims at the characterization of the wave generation capabilities of the experimental wave flume (EWF) as well as the validation of a numerical model that reproduces computationally the different sea wave conditions tested.

2 EXPERIMENTAL AND COMPUTATIONAL METHODOLOGY

The waves in the experimental flume are generated using the commercial software Delta-ASDA (V5) that controls the Delta AC (ASDA-A2 series) servo drive and servo motor. The servo motor is connected to a K series linear actuator (KM60-10 roller screw model), which is attached to a paddle submerged in water. The final movement of the paddle is the responsible for generating waves. The data of the surface elevations were acquired using two ultrasonic wave probes (Pepperl+Fuchs UC500-L2-I-V15 model) that were controlled by means of an ad-hoc LABVIEW program [9]. This software makes it possible to obtain experimental values (sampling time interval of $\Delta t = 1/50$ [s]), of the paddle position (x [m]) and the displacement of

the free surface (η [m]) as a function of time (t [s]). The Delta ASDA software provides the possibility to specify the desired amplitude (A_p [m]), acceleration-deceleration (a_p [m/s^2], both always equal) and velocity (U [m/s]) of the paddle as an input variables to establish the linearly oscillating motion. This information permitted the characterization of the waves as they were generated at a certain depth (h [m]), as a function of time (t [s]), in terms of the velocity of the wave propagation (c [m/s]), the wavelength (λ [m]), the wave period (T [s]) and the wave height (H [m]). The laboratory experiments and the numerical simulations were performed in water at several depths (h [m] of 0.3, 0.4, and 0.5), using the piston-type wave maker at different amplitudes ($0.02 < A_p$ [m] < 0.06), constant accelerations-decelerations (a_p of 200 ms) and velocities ($0.03 < U$ [m/s] < 0.1).

The physical effects are modelled on a 2D computational model (STAR CCM+ v12.06) with meshes of different sizes depending on the depth of study. However, the all the meshes have less than 1 million cells in order to optimize the computational cost of the simulations. Each mesh consist different volumes of study. The volumes around the wave maker and the free surface have smaller cells in order to have a better definition of these areas. User-defined functions are used in order to simulate the paddle movement and to study the free surface variation in different points. The study of the free surface variation will be studied too with sections were the volume fraction function is used. When the computational results are obtained, both, computational and experimental are compared in different terms.

2.1 Experimental wave flume (EWF)

The EWF is 12.5 m long, 0.60 m wide, and 0.7 m high. The structure consists of a stainless steel platform surrounded by a laminated and tempered glass walls. The first probe position was set at 6.0 m from the wave generating side, assuming all the generated waves were at that point fully developed. The distance between the consecutive probes was 30 cm, according to the criteria described in [10].

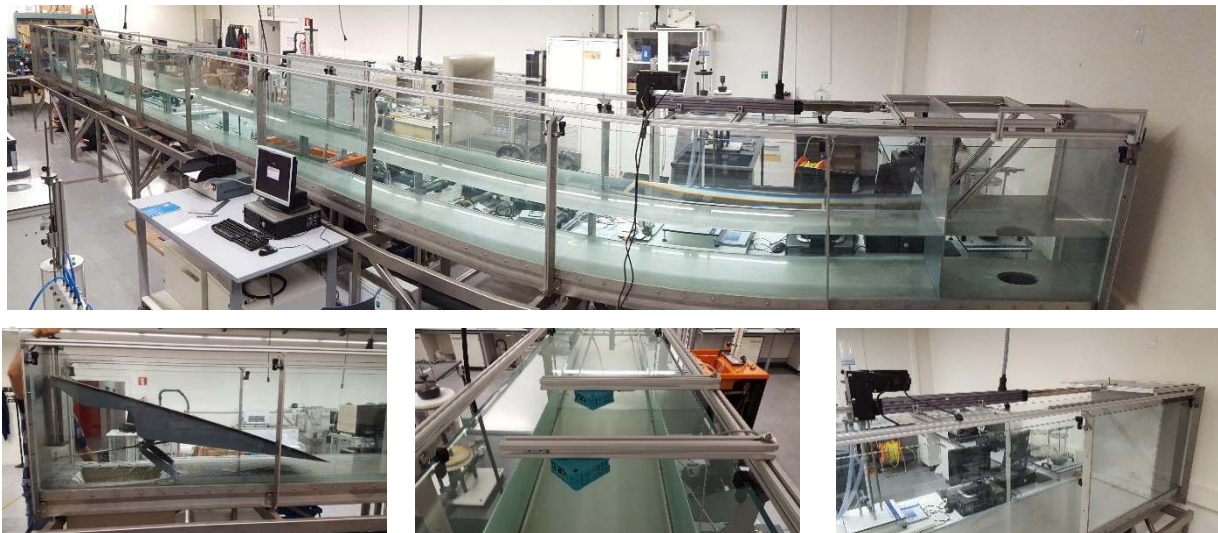


Figure 1: Top: Overall view of the EWF. Bottom: parabolic profile extinction system, wave probes and wave generation system.

The total length of the flume can be divided into three main regions: the wave generation, the wave propagation, and the wave extinction region. For the extinction region A parabolic solid beach, 1.5 m long and with adjustable height and sloping angle, has been designed as extinction passive method.

2.2 Numerical Wave Flume (NWF)

The NWF is a 12.42 m long, 0.7 m high. It aims to simulate the behavior of the EWF and confirm the numerical simulations when comparing them to the experimental results. Besides, two plane sections in position 6 and 6.3 in the X-axis are positioned in order to simulate the existence of the probes.

The simulations are based on the Volume of Fraction (VOF) physical model. The model is suited for simulations of flows where each phase consists of a large structure, with a relative small total contact area between phases [11]. Thus, the model allows to computationally simulate the interaction between two big volumes of air and water that contact in the free surface.

In order to define the depth of each simulation the free surface is determined by defining the y coordinate until the cells have water in the initial moment of the simulation. Then the paddle movement is simulated by using a user created field function. This was made by creating a cyclic motion with constant and opposed velocities. Then the velocity mandates are linked to the sinusoidal wave. This allow us to impose the paddle movement depending on the time of simulation. This movement is determined by taking into account the small acceleration moments, which are neglected, and then the maximum velocity of the paddle is imposed.

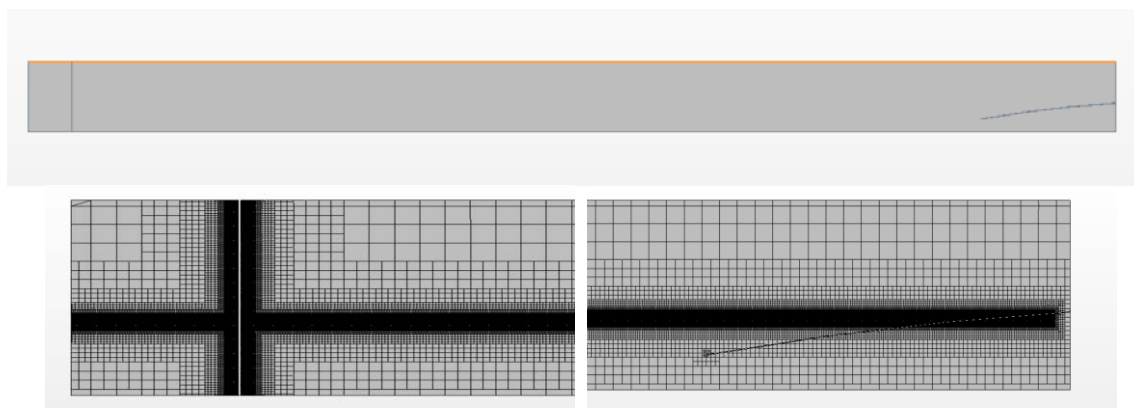


Figure 2: Geometry (up) of the NWF. Mesh construction around the wavemaker (bottom-left) and around the beach (bottom-right).

The computational meshes have different cell sizes depending on the depth of study. This is because the volumes of control for the paddle and the free surface variation are optimized to the wave velocities and heights. Figure 2 shows the mesh for the cases of 30 cm of depth, which has the smaller cells.

Table 1: Relation between depth of study and cell size.

| Depth of study (m) | h= 0.3 | h=0.4 | h=0.5 |
|--------------------|--------|--------|--------|
| Cell Size (m) | 0.0025 | 0.0030 | 0.0039 |

In Table 1 the relation between the depth of study and the cell size used is shown. Although the sizes are different, the objective of create different meshes was to have the closest value possible to Courant Number equal to 1 in each simulation with a time-step of 0.002 seconds.

3 VALIDATION OF THE CFD MODEL

The main objective of the computational simulations is to test the paddle movement and see if it provokes the same free surface variation in the points were the sensors are located in the EWF. The study focus in the first waves in order to minimize, as much as possible, the effect of reflection due to existence of the beach.

3.1 Experimental campaign

For the purpose of having the best results possible, and see if the type way selected to simulate the free surface variation was correct, different depth and wave periods were simulated. Each simulation studies the free surface variation by a user-defined function called Level, which study the lowest y-coordinate of the cells with a 50% of volume fraction of water or less. That command defines the position of the free surface in the locations where the probes are installed in the EWF.

Table 2: Experiments run with the velocity of the wave maker and the period, as well as the depth of work.

| Experiment | Depth (m) | Maximum Velocity of the paddle (m/s) | Period (s) |
|------------|-----------|--------------------------------------|------------|
| 1 | 0.3 | 0.071 | 0.828 |
| 2 | 0.3 | 0.072 | 1.090 |
| 3 | 0.3 | 0.073 | 1.363 |
| 4 | 0.3 | 0.072 | 1.624 |
| 5 | 0.4 | 0.078 | 1.031 |
| 6 | 0.4 | 0.065 | 1.473 |
| 7 | 0.4 | 0.080 | 1.761 |
| 8 | 0.5 | 0.089 | 1.182 |
| 9 | 0.5 | 0.033 | 1.417 |
| 10 | 0.5 | 0.100 | 1.703 |

Besides, an average of the volume of fraction of the water in a section plane is made in both locations. Each panel section creates the average of the volume fraction of water in it giving a percentage value that defines the position of the free surface. Both methods are used in order to see if the size of the cells creates a noticeable deviation from or not.

Table 2 shows the main parameter that were taken into account when simulating the movement of the paddle, and in the creation of the meshes. The maximum velocity of the paddle that, which is the constant velocity of it without taking into account accelerations, and the period are used to create the paddle movement equation.

3.2 Comparison of experimental and computational free surface displacement

In order to compare the results from the experiments and the numerical simulations some graphics are made. In them, it can be seen the free surface variation in the experiments and the surface variation of the numerical methods through the length time of the numerical simulations. Then, the experimental data is shorted to the same time range.

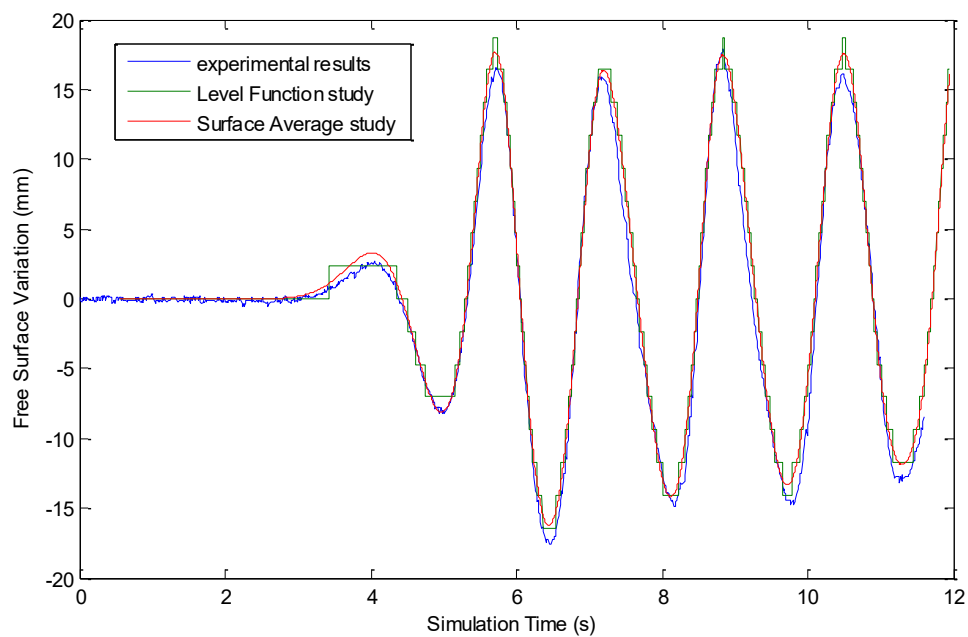


Figure 3: Comparison of the free surface location between experimental and computational signals.

Figure 3 shows the comparison defined above. It can be seen that the free surface variation matches in the three experiments the majority of the time. The blue line is the experimental results, the red one is the results obtained from the average surface of the volume fraction of water and the green one shows the results obtained by the user defined function. The green line is stepped because it measures the y coordinate of the cell and, hence, it cannot be a smoothed line.

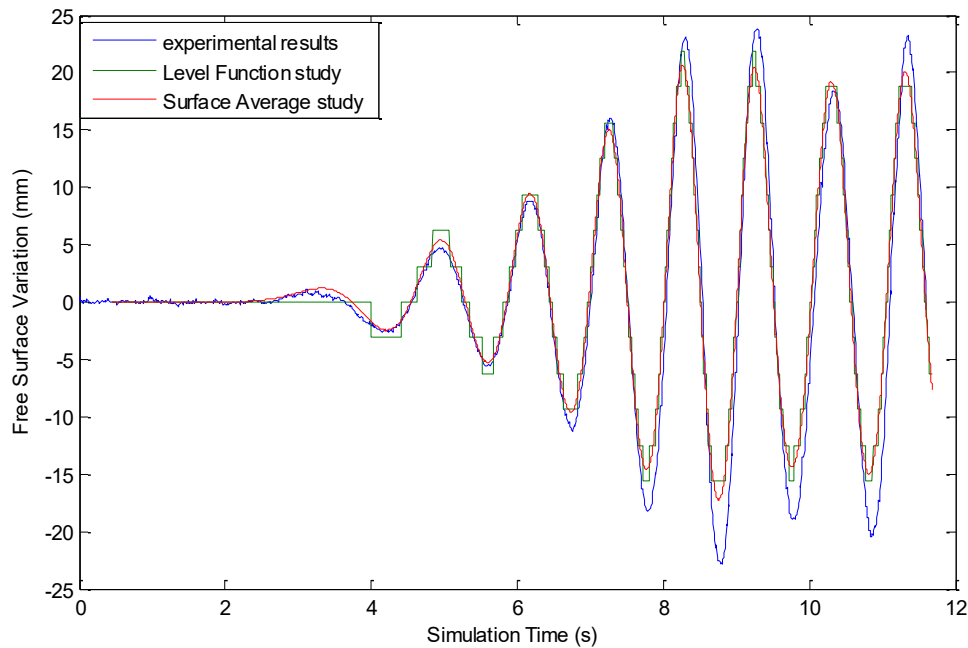


Figure 4: Comparison of the free surface location between experimental and computational signals.

However, reflection has to be taken into account and some of the simulations have shown noticeable differences with the experimental result due to the lower density of the mesh around the beach. This can be seen in Figure 4 where the first waves match perfectly in experimental and numerical results, but an error can be seen in the next waves, where the reflection starts to affect.

This is because the main objective of this phase of research is to see if the behavior of the wave maker and the models used could simulate adequately the EWF results. This has been a success and will be the first step into a better modelling in the future.

4 RESULTS AND DISCUSSION

4.1 Wavemaker Theory

The type of wave maker selected is a piston-type one. Wave maker theory takes into account the type of the wave generator and express it graphically making the relation between the wave height, wave number the depth of study and the stroke of the wave maker [12].

The results show a wide range of error between experiments, but always below the 10%. Although the simulations match greatly in the first waves, and that is the main aim of this study, the error increases considerably with the effect of the reflection. This is due to the non-refinement of the mesh around the beach to not increase the number of cells. Because of that, the effect is not simulated correctly and induces an error that affects in the comparison with the experimental results.

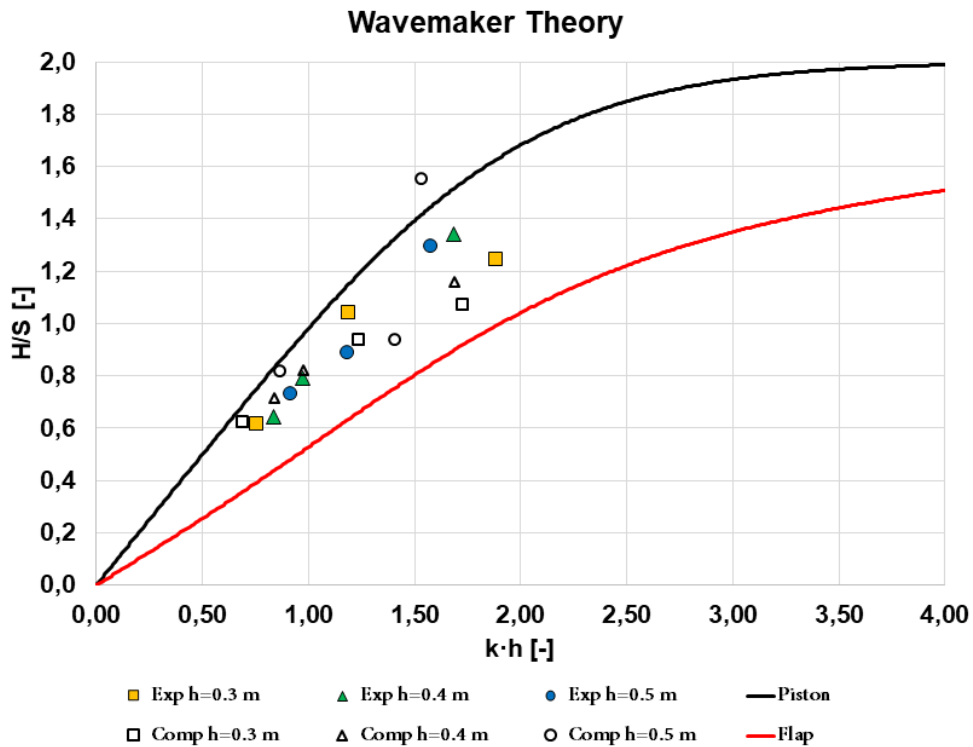


Figure 5: Experimental and numerical results captured in the Wavemaker theory.

Figure 5 shows that the numerical results follow, in its majority, the same tendencies that the experimental results. In the data treatise, the error between the experiments and the simulations does not increase having good matches. Nevertheless, it is important to remember that the reflection was not aimed to be studied in this study and its existence has altered results, in these comparisons between theory, experiments and numerical simulations.

4.2 Phase velocity and period of wave as function of wavelength

Apart from the linear theory, the computational results are compared with the tendency lines created from theory. In this section, both experimental and numerical experiments are compared with these lines, in order to see if the error of the simulations follows the error of the experiments or if it is because of the computational domain.

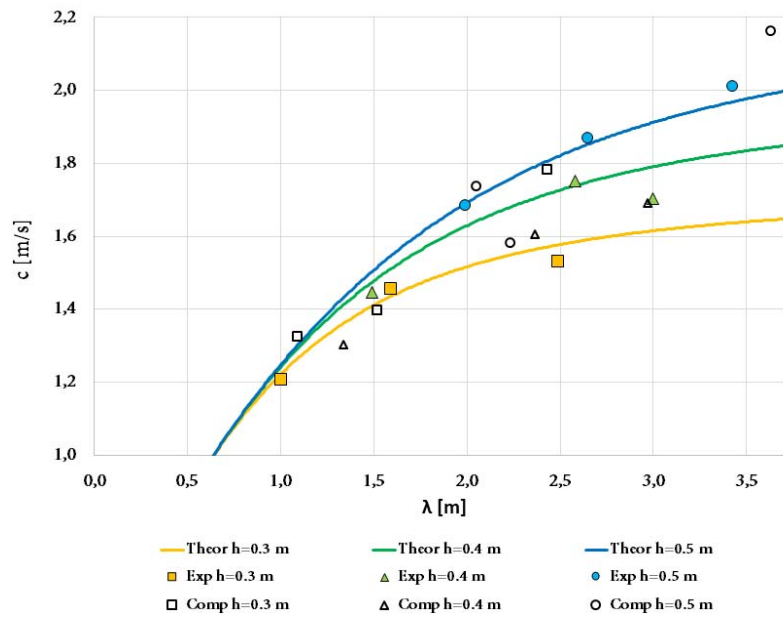


Figure 6: Relation between wavelength and wave celerity.

Figure 6 shows the relation between the wavelength and the wave celerity and the error that both, experiments and numerical simulations, have regarding the tendency lines that are defined by theory. Figure 6 shows that experiments follow closely the tendency lines while the numerical simulations slightly recede from them. Although in the simulations the error between experimental and numerical values is lower than 10%, these errors add up and create the distancing from the theoretical tendencies.

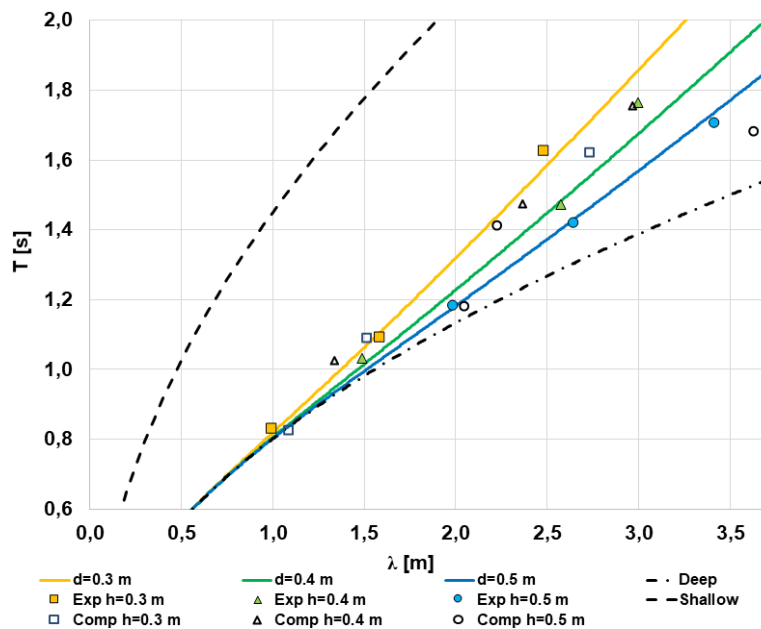


Figure 7: Relation between wavelength and period.

Figure 7 shows the relation between the wavelength and the wave period. In it, it can be observed that the relation between experiments and numerical simulations, the wave period has small errors. Thus, both experiments and numerical simulations follow the theoretical tendencies better than in Figure 6.

5 CONCLUSIONS

Analyzing the results from the nine simulations the first conclusion obtained is that the VOF model approach is correct. The great accuracy of the simulations and the similarity of them in the first waves when the reflection does not affect the measurements, show the success of the approach of the simulations.

However, some modifications in both the grid and physic models have to be done in order to reduce the error when reflection affects to the measurements. Besides continuous improvements in the paddle control of the EWF aim to have more constant waves and approach the theoretical models. Moreover, the inclusion of acceleration in the numerical simulations should create an approximation to the experimental results.

Thus, this study exists as an initial work in the area of numerical simulations of the EWF. Studies of physical effects, as reflection, and of the behavior of offshore structures, as wave energy converters or floating structures for offshore wind, will be the next steps of the research group. With a proper NWF the simulations of a wide range of waves and depths will be possible in order to validate these type of structures.

6 ACKNOWLEDGEMENTS

The authors are very grateful for the support of the government of the Basque Country through IT1314-19.

REFERENCES

- [1] UNFCC (United Nations Framework Convention on Climate Change), Paris Agreement (Spanish), (2015).
- [2] F. M. M. Machado, A. M. G. Lopes and A. D. Ferreira, Numerical simulation of regular waves: Optimization of a numerical wave tank, *Ocean Eng.*, (2018) **170**:89–99.
- [3] N. Bruinsma, B. T. Paulsen, and N. G. Jacobsen, Validation and application of a fully nonlinear numerical wave tank for simulating floating offshore wind turbines, *Ocean Eng.*, (2018) **147**:647–658.
- [4] D. Stagonas, D. Warbrick, G. Muller, and D. Magagna, Surface tension effects on energy dissipation by small scale, experimental breaking waves, *Coast. Eng.*, (2011) **58**:826–836.
- [5] S. Kim, K. Kim, J. Park, G. Jeon, and H. Chun, Numerical simulation of wave and current interaction with a fixed offshore substructure, *Int. J. Nav. Archit. Ocean Eng.*, (2016) **8**:188–197.
- [6] S. Saincher and J. Banerjee, Design of a numerical wave tank and wave flume for low

- steepness waves in deep and intermediate water,(2015) **116**:221-228.
- [7] U. Izquierdo, G. A. Esteban, J. M. Blanco, I. Albaina, and A. Peña, Experimental validation of a CFD model using a narrow wave flume, *Appl. Ocean Res.*, (2019) **86**:1-12.
- [8] M. Anbarsooz and M. Moghiman, Fully nonlinear viscous wave generation in numerical wave tanks, *Ocean Eng.*, (2013) **59**:73–85.
- [9] National Instruments, LabVIEW 2016 (64-bit) - English. Austin - Texas - United States, (2016).
- [10] M. Isaacson, Measurement of regular wave reflection, *J. Waterw. port Coast. Ocean Eng.*, (1991) **117**:553–569.
- [11] U. Guide, STAR-CCM + ® Documentation, (2015).
- [12] R. G. Dean and R. A. Dalrymple, *Water Wave Mechanics for Engineers and Scientists*. World Scientific, (1984).

ON THE IMPORTANCE OF ADVANCED MESH MOTION METHODS FOR WEC EXPERIMENTS IN CFD-BASED NUMERICAL WAVE TANKS

Christian Windt^{1†}, Josh Davidson², Dominic Chandar³ and John V. Ringwood¹

¹ Centre for Ocean Energy Research, Maynooth University
North Campus, Maynooth, Co. Kildare, Ireland
†e-mail: christian.windt.2017@mumail.ie

² Department of Fluid Mechanics, Faculty of Mechanical Engineering
Budapest University of Technology and Economics
H-1111 Budapest, Hungary

³ Institute Of High Performance Computing
1 Fusionopolis Way, #16-16 Connexis North, Singapore 138632

Key words: Mesh motion, Overset grids, Numerical wave tank, Control, OpenFOAM

Abstract. For the economical operation of wave energy converts (WECs), energy maximising control systems (EMCSs) are included in the device design, introducing large structural motions. During the numerical modelling of WECs in CFD-based numerical wave tanks (NWTs), the structural motions must be explicitly accommodated in the finite volume domain. Using well known mesh morphing methods, large amplitude WEC oscillations may deteriorate the quality of the spatial discretisation, and push the NWT beyond the limits of numerical stability. To overcome this issue, advanced mesh motion methods, such as overset grids, have been developed; however, these methods are rarely used in numerical WEC experiments. To this end, the present paper aims to highlight the importance of advanced mesh motion methods, when modelling WECs under controlled conditions. To furthermore prove the feasibility of the overset method, implemented in the OpenFOAM framework, simulations of an uncontrolled WEC are performed, and results are compared to simulations using the mesh morphing method. It is shown that the overset method has potential to improve CFD-based models of controlled WECs, but, at the expense of increased computational cost.

1 INTRODUCTION

Extensive numerical modelling is required during the research and development of WECs, to design cost competitive and durable devices. A range of numerical models, with varying computational cost and fidelity, are available for wave-structure interaction (WSI) problems

[1]. While lower fidelity models, based on linear hydrodynamic modelling techniques, such as boundary element method-based NWTs, are computationally efficient, their accuracy decreases when the amplitude of the waves and the WEC motion increase beyond the validity of the underlying linearising assumptions. In contrast, higher fidelity models, including the relevant non-linear hydrodynamic effects, such as CFD-based numerical wave tanks (CNWTs), remain accurate over a wide range of operational conditions, at the expense of increased computational cost [2].

The relative strengths and weaknesses of the various numerical models can be leveraged for different problems, at different stages of device development. During early stage development, lower-fidelity models are suitable for parametric studies, where a vast number of simulations are required to sweep a broad parameter space. At higher technology readiness levels, the system under investigation becomes more refined and a higher level of accuracy is required to evaluate the performance of the system, e.g. evaluating array effects [3] or EMCSs [4]. The use of a high fidelity model, able to capture all relevant hydrodynamic non-linearities, has been shown to be particularly vital for accurate assessment of EMCSs, which drive the WEC into resonance with the incoming wave field, resulting in large amplitude motions outside the limits in which lower fidelity models are reliable [5, 6].

Although the fidelity of a CNWT is well suited to the evaluation of EMCSs [6], the relatively large amplitude body motions can introduce numerical instabilities due to the required motion of the CFD mesh. A number of different mesh motion methods are available, whose usage and suitability for WEC experiments is reviewed in [7]. Among these, the overset grid method shows particular promise for handling large amplitude, multi-degree of freedom, motions which may occur in WEC experiments. To date, only a relatively small number of CNWT WEC experiments have employed the overset method [8]–[15]. The limited usage of the overset method in the wave energy field can be attributed to (1) the extensively larger computational cost [19], (2) the introduction of numerical errors in a Volume Of Fluid (VOF) environment, such as violation of mass conservation [18], and (3) the limited availability of the algorithm in CFD software. Previously, the overset method was only available in commercial CFD software packages, and initial studies were all implemented in the commercial CFD solver STAR-CCM+ [8]–[13]. However, recently the limitation in (3) has been removed through the code release of the overset method for the open-source CFD toolbox OpenFOAM (OF), making it freely available to a wider user community. Overset grids in OF have been applied to WEC experiments in Windt *et al.* [14] and Chen *et al.* [15].

In a previous study by the authors [14], the performance of the overset implementation in the OF version v1706 has been assessed. Major drawbacks in terms of accuracy of the solution, computational overhead and parallelisation of the solution process were revealed. Since the publication of [14], some updates of the overset method have been implemented and released in OF v1712 and v1812. To this end, the present paper follows two main objectives:

1. Highlight the importance of advanced mesh motion methods, in particular overset grids, for the analysis of WECs in CNWTs, under controlled conditions. While the initial study in [14] only considered simple free decay tests, the case study in this paper presents an optimally controlled, moored, point-absorber WEC device in irregular waves.

2. To investigate the improvements of the overset method, implemented in the latest OF v1812 release, the results of the case study are analysed under the criteria of accuracy and computational overhead, and are compared against results using the conventional mesh morphing method, as well as a second overset implementation, *opera*¹, developed at the Institute Of High Performance Computing, Singapore [16].

The remainder of the paper is organised as follows. First, a brief overview of the dynamic mesh motion methods utilised is given in Section 2. Next, the case study is detailed in Section 3, providing information of the WEC device, the considered test cases, and the optimal control. Section 4 presents the numerical setup for the considered CNWTs, followed by the presentation and discussion of the results in Section 5. Finally, conclusions are drawn in Section 6.

2 DYNAMIC MESH MOTION

The mesh morphing and overset mesh motion methods employed in this paper are briefly introduced in this section. For more details, the interested reader is directed to [7] and [14].

2.1 Mesh morphing

If grid connectivity should be retained, mesh morphing is the common method to accommodate body motion in the CNWTs. The displacement of the body (boundary) is diffused within the domain, by solving the Laplace equation:

$$\nabla \cdot (k \nabla \mathbf{u}) = 0, \quad (1)$$

where k describes the diffusivity and \mathbf{u} the velocity of the moving boundary. The displacement of the body leads to a deformation of single control volumes and careful model setup is required to maintain sufficient grid quality throughout the spatial domain over the course of the simulation [17]. Depending on the implementation, the diffusivity factor, k , gives control over the grid quality during mesh deformation. In the OF environment, distance-based diffusivity is employed, where the user specifies an *inner* and *outer* distance, between which mesh deformation is allowed, and prohibited elsewhere.

2.2 Overset grids

In the overset method, (at least) two grids (background and body-fitted) are defined, which may arbitrarily overlay each other. The different grids are internally static, thereby retaining their original structure and quality, but can move relative to each other. Transferring information between the grids requires interpolation, which can lead to conservation and convergence issues, and represents the biggest challenge of this method [18]. At each time step, the overset method performs the following sequential steps (1) Identification of hole cells, (2) Identification of fringe cells, (3) Identification of donor cells, and (4) Interpolation between fringe and donor cells.

¹Note that *opera* works as an additional application in the OF environment and is not a standalone version of OF

3 CASE STUDY

To illustrate the importance of utilising advanced mesh motion methods when performing WEC experiments in a CNWTs, and investigate the performance of the overset method implemented in OF v1812 and *opera*, this section presents a case study of a WEC under controlled conditions. Section 3.1 describes the considered WEC, Section 3.2 the input wave, and Section 3.3 the control design.

3.1 WEC structure

The WEC structure is chosen based on the Blind Test Series 2 of the Collaborative Computational Project in Wave Structure Interaction (CCP-WSI) [20]. An axisymmetric, cylindrical geometry, featuring a sharp-cornered bottom and a moon-pool is considered (see Figures 1 and 2). All relevant structural dimensions, as well as the mass and inertial properties of the device are shown in Figure 1 and listed in Table 1.

The structure is moored to the tank floor, using a linear spring, with a stiffness of 67N m^{-1} . Based on the spring stiffness, the draft, and the buoyancy properties, a mooring pretension (in equilibrium position) of 31.55N can be measured (see Table 1).

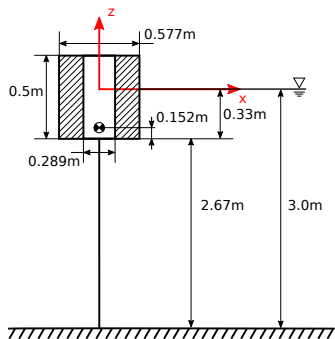


Figure 1: Schematic (not at scale) of the WEC structure

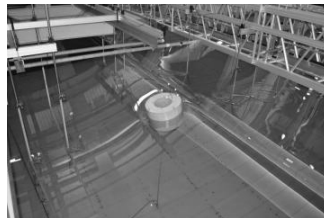


Figure 2: WEC structure in the ocean basin at the COAST Laboratory

Table 1: Properties of the considered WEC structure

| | | |
|------------|----------------------|--------|
| Mass | [kg] | 61.459 |
| Ixx | [kg m ²] | 3.56 |
| Iyy | [kg m ²] | 3.56 |
| Izz | [kg m ²] | 3.298 |
| Mooring | [N] | 31.55 |
| Pretension | | |

3.2 Input wave

For this case study, an irregular polychromatic JONSWAP sea state with a significant wave height, H_s , of 0.25m , and a peak period, T_p , of 1.66s , is chosen. According to the linear dispersion relationship, at a water depth, d , of 3m , this results in a wave length, λ_p , of 4.3m . Simulations are run for 66s ($\approx 40 T_p$). The time trace of the recorded free surface elevation (FSE), measured at the intended WEC location during a preliminary simulation, without the WEC in the CNWT, as well as the according spectral density distribution, are shown in Figure 3.

3.3 Optimal control input

In this study, the power take-off (PTO) acts in the heave direction. A PD complex conjugate controller, realised as a linear spring-damper system, is employed. The control force, $u(t)$,

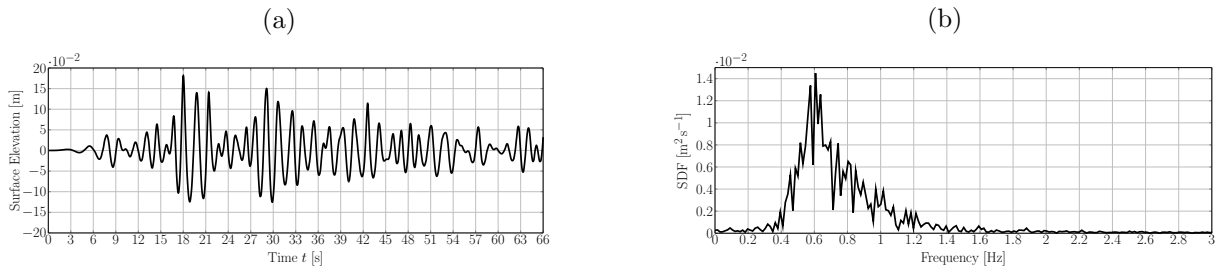


Figure 3: (a) Surface elevation time trace, (b) Spectral density distribution of the FSE signal

follows:

$$u(t) = -b \cdot \dot{x}_{\text{WEC}}(t) - c \cdot x_{\text{WEC}}(t), \quad (2)$$

where b denotes the damping parameter, c is the spring stiffness, and $x_{\text{WEC}}(t)$ and $\dot{x}_{\text{WEC}}(t)$ are the WEC heave position and velocity, respectively. To identify the optimal control parameters, c and b , the procedure detailed in [6, 21] is employed. The spring stiffness, c , is chosen to shift the uncontrolled resonant period of the WEC, T_{WEC} , in-line with the peak period of the input wave spectrum, T_p :

$$c = \frac{k \cdot T_{\text{WEC}}^2}{T_p^2} - k, \quad (3)$$

where k is the linear hydrostatic restoring force coefficient of the WEC. The value of T_{WEC} and k are identified using data from heave free decay test simulations.

To determine k , a second-order parametric state-space model is identified, with the transfer function $H(s) = s / ((m + m_\infty)s^2 + b_r s + k)$, optimising the value k to fit the model to an input data set, stemming from the heave free decay test. The required data for the device mass, m , is given from the structural properties of the device. The added mass at infinite frequency, m_∞ , and the hydrodynamic radiation damping parameter, b_r , are calculated using the boundary element method code WAMIT.

Based on the impedance matching control approach, the hydrodynamic radiation damping parameter, at the peak wave period, directly serves as PTO damping parameter b of the PTO.

From this procedure, the optimal control parameters, for the sea state given in Section 3.2, are $b = 37.3 \text{ N s m}^{-1}$ and $c = -664 \text{ N m}^{-1}$.

4 NUMERICAL WAVE TANK SETUP

In this section, the CNWT setup is detailed. The governing equations are presented (Section 4.1), as well as the treatment of numerical wave generation and absorption (Section 4.2), and the specific details for the three different dynamic mesh motion methods utilised: mesh morphing (Section 4.3), the overset method as implemented in v1812 of OF and *opera* (Section 4.4).

4.1 Governing equations

The hydrodynamics in the CNWT are modelled by solving the incompressible Reynold Averaged Navier-Stokes Equations (RANSE), describing the conservation of mass (Equation (4))

and momentum (Equation (5)).

$$\nabla \cdot \mathbf{U} = 0 \quad (4) \quad \frac{\partial \rho \mathbf{U}}{\partial t} + \nabla \cdot \rho \mathbf{U} \mathbf{U} = -\nabla p + \nabla \cdot \mathbf{T} + \rho \mathbf{f}_b \quad (5)$$

In Equations (4) and (5), t denotes time, \mathbf{U} is the fluid velocity, p the fluid pressure, ρ the fluid density, \mathbf{T} the stress tensor, and \mathbf{f}_b , the external forces, such as gravity. The water wave advection is captured via the VOF method, proposed in [22], following:

$$\frac{\partial \alpha}{\partial t} + \nabla \cdot (\mathbf{U}\alpha) + \nabla \cdot [\mathbf{U}_r \alpha (1 - \alpha)] = 0 \quad (6) \quad \Phi = \alpha \Phi_{\text{water}} + (1 - \alpha) \Phi_{\text{air}} \quad (7)$$

where α denotes the volume fraction of water, \mathbf{U}_r is the relative velocity between liquid and gaseous phase [23], and Φ is a specific fluid quantity, such as density. Laminar flow conditions are assumed for all simulations presented herein.

To measure the FSE, the iso-surface of the volume fraction $\alpha = 0.5$ is recorded throughout the course of the simulation, and can be extracted at specific locations in a post-processing step.

4.2 Numerical wave generation & absorption

The IHFOAM [24] toolbox is employed for wave generation and absorption. IHFOAM is readily implemented in OF v1812, and can be classified as a static boundary method [25]. Waves are generated at the up-wave boundary of the CNWT, by prescribing the water level, through the water volume fraction, and the fluid velocity. For an irregular, polychromatic sea state, the wave amplitudes and phases for each frequency component of the wave act as inputs to the wave maker. For wave absorption, a correction velocity, based on the shallow water theory, is imposed at the down-wave domain boundary, to cancel out the incoming wave.

4.3 Mesh morphing

In this section, the setup of the CNWT employing mesh morphing will be only described briefly. A detailed description, including convergence studies and investigations into the necessity of turbulence modelling are given in [26].

The CNWT spans a length of $4.9\lambda_p$ (in the x-direction, see Figure 4) and $1.8\lambda_p$ in the y-direction, perpendicular to the wave propagation direction. In the z-direction, the CNWT spans $2d$, where d is the water depth. The still water level is located at $z = 0$. The structure is located $1.7\lambda_p$ down wave from the wave generation boundary, and $3.2\lambda_p$ up wave from the absorption boundary, which refers to $(x, y, z) = (0, 0, 0)$.

The symmetry of the problem is exploited, and a symmetry boundary condition is applied in the xz-plane, at $y = 0$. This enforces constraints on the motion of the device, only allowing translational motion in surge and heave, as well as rotational motion in pitch.

In the free surface interface region, and around the body, the domain is discretised with 10 cells per H_s (in z-direction), featuring an aspect ratio of 2. Towards the down wave boundary of the CNWT, cell stretching is applied to enhance wave absorption and reduce the overall cell count. In the y-direction, cells feature an aspect ratio of 1, over a length of $2R$, where R is the device radius. Further away from the structure, cell stretching is applied. The overall cell count

in the domain is 776248. A screen-shot of the spatial discretisation of the CNWT is shown in Figure 4. The field variable α , at time $t = 0$, is depicted in Figure 5.

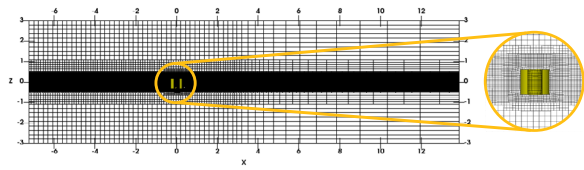


Figure 4: Two-dimensional (2D) slice (xz -plane) of the spatial problem discretisation. The WEC structure is (yellow colour code) is located at $(x, y, z) = (0, 0, 0)$.

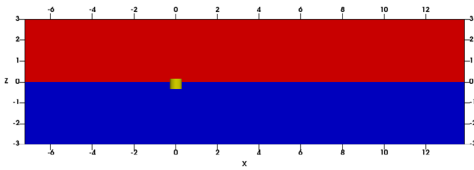


Figure 5: 2D slice (xz -plane) of the CNWT. The water (blue) and air (red) phase are depicted, together with the WEC structure (yellow).

4.4 Overset grid

In terms of CNWT setup, the two implementations of the overset method do not differ and the same CNWT can be employed, excepting an alteration between the boundary conditions used to identify overset patches. The setup of the CNWT follows the setup outlined in [14]. The domain comprises a background and an overset mesh (see Figure 6). The dimensions, as well as the spatial discretisation of the background mesh, is virtually the same as for the mesh morphing CNWT, and the symmetry boundary condition is also applied in the xz -plane, at $y = 0$. The overset mesh region (red color code in Figure 6), spans over $1.57R \times 1.57R \times 0.88R$ in the x -, z -, and y -directions. The device is located in the centre of the overset mesh. The overall cell count for the overset CNWT is 966766.

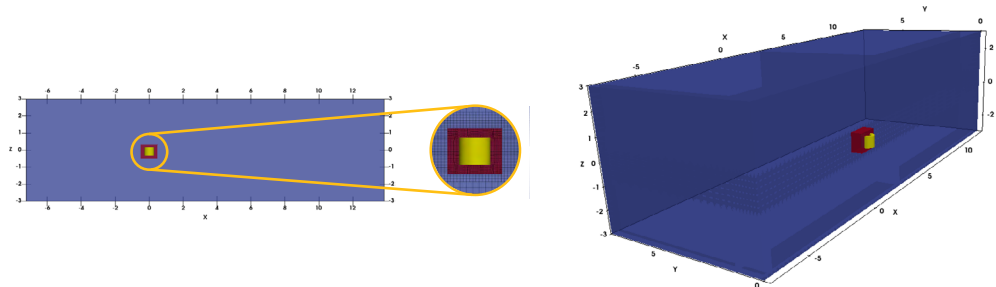


Figure 6: 2D slice (xz -plane) and 3D screen shot of the CNWT for the overset method, where the background mesh is blue, the overset region is red and the WEC structure is yellow.

5 RESULTS & DISCUSSION

In this section, the results for four different simulations are presented and discussed. In Section 5.1, results for an uncontrolled versus controlled device, employing the mesh morphing method, are shown. Next, in Section 5.2, results of the uncontrolled device, simulated with mesh

morphing, are compared to the equivalent results from simulation with the two implementations of the overset method.

5.1 Uncontrolled vs. controlled

Figure 7 shows the time traces of the surge and heave displacement for the case of an uncontrolled (black solid) and controlled (dashed red) WEC, using the mesh morphing method. For reference, Figure 7 also includes the FSE time trace, at the device location, from the empty tank simulation.

For the case of the uncontrolled WEC, it can be observed that the WEC surges in the wave propagation direction, and oscillates back due to the mooring forces, with a maximum displacement of 1m (from its equilibrium position) at $t = 22$ s. In heave, the maximum amplitude is 0.2m (at $t = 30$ s) and the overall trajectory is seen to closely follow the FSE. For the case of the controlled device, results are only available up to 22.5s, at which time the simulation aborts, due to poor mesh quality. Larger WEC displacements, in surge and heave, can be observed compared to the uncontrolled device, which can be expected since the EMCS enhances the body motion.

Figure 8 shows screen-shots of the CNWT, for the cases of an uncontrolled and controlled WEC, taken at four different time instances, representing: zero surface elevation ($t = 9$ s), maximum positive surface elevation ($t = 18$ s), maximum negative surface elevation ($t = 19$ s) and the last time instance simulated for the controlled device ($t = 22.5$ s). It can readily be seen that the two simulations result in significantly different body motions. At $t = 22.5$ s, the mesh in the down wave of the controlled WEC is highly skewed, resulting in the abortion of the simulation.

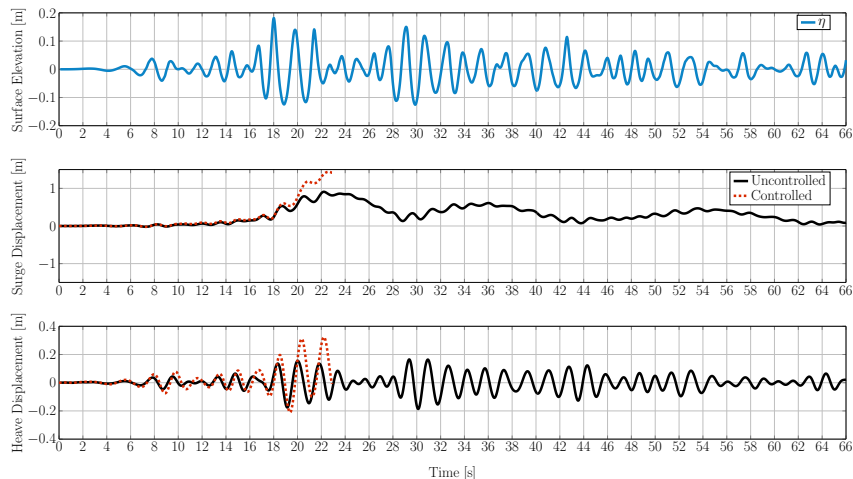


Figure 7: Time traces of the FSE, and the surge and heave displacements of the WEC which are plotted for an uncontrolled (black solid) and controlled (dashed red) device.

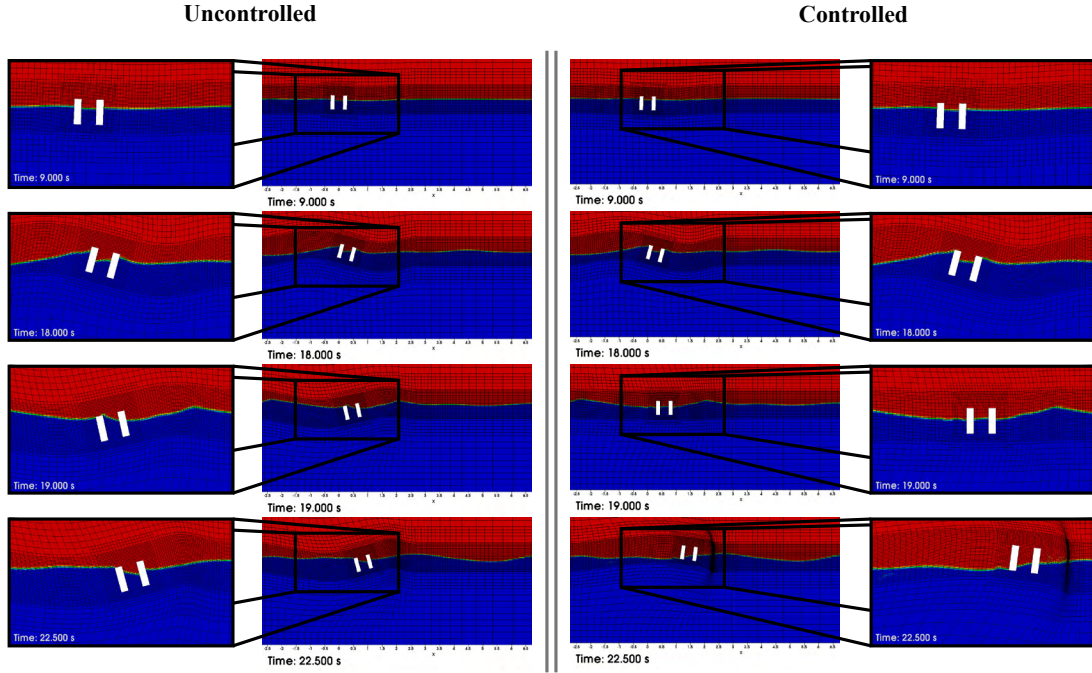


Figure 8: Mesh deformation in the NWT for the mesh morphing method. After 22.5s, the simulation of the controlled WEC aborts, due to poor mesh quality.

5.2 Mesh morphing vs. overset grids

The results in Section 5.1 highlight the importance of advanced mesh motion methods, when modelling WECs under controlled conditions. To evaluate the feasibility of the overset method, as an alternative to mesh morphing, the uncontrolled device is modelled, using the overset method, as implemented in OF v1812 and *opera*, and results are compared to the mesh morphing method. Figure 9a shows the time traces of the surge and heave displacement for the mesh morphing (black solid) and overset grid (v1812) (dashed red) methods. To quantify the agreement between the mesh morphing and overset method, the Mean Average Percentage Errors (MAPEs) (see Equation (8)) are evaluated. In Equation (8), n is the number of samples, y_i denotes the data of the mesh morphing method and \tilde{y}_i the data of the overset method. To compare the relative computational efficiency of the dynamic mesh motion methods, the normalised runtime $\Delta t_{r,n}$ is employed, following Equation (9). In Equation (9), $t_{s,MM}$ and $t_{r,MM}$ denote the simulated time and required run time of the mesh morphing method, while $t_{s,OSG}$ and $t_{r,OSG}$ denote the simulated time and required run time of the overset method.

$$\text{MAPE} = \frac{1}{n} \sum_{i=1}^n \left(\frac{y_i - \tilde{y}_i}{y_i} \right) \cdot 100\% \quad (8) \quad \Delta t_{r,n} = \frac{t_{s,MM}/t_{r,MM}}{t_{s,OSG}/t_{r,OSG}} \quad (9)$$

A relatively good match between the mesh morphing and the overset method (v1812) can be observed, with MAPEs of $\text{MAPE}_{\text{Surge}} = 9.2\%$ and $\text{MAPE}_{\text{Heave}} = 0.5\%$. For the results of the overset method (*opera*) (see Figure 9b), a similarly good match with the mesh morphing can be observed, with $\text{MAPE}_{\text{Surge}} = 5.7\%$ and $\text{MAPE}_{\text{Heave}} = 0.3\%$.

In terms of computational efficiency, the normalise runtime, $\Delta t_{r,n} = 3.7$ for the implementation in v1812, and $\Delta t_{r,n} = 2.6$ for the implementation in *opera*, indicate an overall longer computation time for the overset method, compared to mesh morphing, which is consistent with findings in [14] and [15]. Furthermore, it can be observed that the implementation of the overset method in *opera* is computationally more efficient, compared to the implementation in v1812.

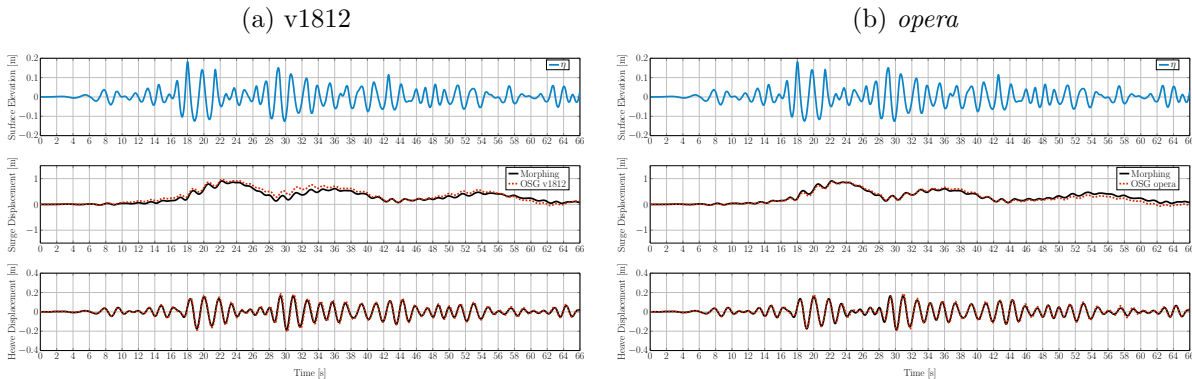


Figure 9: Time traces of the FSE, and the surge and heave displacement of the uncontrolled WEC, for the mesh morphing (black solid) and overset (dashed red) methods.

6 CONCLUSIONS

This paper present the modelling of a WEC device, using two different dynamic mesh motion methods. Comparing the results for the uncontrolled and controlled WEC device, when considering mesh morphing, highlights the importance of advanced mesh motion method, for the modelling of WECs under controlled conditions.

Overset grids prove to be a feasible alternative, showing potential for the analysis of WECs under controlled conditions, by avoiding the deterioration of the mesh quality. In the light of the results found in [14], significant improvements can be observed in the current release of the overset method in v1812, in terms accuracy and computational efficiency, compared to the initial release in v1706. Although the implementation of the overset method in *opera* proves to be of slightly higher accuracy and computational efficiency, compared to the implementation in v1812, the computational expense for overset methods is still significantly higher, compared to the mesh morphing method.

ACKNOWLEDGEMENTS

This paper is based upon work supported by Science Foundation Ireland under Grant No. 13/IA/1886. Josh Davidson is supported by the Higher Education Excellence Program of the Ministry of Human Capacities in the frame of Water science & Disaster Prevention research area of Budapest University of Technology and Economics (BME FIKP-VÍZ). Dominic Chandar is supported by the Institute Of High Performance Computing, Singapore.

REFERENCES

- [1] Penalba, M. and Giorgi, G. and Ringwood, J.V. Mathematical modelling of wave energy converters: a review of nonlinear approaches. *Renewable and Sustainable Energy Reviews* (2017) **78**:1188–1207.
- [2] Folley, M. *Numeircal Modelling of Wave Energy Converters*. Academic Press (2016).
- [3] Ruehl, K. and Bull, D. Wave Energy Development Roadmap: Design to commercialization. *OCEANS 2012 MTS/IEEE: Harnessing the Power of the Ocean* (2012) **78**:1188–1207.
- [4] Ringwood, J.V. and Bacelli, G. and Fusco, F. Energy-maximizing control of wave-energy converters: The development of control system technology to optimize their operation. *IEEE Control Systems* (2014) **34**:30–55.
- [5] Giorgi, G. and Penalba, M. and Ringwood, J.V. Nonlinear Hydrodynamic Models for Heaving Buoy Wave Energy Converters. *in the Proceedings of the 3rd Asian Wave and Tidal Energy Conference, Marina Bay Sands, Singapore* (2016).
- [6] Davidson, J. and Windt, C. and Giorgi, G. and Genest, R. and Ringwood, J.V. Chapter: Evaluation of energy maximising control systems for wave energy converters using OpenFOAM. *OpenFOAM - Selected papers from the 11th workshop, Guimaraes* (2018).
- [7] Windt, C. and Davidson, J. and Ringwood, J.V. High-fidelity numerical modelling of ocean wave energy systems: A review of CFD-based numerical wave tanks. *Renewable and Sustainable Energy Reviews* (2018) **93**: 610–630.
- [8] Stansby, P. and Gu, H. and Moreno, E.C. and Stallard, T. Drag minimisation for high capture width with three float wave energy converter M4. *in the Proceedings of the 11th European Wave and Tidal Energy Conference, Nantes* (2015).
- [9] Bharath A. and Penesis, I. and Nader, R.R. and Macfarlane, G Non-Linear CFD Modelling of a Submerged Sphere Wave Energy Converter. *in the Proceedings of the 3rd Asian Wave and Tidal Energy Conference, Singapore* (2016).
- [10] Coiro, D.P. and Troise, G. and Calise, G. and Bizzarrini, N. Wave energy conversion through a point pivoted absorber: Numerical and experimental tests on a scaled model. *Renewable Energy* (2016) **87**:317–325.
- [11] Lu, X. and Denver, D. and Chandar, J. and Chen, Y. and Lou, J. An overlapping domain decomposition based near-far field coupling method for wave structure interaction simulations. *Coastal Engineering* (2017) **126**:37–50.
- [12] Elhanafi A, and Macfarlane, G. and Fleming, A. and Leong, Z. Experimental and numerical investigations on the hydrodynamic performance of a floating-moored oscillating water column wave energy converter. *Applied Energy* (2017) **205**:369–390.
- [13] Elhanafi A, and Macfarlane, G. and Fleming, A. and Leong, Z. Experimental and numerical investigations on the intact and damage survivability of a floating-moored oscillating water column device. *Applied Ocean Research* (2017) **68**:276–292.

- [14] Windt, C. and Davidson, J. and Akram, B. and Ringwood, J.V. Performance assessment of the overset grid method for numerical wave tank experiments in the OpenFOAM environment. *in the Proceedings of the 37th International Conference on Ocean, Offshore and Arctic Engineering, Madrid* (2018) V010T09A006-1–V010T09A006-10.
- [15] Chen, H. and Qian, L. and Ma, Z. and Bai, W. and Li, Y. and Causon, D. and Mingam, C. Application of an overset mesh based numerical wave tank for modelling realistic free-surface hydrodynamic problems. *Ocean Engineering* (2019) **176**:97–117.
- [16] Chandar, D.D.J. On overset interpolation strategies and conservation on unstructured grids in OpenFOAM. *in press in Computer Physics Communications* (2019).
- [17] Ingram, D.M. and Causon, D.M. and Mingham, C.G. Developments in Cartesian cut cell methods. *Mathematics and Computers in Simulation* (2003) **61**:561–572.
- [18] Ferziger, J.H. and Peric, M. *Computational Methods for Fluid Dynamics*. Springer (2001).
- [19] Jung, M.S. and Kwon O.J. A Parallel Unstructured Overset Mesh Technique for Unsteady Flow Simulations. *in the Proceedings of the 4th International Conference on Computational Fluid Dynamics ICCFD, Ghent* (2006).
- [20] CCP-WSI website Focused wave interactions with floating structures: Blind Test Series 2. https://www.ccp-wsi.ac.uk/blind_test_series_2 Last accessed 10/12/2018.
- [21] Davidson, J. and Giorgi, S. and Ringwood, J.V. Linear parametric hydrodynamic models for ocean wave energy converters identified from numerical wave tank experiments. *Ocean Engineering* (2015) **103**:31–39.
- [22] Hirt, C.W. and Nichols, B.D. Volume of Fluid (VOF) Method for the Dynamics of Free Boundaries. *Journal of Computational Physics* (1981) **39**:201–225.
- [23] Berberović, E. and van Hinsberg, N.P. and Jakirlić, S. and Roisman, I.V. and Tropea, C. Drop impact onto a liquid layer of finite thickness: Dynamics of the cavity evolution. *Physical Review E* (2009) **79**:036306-1–036306-15.
- [24] Higuera, P. and Lara, J.L. and Losada, I.J. Simulating coastal engineering processes with OpenFOAM®. *Coastal Engineering* (2013) **71**:119–134.
- [25] Windt, C. and Davidson, J. and Schmitt, P. and Ringwood, J.V. On the assessment of numerical wave makers for CFD simulations. *Journal of Marine Science and Engineering* (2019) **7**:47.
- [26] Windt, C. and Davidson, J. and Schmitt, P. and Ringwood, J.V. Contribution to the CCP-WSI Blind Test Series 2: CFD-based numerical wave tank experiments employing an impulse source wave maker. *Submitted to the 13th European Wave and Tidal Energy Conference, Naples* (2019).

UNCERTAINTY QUANTIFICATION OF THE DYNAMICS OF A WAVE ENERGY CONVERTER

Guilheme Moura Paredes^{*1}, Claes Eskilsson^{*2} Jens Peter Kofoed^{*3}

*Aalborg University
Department of Civil Engineering
Thomas Manns vej 23, DK-9220 Aalborg Ø, Denmark
e-mail: ¹gmp@civil.aau.dk, ²cge@civil.aau.dk, ³jpk@civil.aau.dk

Key words: Uncertainty Quantification, Sensitivity Analysis, General Polynomial Chaos, Wave Energy Converter, Power Take-off; Numerical Simulation

Abstract. Since time-domain simulations of wave energy converters are computationally expensive, how can we analyse their dynamics and test wide ranges of design variables, without simplifying the physics involved? One possible solution is the use of General Polynomial Chaos (gPC). GPC provides computationally efficient surrogate models for partial differential equation based models, which are particularly useful for sensitivity analysis and uncertainty quantification. We demonstrate the application of gPC to study the dynamics of a wave energy converter in an operational sea-state, when there is uncertainty in the values of the stiffness and damping coefficient of the power take-off.

1 INTRODUCTION

In wave energy, time-domain simulations are unappealing because of the complexity of non-linear effects and the long computational time required. Even the most simple simulations resorting to linear potential flow theory can be time consuming. To complicate this situation, in uncertainty quantification traditional Monte-Carlo (MC) based methods require thousands upon thousands of time-domain simulations to obtain statistical distributions of the quantities of interest. However, this situation can be overcome using General Polynomial Chaos (gPC), and we will demonstrate its application to study the operation of a wave energy converter.

Our case study, described in Section 3, will be a simple two-body heaving point absorber, with a quadratic power take-off, and a three-leg catenary mooring system. In this example, the stiffness and the damping coefficient of the power take-off (PTO) will be the variables subjected to uncertainty, and we will study how the mooring tension, the body motions and the absorbed power is influenced by the uncertainty (Section 4).

General Polynomial Chaos, briefly explained in Section 2.1, provides a polynomial expansion surrogate model for partial differential equation (PDE)-based numerical models with random inputs [1]. Its application to study random processes and uncertainty quantification has several advantages over traditional MC-based methods. Unlike MC methods, gPC does not require

thousands of simulations to obtain stable values for the mean and variance. Using gPC, depending on the specific method, chosen the mean and variance can be obtained with only tens of simulations. Another advantage is that the statistical distributions of the quantities of interest can be obtained by running very large samples of the random inputs through the gPC surrogate model, which can be orders of magnitude faster to run than the PDE-based numerical model.

Polynomial Chaos was first described in 1938 by Norbert Wiener [2], for expansions using only Gauss's distribution. In 2002 it was expanded by Xiu and Karniadakis [3] to expansions using other statistical distributions, for improved convergence in cases where the quantities of interest do not have a gaussian distribution. Since then it has been used in a wide range of applications. One expected application, which drives many of the publications regarding gPC is uncertainty quantification in CFD [4, 5, 6]. Other applications are the study of the dynamics of train wagons [7], electronic circuits [8], particle physics [9], among many more. In ocean and coastal engineering, gPC has been applied in the analys wave scattering from an ice floe [10], propagation of water waves over uneven bottoms [11], to study a heaving buoy in irregular waves [12], just to name a few. More interestingly, in 2018 Lim *et al* [13] applied gPC to determine the extreme loads on the power take-off of a heaving wave energy converter.

2 THEORY

2.1 General polynomial chaos

Consider a process with both deterministic and uncertain inputs:

$$\mathbf{f} = \mathbf{f}(\mathbf{x}, \mathbf{Z}) \quad (1)$$

where \mathbf{f} is a general function, \mathbf{x} is the vector of deterministic inputs and \mathbf{Z} is the vector of uncertain inputs (or random variables) with dimension d . The gPC surrogate model of \mathbf{f} is given by a polynomial expansion of the form [1]:

$$\mathbf{f}_{\text{gPC}}(\mathbf{x}, \mathbf{Z}) = \sum_{|\mathbf{k}|=0}^{\infty} \hat{\mathbf{f}}_{\mathbf{k}}(\mathbf{x}) \Psi_{\mathbf{k}}(\mathbf{Z}) = \sum_{|\mathbf{k}|=0}^{\infty} \hat{\mathbf{f}}_{\mathbf{k}}(\mathbf{x}) \psi_{k_1}(Z_1) \psi_{k_2}(Z_2) \dots \psi_{k_d}(Z_d) \quad (2)$$

where $\hat{\mathbf{f}}_{\mathbf{k}}$ are the polynomial coefficients, $\mathbf{k} = (k_1, k_2, \dots, k_d) \in \mathbb{N}_0$ is a multi-index, $|\mathbf{k}| = k_1 + k_2 + \dots + k_d$, and $\psi_{k_i}(Z_i)$ is the polynomial basis function of the variable Z_i , of degree k_i . Because the expansion in Eq. (2) is an infinite series, it needs to be truncated to a chosen polynomial degree p for practical use, becoming:

$$\mathbf{f}_{\text{gPC}}(\mathbf{x}, \mathbf{Z}) \approx \sum_{|\mathbf{k}|=0}^p \hat{\mathbf{f}}_{\mathbf{k}}(\mathbf{x}) \Psi_{\mathbf{k}}(\mathbf{Z}) = \sum_{|\mathbf{k}|=0}^p \hat{\mathbf{f}}_{\mathbf{k}}(\mathbf{x}) \psi_{k_1}(Z_1) \psi_{k_2}(Z_2) \dots \psi_{k_d}(Z_d) \quad (3)$$

The degree p of the polynomial expansion must be selected depending on the needs of each particular case study. It can be chosen by trial and error, until a sufficiently accurate representation of the model is achieved, or by examining the value of the polynomial coefficients which, for smooth solutions, decay quickly with increasing p . For the selection of the polynomial family

$\psi_{k_i}(Z_i)$, the Weiner-Askey scheme provides the polynomials that converge optimally to solution of some of the most common statistical distributions [3].

There are two ways to apply gPC to a PDE-based model: the Stochastic Galerkin method and the Stochastic collocation method. The Stochastic Galerkin method is classified as intrusive because it needs the underlying equations of the numerical model to be reformulated. This can be complicated, and sometimes impossible, either because of mathematical complexity, or simply because there is no access to the code of the numerical model. The Stochastic collocation method is much simpler to apply because it does not depend on the numerical model, it does not need access to the code, nor re-casting of the differential equations. All that is needed is to run simulations on a selected number of collocation nodes \mathbf{z}_j , and post-process the results.

In our analysis we will be studying a process with only two random variables, $d = 2$. In this case, the gPC coefficients can be efficiently computed using the projection method. This is the inner product of the process $\mathbf{f}(\mathbf{x}, \mathbf{Z})$ and the polynomial basis functions $\Psi_{\mathbf{k}}(\mathbf{Z})$, with respect to the probability density function of the random variables, $\rho(\mathbf{Z})$ Eq. (4):

$$\langle \hat{f}_{\mathbf{k}}(\mathbf{x}), \Psi_{\mathbf{k}}(z) \rangle = \frac{\int f(\mathbf{x}, \mathbf{z}) \Psi_{\mathbf{k}}(\mathbf{z}) \rho(\mathbf{z}) d\mathbf{z}}{\int \Psi_{\mathbf{k}}^2(\mathbf{z}) \rho(\mathbf{z}) d\mathbf{z}} \quad (4)$$

The integration of Eq. (4) is done using quadrature rules, such as Gauss quadrature, which provide the points $\mathbf{z}^{(j)}$ where the model is to be evaluated, and the quadrature weights, $\mathbf{w}^{(j)}$.

The interaction between the different univariate polynomials in the tensor product can be controlled through the q -norm. A q -norm of 1 allows the tensor product of any set of univariate polynomials to reach the maximum selected polynomial order; decreasing the q -norm, until the minimum value of zero, decreases the maximum polynomial order allowed for products of univariate polynomials, reducing the total number of polynomial terms.

For smooth solutions, gPC shows exponential convergence. It is because of this, and because the mean and variance are encoded in the gPC coefficients, that it is possible to obtain stable values of the mean and variance using fewer simulations than in MC-based methods. Depending on the normalization used for the polynomials $\psi_{k_i}(Z_i)$, the mean is $\hat{\mathbf{f}}_0$, while the variance is the sum of the squares of $\{\hat{f}_k(\mathbf{x})\}_{k=1}^p$ (or scaled values of these).

For the computation of the gPC model we used UQLab's version 1.0.0, Polynomial Chaos Expansions Module [14].

2.2 Hydrodynamic, cable, and PTO models

The dynamics of the wave energy converter were modelled in WEC-Sim [15, 16], a time-domain solver for wave energy converters based on Cummins's equation [17]. The PTO selected for the wave energy converter was an hydraulic one, represented by the following model [18]:

$$f_{\text{pto}}(u, v) = ku + c_{\text{hyd}}v|v| \quad (5)$$

where f_{pto} is the force applied by the PTO, k is the linear stiffness of the PTO, u and v are, respectively, the relative displacement and velocity between the bodies driving the PTO, and c_{hyd} is the hydraulic damping coefficient of the PTO.

The mooring system was modelled in MooDy [19]. MooDy is an *hp*-adaptive discontinuous Galerkin (DG) numerical model for mooring cables, based on the equation of motion of cables with neither bending nor torsional stiffness. WEC-Sim and MooDy were coupled for the simultaneous simulation of dynamics of the wave energy converter and of the mooring systems; this coupling has been validated and demonstrated in [20].

2.3 Model equations with random inputs

Because of the uncertainty in the inputs, the model equations describing the dynamics of a moored wave energy converter become stochastic equations, with some variables becoming dependent on the uncertain inputs, \mathbf{Z} . In our analysis, the uncertain inputs are the stiffness, k , and damping coefficient, c_{hyd} of the PTO:

$$\mathbf{Z} = (k, d) \quad (6)$$

As presented in [21], Cummins's equation is now written as:

$$\mathbf{M} + \mathbf{A}_{\infty} \ddot{\mathbf{x}}(t, \mathbf{Z}) + \int_{-\infty}^t \mathbf{K}(t - \tau) \dot{\mathbf{x}}(t, \mathbf{Z}) d\tau + \mathbf{C}\mathbf{x}(t, \mathbf{Z}) = \mathbf{f}_{\text{ext}}(t) + \mathbf{f}_{\text{moor}}(t, \mathbf{Z}) + \mathbf{f}_{\text{pto}}(t, \mathbf{Z}) \quad (7)$$

where \mathbf{M} is the generalised mass matrix, \mathbf{A}_{∞} is the matrix of added mass at infinity, \mathbf{K} is the radiation impulse response function, \mathbf{C} is the stiffness matrix, $\ddot{\mathbf{x}}$, $\dot{\mathbf{x}}$, and \mathbf{x} are, respectively, the acceleration, velocity, and position vectors of the floating bodies, $\mathbf{f}_{\text{moor}}(t, \mathbf{Z})$ is the mooring force, $\mathbf{f}_{\text{pto}}(t, \mathbf{Z})$ is the PTO force, $\mathbf{f}_{\text{ext}}(t)$ is the vector of remaining external forces non-dependent on the uncertain input \mathbf{Z} , and t is time. In its turn, the equation of motion of mooring cables becomes [21]:

$$m_1(s) \frac{\partial^2 \mathbf{r}(s, t, \mathbf{Z})}{\partial t^2} = \left(\frac{T(\epsilon(s, t, \mathbf{Z}))}{1 + \epsilon(s, t, \mathbf{Z})} \frac{\partial \mathbf{r}(s, t, \mathbf{Z})}{\partial s} \right) + \frac{\partial}{\partial s} + \mathbf{f}_e(s, t, \mathbf{Z}), \quad (8a)$$

$$\epsilon(s, t, \mathbf{Z}) = \left| \frac{\partial \mathbf{r}(s, t, \mathbf{Z})}{\partial s} \right| - 1 \quad (8b)$$

where m_1 is the mass per unit length of the cable, \mathbf{r} is the position vector of a point s of the cable, where s is measured along the unstretched length of the cable, T is the tension magnitude, ϵ is the extension, and \mathbf{f}_e is the vector of external forces acting on the cable. Finally, the equation of the hydraulic PTO, Eq. (5) becomes

$$f_{\text{pto}}(u, v, \mathbf{Z}) = f_{\text{pto}}(u, v, k, c_{\text{hyd}}) = ku + c_{\text{hyd}}v|v| \quad (9)$$

where k and c_{hyd} are now random variables.

3 CASE STUDY

Our case study is based on the moored RM3 device tutorial distributed with WEC-Sim, Figure 1. The RM3 device is an axisymmetric two-body heaving point-absorber, using the relative motion between the two bodies to generate energy. The mooring system has been simplified from its original set-up, and here it is composed only of simple chains without floaters, Figure 1 and Table 1.

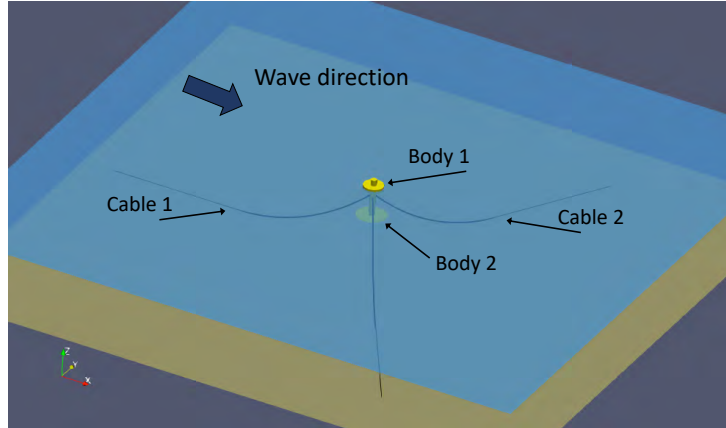


Figure 1: The RM3 case device and set-up.

Table 1: Parameters of the mooring cables.

| Quantity | Value |
|--|------------------------|
| Diameter (D_c) | 0.144 m |
| Density (γ_c) | 7736 kg/m ³ |
| Stiffness (EA) | 583.376 MN |
| Normal drag coefficient (C_{dn}) | 1.6 |
| Tangential drag coefficient (C_{dt}) | 0.5 |
| Normal added mass coefficient (C_{an}) | 1 |
| Cable length | 280 m |

We attributed to the PTO's stiffness, k , and damping coefficient, c_{hyd} , uniform distributions with the parameters presented in Table 2. The uniform distribution, attributing equal probability to all values, can both represent uncertainty and be used for sensitivity analysis. In WEC-Sim, the device was modelled using the one-hour irregular wave time-series umpqua46229_6_2008 provided with the tutorial, and a time-step of 0.01 s. The mooring systems was simulated in Moody [19], using, for each cable, 10 elements of order 5, with an adaptive time-step to ensure the Courant-Friedrichs-Lewy condition did not exceed 0.9.

To create the gPC model we used the quadrature method, testing increasing polynomial

Table 2: Probabilistic distributions for the parameters of the PTO.

| Parameter | Deterministic value | Distribution | Lower bound | Upper bound |
|------------------|---|--------------|---|---|
| k | $1.0 \times 10^4 \text{ N/m}$ | Uniform | $7.0 \times 10^3 \text{ N/m}$ | $1.3 \times 10^4 \text{ N/m}$ |
| c_{hyd} | $1.20 \times 10^6 \text{ N s}^2/\text{m}^2$ | Uniform | $4.80 \times 10^5 \text{ N s}^2/\text{m}^2$ | $1.92 \times 10^6 \text{ N s}^2/\text{m}^2$ |

orders until we achieved convergence of the probability distribution functions (PDF). The PDFs were created, for each time-step and for each output variable, by first running 3000 random sample pairs of k and c_{hyd} through the gPC model; then, using kernel density estimation, the probability density functions were smoothed. The final polynomial order selected for the gPC model was 9, requiring 100 simulations in total to determine the gPC coefficients.

4 RESULTS

In Figure 2 we show the time-series of the rigid body motions, power absorbed, and tension in the mooring cables of the RM3 device, for the simulation using the deterministic values of k and c_{hyd} . In Figure 3 we show the evolution of the PDFs of the same variables at $t = 3000 \text{ s}$, as we increase the polynomial order of the gPC model. We can see that, for a polynomial order of 9, all the PDFs have converged. However, some PDFs converged much earlier: the PDF of the heave motion of body 2 had already converged for order 1, presenting an almost uniform distribution of its values.

In Figure 4 we show the 95% confidence intervals for the different output variables. We plot only a small portion of the whole time-series, centred around $t = 3000 \text{ s}$, because otherwise it was not possible to visualise the confidence intervals. For comparison, this figure shows also simulation results using the deterministic values of k and c_{hyd} . Although k has a variation of 30% around its deterministic value, and c_{hyd} has a variation of 60%, the confidence intervals are quite narrow. The only exception is the confidence interval for the absorbed power, which shows a wide confidence interval at highest power peaks. This means that, to some extent, the power extracted by the device can be increased, without significantly changing motions of the floating WEC or the loads on the mooring cables. One possible explanation for narrow confidence intervals is the small value of the PTO's damping coefficient, associated with small velocities induced by the waves. For the RM3 device equipped with a linear PTO, values of linear damping coefficient up to around $2.5 \times 10^6 \text{ N s/m}$ correspond to very under-damped motions [22]. In our case, the PTO depends on the square of the velocity and the maximum value is $1.92 \times 10^6 \text{ N s/m}$, which, when motions are small, place it in the under-damped region. In this range of operation, even the relatively large variations of k and c_{hyd} generate only relatively small perturbations of the dynamics of the device.

Other reason for the narrow confidence intervals is the possibility that the WEC might not be operating in its most favourable sea-state (or the relatively small amplitude of the waves in the tested sea-state) which might not induce large enough motions. Finally, because WEC-Sim does not account for second order drift forces, the loads in the mooring cables are somewhat smaller than they would be if second order loads were accounted for, which might also help to explain the narrow confidence intervals.

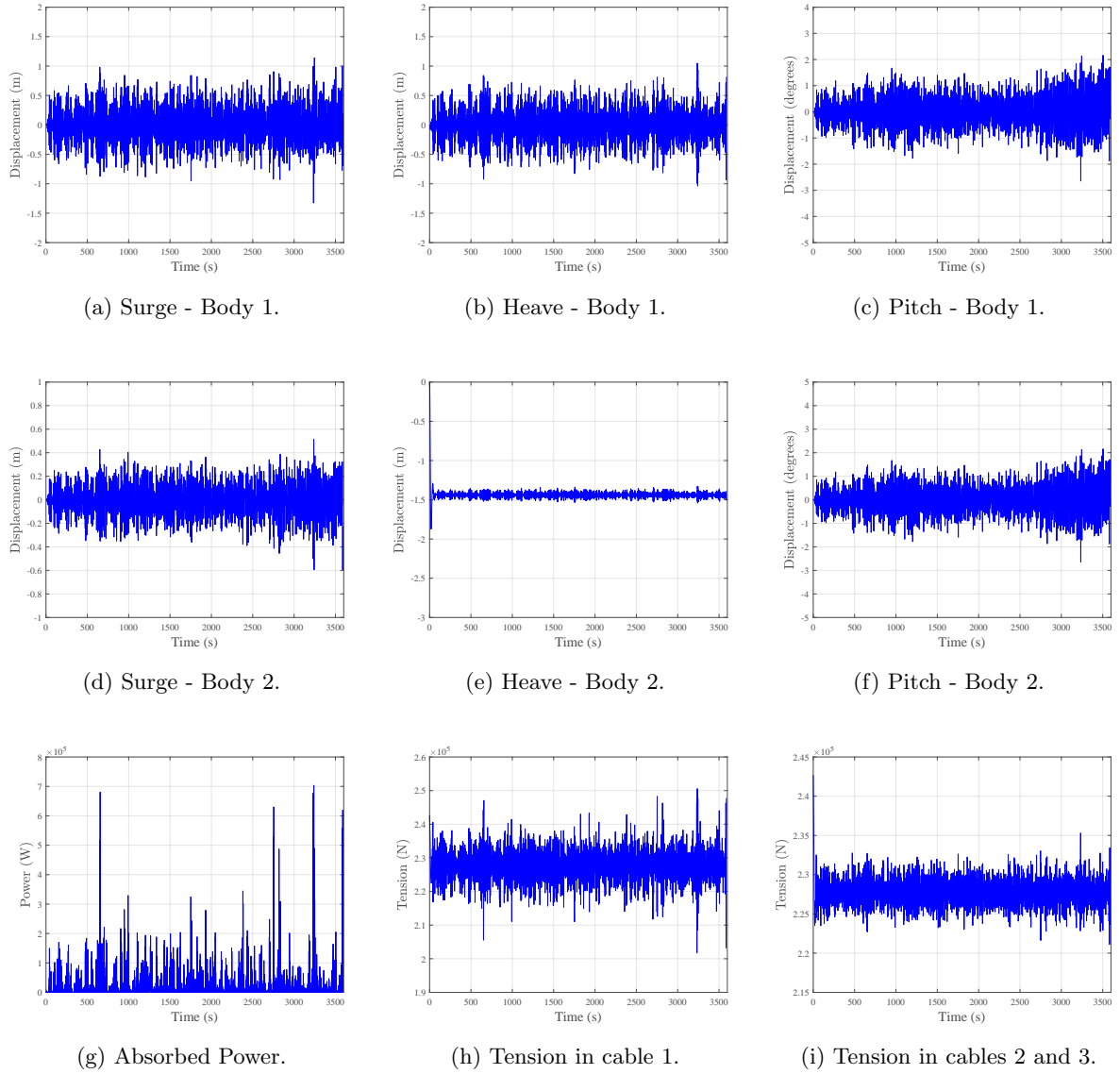


Figure 2: Time-series of displacement in surge, heave and pitch, absorbed power, and tension in the mooring cables for the RM3 device.

In Figure 4 we did not plot mean values of the simulation results, because they are almost the same as the simulation results using the deterministic values of k and c_{hyd} . Since the deterministic values of k and c_{hyd} are also their mean, this shows that the mean of the outputs is similar to the outputs computed using the mean inputs. In other other words, the simulations are almost linear. This is probably due to the device having only small motions in the tested sea-state, that do not generate large velocities in the power take-off, nor fast motions of the mooring cables, which are the major non-linear components.

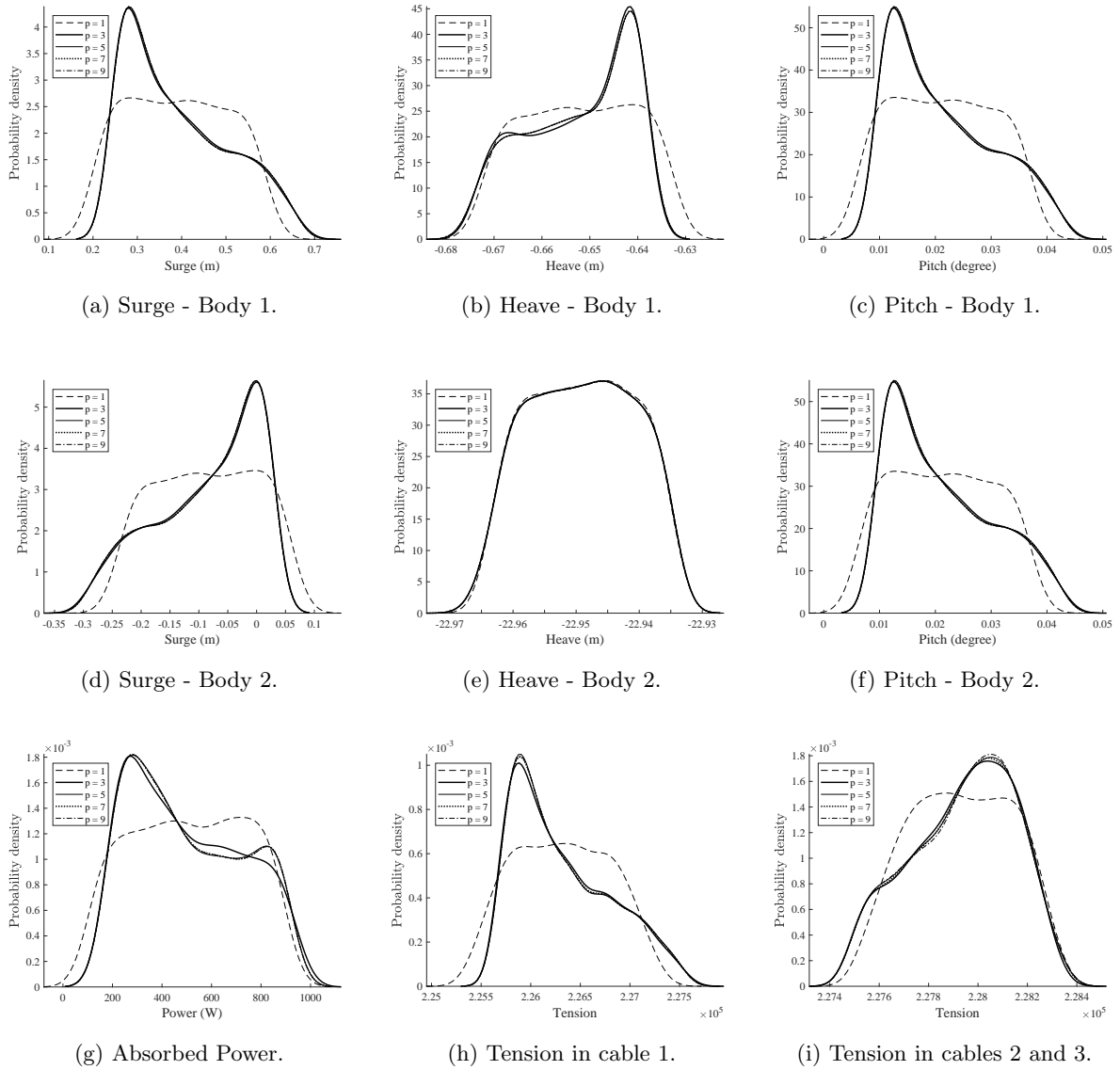


Figure 3: Convergence of the probability density function of displacement, power, and tension in the cables at time instant $t = 3000$ s.

Looking at the confidence interval for heave of body 2, Figure 4e, we can see that both the mean and the deterministic value lie almost in the center of the confidence interval. This, and its almost uniform PDF at $t = 3000$ s, Figure 3e, point to heave in body 2 being a linear function of k and c_{hyd} .

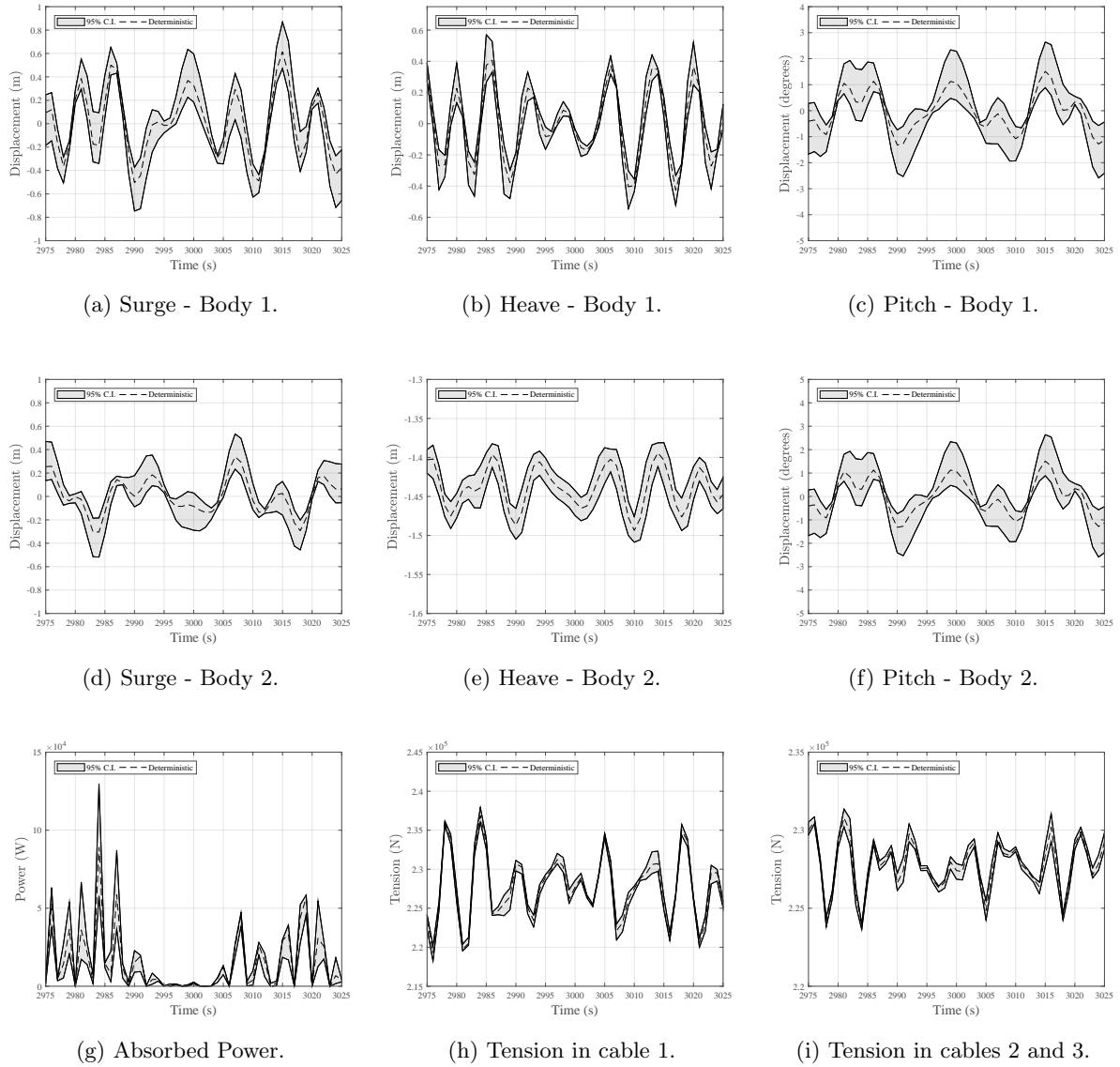


Figure 4: 95% confidence interval and deterministic value of displacement, power, and tension in the cables of the RM3 device.

5 CONCLUSIONS

We presented a case study of the dynamics of moored a wave energy converter, when the stiffness and damping coefficient of its quadratic hydraulic power take-off are uncertain. The wave energy converter analysed was the RM3 two-body heaving point absorber developed by NREL and Sandia. To propagate the uncertainty in the parameters of the PTO to the dynamics of the converter, we used general Polynomial Chaos, in its Stochastic Collocation formulation. Our general Polynomial Chaos model used 9th order polynomials to represent surge, heave, pitch, mooring cable tension, and extracted power as a function of PTO stiffness and damping coefficient.

By applying general Polynomial Chaos, we were able to obtain the equivalent of 3000 time-domain simulations of the RM3 device with as many different values of PTO stiffness and damping coefficients, when in fact we ran only 100 simulations in the numerical model. General Polynomial Chaos allows a fast and efficient analysis of non-linear processes and time-consuming simulations. For the particular case of wave energy, general Polynomial Chaos is useful even for devices with a linear PTO, as, for a large number of test cases, or when modelling non-linear mooring systems, the simulations will take considerable time.

The results we obtained showed that, for the case analysed, even though there was a significant uncertainty attributed to the stiffness and damping coefficient of the power take-off (30% and 60%, respectively), the motions and tensions in the mooring cables did not show a wide variability. This might be due to the damping coefficient of the power take-off being too low, even at the maximum value of the uncertainty interval, to have a significant influence on the dynamics of the wave energy converter. It can also be due to the wave amplitude and periods of the sea-state not inducing large enough motions on the device.

Because what we presented was a relatively simple application case of general Polynomial Chaos, future work on this topic should focus on testing a wider range of PTO stiffness and damping coefficient values, different distributions, a larger variety of sea-states, as well as longer sea-states.

REFERENCES

- [1] Dongbin Xiu. *Numerical Methods for Stochastic Computations - A Spectral Method Approach*. Princeton University Press, Princeton, New Jersey, 2010.
- [2] Norbert Wiener. The Homogeneous Chaos. *American Journal of Mathematics*, 60(4):897, 1938.
- [3] Dongbin Xiu and George Em Karniadakis. The Wiener-Askey Polynomial Chaos for Stochastic Differential Equations. *SIAM Journal on Scientific Computing*, 24(2):619–644, jan 2002.
- [4] O. P. Le Maître and Omar M. Knio. *Spectral Methods for Uncertainty Quantification*. Scientific Computation. Springer Netherlands, Dordrecht, 2010.
- [5] Vincent Couaillier and Eric Savin. Generalized Polynomial Chaos for Non-intrusive Uncertainty Quantification in Computational Fluid Dynamics. In *Uncertainty Management for Robust Industrial Design in Aeronautics*, pages 123–141. 2018.

-
- [6] Chris Lacor and Éric Savin. *General Introduction to Polynomial Chaos and Collocation Methods*, pages 109–122. Springer International Publishing, 2019.
- [7] D. Bigoni, H. True, and A.P. Engsig-Karup. Sensitivity analysis of the critical speed in railway vehicle dynamics. *Vehicle System Dynamics*, 52:272–286, 2014.
- [8] P. Manfredi, D. Vande Ginste, D. De Zutter, and F. G. Canavero. Generalized decoupled polynomial chaos for nonlinear circuits with many random parameters. *IEEE Microwave and Wireless Components Letters*, 25(8):505–507, Aug 2015.
- [9] M. M. R. Williams. Polynomial chaos functions and neutron diffusion. *Nuclear Science and Engineering*, 155(1):109–118, 2007.
- [10] J. E. M. Mosig, F. Montiel, and V. A. Squire. Water wave scattering from a mass loading ice floe of random length using generalised polynomial chaos. *Ocean Modelling*, 70:239, 2017.
- [11] Daniele Bigoni, Allan P. Engsig-Karup, and Claes Eskilsson. Efficient uncertainty quantification of a fully nonlinear and dispersive water wave model with random inputs. *Journal of Engineering Mathematics*, 101:87–113, 2016.
- [12] Edwin Kreuzer and Eugen Solowjow. Polynomial Chaos and the Heave Motion of a Cylinder in Random Seas. In *Proceedings in Applied Mathematics and Mechanics*, volume 15, pages 559–560. Springer, 2015.
- [13] HyeongUk Lim, Lance Manuel, and Ying Min Low. On Efficient Long-Term Extreme Response Estimation for a Moored Floating Structure. In *Volume 3: Structures, Safety, and Reliability*, page V003T02A043. ASME, 2018.
- [14] S. Marelli and B. Sudret. Uqlab user manual - polynomial chaos expansions. Technical report, Chair of Risk, Safety & Uncertainty Quantification, ETH Zurich, Zurich, 2018.
- [15] National Renewable Energy Laboratory and Sandia Corporation. WEC-Sim (Wave Energy Converter Simulator) WEC-Sim documentation, 2015.
- [16] Yi-Hsiang Yu, Michael Lawson, Kelley Ruehl, and Carlos Michelen. Development and demonstration of the WEC-Sim wave energy converter simulation tool. In *Proceedings of the 2nd Marine Energy Technology Symposium METS2014*, page 8, Seattle, WA, USA, 2014. Marine Energy Technology Symposium.
- [17] W. E. Cummins. The impulse response function and ship motions. Technical report, David Taylor Model Basin, Washington D. C., 1962.
- [18] Helen Louise Bailey. *Effect of a nonlinear power take off on a wave energy converter*. PhD Thesis, The University of Edinburgh, 2011.
- [19] Johannes Palm, Claes Eskilsson, and Lars Bergdahl. An hp-adaptive discontinuous Galerkin method for modelling snap loads in mooring cables. *Ocean Engineering*, 144:266–276, 2017.

- [20] Guilherme Moura Paredes, Claes Eskilsson, Johannes Palm, Jens Peter Kofoed, and Lars Bergdahl. Coupled BEM/hp-FEM Modelling of Moored Floaters. In *Proceedings of the 1st Vietnam Symposium on Advances in Offshore Engineering. VSOE 2018*, pages 504–510. Hanoi, 2018.
- [21] Guilherme Moura Paredes, Claes Eskilsson, and Allan P.; Engsig-Karup. Uncertainty Quantification in Mooring Cable Dynamics Using Polynomial Chaos Expansions. *Submitted for possible publication*, 2019.
- [22] Vincent S Neary, Michael Lawson, Mirko Previsic, Andrea Copping, Kathleen C Hallett, Alison Labonte, Jeff Rieks, and Dianne Murray. Methodology for Design and Economic Analysis of Marine Energy Conversion (Mec) Technologies. Technical report, Sandia National Laboratories, 2014.

**3D STRUCTURAL DESIGN TOOL FOR MONOHULL AND
MULTIHULL VESSELS****MARINE 2019****JEROD WYMAN^{1*}, JOSHUA KNIGHT² AND DAVID KRING³**^{1,3} Navatek LTD

10 Free St, Suite 2, Portland, Maine, USA 04101

* Corresponding author e-mail: jwyman@navatekltd.com

² Navatek LTD

4300 Wilson Blvd, Suite 350, Arlington, Virginia, USA 22203

Key words: Structural Design, Ultimate Limit State

Abstract. An Ultimate Limit State (ULS) based design tool has been developed, which calculates discrete 2D ship sections for computational efficiency, while supporting a 3D geometry model. This tool, called Brokkr, uses a medium fidelity methodology which allows the user to determine scantlings and plate thickness earlier in a design process and with less computational time than typical Finite Element Analysis (FEA). Individual structural components within the vessel can be analyzed to a level of accuracy superior to rules-based structural development. The ULS principles allow the tool to be equally accurate for calculating stresses and designing structure for monohull or multihull vessels. The 3D modeling aspect also allows for accurate assessment of structural weights, mass distribution, and secondary loading forces. The program has been validated against a midship section of the David Taylor Model Basin (DTMB) 5415 hull form, generating structure which was within 1% of the weight of the actual design scantlings. An analysis based on the trimaran RV Triton is being performed currently, beginning with calculation of global and local loading for a model scale representation. These calculations will be validated with actual model test data. Then the full-scale Triton will be modeled with expected seaway loading, the loads will be analyzed by Brokkr, and a scantling design will be developed. The program provides 3D visualization of hull sections. Its hierarchical approach will design a primary hull module, generally at midship where global bending loads are highest, and optimize plate thicknesses and stiffener size/spacing. This information is then utilized to govern design of secondary hull modules who inherit the same girder and stiffener spacing. Plate thicknesses are calculated using combined loading conditions, with redesign as necessary.

**Figure 1:** Brokkr is designed for accuracy and computational efficiency

1 INTRODUCTION

Modern military and commercial vessels are being designed today with more focus on optimizing performance and fuel economy than in the past. A preliminary design process that helps to mitigate unnecessary system weight and prevent costly redesign during later development phases can ensure that a vessel is delivered at reduced displacement while meeting mission requirements. The most critical aspect to maintaining overall vessel weight is to optimize structural weight using efficient plate and stiffener combinations. A typical military combatant will have approximately half of its lightship weight in structure. For transports and commercial ships, this ratio can be much higher as their mission is focused less on speed and auxiliary capabilities, and more on transporting as much cargo as possible.

While steel monohull vessels can leverage past practice with low to moderate risk, there have not been a sufficient number of large multihulls built to afford the same level of early risk abatement. Consequently, rules-based approaches to these designs are not as robust as with monohull vessels. Multihulls must consider a wider variety of secondary loading (under-deck wave slap and transverse bending) which makes rules-based approaches more difficult to develop, despite the fact that all the designs are governed by the same first principles.

This Ultimate Limit State (ULS) based design tool which has been developed focuses on these first principles and assesses monohull and multihull ship structures as discrete stiffened panels, referred to as grillages. The structure utilized within the program is discussed in the following sections. The ULS method allows for rapid exploration of a large combination of plate and stiffener combinations when provided estimates of longitudinal and transverse loading, hullform geometry, and deck/watertight subdivision bulkhead locations.

2 PROGRAM STRUCTURE

The tool which has been developed using these ULS formulas is called Brokkr. The program will analyze a hull surface file with deck and major watertight subdivision bulkhead locations specified. The hull surface could be the result of conceptual design speed/power and seakeeping work, the deck and longitudinal bulkhead locations set to maximize functionality, and the watertight bulkhead locations based on a floodable length study or damage stability work. This file would be exported from Rhino, Orca, or a comparable 3D modeling tool and brought into the geometry manager as non-uniform rational B-Splines (NURBS) surfaces.

Brokkr will then use primary loading information (hogging, sagging, and torsion about the longitudinal axis) to analyze longitudinal strength. Strength is analyzed in 2-dimensional cut planes similar to the industry-standard practice of utilizing the midship section and calculating a required section modulus or a maximum stress given a quasi-static loading condition. Brokkr will use a ULS based approach described in detail within Section 3. This analysis is performed for any number of cuts in either the longitudinal or transverse directions. Where this methodology utilizes the accuracy of a 3D model and structural geometry, while basing the calculations on a 2D cut plane ensuring accurate and computationally efficient calculations, it is referred to as a 2.5D approach [1,2]. The transverse cut plane capability is especially useful for ensuring an effective design of multihull vessels which can experience significant transverse bending when rolling or during loading / unloading evolutions.

2.1 Brokkr Hierarchy

The first set of 2D cuts will be focused on what is referred to as the primary hull module. This module is typically located near midship, where the global bending loads are the highest. The grillages (intra-module plate stiffener combinations) within this module are designed based on ULS analysis and their governing loads and safety factors. This primary hull module is calculated with maximum flexibility for selection of stiffener size and spacing, plate thickness, and transverse frame size and spacing. This approach is shown in Figure 2 with the primary hull module shown as number 1 in the design hierarchy breakdown.

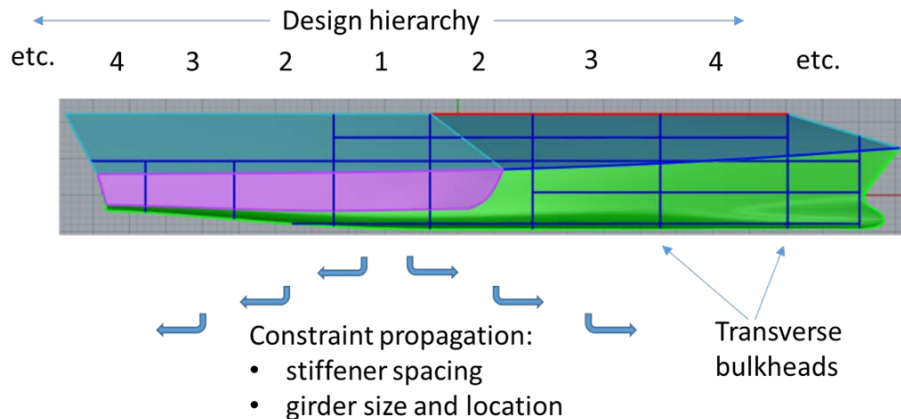


Figure 2: Brokkr design hierarchy

The design priority of each module will be in descending order, with adjacent zones stiffener spacing being governed by the previous module in the design process. Successive modules are allowed to optimize transverse frame spacing, but any single defined module will have the same transverse frame spacing throughout.

2.2 Optimization Methodology

Calculations are performed at the grillage level. Grillages are the components of hull modules which are sections of the ship's structure existing between a transverse bulkhead pair. Components making up the modeled vessel are shown in Figure 3. Certain heuristics are included in the design choices. For example, the lower level members such as stiffeners and stiffened plate thicknesses are selected from a catalogue of available sizes. This adds complexity in doing a true optimization but is an important step to ensure minimal changes as the final detail design of a ship is developed.

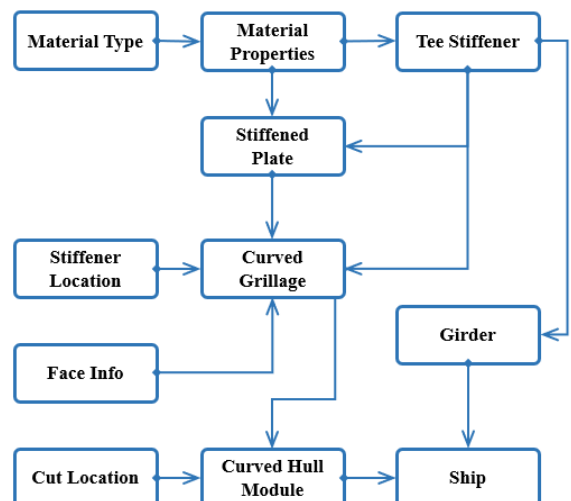


Figure 3: Brokkr modeled component relationship

3 ULTIMATE LIMIT STATE THEORY

Ultimate Limit State theory relies on recent theoretical advances to ensure that a structure's stresses can be accurately calculated in non-linear deflection situations. This method focuses on analyzing the combined effects of lateral pressure, transverse, axial, and shear forces experienced by a structure under load. The von Mises stress is then calculated utilizing the following equation [5]:

$$\left(\frac{\sigma_{xav}}{\sigma_{xu}^{II}}\right)^{c_1} - K \left(\frac{\sigma_{xav}}{\sigma_{xu}^{II}}\right) \left(\frac{\sigma_{yav}}{\sigma_{yu}^{II}}\right) + \left(\frac{\sigma_{yav}}{\sigma_{yu}^{II}}\right)^{c_2} + \left(\frac{\tau_{av}}{\tau_u^{II}}\right)^{c_3} = 1 \quad (1)$$

The structure is below its ULS if the von Mises membrane stresses remain below the yield stress of the material. This method utilizes first principles and approximates physics more accurately than traditional allowable stress methodology such as required section modulus, maximum primary bending stress, or a rules-based approach. ULS calculations are very effective when utilizing the cut-planes methodology discussed in Section 2.

3.1 Membrane Stress Methodology

Structural analysis performed within Brokkr utilizes membrane stress methods for assessing structure in all failure modes discussed above. The methods predict plate collapse by solving the equations governing structural behavior under large deflections, in addition to gross yielding without buckling (Failure Mode 6 in Table 1). Membrane stress method that includes lateral pressure loads is considered as well, which is important for ship structural design. The method accounts for the membrane stress distribution inside of the calculated plate. Prior to buckling, membrane stress is uniform along the loaded edge of the plate panel and is zero on the unloaded edge (assuming unidirectional loading). If the force is sufficient to cause buckling, the plate begins to deflect, and the stresses become non-uniform. For an unloaded edge that is not supported (atypical of ship designs) the edges will move in plane, and no stresses will be developed. If these edges are constrained by other structure, a non-uniform stress field will develop. As the stresses rise due to increased loading, deflections will increase until the von Mises membrane stresses exceed the material's yield strength. At this stress, yield followed by collapse will occur along the boundary and the structure will fail. [3]

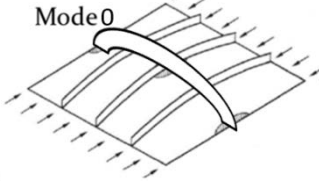
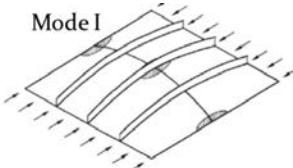
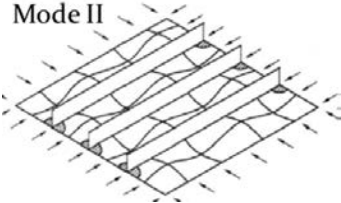
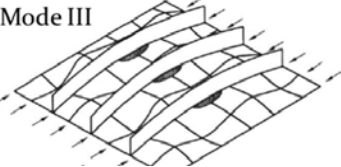
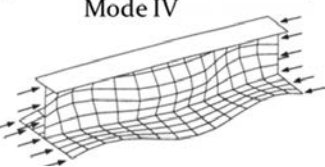
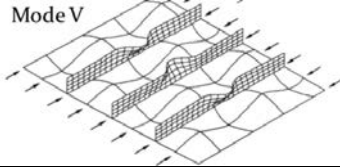
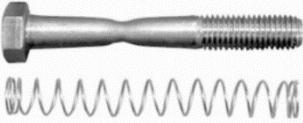
3.2 Assessed Failure Modes

Plate/stiffener combinations can be represented by seven main failure modes, discussed in Table 1 below. As calculated membrane stresses exceed the von Mises stress (Equation 1), the panel will begin to yield. This methodology approximates the physics of structural collapse more closely than relying solely upon overall section modulus, quasi-static still water bending, or rules/experienced based guidelines.

Brokkr utilizes calculations to check all seven failure modes, with user specified stress factors for each mode. The matrix of stress factors is used to assign specific percentages of yield stress that each component of ship structure is allowed to experience before being redesigned to support the necessary loading condition. These stress factors would be applied based on the

severity that a failure in the prescribed area would cause to a vessel and its crew. For example, Mode 0 signifies a massive panel collapse, across multiple frames. This is a significant failure mode anywhere on a vessel and can compromise the overall structural integrity and water tightness. Therefore, a stress factor of no more than 0.5 would be suggested, meaning the grillage would be designed so that no Mode 0 cases experienced von Mises stresses above 50% of the material yield strength. In the case of an interior bulkhead, stress factors for modes 4 and 5 could be selected as high as 0.8 as a locally compromised stiffener is unlikely to be a significant threat to ship safety. Steel and aluminum structures can be analyzed, with the heat affected zone being accounted for within the partial stress factors.

Table 1: Failure modes of steel structures

| Description | Visual Representation | Description | Visual Representation |
|--|---|---|---|
| Mode 0: Inter-frame collapse of plating and stiffeners as one unit. [4] |  | Mode 1: Intra-frame collapse of plating and stiffeners as one unit. [5] |  |
| Mode II: Collapse of plating without failure of stiffeners. [5,6] |  | Mode III: Beam-column collapse of a stiffener with its attached plating. [7] |  |
| Mode IV: Local buckling of the stiffener web. [7] |  | Mode V: Flexural-torsional buckling or tripping of the stiffeners. [7] |  |
| Mode VI: Gross yielding without buckling. [7] |  | | |

3.3 Comparison to Finite Element Modeling

This membrane stress calculation method for ultimate limit strength shows agreement with Finite Element Analysis methodology while utilizing much less computational time and can be applied earlier in the design process. While Brokkr is not intended to be a replacement for detailed FEA, it is important to compare the stresses resulting from a Brokkr analysis to a finite element solution. This helps to bring confidence that a design guided by Brokkr will be similar to one resulting from a finite element analysis that will be used for detail design.

For this validation a single stiffened panel was analyzed. The selected material has a yield stress of 315 MPA and a Young’s modulus of 206 GPA. These properties correspond to a high

strength steel, equivalent to American Bureau of Shipping AH-32 steel, common in shipbuilding. The modeled plate has an aspect ratio of four, with a length of 1.20 meters. Each half-plate is a 0.15 x 1.20 meter rectangle which yielded a mesh size of 22 x 176 elements. The plate was modeled to be simply supported and symmetry is applied along the long edge.

A two-step analysis had been run using a non-linear static solver to determine the ultimate limit state. A uniform pressure load is applied over 100 time steps. Next, a displacement is imposed on an edge over those steps. For each displacement time step, the nodal constraint forces are recorded along the edge opposite to the edge with the applied displacement. Average stress is calculated, and the stress strain curve is created.

The membrane stress/ULS calculations compare well with FEA results for longitudinal and transverse compression. This comparison can be seen in Figures 4 and 5 for plate slenderness ratios of 1.0 to 5.0 for a plate aspect ratio of four. Slenderness ratio was changed by altering plate thickness. The results correlated well with published results for other aspect ratios.

A full explanation of this validation testing is available in Reference [3].

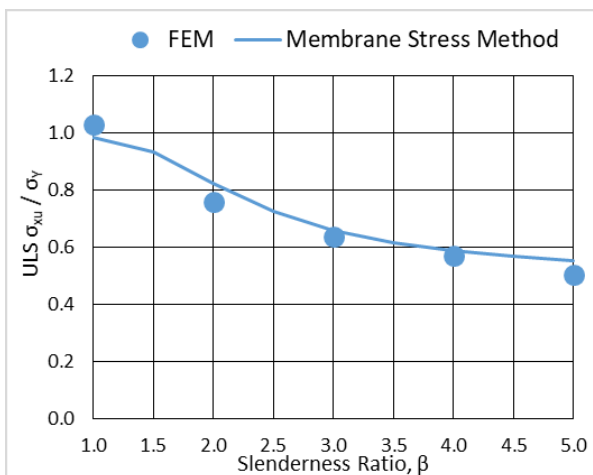


Figure 4: Longitudinal Compression Comparison

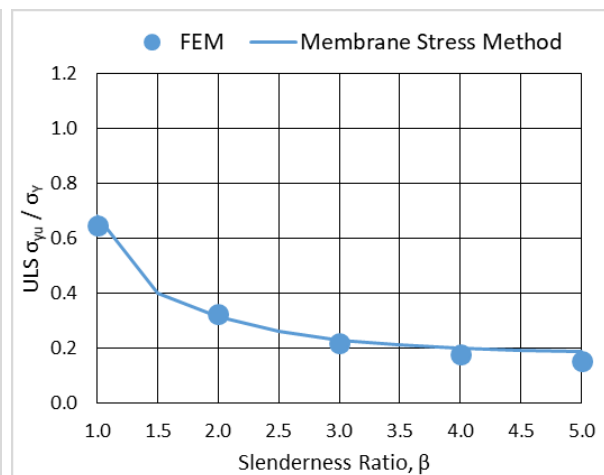


Figure 5: Transverse Compression Comparison

4 VALIDATION OF EXISTING HULLFORM

To confirm that Brokkr generates an accurate structural solution requiring minimal re-engineering during subsequent design steps, results of the program were compared to a vessel which has undergone detail design. There are more monohull than multihulls designs in the medium to large size range. Since the first principles approach that Brokkr employs work equally well for monohulls and multihulls, a proven monohull design was selected.

4.1 The 5415 Hullform

The David Taylor Model Basin (DTMB) 5415 hullform is the preliminary design for the DDG 51 Arleigh Burke class of guided missile destroyers for the United States Navy. This design has undergone full structural analysis based on design loads, safety factors, and best practices of the time. With three flight upgrades and over 60 vessels in service, the Arleigh Burke class has proven reliable and able to accommodate significant upgrades in capability and displacement throughout its life with minor structural modifications.

4.2 Analysis

To verify Brokkr’s structural design capability when compared to a proven design, it was important to understand the specific governing loads and safety factors utilized to create the baseline 5415 structure. The midship section was used for comparison as it was designed for the highest global bending loads. Deck and watertight bulkhead locations, and material types for the parent design were provided as inputs to Brokkr. Deck and shell plate thicknesses, and stiffener sizes and spacing were allowed to vary. Initially, an overall stress factor for all structural members was utilized. Secondly, a set of partial stress factors was developed so that structural components would have allowable stresses set to different percentages of material yield strength, depending on the severity of danger to the vessel that failure to each component would be likely to cause. This methodology is explained in Section 3.2.

4.3 Results

For both verification analyses, the Brokkr generated designs were compared to the 5415 structural configuration. Weight and ULS stress ratios were the primary points of comparison. Table 2 shows the results calculated by Brokkr as a percentage of the 5415 design of record.

Table 2: Brokkr calculations compared to 5415 design

| Safety Factor | Mass % | ULS Stress % |
|---------------|--------|--------------|
| Overall | 75.9 | 99.8 |
| Partial | 99.1 | 99.9 |

Utilizing the partial safety factors method, the weight and ULS stress % of the 5415 design were able to be closely approximated. The Brokkr optimized structure was within 1% of the 5415 weight, obtained with smaller stiffeners at slightly closer spacing. [8]

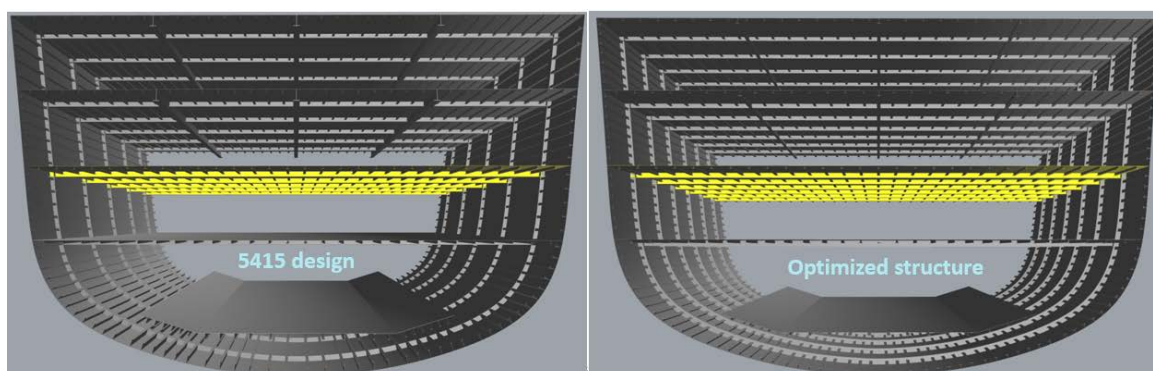


Figure 6: Midship module comparison between the 5415 design and the Brokkr optimized structure

With further adjustment to allowable plate thicknesses, stiffener sizes, and setting a higher “low-limit” for stiffener spacing, Brokkr could have produced a hull module nearly identical to the one designed for the 5415. This functionality allows a design to be both weight efficient and low cost by eliminating potential technical solutions with excessive numbers of stiffeners due to low spacing, which would in turn require excessive welding and fabrication costs.

6 CONCLUSIONS

Ultimate Limit State design can aid in rapid development of the structural configuration for a vessel given design load conditions. The methodology uses first principles with low computational cost when compared with traditional Finite Element Analysis. Brokkr allows for the exploration of a wide design space early in the design process, so that a design can be optimized for reduced weight and/or low production cost by specifying plating thicknesses, stiffener types, and minimum or maximum frame and longitudinal stiffener spacing criteria.

Currently, integration testing is being performed on verifying a loads calculation program utilizing the potential flow code Aegir [9]. This program is showing promising results for the trimaran R/V Triton when compared with model test data. The calculated ship-scale loads will be transferred to Brokkr, along with the hull geometry and deck/bulkhead locations to generate a structural model that will be compared with the structural design of the vessel.

Future development for Brokkr will incorporate Ship Work Breakdown Structure (SWBS) mapping for the modeled ship components so that a weight database for structure can be developed without manual calculation. This will allow additional compatibility with the US Navy's Rapid Ship Design Environment software. Initial studies have begun to assess the viability of including composite structures into the design process, which would expand the scope of hull designs which would benefit from Brokkr analysis.

7 ACKNOWLEDGEMENTS

The author would like to acknowledge the efforts of the United States Office of Naval Research and Naval Surface Warfare Center Carderock, under the technical guidance of Ms. Kelly Cooper and Mr. D. Max Jones via Contract N00014-18-C-2007. Without their support the establishment and development of this structural analysis program would not be possible.

8 REFERENCES

- [1] Knight, J.T. *Rapid, early-stage Ultimate Limit State Structural Design for Multihulls*. MARSTRUCT (2017).
- [2] Ogdon, A. B., Collette, M. D., & Singer, D. J. *Critical Cuts Method*. (2012).
- [3] Smith, M.V, Szlatenyi, C., Field, C. and Knight, J.T. *Improved Ultimate Strength Prediction for Plating Under Lateral Pressure*. IMDC (2018).
- [4] Benson, S., Downes, J. & Dow, R. S. *Overall Buckling of Lightweight Stiffened Panels Using an Adapted Orthotropic Plate Method*. *Engineering Structures*. (2015).
- [5] Paik, J. K., Thayamballi, A. K., & Kim, B. J. *Large deflection orthotropic plate approach to develop ultimate strength formulations for stiffened panels under combined biaxial compression/tension and lateral pressure*. (2001).
- [6] Paik, J. K., & Duran, A. *Ultimate Strength of Aluminum Plates and Stiffened Panels for Marine Applications*. (2004).
- [7] Hughes, O.F. and Paik, J.K. *Ship Structural Analysis and Design*. SNAME (2010).
- [8] Cope, N. and Knight, J. *Verification of an Automated Structural Design Procedure using Ultimate Limit States (Pending)*. PRADS (2019).
- [9] Kring, D. C., Milewski, W. M. and Fine, N. E. *Validation of a NURBS-Based BEM for Multihull Ship Seakeeping*. 25th Symposium on Naval Hydrodynamics. (2004).

AN ADAPTIVE N -FIDELITY METAMODEL FOR DESIGN AND OPERATIONAL-UNCERTAINTY SPACE EXPLORATION OF COMPLEX INDUSTRIAL PROBLEMS

A. SERANI*, R. PELLEGRINI*, R. BROGLIA*,
J. WACKERS†, M. VISONNEAU†, AND M. DIEZ*

*CNR-INM, National Research Council-Institute of Marine Engineering
Via di Vallerano 139, 00128 Rome, Italy
e-mail: {andrea.serani, riccardo.pellegrini}@inm.cnr.it, {riccardo.brogli, matteo.diez}@cnr.it

†LHEEA Lab, Ecole Centrale de Nantes, CNRS-UMR
6598, 44321 Nantes Cedex 3, France
e-mail: {jeroen.wackers, michel.visonneau}@ec-nantes.fr

Key words: Multi-fidelity, adaptive metamodels, simulation-based design optimization, uncertainty quantification, adaptive-grid refinement, multi-grid acceleration

Abstract. An adaptive N -fidelity (NF) metamodel is presented for the solution of simulation-based design optimization and uncertainty quantification problems. A multi-fidelity approximation is built by an additive correction of a low-fidelity metamodel with metamodels of hierarchical differences (errors) between higher-fidelity levels. The metamodel is based on the expected value of an ensemble of stochastic radial-basis functions, which also provides the uncertainty associated to the prediction. New training points are added to the appropriate fidelity level, based on the NF prediction uncertainty and the computational cost. The method is demonstrated for an analytical test function, the shape optimization of a NACA hydrofoil, and the operational-uncertainty quantification of a RoPax ferry. The fidelity levels are defined by adaptive-grid refinement and multi-grid approach, for the NACA hydrofoil and the RoPax ferry, respectively. The generalization of the multi-fidelity concept to N fidelities shows promising results both in terms of accuracy and computational cost.

1 INTRODUCTION

Ship performance depends on design and operational (including environmental) parameters. The accurate prediction of significant design metrics (such as resistance and powering requirements; seakeeping, maneuverability, and dynamic stability; structural response and failure) requires prime-principle-based high-fidelity computational tools (e.g., for computational fluid/structural dynamics, CFD/EFD), especially for innovative configurations and off-design conditions. These tools are generally computationally expensive, making the exploration of design (such as in simulation-based design optimization, SBDO) and operational-uncertainty (such as in uncertainty

quantification, UQ) spaces a technological challenge.

To reduce the computational cost of SBDO and UQ processes, metamodeling methods have been developed and successfully applied in several engineering fields [1]. Among other metamodels, radial basis functions (RBF) methods have demonstrated their accuracy and efficiency in engineering design [2]. Further efficiency is gained using dynamic metamodels, for which the design of experiments (DoE) for metamodel training is not defined a priori but dynamically updated, exploiting the information that becomes available during the analysis process. Thus, training points are added where it is most useful, reducing the number of function evaluations required to properly represent the function. An adaptive sampling criterion based on the maximum prediction uncertainty for dynamic radial basis functions (DRBF) has been presented by [3]. Other sampling approaches are based on the expected improvement [4] and multi-criteria adaptive sampling [5].

In addition to dynamic metamodels, multi-fidelity approximation methods have been developed to further reduce the cost of the SBDO procedure, combining the accuracy of high-fidelity solvers with the computational cost of low-fidelity solvers. Multi-fidelity (MF) metamodels use mainly low-fidelity simulations and few high-fidelity (accurate, expensive) simulations used to preserve the accuracy of the overall model. Several metamodels have been used in the literature with MF data, like non-intrusive polynomial chaos [6], co-kriging [7] and RBF [8]. In SBDO based on CFD computations, high- and low-fidelity evaluations may be obtained by varying the physical model, the size of the computational grid, and/or combining experimental data with numerical simulations [9]. Most MF approaches generally use two fidelity levels.

The objective of the present work is to formulate and assess an N -fidelity (NF) metamodel for design and operational-uncertainty space exploration of complex industrial problems.

The NF metamodel is developed as an extension of the authors' previous work [10]. The methodology is tested on a 1-D analytical problem and then applied to: (i) the shape optimization of a NACA hydrofoil and (ii) the uncertainty quantification of a roll-on/roll-off passengers (RoPax) ferry. CFD computations are based on two unsteady Reynolds averaged Navier-Stokes equations (RANSE) solvers: (1) ISIS-CFD [11], developed at Ecole Centrale de Nantes/CNRS and integrated in the FINE/Marine simulation suite from NUMECA Int, for the SBDO problem; (2) χ navis [12], developed at CNR-INM, for the UQ problem. In ISIS-CFD, mesh deformation and adaptive grid refinement techniques are adopted to allow the automatic shape deformation of the hydrofoil. The fidelity levels are defined by the grid refinement ratio. In χ navis, different fidelities are obtained using multi-grids.

2 N -FIDELITY METAMODEL

Consider $\mathbf{x} \in \mathbb{R}^D$ as the design and/or operational uncertainty vector of dimension D . Let the true function $f(\mathbf{x})$ be assessed by MF simulations: the highest-fidelity level is $f_1(\mathbf{x})$, the lowest-fidelity is $f_N(\mathbf{x})$, and arbitrary intermediate fidelity levels are $\{f_i\}_{i=2}^{N-1}(\mathbf{x})$. Let training sets be available for each level: $\{\mathcal{T}_i\}_{i=1}^N = \{\mathbf{x}_j, f_i(\mathbf{x}_j)\}_{j=1}^{J_i}$, with $\{J_i\}_{i=1}^N$ the training set size. Then an intra-level error $\varepsilon_i(\mathbf{x}) = f_i(\mathbf{x}) - f_{i+1}(\mathbf{x})$ can be defined with an associate training set $\mathcal{E}_i = \{\mathbf{x}, f_i(\mathbf{x}) - f_{i+1}(\mathbf{x}) \mid \mathbf{x} \in \mathcal{T}_i \cap \mathcal{T}_{i+1}\}$.

Using these sets, metamodels \hat{f}_N and $\{\tilde{\varepsilon}_i\}_{i=1}^{N-1}$ are trained, where “ \sim ” denotes metamodel prediction based on a stochastic ensemble of radial basis functions, which also provides the

prediction uncertainty U . Assuming the uncertainty associated to the prediction of the lowest-fidelity $U_{\tilde{f}_N}$ and intra-level errors $U_{\tilde{\varepsilon}_i}$ as uncorrelated, the NF approximation $\hat{f}(\mathbf{x})$ of $f(\mathbf{x})$ and its uncertainty $U_{\hat{f}}$ reads

$$\hat{f}(\mathbf{x}) = \tilde{f}_N(\mathbf{x}) + \sum_{i=1}^{N-1} \tilde{\varepsilon}_i(\mathbf{x}) \quad \text{and} \quad U_{\hat{f}}(\mathbf{x}) = \sqrt{U_{\tilde{f}_N}^2(\mathbf{x}) + \sum_{i=1}^{N-1} U_{\tilde{\varepsilon}_i}^2(\mathbf{x})} \quad (1)$$

The contribution of each fidelity level to $U_{\hat{f}}$ is assessed and used to refine adaptively the training sets as the sampling of the design/operational space progresses.

2.1 Adaptive sampling method

The NF metamodel is dynamically updated by iteratively adding a new training point following a two-step procedure (see Fig. 1): firstly, the coordinates of the new training point \mathbf{x}^* are identified based on the metamodel maximum uncertainty [10], solving the single-objective maximization problem:

$$\mathbf{x}^* = \underset{\mathbf{x}}{\operatorname{argmax}} [U_{\hat{f}}(\mathbf{x})]. \quad (2)$$

secondly, once \mathbf{x}^* is identified, either \mathcal{T}_N or all the training sets from \mathcal{T}_k to \mathcal{T}_{k+1} are refined according to Eq. 3. Defining $\beta_i = c_{i+1}/c_i$, $i = 1, \dots, N-1$, where c_i is the computational cost associated to the i -th level, $\mathbf{U} \equiv \{\beta_1 U_{\tilde{\varepsilon}_1}, \dots, \beta_{N-1} U_{\tilde{\varepsilon}_{N-1}}, U_{\tilde{f}_N}\}$ as the metamodel uncertainty vector, and $k = \max\operatorname{loc}(\mathbf{U})$:

$$\begin{cases} \text{If } k = N & \text{add } \{\mathbf{x}^*, f_N(\mathbf{x}^*)\} \text{ to } \mathcal{T}_N, \\ \text{else,} & \text{add } \{\mathbf{x}^*, f_i(\mathbf{x}^*)\} \text{ to } \mathcal{T}_i \text{ with } i = k, k+1 \end{cases} \quad (3)$$

In the first case, only the lowest-fidelity evaluation is performed, whereas two evaluations are required at the same \mathbf{x}^* in the second case.

2.2 Stochastic radial basis functions

The metamodel prediction $\tilde{f}(\mathbf{x})$ is computed as the expected value (EV) over a stochastic tuning parameter of the RBF metamodel, $\tau \sim \operatorname{unif}[1, 3]$:

$$\tilde{f}(\mathbf{x}) = \operatorname{EV} [g(\mathbf{x}, \tau)]_{\tau}, \quad \text{with} \quad g(\mathbf{x}, \tau) = \sum_{j=1}^J w_j \|\mathbf{x} - \mathbf{x}_j\|^{\tau}, \quad (4)$$

where w_j are unknown coefficients, $\|\cdot\|$ is the Euclidean norm. The coefficients w_j are determined enforcing exact interpolation at the training points $g(\mathbf{x}_j, \tau) = f(\mathbf{x}_j)$ by solving $\mathbf{A}\mathbf{w} = \mathbf{f}$, with $\mathbf{w} = \{w_j\}$, $a_{lj} = \|\mathbf{x}_l - \mathbf{x}_j\|^{\tau}$ and $\mathbf{f} = \{f(\mathbf{x}_j)\}$.

The uncertainty $U_{\tilde{f}}(\mathbf{x})$ associated with the stochastic RBF metamodel prediction is quantified by the 95%-confidence interval of $g(\mathbf{x}, \tau)$, evaluated using a Monte Carlo sampling over τ [3].

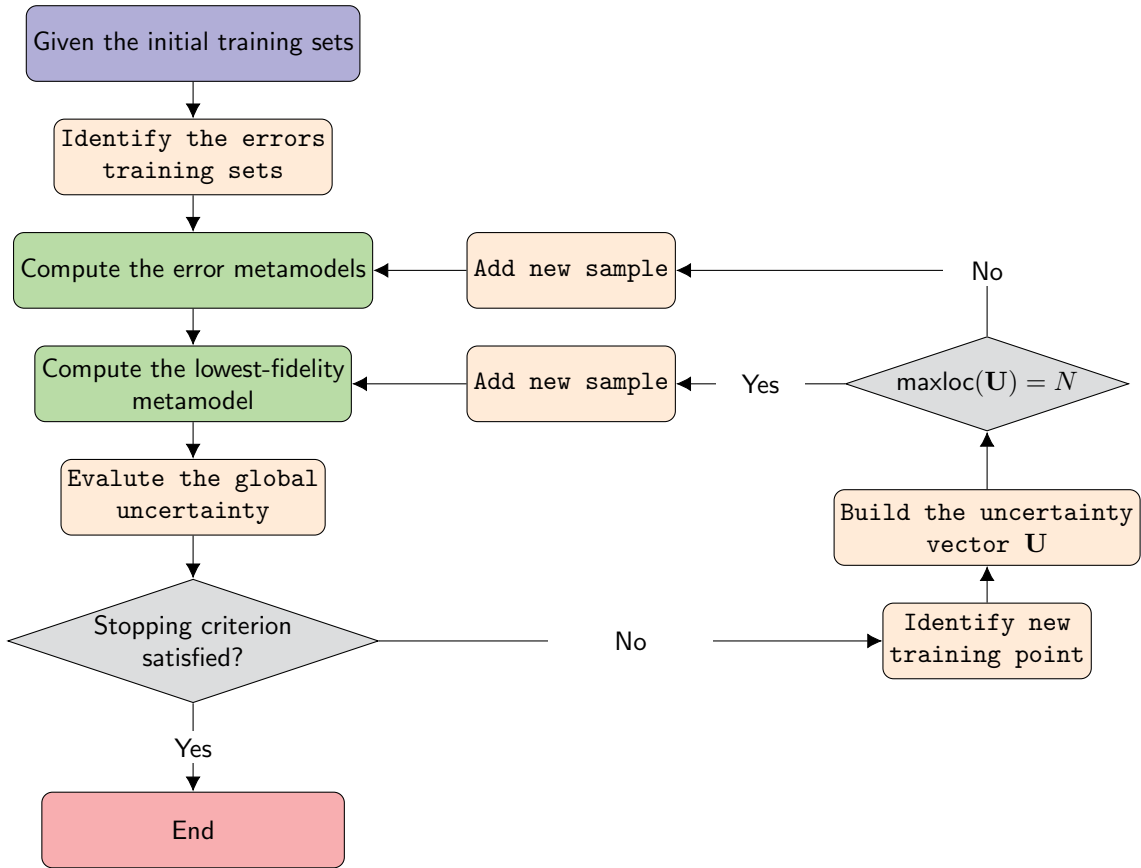


Figure 1: N -fidelity adaptive sampling procedure.

3 ANALYTICAL TEST

One analytical test problem is selected to assess the adaptive NF metamodel performance. It is mono-dimensional and multi-modal. Figure 2a shows the highest-fidelity level (f_1), whereas Figs. 2b and c show, respectively, the same analytical function along with one (f_2) and two ($f_{2,3}$) lower-fidelities and the corresponding errors ($\varepsilon_{1,2}$). The analytical test is defined in Tab. 1.

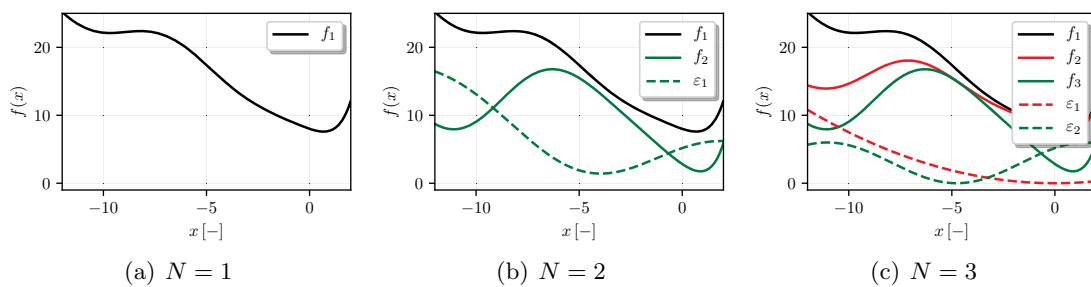


Figure 2: Analytical test problem with different number of fidelities N .

Table 1: Analytical test problem.

| N | Problem | | Domain |
|-----|--------------------|---|------------|
| 1 | $f_1(x)$ | $= -0.5x(\sin(0.25x) \cos(0.5x) + 1 - e^x + 2.0) + 8$ | $[-12, 2]$ |
| 2 | $f_1(x)$ | $= -0.5x(\sin(0.25x) \cos(0.5x) + 1 - e^x + 2.0) + 8$ | $[-12, 2]$ |
| | $f_2(x)$ | $= f_1(x) - \varepsilon_1(x)$ | |
| | $\varepsilon_1(x)$ | $= 0.075(x)^2 + 3 \cos(0.5x - 0.76) + 3$ | |
| 3 | $f_1(x)$ | $= -0.5x(\sin(0.25x) \cos(0.5x) + 1 - e^x + 2.0) + 8$ | $[-12, 2]$ |
| | $f_2(x)$ | $= f_1(x) - \varepsilon_1(x)$ | |
| | $f_3(x)$ | $= f_2(x) - \varepsilon_2(x)$ | |
| | $\varepsilon_1(x)$ | $= 0.075x^2$ | |
| | $\varepsilon_2(x)$ | $= 3 \cos(0.5x - 0.76) + 3$ | |

4 NACA HYDROFOIL SHAPE OPTIMIZATION PROBLEM

This problem addresses the drag minimization of a NACA four-digit airfoil. The following minimization problem is solved

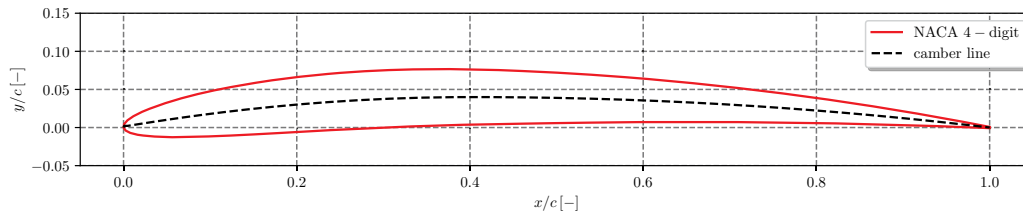
$$\begin{aligned}
 & \text{minimize} && C_D(\mathbf{x}) \\
 & \text{subject to} && C_L(\mathbf{x}) = 0.6 \\
 & \text{and to} && \mathbf{l} \leq \mathbf{x} \leq \mathbf{u}
 \end{aligned} \tag{5}$$

where \mathbf{x} is the design variable vector, C_D and C_L are respectively the drag and lift coefficient, and \mathbf{l} and \mathbf{u} are the lower and upper bound of \mathbf{x} . The equality constraint on the lift coefficient is necessary in order to compare different geometries at the same lift force (typically equal to the weight of the object), since the drag depends strongly on the lift.

The hydrofoil shape (see Fig. 3) is defined by the general equation for four-digit NACA foils. The upper (y_u) and lower (y_l) hydrofoil surfaces are computed as

$$\begin{cases} \xi_u = \xi - y_t \sin \theta \\ \xi_l = \xi + y_t \sin \theta \\ y_u = y_c + y_t \cos \theta \\ y_l = y_c - y_t \cos \theta \end{cases} \quad \text{with} \quad y_c = \begin{cases} \frac{m}{p^2} \left[2p \frac{\xi}{c} - \left(\frac{\xi}{c} \right)^2 \right], & 0 \leq \xi < pc \\ \frac{m}{(1-p)^2} \left[(1-2p) + 2p \frac{\xi}{c} - \left(\frac{\xi}{c} \right)^2 \right], & pc \leq \xi \leq c \end{cases} \tag{6}$$

where ξ is the position along the chord, c the chord length, y_c the mean camber line, p the location of the maximum camber, m the maximum camber value, and y_t the half thickness


Figure 3: NACA 4-digit hydrofoil.

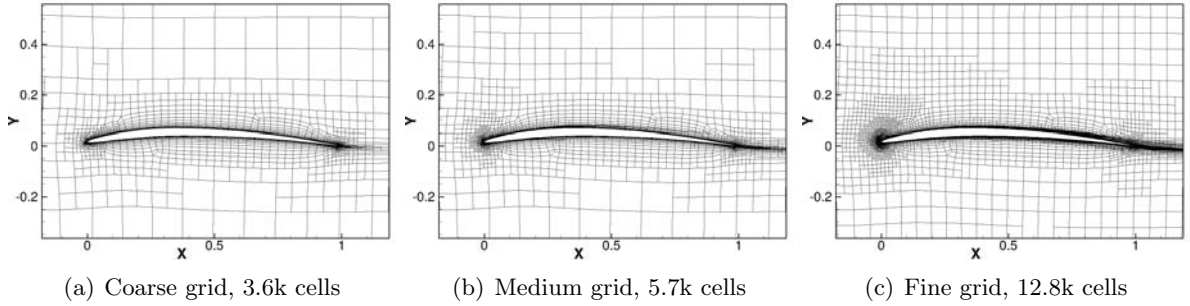


Figure 4: NACA hydrofoil computational grids.

given by

$$y_t = 5t \left(0.2969\sqrt{\xi} - 0.1260\xi - 0.3516\xi^2 + 0.2843\xi^3 - 0.1015\xi^4 \right) \quad (7)$$

In this work, the design variables vector is defined as $\mathbf{x} = \{t, m\}$ with $t \in [0.030, 0.120]$ and $m \in [0.025, 0.065]$. The maximum camber position is fixed at $p = 0.4$. The simulation conditions are: velocity $U = 10$ m/s, chord $c = 1$ m, fluid density $\rho = 1,026$ kg/m³, and Reynolds number $Re = 8.41 \cdot 10^6$.

CFD simulations are performed with the unstructured finite-volume RANSE solver ISIS-CFD developed at ECN – CNRS [11], available in the FINETM/Marine computing suite from NUMECA Int. Computational grids are created through adaptive grid refinement [13, 14] to take into account the need for high and low fidelity. The simulation strategy in the context of metamodel creation is explained by [10]. The adaptive grid refinement method adjusts the computational grid locally, during the computation, by dividing the cells of an original coarse grid, to improve the precision. The decision where to refine comes from a refinement criterion, a tensor field $\mathcal{C}(x, y, z)$ computed from the flow. The tensor is based on the water surface position and on second derivatives of pressure and velocity. The mesh is refined until the dimensions $\mathbf{d}_{p,j}$ ($j = 1, 2, 3$) of each hexahedral cell p satisfy

$$\|\mathcal{C}_p \mathbf{d}_{p,j}\| = T_r \quad (8)$$

The refinement criterion based on the second derivatives of the flow is not very sensitive to grid refinement [14], so the cell sizes everywhere are proportional to the constant threshold T_r .

For NF optimization, the interest of this procedure is that different fidelity results can be obtained by running the same simulations with different thresholds T_r . Herein, three fidelity are used. The initial computational grid has 2,654 cells, the refinement threshold value T_r is set equal to 0.1, 0.2, and 0.4 from highest- to lowest-fidelity. The actual computational grids have 12.8, 5.7, and 3.7k cells, respectively (see Fig. 4). Highest- to lowest-fidelity simulations require about 17, 9, and 5 minutes, respectively, of wall-clock time to converge. The resulting computational cost ratios are about $\beta_1 = 0.5$ and $\beta_2 = 0.3$.

The domain runs from $11c$ in front of the leading edge to $16c$ behind the hydrofoil and from $-10c$ to $10c$ vertically. Dirichlet conditions on the velocity are imposed, except on the outflow side which has an imposed pressure condition. The hydrofoil surface is treated with a wall law and $y^+ = 60$ for the first layer. Turbulence is modeled with the standard $k - \omega$ SST model.

To maintain a constant lift (see Eq. 5), the angle of incidence α for the hydrofoil is adjusted dynamically during the simulations.

The budget is defined in terms of normalized computational cost and is equal to 22. The initial training set for the problem is a set of $2N + 1$ points including the domain center and min/max coordinates for each variable. All fidelities are sampled in these points.

5 ROPAX UNCERTAINTY QUANTIFICATION PROBLEM

This problem addresses the UQ of a RoPax ferry in terms of estimation of expected value (EV) and standard deviation (SD) of the (model-scale) resistance (R_T), subject to operational uncertainty. Specifically, the uncertain parameter is the Froude number with a uniform probability density function from 0.25 to 0.35. The RoPax ferry is characterized by: length between perpendicular $L_{PP} = 162.85$ m, displacement (DWT) of 5,000 t, block coefficient $C_B = 0.5677$. The analysis is performed with a scale factor $\lambda = 27.14$. The parametric geometry of the RoPax is produced with the computer-aided design (CAD) environment integrated in the CAESSES[®] software, developed by FRIENDSHIP SYSTEMS AG, and made available in the framework of the H2020 EU Project Holiship.

The hydrodynamics performance of the RoPax is assessed by the unsteady RANSE code χ navis developed at CNR-INM. It is based on finite volume scheme, with variable co-located at cell centers. Turbulent stresses are taken into account by the Boussinesq hypothesis, with Spallart-Almaras turbulence model. Free-surface effects are taken into account by a single-phase level-set algorithm. Wall-functions are not adopted, therefore $y^+ = 1$ is ensured on the wall. On solid walls, the velocity is set equal to zero and zero normal gradient is enforced on the pressure field; at the (fictitious) inflow boundary, velocity is set to the undisturbed flow value and the pressure is extrapolated from the inside; the dynamic pressure is set to zero at the outflow, whereas the velocity is extrapolated from inner points. On the top boundary, which remains always in the air region, fluid dynamic quantities are extrapolated from inside. Chimera overlapping grid capabilities are used, the numerical solutions are computed by means of a full multi grid–full approximation scheme (FMG–FAS), with four grid levels (from coarser to finer: G4, G3, G2, and G1), each obtained from the next finer grid with a refinement ratio equal to 2, resulting in $\beta_1 = 0.125$ and $\beta_2 = 0.0625$. In the FMG–FAS approximation procedure, the

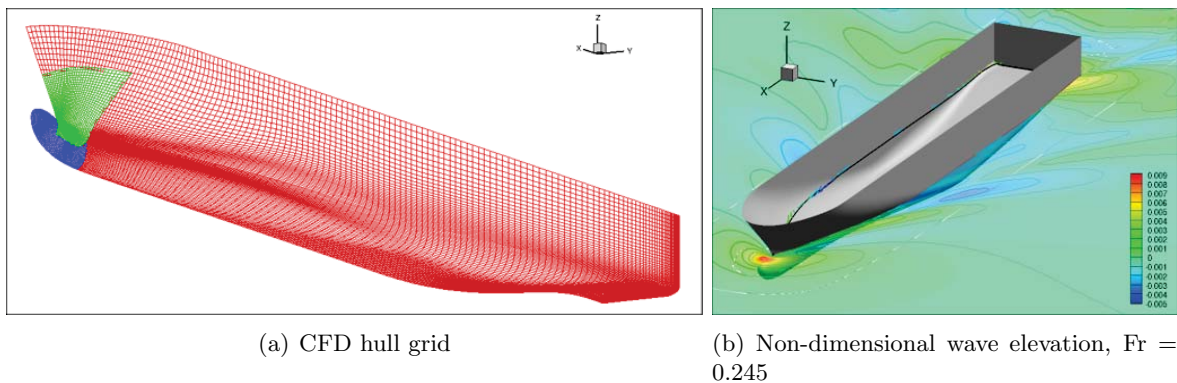


Figure 5: RoPax ferry.

solution is computed on the coarsest grid level first. Secondly, it is approximated on the next finer grid and the solution is iterated by exploiting all the coarser grid levels available with a V-Cycle. The process is repeated up to the finest grid level. For the present UQ problem G1, G2, and G3 grids are used. Simulations are performed considering a water density $\rho = 998.2 \text{ kg/m}^3$, cinematic viscosity $\nu = 1.105\text{E-}6 \text{ m}^2/\text{s}$, gravitational acceleration $g = 9.81 \text{ m/s}$. The grid is composed by 53 blocks, for a total of 4.88 M cells, see Fig. 5; the domain extends to $2L_{PP}$ in front of the hull, $3L_{PP}$ behind, and $1.5L_{PP}$ each side; a depth of $2L_{PP}$ is imposed.

6 NUMERICAL RESULTS

The normalized computational cost is defined as 1 for each f_1 evaluation and β_i , $i = 1, \dots, N-1$ for each f_{i+1} evaluation. It is worth noting that, the normalized computational cost for the CFD problems is defined, considering only the cost of the highest-fidelity level sampled. This is due to the fact that, adaptive grid refinement and FMG-FAS compute the solution at grid level k using solutions from grid level N to k .

The DPSO algorithm presented in [15] is used for the solution of Eqs. 2 and 5.

6.1 Analytical test problem

The performance of the adaptive NF metamodel is assessed in terms of convergence of the normalized root mean square error (NRMSE), the objective function minimum, and the number of highest-fidelity evaluations, as shown in Fig.6.

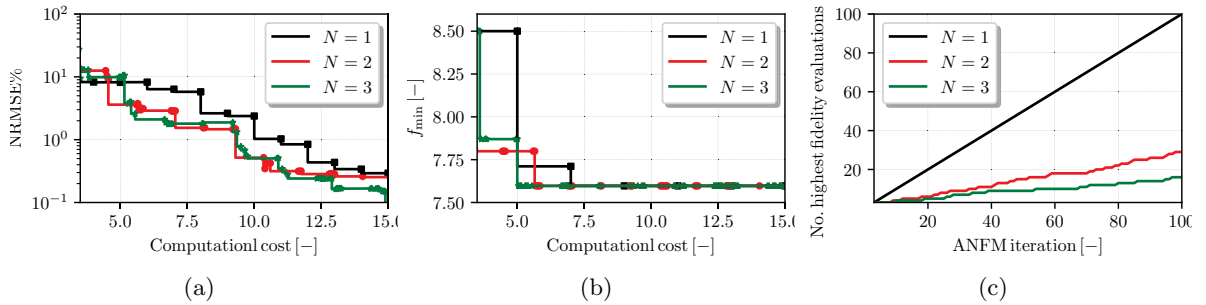


Figure 6: Analytical test problem: convergences of (a) NRMSE, (b) objective function minimum, and (c) the number of the highest-fidelity evaluations versus the sampling procedure iterations.

It is worth noting that for $N = 3$ the NRMSE decreases faster than for $N = 2$ and $N = 1$, achieving an $\text{NRMSE} = 0.01\%$ with the lowest computational cost (see Fig.6a). Similarly, for $N = 3$ the minimum of the objective function is achieved with the lowest computational cost (see Fig. 6b). Finally, Fig. 6c shows the number of highest-fidelity evaluations versus the sampling iteration number. It is worth noting that adding intermediate-fidelity levels decreases the need for highest-fidelity samples.

6.2 NACA hydrofoil shape optimization

Figure 7 shows the training sets at the last iteration of the MF metamodel training for $N = 1$, 2, and 3. For $N = 1$ the training points are evenly distributed. For $N = 2$ the low-fidelity

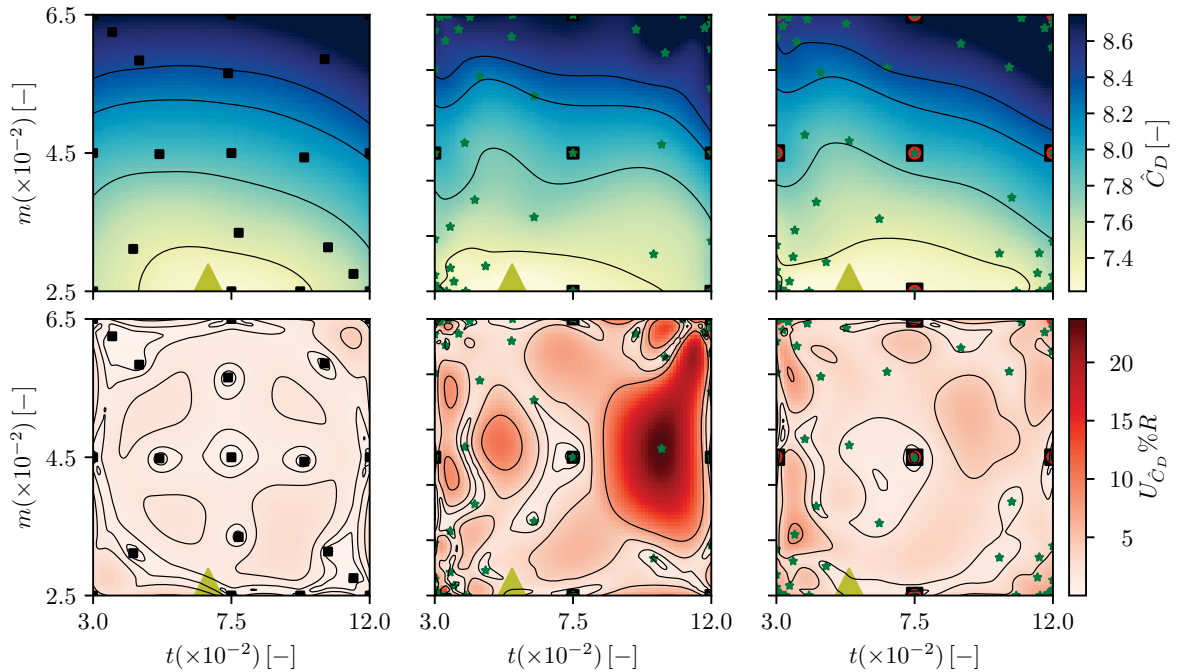


Figure 7: NACA hydrofoil: N -fidelity metamodel prediction and associated uncertainty, with $N = 1, 2$, and 3 from left to right. Black squares, red circles, and green stars are the $i = 1, 2$, and 3 fidelity training sets. Yellow triangles is the minimum position.

evaluations are clustered in three corners. Furthermore, in the latter case the uncertainty of the prediction is significantly higher than for the $N = 1$ case, suggesting the presence of numerical noise. Finally, for $N = 3$ the contour plot of the drag coefficient and the uncertainty look smoother than for $N = 2$. This suggests a regularization effect stemming from the use of a mid-level fidelity. At each iteration the predicted minimum is verified through an highest-fidelity simulation. Fig. 8 shows the convergence of the verified objective function. It is worth noting that the NF metamodel converges faster for both $N = 2$ and 3 . Table 2 summarizes, the training sets size, the normalized cost, the maximum uncertainty of the prediction, the coordinates of the predicted minimum of the C_D , the predicted minimum, its verification, the prediction error, and the improvement with respect to the original configuration. It is worth noting that for

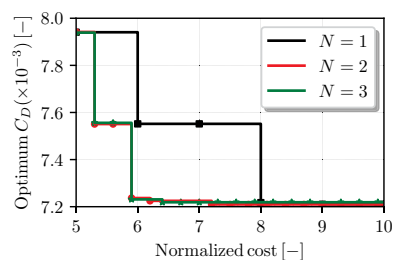


Figure 8: NACA hydrofoil: verified optimum convergence versus the normalized computational cost.

Table 2: Summary of the adaptive NF metamodel performance on the NACA hydrofoil SBDO problem.

| N | $ \mathcal{T}_1 $ | $ \mathcal{T}_2 $ | $ \mathcal{T}_3 $ | Normalized | | minimum position | | minimum value | | | $\Delta C_D\%$ |
|-----|-------------------|-------------------|-------------------|------------|-----------------------|------------------|----------|----------------|----------|-----|----------------|
| | | | | cost | $\max(U_{\hat{f}})\%$ | $t[-]$ | $m[-]$ | $\hat{C}_D[-]$ | $C_D[-]$ | E% | |
| 1 | 22 | | | 22.0 | 3.70 | 6.743E-2 | 0.000E-2 | 7.209E-3 | 7.206E-3 | 0.1 | 9.23 |
| 2 | 8 | | 46 | 21.8 | 23.7 | 5.515E-2 | 0.000E-2 | 7.064E-3 | 7.209E-3 | 2.0 | 9.19 |
| 3 | 5 | 9 | 55 | 20.8 | 8.78 | 5.367E-2 | 0.000E-2 | 7.094E-3 | 7.219E-3 | 1.7 | 9.07 |

$N = 3$ the number of highest-fidelity evaluations decreases compared to $N = 1$ and 2. Similar improvements are achieved using $N = 1, 2,$ and 3.

6.3 RoPax uncertainty quantification

The NF metamodel for UQ is assessed through statistical estimation of the expected value (EV) and standard deviation (SD) of the total resistance, R_T . The training of the NF metamodel is performed considering at most 4 high-fidelity evaluations. The results are compared to the available highest-fidelity CFD data. Figure 9 shows the MF prediction of the total resistance versus the Froude number, with $N = 1, 2,$ and 3. It is worth noting that the increase of N improves the MF prediction. Table 3 summarizes the training sets size, the expected value, standard deviation, and associate errors (E) for $N = 1, 2,$ and 3. It is worth noting that the MF metamodel with $N = 3$ achieves better results than using $N = 1$ and 2. Furthermore, for $N = 3$ only three evaluations of the highest-fidelity are performed.

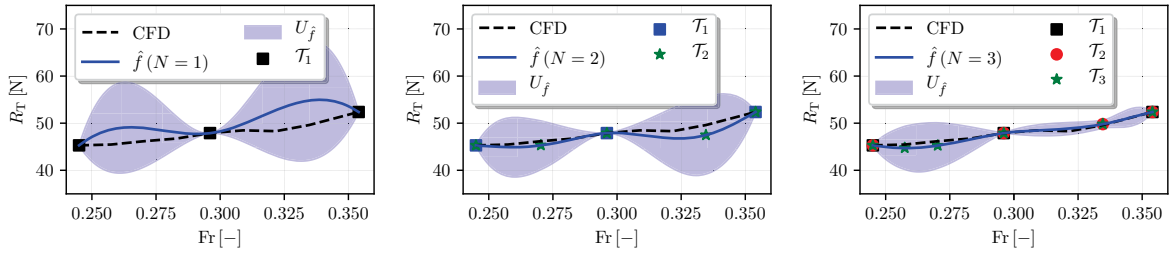

Figure 9: RoPax ferry: model-scale total resistance versus operational uncertainty (Froude number). $N = 1, 2,$ and 3 fidelity metamodels.

Table 3: Summary of the adaptive NF metamodel performance on the RoPax UQ problem.

| N | $ \mathcal{T}_1 $ | $ \mathcal{T}_2 $ | $ \mathcal{T}_3 $ | Normalized cost | EV | E(EV)% | SD | E(SD)% |
|-----------|-------------------|-------------------|-------------------|-----------------|---------|---------|--------|----------|
| 1 | 4 | | | 4.0000 | 48.7053 | 1.8649 | 1.3904 | -38.1179 |
| 2 | 4 | | 5 | 4.2500 | 47.7304 | -0.1739 | 2.1106 | -6.0643 |
| 3 | 3 | 4 | 6 | 3.8125 | 47.7411 | -0.1514 | 2.1953 | -2.2977 |
| Reference | 9 | | | 9 | 47.8136 | - | 2.2469 | - |

7 CONCLUSIONS AND FUTURE WORK

The extension of a two-fidelity metamodel [8] to N -fidelity has been presented for the reduction of the computational cost in solving complex problems by numerical simulations. The method has been tested for an analytical test problem, the simulation-based shape-optimization of a NACA hydrofoil, and the operational-uncertainty quantification of the total resistance of a RoPax ferry at variable advancing speed. The methodology has demonstrated its effectiveness in reducing the computational cost in the problems proposed. For the analytical test problem, the NF method with $N = 3$ has achieved a greater reduction of the highest-fidelity evaluations than with $N = 2$. For the NACA shape-optimization, the NF method with $N = 3$ has achieved comparable solutions to a single-fidelity metamodel, at reduced computational cost. For the operational-uncertainty quantification, the NF method with $N = 3$ has achieved better results than with $N = 1$ and 2, at reduced computational cost. The NACA shape-optimization is likely affected by non-negligible numerical noise for the coarser grids. Therefore, future work will address the presence of numerical noise [16].

ACKNOWLEDGMENTS

CNR-INM is grateful to Dr. Salahuddin Ahmed and Dr. Woei-Min Lin of the Office of Naval Research, for their support through NICOP grant N62909-18-1-2033, and to the Italian Ministry of Education for its support through the Italian Flagship Project RITMARE. The HOLISHIP project (*HOLIstic optimisation of SHIP design and operation for life cycle*, www.holiship.eu) is also acknowledged, funded by the European Union's Horizon 2020 research and innovation programme under grant agreement N. 689074.

REFERENCES

- [1] Viana, F. A. C., Simpson, T. W., Balabanov, V. and Vasilli, T. Special section on multidisciplinary design optimization: Metamodeling in multidisciplinary design optimization: How far have we really come?, *AIAA Journal*, **52** (4), 670–690, (2014).
- [2] Jin, R., Chen, W. and Simpson, T. W. Comparative studies of metamodelling techniques under multiple modelling criteria, *Structural and Multidisciplinary Optimization*, **23** (1), 1–13, (2001).
- [3] Volpi, S., Diez, M., Gaul, N. J., Song, H., Iemma, U., Choi, K. K., Campana, E. F. and Stern, F. Development and validation of a dynamic metamodel based on stochastic radial basis functions and uncertainty quantification, *Structural and Multidisciplinary Optimization*, **51** (2), 347–368, (2015).
- [4] Jones, D. R., Schonlau, M. and Welch, W. J. Efficient global optimization of expensive black-box functions, *Journal of Global Optimization*, **13** (4), 455–492, (1998).
- [5] Diez, M., Volpi, S., Serani, A., Stern, F. and Campana, E. F., (2019), *Simulation-Based Design Optimization by Sequential Multi-criterion Adaptive Sampling and Dynamic Radial Basis Functions*, pp. 213–228. Springer International Publishing.

- [6] Ng, L. W.-T. and Eldred, M. Multifidelity uncertainty quantification using non-intrusive polynomial chaos and stochastic collocation, *53rd AIAA/ASME/ASCE/AHS/ASC Structures, Structural Dynamics and Materials Conference, Structures, Structural Dynamics, and Materials and Co-located Conferences*, (2012).
- [7] Baar, J. d., Roberts, S., Dwight, R. and Mallol, B. Uncertainty quantification for a sailing yacht hull, using multi-fidelity kriging, *Computers & Fluids*, **123**, 185 – 201, (2015).
- [8] Pellegrini, R., Iemma, U., Leotardi, C., Campana, E. F. and Diez, M. Multi-fidelity adaptive global metamodel of expensive computer simulations, *2016 IEEE Congress on Evolutionary Computation (CEC)*, July, pp. 4444–4451, (2016).
- [9] Kuya, Y., Takeda, K., Zhang, X. and Forrester, A. I. J. Multifidelity surrogate modeling of experimental and computational aerodynamic data sets, *AIAA Journal*, **49** (2), 289–298, (2011).
- [10] Pellegrini, R., Serani, A., Diez, M., Wackers, J., Queutey, P. and Visonneau, M. Adaptive sampling criteria for multi-fidelity metamodels in CFD-based shape optimization, *7th European Conference on Computational Fluid Dynamics (ECFD 7)*, Glasgow, UK, 11-15 June, (2018).
- [11] Queutey, P. and Visonneau, M. An interface capturing method for free-surface hydrodynamic flows, *Computers & Fluids*, **36** (9), 1481–1510, (2007).
- [12] Broglia, R. and Durante, D. Accurate prediction of complex free surface flow around a high speed craft using a single-phase level set method, *Computational Mechanics*, **62** (3), 421–437, (2018).
- [13] Wackers, J., Deng, G., Guilmineau, E., Leroyer, A., Queutey, P. and Visonneau, M. Combined refinement criteria for anisotropic grid refinement in free-surface flow simulation, *Computers and Fluids*, **92**, 209 – 222, (2014).
- [14] Wackers, J., Deng, G., Guilmineau, E., Leroyer, A., Queutey, P., Visonneau, M., Palmieri, A. and Liverani, A. Can adaptive grid refinement produce grid-independent solutions for incompressible flows?, *Journal of Computational Physics*, **344**, 364 – 380, (2017).
- [15] Serani, A., Leotardi, C., Iemma, U., Campana, E. F., Fasano, G. and Diez, M. Parameter selection in synchronous and asynchronous deterministic particle swarm optimization for ship hydrodynamics problems, *Applied Soft Computing*, **49**, 313 – 334, (2016).
- [16] Wackers, J., Pellegrini, R., Serani, A., Diez, M. and Visonneau, M. Adaptive multifidelity shape optimization based on noisy cfd data, *To be presented at 2019 International Conference on Adaptive Modeling and Simulation (ADMOS 2019)*, El Campello (Alicante), Spain, 27-29 May.

AN ASSESSMENT OF MULTIFIDELITY PROCEDURES FOR SHIP HULL FORM OPTIMISATION

H.C. RAVEN, T.P. SCHOLCZ

Maritime Research Institute Netherlands (MARIN)
P.O. Box 28, 6700 AA Wageningen, Netherlands
e-mail: h.c.raven@marin.nl

Keywords: Ship design, optimisation, multifidelity

Summary: *Progress in the assessment of multifidelity techniques for ship hull form optimisation at MARIN is described. Surrogate-based optimisation is used, with response surfaces found from a combination of free-surface potential-flow and free-surface RANS computations. A substantial level of correspondence of the trends of the low and high-fidelity methods appears to be required. Applications of multifidelity stern design optimisation for a fast displacement ship and a containership are reviewed. Alternative low-fidelity formulations are considered.*

1 INTRODUCTION

Today's computational tools offer great possibilities for improving a ship's hull form design. At MARIN, RANS methods are frequently used in practical ship design projects since about the year 2000. The design steps were usually based on experience and physical insight, and then checked by computations. This is an effective procedure which is still used, but it is more and more often supplemented by a formal optimisation stage. Optimisation approaches have been introduced that fit in with this procedure, in that the setup of the design space is done based on the same experience and insight, but the optimiser permits a wider exploration and a fine-tuning of the design.

A significant part of the process to minimise the still-water resistance, for forebody wave making in particular, is normally done using a free-surface potential-flow code. The optimisation procedure used [1] is a surrogate-based method, in which the optimiser, typically a genetic algorithm, acts on a response surface found from an initial set of computations. The method is quite effective and fast, and frequently permits significant resistance reductions in just a few days work. However, for ship afterbody design a potential-flow solver is often insufficient, and free-surface RANS codes are used. But because of their computational effort and the limited time available in practical projects, normally the number of parameters varied is small, and the feeling remains that larger resistance gains would be possible.

To alleviate the computational burden of RANS-based ship afterbody optimisation, we consider multifidelity optimisation techniques. By combining a cheap low-fidelity (LF) method and a more expensive high-fidelity (HF) method (in our case, a free-surface RANS code), we hope to achieve efficiency improvements. As a LF method we have mainly used the free-surface potential flow code. Besides its large computational efficiency, this choice has additional benefits. The RANS computations just give frictional and pressure resistance, and

may not clearly indicate the origin of resistance changes. By the parallel work with a potential-flow code, we get useful additional insight in the viscous and wave resistance components and their trends. However, for stern shape optimisation we clearly have to investigate the limits of the use of the potential-flow code as a LF method; and some alternative choices are considered in this paper.

After summarising the tools used, in Section 3 we briefly recall the multifidelity formulation, in particular cokriging, and show that a considerable degree of correspondence of low and high-fidelity results is generally required to benefit from the multifidelity approach. Section 4 reviews some experiences with multifidelity methods for resistance minimisation. We briefly summarise the case from [2], stern design of a fast displacement ship, for which a substantial gain in computational efficiency was obtained. Another case is described here, for a large container ship, which turned out quite differently. Some alternative choices for LF methods are addressed in Section 5.

The research is in progress and additional results will be presented at the symposium.

2 CONTEXT AND TOOLS USED

2.1 Hull form variation

A first essential component is the shape parametrisation. As described in [1], we use a design space defined by parametric deformations of an initial hull form. Specific for the case at hand, we choose design changes considered promising, based on analysis of computations for the initial hull form. We aim at selecting independent deformation modes that are clearly related with the flow features we want to improve. In this way, we normally have a fairly small number of hull form parameters to be varied, most of them hydrodynamically relevant for the design problem. Compared with this, choosing design parameters based on just geometric properties usually leads to a much larger number of parameters.

For each deformation mode, the most deformed hull form is created in the CAD system. The hull form variations are then obtained as a parametric blending of the initial hull form and all of these deformed ones. This blending is generated in the Rhino CAD system, using proprietary plug-ins based on earlier developments [3].

2.2 Surrogate-based optimisation

For the actual optimisation we use primarily the DAKOTA optimisation toolbox [4], which offers a variety of options for response surface generation, optimisation and sensitivity analysis. Once the design space is defined, we generate a set of points spread over that space, using Design of Experiments methods. Usually we choose a Latin Hypercube Sampling, except for small dimensions of the design space. For each point, i.e. each hull form variation defined by the parameters, we run the flow code for all the conditions (e.g. speeds, drafts) to be considered. We feed the results to the Surrogate-Based Global Optimisation algorithm, which for each flow condition generates a response surface based on the computed results; and performs a global optimisation using a genetic algorithm, acting on the response surfaces only. This is a very quick process, normally less than an minute. When conflicting design objectives are present, the multiobjective optimisation problem results in an estimated Pareto front. A selection of points on the front is again evaluated using the flow code to obtain the

true results. If needed, response surfaces can then be updated using the new data points, and the optimisation repeated. The approach, used routinely now in combination with the potential-flow solver, is most effective; in particular as the choice of design parameters that we make often leads to well-defined response surfaces.

2.3 Free-surface potential-flow code

The potential-flow code used is RAPID [5], a panel code that iteratively solves the steady nonlinear free-surface flow problem. The complete inviscid free-surface conditions are imposed, and the dynamic trim and sinkage are incorporated. The computation time is just a few minutes on a desktop PC. Validations have shown that the wave pattern calculated is quite accurate, except for stern waves: those are usually overestimated due to the neglect of viscous effects, the more so for fuller hull forms and lower Froude numbers. Also, for transom sterns only a dry-transom flow can be well modelled.

2.4 Free-surface RANS codes

Two different free-surface RANS codes have been used in the work so far. PARNASSOS [6] is a free-surface fitting code, working on a multiblock structured mesh that deforms to fit the free surface. The steady RANS equations are solved by a multiple-sweep marching iteration, solving the fully coupled momentum and continuity equations. Also the free surface is solved by iteration, using a particular formulation of the steady free-surface boundary conditions [7]. The code is most efficient, but may have occasional robustness issues. Also it is not suitable for large-scale parallelisation. In optimisation this is no large disadvantage though, as on a cluster many computations (e.g. the Design of Experiments) are done simultaneously.

REFRESCO [8,9] is an unstructured-mesh finite-volume code, using free-surface capturing by a volume-of-fluid formulation. The unsteady momentum and pressure equations are solved by a SIMPLE-type algorithm. It is far more general than PARNASSOS, and more robust, but also more time-consuming. In addition, the lower inherent accuracy of the unstructured-mesh discretisation asks for much denser grids. Therefore, if hundreds of computations would need to be done in a practical optimisation, the computational effort would be a disadvantage.

3 A TEST OF MULTIFIDELITY SURROGATES

Suppose we have a set of N_{LF} data points in the design space with results from a low-fidelity method; and for a part of these points, a smaller number N_{HF} , we also have results from a high-fidelity method. We want to exploit both sets to make the best approximation of the high-fidelity function F_{HF} over the design space.

We use a Cokriging formulation, see e.g. [10], defining

$$F_{HF}(\mathbf{par}) = \rho \cdot F_{LF}(\mathbf{par}) + \Delta F(\mathbf{par})$$

in which \mathbf{par} is the vector of parameter values. In the implementation used, first a Kriging approximation of the low-fidelity data set is made. Next, another Kriging approximation is made of the difference $\Delta F(\mathbf{par})$, along with determination of the scale factor ρ . The idea is that ΔF is a smaller quantity with a simpler distribution, therefore it should be better approximated by the limited data set of N_{HF} values ΔF .

Forrester et al [10] show some examples, among which a 1-parameter case:

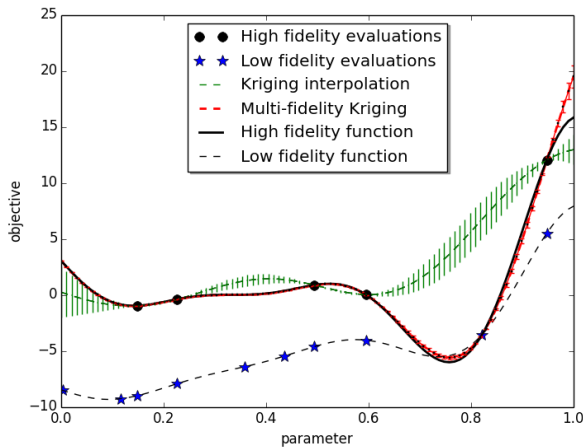


Figure 1 Forrester example, with LF and HF functions, data points, and approximations by Kriging and Cokriging.

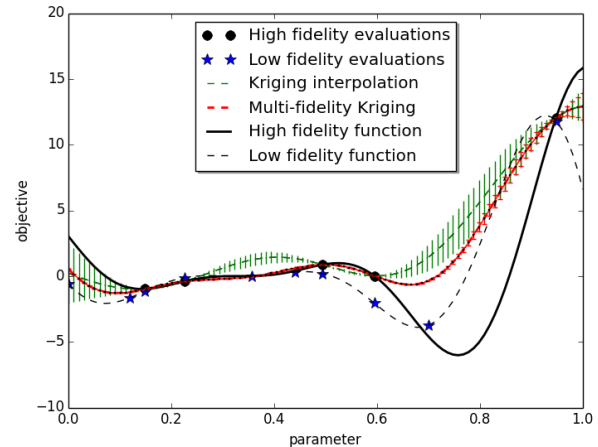


Figure 2 Same with modified LF function.

$$F_{HF} = (6x-2)^2 \sin(12x-4)$$

$$F_{LF} = 0.5 F_{HF} + 10(x-0.5), \text{ for } 0 < x < 1.$$

Fig. 1 shows there is a significant difference between these functions. Kriging on just the 5 HF points (green line with error bars) misses the minimum altogether. Still, with just 10 LF points added, cokriging approximates the high-fidelity function extremely well. The uncertainty implied by the Kriging approximations, shown as ‘error bars’, is also much reduced for cokriging. However, the actual error is 4-5 times larger than this uncertainty, both for Kriging and for Cokriging. We remark that this uncertainty is used in some ‘adaptive sampling’ procedures, in which points are added where maximum improvement is expected; and a better indication of the actual error would be desirable.

However, in this example, for $\rho=2$ it follows $\Delta F = -20x+10$, just a linear function of x without any Kriging approximation involved. We can even choose $-F_{LF}$ as the LF function, with trend completely opposite to F_{HF} , and the Cokriging approximation is still perfect. The example fits the Cokriging formulation nicely but is not general at all. As Forrester et al state, this example is ‘somewhat contrived’, nevertheless it is copied in several other papers, not always indicating its limited validity.

So for the same $F_{HF} = (6x-2)^2 \sin(12x-4)$ let us choose another LF function, $F_{LF} = (6x-2)^2 \sin(12x-3)$, which has a small shift of the minimum --- a most probable situation in practice. Fig. 2 shows that, notwithstanding its similar shape and values, the LF function hardly helps to construct an approximation of the HF function: Cokriging is just marginally better than simple Kriging on the 5 HF points. While the error is much larger than in Fig. 1, the uncertainty is not; therefore it is hardly indicative of the error, and of the location where the largest errors occur. Other small changes to the LF function can even make single-fidelity Kriging more accurate than Cokriging. The 1D example in [10] thus is not representative of what can be expected in case the LF function has its minimum slightly shifted or has other general deviations from the HF function.

This simple example illustrates that in general a significant degree of correspondence between HF and LF functions is needed, such that the difference function ΔF is simpler to model than the HF function itself [10]. Moreover, the relation of the indicated uncertainty and the actual

error is weak and variable; the error here being much larger.

4 MULTIFIDELITY OPTIMISATION COMBINING POTENTIAL FLOW AND RANS CODES

The multifidelity formulations that we have applied mostly used the free-surface potential flow code as the LF method. This method tends to overestimate the stern wave system, which in reality is reduced by viscous effects in a not easily predicted way, and to a different degree for different wave components. The resistance trends for stern variations as predicted by RAPID might thus be different from those from a RANS code, making this a critical test for a multifidelity formulation.

4.1 Stern optimisation for a fast displacement ship

We briefly summarise here the results for the test case from [2], optimisation of the stern of a fast displacement vessel, for $Fr = 0.27$ and 0.37 . We introduced 3 parameters: two stern buttock shape modifications, one parameter changing the deadrise at the stern.

For the LF method, a Design of Experiments of 150 hull forms was generated in this 3D parameter space. For each hull form, computations have been made for both speeds using RAPID. This DoE size surely is an overkill, but could be run overnight on a single PC nonetheless. Total resistance was estimated by adding $(1+k)$ times flat plate friction to the computed wave resistance. Next, an overlapping smaller DoE of 32 hull forms was evaluated by PARNASSOS, for both speeds.

The LF and HF resistance values appeared well correlated, the correlation lines having a

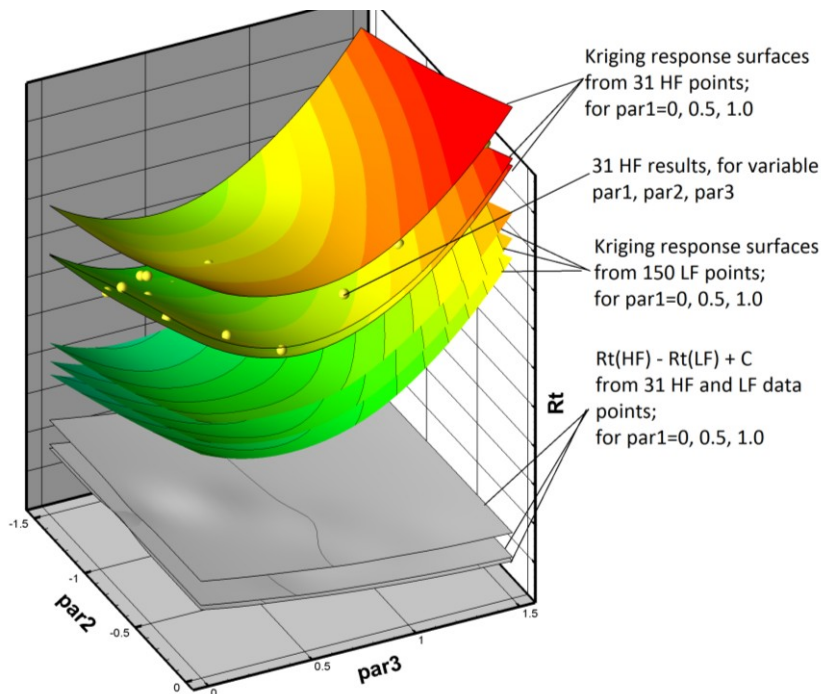


Figure 3 Response surfaces for fast displacement ship. Upper 3 surfaces are for HF method, middle 3 surfaces for LF, lower 3 surfaces show their difference (but increased by a constant to show in the same graph). Each plane is for a constant $par1$.

slope near 1.0. Fig. 3 illustrates that response surfaces, derived separately from the LF and HF computations, have essentially the same shape. Their difference $\Delta R_T(\mathbf{par})$, here assuming that $\rho = 1$, thus is a very simple function of the parameters, as shown in Fig. 3. Instead of using all 31 HF data, a much lower number would sufficiently define it. In [2], it has been checked that the response surfaces for the multifidelity formulations actually did not change much if just 7 HF data points were used in this 3D space; both from visual inspection and from the errors in a set of test points. Instead, a simple Kriging of only the HF data lost more of its accuracy at this reduction of the number of HF data. Subsequently, surrogate-based optimisation was done using these response surfaces; and here again, the multifidelity methods well indicated the optimal hull form even with just 7 HF data points.

In this way, the optimisation of an already refined design indicated some subtle stern shape modifications that reduced the total resistance by 2.6% and 3.6% at the two speeds. However, already the LF method indicated the optimum design and the achievable stern wave reduction very well. To really test the capabilities of MF optimisation, a more challenging case was taken up next.

4.2 Optimisation of a containership stern

The next test case in our search for the limit of multifidelity optimisation is a large containership, at $Fr = 0.20$. The somewhat larger block coefficient and the lower Froude number cause larger viscous effects on the wave making here. The potential flow code predicts a substantially stronger transverse stern wave component than the RANS code, while the diverging components are comparable.

Four parameters are defined for the stern shape modifications. Two of them introduce a slight S-shape to the stern buttock lines, long and short respectively. The 3rd parameter lifts the transom, while the 4th modifies the transom V-shape, decreasing and increasing stern deadrise. A Latin Hypercube Sampling of 240 hull forms is evaluated using RAPID as LF code, followed by surrogate-based global optimisation. The optimum hull form from just the LF method has maximum S-shape of the buttocks, minimum V-shape of the sections, promising 6.2% total resistance reduction owing to a significant reduction of the transverse stern wave (Fig. 8).

Next, a set of 40 hull forms is evaluated using the HF-code (PARNASSOS). Response surfaces are generated for both HF and LF data, and one view is shown in Fig.4. Clearly, they are very different, those from LF having a clear and strong trend and simple shape, those from HF substantially more convoluted. Fig.5 shows the degree of correlation of LF and HF resistance values; a cloud of points without much direction, but showing 8% of variation from LF, 2 % from HF. It seems doubtful whether multifidelity will work in this case.

Upon a detailed inspection of the computed flow fields, the transom flow regime, wetted or dry, is found to play an important role here. The stern variations are such that it is not clear a priori what type of transom flow will be obtained, until it is found from the RANS solutions. In the LF method however, a dry-transom flow was enforced in all cases, since a wetted transom flow cannot be properly modelled by a potential flow. If now we distinguish both transom flow regimes in Fig. 5, we note that the dry-transom results do display some correlation with the LF results: low resistance in RAPID usually means low resistance in PARNASSOS, although the variations are smaller: for these cases we are actually reducing

transverse stern waves, but as these are smaller due to viscous effects, the trend is weakened. For the wetted transom flow cases though, RAPID assumes a dry transom and predicts a high resistance for most, but some have actually a low resistance.

This change in the transom flow regime is not easily anticipated from just hull shape parameters. While in most views of the design space the occurrence of wetted or dry transoms seems arbitrarily spread, the exception is Fig.6, which shows that lower values of the S-shape parameter and higher values of the V-shape tend to promote a wetted transom.

Response surfaces from the HF data are then derived separately for both types of transom flow, and are shown in Fig.7, now based on an increased set of 77 HF data points. We observe that design trends more or less reverse in the middle of the design space at the change of the transom flow regime, for these 2 parameters. Also we observe that the wetted-transom cases actually have a slightly lower resistance. The initial design has a wetted transom and thereby is rather favourable. Because the design space has been set up with trends for dry-transom flow in mind, it is hard to make any gains without redefining the design space. This is why most points in Fig.5 are worse than the initial design. The lowest resistance found is 0.7% lower than that of the original. Fig.8 shows the substantial reduction of transverse stern waves promised by the potential-flow code, and the small reduction actually achieved: we have gone from a wetted transom to a dry transom, which in itself would increase the stern wave amplitude, and which here cancels most of the promised reduction. While the viscous losses in the recirculating flow aft of the transom have been eliminated, the net gain is small.

To optimise the hull form in this situation, a multifidelity formulation with a potential-flow code as the LF method seems inadequate. Either another LF formulation needs to be used, or we simply optimise using the HF method. A much larger number of HF computations would then be needed; not only because of the more complicated response in the present case, but also because the different design trends for wet and dry transoms would necessitate introducing a larger number of design parameters to find the optimum design.

4.3 Practical ship design project

We mention the approach we have used in a practical project to illustrate how multifidelity methods can also be applied somewhat informally. It concerned a slender vessel at a rather high speed, with significant stern wave making. A dry-transom flow was found from an initial RANS computation using REFRESCO. In a first stage, RAPID has been used to estimate design trends and useful modification directions. This helped to preselect relevant parameters to optimise. For two stern design parameters for which the validity of the potential-flow code was less certain, a set of 13 RANS computations was carried out. The response surface derived from it was found to be somewhat complex in shape, and a set of 75 potential-flow computations was made in addition to clarify the picture. A fair agreement of the trends from the LF and HF code could then be observed, and a multifidelity response surface was derived and used to locate the optimum. While the multifidelity approach was no breakthrough, the complementary use of both tools, and exploiting the correspondence of trends, led to a more reliable answer than if just these HF data would have been available.

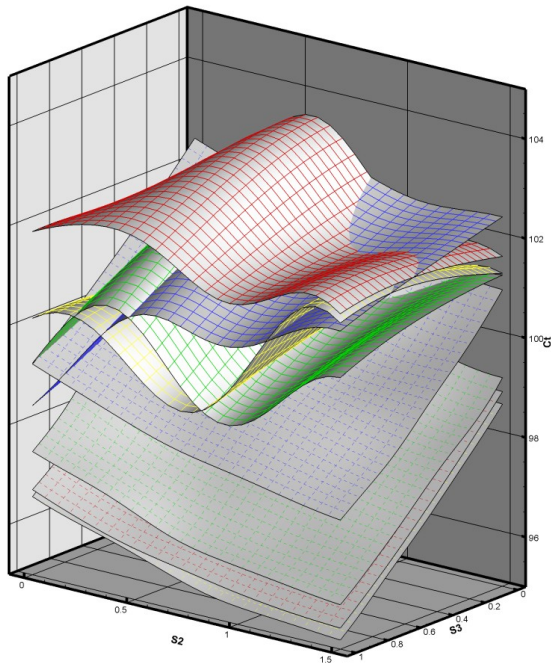


Figure 4 Response surfaces for containership case. Upper surfaces are HF results, lower are LF. Surfaces have constant V-shape parameter.

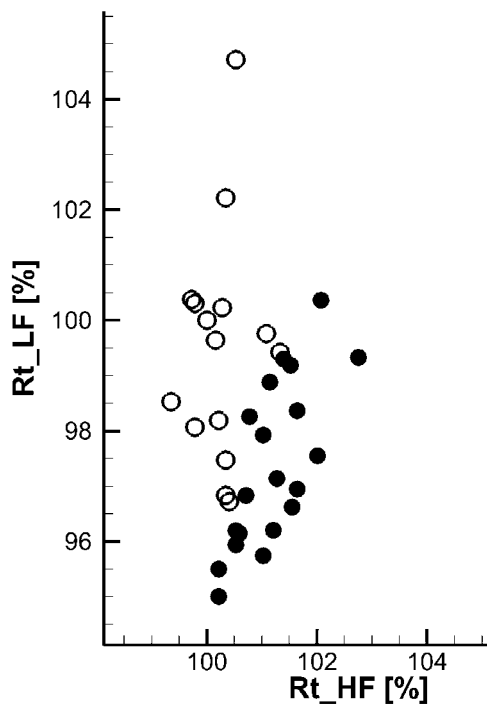


Figure 5 Correlation of HF and LF resistance values. Solid markers: dry transom. Open markers: wetted transom.

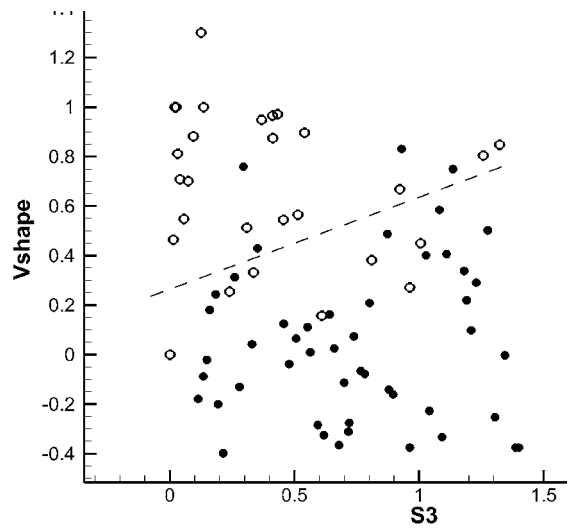


Figure 6 Dry (solid markers) and wetted (open markers) transom flows against parameters S3 and V-shape.

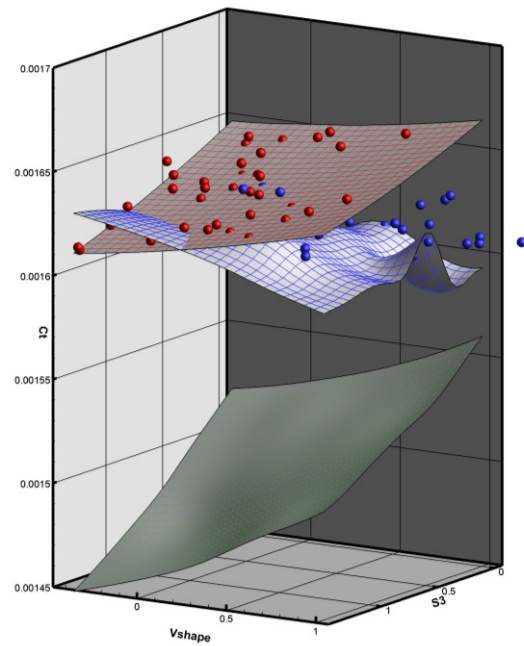


Figure 7 Response surfaces against parameters 1 and 4, for fixed par2 and par3. Red mesh and markers: dry transom. Blue: wetted transom. Lower plane is from LF method.

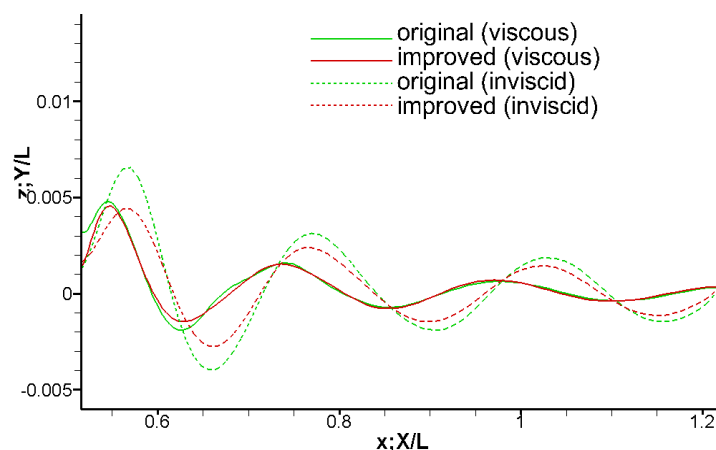


Figure 8 Wave cut along centreline aft of transom. Dashed lines from LF, solid lines from HF method.

5. ALTERNATIVE LOW-FIDELITY METHODS

The free-surface potential flow method has the clear advantage of a very low computation time, little setup time and a clear physical meaning of the results. Therefore, we will surely use it for a class of ships for which correspondence of trends may be expected. However, as expected, it has limitations. Alternative low-fidelity methods can be envisaged.

5.1 Linearised free surface solutions

A possible alternative LF method has been mentioned in [2]. In free-surface computations using PARNASSOS, the wave surface is iteratively updated, and in each iteration, steady free-surface boundary conditions linearised in the wave elevation updates are imposed. If computations for all variations are started from the final result of the original design, the linearised solution (1st iteration) may already be accurate enough, at least to indicate the design trends. The advantage is a significant reduction of the computation time, and an improved robustness as no grid deformations are required.

For the case of Section 4.1, the resistance values so obtained were well correlated with the HF data; and this linearised solution could well serve as a LF method. For the containership of Section 4.2, for the majority of the hull forms the linearised solution already indicated whether the transom would be dry or wetted; but nonetheless, the correlation of resistance values was comparable to that in Fig. 5. This does not offer a suitable alternative for that case.

5.2 Coarse-grid RANS computations using PARNASSOS

While a sufficient grid density in the RANS computations is needed for an accurate prediction, coarser-grid solutions may still predict the trends of resistance correctly; as correlated bias errors in different solutions drop out. In that case, a set of dense-grid solutions may be supplemented by a larger number of coarse-grid computations in a multi-fidelity formulation. At equal total computational cost this might yield better accuracy than just a larger set of dense-grid computations.

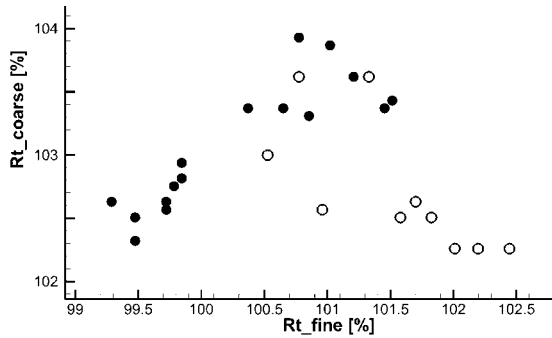


Figure 9 Correlation of LF and HF resistance values. Solid markers: equal transom flow type. Open markers: different transom flow type.

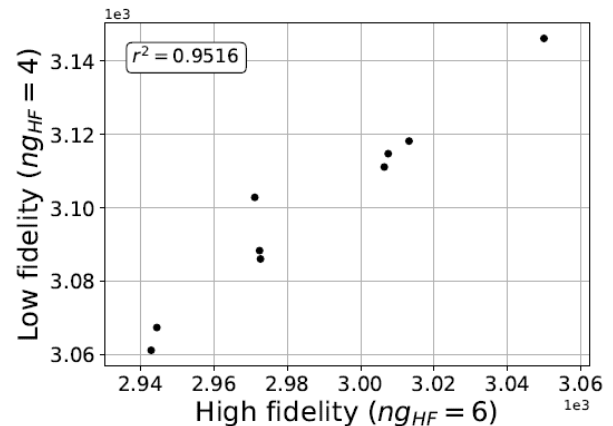


Figure 10 Correlation of coarse and fine grid resistance values. Refresco study.

For the same container ship afterbody considered in Section 4.2, we try to use a coarse-grid RANS solution as a LF method. The grid spacing in longitudinal and transverse directions is doubled, yielding a coarse grid with just 1.7 M cells, but still having full resolution of the boundary layer.

Fig.9 shows the correlation of the coarse and fine grid resistance coefficients. Taking all points together the correlation is poor. However, if we just consider the cases that have the same transom flow regime on coarse and fine grids, the correlation is reasonable; both for dry and wetted transoms. But there is a number of cases that have a dry transom on the fine grid, but wetted on the coarse grid; and again, the change of flow regime destroys the correlation, and thereby, the practicality of the coarse-grid solution. Apparently, the coarse grid here is at least locally too coarse for this purpose.

5.3 Coarse-grid RANS computations using ReFRESKO

A similar test has been done for the case of another large containership, for Froude number 0.185. Two parameters are used to modify the stern, one changing the level of the transom edge, the other the V-shape at the stern. Here all stern flows were of dry-transom type.

The RANS code used here is REFRESKO, and unstructured grids are generated using HEXPRESS. While coarse grids can be generated in a variety of ways, it is considered best to aim for some overall geometrical similarity, by coarsening the initial grid in each direction while maintaining the surface refinement levels [9]. As high-fidelity data, results on a grid of 10.8 million cells are used. For low-fidelity, grids with 4.6 million cells are adopted. Mean computation time on the coarse grids is found to be 32% of that on the fine grids.

Fig.10 illustrates the correlation of resistance values found on both grids, for a 9-point full factorial DoE. There is a reasonable correlation ($R^2 = 0.95$), the variation on the finer grids is about 1.5 times as large as on the coarse grids, and the resistance level is some 4% lower. The coarse-grid results themselves are clearly less accurate, but they may well be helpful to determine the trends.

Toal [11] has given guidelines for when a MF Kriging method is preferred above single-fidelity Kriging:

- The correlation between the low and high-fidelity solver is high: $R^2 > 0.9$;
- Between 10% and 80% of the total computing time is spent to LF computations;
- The fraction of HF data replaced by LF data should be $f_r > 1.75/(1+1/C_r)$; in which C_r is the ratio of computation times (here 0.32).

Following this we replace 5 of the 9 HF evaluations by LF evaluations, keeping the total computational cost roughly equal; i.e. we do 17 LF and 4 HF computations. An accuracy test using a set of 12 additional HF test points was then done (Fig.11). Disappointingly, there is no clear improvement from the use of the MF method. The RMS error in the test points is slightly larger than for SF Kriging. As the overall computation time is roughly equal, this is not helpful. Possibly, for larger grid density ratio's better results could be obtained.

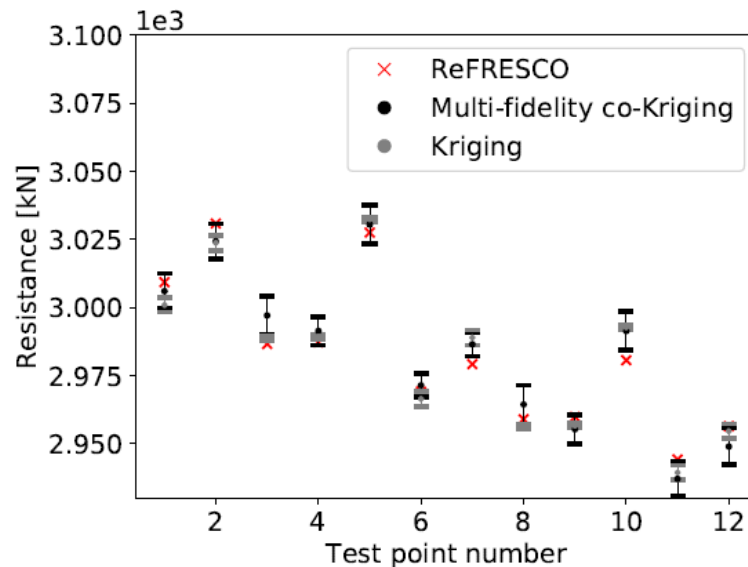


Figure 11 Validation of response surfaces from single and multi-fidelity Kriging. Error bars indicate 2σ confidence interval.

6 CONCLUSIONS

This paper has outlined our progress in the study of possibilities to accelerate and enhance ship afterbody design optimisation using multifidelity formulations. Main points are summarised as follows.

- Surrogate-based global optimisation is being used in ship hull form design at MARIN. For forebody wave making, this is based on just the free-surface potential-flow code RAPID. For afterbody design, evaluation by free-surface RANS codes is required.
- To reduce the computational effort of such a RANS-based optimisation, multifidelity methods have been tested, combining potential flow and RANS codes to determine the response surfaces. For a fast displacement vessel this was found successful and resulted in a significant reduction of the number of high-fidelity evaluations. For a containership however, the correlation between low and high-fidelity resistance values was found to be poor, as a result of a change of the transom flow regime in the middle of the design space. Wetted transoms appeared to have significantly different trends with the design parameters than dry transoms.
- Using coarse-grid RANS solutions as low-fidelity simulations is a possibility, but finding

the right balance between a good correlation with the HF resistance trends, and a large reduction of the computation time, proved not easy.

- Both an additive multifidelity formulation and cokriging require a large degree of correspondence of the HF and LF trends to really contribute to the accuracy of the response surface. In some 1D examples the uncertainty connected with the Kriging approximation appeared not well correlated with the actual error, and hardly suitable to be used for adaptive sampling.
- While for a class of cases we already use multifidelity optimisation incidentally in practical projects, further developments are required to apply it in daily practice.

ACKNOWLEDGEMENT

This research has been partly funded from the TKI-allowance of the Dutch Ministry of Economic Affairs.

REFERENCES

- [1] Raven, H.C., and Scholcz, T.P., Wave resistance minimisation in practical ship design. *Proc. MARINE 2017*, Nantes, France.
- [2] Raven, H.C., Minimising ship afterbody wave making using multifidelity techniques. *32nd Symp. Naval Hydrodynamics*, Hamburg, Germany, Aug. 2018.
- [3] Hoekstra, M., and Raven, H.C., A practical approach to constrained hydrodynamic optimization of ships. *NAV 2003 Symp.*, Palermo, Italy, June 2003.
- [4] Adams, B.M., Bauman, L.E., Bohnhoff, W.J., Dalbey, K.R., Ebeida, M.S., Eddy, J.P., Eldred, M.S., Hough, P.D., Hu, K.T., Jakeman, J.D., Stephens, J.A., Swiler, L.P., Vigil, D.M., and Wildey, T.M., "Dakota, A Multilevel Parallel Object-Oriented Framework for Design Optimization, Parameter Estimation, Uncertainty Quantification, and Sensitivity Analysis: Version 6.0 User's Manual," *Sandia Technical Report SAND2014-4633*, July 2014. Updated November 2015.
- [5] Raven, H.C., A solution method for the nonlinear ship wave resistance problem, *PhD Thesis, Delft Univ. Techn.*, 1996.
- [6] Hoekstra, M., Numerical simulation of ship stern flows with a space-marching Navier-Stokes method, *PhD Thesis, Delft Univ. Techn.*, Netherlands, 1999
- [7] Raven, H.C., van der Ploeg, A. and Starke, A.R., "Computation of free-surface viscous flows at model and full scale by a steady iterative approach", *Proceedings 25th Symposium on Naval Hydrodynamics*, St. John's, Newfoundland, Canada, August 2004.
- [8] Klaij C. M., Hoekstra, M, and Vaz, G., Design, analysis and verification of a volume-of-fluid model with interface-capturing scheme. *Computers and Fluids*, 2018
- [9] P. Crepier, "Ship resistance prediction: Verification and validation exercise on unstructured grids", *MARINE 2017 symposium*, Nantes, 2017.
- [10] Forrester, A.I.J., Sóbester, A. and Keane, A.J., "Multi-fidelity optimization via surrogate modelling", *Proceedings Royal Society A*, Dec. 2007.
- [11] D. J. Toal, Some considerations regarding the use of multi-fidelity kriging in the construction of surrogate models, *Struct. Multidiscip. Optim.* 51 (6) (2015) 1223-1245. doi:10.1007/s00158-014-1209-5. URL <http://dx.doi.org/10.1007/s00158-014-1209-5>

EFFICIENT REDUCTION IN SHAPE PARAMETER SPACE DIMENSION FOR SHIP PROPELLER BLADE DESIGN

ANDREA MOLA*, MARCO TEZZELE*, MAHMOUD GADALLA*,
FEDERICA VALDENAZZI†, DAVIDE GRASSI†, ROBERTA PADOVAN‡ AND
GIANLUIGI ROZZA*

*Mathematics Area, mathLab, SISSA, International School of Advanced Studies,
via Bonomea 265, I-34136 Trieste, Italy
e-mail: andrea.mola@sissa.it, marco.tezzele@sissa.it, mahmoud.gadalla@sissa.it,
gianluigi.rozza@sissa.it

†CETENA S.p.A., via Ippolito D'Aste 5, I-16121 Genova, Italy
e-mail: federica.valdenazzi@cetena.it, davide.grassi@cetena.it

‡CETENA S.p.A., Branch Office Trieste Passeggio S. Andrea, 6/A - 34100 Trieste, Italy
e-mail: roberta.padovan@cetena.it

Key words: Propeller Optimization, Shape Parameterization, Parameter Space Reduction, Active Subspaces

Abstract. In this work, we present the results of a ship propeller design optimization campaign carried out in the framework of the research project PRELICA, funded by the Friuli Venezia Giulia regional government. The main idea of this work is to operate on a multidisciplinary level to identify propeller shapes that lead to reduced tip vortex-induced pressure and increased efficiency without altering the thrust. First, a specific tool for the bottom-up construction of parameterized propeller blade geometries has been developed. The algorithm proposed operates with a user defined number of arbitrary shaped or NACA airfoil sections, and employs arbitrary degree NURBS to represent the chord, pitch, skew and rake distribution as a function of the blade radial coordinate. The control points of such curves have been modified to generate, in a fully automated way, a family of blade geometries depending on as many as 20 shape parameters. Such geometries have then been used to carry out potential flow simulations with the Boundary Element Method based software PROCAL. Given the high number of parameters considered, such a preliminary stage allowed for a fast evaluation of the performance of several hundreds of shapes. In addition, the data obtained from the potential flow simulation allowed for the application of a parameter space reduction methodology based on active subspaces (AS) property, which suggested that the main propeller performance indices are, at a first but rather accurate approximation, only depending on a single parameter which is a linear combination of all the original geometric ones. AS analysis has also been used to carry out a constrained optimization exploiting response surface method in the reduced parameter space, and a sensitivity analysis based on such surrogate model. The few selected shapes were finally used to set up high fidelity RANS simulations and select an optimal shape.

1 Introduction

In several fields of engineering, virtual prototyping simulations results depend on a wide range of different design parameters. When the number of such input parameters becomes too large, the problem of finding their combination resulting in the optimal solution can be easily affected by the curse of dimensionality. Depending on the computational cost of the single simulations, even with a relatively small parameter space dimension, a full optimization campaign could require months to be completed. Thus, reducing the dimension of such space is crucial to allow for quality optimization in engineering design processes.

In recent years, several interesting applications of shape parameter reduction techniques have been documented in the literature. Among them, we mention [5, 6], in which the authors apply both nonlinear extensions of the Principal Component Analysis (PCA) [14] and methods based on Artificial Neural Networks (ANN) [9] to approximate in low dimensional spaces the parametric deformation of ship hulls. A common feature of such works, is that they act in an *offline* fashion, since they solely operate on the relationship between shape parameters and hull geometry, rather than on the one between shape parameters and simulations output. This leads to the advantage that less simulations are required in the *online* optimization phase. In this work, we make instead use of an analysis based on the Active Subspaces (AS) property [3] to obtain parameter space reduction in the framework of a ship propeller shape optimization campaign. A main trait of the present analysis is that, differently from the ones described, it is carried out in the online phase of the optimization so as to construct a reduced parameter space to approximate the relationship between the simulations output and the parameters. Although this might lead to increased computational cost, the analysis has the fruitful benefit of identifying which of the original parameters bear a higher influence on the physical output. Such information can of course lead the work of design engineers. In addition, to mitigate the disadvantage of possibly high computational cost associated to the high number of simulations required for the analysis, in this work we made use of the potential flow solver PROCAL [19], which despite its low computational cost, is able to provide accurate predictions of the fluid dynamic outputs of interest. Moreover, we also explore the use of AS for constrained optimization exploiting response surface method in the reduced parameter space, to identify propeller shapes with increased hydroacoustic performance (i.e.: reduced tip vortex-induced maximum pressure) without thrust reductions. The most promising shapes are the only ones tested with the high-fidelity RANS solver, with considerable reduction of the whole optimization campaign.

2 Blade reconstruction and morphing

A very important ingredient of the multidisciplinary propeller optimization methodology here described is represented by an efficient shape parameterization tool. In fact, as well known, optimization algorithms are mathematical tools which operate on numerical variables, identifying the input parameters combination which maximizes or minimizes the output values of a specific model or system. In such framework, optimization algorithms cannot be used to find shapes of optimal performance, unless a shape parameterization strategy is devised to associate each possible shape modification with numbers characterizing the points in the parameter space. Such numbers are the input used to feed the optimization algorithm. Thus, the main task of shape parameterization is that of creating a — possibly — one-to-one correspondence between

propeller shapes and sample points in the parameter space. There are several multi-purpose parameterization methodologies available in the literature, which are designed to deform bodies of arbitrary shapes. Such algorithms, among which we mention Free Form Deformation (FFD) [?] and Radial Basis Functions (RBF), are implemented in open source software libraries and packages [?, 13, 17] which could be in principle readily downloaded and employed. Unfortunately, in their original formulation such multi-purpose deformation strategies are not suitable for a highly engineered shape as a ship propeller. Among other things, their application would in fact result in altering in an undesired way the specific airfoils selected by the engineers at each blade section for their well assessed hydrodynamic performance. Rather than tweaking FFD or RBF to account for constraints on the shape deformations generated, we decided to exploit the procedure used by the engineers for the bottom-up generation of 3D propeller geometries.

2.1 Bottom-up blade construction of parameterized propeller

A 3D propeller blade is generated (see for instance [2]) as the surface passing through a set of sectional airfoil shapes, which are originally specified in a 2D space and are successively located in the 3D space according to a set of transformations which vary along with the radial coordinate of each section. Such transformations include scaling, translations and rotations to obtain the blade with the desired radial distribution of airfoil section chord length, rake and skew displacements, and pitch angle respectively. Such standard propeller blade design procedure has been implemented in the open source python package BladeX [8]. As illustrated in Figure 1, after the coordinates of blade airfoil sections and radial distribution curves are read from external files, the airfoil sections are placed in the correct three dimensional position and the CAD surface passing through the sections is generated and exported in *iges* format.

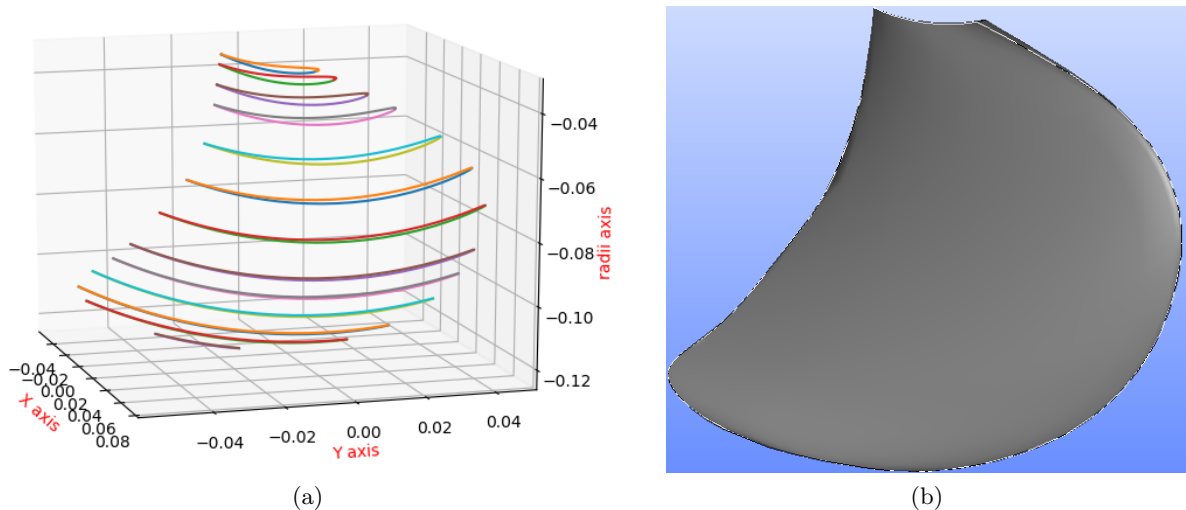


Figure 1: PPTC blade bottom-up construction with BladeX: (a) Cylindrical blade sections in their final three dimensional position. (b) The generated CAD surface (saved in *iges* file format).

In the framework of the described blade construction procedure, BladeX allows for recon-

structuring with user specified degree splines, the radial distribution curves for chord length, pitch angle, skew and rake displacements. By means of constrained least squares minimization, the algorithm will in fact identify the spline control points position minimizing the distance between the original curves and their splines counterparts. A further method has been added to allow for spline reconstruction of the radial distribution of the sectional airfoils maximum camber deflection. Once chord, pitch, skew, rake and camber radial distributions have been reconstructed by means of splines, the user introduces a set of splines control points displacements to alter the blade characteristic curves and ultimately its shape. Thus, a parameterized blade geometry can be generated through variations of the position of an arbitrary number of the control points associated with the spline reconstruction of the original blade characteristic curves. This obviously leads to the convenient possibility of generating parameter spaces having the desired dimension. In addition, a further relevant advantage of such parameterization strategy based on splines control points displacement, is that all the blades generated are smooth deformations of the original one. Figure 2 shows a pitch curve reconstruction by means of a 10 control points 3rd order spline carried out through BladeX. In the example, non null displacements are also assigned to control points 6 and 7, to generate a modified pitch distribution, which would ultimately result in a different blade geometry.

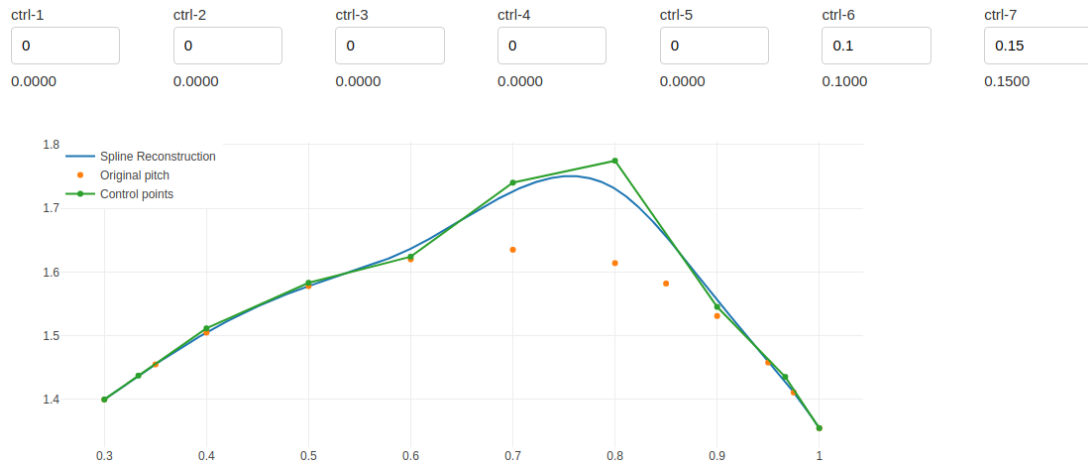


Figure 2: A sketch of the PPTC blade pitch radial distribution curve modification carried out with BladeX. The plot shows the original blade points (yellow dots), and the corresponding splines reconstruction (blue continuous line) with its control polygon (green dots and line). The example shows how control points 6 and 7 are modified to alter the pitch curve retaining smoothness.

Once the parameterized blade geometry has been generated, the full propeller geometry can be finalized by replicating the blade for the desired number of times, and attaching it to the imported hub geometry.

2.2 A family of PPTC SVA-VP1304 blade deformations for the optimization campaign

We based our analysis on the shape of the PPTC SVA-VP1304 benchmark propeller ¹, originally designed for the SMP workshops [1]. To carry out the numerical experiments, we produced a set of 1100 blade variants, based on deforming the pitch and camber radial distributions along the blade. More specifically, the deformations were obtained displacing the 10 control points of the splines reconstructing the pitch and camber profiles, within 15% and 20% of the original blade maximum local pitch and maximum local camber, respectively. We point out that the camber modification is carried out by scaling the camber line points of each sectional airfoil so as to obtain the specified local maximum camber deflection. The described methodology resulted in a family of deformations depending on 20 parameters. As the blade profiles obtained from such procedure might suffer from inflections which might lead to unfeasible manufacturing as well as the poor hydrodynamic performance, the local deformation bounds were also constrained in a way that ensures smooth profiles.

3 Parameter space analysis through active subspaces

In this section, we present the active subspaces analysis of the fluid dynamic performance results obtained for each PPTC SVA-VP1304 benchmark propeller variation produced. Such results were obtained using the potential flow solver PROCAL [19] to simulate the flow past the propeller in an open water test setup.

The present study was carried out for a single value of the propeller advance ratio $J = \frac{V_a}{n \cdot D} = 1.019$ where V_a is the streamwise velocity, $D = 0.25m$ is the propeller diameter, and n is the rotational speed in (rps). While J is a parameter summarizing the fluid dynamic inputs to the simulations, the first outputs of interest for the designers are quite naturally an estimation of the hydrodynamic forces and moments acting on the propeller. In particular, the thrust force T generated by the propeller along its axial direction is the quantity that the designers typically want to maximize. At the same time, the resisting torque Q around the propeller axis needs instead to be minimized to increase performance. Based on such considerations, the first output parameter considered in this work is the thrust coefficient $K_T = \frac{T}{\rho n^2 D^4}$ (ρ being the fluid density). As for the second output parameter, we preferred using the propeller efficiency $\eta = \frac{J}{2\pi} \cdot \frac{K_T}{K_Q}$ rather than simply using the torque coefficient $K_Q = \frac{Q}{\rho n^2 D^5}$. A high propeller efficiency is in fact a significant indicator of the propeller ability to generate thrust, without requiring high torque values from the engine to maintain the indicator of the propeller ability to generate thrust, without requiring high torque values from the engine to maintain the specific rotational speed. For the value of J herein considered, the efficiency and thrust coefficient obtained for the original PPTC SVA-VP1304 benchmark propeller are $\eta = 0.629$, $K_T = 0.3835$ respectively. As shown in Figure 3a, at the selected advance ratio the propeller thrust coefficient as predicted by a non-cavitating unsteady PROCAL computation is very close to the experimental thrust coefficient (SMP'11 workshop; test case 2.3.1 [1]), the difference amounting to less than 1%. Along with the aforementioned propeller thrust coefficient K_T and efficiency η , the output parameters also

¹Geometry and documentation available at <https://www.sva-potsdam.de/en/potsdam-propeller-test-case-pptc>

considered in the analysis were the vortex-induced maximum pressure (P_{max}), and the frequency (f_{max}) associated to (P_{max}). A summary of the values of the four outputs for the benchmark propeller are presented in Figure 3b.

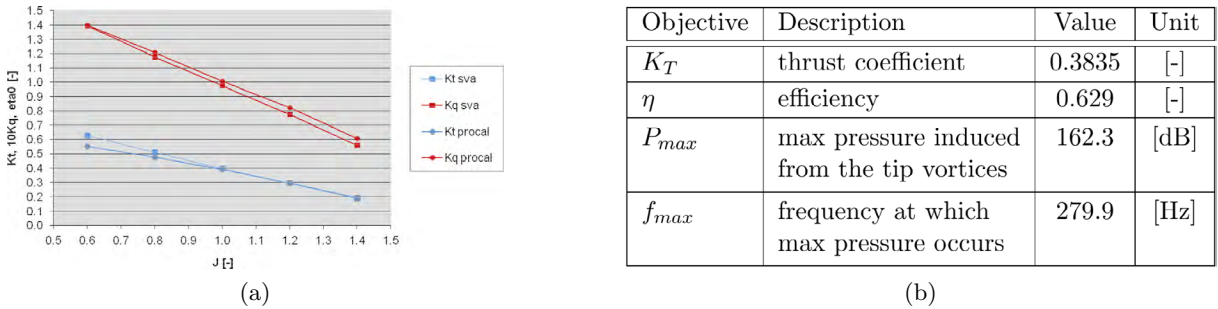


Figure 3: (a) PROCAL prediction of the thrust and torque coefficients of the PPTC SVA-VP1304 at various advance ratios. Results are compared with the corresponding experimental data from the SMP workshop. (b) Computed output parameters at $J = 1.019$.

The procedure adopted in the present study is composed as follows: (i) dimension reduction via the active subspaces analysis on the geometrical parameter space defined by the the control points deformations, (ii) sensitivity analysis and optimization of the propeller performance based on the reduced parameter obtained from the active subspaces analysis. In the following subsections, we first provide a brief description of the active subspaces property theory, and then report the results of the analysis carried out on the potential flow results database.

3.1 Background and formulations

The active subspaces (AS) property has been recently establishing as one of the emerging techniques for dimension reduction in parametric studies [3, 4]. Since its introduction, AS has been widely applied in several research topics, including marine engineering [18, 16, 7], and cardio-vascular flows [15]. A parameter study of an objective function $f(\boldsymbol{\mu})$ becomes challenging when the dimension of $\boldsymbol{\mu}$ (i.e.: the number of input parameters considered) is relatively large. In that regard AS offer a sophisticated approach to reduce the study's dimensions by seeking a set of important directions in the parameter space along which f varies the most. Such directions are linear combinations of all the parameters, and span a lower dimensional subspace of the input space, which can be also exploited to carry out optimization campaigns in an extremely inexpensive fashion.

Consider the objective $f(\boldsymbol{\mu}) : \mathbb{D} \subset \mathbb{R}^m \rightarrow \mathbb{R}$ as a differentiable, square-integrable scalar function of the normalized inputs. In order to determine the directions of maximum variability we evaluate the uncentered covariance matrix of gradients $\mathbf{C} = \mathbb{E}[(\nabla_{\boldsymbol{\mu}} f)(\nabla_{\boldsymbol{\mu}} f)^T] = \int_{\mathbb{D}} (\nabla_{\boldsymbol{\mu}} f)(\nabla_{\boldsymbol{\mu}} f)^T \rho d\boldsymbol{\mu}$, where $\mathbb{E}[\cdot]$ is the expectation operator, and $\rho : \mathbb{D} \rightarrow \mathbb{R}^+$ is the probability density function. The symmetric positive definite (SPD) structure of \mathbf{C} allows for an eigendecomposition, $\mathbf{C} = \mathbf{W}\boldsymbol{\Lambda}\mathbf{W}^T$, where \mathbf{W} is the $m \times m$ column matrix of eigenvectors, and $\boldsymbol{\Lambda}$ is the diagonal matrix of non-negative eigenvalues arranged in descending order.

Now by partitioning $\Lambda = \begin{bmatrix} \Lambda_1 & \\ & \Lambda_2 \end{bmatrix}$ into the larger eigenvalues, $\Lambda_1 = \text{diag}\{\lambda_1, \dots, \lambda_M\}$, and the smaller ones, $\Lambda_2 = \text{diag}\{\lambda_{M+1}, \dots, \lambda_m\}$, subsequently $\mathbf{W} = [\mathbf{W}_1 \quad \mathbf{W}_2]$ such that $\mathbf{W}_1 \in \mathbb{R}^{m \times M}$, $\mathbf{W}_2 \in \mathbb{R}^{m \times m-M}$, then the low eigenvalues Λ_2 suggest that the corresponding vectors \mathbf{W}_2 are in the null space of the covariance matrix \mathbf{C} , and such vectors can be discarded to form an approximation. Therefore the lower dimensional parameter subspace spanned by \mathbf{W}_1 is considered as the active subspace, while the inactive subspace is spanned by \mathbf{W}_2 . At this stage, the dimension reduction is achieved by projecting $\boldsymbol{\mu}$ onto the active subspace to obtain the active variables $\boldsymbol{\mu}_M = \mathbf{W}_1^T \boldsymbol{\mu} \in \mathbb{R}^M$, whereas the inactive variables are $\boldsymbol{\zeta} = \mathbf{W}_2^T \boldsymbol{\mu} \in \mathbb{R}^{m-M}$. The relationship between the full parameter space $\boldsymbol{\mu} \in \mathbb{D}$ and the active variables $\boldsymbol{\mu}_M$ is described as $\boldsymbol{\mu} = \mathbf{W}_1 \mathbf{W}_1^T \boldsymbol{\mu} + \mathbf{W}_2 \mathbf{W}_2^T \boldsymbol{\mu} = \mathbf{W}_1 \boldsymbol{\mu}_M + \mathbf{W}_2 \boldsymbol{\zeta}$, and the objective function $f(\boldsymbol{\mu})$ is approximated by $g(\boldsymbol{\mu}_M)$ which can be further exploited to construct a response surface.

3.2 Sensitivity analysis and optimization using active subspaces

Accordinging the AS formulation presented, we consider the geometrical parameters $\boldsymbol{\mu} \in \mathbb{R}^{1100 \times 20}$ which represent the displacements of the 20 control points of all the 1100 shapes. As for the parameters ordering in vector $\boldsymbol{\mu}$, the first 10 parameters represent the pitch spline control point displacements, going from the blade root to the tip. The last 10 parameters are the camber line spline control point displacements, again ordered from root to tip. The objective function is $f_i(\boldsymbol{\mu}) \in \mathbb{R}^{1100}$, where the index $i = 1, \dots, 4$ indicates the specific output parameter considered, in the order K_T , η , P_{max} , or f_{max} . The eigendecomposition was performed on the covariance matrices corresponding to each output parameter and the resulting eigenvalues magnitudes are presented in Figure 4. The plots clearly show that for all the output parameter considered, a significant gap exists between the magnitude of first eigenvalue and that of the remaining eigenvalues. This observation suggests that each of the the input to output relationships can be rather accurately represented with a one dimensional approximation. Such one dimensional relationship is computed as the projection of the parameter space $\boldsymbol{\mu}$ onto the active subspace corresponding to the first eigenvalue (i.e.: the first eigenvector), namely $\boldsymbol{\mu}_M = \boldsymbol{\mu} \cdot \mathbf{W}_1 \in \mathbb{R}^{1100}$. In Figure 5 we show present an attempt to visualize the subspace $\mathbf{W}_1 \in \mathbb{R}^{20}$. The 20 components in each plots represent in fact the weights needed to obtain the active variable as a linear combination of the of the original input parameters. So, such visualization is able to indicate which parameters have a higher influence on the output, as the corresponding components will be characterized by higher weight magnitudes. The results suggest that both K_T and η are mostly sensitive to the mid-to-near-tip region of the pitch profile, whereas the P_{max} and f_{max} are mostly sensitive to the near-tip region of the pitch curve. In fact, the resulting sensitivity analysis coincides with the hydrodynamic experience and the design practice, where the pitch is directly related to the loading on the propeller and to the tip vortex strength. In addition, the efficiency is directly proportional to the thrust by definition, and the blade loading, thus the K_T , is much affected by the pitch at the radial coordinate range around $0.7r/R$. Such radial coordinate is in fact used in common propeller descriptions, to provide a meaningful reference value for pitch and loading. Moreover, the plots suggest that the pitch at the tip has the largest impact on the tip vortex pressure P_{max} and subsequently f_{max} . As for the camber modifications, they appear to have on the loading a lower but still significant impact with respect to the pitch deformations, and an even less relevant effect on the tip vortex strength. A complete

summary of the parameters influence on the propeller performance is presented in Table 1.

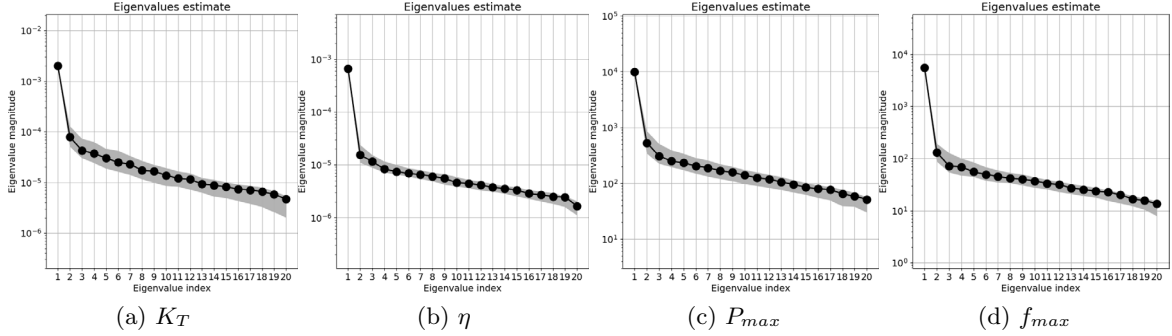


Figure 4: Eigenvalues of the uncentered covariance matrix of gradients, relating the geometrical parameters $\boldsymbol{\mu} \in \mathbb{R}^{1100 \times 20}$ to each of K_T , η , P_{max} , or f_{max} represented by $f(\boldsymbol{\mu}) \in \mathbb{R}^{1100}$. The low eigenvalues suggest the corresponding eigenvectors are in the null space of the covariance matrix, and thus a one dimensional active variable can be achieved as an approximation of $\boldsymbol{\mu}$.

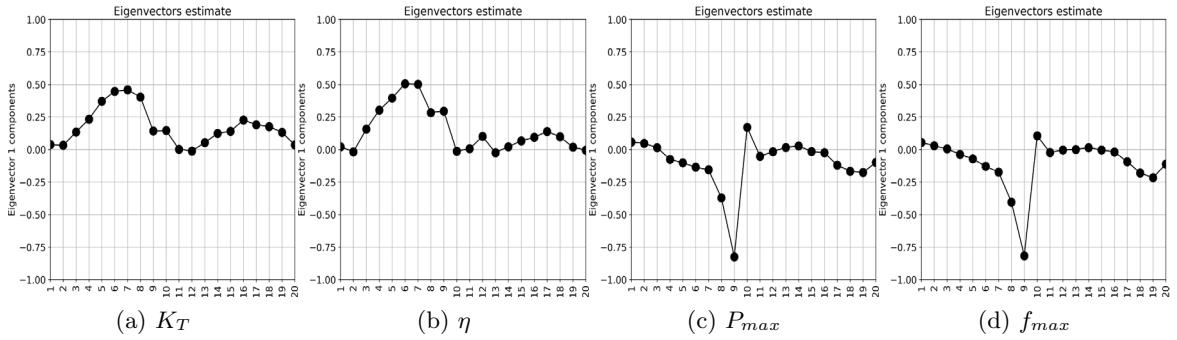


Figure 5: Components of the first eigenvector, i.e. the active subspace \mathbf{W}_1 , which describes the contribution of each of the 20 parameters in the AS approximation. The plots show that K_T and η are mostly sensitive to the mid-to-near-tip region of the pitch profile, while P_{max} and f_{max} are mostly sensitive to the near-tip region of the pitch curve.

We now describe a further possibility offered by AS analysis. We in fact exploit the input to output relationship in the active subspace to carry out an optimization campaign in a low dimensional —hence reduced— space. For instance, if we consider the tip vortex-induced pressure P_{max} , we can readily represent its dependence on its active variable $\boldsymbol{\mu}_M$ with a one dimensional response surface, as depicted in Figure 6a. Such response surface is then conveniently used to determine the active variable corresponding to the minimal P_{max} . The resulting optimal $\boldsymbol{\mu}_M$ value is then mapped back to the actual parameter space so as to identify the exact root-tip deformations yielding the minimal acoustic pressure, as reported in Figures 6b and 7. The deformed

Table 1: Summary of the PPTC performance sensitivity towards the pitch and camber root-tip parametric curves. In the table, (++) represents a dominating influence, (+): significant influence, (+-): small influence, and (-): can be neglected.

| Control points | k_t | η | p_m | f_m | Control points | k_t | η | p_m | f_m |
|----------------|-------|--------|-------|-------|----------------|-------|--------|-------|-------|
| pitch - 1 | - | - | + - | + - | camber - 1 | - | - | + - | - |
| pitch - 2 | - | - | + - | - | camber - 2 | - | + - | - | - |
| pitch - 3 | + | + | - | - | camber - 3 | - | - | - | - |
| pitch - 4 | + | + | + - | - | camber - 4 | + | - | - | - |
| pitch - 5 | ++ | + | + | + - | camber - 5 | + | + - | - | - |
| pitch - 6 | ++ | ++ | + | + | camber - 6 | + | + - | - | - |
| pitch - 7 | ++ | ++ | + | + | camber - 7 | + | + - | + | + - |
| pitch - 8 | ++ | + | ++ | ++ | camber - 8 | + | + - | + | + |
| pitch - 9 | + | + | ++ | ++ | camber - 9 | + | - | + | + |
| pitch - 10 | + | - | ++ | + | camber - 10 | - | - | + | + |

profiles were utilized via BladeX to construct the morphed blade, Figure 6b. Finally, since the ultimate goal was to minimize P_{max} and f_{max} , maximize η without altering K_T , such procedure had to be implemented by introducing a shared subspace [10] among the four objectives, and a constrained optimization needed to be carried out on the resulting response surface in order to find the optimal propeller. Among the 1100 variants produced, the shape resulting from the procedure described was eventually selected to undergo a high fidelity RANS simulations.

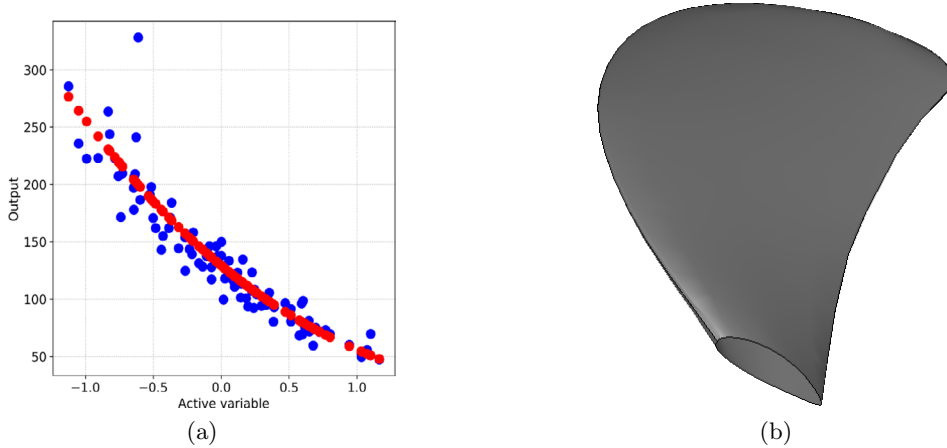


Figure 6: (a) Response surface (RS) of the reduced parameter μ_M vs. P_{max} constructed as a best-fit polynomial trained from 80% of the dataset, the remaining 20% are used to validate the output (in blue) and the corresponding RS (in red). (b) The morphed PPTC blade to produce a minimal P_{max} .

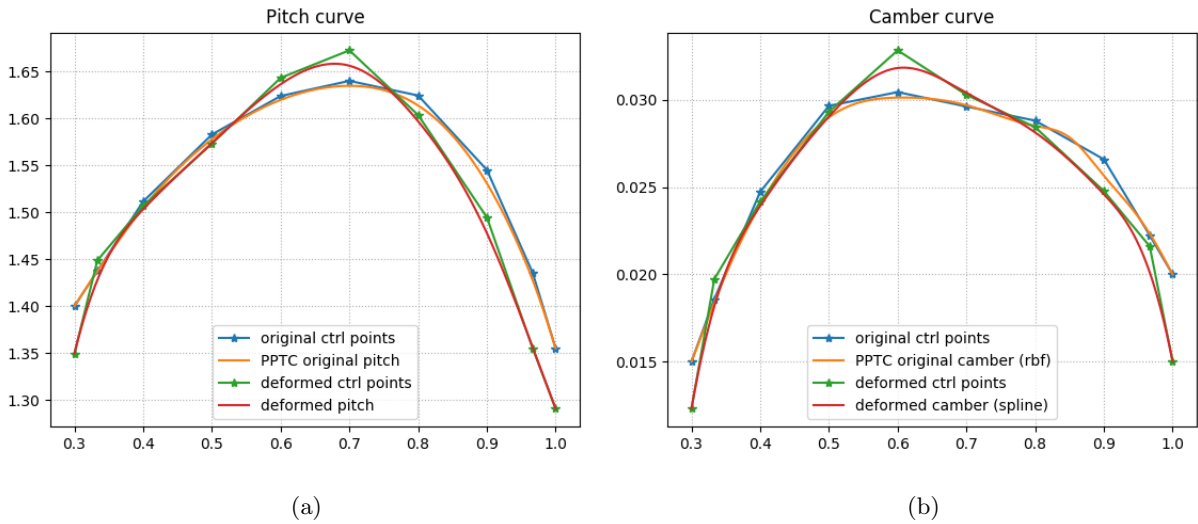


Figure 7: Deformed parametric curves resulting from the minimization procedure for P_{max} . (a) Pitch, (b) camber.

4 Conclusions and perspectives

In the present contribution, we presented an application of parameter space reduction based on the Active Subspaces (AS) property, in the framework of the hydroacoustic optimization of ship propellers. Making use of the open source Python package BladeX, we produced a large number of parameterized modifications of the PPTC SVA-VP1304 benchmark propeller, which were used to carry out potential flow simulations with the software PROCAL. The AS analysis suggested that for all the propeller performance parameters considered the input to output relationships can be rather accurately represented with a one dimensional approximation, in which the single active parameter is a linear combination of the 20 original shape parameters. A further sensitivity analysis based on the weights of such linear combination suggested that, at a first approximation, the pitch modifications in the mid-to-tip region and — at a lesser extent — the camber modification in the blade middle portion have higher impact on the output.

These results open interesting perspective on the application of parameter space reduction in naval engineering problems. Possible developments could be obtained by testing the possibility of carrying out similar investigations employing reduced fluid dynamic models, as the ones broadly described in [11] and [12]. In particular, the use of reduced order models based on POD would allow for fluid dynamic simulations that account for all the relevant physical phenomena in the flow, at a computational cost compatible with the present analysis. Ongoing work in the PRELICA project is directed in such direction.

Acknowledgements

This work was partially performed in the context of the PRELICA - “Advanced methodologies for hydro-acoustic design of naval propulsion”, supported by Regione FVG, POR-FESR 2014-2020, Piano Operativo Regionale Fondo Europeo per lo Sviluppo Regionale, and partially

supported by European Union Funding for Research and Innovation — Horizon 2020 Program — in the framework of European Research Council Executive Agency: H2020 ERC CoG 2015 AROMA-CFD project 681447 “Advanced Reduced Order Methods with Applications in Computational Fluid Dynamics” P.I. Gianluigi Rozza.

REFERENCES

- [1] U. H. Barkmann. Potsdam propeller test case (pptc) - open water tests with the model propeller vp1304, report 3752. Technical report, Schiffbau - Versuchsanstalt Potsdam, 2011.
- [2] J. Carlton. *Marine propellers and propulsion*. Butterworth-Heinemann, 1994.
- [3] P. G. Constantine. *Active subspaces: Emerging ideas for dimension reduction in parameter studies*, volume 2. SIAM, 2015.
- [4] P. G. Constantine, E. Dow, and Q. Wang. Active subspace methods in theory and practice: applications to kriging surfaces. *SIAM Journal on Scientific Computing*, 36(4):A1500–A1524, 2014.
- [5] D. D’Agostino, A. Serani, E. F. Campana, and M. Diez. Nonlinear methods for design-space dimensionality reduction in shape optimization. In *International Workshop on Machine Learning, Optimization, and Big Data*, pages 121–132. Springer, 2017.
- [6] D. D’Agostino, A. Serani, E. F. Campana, and M. Diez. Deep autoencoder for off-line design-space dimensionality reduction in shape optimization. In *2018 AIAA/ASCE/AHS/ASC Structures, Structural Dynamics, and Materials Conference*, page 1648, 2018.
- [7] N. Demo, M. Tezzele, A. Mola, and G. Rozza. An efficient shape parametrisation by free-form deformation enhanced by active subspace for hull hydrodynamic ship design problems in open source environment. In *The 28th International Ocean and Polar Engineering Conference*, 2018.
- [8] M. Gadalla, M. Tezzele, A. Mola, and G. Rozza. BladeX: Python Blade Morphing. *The Journal of Open Source Software*, 4(34):1203, 2019.
- [9] G. E. Hinton and R. R. Salakhutdinov. Reducing the dimensionality of data with neural networks. *Science*, 313(5786):504–507, July 2006.
- [10] W. Ji, J. Wang, O. Zahm, Y. M. Marzouk, B. Yang, Z. Ren, and C. K. Law. Shared low-dimensional subspaces for propagating kinetic uncertainty to multiple outputs. *Combustion and Flame*, 190:146–157, 2018.
- [11] G. Rozza, M. W. Hess, G. Stabile, M. Tezzele, and F. Ballarin. Preliminaries and warming-up: Basic ideas and tools. In P. Benner, S. Grivet-Talocia, A. Quarteroni, G. Rozza, W. H. A. Schilders, and L. M. Silveira, editors, *Handbook on Model Order Reduction*, volume 1, chapter 1. De Gruyter, 2019.

- [12] G. Rozza, M. H. Malik, N. Demo, M. Tezzele, M. Girfoglio, G. Stabile, and A. Mola. Advances in Reduced Order Methods for Parametric Industrial Problems in Computational Fluid Dynamics. Glasgow, UK, 2018. ECCOMAS Proceedings.
- [13] F. Salmoiraghi, F. Ballarin, G. Corsi, A. Mola, M. Tezzele, and G. Rozza. Advances in geometrical parametrization and reduced order models and methods for computational fluid dynamics problems in applied sciences and engineering: Overview and perspectives. *ECCOMAS Congress 2016 - Proceedings of the 7th European Congress on Computational Methods in Applied Sciences and Engineering*, 1:1013–1031, 2016.
- [14] B. Schölkopf, A. J. Smola, and K.-R. Müller. Nonlinear component analysis as a kernel eigenvalue problem. *Neural Computation*, 10:1299–1319, 1998.
- [15] M. Tezzele, F. Ballarin, and G. Rozza. Combined parameter and model reduction of cardiovascular problems by means of active subspaces and POD-Galerkin methods. In D. Boffi, L. F. Pavarino, G. Rozza, S. Scacchi, and C. Vergara, editors, *Mathematical and Numerical Modeling of the Cardiovascular System and Applications*, pages 185–207. Springer International Publishing, 2018.
- [16] M. Tezzele, N. Demo, M. Gadalla, A. Mola, and G. Rozza. Model order reduction by means of active subspaces and dynamic mode decomposition for parametric hull shape design hydrodynamics. In *Technology and Science for the Ships of the Future: Proceedings of NAV 2018: 19th International Conference on Ship & Maritime Research*, pages 569–576. IOS Press, 2018.
- [17] M. Tezzele, N. Demo, A. Mola, and G. Rozza. An integrated data-driven computational pipeline with model order reduction for industrial and applied mathematics. *Submitted, Special Volume ECMI*, 2018.
- [18] M. Tezzele, F. Salmoiraghi, A. Mola, and G. Rozza. Dimension reduction in heterogeneous parametric spaces with application to naval engineering shape design problems. *Advanced Modeling and Simulation in Engineering Sciences*, 5(1):25, Sep 2018.
- [19] G. Vaz. *Modelling of Sheet Cavitation on Hydrofoils and Marine Propellers using Boundary Element Methods*. PhD thesis, Technical University of Lisbon -IST, 2005.

A HIGH-ORDER AND MESH-FREE COMPUTATIONAL MODEL FOR NON-LINEAR WATER WAVES

Morten E. Nielsen*, Bengt Fornberg[†] and Lars Damkilde[‡]

* Department of Civil Engineering
Aalborg University
Niels Bohrs Vej 8, 6700 Esbjerg, Denmark
e-mail: men@civil.aau.dk

[†] Department of Applied Mathematics
University of Colorado
526 UCB, Boulder, CO 80309, USA
e-mail: bengt.fornberg@colorado.edu

[‡] Department of Civil Engineering
Aalborg University
Thomas Manns Vej 23, 9220 Aalborg Ø, Denmark
e-mail: lda@civil.aau.dk

Key words: mesh-free methods, radial basis function-generated finite differences, high-order, node generation, water waves.

Abstract. In this paper, we present the ongoing developments of a novel computational model for non-linear water waves that aims to provide a suitable framework for wave-structure interaction. The proposed model is based on radial basis function-generated finite differences, which allow for arbitrary and moving boundaries without the use of ghost nodes. In order to take advantage of the mesh-free setting, we propose a node generation strategy, suitable for moving boundaries. Numerical properties of the proposed model are investigated and finally the model is benchmarked. The proposed model is expected to provide a suitable computational framework for wave-structure interaction problems, due to its geometric flexibility and high-order nature.

1 INTRODUCTION

During the latest decades, the interest in computational models for wave-structure interaction has increased, e.g. due to an increased demand for renewable energy. On the basis of this interest, several research projects [1, 2, 3] have been initiated, which seek to improve existing computational models for wave-structure interaction. Overall the improvements concern non-linear interactions, high fidelity fluid models and computational efficiency. Ultimately, the goal is to enhance the computational models that are used for analysis and optimization of offshore structures, such as e.g. floating offshore wind turbines and wave energy converters.

Several models have been proposed for the non-linear water wave problem, see e.g. [4, 5, 6, 7, 8, 9, 10, 11], which are based on different discretizations, ranging from traditional finite differences to spectral elements. The main concerns regarding computational modelling of non-linear water waves, in relation to wave-structure interaction, are (1) temporal stability, (2) accuracy, (3) geometric flexibility and (4) computation speed. This paper deals with the development of a novel computational model that aims to deal with the difficulties stated above, while providing a suitable framework for future coupling with structural models, e.g. the one used in [12, 13]. Specifically, we address (1) and (2) by investigating the use of radial basis function-generated finite differences (RBF-FD). The advantages of RBF-FD are geometric flexibility and high-order approximations [14, 15, 16].

Initially, the non-linear water wave problem is introduced in section 2. Next, the methodology is outlined in section 3, including a node generation strategy for the time-varying computational domain. Numerical properties of the resulting computational model are investigated in section 4, while non-linear stream functions waves are used for benchmarking of the non-linear stability and accuracy in section 5. Finally, some conclusions are stated in section 6.

2 MATHEMATICAL FORMULATION

In this paper, the formulation of the fully non-linear water wave problem is based on potential flow theory and the assumption of no wave breaking to occur. In the following subsections, the governing equation and boundary conditions are presented for the two-dimensional case, which will be used in this paper.

2.1 Interior fluid domain

Non-linear water waves may be modelled by means of potential flow theory, which makes it possible to describe the fluid flow by the scalar velocity potential function $\Phi(\mathbf{x}, t)$ found by solving the Laplace equation expressed as

$$\nabla^2 \Phi = 0, \quad \mathbf{x} \in \Omega(t), \quad (1)$$

where $\nabla = [\frac{\partial}{\partial x} \quad \frac{\partial}{\partial z}]^T$ is the gradient operator. Thus, equation (1) must be fulfilled within the time-varying fluid domain $\Omega(t)$, as illustrated in figure 1.

2.2 Free surface conditions

For the fluid flow to evolve over time, the free surface boundary conditions must be updated over time. In the Lagrangian frame of reference, the kinematic and dynamic free surface conditions can be expressed as

$$\frac{D\mathbf{r}}{Dt} = \nabla\Phi, \quad \mathbf{x} \in \Gamma_\eta(t), \quad (2)$$

$$\frac{D\Phi}{Dt} = -g\eta + \frac{1}{2}(\nabla\Phi \cdot \nabla\Phi) = 0, \quad \mathbf{x} \in \Gamma_\eta(t), \quad (3)$$

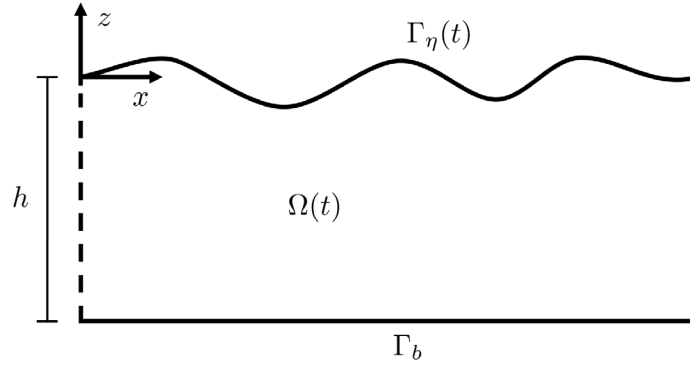


Figure 1: Fluid domain $\Omega(t)$ with specification of the free surface $\Gamma_\eta(t)$ and bottom boundary Γ_b .

where g is the gravitational acceleration, $\mathbf{r} = [x \ \eta]^T$ is the material node position vector, $\frac{D}{Dt}$ is the material derivative and $\Gamma_\eta(t)$ is the subset illustrated in figure 1.

2.3 Bottom boundary condition

The free-slip condition is enforced at the seabed,

$$\frac{\partial \Phi}{\partial \mathbf{n}} = 0, \quad \mathbf{x} \in \Gamma_b, \quad (4)$$

where $\mathbf{n} = [n_x \ n_z]^T$ is the outward-pointing unit normal vector.

2.4 Summary of the periodic non-linear water wave problem

For the sake of simplicity, we assume horizontal periodicity for all computations in this work, i.e. no lateral boundaries are present, and thus the problem is finally stated as

$$\begin{cases} \nabla^2 \Phi = 0, & \mathbf{x} \in \Omega(t), \\ \frac{\partial \Phi}{\partial z} = 0, & \mathbf{x} \in \Gamma_b, \\ \frac{Dx}{Dt} = \frac{\partial \Phi}{\partial x}, & \mathbf{x} \in \Gamma_\eta(t), \\ \frac{D\eta}{Dt} = \frac{\partial \Phi}{\partial z}, & \mathbf{x} \in \Gamma_\eta(t), \\ \frac{D\Phi}{Dt} = -g\eta + \frac{1}{2}(\nabla \Phi \cdot \nabla \Phi), & \mathbf{x} \in \Gamma_\eta(t), \end{cases} \quad (5)$$

where also constant water depth is assumed and $t = [0, T]$ specifies the time interval of the problem.

3 METHODOLOGY

3.1 Radial basis function-generated finite differences

In radial basis function generated-finite differences (RBF-FD), the methodology is similar to the traditional finite difference method. The finite difference weights are approximated as the linear combination

$$\sum_{i=1}^n w_i u_i \approx \mathcal{L}u(\mathbf{x})|_{\mathbf{x}=\mathbf{x}_e}, \quad (6)$$

where \mathcal{L} is a linear operator, w_i are the corresponding weights that approximate $\mathcal{L}u(\mathbf{x})$ at evaluation point $\mathbf{x} = \mathbf{x}_e$ and n is the number of neighboring nodes used in the stencil.

In this paper, the RBF used is the polyharmonic spline $\phi(r) = r^{2m-1}$ where $m \in \mathbb{N}_+$. By augmenting the RBF by polynomial terms, up to an arbitrary order, several advantages may be achieved [14, 15, 16]. In order to compute the weights, we introduce an interpolant as

$$s(\mathbf{x}) = \sum_{i=1}^n \lambda_i \phi(\|\mathbf{x} - \mathbf{x}_i\|) + \sum_{j=1}^l \mu_j p_j(\mathbf{x}), \quad (7)$$

with matching conditions, that seeks to minimize far-field growth, as

$$\sum_{i=1}^n \lambda_i p_j(\mathbf{x}_i) = 0, \quad j = 1, 2, \dots, l, \quad (8)$$

where $l = \binom{k+d}{k}$ is the number of terms in a k th order, d -dimensional polynomial. Now, the linear system for computing the weights w in \mathbb{R}^d , when the RBF is augmented by polynomial terms up to degree k , is expressed as

$$\begin{bmatrix} & & p_1(\mathbf{x}_1) & \dots & p_l(\mathbf{x}_1) \\ & \mathbf{A} & \vdots & \ddots & \vdots \\ p_1(\mathbf{x}_1) & \dots & p_1(\mathbf{x}_n) & & \\ \vdots & \ddots & \vdots & & \\ p_l(\mathbf{x}_1) & \dots & p_l(\mathbf{x}_n) & & \mathbf{0} \end{bmatrix} \begin{bmatrix} w_1 \\ \vdots \\ w_n \\ w_{n+1} \\ \vdots \\ w_{n+l} \end{bmatrix} = \begin{bmatrix} \mathcal{L}\phi(\|\mathbf{x} - \mathbf{x}_1\|)|_{\mathbf{x}=\mathbf{x}_e} \\ \vdots \\ \mathcal{L}\phi(\|\mathbf{x} - \mathbf{x}_n\|)|_{\mathbf{x}=\mathbf{x}_e} \\ \mathcal{L}p_1(\mathbf{x})|_{\mathbf{x}=\mathbf{x}_e} \\ \vdots \\ \mathcal{L}p_l(\mathbf{x})|_{\mathbf{x}=\mathbf{x}_e} \end{bmatrix}, \quad (9)$$

where $\mathbf{A} = A_{ij} = \phi(\|\mathbf{x}_i - \mathbf{x}_j\|)$ is the $n \times n$ RBF collocation matrix and $\mathbf{0}$ is a $l \times l$ zero matrix. Hence, only the differentiation weights $\mathbf{w} = [w_1 \ w_2 \ \dots \ w_n]^T$ are used for approximation of the differential operators described in section 2. In all computations conducted in this paper, the stencil sizes have been chosen to $n \approx 2.5\ell$, and the order of the polyharmonic splines have been chosen as $m = k$ for k odd and $m = k + 1$ for k even.

3.2 Explicit fourth-order Runge-Kutta time stepping

In order to evolve the free surface variables in time, the method of lines approach is used. Specifically, the explicit fourth-order Runge-Kutta method is used, but with a slight modification. At the end of each time step, the free surface variables are reconfigured spatially by means of interpolation, such that the free surface nodes do not become too clustered along the free surface. Other strategies could have been implemented, however, only this strategy will be considered here.

3.3 Node generation strategy

In this paper, the implemented node generation strategy is similar to the ones given in [14, 17]. However, additional steps are introduced due to the time-varying computational domain. The node generation strategy is outlined as follows:

1. Generate nodes on the boundary of the computational domain, $\Omega(t)$.
2. Generate background node set that covers $\Omega(t)$ sufficiently.
3. Remove nodes from the background node set if $r_s < \rho/2$, where ρ is a local node density measure and r_s is the smallest distance to a static boundary node.
4. Perform node repelling on a subset of each of the static boundary nodes' stencil nodes.
5. Save the repelled version of the background node set.
6. Remove nodes from the background node set if $r_d < \rho/2$, where ρ is a local node density measure and r_d is the smallest distance to a dynamic boundary node.
7. Perform node repelling on a subset of each of the dynamic boundary nodes' stencil nodes.
8. Remove nodes from the background node set if they are located outside $\Omega(t)$.
9. Repeat step 6-8 at each substep, where the saved background node set from step 5 is re-used each time.

In the strategy outlined above, static and dynamic boundary nodes refer to their variation over time. Hence, only nodes near moving boundaries are updated at each substep. In this paper, the node generation algorithm from [17] is used to generate the background node set.

3.4 Solution procedure

The overall solution procedure is outlined in algorithm 1. Using an explicit time stepping method, e.g. the RK4 as presented previously, the time derivatives need to be computed, as outlined in section 2 and 3. First the initial- and boundary conditions $\left\{ \Phi_{(x,\eta)_0}^0, \eta_{x^0}^0, x^0 \right\}$ are provided as input. These are used to solve the Laplace equation in (1) for the velocity potential $\Phi(x, z, t) = \Phi_{(x,z)}^t$ within $\Omega(t)$. Next, the particle velocities are computed at the free surface, which are then used to compute the temporal derivatives given in equations (2,3). In this manner, the free surface variables are stepped forward in time. Before proceeding, the new boundary conditions, $\left\{ \Phi_{(x^t, \eta_{x^t}^t)}^t, \eta_{x^t}^t, x^t \right\}$, are interpolated back to their initial horizontal position, x^0 , and the next time step is initialized from this spatial configuration, i.e. $\left\{ \Phi_{(x^0, \eta_{x^0}^t)}^t, \eta_{x^0}^t, x^0 \right\}$.

Algorithm 1: Overall solution procedure

```

Input:  $\{\Phi_{(x,\eta_{x^0}^0)^0}^0, \eta_{x^0}^0, x^0\}$ 
1  $t := 0$ 
2 while  $t < T$  do
3    $\{\Phi_{(x,\eta)_{t+\Delta t}}^{t+\Delta t}, \eta_{x_{t+\Delta t}}^{t+\Delta t}, x^{t+\Delta t}\} \leftarrow \text{RK4}(\mathcal{L}, \Phi_{(x^0, \eta_{x^0}^t)}^t, \eta_{x^0}^t, x^0);$            % Time stepping
4    $\{\eta_{x^0}^{t+\Delta t}\} \leftarrow \text{interp}(\eta_{x_{t+\Delta t}}^{t+\Delta t}, x^{t+\Delta t}, x^0);$            % Interpolate free surface elevation
5    $\{\Phi_{(x^0, \eta_{x^0}^{t+\Delta t})}^{t+\Delta t}\} \leftarrow \text{interp}(\Phi_{(x,\eta)_{t+\Delta t}}^{t+\Delta t}, x^{t+\Delta t}, x^0);$            % Interpolate velocity potential
6    $t := t + \Delta t$ 
7 end
Output:  $\{\Phi_{(x,\eta)^0}^0, \dots, \Phi_{(x^0, \eta^T)}^T\}, \{\eta_{x^0}^0, \dots, \eta_{x^0}^T\}, x^0$ 

```

4 NUMERICAL ACCURACY AND STABILITY

First, the accuracy of computing the vertical particle velocity is examined for different ranges of non-linearities. Next, the temporal stability is investigated and it is demonstrated how to improve the stability by means of a previously proposed method [18].

4.1 Accuracy

The spatial accuracy is illustrated by the relative error between vertical particle velocities, at the free surface, computed by stream function theory and the proposed model, respectively. The wave steepness (H/L), node density (ρ) and order of augmented polynomials (P) are varied, while the wave length $L = 2\pi$ is kept constant. The results are illustrated in figure 2 along with an example of the node set for the corresponding wave steepness. From figure 2, it is noticed that the convergence rate decreases as the wave steepness approaches the breaking limit.

4.2 Linear stability analysis

The purpose of the linear stability analysis is to investigate the temporal stability when different polynomials are used, and to test if instabilities can be removed. First, we express the linearized and semi-discrete counterpart of the system in (5) as

$$\frac{D}{Dt} \begin{bmatrix} x \\ \eta \\ \Phi \end{bmatrix} = \mathcal{J} \begin{bmatrix} x \\ \eta \\ \Phi \end{bmatrix} = \begin{bmatrix} \mathbf{0} & \mathbf{0} & \mathcal{L}_x \\ \mathbf{0} & \mathbf{0} & \mathcal{L}_z \\ \mathbf{0} & -g\mathcal{I} & \mathbf{0} \end{bmatrix} \begin{bmatrix} x \\ \eta \\ \Phi \end{bmatrix}, \quad (10)$$

where \mathcal{I} is the identity matrix and \mathcal{L}_z is derived from the relation

$$\mathbf{D}_z \Phi|_{x=r} = [(\mathbf{D}_z)_{11} \Phi_1 + (\mathbf{D}_z)_{12} \Phi_2] = [(\mathbf{D}_z)_{11} - (\mathbf{D}_z)_{12} \mathbf{L}_{22}^{-1} \mathbf{L}_{21}] \Phi_1 = \mathcal{L}_z \Phi_1, \quad (11)$$

where \mathbf{L} is the differential operator for the Laplace problem, introduced in section 2, \mathbf{D}_z is the differentiation matrix with respect to the vertical direction and the matrices are decomposed as

$$\mathbf{L} = \begin{bmatrix} \mathbf{L}_{11} & \mathbf{L}_{12} \\ \mathbf{L}_{21} & \mathbf{L}_{22} \end{bmatrix}, \quad (12)$$

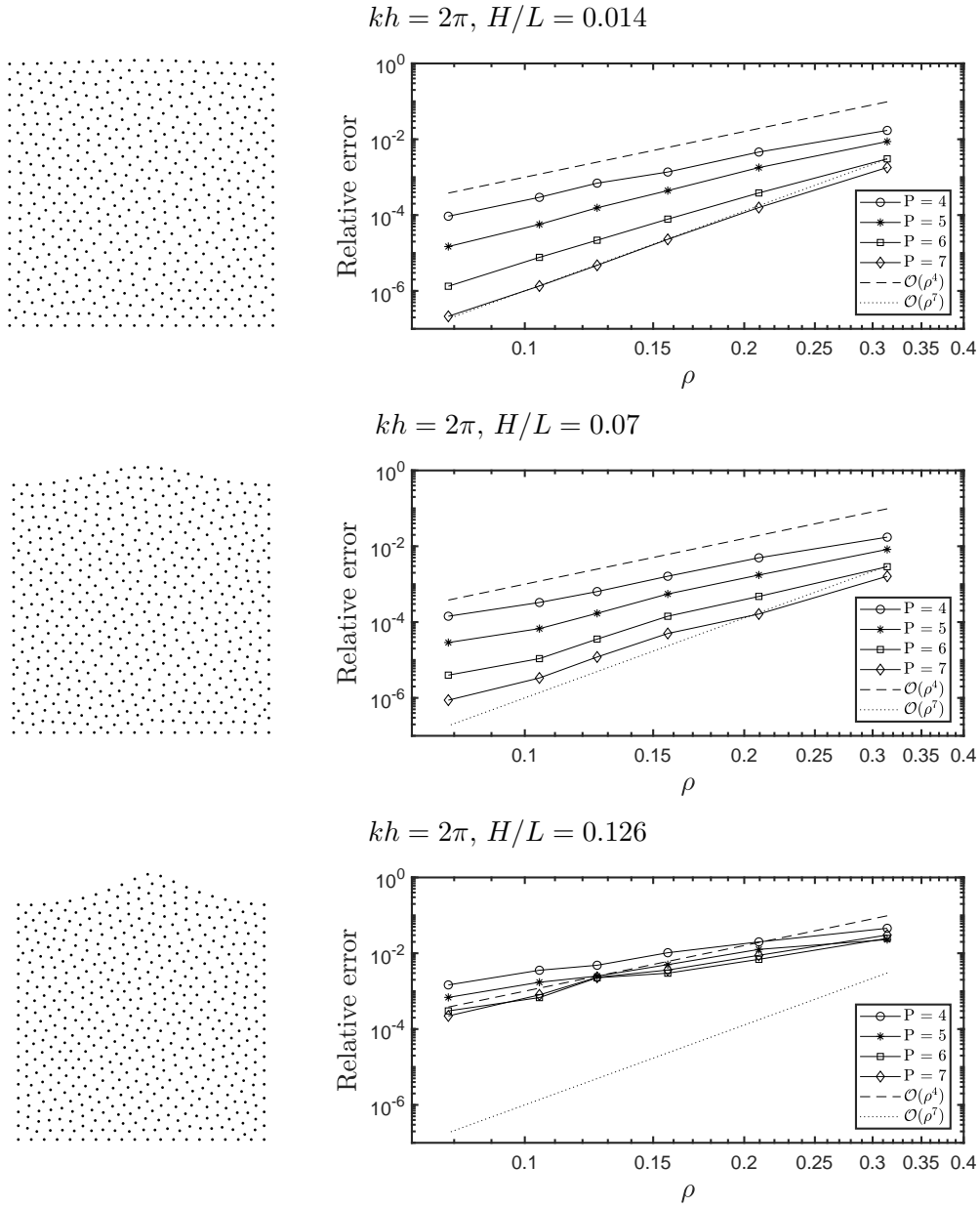


Figure 2: Convergence plots of the relative error computing $\frac{\partial \Phi}{\partial z}$ at the free surface for different H/L ratios and augmented polynomials, while using a node density approximately equal to ρ .

where the subscript indices define whether the nodes are on the free surface (1) or not (2). \mathcal{L}_x is computed in a similar manner as in equation (11). Eigenspectra of the system in equation (10) are illustrated in figure 3.a, where a quasi-uniform node set has been used and also different orders of augmented polynomials. As noticed, the eigenvalues in figure 3.a has positive real parts, which leads to temporal instability. However, as described in e.g. [18], convective PDEs

may be stabilized by adding a slight amount of artificial dissipation, known as hyperviscosity. In this work, a third order Laplacian is used along with a tuning parameter γ , which depends on the discretization used. The effect of adding hyperviscosity to the free surface elevation and velocity potential, in equation (10), is illustrated in figure 3.b. Here $\gamma = 6 \cdot 10^{-6}$ has been used for all cases, although a more suitable choice exist for each individual discretization.

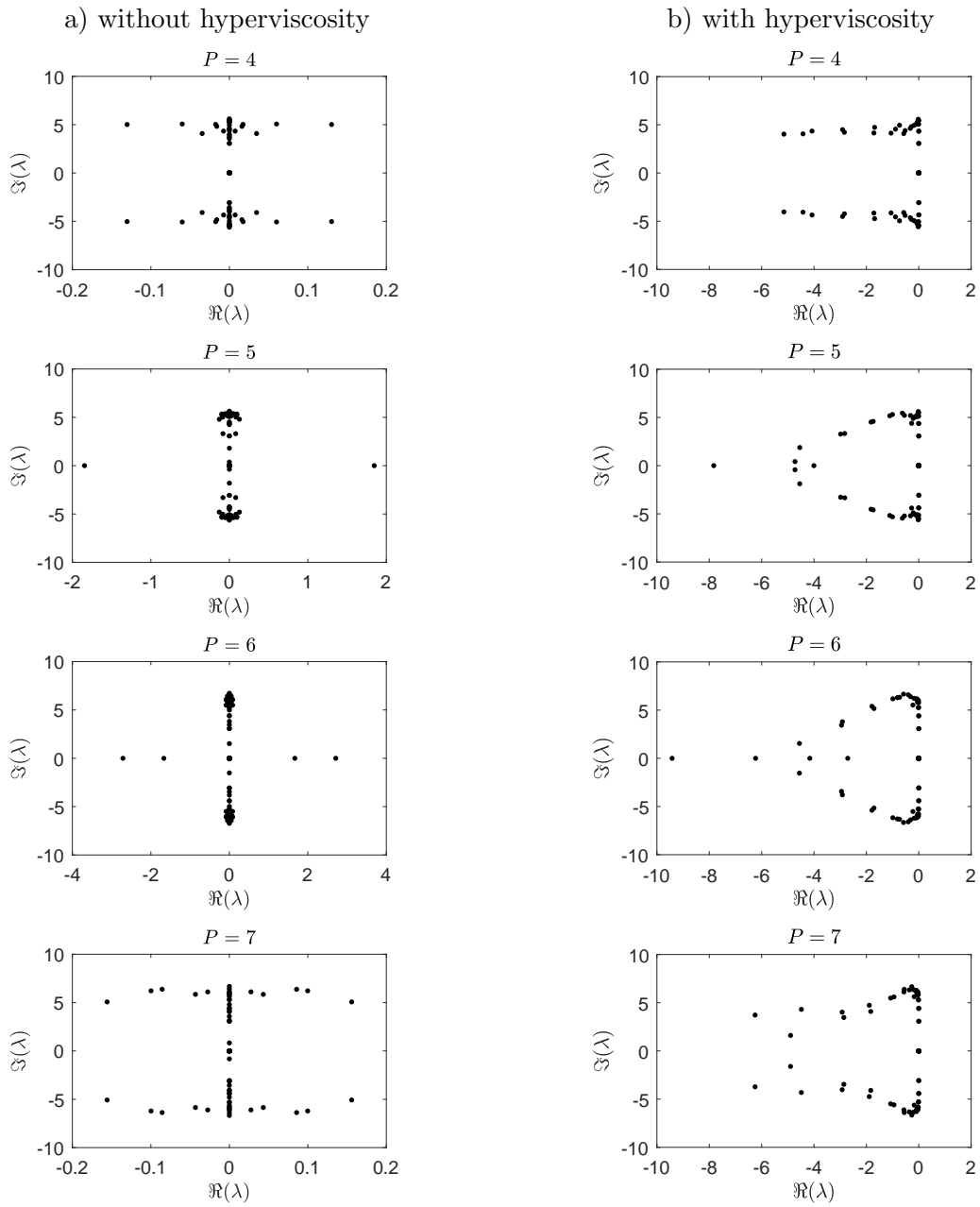


Figure 3: Eigenspectra of \mathcal{J} in equation (10) using a quasi-uniform node set and augmented by up to the P th order polynomial.

5 RESULTS

Stream function waves of varying steepness are used as benchmark for the non-linear stability and accuracy. Each case is simulated for five periods with the time step $\Delta t = 0.025s \approx T/80$, where T is the wave period. The maximum relative errors between the stream function solution and proposed model are shown in figure 4. For each discretization, a suitable γ -value is determined by linear stability analyses.

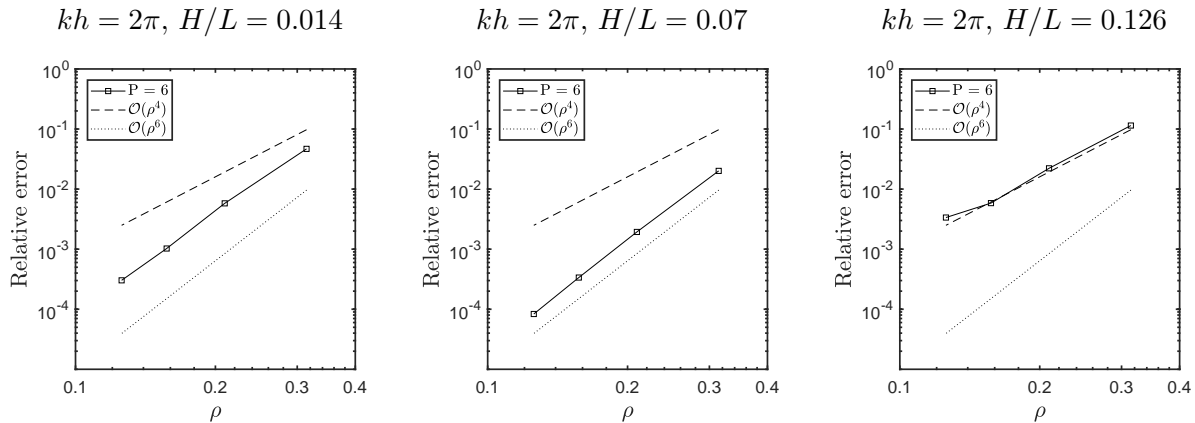


Figure 4: Convergence plots showing the relative error of the free surface elevation after five periods when using a 7th order polyharmonic spline augmented by up to 6th order polynomials.

Once again, it is noticed that the convergence rate tend to decrease as the wave steepness increase. As expected, it drops to the same convergence rate that was noticed in figure 2. However, as quasi-uniform nodes were used, it can be expected that node refinement near the free surface will improve the accuracy without increasing the total number of nodes used.

6 CONCLUSIONS

A novel computational model for non-linear water waves is introduced and the methodology outlined. The main novelty is the application of RBF-FD, which provide high-order approximations along with geometric flexibility for the moving free surface. Additionally, a modification of a previously developed node generation strategy is introduced, such that the computational domain is updated as the boundaries evolve over time. Finally, it is shown that stability can be achieved by adding hyperviscosity to the problem without influencing the convergence rate.

REFERENCES

- [1] DeRisk, <http://www.derisk.dk>, [Online; accessed 11-February-2019] (2015).
- [2] MIDWEST, <https://project.inria.fr/midwest/>, [Online; accessed 11-February-2019] (2016).
- [3] CCP-WSI, <https://www.ccp-wsi.ac.uk/>, [Online; accessed 11-February-2019] (2016).

- [4] A. P. Engsig-Karup, H. B. Bingham, O. Lindberg, An efficient flexible-order model for 3D nonlinear water waves, *Journal of Computational Physics* 228 (6) (2009) 2100–2118.
- [5] G. Wu, R. E. Taylor, Finite element analysis of two-dimensional non-linear transient water waves, *Applied Ocean Research* 16 (6) (1994) 363–372.
- [6] D. G. Dommermuth, D. K. Yue, A high-order spectral method for the study of nonlinear gravity waves, *Journal of Fluid Mechanics* 184 (1987) 267–288.
- [7] I. Robertson, S. Sherwin, Free-surface flow simulation using hp/spectral elements, *Journal of Computational Physics* 155 (1) (1999) 26–53.
- [8] S. Yan, Q. Ma, Qale-fem for modelling 3D overturning waves, *International Journal for Numerical Methods in Fluids* 63 (6) (2010) 743–768.
- [9] S. T. Grilli, P. Guyenne, F. Dias, A fully non-linear model for three-dimensional overturning waves over an arbitrary bottom, *International Journal for Numerical Methods in Fluids* 35 (7) (2001) 829–867.
- [10] A. P. Engsig-Karup, C. Eskilsson, D. Bigoni, A stabilised nodal spectral element method for fully nonlinear water waves, *Journal of Computational Physics* 318 (2016) 1–21.
- [11] C. M. Sanchez, A. P. Engsig-Karup, C. Eskilsson, Nonlinear wave-body interaction using a mixed-eulerian-lagrangian spectral element model, in: *37th International Conference on Ocean, Offshore and Arctic Engineering (OMAE2018)*, 2018.
- [12] M. E. Nielsen, M. D. Ulriksen, L. Damkilde, SOFIA - A simulation tool for bottom founded and floating offshore structures, *Procedia engineering* 199 (2017) 1308–1313.
- [13] M. D. Ulriksen, D. Bernal, M. E. Nielsen, L. Damkilde, Damage localization in offshore structures using shaped inputs, *Procedia engineering* 199 (2017) 2282–2287.
- [14] V. Bayona, N. Flyer, B. Fornberg, G. A. Barnett, On the role of polynomials in RBF-FD approximations: II. Numerical solution of elliptic PDEs, *Journal of Computational Physics* 332 (2017) 257–273.
- [15] N. Flyer, G. A. Barnett, L. J. Wicker, Enhancing finite differences with Radial Basis Functions: Experiments on the Navier–Stokes equations, *Journal of Computational Physics* 316 (2016) 39–62.
- [16] B. Fornberg, N. Flyer, Solving PDEs with Radial Basis Functions, *Acta Numerica* 24 (2015) 215–258.
- [17] B. Fornberg, N. Flyer, Fast generation of 2-D node distributions for mesh-free PDE discretizations, *Computers and Mathematics with Applications* 7 (69) (2015) 531–544.
- [18] B. Fornberg, E. Lehto, Stabilization of RBF-generated finite difference methods for convective PDEs, *Journal of Computational Physics* 230 (6) (2011) 2270–2285.

APPLICATION OF A COUPLED LEVEL SET AND VOLUME OF FLUID METHOD FOR UNSTEADY SIMULATIONS WITH AN UNSTRUCTURED FLOW SOLVER

Benoît É. LeBlanc^{*†}, Christiaan M. Klaij[†], Hamn-Ching Chen[‡], and Andrew G. Gerber^{*}

^{*} Dept. of Mechanical Engineering
University of New Brunswick
15 Dineen Dr., E3B 5A3 Fredericton, Canada
e-mail: bleblan9@unb.ca, web page: <http://www.unb.ca/>

[†] Maritime Research Institute Netherlands (MARIN)
Haagsteeg 2, 6708 PM Wageningen, Netherlands
e-mail: info@marin.nl - web page: <http://www.marin.nl/>

[‡] Zachry Dept. of Civil Engineering
Texas A&M University
College Station, TX 77843-3136, USA
e-mail: easa@tamu.edu - web page: <http://engineering.tamu.edu/>

Key words: Computational Methods, Free Surface, Volume-of-Fluid, Level Set.

Abstract. In this paper, a Coupled Level Set and Volume of Fluid surface capturing method is evaluated alongside the standard Volume of Fluid method against experimental data, using the breaking dam benchmark test case. Results are obtained for simulations on three geometrically similar cartesian meshes for both methods, measuring kinematic and dynamic characteristics of the flow, including arrival time, water front velocity, water heights, impact pressures and rise times. Both methods can predict the kinematics of the initial impact within the interval of experimental data, however, results from both methods show some spreading away from experimental data for the dynamic characteristics of the flow. The coupled method gives better control over the free surface interface thickness, while both methods show the ability to conserve initial water volume. The coupled method must however use a non conservative formulation of the momentum equations for stability.

1 INTRODUCTION

A free surface capturing method for unsteady flows between air and water has been developed for marine applications using a coupled approach, combining the Volume of Fluid (VOF) method^[1] with the Level Set (LS) method^{[2][3]}. The Coupled Level Set and Volume of Fluid method (CLSVOF) method was previously developed^{[4][5]} as an attempt to overcome the difficulties associated with either method. Previous implementations of the method were applied to fully structured unsteady flow solvers^[4]. This study focuses on further development of the algorithm for use in unstructured flow solvers.

Since free surface flows between water and air are characterized by a large density ratio and a very sharp interface transition, this poses significant challenges to their numerical modeling using unsteady

flow solvers. In LS methods, the interface sharpness is controlled to mitigate effects of this transition^[2], whereas in VOF methods, sharpening advection schemes are applied to the transport equation of the free surface marker variable. A tight coupling between the advected free surface marker variable and the momentum equation must be kept with VOF methods to achieve stability^[6]. Drawbacks of the methods are that the pure LS method must include a redistancing step, which brings the density out of phase with the advected momentum, causing fluctuation in total water/air volume^[4], whereas the VOF method needs to resort to compressive advection schemes or interface reconstruction in the advected variable to retain interface sharpness, which still suffer from interface spreading and stability issues. A coupled method is thus designed to mitigate these drawbacks to conserve total water/air volume, while keeping a sharp interface transition which does not depend on an elaborate advection scheme. When the redistancing algorithm is applied to unstructured grids however, the robustness of the discretized redistancing equation also becomes an issue, as a result of the level set gradient calculation^[7]. The gradient calculation is normally done using traditional means such as least-squares or Gauss, however the redistancing equation contains an absolute value function, whose sharpness conflicts with the traditional gradient calculation methods.

In this study, a version of the CLSVOF algorithm has been modified to operate in the fully unstructured solver ReFRESKO (www.refresco.org), developed by MARIN and collaborating universities, for marine applications. ReFRESKO uses SIMPLE-type solvers for the coupled mass and momentum equations^[8]. An unstructured redistancing algorithm was developed and applied to provide the level set solution inside the coupled method, and a non-conservative (or velocity based) formulation of the momentum equation was found to be necessary for stability reasons discussed in Section 2.

The coupled method was then applied to an unsteady flow problems with coupling to pressure and momentum, the Martin and Moyce breaking dam problem^[10]. The problem provides a benchmark for the kinematics and impact dynamics of the free surface method. The coupled method, which uses a non-conservative momentum equation, is compared to a VOF method using both a conservative momentum formulation and a non-conservative formulation in Section 3. Solutions are also compared with experimental data from Lobovsky^[11], showing a difference in the results between all three methods attempted, and permitting to highlight strengths and weaknesses of either approach. Conclusions are drawn in Section 4.

2 COUPLED LEVEL SET AND VOLUME OF FLUID

The CLSVOF method is built upon the Navier-Stokes equations. In this study, we consider the momentum equations either in conservative or in non-conservative form. The conservative form is given by:

$$\frac{\partial \rho \mathbf{u}}{\partial t} + \nabla \cdot (\rho \mathbf{u} \otimes \mathbf{u}) = \nabla \cdot (2\mu \bar{\mathbf{s}}) - \nabla p + \rho \mathbf{g} \quad . \quad (1)$$

with ρ the density, \mathbf{u} the velocity vector, μ the dynamic viscosity, $\bar{\mathbf{s}}$ the rate of strain tensor, p the pressure and \mathbf{g} the gravitational acceleration vector. Furthermore, we consider incompressible flow, so that the mass equation reduces to

$$\nabla \cdot \mathbf{u} = 0 \quad . \quad (2)$$

Using this equation, the momentum equations can be recast into non-conservative form

$$\frac{\partial \mathbf{u}}{\partial t} + \nabla \cdot (\mathbf{u} \otimes \mathbf{u}) = \nabla \cdot (2\nu \bar{\mathbf{s}}) - \frac{\nabla p}{\rho} + \mathbf{g} \quad . \quad (3)$$

with $\nu = \mu/\rho$. In the context of free-surface flows, this non-conservative form has the advantage that the density, which is discontinuous at the interface between air and water, is removed from the convective term, making its discretization less sensitive. Momentum, however, is only conserved in the asymptotic range of grid refinement. The density and viscosity are variable and follow a marker field which is advected with the fluid velocity \mathbf{u} . In the case of VOF, it is the volume fraction field c , while the level set function ϕ is used in the case of LS:

$$\frac{\partial c}{\partial t} + \mathbf{u} \cdot \nabla c = 0 \quad (\text{VOF}) \quad \text{or} \quad \frac{\partial \phi}{\partial t} + \mathbf{u} \cdot \nabla(\phi) = 0 \quad (\text{LS}) \quad . \quad (4)$$

The mass and momentum equations are coupled to the volume fraction or level-set function through the material properties as follows.

For the VOF case, the volume fraction c takes the value of 0 or 1 to indicate water or air, respectively, and varies sharply at the interface. The density and viscosity are given by

$$\rho = c \rho_{\text{air}} + (1 - c) \rho_{\text{water}} \quad \text{and} \quad \mu = c \mu_{\text{air}} + (1 - c) \mu_{\text{water}} \quad , \quad (5)$$

where μ is replaced by ν in the case of the non-conservative formulation (3). A compressive interface-capturing scheme called ReFRICS is used to maintain the sharpness of the interface. This scheme, together with all other details of the discretization and solver for mass, momentum and volume fraction can be found in Ref. [6].

For the LS case, the ϕ field represents a signed distance function from the interface, so the magnitude of its gradient must be unity throughout the field ($|\nabla\phi| = 1$). The relation between ϕ and the material properties are determined via a Heaviside function. In practice, a mollified Heaviside function is used, to smoothen the transition at the interface. In this study, a mollified Heaviside based on a sinusoidal function was used, based on a previous implementation^[4]. The relation is given by

$$\begin{bmatrix} \rho \\ \nu \end{bmatrix} = H(\phi) \begin{bmatrix} \rho_1 \\ \nu_1 \end{bmatrix} + H(-\phi) \begin{bmatrix} \rho_2 \\ \nu_2 \end{bmatrix}, \quad H(\phi) = \begin{cases} 0 & \text{if } \phi < -\varepsilon \\ \frac{1}{2} \frac{(1+\phi)}{\varepsilon} + \frac{1}{2\pi} \sin\left(\frac{\pi\phi}{\varepsilon}\right) & \text{if } -\varepsilon \leq \phi < \varepsilon \\ 1 & \text{if } \varepsilon \leq \phi \end{cases} \quad (6)$$

where ε represents a user prescribed width over which the transition of properties occurs at the interface. In practice, the differential equations must be supplemented by a redistancing equation^[3], which enforces the property of unity gradient ($|\nabla\phi| = 1$). For the CLSVOF method, this property is enforced by explicit integration of the redistancing equation in pseudo time τ ,

$$\frac{\partial \phi}{\partial \tau} = \text{sgn}(c - 0.5) (1 - |\nabla\phi|) \quad , \quad (7)$$

using a forward Euler method, for a small but sufficient number of steps to cover the prescribed interface width. The advection of the ϕ does not require any special advection schemes, and so a standard second order harmonic upwind scheme is used in this case. Both the VOF method and the CLSVOF method are illustrated in the flowchart of Figure 1.

Solving with the CLSVOF method on unstructured grids requires the use of an alternate method for gradient calculation, due to the abruptness of gradient direction change, which is a characteristic of the level set distance field near the interface. Since the level set distance field takes the form of an absolute

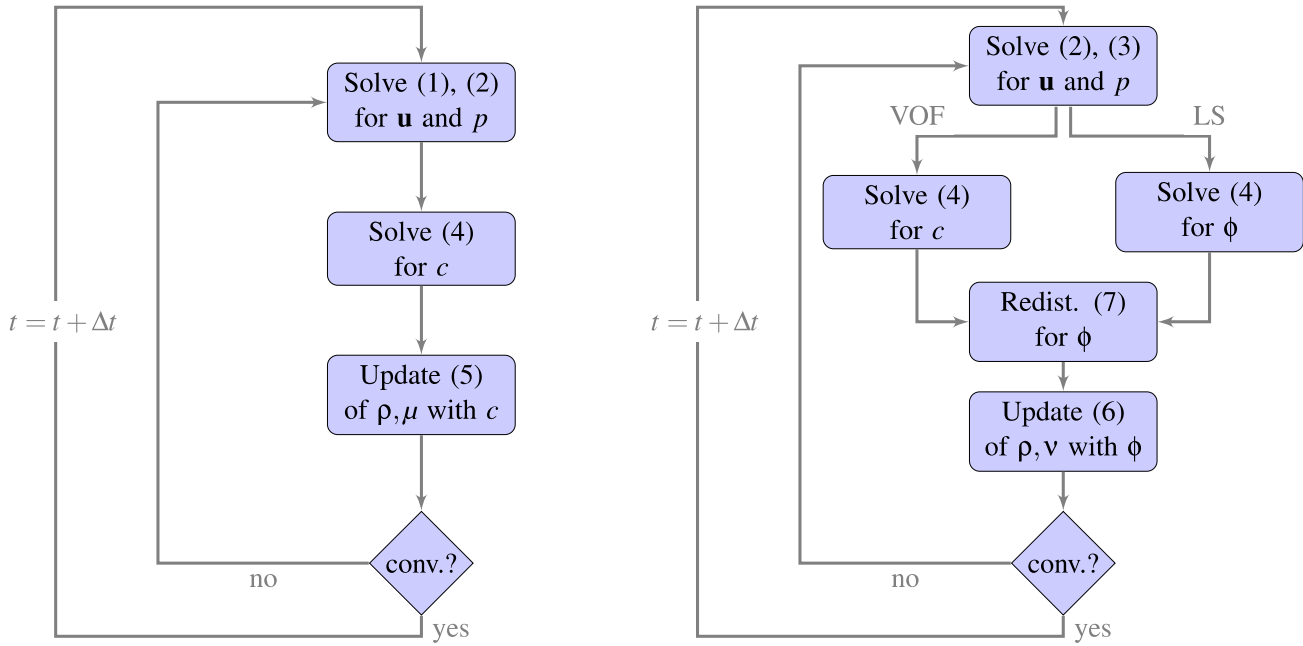


Figure 1: Simplified flowchart of the algorithm for the VOF method (left) and the CLSVOF method (right).

value function at the interface, more common gradient calculation techniques such as Gauss or Least Squares prove insufficient at directing the gradient in the proper direction near the interface or at peaks or valleys of the level set field, regardless of grid density at the surface^[7]. To overcome this challenge, a so-called Flux-Positive (FP) gradient calculation method was used, which is based on the Gaussian method but using only the adjacent contributions which have a positive flux. It consists of two passes, one which calculates a standard Gaussian integral, followed by a second pass which uses information from the previous Gaussian to exclude certain contributions. The method is given by equation (8) (subscripts c and f stand for cell center and cell face, respectively),

$$\nabla\phi_c = \frac{1}{V_c} \sum_{f \in \text{nb}} \phi_f \mathbf{S}_f, \quad \nabla\phi_{\text{FP}} = \frac{1}{V_c} \sum_{f \in \text{nb}} (\min\{0, \nabla\phi_f \cdot \mathbf{n}_f\} \phi_f \mathbf{S}_f) \quad , \quad (8)$$

with $\mathbf{S}_f = |S_f| \mathbf{n}_f$ the face vector and $\nabla\phi_f$ the geometric interpolation of $\nabla\phi_c$ from the first pass. The unstructured CLSVOF method further makes use of corrections at the cells which are intersected by the interface, using an explicit distance extrapolation to obtain values for ϕ in cells where the gradient cannot be calculated. These corrections are described in detail in Ref. [7].

Remark. We found that only the non-conservative formulation of the momentum equations (3) could be used for the CLSVOF method. Our attempts with the conservative formulation (1) were not successful. A possible explanation is found in Section 3.10 of Ref. [9]: in the conservative case, the advection scheme for density must be consistent with the advection scheme for momentum. This is the case for the VOF method, where the density follows directly from the advection (4) of the volume fraction. For the CLSVOF method, however, the density follows from the advected *and redistanced* level-set function.

Table 1: General properties of geometry used

| Grid Size | Δt (s) | Max CFL (theo.) | N cells | $\epsilon_{015}/\Delta x$ | $\epsilon_{03}/\Delta x$ |
|---------------------------------|----------------|-----------------|---------|---------------------------|--------------------------|
| G2 - $113 \times 88 \times 10$ | 0.0004 | 0.1 | 111k | 2.11 | 4.23 |
| G3 - $130 \times 111 \times 13$ | 0.000315 | 0.1 | 205k | 2.66 | 5.32 |
| G4 - $180 \times 140 \times 16$ | 0.00025 | 0.1 | 434k | 3.35 | 6.71 |
| G5 - $227 \times 176 \times 20$ | 0.0002 | 0.1 | 852k | 4.23 | 8.45 |

Whether this is indeed the cause of the observed problems remains to be confirmed.

3 RESULTS

The CLSVOF method has been applied to the free surface breaking dam test case, which serves as a benchmark for feasibility and validation of the kinematics and dynamics of the flow^{[10][11]}. The case is a column of water of height H and width L initially at rest by a sliding gate in a rectangular tank with walls all around. In the experimental setup, the column of water is released at $t = 0$, followed by a fall of the column height and an impact on the far wall.

For the kinematics, the measured variables are the advancing front velocity and the time of impact after release. The heights of water at various points through the domain over time are also measured. The time, height, and advancing front position are all nondimensionalized following Martin^[10], to be $T = t\sqrt{2g/L}$, $H^* = h/H$, $X^* = x/L$, respectively. As for the dynamic variables, the impact pressure is measured at a point on the far wall, as a function of time, and nondimensionalized by the initial maximum pressure in the column (at the deepest point), $P^* = P/\rho gh$.

The computations are done on a Cartesian mesh with wall boundary conditions on all sides and on the bottom, and a pressure condition on the top surface. The top is extended with regards to the experimental case to ease the pressure boundary condition and to prevent the boundary condition to affect the distribution of pressure in the water phase. Note that the solver treats these meshes as if they were unstructured. Tetrahedral meshes were also attempted but these require more cells and showed some stability issues with the redistancing algorithm.

The computation was done for four cases using four geometrically similar meshes. The four cases were: two with a pure VOF model formulation as implemented in ReFRESKO^[6] (one with non-conservative formulation of momentum, and the other with conservative), and two using the CLSVOF model as described in this study, while varying interface width. The simulation was run up until just after the first impact on the opposite wall, accompanied by a pressure peak.

The grids are numbered from G2 to G5, and time step information for the simulations ran can be found in Table 1, including max CFL number, total number N of cells, and interface width in number of cells, for both $\epsilon = 0.015m$ and $\epsilon = 0.03m$. The maximum CFL number is taken from the maximum velocity attained in the run-up to the far wall. It was estimated as being close to 0.1 before the tests, and the real calculated values are given in Table 2.

The convergence criterion was set to 10^{-7} in the L_{inf} norm for the equations of momentum/velocity, mass, and volume fraction, while the error for the level-set transport equation relies on the explicit time-stepping redistancing equation (7) used in the method. For the redistancing equation, 5 pseudo-time steps were used, with a time step size of $\epsilon/5$. Other values were tested but it was found that 5 was sufficient

Table 2: Max CFL Number (real) during run-up

| CFD | VOF | | CLSVOF | |
|-----|--------|----------|------------------------|-----------------------|
| | cons. | noncons. | $\varepsilon = 0.015m$ | $\varepsilon = 0.03m$ |
| G2 | 0.0876 | 0.0907 | 0.0968 | 0.0874 |
| G3 | 0.0871 | 0.0873 | 0.0951 | 0.0856 |
| G4 | 0.0873 | 0.0903 | 0.0964 | 0.0888 |
| G5 | 0.0896 | 0.0868 | 0.0967 | - |

Table 3: Arrival time $T = t\sqrt{2g/L}$ of water on far wall

| CFD | VOF | | CLSVOF | | Exp. Lobovsky |
|-----|-------|----------|------------------------|-----------------------|-------------------------------------|
| | cons. | noncons. | $\varepsilon = 0.015m$ | $\varepsilon = 0.03m$ | |
| G2 | 2.408 | 2.571 | 2.566 | 2.513 | 2.573 |
| G3 | 2.431 | 2.610 | 2.641 | 2.570 | All Studies ^{[12][11][10]} |
| G4 | 2.402 | 2.542 | 2.562 | 2.508 | 2.358-2.894 |
| G5 | 2.401 | 2.55 | 2.522 | - | |

for the redistancing equation to span the interface width.

3.1 Kinematics of the run-up

The arrival time for the different cases on G2 to G5 are given in Table 3, with experimental data from Lobovsky^[11], Dressler^[12], and Martin^[10], displayed as well for comparison. The data from Lobovsky is highlighted since it shows the most recent data and the most thorough statistical study.

Table 4 also shows the peak velocities measured from the same cases in comparison with the same experimental data sets.

The resulting kinematics of the flow show that, with grid refinement, the values for the arrival time and peak velocity do not seem to converge to a single asymptotic value with grid convergence. Though the results for both measured variables fall within the experimental range, the coupled CLSVOF showed to cause problems when the chosen interface width was too large (8.45 cells). This occurred only for the

Table 4: Peak Velocity X^*/T of the advancing water front

| CFD | VOF | | CLSVOF | | Exp. Lobovsky ^[11] |
|-----------|-------|----------|------------------------|-----------------------|-------------------------------------|
| | cons. | noncons. | $\varepsilon = 0.015m$ | $\varepsilon = 0.03m$ | |
| G2 CFL0.1 | 1.715 | 1.649 | 1.652 | 1.709 | 1.56 |
| G3 CFL0.1 | 1.826 | 1.558 | 1.532 | 1.591 | All Studies ^{[12][11][10]} |
| G4 CFL0.1 | 1.827 | 1.684 | 1.655 | 1.712 | 1.33-1.74 |
| G5 CFL0.1 | 1.824 | 1.662 | 1.688 | - | |

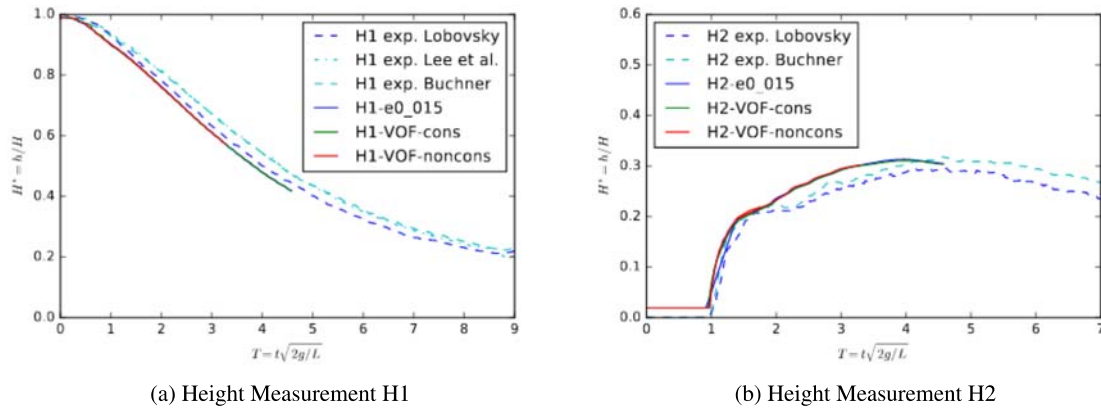


Figure 2: Plots of water height measurements throughout the domain, with respect to time, dimensionless.

case of $\varepsilon = 0.03m$, with Grid 5. This agrees with the findings of Chen^[4].

The water heights throughout the domain for all three simulated models, visible in Figure 2, show very close results with one another, and follow more closely the results of the more recent experimental data from Lobovsky^[11]. It is to be noted that the initial peak visible in the experimental results of Lee^[13] and Buchner^[14] of H3 and H4 has been attributed to the effects of starting without a completely dry bed in the bottom of the tank.

The conservation of water volume has also been observed for the cases, since the purpose of the coupled method is to leverage the advantage of VOF when it comes to mass conservation. The water mass loss/gain plot can be found in Figure 4. The largest mass change for CLSVOF is of the order of 0.00004%, which should not influence the results. This was accompanied by an interface width which was controlled by the redistancing algorithm, even long after the initial impact, as can be seen in Figure 3.

3.2 Dynamics of the impact

The impact values of the breaking dam case have also been measured from the simulations, for comparison with experimental data available. The values measured were the impact pressure at the location of impact (in the lower corner of the domain where the water column initially hits).

The values to be measured were the nondimensionalized impact pressure P and impact rise time, RT . The rise time represents the time window in which the pressure at the impact location goes from zero to its peak value, P_{\max} . In practice, the rise time is approximated by twice the time it takes to get from $P_{\max}/2$ to P_{\max} .

The pressure profiles for the different models, shown in Figure 5, show some discrepancy with experimental results, particularly in the shape of the peak.

The impacts from the simulations show less abrupt slopes, and a smoother drop-off from the peak pressure values can be observed. The conservative VOF model seems to show the slowest impact, whereas the non-conservative VOF model appears to display some more pronounced oscillatory or elastic effects in the results of the pressure peaks, having two very distinct peaks.

Both the experimental results and the CLSVOF model, however, show an initial peak, followed by an

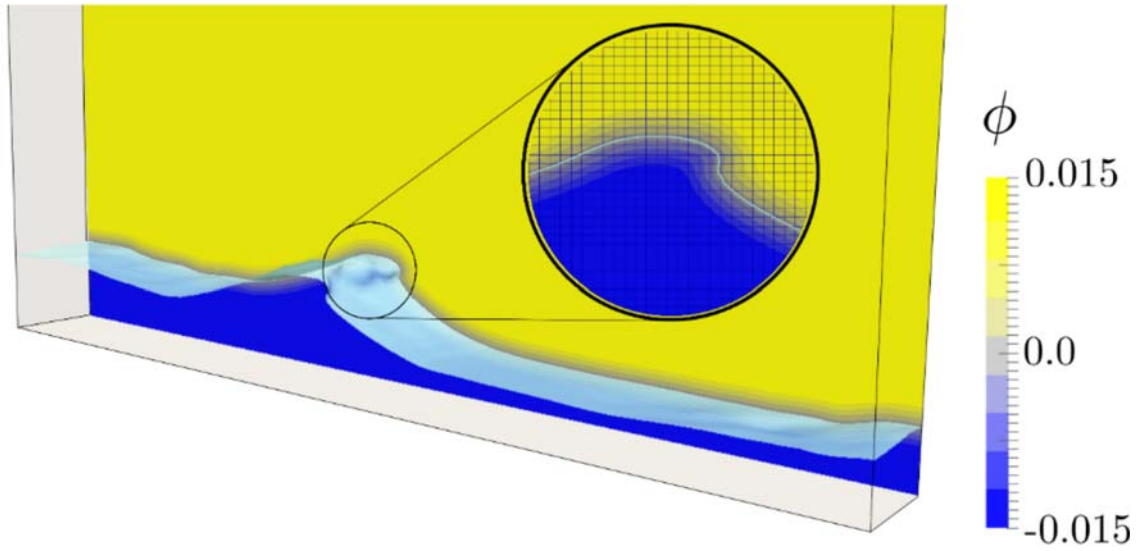


Figure 3: Impression of the free surface and interface width using CLSVOF on G4, after back and forth sloshing, $T = 15.72$. Zoomed view of the slice on the back wall, to see the interface thickness with the cell size. The interface at $\phi = 0$ can be seen in light blue.

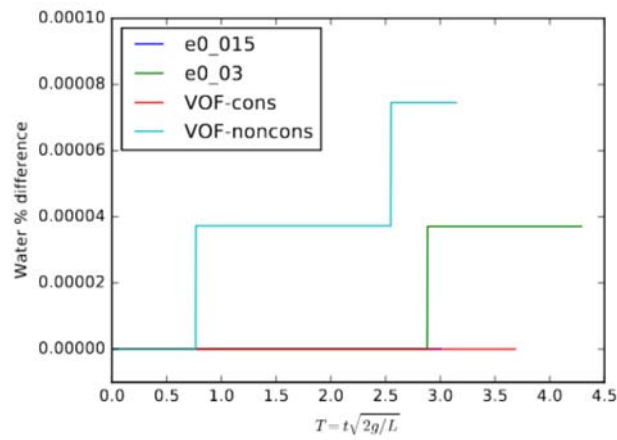


Figure 4: Conservation of water volume in percentage of total initial water volume. Results are shown for G4 with all methods.

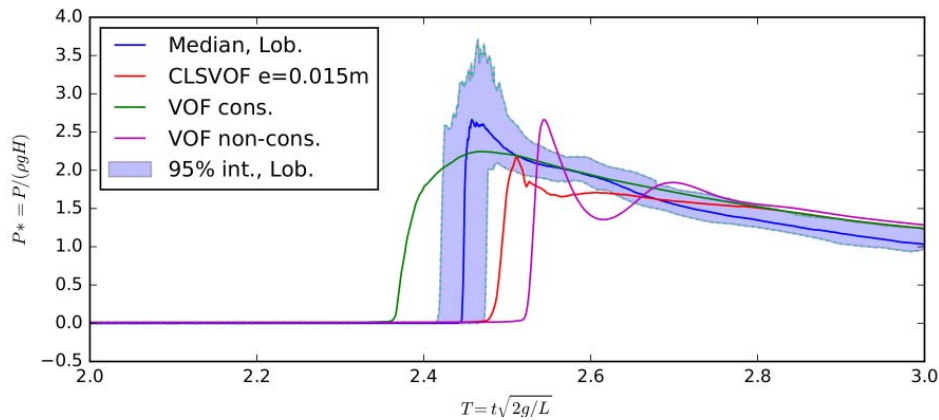


Figure 5: Pressure peaks from breaking dam impact for three methods, VOF (both conservative and non-conservative) and CLSVOF (non-conservative, $\varepsilon = 0.015m$), with the median and the 95% confidence interval from Lobovsky^[11] indicated in blue and light blue, respectively. Simulation results are from G4.

inflection point and, for the case of the CLSVOF model, a second and much less pronounced peak.

The impact rise time were plotted in a scatter plot against those from experiment, using the different grids. They can be seen in the Figure 6. A more precise look at the peak characteristics, from the scatter plot of Figure 6 gives a larger demarcation between the sharpness of the peaks. The grid refinement for the three cases unfortunately does not show a clear convergence of the rise time or pressure peak against grid refinement. There is however a tendency for the results to approach the experimental range, represented by the blue dots.

Surprisingly, the non-conservative VOF case seems to show the most accurate results in terms of rise time and peak pressure, even if the profile of the pressure over time shows a different behavior than in experiment. The conservative VOF case consistently showed the slowest rise time of all three models, while the CLSVOF case showed results just shy of the experimental range.

With the conservative VOF method, the interface on the advancing front (not shown here) is significantly smeared directly before the impact. This may explain the dampened impact and higher rise time for the VOF conservative case, since the momentum $\rho\mathbf{u}$ varies strongly across the smeared interface.

4 CONCLUSIONS

Results were obtained on a breaking dam case using a Coupled Level Set and Volume of Fluid method, on an unstructured solver. Application of the original model required corrections to the redistancing equation, such as a distance gradient correction, as well as an interpolation and an extrapolation correction, to ensure the functionality of the model on benchmark test cases.

The use of a non-conservative form for the momentum equations raises questions about the implications of this assumption on the results, especially with regards to the rise time for peak pressures. Unfortunately not much literature has been found on the comparison between the two for free surface applications. This remains an open question, since the non-conservative VOF and conservative VOF methods showed some variation in qualitative results for the impact.

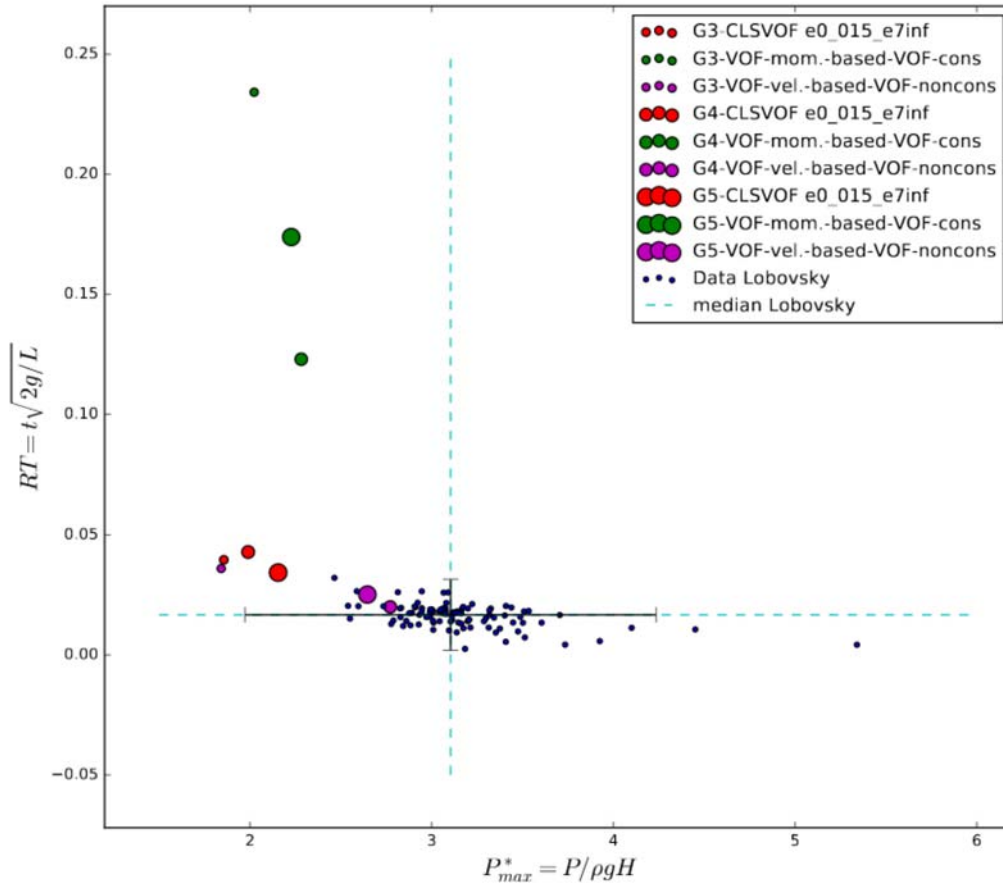


Figure 6: Pressure peaks from breaking dam impact for three methods, VOF (both conservative and non-conservative) and CLSVOF (non-conservative, $\varepsilon = 0.015m$), on G4. Experimental results from Lobovsky^[11] indicated in blue, with bars for 95% confidence interval.

The breaking dam test case has also shown some sensitivity of the CLSVOF model to grid sizing, in particular due to the physics of the transition, which seem to hinge on the number of cells over which the transition occurs. This complicates the standard application of a grid study, since it may require changing the interface width (i.e. changing the physics of the problem) whilst refining or coarsening the grid. Future studies with CLSVOF would have to look at modifying interface width in relation to grid size for comparison. Further study of the redistancing algorithm could also be useful, notably of the corrections used in the present implementation for more challenging unstructured grids.

The CLSVOF model however seems to show an ability to give sloshing impact peak pressure values within the confidence interval of experimental results, all the while ensuring water volume conservation. Most importantly, it does so while succeeding in keeping the interface sharp, which is a desirable characteristic for any free surface applications with folding interfaces, and which is an area where VOF methods traditionally have more difficulty. This suggests that the CLSVOF model could show an interesting avenue for exploration in the case of some sloshing applications where other methods fall short.

5 ACKNOWLEDGEMENTS

This research is partly funded by the Dutch Ministry of Economic Affairs.

REFERENCES

- [1] Hirt, C. W.; Nichols, B. Volume of fluid method for the dynamics of free boundaries. *J. Comput. Phys.*, **39**(1), 201–225, (1981).
- [2] Sethian, J. A. *Level Set methods and fast marching methods: evolving interfaces in computational geometry, fluid mechanics, computer vision, and materials science (Vol. 3)*, Camb. U. Press, (1999).
- [3] Sussman, M.; Smereka, P.; Osher, S. A level set approach for computing solutions to incompressible two-phase flow. *J. Comput. Phys.*, **114**(1), 146–159, (1994).
- [4] Chen, H.-C. CFD simulation of compressible two-phase sloshing flow in a LNG tank. *Ocean Sys. Eng.*, **1**(1), 31–57, (2011).
- [5] Wang, Z.; Yang, J.; Koo, B.; Stern, F. A coupled level set and volume-of-fluid method for sharp interface simulation of plunging breaking waves. *International Journal of Multiphase Flow*, **35**(3), 227–246, (2009).
- [6] Klaij, C. M.; Hoekstra, M.; Vaz, G. Design, analysis and verification of a volume-of-fluid model with interface-capturing scheme. *Comput. Fluids*, **170**, 324–340, (2018).
- [7] LeBlanc, B. É.; Chen, H.-C.; Klaij, C. M. Evaluation of a coupled Level Set and Volume of Fluid Method for Unstructured Meshes. *Num. Towing Tank Symposium*, (2018).
- [8] Klaij, C. M.; Vuik, C. SIMPLE-type preconditioners for cell-centered, colocated finite volume discretization of incompressible Reynolds-averaged NavierStokes equations. *Int. J. for Num. Methods in Fluids*, **17**, 830–849, (2013).
- [9] Tryggvason, G. *Direct Numerical Simulations of Gas-Liquid Multiphase Flows*, Camb. U. Press, (2011).
- [10] Martin, J. C.; Moyce, W. J. An experimental study of the collapse of liquid columns on a rigid horizontal plane. *Phil. Trans. R. Soc. Lond. A*, **244**(882), 312–324, (1952).
- [11] Lobovský, L.; Botia-Vera, E.; Castellana, F.; Mas-Soler, J.; Souto-Iglesias, A. Experimental investigation of dynamic pressure loads during dam break. *J. Fluids Struct.*, **48**, 407–434, (2014)

- [12] Dressler, R. F. Comparison of theories and experiments for the hydraulic dam-break wave. *Int. Ass. Sci. Hydrol. Publi.* , **38**(3), 319-328, (1954).
- [13] Lee, T.; Zhou, Z.; Cao, Y. Numerical simulations of hydraulic jumps in water sloshing and water impacting. *Journal of Fluids Engineering*, **124** (1), 215226, (2002).
- [14] Buchner, B. Green Water on Ship-type Offshore Structures. *Delft University of Technology*, (2002).

EXTENSION OF A FAST METHOD FOR 2D STEADY FREE SURFACE FLOW TO STRETCHED SURFACE GRIDS

Toon Demeester^{1,*}, E. Harald van Brummelen² and Joris Degroote^{1,3}

¹ Department of Flow, Heat and Combustion Mechanics, Ghent University
Sint-Pietersnieuwstraat 41, 9000 Ghent, Belgium, toon.demeester@ugent.be

² Department of Multiscale Engineering Fluid Dynamics, Eindhoven University of Technology
PO Box 513-5600 MB Eindhoven, the Netherlands

³ Flanders Make, Belgium

Key words: free surface flow, fitting method, surrogate model, quasi-Newton, convolution theorem

Abstract. Steady free surface flow is often encountered in marine engineering, e.g. for calculating ship hull resistance. When these flows are solved with CFD, the water-air interface can be represented using a surface fitting approach. The resulting free boundary problem requires an iterative technique to solve the flow and at the same time determine the free surface position. Most such methods use a time-stepping scheme, which is inefficient for solving steady flows. There is one steady technique which uses a special boundary condition at the free surface, but that method needs a dedicated coupled flow solver. To overcome these disadvantages an efficient free surface method was developed recently, in which the flow solver can be a black-box. It is based on quasi-Newton iterations which use a surrogate model in combination with flow solver inputs and outputs from previous iterations to approximate the Jacobian. As the original method was limited to uniform free surface grids, it is extended in this paper to stretched free surface grids. For this purpose, a different surrogate model is constructed by transforming a relation between perturbations of the free surface height and pressure from the wavenumber domain to the spatial domain using the convolution theorem. The method is tested on the 2D flow over an object. The quasi-Newton iterations converge exponentially and in a low number of iterations.

1 INTRODUCTION

Steady free surface flows of incompressible, viscid fluids are often encountered in the field of marine engineering. The most common application is the ship hull resistance problem. These problems tend to be solved using CFD methods, where the free surface poses an additional difficulty as its position is unknown a priori. Methods to solve these flows deal with the free surface in different ways. Two approaches to represent the free surface can be distinguished:

surface capturing and surface fitting. In capturing approaches the free surface intersects the mesh in an arbitrary manner, which makes them more versatile. Examples are the volume-of-fluid [1] and level-set [2] methods. In surface fitting approaches, the mesh is aligned with the free surface so that its position is known more accurately. These methods are very suitable for the envisioned applications and thus the topic of this paper.

For the envisaged applications in marine engineering, the air-phase may be neglected due to the large density difference with water. The free surface then becomes a free boundary of the domain and the interface conditions must be enforced as kinematic and dynamic boundary conditions. The kinematic boundary condition (KBC) requires that the free surface is impermeable: for steady flows the velocity at the free surface must be parallel to it. The dynamic boundary condition (DBC) requires continuity of the stresses. As the air phase is neglected, this condition can be simplified to the requirement of zero shear stress (tangential DBC) and a constant (atmospheric) pressure (normal DBC) at the free surface.

As there are more free surface boundary conditions than can be applied when solving the Navier-Stokes equations with fixed free surface position, the free boundary problem must inherently be solved iteratively for the flow field and free surface position. Existing methods do this by distributing the boundary conditions over two steps: in one step the flow is solved with a fixed free surface position, in the other step the free surface position is calculated and the mesh deformed accordingly. Most of the methods found in literature use the DBC in the flow solver and the KBC to update the free surface position [3, 4]. This leads to a time-stepping scheme, which is inefficient for steady free surface flows due to the slow decay of transient phenomena. The *steady iterative method* by van Brummelen et al. [5] uses a combined boundary condition (KBC + DBC) in the flow solver and the normal DBC for the surface update. This method converges in a low number of iterations, but needs a dedicated coupled solver to deal with the difficult combined boundary condition.

In [6] a new method was presented which avoids the disadvantages of existing methods. By using an efficient quasi-Newton method based on the normal DBC, it converges in a low number of iterations. The other boundary conditions are easily enforced in a general-purpose (black-box) flow solver by using a free-slip wall. The original method was developed for uniform free surface grids and is in this paper extended to stretched free surface grids.

In Section 2 a surrogate model is developed for a black-box flow solver. This surrogate is used in Section 3 to approximate the Jacobian which is needed to solve the free boundary problem with quasi-Newton iterations. In Section 4 the method is tested by solving the 2D free surface flow over an object.

2 FLOW SOLVER SURROGATE MODEL

In Section 3 a quasi-Newton method is outlined to solve the steady free surface flow as described above. The approximate Jacobian which is used is based (partially) on a surrogate model for the black-box flow solver. The surrogate model proposed originally in [6] can only deal with a uniform free surface discretization, as it is based on a Fourier series decomposition. A more versatile surrogate model which can deal with stretched free surface grids is constructed in the following sections. In Section 2.1 a relation between free surface height and pressure is obtained from a 2D potential flow perturbation analysis. As this relation is only valid in the wavenumber

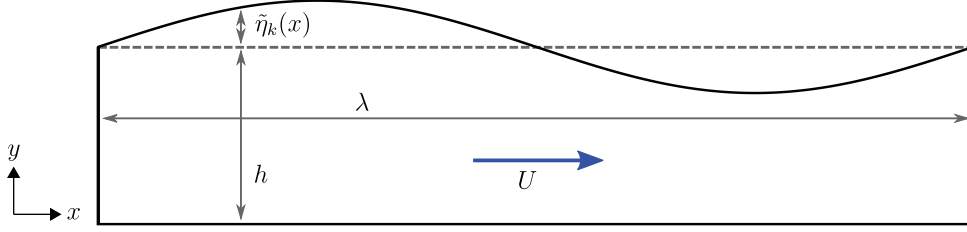


Figure 1: Flow over a horizontal plate with sinusoidal perturbation $\tilde{\eta}$ of the free surface.

domain, it is approximated with linear shape functions and consequently transformed to the spatial domain using the convolution theorem in Section 2.2. The spatial domain relation is then discretized in Section 2.3 to construct the surrogate model. In Section 2.4 the surrogate model is modified to deal with the problematic discretization of high wavenumbers.

2.1 Wavenumber domain relation between free surface pressure and height

A 2D free surface is considered, whose position is determined by a height function $\eta(x)$. The inviscid steady free surface flow over a horizontal plate as shown in Fig. 1 has a flat free surface as solution, as this fulfills all free surface boundary conditions: the velocity is parallel to the free surface and the pressure is constant. A relation between sinusoidal perturbations of free surface height and pressure has been derived by Demeester et al. [7] and is summarized here. The free surface height is perturbed with

$$\tilde{\eta}_k(x) = a \sin(kx + \theta) \quad (1)$$

with $k = 2\pi/\lambda$ the wavenumber, θ the phase angle and a the amplitude which must be small relative to the wavelength λ and flow depth h . The corresponding pressure perturbation $\tilde{p}_k(x)$ is given by a proportional relation:

$$\tilde{p}_k(x) = L(k) \tilde{\eta}_k(x) \quad \text{with} \quad L(k) = \rho g \left(\text{Fr}^2 \frac{kh}{\tanh kh} - 1 \right). \quad (2)$$

ρ is the density, g the gravitational acceleration and $\text{Fr} = U/\sqrt{gh}$ the flow Froude number based on the average velocity U . For subcritical flow ($\text{Fr} < 1$) L can become zero, so that there is no one-to-one relation between pressure and height perturbations. This complicates the steady free surface problem, requiring additional conditions to be added in order to get a unique free surface solution. The original free surface method [6] handles this, but in this paper only the case of supercritical flow ($\text{Fr} > 1$) is considered.

Functions in the spatial domain such as $p(x)$ can be transformed to the wavenumber domain using the Fourier transform \mathcal{F} , and transformed back using the inverse transform \mathcal{F}^{-1} . These are defined as

$$\mathcal{F} \{g(x)\} (k) = \int_{-\infty}^{\infty} g(x) e^{-ikx} dx \quad (3)$$

$$\mathcal{F}^{-1} \{G(k)\} (x) = \frac{1}{2\pi} \int_{-\infty}^{\infty} G(k) e^{ikx} dk \quad (4)$$

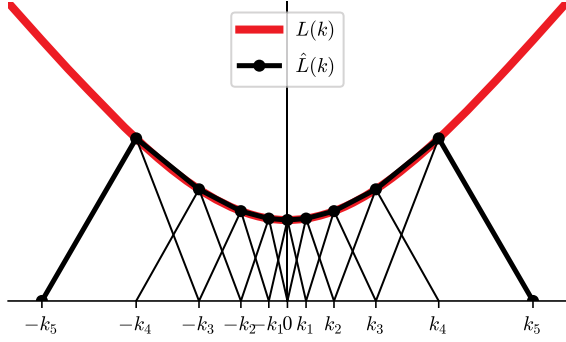


Figure 2: Example of original L and approximation \hat{L} .

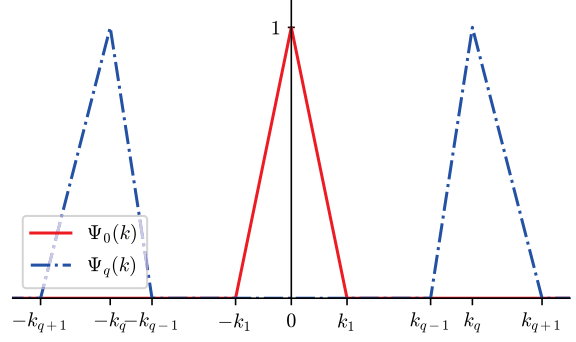


Figure 3: Definition of linear shape functions Ψ_0 and Ψ_q .

Arbitrary –non-sinusoidal– perturbations in the spatial domain then have a wavenumber domain representation

$$\tilde{H}(k) = \mathcal{F} \{ \tilde{\eta}(x) \} (k), \quad (5)$$

$$\tilde{P}(k) = \mathcal{F} \{ \tilde{p}(x) \} (k). \quad (6)$$

In the wavenumber domain the relation between height and pressure perturbations is

$$\tilde{P}(k) = L(k) \tilde{H}(k). \quad (7)$$

This relation is based on a perturbation analysis with potential flow. For more general free surface flows (large perturbations, viscid fluid, different geometry) this relation is not valid, but it can be used to construct a surrogate model which approximates the flow behavior.

2.2 Spatial domain relation based on convolution theorem

The relation between pressure and height perturbations in the wavenumber domain (Eq. 7) is not very practical, as it requires that signals are transformed to the wavenumber domain and back. However, the convolution theorem can be used to transform the relation itself to a spatial domain form. With the convolution defined as

$$(f * g)(x) = \int_{-\infty}^{\infty} f(\tau)g(x - \tau) d\tau, \quad (8)$$

the convolution theorem states that the Fourier transform of a convolution is the product of the Fourier transforms, i.e.

$$\mathcal{F} \{ (f * g)(x) \} = \mathcal{F} \{ f(x) \} \cdot \mathcal{F} \{ g(x) \}. \quad (9)$$

Applying the convolution theorem to the wavenumber domain relation from Eq. (7) leads to the spatial domain relation

$$\tilde{p}(x) = (l * \tilde{\eta})(x) \quad \text{with} \quad l(x) = \mathcal{F}^{-1} \{ L(k) \} (x). \quad (10)$$

The inverse Fourier transform of $L(k)$ is not trivial. First of all, $L(k)$ must be extended to negative wavenumbers in an even way, see Fig. 2 where $L(-k) = L(k)$. This ensures that its

inverse Fourier transform $l(x)$ is real. Furthermore L must be bandwidth limited, i.e. it must go to zero at a certain maximum wavenumber. If this is not done, L is infinitely wide in the wavenumber domain and will therefore have an asymptote in the spatial domain.

The inverse Fourier transform of the bandwidth limited L is not known, but it can be approximated by linear shape functions $\Psi_0(k)$ and $\Psi_q(k)$ as illustrated in Fig. 2. The approximate signal is denoted with a hat, so that

$$\hat{L}(k) = L(0) \Psi_0(k) + \sum_{q=1}^{q_{\max}} L(k_q) \Psi_q(k) \quad (11)$$

with q_{\max} depending on the free surface discretization. The linear shape functions Ψ_0 and Ψ_q are defined in Fig. 3. Ψ_0 is a triangle centered around $k = 0$ and depends only on k_1 . Ψ_q consists of two triangles which constitute an even function and depends on k_q , k_{q-1} and k_{q+1} . Writing out Ψ_q with $q = 0$ and the condition to be even, gives $2\Psi_0$ and not Ψ_0 . That is the reason why the central shape function Ψ_0 is considered separately. To shorten notation, the difference between two neighboring wavenumbers is denoted as $\Delta k_q = k_{q+1} - k_q$. The inverse transforms of $\Psi_0(k)$ and $\Psi_q(k)$ are respectively $\psi_0(x)$ and $\psi_q(x)$ and are known:

$$\psi_0(x) = \frac{1 - \cos k_1 x}{\pi k_1 x^2} \quad (12)$$

$$\psi_q(x) = \frac{(\Delta k_q + \Delta k_{q-1}) \cos k_q x - \Delta k_q \cos k_{q-1} x - \Delta k_{q-1} \cos k_{q+1} x}{\pi \Delta k_q \Delta k_{q-1} x^2} \quad (13)$$

Thanks to the linearity of the Fourier transform, the inverse transformation of \hat{L} is given by

$$\hat{l}(x) = \mathcal{F}^{-1} \left\{ \hat{L}(k) \right\} (x) = L(0) \psi_0(x) + \sum_{q=1}^{q_{\max}} L(k_q) \psi_q(x). \quad (14)$$

This results in an approximate spatial domain relation between height and pressure perturbations:

$$\tilde{p}(x) \approx \left(\hat{l} * \tilde{\eta} \right) (x) \quad (15)$$

Two important choices remain regarding the construction of \hat{l} . Firstly the approximation of L is determined by the choice of the wavenumbers k_q with $q \in [0, q_{\max}]$ in Eq. 11. Secondly \hat{l} will need to be limited to a certain domain when it is discretized. More specifically, a cut-off value x_{co} must be chosen for each term in Eq. (14) so that it can be set to zero for $|x| > x_{\text{co}}$. In the remainder of this section it is shown that these two choices are related and how they can be made.

A closer look is taken at ψ_0 and ψ_q to see where the cut-off is best made for each function. The inverse of the central shape function Ψ_0 can be rewritten as

$$\psi_0(x) = \frac{k_1}{2\pi} \text{sinc}^2 \frac{k_1 x}{2}. \quad (16)$$

A sinc^2 function is plotted in Fig. 4: it damps out with $1/x^2$, and has zeroes at locations $i\pi/\alpha$ with i a non-zero integer. Note that the derivative is also zero in these points, so the zeroes

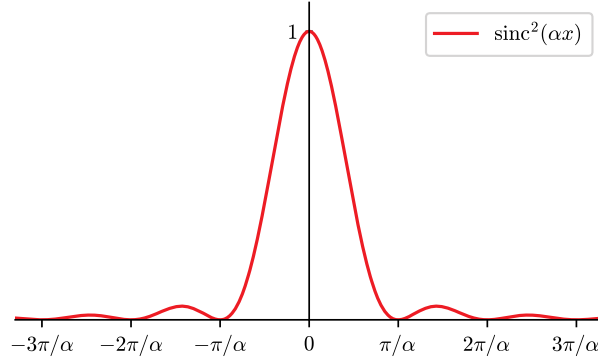


Figure 4: The sinc^2 function.

seem like good cut-off locations for ψ_0 . The inverse transform of a general shape function Ψ_q can be rewritten as

$$\begin{aligned} \psi_q(x) &= \frac{\cos k_q x}{2\pi} \Delta k_{q-1} \text{sinc}^2 \frac{\Delta k_{q-1} x}{2} \\ &\quad + \frac{\cos k_q x}{2\pi} \Delta k_q \text{sinc}^2 \frac{\Delta k_q x}{2} \\ &\quad - \frac{k_q}{\pi} \text{sinc } k_q x (\text{sinc } \Delta k_{q-1} x - \text{sinc } \Delta k_q x). \end{aligned} \quad (17)$$

The first and second term in this expression consist of a sinc^2 function with a low wavenumber multiplied with a cosine with higher wavenumber (namely k_q). The sinc^2 factor acts as an envelope function as it were. A good location for the cut-off could be where the zeroes of the sinc^2 factors coincide, namely locations $x_{\text{co}} = i_1 2\pi / \Delta k_{q-1} = i_2 2\pi / \Delta k_q$. From this expression it follows that the zeroes only coincide when $i_2 / i_1 = \Delta k_q / \Delta k_{q-1}$ with i_1 and i_2 non-zero integers. This means that $\Delta k_q / \Delta k_{q-1}$ must be rational in order for the first two terms to have a common zero. Moreover, it can be shown that at these points the third term in Eq. (17) is also zero and has a zero derivative.

Choosing the ratio $\Delta k_q / \Delta k_{q-1}$ to be 1/1 seems the obvious choice, but it is not the best one. With this choice the envelope of ψ_q stays the same, i.e. for high wavenumber phenomena –which are typically more localized– the signal stays very wide in the spatial domain. It is more logical to have a narrower ψ_q for higher wavenumbers, which corresponds to a wider Ψ_q in the wavenumber domain. Good choices for the ratio $\Delta k_q / \Delta k_{q-1}$ are accordingly 2/1 and 3/2. For these values, ψ_q is plotted in Fig. 5 with $q = 4$, together with its three terms (Eq. (17)). Note that x_{co} is located at the first location where ψ_q and its derivative are both zero.

2.3 Discretization of spatial domain relation to construct surrogate model

In this section discrete variables will be introduced, which requires different notation: all matrices will be denoted by bold symbols and their elements with subscript indices.

Eq. (10) gives a relation between continuous functions $\tilde{\eta}(x)$ and $\tilde{p}(x)$. For use as a surrogate model, this relation must be discretized. Height and pressure perturbations have discrete counterparts which are denoted by the column vectors $\tilde{\boldsymbol{\eta}}, \tilde{\boldsymbol{p}} \in \mathbb{R}^{n \times 1}$ which contain the values

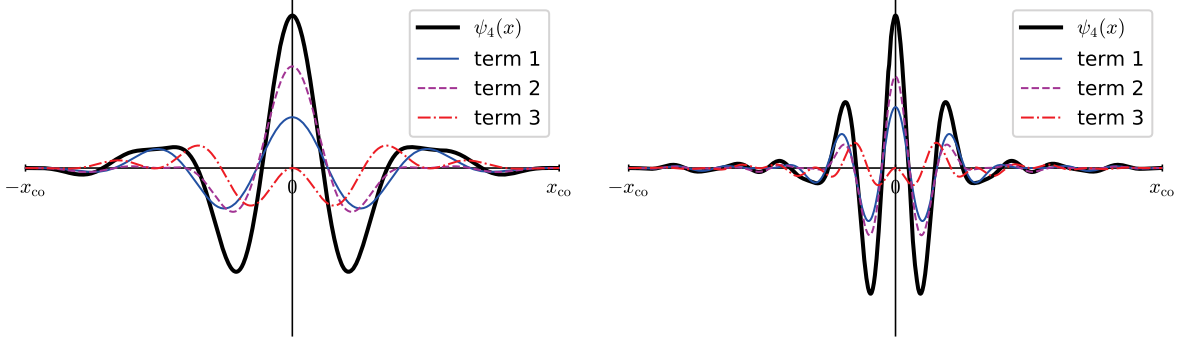


Figure 5: ψ_q for $q = 4$, using ratios $\Delta k_q/\Delta k_{q-1}$ of $2/1$ (left) and $3/2$ (right). The three terms of ψ_q from Eq. (17) are also plotted separately.

that correspond to positions $\mathbf{x} \in \mathbb{R}^{n \times 1}$. Discretization in the x-direction can be non-uniform, but it is assumed that the points are ordered from inlet to outlet, with \mathbf{x}_0 the inlet position. A surrogate model $\mathbf{F} \in \mathbb{R}^{n \times n}$ is now constructed such that

$$\tilde{\mathbf{p}} = \mathbf{F} \tilde{\boldsymbol{\eta}}. \quad (18)$$

The pressure $\tilde{\mathbf{p}}_i$ in point \mathbf{x}_i is found by discretizing Eq. (15). Using the trapezoidal rule, the convolution becomes

$$\tilde{\mathbf{p}}_i = \sum_{j=-\infty}^{+\infty} \tilde{\boldsymbol{\eta}}_j \cdot \hat{l}(\mathbf{x}_i - \mathbf{x}_j) \cdot \frac{\mathbf{x}_{j+1} - \mathbf{x}_{j-1}}{2}. \quad (19)$$

Although the sum is taken from $-\infty$ to $+\infty$, this does not pose a problem as the region where \hat{l} is non-zero is limited and the sum reduces to a limited number of terms. By comparing the expressions in Eqs. (18) and (19), the elements of \mathbf{F} can be identified:

$$\mathbf{F}_{i,j} = \hat{l}(\mathbf{x}_i - \mathbf{x}_j) \cdot \frac{\mathbf{x}_{j+1} - \mathbf{x}_{j-1}}{2} \quad (20)$$

A problem is present near the boundaries of the domain: it is possible that j falls outside the allowed range $[0, n]$. The solution is to extend the height $\tilde{\boldsymbol{\eta}}$ past the boundary. This extension can be even or odd; the best choice is case dependent, as will be explained later. The result is that some elements of \mathbf{F} get additional contributions of a form similar to Eq. (20).

2.4 Adaption of surrogate model for high wavenumbers

The highest wavenumber which can be represented on the free surface grid depends on the local discretization of that grid. The highest wavenumber in each node is collected in the grid wavenumber vector $\mathbf{k}_{\text{grid}} \in \mathbb{R}^{n \times 1}$, defined as

$$\mathbf{k}_{\text{grid}_i} = \frac{2\pi}{\mathbf{x}_{i+1} - \mathbf{x}_{i-1}}. \quad (21)$$

The discretization of \hat{l} becomes problematic for these wavenumbers. On the one hand, it is important that these wavenumbers are taken into account, so $k_{q_{\text{max}}}$ –which is determined locally–

must be at least as high as the grid wavenumber. On the other hand, it is possible to get aliasing in the discretization of \hat{l} , especially for irregular spacing of the points on the free surface. This leads to a wrong result of the convolution.

The solution is to use a filter matrix $\mathbf{W} \in \mathbb{R}^{n \times n}$ in the spatial domain to filter out the wavenumbers close to \mathbf{k}_{grid} . For the lower wavenumbers the convolution matrix \mathbf{F} is still used, but now $k_{q_{\text{max}}}$ can be chosen lower than \mathbf{k}_{grid} to avoid aliasing. The high wavenumbers which were filtered out are treated with a factor L corresponding to \mathbf{k}_{grid} . This is written as a diagonal matrix \mathbf{L}_{grid} defined as

$$\mathbf{L}_{\text{grid},i,i} = L(\mathbf{k}_{\text{grid},i}). \quad (22)$$

For the wavenumbers that are slightly lower than \mathbf{k}_{grid} , \mathbf{L}_{grid} is an overestimation. This reduces the accuracy of the surrogate model, but will still give a stable update in the quasi-Newton iterations (i.e. the change in free surface height will be underestimated, not overestimated). The adapted surrogate model \mathbf{F}^* is constructed from the original model \mathbf{F} as

$$\mathbf{F}^* = \mathbf{F}\mathbf{W} + \mathbf{L}_{\text{grid}}(\mathbf{I}_n - \mathbf{W}) \quad (23)$$

with \mathbf{I}_n the identity matrix.

The filter \mathbf{W} must remove wavenumbers which are high with respect to the grid resolution, i.e. its cut-off wavenumber is chosen with respect to \mathbf{k}_{grid} and not a reference which is physically meaningful to the flow. This means a filter kernel must be calculated only once and then put on every row of the matrix \mathbf{W} . At the boundaries, an even or odd extension must be made in the same way as was done for constructing \mathbf{F} . For the kernel, a windowed-sinc filter is used as described by Smith [8]. A Blackman window is used as this provides low passband and stopband ripples for reasonable rol-off. The kernel is based on two parameters: the cut-off wavenumber and the kernel length.

3 QUASI-NEWTON SOLUTION METHOD FOR STEADY FREE SURFACE FLOW

The free boundary problem which presents itself when the water-air interface is represented by surface fitting, was introduced in Section 1. Using the distribution of free surface boundary conditions proposed in Section 1, the free surface discretization introduced in Section 2.3, and a non-linear black-box flow solver \mathcal{F} , the problem may be stated as:

given the flow solver $\mathcal{F}(\boldsymbol{\eta}) = \mathbf{p}$ which fulfills the KBC and tangential DBC, find $\boldsymbol{\eta}$ so that the normal DBC $\mathbf{p} = p_{\text{cst}}\mathbf{1}$ is fulfilled.

$\mathbf{1}$ denotes the all-ones vector. The KBC and tangential DBC are applied at the free surface by modeling it as a free-slip wall in the flow solver.

Starting from an initial guess $\boldsymbol{\eta}^0$ (a superscript denotes the iteration index), this problem can be solved iteratively with a quasi-Newton method: an approximate Jacobian $\widehat{\mathcal{F}}'$ of the flow solver \mathcal{F} is used to calculate a new free surface height $\boldsymbol{\eta}$:

$$\widehat{\mathcal{F}}' \Delta \boldsymbol{\eta}^m = p_{\text{cst}}\mathbf{1} - \mathbf{p}^m \quad (24)$$

with $\Delta\boldsymbol{\eta}^m = \boldsymbol{\eta}^{m+1} - \boldsymbol{\eta}^m$ and $\mathbf{p}^m = \mathcal{F}(\boldsymbol{\eta}^m)$. The pressure p_{cst} is unknown and not of interest, as only the gradient of the pressure appears in the incompressible Navier-Stokes equations. To remove it from the system, Eq. (24) is split in two parts

$$\begin{cases} \widehat{\mathcal{F}}' \Delta\boldsymbol{\eta}_a^m = -\mathbf{p}^m \\ \widehat{\mathcal{F}}' \Delta\boldsymbol{\eta}_b^m = p_{\text{cst}} \mathbf{1} \end{cases} \quad (25)$$

so that $\Delta\boldsymbol{\eta}^m = \Delta\boldsymbol{\eta}_a^m + \Delta\boldsymbol{\eta}_b^m$. The first part can be solved once an expression for the approximate Jacobian is known (see further). The second part cannot be solved as p_{cst} is not known. However, the perturbation analysis from Section 2.1 predicts that $\Delta\boldsymbol{\eta}_b^m$ should also be constant, which implies that $\Delta\boldsymbol{\eta}_b^m$ determines the (average) flow height. In a practical case however, the flow height will usually be imposed at the inlet (or alternatively the outlet) by requiring that $\boldsymbol{\eta}_0 = h$. Using this condition instead of p_{cst} to determine $\Delta\boldsymbol{\eta}_b^m$ gives

$$\Delta\boldsymbol{\eta}_b^m = (h - \Delta\boldsymbol{\eta}_{a,0}^m) \mathbf{1} \quad (26)$$

The subscript notations a and b will not be used any further as the contribution by $\Delta\boldsymbol{\eta}_b^m$ can simply be written as a correction based on $\Delta\boldsymbol{\eta}_a^m$.

The Jacobian of the flow solver can be approximated using the surrogate model \mathbf{F}^* developed in Section 2, and is accordingly denoted

$$\widehat{\mathcal{F}}'_{\text{sur}} = \mathbf{F}^*. \quad (27)$$

To stabilize the iterations and accelerate convergence, a second approximation of the Jacobian is constructed using the IQN-ILS algorithm by Degroote et al. [9], originally developed to improve convergence in partitioned fluid-structure interaction simulations. Flow solver inputs and outputs from previous iterations are collected in the matrices

$$\mathbf{V}^m = [\Delta\boldsymbol{\eta}^{m-1} \quad \dots \quad \Delta\boldsymbol{\eta}^0], \quad (28)$$

$$\mathbf{W}^m = [\Delta\mathbf{p}^{m-1} \quad \dots \quad \Delta\mathbf{p}^0]. \quad (29)$$

These are used to construct a low-order approximate Jacobian with a least-squares technique as

$$\widehat{\mathcal{F}}'_{\text{IQN}}{}^m = \mathbf{W}^m \mathbf{R}^{m-1} \mathbf{Q}^{mT} \quad \text{with} \quad \mathbf{V}^m = \mathbf{Q}^m \mathbf{R}^m \quad (30)$$

the economy-size QR-decomposition of \mathbf{V}^m . This second approximate Jacobian improves while the iterations progress and more information is stored in \mathbf{V}^m and \mathbf{W}^m . The two approximations now have to be combined. While $\widehat{\mathcal{F}}'_{\text{sur}}$ is a full rank Jacobian approximation, $\widehat{\mathcal{F}}'_{\text{IQN}}{}^m$ only affects the part of $\Delta\boldsymbol{\eta}^m \in \text{range}(\mathbf{V})$, which is equal to $\mathbf{Q}^m \mathbf{Q}^{mT} \Delta\boldsymbol{\eta}^m$. $\widehat{\mathcal{F}}'_{\text{sur}}$ is then used for the remaining part of $\Delta\boldsymbol{\eta}^m$. The full expression for the approximate Jacobian is

$$\widehat{\mathcal{F}}'{}^m = \widehat{\mathcal{F}}'_{\text{IQN}}{}^m \mathbf{Q}^m \mathbf{Q}^{mT} + \widehat{\mathcal{F}}'_{\text{sur}} (\mathbf{I}_n - \mathbf{Q}^m \mathbf{Q}^{mT}) \quad (31)$$

$$= \mathbf{W}^m \mathbf{R}^{m-1} \mathbf{Q}^{mT} + \mathbf{F} (\mathbf{I}_n - \mathbf{Q}^m \mathbf{Q}^{mT}). \quad (32)$$

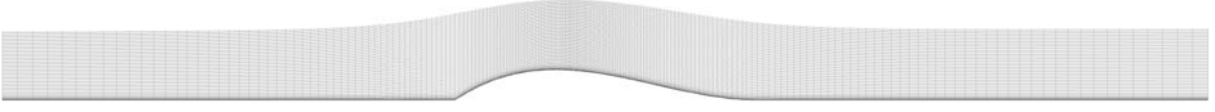


Figure 6: Final solution for flow over object. The free surface grid has a ratio between largest and smallest cell of 10.

Algorithm 1 presents the complete iterative solution method. The convergence criterion is based on the pressure residual r_p . With $d = \mathbf{x}_{n-1} - \mathbf{x}_0$ (assumed positive), the average pressure \bar{p} is computed as

$$\bar{p} = \frac{1}{d} \sum_{i=1}^{n-1} (\mathbf{x}_i - \mathbf{x}_{i-1}) \left(\frac{\mathbf{p}_i + \mathbf{p}_{i-1}}{2} \right). \quad (33)$$

The pressure residual is then defined as the root mean square value of $(\mathbf{p} - \bar{p})$:

$$r_p = \frac{1}{d} \sum_{i=1}^{n-1} (\mathbf{x}_i - \mathbf{x}_{i-1}) \left(\frac{\mathbf{p}_i + \mathbf{p}_{i-1}}{2} - \bar{p} \right)^2 \quad (34)$$

Algorithm 1 Quasi-Newton method for 2D supercritical steady free surface flow.

```

1:  $m = 0$ 
2:  $\mathbf{p}^0 = \mathcal{F}(\boldsymbol{\eta}^0)$ 
3: while  $r_p^m > \varepsilon$  do ▷ Eq. (34)
4:   if  $m > 0$  then
5:     construct  $\mathbf{V}^m, \mathbf{W}^m$ 
6:     QR-decomposition  $\mathbf{V}^m = \mathbf{Q}^m \mathbf{R}^m$ 
7:   end if
8:   construct  $\widehat{\mathcal{F}}^m$  ▷ Eq. (32)
9:   solve  $\widehat{\mathcal{F}}^m \Delta \boldsymbol{\eta}^m = -\mathbf{p}^m$ 
10:   $\Delta \boldsymbol{\eta}^m += (h - \Delta \boldsymbol{\eta}_0^m) \mathbf{1}$ 
11:   $\boldsymbol{\eta}^{m+1} = \boldsymbol{\eta}^m + \Delta \boldsymbol{\eta}^m$ 
12:   $m = m + 1$ 
13:   $\mathbf{p}^m = \mathcal{F}(\boldsymbol{\eta}^m)$ 
14: end while
    
```

4 NUMERICAL RESULTS

The 2D flow over an obstacle as shown in Fig. 6 is used as test case. Experimental data was collected by Cahouet [10] and the case has been used to evaluate several free surface methods [3, 11, 12] for steady flow. The shape of the obstacle is described by

$$y_b = \frac{27}{4} \frac{H_b}{L_b^3} x (x - L_b)^2 \quad \text{for } 0 \leq x \leq L_b \quad (35)$$

with $L_b = 0.42$ m the length and $H_b = 0.042$ m the height of the obstacle. The inlet water depth $h = 0.09545$ m, the Froude number $Fr = 2.05$. The boundary conditions are: a velocity profile

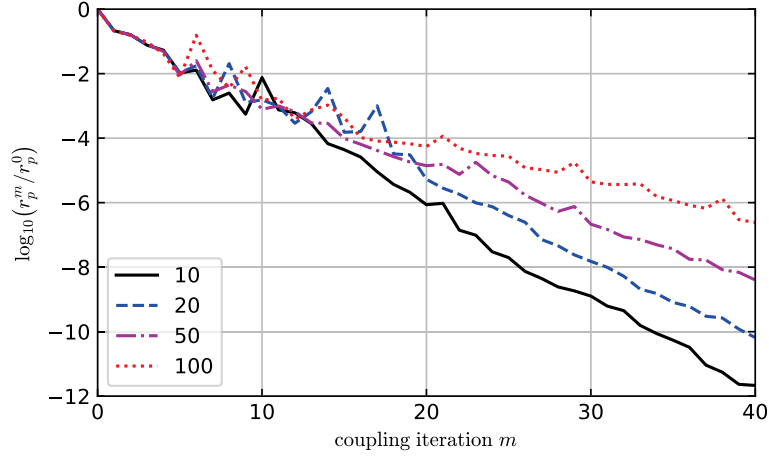


Figure 7: Normalized pressure residual of free surface method on different meshes. The legend shows the ratio between the largest and smallest free surface cells.

[10] at the inlet, a hydrostatic pressure outlet, a no-slip wall at the bottom and a free-slip wall at the free surface. A second order upwind scheme is used for all convection terms. Turbulence modeling is done with the $k\omega$ -SST model. The initial height of the free surface is $\boldsymbol{\eta}^0 = h \mathbf{1}$.

The mesh which is used is structured, but not equally spaced. In the y -direction, the bottom boundary layer is resolved by the mesh, resulting in $1 < y^+ < 5$. In the x -direction mesh stretching is used to have coarse cells near the inlet and outlet of the domain and fine cells at the wave crest as can be seen in Fig. 6. In all simulations, the coarsest cell has length $L_b/20$. The ratio between coarsest and finest cell is varied: ratios 10, 20, 50 and 100 are tested.

For the surrogate model a filter \mathbf{W} with cut-off frequency 0.15 (which corresponds to $k_{co}/k_{grid} = 0.3$) and with kernel length 41 is used. For approximating L , a ratio $\Delta k_q/\Delta k_{q-1} = 1.5$ is used with $k_1 = 2.5\pi/L_b$. To avoid aliasing q_{max} is chosen in each point \mathbf{x}_i as the largest integer so that $3k_{q_{max}} \leq k_{grid_i}$. For both \mathbf{F} and \mathbf{W} , the inlet domain is extended in an odd way and the outlet domain in an even way, as these choices gave the best convergence.

Fig. 7 shows the residual r_p as defined in Eq. (34) for simulations with the four different meshes. In all simulations r_p decreases exponentially and in a low number of iterations. For larger ratios (i.e. finer cells), convergence becomes a bit slower.

5 CONCLUSIONS

A quasi-Newton method for efficiently solving 2D steady free surface flow has been developed recently. It offers the advantage of being compatible with black-box flow solvers. The original method uses an approximate Jacobian based on the one hand on a surrogate model of the flow solver, and on the other hand on flow solver inputs and outputs from previous iterations. Due to the formulation of the surrogate model, it can only be applied when the free surface grid is uniform. In this paper a new surrogate model is constructed, which allows the method to be extended to meshes with stretched free surface grids. This surrogate model is obtained by transforming a relation between perturbations of the free surface height and pressure from the

wavenumber domain to the spatial domain using the convolution theorem. The method is tested by solving the free surface flow over an object. It converges exponentially and in a low number of iterations. When the free surface grid is refined (i.e. ratio of largest to smallest cell increases), convergence slows down a bit.

REFERENCES

- [1] C. W. Hirt and B. D. Nichols, “Volume of fluid (VOF) method for the dynamics of free boundaries,” *Journal of Computational Physics*, vol. 39, no. 1, pp. 201–225, 1981.
- [2] M. Sussman, P. Smereka, and S. Osher, “A level set approach for computing solutions to incompressible two-phase flow,” *Journal of Computational Physics*, vol. 114, no. 1, pp. 146–159, 1994.
- [3] G. Tzabiras, “A numerical investigation of 2D, steady free surface flows,” *International Journal for Numerical Methods in Fluids*, vol. 25, no. 5, pp. 567–598, 1997.
- [4] S. Muzaferija and M. Perić, “Computation of free-surface flows using the finite-volume method and moving grids,” *Numerical Heat Transfer*, vol. 32, no. 4, pp. 369–384, 1997.
- [5] E. H. van Brummelen, H. C. Raven, and B. Koren, “Efficient numerical solution of steady free-surface Navier–Stokes flow,” *Journal of Computational Physics*, vol. 174, no. 1, pp. 120–137, 2001.
- [6] T. Demeester, E. H. van Brummelen, and J. Degroote, “An efficient quasi-Newton method for 2D steady free surface flow.” Manuscript submitted for publication.
- [7] T. Demeester, J. Degroote, and J. Vierendeels, “Stability analysis of a partitioned iterative method for steady free surface flow,” *Journal of Computational Physics*, vol. 354, pp. 387–392, 2018.
- [8] S. W. Smith, *The scientist and engineer’s guide to digital signal processing*. California Technical Pub., 1999.
- [9] J. Degroote, K.-J. Bathe, and J. Vierendeels, “Performance of a new partitioned procedure versus a monolithic procedure in fluid–structure interaction,” *Computers & Structures*, vol. 87, no. 11, pp. 793–801, 2009.
- [10] J. Cahouet, *Etude numérique et expérimentale du problème bidimensionnel de la résistance de vagues non-linéaire*. Ecole Nationale Supérieure de Techniques Avancées, 1984.
- [11] E. H. van Brummelen and A. Segal, “Adjoint shape optimization for steady free-surface flows,” *International Journal for Numerical Methods in Fluids*, vol. 40, no. 3-4, pp. 605–614, 2002.
- [12] J. Wackers and B. Koren, “A surface capturing method for the efficient computation of steady water waves,” *Journal of Computational and Applied Mathematics*, vol. 215, no. 2, pp. 618–625, 2008.

NUMERICAL MODELING OF CONTACT DISCONTINUITIES IN TWO-PHASE FLOW

RONALD A. REMMERSWAAL* AND ARTHUR E. P. VELDMAN†

*†Bernoulli Institute for Mathematics, Computer Science and Artificial Intelligence
University of Groningen, The Netherlands
[*r.a.remmerswaal@rug.nl](mailto:r.a.remmerswaal@rug.nl) †a.e.p.veldman@rug.nl

Key words: two-phase flow, contact discontinuity, Ghost Fluid Method, Cut Cell Method

Abstract. For convection dominated two-phase flow, velocity components tangential to the interface can become discontinuous when interface boundary layers are numerically underresolved. When sharp interface tracking methods are used it is essential that such discontinuities are captured in an equally sharp way.

In this paper we propose to model the velocity component tangential to the interface as discontinuous using an appropriate interface jump condition on the normal component of the pressure gradient. We achieve this numerically using a novel combination of a Multi-dimensional Ghost Fluid Method for the gradient and the Cut Cell Method for the divergence operator. The resulting model is able to accurately and sharply capture discontinuities at large density ratios.

The model is applied to an inviscid dam-break problem. Here we observe that our proposed model accurately captures the shear layer at the interface with the tangential velocity discontinuity.

In future work we will apply this discretization approach to the modeling of viscous two-phase sloshing problems with LNG and its compressible vapour, with a particular interest in studying the development of free surface instabilities.

1 Introduction

Sloshing of fluids in a container is a complex physical phenomena which is present in many engineering problems. For instance the transport of Liquefied Natural Gas (LNG) in LNG carriers. In particular the role of free surface instabilities in measured impact pressures during breaking wave impacts, which may occur during sloshing, is not well understood [2]. Numerical modeling can facilitate this understanding.

The numerical modeling of two-phase flow involves dealing with a multitude of jumps (discontinuities) of fluid properties across the interface separating the fluids. Additional challenges arise when shear layers develop at the fluid-fluid interface, resulting in an interface boundary layer. When such an interface boundary layer is underresolved this can result in unphysical

interaction between the two fluids at the interface. Numerically such an underresolved interface boundary layer effectively results in a velocity field which has a (contact) discontinuity in the tangential direction. We therefore propose to model the underresolved velocity field as being discontinuous in the direction tangential to the interface. As a starting point we consider inviscid two-phase flow modeled by the Euler equations.

In this paper we explore the numerical modeling, in a Finite Volume setting, of contact discontinuities for incompressible and inviscid two-phase flow. To this end we describe the governing equations in Section 2, followed by our proposed discretization at the interface in Section 3. In Section 4 we demonstrate the accuracy of our discretization when applied to a Poisson problem as well as a time-dependent Euler problem in which we model a dam-break. Concluding remarks are made in Section 5.

For simplicity in notation we consider a two-dimensional setting.

2 Mathematical model

Here we briefly describe the underlying mathematical model we use, which are the incompressible Euler equations for each of the two phases $\pi = l, g$ (liquid and gas).

2.1 Primary equations

The primary equations describe the conservation of mass and momentum in each of the phases in an arbitrary control volume $\omega = \omega^l \cup \omega^g$

$$\frac{d}{dt} \int_{\omega^\pi} \rho^\pi dV + \int_{\partial\omega^\pi \setminus I} \rho^\pi u_\eta^\pi dS = 0 \quad (1)$$

$$\frac{d}{dt} \int_{\omega^\pi} \rho^\pi \mathbf{u}^\pi dV + \int_{\partial\omega^\pi \setminus I} \rho^\pi \mathbf{u}^\pi u_\eta^\pi dS = - \int_{\partial\omega^\pi} (p^\pi - \rho^\pi \mathbf{g} \cdot \mathbf{x}) \eta dS, \quad (2)$$

where η denotes the face normal, u_η^π the face normal velocity component, p^π the pressure, \mathbf{g} the gravitational acceleration and ρ^π the density per phase. We consider incompressible flow for which the mass conservation equations result in a volume constraint on the evolution of the interface

$$\frac{d}{dt} |\omega^l| + \int_{\partial\omega^l \setminus I} u_\eta^l dS = 0, \quad (3)$$

where $|\omega^\pi|$ denotes the volume of ω^π .

The influence of surface tension is of interest in our application and we therefore include it via Laplace's law

$$- \llbracket p \rrbracket = \sigma \kappa. \quad (4)$$

Here κ denotes the interface mean curvature and $\llbracket \varphi \rrbracket$ denotes jump of some flow variable φ

$$\llbracket \varphi \rrbracket := \varphi^g - \varphi^l. \quad (5)$$

We assume immiscible fluids without phase change, and therefore

$$\llbracket u_\eta \rrbracket = \eta \cdot (\mathbf{u}^g - \mathbf{u}^l) = 0. \quad (6)$$

Together with appropriate boundary conditions on \mathbf{u}^π and a contact angle boundary condition on κ this results in a closed system of equations. Note that this model does not impose any smoothness on the tangential velocity component $u_\tau = \boldsymbol{\tau} \cdot \mathbf{u}$, where $\boldsymbol{\tau}$ denotes the interface tangent.

2.2 The pressure Poisson problem

Addition of the mass conservation equations, when divided by their respective densities, yields

$$\int_{\partial\omega} u_\eta \, dS = \int_{\partial\omega^l \setminus I} u_\eta^l \, dS + \int_{\partial\omega^g \setminus I} u_\eta^g \, dS = 0, \quad (7)$$

thus showing that the mixture velocity field is divergence free. Taking the time derivative of the divergence constraint, substituting the momentum equation and using $[[u_\eta]] = 0$, yields an equation for the pressure

$$\int_{\partial\omega} \frac{1}{\rho} \partial_\eta p \, dS = - \int_{\partial\omega} \boldsymbol{\eta} \cdot (\mathbf{u} \cdot \nabla) \mathbf{u} \, dS. \quad (8)$$

We supplement the aforementioned equation with Laplace's law (4), an homogeneous Neumann boundary condition on the pressure and the following jump condition on the normal derivative of the pressure gradient

$$\left[\left[\frac{1}{\rho} \partial_\eta p \right] \right] = - \left[\left[\boldsymbol{\eta} \cdot \frac{D\mathbf{u}}{Dt} \right] \right], \quad (9)$$

which follows directly from the strong form of the Euler equations. The latter condition (9) is necessary for having a well-posed coupled Poisson problem.

3 Numerical model

We consider a staggered variable arrangement (Arakawa C grid) on a rectilinear grid. The grid cells are denoted by the set \mathcal{C} , with faces $\mathcal{F}(c)$ for $c \in \mathcal{C}$. The set of all faces is denoted by \mathcal{F} . A subset of the faces are cut by the interface $I(t) \subset \Omega$, we denote this time-dependent set by \mathcal{F}_I . Every interface face is split into its liquid and gaseous part $f = f^g \cup f^l$. This leads to the definition of $\hat{\mathcal{F}}^\pi$ containing all the (possibly cut) faces which are entirely contained in the π -phase. Moreover let $\hat{\mathcal{F}} = \hat{\mathcal{F}}^l \cup \hat{\mathcal{F}}^g$, see Figure 1.

The space of functions defined on \mathcal{C} is denoted by C^h , with e.g. $p \in C^h : c \mapsto p_c \approx p(\mathbf{x}_c)$, where \mathbf{x}_c is the center of cell c . Similarly we have the function space F^h , where the approximations are located at \mathbf{x}_f , the center of the face f . We denote by $\boldsymbol{\eta}_f$ the normal of the face f . The function $\alpha : \mathcal{C} \times \mathcal{F} \rightarrow \{1, -1\}$ encodes the orientation of the face normals such that $\alpha_{c,f} \boldsymbol{\eta}_f$ points out of cell c .

3.1 Interface advection

The interface is represented using the volume fraction field $\bar{\chi} = |c^l|/|c| \in C^h$ as per the Volume-of-Fluid method. Advection of the interface is performed using the Lagrangian-Eulerian Advection Scheme (LEAS) [9].

3.2 Momentum equations

In the interior of each of the phases the momentum equations are discretized using the symmetry-preserving finite-volume discretization by Verstappen and Veldman [8]. Near the interface we choose to discretize the momentum equations in strong form, thereby sacrificing exact momentum conservation at the interface but alleviating difficulties faced with having arbitrarily small cells $|c^\pi|(t)$ and non-smooth in time face areas $|f^\pi|(t)$. At the interface we use a first-order upwind convection scheme *per phase*, which relies on constant extrapolation of velocities.

The time integration is performed under a CFL constraint of 0.5 using a second-order accurate explicit method, followed by a pressure correction step

$$\frac{u_f^* - u_f^{(n)}}{\Delta t} = R \left(\frac{3}{2} u_f^{(n)} - \frac{1}{2} u_f^{(n-1)} \right)_f, \quad u_f^{(n+1)} = u_f^* - \frac{\Delta t}{\rho} (Gp)_f, \quad \forall f \in \hat{\mathcal{F}}. \quad (10)$$

Here R denotes the convection and gravity terms, and $G : C^h \rightarrow \hat{F}^h$ is the gradient operator.

3.3 Pressure Poisson problem

The solution of the Poisson problem plays a central role in the numerical model, since this is where the two phases are implicitly coupled. The gradient of the resulting pressure is used to make the mixture velocity field divergence free and it is therefore important that the Laplace operator can be decomposed in a divergence $\bar{D} : \hat{F}^h \rightarrow C^h$ and a gradient G .

Given \bar{D} and G we may write the Poisson problem as (for notational convenience we let $\Delta t = 1$)

$$\bar{D} \left(\frac{1}{\rho} Gp \right)_c = \bar{D}(u^*)_c, \quad \forall c \in C \quad (11)$$

where the gradient operator G contains the value jump due to surface tension as well as the jump in the normal derivative. We will now precisely define the divergence \bar{D} and the gradient G .

3.3.1 Divergence operator

At the interface our velocity field is discontinuous, and therefore the divergence operator needs to be modified. A finite difference approach such as the Ghost Fluid Method (GFM) [4] will result in an incompatible discretization of the Poisson problem

$$\exists u \in \hat{F}_0^h \quad \text{s.t.} \quad \sum_{c \in C} \bar{D}(u)_c \neq 0, \quad (12)$$

where \hat{F}_0^h is the set of velocity fields which vanish at the boundary. A consequence of this incompatibility is that the resulting linear system of equations, resulting from the pressure Poisson equation, has no solution.

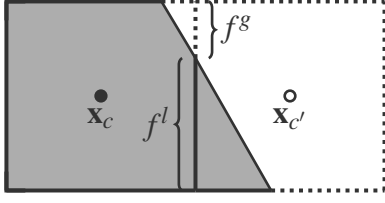


Figure 1: Illustration of the CCM. Each face is split into its liquid and gaseous part $f = f^l \cup f^g$. Shaded region corresponds to the liquid parts c^l, c'^l . Solid nodes correspond to the liquid phase and open nodes to the gas phase.

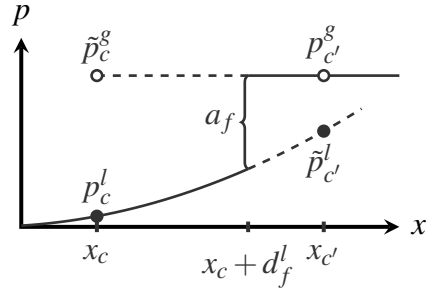


Figure 2: Illustration of the GFM. The pressure values denoted by \tilde{p} are ‘ghost’ pressures and not actually part of the solution.

A finite-volume approach however naturally preserves the flux cancellation property which a divergence operator should satisfy, and therefore we propose to use the cut-cell method [6] for discretization of the divergence operator. To this end we define the face apertures $A_f \in F^h$ (computed from the PLIC reconstruction) as the fraction of the face $f \in \mathcal{F}$ contained in the reference fluid l , so $A_f = |f^l|/|f|$. This results in the following divergence operator

$$|c|\bar{D}(u)_c = \sum_{f \in \mathcal{F}(c)} \alpha_{c,f} |f| \bar{u}_f, \quad (13)$$

where we define the mixture velocity $\bar{u}_f = A^f u_f^l + (1 - A^f) u_f^g$. See also Figure 1. This divergence operator satisfies the discrete equivalent to Gauss’s theorem exactly, and therefore the term in (12) vanishes exactly for all $u \in \hat{F}_0^h$.

3.3.2 The gradient operator

In the interior of the phases we define the gradient G as the standard finite difference operator

$$(Gp)_f = - \sum_{c \in \mathcal{C}(f)} \alpha_{c,f} \frac{p_c}{h_f}, \quad (14)$$

where h_f is the distance between the nodes $\mathbf{x}_c, \mathbf{x}_{c'}$. Near the interface the gradient needs modification to sharply capture the imposed jumps.

The Ghost Fluid Method

We consider a finite-difference approximation for the gradient at a face $f \in \mathcal{F}_I$ near the interface. The pressure $p \in C^h$ is defined point-wise according to the liquid indicator $\chi \in C^h$

$$\chi_c = \begin{cases} 1 & \text{if } \mathbf{x}_c \in \Omega^l \\ 0 & \text{if } \mathbf{x}_c \in \Omega^g \end{cases}. \quad (15)$$

Consider a face f which connects two nodes $C(f) = \{c, c'\}$ from different phases (so $\chi_c \neq \chi_{c'}$). Hence we know the liquid pressure p_c^l on one side of the face and the gas pressure $p_{c'}^g$ on the other side of the face. Moreover we are given the value jump¹ $a_f = -\sigma\kappa_f$ and gradient jump b_f . The unknown scaled gradients are denoted by g_f^π . See also Figure 2.

The scaled mixture gradients, as per the Ghost Fluid Method [4], are then given by

$$\bar{g}_f = \frac{1}{\bar{\rho}_f}(\bar{G}p)_f = \frac{1}{\bar{\rho}_f}(Gp)_f + \frac{\delta_f a_f}{\bar{\rho}_f h_f} - b_f \frac{\hat{\rho}_f}{\bar{\rho}_f}, \quad (16)$$

where $\bar{\rho}_f, \hat{\rho}_f$ are average densities depending on the face aperture A_f and the distance to the interface. The difference between the liquid indicators at opposite sides of the face f is denoted by $\delta_f = h_f(G\chi)_f \in \{-1, 0, 1\}$. We recognize contributions from the standard finite difference operator, the pressure value jump and the pressure gradient jump respectively. If the value jump a_f is known at second order accuracy, it follows that the resulting gradient will be at most first order accurate in h_f .

One-dimensional GFM

From the discussion in Section 2.2 we know that we should not impose a jump on the full pressure gradient, but rather only on the component normal to the interface. In Liu et al. [4] it is assumed that the jump component tangential to the interface vanishes, resulting in

$$b_f = \alpha_{i_f, f} \llbracket u_\eta^* \rrbracket, \quad (17)$$

where $\alpha_{i_f, f} = \eta_{i_f} \cdot \eta_f$ is the face normal component of the interface normal η_{i_f} . We refer to this approach as the ‘one-dimensional’ GFM (1d-GFM).

Multi-dimensional GFM

Whenever the interface is not aligned with the face f (hence $|\alpha_{i_f, f}| \neq 1$), the 1d-GFM is inconsistent. We propose to replace (17) by a formula which consistently imposes the normal derivative jump condition on the gradient (9). Note that (9) involves the dot product of the full gradient with the interface normal, and therefore interpolation to the face f of interface tangential pressure derivatives will be required.

The interface configuration, defined by the indicator χ as well as the face apertures $A \in F^h$, defines two types of interface faces where the gradient will be modified:

- If a face f connects two nodes $C(f) = \{c, c'\}$ from different phases (so $\chi_c \neq \chi_{c'}$) then we call this an interface normal face. See also Figure 3. The set of all interface normal faces is denoted by \mathcal{F}_{I_η} .
- On the other hand, if a face f connects two nodes from the same phase, but with a non-trivial aperture (so $A_f \notin \{0, 1\}$) then we call this an interface tangential face. See also Figure 4. The set of all interface tangential faces is denoted by \mathcal{F}_{I_τ} .

¹The curvature κ_f is interpolated from a cell-based curvature $\kappa \in C^h$ which in turn is computed using local height functions, which are generalized [5] if needed.

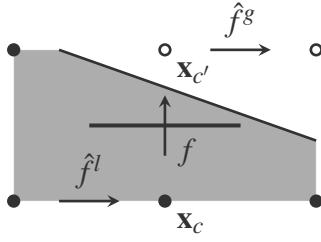


Figure 3: Example Md-GFM gradient stencil for an interface normal face $f \in \mathcal{F}_\eta$.

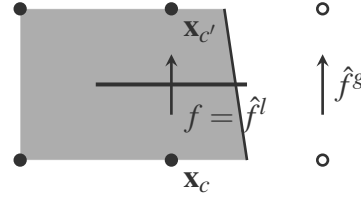


Figure 4: Example Md-GFM gradient stencil for an interface tangential face $f \in \mathcal{F}_\tau$.

The discretization of the gradient operator for an interface normal face is as follows. We define a jump interpolant J which given $u \in \hat{F}^h$ yields a consistent approximation to the jump of the vector-valued function \mathbf{u}

$$J: \hat{F}^h \rightarrow F^h \times F^h, \quad u_f \mapsto (Ju)_f \approx \llbracket \mathbf{u} \rrbracket(\mathbf{x}_f). \quad (18)$$

We choose two faces $\hat{f}^g \in \hat{\mathcal{F}}^g, \hat{f}^l \in \hat{\mathcal{F}}^l$ whose face normals are orthogonal to η_f , from which we define the jump interpolant as

$$(Ju)_f = \eta_f \llbracket u_f \rrbracket + \eta_{\hat{f}^g} u_{\hat{f}^g}^g - \eta_{\hat{f}^l} u_{\hat{f}^l}^l, \quad (19)$$

see also Figure 3. Using this jump interpolant we can consistently impose (9)

$$\eta_{i_f} \cdot [(Jg)_f - (Ju^*)_f] = 0. \quad (20)$$

Combining (19) & (20), and solving for $\llbracket g_f \rrbracket$ yields the jump across the face f

$$b_f^\eta = \frac{\eta_{i_f} \cdot (Ju^*)_f}{\alpha_{i_f, f}} - \frac{\alpha_{i_f, \hat{f}^g}}{\alpha_{i_f, f}} g_{\hat{f}^g}^g + \frac{\alpha_{i_f, \hat{f}^l}}{\alpha_{i_f, f}} g_{\hat{f}^l}^l. \quad (21)$$

The faces \hat{f}^g, \hat{f}^l should be chosen such that the evaluation of the interpolant can be done explicitly, hence $\hat{f}^\pi \notin \hat{\mathcal{F}}_{I_\eta}$. Moreover the interpolant should result in a compact stencil and we therefore restrict ourselves to a 6-point stencil for the Md-GFM gradient.

We found that ensuring $\left| \frac{\alpha_{i_f, \hat{f}^\pi}}{\alpha_{i_f, f}} \right| \leq 1$ greatly improves the quality of the Md-GFM operator in time-dependent problems (this requires further investigation). For faces $f \in \mathcal{F}_{I_\eta}$ for which this ratio exceeds 1 we interpret the face as an interface tangential face instead.

For an interface tangential face $f \in \mathcal{F}_{I_\tau}$ we do not impose the gradient jump condition (9). Instead we select two faces \hat{f}^g, \hat{f}^l (one of which coincides with f itself) with the same face normal direction but each in a different phase, which we use for computing the gradient jump. See also Figure 4. This results in the following gradient jump

$$b_f^\tau = \frac{1}{\rho^g} (Gp)_{\hat{f}^g} - \frac{1}{\rho^l} (Gp)_{\hat{f}^l}. \quad (22)$$

Composition of the CCM divergence operator with the aforementioned modifications to the gradient operator defines our Laplace operator. The stencil is no larger than 3×3 , and the Laplace operator is no longer self-adjoint but can still be shown to be negative semi-definite with only the constant pressure in the null-space.

4 Validation

Here we consider the validation of the proposed discretization. We first assess the accuracy of the discretized Poisson problem and then consider the more exciting dam-break problem.

4.1 Poisson problem

We compare our proposed method to the Immersed Interface Method (IIM) [3] which sharply imposes jump conditions directly on the Laplacian. The 1d-GFM [4], implemented as described in Section 3.3.2, is also included in the comparison. Whenever the methods 1d-GFM or Md-GFM are referred to in the context of a Laplace operator, the composition with the CCM divergence operator (13) is implied.

We consider the following Poisson problem given by Leveque and Li [3] (therein referred to as ‘Problem 3’ with $\beta = \rho^{-1}$)

$$\nabla \cdot \left(\frac{1}{\rho} \nabla p \right) = f, \quad \mathbf{x} \in \Omega = (-1, 1)^2. \quad (23)$$

The right-hand side f , the Dirichlet boundary conditions, as well as the jump conditions at the interface are such the exact solution is given by

$$p = \begin{cases} \exp(x) \cos(y) & \text{if } \mathbf{x} \in \Omega^l \\ 0 & \text{if } \mathbf{x} \in \Omega^g \end{cases}, \quad (24)$$

where Ω^l is the interior of a circle with radius $\frac{1}{2}$ centered at the origin. Note that p is discontinuous and has a jump in the normal as well as tangential derivative.

4.1.1 Mesh refinement

We let $\rho^l = \rho^g = 1$ and vary the mesh-width as $h = 2/N$ where $N = 10 \times 2^l$ for $l = 1, \dots, 5$. The resulting L^∞ errors in the pressure are shown in Table 1. As expected, the 1d-GFM is first-order accurate, whereas the Md-GFM is second-order accurate, and of comparable accuracy to the IIM. The main advantage of using the Md-GFM is that the Laplace operator itself follows from the *composition* of a divergence operator and a gradient operator which is required in the context of solving incompressible two-phase problems.

4.1.2 Varying the density ratio

To assess the dependence of the errors on the density ratio we fix the mesh-width $h = 2/80$, and vary the density ratio. The resulting gradient errors are shown in Table 2. We note that the

| N | IIM | 1d-GFM | Md-GFM | ρ^g/ρ^l | $\ \frac{1}{\rho}\nabla p - \frac{1}{\rho}Gp^h\ _{L^\infty}$ |
|-----|-----------------------|-----------------------|-----------------------|-----------------|--|
| 20 | 4.38×10^{-4} | 7.78×10^{-3} | 2.67×10^{-3} | 10^6 | 3.14×10^{-2} |
| 40 | 1.08×10^{-4} | 6.48×10^{-3} | 6.15×10^{-4} | 10^3 | 3.14×10^{-2} |
| 80 | 2.78×10^{-5} | 6.47×10^{-3} | 1.56×10^{-4} | 10^0 | 3.24×10^{-2} |
| 160 | 7.50×10^{-6} | 3.20×10^{-3} | 3.36×10^{-5} | 10^{-3} | 2.14×10^{-2} |
| 320 | 1.74×10^{-6} | 1.49×10^{-3} | 9.11×10^{-6} | 10^{-6} | 2.14×10^{-2} |

Table 1: The resulting error $\|p - p^h\|_{L^\infty}$ for the Poisson problem defined by (24). Results for IIM are taken from Leveque and Li [3].

Table 2: Dependence of the scaled gradient error on the density ratio ρ^g/ρ^l for the Md-GFM.

accuracy of the gradient is independent of the density ratio. Hence the proposed method can be used to accurately simulate near the one-phase limit $\rho^g \rightarrow 0$.

4.2 A dam-break problem

The proposed discretization has been implemented in our in-house free-surface Navier-Stokes solver ComFLOW. Local and adaptive mesh refinement is used, as detailed in Van der Plas [7]. We validate our model using a smooth version of the classic dam-break problem.

4.2.1 Problem description

The domain is a rectangle of size $20 \times 12m$ with an elliptic bathymetry of half lengths 18 and $2.8m$ whose center lies in the left-hand side bottom corner. Slip boundary conditions are imposed on the velocity field. The liquid density is given by $\rho^l = 10^3 kg/m^3$, the gas density varies and will always be indicated. Both fluids are initially at rest and separated by the following interface profile

$$y(x) = 7.6 + 3.6 \tanh(0.36(x - 12.5)), \quad (25)$$

which will result in a flip-through impact (FTI) [1] in which the wave trough and crest reach the wall at the same time instance, resulting a violent impact. The gravitational acceleration is set to $g = -9.81m/s^2$ and the surface energy coefficient is that of the combination of water and air at $25^\circ C$: $\sigma = 7.2 \times 10^{-2} J/m^2$. A static contact angle boundary condition of 90° is imposed on the curvature.

Our base mesh is uniform with $N_x = 80$ and $N_y = 48$ cells in the x - and y -direction respectively. We consider several levels of mesh refinement, where we refine the mesh near the interface using blocks of size 16×16 . The refinement level at the interface $l \in \{2, 3, 4\}$ will always be indicated, the resulting interface mesh-width is given by $h = 2^{-(l+2)}m$.

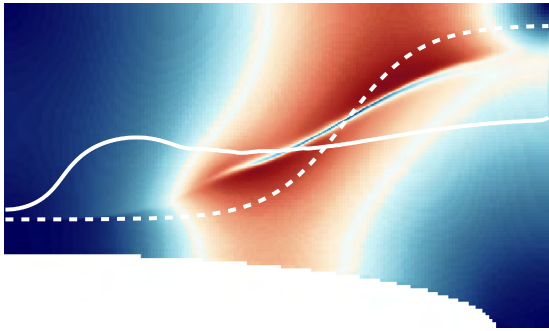


Figure 5: Standard two-phase model. Absolute velocity $|u|$ at $t = 0.75$. Interface is shown at $t = 0$ & 1.47 .

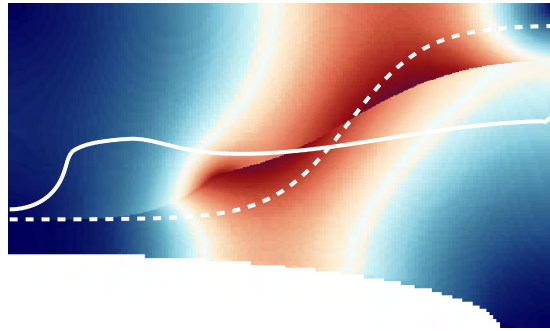


Figure 6: Proposed two-phase model. Absolute velocity $|u|$ at $t = 0.75$. Interface is shown at $t = 0$ & 1.47 .

4.2.2 Comparison to standard two-phase method

Here we demonstrate the efficacy of the proposed model when compared to the standard two-phase model². We let $\rho^g = 1$ and $l = 3$.

In Figures 5 & 6 we show the resulting absolute velocity. We also show the initial interface profile (dashed) and at a later time $t = 1.47$ (solid). Note that the standard two-phase model has a thin region at the interface in which the velocity transitions from gas to liquid. Our proposed model captures this transition in a discontinuity, which allows the breaking wave to develop properly, as seen by the interface profile at $t = 1.47$.

4.2.3 Mesh refinement

We let the gas density be 1 and we consider three levels of refinement $l = 2, 3, 4$. In Figure 7 we show a close-up of the resulting interface profiles, as well as the tangential velocity jump $[[u_\tau]]$ along the interface. Results by the CADYF code³[1] are included.

Except for the highest level of refinement, $l = 4$, we observe convergence towards the reference solution. For the highest refinement level, we observe a small fragmentation of the interface at the location where the velocity discontinuity is largest. Whether this is physical, and occurs only at the finest level because it is underresolved at the coarse level, or a numerical artifact, is unclear. The reference solution clearly does not exhibit this behavior, but this could be attributed to numerical damping.

4.2.4 Varying the density ratio

Furthermore we consider the dependence of the solution on the gas density. To this end we fix the refinement level at $l = 3$, and vary the gas density as $\rho^g = 10^{-3}, 1, 3$ and 5 kg/m^3 . For the

²The numerical scheme was identical except for the condition $[[u_\tau]] = 0$ and the use of first-order upwind throughout the entire domain. For our proposed model the symmetry-preserving central discretization was adequate.

³CADYF is a PSPG-SUPG FEM code which implements the two-phase Navier-Stokes equations using the ALE formulation.

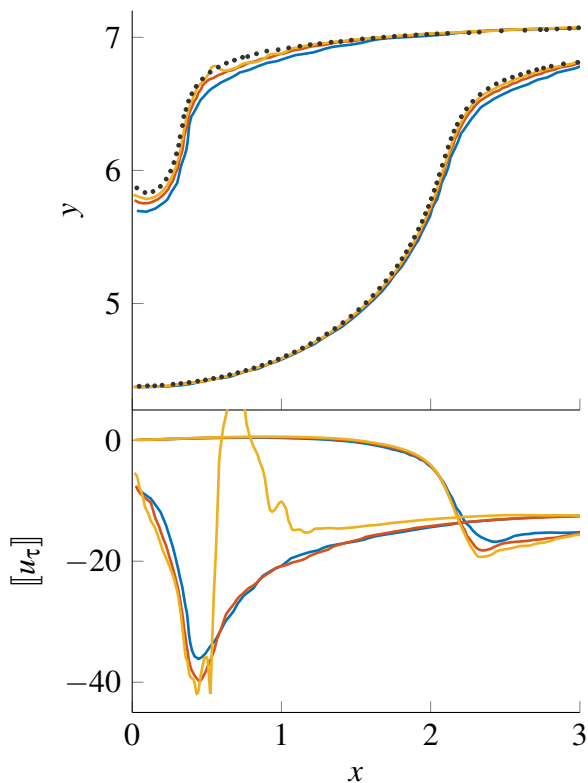


Figure 7: Interface profiles (top) and velocity discontinuity (bottom) for $\rho^g = 1 \text{ kg/m}^3$ at two time-instances $t = 1.47, 1.67$. Refinement levels are $l = 2$ (blue), 3 (red) and 4 (yellow). Reference solution by CADYF (black markers) [1].

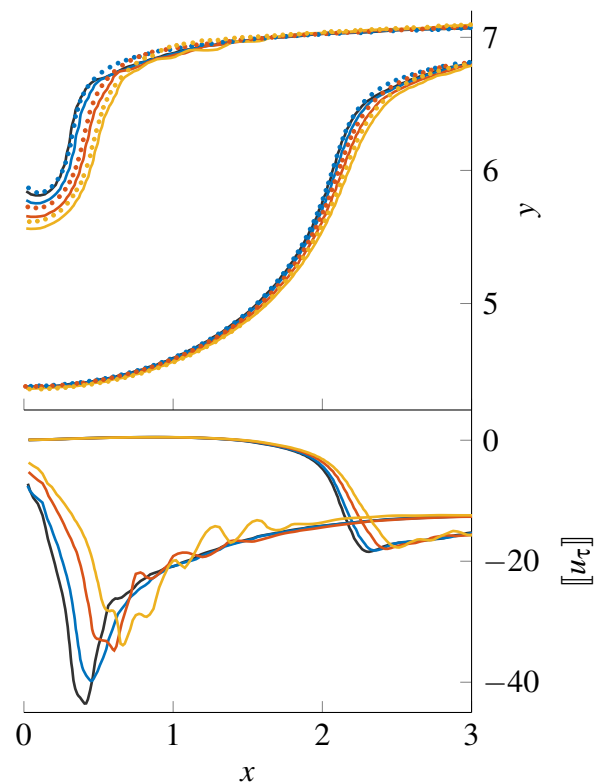


Figure 8: Interface profiles (top) and velocity discontinuity (bottom) for gas densities $\rho^g = 10^{-3}$ (black), 1 (blue), 3 (red) and 5 kg/m^3 (yellow) at $t = 1.47, 1.67$. The refinement level was $l = 3$. Reference solutions by CADYF (colored markers) [1].

latter three we have a reference solution by CADYF [1].

We find fairly good agreement in terms of the interface profile. The maximum tangential velocity jump increases as the gas density decreases, which may be expected. Moreover, for the larger gas densities, oscillations in the tangential velocity jump can be observed just before impact. This suggests that free surface instabilities are about to develop. The fact that such oscillations are not present for $\rho^g = 10^{-3}$ means that we successfully approach the one-phase limit in which no free surface instabilities due to shearing gas flow are present.

5 Conclusion

We presented a discretization approach for capturing contact discontinuities in two-phase flow. The discretization of the pressure Poisson problem plays a central role since it implicitly couples the phases using a gradient jump condition which corresponds to imposing smoothness of the velocity field *only in the interface normal direction*. A novel combination of our proposed Md-GFM and the CCM was used to achieve this. Using the dam-break problem we then

demonstrated that this approach is able to capture contact discontinuities sharply and accurately, even at high density ratios (demonstrated up to 10^{-6}) close to the one-phase limit.

For the discretization presented in this paper there are several aspects that need further investigation: uniquely defining the Md-GFM jump interpolant to improve the properties of the Laplace operator as well as thorough analysis of the convection scheme near the interface.

The model will be extended with gas compressibility and the effects of viscosity will be included. When modeling viscous flow, the velocity jump condition becomes a closure model for underresolved boundary layers. Eventually we want to use this model to study the effects of free surface instabilities in sloshing of LNG and its vapor.

Acknowledgements

This work is part of the research programme SLING, which is (partly) financed by the Netherlands Organisation for Scientific Research (NWO).

References

- [1] Etienne, S., Scolan, Y.-M., and Brosset, L. (2018). Numerical Study of Density Ratio Influence on Global Wave Shapes Before Impact. In 2, pages 1–11.
- [2] Lafeber, W., Brosset, L., and Bogaert, H. (2012). Comparison of Wave Impact Tests at Large and Full Scale : Results from the Sloshe1 Project. In *Twenty-Second (2012) International Offshore and Polar Engineering Conference*, volume 4, pages 285–299.
- [3] Leveque, R. J. and Li, Z. (1994). The Immersed Interface Method for Elliptic Equations with Discontinuous Coefficients and Singular Sources. *SIAM Journal on Numerical Analysis*, 31(4):1019–1044.
- [4] Liu, X.-d., Fedkiw, R. P., and Kang, M. (2000). A Boundary Condition Capturing Method for Poisson’s Equation on Irregular Domains. *Journal of Computational Physics*, 160:151–178.
- [5] Popinet, S. (2009). An accurate adaptive solver for surface-tension-driven interfacial flows. *Journal of Computational Physics*, 228(16):5838–5866.
- [6] Udaykumar, H. S., Kan, H.-c., Shyy, W., and Tran-son tay, R. (1997). Multiphase Dynamics in Arbitrary Geometries on Fixed Cartesian Grids. *Journal of Computational Physics*, 137(2):366–405.
- [7] Van der Plas, P. (2017). *Local grid refinement for free-surface flow simulations*. PhD thesis, Rijksuniversiteit Groningen.
- [8] Verstappen, R. and Veldman, A. E. P. (2003). Symmetry-preserving discretization of turbulent flow. *Journal of Computational Physics*, 187(1):343–368.
- [9] Zinjala, H. K. and Banerjee, J. (2015). A Lagrangian-Eulerian Volume-Tracking with Linearity-Preserving Interface Reconstruction. *Numerical Heat Transfer, Part B*, 68:459–478.

ANALYSIS OF FLEXIBLE NET STRUCTURES IN MARINE ENVIRONMENT

MARINE 2019

A. J. BERSTAD* AND L.F. HEIMSTAD†

* Aquastructures
Kjøpmannsgata 21
7013 Trondheim, Norway
e-mail: are@aquastructures.no, www.aquastructures.no

† Aquastructures
Kjøpmannsgata 21
7013 Trondheim, Norway
e-mail: line@aquastructures.no, www.aquastructures.no

Key words: Computational Methods, Aquaculture, Fish farm, Marine Engineering, Permeable nets, Flexible systems, Hydroelasticity, Coupled analysis

Abstract. The classic aquaculture units are flexible net structures where loads from the marine environment are drag-dominated. Such systems are normally analysed using computer intensive dynamic hydro-elastic analysis. The current analysis culture is to apply a regular design wave analysis to cage grids which are drag dominated, while irregular analysis is applied to barge units which are mass dominated. This is mostly due to time efficiency, but has been under the assumption that the drag dominated systems have less need for irregular analysis to obtain a realistic estimate for the max design response value.

This paper does extensive analysis of a classic aquaculture cage case to compare the regular and irregular response analysis. Response from regular wave analysis is compared to response from three hour long time series of irregular waves. Extreme value statistics are derived and results are discussed.

1 INTRODUCTION

The aquaculture industry in Norway has increased rapidly the last decades. In the early years the industry was regulated only under the laws for free enterprise until the first specific laws were put into place in 1973. Since then, rules and regulations have evolved and in 2003 the Norwegian Standard NS 9415 [3] was introduced, establishing design criteria. In 2009 the NS 9415 was revised and in 2011 corresponding regulations were enforced. Structural integrity to defined load criteria had to be documented. This largely increased the engineering effort within the industry and as more systems were assessed and documented to this regime, the number of escaped fishes plummeted. NS 9415 is currently under revision with scope to enhance safety even further.

The classic aquaculture units are drag-dominated structures. About 90% of the fish farms in Norway are based on polyethylene floating collars with a flexible net underneath as shown in Figure 1.

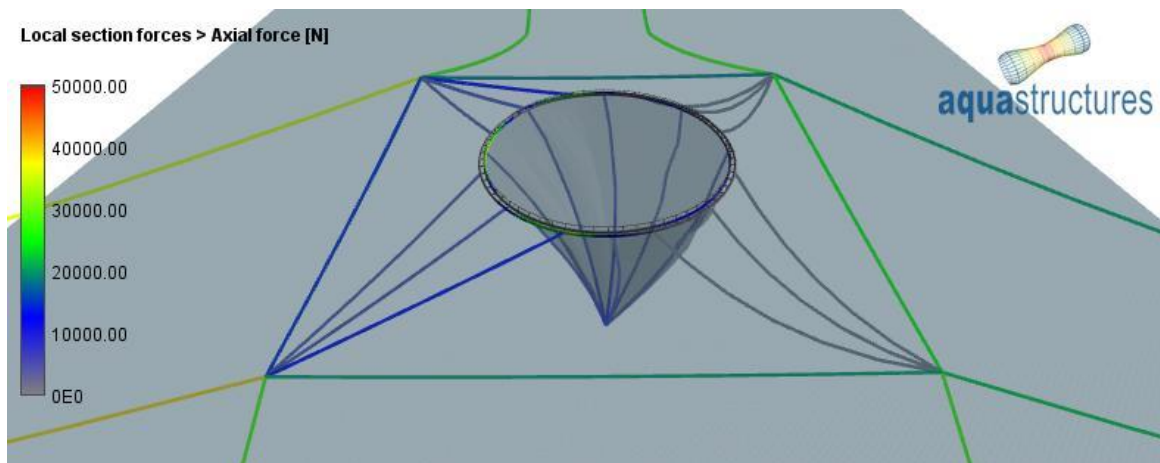


Figure 1 Conically shaped net in floating collar

Figure 1 shows a conically shaped net. The net cages are normally laid out in a grid like the one shown in Figure 2.

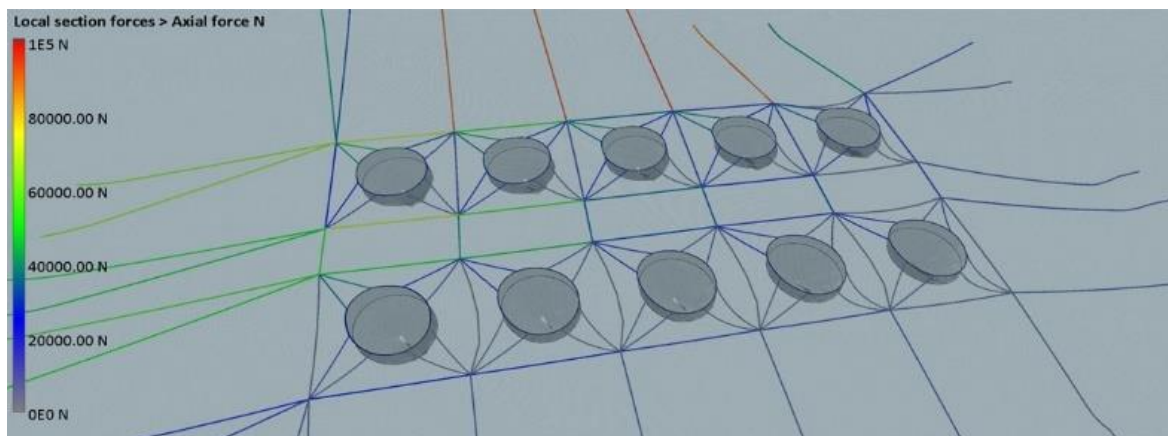


Figure 2 Grid system

2 THEORETICAL BASIS FOR THE AQUASIM ANALYSIS

The analysis presented in this paper are carried out with the FEM software-tool AquaSim. AquaSim is the most commonly used analysis tool for finding response of Aquaculture units from wind, current and waves worldwide. The AquaSim software is based on the finite element method. It utilizes beam and shell elements with rotational degrees of freedom, (DOF's), as well as membrane elements and truss elements with no rotational stiffness. Geometric nonlinearities are accounted for in all element types, such that the program handles large structural deformations. The program is based on time domain simulation where it is iterated to equilibrium at each time instant. Both static and dynamic time domain simulation may be carried out. Features such as buoys, weights, hinges and springs are included in the program.

The basic idea of the FE analysis program is to establish equilibrium between external loads acting on the structure at a given time instant and internal reaction forces:

$$\sum F = R_{ext} + R_{int} = 0 \quad (1)$$

where R_{ext} is the total of the external static forces acting on the structure at a given time instant and R_{int} is the internal forces. The structure is discretized to a finite number of DOF's. Equation 1 is then discretized as:

$$F^{idof} = R_{ext}^{idof} + R_{int}^{idof} = 0, \quad idof = 1, N_{dof} \quad (2)$$

where N_{dof} is the discrete number of DOF's the structure has been discretized into. The current element program deals with strongly nonlinear behaviour both in loads and structural response. To establish equilibrium, the tangential stiffness method is used. External loads are incremented to find the state of equilibrium. Having established equilibrium in time step $i-1$, the condition for displacement r , step i , is predicted as:

$$\Delta R^i(r_{i-1}) = R_{ext}^i(r_{i-1}) + R_{int}^{i-1}(r_{i-1}) = K_t^{i-1} \Delta r \quad (3)$$

where K_t^{i-1} is the tangential stiffness matrix at configuration $i-1$. The external load is calculated based on the configuration of the structure at $i-1$. This gives a prediction for a new set of displacements ($j=1$). Based on Equation 3, a prediction for the total displacement $r_{(j=1)}$, is found as:

$$\bar{r}_{j-i} = r_{i-1} + \Delta r \quad (4)$$

Based on this estimate for new displacements, both external and internal forces are derived based on the new structural geometry and the residual force, ΔR is put into the equation of equilibrium as follows:

$$\Delta R(\bar{r}_i) = R_{ext}^i(\bar{r}_i) + R_{int}^i(\bar{r}_i) = K_t^i \Delta r \quad (5)$$

Note that both the external and internal forces will vary for each iteration due to the strongly hydro-elastic nature of the fluid structure interaction. Equation 5 is solved for the displacement Δr . Incrementing j with one, the total displacement is now updated as:

$$\bar{r}_j = \bar{r}_{j-1} + \Delta r \quad (6)$$

Now if Δr found from Equation 5 is larger than the tolerated error in the displacements, Equation 4 is updated ($j = j+1$) and Equation 5 is solved based on the new prediction for displacements, this is repeated until, Δr is smaller than a tolerated error, then:

$$r_i = \bar{r}_j \quad (7)$$

i is increased with one, and Equation 4 is carried out for the new load increment.

At the default configuration, the software works as this: Static analysis is used to establish static equilibrium including buoyancy. Secondly, current loads are applied then wind and wave loads are added (still static analysis). Then dynamic analysis commences. Waves are introduced with the first wave used to build up the wave amplitude. Both regular waves and irregular waves

may be simulated. Waves are assumed to be sufficiently described by linear wave theory. Inertia and damping are accounted for in the wave analysis, meaning that mass and damping are accounted for in the equations of equilibrium. The Newmark-Beta scheme is applied for the dynamic time domain simulation. Note that the above equations imply using the Euler angles for rotations. This is just a simplification for easy typing. For rotational DOF's AquaSim uses a tensor formulation for the rotations as outlined in e.g. [10] which should be applied to handle 3D rotations in an appropriate manner.

Wave loads may be derived using the Morison formulae [6] or using diffraction theory [9]. For elements where the Morison formulae is applicable the cross-flow principle is applied for beams and truss elements [9]. The drag load term of this equation is quadratic with respect to the relative velocity between the undisturbed fluid and the structure. Both the mass of the structure as well as added mass in the cross-sectional plane is accounted for. Due to the large deflections occurring, the added mass is nonlinear. For permeable nets the method presented in [11] is applied. A main difference in the drag load on permeable net compared with drag loads to truss is the increase of the drag due to the presence of the permeable net. [11] formulated this as an increased drag coefficient:

$$Cd_{mem} = Cd_{cyl} \frac{1}{\left(1 - \frac{Sn}{2}\right)^3} \quad (8)$$

where Sn is the solidity of the net.

A further description of load and response for permeable nets in AquaSim is described in [4] and [11].

AquaSim has been used commercially for more than 15 years and has throughout the years undertaken a versatile verification scheme: Analysis has been carried out on a wide range of computational cases where results have been compared to handbook formula or other programs [4]. As early as in 2004 model experiments were carried out and compared to analysis [5]. AquaSim has been compared to accidents where the capsize origins were known [1], [2]. In addition, experience have been obtained during several years where AquaSim has been the most used software for calculation of the structural integrity of fish farm systems in Norway, as well as in other regions with similar aquaculture systems including Chile, North America and Australia. The cage-system as seen in Figure 2 in general consist of mooring lines, floating collars and nets responding to wave and current in a strongly nonlinear (hydro-elastic) manner. AquaSim is also used for a wide range of offshore applications such as towing for seismic operations [8], operations and installations offshore, mooring analysis of offshore units and structural and mooring analysis of equipment for renewable equipment offshore [7].

3 CASE STUDY: POLYETHYLENE CAGE GRID SYSTEM

The system seen in Figure 1 is used as case study. The system is a 50 meter diameter circular collar with a conically shaped net and mooring as shown in Figure 3 and Figure 4. Details regarding the input-data is given in Appendix.

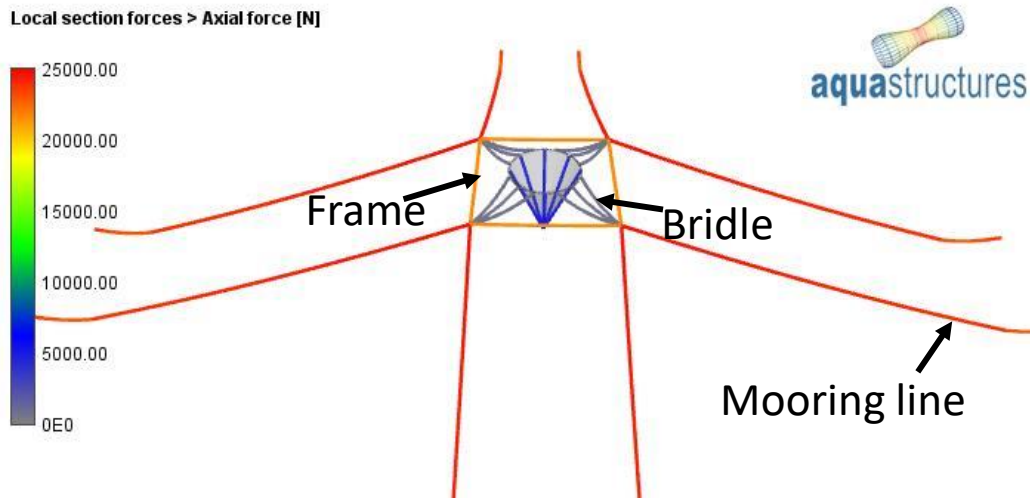


Figure 3 Case study 1, classic polyethylene-based fish farm. Colours represent axial force in still water which is the pretension force. The x- axis points to the right in the figure and the z- axis point upward in ant orthonormal coordinate system.

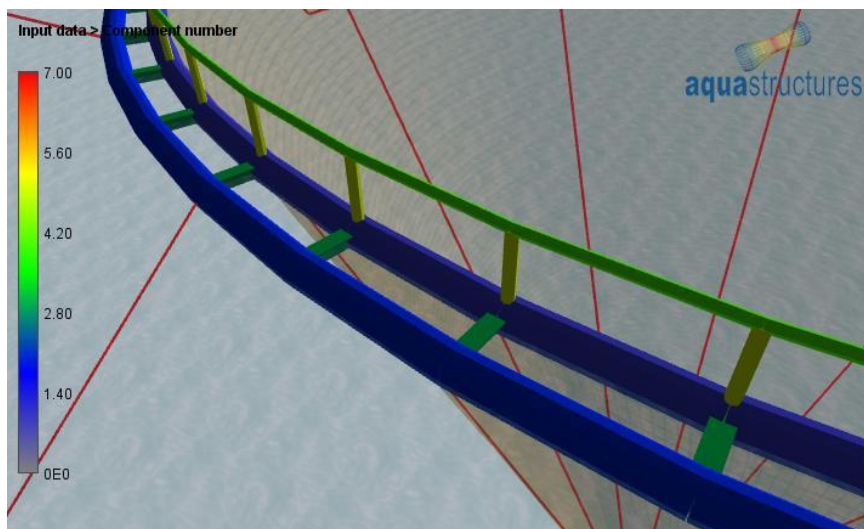


Figure 4 Polyethylene collar. Components are indicated by colour. Component data are given in Appendix.

The most important load component to such system is the drag term of the Morison equation:

$$F = Cd \frac{\rho}{2} dLv^2 \quad (9)$$

Cd is the drag coefficient, d is the diameter of twine or rope and L is the length. The velocity v is the relative velocity between the twine / rope and the flow in the cross-flow direction. Differentiating between velocity cause by waves (v_w), by current (v_c) and by the system (v_s), the combined velocity in the cross-flow direction can be expressed as:

$$v = v_w + v_c - v_s \quad (10)$$

The force acting on the net is squared relative to the sum of the combined cross-flow relative velocity. Hence effects cannot be superposed. The forces depend on both angle of the twine and

the effective solidity in the given position. This means that time domain simulations with all effects combined are a necessity.

In AquaSim the current velocity flow is incremented, and static equilibrium is established. Then waves are incremented over one wave period to its full amplitude for regular waves and over a time period = T_z for irregular waves. Figure 5 shows results in terms of axial forces in mooring components for a load case with the environmental data given in Table 1.

Table 1 Environmental data

| Parameter | Abbreviation | Value |
|-------------------|---------------|---------|
| Current velocity | Vc | 0.5 m/s |
| Current direction | Along x- axis | 0.0 deg |
| Wave type | - | Regular |
| Wave amplitude | - | 2.0 m |
| Wave direction | Along x- axis | 0.0 deg |
| Wind | Not included | - |

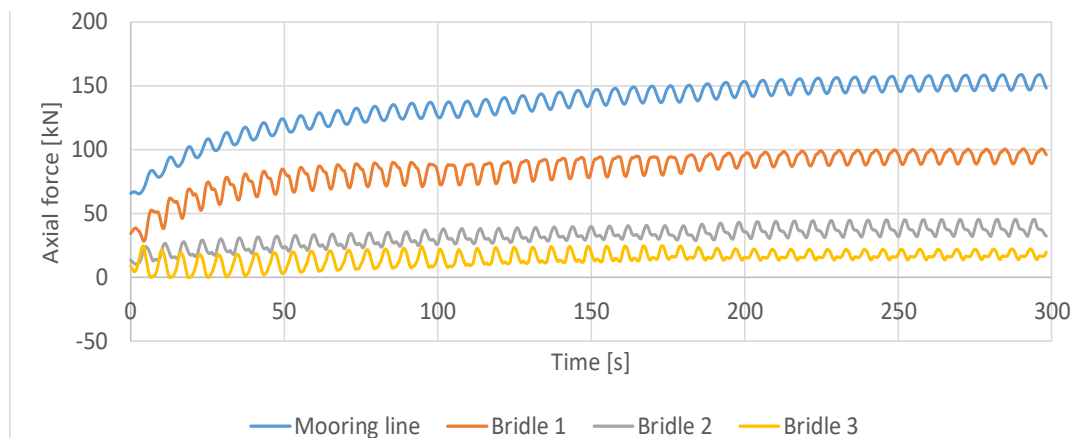


Figure 5 Axial force in 4 lines in the mooring system as function of time. The 4 lines are marked in Figure 6.

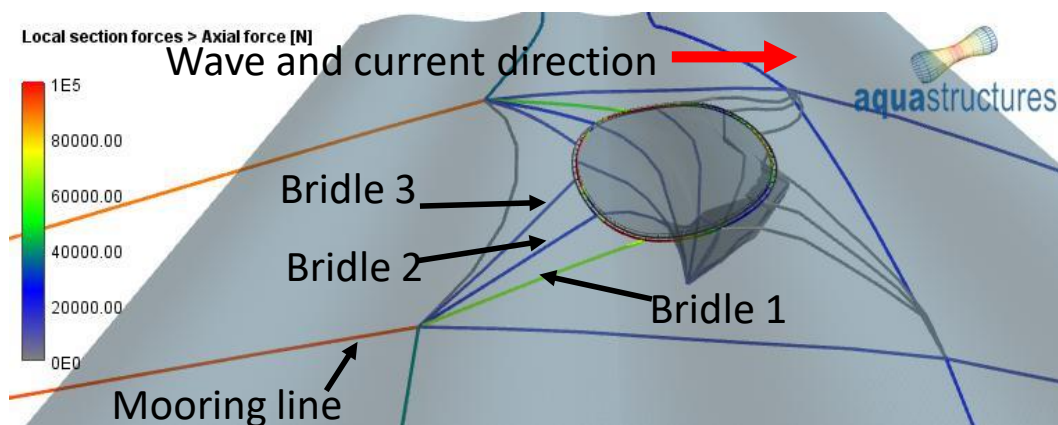


Figure 6 One time instant in the analysis, system is deformed.

As seen from Figure 5 it takes approximately 250 seconds for the response to reach a steady state where the drift-force is fully developed. The fully developed situation for several design waves will of course not occur for the real-life cases. The relation between the response of the n^{th} wave of the regular wave response and peak response in irregular seas is compared.

Figure 7 shows displacement as function of time for the mooring lines.

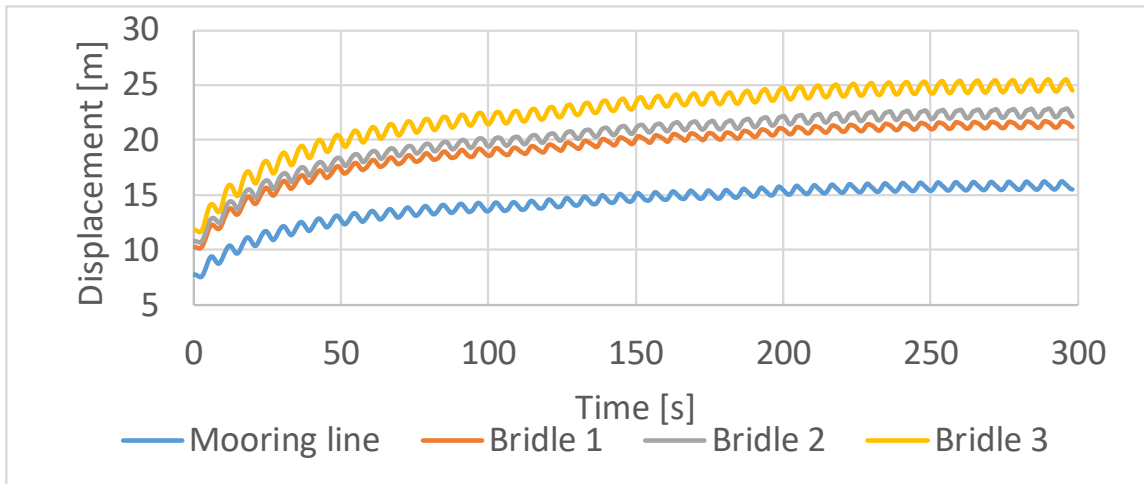


Figure 7 Displacement. Response time series for displacement in mooring lines.

As seen from Figure 7, and comparing to Equation 10 it is seen that the system is pushed in the wave and current direction wave cycle by wave cycle. Since there is an average force in the direction of the wave propagation, the system slides in the wave propagation direction until equilibrium is established, which in this case takes approximately 250 seconds.

Figure 8 presents results for regular waves with amplitude 1.0 meter and a period of 3.0 seconds

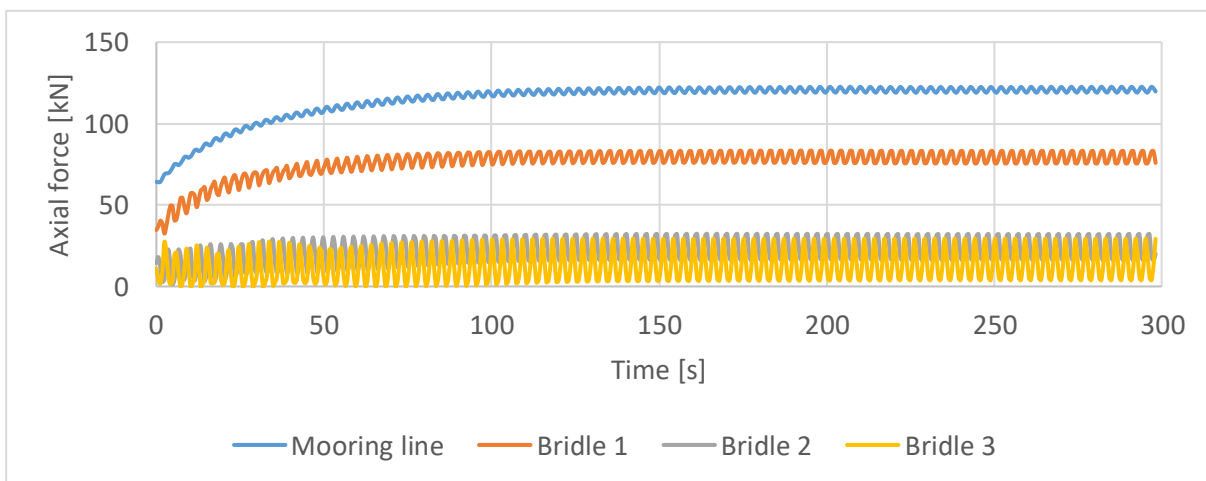


Figure 8 Axial force. Results for regular waves with amplitude 1.0 meter and a period of 3.0 seconds.

Figure 9 shows results for regular waves with amplitude of 3.0 meter and a period of 9.0 seconds

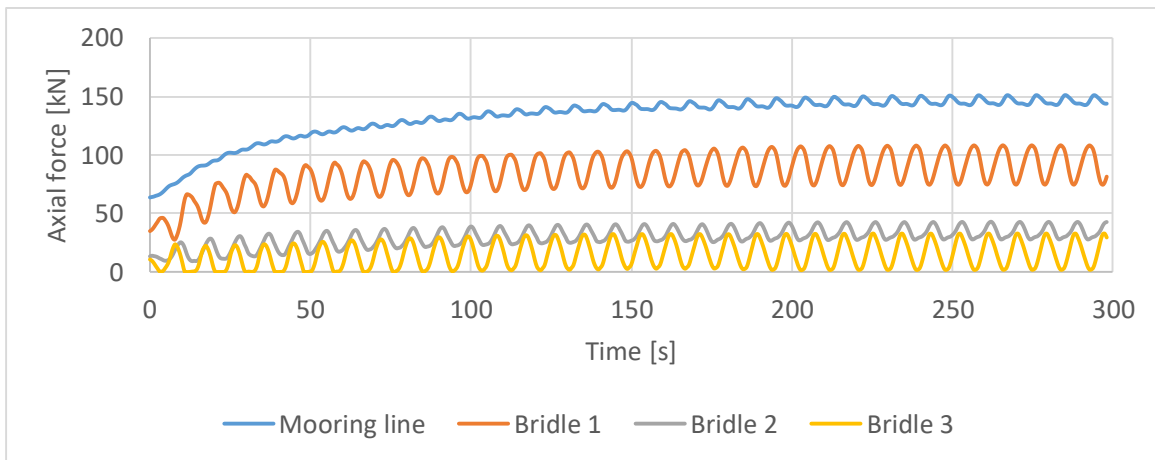


Figure 9 Axial force. Results for regular waves with amplitude of 3.0 meter and a period of 9.0 seconds.

The results presented in Figure 8 and Figure 9 shows the same trend as the results in Figure 5 but note that the wave induced forces in the bridles vary much more for the cases presented in Figure 8 and Figure 9. This illustrates the need for dynamic analysis and it indicates that the closer the mooring component is to the cage (i.e. bridles) the more important the dynamic wave response is. Note that the dynamics relatively is highest for the low loaded bridles. For a design case there are other wave and current directions such that the results seen for Bridle 3 in this paper will not be the dimensioning forces. Hence it is the Mooring line and Bridle 1 that has been chosen for evaluation of results from irregular analysis.

NS 9415 states that the wave in a design wave approach shall be 1.9 times the significant wave height of an irregular wave (i.e. $H_{max} = 1.9 \times H_s$). This paper also analyses this system with irregular waves. The irregular wave parameters are given in Table 2.

Table 2 Key data for analysis in irregular waves

| Parameter | Abbreviation | Value |
|-------------------------|---------------|-----------|
| Current velocity | Vc | 0.5 m/s |
| Current direction | Along x- axis | 0.0 deg |
| Wave type | | Irregular |
| Spectrum | | Jonswap |
| Significant wave height | Hs | 2.1 m |
| Peak wave periode | Tp | 6.0 s |
| Peak factor of spectrum | | 3.1 |
| Wave direction | Along x- axis | 0.0 deg |
| Wind | Not included | - |

Figure 10 shows examples of response from 20 minutes of irregular waves. 10 time series have been generated based on different seed for random phases of the wave components with at time length of 3 hours, whereas the figure shows 20 minutes.

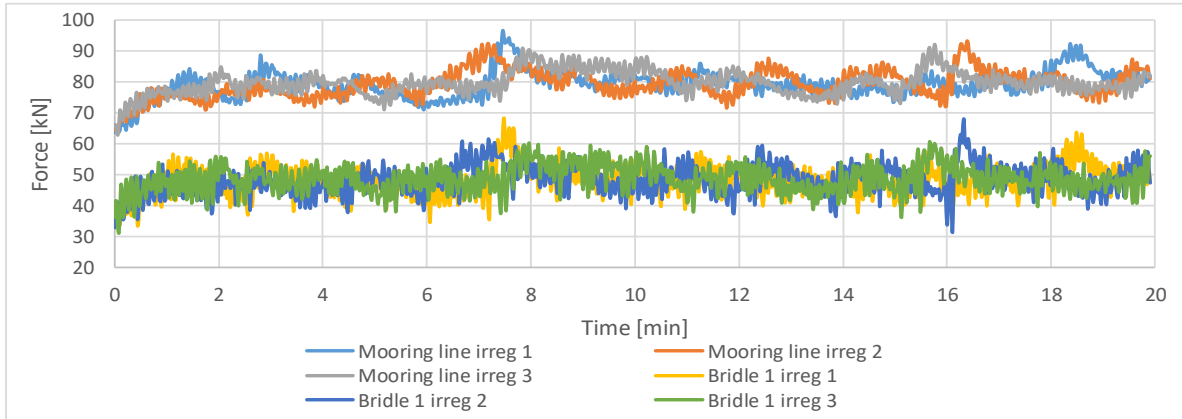


Figure 10 Resulting tensile force in Mooring line and Bridle 1 for three sets of irregular waves.

Discussing the results seen in Figure 10 it is useful to consider the slow drift eigen periods. The eigen periods for the three drifting mode sway, surge and yaw are shown as a function of current velocity in Figure 11.

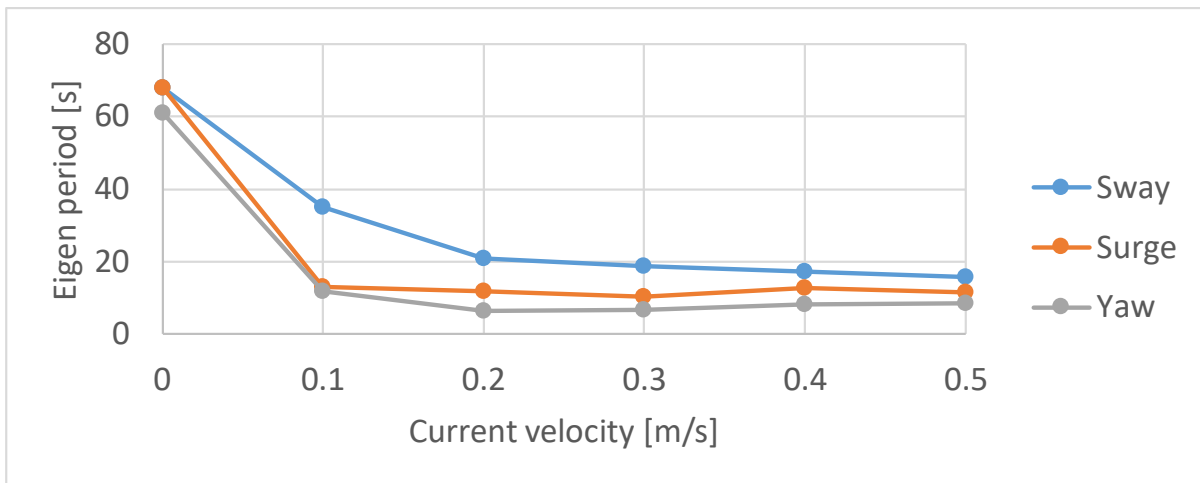


Figure 11 Eigen period for three motions of system as function of current velocity. Surge is transverse to the flow direction.

As seen from Figure 11, the eigen periods of the previously named response modes decrease with increasing current velocity. This is due to that stiffness of the mooring system increase with increasing current velocity. Hence such system will not see frequency domain resonant slow drift behaviour, but rather response better described by an impulse response consideration [12].

The fourth eigen period of this system is not roll, heave or pitch, as are the classic eigen periods for stiff systems, but rather the shape seen in Figure 12.

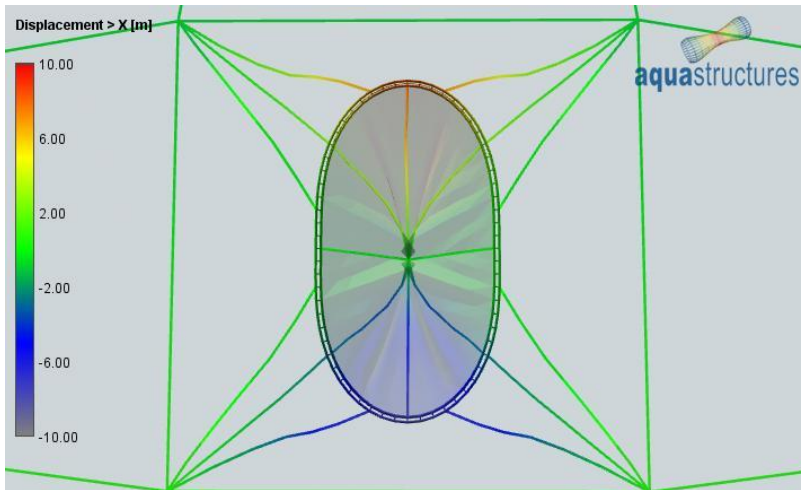


Figure 12 Eigen period at 4.66 seconds (current velocity 0.0 m/s).

As seen from Figure 12 the fourth largest eigen period in this case is an ovalisation of the floating collar. Though the eigen period for this case is in the area of high wave energy. The damping due to drag forces in the net is so high that resonant motions, for classic net pen system, in this shape has not been observed. However, the eigen-shape seen in Figure 12 is an indication to why floating collars may get damage when being stored at sea without nets in them. In such case they do not benefit from the drag damping caused by the net.

Figure 13 presents max force in Mooring line and Bridle 1 from the irregular wave analysis, with 10 different random phases, compared to the max force found from 1 fully developed wave, 2 fully developed waves, 3 fully developed waves and the equilibrium state shown in Figure 5 and Figure 6 (after 250 seconds).

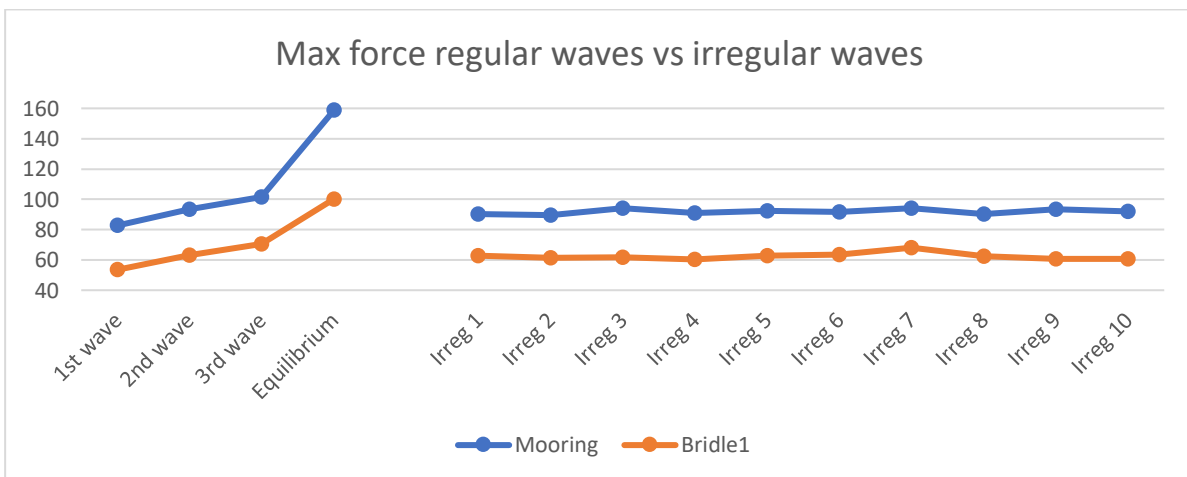


Figure 13 Max force in Mooring line and Bridle 1. Regular and irregular waves.

As seen from Figure 13 the loads from the regular sea analysis are larger after the 3rd wave than for all irregular wave analysis. Whereas the 2nd wave response fall in the range of the irregular sea states and the 1st wave response is lower. Table 3 show the results from the regular wave analysis compared to statistics of the irregular wave analysis. As seen from the

table, there is a good correspondence between the 2nd fully developed wave and the irregular wave analysis, which also is seen in Figure 13.

Table 3 Results regular wave analysis compared to statistics of irregular analysis. For the irregular analysis 3 hour sea state has been analysed.

| Component | 1st wave | 2nd wave | 3rd wave | Fully developed | Irregular average | Irregular 90 % |
|-----------|----------|----------|----------|-----------------|-------------------|----------------|
| Mooring | 82.7 N | 93.5 N | 101.5 N | 158.8 N | 91.8 N | 94.0 N |
| Bridle 1 | 53.5 N | 63.2 N | 70.5 N | 100.2 N | 62.4 N | 63.9 N |

This means that the analysis indicates that when estimating maximum response from regular waves, one should at least simulate two fully developed regular waves.

Comparing the results in general it is seen that the current velocity itself make up for a large component of the forces introduced in the system. This means that the risk introduced by regular wave analysis overall is lower than for systems where waves are the largest load component. This will be the case for most classical fish farm systems.

The standard deviation for the irregular wave results are 1.6 % and 3.3 % of the mean values for the mooring and bridle, respectively.

4 CONCLUSIONS

From the analysis carried out one can conclude that one should at least analyse two fully developed regular waves to be in the same range as the irregular waves. Irregular wave analysis is preferable also for such systems, as it reflects better the actual sea state. The drag- and damping effects plays an important role, such that the spread in results are not high and regular waves would be sufficient for the case analysed in this study.

Slow drift eigen periods for fish farm systems are strongly nonlinear and one should consider whether impulse response could be of importance, but for this case the damping was so large that no response to eigen periods were seen. This will be the case for the classical net pen systems with large damping. In case nets are removed or changed to impermeable nets one should investigate if response caused by eigen periods will be of importance.

In further studies, similar analysis should be carried out for a mass dominated system, such as feeding barges and systems with impermeable nets (e.g. lice skirts) or other structures leading to closed water (and hence mass) compartments and relatively lesser damping.

5 REFERENCES

- [1] Aquastructures (2003) "Havari Laksefjord" (in Norwegian). Report no.2003-132. Aquastructures, Kjøpmannsgata 21 7013 Trondheim. www.aquastructures.no.
- [2] Aquastructures (2005) "Teknisk vurdering av anlegg, Tustna kommune" (in Norwegian). Report no. HR-300083-103, Aquastructures, Kjøpmannsgata 21 7013 Trondheim. www.aquastructures.no.
- [3] NS 9415(2009) Marine fish farms, Requirements for design, dimensioning, production, installations and operation. Pronorm. Postboks 252, 1326 Lysaker.
- [4] Aquastructures (2018) "THE AQUASIM PACKAGE THEORY USER MANUAL" TR-30000-2049-2018 02.01.2018. Aquastructures, Kjøpmannsgata 21 7013 Trondheim. www.aquastructures.no.
- [5] Berstad, A. J., Tronstad, H., Ytterland, A. (2004)" Design Rules for Marine Fish Farms in Norway. Calculation of the Structural Response of such Flexible Structures to Verify Structural Integrity." Proceedings of OMAE2004 23rd International Conference on Offshore Mechanics and Arctic Engineering June 2004, Vancouver, Canada. OMAE2004-51577
- [6] Morison, J. R., M.P. O'Brien, J.W. Johnson and S.A. Schaaf (1950), "The Force Exerted by Surface Waves

- on Piles," *Petroleum Transactions*, AIME. Vol. bold 189, 1950, 149-154
- [7] Berstad, A. J. and H. Tronstad (2007) "Development and design verification of a floating tidal power unit" OMAE 2007, The 26th International Conference on Offshore Mechanics and Arctic Engineering San Diego, California, 10-15 June, 2007. Paper 29052.
- [8] Berstad, A.J. and H. Tronstad (OMAE 2008) "Use of Hydroelastic Analysis for Verification of Towed equipment for Aquisition of Seismic Data" Proceedings of OMAE2008 27th International Conference on Offshore Mechanics and Arctic Engineering June 15-20 2008 Estoril, Portugal OMAE2008-57850
- [9] Faltinsen, Odd M. (1990) "Sea loads on ships and offshore structures." Cambridge university press ISBN 0 521 37285 2
- [10] Eggen, T.E. (2000) "Buckling and geometrical nonlinear beam-type analyses of timber structures" PhD Thesis Institute of civil engineering NTNU.
- [11] Berstad, A.J., J. Walaunet and L. F. Heimstad (2012) "Loads From Currents and Waves on Net Structures" Proceedings of the ASME 2012 31st International Conference on Ocean, Offshore and Arctic Engineering OMAE2012 July 1-6, 2012, Rio de Janeiro, Brazil OMAE2012-83757
- [12] Berstad A. J. and L F. Heimstad (2017) "Experience from Introduction of the Design code NS 9415 to the Aquaculture Industry in Norway and Expanding the Scope to Cover also operations" Proceedings of the 36th International Conference on Ocean, Offshore & Arctic Engineering OMAE 2017 June 25-30, 2017, Trondheim, Norway OMAE2017-62426

APPENDIX

This appendix contains model descriptions of the floating collar system used as case study.

Table 4 Properties belonging to the floating collar, beam elements.

| Parameter | Inner collar | Outer Collar | Brackets | Handrail | Pole |
|-----------------------------------|--------------|--------------|----------|----------|----------|
| E-modulus [N/m ²] | 9.00E+08 | 9.00E+08 | 8.00E+08 | 8.00E+08 | 8.00E+08 |
| G-modulus [N/m ²] | 3.46E+08 | 3.46E+08 | 3.08E+08 | 3.08E+08 | 3.08E+08 |
| Area [m ²] | 4.43E-02 | 4.43E-02 | 1.53E-02 | 3.74E-03 | 4.75E-03 |
| Iy [m ⁴] | 1.23E-03 | 1.23E-03 | 3.15E-04 | 9.05E-06 | 1.48E-05 |
| Iz [m ⁴] | 1.23E-03 | 1.23E-03 | 6.01E-05 | 9.05E-06 | 1.48E-05 |
| It [m ⁴] | 2.46E-03 | 2.46E-03 | 6.79E-05 | 1.79E-05 | 2.92E-05 |
| Volume [m ³ /m] | 1.96E-01 | 1.96E-01 | - | - | - |
| Mass density [kg/m ³] | 9.53E+02 | 9.53E+02 | 9.56E+02 | 9.59E+02 | 9.50E+02 |
| Weight in air [kg/m] | 4.22E+01 | 4.22E+01 | 1.46E+01 | 3.55E+00 | 4.06E+00 |

Table 5 Properties of truss elements

| Parameter | Type | Dia. [m] | E-modulus [N/m ²] | Length [m] | Depth [m] |
|-------------------|-------|----------|-------------------------------|------------|-----------|
| Vertical net rope | Rope | 14 | 2.00E+09 | 60.4 | - |
| Grid | Rope | 48 | 1.80E+09 | 100x100 | 6 |
| Bridle | Rope | 48 | 1.80E+09 | 45 - 50 | - |
| Anchor lines | Rope | 52 | 1.80E+09 | 320 | 106 |
| Anchor chain | Chain | 32 | 8.00E+10 | 50 | 106 |

Table 6 Properties for membrane elements.

| Type | Dia. Twine [mm] | 1/2 mesh width [mm] | E-modul [N/m ²] | Solidity incl. fouling [%] |
|-------|-----------------|---------------------|-----------------------------|----------------------------|
| Nylon | 2.0 | 25.0 | 1.00E+09 | 24.0 |

APPLICATION OF FHSIM FOR THE ANALYSIS OF ENVIRONMENTAL LOADS ON A COMPLETE FISH-FARM SYSTEM

ANDREI TSARAU* AND DAVID KRISTIENSEN†

* SINTEF Ocean AS, Trondheim, Norway
e-mail: andrei.tsarau@sintef.no, web page: <http://www.sintef.no>

† SINTEF Ocean AS, Trondheim, Norway
e-mail: david.kristiansen@sintef.no

Key words: Computational Methods, Aquaculture Structures

Abstract. Fish farming at exposed locations requires robust and reliable structures that facilitate sustainable, safe and efficient production. There is also a need for proper numerical tools and analysis methods that can be utilised for designing such structures and evaluating their performance under increased exposure. Some recent advances in developing and applying such tools are highlighted in the present paper. An analysis of the mooring loads of a complete multi-cage fish farm exposed to currents and waves is presented. This analysis is based on numerical simulations performed with FhSim, which is a software framework developed at SINTEF Ocean for simulating marine systems and flexible net structures in the time domain. Previously, FhSim has been used to simulate loads on a single net cage, and the results have shown a good agreement with experimental data. In the present work, a numerical model of a conventional fish farm with multiple interconnected net cages was built, and the effects of environmental conditions on the mooring loads and their distribution in the mooring system were investigated. Additionally, the sensitivity of the mooring loads to various parameters of the model were studied.

The results have shown that for fish farms operating in marine areas with high current velocities (over 0.5 m/s) under typical wave conditions, the mooring loads are dominated by the current-induced forces rather than the wave forces. Consequently, the assumptions and uncertainties associated with the model for viscous drag on the flexible net structure have the strongest effect on the mooring forces and thus the results of this analysis. Other considered uncertainties associated with the structural parameters of the model did not show such a strong effect on the predicted results. Thus, to significantly improve the present model, more research should be done to refine the load model for net structures.

1 INTRODUCTION

Calculating environmental loads on and corresponding motions of a large-scale aquaculture system under offshore conditions is a relatively new and very complicated task. The interest to this problem is growing in the light of the emerging tendency to develop fish-farming facilities in open sea areas of the coastal zone, where the waves and currents are

stronger than they are in sheltered and thus more favourable for the traditional aquaculture areas of the Norwegian coast. Although it may take several years to collect relevant experience and experimental data on the behaviour of new aquaculture structures offshore, attempts have already been made to simulate possible scenarios numerically. As discussed below, various numerical models for aquaculture systems, including net cages, exist and are continuously developing. Meanwhile, laboratory experiments on structural response of net cages subjected to high flow velocities help revealing the weaknesses of existing numerical models, e.g., their prediction of inaccurate drag forces on the net structure for high solidities and large deformations (Moe-Føre et al., 2016). It is believed that appropriate numerical tools together with laboratory testing will help to design more reliable aquaculture structures, which will reduce the risk of fish escapes and thus also the impact of future fish farming on the environment.

In this paper, we test the capabilities of available numerical methods to simulate environmental loads on a flexible multi-cage system exposed to high currents and waves. The focus is placed on analysing the mooring loads and their distribution among the structural elements of the entire system. Several scientific papers on similar problems have emerged in the recent years, e.g., Shen et al. (2018), Chen and Christensen (2017), Kristiansen and Faltinsen (2015) and Endresen et al. (2014). However, the authors of these papers focused on modelling a single net-cage and therefore did not discuss, e.g., how environmental conditions and the loads due to them may be distributed over a large-scale fish farm consisting of multiple interconnected cages. Fredriksen et al. (2018) studied the loads due to waves and currents on a complete fish farm but did not evaluate the effects of the model parameters on the obtained loads. Thus, the objective of this paper is not only to predict loads on a complete fish-farm system using a numerical model, but also to conduct a sensitivity analysis of the obtained mooring loads by varying the model parameters.

2 MODEL CHARACTERISTICS

The numerical analysis in this paper was conducted by utilising FhSim (Reite et al., 2014), which is a framework for software development and numerical modelling that has been under constant development at SINTEF Ocean. This software is designed for simulating marine systems in the time domain, using models described as ordinary differential equations (ODEs). The primary ODE models for simulating marine fish farms in FhSim include: net structures, cables, ropes, floating collars and buoys (Fig. 1). Detailed descriptions of all these models are provided by Endresen et al. (2014), and only general highlights are given below.

Moorings

All mooring lines and cable elements shown in Fig. 1 are modelled as collections of interconnected rigid-bar elements constrained to provide desired structural properties of a cable, such as bending, axial and torsional stiffness, as well as buckling behaviour under compression forces. The constraint forces are applied to the ends of each rigid-bar element and are controlled through an elastic version of the Baumgarte stabilisation method (Johansen, 2007) to avoid numerical instabilities. The parameters of the Baumgarte stabilisation are directly related to the physical properties of a cable, such as Young's modulus, length and diameter.

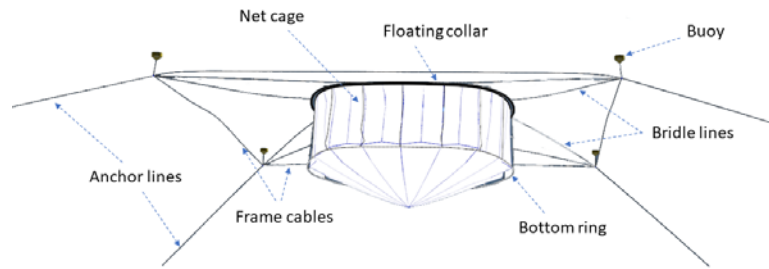


Figure 1: Illustration of the main elements of a net-cage system for fish farming.

Floating collar

The floating collar is modelled as a flexible continuous circular ring with six degrees of freedom with regards to rigid-body motion. Elastic deformation due to bending is accounted for by Euler-Bernoulli beam theory, while axial- and shear forces as well as torsion of the floater cross section are ignored. The structural response of the ring is modelled using the principle of modal superposition, where the responses for a finite number of the generalised natural modes are summed to give the total response of the ring. Forces that may act on the ring include wave excitation loads, added mass and additional structural- and viscous damping. The derivation of the hydrodynamic forces and modal responses for a floating-ring model can be found in Li and Faltinsen (2012).

Net cage

A net cage consists of a net structure and embedded into it cable elements reinforcing the cage. As the net is flexible, it will deform when exposed to waves and currents and thus will reduce its exposure. Therefore, it is important to account for such deformations in the present analysis.

In FhSim, the net structure is modelled according to Priour (1999) as a collection of triangular elements that are interconnected through nodes. All forces acting on the net and its mass are distributed among these nodes. Two expressions of the viscous hydrodynamic load on nets are available in FhSim: a Morison-type expression with a modified drag law and so-called Screen model. The former is based on Morison's equation and is validated for certain flow conditions by, e.g., Endresen et al. (2014). The latter is presented and validated by Kristiansen and Faltinsen, (2012). Additionally, the flow reduction due to the presence of a net structure is considered according to Endresen et al. (2013).

A sinker (bottom ring) is connected to the net structure as shown in Fig. 1. It is modelled similarly to a mooring cable but has a higher mass, and its both endpoints are connected forming a continuous cable structure.

Environmental conditions

All the abovementioned components of the fish farm can be simulated under forcing from both waves and a current. The hydrodynamic forces that may act on the fish-farm elements

include wave excitation forces and viscous-drag forces from the water current. Wave excitation forces include Froude-Kriloff pressure forces, diffraction forces and non-linear forces due to relative velocity. Linear long-wave theory is used to calculate the excitation forces, as well as the velocities of water particles under wave conditions.

Model validity

The validity of the abovementioned numerical models was studied by Endresen et al. (2014) by comparing FhSim simulations against data from experiments with a scaled model of a net cage on moorings as the one shown in Fig. 1. In their study, the authors compared the tensions in anchor lines, bridles and buoys from the simulator to the corresponding data series obtained in the experiment. They concluded that FhSim was able to reproduce the main dynamics and responses of the net cage when it was exposed to currents and waves. For two cases with different current velocities, 0.5 and 0.7 m/s in full scale, and no waves, the highest discrepancies of the forces in the anchor lines were 31% and 17%, respectively. In two cases with both current and waves, forces on anchor lines were 56% and 35% higher in the simulation than in the experiments.

3 NUMERICAL SETUP

The numerical setup chosen for this study represents a typical marine fish farm, which consists of eight net cages and a frame-type mooring system as shown in Figs. 2 and 3. Each net cage consists of a floating collar (two buoyant rings), a bottom ring, a cylindrical net structure with a conical bottom and bridles connecting the cage system to the frame moorings. All relevant parameters of the model setup are summarized in Table 1 and Table 2.



Figure 2: The fish-farm model in FhSim.

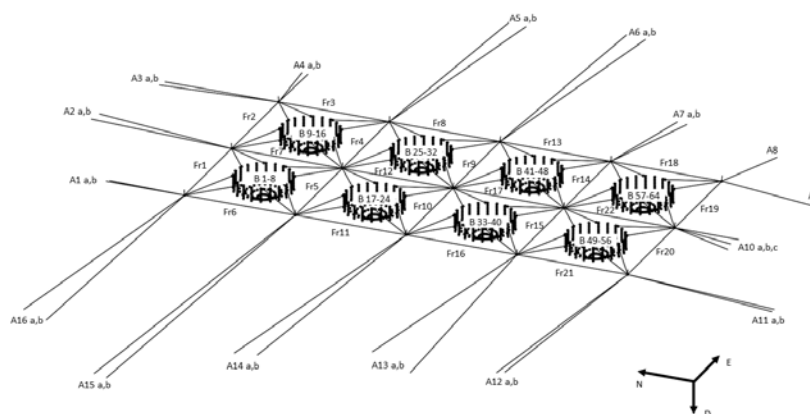


Figure 3: A sketch of the complete fish-farm model showing the mooring system.

Table 1: Characteristics of the net-cage system.

| Parameter | Value | Unit |
|---------------------------|---------|------|
| Collar diameter | 51 | m |
| Collar pipe diameter | 0.5 | m |
| Collar elastic modulus | 900 | MPa |
| Collar drag coefficient | 1.0 | - |
| Number net connections | 20 | - |
| Number sinker connections | 20 | - |
| Cage vertical wall depth | 15 | m |
| Cage cone-tip depth | 32.5 | m |
| Bottom ring depth | 17.5 | m |
| Bottom ring mass | 80 | kg/m |
| Ring diameter | 51 | m |
| Ring pipe diameter | 0.4 | m |
| Ring elastic modulus | 900 | MPa |
| Ring drag coefficient | 1.2 | - |
| Bridle length | 48.4 | m |
| Bridle diameter | 0.05 | m |
| Bridle weight | 1.66 | kg/m |
| Bridle elastic modulus | 1870 | MPa |
| Mooring frame size | 100x100 | m |
| Frame configuration | 2x4 | - |
| Mooring frame depth | 8 | m |
| Mooring rope diameter | 0.064 | m |
| Mooring rope weight | 1.66 | kg/m |
| Mooring elastic modulus | 1670 | MPa |
| Anchor line diameter | 0.056 | m |
| Anchor line weight | 1.66 | kg/m |

Table 2: Anchor lines.

| Line | Length [m] | Line | Length [m] |
|-------|------------|----------|------------|
| A1a/b | 70/70 | A9 | 91 |
| A2a/b | 130/131 | A10a/b/c | 57/55/58 |
| A3a/b | 112/111 | A11a/b | 133/133 |
| A4a/b | 60/60 | A12a/b | 199/201 |
| A5a/b | 235/235 | A13a/b | 212/210 |
| A6a/b | 259/258 | A14a/b | 248/256 |
| A7a/b | 108/108 | A15a/b | 335/335 |
| A8 | 84 | A16a/b | 246/240 |

4 TEST MATRIX

Several simulations were performed using the numerical setup described above with various environmental conditions to evaluate the effect of the latter on the mooring loads for the entire fish farm. Additionally, structural parameters were modified in some of the simulations to identify how strongly the mooring loads depend on those parameters. The test matrix in Table 3 summarizes all the simulations analysed in this paper.

Table 3: Test matrix.

| Case | H_s [m] | T_p [s] | Wave direction [°] | Current [m/s] | Current direction [°] | Comment |
|------|-----------|-----------|-----------------------|---------------|--------------------------|-------------------------|
| #1 | 3 | 6 | 0 | 0 | - | Irregular waves |
| #2 | 3 | 6 | 0 | 0.5 | 0 | -/- |
| #3a | 1.6 | 4 | 272 | 0.67 | 272 | -/- |
| #3b | 1.6 | 4 | 272 | 0.67 | 272 | Stiff collar |
| #4 | 1.6 | 4 | 0 | 0.67 | 272 | |
| #5 | 1.6 | 4 | 192 | 0.67 | 192 | |
| #6 | $H=6$ | $T=6$ | 0 | 0 | - | Regular waves |
| #7 | 0 | - | - | 0.67 | 0 | |
| #8 | 0 | - | - | 0.67 / 0 | 0 | Surface current |
| #9 | 0 | - | - | 0 / 0.67 | 0 | Deep current |
| #10* | 1.6 | 4 | 272 | 0.67 | 272 | Screen model |
| #11* | 1.6 | 4 | 272 | 0.67 | 272 | Shorter anchor lines |
| #12* | 1.6 | 4 | 272 | 0.67 | 272 | Shorter frame cables |

*Simulations with the screen model

The environmental loads that are considered in this study are those due to waves and current. Irregular waves (cases #1 – 6 and #10) were modelled according to JONSWAP wave spectrum with various significant wave heights (H_s), mean wave periods (T_p) and wave directions. In one of the cases (#6) a regular wave field was modelled with a constant wave height H and wave period T . The current velocities were modelled as time-independent and

uniform within a given layer but were depth-dependent in two of the simulation cases (#8 – 0.67 m/s on surface and 0 m/s from 0.6 m depth; #9 – 0 m/s on surface and 0.67 m/s from 0.6 m depth). For convenience, both wave- and current directions in Table 3 are specified by giving the directions in which they are progressing, measured as azimuth angles (e.g., 0° is the direction towards north).

The only difference between Cases #3a and Case #3b is the values of the elastic modulus for the floating collars: 0.9 GPa (normal value) and 90 GPa (artificially high value to model rigid-body behaviour), respectively. These simulations are performed to find out if the stiffness of the floating collars has a significant effect on the mooring forces. In Case #10, the collar stiffness is the same as in Case #3a, while a different model for hydrodynamic forces on the net structure is applied (the screen model). Cases #11 and #12 differ from Case #10 only due to changes in the mooring system: anchor lines A6 – A8 are shortened by 10 %, respectively, and the corresponding anchor positions are moved from their original locations (Fig. 3) by 10 – 20 m in Case #11; the length of frame cable Fr14 is modified from 100 to 95 m in Case #12. These modifications are made to study the variation of the mooring forces due to uncertainties in cable length and anchor positions.

5 SIMULATION RESULTS

From each simulation in Table 3, time series of the loads for all anchor lines, frame cables and bridles were obtained, and corresponding mean and maximum values were determined. A summary of the maximum mooring loads is given in Table 4. An example of typical time series of the mooring loads obtained from Case #10 is demonstrated in Fig. 4.

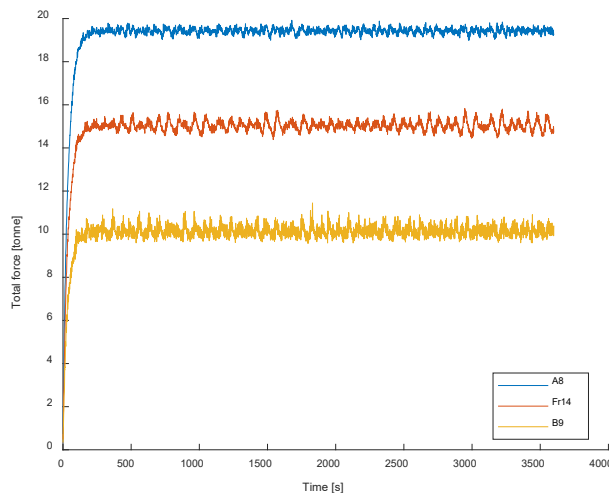


Figure 4: Mooring loads due to irregular waves and a current (Case #10).

Table 4: Cables with maximum mooring loads.

| Case | Force [tonne] | | |
|------|---------------|-------------|------------|
| | Anchor lines | Frames | Bridles |
| #1 | 2.8 (A8) | 4.7 (Fr22) | 2.4 (B46) |
| #2 | 22.1 (A10a) | 30.3 (Fr22) | 14.5 (B62) |
| #3a | 24.4 (A8) | 18.5 (Fr14) | 14.0 (B9) |
| #3b | 25.2 (A8) | 18.1 (Fr14) | 16.0 (B9) |
| #4 | 22.9 (A8) | 16.6 (Fr14) | 12.9 (B44) |
| #5 | 25.4 (A3b) | 31.2 (Fr3) | 17.1 (B10) |
| #6 | 2.9 (A9) | 4.4 (Fr22) | 2.2 (B62) |
| #7 | 24.6 (A10a) | 33.9 (Fr22) | 15.1 (B62) |
| #8 | 2.2 (A10a) | 4.2 (Fr22) | 0.7 (B62) |
| #9 | 21.8 (A10a) | 30.5 (Fr22) | 13.3 (B62) |
| #10 | 19.9 (A8) | 15.8 (Fr14) | 11.4 (B9) |
| #11 | 20.2 (A8) | 15.9 (Fr14) | 11.0 (B9) |
| #12 | 22.0 (A8) | 17.3 (Fr14) | 10.7 (B9) |

The loads shown in Fig. 4 are due to the superposition of irregular waves and a current. This graph can be compared to Fig. 5 showing the loads in a frame cable due to only currents, and to Fig. 6, which depicts the load in a bridle induced by regular waves.

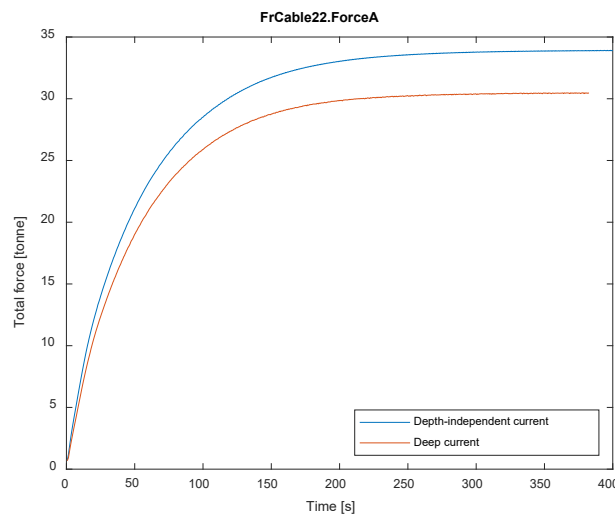


Figure 5: Current-induced loads in a frame cable (Cases #7 – blue and #9 – red).

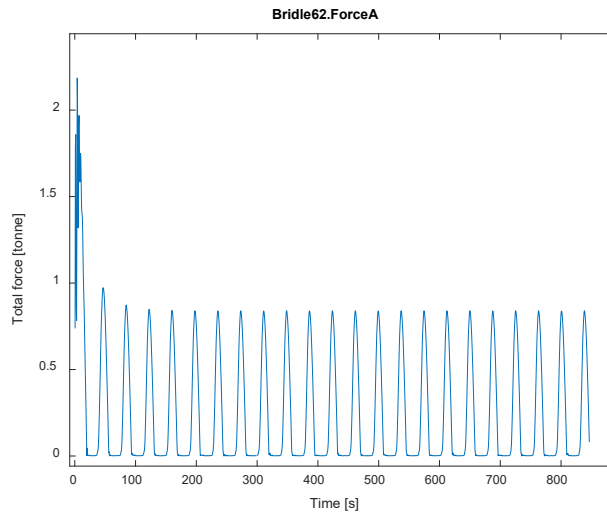


Figure 6: Bridle force due to regular waves (Case #6).

Finally, additional simulation results needed for the analysis of the effect of collar stiffness on the distribution of mooring loads is presented in Table 5. Here the maximum, mean and standard deviations of the forces in selected mooring lines are given for both Case #3a and Case #3b.

Table 5: Comparison of the results from the simulations with flexible and stiff collars (Cases #3a and #3b).

| Moorings | Force [tonne] Case #3a / Case #3b | | |
|----------|-----------------------------------|-------------|--------------------|
| | Maximum | Mean | Standard deviation |
| A8 | 24.4 / 25.2 | 23.1 / 23.9 | 2.8 / 2.8 |
| Fr14 | 18.5 / 18.1 | 17.3 / 16.5 | 2.2 / 1.9 |
| B9 | 14.0 / 16.0 | 12.6 / 14.7 | 1.6 / 1.7 |

6 ANALYSIS AND DISCUSSIONS

Mean mooring loads

All simulations in this study indicate that the mean tension forces in the anchor lines, frame cables and bridles approached steady-state values within the first 15 minutes of the simulation, in full scale. Typically, the mooring forces were essentially transient within the first 5 minutes, especially in the simulations with high current velocities (see, e.g., Fig. 4 and 5). In the simulation with only regular waves, the transient response decayed within approximately 100 seconds, as shown in Fig. 6.

Thus, based on the above observations, we established a simple empirical rule that suggests using at least 15-minute long time series, in full scale, to identify mean mooring

loads with a 10% accuracy. Note, however, that most of the simulations from Table 3 resulted in time series that are much longer than 15 minutes (see, e.g., Fig. 4 showing a 1-hour simulation).

It was also found that the mean and maximum loads were distributed among all the cables of the entire fish farm in a similar way, i.e., the same anchor line typically showed both the maximum peak force and the largest mean force, compared to the forces in all other anchor lines of the system. This conclusion is also valid for frame cables and bridles, respectively. Moreover, under realistic environmental conditions with both waves and a current (Cases #3 – #5 and #10), the highest mean load was typically 80 – 90 % of the maximum observed load in the same cable. In the latter cases, the current-induced forces were obviously dominant.

Maximum mooring loads

The maximum observed loads for anchor lines, frame cables and bridles, respectively, are given in Table 4. These values appeared to be strongly dependent on the magnitude of the current velocity and its direction as well as the wave parameters. The most unfavourable combination is when the waves and current act in the same direction (e.g., Case #5).

A sea state with the significant wave height equal to 1.6 m and the mean wave period equal to 4 s and a current of 0.67 m/s are considered as realistic environmental conditions for the considered fish farm. The simulations showed that under these conditions, the loads in the anchor lines may reach up to 25.4 tonnes (Case #5), in the frame cables – 33.9 tonnes (Case #7) tonnes, and in the bridles – 17.1 tonnes (Case #5). These values correspond to the scenarios when the wave and current direction was approximately aligned with the longest side of the fish-farm rectangle, i.e., from north to south or the opposite (see Fig. 3).

One of the objectives of this study was to investigate how the load due to environmental forces is distributed among all ropes and cables of the entire mooring system of the fish farm, including the frame, anchor lines and bridles. For this purpose, the locations of the mooring elements with maximum loads were identified as given in Table 4. It can be noticed that the cables with maximum forces are typically located upstream with respect to the current and/or wave directions. This is illustrated in Figs. 7 and 8.

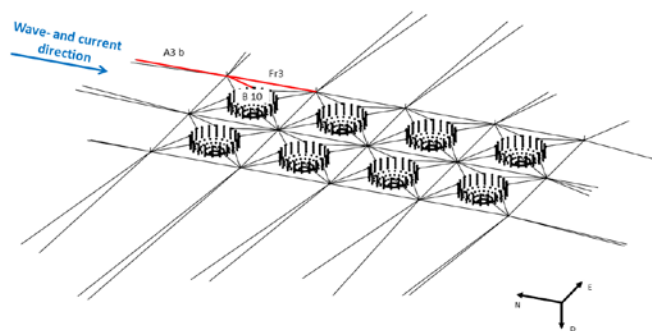


Figure 7: Locations of the moorings with highest loads (shown in red) with respect to the wave- and current direction in Case #5.

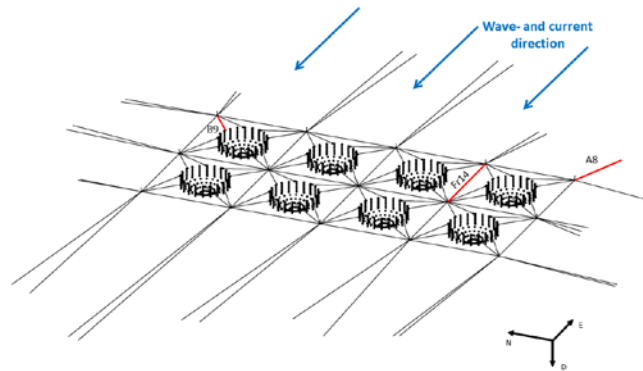


Figure 8: Locations of the moorings with highest loads (shown in red) with respect to the wave- and current direction in Case #3a.

Wave and current effects on the total load

Relatively high sea states were considered in Cases #1 and #2. This was done to identify the wave effect on the mooring loads of the farm and to compare these loads with those due to a current. By comparing the results from Table 4, it can be seen that the loads due to a relatively high sea state (Case #1) are more than 5 times lower than the combined loads from a relatively high current and the same sea state (Case #2). Moreover, the simulation results from Case #7 show that the loads due to the current, in the absence of any waves, are also significantly higher than the wave-induced loads observed in Cases #1 and #6. Thus, for marine farming areas with high currents (over 0.5 m/s), the total load on the fish farm is found to be dominated by the current-induced forces rather than the wave forcing, provided that H_s does not exceed 3 m and T_p is lower than 6 s.

Effects of model parameters

As presented above, each component of the fish farm in FhSim is represented by its own mathematical model, e.g., cable elements, net and floating collars. This representation involves a number of model parameters that control the physical properties and behaviour of a simulated component. By manipulating these parameters, very detailed or rather simplified simulations can be accomplished.

Although the objective of this study was to use a fish-farm model that is as accurate as possible, some simulations were conducted with modified model parameters that intentionally simplified the underlying physics of the modelled system. This was done to study the sensitivity of the mooring loads to certain model parameters, such as the structural stiffness, wave-spectrum and hydrodynamic-drag law. The results of this study may be useful for future work related to numerical modelling of fish farms, where simplifications are needed for, e.g., reducing the computation time.

In Case #6, a monochromatic wave was simulated instead of the more realistic irregular-wave spectrum as in Case #1. The simulation results (Table 4) suggest that similar maximum load levels can be achieved in these two cases if the monochromatic wave period T is equal to T_p and the wave height H is equal $2H_s$ (see Table 3). However, this conclusion can not be generalised as only two simulations were considered.

Another parameter that was investigated is the floating-collar elastic modulus E . In Case #3a, a realistic value of E equal to 900 MPa was utilised, whereas in Case #3b E was set to 900 GPa, which corresponds to a very stiff structure. Although the hydroelastic response of the flexible floater is very different from that of the stiff floater, which essentially behaved as a rigid body, the mooring loads obtained from these two cases differed by only approximately 5 % for anchor- and frame cables and by 20 % for bridles (Table 5).

Force contribution from the viscous-drag model on the net structure seems to be the most influencing factor for the analysis of the mooring loads on the considered fish farm. This was concluded by comparing the results from Cases #7, #8 and #9. In the latter case, the drag forces induced by a current (0.67 m/s) affected only the lower parts of the net cages below 0.6 m from the sea surface, whereas the floating collars and buoys were not subject to significant viscous forces as no current or waves were modelled at the sea surface. However, the magnitudes of the mooring forces from this case are comparable to those from Case #7, where the entire net-cage system, buoys and floating collars were subject to a uniform current with a depth-independent speed of 0.67 m/s. This result implies that the mooring loads due to the uniform current were dominated by the forces on the net structure rather than those on the surface-piercing elements of the fish farm. The contribution of the latter was approximately 10 %, according to Case #8, where only a surface current was simulated.

Another important aspect of the net-cage modelling is the wake effect of the net twine in a current. As the downstream flow is reduced in the turbulent wake of the net twine, the total hydrodynamic force on the net cage becomes dependent on its shape and orientation relative to the undisturbed current direction. Various approximations can be used to model such hydrodynamic forces on a net structure. In this paper, a rather conservative Morison-type model was employed for all cases, except Case #10. In the latter, a screen-type model of the hydrodynamic forces was utilised. Kristiansen and Faltinsen (2012) demonstrated the validity of this model and its advantage compared to Morison-type models for high flow velocities and net solidity. Our simulation with the screen model predicted mooring forces 20 – 30 % lower than those from Case #3a, where the same environmental conditions were simulated. Thus, these simulations demonstrate the importance of the correct choice of the net model for the accurate prediction of the mooring loads of a complete fish farm.

Effect of mooring configuration

The mooring system of a fish farm may slightly deviate from its design configuration due to various reasons, e.g., the anchors may move some distance under actions from waves and currents. Moreover, the lengths of the mooring lines and frame cables may not precisely match their design values. An attempt to account for such deviations was made in Cases #11 and #12, where some moorings were shorter than the original ones in Case #10. The results from these simulations (see Cases #10 and #11 in Table 4) suggest that minor uncertainties in the length and position of an anchor line have a negligible effect on the maximum mooring loads measured for the whole fish farm. However, as shown by Case #12, maximum mooring loads may increase almost proportionally with a decrease of the frame-cable length.

7 CONCLUSIONS

The FhSim-based numerical model of a complete fish farm presented in this paper was found to be a flexible tool for the analysis of the mooring loads under exposed conditions. From the performed numerical analysis, the following conclusions were drawn:

- For marine farming areas with high currents (over 0.5 m/s), the mooring loads were found to be dominated by the current-induced forces rather than the wave forces, provided that H_s does not exceed 3 m and T_p is lower than 6 s.
- Mooring cables with maximum forces were typically located upstream with respect to the current and/or wave directions.
- The assumptions and uncertainties of the model for viscous drag on the net structure had the strongest effect on the predicted mooring forces, compared to the effects of other possible uncertainties in parameters such as the floating-collar stiffness, cable length and anchor positions.

Note, however, that all results in this study were obtained based on a limited number of simulation cases with only one fish-farm system and therefore may not be directly generalised. Moreover, this analysis is rather conservative with respect to current modelling, whereas nonlinear wave effects are not fully accounted for.

ACKNOWLEDGMENTS

This work was funded by the Research Council of Norway through the Centre for Research based Innovation (SFI) Exposed.

REFERENCES

- Chen, H., Christensen, E. D., 2017. Development of a numerical model for fluid-structure interaction analysis of flow through and around an aquaculture net cage. *Ocean Engineering* 142 (2017) 597–615.
- Endresen, P. C., Føre, M., Fredheim, A., Kristiansen, D., and Enerhaug, B., 2013. Numerical modeling of wake effect on aquaculture nets. In *Proceedings of OMAE 2013*.
- Endresen, P. C., Birkevold, J., Føre, M., Fredheim, A., Kristiansen, D., and Lader, P., 2014. Simulation and validation of a numerical model of a full aquaculture net-cage system. In *Proceedings of OMAE 2014*.
- Fredriksen, A.G., Bonnemaire, B., Nilsen, Ø., Aspelund, L., Ommundsen, A., 2018. Irregular wave and current loads on a fish farm system. In *Proceedings of OMAE2018*, paper 77482.
- Johansen, V., 2007. Modelling of flexible slender systems for real-time simulations and control applications. PhD Thesis, Norwegian University of Science and Technology.
- Kristiansen, T., Faltinsen, O.M., 2012. Modelling of current loads on aquaculture net cages. *J. Fluids Struct.* 34, 218–235.
- Kristiansen, T., Faltinsen, O.M., 2015. Experimental and numerical study of an aquaculture net cage with floater in waves and current. *J. Fluids Struct.* 54,1–26.
- Li, P., Faltinsen, O.M., 2012. Wave-induced vertical response of an elastic circular collar of a floating fish farm. 10th International Conference on Hydrodynamics, St. Petersburg, Russia.

Moe-Føre, H., Lader, P.F., Lien, E., Hopperstad, O.S., 2016. Structural response of high solidity net cage models in uniform flow. *J. Fluids Struct.* 65 (2016) 180–195.

Priour, D., 1999. Calculation of net shapes by the finite element method with triangular elements. *Communications in Numerical Methods in Engineering*, 15(10), pp. 755–763.

Reite, K.-J., Jensen, J., Aarsæther, K. G., Føre, M., Endresen, P. C., Kristiansen, D., Kyllingstad, L. T., Rundtop, P., Johansen, V., and Fredheim, A., 2014. Fhsim - time domain simulation of marine systems. In *Proceedings of OMAE 2014*.

Shen Y.G., Greco M., Faltinsen O.M., Nygaard, I., 2018. Numerical and experimental investigations on mooring loads of a marine fish farm in waves and current. *J. Fluids Struct.* 79: 115–136.

EULERIAN-LAGRANGIAN SIMULATION ON MICROBUBBLES IN TURBULENT CHANNEL FLOW

XIAOSONG ZHANG, JIANHUA WANG AND DECHENG WAN*

Collaborative Innovation Center for Advanced Ship and Deep-Sea Exploration, State Key Laboratory of Ocean Engineering, School of Naval Architecture, Ocean and Civil Engineering, Shanghai Jiao Tong University, Shanghai, China

*Corresponding author: dcwan@sjtu.edu.cn

Key words: Microbubbles; Euler-Lagrange method; Turbulent channel flow; Drag reduction

Abstract. Microbubble drag reduction technology has been proved by many experiments that it can reduce frictional resistance of ships significantly. The underlying physical mechanism of drag reduction needs to be studied by means of numerical simulation. In this paper, Eulerian-Lagrangian method is used to study the interaction between microbubbles and a fully developed turbulent channel flow. Turbulent flow field is solved using large eddy simulation (LES) method. The microbubble trajectories were tracked by the motion equation following Newton's second law in Lagrangian framework. The interaction between microbubbles and liquid is fully considered in the simulation. The computational code is developed based on the open-source platform OpenFOAM. Before introducing bubbles, a fully developed single-phase turbulent channel flow is obtained at friction Reynolds number. The mean streamwise velocity, turbulent normal and shear stresses are verified by comparison with standard DNS results. Microbubbles are injected uniformly into the channel and eventually form a bubble layer on the upper plate due to buoyancy. The drag reduction of the upper plate is calculated and detailed analysis is carried out about the interaction between microbubbles and turbulent boundary layer.

1 INTRODUCTION

During the past several years, reducing ship resistance has become one of the most important objectives of ship research. It has been reported that skin frictional resistance accounts for as much as 60%-70% of the total drag for cargo ship, and about 80% of that for a tanker. Therefore, reducing frictional resistance is an important way to save cost in shipping industry in the marine transportation business^[1]. Microbubble drag reduction technology takes advantage of blower and porous plate to inject microbubbles to the bottom of ship, which can significantly reduce frictional resistance. In order to investigate the underlying physical mechanism. Many scholars simplified the bottom plate of a ship into a flat plate and studied the interaction between microbubbles and the flow field around the plate.

Madavan et al.^[2-3] and Merkle et al.^[4] carried out experimental studies on the microbubble drag reduction in a channel very early. Drag reduction effect was obtained under different air flow rate. Their analysis showed that the region where the bubbles mainly acted on the fluid was in the turbulent boundary layer, rather than the fluid outside the boundary layer. A series

of bubble drag reduction experiments^[5-7] were carried out on a long plate in the USA Navy's Large Cavitation Channel. The experiment results showed that bubbles tend to concentrate on the plate and the highest drag reduction rate can be up to 90% under the low velocity condition. These experiments confirm the drag reduction effect of the microbubble drag reduction technology.

However, it is difficult to extract and analyze the detailed flow information in the experiment. Thus, CFD method is needed to investigate the deep mechanism. Eulerian-Eulerian and Eulerian-Lagrangian are two methods that are mostly used to simulate the fluid carried discrete bubbles. Eulerian-Eulerian method means that liquid and bubble are both solved under Eulerian framework, whose most prominent advantage is the low computational cost. Kunz et al.^[8-9] developed an Eulerian-Eulerian code for the modeling of high Reynolds number external flows with microbubble drag reduction, the code has been validated by comparison with experimental results that it can predict drag reduction effect correctly across a wide range of Reynolds numbers. Qin et al.^[10] combine the CFD method in Eulerian framework with population balance model (PBM) to simulate the bubbly flow. The PBM method was used to predict the coalescence and breakup of bubbles. The numerical results were qualitatively correct compared with the experimental results. The Eulerian-Eulerian method can be used in industrial applications because of the lower expense, but detailed behavior of bubbles cannot be resolved. To get more accurate results, many scholars use Eulerian-Lagrangian method for mechanism investigation. In this method, the bubble motion is obtained by solving the kinetic equation in the Lagrangian framework. Xu et al.^[11] firstly carried out numerical simulation of drag reduction of microbubbles in a channel flow. Bubbles were tracking using Lagrangian method and fluid was solved using Direct Numerical Simulation (DNS) method. Their results proved that smaller bubbles have a greater impact on turbulent flow. The same method was used by Ferrante et al.^[12] to investigate the mechanism for drag reduction in a microbubble laden turbulent boundary layer over a flat plate. Early studies often made a lot of simplifying assumptions such as ignoring bubble gravity and buoyancy, bubble free from collide. The number of bubbles were also relatively small. More recently, Pang et al.^[13] used two-way coupling Eulerian-Lagrangian method to study the interaction between microbubbles and liquid turbulence with the help of interphase forces in channel flow. Asiagbe et al.^[14] also carried out bubbly channel flow simulation, specially, they adopt Large Eddy Simulation (LES) method to solve the fluid. In contrast with DNS method, LES method requires less computing resources and can also reasonably reproduce the bubble-induced velocity fluctuations in the liquid. The uses of LES makes it possible to study drag reduction at high Reynolds number and bubble fraction. In the previous studies, simulation of microbubbles is highly simplified. Interaction between microbubble was usually ignored^[13] or was described by simple hard sphere model^[14]. Soft sphere model is used to simulate bubble interaction in this paper in order to simulate the bubble-bubble interaction and bubble-wall interaction more veritably.

The present paper is organized as follows. The numerical method is presented at first including liquid phase solving and discrete phase solving. The computational conditions are introduced next. Computational results for single phase turbulent flow and bubbly flow are shown in the simulation part, where the impact of microbubbles on the mean velocity profile, turbulent intensities and Reynolds stress are analyzed in detail. A brief conclusion is given in the end.

2 NUMERICAL METHOD

In Eulerian-Lagrangian method, liquid phase and discrete phase are treated in different frameworks. In this paper, the fluid is solved using LES method in Eulerian framework, while microbubbles are tracked by the motion equation following Newton's second law. The coupling between two phases is considered by interphase interaction forces, which are described as momentum source term of the momentum equation. For the liquid-phase calculation, temporal discretization adopts a second-order implicit scheme, and second-order scheme is used for spatial discretization.

2.1 Liquid phase solving

LES is adopted to simulate the carrier phase. The flow field is decomposed into large-scale motions and small-scale motions using a filter function. The larger three-dimensional unsteady turbulent motions are directly represented, whereas the effects of the smaller-scale motions are modelled^[15]. The filtered continuity and momentum equations are as follows:

$$\frac{\partial \bar{u}_i}{\partial x_i} = 0 \quad (1)$$

$$\frac{\partial \bar{u}_i}{\partial t} + \bar{u}_j \frac{\partial \bar{u}_i}{\partial x_j} = -\frac{1}{\rho} \frac{\partial \bar{p}}{\partial x_i} - \frac{\partial}{\partial x_j} (\bar{\sigma}_{ij} + \tau_{ij}) + S_u + \frac{f_{pf}}{\rho} \quad (2)$$

where the overbar identifies filtered quantities. \bar{u}_i is fluid velocity in three direction ($i = x, y, z$), ρ is the fluid density, p is pressure, σ_{ij} is viscous stress, τ_{ij} is the sub-grid scale stress tensor, which is required to close the equations. S_u represents the mean momentum source term, which is required to drive the channel flow. The SGS stress is modelled using Wall Adapting Local Eddy-Viscosity Model (WALE)^[16]. The turbulent kinematic eddy-viscosity is defined as:

$$\nu_t = (C_w \Delta)^2 \frac{(S_{ij}^d S_{ij}^d)^{3/2}}{(\bar{S}_{ij} \bar{S}_{ij})^{5/2} + (S_{ij}^d S_{ij}^d)^{5/4}} \quad (3)$$

where S_{ij} is the strain-rate tensor, Δ is the filter width. C_w is a constant, which is set to be 0.325 in the present study.

The effect of bubbles on the fluid is reflected in the last term of the Eq. (2). The hydrodynamic forces on all bubbles in each grid are added up and averaged by grid volume. According to Newton's third law, the coupling effect is achieved by apply the force to the fluid.

2.2 Discrete phase solving

Bubbles are assumed to be homogeneous spheres with constant diameters in this study. Collision between bubbles are considered but coalescence and breakup are ignored in the present work. Each bubble is tracked individually by solving the motion equation as follows:

$$m \frac{dv}{dt} = mg \left(1 - \frac{\rho_l}{\rho_b} \right) + \frac{3mC_D}{4d} |u-v|(u-v) + \frac{m\rho_l}{\rho_b} C_L (u-v) \times (\nabla \times u) + f_c \quad (4)$$

where the terms on the right side of Eq.(4) represent the gravity-buoyancy, drag force, shear-lift force, collide force, respectively. Drag coefficient C_D and lift coefficient C_L are determined by Tomiyama's drag model^[17] and lift model^[18] as follows:

$$C_D = \max\left(\min\left(\frac{16}{\text{Re}}(1+0.15\text{Re}^{0.687}), \frac{48}{\text{Re}}\right), \frac{8}{3} \frac{Eo}{Eo+4}\right) \quad (5)$$

$$C_L = \begin{cases} \min[0.288 \tanh(0.121\text{Re}), f(Eo_d)] & Eo_d < 4 \\ f(Eo_d) & 4 \leq Eo_d \leq 10.7 \end{cases} \quad (6)$$

Previous studies usually ignored the interaction between bubbles^[13] or used hard sphere model to simulate the collision^[14]. However, it is the soft sphere model that can describe the bubble-bubble interaction and bubble-wall interaction more realistically. In this paper, a non-linear spring-dashpot-slider model is used to calculate contact forces. The normal and tangential contact forces can be obtained by:

$$f_c^n = -k_n \delta_n^{1.5} - \eta_n u_n \quad (7)$$

$$f_c^t = \begin{cases} -k_t \delta_t - \eta_t u_t & |f_c^t| < \mu |f_c^n| \\ -\mu |f_c^n| & |f_c^t| \geq \mu |f_c^n| \end{cases} \quad (8)$$

where k and η represent spring stiffness coefficient and damping coefficient, respectively. δ is overlap, u is the relative velocity, and μ is the friction coefficient. The subscript n and t represent the normal and tangential components, respectively. The spring stiffness coefficient is derived from surface tension σ as reference^[19].

3 COMPUTATIONAL CONDITIONS

A turbulent channel flow laden with microbubbles is simulated. Dimension of the channel geometry and the coordinate system is shown in Figure 1 (a). In particular, the channel half height h is equal to 0.025m. The computational domain is discretized using grids in the streamwise, wall-normal and spanwise directions, respectively. The grids were distributed uniformly along the streamwise and spanwise directions, equal-ratio distribution is used for the wall-normal direction. Grid distribution can be seen in Figure 1 (b).

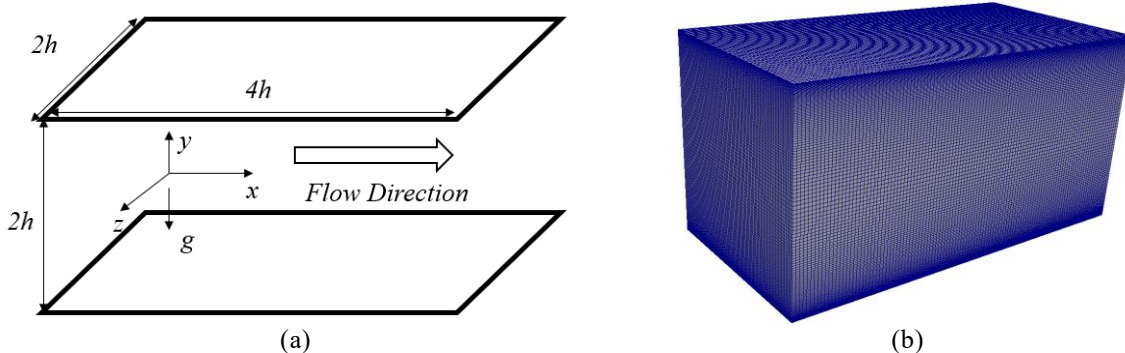


Figure 1: Computational domain and grid distribution. (a) Channel sketch. (b) Grid distribution.

Periodic boundary conditions are used in both the streamwise and spanwise directions for the liquid flow to obtain a fully developed turbulent flow. At the same time, periodic boundary is also applied to microbubble motion to keep void fraction the same. No-slip boundary conditions are exerted on the channel top and bottom walls for the liquid flow, where microbubbles will collide with the walls. The bubble-wall collision is solved by Eqn(7). Turbulent channel flow is developed with friction Reynolds number $Re_\tau = 375$. At first, a single phase turbulent channel flow is obtained by long-time simulation. After a statistically steady state of the liquid-phase turbulence is reached, the microbubbles are injected into the channel uniformly. The density of bubble is set to 1.2 kg/m^3 , and the bubble diameter is $110 \mu\text{m}$. The corresponding total number of bubbles are 39366. The bubble volume fraction is chosen as $\alpha_b = 1.12 \times 10^{-4}$ refer to the literature^{[13][14]}, which has been proved large enough to have influence on the flow field. The initial velocity of microbubbles is equal to zero. Under these conditions, the interaction between liquid phase and microbubbles can be investigated by the bubble motion and turbulence changes.

4 RESULTS AND DISCUSSIONS

In this section, a fully developed single-phase turbulent channel flow is simulated firstly, and the turbulent flow field is validated by comparison with DNS results of Moser et al.^[20]. Then, turbulent bubbly flow is simulated to investigate the interaction between microbubbles and turbulent flow.

4.1 Fully developed turbulent flow simulation

The evolutionary process from laminar flow to turbulence in channel flow can be reproduced in a long time simulation with the use of periodic boundary conditions. Figure 2 shows the change of friction Reynolds number Re_τ with time and the corresponding flow field. The dimensionless time is defined as $t^+ = tu_\tau^2 / \nu$.

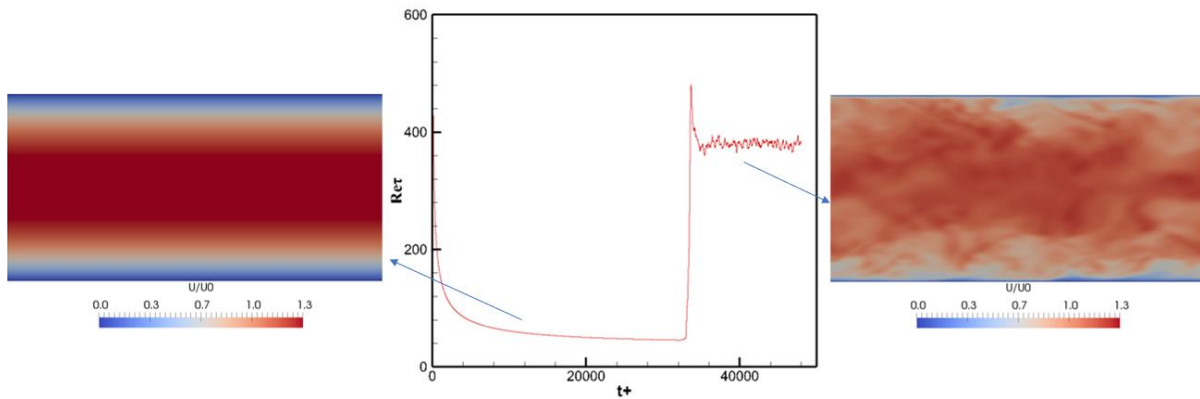


Figure 2: Time history of friction Reynolds number Re_τ and the corresponding flow field.

There is regular laminar flow in the channel for a long time at first as shown in the left figure in Figure 2. Frictional stress near the channel wall decreases with time. Then the

transition happens, frictional stress increase suddenly. The flow field begins to become disordered as shown in the right figure in Figure 2. The friction Reynolds number Re_τ oscillates around a fixed value. The flow field has become fully developed turbulence at this point.

The simulation of single phase turbulent flow is validated by comparison with DNS results of Moser et al.^[20]. Figure 3 presents the comparison of mean velocity profile, while Figure 4 presents the comparison of turbulent intensities and Reynolds stress. These profiles have been obtained after averaging over time and space. The mean velocity profile shows good agreement with DNS results and the empirical formula. At the same time, the turbulent intensities and Reynolds stress are slightly under-predicted near the centre of the channel. It is worth noting that the simulation carried out by Moser et al.^[20] is in the friction Reynolds number $Re_\tau = 395$, which is slightly larger than $Re_\tau = 375$ in the present work. It is the difference in Reynolds number that causes the difference in stress. In summary, the LES simulation has the ability to resolve the main characteristics of the turbulent flows.

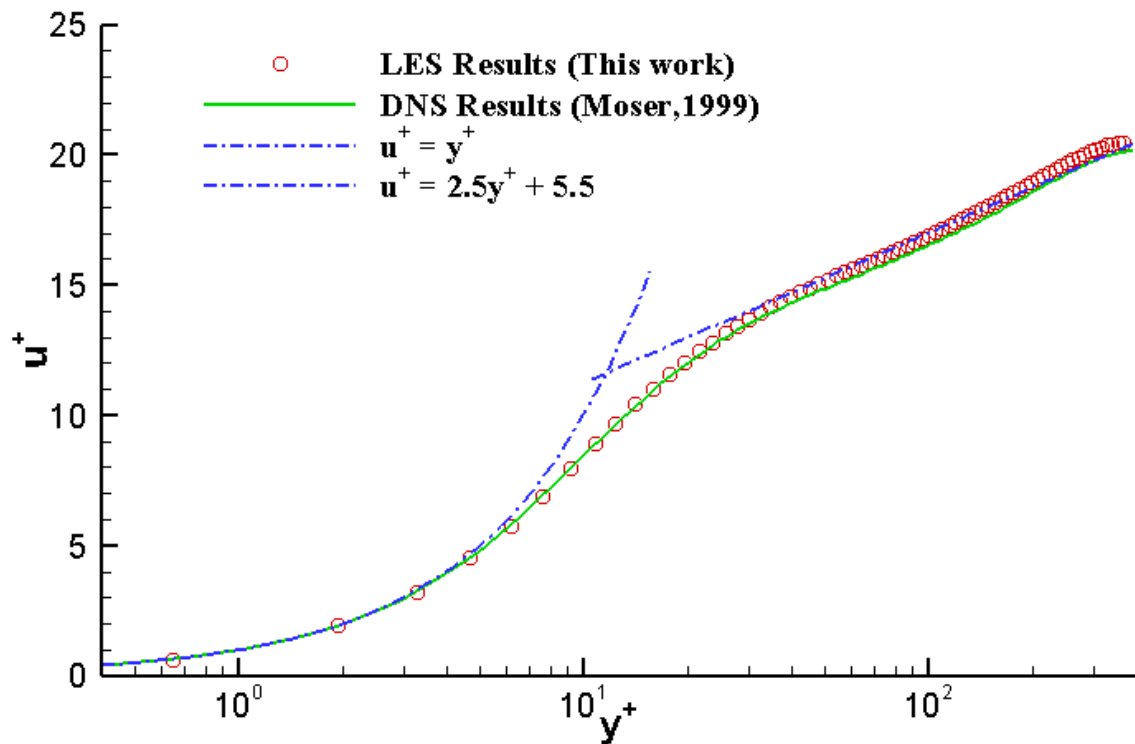


Figure 3: Comparison of mean velocity profile.

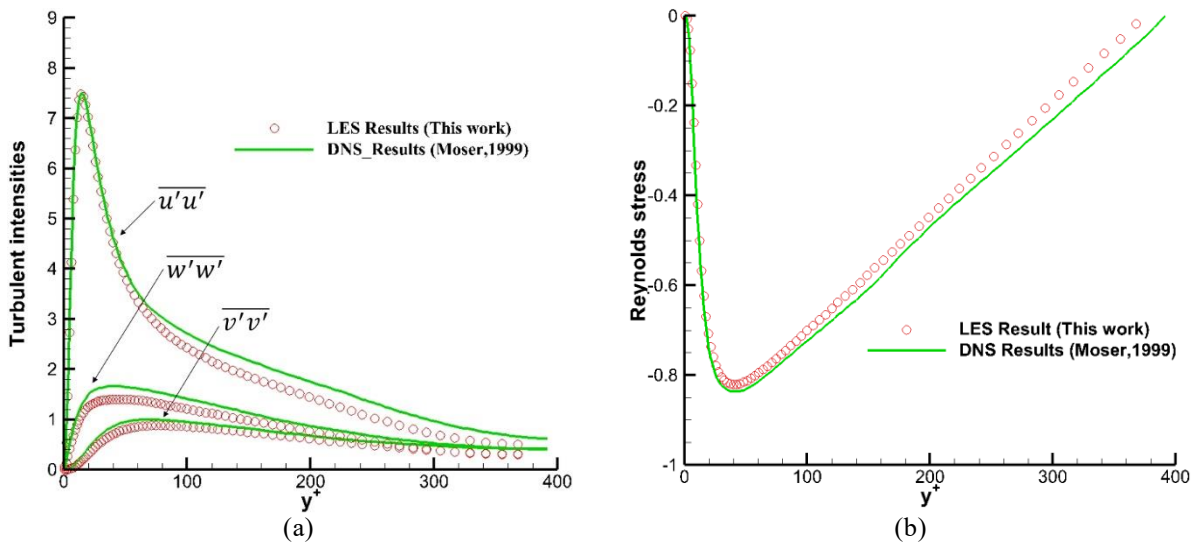


Figure 4: Comparison of turbulent intensities and Reynolds stress. (a) Turbulent intensities in three directions. (b) Reynolds stress

4.2 Bubbly channel flow simulation

In this section, the two phase coupled turbulent flow is simulated. Figure 5 presents the bubble transport process in the channel.

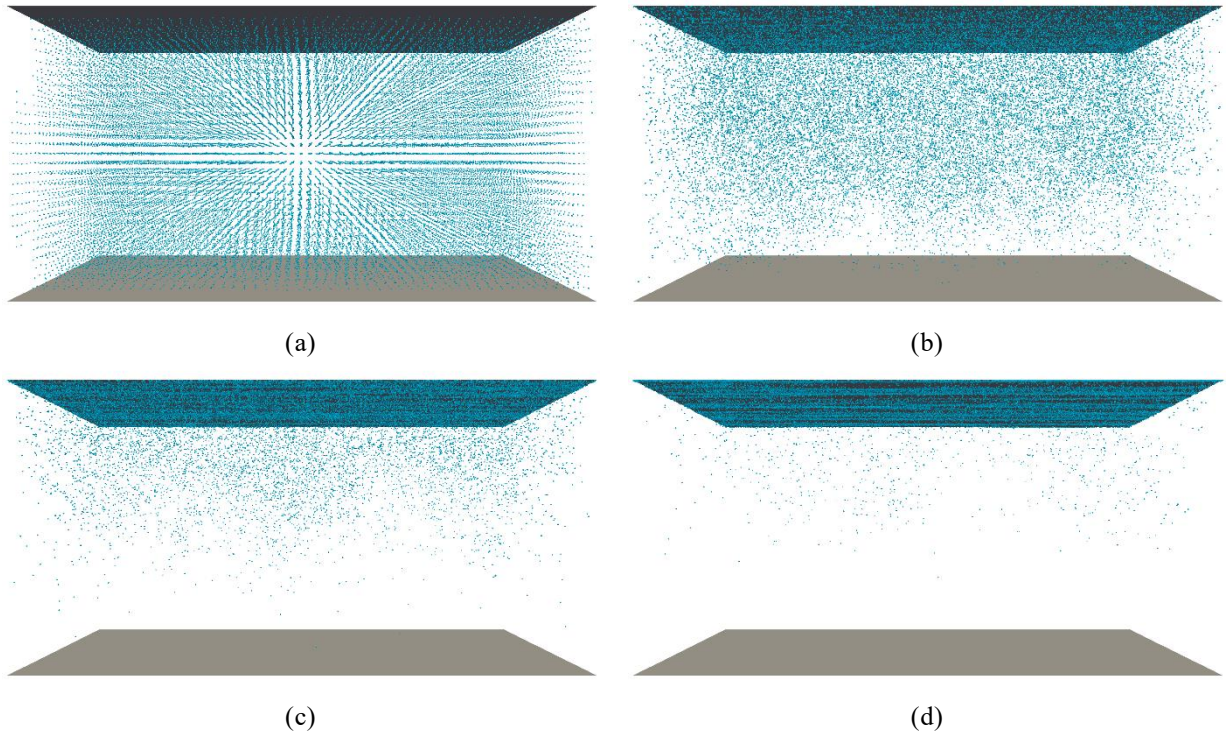


Figure 5: Microbubble transport process in the channel. (a) $t^+ = 0$ (b) $t^+ = 450$ (c) $t^+ = 1125$ (d) $t^+ = 1800$

After $t^+ = 1800$, most of microbubbles have moved close to the upper wall. It can be concluded that gravity-buoyancy is the dominant force in the wall-normal direction. The buoyancy force from the large density difference leads to the floating motion of bubbles to the upper wall gradually. At the same time, the lift force on the bubbles also causes them to move towards the wall. On the other hand, drag force is the dominant force in the streamwise direction. After the bubbles are initialized with zero speed in the channel, they are affected by the drag force of the fluid to produce velocity in the flow direction, which is almost the same as the local fluid velocity. It is worth noting that not all the bubbles are sticking to the upper wall after the flow field reaches stability. There are still many microbubbles move towards or away from the wall in the turbulent boundary layer, which leads to the suppression of turbulent vortex and turbulent drag.

Figure 6 shows the time histories of steady state frictional drag coefficient τ_w^+ ($\tau_w^+ = \tau_w / \frac{1}{2} \rho u_\tau^2$) on the upper wall with and without microbubbles. In the steady state, drag force oscillates randomly around a fixed value. It can be seen that the existence of microbubbles results in a certain degree of drag reduction. Quantitatively, about 6% drag reduction effect is obtained. The effect is much larger than the drag reduction of Pang et al.^[13] with the same bubble size and void fraction. The reason is that the microbubbles are considered to be as points in their paper, the change in viscosity of the mixed fluid was neglected. In this paper, The viscosity change is considered in the drag calculation. It can be probed from the results that the viscosity change caused by the microbubbles sticking to the wall can obviously improve the effect of drag reduction.

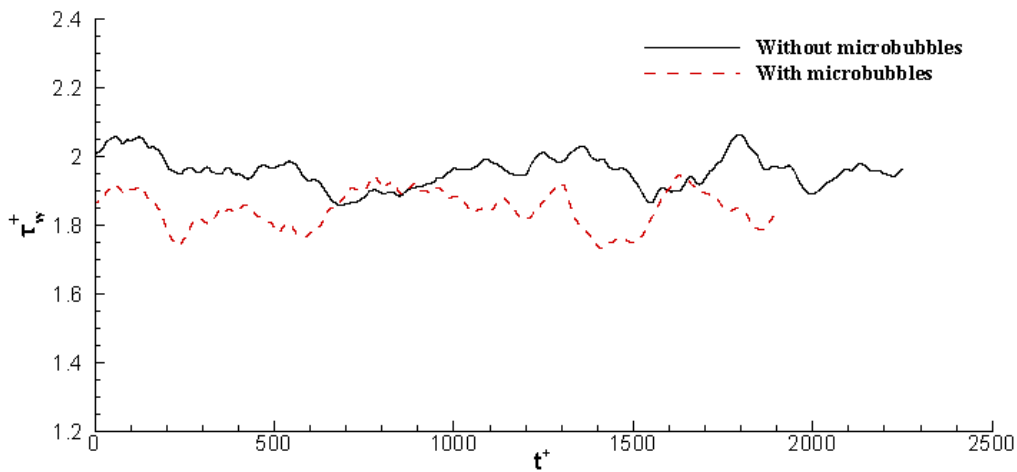


Figure 6: Time history of steady state frictional drag coefficient

Next, the influence of microbubbles on the turbulent flow is discussed in detail. The mean streamwise velocity profiles of the liquid phase with and without microbubbles are plotted in Figure 7. It is obvious that the mean velocity profile of the liquid phase with microbubbles displays a asymmetric shape in contrast with pure liquid flow. Specifically, the two profiles coincide completely in the lower half of the channel ($0 < y^+ < 375$), because there is no microbubble in that region. On the other hand, microbubbles concentrate in the upper half of the channel especially near the wall, which leads to a

squeeze on the fluid away from the wall. As a consequence, velocity near the channel centre is slightly higher than that in the pure liquid condition. At the same time, the velocity gradient near the wall is slightly decreases due to the presence of microbubbles, which contribute to drag reduction.

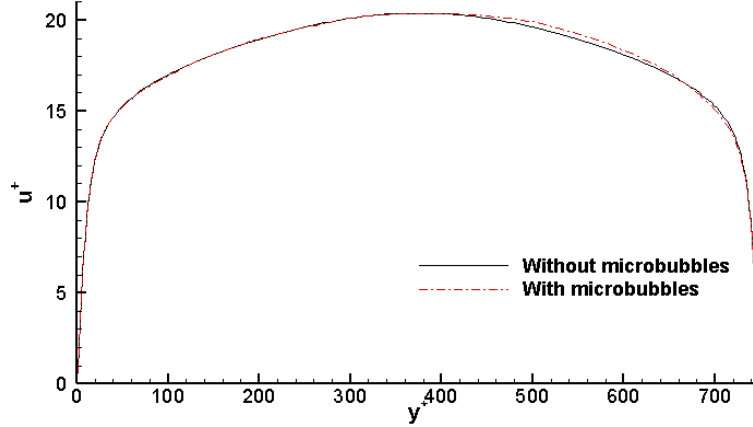


Figure 7: Mean velocity profiles of liquid.

Figure 8 presents the effect of microbubbles on the turbulent intensities and Reynolds stress in the upper half of the channel. It can be seen in Figure 8 (a) that the turbulent intensities of the liquid decrease by the impact of microbubbles. The decrease is more obvious in the wall-normal and spanwise directions, which indicates that microbubble has more obvious inhibitory effect on turbulent vortices in the wall-normal and spanwise directions. The results are in qualitative agreement with the results of Pang et al.^[13]. Figure 8 (b) shows that the distribution of Reynolds stress in the direction of channel height changes due to the presence of microbubbles. The magnitude of Reynolds stress decreases in the region near the wall ($y^+ < 250$). In the region away from the wall, Reynolds stress becomes slightly larger in the two phase flow than that in the single phase flow. In addition, the balance point is away from the channel center.

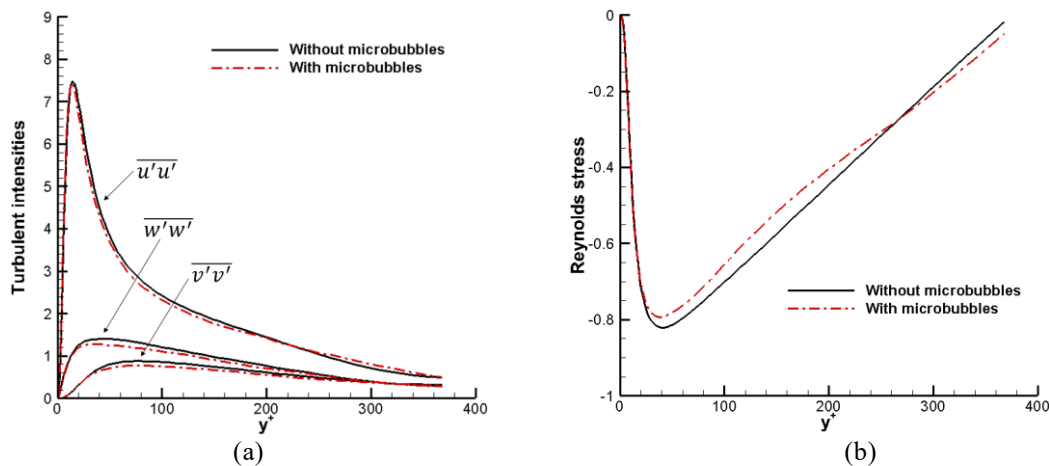


Figure 8: Turbulent intensities and Reynolds stress. (a) Turbulent intensities in three directions. (b) Reynolds stress

5 CONCLUSION

In this paper, Euler-Lagrange method is used to simulate a turbulent channel flow with a large number of microbubbles. LES method is applied to capture the detail turbulent flow, while microbubble is tracked individually in Lagrangian framework. Interaction between liquid and microbubbles is solved. The simulation is carried out by the code developed base on OpenFOAM.

Firstly, a fully developed turbulent flow is simulated. Mean velocity profile, turbulent intensities and Reynolds stress are validated by comparison with DNS results. Then, microbubbles are injected into the channel. Bubbles moves towards the upper wall due to the action of buoyancy. About 6% drag reduction effect is obtained in the steady state. The drag reduction effect results from two aspects: On the one hand, microbubbles attached to the wall change the local viscosity. On the other hand, turbulent vortexes are inhibited by microbubbles in a certain degree. Both turbulent intensities and Reynolds stress decrease in the presence of microbubbles.

The drag reduction effect achieved in the present simulation is very limited. At the same time, there are also some unreal assumptions about the calculation conditions like the fixed bubble size. Future work will be focused on the simulation with larger void fraction, and the breakup and coalescence of bubbles will also be considered.

REFERENCES

- [1] Fukuda, K., Tokunaga, J., Nobunaga, T., Nakatani, T., Iwasaki, T. Frictional Drag Reduction with Air Lubricant Over a Super-Water-Repellent Surface. *Journal of Marine Science and Technology*. (2000) **5**:123-130.
- [2] Madavan, N. K., Detusch, S. & Merkle, C. L. Reduction of turbulent skin—friction by microbubbles. *Physics of Fluids*. (1984) **27(2)**: 356-363.
- [3] Madavan, N. K., Detusch, S. & Merkle, C. L. Measurements of Local Skin Friction in a Microbubble Modified Turbulent Boundary Layer. *Journal of Fluid Mechanics*. (1985) **156**: 237-256.
- [4] Merkle, C. L., Detusch, S. Microbubbles drag reduction. *Springer, Berlin, Gad-el-Hak M(ed) Frontiers in experimental fluid mechanics*. (1989) **46**: 291-335.
- [5] Eric S., Winkel, Steven L., Ceccio, David R., Dowling. Marc Perlin Bubble-size distributions produced by wall injection of air into flowing freshwater, saltwater and surfactant solutions. *Experiments in Fluids*. (2004) **37**: 802-810.
- [6] Sanders, W. C., Winkel, E. S., Dowling, D. R., Perlin, M. & Ceccio, S. L. Bubble friction drag reduction in a high-Reynolds-number flat-plate turbulent boundary layer. *Journal of Fluid Mechanics*. (2006) **552**: 353-380.
- [7] Brian R. Elbing, Eric S. Winkel, Keary A. Lay, Steven L. Ceccio, David R., Dowling & Marc Perlin. Bubble-induced skin-friction drag reduction and the abrupt transition to air-layer drag reduction. *Journal of Fluid Mechanics* (2008) **612**: 201-236.
- [8] Kunz, R. F., Deutsch, S., and Lindau, J. W. Two Fluid Modeling of Microbubble Turbulent Drag Reduction. *Proceedings of FEDSM'03: 4TH ASME-JSME Joint Fluids Engineering Conference*. (2003) Honolulu, Hawaii, ASME Paper No. FED2003-45640.
- [9] Kunz, R. F., Gibeling, H. J., Maxey, M. R., Tryggvason, G., Fontaine, A. A., Petrie, H. L., Ceccio, S. L., Validation of two-fluid Eulerian CFD modelling for microbubble drag

- reduction across a wide range of Reynolds numbers. *Journal of Fluids Engineering*. (2007) **129**: 66-79.
- [10] Shijie Qin, Ning Chu, Yan Yao, Jingting Liu, Bin Huang, and Dazhuan Wu. Stream-wise distribution of skin-friction drag reduction on a flat plate with bubble injection. *Physics of Fluids* (2007) **29**: 037103.
- [11] Jin Xu, Martin R. Maxey and George Em Karniadakis. Numerical simulation of turbulent drag reduction using micro-bubbles. *Journal of Fluid Mechanics*. (2002) **468**: 271-281.
- [12] Antonini Ferrante and Said Elghobashi. On the physical mechanisms of drag reduction in a spatially developing turbulent boundary layer laden with microbubbles. *Journal of Fluid Mechanics*. (2004) **503**: 345-355.
- [13] M.J. Pang, J.J. Wei, B. Yu. Numerical study on modulation of microbubbles on turbulence frictional drag in a horizontal channel. *Ocean Engineering*. (2014) **81**: 58-68.
- [14] Kenneth S. Asiagbe, Michael Fairweather, Derrick O. Njobuenwu, Marco Colombo. Large eddy simulation of microbubble transport in a turbulent horizontal channel flow. *International Journal of Multiphase Flow*. (2017) **94**: 80-93.
- [15] Stephen B. Pope. Turbulent Flows. *Turbulent Flows*. (2000) **12**, (11).
- [16] F. Nicoud and F. Ducros. Subgrid-Scale Stress Modelling Based on the Square of the Velocity Gradient Tensor Flow. *Turbulence and Combustion*. (1999) **62**: 183-200.
- [17] A. Tomiyama, G.P. Celata, S. Hosokawa, S. Yoshida. Terminal velocity of single bubbles in surface tension force dominant regime. *International Journal of Multiphase Flow*. (2002) **28**: 1497-1519.
- [18] Akio Tomiyama, Hidesada Tamai, Iztok Zun, Shigeo Hosokawa. Transverse migration of single bubbles in simple shear flows. *Chemical Engineering Science*. (2002) **57**: 1849 - 1858.
- [19] Van Hecke, M. Jamming of soft particles: geometry, mechanics, scaling and isostaticity. *Journal of Physics*. (2010) **22**: 3, 033101.
- [20] Moser, R.D., Kim, J., Mansour, N.N. Direct numerical simulation of turbulent channel flow up to $Re \tau = 590$. *Physics of Fluids*. (1999) **11**: 943-945.

A PRACTICAL TOOL FOR THE HYDRO-ACOUSTIC OPTIMIZATION OF NAVAL PROPELLERS

FEDERICA VALDENAZZI*, FRANCESCO CONTI†, STEFANO GAGGERO‡,
DAVIDE GRASSI*, CRISTINA VACCARO† AND DIEGO VILLA‡

*CETENA S.p.A.

Via Ippolito d'Aste, 5, 16121 Genova, Italy
e-mail: federica.valdenazzi@cetena.it, www.cetena.it

‡Department of Naval Architecture, Electric and Electronic Engineering
University of Genoa
Via Montallegro,1, 16145 Genoa, Italy
email: stefano.gaggero@unige.it, www.unige.it

†Fincantieri Naval Vessel Business Unit
Via Cipro, 11, 16129 Genoa, Italy
email: cristina.vaccaro@Fincantieri.it – www.Fincantieri.it

Key words: Optimization, design, propeller, acoustics, tip vortex

Abstract. *Propeller optimisation is always the focus of the propeller design process, as such process is aimed at finding the best compromise between often conflicting objectives accounting for many design constraints. The use of optimization algorithms combined with blade shape modification techniques has been proposed by a number of research groups in the past few years and has proved to have a potential for practical applications, but integration in the everyday propeller design process is still beyond to be so consolidated.*

In the past one and a half year, CETENA, University of Genoa and the Fincantieri's Naval Vessels Business unit have teamed to set up a propeller optimization software environment to be used by Fincantieri's propeller designers in their everyday design work. A specification of the optimisation environment was worked out based on an analysis of the current design process, in order for the new procedures and tools to allow continuity of current practices while offering new possibilities in the comparative investigation of design variants and the identification of the very best design solution.

The resulting optimisation environment integrates different software tools and consists of three main components linked by JAVA script architecture: a software tool for blade shape modification and definition (1), a BEM code for the evaluation of the propeller performance (2) and the open-source software DAKOTA to guide the optimisation (3).

The software suite has been setup such as to be compatible with both Windows and Linux operating systems, in order to take advantage of all available computational resources, from single Windows workstations to the company's cluster, which operates under Linux.

An ad-hoc '2D modeler' has been developed by the University of Genoa to model and modify the propeller design table, while a 3D modeller has been developed by CETENA to generate the 3D propeller description suitable for CFD RANS computations, starting from the 2D

propeller design curves. The propeller performance is evaluated using CRS BEM code PROCAL and the CRS Empirical Tip Vortex model. Measures of merit usually include: the propeller efficiency, pressure coefficients at specific locations on the blade back and face sides and, for an hydro-acoustic optimization, also the tip vortex induced pressure.

The paper will provide details of the setup of the optimization environment focusing on an industrial application to design by optimization a naval propeller. The specific needs of the final users of the optimization suite will be highlighted and the expected benefits will be discussed, related to the time frame of the design process and the possibility of performing thorough investigations of design variants.

1 INTRODUCTION

Formal optimization techniques and tools are well-developed and it is well-known and demonstrated that they can help to improve the industrial design process. In order to be really effective, such techniques and tools need to be associated to equally effective tools to generate design variants and to a flexible and friendly post-processing, allowing the designer to quickly select the variants that fully answer his/her design purposes.

In this paper, the optimization environment designed by the authors to support the hydrodynamic design of propellers in the Naval Vessels Business Unit of Fincantieri is presented. The environment integrates an existing open source optimization software and existing and well-validated performance assessment tools. Focus of the activities has been the development of in-house tools for the generation of blade shape variants and the setup of the whole optimization process such that it can be fast and seamlessly integrated into the existing design process.

Minimization of computational time, possibility of carrying out optimization tasks on both Windows workstations and the company's Linux cluster and easiness of post-processing have been the priorities of the developments. Based on existing or desired design procedures, optimization templates have been created to allow the user to quickly start his/her propeller optimization.

In the following of this paper, the choices informing the development of the optimization environment are discussed; the tools and steps of the optimization process are presented and, finally, a specific optimization case is presented and discussed.

2 PROPELLER OPTIMIZATION AS A DESIGN ISSUE

The propeller design process is a very good example of optimization process. The designer has to deal with a set of objectives and constraints of various nature and he has to find the best solution accounting for all of them.

In this paper, the focus is on the hydrodynamic design of propellers, intended as the process that leads to a propeller providing the required thrust with the best possible hydrodynamic performance; the latter generally meaning maximum efficiency, minimum cavitation, minimum induced pressures. These objectives must be met accounting for quite a few constraints, some expressing requirements of the subsequent design and production phases, such as those related to robustness and structural performance and those deriving from production procedures and costs.

Interviewing designers prior to starting the research program that led to this paper

highlighted the criticalities in the hydrodynamic design process. They can be summarized as follows:

- constraints are so many that finding the optimal design or designs is difficult;
- available time to complete the design process is limited and too much of it is spent in the process of generating shape variants and setup and run the computations for performance verification.

After some discussion, it was agreed that making the design process more ‘formal’ can indeed help deal with the many constraints. It was also agreed to give priority to the development of tools to easily change the blade shape and setup the performance verification. It was finally, and importantly, agreed, that the new procedures should reflect, at least in part, the current practices, in order to create continuity between the old and new way of optimizing the propeller shape.

Following an analysis of current practices, it was decided to set three subsequent levels of shape optimization:

- Level 1 - exploration
- Level 2 - optimization
- Level 3 - refinement

The three levels differ essentially in the dimensions of the design space. In Level 1, there is a certain freedom in modifying the blade shape. It is accepted that design variants with shapes that are not acceptable for production are generated, provided they can be easily discarded. The freedom allowed in shape modification is meant to allow to identify areas of the design space that are promising and can be subsequently further investigated. Main objective is to increase efficiency at fixed thrust coefficient, while achieving a good blade pressure distribution. In this phase, the propeller performance is computed in open water conditions.

In Level 2, the blade shape modifications are more limited, with the design space defined based on the previous Level 1. The propeller performance is evaluated in behind hull conditions. Scope of the optimization is still to increase efficiency at fixed thrust coefficient, but two additional objectives can be added for this level: near field pressure at the first blade passing frequency and maximum pressure induced by the tip vortex in the near field. The latter is a preliminary measure of the propeller acoustic performance in the far field. For a naval propeller, accounting for the acoustic performance since early in the design process is quite important.

In Level 3, a limited number of variants from the previous levels are further investigated with a high-fidelity viscous CFD solver. No formal optimization is performed, but rather an assessment of the performance of the selected variants with numerical tools that model more accurately the physics behind the propeller behavior with respect to the previous levels.

Though they reflect the current design practices, the three levels are expected to allow a better exploration of the design space in a limited time. In the end, the goal is to have more chances to identify a very good solution in the same, or possibly reduced, time as before.

3 THE OPTIMIZATION ENVIRONMENT – GENERAL REQUIREMENTS AND SETUP

Prior to starting the tool development, the requirements on the optimization environment were discussed and decided upon. An optimization environment is intended here as the suite of software tools that allow to setup and perform an optimization task and analyze the optimization results. It can be seen as a computational box whose input is an initial blade shape and a set of objectives and constraints and whose output consists in a few blade shape variants that meet the objectives and comply with the constraints. Both initial shape and final shapes must be provided in a format that allow easy interfacing with the other software tools adopted by the design department.

Since the beginning, it was decided that DAKOTA [4] would be the optimization software: it is available under a GNU Lesser General Public License, it runs on Windows and Linux and the literature review demonstrates its potentialities to deal with complex optimization problems and its flexibility for the integration of heterogeneous tools in the optimization process. Version 6.7 of DAKOTA has been used for the study presented in this paper.

Importantly, it was decided that the optimization environment should be developed for use on both dedicated Windows workstations and FINCANTIERI's and CETENA's Linux computational clusters. This led to the decision to develop all the necessary scripts in Java. It also made it necessary to select verification tools with executables available for both Windows and Linux.

Finally, in order to simplify the setup of the optimization process, it was agreed that templates would be provided for the various optimization levels, so that the user would simply have to choose the template and define the desired boundaries of the design space to be able to start the optimization.

4 THE OPTIMIZATION PROCESS

The propeller optimization process consists in iteratively performing the following steps:

1. Generate blade shape variants, starting from an initial shape;
2. Evaluate the hydrodynamic performance of the variants;
3. Further modify the shape based on the outcome of the hydrodynamic evaluation;

Steps 1 and 3 are driven by the optimization algorithms and the three steps are repeated until convergence is achieved (or the maximum number of steps/iterations is reached).

Three tools, or set of tools, are required to perform these three steps:

- A tool for blade shape modification;
- Tools to estimate the hydrodynamic performance of shape variants;
- Optimization algorithms.

In the following of this section, the tools developed for the FINCANTIERI's optimization environment are presented and discussed in detail.

4.1 Blade shape modification

In the current design practices, the propeller blade shape is defined through a design table and a specification of the shape of blade sections at constant radii (radial sections). Propeller designers and hydrodynamics specialists usually relate the physics of the propeller behavior to the properties of the curves in the design table and of the radial sections, and such curves are also very suitable to an easy comparison of shape variants. This type of shape description, consisting in a set of 2D curves, has therefore been chosen as the starting point of the blade shape modeling.

The blade shape modeler developed by DITEN (hereafter called 2D modeler) is a Java code that allows to modify the design table based on user's requirements and to generate a new design table and radial sections suitable for the analysis with the hydrodynamic tools selected for the optimization process. The 2D modeler describes the propeller curves through a B-Spline approach [5]. Each curve of the initial design table (that of the reference propeller used as starting point for the design space exploration) is approximated with a B-Spline curve handled by a polygon with the lowest possible number of control points necessary to describe the curve within a given tolerance. This approach is suitable to reduce the dimensionality of the design space investigated by the optimizer. Preliminarily, only the spanwise curves have been considered: the shape of the radial sections is not modified, except for adapting it to the updated maximum sectional camber and thickness specified by the modification of the design table. The modification of the radial sections, which is not currently implemented with the 2D modeler, is meant to be part of a future level of detail.

The 2D modeler is able to:

- read the geometry file and upload the design table and radial sections;
- model the design table curves with B-Spline curves;
- allow the user to select a few control points and fix the range and step of variation of the point positions;
- generate all the variants in the fixed range, in terms of design table and radial sections;

The modeler identifies the number and position of the control points that best approximate the design table curves but allows the user to modify the number of control points. This is a useful feature, as a lower number of control points may result in a less accurate reproduction of the initial curves, but may be beneficial during shape modifications, as a lower number of control points tends to generate smoother curves with a limited number of inflexions. On the other hand, more control points are needed to modify and control curves locally. The choice of the number of control points to be used is part of the setup of the optimization process.

The figure hereafter shows the graphical interface of the 2D modeler. The propeller designer interacts with the modeler using this interface; there is no need to act on text files, as the control point variations are fixed through the graphical interface. The figure shows how the range of variation is chosen through a dedicated box that is associated to each control point. Once the control points and their range of variations are fixed, they can be exported into a text that can be copied directly in the input file used by DAKOTA to run the optimization.

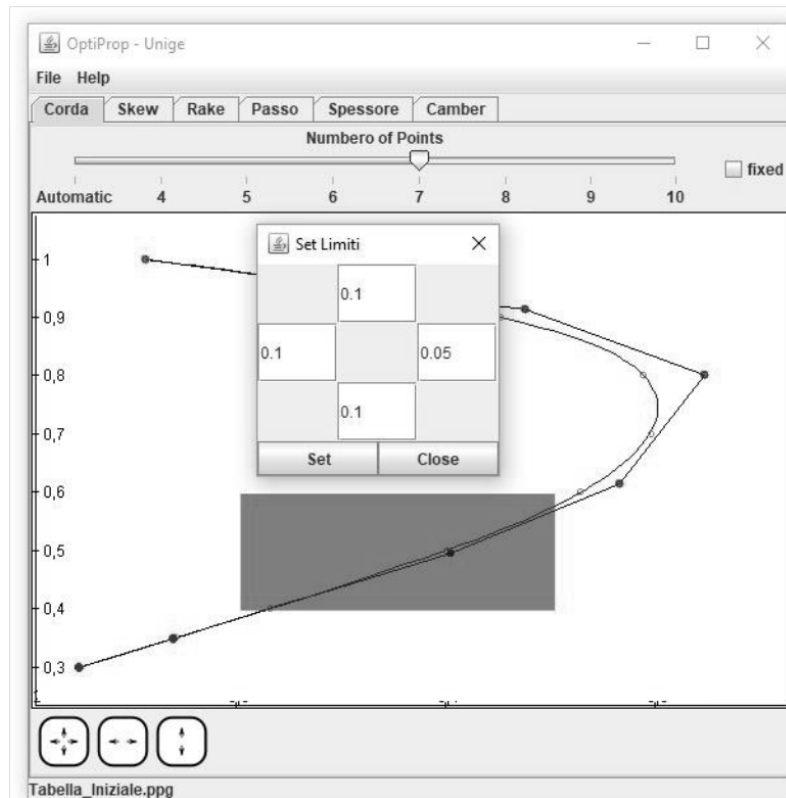


Figure 1: 2D modeller – graphical interface. The red box indicates the allowed variations in the position of the control point in the box.

The 2D modeller provides the blade shape in the format required by potential flow computations. In case CFD computations are to be carried out, a 3D model of the blade is necessary. A 3D modeller was therefore developed, using the Rhinoceros Grasshopper ©. The modeller uploads the design table and allows to select the shape of the radial sections in a database of NACA profiles. Using this data, it builds a 3D model of the blade through NURBS surfaces interpolating the given foil profiles. The 3D model is meant to be used for CFD computations and not production, which leads to a modeling of leading and trailing edge that, in the authors' experience, favours numerical convergence. Figure 2 shows a representation of the 3D blade and the blade sections generated by the modeller.

4.2 Performance verification

The assessment of blade shape variants is carried out using different hydrodynamic tools, depending on the level of the optimization process. For Level 1 and 2, potential flow code CRS PROCAL is used. It is a BEM code developed by and belonging to the Cooperative Research Ship (CRS) [1]. For Level 1, open water computations are performed and for Level 2 unsteady wetted computations are carried out. Prior to starting the optimization, PROCAL computations are performed for the initial blade shape and a sensitivity study is carried out to select the minimum number of panels necessary to obtain converged results. Unsteady wetted computations by PROCAL provide, amongst the output data, the circulation around the blade tip and, from circulation, an estimate of the maximum hull pressure induced by the tip vortex.

This estimate is made using the Empirical Tip Vortex (ETV) method developed by the CRS [2], which is integrated in PROCAL as far as near field pressures are concerned.

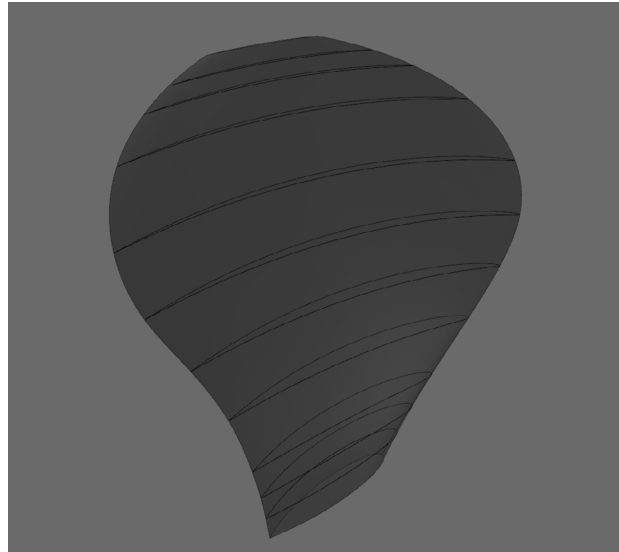


Figure 2: representation of the blade and sectional profiles from the 3D modeler.

From the PROCAL unsteady wetted computations it is also possible to derive the pressure amplitude at the first blade passing frequency at a user chosen location above the propeller tip, which can be taken as representative of the induced pressure on the hull above the propeller in the low frequency range.

A dedicated PROCAL post-processing piece of code has been developed to extract from the PROCAL output the data required by the optimization setup and write them in a simple text file in the format required by DAKOTA.

One of the main tasks of the post-processor is to extract from the standard PROCAL output the minimum value of the pressure coefficient on different blade regions, since the optimization process is based on cavitation avoidance using the simplest cavitation inception criterion ($-C_{PN} < \sigma_{N \text{ design}}$) and wetted calculations only [7]. Back and face of the blades are divided into four regions, as detailed in the following table:

Table 1: blade regions for estimation of minimum pressure

| | Radial position | Position along section chord |
|--------------------|--------------------|------------------------------|
| Lower Leading Edge | $r/R < 0.5$ | $x/C < 0.1$ |
| Upper Leading Edge | $0.5 < r/R < 0.95$ | $x/C < 0.1$ |
| Lower Centre Blade | $r/R < 0.5$ | $0.1 < x/C < 0.7$ |
| Upper Centre Blade | $0.5 < r/R < 0.95$ | $0.1 < x/C < 0.7$ |

Minimum value of the pressure coefficient is estimated for each of the regions defined in the table. The first panels along the leading edge are not included in the estimation of the pressure coefficient. A series of preliminary testing showed that pressure on the first panel can in some cases be rather high in absolute value for numerical reasons and this can mislead

the pressure assessment process. It was agreed that local effects at the leading edge are to be investigated and estimated with CFD rather than with potential flow methods.

One of the issues that were investigated in the first phases of the setup of the optimization environment is related to the PROCAL computational time. Though the time required by the single potential flow computation is indeed very short, when thousands of shape variants are to be assessed in an optimization process, even a few additional seconds can make a noticeable difference in the overall computational time. To investigate this aspect, tests were carried out to estimate the time needed to perform an open water computation and an unsteady wetted computation with PROCAL. Two different workstations were used, with respectively, a 3.2 GHz processor with 8.0 GB RAM and a 3.5 GHz processor with 16 GB RAM. Open water computations with standard paneling were found to require between 9 and 15 seconds. Unsteady wetted computations were found to require between 30 and 60 seconds. These data refer to a specific propeller but computation time was checked for other propellers and is very similar. These computational times are fully compatible with a full optimization process in the time frame required by the designers.

4.3 Optimization algorithms, objective and constraints

The selected optimization algorithm is a Multi Objective Genetic Algorithm (MOGA), as it allows to deal with multiple objectives and constraints. The MOGA parameters, such as population size and maximum function evaluations, were set by DITEN based on previous experience [5,6,7,8,9]. Such experience led to the choice of setting some objectives without constraints and using the genetic algorithm to drive the optimization process towards promising solutions without necessarily achieve a full convergence.

Objectives for Level 1 are:

- maximization of efficiency
- minimization of change of thrust coefficient with respect to initial value
- maximization of pressure coefficient on a few or all the blade zones of Table 1.

Objectives for Level 2 are:

- maximization of efficiency
- minimization of change of thrust coefficient with respect to initial value
- minimization of tip vortex pressure
- maximization of pressure coefficient on a few or all the blade zones of Table 1.

Regarding the pressure coefficients, for the unsteady computations, the minimum values over one revolution are used.

As far as Level 3 is concerned, it consists in a comparative CFD assessment of previously identified solutions with no formal optimization process. The CFD computations are expected to provide the details that potential flow computations are not able to predict and, due to the different physics, additional information on the performance of the selected shape variants.

5 DATA MANAGEMENT AND POST-PROCESSING TOOLS

An optimization process can generate a large amount of data, depending on the size of the

files generated by the software codes used for the assessment of variants. To avoid occupying a lot of memory with data unlikely to be used, it was decided to retain, for each shape variant, only the values of free variables and objectives. At the end of the optimization process, once the user has selected a few solutions that are promising and should be further analyzed, a dedicated script re-runs PROCAL for the selected solutions, so that pressure distribution over the blades and other results can be used for a complete assessment of such solutions.

To help selection and discussion of results, a dedicated visualization of results based on “Parallel Plots” was developed and customized for the optimization environment since parallel coordinates are a common way of visualizing high-dimensional geometry and analyzing multivariate data like those involved in the multi-objective parametric optimization of marine propellers. The developed graphical interface can be seen in Figure 2. A broken line, connecting the values of free variables and objectives, represents each design variant. The interface allows to restrict the range of variation of each free variable and objective and identify the variants that stay within the restricted intervals. This way, a limited number of variants with desired characteristics can be easily identified; the list of selected variants can be exported in a text file that is then used to re-run PROCAL in the cases of interest.

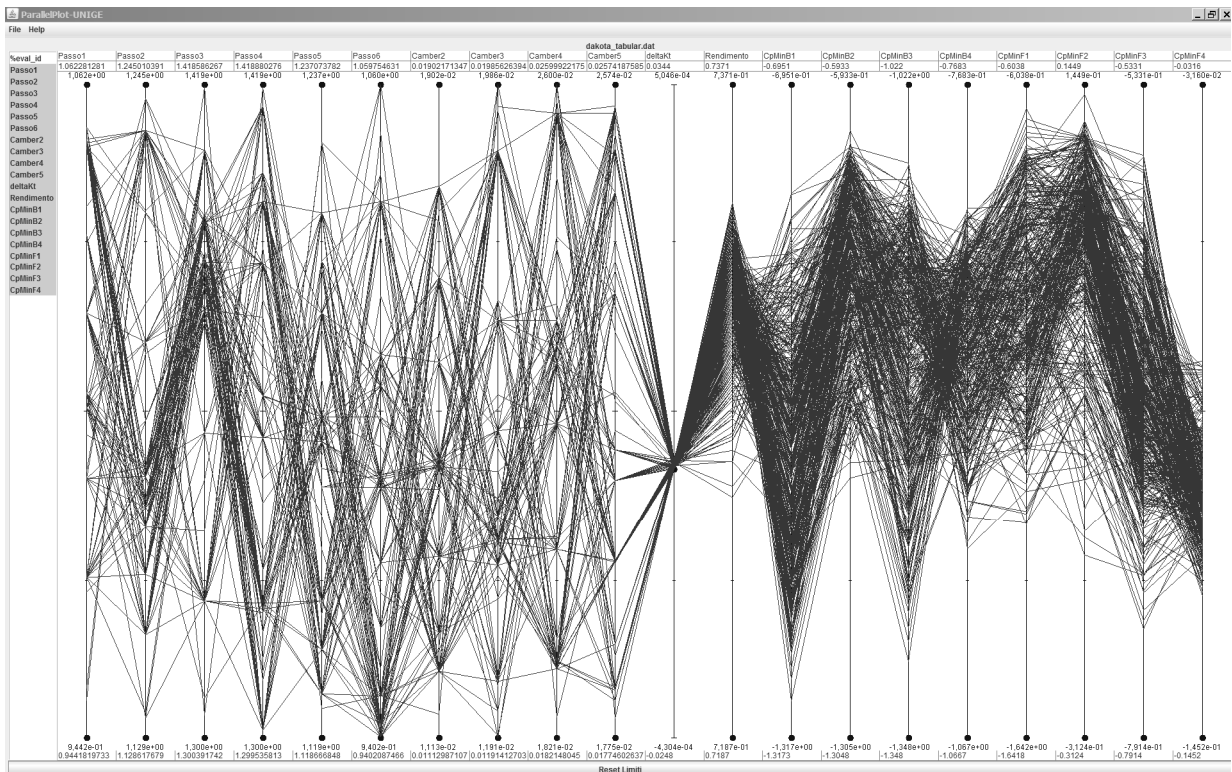


Figure 3: Parallelplot, graphical interface

6 A DESIGN OPTIMIZATION CASE

The optimization environment and process presented in the previous sections has been tested in the case of a naval propeller. The reference geometry is that of a four-bladed controllable pitch propeller designed for a high-speed twin screw vessel, with an advance

ratio close to 1.

Optimization has been performed in uniform flow. Both Level 1 and Level 2 optimization have been carried out. Hereafter the results of the Level 2 exercise are presented.

The free variables of the optimization were chosen as the control points of the chord, pitch and camber curves. As far as the chord is concerned, it was decided to allow only the control points governing the upper part of the blade (non-dimensional radial position $r/R > 0.8$) to be varied. Regarding the pitch curve, all the 6 control points describing the curve were allowed to move, while for the camber curve, described by 6 control points, only 4 points were allowed to move, the points with lowest and largest r/R having been set as fixed. For all the control points, the radial position was not allowed to change, leading to a total of 12 free variables.

The range of variation of pitch and camber were chosen as follows:

- Pitch +/-10% of maximum pitch;
- Camber +/-15% of maximum camber;
- Chord +/-10% of the maximum chord for the last but one point towards the tip, +/-5% for the tip point;

Optimization was run on a Windows workstation using four processors. Time to complete the process was 29 hours. Following completion of the optimization process, the results were analyzed using the Paralleplot. A few shape variants were selected amongst those with high efficiency and low tip vortex induced pressure, all of them having a K_T value within 2.5% of the initial value and chord lengths in the upper range of variation. Allowing longer chords towards the tip is not favourable to efficiency but allows to achieve a smoother pressure distribution and improve cavitation-related behavior.

The following figures show the pitch and camber curves for the selected variants.

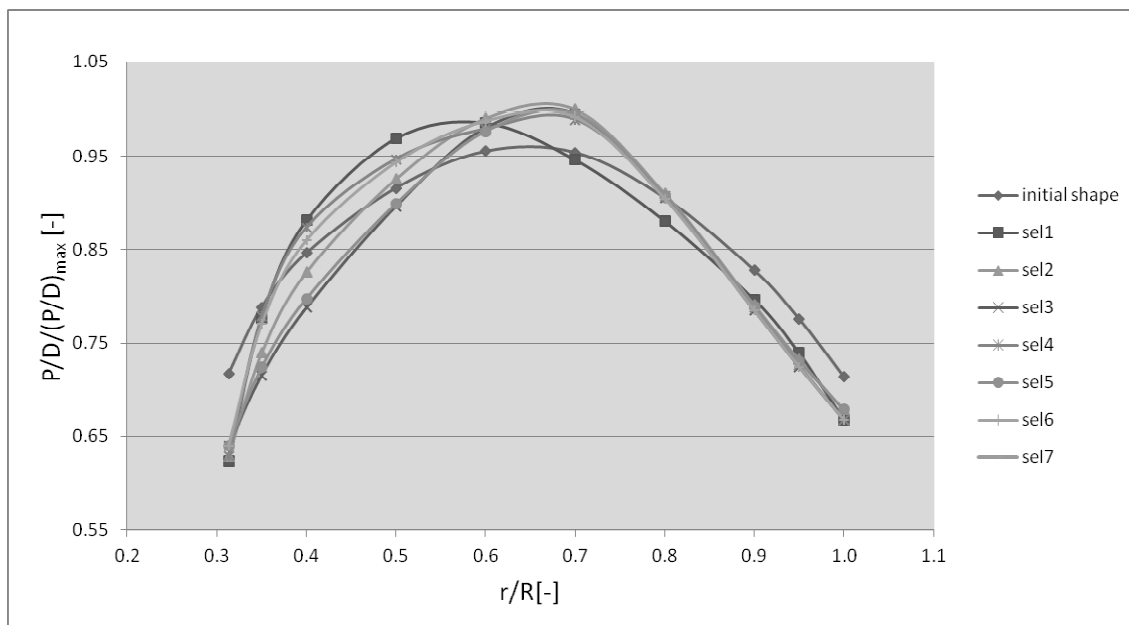


Figure 4: Pitch distribution of selected shape variants

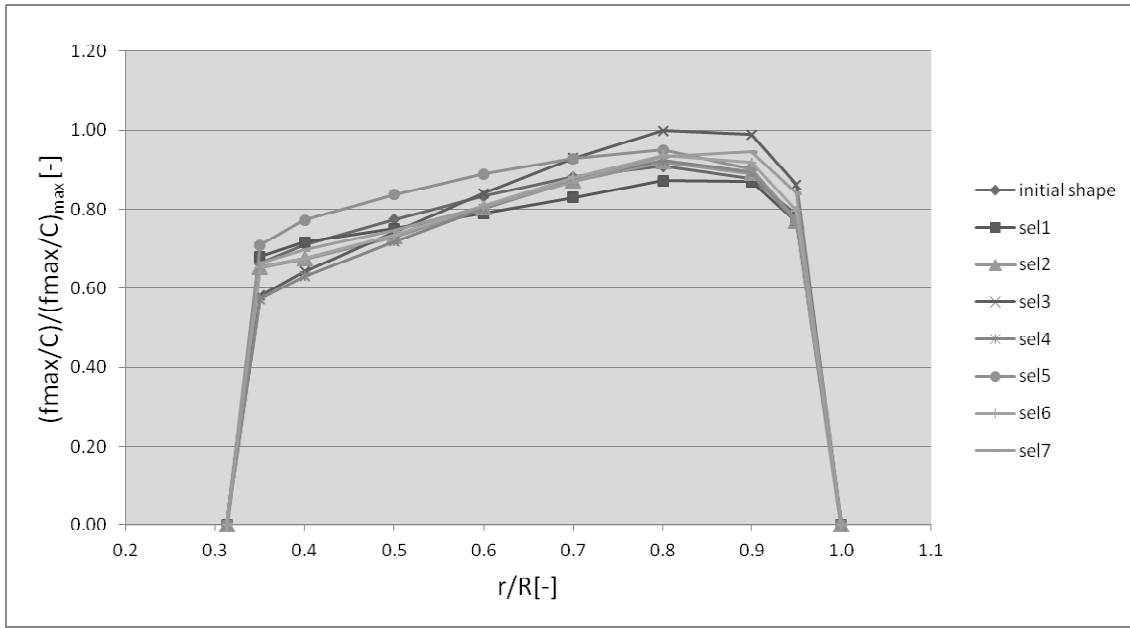


Figure 5: Camber distribution of selected shape variants

The curves in the figures are well behaved, in the sense that they are rather smooth and feature no inflexions. This is an effect of the limited number of control points used for the B-Spline approximation and a result of the optimization process, which drives the blade shape in the direction of a smooth pressure distribution through maximization of the pressure coefficient in the blade regions of Table 1; and a smooth pressure distribution tends to be associated to well behaved radial curves.

The selected solutions feature a slightly reduced efficiency with respect to the initial shape, but the tip vortex pressure is always reduced; in the best case (number 6 in the figures), the pressure is 3.5 dB lower than the pressure of the original design, with a reduction in efficiency of 0.7%.

The objective to reduce the tip vortex strength and induced pressure leads to a reduction of the pitch in the tip area of the blade; the best solutions are found to be those that combine a reduced tip pitch with suitable changes in the camber curve. This result is no surprise to the designer, but the optimization process allows to identify good blade shapes with such features with less effort in less time.

Blade pressure distribution is satisfactory in terms of both pressure levels and distribution over the blade, as shown in the figure hereafter, where the pressure coefficient CPN at radial position $r/R = 0.7$ is shown for the original blade shape (solid line) and the seven variants of the previous figures (dotted lines). The curves feature a more peaked CPN in the leading edge region, as an effect of the pitch and camber modifications and they reflect the fact that most of the variants have an increased loading at radial positions between $r/R=0.6$ and $r/R=0.7$. The pressure coefficient is always lower than the cavitation number, as desired.

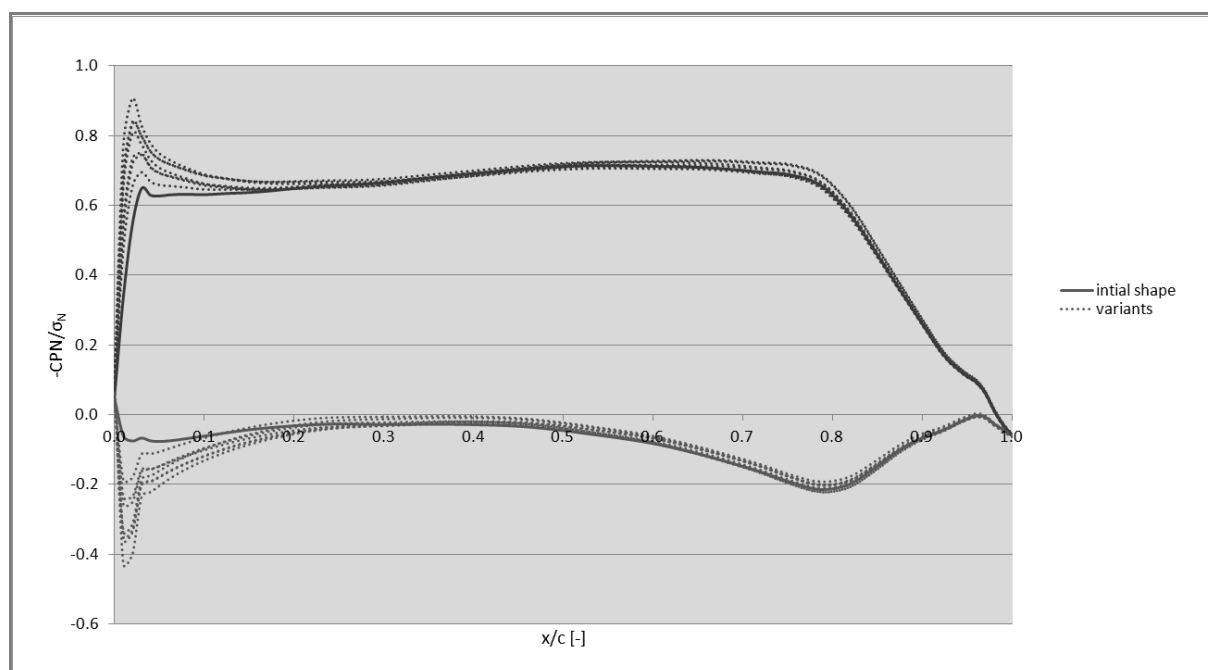


Figure 6: Pressure coefficient at radial position $r/R = 0.7$, for the initial blade shape and selected variants.

7 CONCLUSIONS

In the previous sections of this paper, the propeller optimization environment developed by the authors to support the everyday propeller design work of the Fincantieri Naval Vessels Business Unit has been presented and a specific application to the design of a naval propeller has been discussed.

Focus of the authors work has been on integrating existing and well-validated performance assessment tools and optimization algorithms into a new design optimization environment reflecting and enhancing the current design practice. A 2D blade modeler for the generation of design variants starting from the classical blade description in terms of design table and radial sections has been developed on purpose for the optimization environment; a new 3D modeler allows to easily generate 3D surface descriptions of promising variants for subsequent CFD analysis.

Limited computational time and easiness of post processing have been priorities; the propeller optimization process must fit into the tight time schedules of the design office.

An application to the optimization of a four-bladed naval propeller designed for installation on a fast naval vessel has proved that the environment answers the needs of the designers and can provide a number of good design alternatives in a limited time frame.

ACKNOWLEDGEMENTS

The work presented in this paper has been funded by the Fincantieri's Naval Vessels Business Unit in the frame of their Research & Innovation Program. Codes PROCAL and ETV have been developed by and belong to the Cooperative Research Ship.

REFERENCES

- [1] Vaz, G. and Bosschers, J., Modelling Three Dimensional Sheet Cavitation on Marine Propellers using a Boundary Element Method. *Sixth International Symposium on Cavitation CAV 2006, Wageningen, the Netherlands* (2006)
- [2] Bosschers, J., A Semi-Empirical Method to Predict Broadband Hull Pressure Fluctuations and Underwater Radiated Noise by Cavitating Tip Vortices. *Fifth International Symposium on Marine Propulsors, smp'17, Espoo, Finland* (2017)
- [3] Firenze, E. and Valdenazzi, F. A Method to predict underwater noise from cavitating propellers. *OCEANS 2015, Genoa*, (2015)
- [4] Adams, B.M., Bauman, L.E., Bohnhoff, W.J., Dalbey, K.R., Ebeida, M.S., Eddy, J.P., Eldred, M.S., Hough, P.D., Hu, K.T., Jakeman, J.D., Stephens, J.A., Swiler, L.P., Vigil, D.M., and Wildey, T.M., Dakota, A Multilevel Parallel Object-Oriented Framework for Design Optimization, Parameter Estimation, Uncertainty Quantification, and Sensitivity Analysis: Version 6.7 User's Manual, *Sandia Technical Report SAND2014-4633, July 2014. Updated November 2017 (Version 6.7)*, (2017)
- [5] Bertetta D., Brizzolara S., Gaggero S., Viviani M. and Savio, L., CPP propeller cavitation and noise optimization at different pitches with panel code and validation by cavitation tunnel measurements, *Ocean Engineering*, Volume 53 (2012)
- [6] Gaggero S., Gonzalez-Adalid J.G. and Perez Sobrino M., Design and Analysis of a New Generation of CLT Propellers, *Applied Ocean Research*, Vol. 59, (2016)
- [7] Gaggero, S., Tani, G., Villa, D., Viviani, M., Ausonio, P., Travi, P., Bizzari, G. and Serra, F., Efficient and multi-objective cavitating propeller optimization: an application to a high-speed craft, *Applied Ocean Research*, Vol. 64, (2017)
- [8] Gaggero, S., Design of PBCF energy saving devices using optimization strategies: A step towards a complete viscous design approach, *Ocean Engineering*, Vol. 159, (2018)
- [9] Gaggero, S., Villa, D., Tani, G., Viviani, M. and Bertetta, D., Design of ducted propeller nozzles through a RANSE-based optimization approach, *Ocean Engineering*, Vol. 145, (2017)

DATA DRIVEN UNCERTAINTY QUANTIFICATION FOR COMPUTATIONAL FLUID DYNAMICS BASED SHIP DESIGN

T.P. Scholcz

Maritime Research Institute Netherlands (MARIN)
Haagsteeg 2, 6708 PM Wageningen, The Netherlands
e-mail: t.p.scholcz@marin.nl, web page: <http://www.marin.nl/>

Key words: Robust ship design, data-driven, uncertainty quantification, computational fluid dynamics

Abstract. Maritime transport is responsible for an annual emission of around 1000 million tonnes of CO₂, which is around 2.5% of the global greenhouse gas emissions. Nowadays, ships are designed using simplified operational profiles representing the expected operational profile during the lifetime of the ship. However, there is a discrepancy between these simplified profiles used for design and the actual full operational profile of a ship during its lifetime. This discrepancy leads to inefficient hydrodynamic ship design resulting in a waste of fuel and an increase of greenhouse gas emissions.

The amount of available data on actual operational conditions of ships is rapidly increasing. The Automatic Identification System (AIS) and onboard monitoring systems produce a huge amount of historical data on ship operations. These developments call for efficient data-driven methods that account for this data. Knowledge of operational conditions can be used for Computational Fluids Dynamics (CFD) -based probabilistic uncertainty quantification leading to robust design: A hull shape that is optimal with respect to uncertain operational conditions. Robust design is a promising approach since it makes ships energy efficient for the real usage situation.

Three UQ-methods are discussed: The perturbation method, the Polynomial Chaos Expansion (PCE) method and the multi-fidelity PCE method. The methods are applied to a simple one-dimensional test case to compute the stochastic moments of the effective power. The multi-fidelity Polynomial Chaos Method is found to be the most efficient UQ method. Moreover, the multi-fidelity PCE can be used as a surrogate for efficient Monte Carlo integration. This makes the method suitable for an Optimisation Under Uncertainty (OUU) algorithm leading to robust design.

1 INTRODUCTION

Greenhouse gas emissions from the combustion of oil-based fuels are directly proportional to fuel consumption. Some options to reduce fuel consumption are, amongst others, hull optimisation, weather routing, propeller polishing, slow steaming and trim optimisation, see [1]. Here, we will focus on improving hull optimisation techniques to reduce fuel consumption. By including realistic operational conditions in the hull form optimisation process it is expected that ships can be made more robust with respect to these conditions, leading to an improved energy efficiency.

Robust design optimisation is a promising technique that enables the ship designer to optimise the hull for the actual usage situation [2, 3]. When operational data is available of comparable ships and missions, *new* ships can be optimised to account for exactly these conditions. The resulting ship designs will be more energy efficient than designs resulting from optimisation using only a few representative design conditions.

In order for robust design optimisation to be useful it is critical to have reliable operational data relevant to the ship and mission to be designed. Sources of data are for example the Automatic Identification System (AIS) [2] and onboard monitoring systems [1]. Using AIS data, speed is recorded during the voyage and displacement at the beginning of the voyage. AIS signals are detected by satellites which provide a capability for monitoring all vessels with AIS equipment. When operational data is collected onboard, the ship has a data logging system which processes the data from on board sensors.

Robust design optimisation requires efficient Uncertainty Quantification (UQ) methods to propagate the uncertain operational conditions to the uncertain design objectives. This contribution will focus on UQ using Polynomial Chaos Expansions (PCE). The methods are ranked on computational efficiency and the capability to predict uncertainty for large input data. A simple one-dimensional test case is defined in Section 1.1 involving a container ship sailing at random speed. Two deterministic solvers are used: a cheap to evaluate low fidelity solver and an expensive high fidelity solver.

1.1 Numerical test case: 22000 TEU container vessel

The particulars of the containership are summarized in Table 1. The speed is assumed to be a random

Table 1: Main particulars

| Parameter | Symbol | Value | Units |
|---------------|--------|-----------------------|-------|
| Ship | Lpp | 383 | m |
| Beam | B | 61.2 | m |
| Draft | T | 14.5 | m |
| Froude number | Fn | $N(0.1847, 0.008397)$ | [-] |

variable which can be decomposed in m standard independent random variables:

$$V = V(\xi_i) \quad \xi_i = i, \dots, m \quad (1)$$

For simplicity, here the speed is assumed to be a function of a single standard Gaussian random variable

$$V = V_0 + \sigma_V \cdot \xi, \quad (2)$$

where the speed V_0 and σ_V are chosen to represent a 'realistic' operational profile. Here, we choose $V_0 = 22$ knots and $\sigma_V = 1$ knot which leads to a random Froude number $Fn = N(0.1847, 0.008397)$. The deterministic design objective is the effective power of the ship

$$P_E = R \cdot V, \quad (3)$$

where R is the total resistance of the ship. The total resistance can be predicted using the low fidelity potential flow solver RAPID in order to compute a quick and rough estimate and using the viscous high fidelity solver ReFRESKO to compute a reliable value.

1.1.1 Low fidelity solver: free-surface potential code RAPID

The fully nonlinear free-surface potential flow solver Raised-Panel Iterative Dawson (RAPID) [4] is a panel method neglecting viscous effects. Using RAPID, the total (viscous) resistance is estimated using

$$R = (1 + k)R_{f_0} + R_w, \quad (4)$$

where R_{f_0} is the frictional resistance of a flat plate with a surface equal to the wetted surface area S moving at speed V , the factor k is an estimated form factor and R_w is the wave resistance computed from integration of the pressure resistance along the hull. Expression (4) yields a Low Fidelity (LF) prediction of the total resistance which is computed in a few minutes on a desktop PC.

1.1.2 High fidelity solver: free surface RANS code ReFRESO

The free surface RANS code ReFRESO solves incompressible viscous flows using the Navier-Stokes equations, see [5]. ReFRESO is used for High Fidelity (HF) predictions of the resistance. ReFRESO is an unstructured finite volume code based on the volume-of-fluid formulation. To assess the prediction accuracy, the numerical uncertainty needs to be estimated using a grid refinement study. Richardson extrapolation is used in the least square sense since scatter in the solution may deteriorate the observed order of convergence p . The goal is to obtain the discretisation uncertainty U of prediction \hat{R} such that with 95% confidence: $\hat{R} - U \leq R^* \leq \hat{R} + U$, where R^* denotes the exact solution. Equivalently, this can be written as

$$P \left[|\varepsilon_R| \geq \frac{U}{R^*} \right] \leq 1 - C \quad \text{with} \quad \varepsilon_R = \frac{\hat{R} - R^*}{R^*}, \quad (5)$$

where ε_R is the discretisation error and $C = 0.95$. The uncertainty U is obtained using the method described in [6]. Four solutions on geometrically similar grids with sizes $N = 2.7, 4.6, 7.4$ and 10.8 million cells are used to fit $\delta_{RE} = R_i - R^* = \alpha h_i^p$. When the observed order p satisfies $1.0 \leq p \leq 2.1$ and the standard deviation of the fit $\hat{\sigma}$ is smaller than the mean change in the data, the value for U is estimated using

$$U = F_s \delta_{RE} + \hat{\sigma} + |\hat{R} - R_{\text{fit}}|, \quad (6)$$

with a safety factor $F_s = 1.25$. A distinction is made between the friction resistance and the pressure resistance, see Figure 1.

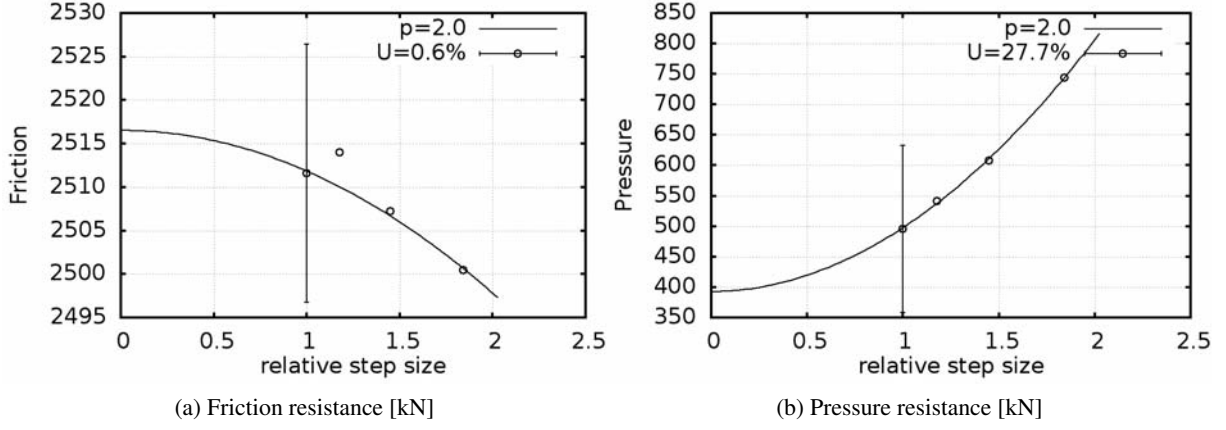


Figure 1: Grid convergence of the friction and pressure resistance.

The results for the finest grid with $N = 10.8$ million cells are summarized in Table 2.

Table 2: Errors and uncertainties of the finest grid ($N=10.8$ million cells)

| | Friction | Pressure | Total |
|-----------------------------|-----------------------|-----------------------|-----------------------|
| Approximation (\hat{R}) | 2512 kN | 496 kN | 3007 kN |
| Uncertainty (U/\hat{R}) | 5.90×10^{-3} | 2.77×10^{-1} | 4.60×10^{-2} |

The uncertainty of the total resistance is obtained using $U_T = \sqrt{U_f^2 + U_p^2}$, which assumes independent convergence of pressure and friction. Note that the numerical uncertainty of the pressure is much higher than the uncertainty of the friction and that the total uncertainty is almost 5% of the estimated resistance. However, grid convergence is observed such that this uncertainty can always be reduced when more grid cells are used for the computation. To limit computational costs, we use $N = 10.8$ million cells in the remainder of the paper.

1.1.3 Quantities of Interest

The Quantities of Interest (QoI) are the stochastic moments of the effective power with respect to the uncertain operational conditions. The effective power depends on the random variable as

$$P_E(\xi) = R(V(\xi)) \cdot V(\xi). \quad (7)$$

The statistical moments of the effective power are then defined by

$$\begin{aligned} \mu_{P_E} &= \int P_E(\xi) p_\xi d\xi \\ \sigma_{P_E}^2 &= \int (P_E(\xi) - \mu_{P_E})^2 p_\xi d\xi, \end{aligned} \quad (8)$$

where p_ξ denotes the probability density function of random variable ξ . Computing the integrals in (8) efficiently is required in order to be able to optimise the hull shape for minimal expected power. Efficient UQ methods are the subject of Section 2.

2 Uncertainty Quantification Methods

The Monte Carlo method is the most general and reliable method to propagate uncertainty to the objectives. Unfortunately, it is also the most expensive method which makes it not suitable for robust optimisation. More efficient UQ methods exploit the smoothness of the objectives with respect to the uncertain variables. Three UQ methods are applied: The perturbation method, the Polynomial Chaos Expansion method and the multi-fidelity Polynomial Chaos Expansion method. To this end, Sandia National Laboratories open-source DAKOTA tool is used, see [7].

2.1 Perturbation method

If the objective function is smooth, the effective power can be expanded in a multi-dimensional second-order Taylor expansion around a point α (see [8])

$$\begin{aligned} P_E(\xi) &= P_E \Big|_\alpha + \nabla P_E \Big|_\alpha (\xi - \alpha) + \frac{1}{2} (\xi - \alpha)^T \nabla^{(2)} P_E \Big|_\alpha (\xi - \alpha) \\ &= a + \mathbf{b}^T \xi + \frac{1}{2} \xi^T \mathbf{C} \xi, \end{aligned} \quad (9)$$

where a , \mathbf{b} and \mathbf{C} are given by

$$\begin{aligned} a &= P_E \Big|_\alpha - \nabla P_E \Big|_\alpha \alpha \\ \mathbf{b}^T &= \nabla P_E \Big|_\alpha - \alpha^T \nabla^{(2)} P_E \Big|_\alpha \\ \mathbf{C} &= \nabla^{(2)} P_E \Big|_\alpha. \end{aligned} \quad (10)$$

Here, ∇P_E denotes the gradient of the effective power with respect to the uncertain variables and $\nabla^{(2)} P_E$ the Hessian of the effective power. From equation (7), the gradient and Hessian are computed as

$$\frac{dP_E}{d\xi_i} = \left(\frac{\partial R}{\partial V} \cdot V + R \right) \cdot \frac{\partial V}{\partial \xi_i} \quad \text{for } i = 1, \dots, m \quad (11)$$

and

$$\frac{d^2 P_E}{d\xi_i d\xi_j} = \left(\frac{\partial^2 R}{\partial V^2} \frac{\partial V}{\partial \xi_j} V + 2 \frac{\partial R}{\partial V} \frac{\partial V}{\partial \xi_j} \right) \cdot \frac{\partial V}{\partial \xi_i} + \left(\frac{\partial R}{\partial V} \cdot V + R \right) \cdot \frac{\partial^2 V}{\partial \xi_i \partial \xi_j} \quad \text{for } i, j = 1, \dots, m. \quad (12)$$

If the random variables are independent and Gaussian distributed, the statistical moments follow from

$$\begin{aligned} \mu_{P_E} &= a + \frac{1}{2} \text{Tr}[\mathbf{C}] \\ \sigma_{P_E}^2 &= \mathbf{b}^T \mathbf{b} + \frac{1}{2} \text{Tr}[\mathbf{C}^2], \end{aligned} \quad (13)$$

where $\text{Tr}[\cdot]$ is the trace operator. The mean-centred perturbation method results when the center of expansion α equals the mean of the input random variables: $\alpha = 0$ in case of Gaussian distributed variables.

2.2 Polynomial Chaos Expansion Method

A (truncated) polynomial chaos expansion is an expansion in a finite number of basis functions. The basis functions ψ_i with $i = 0 \dots P$ are chosen such that

$$\langle \psi_i(\xi) \psi_j(\xi) \rangle = \int \psi_i(\xi) \psi_j(\xi) p_\xi(\xi) d\xi = \delta_{ij}, \quad (14)$$

where $\delta_{ij} = 1$ if $i = j$ and $\delta_{ij} = 0$ if $i \neq j$. The effective power is expanded in the basis functions

$$\begin{aligned} P_E(\xi) &= a_0 B_0 + \sum_{i_1=1}^{\infty} a_{i_1} B_1(\xi_{i_1}) + \sum_{i_1=1}^{\infty} \sum_{i_2=1}^{i_1} a_{i_1 i_2} B_2(\xi_{i_1}, \xi_{i_2}) + \dots \\ &\approx \sum_{i=0}^P \alpha_i \psi_i(\xi), \end{aligned} \quad (15)$$

where P is the expansion order. Standard Hermite functions are used for the (Askey) polynomial basis which satisfy (14) in case p_ξ is normally distributed. Two options are available to compute the expansion coefficients: the spectral method and the regression method ([9]). Once the coefficients are computed, the statistical moments of the effective power are determined using

$$\begin{aligned} \mu_{P_E} &= \alpha_0 \\ \sigma_{P_E}^2 &= \sum_{i=1}^P \alpha_i^2 \langle \Psi_i^2 \rangle. \end{aligned} \quad (16)$$

Using the spectral method, Equation (15) is multiplied with basisfunctions ψ_i and integrated over the random variable space to obtain

$$\alpha_i = \frac{\langle P_E(\xi), \psi_i(\xi) \rangle}{\langle \psi_i^2(\xi) \rangle} = \frac{1}{\langle \psi_i^2(\xi) \rangle} \int P_E(\xi) \psi_i(\xi) \rho(\xi) d\xi, \quad (17)$$

where use has been made of the orthogonality of the basis functions with respect to the inner product $\langle \cdot \rangle$. To evaluate the integrals in (17) sparse grid integration can be used. So called Genz-Keister ([10]) quadrature results in a number of quadrature points and corresponding expansion orders that depend on the dimension of the problem and the level of the grid. For example, in one dimension, the number of required quadrature points is given in Table 3. For higher dimensions, tables can be found in [10, 11].

Table 3: Number of quadrature points (samples) for a 1-dimensional Genz-Keister quadrature

| Level | N_l | P | Number of samples |
|-------|-------|----|-------------------|
| 0 | 1 | 0 | 1 |
| 1 | 3 | 2 | 3 |
| 2 | 7 | 6 | 9 |
| 3 | 15 | 14 | 19 |

As can be seen in Figure 2 the quadrature rule is nested which means there is an overlap between the quadrature points on different grid levels. The advantage of nested quadrature rules is the possibility of

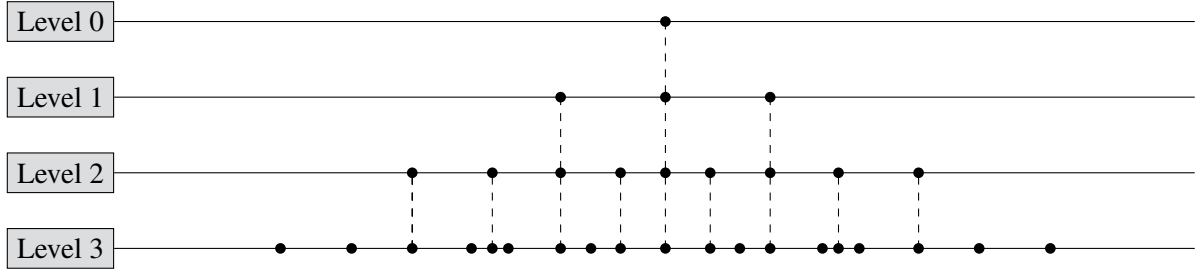


Figure 2: Genz Keister quadrature points in 1 dimension. The dashed lines indicate the overlap/nesting.

reusing results from one grid to the other and the possibility of combining high and low fidelity results on different grid levels in a multi-fidelity method. Using Genz-Keister quadrature, the PCE coefficients can be computed from (17) and substituted in (16) to compute the stochastic moments.

2.2.1 Multi-fidelity Polynomial Chaos Expansion

In case of an additive multifidelity correction model, the model discrepancy is defined as

$$\Delta(\xi) = P_E^{\text{HF}}(\xi) - P_E^{\text{LF}}(\xi), \quad (18)$$

which can be expanded in the polynomial basis as

$$\Delta(\xi) = \sum_{i=0}^{P_{\text{HF}}} \delta_i \psi_i(\xi). \quad (19)$$

If the HF-solver is used at a certain grid level and the LF-solver at a higher grid level, the model discrepancy can only be computed on the overlapping points, see Figure 2. The discrepancy expansion is therefore constructed on the lower grid level. Once the model discrepancy expansion is constructed it can be evaluated at the higher grid level to correct the LF prediction:

$$P_E \approx \sum_{i=0}^{P_{\text{HF}}} \delta_i \psi_i(\xi) + \sum_{i=0}^{P_{\text{LF}}} \alpha_i^{\text{LF}} \psi_i(\xi) \quad (20)$$

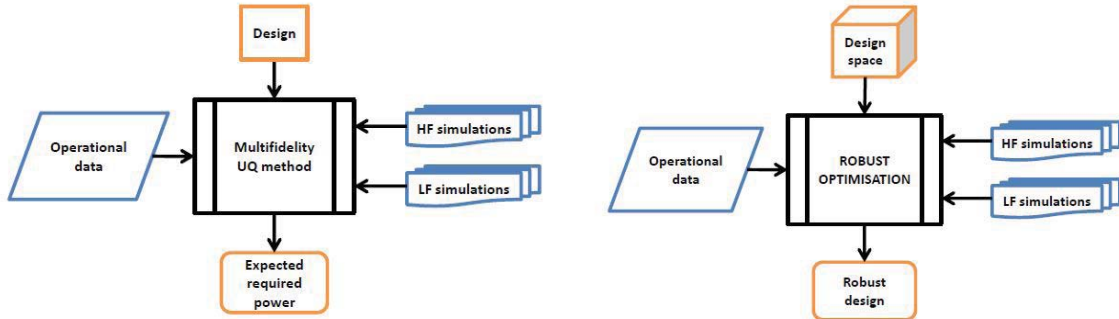
$$= \sum_{i \in \text{CB}} (\alpha_i^{\text{LF}} + \delta_i) \psi_i(\xi) + \sum_{i \in \text{B}_{\text{LF}} \setminus \text{CB}} \alpha_i^{\text{LF}} \psi_i(\xi). \quad (21)$$

Here, B_{rapid} is the polynomial basis for the LF expansion and CB the Common polynomial Basis of the HF and LF expansion, see [12, 13]. The stochastic moments μ_{P_E} and $\sigma_{P_E}^2$ are then computed in the same way as in Equation (16)

$$\begin{aligned} \mu_{P_E} &= \alpha_0^{\text{LF}} + \delta_0 \\ \sigma_{P_E}^2 &= \sum_{i \in \text{CB} \setminus 0} (\alpha_i^{\text{LF}} + \delta_i)^2 \langle \Psi_i^2 \rangle + \sum_{i \in \text{B}_{\text{LF}} \setminus \text{CB}} (\alpha_i^{\text{LF}})^2 \langle \Psi_i^2 \rangle. \end{aligned} \quad (22)$$

3 Robust optimisation using data driven UQ

An Optimisation Under Uncertainty (OUU) procedure allows to account for the uncertainties in the operational conditions during the hull form optimisation. The challenge is to efficiently and reliably include the uncertainties in the analysis such that the result will be a hull design which is robust with respect to given representative operational conditions.



(a) Multifidelity Uncertainty Quantification of the expected required power for representative operational data

(b) Robust Optimisation of the expected required power. Optimisation Under Uncertainty (OUU), see [14].

Figure 3: Data driven design methodology: (a) Prediction (b) Optimisation.

Figure 3a shows the procedure to predict the expected required power using a multifidelity UQ method. When for example a PCE surrogate is constructed from multifidelity simulations it is possible to predict the expected required power in a very cheap and efficient way since the surrogate can be evaluated at a negligible cost. Any operational data can be used as long as the surrogate represents the high fidelity objective in the range of conditions.

Figure 3b shows the procedure to optimise a hull form for expected required power given representative operational data. Here, the operational data drives the design which means that representative operational conditions will determine the optimal hull shape from the design space. Different formulations exist to perform the optimisation: Nested, Layered/Nested, Nested/Layered and Layered/Nested/Layered, see [14]. The latter constructs a surrogate at the UQ level *and* at the optimisation level. In other words, each point (hull shape) of the Design of Experiment at the optimisation level contains an entire surrogate based UQ analysis to predict the expected required power. This is the most attractive option from a computational point of view but only works if the quality of the surrogates are verified.

4 Results and discussion

In this section we examine the quality of the UQ methods from section 2. Assuming converged moments $\mu_{P_E}^*, \sigma_{P_E}^*$ at grid level 3, the errors in the predicted moments $\hat{\mu}_{P_E}, \hat{\sigma}_{P_E}$ are defined as

$$\varepsilon_{\mu_{P_E}} = \frac{\hat{\mu}_{P_E} - \mu_{P_E}^*}{\mu_{P_E}^*} \quad \text{and} \quad \varepsilon_{\sigma_{P_E}} = \frac{\hat{\sigma}_{P_E} - \sigma_{P_E}^*}{\sigma_{P_E}^*} \quad (23)$$

As can be seen from Table 3 and Figure 2, 19 high fidelity calculations (samples) were required to compute $\mu_{P_E}^*$ and $\sigma_{P_E}^*$. Figure 4a and 4b show the convergence of the mean and standard deviation of the effective power with respect to the number of required samples for each method from section 2.

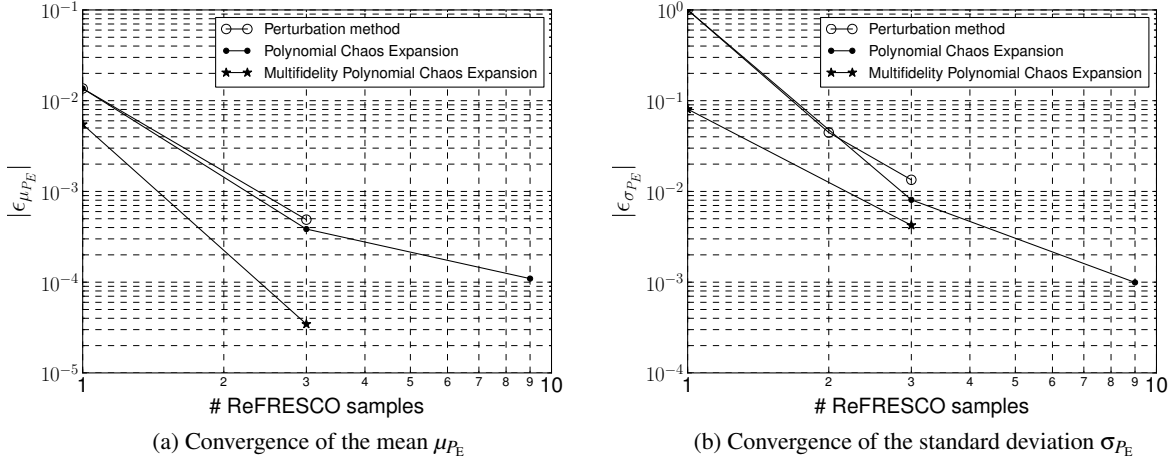


Figure 4: Convergence of statistical moments with the number of required ReFRESKO samples

The predictions are collected in Table 4 and ranked in performance for predicting the expected effective power μ_{P_E} . It can be seen that the UQ methods all converge rapidly to $\mu_{P_E}^*$ and $\sigma_{P_E}^*$ and that the multifidelity PCE method is the most efficient UQ technique. Multi-fidelity PCE at levels 1,2 is even more accurate in predicting the expected effective power than PCE at level 2. However, note that this is not true for the standard deviations of the effective power. The accuracy of multi-fidelity PCE at levels 0,1 falls exactly between the accuracy of the first and second order perturbation method: a constant correction to the LF data performs better than linearisation but worse than a curved approximation. Due to the uncertain speed ($\sigma_V = 1$ knot), the expected power is about 1.4% higher than the power at $V_0 = 22$ knots.

| Method | Resistance | | Effective power | |
|--------------------------------|--------------------------------|--------------------------------------|------------------------------------|--|
| | $\mu_R (\varepsilon_\mu)$ [kN] | $\sigma_R (\varepsilon_\sigma)$ [kN] | $\mu_{P_E} (\varepsilon_\mu)$ [kW] | $\sigma_{P_E} (\varepsilon_\sigma)$ [kW] |
| PCE, level = 3, 'truth' | 3035.0 (0.00%) | 306.1 (0.00%) | 34505.6 (0.00%) | 5069.3 (0.00%) |
| Multi-fi PCE, levels = 1,2 | 3035.5 (0.01%) | 307.5 (0.47%) | 34506.7 (0.00%) | 5090.8 (0.42%) |
| PCE, level = 2 | 3035.4 (0.01%) | 305.5 (-0.18%) | 34509.3 (0.01%) | 5064.3 (-0.10%) |
| PCE, level = 1 | 3036.4 (0.05%) | 309.5 (1.11%) | 34518.8 (0.04%) | 5110.3 (0.81%) |
| Second order perturbation | 3034.1 (-0.03%) | 299.8 (-2.04%) | 34488.7 (-0.05%) | 5001.2 (-1.34%) |
| Multi-fi PCE, levels = 0,1 | 3020.1 (-0.49%) | 276.4 (-9.71%) | 34316.5 (-0.55%) | 4660.1 (-8.07%) |
| First order perturbation | 3007.2 (-0.91%) | 290.6 (-5.06%) | 34035.4 (-1.36%) | 4843.5 (-4.46%) |
| PCE, level = 0 | 3007.2 (-0.91%) | - | 34035.4 (-1.36%) | - |
| Zeroth order perturbation | 3007.2 (-0.91%) | - | 34035.4 (-1.36%) | - |

Table 4: Comparison of UQ methods

PCE can also be used as a surrogate for the high fidelity solver in order to estimate the effective power. Using Monte Carlo integration, stochastic moments can be computed for arbitrary input data at almost negligible cost. This is the subject of section 4.1.

4.1 Comparison of surrogates and Monte Carlo integration

The surrogates of each UQ method from section 2 are shown in Figure 5a together with the high fidelity evaluations at grid level 1 and the low fidelity evaluations at grid level 2. The conclusions of the previous section are now visualised: Multi-fidelity PCE at grid levels 1,2 performs best and the multi-fidelity PCE at grid levels 0,1 falls exactly between the first and second order perturbation curves. Figure 5b shows the model discrepancy expansions of the multi-fidelity PCEs. The discrepancies are small such that the multi-fidelity approach works well in this case.

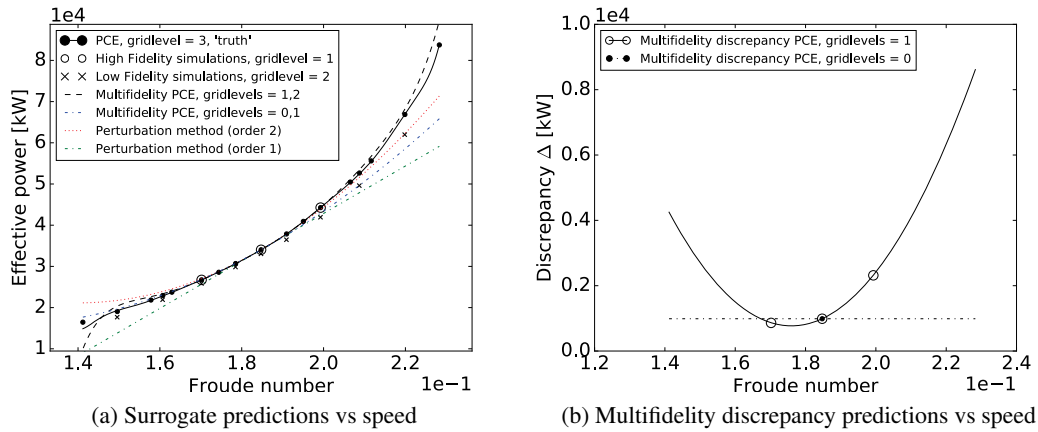


Figure 5: UQ Surrogate comparison

Monte Carlo integration is now applied to the multi-fidelity PCE surrogate at grid levels 1,2 using 100,000 samples drawn from three Gaussian distributions with $\sigma_V = 1, 2, 3$ knots, see Figure 6. A rapid increase in expected effective power is observed due to the stretched tail which is a consequence of increased effective power at high speeds. The entire computation takes only a few seconds.

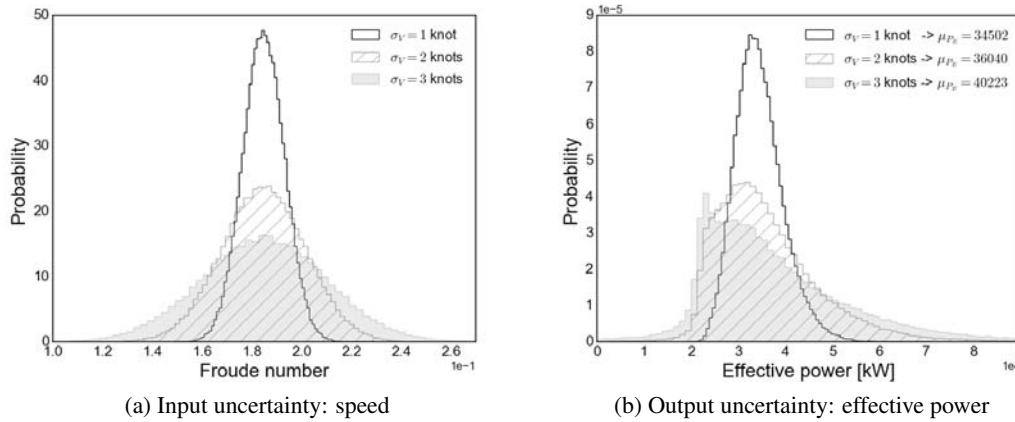


Figure 6: Monte Carlo on the multi-fidelity PCE surrogate constructed at grid levels 1,2. $N_{mc} = 100,000$.

5 Conclusions

Greenhouse gas emissions are directly proportional to fuel consumption. One option to mitigate fuel consumption is to optimise the ship hull with respect to realistic operational conditions leading to a so called 'robust design'.

Robust design optimisation requires efficient Uncertainty Quantification in order to propagate the uncertainty to the objectives. In addition to efficiency, the UQ method should also be able to deal with large (measured) input data. Three UQ methods are discussed: the perturbation method, the Polynomial Chaos Expansion method and the multi-fidelity Polynomial Chaos Expansion method. The methods are applied to a simple one-dimensional test case: a container ship sailing at random speed.

The multi-fidelity Polynomial Chaos Expansion is found to be the most efficient UQ method for this test case. Moreover, the PCE method can be used as a surrogate for efficient Monte Carlo integration in case large input data of arbitrary distribution is available. Since surrogate evaluations are computationally cheap, they are well suited for an Optimization Under Uncertainty (OUU) algorithm leading to robust design. Such a data-driven hull optimisation approach will be the subject of future work.

6 Acknowledgements

This research was funded from the TKI-allowance of the Dutch Ministry of Economic Affairs. The support is gratefully acknowledged.

REFERENCES

- [1] Coraddu, A., Oneto, L. and Anguita D. Vessels Fuel Consumption: A Data Analytics Perspective to Sustainability. in: Cruz Corona C. (eds) *Soft Computing for Sustainability Science. Studies in*

- Fuzziness and Soft Computing*, vol 358. Springer, Cham (2018).
- [2] Peri, D. 'Robust Design Optimization for the refit of a cargo ship using real seagoing data' , *Ocean Engineering*, Vol. 123, pp. 103-115, (2016).
- [3] Wei, H., Diez, M, Campana, E., Stern, F. and Zao-jian, Z. 'A one-dimensional polynomial chaos method in CFD-Based uncertainty quantification for ship hydrodynamics performance' *Journal of Hydrodynamics*, Vol. 25(5), pp. 655–662, (2013).
- [4] Raven, H. C., "A solution Method for the Nonlinear Ship Wave Resistance Problem" PhD Thesis Delft University of Technology (1996).
- [5] Vaz, G., Jaouen, F., Hoekstra, M. "Free-surface viscous flow computations. Validation of URANS code FRESKO", *Proceedings of OMAE2009*, Hawaii, USA, (2009).
- [6] Eça, L., Hoekstra, M., "Evaluation of numerical error estimation based on grid refinement studies with the method of the manufactured solutions", *Computer & Fluids*, Vol. 38, pp. 1580–1591, (2009).
- [7] Adams, B.M., Ebeida, M.S., Eldred, M.S., Geraci, G., Jakeman, J.D., Maupin, K.A., Monschke, J. A., Stephens, J.A., Swiler, L.P., Vigil, D.M., Wildey, T.M., "Dakota, A Multilevel Parallel Object-Oriented Framework for Design Optimization, Parameter Estimation, Uncertainty Quantification, and sensitivity Analysis: Version 6.9 User's Manual" *Sandia Technical Report SAND2014-4633*.
- [8] Verhoosel, C.V., Scholcz, T.P., Hulshof S.J. and Gutierrez, M.A. 'Uncertainty and reliability analysis of fluid-structure stability boundaries', *AIAA Journal*, Vol. 47(1), pp. 91-104, (2009).
- [9] Duz, B., Ypma, E. "Uncertainty quantification in numerical simulations of parametric roll", *Proceedings of the ASME 2018 37th International Conference on Ocean, Offshore and Arctic Engineering OMAE2018*, 17-22 June 2018, Madrid, Spain. OMAE2018-77801
- [10] Genz, A. and Keister, B.D. 'Fully symmetric interpolatory rules for multiple integrals over infinite regions with Gaussian weight', *Journal of Computational and Applied Mathematics*, Vol. 71, pp. 299-309, (1996).
- [11] Chen, P. 'Sparse quadrature for high dimensional integration with Gaussian measure', *ESAIM Journal*, Vol. 52(2), pp. 631-657, (2018).
- [12] Ng, L. W. T. and Eldred, M. S. 'Multifidelity uncertainty quantification using non-intrusive polynomial chaos and stochastic collocation', *53rd AIAA/ASME/ASCE/AHS/ASC Structures, Structural Dynamics and Materials Conference*, 23-26 April 2012, Honolulu, Hawaii. AIAA 2012-1852
- [13] Palar, P.S., Zuhail, L.R., Shimoyama, K., Tsuchiya, T. 'Global sensitivity analysis via multi-fidelity polynomial chaos expansion', *Reliability Engineering & System Safety*, Vol. 170, pp.175–190, (2018).
- [14] Eldred, M. S., Giunta, A. A., Wojtkiewicz, S. F. and Trucano, T. G. "Formulations for surrogate-based optimization under uncertainty", *9th AIAA/ISSMO Symposium on Multidisciplinary Analysis and Optimization*, AIAA-2002-5585 (2002).

IMPROVED HULL DESIGN WITH POTENTIAL-FLOW-BASED PARAMETRIC COMPUTER EXPERIMENTS

OSCAR F.A. VAN STRATEN*, EGEMEN CELIK*, JOUKE H.S. DE
BAAR†, BLANKA ASCIC† AND JOCHEM S. DE JONG†

*Damen Schelde Naval Shipbuilding
De Willem Ruysstraat 99, Vlissingen, The Netherlands
e-mail: o.van.straten@damennaval.com
web page: <https://www.damennaval.com>

†Damen Shipyards Gorinchem
Avelingen West 20, Gorinchem, The Netherlands
e-mail: jouke.de.baar@damen.com
web page: <https://www.damen.com>

Key words: Computational Methods, Marine Engineering, Design-of-Experiments, Meta-Model, Potential Flow, DACE

Abstract. There is a significant market pull and technology push to incorporate computational fluid dynamics (CFD) in the early vessel design phase. In this phase, one allows for large-impact changes in the hull geometry. The computational cost of CFD deployment in this early phase has two important drivers. Firstly, for an individual CFD simulation, accuracy is correlated with cost—both in man and CPU hours. Secondly, when we increase the number of shape parameters, we face the ‘curse of dimensionality’, an exponential increase of the number of individual simulations that are required to obtain a target accuracy. By applying design and analysis of computer experiments (DACE) methodology, as well as by employing potential flow simulations, we can gather valuable insight in the performance of the vessel within a short amount of time. In this paper, we present the multi-objective automatic shape optimisation of a combatant with eight design parameters, as well as the inverse design of an offshore patrol vessel with seven design parameters.

1 INTRODUCTION

During the initial design phase of a vessel, a number of important changes in the geometry can have a large impact in various areas, one of which is the predicted hydromechanical performance. In order to allow swift analysis of the result of such geometric modifications, thus enabling speedy yet well-informed product development, it is important for a shipyard to develop and maintain the ability to make quick updates of the performance predictions.

The subject of this paper is the design and analysis (DACE) of the performance of a combatant and an offshore patrol vessel. DACE was introduced in the seminal 1989 paper by Sacks *et al.* [1]. In this paper, Sacks *et al.* extended the idea of large-scale experimental set-up and analysis to systematic sampling of the output of complex computer codes. Instead of providing an analysis of the Physics of the computer model, DACE considers the computer code as a black box, and provides a statistical analysis of the input/output relation. The objective of the DACE analysis is to, efficiently, arrive at an accurate on-the-fly prediction of the output of the computer code, without requiring a new, expensive, code evaluation.

The scope of coverage is the theoretical, computational fluid dynamics (CFD)-based resistance analysis of two hull forms. The analysis is limited to a user-defined parametric description of the hull, defined by eight shape parameters in the first application and seven shape parameters in the second application. Both base-line hulls are closely related to vessels that are currently being developed within our shipyard. Therefore, we are very grateful for your kind understanding that we cannot publicly share all details of the designs and results.

The purpose of the paper is to emphasise the role that DACE can play in the early design phase of a vessel. Our point of view is that the regression of a large number of purpose-dedicated hull variations can be valuable for multi-objective optimisation as well as inverse design.

The paper is organised as follows. Section 2 provides an overview of the methodology—the design-of-experiments, flow solvers, and meta-modeling. Section 3 provides the case descriptions. In Section 4 we present our results. Section 5 is the conclusion.

2 METHODOLOGY

The DACE methodology consists of four consecutive steps: creating a design-of-experiments, running the flow solver, building a meta-model and, finally, exploiting the meta-model. These steps are discussed in more detail in the following sub-sections.

The methodology used for the first application is the Python code HYDRA, which has been developed by the Maritime Research Institute Netherlands (MARIN). This method combines a 3D CAD model in Rhinoceros through the use of a Grasshopper script to a flow solver RAPID and finally to an optimiser Dakota [2]. In this paper the solver is a potential flow solver, but this can also be a full RANS solver. The methodology used in the second application is an in-house development, which acts as a pre- and post-processor for the potential flow solver ν -SHALLO.

2.1 Design-of-experiments

The design-of-experiments (DoE), alternatively known as a sampling plan, determines which combinations of shape parameters, and therefore which hull shapes, will be simulated. The most straight-forward, and perhaps most intuitive, is a full-factorial DoE. However, for a full-factorial DoE, the required number of samples, and thus computational cost, increases exponentially with the number of shape parameters—an effect known as the ‘curse of dimensionality’ [3]. Therefore, alternative sampling strategies have been developed, which aim to mitigate this curse. The two most important approaches are the deterministic sparse grid approach [4, 5, 6, 7] and the pseudo-random space-filling approaches. The full-factorial, sparse grid and space-filling sampling strategies are illustrated in Figure 1.

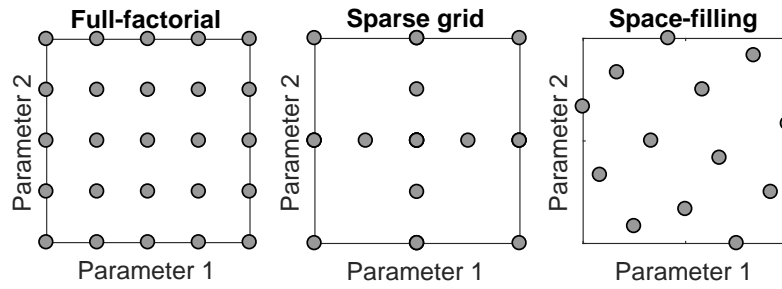


Figure 1: Illustration of the three main types of DoE for two shape parameters. In both applications, we use a space-filling DoE.

Presently, in the first application, where we consider multi-objective optimisation of a combatant, we use a statistical method for generating a near-random range of samples from a multi-dimensional distribution, to be used as the DoE, generating the form variations in Rhino by using a Grasshopper script, developed by Damen Schelde Naval Shipbuilding (DSNS), which is coupled to the MARIN HYDRA framework. The space-filling DoE in Figure 1 presents an indicative DoE as used in this application. Rhinoceros 3D is a software package from Robert McNeel & Associates for 3D modelling of NURBS and mesh objects. Rhino can create, edit, analyze, document, render, animate, and translate NURBS* curves, surfaces, and solids, point clouds, and polygon meshes.[8] Grasshopper is a visual programming editor developed by David Rutten at Robert McNeel & Associates. As a plug-in for Rhino, Grasshopper is integrated with the robust and versatile modelling environment used by creative professionals across a diverse range of fields, including architecture, engineering, product design, and more. [9] All 3D objects are created based on given parameters and they are generated instantly when a parameter is modified.

In the second application, for which Damen Shipyards Gorinchem (DSGo) considers simulation and inverse design of an offshore patrol vessel (OPV), we use a space-filling approach for our DoE. In the space-filling approach, the distribution of samples is pseudo-random, but is then optimized to maximize a performance measure of the sample distribution. The exact measure we use remains confidential.

2.2 Potential flow simulation

In comparison to viscous simulations, potential flow simulations provide a rough resistance estimate at a relatively small number of man-hours and at low computational cost. The simulation is based on a mesh representation of the vessel surface, to which a mesh representation of the free surface is added by the solver. The panels above the free surface are iteratively deformed to track the wave profile, therefore, breaking waves and spray cannot be modelled.

The code is mainly used in a comparative way during hull form optimisation. The potential flow simulation provides an estimate of the wave making resistance—an ITTC friction line [10] based estimate of the viscous resistance can be added a posteriori. It is up to the user to either optimise for wave-making or for total resistance. Within the Damen group, we use two codes for this purpose, RAPID and ν -SHALLO.

2.2.1 RAPID

The computer code RAPID, used in the first application, is a non-linear free surface potential flow solver for the computation of the steady inviscid flow around a ship hull, the wave pattern and the wave resistance [11, 12]. The code has been developed by MARIN. The code takes into account dynamic trim and sinkage and optionally an actuator disc can be defined for taking into account the pressure field around the propeller disc. The form factor for estimation of viscous resistance is pre-determined. RAPID is in use at DSNS for almost twenty years, it has been validated for a range of vessels and is being used for all new designed vessels during the hull form optimisation phase.

2.2.2 ν -SHALLO

ν -SHALLO, used in the second application, is a FORTRAN 90 non-linear free surface potential flow solver for the computation of inviscid flow around ships [13]. The code has been developed by the Hamburg Ship Model Basin (HSVA). It uses panels to discretise the hull as well as the free surface, and uses Rankine point sources. The code predicts a form factor for estimation of viscous resistance. In an internal project, DSGo has validated ν -SHALLO for a range of relevant hull shapes and ship speeds.

2.3 Meta-model construction

The next step is the construction of meta-models for all solver outputs. In both applications, we use a kriging meta-model. Regressing spatial data by means of a kriging predictor was introduced independently in the field of meteorology by [14, 15] and in the field of geostatistics by [16]. A discussion of kriging methodology is provided by [17, 18, 19]. In the present paper we follow [20], who present kriging as a method within the framework of Bayesian data assimilation.

The aim of kriging is to predict a function—known as a meta-model, surrogate, or emulator—which is, essentially, a prediction of the QoI (the output of the potential flow solver) as a result of the selected input (the hull shape). On a computer, we do not represent the continuous function, but rather the discrete predicted realisations \mathbf{X} . In the present paper, \mathbf{X} represents each of the outputs of the solver, such as the resistance of the selected hull shape at a certain speed—where it should be noted that each solver output is treated as a separate QoI. As in [20], we assume that we have a normally distributed prior

$$\mathbf{X} \sim \mathcal{N}(\boldsymbol{\mu}, P), \quad (1)$$

where $\boldsymbol{\mu}$ is the drift and P is the process covariance matrix. In the present paper, we assume $\boldsymbol{\mu}$ to be constant.

In order to make the prediction, we first compute values \mathbf{y} , which form a subset of \mathbf{X} . In the present paper, an individual y represents, for example, the resistance of the vessel at a certain speed, obtained from the solver, for a particular hull shape generated from the DoE. For the computed values, we assume a normally distributed likelihood

$$\mathbf{Y}|\mathbf{x} \sim \mathcal{N}(H\mathbf{x}, R), \quad (2)$$

where H is the observation matrix, while R is the observation error covariance matrix. The observation matrix H is an incidence matrix, which has elements of either zero or one, thus selecting the simulated hull variations from the total number of predicted variations.

Using the prior (1) and likelihood (2), we apply Bayes' Theorem [21, 22]

$$\pi(\mathbf{x}|\mathbf{y}) = \frac{\pi(\mathbf{y}|\mathbf{x})\pi(\mathbf{x})}{\pi(\mathbf{y})}, \quad (3)$$

to find that the posterior mean of the predicted QoI is given by [20]

$$\mathbb{E}(\mathbf{X}|\mathbf{y}) = \boldsymbol{\mu} + K(\mathbf{y} - H\boldsymbol{\mu}), \quad (4)$$

where we have used the (Kalman) gain matrix

$$K = PH^T(R + HPH^T)^{-1}. \quad (5)$$

The predicted kriging covariance[20] is presently not exploited. In the present paper, (4) is the kriging prediction of, for example, the resistance of the vessel at a certain speed, conditional on the output of p solver runs.

So far, our analysis has not directly involved the shape parameters of the different hulls in the DoE. We include the shape parameters during the construction of the covariance matrices P and R . In the present paper, we use a process covariance function $c(\cdot, \cdot)$ to generate the process covariance matrix.

$$P_{ij} = \sigma^2 c(\mathbf{h}, \boldsymbol{\theta}), \quad (6)$$

in which σ^2 is the variance of the process, while θ_d is the correlation length for dimension d , where each dimension represents one of the shape parameters, and $h_d = \|\xi_d^{(j)} - \xi_d^{(i)}\|$ is the lag for each dimension d . Our exact choice for the covariance function is confidential. In the present paper, $\xi^{(i)}$ represents a particular hull variation, defined by the shape parameters in the DoE, for which we are running the potential flow solver. The correlation lengths $\boldsymbol{\theta}$ are found from a maximum likelihood estimate (MLE)[23, 24, 25, 26], which is equivalent to minimising the negative log-likelihood

$$\log |R + HPH^T| + (\mathbf{y} - H\boldsymbol{\mu})^T (R + HPH^T)^{-1} (\mathbf{y} - H\boldsymbol{\mu}), \quad (7)$$

where, for optimisation, it should be considered that P depends on $\boldsymbol{\theta}$ through the process covariance function (6).

The error covariance matrix contains the measurement uncertainty in the outputs y . It should be noted that this is not the modeling error, but rather the change in output observed when making small changes in the input—that is, the ‘noisiness’ of the solver. We presently include a small ‘white noise’ uncorrelated observation uncertainty, such that we have

$$R_{ij} = \epsilon^2 \delta_{ij}, \quad (8)$$

with ϵ estimated to be 1 % of the standard deviation of the output. As a result of this choice, the kriging predictor slightly smoothens the solver data.



Figure 2: The base-line combatant

2.4 Meta-model exploitation

After constructing the meta-model, it can be exploited for various purposes, such as uncertainty quantification, shape optimisation, and inverse design. In the present paper we present two different applications: the aim of the first application is multi-objective optimisation, the aim of the second application is inverse design. With multi-objective optimisation, we visualise and/or quantify the trade-off between designing optimal hull forms for different objectives. With inverse design, we allow the user to reverse the input/output relation.

3 CASE DESCRIPTION

In this paper we present two applications, a combatant and an offshore patrol vessel.

3.1 Combatant

The first application is of the new large combatant design family of DSNS. This new design family is to provide the best mission capabilities to the navies with a flexible, scalable approach for full customization—outfitted with the latest technologies to create a new frontier for combatant vessels. A random design point within this family is created for this study and the starting point is a new combatant type hull form with a round bilge mid ship section, deep V-sections in the forebody and more pram type sections towards a flat transom stern. The propulsion for this type of vessel typically consists of a twin shaft twin rudder arrangement with a centreline skeg. The lines plan and main particulars of the parent hull remain confidential. An artistic impression of the design is presented in Figure 2.

For the exploration of optimal hull forms in terms of resistance, we have defined a range of eight parameters, being length L_{pp} , beam B , draught T , block coefficient C_B , midship coefficient C_m , longitudinal centre of buoyancy L_{CB} , stem angle and transom immersion. For each parameter, we define an allowable range, with lower and upper bounds.

**Figure 3:** Side-view of the base-line modified OPV**Table 1:** Main particulars of the OPV

| Quantity | Value | Unit |
|---------------------|-------------------|--------------|
| Length on waterline | 77 | m |
| Beam on waterline | 12 | m |
| Draft | 3.8 | m |
| Displacement | 1.5×10^3 | m^3 |
| Block coefficient | 0.43 | - |

3.2 Offshore patrol vessel

Our second application is inverse design of a modified offshore patrol vessel (OPV). A side-view of the OPV is presented in Figure 3, while the main particulars are shown in Table 1. The lines plan of this vessel remains confidential.

For the OPV, we consider changes in seven shape parameters. We shift an aft frame position x_a , the mid frame position x_m and a fore frame position x_f (it should be noted that the frame shifts are set up such that they are independent parameters). Also, we change the dead-rise in the stern z_s , mid ship z_m and bow section z_b . Finally, we increase or decrease the draft T .

4 RESULTS

In this section, we present the results of the DACE analysis of the two different hull types.

4.1 Combatant

We create a DoE using the eight parameters mentioned in Section 3.1 for a fixed displacement for the design of a new vessel. As a full-factorial DoE with a total of eight parameters and a few steps in all directions will lead to a massive amount of possible combinations, we create a more efficient DoE using a space-filling method as mentioned in Section 2.1. During the creation of the DoE a check of the metacentric height is done in order to have a range of candidates which are likely to fulfil the stability criteria.

For each of the samples in the DoE we run a RAPID calculation at a number of speeds. Of course one speed can be taken for the optimisation; traditionally this is the top speed as this determines the size of the propulsion system. However, nowadays more and more focus is put on design for service, which requires the ship designer to look at optimal fuel consumption over the operational profile. But since naval vessels usually have quite a broad operational profile a

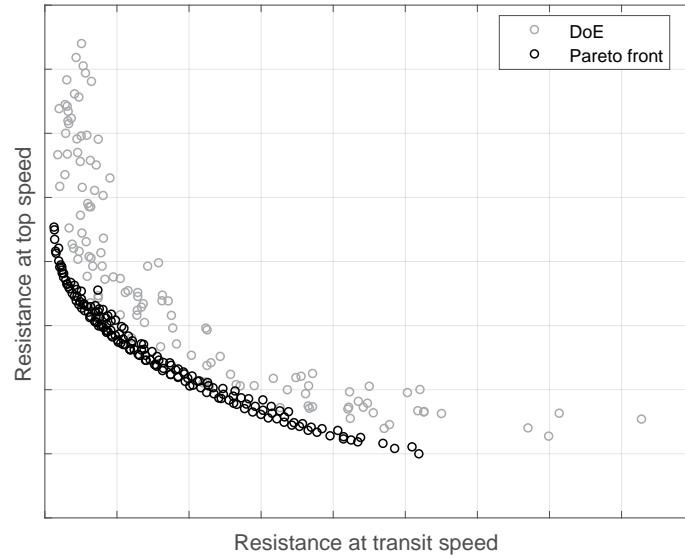


Figure 4: Example of a Pareto front, as envisaged for the combatant

minimum of two speeds is to be taken; e.g. the transit speed and the top speed. More speeds can be added depending on the operational profile of the vessel.

A further extension can be made by using two displacements; e.g. full load and light load condition. This will of course increase the size of the total design space, but it will provide with the possibility of optimising not only over the speed profile, but also over the loading range. However, since the displacement range for typical combatant does not change that much it is usually sufficient to look only at an average loading condition.

Based on the calculated wave resistance from RAPID and the frictional resistance multiplied with a form factor the total resistance for all of the samples is calculated automatically. The form factor has been estimated a priori, and is, for now, equal for all cases. Using the Kriging surrogate model a Pareto front is found. The optimal solution in terms of low resistance lies on this Pareto front. The DoE can now be extended by calculating the resistance of a number of design variants on the Pareto front and adding these to the DoE. After this extension of the DoE a new Pareto front can be calculated, which is closer to the optimum solution. This Pareto front can be displayed for two or three parameters; e.g. the resistance at two or three speeds under investigation. In Figure 4 an example of the resulting resistance for the DoE at transit and top speed is presented as well as the Pareto front. It illustrates that it is not possible to have the lowest resistance in both speed regimes. Based on this Pareto front and weight factors for the different speeds the optimum design point can be found for a particular operational profile.

Since this whole investigation has been done on potential flow calculations there is quite some uncertainty when it comes to the actual value of the resistance. So as a final step, to obtain more confidence over the total resistance and validity of the optimum design variants a full RANS CFD calculation can be done.

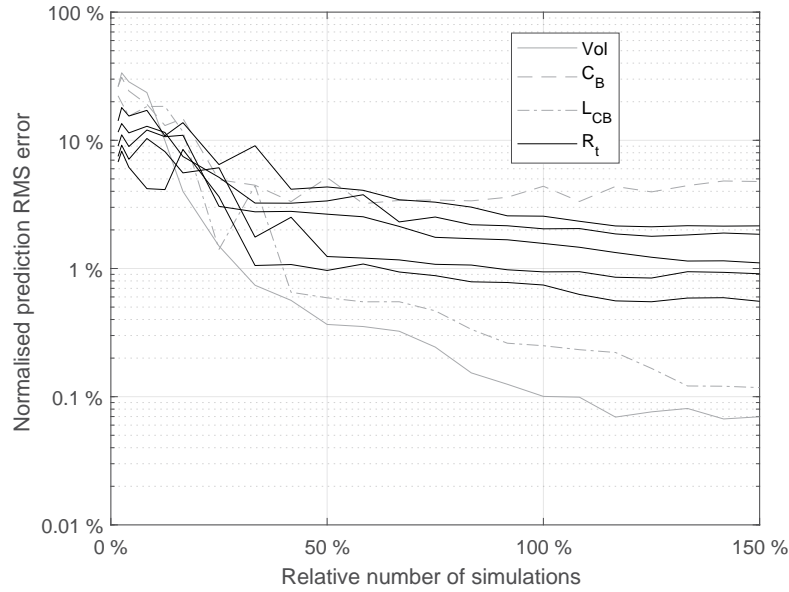


Figure 5: Convergence of the meta-model prediction error for the OPV, showing the various interpolated solver outputs using an increasing number of hull variations

4.2 Offshore patrol vessel

For all hull variations, we compute the displaced volume, the block coefficient C_B , the length-wise centre of buoyancy L_{CB} as well as the resistance R_t for a uniformly increasing range of five Froude numbers. Because the results are confidential, in the present paper all shape parameters and outputs have been normalised, by dividing by the range of the quantity, and by the range of resistances for all speeds for the resistance.

Firstly, we create a space-filling design-of-experiments and run the simulations for those hull variations. Secondly, we create meta-models for each output present and analyse the interpolated results. Thirdly, we impose our desired outputs, and present the updated design variables and outputs.

Figure 5 illustrates the convergence of the meta-models that are constructed from the solver output. In general, an increase in the number of samples—i.e. the number of simulated hull variations—leads to a decrease of the relative prediction error. It should be noted that the present method of computing the block coefficient, which converges slowly, is rather crude; this could be improved in future implementations. The exact number of samples we typically use for a study like this, corresponding to 100 % on the horizontal axis, remains confidential. Importantly, for 100 % of the number of samples, the normalised regression error in the resistance values—important for hull-to-hull comparison—is in the order of magnitude of 1 %. The uncertainty of the solver output would have to be added to this.

Figure 6 is an observed density plot of the solver output versus the shape parameters before inverse design. The spread of the distributions is a result of the uniform spread, throughout the

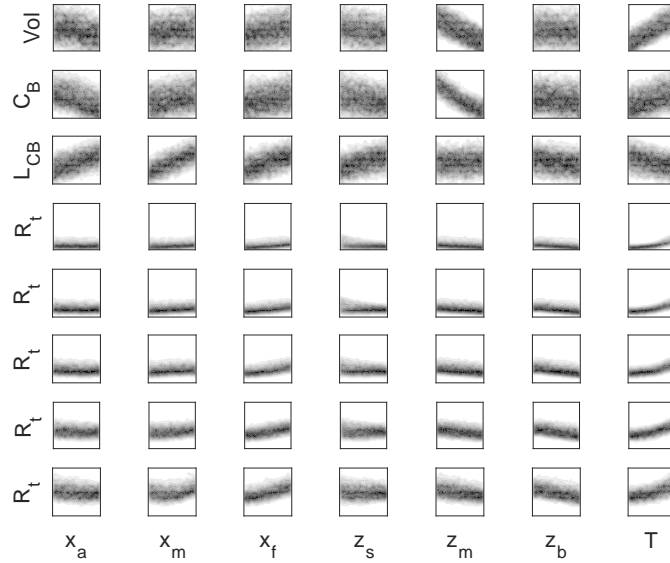


Figure 6: Density plots of interpolated solver output versus shape parameters for the OPV

design space, of the simulated hulls. Some important correlations can be observed. For example, in general, shifting frame positions forward moves the lengthwise centre of buoyancy forward and increasing the mid-ship dead-rise decreases the block coefficient. Further correlations can be observed between the resistance, at different speeds, and the design parameters. For example, increasing the draft generally increases resistance at all speeds.

Figure 7 is an observed density plot of the solver output versus solver output before inverse design. It is interesting to note that, although the shape parameters are distributed uniformly, the resulting resistances are distributed close to normal. Important correlations between various solver outputs can be observed, for example between resistances at different speeds. As could be expected, on average, resistance increases with increasing speed.

At this point we impose our—partly conflicting—design preferences. We would like to increase displacement, and, at the same time, modify our resistance curve. At the lowest speed, we would like to keep the resistance we have, while we prefer a small decrease in resistance at medium speed combined with a larger decrease at high speed. Figure 8 shows the baseline values of the design parameters and outputs, as well as the preferred values and the values resulting from the inverse design procedure. The inverse design procedure results in an aftward shift of the frame parameters, as well as a decrease in dead-rise in the stern and mid section and an increase in dead-rise in the bow section. The draft is decreased by a small amount. The exact inverse design procedure remains confidential.

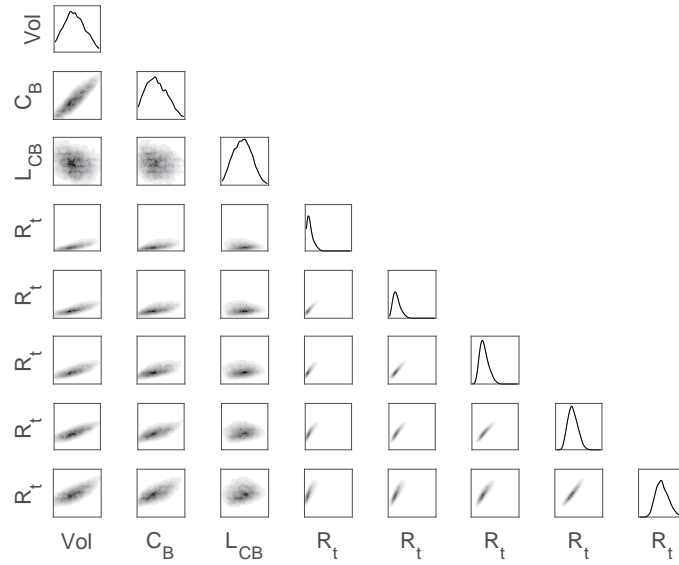


Figure 7: Density plots of interpolated solver output versus solver output for the OPV

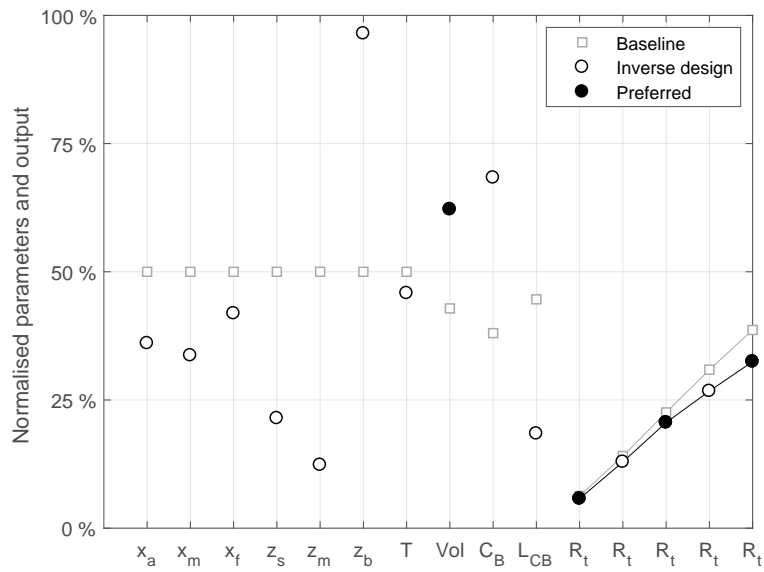


Figure 8: Design parameters and interpolated solver output for the OPV, before (base-line) and after (inverse design) imposing design preferences

5 CONCLUSIONS

Summing up, in this paper we have outlined two implementations of the design and analysis of computer experiments (DACE) methodology, as they are currently utilised within our shipyard. We have illustrated this approach with two design studies, one focusing on multi-objective shape optimisation, the other focusing on inverse design.

We conclude that efficient DACE methodology can be an important tool in the early design phase of a vessel. Both optimisation and inverse design offer the ability of making quick yet well-informed design choices, which can accelerate product development.

The main recommendation is to further investigate the methodology of parametrisation of the hull, the morphing methodology, and the recovery of the optimised or inverse-designed hull geometry.

In the end, there is another important consideration. With the development of CFD, the prediction and analysis of hydromechanic performance has been—more and more—pulled into the domain of the CFD specialist. With DACE, we see the opportunity of transferring at least part of this analysis and computation-based design trade-off back to the ship designer.

REFERENCES

- [1] Sacks, J., Welch, W.J., Mitchell, T.J. and Wynn, H.P., Design and analysis of computer experiments. *Statistical Science*, Vol. 4, No. 4, pp. 409–423, (1998).
- [2] B. M. Adams, L. E. Bauman, W. J. Bohnhoff, K. R. Dalbey, J. P. Eddy, M. S. Ebeida, M. S. Eldred, P. D. Hough, K. T. Hu, J. D. Jakeman, L. P. Swiler, Stephens J. A., D. M. Vigil, and T. M. Wildey. *Dakota, a multilevel parallel object-oriented framework for design optimization, parameter estimation, uncertainty quantification, and sensitivity analysis: Version 6.0 users manual*. Technical Report SAND2014-4633, Sandia National Laboratories, Albuquerque, NM. (2014).
- [3] Bellman, R.E., *Dynamic programming*. Princeton University Press, (1957).
- [4] M. Griebec, M. Schneider and C. Zenger, A combination technique for the solution of sparse grid problems *Iterative Methods in Linear Algebra*, pp. 263–281, IMACS, Elsevier, North Holland. (1992).
- [5] Hans-Joachim Bungartz and Michael Griebel, Sparse grids, *Acta Numerica*, **13**, No. 5, pp. 147–269. (2004).
- [6] Hans-Joachim Bungartz and Stefan Dirnstorfer, Higher Order Quadrature on Sparse Grids, *International Conference on Computational Science*, pp. 294–401. (2004).
- [7] Jochen Garcke, Sparse Grids and Applications, *Lecture Notes in Computational Science and Engineering*, **88**, pp. 57–80, Springer Berlin Heidelberg. (2013).
- [8] Rhinoceros 3D: <https://www.rhino3d.com/>
- [9] Akos, G., Parsons, R., *Foundations – The Grasshopper Primer Third Edition*, (2014).

- [10] International Towing Tank Conference, *ITTC – Recommended Procedures, 7.5-02 -02-02, Resistance Uncertainty Analysis, Example for Resistance Test*. (2002).
- [11] Raven, H.C., *A solution method for the nonlinear ship wave resistance problem*. PhD Thesis, Delft University of Technology, (1996).
- [12] H.J.Prins, H.C. Raven, M.A. Deij and M.S. de Ruyter de Wildt, *RAPID user’s guide, version 4.7.0*. (2018).
- [13] Marzi, J. and Hafermann, D., *The ν -shallo user guide—release 1.8.6*. HSVA Report 1646/4.
- [14] L. S. Gandin. The problem on optimal interpolation: Trudy GGO, v. 99. pages 67–75, (1959).
- [15] L. S. Gandin. *Objective analysis of meteorological fields: Gidrometeorologicheskoe Izdatel’stvo (GIMIZ), Leningrad*. Translated by Israel Program for Scientific Translations, Jerusalem, (1965).
- [16] G. Matheron. Principles of geostatistics. *Economic Geology*, **58**, pp. 1246–1266, (1963).
- [17] Noel Cressie. *Statistics for spatial data*. Wiley, (1993).
- [18] Michael L. Stein. *Interpolation of spatial data, some theory for Kriging*. Springer, (1999).
- [19] Richard Webster and Margaret A. Oliver. *Geostatistics for environmental scientists 2nd edition*. Wiley, (2007).
- [20] Christopher K. Wikle and L. Mark Berliner. A Bayesian tutorial for data assimilation. *Physica D: Nonlinear Phenomena*, **230** (1-2), pp. 1–16, (2007).
- [21] Thomas Bayes. An essay towards solving a problem in the doctrine of chances. *Philosophical Transactions of the Royal Society of London*, **53**, pp. 370–418, (1763).
- [22] Pierre-Simon Laplace. Memoire sur la probabilitie des causes par les evenements. *Memoires de Mathematique et de Physique Presentes a l’Academie Royale des Sciences, Par Divers Savans, & Lus dans ses Assemblies*, **6**, pp. 621–656, (1774).
- [23] K. V. Mardia and R. J. Marshall. Maximum likelihood estimation of models for residual covariance in spatial regression. *Biometrika*, 71(1):135–146, (1984).
- [24] Peter K. Kitanidis and Robert W. Lane. Maximum likelihood parameter estimation of hydrologic spatial processes by the Gauss-Newton method. *Journal of Hydrology*, **79** (1-2), pp. 53 – 71, (1985).
- [25] Peter K. Kitanidis. Parameter uncertainty in estimation of spatial functions: Bayesian analysis. *Water Resources Research*, **22** (4), pp. 499–507, (1986).
- [26] K. V. Mardia. Maximum likelihood estimation for spatial models. *Proceedings from the symposium on Spatial Statistics: Past, Present, and Future*, pp. 203–253, (1989).

A SYNERGETIC DESIGN STUDY OF A PASSENGER-HYDROFOIL FLAPPED SURFACE: EXPERIMENTAL AND COMPUTATIONAL FLUID DYNAMICS, OPTIMIZATION, AND CONTROL

L. ANTOGNOLI[†], M. BIBULI^{*}, M. DIEZ^{*}, D. DURANTE^{*}, S. FICINI[†],
S. MARRONE^{*}, A. ODETTI^{*}, I. SANTIC^{*}, AND A. SERANI^{*}

^{*}CNR-INM, National Research Council-Institute of Marine Engineering
Via di Vallerano 139, 00128 Rome, Italy
e-mail: matteo.diez@cnr.it, web page: www.inm.cnr.it

[†] Roma Tre University, Department of Engineering
Via Vito Volterra 62, 00146 Rome, Italy

Key words: Hydrofoil, Optimization, Metamodels, Control

Abstract. A hydrodynamic design procedure is presented, combining multi-objective sampling, metamodeling, and optimization. A design study of a flapped surface for a passenger hydrofoil is discussed. Hydrodynamics, stability and control are optimized with focus on maximum lift, minimum drag, and maneuverability/stability performance during take-off and turning maneuvers. Shape optimization and control design are applied in combination with validated CFD simulations. Specifically, the hydrodynamic design of the foil sections is achieved through optimization, combining automatic shape/grid modification, adaptive sampling and metamodeling, and multi-objective optimization algorithms for maximum lift and minimum drag. A robust control scheme is designed for the optimized shape. Flaps and rudders are commanded to stabilize roll and pitch motions, as well as steering the vessel during the desired maneuvers.

1 INTRODUCTION

When in flight conditions, hydrofoils have low sensitivity to waves both in terms of speed loss and seakeeping performance, furthermore they have small wake/wave washing effects and reduced fuel consumption, if compared to fast displacement ships with same payload and speed. These characteristics are particularly evident in the case of submerged-wings hydrofoils. Their initial development dates back to the 60s, when several Navies began to develop submerged-wings hydrofoils for military purposes. In those years, the American Navy together with Boeing developed the first Jetfoil as a missile launcher. Later in the 70s, the Italian Navy started the development of a Sparviero-class immersed-wing missile launcher. In the 90s, catamarans equipped with submerged wings were built in both Norway and Japan. The Norwegian design Foilcat 2900 used a pair of inverted-T wings at the bow and an inverted Greek "Pi" wing

at the stern. The Japanese design by Mitsubishi, the Super Shuttle 400 Rainbow, used an inverted Greek "Pi" aft wing. In recent years, the Italian company Rodriquez, now Intermarine, developed a prototype of fully-submerged wing hydrofoil, which requires the improvement of some aspects including flight efficiency and safety, along with the in-crease of payload to be competitive on the market. Despite its early developments, immersed-wings designs have not found extensive applications on the market of fast vehicles and their production has been limited to a few examples. This is because alongside the undeniable advantages, this solution has presented some limitations that have not facilitated its wide commercial use. Critical issues are: overall efficiency of the wing complex; take-off phase stability and control; efficiency of the propulsion system both in the take-off and cruising phases; maintenance of control surfaces; pay-load versus installed power; safety and stability during navigation.

In the present paper, the study a new vehicle with hybrid features is outlined. This new design aims at: maintaining the typical advantages of submerged-wings hydrofoils; overcoming problems related to the in-flight stability; improving, compared to the state of the art, payload, wing efficiency, etc. Specifically, a synergetic design study of a flapped surface for a passenger hydrofoil is presented, where the vessel is characterized by immersed fore and aft foils. The fore foil is attached to the hull by a single strut that embeds a vertical rudder; the fore foil has two independent flaps for the motion stabilization. The aft foil is attached by means of three vertical struts (each equipped with an independent rudder); the aft foil has two lateral and two central flaps. Foils are straight/tapered and have NACA 16-3075 sections.

Experimental and computational fluid dynamics (EFD, CFD) are used to assess design performance, which are later optimized for maximum lift, minimum drag, and maneuverability/stability performance during take-off/turning via shape design and control. The aim of EFD is the collection of data for hydrodynamic characterization and CFD validation of the forward fully-submerged inverted T-foil. A 1:7 scale model has been designed and manufactured at CNR-INM laboratories by rapid prototyping techniques, using a performing 3D printing polylactic acid (PLA) with steel stiffening. The prototype has been tested at CNR-INM towing tank covering a wide range of speeds and deflection angles of the flap. An in-house finite volume method (FVM) is used for unsteady Reynolds-averaged Navier-Stokes equation (RANSE) calculations [1, 2, 3]. The agreement with the EFD data indicates reliable predictions and suitability for simulation-based design optimization and control (by accurate definition of hydrodynamic coefficients). The shape design of the foil sections is achieved through optimization, combining automatic shape/grid modification, adaptive sampling and metamodeling, and multi-objective optimization algorithms for maximum lift and minimum drag. Finally, the development of the control system has been achieved, overcoming two major difficulties: the hard-nonlinear behavior of the overall craft and the presence of unstable dynamics that require reliable and robust stabilization schemes. A robust control scheme is designed for the optimized shape. Flaps and rudders are commanded to stabilize roll and pitch motions, as well as steering the vessel during the desired maneuvers. A preliminary version of the present work has been presented in [4].

2 COMPUTATIONAL FLUID DYNAMICS

The numerical solution of the unsteady RANSE is achieved through an in-house developed numerical algorithm. The latter is based on a finite volume scheme, with variables co-located

at cell centers. Turbulent stresses are taken into account by the Boussinesq hypothesis, and several turbulence models (both algebraic and differential) are implemented. Here the Spalart-Allmaras turbulence model is adopted. The free surface is also taken into account through a single-phase level set algorithm [3]. The 3D wing geometry is fully discretized together with flaps, struts and anti-rolling fin with a body-fitted structured grid, allowing for an in-depth analysis of the flow features near the body. In order to treat complex geometries or bodies in relative motion, the numerical algorithm is discretized on a block-structured grid with partial overlap, possibly in relative motion. This approach makes domain discretization and quality control of the calculation grid much easier than with similar discretization techniques implemented on meshes structured with adjacent blocks. Of course, grid connections and overlaps are not trivial, as with standard multi-block approaches, but must be calculated in the pre-processing phase. The coarse/fine grain parallelization of the RANSE code is obtained by distributing the structured blocks among available distributed memory (nodes) or shared memory (threads) processors. Pre-processing tools, which allow the subdivision of structured blocks and their distribution among the processors, are used for load balancing, while fine tuning is left to the user. The communication between the processors for the coarse grain parallelization is obtained using the standard message passing interface (MPI) library, while the fine grain parallelization (shared memory) is achieved through the open message passing library (OpenMP). The efficiency of the parallel code has been examined in earlier research, showing satisfactory results in terms of acceleration for different test cases [5]. More details on the code implementation and application may be found in [6].

The wing group at the bow region was characterized by an extensive analysis of the loads at different regimes. Four different angles of attack of the whole group were considered (in addition to the built-in angle of 1.5 deg): 0, 3, 5, 7 deg. For each of them the flap was also rotated by: -15, -10, -5, +5, +10, +15 deg where with the plus sign (+) a rotation downwards of the flap is intended.

Being the total number of simulations quite demanding in terms of computational time, steady computations were performed. According to the present numerical scheme, which is based on a pseudo-compressible technique, a steady approach is intended as an average of a time varying solution, which is correct in view of the mere evaluation of the forces acting on the body. For the flap rotation, the Chimera overlapping grid technique was widely exploited. For every angle of rotation of the flap, a new grid is designed to make the solution as smooth as possible. When the angle of attack of the wing group is varied, we preferred to rotate the inflow direction rather than the whole grid, so that the shown solutions are coherently counter-rotated.

Figure 1 shows on the top row the pressure distribution on the sides of the forward wing: as it can be seen, as the angle of attack increases the back of the wing is in a condition of increasing depression. In general, the bow wing group is characterized by a regular pressure distribution for angles of attack of 0, 3, and 5 deg, whereas at 7 deg there are problems for angles of rotation of the flap of +10 and +15 deg (see Fig. 1). From the velocity field shown in the bottom rows of Fig. 1, it appears evident how the flow over the back of the profile is completely separated, thus indicating a stall condition.

Finally, Fig. 2 shows the anti-rolling fin effect. On the left frame the span vorticity iso-surfaces are shown in blue (positive) and red (negative) colors. In correspondence of the fin, the surfaces are strongly enroled with the presence of two counter rotating vortices, shown in

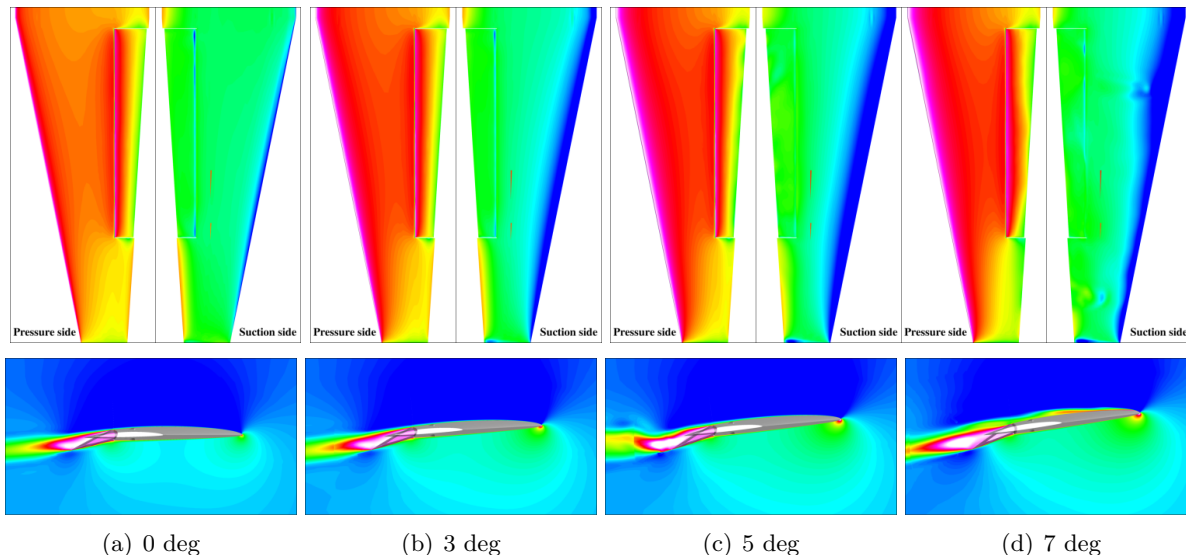


Figure 1: Pressure coefficient distribution (top, colour map (red/blue) goes from -0.5 to 0.5) and stream-wise velocity distributions on a domain section at the center of the flap (bottom, colour map (white/blue) goes from -0.78 m/s to 8.55 m/s) with +15 deg flap angle.

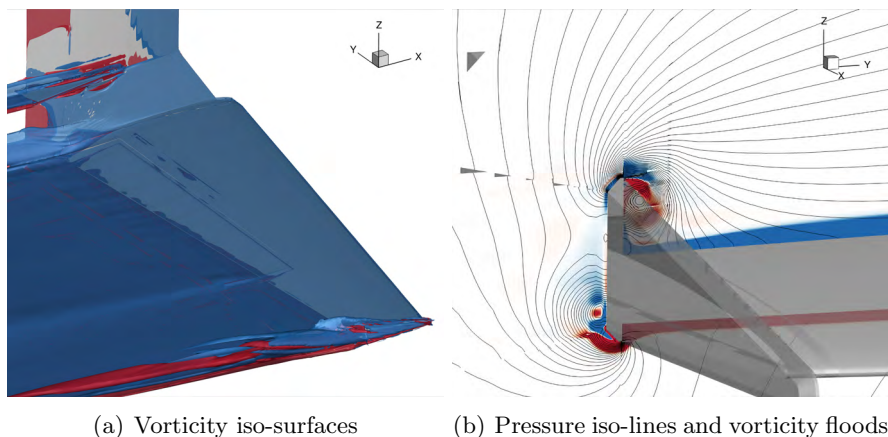


Figure 2: Effect of anti-rolling fin. Example at angle of attack 5 deg, 0 deg flap rotation and 15 kn of advancing speed.

the right frame. The fin acts in stabilizing the undesired rolling instabilities by damping them through the inception of a pair of counter rotating vortices which induce a local stabilizing moment.

3 EXPERIMENTAL FLUID DYNAMICS

In order to develop a scaled model of the bow wing group with strut and flaps, the loads acting on the body are numerically evaluated, in some meaningful condition. Specifically, a finite element simulation of the loaded model was performed in order to assess the maximum

deformation of the wing. 3D printing is used and a model at scale 1:7 with moving flaps is obtained (see Fig. 3a). Towing-tank experiments at different angle of attacks and flap deflections were performed. Significant deformations of the wing at high speed (20 kn, 25 kn) are a concern. For this reason, more rigid models are currently in the design phase to be tested in the near future. A preliminary comparison of numerical and experimental results is included in Fig. 3b), showing lift versus speed at the built-in angle of attack of 1.5 deg.

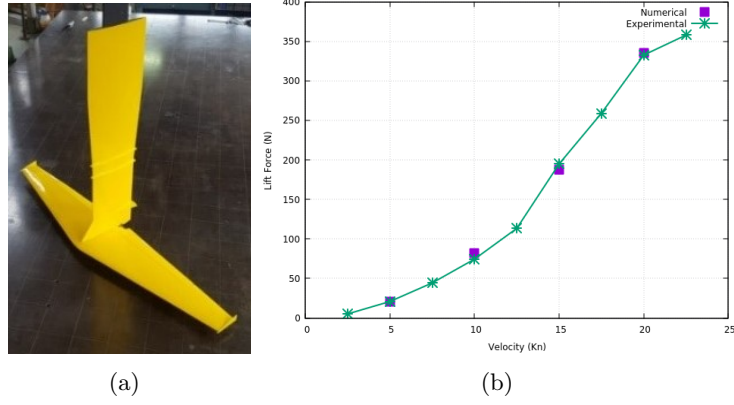


Figure 3: EFD (a) model and (b) comparison to CFD.

4 OPTIMIZATION PROCEDURE OF HYDRODYNAMICS PERFORMANCE

4.1 Problem formulation

A 2D section is considered for this preliminary optimization (namely a NACA 16-3075 profile), assuming take-off conditions. The built-in angle of attack is set here to 2 deg, whereas the flap is deflected by 15 deg (downwards). No additional pitch angle is considered. A Reynolds number of about 10^6 is used. An idealized flapped profile with no gaps is considered. The optimization aims at reducing the drag coefficient C_D , while maintaining the lift coefficient at least equal to the original value, C_L^* . The optimization problem is formulated as

$$\begin{aligned} & \text{minimize } C_D \text{ and maximize } C_L, \\ & \text{subject to } C_L \geq C_L^*, \end{aligned} \quad (1)$$

4.2 Shape modification

The profile is modified by adding in z -direction both to the pressure and the suction side a Hicks-Henne function [7], with one bump, $b(\xi)$:

$$b(\xi) = a \left[\sin \left(\pi \xi \frac{\log 0.5}{\log t_1} \right) \right]^{t_2} \quad (2)$$

ξ is a nondimensional curvilinear coordinate (where 0 is the leading edge and 1 the trailing edge of the unflapped section), a the maximum bump amplitude, t_1 controls the bump location, t_2 defines its width. Two design variables are chosen, namely the amplitude a and the position

t_1 of the bump, whereas t_2 is kept fixed equal to 2. The variables' range of variation is set to $\pm 3\%c$ (c is the unflapped chord) and 0.2-0.6, respectively. In the following, both variables are normalized between 0 and 1.

Equation 2 is applied to both sides, therefore the section thickness remains constant. Furthermore, shape and RANSE computational grid are automatically modified according to Eq. 2.

4.3 Multi-objective optimization method

A multi-objective version of the deterministic particle swarm optimization (MODPSO) method is used to solve the problem of Eq. 1. Details can be found in [8].

4.4 Adaptive metamodeling

Two metamodeling techniques are used, namely stochastic radial basis functions (RBF) and Gaussian processes (GP), and combined with adaptive sampling methods as described in the following.

4.4.1 Stochastic radial basis functions

Consider an objective function $f(\mathbf{x})$, where $\mathbf{x} \in \mathfrak{R}^N$ is the design variable vector and N the design space dimension. Let the true function value be known in J training points \mathbf{x}_j with associated objective function values $f(\mathbf{x}_j)$. The metamodel prediction $\tilde{f}(\mathbf{x})$ is computed as the expected value (EV) over a stochastic tuning parameter of the RBF metamodel, e.g., $\tau \sim \text{unif}[1, 3]$:

$$\tilde{f}(\mathbf{x}) = \text{EV}[g(\mathbf{x}, \tau)], \quad \text{with} \quad g(\mathbf{x}, \tau) = \sum_{j=1}^J w_j \|\mathbf{x} - \mathbf{x}_j\|^\tau \quad (3)$$

w_j are unknown coefficients and $\|\cdot\|$ is the Euclidean norm. The coefficients w_j are determined enforcing exact interpolation at the training points $g(\mathbf{x}_j, \tau) = f(\mathbf{x}_j)$ by solving $\mathbf{A}\mathbf{w} = \mathbf{f}$, with $\mathbf{w} = \{w_j\}$, $a_{ij} = \|\mathbf{x}_i - \mathbf{x}_j\|^\tau$, and $\mathbf{f} = \{f(\mathbf{x}_j)\}$.

The uncertainty $U_{\tilde{f}}(\mathbf{x})$ associated with the prediction is quantified as four times the square root of the variance. The maximum-uncertainty adaptive sampling (MUAS) method identifies new training points by solving the following single-objective maximization problem:

$$\mathbf{x}^* = \underset{\mathbf{x}}{\text{argmax}}[U_{\tilde{f}}(\mathbf{x})] \quad (4)$$

Accordingly, new training points are adaptively placed where the prediction uncertainty is maximum. Details of methodology, implementation, and example applications are found in [9] and [10]. Here, both C_L and C_D are interpolated by the RBF model and their prediction and associated uncertainty considered for optimization and adaptive sampling. The latter is performed considering the largest uncertainty associated to lift and drag coefficients, respectively.

4.4.2 Gaussian process

A Gaussian process (GP) is a collection of random variables, any finite number of which have a joint Gaussian distribution. The mean function $m(\mathbf{x})$ and the covariance function $k(\mathbf{x}, \mathbf{x}')$ of

a real process $f(\mathbf{x})$ are defined as [11]

$$m(\mathbf{x}) = \text{EV}[f(\mathbf{x})] \quad (5)$$

and

$$k(\mathbf{x}, \mathbf{x}') = \text{EV}[(f(\mathbf{x}) - m(\mathbf{x}))(f(\mathbf{x}') - m(\mathbf{x}'))] \quad (6)$$

where $f(\mathbf{x})$ may be approximated as

$$f(\mathbf{x}) = \tilde{f}(\mathbf{x}) = \text{GP}(m(\mathbf{x}), k(\mathbf{x}, \mathbf{x}')) \quad (7)$$

The covariance functions is evaluated as $k(x_{p,i}, x_{p,j}) = \exp^{-\Theta_p \|x_{p,i} - x_{p,j}\|^2}$ with a set of free tuning parameters Θ_p , where i and j are training set indices and p is the design variable index. The parameters are defined so as to maximize the log likelihood. Mean and variance associated to the prediction are calculated accordingly [12].

Finally, the uncertainty $U_{\tilde{f}}$ associated with the prediction is quantified as four times the square root of the variance. The MUAS criterion of Eq. 4 is used for the adaptive sampling procedure, considering the largest uncertainty between lift and drag coefficients.

4.5 Optimization results

Five points are selected as initial training set in the nondimensional domain, specifically $[(0.5, 0.5); (0.5, 0); (0, 0.5); (0.5, 1); (1, 0.5)]$. Five additional points are defined based on the adaptive sampling methodology described above (see Figs. 4). Four points are placed at the domain corners with both RBF and GP. Although the global trend of C_L and C_D provided by RBF and GP is reasonably similar, their uncertainty structure is quite different. Therefore, the fifth RBF point is different than the fifth GP point.

The two Pareto fronts obtained by MODPSO with both RBF and GP are shown in Fig. 5. It may be noted how they span the same objective function region. Nevertheless, they are

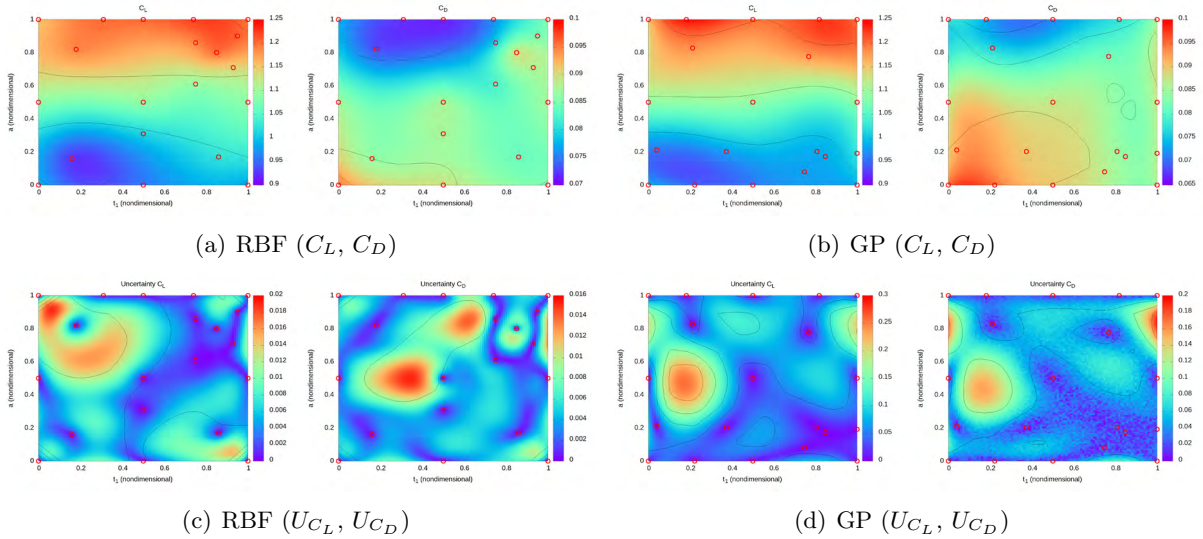


Figure 4: Metamodel prediction (left) and associated uncertainty (right) for lift and drag coefficients.

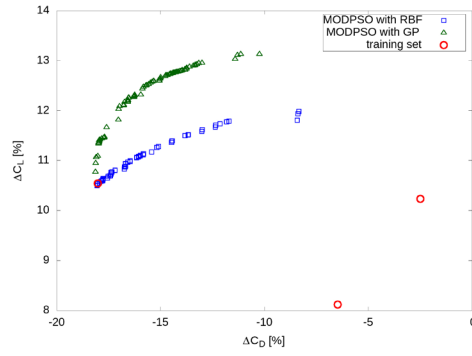


Figure 5: Multi-objective optimization results.

quite different to each other, indicating convergence of the metamodel training has not been achieved yet. The training point (in red) belonging to the front is used for comparison to the original profile. Specifically, the drag coefficient is reduced by 18%, whereas the lift coefficient is increased by 10%. As a consequence, the hydrodynamic efficiency is increased by 35%. As a comparison, Fig. 6 shows the section along with the pressure distribution and the y -component of the vorticity vector of original and optimized profile.

Finally, and in addition to the current design space, a bio-inspired wing section (taken from owl wings) named ISHII is also considered. Figure 7 shows a comparison between the original profile and an ISHII section. As visible, a second curvature on the pressure side allows the flow to remain more attached giving a global increase of 1.5 to 2 times the efficiency of the original NACA. The vorticity fields in the depicted configuration (7 deg angle of attack and 20 kn advancing speed) allow to appreciate the lower shedding and the back reattachment of the

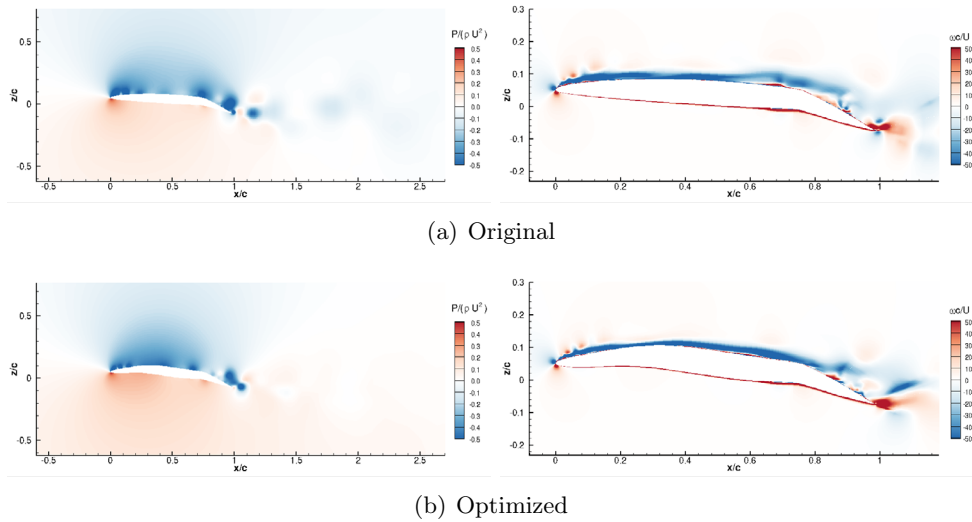


Figure 6: Comparison between the original and optimized NACA 16-3075 profile. On left the pressure fields, on right the vorticity fields.

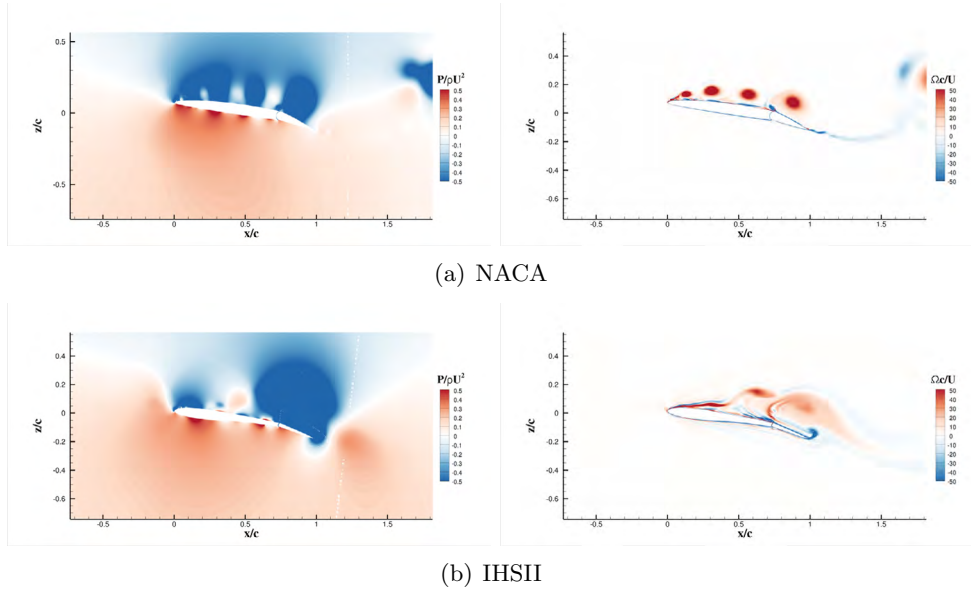


Figure 7: Comparison between the original NACA 16-3075 and a bio-inspired ISHII profile at 20 kn, 7 deg angle of attack and 10 deg flap rotation. On left the pressure fields, on right the vorticity fields.

flow for the the ISHII profile, when com-pared to the NACA. As a drawback, the thickness of the ISHII profile is fairly reduced, resulting in poor manufacturing and structural performance.

Obviously, being the simulations 2D, the vorticity intensity is significantly greater than the corresponding 3D. This means that the 2D simulations must be considered only in the sense of a first estimation of the global performances of an optimized design.

5 HYDROFOIL CONTROL OF FLAPPED SURFACES

The control system development for a hydrofoil vessel is a challenging problem to be tackled for two main reasons: the first is the hard non-linear behavior, [13], of the overall craft, making a demanding task the design of a suitable mathematical model, the second is the presence of unstable dynamics that require the development of reliable and robust stabilization schemes, [14], in such a way to guarantee the regulation of the vessel motion within the operative limits.

Figure 8 shows the actual vessel sketch with the relevant parameters used to design the control system. The results of a combined take-off and turning maneuver is reported in Figs. 9 and 10, showing the combined action of the control scheme acting on the different control surfaces (flaps and rudders) to stabilize successfully the motion on the different axes while at the same time tracking the desired references.

The first issue requires the design of a mathematical model based on ordinary differential equations (which represent a much more handy tool from a control standpoint, with respect to distributed parameters or numerical models) that captures the main motion behaviors and embeds the controllability and observability characteristics of the system for the stabilization-oriented analysis. The second point is related to the development and performance evaluation of the control system devoted to the regulation of roll, pitch and yaw motions during the different

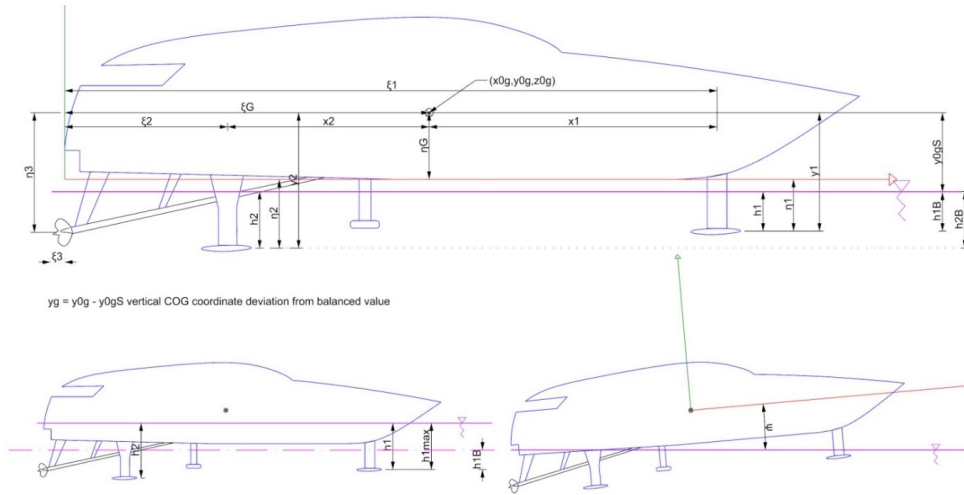


Figure 8: Representation of the overall vessel, used for control.

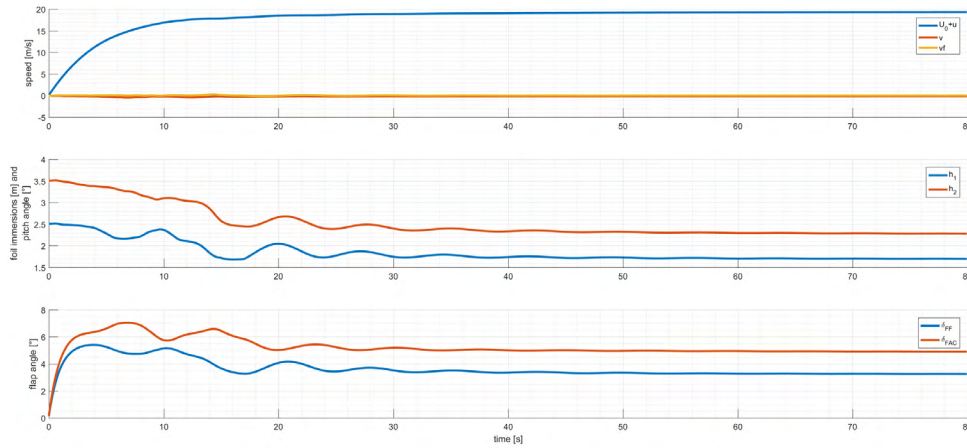


Figure 9: Combined take-off and turning maneuver. Top plot depicts the speed profile, central plot reports the immersion values of fore and aft foils, bottom plot shows the angle values commanded to the fore and aft central flaps for pitch control.

operative phases (take-off, cruise, turning). In particular, given the unstable dynamics of the roll motion, a robust control scheme is designed to ensure a stabilized motion within the predefined operating limits and external disturbances. A robust control scheme based on local linearization and custom-shape of the desired closed-loop dynamics is designed to command the proper driving of flaps and rudders in order to stabilize the roll and pitch motions, as well as steering the vessel where intended.

6 CONCLUSIONS AND FUTURE WORKS

A hydrodynamic design procedure of a passenger-hydrofoil flapped surface has been presented, combining adaptive multi-objective sampling, metamodeling, and optimization. Hydrodynam-

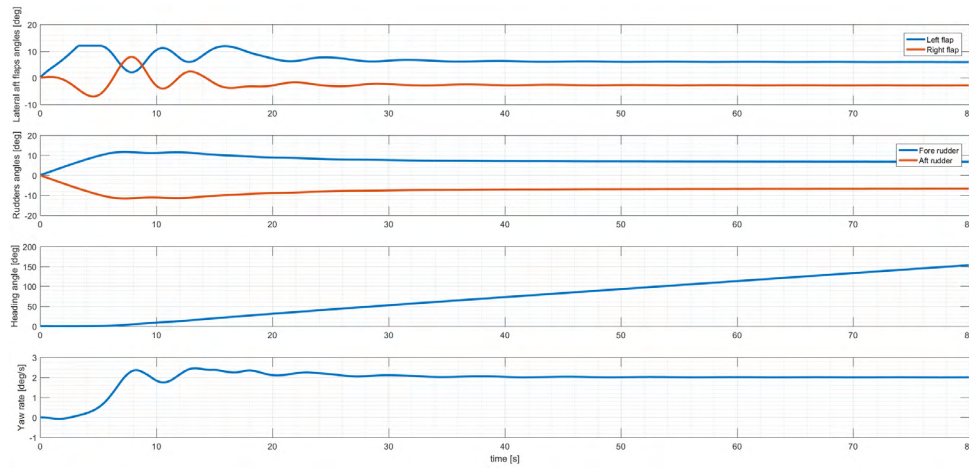


Figure 10: Combined take-off and turning maneuver. From the top, the first plot depicts the angle values commanded to aft lateral flaps for roll control; the second plot reports the commanded rudder angle for the steering actions; the third plot represents the heading of the vessel and the fourth plot reports the yaw-rate (i.e. the turning speed).

ics, stability and control were assessed and optimized with focus on maximum lift, minimum drag, and maneuverability/stability performance during take-off and turning maneuvers. Validated CFD simulations were used for hydrodynamic performance predictions, provided by a RANSE solver. Stochastic radial basis functions and Gaussian processes were used as adaptive metamodels. CFD results pertained to the 3D submerged wing under a variety of conditions, whereas current optimization results are limited to a flapped 2D section of the foil in take-off phase. Two design variables were used, with shape modifications provided by the Hicks-Henne function. Despite the use of an idealized 3D geometry and a low-dimensional design space, results are promising as the drag coefficient is reduced by 18%, whereas the lift coefficient is increased by 10%. The hydrodynamic efficiency is increased by 35%. Future work includes use of 3D simulations in the optimization phase possibly under multiple conditions, definition of higher-dimensionality design spaces, along with final EFD campaign for the optimized wing.

ACKNOWLEDGEMENTS

The work is part of the CNR-INM activities within the research project IBRHYDRO, led by the Italian shipyard "Intermarine S.p.A." and financially supported by the Italian Ministry of Infrastructures and Transport.

REFERENCES

- [1] Di Mascio, A., Broglia, R. and Favini, B., (2001), A second order godunov-type scheme for naval hydrodynamics. *Godunov Methods*, pp. 253–261, Springer.
- [2] Muscari, R., Broglia, R. and Di Mascio, A. An overlapping grids approach for moving bodies problems, *16th Int. Offshore and Polar Eng. Conf.*, 01, pp. 243–248, (2006).
- [3] Broglia, R. and Durante, D. Accurate prediction of complex free surface flow around a

- high speed craft using a single-phase level set method, *Computational Mechanics*, **62** (3), 421–437, (2018).
- [4] Antognoli, L., Ficini, S., Bibuli, M., Diez, M., Durante, D., Marrone, S., Odetti, A., Santic, I. and Serani, A. Hydrodynamic design procedure via multi-objective sampling, metamodelling, and optimisation, *Proceedings of the 18th International Conference on Computer Applications and Information Technology in the Maritime Industries*, Tullamore, Ireland, 25-27 March, pp. 438–450, (2019).
- [5] Broglia, R., Zaghi, S., Muscari, R. and Salvatore, F. Enabling hydrodynamics solver for efficient parallel simulations, *2014 International Conference on High Performance Computing & Simulation (HPCS)*, pp. 803–810, IEEE, (2014).
- [6] Di Mascio, A., Broglia, R. and Muscari, R. Prediction of hydrodynamic coefficients of ship hulls by high-order godunov-type methods, *Journal of Marine Science and Technology*, **14** (1), 19–29, (2009).
- [7] Masters, D. A., Taylor, N. J., Rendall, T., Allen, C. B. and Poole, D. J. Review of aerofoil parameterisation methods for aerodynamic shape optimisation, *53rd AIAA Aerospace Sciences Meeting*, p. 0761, (2015).
- [8] Pellegrini, R., Serani, A., Leotardi, C., Iemma, U., Campana, E. F. and Diez, M. Formulation and parameter selection of multi-objective deterministic particle swarm for simulation-based optimization, *Applied Soft Computing*, **58**, 714–731, (2017).
- [9] Volpi, S., Diez, M., Gaul, N. J., Song, H., Iemma, U., Choi, K. K., Campana, E. F. and Stern, F. Development and validation of a dynamic metamodel based on stochastic radial basis functions and uncertainty quantification, *Structural and Multidisciplinary Optimization*, **51** (2), 347–368, (2015).
- [10] Pellegrini, R., Serani, A., Diez, M., Wackers, J., Queutey, P. and Visonneau, M. Adaptive sampling criteria for multi-fidelity metamodels in CFD-based shape optimization, *7th European Conference on Computational Fluid Dynamics (ECFD 7)*, Glasgow, UK, 11-15 June, (2018).
- [11] Rasmussen, C. E., (2004), *Gaussian Processes in Machine Learning*, pp. 63–71. Springer Berlin Heidelberg.
- [12] Williams, C. K. I., (1998), *Prediction with Gaussian Processes: From Linear Regression to Linear Prediction and Beyond*, pp. 599–621. Springer Netherlands.
- [13] Khalil, H. K. and Grizzle, J., *Nonlinear systems*, Vol. 3, Prentice hall Upper Saddle River, NJ (2002).
- [14] Zhou, K., Doyle, J. C., Glover, K., et al., *Robust and optimal control*, Vol. 40, Prentice hall New Jersey (1996).

CFD INVESTIGATION OF VENTILATION-CAVITATION COUPLING ON SURFACE-PIERCING SUPER-CAVITATING HYDROFOILS

STEFANO BRIZZOLARA *

* iShip lab., Department of Aerospace and Ocean Engineering,
Virginia Tech, Blacksburg, VA, 24061, USA
e-mail: stebriz@vt.edu, web page: <https://www.aoe.vt.edu/people/faculty/brizzolara.html>

Key words: Ventilation, Cavitation, Super-cavitating hydrofoils, CFD, multi-phase flow

Abstract. Results of time-accurate N-S on a model scale Super-Cavitating Surface-Piercing hydrofoil are presented. The CFD model considers three immiscible flow phases: water, vapor and air, tracked by means of a multiple species mixture of fluid approach. A homogeneous cavitation model is used to solve the production and condensation of the vapor phase. Three cavitation numbers are considered, corresponding to full scale speeds of about 18, 50 and 120 knots. Unsteady flow features around the foil are presented through sequences of snapshots captured at high frequency rate and from different viewpoints. The mechanisms of ventilation and cavitation interaction can then be more effectively observed and understood. Cavitation, when present, is shown to play a primary role for the air to penetrate and ventilate different portions of the foil. Interaction between the dynamics of the two different mechanisms leading to gaseous cavity formation on the foil are discussed and visually rendered in the paper. Average forces and span-wise and chord-wise location of the center of pressure in the different flow regimes are also given and shown to be intimately and consistently related to the ventilation and cavitation patterns observed on the foil.

1 INTRODUCTION

The physics of ventilation inception and growth on super-cavitating (SC) surface-piercing (SP) hydrofoils has still open issues since the mechanism that leads to partial and full ventilation completely understood [1]. In particular ventilation prediction at high Froude numbers and low cavitation numbers has still open issues, yet critical since more often high speed crafts are equipped with shallow-submerged or surface-piercing hydrofoils to improve resistance and seakeeping performances. Early experiments of Swales et al. [3] and more recently [2] highlighted three different mechanisms for ventilation occurring on vertical surface piercing struts with different section shapes (blunt, sharp and rounded nose): separation bubble near the tail, near the nose or full separation at high angles of attack or for blunt bodies. Inception happens quite abruptly at critical speed, once the air finds its way and breach through a thin unseparated (energetic) flow stream that seals the low energetic (separated) flow region on the hydrofoil from the free surface. Ventilation is initially very unstable and in some cases it shows undulations, similar to Taylor instabilities, in the internal ventilated free surface.

These unsteady hydrodynamic phenomena, involving three fluid phases (air, water and vapor) are quite challenging to simulate by computational fluid dynamics. This paper presents

a contribution in this field, following a pioneer study made few years ago [13]. The numerical models are substantially changed with respect to the mentioned study: from URANSE we move to time-accurate Navier-Stokes (N-S) solvers, using highly refined meshes in the area of interest and adequately small time steps.

Current research projects of the Virginia Tech innovative Ship design laboratory, VT-iShip, gravitate around the study of different high speed craft using super-cavitating surface-piercing dihedral or anhedral hydrofoils, designed to work in the stern of innovative crafts [5] [6] at speeds ranging from 50 to 120 knots, i.e. in partially or super-cavitating (ventilated) conditions. So, the reference case addressed in this paper consists in a SC-SP dihedral V-hydrofoil, recently designed and built for model scale tests.

Application of the numerical model proposed to the considered case allows the discovery of fundamental aspects of ventilation dynamic, illustrated in section 4. Last section completes the qualitative analysis with quantitative estimation of the effect of cavitation/ventilation on forces and moments on the hydrofoil working in different cavitating regimes.

2 SUPER-CAVITATING SURFACE-PIERCING DIHEDRAL HYDROFOIL

A series of dihedral (V-shaped) super-cavitating surface-piercing hydrofoil were designed and studied [7] for application on a new high speed planing hull concept, the SCPH² concept [5]. A mini-family was designed considering different chord and sweep angle distribution along the span. The hydrofoil considered in this paper is the one having constant cord along the span and a constant dihedral angle of 20 degrees over the horizontal. The foil is shown in Figure 1, its principal characteristics are given in Table 1. The span is measured along the leading edge line of the hydrofoil. The design semi-span, i.e. the submerged semi-span at the design draft, corresponds to the seventh section from the symmetry plane indicated in the drawing. The small size was chosen in order to respect the Froude similitude while towing the model at about 30ft/s in the large ship model basin of the US Naval Academy.

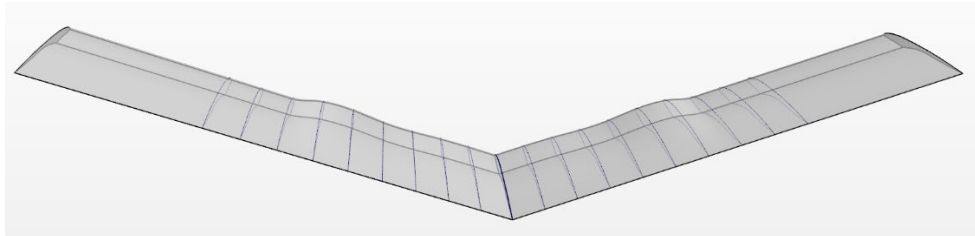


Figure 1: Surface-piercing V-Hydrofoil using the new super-cavitating SBSC2-5-32 profile [10]

Table 1: Principal Characteristics of the SC-SP Dihedral Hydrofoil model

| Parameter | Symbol | Value | Parameter | Symbol | Value |
|--------------------|----------------------|---------|-----------------------|---------------|-------------------|
| Max Chord | c_{MAX} | 1.85 in | Max Span | S_{MAX} | 5.72 in |
| Effective SC Chord | c_{SC} | 1.35 in | Reynolds in SC regime | $Re_{c_{SC}}$ | $0.28 \cdot 10^6$ |
| Design Semi Span | S | 2.86 in | Froude on chord | $Fr_{c_{SC}}$ | 15.8 |
| Dihedral Angle | β | 20 deg | Froude on draft | Fr_T | 18.0 |
| Design Draft | $T (= S \tan \beta)$ | 1.04 in | Des. Cav. number | σ_o | 0.13 |

The foil was designed using the Viscous Lifting Line Model (VLLM), specifically devised to allow for the non-linear dependence of lift on the angle of attack that characterizes super-cavitating hydrofoils [8]. The code has been enhanced [7] with symmetric images to impose the boundary condition on the dihedral hydrofoil symmetry plane and anti-symmetric images to approximate the free surface boundary condition, as represented in the sketch of Figure 2. In fact, as well known, at high Froude numbers, the linearized free surface boundary condition reduces to force a null value for the potential on the undisturbed waterplane [11] and this is very efficiently achieved by the anti-symmetric vortex images. This approximate boundary condition, though, neglects the physical presence of the emerged portion of the hydrofoil which is interested by pile up and stagnation of the flow beneath the face, hence neglecting an extra portion of lift.

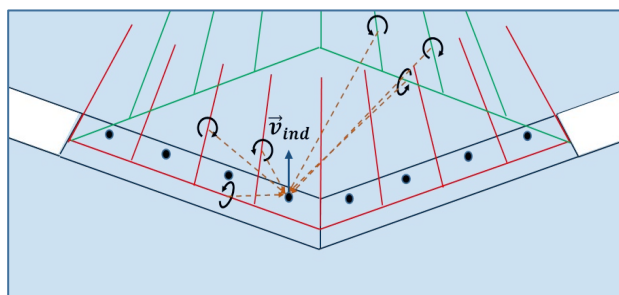


Figure 2: Symmetric vortex segments (red on the left) and anti-symmetric (green on top) used to represent the hydrofoil with free surface boundary condition [7] using viscous lifting line model [8]

The wing design is based on the SCSB2 unconventional super-cavitating section [10], specifically designed to have high hydrodynamic efficiency both in super-cavitating and fully-wet conditions. The SCSB2 section is characterized by a sharp leading edge, a step-type cavitator on the face and a high-curvature cavitator on the back, distinguishable in the sections drawings of Figure 1.

The distribution of angles of attack along the span of the hydrofoil obtained with the VLLM shows an increase of angle of attack right below the design water level which causes the bump visible in the perspective view of Figure 1. The presence of this localized increase of angle of attack is relevant, since it is one of the ventilation triggers observed in the numerical simulation study.

2 MULTIPHASE CFD MODELLING OF SP-SC HYDROFOILS

The unsteady time accurate viscous simulations are implemented using StarCCM+ v.13. The segregated flow implicit solver is used with no sub-grid turbulence model approximation, due to the relatively low model scale Reynolds number. Time integration scheme is second order accurate. A constant time step of $20\mu\text{s}$ is used.

A single fluid with three immiscible phases is considered: water, vapor and air. Transport equation of VoF is solved with a second order integration scheme for the convection term and no artificial diffusion limiter is used.

Schnerr-Sauer cavitation model is used to model the phase change from water to vapor phases. Standard values for condensation and vaporization factors and nuclei number and sizes were used, as this values proved to lead to good correlation with experiments in different

validation studies.

The mesh is an unstructured trimmed mesh with about 13.5M cells with different level of refinement around the hydrofoil and the free surface, as represented in Figure 3. Maximum cells size on the hydrofoil is 100 μ m, refined around the foil sharp edge lines, in order to accurately define the flow features induced by these feature lines that are typical of super-cavitating profiles.

Usual boundary conditions used in virtual cavitation tunnel simulations are applied: velocity inlet with hydrostatic pressure starting from the free surface level, zero gradient outlet with the same hydrostatic pressure. The simulation is initialized with uniform calm water flow and hydrostatic pressure.

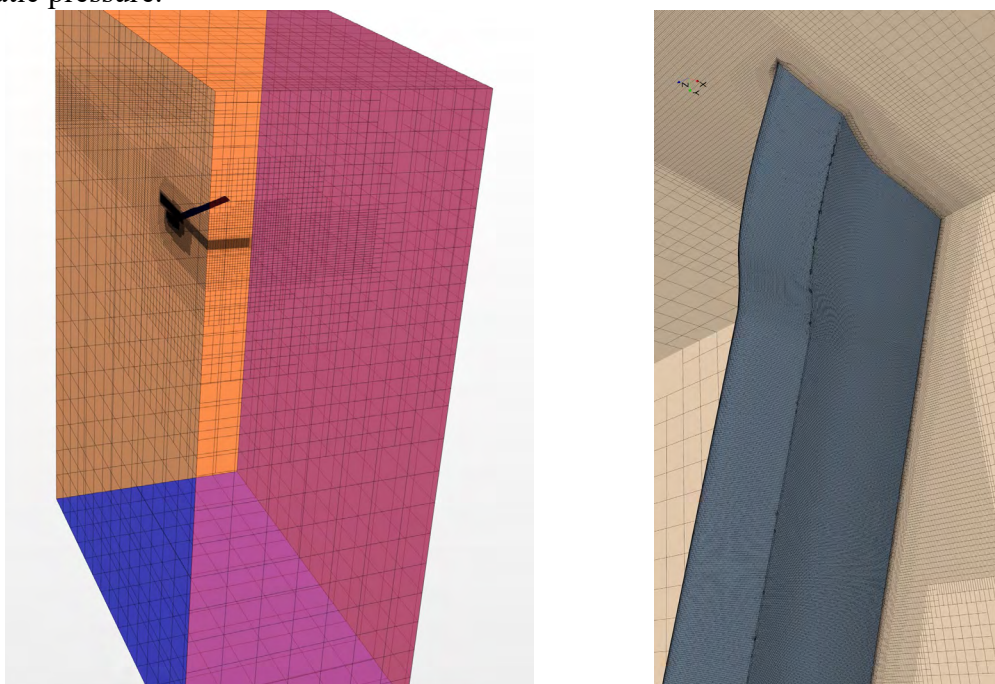


Figure 3: Unstructured mesh around the V-Hydrofoil, domain (left) and close-up on the face of the foil (right)

3 CFD INVESTIGATION OF VENTILATION-CAVITATION DYNAMICS

3.1 Ventilation Physics at Variable Cavitation Numbers

The effect of cavitation on ventilation phenomena has been investigated by running simulations at the design angle of attack, changing the cavitation number calculated at the free surface σ_0 , defined as follows:

$$\sigma_0 = \frac{p_{amb} - p_{vap}}{\frac{1}{2} \rho_w V_0^2} \quad (1)$$

The ambient pressure p_{amb} is the atmospheric pressure in full scale, where the speed varies to change the cavitation number. It corresponds to the static air pressure and it can be regulated in a free surface cavitation tunnel to achieve different cavitation numbers at constant inflow

speed V_0 . The vapor tension of water at ambient temperature is p_{vap} (3170 Pa, at 25 °C).

Cavitation numbers investigated in this study span the range [0.05 – 2.35], to cover applications also to higher speeds (low cavitation numbers). Obviously Froude number changes with the inflow speed, but its influence on ventilation is deemed to be negligible beyond 4-5. Reynolds number considered in this study follows model scale values. Turbulence models used in the RANSE solver assume the flow to be fully turbulent as obviously in full scale. Reynolds number scaling is beyond the scope of this study, although surely interesting.

Following the experiment practice, unsteady simulations are initialized with uniform inflow speed V_0 and atmospheric ambient pressure ($\sigma_0 = 2.35$). The simulation is run long enough for the flow to reach the steady state at ambient pressure. The steady state is reached after the ventilation on the back stabilizes, covering a stable portion of the hydrofoil span on the back from the free surface towards the bottom.

A sequence of consecutive snapshots (still frames) that follows the flow evolution on the back, face and on a spanwise section for is presented in Appendix A, Figure 4 to Figure 6, in order. Time instants find correspondence from one frame sequence to another.

At this high cavitation number ($\sigma_0 = 2.35$), cavitation does not occur, so ventilation physics follows the mechanisms described in [12], plus new others, as in this case the foil uses a particular type of super-cavitating section, the SCSB2 profile [10].

Analyzing the sequence in the first two rows of Figure 4, we notice that the ventilation, or air infiltration into a pocket between the hydrofoil back surface and the surrounding water flow, happens from the side: the sharp leading edge having a relatively high angle of attack at the surface, creates a pocket of separate flow with low pressure that draws the air in from the side. The ventilation from the side advances more rapidly at the trailing edge, due to the high suction pressure created by the curvature-cavitator on the back of the SCSB2 profile. The suction of air and consequent growth of the cavity height along the trailing edge is slower than the initial dynamics and it is captured by the images of the second to fourth row, captured at much lower frequency than the first row.

The cavity growth in a spanwise section close to the trailing edge can be followed also in the sequence of Figure 6 that shows the volume fraction of water in color: red solid water, blue pure air. Two longitudinal planes are also included in the picture of Figure 6: the symmetry plane and a plane at mid-span. The rapid initial growth of the ventilated cavity on the side is evident, again, in the frames of the first row, captured at the same time instant of those in Figure 4 (or Figure 5). Then a time of about 1/10 of a second is necessary to reach the stable ventilation regime captured in the last few frames of the sequence.

The ventilation dynamics on back influences the pressure distribution on the face, since it changes the effective incidence on the foil. This is well visible from the change of pressure distribution given in the sequence of frames in Figure 5: initially the area of stagnation (high pressure coefficients) at the leading edge and in front of the step is larger; after the ventilation on the back is stabilized, the extension of these two regions with $C_p > 0.3$ shrink down.

It can be also noted that at this high cavitation number the step-cavitator on the face is not able to cause cavitation nor ventilation (green and blue areas in Figure 5): the flow does separate from the step and forms the blue area where $C_p < -0.3$, but the suction pressure is not enough to cause cavitation nor to draw air from the trailing edge.

In summary, result is that ventilation on the hydrofoil back surface is only partial, interesting

the whole trailing edge of the foil and only a small portion of the leading edge close to the free surface. A trapezoidal portion of the back about half span wide at the leading edge and three quarter span wide at the trailing edge, as it appears from the last snapshots of Figure 4. The wet/ventilated regions on the back, in fact, are separated by an oblique line with respect to the inflow direction.

The dynamic of ventilation completely changes when cavitation occurs.

The flow simulations at the lower cavitation indexes are initialized with the non-cavitating steady state flow solution obtained at $\sigma_0 = 2.35$. Then the cavitation index is progressively reduced to the desired value and the simulation is continued until steady state regime is reached.

We focus our attention on the transient flow solution that leads to the different steady state ventilation in cavitating conditions.

Ventilation dynamics at $\sigma_0 = 0.05$ is rendered in the snapshots sequences of Appendix – C, Figure 10 to Figure 12. In these pictures, the free surface at the interface between the vapor phase (generated by cavitation) and the other two phases is highlighted in magenta.

The free surface separating air phase from water phase is colored in blue. The top view (Figure 10) shows the initial growth of the vapor cavity that progressively occupies the wet portion of the back of the supercavitating hydrofoil, i.e. the area of the back that is not ventilated.

Vapor tension (or saturation pressure) is considerably lower than the almost atmospheric pressure of the air filling the ventilated cavity, so soon enough the air in the adjacent cavity expands and takes the place of the vapor. This dynamics is happening in the second row of the frame sequence. The vapor phase gets convected by the flow in the wake and at the beginning of the third frame row the back of the hydrofoil is fully ventilated from the free surface down to the apex.

This dynamics is also well captured in Figure 12 sequence that shows the volume fraction of water on a spanwise section close to the trailing edge, where solid water is represented in red, pure air in blue and the vapor phase is again magenta. As expected, the thickness of the initial vapor cavity significantly expands when the air takes place.

The infiltration of air flow into the vapor cavity happens mostly from the lateral direction due to a fairly strong cross flow. In minor extent air infiltrates from the trailing edge.

As regards the face of the super-cavitating hydrofoil, presented in Figure 11, the difference between this case and the previous is the ventilated portion of the tail aft of the step-cavitator. The mechanism of this ventilation is similar to that at the other will be described for the next case with a higher cavitation number. At this very low cavitation number, this dynamics is too quick to be rendered in the extracted frames.

At the *design cavitation number*, $\sigma_0 = 0.15$, the situation is somehow intermediate between the extreme cases presented above. The unsteady flow snapshots are presented in Appendix-B.

The first four frames of Figure 8 well capture the ventilation dynamics of the tail on the face of the SCSB-2 profile. The cavitation bubble forms at the step-cavitator and then quickly expands until it reaches the trailing edge of the foil where it meets the ventilated cavity coming from the back. At that point air quickly infiltrates and fills the cavity even running upstream, being at a considerably higher pressure.

In the meantime, Figure 7, a vapor cavity forms on the wet portion of the back surface, rapidly growing and reaching the trailing edge too. The thickness of the vapor cavity, due to the low angle of attack is small and the air ventilation flow from the side and the trailing edge finds considerable resistance to enter. It does enter, mainly from the trailing edge, but it cannot fill

the entire vapor cavity which continue to grow, ventilate, shed vapor, and grow again, periodically (in an irregular fashion).

A thin film of water seems to form and seal the ventilated cavity laying above from the vapor cavity below. The cross section of this sealing strip is well visible in Figure 9 that also evidences the small height of the vapor cavity, compared to the ventilated portion of the cavity.

3.2 Ventilation-Cavitation Effect on Forces and Moments

Forces and moments were calculated for the three transient simulations described in the previous section. Numerical results are summarized in Table 2. The lift and drag coefficients are non-dimensionalized with the effective planform area $S \cdot c_{sc}$. The vapor phase volume is non-dimensionalized with the cube of the effective chord c_{sc} and multiplied by 10^3 for easy reading.

Table 2: Principal hydrodynamic characteristics calculated at three different cavitation numbers for the SCSP Hydrofoil.. All values are time averaged

| σ_0 | C_L | $10 \cdot C_D$ | L/D | Y_{cp}/S | X_{cp}/c | $C_{vol}/(c/10)^3$ |
|------------|-------|----------------|------|------------|------------|--------------------|
| 0.05 | 0.384 | 0.5606 | 6.84 | 0.60 | 0.54 | 50 |
| 0.15 | 0.448 | 0.5591 | 8.00 | 0.53 | 0.52 | 27 |
| 2.35 | 0.158 | 0.2358 | 6.69 | 0.45 | 0.22 | 0 |

A considerable variation of the lift coefficient is noted between the lowest and the highest simulated cavitation indexes. This is typical of super-cavitating foil passing from a partially wet ($\sigma_0 = 2.35$) regime to a super-cavitating (ventilated) regime ($\sigma_0 = 0.05$). The missed ventilation of the foil tail on the face, aft of the step, noted and discussed earlier at the atmospheric cavitation number is responsible for an additional drop in lift coefficient (blue area in Figure 5). The chord-wise position of the center of pressure moves from a point close to the quarter chord (22% from the leading edge), typical of thin profiles, to about mid chord (52%-54%) as it is expected for the specific SCSB2 2D-section used.

Lift increases at the higher cavitation number $\sigma_0 = 0.15$, compared to its value at the lowest one. This is due to the contribution to lift given by the vapor cavity forming on the back. The hydrofoil is still essentially super-cavitating, as it is at the lowest cavitation index, but now about half of back surface is enveloped in a vapor cavity, not filled with air, and the vapor pressure in the cavitation bubble is lower than the ambient pressure. This justifies the higher value of lift found in the partially cavitating condition with respect to the fully ventilated condition. The volume occupied by the vapor phase is given in in the last column of Table 2. Vapor production is still copious at $\sigma_0 = 0.05$, even if the foil is cavity is ventilated. This is another confirmation that cavitation poses the foundations for ventilation to fully occur.

4 CONCLUSIONS AND PLAN OF FUTURE STUDIES

This paper brings multiple contributions to the fundamental understanding of ventilation mechanics on super-cavitating surface-piercing hydrofoil.

The definition and setup of high fidelity numerical models to simulate the unsteady viscous multiphase (air, vapor and water) flow, using volume of fluid technique and homogeneous cavitation model is described. Detail of the mesh resolution and physical/numerical parameters are also supplied. The introduction of sequential snapshots that visually capture flow features

at high sampling frequency, reveal as a crucial tool to understand the ventilation and cavitation coupled dynamics. In particular, we introduce and analyze perspective views of the face and back of the hydrofoil colored by pressure distribution, with simultaneous overlay of free surface between water/air and water/vapor.

The analysis of simulations made at different cavitation indexes allows for the phenomenological description of the unsteady ventilation/cavitation interaction mechanisms that lead to the final steady state.

The general conclusion is that cavitation needs to be considered for an accurate prediction of ventilation on SC-SP hydrofoils working at cavitation numbers corresponding to speeds higher than 50 knots. We suspect cavitation is important also at lower speeds, but we have no evidence yet, since more simulations need to be completed.

Ongoing studies, in fact, are aimed to extend the numerical investigation to a larger number of cavitation number and angle of attack of the considered foil. In parallel, experimental tests have been conducted in towing tank in order to validate the results of the numerical predictions. Preliminary results of the tests seem to confirm the validity of the CFD predictions.

ACKNOWLEDGMENTS

The support of the Office of Naval Research, through grant N00014-17-1-2344 is gratefully acknowledged. CFD simulations were run on Blueridge, a 6000 cores high performance computing cluster of the Advanced Research Center at Virginia Tech.

REFERENCES

- [1] Brizzolara S., Young Y.L. (2012). Physical and Theoretical Modeling of Surface-Piercing Hydrofoils for a High-Speed Unmanned Surface Vessel. Proceedings of the ASME 2012 31st International Conference on Ocean, Offshore and Arctic Engineering. OMAE2012. Rio de Janeiro, Brazil. June 10-15, 2012.
- [2] Harwood, C., Young, Y., & Ceccio, S. (2016). Ventilated cavities on a surface-piercing hydrofoil at moderate Froude numbers: Cavity formation, elimination and stability. *Journal of Fluid Mechanics*, 800, 5-56. doi:10.1017/jfm.2016.373.
- [3] Swales, P.D., Wright, A.J., McGregor, R.C., Cole, B.N. (1973). Separation and Ventilation Interaction Studies. *Hovering Craft and Hydrofoil*, Vol. 13, No.3, pp. 8-12.
- [4] Harwood, C. M., Young, Y. L., and Ceccio, S. L. (2016). Ventilated cavities on a surface piercing hydrofoil at moderate Froude numbers: cavity formation, elimination, and stability, *J. Fluid Mechanics*, 800: 5-56
- [5] Brizzolara S., Judge C., Beaver W. (2016). High Deadrise Stepped Cambered Planing Hulls with Hydrofoils: SCPH2. A Proof of Concept. *SNAME Transactions*, Volume 124, 2016, pp.312-321.
- [6] Williams S., Brizzolara S. (2017). Dynamic Stability of Foilborne Hydrofoil/SWATH with Anhedral Foil Configuration. *Transactions RINA*, Vol 159, Part B2, Intl J Small Craft Technology, pp.65-80, July-Dec. 2017.
- [7] Dutton T. (2017). An investigation into the design of surface piercing super cavitating hydrofoils. MS thesis in Naval Engineering, Massachusetts Institute of Technology. Department of Mechanical Engineering.
- [8] Vernengo G., Bonfiglio L., Brizzolara S. (2017). Super-Cavitating 3D Hydrofoil Analysis

- by Viscous Lifting Line Approach. *AIAA Journal*, 55(12): 4127-4141, Dec. 2017, doi: 10.2514/1.J055504
- [9] Brizzolarà S., Bonfiglio L. (2015). Comparative CFD Investigation of the Performance of a New Family of Super-Cavitating Hydrofoils. *Journal of Physics: Conference Series (JPCS)*, Volume 656, Number 1, 2015, pp. 12147-12150.
- [10] Vernengo G., Bonfiglio L., Gaggero S., Brizzolarà S. (2016). Physics-Based Design by Optimization of Unconventional Supercavitating Hydrofoils. *Journal of Ship Research*, 60(4):1–16. <http://dx.doi.org/10.5957/JOSR.60.4.150074>
- [11] Newman N. (2018) *Marine Hydrodynamics*. MIT Press.
- [12] Young, Y.L., Harwood, C.M., Montero, F.M., Ward, J.C., Ceccio, S.L. (2017) Ventilation of Lifting Bodies: Review of the Physics and Discussion of Scaling Effects. *Applied Mechanics Reviews*, Vol. 69, 010801, 2017
- [13] Brizzolarà S., Villa D. (2012). Three Phase RANSE Calculation for a Surface Piercing Supercavitating Hydrofoil. *Proceedings of the Eighth International Symposium on Cavitation (CAV 2012)*, Research Publishing Services. doi:10.3850/978-981-07-2826-7-084.

APPENDIX - A

Snapshots of N-S simulations, $\sigma_0 = \sigma_{atm} = 2.35$

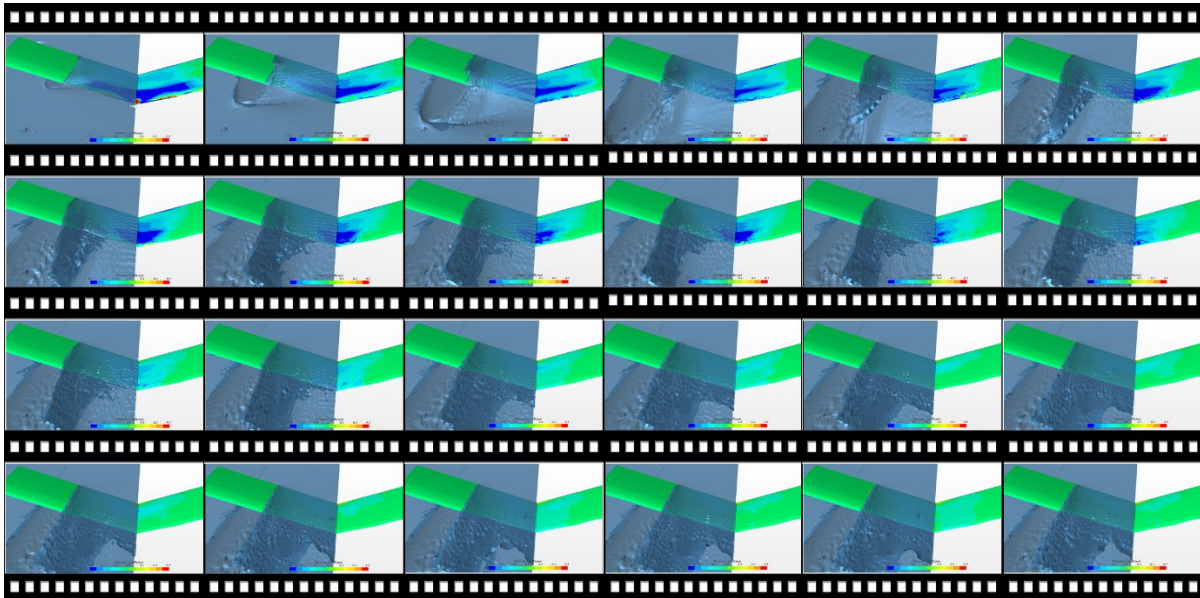


Figure 4: Flow field snapshots of N-S simulations at $\sigma_0 = 2.35$. Top view (on foil back). Frame sampling rate: first row $\Delta t=2.4$ ms, second row $\Delta t=4.8$ ms, third/fourth rows $\Delta t=9.6$ ms. Color contours indicate pressure coefficient, air/water free surface rendered in transparent blue (on left side of V-hydrofoil only).



Figure 5: Flow field snapshots of N-S simulations at $\sigma_0 = 2.35$. Bottom view (on foil face). Frame sampling rate: first row $\Delta t=2.4$ ms, second row $\Delta t=4.8$ ms, third/fourth rows $\Delta t=9.6$ ms. Color contours indicate pressure coefficient, air/water free surface rendered in transparent blue (on left side of V-hydrofoil only).

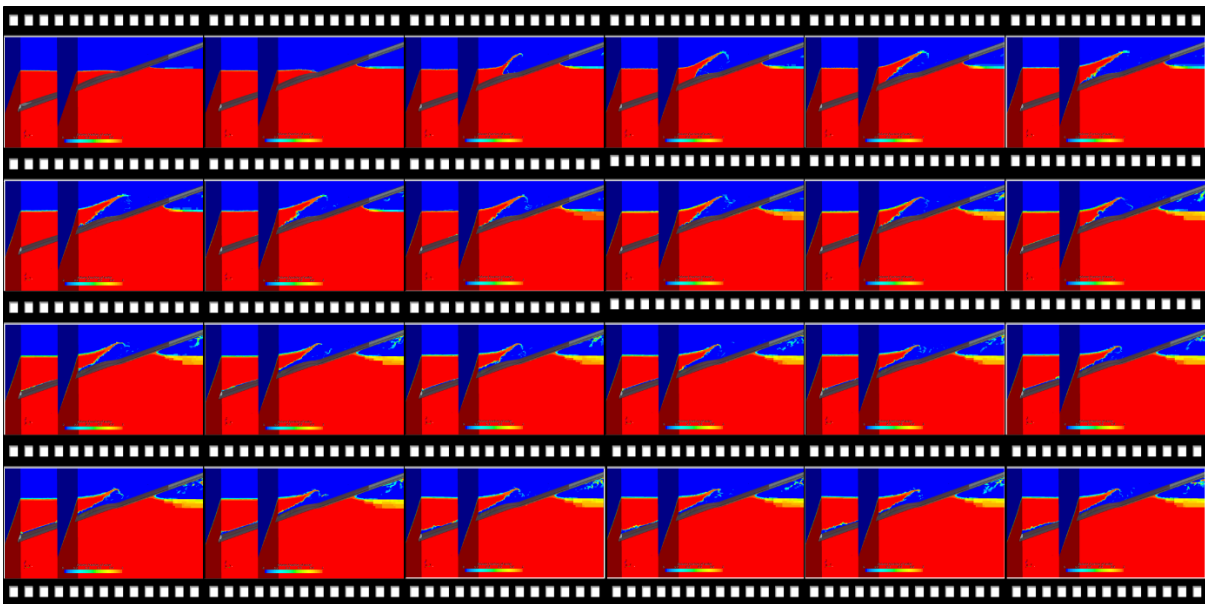


Figure 6: Flow field snapshots of N-S simulations at $\sigma_0 = 2.35$. Color contours indicate the volume of fluid of water on a spanwise section close to hydrofoil trailing edge. View is from upstream. Two longitudinal sections are included (symm. and midspan planes). Frame sampling rate: 1st row $\Delta t=2.4$ ms, 2nd row $\Delta t=4.8$ ms, 3rd/4th rows $\Delta t=9.6$ ms.

APPENDIX - B

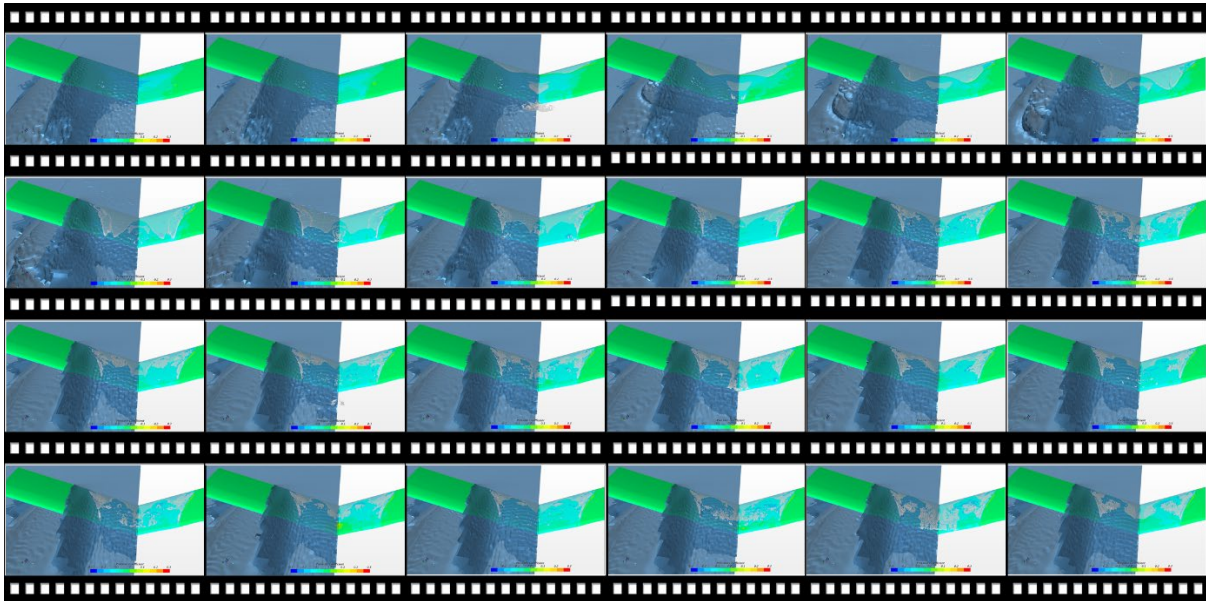
Snapshots of N-S simulations, $\sigma_0 = 0.15$ 

Figure 7: Flow field snapshots of N-S simulations at $\sigma_0 = 0.15$. Top view (on foil back). Frame sampling rate: $\Delta t = 2$ ms. Color contours indicate pressure coefficient, air/water free surface rendered in transparent blue, water/vapor free surface is colored in white (on left side of V-hydrofoil only).

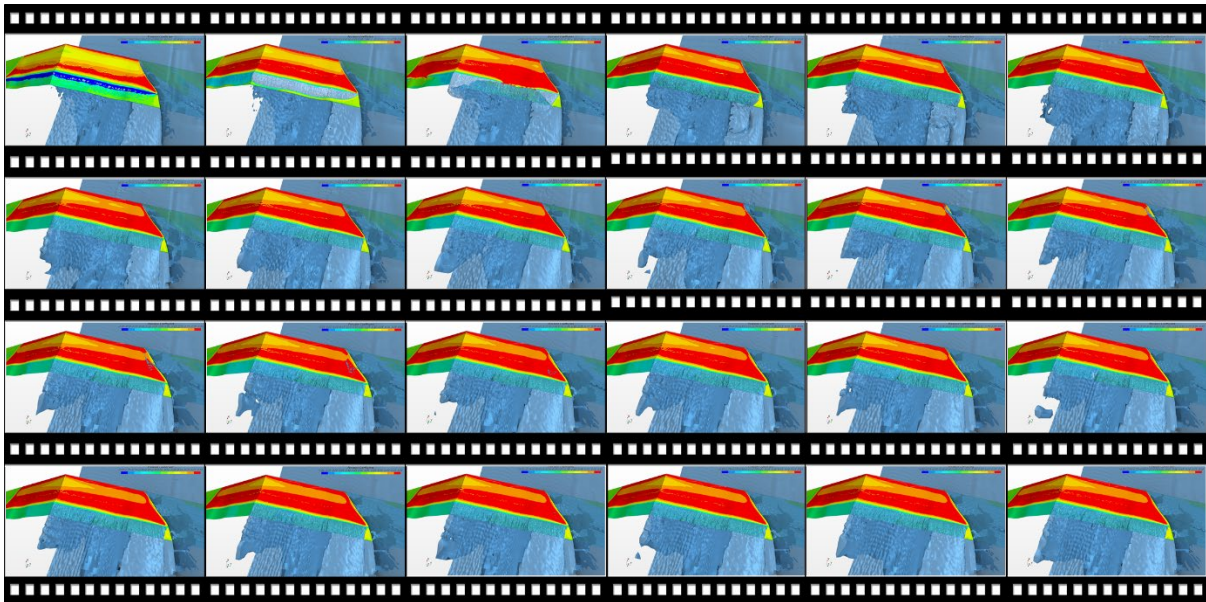


Figure 8: Flow field snapshots of N-S simulations at $\sigma_0 = 0.15$. Bottom view (on foil face). Frame sampling rate: $\Delta t = 2$ ms. Color contours indicate pressure coefficient, air/water free surface rendered in transparent blue, water/vapor free surface is colored in white (on left side of V-hydrofoil only).

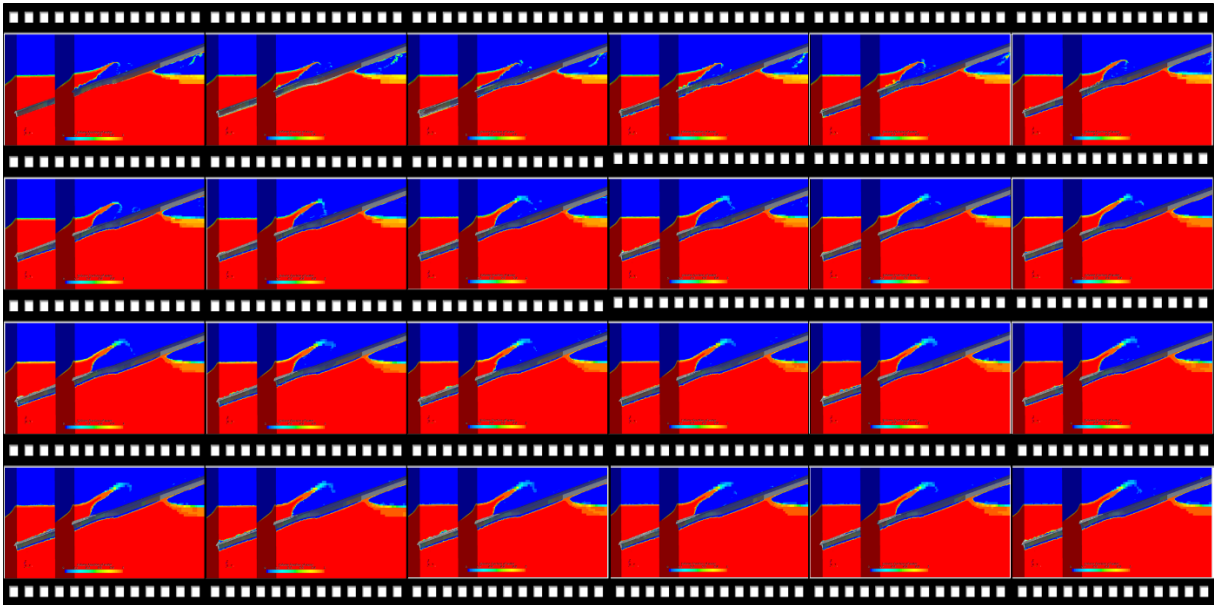


Figure 9: Flow field snapshots of N-S simulations at $\sigma_0 = 0.15$. Color contours indicate the volume of fluid of water on a spanwise section close to hydrofoil trailing edge. Water/vapor free surface is colored in white. View is from upstream. Two longitudinal sections are included (symm. and midspan planes). Sampling rate: $\Delta t = 2.0$ ms.

APPENDIX - C

Snapshots of N-S simulations, $\sigma_0 = 0.05$

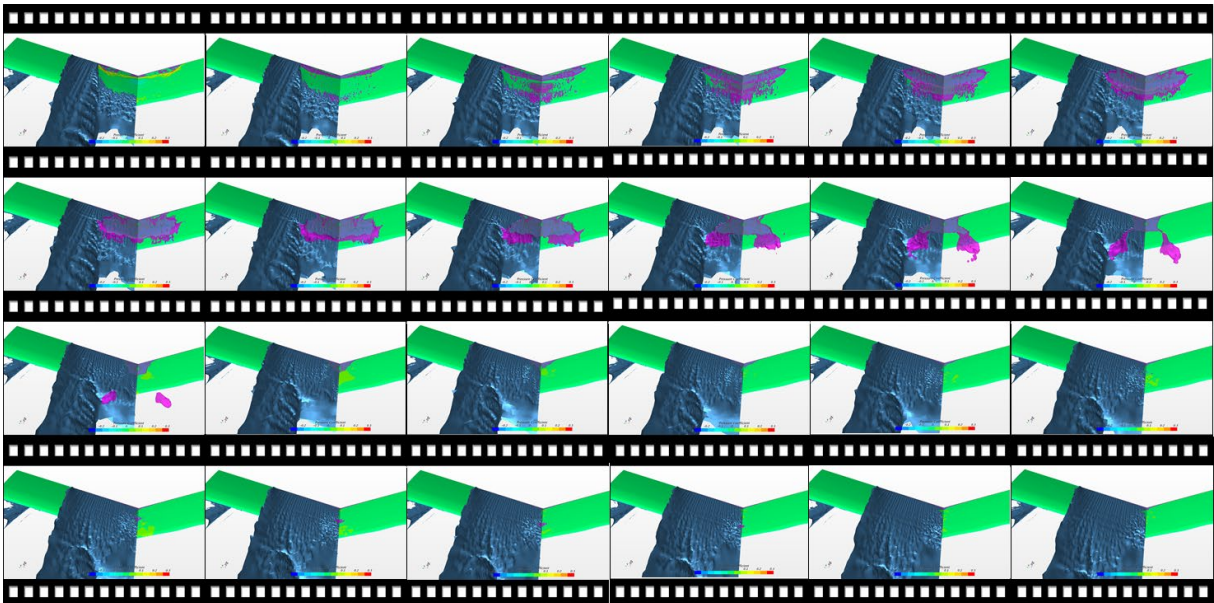


Figure 10: Flow field snapshots of N-S simulations at $\sigma_0 = 0.05$. Top view (on foil back). Frame sampling rate: $\Delta t = 0.6$ ms. Color contours indicate pressure coefficient, air/water free surface rendered in transparent blue, water/vapor free surface is colored in magenta (on left side of V-hydrofoil only).

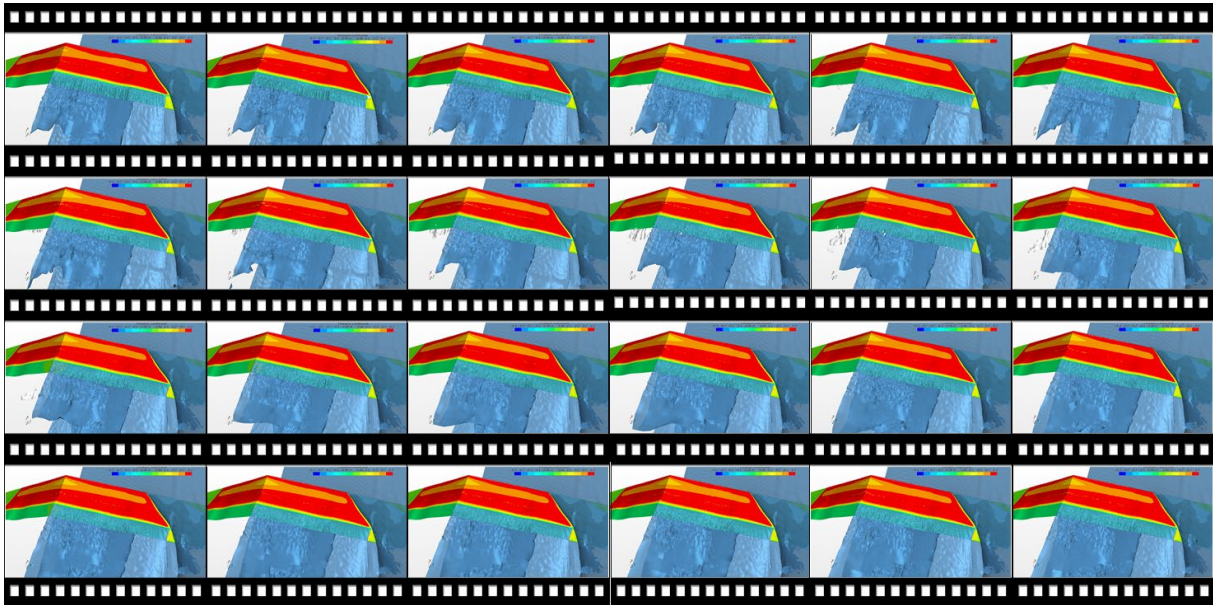


Figure 11: Flow field snapshots of N-S simulations at $\sigma_0 = 0.05$. Bottom view (on foil face). Frame sampling rate: $\Delta t = 0.6$ ms. Color contours indicate pressure coefficient, air/water free surface is rendered in transparent blue, water/vapor free surface is colored in magenta (on left side of V-hydrofoil only).

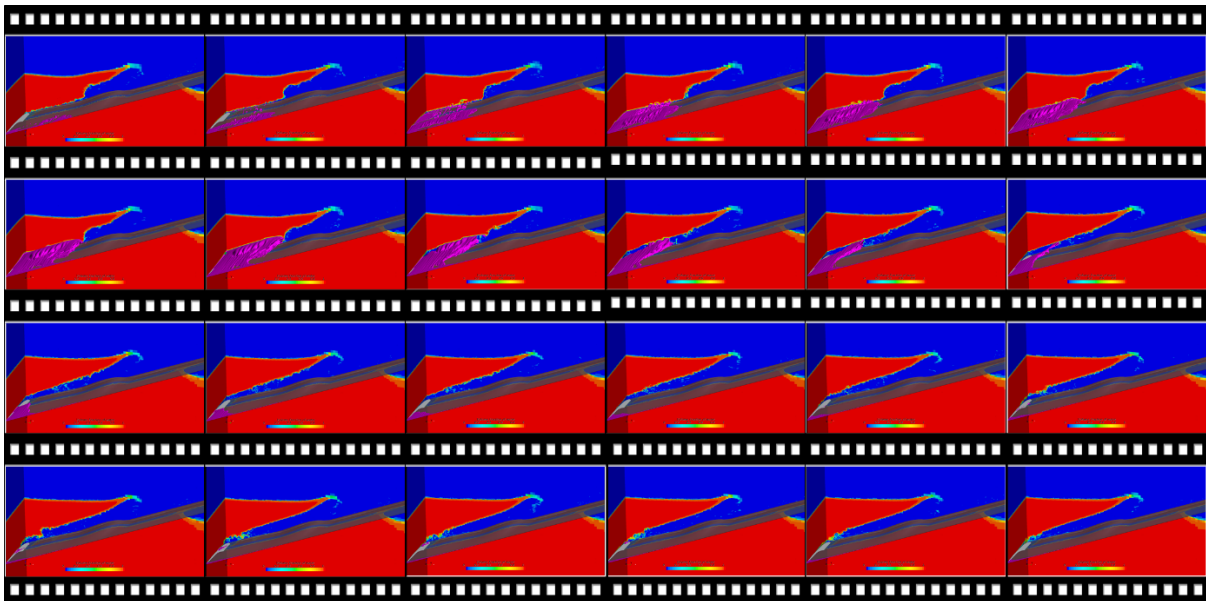


Figure 12: Flow field snapshots of N-S simulations at $\sigma_0 = 0.05$. Color contours indicate the volume of fluid of water on a spanwise section close to hydrofoil trailing edge. Water/vapor free surface is colored in magenta. The longitudinal symmetry plane is included too. View is from upstream. Frame sampling rate: $\Delta t = 0.6$ ms.

NUMERICAL HYDRODYNAMIC STUDY ON THE EFFECTS OF BODY-CURVATURE DURING DITCHING

Jose D. Mesa, Kevin J. Maki

Dept. of Naval Architecture and Marine Engineering
University of Michigan
2600 Draper Drive, Ann Arbor, MI 48109
e-mail: jmesa@umich, kjmaki@umich.edu

Key words: ditching, forward-speed water entry, body surface curvature effects, computational fluid dynamics, volume-of-fluid method

Abstract. In this paper, we discuss the effects of the body curvature on the high-forward-speed water entry problem. The flow caused by aircraft ditching or planing craft slamming is characterized by a complex time-dependent wetness that is often coupled with the resulting structural dynamical response. The interaction of the complex body geometry and three-dimensional nature of the flow pose significant challenges for analytical solution development. The majority of the previous studies of this problem have been focused on pure vertical motion and flat-plate geometries, we focus on the effects of body surface curvature and large forward speed.

The present numerical study assumes the air-water flow to be governed by the Navier-Stokes equations of an incompressible two-phase but single-fluid medium. The volume-of-fluid method is employed to track the air-water interface.

The numerical framework is validated through the comparison with experiment of the force and pressure at distinct points on the body for plates that are either flat, concave, or convex. The simulations show that the body curvature produces a slight increase in the hydrodynamic force for the case of a concave plate and a reduction in force for the convex plate. An underprediction of the highly localized maximum pressure is observed between the numerical and experimental results, suggesting that a higher mesh resolution is required to fully resolve this feature. Finally, the numerical results are used to provide data for the air-water interface profile and the pressure distribution on the entire plate.

1 INTRODUCTION

The design and certification process of elastic structures that enter the water at high horizontal velocity requires the understanding of complex hydrodynamic phenomena. In the aeronautical industry, the primary concern relates to the emergency landing of an aircraft in water, referred to as ditching. A related physical process is known in naval architecture as planning-

craft slamming, where a hull experiences a violent impact on the water when traveling with large forward speed. The impact of the body develops large hydrodynamic loading that can lead to structural failure. Thus accurate prediction of the force and pressure distribution is an essential for the design and certification of aircraft and planning craft structures.

The analysis of water entry problems is challenging because air-water interface topology is complicated with a wide range of length scales (*i.e.* highly localized large surface curvature), time-dependent wetness that strongly influences the maximum value of pressure and determines the force magnitude, and large fluid density relative to the effective density of structures. The last factor requires a coupled fluid-structure interaction (FSI) analysis, and although the FSI aspect of flat-plate ditching has been studied intensely for the flat problem, the present work examines only the hydrodynamical aspects of ditching of curved surfaces.

Today the design and certification of aircraft and planning boat structures involves experimental testing and approaches based on two-dimensional hydrodynamical theory. The primary challenge in experimental campaigns is to difficulty in properly scaling for all physical process as mentioned in [1]. Furthermore, experimental testing is expensive since a specialized facility and a model is required for each structure. In the majority of theoretical approaches, the salient feature of the water entry problem such as three-dimensional effects and hydroelastic coupling is neglected [8]. Therefore, it is of interest to develop and validate high-fidelity numerical tools capable of capturing all the salient features of the water entry problem.

This numerical study aims to validate a high-fidelity numerical framework for curve bodies under high-velocity water entry problems with the experimental data presented in [6] and [5]. The successful validation of the FSI framework with high horizontal velocity for the flat-plate ditching experiments in several impact conditions is presented in [9]. While the majority of the studies of this problem have been focused on pure vertical motion and flat-plate geometries such as in [2] and [3], we focus on the effects of body surface curvature and large forward speed on the ditching hydrodynamics.

2 Numerical Framework

A detailed description of the numerical tightly-coupled fluid-structure interaction framework is found in [9]. For clarity, a brief discussion of the method fluid domain solver is presented since the structural response is not part of the scope for the current study.

The fluid domain solution is determined using computational fluid dynamics (CFD) with the volume-of-fluid (VoF) approach. The Navier-Stokes equations govern the fluid solution considering an incompressible flow of a two-phase viscous-fluid system. The finite-volume discretization combined with Arbitrary Lagrangian-Eulerian (ALE) method allows for moving and deforming fluid meshes. In this study, the ALE approach is used to rigidly move the fluid mesh. The VoF approach is suitable for complex geometries and can accurately capture the nonlinear air-water interface that develops during the ditching problem. Mainly, VoF can resolve the thin jet root, the high local pressure, the pile-up of water in front of the structure, and the three-dimensional

effects, all subject to sufficient grid resolution.

VoF is used with the Navier-Stokes equations to combine the properties of fluids (air and water) into one single continuous fluid using the volume fraction variable α . The volume fraction variable α can have any value between 0 and 1, where a value of 0 represents air, and a value of 1 represents water. Values of α between 0 and 1 represent the interface between the two fluids. The combination of VoF and the Navier-Stokes equations are shown in Equations 1 through 5.

$$\nabla \cdot \vec{u} = 0 \quad (1)$$

$$\frac{\partial \rho \vec{u}}{\partial t} + \nabla \cdot \rho \vec{u} \vec{u} = -\nabla \bar{p} + \nabla \cdot [\mu (\nabla \vec{u} + \nabla \vec{u}^T)] + \rho \vec{g} \quad (2)$$

where \vec{u} is the fluid velocity, ρ is the fluid density, μ the fluid viscosity, \bar{p} the fluid pressure and \vec{g} the gravitational acceleration. The combination of the Navier-Stokes equations with the volume of fraction α is as follows:

$$\rho(\vec{x}, t) = \rho_{\text{water}}\alpha(\vec{x}, t) + \rho_{\text{air}}(1 - \alpha(\vec{x}, t)) \quad (3)$$

$$\mu(\vec{x}, t) = \mu_{\text{water}}\alpha(\vec{x}, t) + \mu_{\text{air}}(1 - \alpha(\vec{x}, t)) \quad (4)$$

$$\frac{\partial \alpha}{\partial t} + \nabla \cdot (\alpha \vec{u}) + \nabla \cdot (\alpha(1 - \alpha)\vec{u}_r) = 0 \quad (5)$$

The flow solver used in this work is based on the OpenFOAM CFD library, see [9] for additional details.

3 Experimental Ditching Tests and Numerical Setup

3.1 Experimental Validation Data

As previously mentioned, the understanding of the fundamental physics of high-speed water entry impact is essential for the design and certification process of complex aeronautical and marine structures. A pioneering study of high-forward-speed impact can be found in [11]. The maximum velocity during these tests was limited to 30 m/s, and the velocity during impact reduces significantly due to the small mass of the test apparatus relative to the hydrodynamic force. The data set provided in [11] provides an insight into the physical phenomena, but due to limited resolution and accuracy in measurements, the data set is not directly used for numerical tool validation.

A similar and extensive flat-plate ditching experimental campaign was carried out in [4]. Among the major improvements in [4] are use of advanced field measurement technologies, and the significantly larger mass of the system which reduces the deceleration of the test specimen

during the impact phase of the body trajectory. Also, facility uncertainty analysis performed in [7] to provide reliability in the experimental data set used for the numerical framework validation. The experimental campaign carried out in [4] for flat-plate ditching tests is further expanded in [6] and [5] to incorporate curved plates ditching tests. These latter two references form the dataset that will be used for comparison in this work.

The experimental condition simulated in this study uses shapes that are made of aluminum alloy (AL2024-T3) plate. The basic dimensions of the test specimens are 1 m long, 0.5 m wide and 15 mm thick. The radius of curvature of the surface in contact with the water is 2000 mm for both the convex and concave plates. The plate is oriented with with a 6° pitch angle, and the plate velocity is $(U, V) = (40, 1.5)$ m/s. The test condition is labeled as condition 1322 (concave plate) and 1222 (convex plate) in [5]. The experimental tests used guide rails to enforce the test-specimen body trajectory. The experiments do exhibit small reduction in velocity during the impact phase. In the numerical simulations the velocity is held constant.

3.2 Numerical Setup

Figure 1a shows the centerplane of the fluid mesh. The spatial discretization is constant in a region that extends from the leading edge of the plate through to the downstream boundary of the domain. The uniformly refined region gives a more accurate resolution of the free-surface. The computational domain has a length of three meters downstream and two meters upstream. The upstream region contains a damping relaxation zone which starts approximately 0.72 m from the leading edge of the plate and extends to the start of the domain. The damping relaxation zone ensures a calm-water-free-surface constraint in front of the plate. The total width of the numerical domain is two meters, and the plate is modeled with a symmetry plane at $y = 0$. The mesh is generated with two boundary-layer prisms with a thickness of 1 mm that are helpful to resolve the flow near the body. The numerical grid setup is based on the findings of the rectangular flat-plate ditching simulations that are presented in [10].

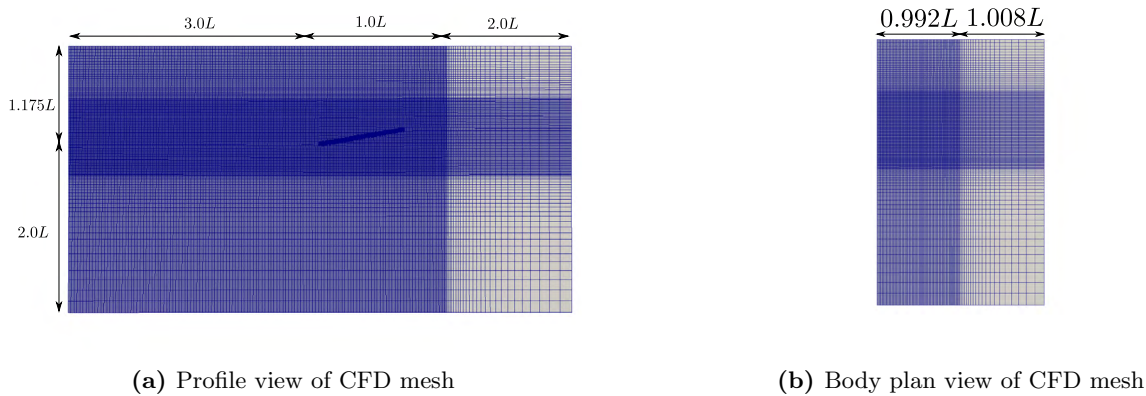


Figure 1: Fluid domain discretization for coarse grid G1 ($L = 1$ m and $\Delta x = 4$ mm).

Three grids are used to analyze resolution requirements for the different quantities of interest.

A summary of the grid resolutions is shown in Table 1. Figure 2 shows the mesh on the each of the three plates for the medium grid G2.

Table 1: CFD grid resolution

| Label | Convex Plate | | Flat Plate | | Concave Plate | | Nominal Δx |
|-------|--------------|------------------|------------|------------------|---------------|------------------|--------------------|
| | # of Cells | # Faces on Plate | # of Cells | # Faces on Plate | # of Cells | # Faces on Plate | |
| G1 | 3,102,608 | 35,256 | 3,047,171 | 32,745 | 3,139,994 | 32,452 | 4 mm |
| G2 | 6,078,590 | 57,526 | 5,971,567 | 57,607 | 6,031,780 | 57,769 | 3 mm |
| G3 | 16,008,341 | 129,480 | 15,583,565 | 130,170 | 16,026,476 | 130,296 | 2 mm |

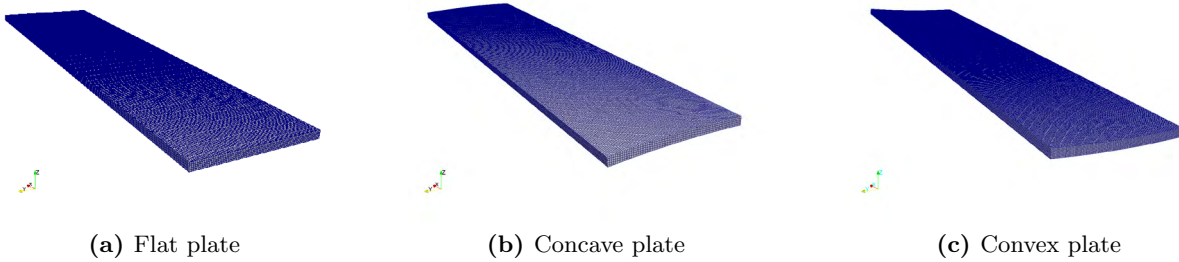


Figure 2: Fluid mesh for G2

4 Results

4.1 Force on Plate

Figure 3 shows the vertical force on the three plates as predicted by each of the three numerical grids and the experimental measurements. Figure 3a is reprinted from [9]. Figure 3b displays the comparison between the numerical and experimental results for the concave plate. The concave ditching simulations display excellent agreement in the slope of the force and for the peak value that occurs around $t \approx 0.045$ s. The force decreases after the jet-root leaves the body, and this occurs earlier in the numerical simulations than it does in the experiment. As previously explained, the experimental test rig is freely moving along a fixed trajectory, and hence experiences a small deceleration that results in a small reduction in velocity during the impact phase. The time delay observed for the concave plate is slightly greater than the time delay observed for the flat-plate. The numerical results indicate a slightly increased force for the concave plate, which would cause a greater deceleration in the experiment and to explain the larger time shift between the numerical and experimental results. The slight increase in force could be attributed to the nature in which the water escapes from the side of the test specimen. For the concave shape the water is forced inwards towards the centerline of the body, whereas

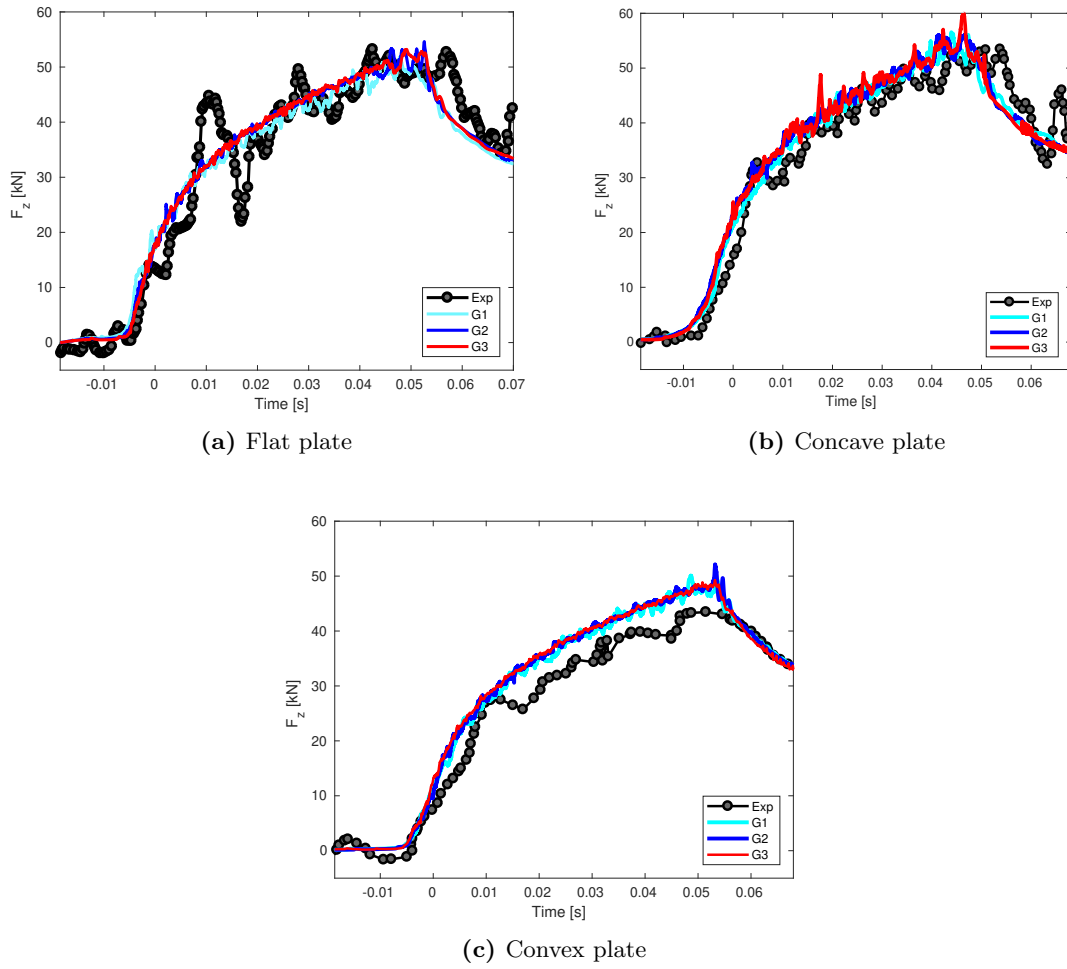


Figure 3: Time history of the vertical force component for G1, G2, G3, and experiment (Exp) for the flat, concave and convex plates.

for the flat plate a greater amount of water can flow outwards and away from the body. Finally, it is important to note that all three grids agree strongly with each other indicating the grid resolution is sufficient for the purposes of predicting the force on the body.

Figure 3c shows the force on the convex plate. Again the agreement between the three numerical grids is very good. The comparison between the numerical and experimental results shows that the time delay due to the body deceleration is not evident, and the force in the numerical prediction is slightly larger than the experimental measurement. Overall the force for the convex plate is of smaller magnitude when compared to the concave or flat plates, and again this can be explained in the way that water can flow away from the body. This is very similar to the wedge impact problem where larger deadrise angle results in smaller forces.

In general the numerical results compare very strongly with the experimental measurements. The conclusions that can be drawn from both sources of information indicate that the force slightly increases for the concave plate when compared to a flat plate. The convex plate shows the force decreases relative to the flat plate. The small changes in force are attributed to the nature of how the flow escapes from under the body. In all three geometries the numerical results show strong agreement amongst themselves.

4.2 Pressure Probe Analysis

Figure 4 compares the local pressure coefficient time history from the experimental data and grids G1, G2 and G3. The probes are located at distances of 0.125, 0.250, 0.400, 0.600 and 0.800 m from the trailing edge along the centerline of each plate. The pressure coefficient C_p is defined as $2p/\rho(U^2 + V^2)$, where p is the total pressure acting on the plate, ρ is the fluid density, U is the horizontal plate velocity, and V is the plate vertical velocity. The reference time used in Figure 4 corresponds to the time where the pressure is maximum at the first probe P4 (0.125 m).

A considerable underprediction between the experimental and numerical results can be observed for the flat and convex plate results as shown in Figure 4a and 4c respectively. The peak values of the experimental pressure for each probe exhibits significant variation for this particular ditching condition. It is noted in [4] that for pitch angles between 4° and 6° , substantial air entrapment was observed during the experiment. This complex multiphase phenomenon of spray and bubble dynamics is not accurately represented using the current grid resolution in the numerical simulations.

In contrast, the concave experimental and numerical results display a better agreement for the local pressure at locations near to the trailing and leading edges (*e.g.* 0.125, 0.250 and 0.800 m). There are larger differences between the experiments and simulations for the centrally located pressure probes which are highlighted using the green box in Figure 4b. It is believed that during impact, the first two corners of the body generate a jet-like flow that is directed towards the center of the body. When the jet flows meet on the centerline they continue to interact with each other and move together in the forward direction. This complicated flow contains spray and bubbles that are only coarsely represented in the numerical simulations.

This effect is presented in Section 4.3 and Figure 6d.

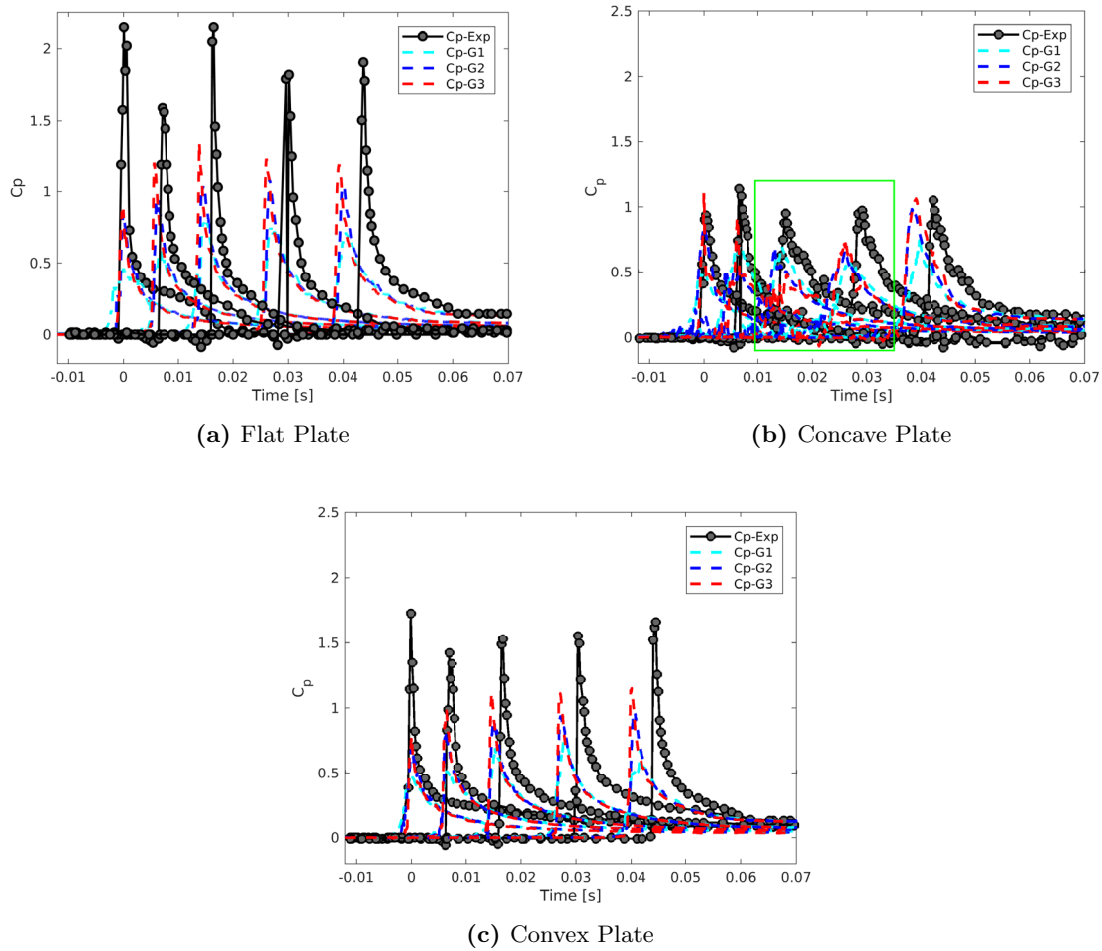


Figure 4: Time history of pressure coefficient C_p recorded at locations of 0.125, 0.250, 0.400, 0.600 and 0.800 m along the centerline of the flat (a), concave (b) and convex (c) plates for G1, G2, G3 grids and experiment ($C_p - \text{Exp}$).

In general it is observed that the effect of curvature is to reduce the maximum pressure on the plate. This effect is more pronounced for the concave plate than for the convex plate. It is very interesting to see that the effect of concavity produces a slight increase in force, but a more pronounced decrease in maximum pressure. This is believed to be due to the complex flow that develops due to the two inward-oriented jets that are produced by the edges of the concave shape that first impact the water.

The underprediction of the value of the peak in each of the numerical pressure time histories is due primarily to the lack of resolution of the numerical grid. It can be seen that as the grid is refined, the maximum value of the pressure in each probe increases and grows closer to the

experimental value. Hence the solution is not fully converged, and for the purposes of prediction of the maximum value of pressure, a finer grid yet is necessary.

4.3 Spatial Flow Field Analysis

Lastly, to provide an insight into how body curvature affects the flow during ditching, the air-water interface and pressure-profile on the plate are presented. Figure 5 displays a transverse profile of the water surface elevation η . The profile is located at a streamwise position of the plate trailing edge for plates at an instant in time when the jet root has approximately reached 0.400 m along the plate. The horizontal axis is the dimensionless transverse coordinate defined as $\xi = y/B$. Close agreement is observed for the free surface topology as the grid resolution increases for all plate geometries. The water surface elevation maximum value is highest for the flat plate and slightly reduces for the concave and convex plate respectively.

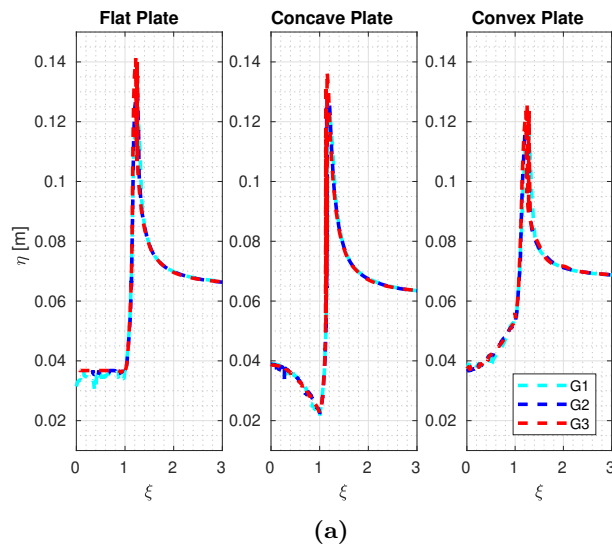
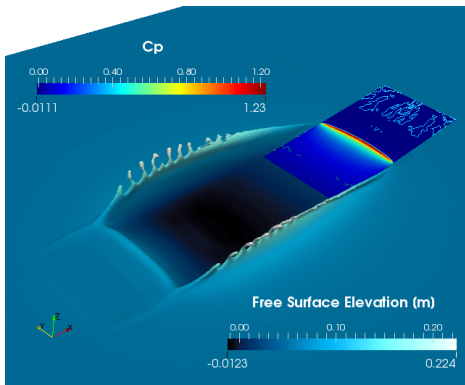
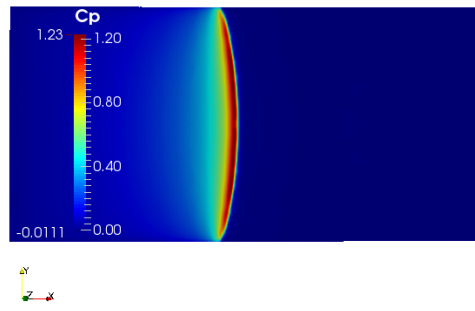


Figure 5: Water surface transverse profile.

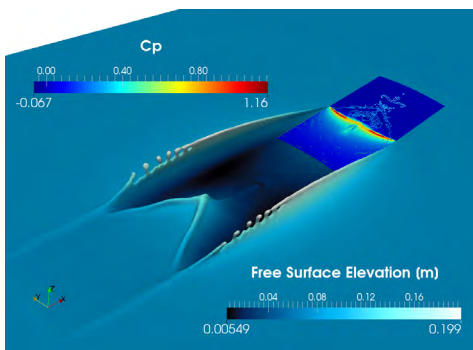
A full three-dimensional view of the water surface is shown together with the pressure coefficient on the plate in Figure 6. The imprint of the different body shapes is clearly seen in the region where the body first impacts the water surface. For the flat plate, the initial depression in the calm water appears as a straight line behind the trailing edge of the plate. In the case of the concave and convex plates, the depression follows either a V or U behind the trailing edge of the plate. The pressure coefficient distribution for the flat plate follows a parabolic shape with a smaller curvature compared to the convex plate. In the case of the concave plate the unique feature along the center of the plate shows the interacting edge-generated jets that are discussed previously in the text with regard to the pressure probe data.



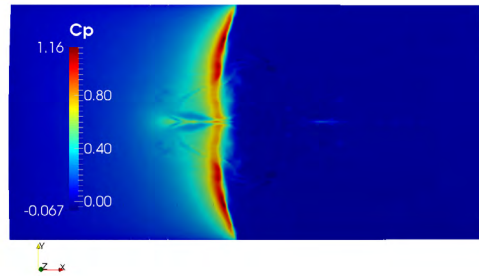
(a) Flat plate isometric view



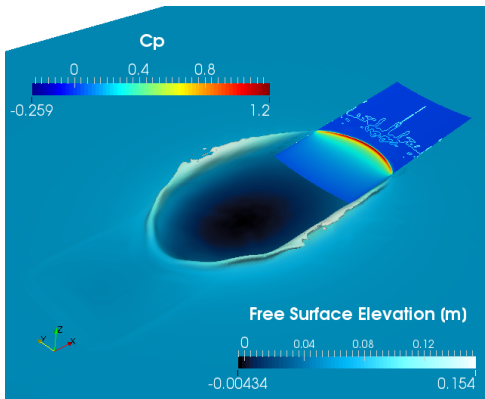
(b) Flat plate top view



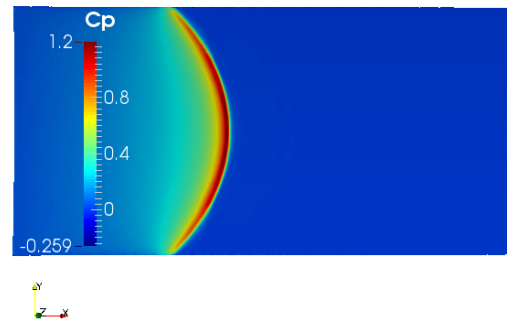
(c) Concave plate isometric view



(d) Concave plate top view



(e) Convex plate isometric view



(f) Convex plate top view

Figure 6: Visualization of the water surface and pressure coefficient distribution on the plate during the time when the jet root approximately reaches 0.400 m.

5 CONCLUSIONS

In this paper the hydrodynamics of a body entering the water with high forward speed are studied with a numerical computational fluid dynamics solver. In particular the effect of body curvature is analyzed by comparing results of a concave and convex shape to those of a flat plate. Comparison with an extensive experimental campaign is used to assess the accuracy and convergence of the numerical results.

The numerical solution captures the curvature effects on the hydrodynamic force and is in strong agreement with the experimental data. For the concave plate a slight increase in force is observed, but overall the force component follows the same trend as the flat plate. On the other hand, for the convex plate a more noticeable force reduction is observed.

It is observed that the overall effect of plate curvature on the maximum pressure along centerline is to reduce the local pressure magnitude. The reduction in local pressure is more significant for the concave plate due to the complex interacting jet flow that forms with the two edges of the plate that first impact the water and generate spray and bubbles.

The numerical results demonstrate that the grids used in this work are sufficient for force prediction purposes. The maximum pressure is not fully converged, and grids with additional resolution on the body are required to more confidently predict the maximum value. The numerical results are useful to predict the full flow field including the pressure distribution on the plate and the water surface distribution.

REFERENCES

- [1] H. Climent, L. Benitez, F. Rosich, F. Rueda, and N. Pentecote. Aircraft ditching numerical simulation. In *25th Int. Congress of the Aeronautical Sciences, Hamburg, Germany*, 2006.
- [2] O. M. Faltinsen. The effect of hydroelasticity on ship slamming. *Philosophical Transactions of the Royal Society of London A: Mathematical, Physical and Engineering Sciences*, 355(1724):575–591, 1997.
- [3] O. M. Faltinsen, J. Kvålsvold, and J. V. Aarsnes. Wave impact on a horizontal elastic plate. *Journal of Marine Science and Technology*, 2(2):87–100, 1997.
- [4] A. Iafrati. Experimental investigation of the water entry of a rectangular plate at high horizontal velocity. *Journal of Fluid Mechanics*, 799:637–672, 2016.
- [5] A. Iafrati. Effect of surface curvature on the hydrodynamics of water entry at high horizontal velocity. In *ASME 2018 37th International Conference on Ocean, Offshore and Arctic Engineering*, pages V009T13A034–V009T13A034. American Society of Mechanical Engineers, 2018.
- [6] A. Iafrati. Effect of the body curvature on aircraft ditching hydrodynamics. In *33th IWWF, Guidel-Plages, France*, 2018.

- [7] A. Iafrati, S. Grizzi, M. Siemann, and L. B. Montañés. High-speed ditching of a flat plate: Experimental data and uncertainty assessment. *Journal of Fluids and Structures*, 55:501–525, 2015.
- [8] A. Iafrati and Korobkin. Self-similar solutions for porous/perforated wedge entry problem. In *20th IWWFEB, Longyearbyen, Norway*, 2005.
- [9] J. D. Mesa. *Hydroelastic Analysis of Aluminum and Composite High-Speed Planing Craft Structures During Slamming*. PhD thesis, The University of Michigan, 2018.
- [10] J. D. Mesa and K. J. Maki. Numerical investigation of rectangular flat plate slamming. In *ECCOMAS Congress 2018, Glasgow, UK*, 2018.
- [11] R. F. Smiley. An experimental study of water-pressure distributions during landing and planing of a heavily loaded rectangular flate-plate model. Technical report, National Aeronautics And Space Administration Washington DC, 1951.

EXPERIMENTAL AND NUMERICAL INVESTIGATION OF BLADE GEOMETRY EFFECT ON PROPELLER CAVITATION AND NOISE

MARINE 2019

XIAO-QIAN DONG*, QI WANG, CHEN-JUN YANG

State Key Laboratory of Ocean Engineering(SKLOE)
Collaborative Innovation Center for Advanced Ship and Deep-Sea Exploration(CISSE)
Shanghai Jiao Tong University, Shanghai 200240, China
*e-mail: xiaoqiandong0330@sjtu.edu.cn

Key words: Propeller, Blade geometry, section profile, skew, tip rake, Cavitation, Noise

ABSTRACT: In this paper, the effects of propeller blade geometry on cavitation and noise were studied by model tests and numerical simulations. Section thickness distribution, skew and tip rake are considered. Propeller model tests were carried out in SJTU Cavitation Tunnel. Test results of open water performance, cavitation inception and noise were compared. Then the hydrodynamic performances were simulated by solving the Reynolds-averaged Navier-Stokes (RANS) equations using the Fluent software. The boundary layer grids were set on blades. Numerical results of open water performance, section pressure distribution and propeller wake flow field were compared. It is shown that increasing skew can delay cavitation inception, and reduce the area of sheet and sound pressure level after cavitation occurs; increasing skew near blade tip can delay tip vortex cavitation inception further at low advance coefficients; thickening the section near leading edge can delay the suction side and pressure side cavitation inception, and make cavitation stable when cavitation incepts; tip rake can reduce the strength of tip vortex, and delay the tip vortex cavitation inception significantly.

1 INTRODUCTION

With Modern ships developing towards larger size and higher speed, cavitation and noise performances of propeller are increasingly important. One of the key objectives of propeller optimization is to delay propeller cavitation inception and reduce propeller noise. When propeller blades rotate, there is pressure differences between the upstream and downstream surfaces, which drives the secondary flow around the blade tip, and leads to the tip vortex. The low pressure at the core of the tip vortex will cause cavitation, and the tip vortex cavitation is generally earlier than the sheet cavitation. Once cavitation occurs, the noise of propeller will increase significantly, sometimes even cause the vibration on ship stern.

In propeller design, tip unloading (reducing pitch and camber of tip), is usually used to delay the tip vortex cavitation inception, but tip unloading has a negative impact on propulsion efficiency^{[1][2]}. On the other hand, some researchers began to study how to delay the tip vortex cavitation inception by changing skew and rake near the tip. Kuiper^[3] studied the effects of skew and rake on cavitation inception, and the results show that tip rake towards pressure side can delay the tip vortex cavitation inception. Choi^[4] also studied the effects of skew and rake

on the cavitation and fluctuating pressure. Yamasaki^[5] compared the effects of tip unloading and tip rake on the hydrodynamics, cavitation and fluctuating pressure through experimental study. It was found that tip rake is better than tip unloading in reducing the area of cavitation and fluctuating pressure. Subsequently, Yamasaki^[6] made further research on the influence of tip rake on the fluctuating pressure, the size and distribution of tip rake were studied experimentally, and the relationship between the reduction of the fluctuating pressure and tip rake was regressed according to the experimental data. Xin^[7] studied the effects of tip thickness, skew and rake on tip vortex flow and cavitation inception with three-dimensional twisted hydrofoil. Using geometry with rake towards pressure side can prevent the leading edge vortex rolling into the local tip vortex and weaken the transverse flow around tip.

In this paper, the effects of propeller blade geometry, section thickness distribution, skew and tip rake, on cavitation and noise were studied by model tests and numerical simulations. Propeller model tests were carried out in SJTU Cavitation Tunnel. Also the hydrodynamic performances were simulated by solving the Reynolds-averaged Navier-Stokes (RANS) equations using the Fluent software. Test results of open water performance, cavitation inception and noise were compared. The boundary layer grids were set on blades. Numerical results of open water performance, section pressure distribution and propeller wake flow field were compared.

2 EXPERIMENTAL RESEARCH

2.1 Test facility and measuring equipments

Propeller model tests were carried out in the cavitation tunnel of Shanghai Jiao Tong University (SJTU CT), as shown in Figure 1. The test section is 6.1m in length, and its cross section is 1m×1m with rounded corners. The axial flow velocity over the test section ranges from 0.5m/s to 15.8m/s, and the static pressure at the centerline of the test section ranges from 25kPa to 300kPa. The non-uniformity of axial flow velocity is less than 1%.

Figure 2 shows the equipments used in the model tests. The measuring ranges of the single propeller dynamometer are $\pm 3000\text{N}$ for thrust and $\pm 300\text{Nm}$ for torque, respectively. The maximum rotating speed is 1750r/min. The propeller model was mounted upstream the dynamometer. Propeller noise was measured by Brüel & Kjær 8103 hydrophone, which was just below the propeller model, with a distance of 0.725m, fixed in the acoustic measurement tank. The frequency response range of the hydrophone is 0.1Hz ~ 180Hz, and the sensitivity is $-211\text{dB re } 1\text{V} / \mu\text{Pa} \pm 2\text{dB}$.



Figure 1: The cavitation tunnel of Shanghai Jiao Tong University

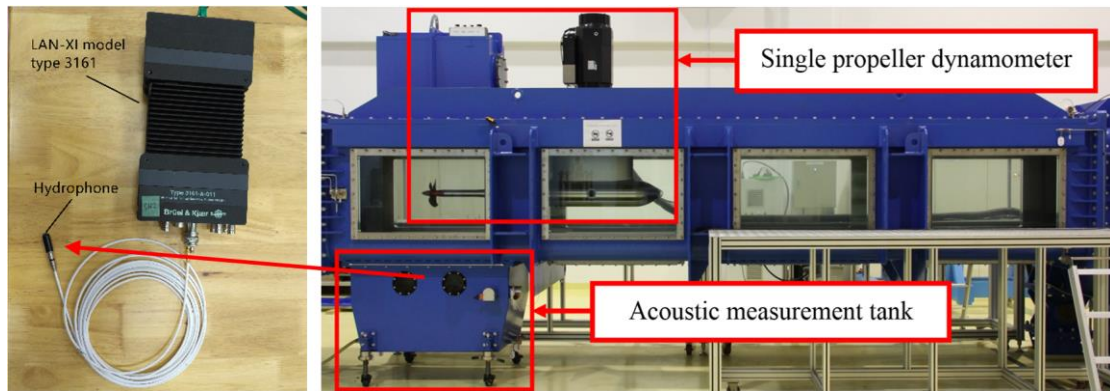


Figure 2: The equipments used in propeller model tests

2.2 Propeller models

Five propeller models with different skew, tip rake and section thickness distribution are used for model tests. The model diameter D is 250mm. DTMB 4381 propeller^[8] was used as the initial model, which is a five-blade propeller without skew. DTMB 4382 propeller, a five-blade propeller with a linear skew of 36° , was used to study effect of skew angle. (Pitch and camber of 4382 propeller are correct due to skew, the pitch distributions are shown in Figure 1.) Based on the 4382 propeller, another three propellers were designed. For the 4382-1 propeller, the maximum thickness of section profile is unchanged, but the thickness near leading and trailing edges is increased, as shown in Figure 4. Comparing with 4382-1 propeller, a balance skew distribution is used on 4382-2 propeller, as shown in Figure 5. Comparing with 4382-2 propeller, a tip rake of $2\%D$ towards pressure side is used on 4382-3 propeller, as shown in Figure 6. The pitch (Figure 1), camber and chord for these three propellers are same with 4382 propeller. Figure 7 shows the comparison of blade profiles, while Figure 8 give a 3D viewer of the tip rake. Figure 9 shows the photos of five propeller models.

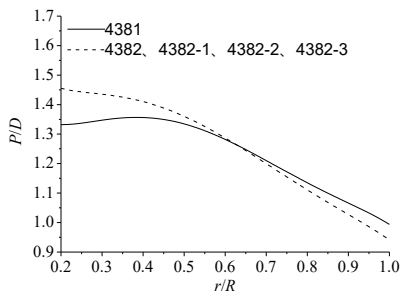


Figure 3: Pitch distribution

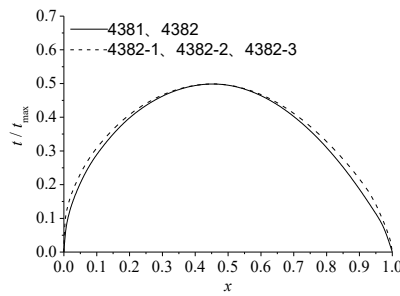


Figure 4: Section profile

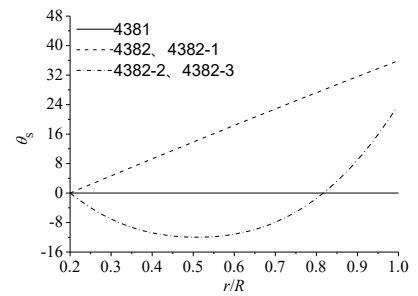


Figure 5: Skew distribution

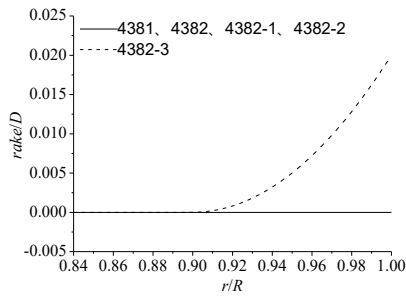


Figure 6: Tip rake

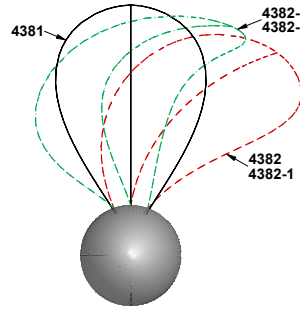


Figure 7: Blade outline

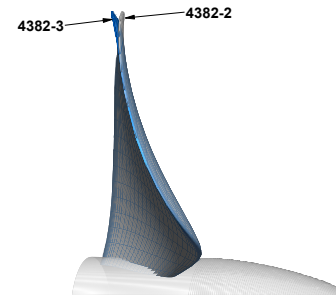


Figure 8: 3D view of tip rake

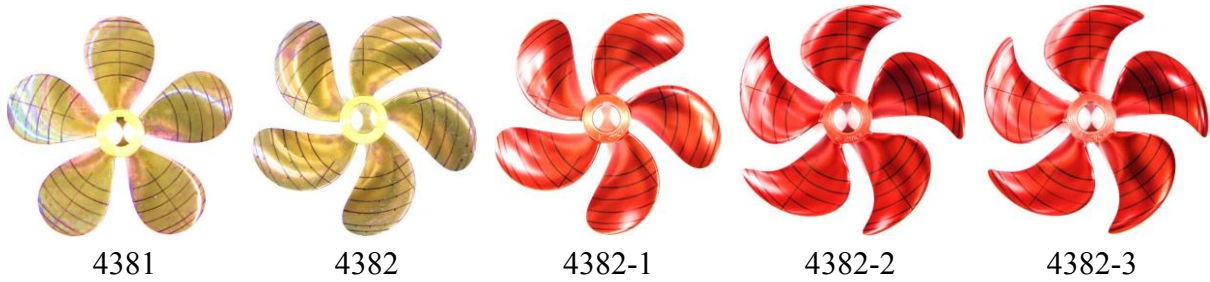


Figure 9: Photos of propeller models

2.3 Test results and analysis

- Open Water Performance

The open water test was carried out with a constant rotating speed of 20r/s. The Reynolds number ranges from 7.5×10^5 to 8.7×10^5 , which is defined as

$$Re = \frac{C_{0.7R} \sqrt{V_A^2 + (0.7\pi nD)^2}}{\nu} \quad (1)$$

where $C_{0.7R}$ is the chord length at $0.7R$, V_A is the advance velocity, n is propeller rotating speed and ν is the kinematic viscosity of water.

Figure 10 shows the comparison of SJTU CT test results and DTNSRDC test results^[8]. For the SJTU CT test results, thrust and torque are larger at most J conditions. One possible reason is that the test results in SJTU CT is not corrected with blockage effect of cavitation tunnel and dynamometer.

Figure 11 compares the open water performance of five propellers, and K_T , K_Q and η_0 at design condition $J=0.889$ are presented in table 1. The performances of five propellers are close at most J conditions, the relative differences of K_T , K_Q and η_0 between each propeller are within 3.9%, 4.5% and 1.2%, respectively, at design condition $J=0.889$. It can be approximately considered that performances of the five propellers are the same under design condition.

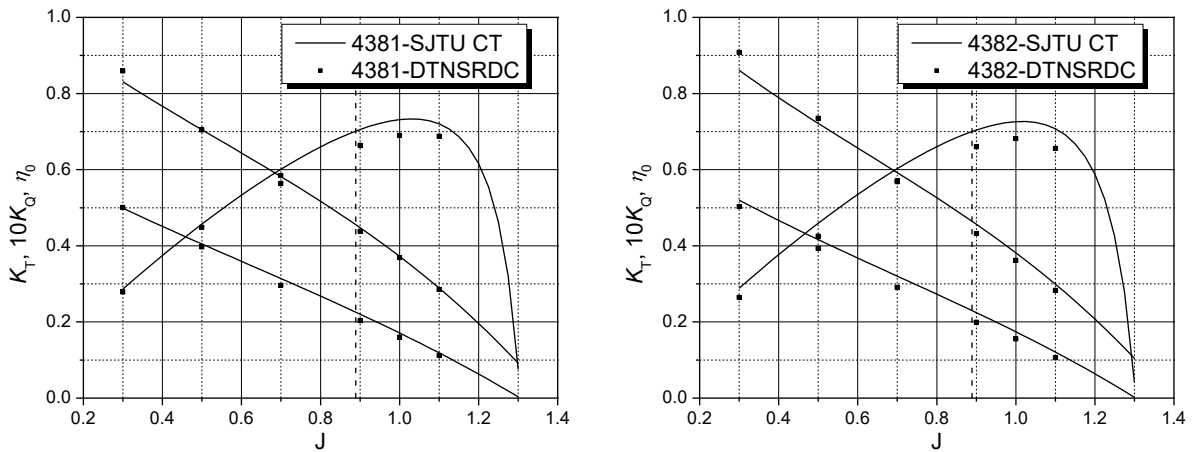


Figure 10 Comparison of open water performance test results with DTNSRDC (Left: 4381 propeller, Right: 4382 propeller)

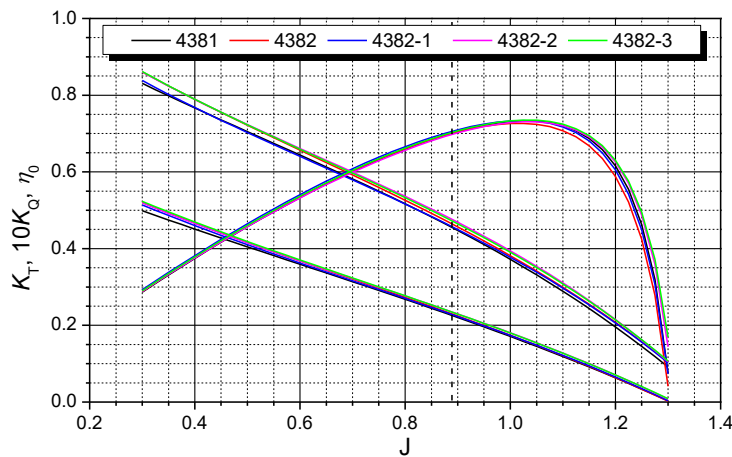


Figure 11: Comparison of open water performance of the five propellers

Table 1: The open water performance at design condition ($J=0.889$)

| | 4381 | 4382 | 4382-1 | 4382-2 | 4382-3 |
|----------|-------|-------|--------|--------|--------|
| K_T | 0.226 | 0.230 | 0.228 | 0.235 | 0.235 |
| $10K_Q$ | 0.455 | 0.464 | 0.457 | 0.476 | 0.473 |
| η_0 | 0.701 | 0.700 | 0.706 | 0.698 | 0.703 |

- Cavitation Inception

The cavitation inception test was carried out with a constant rotating speed of 20r/s. At each advance coefficient J , the cavitation test was conducted by starting from a noncavitating condition and reducing the cavitation tunnel pressure until one kind of cavitation appeared. The cavitation number is defined as

$$\sigma_n = \frac{P_0 - P_v}{\frac{1}{2}\rho n^2 D^2} \quad (2)$$

where P_0 is the static pressure at the propeller shaft, P_v is the vapor pressure of water, and ρ is the density of water. Figure 12 shows the comparison of cavitation inception curves of the five propellers.

Compared with 4381 propeller, the cavity bucket of 4382 propeller (with a linear skew of 36°) became much wider. Both of the suction side and pressure side cavitation inceptions were delayed a lot. Also the tip vortex cavitation inception was delayed, which is more obvious at low advance coefficients.

Compared with 4382 propeller, the suction side and pressure side cavitation inceptions of 4382-1 propeller (with a section profile thickened near leading and trailing edges) were delayed slightly. The tip vortex inception was only delayed near design condition. And during cavitation test, it was seen that inception of sheet cavitation on 4381 and 4382 propeller was highly unstable, the inception pressure in each decompression cannot repeat well, which was much better on 4382-1 propeller.

Compared with 4382-1 propeller, using a balanced skew distribution made the cavitation inception of 4382-2 propeller delay further. Delay of tip vortex inception was very obvious at low advance coefficients, which was similar to the delay of tip vortex cavitation between 4381 and 4382 propeller. Using the balanced skew distribution corresponds to increasing the skew at outer radius.

Compared with 4382-2 propeller, by using tip rake (towards pressure side), the tip vortex cavitation inception of 4382-3 propeller was delayed significantly. On the suction side, the cavitation inception was delayed at low advance coefficients; while tip rake had little effect on the pressure side cavitation inception.

In summary, increasing skew can delay tip vortex cavitation, suction side cavitation and pressure side cavitation inception significantly, and increasing skew near blade tip can delay tip vortex cavitation inception further at low advance coefficients; thickening the section profile near leading edge can delay the suction side and pressure side cavitation inception, and make cavitation stable when cavitation incepts; tip rake can delay the tip vortex cavitation inception significantly.

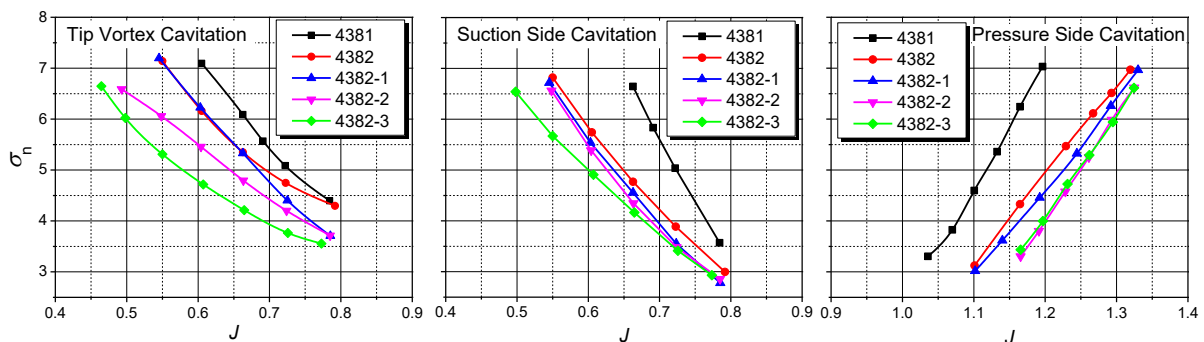


Figure 12: Cavitation inception test results

- Noise

Propeller noise measurements were conducted under $J=0.5$ and $\sigma_n=5.73$. The background noise was also measured under the same condition.

Figure 13 shows the cavity patterns on the five propellers under the noise test condition. Sheet cavitation was seen on 4381, 4382, 4382-1 propeller, and the cavitation area decreased along radial and chordwise directions one by one. Stable and strong tip vortex cavitation was observed on these three propeller. Cavitation on 4382-2 and 4382-3 propeller were much weaker, both of the sheet and tip vortex cavitation appears intermittently, and the tip vortex cavitation on 4382-3 propeller was weaker due to the tip rake.

Figure 14 shows the sound pressure level of five propellers. Increasing skew can decrease the sound pressure level, at high frequency, larger than 10kHz, based on comparison of 4381 and 4382 propeller, as well as 4382-1 and 4382-2 propeller. At low frequency, between 300Hz to 2000Hz, two peaks appeared in the noise spectrum of 4381 propeller, at about 600Hz and 1000Hz; noise spectrum of 4382 had the same shape but lower peak value; from 4382-1 propeller to 4382-3 propeller, noise spectrum at low frequency became smooth one by one, and the maximum sound pressure level decreased correspondingly.

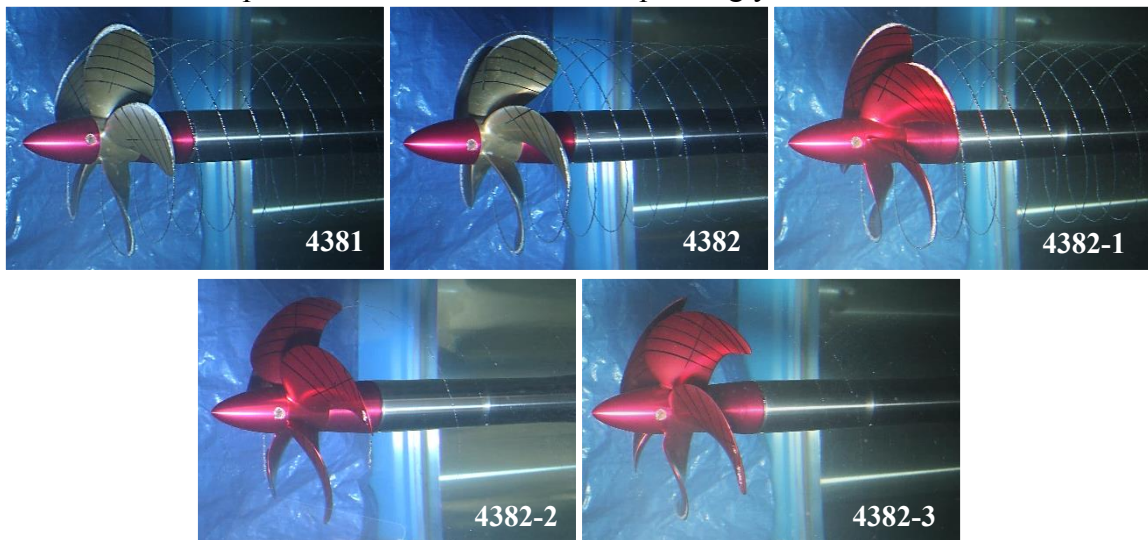


Figure 13: Comparison of cavity patterns of five propellers ($J=0.5$, $\sigma_n=5.73$)

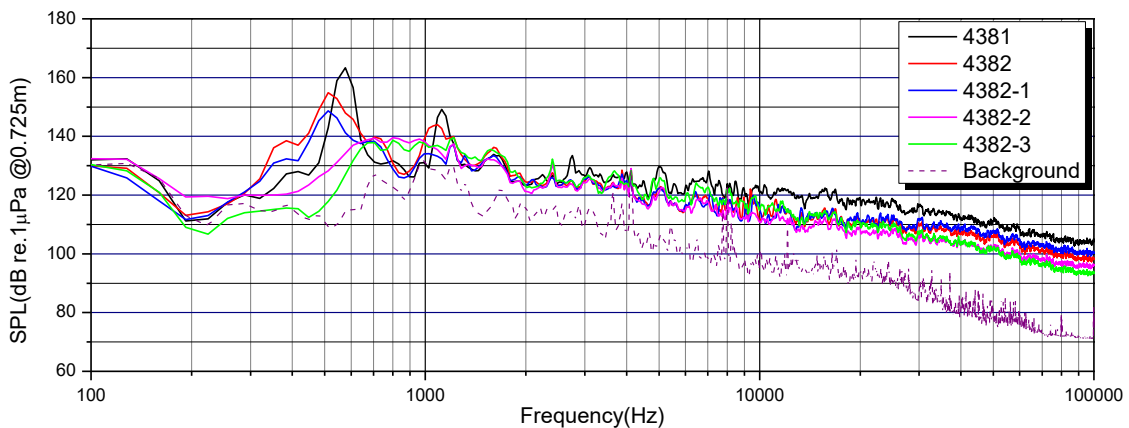


Figure 14: Comparison of sound pressure level of five propellers ($J=0.5$, $\sigma_n=5.73$)

3 NUMERICAL SIMULATION

3.1 Modeling

Since flow in open water is assumed to be steady and periodic for all blades in the coordinate system fixed to the propeller, a single blade passage suffices for the simulation. As illustrated in Figure 15, the computational domain is a portion of the cylinder which is coaxial with the propeller shaft. It is bounded by a pair of periodic surfaces which pass through the shaft axis and make an angle of $360/Z$ degrees, where Z is the number of blades, and here $Z=5$. The inlet and outlet of the domain are $5D$ upstream and $10D$ downstream of the propeller. The radial size of the domain is $5D$. As shown in Figure 16, the periodic boundary surfaces pass through the leading and trailing edges of adjacent blades, hence the back and face of the adjacent blades, instead of the same blade, become boundaries of the domain. By doing so, prism layer grids of high quality can be generated easily on blade surfaces, as shown in Figure 17. Using the SST $k-\omega$ model for turbulence closure, the boundary layer flow is resolved down to the viscous sub-layer. The wall distance averaged over blade surfaces, y^+ , and total number of cells are presented in table 2. All the boundary surfaces are discretized via triangular grids, while the space outside the prism layers is discretized via tetrahedral cells.

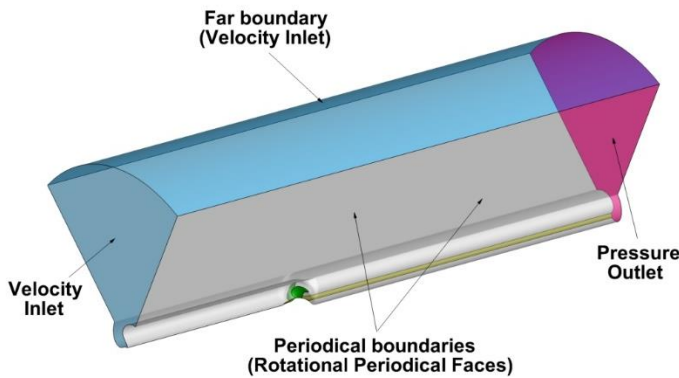


Figure 15: The computational domain

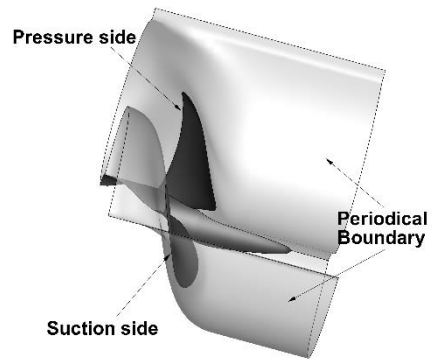


Figure 16: Geometry of the sub-domain enclosing the back and face of adjacent blades

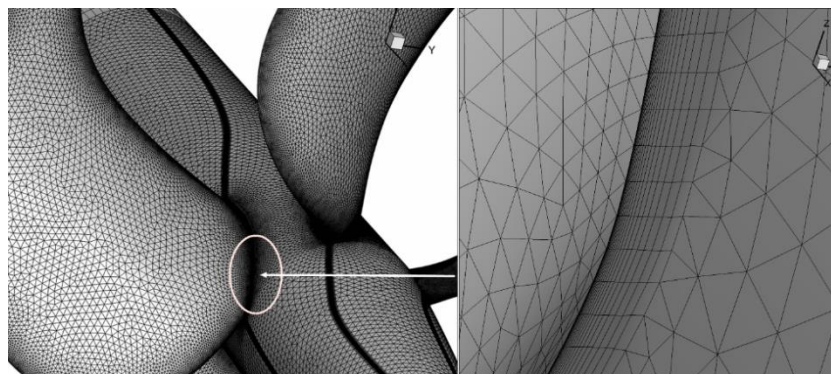


Figure 17: Zoom-up view of blade-surface prism layer grids

Table 2: Wall distance averaged over blade surfaces (y^+) and total cells number

| | 4381 | 4382 | 4382-1 | 4382-2 | 4382-3 |
|------------------------------|------|------|--------|--------|--------|
| y^+ | 1.41 | 1.47 | 1.19 | 1.16 | 1.38 |
| Total cells number (million) | 5.31 | 5.40 | 5.45 | 6.57 | 5.93 |

The blade, hub, and shaft surfaces are set as stationary no-slip walls in the rotating frame. As shown in Figure 15, the inlet and far boundary are set as velocity inlets, while the outlet as the pressure outlet. For a fixed rotation speed of the propeller, the inlet velocity is specified according to the desired value of J , the advance coefficient. The convection terms in all the governing equations are discretized with 2nd-order upwind schemes. The SIMPLE scheme is employed for velocity-pressure coupling.

3.2 Numerical results and analysis

Figure 18 compares the numerical results of the open water performance for five propellers, and K_T , K_Q and η_0 at design condition $J=0.889$ are presented in table 3. The numerical results that the performances of five propellers are close except low advance coefficient, the relative differences of K_T , K_Q and η_0 between each propeller are within 3.0%, 3.3% and 1.3% at design condition, respectively.

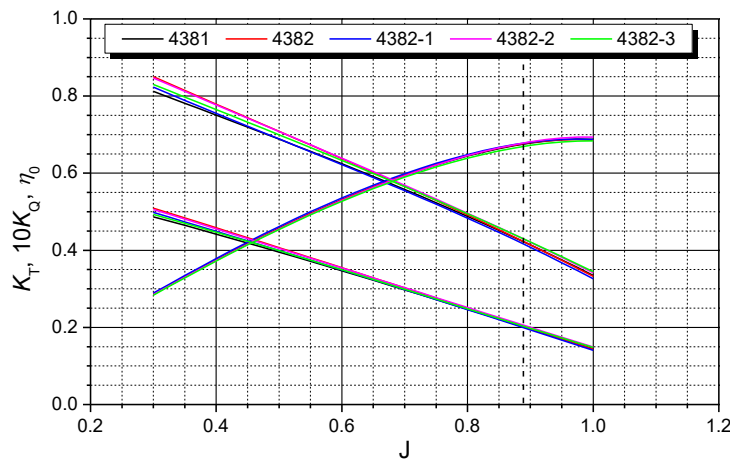


Figure 18: Numerical results of open water performance of the five propellers

Table 3: Numerical results of open water performance at design condition ($J=0.889$)

| | 4381 | 4382 | 4382-1 | 4382-2 | 4382-3 |
|----------|-------|-------|--------|--------|--------|
| K_T | 0.202 | 0.202 | 0.200 | 0.206 | 0.203 |
| $10K_Q$ | 0.422 | 0.423 | 0.416 | 0.429 | 0.430 |
| η_0 | 0.675 | 0.677 | 0.678 | 0.678 | 0.669 |

Figure 19 and 20 shows the section pressure coefficient distribution along the chord of $0.75R$ and $0.97R$ at $J=0.7$ and $J=0.889$. The horizontal axis is dimensionless chordwise coordinate x/C , and $x/C=0$ at leading edge, $x/C=1$ at trailing edge. The peak of negative pressure near leading edge decreases from 4381 propeller to 4382-2 propeller at $0.75R$ under $J=0.7$ and $J=0.889$,

which agrees with the cavitation test that the radial range of sheet cavitation decreases from 4381 propeller to 4382-2 propeller. And for 4382-3 propeller, the tip rake affects little at 0.75R. Comparing 4382-2 and 4382-3 propeller, the load on tip is reduced due to the tip rake. At 0.97R, comparing 4382-1 and 4382-2 propeller, increasing skew at outer radius reduces the pressure difference between the suction and pressure side near the leading edge at $J=0.7$, which can explain the reason of tip vortex inception delay with balance skew distribution at low advance coefficients.

Figure 19 and 20 shows the pressure coefficient contour of the plane perpendicular to the shaft axis, $0.1D$ downstream from the blade tip, at $J=0.7$ and $J=0.889$. It is seen that the strength of tip vortex decreases in turn from 4381 propeller to 4382-3 propeller, which coincides with the test results of tip vortex cavitation inception.

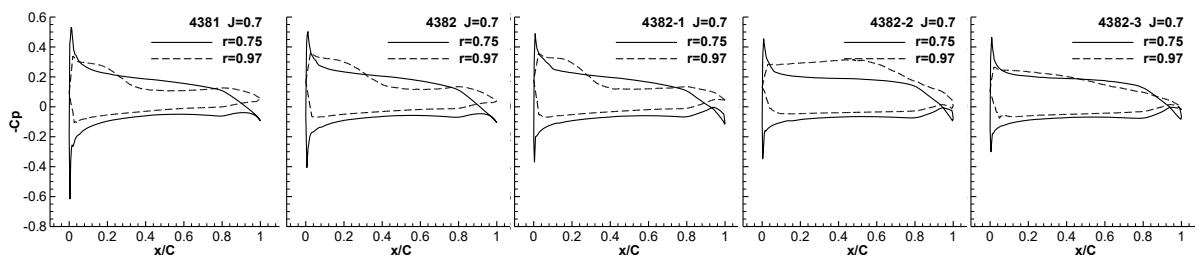


Figure 19: Section pressure at 0.75R and 0.97R ($J=0.7$)

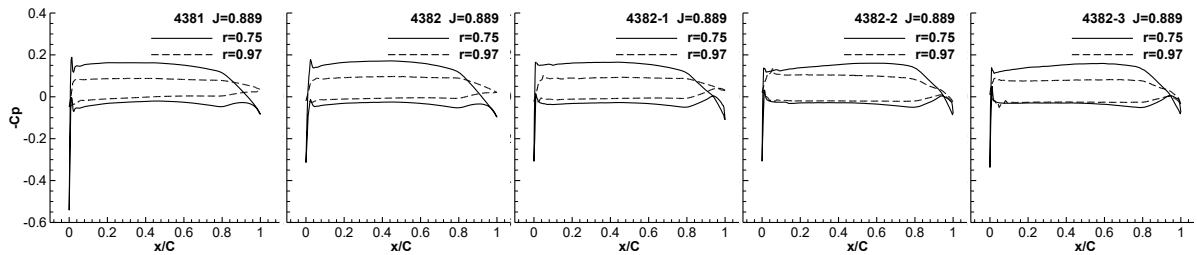


Figure 20: Section pressure at 0.75R and 0.97R ($J=0.889$)

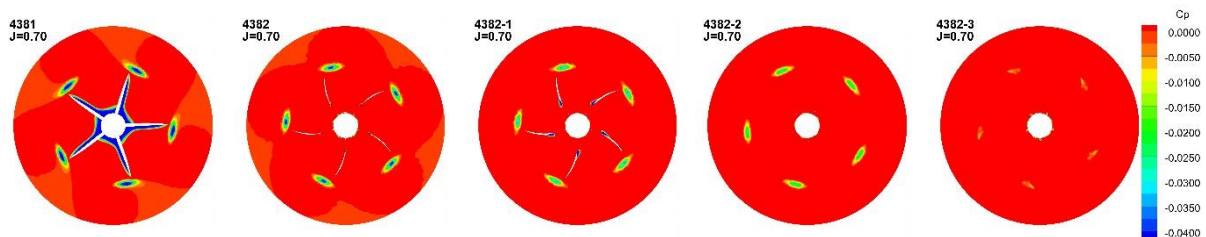


Figure 21: Pressure fields in the cross section $0.1D$ downstream of the tip ($J=0.7$)

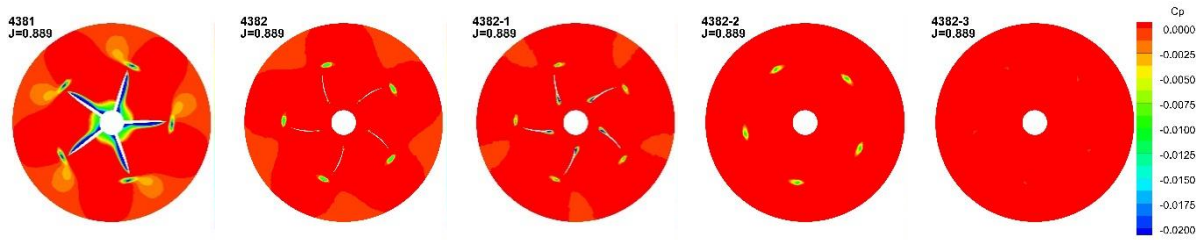


Figure 22: Pressure fields in the cross section $0.1D$ downstream of the tip ($J=0.889$)

4 CONCLUSIONS

In this paper, the effects of propeller blade geometry, section thickness distribution, skew and tip rake, on cavitation and noise were studied by model tests and numerical simulations. Propeller model tests were carried out in SJTU Cavitation Tunnel. Also the hydrodynamic performances were simulated by solving the Reynolds-averaged Navier-Stokes (RANS) equations using the Fluent software. According to the test and numerical results, the following conclusions are drawn,

- Increasing skew can delay tip vortex cavitation, suction side cavitation and pressure side cavitation inception significantly. Increasing skew near blade tip can delay tip vortex cavitation inception further at low advance coefficients. After the cavitation occurs, increasing skew can reduce the area of the sheet cavitation, and decrease the sound pressure level at high frequency.
- Thickening the section profile near leading edge can delay the suction side and pressure side cavitation inception, and make cavitation stable when cavitation incepts.
- Both of skew and section thickening at leading edge can decrease the peak of negative pressure near leading edge.
- Tip rake can reduce the strength of tip vortex, and delay the tip vortex cavitation inception significantly.

REFERENCES

- [1] Chiba N., A relation between circulation distribution and tip vortex cavitation of marine propellers [C]. AIAA, 27th Joint Propulsion Conference, Sacramento, CA, USA, June 24-26, 1991.
- [2] Stainer M.J., The effect of radial circulation distribution on propeller cavitation [C]. PROPCAV '95 Conference on Propeller Cavitation, Newcastle upon Tyne, UK, 1995.
- [3] Kuiper G., Effects of skew and rake on cavitation inception for propellers with thick blade sections [C]. 20th Symposium on Naval Hydrodynamics, Santa Barbara, USA, 1994.
- [4] Choi G.I., The effect of propeller skew and rake on the fluctuating pressure [J]. Journal of the Korean Society of Marine Engineering, 21(4), 1997, pp364-371.
- [5] Yamasaki S., Okazaki A., Design and model tests of a backward tip rake propeller for a low speed ship [J]. The Japan Society of Naval Architects and Ocean Engineers, Vol.5, 2007, pp163-168.
- [6] Yamasaki S., Okazaki A., et al., The effect of tip rake on propeller induced pressure fluctuations [J]. The Japan Society of Naval Architects and Ocean Engineers, Vol.17, 2013,

- pp9-17.
- [7] Xin G.Z., The Investigation of the effect of blade geometry on tip vortex cavitation inception and its mechanism[D], China Ship Research & Development Academy, March 2014.
 - [8] Boswell R.J., Design, cavitation performance, and open-water performance of a series of research skewed propellers [R]. Report No.3339, America: Naval Ship Research and Development Center, 1971.

PROPELLER TIP VORTEX CAVITATION MITIGATION USING ROUGHNESS

Abolfazl Asnaghi*, Urban Svennberg[†], Robert Gustafsson[†] and Rickard E.
Bensow*

*Department of Mechanics and Maritime Sciences, Chalmers University of Technology, Sweden
e-mail: asnaghi@chalmers.se, rickard.bensow@chalmers.se

[†] Rolls-Royce Hydrodynamic Research Center, Rolls-Royce AB, Kristinehamn, Sweden
e-mail: urban.svennberg@rolls-royce.com, robert.gustafsson@rolls-royce.com

Abstract. This paper presents an investigation of roughness application on marine propellers in order to alter their tip vortex properties, and consequently mitigate tip vortex cavitation. SST $k - \omega$ model along with a curvature correction is employed to simulate the flow on an appropriate grid resolution for tip vortex propagation, at least 32 cells per vortex diameter. The roughness is modelled by using a rough wall function to increase the turbulent properties in roughed areas. In one case, roughness geometry is included as a part of the blade geometry, and the flow around them are resolved. To minimize the negative effects of the roughness on the propeller performance, the roughness area is optimized by simultaneous consideration of the tip vortex mitigation and performance degradation. For the considered operating condition, it is found that having roughness on the tip region of suction side can reduce the cavitation inception by 18 % while keeping the performance degradation in a reasonable range, less than 2%.

Key words: Cavitation, Mitigation, Tip Vortex, Inception, CFD

1 INTRODUCTION

Tip vortex cavitation (TVC) is usually the first type of cavitation that appears on a propeller. Therefore, it is considered as the main controlled cavitation characteristics in the design procedure of low-noise propellers, where their operating profiles require very low radiated noise emissions. Several approaches are proposed and tested to modify tip vortex structures in order to prevent or at least delay tip vortex cavitation inception. Among these approaches, the application of roughness is a promising way [1]. Surface roughness affects the tip vortex roll-up as the roughness elements promote transition to turbulence in laminar boundary layers and therefore alter the near-wall flow structures. If size, pattern, and location of roughness elements are selected appropriately, the alteration can lead to tip vortex breakdown, and consequently lead to TVC mitigation.

The selected propeller is from a research series of highly skewed propellers having a low effective tip load and is typical for yachts and cruise ships, where it is very important to suppress

and limit propeller-induced vibration and noise. In this type of propellers, the main source of noise and vibration is the vortex cavitation in the tip region. In our previous studies, numerical simulations of tip vortex flows around this propeller having smooth blades were carried out and successfully compared with experimental measurements [2]. The aim of the present study is to provide further knowledge about the effects of the surface roughness on the TVC and the possibility of using roughness to delay the cavitation inception.

The tip vortex flows around the propeller are simulated by the two equation SST $k-\omega$ model of OpenFOAM on appropriate grid resolutions for tip vortex propagation, at least 32 cells per vortex diameter according to previous studies guidelines [3, 4]. The η_3 curvature correction method is employed to prevent overprediction of turbulent viscosity in highly swirling tip regions [5, 6].

The roughness is included in the simulations by employing two different approaches. In the first approach, rough wall functions are used to mimic the effects of roughness by increasing the turbulent properties in roughed areas [7]. The second approach modifies the mesh topology by removing cells in roughed areas to create random roughness elements. While the first approach models the roughness effects, the second one actually includes the geometry change into the simulations. However, as the roughness elements have very small sizes, resolving the flow around them demands a very fine mesh resolution.

Roughness application on different blade areas, e.g. suction side and pressure side are considered. It is evaluated how roughness alters the vortical structures on the blade and as a result in the tip vortex region. The analysis provides further knowledge on how roughness changes the flow pattern around the blade tip and mitigates the cavitation. The propeller performance degradation in different roughness conditions is computed and by considering the tip vortex cavitation inception improvement, the most optimum roughness pattern is proposed.

2 EQUATIONS

To model the roughness effect, the wall function developed by Tapia [8] for the inner region of the turbulent boundary layer or the log-law region (e.g. $11 \leq y^+$ in OpenFOAM wall functions) is used,

$$u^+ = \frac{1}{\kappa} \ln(Ey^+) - \Delta B, \quad (1)$$

with the von Karman constant $\kappa = 0.41$, the constant $E=9.8$, the dimensionless wall distance $y^+ = u_\tau y/\nu$, and the velocity shift correction ΔB due to the roughness elements. The nondimensional roughness height is presented by $K_s^+ = u_\tau K_s/\nu$ where K_s is the roughness height, $u_\tau = \sqrt{\tau_w/\rho}$ is the shear velocity, and τ_w is the wall shear stress. In this approach, the height of the elements should be smaller than the height of the cells adjacent to the wall, i.e. $K_s^+ \leq y^+$. Otherwise, the part of roughness elements located outside the adjacent cells will not be included in the modelling.

In a smooth regime represented by $K_s^+ \leq 2.5$, the correction ΔB is set to zero and the wall function recalls the smooth wall function. For a transitionally rough regime, $2.5 < K_s^+ < 90$, the correction reads,

$$\Delta B = \frac{1}{\kappa} \ln \left[\frac{K_s^+ - 2.25}{87.75} + C_s K_s^+ \right] \sin(A), \quad (2)$$

where $A = 0.425[\ln(K_s^+) - 0.811]$, and C_s is a constant representing shape and form of roughness elements. It is suggested that C_s varies from 0.5 to 1 where $C_s = 0.5$ corresponds to the uniformly distributed sand grain roughness. If the roughness elements deviate from the sand grains, the constant roughness should be adjusted by comparing the results with experimental data.

For a fully rough regime having $90 \leq K_s^+$, the ΔB correction is represented by,

$$\Delta B = \frac{1}{\kappa} \ln \left[1 + C_s K_s^+ \right]. \quad (3)$$

The turbulent viscosity of cells adjacent to the rough wall is then recalculated using the following formula,

$$\mu_t = \mu \left[\frac{y^+ \kappa}{\ln(Ey^+/e^{\kappa \Delta B})} - 1 \right]. \quad (4)$$

The flow is simulated by employing the SST $k - \omega$ model [3]. To include the effects of curvature correction, the production term of the ω equation is multiplied by F_{rc} ,

$$F_{rc} = 1 + \alpha_1 |\eta_3| + 3\alpha_1 \eta_3, \quad (5)$$

where $\alpha_1 = -0.2$, and $C_r = 2.0$. η_3 is a velocity gradient invariants [5],

$$\eta_1 = \bar{S}_{ij}^* \bar{S}_{ij}^*, \quad \eta_2 = \bar{\Omega}_{ij}^* \bar{\Omega}_{ij}^*, \quad \eta_3 = \eta_1 - \eta_2, \quad (6)$$

defined through the non-dimensional strain rate and rotational rate tensors,

$$\bar{S}_{ij}^* = \tau \bar{S}_{ij}, \quad \bar{\Omega}_{ij}^* = \tau \bar{\Omega}_{ij}^{mod}, \quad (7)$$

where the strain rate and rotational rate tensors are defined by,

$$\bar{S}_{ij} = \frac{1}{2} \left(\frac{\partial \bar{u}_i}{\partial x_j} + \frac{\partial \bar{u}_j}{\partial x_i} \right), \quad \bar{\Omega}_{ij} = \frac{1}{2} \left(\frac{\partial \bar{u}_i}{\partial x_j} - \frac{\partial \bar{u}_j}{\partial x_i} \right). \quad (8)$$

As can be seen, η_1 represents the non-dimensional strain rate magnitude, η_2 represents the non-dimensional vorticity magnitude, and η_3 is a linear combination of these two independent velocity-gradient invariants. Please refer to [3] for further information.

3 CASE DESCRIPTION

The basic design of the propeller is from a research series of five-bladed highly skewed propellers having low effective tip load where it is very important to suppress and limit propeller-induced vibration and noise. The main or first source of noise, for this type of propellers, is cavitation in the tip region.

The computational domain of the propeller is presented in Figure 1. The domain is simplified to a cylinder extending 4D upstream the propeller and 8D downstream of the propeller where $D=0.2543$ m is the diameter of the propeller. In order to model the moving mesh (i.e. relative motion between the propeller and the external domain), the computational domain has been decomposed into two regions connected to each other through AMI (Arbitrary Mesh Interpolation) boundaries. While the outer region is stationary, the rotation of the region close to the propeller where all interesting flow phenomena occur has been handled by MRF.

The simulations are conducted at a constant inlet velocity, a fixed pressure outlet boundary and the advance ratio of the propeller is then set by adjusting the rotational rate of the propeller. No-slip wall boundary condition is used for the propeller and the shaft. The outer cylinder boundary is set as a slip boundary to reduce the mesh resolution requirements far from the propeller. Then, the blockage effects are considered in comparing the numerical results with related experimental measurements. All of the simulations are conducted at one J value where the tip vortex forms on the suction side of the blade. The comparison between numerical simulations and the experimental measurements of the smooth propeller is presented and discussed in [2].

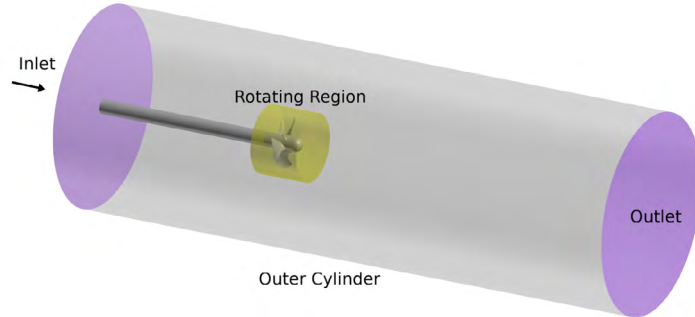
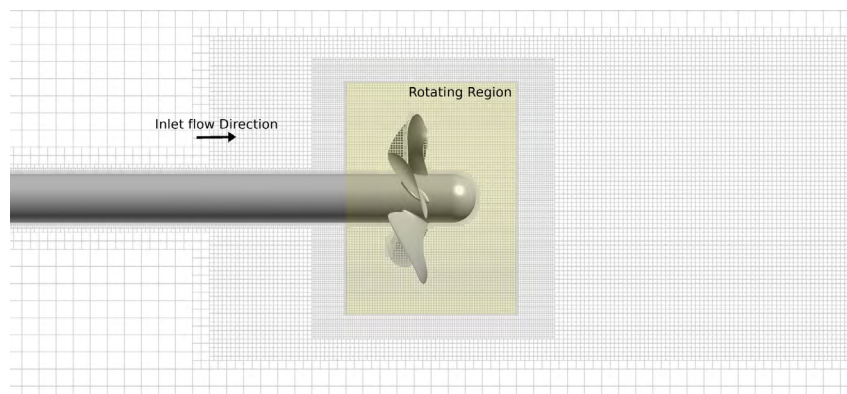


Figure 1: Computational domain of the propeller.

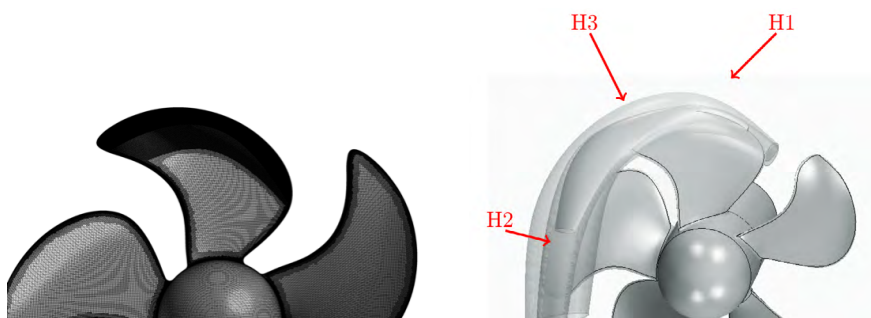
The distribution of the propeller mesh is presented in Figure 2. Different refinement boxes are applied to provide finer resolutions around the rotating propeller region, Figure 2a. The baseline mesh resolution on the blades gives x^+ and $z^+ < 250$, where finer resolutions are provided at the leading edge and trailing edge of the blades. Further finer resolution is achieved where tip refinement is applied. The nominal values given above are calculated based on the inlet velocity and the propeller diameter as the reference length and verified afterwards. The prismatic layers of the refined blade consists of 20 layers having extrusion factor of 1.15 where the first cell wall normal resolution is $y^+ = 35$.

The tip vortex refinement is applied on one blade only, where three helical shape refinement zones are defined based on the primary vortex trajectory. The refinement zones cover the tip of the blade, and therefore provide more refined grid resolutions on the tip of this blade, Figure 2b. These helical refinement regions provide spatial resolutions as fine as 0.2 mm, 0.1 mm, and 0.05 mm in H1, H2, and H3 regions, respectively.

The roughness pattern is tested on the suction side and pressure side of the refined blade tip, Figure 3. The study consist of the roughness modelling on the blade tip of the suction side, SS, of the pressure side, PS, and of the suction and pressure sides, SS+PS. The fully rough, FR, blade condition is also included. For one case where the roughness is only applied on the suction side tip region, the mesh topology is modified by removing cells to include the roughness elements into the simulations, Figure 3c. This will provide the opportunity to resolve the flow around these roughness elements.



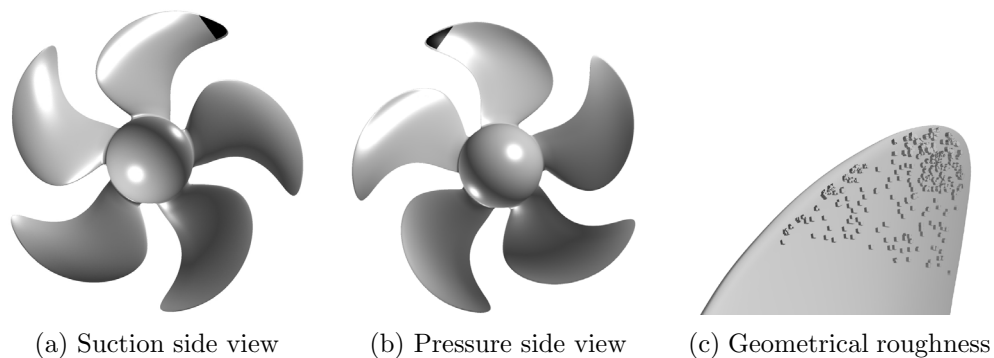
(a) Streamwise resolution



(b) Blade surface resolution

(c) Helical tip refinement

Figure 2: Mesh distribution of the propeller.



(a) Suction side view

(b) Pressure side view

(c) Geometrical roughness

Figure 3: (a) and (b): Roughness areas on the suction side and pressure side of the refined blade; (c): distributions of roughness elements on the SS.

4 RESULTS

The numerical results are presented in two parts. In the first part, effects of having roughness on different areas of the blade are evaluated. It includes tip vortex cavitation inception

prediction, and also the propeller performance. The roughness size is selected to be equal to 250 μm and it is assumed that the roughness is distributed uniformly, i.e. $C_s = 0.5$. In the second part, for the case where the roughness is only applied on the suction side of the blade, the flow around the roughness elements are resolved.

4.1 Evaluation of roughness patterns

The performance of the propeller for different surface conditions are presented in Table 1. Thrust and torque coefficients as well as the efficiency, are presented relative to the smooth propeller condition. The results indicate an increase in the torque coefficient when roughness is included. The thrust coefficient, however, is more dependent on the roughness pattern. For the FR blade, the maximum thrust decrease, -13.4 %, and efficiency drop, -16.6 %, are observed. Having roughness on the PS leads to higher K_t but it also demands for higher K_q . This eventually results in a lower propeller efficiency, around -2.5 %. When roughness is only applied on the SS, the variation of the thrust and torque is minimum. Further quantitative justification of these results demands uncertainty analysis which has been postponed for future studies. The results, however, clearly confirm that in order to minimize the negative effects of roughness on the propeller performance, the roughness area should be optimized.

Table 1: Variation of thrust, torque and efficiency relative to the smooth foil condition for different roughness patterns. Refer to Figure 3 for descriptions of SS, PS, and SS+PS.

| Case | K_t (%) | K_q (%) | Efficiency (%) |
|--------|-----------|-----------|----------------|
| Smooth | – | – | – |
| SS | -0.8 | 0.2 | -1.0 |
| PS | 1.2 | 3.8 | -2.5 |
| SS+PS | 2.1 | 4.6 | -2.4 |
| FR | -13.4 | 3.8 | -16.6 |

In Figure 4, the predicted cavitation inception based on the minimum pressure criterion is presented for different roughness patterns. As the propeller was not tested at the selected condition, the experimental data is extrapolated to this operating condition. Among the results, the FR condition has the lowest cavitation inception comparing to other patterns. The predicted cavitation inception in SS and SS+PS patterns is close to each other, and the difference between them is believed to lie in the uncertainty of the numerical results in the current simulations. The results indicate the necessity of having roughness on the side where the tip vortex forms, e.g. suction side in the evaluated operating condition. We also observed some stability and convergence issues with the simulations related to PS and SS+PS. These could be related to the flow gradients at the low quality cells on the edge of the blades at the interface of the prismatic layers and the volumetric cells. Another reason could be related to the nature of curvature correction model. The curvature correction reduces the turbulent viscosity and by that increases the formation of vortical structures and therefore increases the unsteadiness of the flow.

It is noted that compared to the LES simulations on the fully resolved resolution for the same operating condition of the smooth blade [2], the tip vortex is under predicted in the RANS

simulations. Where in LES simulations of fully resolved boundary layer resolution the cavitation inception is found to be around 7.4, for wall modelled RANS simulation the cavitation inception is around 5.5. This, however, is not a major issue in the current study, as the main objective is to compare different roughness patterns and to compare how the tip vortex forms on them rather than exact prediction of tip vortex.

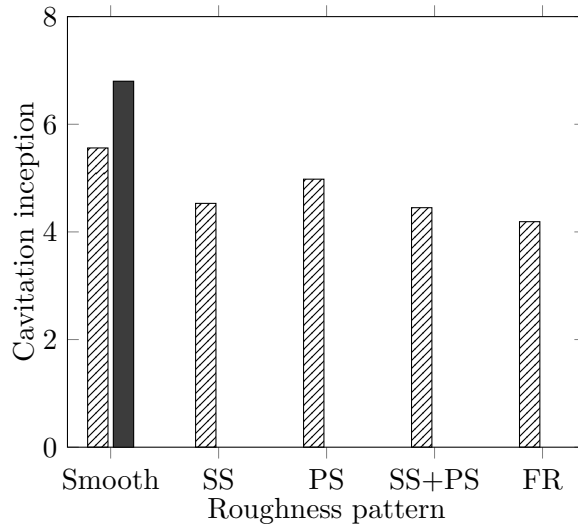


Figure 4: Variation of the cavitation inception versus different surface roughness areas, solid bar is the extrapolated experimental measurements for the smooth blade.

Among the studied cases, the lowest cavitation inception points belong to the FR blade, and then SS or SS+PS which have similar inception prediction. However, as the performance degradation is much lower in SS, this case is considered as the outcome of the roughness area optimization.

4.2 Evaluation of roughness modelling

Modelling of roughness with a wall function has some limitations, especially for the employed wall function where the roughness pattern is included into the CFD with only two representing values, i.e. roughness height and C_s . Depending on the topology of roughness elements, modelling them with an averaged value as sand grains may increase the deviation between numerical results and experimental observations. As a first attempt, in this section the numerical simulations of wall modelled roughness is compared with resolving the flow around the roughness elements.

In Figure 5 and 6, numerical results of resolved flow around the roughness elements are presented. The figures are the zoomed view of the blade having the roughness elements on its suction side where the blade is colored with the turbulent viscosity. The figures include the pressure iso-surface of the saturation pressure colored black, and the vortical structure based on $Q=1000$ presented with transparent gray color.

The low turbulent viscosity around the roughness elements indicates formation of vortical

structures around them. The location of these structures are predicted by the curvature correction model, and then the turbulent viscosity is lowered there to allow the flow development. This can be noted from Figure 6 where the distribution of Q is represented.

Formation of vortical structures around the roughness elements weakens the tip vortex, and mitigates the tip vortex cavitation inception. However, they lead to formation of several low pressure spots on the blade. These spots can intensify the cavitation on the blade as the roughness elements can easily introduce the nuclei into these low-pressure region. This poses the demand for the simultaneous analysis of cavitation inception in tip vortex and on the blade.

It should be noted that although the spatial resolution around the roughness elements is very coarse to accurately resolve the flow around them, it is still possible to decently predict their impact on the tip vortex.

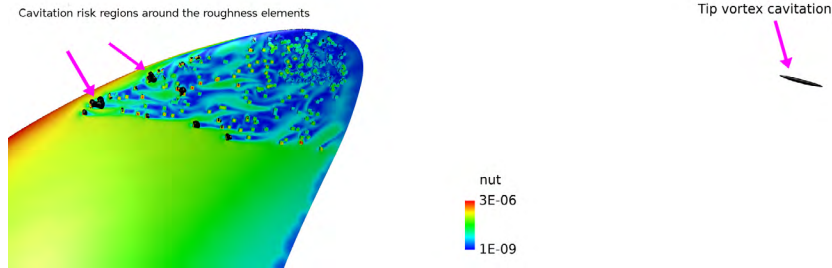


Figure 5: Distribution of the turbulent viscosity around the roughness elements along with the iso-surface of pressure colored black, zoomed view of the roughness elements on the SS.

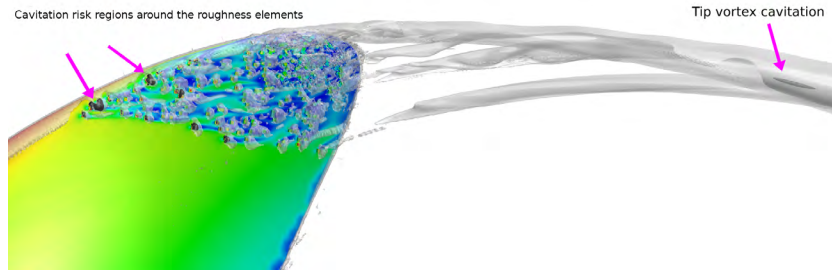


Figure 6: Distribution of the vortical structures around the roughness elements along with the iso-surface of pressure colored black, zoomed view of the roughness elements on the SS.

Table 2: Variation of thrust, torque and efficiency relative to the smooth foil condition for different roughness modelling approaches.

| Case | K_t (%) | K_q (%) | Efficiency (%) |
|-----------------------|-----------|-----------|----------------|
| Smooth | – | – | – |
| SS Wall modelled | -0.8 | 0.2 | -1.0 |
| SS Roughness modelled | -1.9 | 0.1 | -1.8 |

For the resolved flow around the roughness elements, the cavitation inception is found to be around 3.28 while with wall-modelling approach the predicted inception point is 4.53. Lower propeller performance is noted for the resolved flow as well, Table 2. When conducting a comparative analysis, e.g. comparing different patterns, the large difference between the cavitation inception predictions has less importance. But when it comes to find the balance between the cavitation tip vortex and the blade cavitation, the accurate prediction of flow around roughness elements is inevitable.

5 CONCLUSIONS

The results on the tested propeller show that the application of roughness can be a solution to mitigate a tip vortex. It is found that the area where the roughness is applied has a direct impact on the interactions between the roughness elements and boundary layers over the blade, and eventually on the strength of the tip vortex. The presence of roughness alters the boundary layer distribution and consequently affects the tip vortex formation and development. This leads to a weaker tip vortex, and mitigation of tip vortex cavitation.

It is noted that the negative effects of roughness on the propeller performance can be minimized when the roughness area is optimized. This can be done by considering different roughness patterns on the suction side and pressure side of the propeller. For the tested propeller having full rough blades, the performance efficiency drops 16.6 % while in the optimum roughness area the performance degradation can be kept below 2 %.

The difference between the cavitation inception predicted by the wall modelled roughness and resolved flow is found to be considerable where the predicted cavitation inception by wall modelled approach is 4.53 and for the resolved flow the inception point is 3.28. However, there are still some uncertainties about resolving the flow over the roughness elements by RANS modelling that demands for further investigations.

When the flow around the roughness elements are resolved, several low pressure spots on the blade are observed. These low pressure regions can lead to bubble or sheet cavitation on the blade. Therefore, the compromise between tip vortex and bubble cavitation is needed when roughness patterns are compared.

It is found that having roughness on the tip region of blade suction side is sufficient to mitigate the tip vortex and at the same time keep the performance degradation at a reasonable level. However, it should be considered that the current study focuses only on one operating condition where the tip vortex is formed on the suction side of the blade. To generalize the finding further studies with a wider range of operating conditions are necessary.

ACKNOWLEDGEMENTS

Financial support for this work has been provided by Vinnova through the RoughProp project, Grant number 2018-04085. The simulations were performed on resources at Chalmers Centre for Computational Science and Engineering (C3SE) provided by the Swedish National Infrastructure for Computing (SNIC).

REFERENCES

- [1] Kruger, C. and Kornev, N. and Greitsch, L. *Influence of propeller tip roughness on tip vortex strength and propeller performance*. Ship Technology Research, 63(2):110120, 2016.
- [2] Asnaghi, A. and Svennberg, U. and Bensow, R.E. *Numerical and experimental analysis of cavitation inception behaviour for high-skewed low-noise propellers*, Applied Ocean Research, 79:197214, 2018.
- [3] Asnaghi, A. *Computational modelling for cavitation and tip vortex flows*, PhD -thesis, Chalmers University of Technology, 2018.
- [4] Asnaghi, A. and Bensow, R.E. and Svennberg, U. *COMPARATIVE ANALYSIS OF TIP VORTEX FLOW USING RANS AND LES*, VII International Conference on Computational Methods in Marine Engineering, MARINE 2017At: Nantes, France, 2017.
- [5] Arolla, S.K. *Modeling and eddy simulation of rotating and curved turbulent flows*, Doctoral Thesis, Iowa State University, Ames, Iowa, 2013.
- [6] Arolla, S.K. and Durbin, P.A. *Modelling rotation and curvature effects within scalar eddy viscosity model framework*, Int. J. Heat Fluid Flow, 39 (1), 2013.
- [7] Asnaghi, A. and Svennberg, U. and Gustafsson, R. and Bensow, R.E. *Roughness Effects on the Tip Vortex Strength and Cavitation Inception*, Sixth International Symposium on Marine Propulsors: smp19, Rome, Italy, May 2019.
- [8] Tapia, X.P. *Modelling of wind flow over complex terrain using OpenFoam*, Master thesis, University of Gavle, 2009.

ASSESSMENT OF COMPUTATIONAL TECHNIQUES FOR THE PREDICTION OF ACOUSTIC SOURCES FROM LIFTING SURFACES USING LES AND DNS

Tom A. Smith* and Yiannis Ventikos*

* University College London, Dept. Mechanical Engineering, London, WC1E 7JE, United Kingdom
e-mail: tom.smith.17@ucl.ac.uk

Key words: DNS, LES, Boundary Layer Transition, Trailing Edge Flow

Abstract. The acoustic field produced by the flow over a lifting surface is closely linked to the dynamics of the boundary layer. The location and mechanism of the transition strongly influences the character of the trailing edge flow and surface pressure fluctuations and so accurately predicting the transition process is critical for acoustic analyses. In this study, a comparison of DNS and LES is undertaken for a transitional boundary layer flow over a foil at a moderate Reynolds number. The effects of the of sub-filter scale model, discretisation scheme and mesh resolution are considered to better understand how LES can be used to accurately resolve external boundary layer and trailing edge flows. Significant differences are seen for the different modelling approaches and the reasons for this are explored. A second case is then considered using LES which has a very different boundary layer and trailing edge flow. This case highlights the important link between the transitional boundary layer dynamics, trailing edge flow and the acoustic field.

1 INTRODUCTION

Transitional boundary layers represent an important class of flows in marine engineering. For flows over lifting surfaces at moderate to high Reynolds numbers such as propeller, hydrofoil and pump flows, the boundary layer dynamics have a significant influence on the trailing edge flow and resulting noise. It has been shown experimentally, for example [1], that large amplitude tonal noise can be generated at a foil trailing edge if the pressure-side boundary layer is still transitional at the trailing edge. This occurs if the Tollmien-Schlichting (T-S) instabilities responsible for the transition become amplified by a separated region at the trailing edge. If the transition occurs closer to the leading edge, the 2D structures associated with the Tollmien-Schlichting instabilities will have broken down into 3D structures that will scatter as broadband noise at the trailing edge. Accurately capturing the location and mechanism of the transition is therefore paramount for acoustic analyses.

Whilst DNS has provided detailed insights into the flow physics of transitional boundary layers, for example in [2], [3], this method is still far too expensive to apply to many practical flows of interest in hydro-acoustics. Therefore, attention over the past decade has turned to the use of large eddy simulations for acoustic analyses, which allow for the larger turbulent scales to be resolved whilst modelling the smaller scales. A number of recent studies into trailing edge noise, e.g. [4], [5] have used large eddy simulations to provide the source terms for acoustic models such as those developed by Curle, [6] and Ffowcs-Williams and Hawkings, [7]. Most such studies provide only limited verification and uncertainty analysis, and grid sensitivity studies are far less common than for RANS-based analyses. A wide range of approaches are used in terms of sub-filter scale modelling and discretisation, with little published information on the sensitivity of the boundary layer dynamics to the different methods used. Experimental results such as [1], [8] have shown that small changes in the operating conditions can lead to large changes in the boundary layer and acoustic field. Therefore, in order to use LES as a predictive tool, a better understanding of how well different modelling techniques capture these dynamics is needed.

In this study, 2 separate cases are considered. For Case 1, both LES and DNS are used to model the flow over a NACA0012 foil at a Reynolds number of $Re = 10^5$ and an angle of attack of $\alpha = 4^\circ$. Two sub-filter scale models are used and different approaches to the discretisation of the convective terms are considered. Grid independent DNS data are obtained which provide an excellent benchmark against which a number of large eddy simulations are compared. This provides a better understanding of how well different modelling approaches capture the transition process and resulting turbulent boundary layer. Case 2 then takes the best approaches from Case 1 and considers the flow with a Reynolds number of $Re = 1.5 \times 10^5$ and a 0° angle of attack. Unlike the broadband trailing edge flow and surface pressure field observed for Case 1, experiments in [8] have shown that the second case is dominated by narrowband fluctuations due to the presence of Tollmien-Schlichting waves close to the trailing edge. Thus by considering these cases we are able to explore the physical relationship between the boundary layer transition and the trailing edge flow as well as understand how LES can be used to analyse this important class of flows.

2 METHODS

The governing equations for an incompressible Newtonian fluid are given below.

$$\frac{\partial U_i}{\partial x_i} = 0 \quad (1)$$

$$\frac{\partial U_j}{\partial t} + U_i \frac{\partial U_j}{\partial x_i} = -\frac{1}{\rho} \frac{\partial p}{\partial x_j} + \nu \frac{\partial^2 U_j}{\partial x_i^2} \quad (2)$$

For Direct Numerical Simulation, all of the flow scales are resolved and so no further modelling is required. For large-eddy simulation, the flow field is split into a resolved part and a modelled part by spatially filtering the continuity and momentum equations. The latter part, representing the higher wave-number turbulence, is then modelled using a sub-filter scale model analogous

to the turbulence models used in a RANS approach. The filtered equations are derived by introducing a general filtering operator, G , to each variable:

$$\bar{\phi}(\mathbf{x}, t) = \int_V G(\mathbf{r}, \mathbf{x}) \phi(\mathbf{x} - \mathbf{r}, t) d\mathbf{r} \quad (3)$$

Applying the filter to each of the variables, the filtered equations are obtained:

$$\frac{\partial \bar{U}_j}{\partial t} + U_j \frac{\partial \bar{U}_i}{\partial x_i} = -\frac{1}{\rho} \frac{\partial \bar{p}}{\partial x_j} + \nu \frac{\partial^2 \bar{U}_j}{\partial x_i \partial x_i} - \frac{\partial \tau_{ij}}{\partial x_i} \quad (4)$$

where

$$\tau_{ij} = \overline{U_i U_j} - \bar{U}_i \bar{U}_j \quad (5)$$

The filtered equations given by equation 4 are not closed and so we must introduce an additional model to account for the effects of the sub-filter scale (SFS) stresses, τ_{ij} . In this study, two different models for the sub-filter scale stresses are considered: the Smagorinsky model and the Local Dynamic k model. The Smagorinsky model, [9], is widely used and is an eddy viscosity model based on a characteristic length, which is usually defined by the grid size. It is also necessary, when using this model, to apply a damping function at walls to force the sub-filter scale viscosity to zero. To this end, a van Driest damping function, [10], is applied in this work. The second sub-filter scale model considered is the Localised Dynamic k Model developed by Kim and Menon, [11]. This is a one-equation transport model for the sub-filter scale turbulent kinetic energy. A dynamic procedure is used to determine the model coefficients which allows for the model to be tuned based only on the smaller resolved local flow scales.

The filter width is most commonly taken as the cube-root of the cell volume. However, this definition can result in the filter width being less than the stream-wise cell length for near-wall meshes, where anisotropic elements are used. This will introduce errors into the flow-field, as the smallest resolved scales will be under-resolved. To mitigate this problem, the following definition is therefore used:

$$\Delta = \lambda \cdot \max(h_x, h_y, h_z), \quad \lambda \in \mathbb{N} \quad (6)$$

In this work, a value of $\lambda = 4$ is used which is based on the work in [12]. The coupled pressure/velocity fields are solved at each time step using the PISO algorithm with an algebraic multi-grid solver for the pressure correction equation. The time derivative is discretised using a 3-point backward scheme and a second-order central scheme is used for the spatial derivatives. The convective terms are also discretised using second-order schemes. For the direct numerical simulations, a pure central scheme is used exclusively whereas for the large eddy simulations, a range of blended approaches are considered which introduce a level of up-winding. The impact of this is discussed in the results.

The geometry considered is a NACA0012 foil with a chord length of 0.3m. For Case 1, a span of $s = 0.2c$ is used whereas a span of $s = 0.1c$ is used for Case 2. The foil has a trailing edge bluntness of $h_{TE} = 0.0025c$, which represents a sharp but physically realistic geometry. A block-structured mesh design is used with a C-grid around the foil. The mesh parameters are

| Case | Mesh | Turbulence | N cells ($\times 10^6$) | Δx^+ | Δy^+ | Δz^+ |
|------|------|------------|------------------------------|--------------|--------------|--------------|
| 1 | A | LES | 1.8 | 42 | 38 | 0.6 |
| | B | LES | 4.1 | 29 | 23 | 0.6 |
| | C | LES | 8.7 | 16 | 15 | 0.6 |
| | D | DNS | 25 | 8 | 8 | 0.6 |
| | E | DNS | 58 | 6 | 5 | 0.4 |
| 2 | F | LES | 2.4 | 29 | 22 | 0.6 |
| | G | LES | 6.7 | 17 | 15 | 0.6 |

Table 1: Near wall mesh parameters for cases 1 and 2.

shown in table 1. Freestream boundary conditions are used at the inlet and outlet for both the pressure and velocity fields. The foil wall is treated as a no-slip boundary and the sub-filter scale turbulence quantities are set equal to zero on all boundaries apart from the outlet, where a zero-gradient condition is applied. Symmetry conditions are used for the side walls.

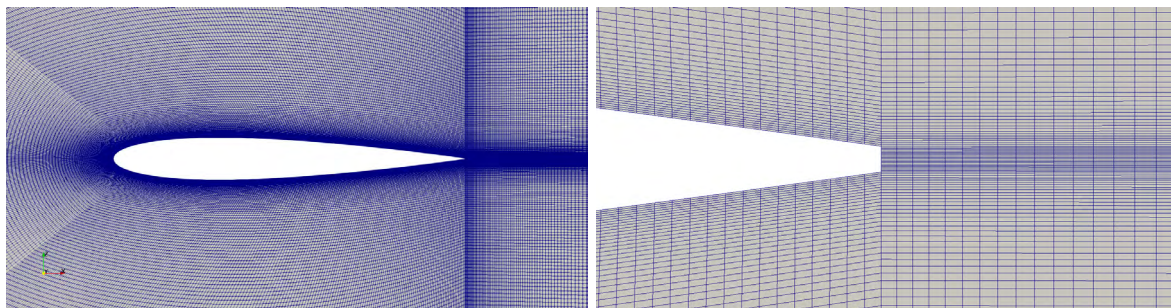


Figure 1: Design of mesh C showing the mesh around the foil and at the trailing edge

3 RESULTS AND DISCUSSION

3.1 Comparison of LES and DNS for Case 1

The DNS data for Case 1 show the growth of a separation bubble on the suction side prior to the transition of the boundary layer. The boundary layer re-attaches at around $x/c = 0.56$, after which a fully turbulent boundary layer forms. Results from meshes D and E are in excellent agreement, indicating grid independence of the results. A comparison of the suction-side boundary layer velocity profiles from the 2 meshes is shown in figure 2. Within the separation bubble, there is a region of reversed flow close to the wall which results in an unstable shear layer. Growing streamwise fluctuations are observed within this region which grow until the reattachment point. These fluctuations are dominated by a narrowband component centred around 140 Hz. After the boundary layer becomes fully turbulent, this component is lost and only broadband fluctuations are seen, as shown in figure 3. The turbulent boundary layer is then convected over the trailing edge, with the broadband turbulent structures decaying into the far

field. The pressure side of the foil remains laminar and attached all the way to the trailing edge.

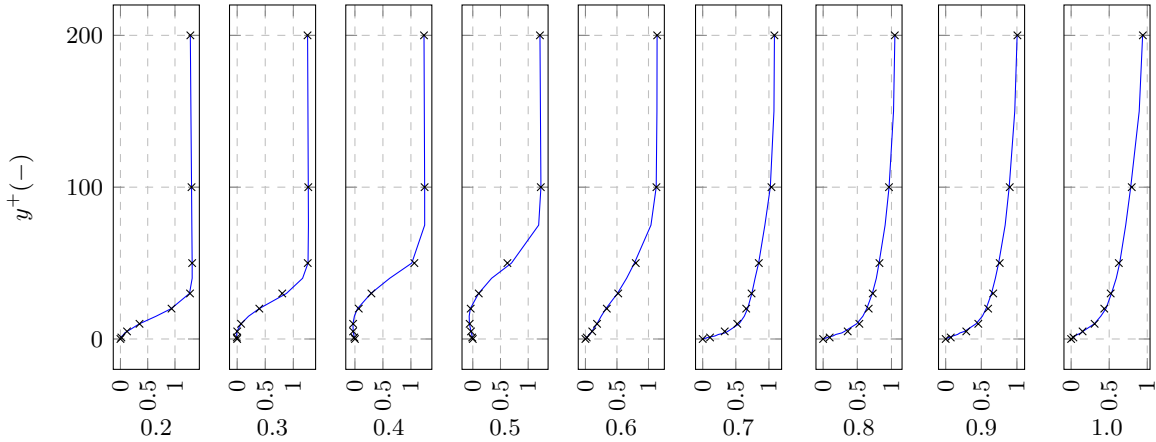


Figure 2: Mean streamwise velocity, U_x/U_∞ , in the boundary layer at different chord-wise locations. The solid line represents mesh E and the markers (x) represent mesh D.

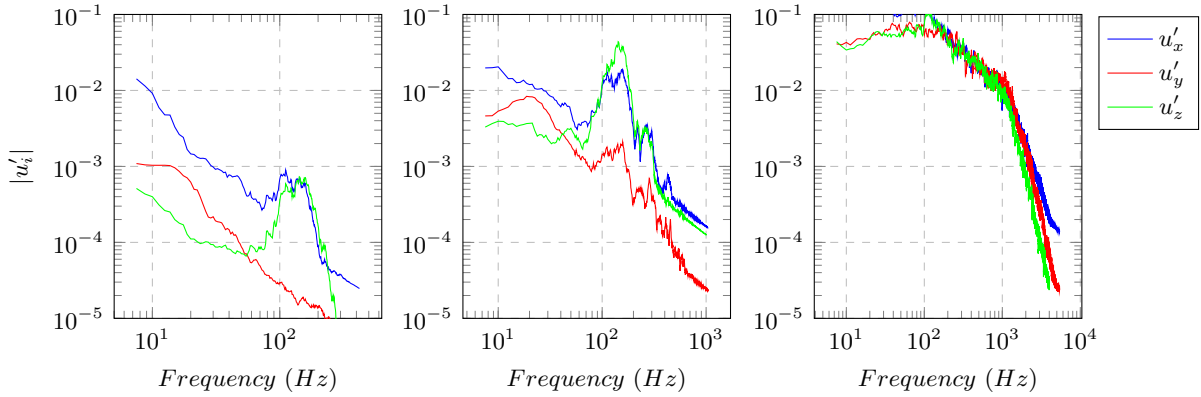


Figure 3: Spectral plots of the streamwise and spanwise velocity fluctuations from mesh E at $y^+ = 30$ for $x/c = 0.4, 0.5, 0.6$.

The large eddy simulations show very different results depending on the sub-filter scale modelling, discretisation scheme and mesh resolution. The interaction between these different components is complex and some of the key findings are explored here. Simulations conducted using the Smagorinsky model do not show any transition and so the boundary layer remains laminar on both the pressure and suction sides of the foil. This is irrespective of what discretisation scheme is used. For all three meshes, there is a separated region close to the trailing edge on the suction side which grows as the mesh is refined. Convergence towards the DNS data is not seen for these simulations. Instead, all exhibit trailing edge flows consistent with laminar boundary layers, with tonal fluctuations corresponding to von Kármán vortex shedding. This can be seen

in the velocity contour plots shown in figure 4. This behaviour contrasts sharply with that seen for the Dynamic k model, which does capture a transition in all cases.

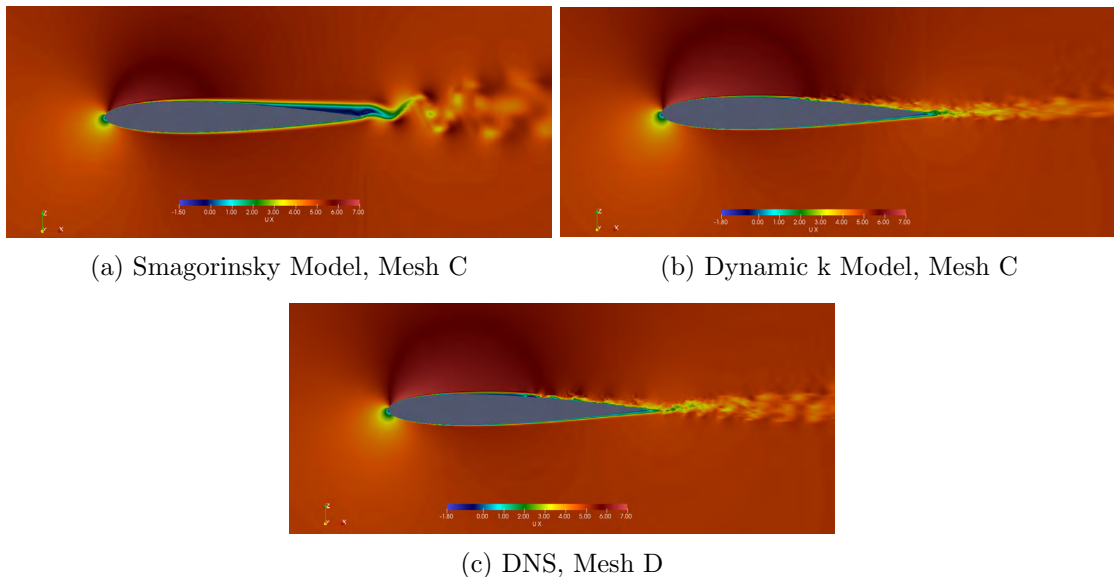


Figure 4: Instantaneous streamwise velocity contours for $t = 20c/U$.

To explain the differences in the flow fields resolved by the two models, we consider the sub-filter scale viscosity in the boundary layer at $x/c = 0.4, 0.5, 0.6$, which covers the region over which the transition should occur. This is shown in figure 5. It can be seen that the dynamic k model is not active in the boundary layer for $x/c = 0.4$, with the sub-filter scale viscosity more than 2 orders of magnitude smaller than the molecular viscosity. The Smagorinsky model predicts a peak sub-filter scale viscosity of $6 \times 10^{-5} \text{ m}^2\text{s}^{-1}$, which is 4 times larger than the molecular viscosity. This prevents the growth of any disturbance in the boundary layer and so prevents the transition from occurring. The dynamic k model only becomes active at $x/c = 0.6$, which the DNS data show corresponds to the emergence of the smallest turbulent scales.

The effect of the differences in the SFS models on the prediction of the trailing edge noise can be seen by looking at the spectra of the trailing edge pressure fluctuations, shown in figure 6. The Smagorinsky model leads to a pressure spectrum dominated by tonal components at multiples of 65 Hz whereas a broadband spectrum is observed for the Dynamic k model, which is in agreement with the DNS data.

The errors associated with the discretisation scheme are small compared to the dissipative effects of the Smagorinsky model but become important when the Dynamic k model is used. For coarser meshes that use a pure central scheme, the flow field is dominated by unphysical velocity fluctuations caused by dispersion errors. These reduce as the mesh is refined, or as larger amounts of up-winding are introduced into the discretisation scheme. These errors can

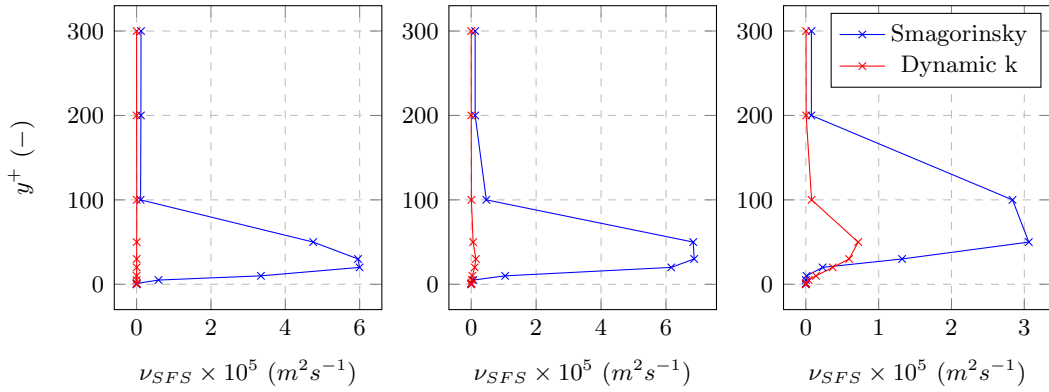


Figure 5: Comparison of the mean sub-filter scale viscosity in the boundary layer at $x/c = 0.4, 0.5, 0.6$ for the two SFS models. Results are for mesh C using a pure central scheme.

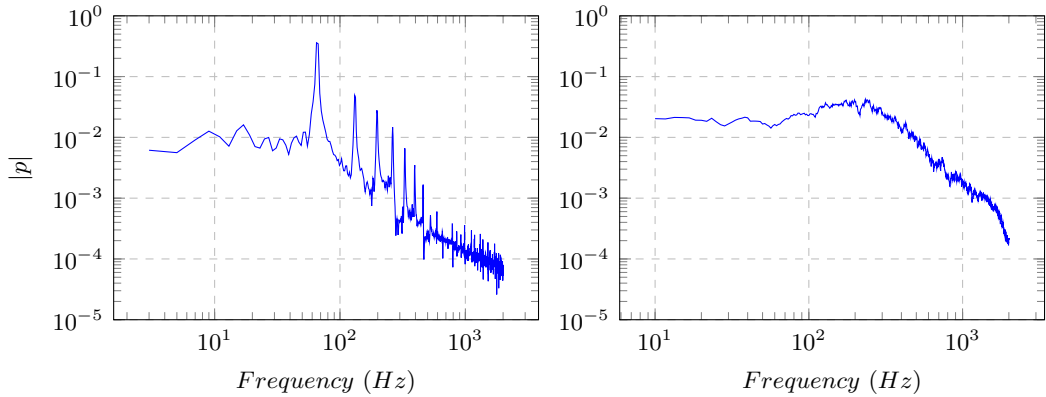


Figure 6: Trailing edge pressure spectra for (a) Smagorinsky model and (b) Dynamic k model. Results are taken from simulations using mesh C with a pure central scheme.

be visualised by looking at the vorticity in the flow field around the foil using the Q-criterion, as shown in Figure 7. It is also seen that coarser meshes, when combined with a pure central scheme fail to capture the separation bubble. Simulations using a blended scheme capture a separation bubble in all cases, with increasing agreement with the DNS data as the mesh is refined.

The effect of the dispersion errors on the boundary layer dynamics can be seen by looking at the change in the turbulent kinetic energy (TKE) in the boundary layer along the chord. This is shown for both the central scheme and a blended scheme with 25% upwinding in figures 8 and 9. While the DNS results show a sharp growth in the TKE between $x/c = 0.5$ and $x/c = 0.6$, the coarser meshes show a more gradual increase starting closer to the leading edge. This indicates that the transition is occurring earlier, and by a different mechanism. Analysis of the velocity fluctuations in the boundary layer reveal that the dispersion errors act in a similar way to free-stream turbulence and by-pass the natural transition of the boundary layer. This also explains

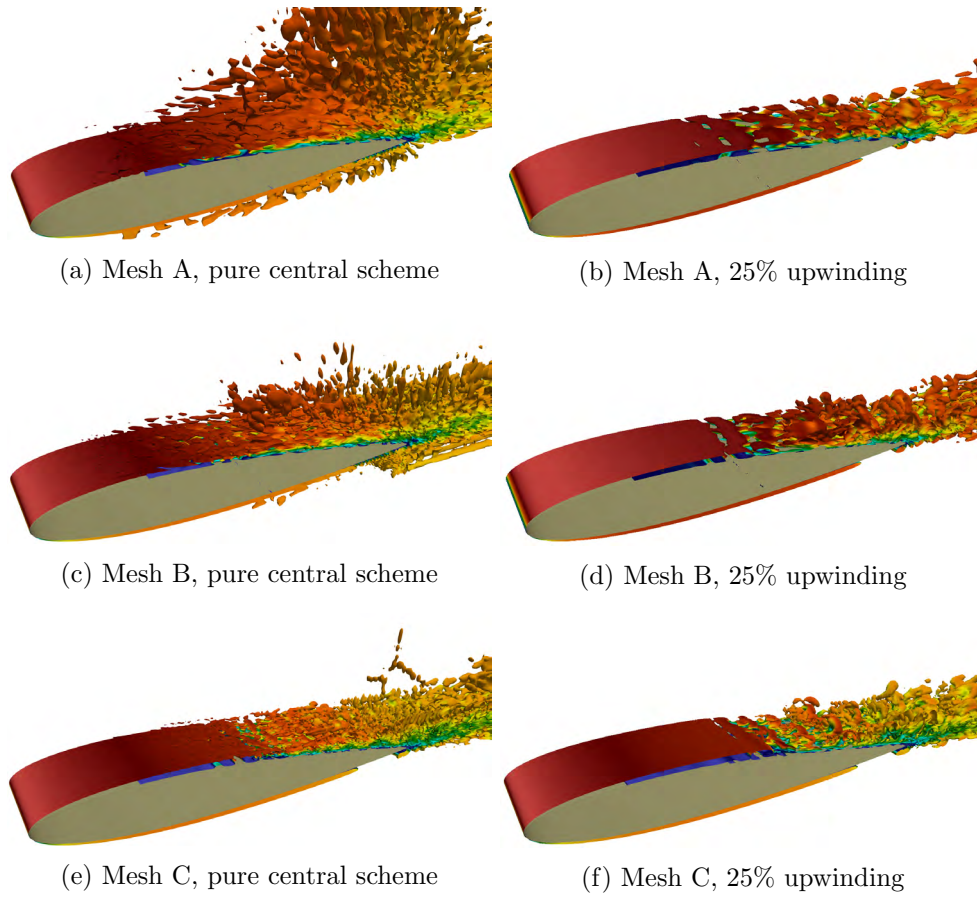


Figure 7: Iso-contours of $Q = 100$ for different mesh resolutions and discretisation schemes. Contours coloured by velocity magnitude.

why no separation bubble is resolved in these cases, as the boundary layer is already turbulent.

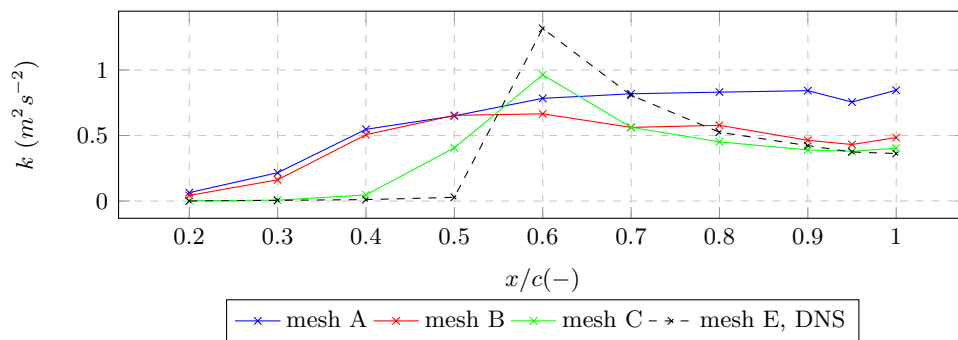


Figure 8: Resolved rms turbulent kinetic energy at $y^+ = 30$. DNS compared with LES with pure central differencing.

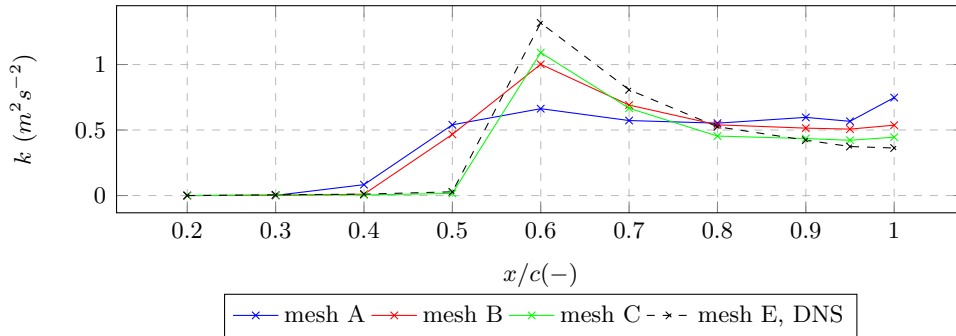


Figure 9: Resolved rms turbulent kinetic energy at $y^+ = 30$. DNS compared with LES with blended scheme using 25% upwinding.

The earlier transition leads to higher levels of turbulent kinetic energy at the trailing edge, particularly at lower frequencies. The effect of this is to increase the energy that is scattered as acoustic waves at the trailing edge. The dispersion errors will also create additional quadrupole noise sources if they are present in the acoustic source region. Spectral analysis of the erroneous fluctuations in the boundary layer reveals that they occur across a wide range of scales. As the dynamic SFS model is effective only in dissipating the smallest scales, the model does not remove the dispersion errors from the flow. From the perspective of the sub-filter scale modelling, this behaviour is correct as the SFS model should only be effective at the smaller scales. Therefore, the dispersion errors must be controlled in a different way. The most accurate and obvious way of achieving this is of course to increase the resolution. However, to remove such effects completely from the boundary layer, the mesh resolution needs to be far higher than is achievable for many practical flows of interest. Therefore for coarser meshes, the dispersion can be controlled by increasing the level of up-winding in the discretisation scheme. This will introduce artificial dissipation but does not appear to delay or prevent the transition from occurring in any of the simulations considered here. From these results, it is recommended that if a very fine mesh cannot be obtained due to the complexity of the geometry or the Reynolds number, then a scheme that minimises the dispersion errors is needed, as these have a significant impact on the boundary layer flow.

3.2 Case 2

Using the preceding analysis, Case 2 has been considered using LES with the Dynamic k SFS model and a blended scheme with a 10% level of up-winding. A smaller level of blending has been used here to reduce the dissipation and the presence of dispersion errors will be assessed in the results. Two mesh resolutions are considered, with the parameters shown table 1. Experimental results in [8] show that the acoustic field for this case is dominated by a narrowband component that results from Tollmien-Schlichting waves close to the trailing edge.

The results from both mesh F and mesh G show the growth of a stream-wise instability close to the trailing edge of the foil on both sides. The spectral plots in figure 10 show good agreement

between the two meshes, with both predicting the rapid growth of a narrowband fluctuation towards the trailing edge. Both the upper and lower sides exhibit the same behaviour. The similarity of the amplitude of the fluctuations for the two meshes suggests that the transition region is not contaminated by dispersion errors. These would be identified if the coarser mesh showed larger fluctuations than the finer mesh, particularly upstream of the transition.

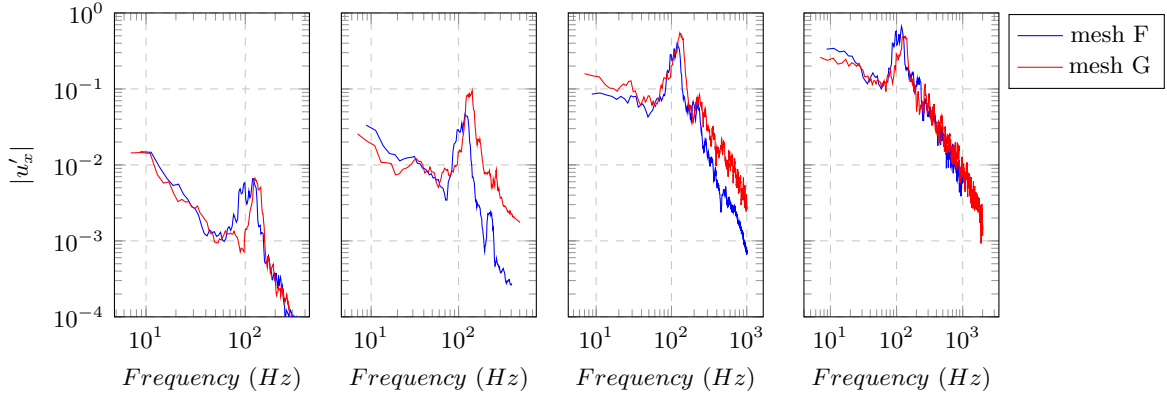


Figure 10: Spectral plots of the streamwise velocity fluctuations in the lower-side boundary layer at $x/c = 0.8, 0.9, 0.95, 1.0$.

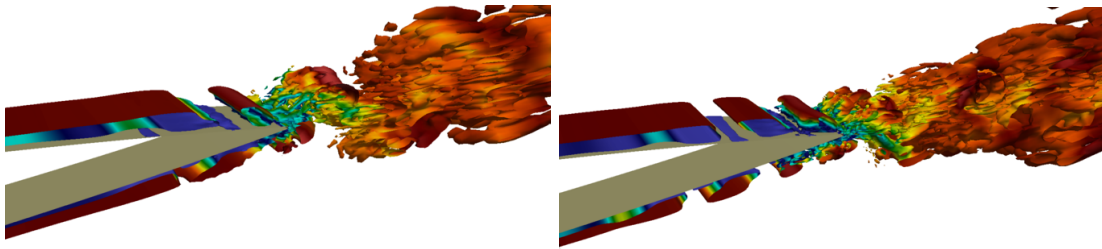


Figure 11: Instantaneous Iso-contours of $Q = 100$ at the trailing edge for Meshes F and G at $t = 20c/U$.

At the trailing edge, the 2D vortical structures on the upper and lower sides interact, creating span-wise fluctuations which lead to fully three-dimensional structures being convected into the near wake of the trailing edge, as shown in figure 11. This behaviour appears to be inconsistent with the experimental analysis in [1], which shows that the amplified T-S waves should produce a mostly 2D near-wake flow field. However, this 2D behaviour was observed for experiments where the foil was at a non-zero angle of attack, with the T-S waves only present at the trailing edge on the pressure side of the foil. For Case 2, we have T-S waves creating large 2D structures on both sides of the foil at the trailing edge, and so it may be that their interaction induces a stronger span-wise instability than is seen in that particular experiment.

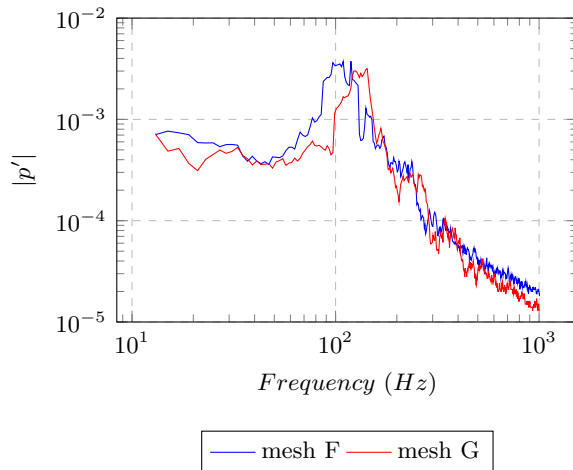


Figure 12: Spectral analysis of the surface pressure fluctuations for Case 2.

The spectral content of the foil surface pressure contains a narrowband component at the same frequency as the instability waves in the boundary layer. This is shown in figure 12 for both meshes. It is noted that mesh G predicts the peak frequency to be 130 Hz whereas mesh F predicts a lower value of 110 Hz. This was also observed for the boundary layer fluctuations.

4 CONCLUSIONS

In this study, simulations of the flow over a NACA0012 foil have been conducted using LES and DNS. Two different cases have demonstrated very different behaviours allowing for the relationship between the transition of the boundary layer and the trailing edge flow to be explored. It has been shown that if the boundary layer becomes fully turbulent upstream of the trailing edge, the narrowband fluctuations present during the transitional stage will have disappeared and so will not contribute to the trailing edge noise. If the boundary layer is transitional at the trailing edge, the surface pressure fluctuations will contain tonal components with frequencies equal to those of the instabilities in the boundary layer.

The assessment of the large eddy simulations has identified some important considerations for the sub-filter scale modelling and the discretisation. In order to capture the transition process, the SFS model must remain inactive during the early stages. The constant coefficient Smagorinsky model was shown to be incapable of capturing this process, even for highly resolved meshes and so is not recommended for flows involving transitional boundary layers. Regardless of the modelling approach taken, the importance of grid sensitivity and uncertainty analysis has been highlighted here. By considering how the boundary layer fluctuations change with mesh resolution, dispersion and dissipation errors can be identified. It has been shown that dispersion errors can change the boundary layer dynamics substantially by triggering an earlier transition and so understanding such errors is vital for acoustic analyses. Future work should focus quantifying the contributions of the different error sources and identify a more robust

approach to the discretisation, particularly regarding the use of blending. The impact of the different error sources on the far-field acoustics should also be considered.

Acknowledgements

This research was sponsored by the Naval Authority Group at the UK Ministry of Defence and by BMT Group. The Authors also wish to acknowledge the use of the UCL Grace High Performance Computing Facility and associated support services in the completion of this work.

REFERENCES

- [1] Nash, E.C., Lowson, M.V. and McAlpine, A., 1999. Boundary-layer instability noise on aerofoils. *Journal of Fluid Mechanics*, 382, pp.27-61.
- [2] Shan, H., Jiang, L. and Liu, C., 2005. Direct numerical simulation of flow separation around a NACA 0012 airfoil. *Computers and Fluids*, 34(9), pp.1096-1114.
- [3] Jones, L.E., Sandberg, R.D. and Sandham, N.D., 2008. Direct numerical simulations of forced and unforced separation bubbles on an airfoil at incidence. *Journal of Fluid Mechanics*, 602, pp.175-207.
- [4] Solís-Gallego, I., Meana-Fernández, A., Oro, J.F., Díaz, K.A. and Velarde-Suárez, S., 2018. LES-based numerical prediction of the trailing edge noise in a small wind turbine airfoil at different angles of attack. *Renewable Energy*, 120, pp.241-254.
- [5] Wang, J., Zhang, C., Wu, Z., Wharton, J. and Ren, L., 2017. Numerical study on reduction of aerodynamic noise around an airfoil with biomimetic structures. *Journal of Sound and Vibration*, 394, pp.46-58.
- [6] Curle, N., 1955. The influence of solid boundaries upon aerodynamic sound. *Proc. R. Soc. Lond. A*, 231(1187), pp.505-514.
- [7] Williams, J.F. and Hawkings, D.L., 1969. Sound generation by turbulence and surfaces in arbitrary motion. *Phil. Trans. R. Soc. Lond. A*, 264(1151), pp.321-342
- [8] Chong, T.P., Joseph, P.F. and Kingan, M.J., 2013. An investigation of airfoil tonal noise at different Reynolds numbers and angles of attack. *Applied Acoustics*, 74(1), pp.38-48.
- [9] Smagorinsky, J., 1963. General circulation experiments with the primitive equations: I. The basic experiment. *Monthly Weather Review*, 91(3), pp.99-164
- [10] Van Driest, E. R., 1956. On turbulent flow near a wall. *Journal of the Aeronautical Sciences*, 23(11), pp.1007-1011.
- [11] Kim, W.W. and Menon, S., 1999. An unsteady incompressible Navier–Stokes solver for large eddy simulation of turbulent flows. *International Journal for Numerical Methods in Fluids*, 31(6), pp.983-1017.
- [12] Chow, F.K. and Moin, P., 2003. A further study of numerical errors in large-eddy simulations. *Journal of Computational Physics*, 184(2), pp.366-380.

Experimental validation of aerodynamic computational results in the aft-deck of a simplified frigate shape (SFS2)

MARINE 2019

R. BARDERA[†], J.C. MATIAS*, A. GARCIA-MAGARIÑO[†]

Instituto Nacional de Técnica Aeroespacial (INTA)

Ctra. Ajalvir, km 4.5

Torrejón de Ardoz, 28850 Madrid, Spain

[†]e-mail: barderar@inta.es, web page: <http://www.inta.es>

*e-mail: matiasgjc@inta.es, web page: <http://www.inta.es>

[†]e-mail: garciamga@inta.es, web page: <http://www.inta.es>

Key words: aerodynamics, frigate, helicopter, flight-deck, wind-tunnel, CFD validation, PIV.

Abstract. Military frigates develop an essential tactical element and have a great importance in all navies operations around the world since they provide marine and submarine surveillance, as well as support for different emergencies, rescue, and humanitarian aid. These operations increase their range, even more, when the frigate allows for helicopter operations on its deck. Thus, troops can be transported between frigates and surveillance and rescue operations can be done faster. However, the aerodynamic interference between frigate and helicopter results in a complex airflow which causes an increase in the pilot's workload during aircraft operations above the helideck. This complex airflow is due to the fact that the frigate has a non-aerodynamic design with sharp surfaces. They cause large areas of turbulent detached flow and low-velocity recirculation zones above the flight deck endangering helicopter take-off and landing maneuvers. For this reason, a large number of tests must be carried out on all frigates which can host helicopters operations. Tests have traditionally been performed in wind tunnels. Advances in the computing power of computers and their costs reduction have allowed better *computational fluid dynamics* (CFD) analysis reducing the need for experimental testing. However, CFD still has certain problems in predicting some complex flows such as the perturbed flow over the flight deck located in the wake of a frigate resulting in a necessity of validation by experimental data. The aim of this paper is to conduct a comparative study between numerical and experimental results of the flow around a *simplified frigate shape* (SFS2). The numerical study has been performed using a commercial software (FLUENT). The experimental study has been carried out in *Instituto Nacional de Técnica Aeroespacial* INTA (Spain) by wind tunnel testing a sub-scaled SFS2 model by means of *Particle Image Velocimetry* (PIV). The assessment is made by comparing point by point the velocity values obtained from experimental maps with those obtained in the numerical study. The comparison focuses on the helicopter rotor plane during its approach to the frigate. All the results presented could be a step forward in solving computational problems and improve their results related to marine engineering. They also could provide an important basis as a powerful validation method for future researches.

1. INTRODUCTION

Helicopters are currently a very useful operational tool for military operations on frigates. They make it possible to support anti-submarine and surface warfare, surveillance tasks, or even to transfer troops between different frigates [1]. For this reason, helicopters operation in frigates is presented as an essential element among modern naval operations.

In general, a frigate superstructure is essentially a combination of non-aerodynamic bodies that generate a very complex flow around them, affecting the helicopter operations on the ship [2-4]. This makes take-off and landing operations at its deck difficult and in certain circumstances risky. The most common position for the helicopter platform on a frigate is at the stern. It is a point where the ship's superstructure generates a large recirculation bubble caused by the detachment of the flow [5-7]. This flow structure, in contrast to the free stream wind velocity experienced by the helicopter during the approach procedure to the frigate, is what causes oscillations and low-frequency movements on the helicopter, increasing pilot workload during the maneuver [8-13].

The aim of this paper is to obtain velocity maps above the helideck of a "Simplified Frigate Shape" (SFS2) by means of numerical results and Particle Image Velocimetry (PIV) in wind tunnel tests. Thus, the flow structure, which affects the helicopter rotor during the landing maneuver of a helicopter, will be analyzed and the differences founded in the results using numerical and experimental methods will be compared.

2. HELICOPTER LANDING MANEUVER ON FRIGATES

All navies have standardized procedures related to aircraft operations on military ships. The case of the helicopter landing on decks is not an exception, and one of the most common maneuvers is the fore/aft approach [14]. This maneuver is performed in three steps, as can be seen in *figure 1*.

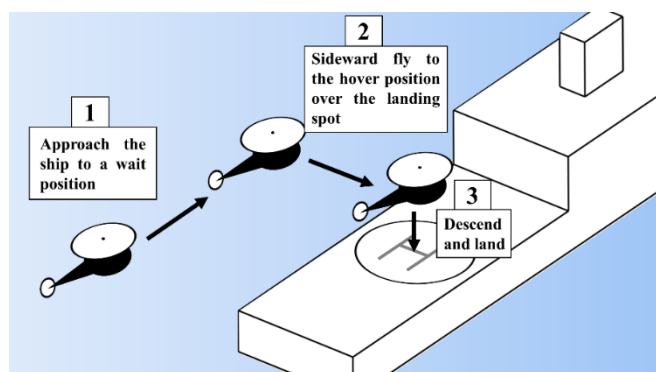


Figure 1: Diagram of the procedure for aft landing on a frigate.

For the tests, a distance equal to the beam of the frigate will be taken for the helicopter waiting point on the port side of the frigate (point 2 in *figure 1*). In this way, the sideward displacement flies half over the water and half over the deck.

3. NUMERICAL STUDY SETUP

In this section, the process followed to get numerical results of the flow around a simplified frigate model is explained.

3.1. Simplified frigate model geometry

Figure 2 (left) shows the dimensions of the frigate model used for the tests. It is a simplified frigate model proposed by NATO, on a scale of 1:85, called SFS2 (“Simplified Frigate Shape”). Its shape represent the part of the frigate above the waterline i.e. the superstructure and exhaust gases stack by means of simple prismatic blocks, which imitate the poorly aerodynamic geometries presents in conventional frigates. This model has been widely used for aerodynamic research. Its simplicity allows easy numerical implementation or simple manufacturing for experimental tests. [15-17].

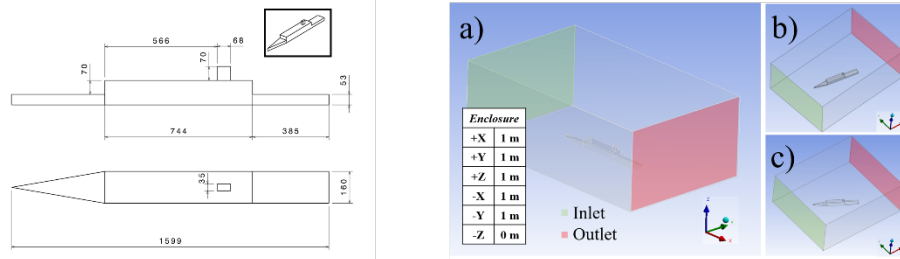


Figure 2: At the left, 1:85 SFS2 dimensions (mm). At the right, control volume of the problem in the ANSYS Design Modeler for $WOD = 0^\circ$ (a), 15° (b) and 30° cases (c).

For the numerical study, the model was created as a 3D virtual model using CATIA V5 software. The model was imported in .igs format to the Design Modeler program available in ANSYS Workbench. The Design Modeler allows creating a contour around the full body using the enclosure function. The contour dimensions selected for this study were $-z = 0\text{ m}$ (representing the sea level surface) and 1 m in all directions, measured from the surface of the body, figure 2a. Finally, a boolean operation was made to the body and the contour created to define the control volume of the fluid.

As both experimental and numerical studies were made in three different inlet configurations (*Wind Over Deck angle*, $WOD = 0^\circ, 15^\circ$ and 30°), three different control volumes were created with the model turned, figure 2 (right), 2a, 2b, 2c.

3.2. Mesh generation

Once the model geometry and the control volume is defined, the next step is to generate the mesh. Using the *Mesh Generator* from ANSYS Workbench and limiting the tetrahedral elements size to a maximum of $4 \times 10^{-2}\text{ m}$, a 475K cells mesh was created. It was under the FLUENT Student limit of 512K elements and it allowed to obtain results considerably quickly. Mesh refinements were made to improve results quality close to the body. Finally, *Named selections* were created for the *inlet* and *outlet* surfaces to help the solver to boundary conditions definition. Figure 3 shows the mesh generated for the control volumes created.



Figure 3: Mesh generated for $0^\circ, 15^\circ$ and 30° (a, b, c) cases in ANSYS Mesh Generator.

3.3. Solver settings

The software used to get the fluid mechanics results was FLUENT. The program was adjusted for calculating the results using four processors working in parallel with a dedicated GPU. The energy equation was disabled and the k-epsilon Realizable viscous model with standard wall functions was used. The boundary conditions were similar for the three cases studied: a constant velocity magnitude of 10 m/s at the inlet and a null gauge pressure at the outlet ($P_{out} = P_{ambient}$). Both inlet and outlet were adjusted with a turbulence intensity of 10 % and a turbulence length scale of 0.16 m, based on the width of the scaled model.

The calculation methods selected for the turbulent kinetic and dissipation rate were first order upwind schemes in a first attempt. For the final and more accurate results, a second order was used. A standard initialization computed from the inlet surface data was used. Finally, a limit of 3.000 iterations was imposed. However, the real number of iterations enough to get the solution convergence were less than 200 in the three cases.

3.4. Exporting results

The first step to get the numerical results of each case was to create contours from plane surfaces. The contours can present different magnitudes of interest such as pressures, velocities, turbulence or vorticity. *Figure 4* presents the velocity contours obtained for the 0° of inlet velocity case in two different planes: the symmetry plane and the rotor plane. The symmetry plane is a vertical plane created from the center line of the frigate. The rotor plane is a horizontal plane located at a height in which the rotor is working during the helicopter approach (5 m above the deck at the real case, 58 mm scaled).

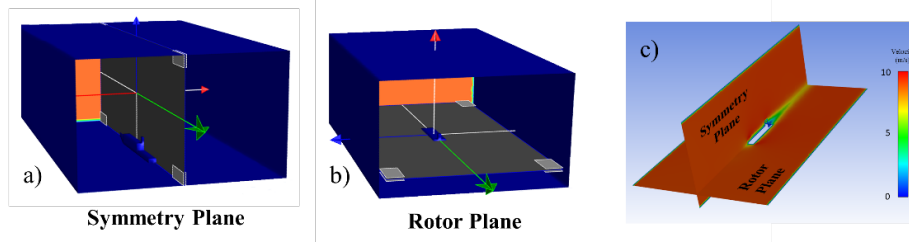


Figure 4: Symmetry (a) and rotor (b) planes defined in the control volume. Velocity contours of symmetry and rotor plane for 0° case (c).

All data contained on the rotor plane, which contains the results that are the objective of this study, was exported as an ASCII file in order to be able to make calculations using these results. For example to make velocity values non-dimensional or to get a specific point value through interpolation to compare with experimental data (see *section 5.3: comparison*).

4. EXPERIMENTAL SETUP

4.1. Wind tunnel

In order to experimentally characterize the flow over the flight deck of the frigate, experimental tests were carried out in wind tunnel T1 at the Instituto Nacional de Técnica Aeroespacial (INTA), Spain. This wind tunnel has a closed circuit with an open test section ($3 \times 2 \text{ m}^2$). In the test section a maximum flow velocity up to 60 m/s with a turbulence intensity under 0.5 % can be reached.

4.2. Simplified frigate model

The same model presented in *figure 2* was made of wood for wind tunnel testing. For the tests, due to the fact that the PIV laser plane available in the wind tunnel is vertical, and horizontal velocity maps are desired, the model was fixed to a vertical wall as can be seen in *figure 5*. In addition, a bolt was used to fix the model to the wall at the proper wind incidence angle (WOD which means *Wind Over Deck* angle). As the helicopter maneuver must be carried out at 5 meters height above the deck, the planes were taken at a distance of 58 mm from the deck of the model (scale 1:85).

All tests were performed at 10 m/s, which results in a Reynolds number based on the beam of the frigate of 1.09×10^5 . This value is above the critical value that is necessary to satisfy the laws of dynamic similarity between the flow on the model and on the real frigate [18].

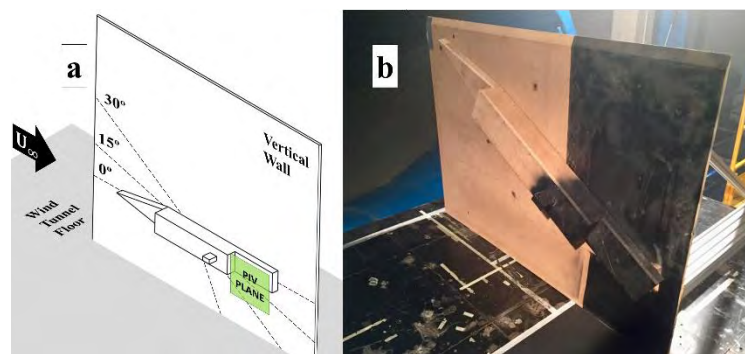


Figure 5: a) Positioning diagram of the frigate and the velocity measuring plane PIV b) Frigate model SFS2 placed in the wind tunnel test chamber at WOD = 30°.

4.3. Particle Image Velocimetry

Particle Image Velocimetry (PIV) was used for the experimental tests. It is an advanced and non-intrusive velocity measurement technique that needs an airflow seeded with small tracer particles which are illuminated by means of a laser plane in order to capture them in two pictures, separated a short time Δt [19-22]. Thus, by making a correlation between the pair of images captured, it is possible to measure the displacement of the particles (ΔX). As the time between captures (Δt) is known, it is possible to obtain the local speed \bar{u} with the following expression contained in *figure 6*,

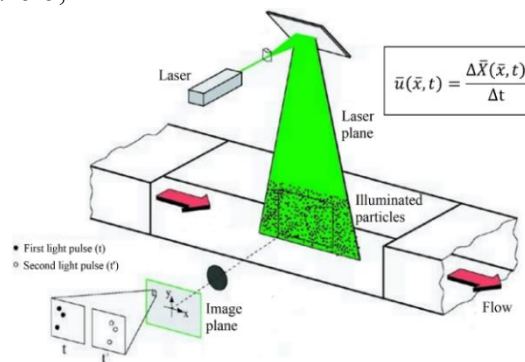


Figure 6: Operating diagram of PIV system

The required equipment for this technique consisted of a particle generator, a laser light source, an image recording system, a synchronizer and a processor system. Laskin atomizers were used as particle generators, which allow the production of very small particles ($\sim 1 \mu\text{m}$) that are able to acquire quickly the local velocity of the flow [23, 24]. The laser light source consists of two Nd:YAG pulsed lasers (Neodymium: Yttrium Aluminium Garnet). To capture the images, a digital camera was used, which consisted of a CCD sensor of 2048×2048 pixels and a lens that allows regulating the entry of light and focus. A synchronizer is required to trigger the lasers at the appropriate time and synchronize them with the captures taken by the camera. Finally, a processing system must correlate the small interest windows of 32×32 pixels of each pair of images taken, to obtain the particle displacement and then their velocity. After this correlation, the velocity maps can be obtained. *Figure 6* shows the simplified scheme of operation of the PIV system.

5. RESULTS

5.1. Numerical results

Figure 7 shows the non-dimensional velocity maps of the rotor plane locations obtained directly from FLUENT results. Dashed black squares represent the interest windows in which the experimental and numerical comparison will be focused.

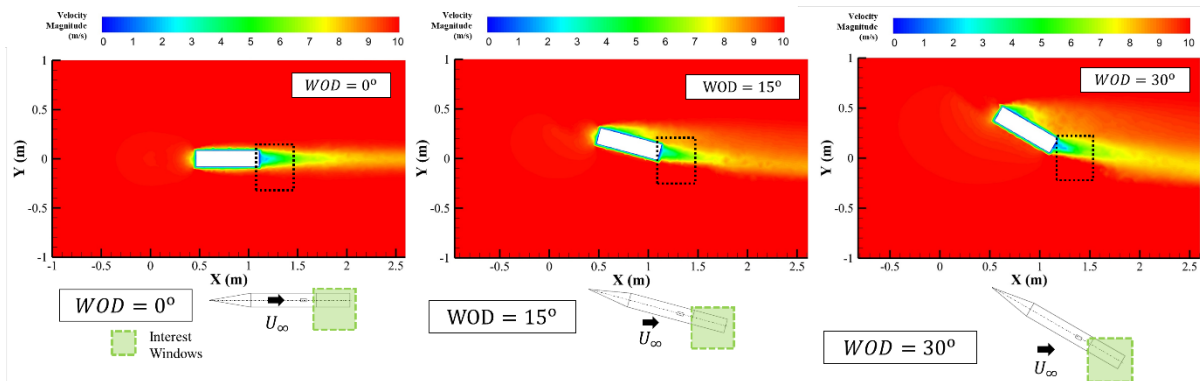


Figure 7: Numerical results of Velocity maps at 0° , 15° and 30°

In all of three cases presented, it can be observed an airflow wake with a huge recirculation region of the flow, caused by the presence of the frigate superstructure. This flow structure could negatively affect the helicopter approach operation to the frigate.

5.2. Experimental results

Figure 8 shows the PIV non-dimensional velocity maps for $WOD = 0^\circ$, 5° , 30° obtained from experimental tests performed. All of them were captured at the same 58 mm above the frigate flight deck. The black line in the maps represents the helicopter trajectory during the landing maneuver towards the helideck at the stern described in *section 2*. Dashed red lines indicate the area of the rotor occupied during helicopter landing procedure.

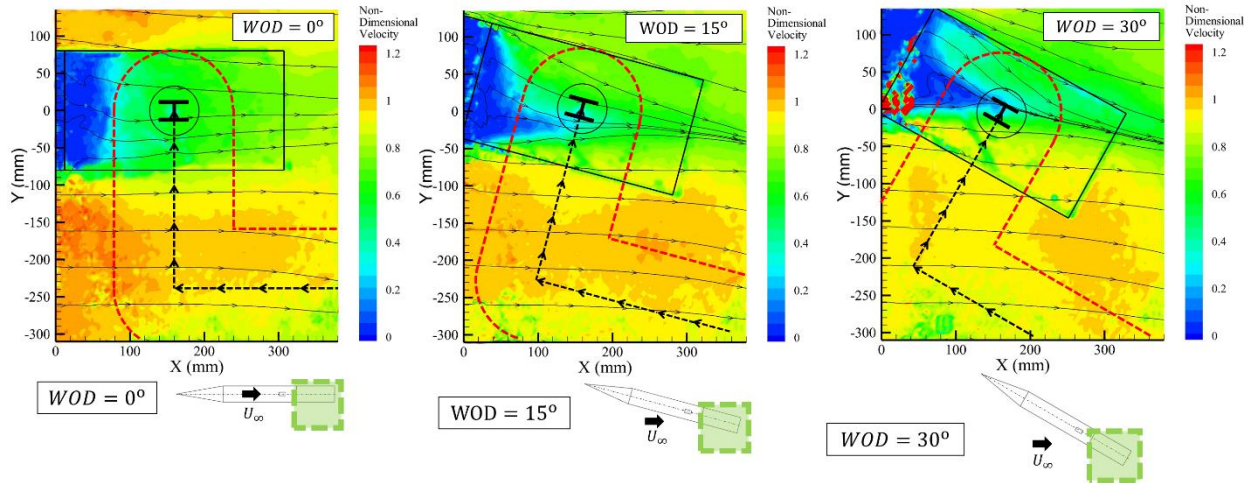


Figure 8: PIV non-dimensional velocity maps at $WOD = 0^\circ$, 15° and 30° . Landing path of the helicopter marked in black lines.

As can be observed at the previous maps, in all three cases there is a low-velocity area caused by the detachment of the airflow caused by the frigate superstructure ($x \sim 50 \text{ mm}$; $y \sim 0 \text{ mm}$). This is a typical path of a flow, which is immediately behind from a descending step. For the helicopter landing procedure, it is clearly visible that although most of the maneuver is immersed to clean airflow condition, in the last phase of the approach when the helicopter moves laterally towards the point of descent, its rotor experiences a large change in incident velocities, caused by the presence of the frigate superstructure.

5.3. Comparison

As the same velocity maps have been obtained by experimental and numerical methods, they can be compared. However, the coordinates of the points in which the values are known on both tests do not exactly match. The experimental maps points are distributed according to the interest windows size of PIV (32×32 pixels), while in the numerical results, each point associated with a value coincides with the mesh nodes. This problem has been solved by interpolating the numerical results in the same coordinates of the experimental results as shown in *figure 9*. In this figure, V_{CFD_i} are the velocities obtained by numerical results, h_i are the distances between each point i and the desired CFD_PIV , and V_{CFD_PIV} is the desired interpolated velocity at the same point where the PIV velocity is already known.

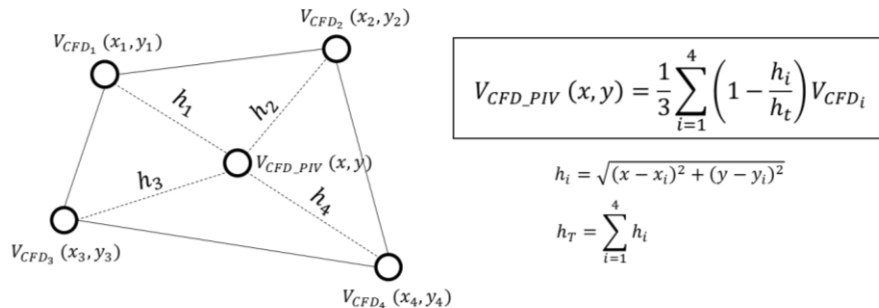


Figure 9: Interpolation to get CFD velocity values at experimental PIV coordinates.

Applying the above formula to the numerical results and representing the values in similar maps than PIV results, CFD Velocity maps in *figure 10* are obtained. Results presented show a big resemblance of the main flow patterns and velocity values over the aft-deck using both methods. In all maps, the helicopter trajectory is represented with black arrowed lines and the volume occupied by the rotor position during the maneuver with dashed red lines.

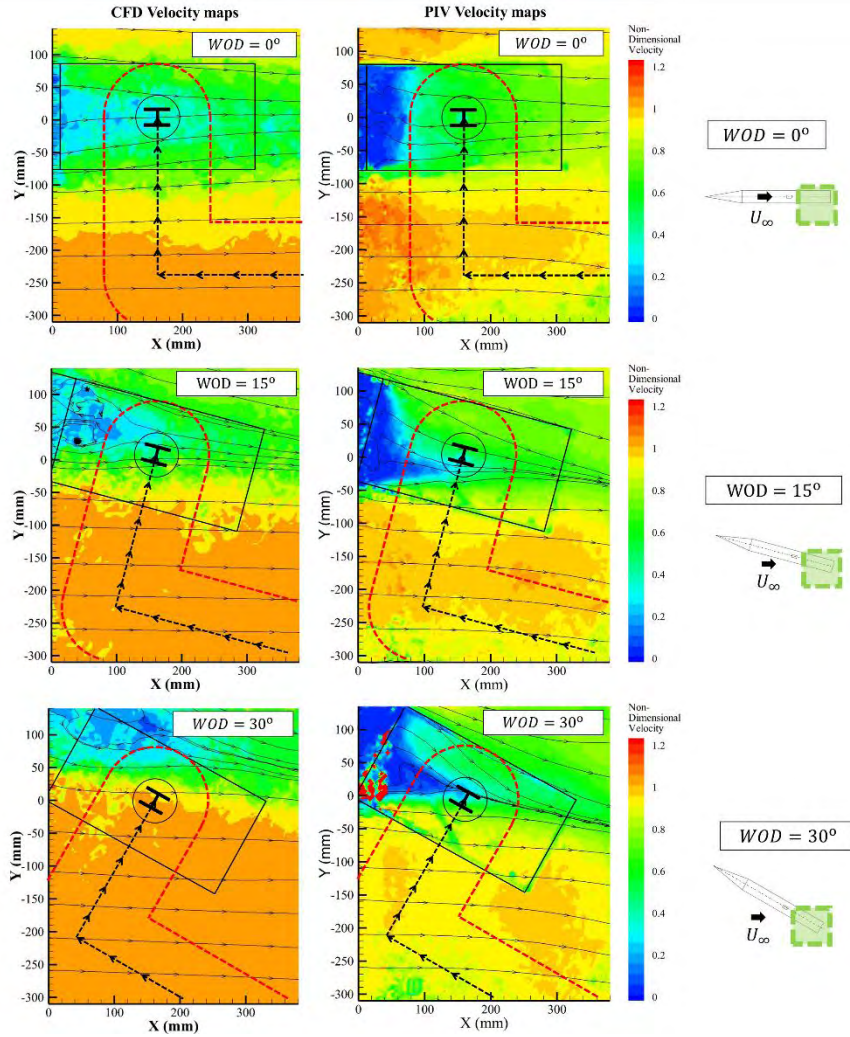


Figure 10: Interpolated CFD (left) and PIV non-dimensional velocity maps (right) at 0° and 15° and 30°.

For a more detailed comparison, a new set of maps has been obtained in *figures 11 to 13*. They represent the magnitude differences (ϵ) between experimental PIV and numerical maps,

$$\epsilon (\%) = |V_{PIV} - V_{CFD}| \times 100 \quad (1)$$

In each of the following figures, the helicopter trajectory is represented again with black arrowed lines. The helicopter incident non-dimensional velocity profiles during these paths are plotted for the experimental (PIV) and numerical (CFD) results. The magnitude of relative differences (ϵ) between them are also plotted. Some important points are marked with letters to

match the helicopter position on the map and graphs (A, B, C, D). The helicopter position plotted in the graphs is the distance travelled by the helicopter when it follows the black arrowed lines.

Figure 11 represents the magnitude difference maps for $WOD = 0^\circ$ case. Map and plots show that the differences between experimental and numerical results are not so high in this case. Also, the incident velocities to the helicopter during the approach follow the same tendency. However, in the last phase of the maneuver (points B, C and D), the numerical results are always under the experimental, with maximal differences in magnitude of 20 and 30 %.

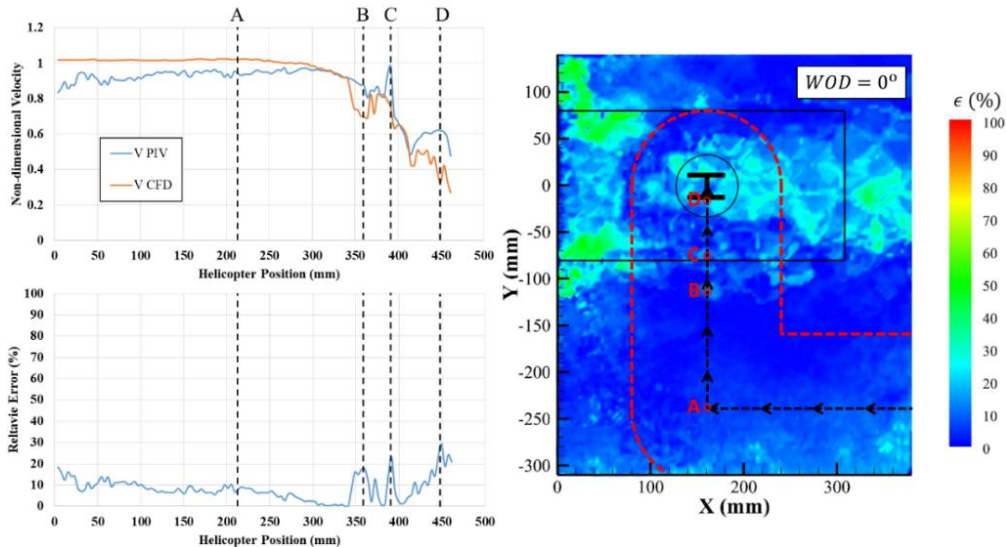


Figure 11: Magnitude difference maps for $WOD = 0^\circ$. Plot of helicopter incident velocity during landing approach and magnitude difference between PIV and CFD.

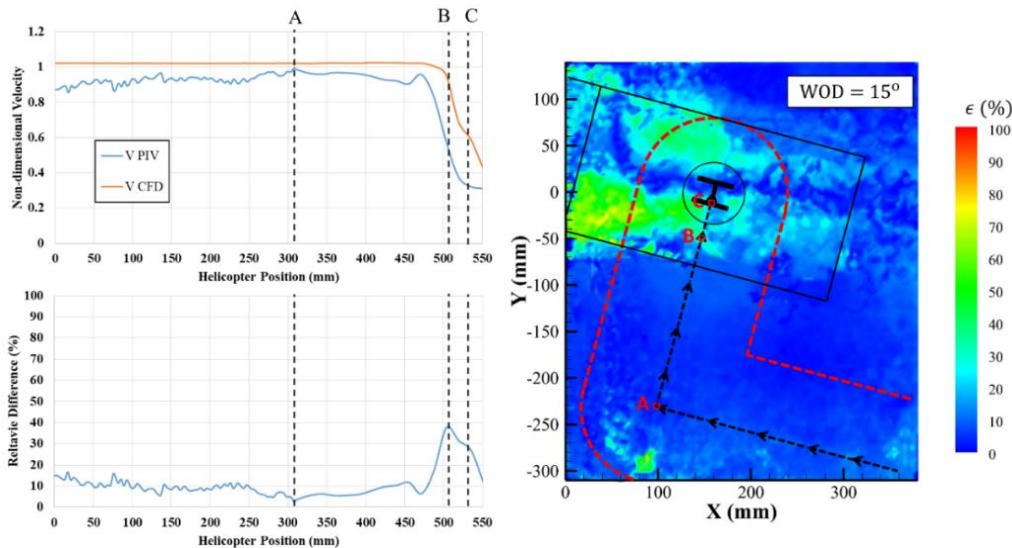


Figure 12: Helicopter incident velocity during landing approach. Interpolated CFD and PIV relative error for $WOD = 15^\circ$.

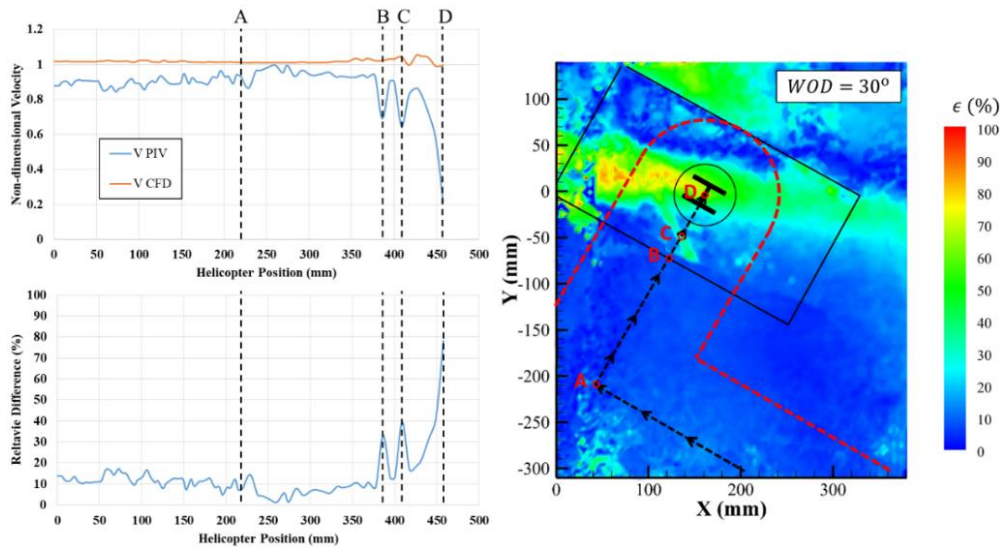


Figure 13: Helicopter incident velocity during landing approach. Interpolated CFD and PIV relative error for $WOD = 30^\circ$.

Figure 12 represents the magnitude difference maps for $WOD = 15^\circ$ case. Map and plots show a similar tendency for the numerical and experimental results. However, higher relative differences are observed (up to 40 %). Contrary to the previous case, in the last phase of the maneuver, the numerical results show a higher value of incident wind velocity than the experimental results. This is because the numerical simulation predicts a recirculation bubble in an area above the final descending point (C), see figure 10, CFD map ($WOD = 15^\circ$).

Figure 13 shows the magnitude difference maps for $WOD = 30^\circ$ case. In this case, the relative differences were higher between experimental and numerical results. The reason for this may be that the recirculation bubble in the numerical results is predicted in a far zone from the helicopter descent point (D), see figure 10 CFD map ($WOD = 30^\circ$). And experimental results obtained from PIV technique show a recirculation bubble near from this point and a huge descent in incident velocities is produced for the helicopter, as seen in the non-dimensional PIV velocity profiles in figure 15.

6. CONCLUSIONS

Both numerical and PIV velocity maps obtained have shown that the helicopter landing approach on frigates is a very complex maneuver for pilots. This is due to the great change in its incident velocities and the turbulence intensity during its lateral approach to the contact point experienced by the helicopter rotor. And it is worse when the incident wind angle increases.

In general, the comparison between numerical and experimental results obtained on the rotor plane above the helicopter aft-deck have shown a great resemblance. This means that the streamlines, velocity magnitude and main flow patterns of the maps obtained experimentally (PIV) and numerically (CFD) are very similar. However, in a more detailed comparison, when the incident velocities during the path of the helicopter approach are compared, differences are more significant (up to 40 % at certain points). In addition, differences between numerical and experimental results become higher with the increment of wind over deck angle. This difference could be due to the fact that numerical simulation predicts a smaller recirculation bubble behind the superstructure. Another reason is that the numerical results show always this bubble aligned

with the incident wind velocity and its direction does not change significantly with the change in WOD (Wind Over Deck) angle.

All data presented in this paper could be a very useful basis for future comparatives and validation of numerical results obtained by Computational Fluid Dynamics codes (CFD). This is because a standardized and simplified frigate shape (SFS2), which is easy to study numerically due to its geometry, has been used. In addition, the simple interpolation process followed to compare experimental PIV data and numerical, could be useful to enable effective collaboration between both ways of dealing with the aerodynamic problem on frigates. Numerical tests could help the process to save time and money avoiding expensive long wind-tunnel testing campaigns. Experimental tests could do the same providing results that help to improve turbulence models and the accuracy of numerical results.

Finally, it has been shown that is very important to carry out wind tunnel tests and numerical predictions to certify and establish operational limits related to helicopters maneuvers on frigates. It should also be noted that any new frigate should be tested in this way to detect possible aerodynamic peculiarities caused by its superstructure geometry and thus correctly determine the flight envelopes of aircraft maneuvers on its deck. In the future, these tests and its results will increase the safety of helicopter operations on frigates.

REFERENCES

- [1] Kääriä, C. Wang Y., White M. and Owen I. An experimental technique for evaluating the aerodynamic impact of ship superstructures on helicopter operations", *Ocean Engineering*, vol. 61, pp. 97-108, 2013. Elsevier Publishing.
- [2] Swales, C. and Breeze, G. LDV measurements above the flight deck of a model frigate. In: 35th aerospace sciences meeting & exhibit, Reno, NV, 6-9 January 1997. Reston, VA: AIAA.
- [3] Wakefield, N. Newman S. and Wilson P., Helicopter flight around a ship's' superstructure. *Proceedings of the Institution of Mechanical Engineers, Part G: Journal of Aerospace Engineering*, vol. 216, no. 1, pp. 13-28, 2002.
- [4] Kääriä, C. Investigating the impact of ship superstructure aerodynamics on maritime helicopter operations. PhD Thesis, School of Engineering, University of Liverpool, UK, 2012
- [5] Lumsden, R. B. Ship air-wake measurement, prediction, modelling and mitigation *Defence Science and Technology Laboratory, UK*, 2003.
- [6] Rajasekaran, J. On the flow characteristics behind a backward-facing step and the design of a new axisymmetric model for their study. *Doctoral dissertation, University of Toronto*, 2011.
- [7] Nacakli, Y. Landman, D. and Doane, S. Investigation of Backward-Facing-Step Flow Field for Dynamic Interface Application, *Journal of the American Helicopter Society*, vol. 57, no. 3, pp. 1-9, 2012.
- [8] Shafer, D.M. Ghee, T.A. Active and passive flow control over the flight deck of small naval vessels. 35th AIAA Fluid Dynamics conference and Exhibit, Fluid Dynamics and Co-

- located Conferences, Toronto, Ontario, Canada, 2005.
- [9] Bardera-Mora, R. Barcala-Montejano, M. Rodríguez-Sevillano, A. de Diego, G. and de Sotto, M. A spectral analysis of laser Doppler anemometry turbulent flow measurements in a ship air wake, *Proceedings of the Institution of Mechanical Engineers, Part G: Journal of Aerospace Engineering*, vol. 229, no. 12, pp. 2309-2320, 2015.
- [10] Brownell, C. Luznik, L. Snyder, M. Kang, H. and Wilkinson, C. In Situ Velocity Measurements in the Near-Wake of a Ship Superstructure, *Journal of Aircraft*, vol. 49, no. 5, pp. 1440-1450, 2012.
- [11] Lee, R. and Zan, S. "Wind tunnel testing to determine unsteady loads on a helicopter fuselage in a ship airwake". In *ICAS 2002 Congress* (pp. 3111-1), 2002.
- [12] Lee, R. and Zan, S. Wind Tunnel Testing of a Helicopter Fuselage and Rotor in a Ship Airwake. *Journal of the American Helicopter Society*, vol. 50, no. 4, pp. 326-337, 2005.
- [13] Doane, S. R. and Landman, D. A. A wind tunnel investigation of ship airwake/rotor downwash coupling using design of experiments methodologies. In *Proceedings of the 50th AIAA Aerospace Sciences Meeting including the New Horizons Forum and Aerospace Exposition* (pp. 2012-0767), 2012.
- [14] Foeken, M. Pavel, M. D. Investigation on the simulation of helicopter/ship operations. Faculty of Aerospace Engineering, Delft University of Technology Kluyverweg 1, 2629 HS, Delft, The Netherlands.
- [15] Yuan, W., Wall, A. and Lee, R. Combined numerical and experimental simulations of unsteady ship airwakes, *Computers & Fluids*, vol. 172, pp. 29-53, 2018.
- [16] Yuan W., Lee R., Wall A., "Simulation of Unsteady Ship Airwakes Using Openfoam". 30th Congress of the International Council of the Aeronautical Sciences. DCC, Daejeon, Korea: September 25-30, 2016.
- [17] Mora, R. "Experimental Investigation of the Flow on a Simple Frigate Shape (SFS)", *The Scientific World Journal*, vol. 2014, pp. 1-8, 2014.
- [18] White, F. *Fluid Mechanics*, 4th Edition. McGraw Hill Companies, 2002, pp. 298-299.
- [19] Raffel, M. Willert, C. Scarano, F. Kähler, C. Wereley, S. and Kompenhans, J. *Particle Image Velocimetry*. Springer, 2007.
- [20] Adrian, R. and Westerweel, J. *Particle Image Velocimetry*. Cambridge: Cambridge University Press, 2011.
- [21] Prasad, A. K. *Particle Image Velocimetry*. *Curr Sci* 2000; 79(1): 10
- [22] Adrian, R. Particle-Imaging Techniques For Experimental Fluid-Mechanics, *Annual Review of Fluid Mechanics*, vol. 23, no. 1, pp. 261-304, 1991.
- [23] Kähler, C. Sammler, B. and Kompenhans, J. Generation and control of tracer particles for optical flow investigations in air, *Experiments in Fluids*, vol. 33, no. 6, pp. 736-742, 2002.
- [24] Echols, W. H. and Young, J. A. Studies of portable air-operated aerosol generators (No. NRL-5929). NAVAL RESEARCH LAB WASHINGTON DC, 1963.

A NUMERICAL AND ANALYTICAL WAY FOR DOUBLE-STEPPED PLANING HULL IN REGULAR WAVE

RASUL NIAZMAND BILANDI^{*,♀}, SIMONE MANCINI^{†,♀}, ABBAS
DASHTIMANESH^{*}, SASAN TAVAKOLI[‡] AND MARIA DE CARLINI[♀]

^{*} Faculty of Engineering,
Persian Gulf University, Bushehr, Iran; Post Code: 7516913817,
rasool.niazmand@mehr.pgu.ac.ir
a.dashtimanesh@pgu.ac.ir

[†] Department of Industrial Engineering (DII),
University of Naples “Federico II”, Naples, Italy, Post code 80125,
simone.mancini@unina.it

[‡] Department of Infrastructure Engineering,
University of Melbourne, Parkville, Melbourne, Victoria, Australia
stavakoli@student.unimelb.edu.au

[♀] Eurisco Consulting Srls - R&D Company,
Torre del Greco, Italy, Post code 80059;
maria.decarlini@euriscoconsulting.com

Keywords: Seakeeping, 2D+T theory, Head sea, CFD simulation, Stepped hull design, Nonlinear mathematical model.

Abstract. The paper presents a comparison analysis between numerical method and nonlinear mathematical model for the prediction of the vertical motions of a double stepped planing hull in regular wave. The numerical method is to Unsteady Reynolds Averaged Navier-Stokes (URANS) equations solution via moving mesh techniques (overset/chimera), performed at different model speeds, wavelengths, and wave heights using the commercial software Siemens PLM Star-CCM+. Instead, the analytical solution is obtained using non-linear mathematical model. The presented non-linear mathematical model is developed using a combined approach based on 2D+T theory, momentum theory, and linear wake profile. Under such assumption, the double stepped planing hull is divided into three planing surfaces, and hydrodynamic forces acting on each planing surface is found by extension of simulation of symmetric water entry of two-dimensional wedge section bodies. Then, each sub-problem is solved by extending the mathematical simulation of wedge penetrating water. Final vertical force and pitching moment are found and substituted in motion equation. The mathematical model is able to compute heave and pitch motion in calm water and regular waves. Results of numerical method and novel 2D+T analytical method are compared against each other.

1 INTRODUCTION

In recent year, research on motion of stepped planing hulls in wave is important for military, recreational, racing, and transportation applications. The design of stepped planing hull reduces the friction drag creating air cavity and new hydrodynamic forces. For this

reason this kind of hull is characterized by a complex dynamic, in particular in the wave condition. Hence, understanding the behavior of a stepped planing hull in a real seaway is critical for determining its performance. Accordingly, a numerical setup and mathematical tool are directly needed to predict motion of stepped planing hull in wave.

First work on prismatic planing hull in wave has been done with Fridsma [1, 2] experimental work and regression formulas. Fridsma's work considered sixteen model with different L/B, deadrise angle and sea state to calculate added resistance, hull motions, and the vertical impact accelerations. Fridsma found accelerations at the CG and bow and added resistance to have a nonlinear relationship with wave length. Based on the Fridsma works, Savitsky and Brown [3] developed an empirical equation for the measure of vertical acceleration and added resistance of planing hull in wave. Martin [4, 5] developed a linear frequency-domain model for prismatic planing hull in regular waves. Later, Zarnick [6], following the work of Martin, developed a nonlinear mathematical model based on time domain and 2D+T theory for planing hull in head sea. Keuning [7] further extended the basic model of Zarnick [6] to combine a formulation for the sinkage and trim of the ship at wider speed range. He calculated nonlinear added mass for each two dimensional section and wave exciting force in both (ir)regular waves. After Keuning [7], many of researchers similar to Hicks [8] and Alker [9] decided to modify the Zarnick model. Nevertheless, Alker [9] was able to develop power sea software. Then, the researchers were trying to develop the 2D+T theory method for other planing hull motions.

Later, Von Deyzen [10] extended mathematical models of Zarnick [6] and Keuning [7] to three degree of freedom of surge, heave and pitch motion in (ir)regular head sea. On the other hand, Sebastiani et al. [11] presented a mathematical model for roll, heave and pitch motions of planing hull. Then, Ghadimi et al. [12, 13] extended the Sebastiani et al. [11] model to four and six degree of freedom. Finally, Tavakoli et al. [14, 15] developed several mathematical models in order to compute coupled heave, pitch, roll motions, and planar mechanism motion of planing hulls. Then, the researchers were trying to develop mathematical model to reduce the drag-to-lift ratio for planing hulls in calm water and wave. As pointed out by Savitsky and Morabito [16], the stepped hull is characterized by a low hydrodynamic drag-to-lift ratio at high speeds (see Dashtimanesh et al. [17, 18], Niazmand Bilandi et al. [19-21], Di Caterino et al. [22] and De Marco et al. [23]).

In this paper, numerical and analytical method are applied in order to investigate double stepped planing hull in regular head waves. The analytical method has been based on 2D+T theory, added mass theory, momentum theory, and linear wake theory in order to compute vertical motion (heave and pitch) of double-stepped planing hulls. In stepped planing hulls, the flow creates a dry area over the bottom body after passing through the steps. The correct prediction of the profile created by the steps will have a great effect on the accuracy of the existing equations. Hull of a double-stepped planing hull has been divided into three parts, and for each part a water entry problem has been simulated. To determine the forces for each planing surface, added mass is considered and it is computed by using the momentum variation. To determine the wetted half-beam for each planing surface, two phases are considered. The analytical approach used here follows the works of Niazmand Bilandi et al. [21]. For numerical way, URANS methods have been used. Afterward, the two methods are compared with each other.

2 HULL GEOMETRY AND CONDITION

The seakeeping analysis using the two different approaches was done on a double stepped hull. In Figure 1 the double stepped hull is shown and in Table 1 are summarized the main non-dimensional data of the hull.



Figure 1: Double stepped hull - side view.

Table 1: Main non-dimensional data of the hull

| | |
|--------------------------------|-------|
| C_B | 0.30 |
| L/B | 3.04 |
| B/T | 4.96 |
| $L/\nabla^{1/3}$ | 5.33 |
| LCG (% from transom) | 34 |
| $K_{xx}/B,$ | 0.912 |
| $K_{yy}/L_{WL}, K_{zz}/L_{WL}$ | 0.082 |

The seakeeping analysis was performed at a one speed, as listed in Table 2. The encountered frequency (f_e) has been evaluated according with the following equation:

$$f_e = \sqrt{\frac{g}{2\pi\lambda}} - \frac{V}{\lambda} \tag{1}$$

Table 2: Tests summary

| Speed (Kn) | Fr | Wave length: λ (m) | Wave Height: H (m) | Wave Period: T (s) | Encountere frequency(Hz) |
|------------|------|----------------------------|--------------------|--------------------|--------------------------|
| 30 | 1,44 | | | calm water | |
| 30 | 1,44 | 30 | 11 | 0175 | 1.78 |

3 MATHEMATICAL MODEL

In this sub-section, motion in vertical plane of double-stepped planing hull has been considered. It is assumed that the boats under the trim angle τ is moving forward with velocity u in regular head wave. Two coordinate systems of $CG\xi\eta\zeta$ and $Oxyz$ are considered for the mathematical model (see Figure 1). For this motion, the governing equation for each planing surface is given as

$$M\ddot{z}_{CG}(t) = F_z(t) = \sum_{i=1}^3 F_{\tau_{\xi_i}}(t) + F_{\tau_{\eta_i}}(t) + F_{\tau_{\eta_j}}(t) \tag{2}$$

$$I_{\zeta\zeta} \ddot{\theta}(t) = F_{\theta}(t) = \sum_{i=1}^3 F_{\theta_{R_i}}(t) + F_{\theta_{H_i}}(t) + F_{\theta_{W_i}}(t) \quad (3)$$

where, z_{CG} and θ represent vertical (heave) and pitch motions respectively, M is mass of boat, $I_{\zeta\zeta}$ is the mass moment of inertia about η -axis. Subscripts R_i , H_i and W_i refer to restoring, hydrodynamic, and wave induced forces for each planing surface, respectively. The main problem is to find the forces acting to the double stepped planing hull using a previous mathematical model (Niazmand Bilandi [21]). To this end, similar to previous mathematical models, 2D+T method is used. So, three observation planes for each planing surface in the path of boat as shown in Figure 1. Using 2D+T method, three dimensional problem changes to 2D water entry problem and can be theoretically (added mass variation) solved. To calculate flow separation from the steps, linear wake profile has been considered (see Dashtimanesh et al. [17, 18], and Niazmand Bilandi et al. [19-21]).

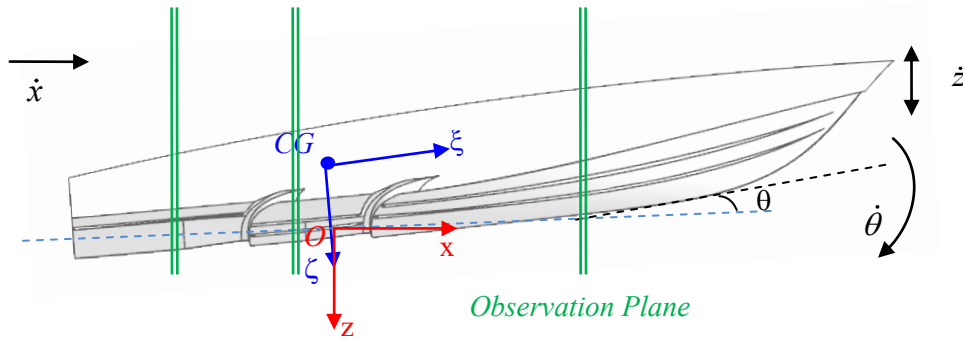


Figure 2: View of the coordinate system and 2D+T method for modeling of double stepped planing hull in regular head waves.

In the 2D+T theory, the forces acting on the wedge section entry water for each planing section can be found using momentum variation as in

$$f_i(\xi) = -\{f_{M_i} + f_{CD_i} + f_{HS_i}\}; \quad (i = 1, 2, 3) \quad (4)$$

where, f_{M_i} is the hydrodynamic lift force due to momentum changes in fluid for each planing surface, f_{CD_i} is the viscous lift force due to cross-flow drag forces, and f_{HS_i} is the hydrostatic force for each planing surface. It should be noted that, forces and moments acting on the vessel are found using the added mass theory (see Equations 5 and 6). Formula for calculation mentioned forces can be found in previous work (Niazmand Bilandi [21]). So, equations for determination of heaving force and pitching moment of double stepped planing hull are obtained as shown in Equation 5 and 6, respectively.

$$\begin{aligned}
 F_z(t) = & \sum_{i=1}^3 \int_{L_i} (f_{M_i} + f_{CD_i}) \sin(\theta + \tau_i) d\xi + \int_{L_i} f_{HS_i} d\xi = \sum_{i=1}^n -M_{a_i}(\xi, t) \cos^2(\theta + \tau_i) \ddot{\theta} + Q_{a_i}(\xi, t) \cos(\theta + \tau_i) \ddot{\theta} + \\
 & M_{a_i}(\xi, t) \dot{\theta} (\dot{z}_{CG}(\xi, t) \sin(\theta + \tau_i) - \dot{x}_{CG}(\xi, t) \cos(\theta + \tau_i)) + \\
 & \left\{ \int_{L_i} c_{r_i}(\xi, t) \frac{dw_z(\xi, t)}{dt} d\xi \right\} \cos(\theta + \tau_i) - \left(\int_{L_i} c_{r_i}(\xi, t) w_z(\xi, t) d\xi \right) \sin(\theta + \tau_i) - \\
 & \left(\int_{L_i} c_{r_i}(\xi, t) V_i \frac{dw_z(\xi, t)}{d\xi} d\xi \right) \sin(\theta + \tau_i) + \left(\int_{L_i} c_{r_i}(\xi, t) U_i(\xi, t) \frac{dw_z(\xi, t)}{d\xi} d\xi \right) \cos(\theta + \tau_i) \\
 & - U_i(\xi, t) V_i(\xi, t) \rho c_{r_i}(\xi, t) \Big|_{\text{end of step or transom}} - \left(\int_{L_i} c_{r_i}(\xi, t) V_i(\xi, t) d\xi \right) \\
 & - \left(\int_{L_i} c_{r_i}(\xi, t) \rho C_{D,c_i} V_i^2(\xi, t) d\xi \right) \cos(\theta + \tau_i) \Big\} + \int_{L_i} c_{r_i}(\xi, t) \rho \frac{d_i}{2} (c_{1i} + c_{2i}) \xi
 \end{aligned} \tag{5}$$

$$\begin{aligned}
 F_\theta(t) = & \sum_{i=1}^3 \int_{L_i} (f_{M_i}(\xi, t) \xi + f_{CD_i}(\xi, t) \xi) d\xi + \int_{L_i} f_{HS_i} \cos(\theta + \tau_i) d\xi = \sum_{i=1}^n -Q_{a_i}(\xi, t) \cos(\theta + \tau_i) \times \ddot{\theta}_{CG} + I_{a_i}(\xi, t) \ddot{\theta} \\
 & + Q_{a_i}(\xi, t) \dot{\theta} (\dot{\theta}_{CG}(\xi, t) \sin(\theta + \tau_i)) + \left\{ \int_{L_i} c_{r_i}(\xi, t) \frac{dw_z(\xi, t)}{dt} d\xi \right\} \cos(\theta + \tau_i) \\
 & - \left(\int_{L_i} c_{r_i}(\xi, t) w_z(\xi, t) d\xi \right) \sin(\theta + \tau_i) - \left(\int_{L_i} c_{r_i}(\xi, t) V_i \frac{dw_z(\xi, t)}{d\xi} d\xi \right) \sin(\theta + \tau_i) \\
 & + \left(\int_{L_i} c_{r_i}(\xi, t) U_i(\xi, t) \frac{dw_z(\xi, t)}{d\xi} d\xi \right) \cos(\theta + \tau_i) - U_i(\xi, t) V_i(\xi, t) \rho c_{r_i}(\xi, t) \Big|_{\text{end of step or transom}} \\
 & - \left(\int_{L_i} c_{r_i}(\xi, t) V_i(\xi, t) d\xi \right) - \left(\int_{L_i} c_{r_i}(\xi, t) \rho C_{D,c_i}(\xi, t) V_i^2(\xi, t) d\xi \right) \Big\} + \int_{L_i} c_{r_i}(\xi, t) \rho \frac{d_i}{2} (c_{1i} + c_{2i}) \xi d\xi
 \end{aligned} \tag{6}$$

By substituting the 3D force obtained in equations 5 and 6 into the motion equation (Equations 2 and 3), it is found to be:

$$\rightarrow \sum_{i=1}^3 \{ M_{a_i} \sin(\theta + \tau_i) \cos(\theta + \tau_i) \ddot{x}_{CG} + (M + M_{a_i} \cos^2(\theta + \tau_i)) \ddot{z}_{CG} - (Q_{a_i} \cos(\theta + \tau_i)) \ddot{\theta} \} = \tag{7}$$

$$T_z + F'_z - \sum_{i=1}^n D_i \times \cos(\theta + \tau_i) + W$$

$$\rightarrow \sum_{i=1}^3 \{ -Q_{a_i} \sin(\theta + \tau_i) \ddot{x}_{CG} - (Q_{a_i} \cos(\theta + \tau_i)) \ddot{z}_{CG} - (I + I_{a_i}) \ddot{\theta} \} = F'_\theta + Tx_p - \sum_{i=1}^n D_i x_d \tag{8}$$

where, M is mass, W is weight, T is thrust force, D_i is drag force for each planing surface, x_p and x_d are distance from CG to the center of action, and F'_z and F'_θ signifies the total force without considering the defined parameters M_{ai} , Q_{ai} , and I_{ai} . These equations (7 and 8) are second order nonlinear differential. Hence, to solve the equations 6 and 7, the Runge–Kutta–Merson method has been applied.

4 NUMERICAL SIMULATION

A Semi- Implicit Method for Pressure-Linked Equations (SIMPLE) to conjugate pressure and velocity field has been used to find the field of all hydrodynamic unknown quantities, and an Algebraic Multi-Grid (AMG) solver was used to accelerate the convergence of the solution. A segregated flow solver approach has been used for all simulations. The free surface has been modeled with the two phase VOF approach with a High-Resolution Interface Capturing (HRIC) scheme based on the Compressive Interface Capturing Scheme for Arbitrary Meshes (CICSAM). The wall function approach was used for the near wall treatment, in particular, the All wall y^+ model. It is a hybrid approach, that attempts to emulate the high y^+ wall treatment for coarse meshes, and the low y^+ wall treatment for fine meshes. For turbulent flows, y^+ values in the range of 30 - 300 are generally acceptable (CD-Adapco, [24]). The values of wall y^+ on the hull surface are shown in Figure 2. The Reynolds stress is solved by means of the $k-\omega$ SST turbulence model.

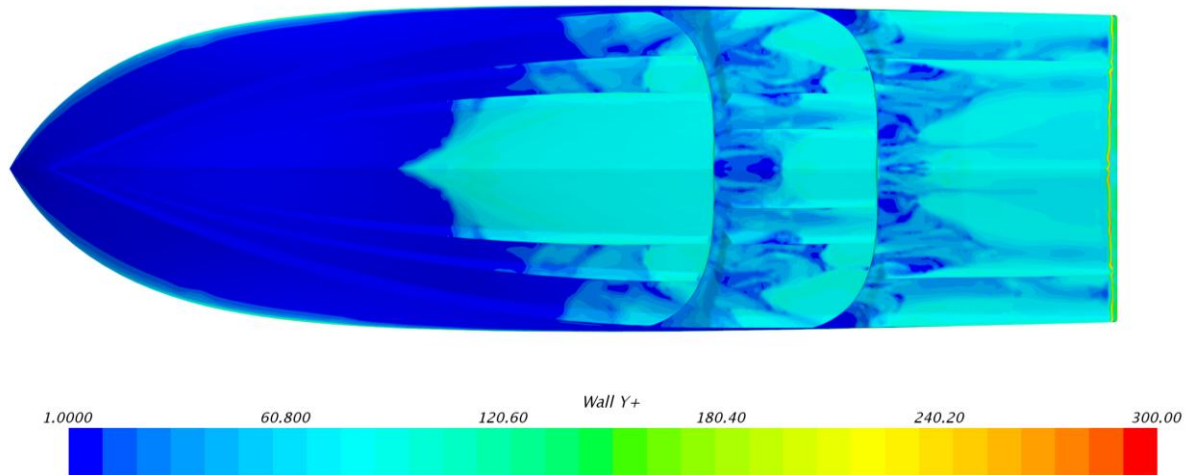


Figure 3: View of the wall y^+ on hull in calm water test at 30 Kn.

The URANS simulations were carried out using the technique of the Overset/Chimera grid mesh in order to take into account the hull motion in wave. This technique requires the definition of two different regions: a static region defined background region and a moving region, that incorporates the hull, defined Overset region (Figure 4). More details about this approach in the simulation of hull motion in wave and for calm water resistance simulation are available in Tezdogan et al. [25] and De Luca et al. [26] respectively. The computational domain dimensions are shown in Figure 4 and these dimensions are in compliance with the ITTC [27] recommendations and are close to similar studies, such as Tezdogan et al. [25].

About the time-step value for resistance computations in calm water, the time step size is determined by the following formula:

$$\Delta t = 0.005 - 0.01 L/V \quad (9)$$

where L is the length between perpendiculars, in accordance with the related procedures and guidelines of ITTC [27]. For the prediction of vessel responses to incident regular waves, at least 100 time steps per encounter period were used, as recommended by ITTC [27].

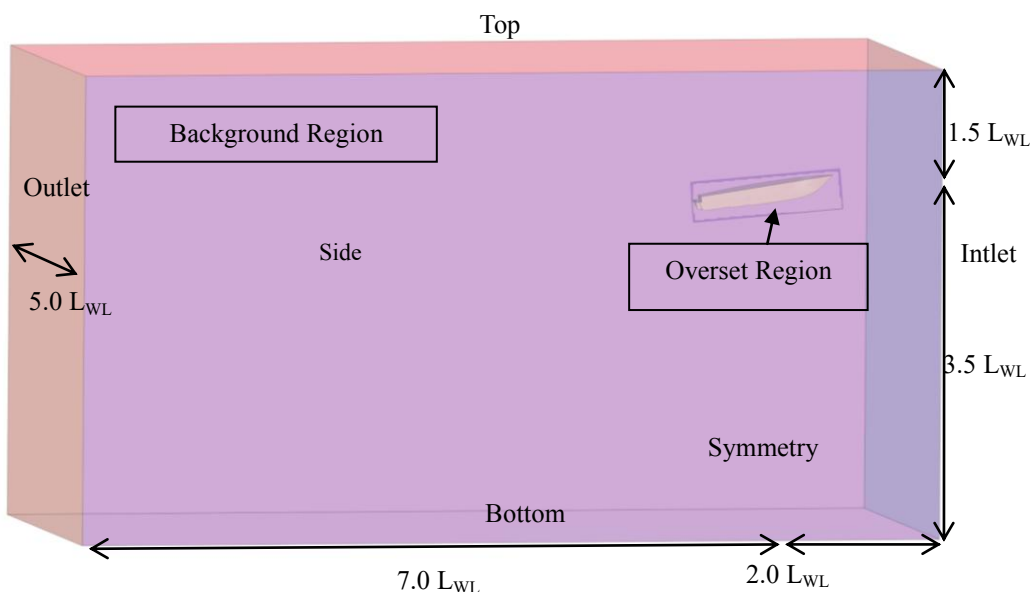


Figure 4: Computational domain dimensions and boundary conditions applied.

5 RESULTS AND DISCUSSION

In this sub-section results analytical and simulation method for motion of double stepped planing hull in calm water and regular wave compared each other. The main aim of this stage of analysis is to verify the accuracy of the analytical method predicting the heave and pitch motions, CG acceleration, and added resistance of the double stepped planing hull in regular head wave. It should be noted that there is a lack in the literature because there are not available experimental data regarding the motions of double stepped planing hull in head sea.

5.1 Motions in regular wave

The amplitude ratio of heave, pitch and CG acceleration obtained by numerical simulation and analytical method using FFT analysis are shown in table 3. Comparing the time history plots, the amplitude ratio from the analytical and numerical results follows the same trend (see table 3). Comparison of analytical method against numerical study shows error in prediction of pitch, heave, and CG acceleration around 1%, 14%, and 16%, respectively.

Table 3: results of pitch, heave, and CG acceleration amplitude by FFT analysis.

| z/A (analytical) | z/A (simulation) | θ/KA (a) | θ/KA (s) | a_{CG}/g (a) | a_{CG}/g (s) |
|--------------------|--------------------|-----------------|-----------------|----------------|----------------|
| 0.093 | 0.094 | 3.2 | 2.8 | 0.5 | 0.43 |

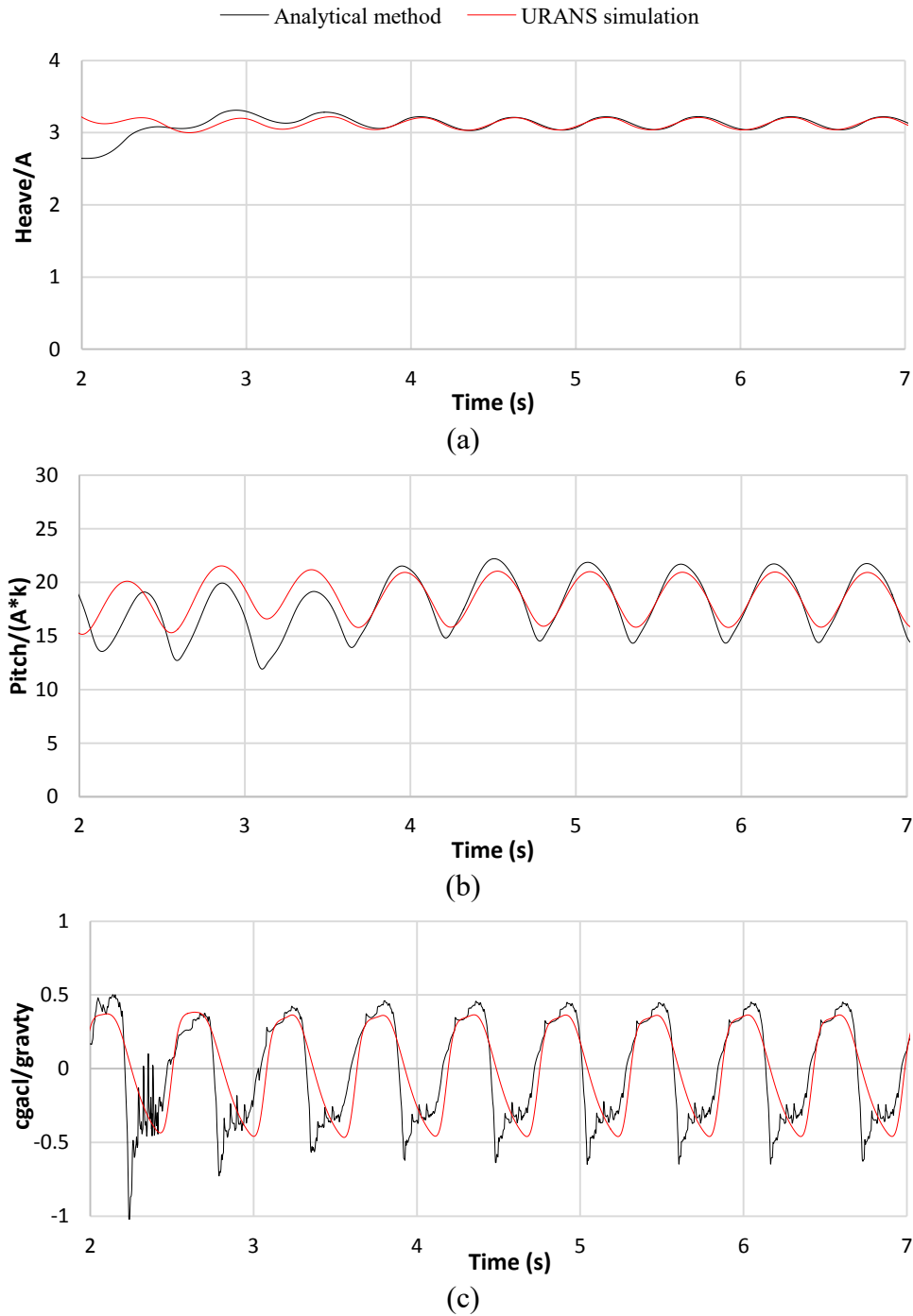


Figure 5: Time histories: a) heave motion, b) pitch angle, and c) CG acceleration.

5.2 Added resistance

The resultant added resistance of the double stepped planing hull using the different methods are tabulated in Figure 6 and Table 4. The added resistance is defined as the difference between the steady and 0th-order harmonic component of resistance. Added resistance calculation is based on the following equation.

$$R_{AW} = \overline{R_{AW}} - R_T \quad (10)$$

$\overline{R_{AW}}$ is the mean resistance in waves and R_T is the calm water resistance. Hence, the effective power due to the added resistance in wave has calculated as follow.

$$\Delta P_E \% = \frac{\overbrace{P_{E_{wave}} - P_{E_{calm\ water}}}^{\Delta P_E}}{P_{E_{calm\ water}}} \times 100 \tag{11}$$

It is observed that the results of both methods (analytical and numerical methods) are relatively accurate (similar manner) to the ship motion predictions in regular wave. Verification of analytical method against numerical study for prediction added resistance in regular wave is around 3%. So, this analytical method was applied, in the preliminary design stage, in order to evaluate the performance in regular wave of several concurrent hull geometries. Hence, this method represents a very fast tool for the designers, in particular in the early design stage, when several configurations (hull shapes, different displacement conditions, different position of CG, etc.) have to be evaluated and compared quickly.

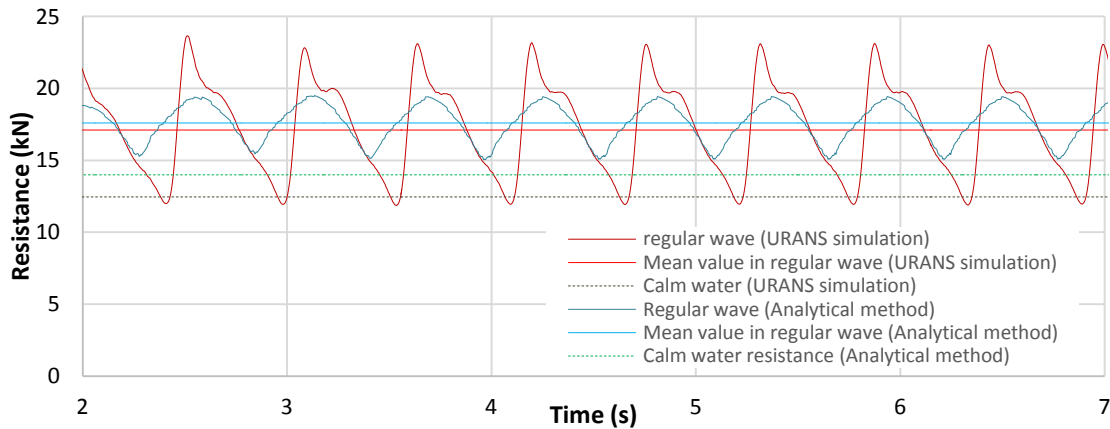


Figure 6: comparison of the added resistance – analytical method vs URANS simulations.

Table 4: Added resistance analysis of wave with H=0.75 (m) using different methods.

| | Encountered Freq. (Hz) | Encountered Freq. by FFT (Hz) | Error (%) | ΔP_E (kW) | ΔP_E (%) |
|-------------------|------------------------|-------------------------------|-----------|-------------------|------------------|
| Star CCM+ | 1.780 | 1.753 | 1.53% | 71.978 | 37.29% |
| Analytical method | 1.780 | 1.753 | 1.53% | 64.466 | 28.81% |

6 CONCLUSIONS

In the current paper, a mathematical model and numerical simulation for vertical motion (heave and pitch) of a double stepped planing hull in head sea has been developed. The analytical method represents a very fast way compared with the URANS simulations. A verification of analytical method has been performed against the current numerical simulation study, and error in prediction of added resistance, pitch, heave, and CG acceleration are around 3%, 1%, 14%, and 16%, respectively.

This combined solution demonstrates a very fast way for the designers in order to analyze and compare a high number of concurrent hulls for calculation resonance region in head sea.

In the near future, will be attempt to solve other motions such as roll motion, sway motion, couple heave, pitch, and roll of double stepped planing hull in calm water and regular wave.

REFERENCES

- [1] Fridsma, G., A systematic study of the rough-water performance of planing boats, Davidson Laboratory, Stevens Institute of Technology, Hoboken, NJ, USA, (1969), R-1275.
- [2] Fridsma, G., A systematic study of the rough-water performance of planing boats (irregular waves—part II), Davidson Laboratory, Stevens Institute of Technology, Hoboken, NJ, USA, (1971), R-11495
- [3] Savitsky D., Brown P.W., Procedures for hydrodynamic evaluation of planing hulls in smooth and rough water, *Marine Technology*, (1976), 13(4), 381-400.
- [4] Martin, M., Theoretical prediction of motions of high-speed planing boats in waves. DTNSRDC, (1976), Report 76-0069. Bethesda, MD, USA.
- [5] Martin, M., Theoretical determination of porpoising instability of high-speed planing boats. DTNSRDC, (1976), Report 76-0058. Bethesda, MD, USA.
- [6] Zarnick E.E., A nonlinear mathematical model of motions of a planing boat in regular waves, Bethesda Maryland: David Taylor Naval Ship Research and Development Center, (1978).
- [7] Kuening, J.A., The nonlinear behavior of fast mono-hulls in head waves, PhD Thesis, Delft TU, Delft, Netherlands, (1994).
- [8] Hicks, J.D., Troesch, A.W., Jiang, C., Simulation and nonlinear dynamics of planing hulls, *Journal of Offshore Mechanics and Arctic Engineering*, (1995), Vol. 117, p.p. 38-45.
- [9] Akers, R.H., Dynamic analysis of planing hulls in vertical plane. In *Proceedings of the Society of Naval Architects and Marine Engineers, New England Section*, (1999).
- [10] van Deyzen, A., A nonlinear mathematical model for motions of a planing monohull In head seas, *Proceedings of the 6th International Conference on High Performance Marine Vehicles*, Naples, Italy, (2008).
- [11] Sebastiani, L., Bruzzone, D., Gualeni, P., et al., A practical method for the prediction of planing craft motions in regular and irregular waves, *Proceedings for the 27th International Conference on Offshore, Mechanics and Arctic Engineering*, Estoril, Portugal, (2008).
- [12] Ghadimi, P., Dashtimanesh, A., Djeddi, S.R., Faghrfour Maghrebi, Y., Development of a mathematical model for simultaneous heave, pitch and roll motions of planing vessel in regular waves. *International Journal of Scientific World*, (2013), 1: 44-56.
- [13] Ghadimi, P., Dashtimanesh, A., Faghrfour Maghrebi, Y., Initiating a mathematical model for prediction of 6-DOF motion of planing crafts in regular waves, *International Journal of Engineering Mathematics*, (2013), 1-16.
- [14] Tavakoli, S., Ghadimi, P., Dashtimanesh, A., A nonlinear mathematical model for coupled heave, pitch and roll motions of a high-speed planing hull. *Journal of Engineering Mathematics*, (2017), 104(1), 157-194.
- [15] Tavakoli, S., Dashtimanesh, A., Mathematical simulation of planar motion mechanism test for planing hulls by using 2D+ T theory. *Ocean Engineering*, (2018), 169, 651-672.
- [16] Savitsky, D., Morabito, M., Surface Wave contours associated with the fore body wake of stepped planing hulls. *Marine Technology*, (2011), 47.
- [17] Dashtimanesh, A., Tavakoli, S., Sahoo, P., Development of a simple mathematical model for calculation of trim and resistance of two stepped planing hulls with transverse steps,

- Proceedings of 1st International Conference on Ships and Offshore Structures, Hamburg, Germany, (2016).
- [18] Dashtimanesh, A., Tavakoli, S., Sahoo, P., A simplified method to calculate trim and resistance of a two-stepped planing hull, *Ships and Offshore Structures*, (2017), 12 (sup1), S317-S329.
- [19] Niazmand Bilandi, R., Dashtimanesh, A., Tavakoli, S., Development of a 2D+ T theory for performance prediction of double-stepped planing hulls in calm water. *Proceedings of the Institution of Mechanical Engineers, Part M: Journal of Engineering for the Maritime Environment*, (2018).
- [20] Niazmand Bilandi, R., Mancini, S., Vitiello, L., Miranda, S., De Carlini, M., A Validation of Symmetric 2D + T Model Based on Single-Stepped Planing Hull Towing Tank Tests, *J. Mar. Sci. Eng.*, (2018), 6, 136.
- [21] Niazmand Bilandi, R., Dashtimanesh, A., Tavakoli, S., A Nonlinear Mathematical Model for Hydrodynamic Analysis of Unsteady Vertical Motion of Double-Stepped Planing Boats in Regular Waves, *Journal of Ship Research*, Revised, Jan. (2019).
- [22] Di Caterino, F., Niazmand Bilandi, R., Mancini, S., Dashtimanesh, A., De Carlini, M. Numerical Way for a Stepped Planing Hull Design and Optimization. In *Proceedings of the 19th International Conference on Ship & Maritime Research*, Trieste, Italy, 20–22 June (2018).
- [23] De Marco, A., Mancini, S., Miranda, S., Vitiello, L., Scognamiglio, R., Experimental and numerical hydrodynamic analysis of a stepped planing hull. *Appl. Ocean Res.*, (2017), 64, 135–154.
- [24] CD-adapco, STAR CCM+ User's Guide Version 13.06.011, (2018).
- [25] Tezdogan, T., Demirel, Y. K., Kellett, P., Khorasanchi, M., Incecik, A., Turan, O., Full-scale Unsteady RANS CFD Simulations of Ship Behaviour and Performance in Head Seas due to Slow Steaming, *Ocean Engineering*, (2015), 97, 186-206.
- [26] De Luca, F., Mancini, S., Miranda, S., Pensa, C., "An Extended Verification and Validation Study of CFD Simulations for Planing Hulls", *Journal of Ship Research*, (2016), 60(2), 101–118.
- [27] International Towing Tank Conference (ITTC), Practical guidelines for ship CFD applications. *Proceedings of the 26th ITTC*, (2011).

VERIFICATION AND VALIDATION STUDY OF OPENFOAM ON THE GENERIC PRISMATIC PLANING HULL FORM

JIAHUI LI*, LUCA BONFIGLIO[†] AND STEFANO BRIZZOLARA*

*iShip lab., Department of Aerospace and Ocean Engineering
Virginia Tech
420 Old Turner Street, Blacksburg, VA 24061, USA.
e-mail: jiahui37@vt.edu; stebriz@vt.edu

[†] MIT-Sea Grant College Program
Massachusetts Institute of Technology
12 Emily St. NW98-180, Cambridge, MA 02139, USA
e-mail: bonfi@mit.edu

Key words: Planing hulls, GPPH, OpenFOAM, URANS

Abstract. The paper presents the first series of results obtained in an ongoing validation and verification study of inter-dynamic OpenFOAM solver framework on a new set of high quality experimental tests performed on a large (2.4m long) generic planing hull model (GPPH) with high deadrise (18deg), from the pre-planing ($Fn_{\nabla}=2.6$) to fully planing ($Fn_{\nabla}=5.7$) regimes. This test case is a good benchmark for the free surface capturing model implemented in OpenFOAM which is based on a rather simple transport equation for an additional scalar field that defines the fraction of water in each cell of the computational mesh. This model, in spite of its simplicity seems capable of reproducing complex violent free surface flows such as that observed in planing hulls, that includes jet spray forming on the bottom and detaching from the chine of the planing hull and overturning waves off the wet chine region, with some nuances. The dependence of the flow solution on the mesh quality is presented and discussed. Practical indication of the level of uncertainty of CFD models for the prediction of the calm water hydrodynamics of the GPPH is given at the highest simulated speed. Predictions are then extended to the whole speed range, including dynamic trim and sinkage.

1 INTRODUCTION

CFD is taking the place of experimental tests in many engineering fields. In naval architecture, the accuracy and reliability of numerical simulations have been extensively validated with model scale experiments performed on different displacement hull forms [1] and the conclusion is that RANSE solvers are a mature tool for displacement ship design.

Validation and Verification (V&V) studies for high speed planing crafts are very less in comparison with larger displacement hull forms and often lack of high quality experimental

reference data on modern hull forms. Previous validation studies have considered old systematic planing hulls series [2] [3] that hardly reflect contemporary planing hull forms. Only few studies have considered modern planing hull shapes for practical seagoing application [4] [5] [6].

In the case of planing crafts, the free surface flow regime changes completely with respect to displacement hulls. The free waves patterns loose importance while the accurate estimation of the dynamic pressure distribution on the hull due to a water entry like flow becomes essential. In fact, the dynamic equilibrium of the vessel derives from the accurate prediction dynamic forces (mostly dynamic lift and not buoyancy) acting on the dynamic wetted portion of the planing hull. Hence, it can be argued that the running attitude of planning craft might be strongly dependent on the mesh resolution close to hull regions interested by jet spray formations such as the fore body (spray root line), chine and transom where flow separation phenomena occur.

In fact recent studies have appeared correct modeling of the non-linear free surface dynamics [4] even in presence of steps and ventilation [5]. The significant pressure field on the hull surface due to high Froude number and the sharp edges characterizing both the chine and the transom of planing craft induce jet sprays that need to be correctly modeled to achieve high accuracy in the prediction of the hydrodynamic forces exerted on the hull.

Under this perspective, the study aims to investigate the performance of the standard OpenFOAM solver interdympfoam, which combines mesh morphing to allow for the hull kinematic and a volume of fluid solver based on a rather simple transport equation for an additional scalar field that defines the fraction of water in each cell of the computational mesh. This model, in spite of its simplicity seems capable of reproducing complex violent free surface flows (see for instance [7]), such as that observed in planing hulls, that includes jet spray forming on the bottom and detaching from the chine of the planing hull and overturning waves off the wet chine region. The Validation and Verification study on the GPPH hull at the highest speed presented in this paper, shows that for planing hulls the flow mixture predicted by the volume of fluid solver is highly dependent on the mesh quality and refinement in high pressure regions. Typical problems noted by other researchers [2] [3] such as numerical (non-physical) diffusion of air under the hull, are noted also in this case and systematically addressed by the V&V study at the highest speed. The CFD predictions of resistance, dynamic trim and sinkage are then extended to the whole pure planing speed range ($Fn_{\nabla} = 4.2 - 5.7$) in the last section.

2 PHYSICAL AND NUMERICAL MODEL

The numerical model proposed in the present study is based on the solution of the Unsteady Reynolds Averaged Navier Stokes equations. The system is a set of partial differential non linear equations in the unknowns of pressure and velocity components. The physical problem is described in terms of mass and momentum conservation equations which are solved in a Cartesian reference frame for the pressure and velocity unknowns:

$$\begin{aligned} \frac{\partial(\rho u_i)}{\partial x_i} &= 0, \\ \frac{\partial u_i}{\partial t} + \frac{\partial(u_i u_j)}{\partial x_j} &= \frac{\partial}{\partial x_j} \left(\nu \frac{\partial u_i}{\partial x_j} \right) - \frac{1}{\rho} \frac{\partial p}{\partial x_i} + g_i. \end{aligned} \tag{1}$$

Even in model scale, the fluid dynamic problems considered in the present study is characterized by a high Reynolds number ($R_E \in [1e7, 3e7]$) inducing fully turbulent flow. We solve the fluid

dynamic problem by applying a Reynolds averaging technique to the solution of N-S equations. In particular, we have used the $k-\omega$ turbulence model (see [8]) reformulated in the Shear Stress Transport version (SST) by [9, 10]) with the goal to improve the model independence from freestream turbulent intensity through a formulation which blends the $k-\epsilon$ model (used in the free stream) and the $k-\omega$ model (used in the boundary layer). Freestream values of the turbulent quantities are calculated according to the turbulent intensity and length scale based on the flat plate boundary layer thickness formulation:

$$k = \frac{3}{2} (UI)^2 \quad \omega = \frac{k}{\nu_T} \quad \nu_T = \frac{1}{\rho} \sqrt{\frac{3}{2}} UI l \quad (2)$$

In equation (2) l indicates the turbulent length scale and has been selected according to the boundary layer thickness δ_{99} of a turbulent flow on a flat plate.

$$l = 0.4\delta_{99} \quad \frac{\delta_{99}}{L} = \frac{0.374}{Re^{\frac{1}{5}}} \quad (3)$$

A volume of Fluid (VOF) surface capturing technique ([11]) is here used to predict the wave pattern generated by the hull advancing at the free surface. URANS equations are solved for a fluid mixture of water and air whose characteristics are determined on the basis of the scalar function γ :

$$\rho = (1 - \gamma) \rho_W + \gamma \rho_A \quad (4)$$

$$\mu = (1 - \gamma) \mu_W + \gamma \mu_A \quad (5)$$

At each time-step the local value of γ is determined by the solution of the following equation:

$$\frac{\partial \gamma}{\partial t} + \nabla \cdot (\gamma U) + \nabla \cdot [\gamma (1 - \gamma) U_r] = 0 \quad (6)$$

In equation (6) the term U_r indicates the relative velocity between water and air and it is here used to steepen the gradient of the VoF scalar function γ close to the interface. U_r is tuned through the parameter C_f as follow:

$$U_r = n_f \min \left[C_f \frac{\phi}{S_f}, \max \left(\frac{\phi}{S_f} \right) \right] \quad (7)$$

In particular $\nabla \cdot [\gamma (1 - \gamma) U_r]$, also called artificial compression, is effective when $\gamma \neq 0$ and $\gamma \neq 1$ and it is opportunely tuned to increase the compression of the free surface hence reducing the interface smearing often experienced when surface capturing techniques are used to predict free surface flows.

A constant flow velocity is imposed at the inlet according to the specific operating conditions. Neumann boundary condition is used for the dynamic pressure field at the inlet (zero gradient). Constant zero dynamic pressure is enforced at the outlet of the computational domain where a Neumann boundary condition is instead used for the velocity field (zero gradient). No-slip condition is imposed at the hull surface where a zero gradient dynamic pressure condition is used together with a zero velocity field. Top, bottom and side boundaries have been modeled as slip walls.

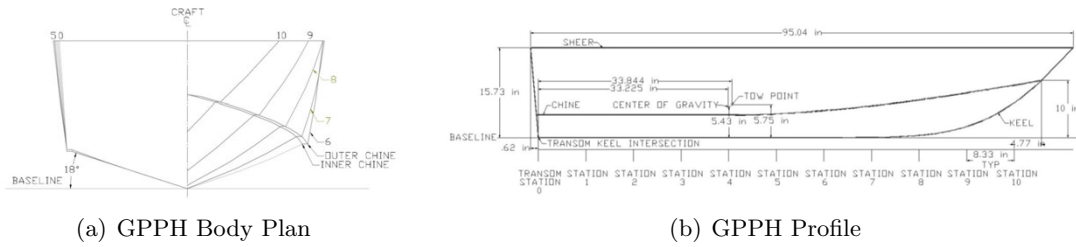


Figure 1: GPPH Test Model [14]

Ship motion is obtained using a dynamic mesh strategy supported by grid morphing algorithm that diffuse boundary motion through internal grid points. Mesh motion is computed from the pressure field on the hull. In particular, at each time-step the position and the velocity of the hull are known as well as the forces and moments acting on the rigid body (which result from pressure and velocity fields integration). We solve the forward dynamic problem using a 6 Degrees of Freedom solver in which surge, sway, roll and yaw motions are constrained, while heave and pitch accelerations are computed using a Newmark solver (see [12]). A pseudo-solid Laplace smoothing equation distributes hull motion to the internal grid points through a diffusivity coefficient Γ following equations (8) and (9):

$$\nabla \cdot (\Gamma \nabla V) = 0 \quad (8)$$

Once mesh deformation velocity (V) is known at each point, grid displacement is found at each new time step t^n solving a linear motion equation:

$$x_n = x_{n-1} + V \Delta t \quad (9)$$

Equation (9) describes the deformation of an initially valid mesh (t_{n-1}) into a deformed mesh at t_n . The quality of the grid is verified at each time step to ensure that no faces and no cells were inverted during motion. This method has been applied with success for the solution of forced oscillation problems (see [13])

The numerical solution of the aforementioned physical problem is obtained using a Finite Volume approach with collocated arrangement of variable. In particular, we have used OpenFOAM libraries to numerically solve the non-linear system of PDEs describing the fluid dynamic problem on a computational domain discretized through unstructured grid (see [15]). More in details, the solution of the dynamic pressure term is here obtained using an algebraic multigrid method (*GAMG* - Geometric Algebraic Multi Grid) with a *DIC* (Diagonal Incomplete Cholesky) smoother. The tolerance has been set up to $5e-8$. Velocity U and transported quantities (turbulent kinetic energy k and specific dissipation rate ω terms) have been solved using a smooth solver suitable for asymmetric matrices with a symmetric Gauss Seidel smoother with a tolerance of $1e-7$. Volume of fluid term γ , has been solved with a smooth solver used also for other transported quantities, but in this case we have used a *MULES* (Multi-dimensional Limiter for Explicit Solution) to guarantee boundedness of γ . The tolerance has been constrained to $1e-10$ and the artificial compression of the free surface (see (7)) has been tuned through the parameter C_f ($C_f=1$). This solver is particularly effective when used in combination with an adjustable

Table 1: Tested GPPH Characteristics

| Parameter | Value |
|--|------------------|
| Length Between Particulars, L_{pp} | 2.4140 (m) |
| Maximum Projected Chine Beam, B_{PX} | 0.6274 (m) |
| Deadrise Angle to Outer Chine, β | 17.2000 (degree) |
| Displacemet, ∇ | 101.5140 (kg) |
| Longitudinal Center of Gravity, LCG | 0.8439 (m) |
| Vertical Center of Gravity, VCG | 0.1379 (m) |
| Longitudinal Center of Tow Point, LTP | 0.8596 (m) |
| Vertical Center of Tow Point, VTP | 0.1461 (m) |
| Hydrostatic Draft at Transom Above Baseline, $T_{Transom}$ | 0.1476 (m) |
| Hydrostatic Trim Angle from Baseline (+bow \uparrow) | 0.1270 (degree) |

time-step strategy that at each time iteration select the time-step in order to satisfy a given constraints on the Courant number, which in a 1-D case is defined as:

$$Co = u \frac{\Delta t}{\Delta x} \quad (10)$$

In particular, the unsteady solution of RANS equations is achieved differentiating in time with an implicit Euler scheme and adjustable time step selected according to the maximum Courant number ($Co < 0.5$ at the free surface and $Co < 1$ everywhere else). Navier-Stokes equations have been solved including gravity effects but dropping the hydrostatic component from the pressure field. The pressure-velocity coupling is here solved using the PISO scheme.

3 TEST CASE

The test model of Generic Prismatic Planing Hull is designed by the Naval Surface Warfare Center as assessment for CFD simulation tools. This model uses a modern planing hull bow shape and a prismatic hull aft of the bow area to minimize the geometric variables, thus to have the physics and response to waves of a typical planing hull. [14] The test data used in this paper is from the November 2015 test performed at Naval Surface Warfare Center Carderock Division (NSWCCD). Figure 1(a) shows the body plan of the model, Figure 1(b) shows profile view of the model.

The model is only allowed to be free to heave and pitch while it was restrained in surge, sway, roll and yaw by the experimental setup. The model was tested under 7 different speeds from pre-planing to fully planing regimes.

4 VERIFICATION & VALIDATION STUDY

The solution of the physical problem described in section 2 is obtained through a finite volume numerical technique with collocated arrangement of variables. Figure 3 presents RANSE predictions obtained at $V=12.24$ m/s corresponding to the highest volumetric Froude number tested by [14] ($F_{\nabla} = \frac{V}{\sqrt{g\nabla^{1/3}}}=5.723$). The accuracy of the numerical solution depend on the

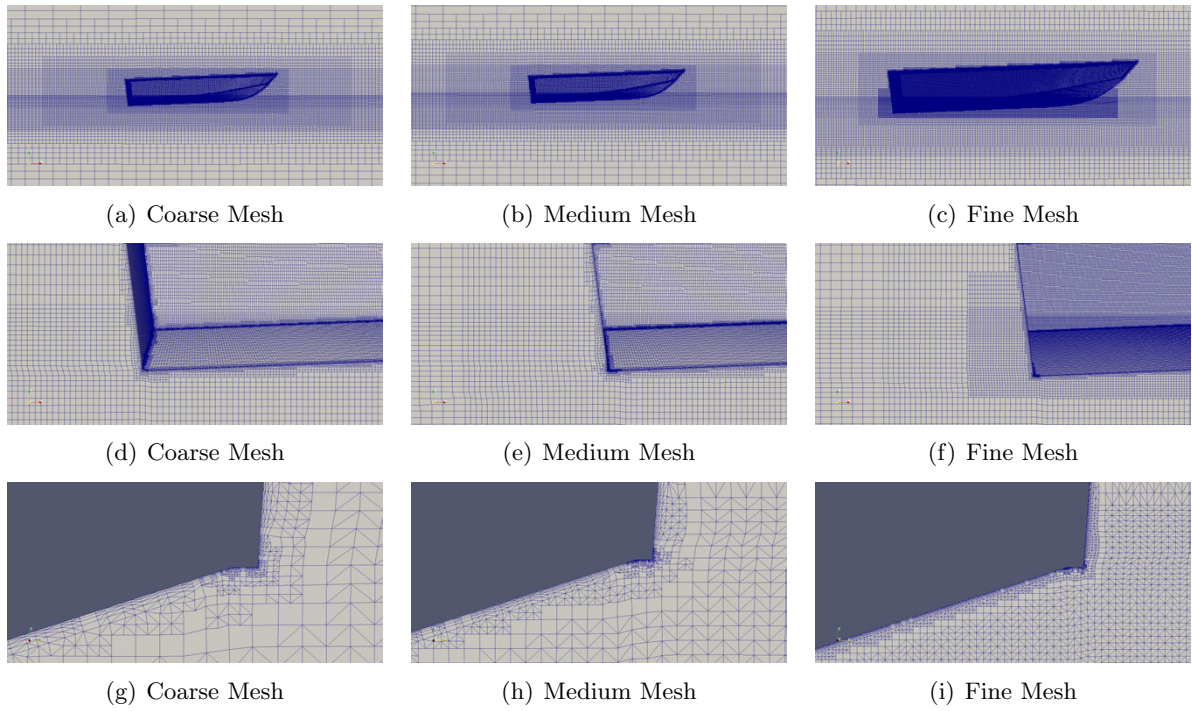


Figure 2: Overview of the three numerical grids used for the grid verification and numerical uncertainty estimation study. Top three panels (2(a),2(b) and 2(c)) present a longitudinal view of the grid including the hull and the surrounding free surface region). Middle panels (2(d),2(e) and 2(f)) show grid refinements in proximity of the flat transom. Bottom panels (2(g),2(h) and 2(i)) present grid refinements on the hull bottom with specific focus to the chine region.

Table 2: Numerical Results obtained with the three meshes at the highest speed $V=12.24$ m/s

| | Coarsest Mesh | Relative Error (%) | Medium Mesh | Relative Error (%) | Fine Mesh | Relative Error (%) | Experimental Result | Savitsky Short Method |
|--------------------------|------------------|-----------------------|----------------|-----------------------|--------------|-----------------------|------------------------|--------------------------|
| Mesh (Number of Cells) | 1141900 | — | 2424676 | — | 4560229 | — | — | — |
| Grid step size (h_i) | 1.587 | — | 1.234 | — | 1 | — | — | — |
| Resistance [N] | 220.4 | 18.32 | 244.0 | 9.57 | 252.0 | 6.61 | 269.83 | 231.32 |
| Friction Drag [N] | 158.0 | — | 182.1 | — | 190.0 | — | — | 181.98 |
| Pressure [N] | 62.4 | — | 61.9 | — | 62.0 | — | — | 49.34 |
| Trim Angle [degree] | 1.87 | 34.15 | 2.14 | 1.46 | 2.19 | 1.08 | 2.17 | 2.84 |
| Heave [cm] | 10.32 | 7.54 | 9.99 | 4.08 | 9.89 | 3.14 | 9.60 | 10.33 |
| L_C [cm] | 43.45 | 2.25 | 43.11 | 3.01 | 42.97 | 3.55 | 44.45 | 50.54 |
| L_K [cm] | 168.94 | 2.19 | 173.21 | 0.28 | 174.01 | 0.74 | 172.72 | 175.31 |

numerical set-up and the strategy adopted for the discretization of the computational domain. In this section we describe the grid generation strategy and we present a verification study having the goal to characterize the uncertainty of the numerical solution.

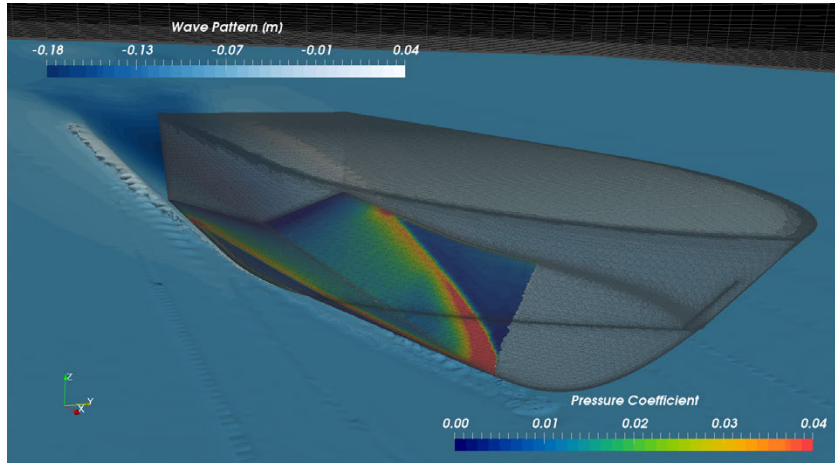


Figure 3: Perspective view of the pressure coefficient contours on the bottom of the planing hull. Red color indicate the spray root line. Blue colors indicate the wave pattern at $V=12.24$ m/s. Results obtained using the medium mesh described in table 2.

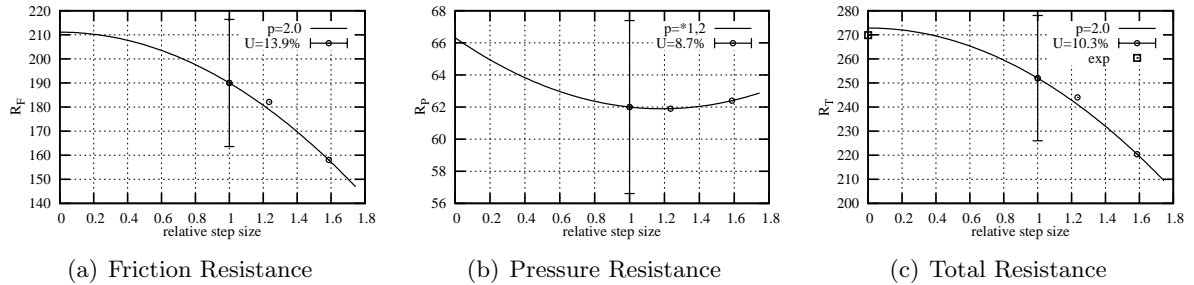


Figure 4: Convergence of the friction (4(a)), pressure (4(b)) and total (4(c)) calm water resistance with respect to the relative step size $\frac{h_i}{h_1}$ defined in equation (11).

4.1 Grid Generation Strategy

The computational domain covers a total length of 36.21 m, corresponding to 15 ship lengths, a total breadth of 36.21 and a total height of 9.242 m. With reference to a Cartesian coordinates system (xyz) , the tow point of the planing hull is positioned at $(0,0,0)$. The longitudinal distance between the tow point and inlet is 12.07 m, corresponding to 5 ship lengths. The bottom of the domain is positioned at 7.242 m, corresponding to 3 ship lengths, while the top is located at 2 m from the free surface at rest (approximately 1 ship length). The computational domain is divided in 6 vertical regions, each representing a specific depth-wise layer. With reference to the design water line (free surface at rest), three layers are used to discretize the water region while the remaining three are employed in the air region. Each depth-wise region extends from inlet to outlet without any geometrical progression in the length- (x) or breadth-wise (y) direction. Geometrical progressions are used in the bottom and top layer to coarsen the grid resolution from the internal volume to the top and bottom boundaries of the computational domain. We first construct a background mesh of structured elements discretizing the 6 depth-wise layers

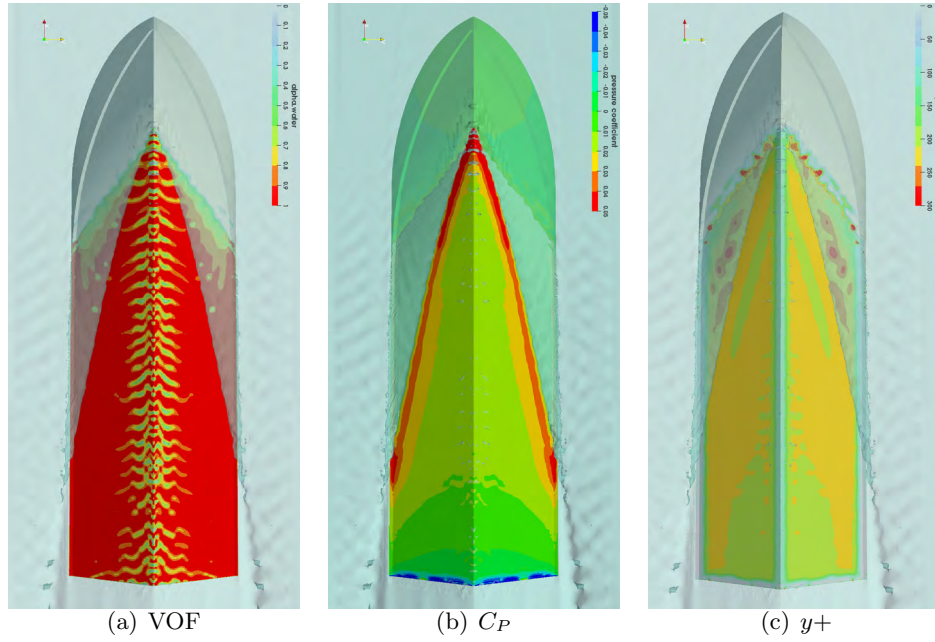


Figure 5: Numerical solution obtained using the coarse grid described in table 2. Results presented in terms of Volume of Fluid, pressure coefficient and non-dimensional wall distance contours on the hull bottom. Steady-state solution at $V=12.24$ m/s.

previously described. This structured grid is successively refined in the $x - y$ direction by iteratively selecting sub-domain regions containing the hull and refining them in the length-breadth direction. The refinement in the direction perpendicular to the free surface is performed only using the aforementioned depth-wise layers for the construction of the structured grid. Refinement in the $x - y$ directions are performed using 6 refinement boxes containing the hull. The plane-wise refinement process leads to an unstructured background grid that is then intersected with the hull surface. The hull is represented by means of a triangulated surface mesh serving as input for the generation the unstructured grid. The hull surface mesh is intersected with the unstructured background grid through an iterative procedure that first increases mesh resolution at the hull-surface/background-grid intersections and then discards cells with centroid inside the hull surface. Cell vertices of this jagged mesh are successively projected on the hull surface and repeatedly extruded in order to obtain layers of prismatic cells suitable for boundary layer flow resolution. The background grid has been constructed using *blockMesh* and successively refined in the $x - y$ direction using six *topoSet-refineMesh* iterative loops. The hull-background intersection has been performed using *snappyHexMesh* utility (see [15] for further details).

4.2 Grid verification

A mesh convergence study is performed at the highest speed, 12.24 m/s corresponding to $Fr_{\nabla} = 5.75$. The grid verification analysis has the goal to estimate the numerical uncertainty of CFD predictions for friction, pressure and total calm water resistance. To this end, we consider three different computational domain discretizations. With reference to the mesh description

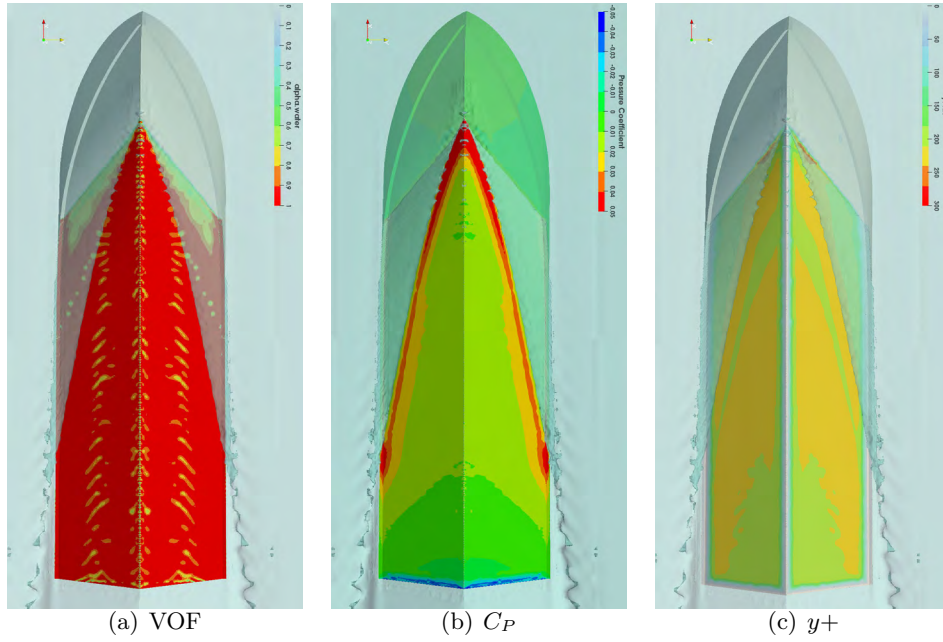


Figure 6: Numerical solution obtained using the coarse grid described in table 2. Results presented in terms of Volume of Fluid, pressure coefficient and non-dimensional wall distance contours on the hull bottom. Steady-state solution at $V=12.24$ m/s.

previously provided, we have systematically increased the resolution of the background grid as well as the mesh resolution in proximity of the hull. During this process we ensured conformity of several mesh quality indicators, such as maximum aspect ratio, number of non-orthogonal faces, maximum skewness. Figure 2 presents a comparison between the three different discretizations used in the grid verification study. Numerical predictions are presented in terms of total resistance as well as shear and pressure drag components in Table 2. At this high Froude number, the prevalent resistance component is the friction drag which accounts for more than 75% of the total resistance. The ration of the two resistance components is confirmed by the estimation obtained with Savitsky short method that are reported in the last column. Apparently the numerical predicted pressure drag does not change considerably with mesh resolution, this is

Uncertainty U and order of convergence p have been estimated using power series expansions as a function of the relative grid size, following the procedure described by [16]. Figure 4 presents convergence of friction resistance (Figure 4(a)), pressure resistance (Figure 4(b)) and total resistance (Figure 4(c)) with respect to grid relative step size defined as follows:

$$\frac{h_i}{h_1} = \left(\frac{n_1}{n_i} \right)^{\frac{1}{3}} \quad (11)$$

Where n_i represents the total number of cells used in the unstructured grids previously presented and n_1 is the total number of cells of the finest grid used in the numerical uncertainty estimation. Grid step size h_i is reported in table 2 for the three grids used in the verification study. Discretization error ϵ is estimated for pressure R_P , friction R_F and total resistance R_T

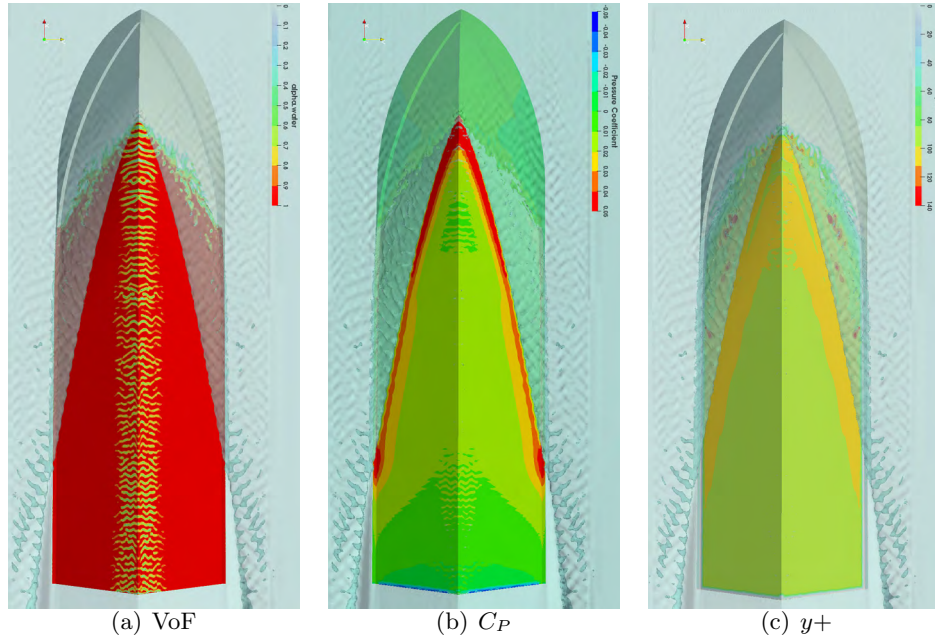


Figure 7: Numerical solution obtained using the coarse grid described in table 2. Results presented in terms of Volume of Fluid, pressure coefficient and non-dimensional wall distance contours on the hull bottom. Steady-state solution at $V=12.24$ m/s.

using the following truncated power series expansion:

$$\begin{aligned}
 \epsilon_{R_F} &\approx R_{F_i} - R_{F_0} = \alpha h_i^2 \\
 \epsilon_{R_P} &\approx R_{P_i} - R_{P_0} = \alpha_1 h_i + \alpha_2 h_i^2 \\
 \epsilon_{R_T} &\approx R_{T_i} - R_{T_0} = \alpha h_i^2
 \end{aligned} \tag{12}$$

Equation (12) suggest that friction and total resistance are monotonically converging, contrarily from pressure resistance which is instead non-monotonically convergent. The approximate exact solutions for pressure resistance is $R_{P_0} = 66.3$ N with uncertainty $U=8.69\%$, for friction resistance is $R_{F_0} = 211.1$ N with uncertainty $U=13.9\%$ while for total resistance is $R_{T_0} = 272.8$ N with uncertainty $U=10.3\%$. The approximate exact solution for the total resistance present a relative error w.r.t. experiments of about 1%. Despite the polynomial fitting suggest an approximate exact solution for pressure resistance of about 66.3 N with 8.7% of uncertainty, we believe that the discrepancy characterizing CFD predictions of total resistance should be mostly imputed to an inaccurate solution of the friction resistance on the hull bottom. Figure 5, 6 and 7 present CFD results obtained for the coarse, medium and fine mesh as defined in table 2. More in detail, figures 5(a) 6(a) and 7(a) show VOF contours on the hull bottom at the latest time-step (corresponding to a non-dimensional time Ut/L of 16.3). VOF contours as predicted by the coarsest grid (figure 5(a)) present extensive numerical ventilation in proximity of the keel in the pressure area. The medium mesh, characterized by similar values of non-dimensional wall distance $y+ = \frac{u_* y}{\nu}$ (see figures 5(c) and 6(c)), partly mitigate this numerical inaccuracy (see figure 6(a)), however for the finest grid, characterized by lower values of $y+$ (figure 7(c)),

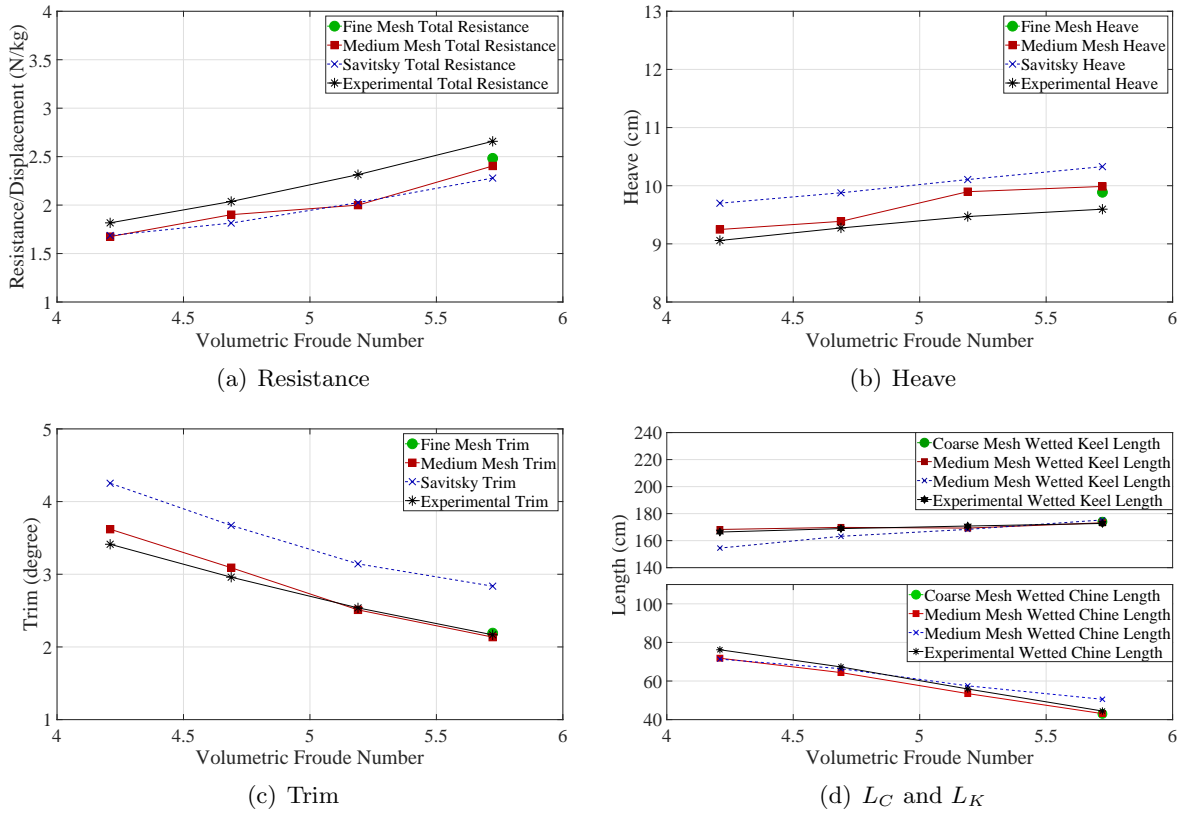


Figure 8: Comparison Plot vs Volumetric Froude Number

this inaccuracy seems to be as marked as in the coarse grid case. VOF contours in the hull bottom pressure area suggest higher friction drag predicted by the medium mesh. However, this is not confirmed by results presented in figure 4(a). The reason might be related to the solution obtained in the spray area, in which the coarse grid predicts extensive ventilation (more extensive green/blue colors), while the medium and the fine resolution leads to higher values of γ (VOF). Pressure solution on the hull bottom is not significantly affected by grid resolution as demonstrated in figure 4(b) in terms of pressure drag and in figures 5(b), 5(b) and 7(b) terms of pressure coefficient $C_P = \frac{p - \rho gh}{0.5 \rho v^2}$.

5 PREDICTIONS AT DIFFERENT SPEEDS

The mesh verification study and the assessment of the numerical uncertainty highlighted the necessity of using high mesh resolution close to the hull in order to capture the correct dynamic of the free surface and in general of the γ (VOF) on the spray and the pressure area of planing hulls. However the computational budget at our disposal is insufficient to perform a validation of CFD predictions in a wide range of volumetric Froude numbers ($F_{n\triangledown}$). For this reason we present results obtained using the medium mesh (see table 2) for the solution of the hydrodynamic problem at $F_{n\triangledown}=4.210$, $F_{n\triangledown}=4.689$, $F_{n\triangledown}=5.190$ and $F_{n\triangledown}=5.723$. Results are presented in figure 8 in terms of non-dimensional calm water resistance, $\frac{R_T}{\Delta}$ (figure 8(a)),

heave of the Center of Gravity (figure 8(b)), trim angle (figure 8(c)) as well as wetted lengths of the chine L_C and the keel L_K (figure 8(d)). CFD predictions of total resistance averagely underestimates experimental measurements of about 9.5%. This discrepancy is minimum at $\text{Fn}_\nabla=6.689$ where CFD predictions are characterized by a relative error w.r.t. experiments of about 6.9%. A maximum discrepancy of 13.7% is experienced at $\text{Fn}_\nabla=5.190$. The average relative error of CFD predictions w.r.t. experiments is consistent with the numerical uncertainty estimation determined at the highest speed ($\text{Fn}_\nabla=5.723$) in section 4. The dynamic attitude of the planing hull is well predicted in the range of speeds considered in the present study. This is demonstrated in figures 8(b), 8(c) comparing the experimental with the numerically predicted dynamic heave motion and trim angle and in figure 8(d) where the wetted chine and keel length are compared at different volumetric Froude numbers.

6 CONCLUSIONS

The Generic Prismatic Bull tested at the NSWCCD provides a valuable opportunity to test numerical models and tune their parameters against a modern set of experiments. The grid verification study and numerical uncertainty assessment presented in this paper highlighted the complexities in accurately capturing the free surface dynamics in case of violent flows caused by high velocity and pressure fields. The problem of numerical ventilation was partially mitigated by increasing the grid resolution while keeping relatively high values of y_+ . However further studies are needed to understand the influence of wall functions on VOF diffusion on the pressure area of planing hulls and to characterize the importance of numerical solution of the partial differential equation describing the transport of VOF. The accuracy of the results obtained at different speeds is consistent with the relative error of CFD predictions w.r.t. experiments found using other CFD solvers.

Acknowledgements

The support of the Office of Naval Research, grant N00014-17-1-2344, is gratefully acknowledged. Computations were run on the high performance computing clusters of Virginia Tech Advanced Research Computing Center.

References

- [1] Lars Larsson, Frederick Stern, and Michel Visonneau. *Numerical ship hydrodynamics: an assessment of the Gothenburg 2010 workshop*. Springer, 2013.
- [2] Brizzolara S. and Villa D. Cfd simulations of planing hulls. In *Proceedings of the Seventh International Conference on High-Performance Marine Vehicles, HIPER 2010*, pages 16–24, Melbourne, 2010. Florida Institute of Technology.
- [3] Gaggero S. Ferrando M. and Villa D. Open source computations of planing hull resistance. *Transactions of the Royal Institution of Naval Architects Part B: International Journal of Small Craft Technology*, 157:83–98, 2015.
- [4] R. Broglia and D. Durante. Accurate prediction of complex free surface flow around a high

- speed craft using a single-phase level set method. *Computational Mechanics*, 62:421–437, September 2018.
- [5] Brizzolara S. and Federici A. Cfd modeling of planing hulls with partially ventilated bottom. In *The William Froude Conference: Advances in Theoretical and Applied Hydrodynamics Past and Future*, pages 1–17, London, 2010. Royal Institution of Naval Architects.
- [6] Brizzolara S. and Serra F. Accuracy of cfd codes in the prediction of planing surfaces hydrodynamic characteristics. In *Proceedings of the 2nd International Conference on Marine Research and Transportation, ICMRT'07*, pages A:1–12, Italy, 2007. U. of Napoli Federico II.
- [7] Luca Bonfiglio and Stefano Brizzolara. Amplitude induced nonlinearity in piston mode resonant flow: A fully viscous numerical analysis. *Journal of Offshore Mechanics and Arctic Engineering*, 140(1):011101, 2018.
- [8] D.C. Wilcox. Reassessment of the Scale-Determining Equation for Advanced Turbulence Models. *The American Institute of Aeronautics and Astronautics (AIAA)*, 26:1299–1310, 1988.
- [9] F.R. Menter. Zonal two equation $k-\omega$ Turbulence Models for Aerodynamic Flows. In *24th AIAA Fluid Dynamics Conference, July 6-9, Orlando, Florida*, page 2906, 1993.
- [10] F.R. Menter. Two-equation eddy-viscosity turbulence models for engineering applications. *AIAA journal*, 32(8):1598–1605, 1994.
- [11] C.W. Hirt and B.D. Nichols. Volume of fluid (VOF) method for the dynamics of free boundaries. *Journal of Computational Physics*, 39(1):201–225, 1981.
- [12] R. Featherstone. *Rigid body dynamics algorithms*. Springer, 2014.
- [13] Luca Bonfiglio and Stefano Brizzolara. Unsteady viscous flow with non linear free surface around oscillating SWATH ship sections. *WSEAS Trans. Fluid Mech*, 9:49–57, 2014.
- [14] Weil C.R. Lee E. and Fullerton A. Experimental results for the calm water resistance of the generic prismatic planing hull (gppl). Technical report.
- [15] OpenFOAM Foundation. *OpenFOAM user guide*. OpenFOAM Foundation, 2014.
- [16] Luis Eça and Martin Hoekstra. A procedure for the estimation of the numerical uncertainty of cfd calculations based on grid refinement studies. *Journal of Computational Physics*, 262:104–130, 2014.

DESIGN OF LOW DRAG-TO-POWER RATIO HYDROKINETIC TURBINE MARINE 2019

ABOLFAZL SHIRI^{*}, JAN HALLANDER^{*} AND BJÖRN BERGQVIST[†]

^{*} SSPA Sweden AB
Chalmers Tvärgata 10, Göteborg, Sweden
email: ash@sspa.se, www.sspa.se

[†] Minesto AB
Vita gavelns väg 6, Göteborg, Sweden
email: Bjorn.Bergqvist@minesto.com, www.minesto.com

Key words: Computational Fluid Dynamics, Tidal Turbine, Ocean Energy, Horizontal Axis Hydrokinetic Turbine, Deep Green.

Abstract. The abundant power in tidal current is a reliable source of renewable energy for electricity production in coastal areas. With Deep Green technology, Minesto has presented a cost-effective unique approach to extract energy even from low speed water currents and increase the potential of ocean energy extraction. In PowerKite project, funded by EU Horizon 2020, we designed and tested a special type of horizontal axis hydrokinetic turbine for Minesto's tidal kite. The operational condition for this turbine is very different from stationary hydrokinetic turbines due to correlation between the kite's maneuvering speed, turbine drag and power production. In this paper, we present the procedure of turbine blade design for reducing drag forces while producing maximum torque. We used OpenProp, a lifting line method open-source code, combined with CAESSES modeler to establish the design space. To select the suitable design parameters with regard to cavitation and viscous effect, we also used RANS CFD solver OpenFOAM and improved the turbine performance. Computational studies as well as experimental test in cavitation tunnel are presented and the result is compared with a baseline turbine performance. The new design is currently being evaluated in sea-trial with a quarter-scale kite.

1 INTRODUCTION

With the advancement of renewable energy technologies in the world, the electricity production is becoming diverse and decentralized. In future, communities will prefer to exploit the local renewable resources at their disposal. Wind and solar energies, despite their low capacity factor, are gaining momentum in this "green market". Historically hydroelectricity dominated the renewable energy production but it was limited to certain geographical area near big rivers and required excessive infrastructure investment. Hydrokinetic ocean energy would expand the global energy potential and open up a reliable local resource for coastal area.

Tidal power as an abundant and predictable form of hydrokinetic energy has traditionally suffered from high utilization cost. Laws and Epps [14] offer an in-depth comparison of different hydrokinetic energy conversion (HEC) technologies and the challenges faced by

conventional techniques. The main problem is limited suitable sites for installation and low tidal water speed. Deep Green technology, invented and developed by Minesto, aims to address these issues by mounting the turbine on an underwater kite, which can operate in depth of up to 120 meters.

The tidal kite is capable of sweeping through low velocity tidal stream (1.2–2.4 m/s) with the speed several times higher than current due to hydrodynamic lift forces acting on the wings. The turbine is located in front of the kite and extracts kinetic energy from the motion of kite in the tidal stream. *Figure 1* shows an artistic illustration of the subsea tidal kite with the turbine positioned in front of the electrical generator in the nacelle. The nacelle is connected under the buoyant wing and kite is connected by tether to the bottom joint on seabed.

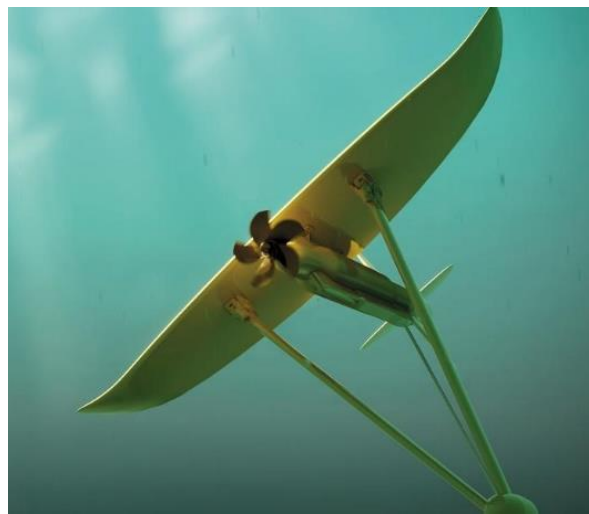


Figure 1 - The Deep Green subsea tidal kite.

In conventional stationary hydrokinetic turbine, the structural support counteracts the drag forces on the turbine. In tidal kite, excessive drag caused by higher loading of turbine blades prohibits the kite to reach design speed. Since the produced power is proportional to cube of water velocity entering the turbine, a lower drag is desirable to increase the kite speed. Therefore, conventional turbine design approach was not suitable for this project.

The Powerkite project developed a new power take-off system (PTO) for Deep Green tidal kite. The overall objective of the Powerkite project was to enhance the performance of the PTO for the next generation kite and to ensure high survivability, reliability, low environmental impact and competitive cost of energy in future commercial phases. As a part of PTO system, a special type of horizontal axis hydrokinetic turbine was designed starting from scratch with the goal of minimizing the drag-to-power ratio.

For the overall concept of turbine, we chose the open-blade design since the total weight and excessive drag from a shroud had adverse effect on kite performance. Shahsavarifard et.al. [17] argues that by extending blade length we can achieve the same power enhancement as by using a shroud. Moreover, to reduce the overall weight of the kite, the turbine design was limited to open blade version (without duct).

We started the turbine development procedure by defining the design parameters based on the operational conditions of the tidal kite in open sea. A matrix of design space was created based on these parameters using low fidelity numerical code. For further improvement, we selected a series of designs with highest drag to power coefficient ratio and desired output power of range. For those selections, we performed detailed simulations using viscous CFD solver to determine blade section properties and type of hydrofoil with highest performance without risk of cavitation inception. In the next step, the structural stiffness and the total weight of the blades were the criteria to consider for the final design.

With the selected blade geometry, series of model test were carried out in SSPA cavitation tunnel in different cavitation numbers and tip speed ratios. The model test resulted in minor improvement of the blade shape and the final new design was used to build a quarter of scale prototype for open sea test. The quarter-scale sea trial is currently underway in Minesto's test site in Strangford Lough, UK, using a 3-meter wing prototype of tidal kite.

2 HYDRODYNAMICS OF MARINE TURBINE

Many of the theoretical foundation of marine hydrokinetic turbine are similar to wind turbine blade design [5]. Considering that water is about 800 times denser, we expect that a small size hydro-turbine produce same power as a larger wind turbine. To describe the turbine performance, we define power coefficient as non-dimension parameter:

$$C_p = \frac{P}{\frac{1}{2} \rho A V^3} \quad (1)$$

where P is shaft power, A is turbine's projected area, ρ is the density of water and V is the water flow speed. Similarly, the drag coefficient (or thrust as in propellers) can be expressed as:

$$C_T = \frac{T}{\frac{1}{2} \rho A V^2} \quad (2)$$

where T is the drag force due to blade rotation.

Maximum theoretical limit of power coefficient C_P is 0.593, calculated by Betz's law[4]. C_P is also a function of Tip Speed Ratio (TSR or λ) which is a non-dimensional rotational speed of the turbine in relation to the passing water speed. It is expressed as:

$$\lambda = \frac{\omega R}{V} \quad (3)$$

where $\omega = 2\pi.n$ is rotational speed of the turbine in radians per second, n is revolution per second, R is the turbine radius and V is the passing flow speed. Power output of the turbine can also be expressed as generated torque multiplied by rotational speed:

$$P = Q . \omega \quad (3)$$

Normally for turbines, C_P is considered the most important parameter and the drag (thrust) force would to be handled by the support structure. The Minesto turbine however, is mounted on a flying wing and their combined performance finds a different maximum operating point, somewhere between high vehicle speed and high turbine power extraction. In horizontal axis

turbines, higher power production is achieved through loading the blades. For such condition the thrust (drag) force is also increased which in return reduces kite speed. Hence, the ratio of C_P/C_T , which is a measure of the efficiency, is more important than the C_P .

$$\frac{C_p}{C_T} = \frac{Q \cdot \omega}{T \cdot V} \quad (4)$$

Unlike wind turbine, the cavitation corrosion can occur on hydrokinetic turbine blades. The parameter to define this critical condition is cavitation number

$$C_a = \frac{p - p_v}{\frac{1}{2} \rho V^2} \quad (5)$$

where p is local pressure, p_v is the vapor pressure of the fluid. As a design criterion, we preferred to avoid excessive low-pressure region on the suction side of the blade and selected hydrofoil profiles for the blade sections that minimize cavitation inception in the normal operational condition.

3 DESIGN CRITERIA

The full-scale kite is designed so that in a tidal stream with the speed between 1.2-2.4m/s, it would maintain the water velocity into the turbine at an average of 10m/s. The blade design for turbine considered this velocity as the initial design parameter along with some other limitations dictated by kite specifications. The turbine output power is proportional to the area swept by the blades. Increase in the rotor diameter is preferable but the size is limited by cost, weight and dynamics of kite. In addition, for the same reason, we did not consider pitch control mechanism for the blades.

The turbine diameter was limited to 2m and the desired mechanical power output was 0.5MW. The rotational speed was also set to a range suitable for the electrical generator in power take-off unit. To avoid cavitation at high speed, we selected a lower range of tip speed ratio λ for the turbine compared to values usually used in wind turbine. Lower rotational speed reduces the performance of electrical generator therefore the shaft RPM would be converted to a suitable speed using a gearbox in full-scale kite.

For design-space, the emphasis is on important operational parameters to maximizing the power to drag ratio. We should also include the turbine blade specifications, such as number of blades, solidity, blade profile, chord-length profile, thickness, pitch angle, camber profile, skew and rake into the list.

In our approach, the limiting factor is a suitable range of TSR for avoiding cavitation, especially on the tip section of the blade. Considering a constant inflow speed, there are combination of turbine radius and RPM to provide the desired TSR. The range of 350 to 500 rpm is suitable for low TSR values ($3 < \text{TSR} < 4$) and inflow speed of 10 m/s.

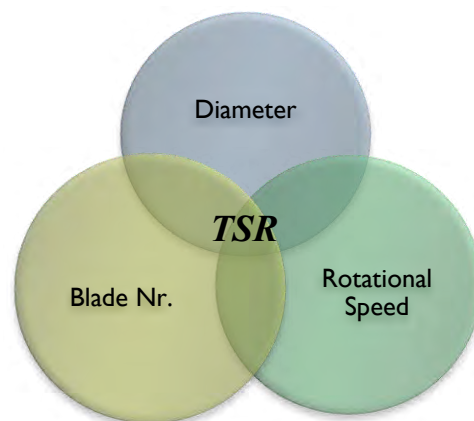


Figure 2 – Design space's initial parameters.

Next variable in the list of design parameters is the number of blades. For a given turbine diameter with a constant working speed, the increase in number of blades (if designed properly) increases both power (torque) and drag. Also, if the number of blades increases for a certain design, we can decrease the loading of each individual blade in favor of delaying cavitation inception. The solidity of the turbine is based on the number of blades and suggests the optimum chord-length and pitch for each blade. Therefore, it is important to have the number of blades also in the list of initial parameters for the selection procedure. The combination of these parameters gave us the design space. We performed numerical simulations for the cases in design space and selected those with the maximum C_P/C_T ratio. The design space produced a range of different power outputs within the selected range of acceptable TSR. Further numerical and experimental studies were carried out on the preferred designs to choose the best based on strength, weight and actual power output.

During several simulation iterations, we included different blade profiles in our investigation. Other studies on conventional hydrokinetic turbines have suggested a high lift NACA638-xx family as their choice of hydrofoils ([12],[10],[1]). This proved to be problematic as certain regions of the blade became prone to cavitation inception due to very low pressure on suction surface of blade. For most marine applications, the safe choice for the blade profile is the foil with smaller camber and less prominent low-pressure areas on suction side. Therefore, the family of NACA66a08-xx was used in this project.

4 COMPUTATIONAL MODEL

Different numerical tools are available for designing turbine blades. RANS codes calculate both pressure and viscous forces accurate but the high cost of simulation makes them suitable only for fine adjustments at the final stage of the design. Semi-empirical methods like blade element momentum (BEM) theory are used widely in turbine blade design [11]. Da Silva et al. [9] presents a design methodology for blade optimization considering cavitation inception on blades using (BEM) theory. This method uses 2-D blade profile's lift and drag values and calculate the chord and twist angle of sections along the radius of blade. Gue et al. [12] attempted to combine BEM with RANS code and simulate a rotor in high Tip Speed Ratio.

4.1 Lifting Line Method

Lifting Line method is mainly used in propeller design but recent attempts by Kinnas [13], Menendez [15] and Epps [8] provided different approach for using this method in turbine design. While Kinnas et al. [13] utilized lifting line code LLOPT in combination with unsteady wake alignment code MPUF-3A, Epps et al. [6] developed a "unified lifting line" method suitable for the axial flow turbines.

To evaluate the cases included in the design space, we used software "OpenProp". OpenProp is an open-source code developed for the design and analysis of marine propellers and horizontal-axis turbines and uses Lifting Line optimization method [7]. By using this code, we calculated blade chord, twist angle and blade thickness and estimated turbine performance.

The input values given to the code are number of blades, RPM, rotor diameter, inflow speed, chord length distribution and hydrofoil type. The output of this potential flow code is the main parameters such hydrofoil chord and twist angle. In order to have a complete geometry of the blades from these basic parameters, we have to use a blade generator program that creates

complete CAD geometry of the design. CAESES software contains a blade generator engine that seamlessly converts the main parameters into a CAD output and couples the CFD solver for optimization purpose. We used CAESES to generate the geometry for both model production and CFD simulation.

4.2 RANS Simulation

To investigate the viscous force effect on the selected cases generated by OpenProp, we used Reynolds-Averaged Navier-Stokes (RANS) solver. Different RANS codes have been used in studies of marine tidal turbines. Gharraee et al.[10] used ReFRESKO to simulate Horizontal Axis Tidal Turbines (HATT) developed by Southampton university. For our study, we used open-source solver OpenFOAM for investigating viscous effect and cavitation inception on the blades. We performed simulations using $k-\omega$ SST turbulence model with steady-state solver. Even though the steady state solver does not simulate the full rotational effect of the turbine, it is accurate for calculating the force and momentum on the blades. To simulate the effect of rotating blades, we chose the Single Rotating Reference Frame (SRF) method, which converts the rotational momentum to a body force and applies the effect to the entire domain. Since the simulation does not include the stationary part of the turbine, SRF offers an accurate measure of the flow. The reason for excluding the stationary sections of the turbine and nacelle was to narrow down the focus of the simulation result to the blade design and minimize the complexity of the blade-nacelle interaction.

The cylindrical domain of simulation had a size of $4D$ in length and $6D$ in diameter where D is the turbine diameter. All the geometries were created using CAESES blade generator and unstructured meshes were generated by snappyHexMesh tool. 3D meshes contained hexahedra and split-hexahedra from triangulated surface geometries. The hexahedral mesh snaps on the curved surfaces and at the final stage a prism layer is added between the mesh and solid surfaces to resolve the mesh size to the suitable $y^+ < 5$. The total number of cells for the model-scale simulation was approximately 8.6 million. *Figure 3* presents the mesh created for this study.

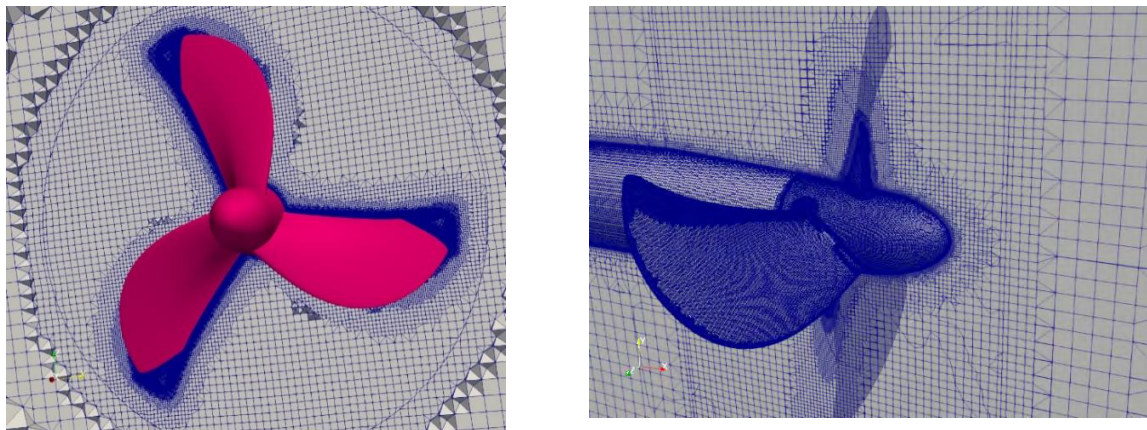


Figure 3 - SRF mesh created by snappyHexMesh.

Four series of simulations were performed for different scales of the turbine. These scales were model scale, used in cavitation tunnel test, design scale, quarter scale for using in

Strangford Lough demonstration test and up scaled version. (see Table 1)

Table 1- scales used in CFD study.

| Case | Model scale | Quarter scale | Design scale | Up scaled |
|-------|-------------|---------------|--------------|-----------|
| Scale | 14.7% | 28% | 100% | 114% |

Since the SSPA’s turbine performed better than base-line turbine for kite and had less drag, there was room to scale up the new design. Therefore, we investigated the up-scaled turbine with the 14% larger diameter and compared its result with the model size tested in cavitation tunnel and the quarter scale model for Strangford Lough.

The change in diameter theoretically results in higher power production by the square of radius and maximum possible power produced by up-scaled turbine should be 29% higher than the design turbine. Considering that the blade loading is not uniformly distributed and the tip section of blade is lightly loaded, this value expected to be smaller.

The CFD computation for the power at the design tip speed ratio (TSR=3.1) shows 27.7% power increase due to increased size of the turbine, while the power to drag ratio (C_P / C_T) remains the same.

Comparing the performance of the full-scale turbine with the model-scale and quarter-scale shows that the value of power to drag increases in higher TSR numbers. Figure 4 and Figure 5 present the CFD computation results for three different scales of the turbine. The maximum power to drag ratio occurs between the TSR 3 and 4, which is the region close to the design point. The C_P / C_T value in lower TSR numbers are similar for different scales. Deviation in higher TSR suggests performance improvement due to scale effect.

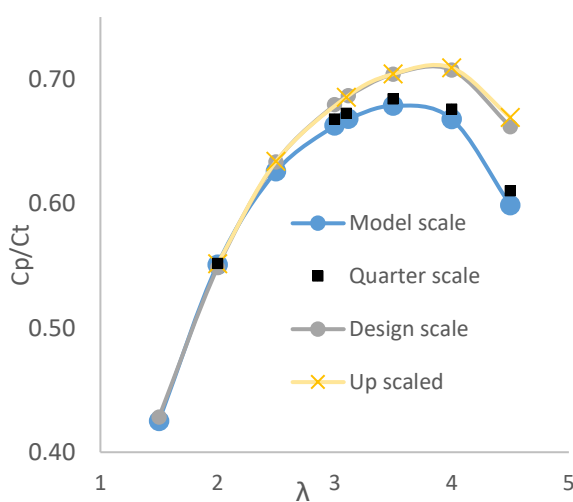


Figure 4 - Performance improves in full scaled turbine

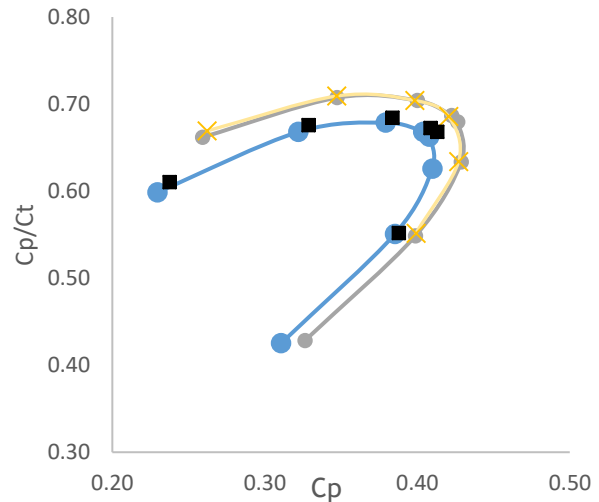


Figure 5 - Maximum power production occurs close to the design point for all scales.

Another question for the change in the scale is the cavitation inception at higher radii. Since the design TSR is kept constant by reducing the RPM, we do not expect any significant difference in the cavitation risk. Comparing the pressure distribution on the blades verified that low-

pressure area is not much different; therefore, we do not expect the cavitation inception to differ in the up-scaled model.

To have a better understanding of the turbine performance in real operational condition, we simulated the quarter scale turbine with the inflow angle of 5 and 10 degree. The turbine was operating at design point (Tip Speed Ratio = 3.1) and the free-stream flow speed was constant. Figure 6 – Free-stream flow enters the turbine at 10 degree angle. *Figure 6* illustrates the free stream flow entering turbine at 10 degree angle.

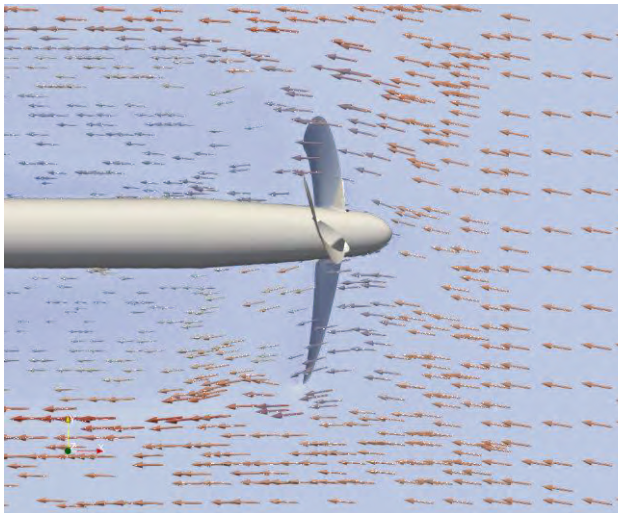


Figure 6 – Free-stream flow enters the turbine at 10 degree angle.

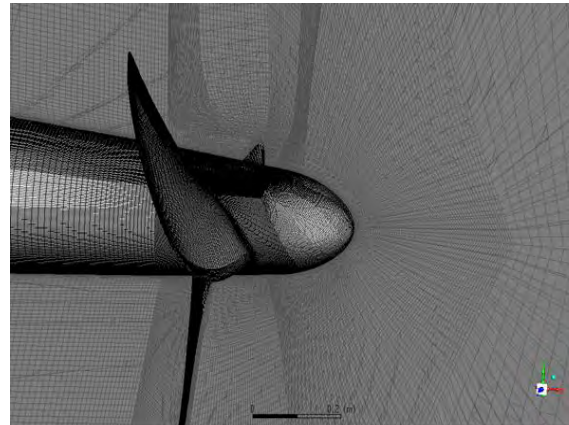


Figure 7- Structured mesh created by ICEM-CFD and used in simulation using ANSYS-FLUENT.

The result showed between 1% to 6% power reductions when the inflow was inclined 5 and 10 degree respectively. To study the mesh and solver dependency of simulations, the simulation was repeated at the design point (TSR = 3.1) using ANSYS-FLUENT solver using structured mesh created by ICEM-CFD. The original mesh was an unstructured cut-cell mesh created by SnappyHexMesh (Figure 3) and had approximately 8.6 million cells including prism layer. The new mesh (Figure 7) was a structured hexahedral mesh created by ICEM-CFD and $y^+ < 3$. Total number of cells for this mesh was 13 million and power production in two simulations differs only by 0.5%.

5 EXPERIMENTAL TEST

Most of the available experimental studies on marine turbines are performed on the models suitable for low water velocity and high tip speed ratio. Model test in towing tank and cavitation tunnel by Bahaj [2][3] and Batten [1] are examples of horizontal hydrokinetic turbine developed for these conditions with the design approach similar to wind turbine.

We carried out two rounds of model scale test in the SSPA cavitation tunnel with the turbines developed by SSPA. After first round of test, the initial design was improved by fine adjustment of blade thickness, pitch angle and blade's tip profile. The results discussed in this paper is for the final design after improvement. During test, turbine performance in terms of thrust, power, efficiency and cavitation were investigated.

5.1 Test Facilities

At the cavitation test, the turbine was mounted on a Kempf & Remmers H33 Open Water dynamometer in cavitation tunnel test section #1 (cross section diameter 1 m, see *Figure 8*). As shown in *Figure 9*, the turbine was mounted upstream of dynamometer, and equipped with a hubcaps. Fairings were mounted between the turbine hub and the dynamometer.



Figure 8 - The SSPA cavitation tunnel. Measurement section #1 to the right.

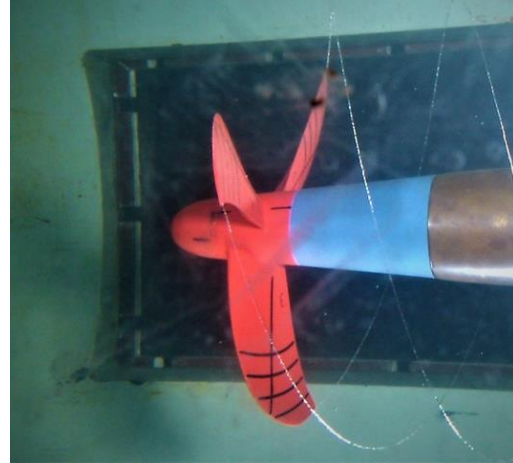


Figure 9 - Cavitation observation in SSPA testing facility.

5.2 Model Turbine, Test Arrangement and Test Results

Before test, the blades were painted with a special paint to obtain a certain roughness on the blade surfaces for cavitation stimulation. The radii $0.6R$, $0.7R$, $0.8R$, $0.9R$ and generator line were marked on all blades. The cavitation number is based on the static pressure at the shaft centerline. The static pressure in the cavitation tunnel is adjusted to achieve the preferred cavitation number at the given flow speed.

Turbine force measurement at the atmospheric condition was performed in order to determine the effective velocity of advance. Further measurements carried out at different cavitation numbers to determine the effect of cavitation thrust breakdown. In the turbine force measurements, the shaft rate varied to cover the loading range of interest. Measurement points are taken at both decreasing and increasing shaft speed in order to check for hysteresis effects.

The turbine design surpassed the expected efficiency by 17 to 23 % and sufficient cavitation performance compared to the baseline for kite operation and fulfilled the design goal of $C_P/C_T \geq 0.6$ at a Tip Speed Ratio of $\lambda = 3$. The cavitation on the turbine blade was studied at different loading conditions and the extension and character of the cavitation at different blade positions were documented by video recording. All observations are made with the turbine illuminated by stroboscope synchronized to the shaft rate frequency. During an incipient cavitation test the shaft rate and thus the tip speed ratio is varied at several constant static pressure levels until the different types of cavitation could be observed.

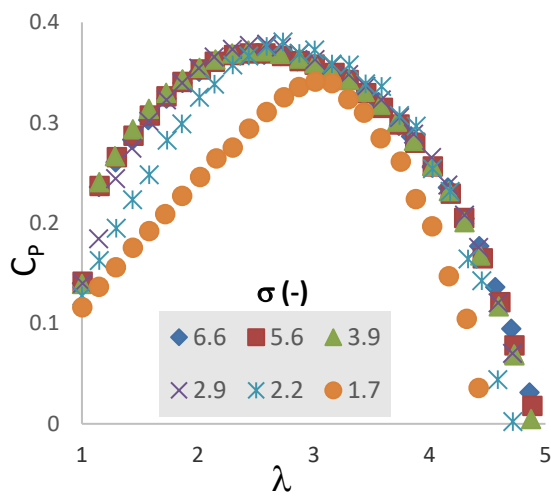


Figure 10 - Power coefficient of model test for different cavitation number

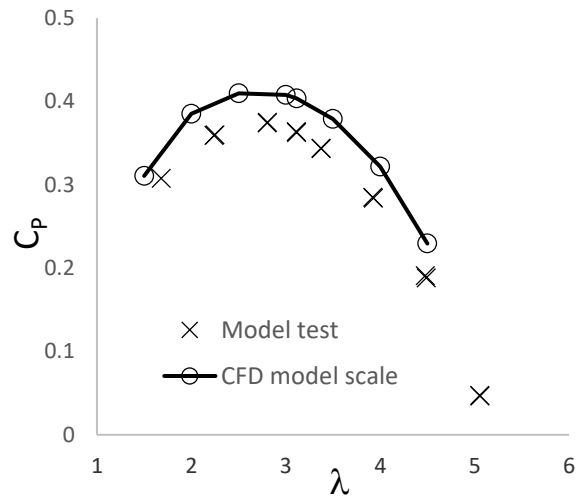


Figure 11 - Power coefficient comparison between CFD simulation and model test.

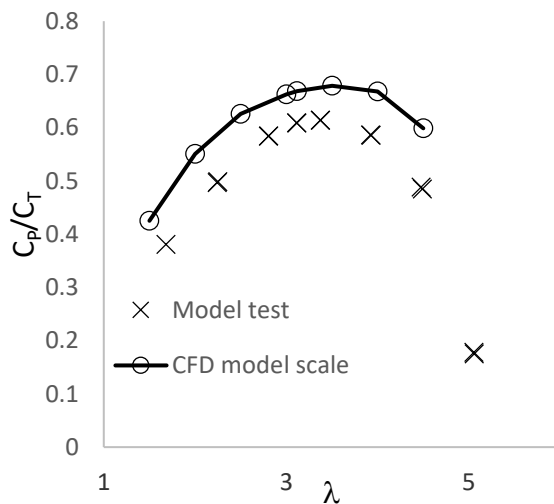


Figure 12 - Power to drag ratio comparison between CFD and model test.

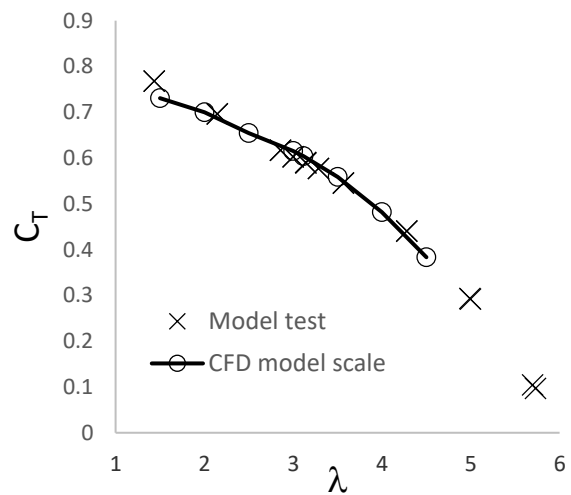


Figure 13 - Thrust (drag) coefficient comparison between CFD and model test.

Figure 10 presents the test result for different cavitation numbers σ . For cavitation numbers higher than 3, power coefficients in different TSR are similar. Since we did not simulate the turbine performance with the cavitation model, the comparison between test result and CFD are with the cases that cavitation does not contribute in power loss. The turbine was designed to operate at $TSR = 3.1$ but tests were performed also in off-design conditions between $TSR = 1$ to 6.

Figure 11 shows power coefficients in different tip speed ratios and Figure 13 compares turbine thrust (drag) coefficient with the CFD result. CFD simulation over-predicts the power but is more accurate in predicting thrust. CFD simulation seems to predict both power and thrust trends correctly. The higher torque predicted in CFD simulation might be due to deficiency of

the simulation as the results were not corrected for blockage effect in the test section. The performance of the turbine in *Figure 12* is plotted as ratio of power to drag coefficient vs. different TSR.

The cavitation tests showed that the design point ($\sigma=3.14$, $\sigma=5.8$) was located inside the cavitation bucket, thus there is no cavitation at this point. If the cavitation number or TSR decreases, tip vortex cavitation (TVC) will occur first and then suction side sheet cavitation (SS SC). There is a large margin against pressure side cavitation and bubble cavitation. There are no signs of erosive cavitation. In summary, the new turbine design has very good performance from cavitation point of view.

6 SUMMARY AND CONCLUSION

We presented the design process and CFD simulations of a new turbine designed for Powerkite project. At kite speed of 10 m/s and $TSR \approx 3$, estimated power produced by the full-scale turbine reached the expected value of 0.5 MW. We also investigated the possibility of scaling up the turbine size by 14%.

The Powerkite turbine had a maximum $C_p/C_T > 0.6$ at design TSR, which satisfies the operational condition of the kite. Cavitation tunnel tests were performed using model scale of the turbine and results were used to further improve the performance. Test results were also compared with CFD simulation. Power coefficient was over-predicted in CFD computation by less than 10% and thrust coefficient was very similar to test result.

The full-scale turbine with the larger diameter and quarter of scale model were simulated using CFD software. The result showed an improvement in the performance of the larger scale turbine because of the Reynolds scaling. The power to drag ratio for full-scale turbine did not change in lower TSR value but increased in larger TSR which is very good overall performance of the scaled-up turbine. The simulation did not show any sign of cavitation risk on the full-scale and quarter-scale turbine blade.

The simulation for the inclined inflow presented less than 6% power production decrease while the kite manoeuvres in its track (10 degrees drift angle). We also investigated the mesh and solver dependency of CFD simulations and results were similar with difference of less than 1%.

ACKNOWLEDGEMENTS



This project has received funding from the European Union's Horizon 2020 research and innovation programme under grant agreement number 654438. The authors also would like to thank the Region of Västra Götaland for their support.



REFERENCES

- [1] Batten W.M.J., Bahaj A.S., Molland A.F. and Chaplin J.R. Hydrodynamics of marine current turbines. *Journal of Renewable Energy*, vol. 31, no. 2 (2006) pp249-256
- [2] Bahaj A.S., Batten W.M.J. and McCann G. Experimental verifications of numerical predictions for the hydrodynamic performance of horizontal axis marine current turbines. *Journal of Renewable Energy*, vol. 32, no. 15 (2007) pp2479-2490
- [3] Bahaj A.S., Molland A.F., Chaplin J.R. and Batten W.M.J. Power and thrust measurements of marine current turbines under various hydrodynamic flow conditions in a cavitation tunnel and a towing tank. *Journal of Renewable Energy*, vol. 32, no. 3 (2007) pp407-426
- [4] Carlton J.S., *Marine Propellers and Propulsion*, Third Edition, Elsevier.
- [5] Chica E., Perez F., Rubio-Clemente A. and Agudelo S. Design of a hydrokinetic turbine. *Energy and Sustainability VI*. WIT Press (2015), pp.137-147
- [6] Epps B.P. On the rotor lifting line wake model. *Journal of Ship Production and Design* (2016) vol. 32, no. 3, pp.1-15.
- [7] Epps B.P. and Kimball R.W. *OpenProp v3: Open-source software for the design and analysis of marine propellers and horizontal-axis turbines*. (2013)
URL: <http://engineering.dartmouth.edu/epps/openprop>
- [8] Epps B.P. and Kimball R.W. Unified Rotor Lifting Line Theory. *Journal of Ship Research*, (2013) vol. 57, no. 4, pp. 1-21.
- [9] Freitas da Silva P.A.S., Shinomiya L.D., Felamingo de Oliveira T., Vaz J.R.P., Amarante Mesquita A.L. and Pinho Brasil A.C. Design of Hydrokinetic Turbine Blades Considering Cavitation. *Journal of Energy Procedia* (2015), vol.75, pp.277-282.
- [10] Gharraee, B., Eskilsson, C., Bensow, R. and Vaz, G. Numerical Simulation of Cavitation on a Horizontal Axis Tidal Turbine. *ISOPE 26th International Ocean and Polar Engineering Conference, Rhodes, Greece*. June (2016)
- [11] Goundar J.N. and Ahmed M.R. Design of Horizontal Axis Tidal Current Turbine. *Journal of Applied Energy*, (2013) vol.111, pp.161-174.
- [12] Guo Q., Zhou L. and Wang Z. Comparison of BEM-CFD and full rotor geometry simulations for the performance and flow field of a marine current turbine. *Journal of Renewable Energy* (2015), vol.75, pp.640-648.
- [13] Kinnas A.S., Xu Wei, Yu Yi-Hsiang and He Lei. Computational Methods for the Design and Prediction of Performance of Tidal Turbines. *Journal of Offshore Mechanics and Arctic Engineering*. (2012) vol.134, 011101.
- [14] Laws N.D. and Epps B.P. Hydrokinetic energy conversion: Technology, research, and outlook. *Journal of Renewable and Sustainable Energy Reviews* (2016), vol.57, pp1245-1259.
- [15] Menéndez Arán D.H. and Kinnas S.A. Hydrodynamic optimization of marine current turbines. *Proceedings of the 17th Offshore Symposium- SNAME* (2012) Texas D15-D21.
- [16] Schubel P.J. and Crossley R.J. Wind Turbine Blade Design. *Energies* (2012). ISSN 1996-1073, vol.5, pp 3425-3449.
- [17] Shahsavarifard M., Louis Bibeau, E.L. and Vijay C. Effect of shroud on the performance of horizontal axis hydrokinetic turbines. *Journal of Ocean Engineering* (2015) vol.96, pp215-225.

NUMERICAL MODELLING OF THE INTERACTION BETWEEN A FISH NET AND FLUID USING CFD

TOBIAS MARTIN*, ARUN KAMATH AND HANS BIHS

* Department of Civil and Environmental Engineering
Norwegian University of Science and Technology
Høgskoleringen 7a, 7491 Trondheim, Norway
e-mail: tobias.martin@ntnu.no

Key words: Fluid-structure interaction, Net modelling, Porous media, CFD

Abstract. A numerical model for the determination of the deformed shape of nets under consideration of hydrodynamic loads and elastic twines is presented. The hydrodynamic forces are incorporated using Morison's formula and force coefficients evaluated from experiments. The model is coupled to a CFD fluid model by representing the net's influence on the fluid as a porous medium. For this purpose, the volume-averaged Navier-Stokes equations, which include porosity and an additional resistance term, are solved. The source term is calculated from an adapted version of Forchheimer's equation for flow in porous media. A validation part focusing on forces and deformation of a net wall in steady current provides insight into the accuracy of the chosen concept.

1 INTRODUCTION

The aquaculture industry has seen strong growth over the last decades due to its potential to meet the rising global food demand. Offshore fish production becomes relevant as the size of the structures increases and greater concerns about the environmental impact on the nearshore zone arise. In the open sea, severe environmental loadings from high energy sea states necessitate accurate analysis of motion and fatigue for the design of reliable and economical marine fish farm structures. Separated studies on either the motion of the structure or the fluid around the structure using experimental or simple numerical tools were predominant in the past. However, these approaches are not suitable for real sea state conditions due to the strong and non-linear fluid-structure interaction. In contrast, computational fluid dynamics can be applied to understand the structural and environmental challenges in the operation of the whole structures by studying the forces on and the fluid dynamics in and around the cages.

Several experimental studies were presented for nets in current. Patursson [1] published a series of measurements of drag and lift forces on a fixed net panel and the velocity reduction behind the net for different inflow velocities and angles between fluid and panel. Similar studies were presented in [2] where the authors investigated the deformation of a square net in different current velocities. Lader and Enerhaug [3] analysed the forces and deformation of a net cage in

current. They found a strong coupling between occurring forces and deformation and concluded that existing simple drag formulae for stiff net panels are not suitable for calculating the forces on flexible cage structures. Less research focused on experiments including waves. Lader et al. [4, 5] studied wave forces on net panels in a small wave flume and compared the results with different wave force models. They could show the increasing influence of the net on the wave with increasing wave steepness. A complete study of a net cage in current and waves including an elastic floater, mooring and net is presented in [6], where the authors investigated the validity of different rational hydrodynamic load models for more complex wave situations.

The numerical representation of the net is mostly based on a finite element method (FEM). Tronstad [7] developed a non-linear FEM applying membrane elements suitable for static analyses of net deformation. Priour [8] generalised this idea for triangular elements and in [9], a similar approach is used for dynamic calculations. All the approaches rely on super elements which represent a certain area of the net. In contrast, Tsukrov et al. [10] presented a consistent net element method. Here, the discrete net consists of several 1D truss elements which move due to tension and external forces from a modified Morison equation. Marichal [11] developed an elastic truss element method with kinematic constraints. A similar approach is presented in [12]. It is a quasi-static approach which leads to an efficient overall computation due to missing time step restrictions. The coupling of a net model to a fluid solver is advanced by different researches. Patursson et al. [13] incorporated the net as a porous medium and solved the volume-averaged Navier-Stokes equations. Good agreements with experiments for a fixed net panel could be shown, but the deformation of the net is not included in the study. Bi et al. [2] and Zhao et al. [14] followed the same approach but included the net deformation using a lumped-mass model. They validated the model for current and waves and could show good agreement with the experiments. Chen and Christensen [15, 16] extended this idea for net cages and provided a comprehensive validation of their approach. The good accuracy of the model for current cases shows the validity of this approach.

The presented net model is implemented in the open-source CFD code REEF3D [17]. The fluid solver has been validated for a wide range of marine applications which are relevant for this research. Kamath et al. [18] tested successfully the code for shoaling and decomposition of non-breaking and breaking waves over varying bathymetry. In [19], the code showed good agreement with experiments for the fluid-structure interaction with fixed cylinders. Further, floating structures [20] including a numerical mooring model [21] were incorporated using a directional immersed boundary method. In the following, details about the numerical fluid and net models are given. The coupling between the two models is mainly based on the ideas in [13, 16]. The paper concludes with a validation of the presented approach for the deformation of a net in current and the forces acting on the net.

2 NUMERICAL MODELS

2.1 Fluid model

The Reynolds averaged continuity equation and Navier-Stokes (RANS) equations for incompressible fluids are the typical set of equations solved for describing the fluid. In non-conservative

term, they are given as

$$\begin{aligned} \frac{\partial u_i}{\partial x_i} &= 0, \\ \frac{\partial u_i}{\partial t} + u_j \frac{\partial u_i}{\partial x_j} &= -\frac{1}{\rho} \frac{\partial p}{\partial x_i} + \frac{\partial}{\partial x_j} \left(\nu_{\text{eff}} \left(\frac{\partial u_i}{\partial x_j} + \frac{\partial u_j}{\partial x_i} \right) \right) + g_i, \end{aligned} \quad (1)$$

with u_i the velocities in the principal directions, p including the pressure and the root mean square of the turbulent velocity fluctuations, and \vec{g} accounting for gravitational forces. In a two phase approach, the density ρ and the viscosity ν_{eff} have to be determined from the two material properties. The effective viscosity is the sum of the kinematic viscosity ν and the turbulent viscosity ν_t , which is calculated using Boussinesq's approximation and the two-equations $k - \varepsilon$ turbulence model.

The set of equations (1) is computed on a rectilinear staggered grid using a finite difference method. Chorin's projection method for incompressible flows [22] is implemented with a third-order accurate Runge-Kutta discretisation scheme for temporal terms [23] and a fifth-order accurate weighted essentially non-oscillatory (WENO) scheme [24] for convection terms. The resulting Poisson equation for pressure is solved by HYPRE's MPI parallelized BiCGStab method [25] with a geometric multigrid method as preconditioner.

Resolving the twines of the net would incorporate a very large number of cells. Therefore, the effect of the net on the fluid is incorporated as a porous medium. For this purpose, a volume averaging operator according to

$$\langle a \rangle = \frac{1}{V} \int_{V_f} a \, dV, \quad (2)$$

is introduced. The portion fluid volume V_f in the control volume V is expressed through the porosity Φ which is defined as

$$\Phi = \frac{V_f}{V}, \quad (\Phi \in [0, 1]). \quad (3)$$

Without presenting the derivation, the introduction of the operator in (1) results in the volume-averaged RANS (VARANS) equations [26]

$$\begin{aligned} \frac{\partial \langle u_i \rangle}{\partial x_i} &= 0, \\ (1 + c_a) \frac{\partial \langle u_i \rangle}{\partial t} \frac{1}{\Phi} + \frac{\langle u_j \rangle}{\Phi} \frac{\partial \langle u_i \rangle}{\partial x_j} \frac{1}{\Phi} &= -\frac{1}{\rho} \frac{\partial \langle p \rangle}{\partial x_i} + \frac{1}{\Phi} \frac{\partial}{\partial x_j} \left(\nu_{\text{eff}} \left(\frac{\partial \langle u_i \rangle}{\partial x_j} + \frac{\partial \langle u_j \rangle}{\partial x_i} \right) \right) + g_i + S_i. \end{aligned} \quad (4)$$

The added mass coefficient c_a takes the transient interaction of fluid and twines into account but is not well investigated for nets yet. In this study, the value is calculated as given in [15]. The source term S_i includes the drag resistance of the porous zone and can be calculated under consideration of the equation of Forchheimer as [13]

$$S_i = -\rho \cdot \left(\nu D_{ij} \langle u_i \rangle + \frac{1}{2} C_{ij} |\langle u \rangle| \langle u_j \rangle \right). \quad (5)$$

The material matrices D_{ij} and C_{ij} include the porous media resistance coefficients in normal and tangential directions of a net element in their main diagonal. If the element is not aligned with the principal directions of the fluid flow, a coordinate transformation as given in [13] is applied to the matrices.

2.2 Net model

In this paper, the tension element method [12] is utilised for the simulation of the deformation of a net plane. It is assumed that the net consists of square meshes such that the solidity ratio S can be approximated as [27]

$$S = \frac{2d}{l} - \left(\frac{d}{l}\right)^2, \quad (6)$$

where d is the diameter and l is the length of each twine. The porosity defined in (3) equals then $1 - S$.

The net is represented as a finite number of massless bars connected with mass points P . Further, the elasticity of the twines is incorporated, and bending stiffness is neglected such that a flexible system is assumed. A static force equilibrium can then be stated for each of the N_{ik} inner knots of the net $P^{(\nu)}$ as (see Fig. 1)

$$\sum_{j=1}^{N_{b,\nu}} \left(\vec{f}^{(j)} T^{(j)} + \frac{1}{2} \cdot \vec{H}^{(j)} \right) + \vec{G}^{(\nu)} = \vec{0}, \quad \nu = 1, \dots, N_{ik}. \quad (7)$$

Here, the $N_{b,\nu}$ bars which are connected to $P^{(\nu)}$ point in the direction of the unit vectors \vec{f} and include the tension forces T . Once these forces are known for each of the bars, the length can be updated from e.g. Hooke's law

$$l^{(j)} = l_0^{(j)} \cdot \left(1.0 + \frac{T^{(j)}}{EA} \right). \quad (8)$$

The gravity forces \vec{G} are known forces and uniformly distributed on all knots. The hydrodynamic forces \vec{H} are calculated from the surrounding fluid using Morsion's drag formula

$$\vec{H}^{(j)} = \frac{\rho d l^{(j)}}{2} \cdot \left[c_n \left(\vec{v} - (\vec{v} \cdot \vec{f}) \vec{f} \right) \left| \vec{v} - (\vec{v} \cdot \vec{f}) \vec{f} \right| + c_t \left(\vec{v} \cdot \vec{f} \right) \left| \vec{v} \cdot \vec{f} \right| \cdot \vec{f} \right]^{(j)}, \quad (9)$$

with c_n and c_t the normal and tangential drag coefficients. The chosen velocity \vec{v} is due to the fluid because of the quasi-static assumption for the net motion. The coefficients are calculated using formulae for flow around cables [28]

$$c_n = \begin{cases} \frac{8\pi}{\text{Re} \cdot s} \cdot (1 - 0.87s^{-2}), & (0 < \text{Re} \leq 1) \\ 1.45 + 8.55 \cdot \text{Re}^{-0.9}, & (1 < \text{Re} \leq 30) \\ 1.1 + 4 \cdot \text{Re}^{-0.5}, & (30 < \text{Re} \leq 10^5) \end{cases}, \quad (10)$$

$$c_t = \pi 1.05^{-3} \cdot \left(0.55 \sqrt{\text{Re}} + 0.084 \cdot \text{Re}^{\frac{2}{3}} \right),$$

with $s = -0.077215665 + \ln\left(\frac{s}{\text{Re}}\right)$ and $\text{Re} = \frac{v_n d}{\nu}$. The same approach was used by Tsukrov et al. [10] for developing their consistent net element model.

The solution of (7) is found by separating internal and external forces. This leads to

$$\sum_{j=1}^{N_{b,\nu}} \left(\vec{f}^{(j)} T^{(j)} \right) = \sum_{j=1}^{N_{b,\nu}} \frac{1}{2} \cdot \vec{H}^{(j)} + \vec{G}^{(\nu)}, \quad \nu = 1, \dots, N_{ik}. \quad (11)$$

The arising system of equations is solved for the unit bar vectors using a successive approximation method. A net of rectangular meshes always contains more twines than knots such that the system is undetermined. To overcome this issue and include physical coherence into the model, appropriate geometrical constraints in form of boundary and internal mesh equations are added as described in [12].

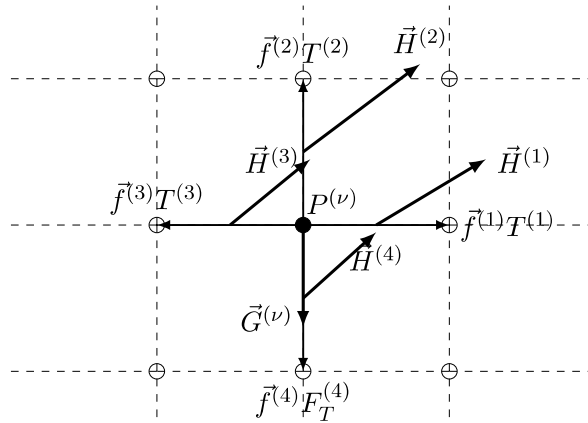


Figure 1: Acting forces at knot P^ν of the net.

2.3 Coupling algorithm

The algorithm developed for simulating the fluid-structure interaction of a moving net is shown in figure 2. In the first step of the iterative process of the net model, the hydrodynamic forces are updated using (9) and (10). The necessary fluid velocity information is provided by interpolating the velocity field at all knots of the net and averaging them accordingly for each intermediate bar. Additionally, the elasticity of the twines is incorporated using (8). The system is then solved and corrected as described above, and the new net position is stored when convergence has been reached. In the fluid solver, a zone of porous medium is then generated based on the current position of the net. Here, the authors follow the idea of Chen and Christensen [16], which defines prisms of thickness t around the triangulated net and checks for each fluid cell whether it is within these prisms. Due to the time and space dependency of the angles of attack, the porous media resistance coefficients have to be calculated for each mesh in each time step. The drag resistance is then determined for each cell in the porous zone using the coefficients from the corresponding mesh and (5). A porosity value is assigned, and the fluid problem is solved with the VARANS equations as given in section 2.1.

3 VALIDATION

For validation purposes, two cases are compared to experimental data from the literature. For both cases, the resistance coefficients are taken from [13]. They are based on comparisons between a simple analytical model and experimental data for nets with different solidity.

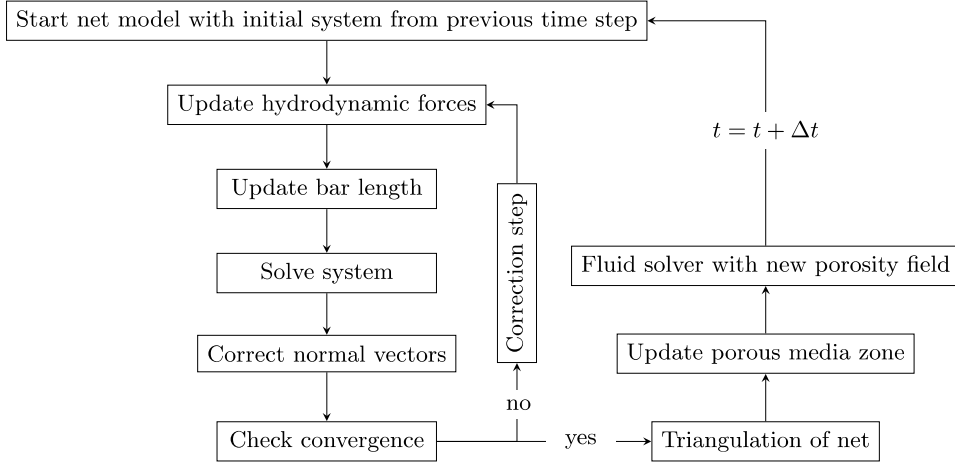


Figure 2: Flowchart of the presented fluid-structure interaction algorithm.

3.1 Fixed net panel in steady current flow

A fixed net panel in current flow under several angles of attack α and current velocities shall be compared to the experimental data of Patursson et al. [13]. Here, the drag and lift force coefficients and the velocity reduction factor behind the net u_r are considered. The latter is defined as

$$u_r = \frac{u_\infty - u_{2.5}}{u_\infty}, \quad (12)$$

with $u_{2.5}$ the measured velocity $2.5m$ behind the net. The force coefficients are calculated by integrating the source term in x- and z-direction over the porous zone

$$c_d = \frac{S_x t A}{\frac{\rho}{2} A u_\infty^2}, \quad c_l = \frac{S_z t A}{\frac{\rho}{2} A u_\infty^2}. \quad (13)$$

The thickness of the zone is set to be $50mm$. The net is fixed in a frame of $1m \times 1m$ and has a solidity of 0.184. Three different angle of attacks, i.e. $\alpha = 15^\circ, 45^\circ, 90^\circ$ and four different inflow velocities between $0.125m/s$ and $0.75m/s$ are investigated. The chosen porous resistance coefficients are $C_{11} = 5.098, C_{22} = C_{33} = 1.6984$ and $D_{11} = 51730, D_{22} = C_{33} = 26379$. A computational domain of $4.5m \times 3.66m \times 2.44m$ consisting of 0.6Mio. cells is chosen. The nets middle position is kept at $(1.5m, 1.83m, 1.22m)$ for all angle of attacks.

A slice of the domain at $y = 0.915m$ is shown for the different angles of the net and $u_\infty = 0.5m/s$ in Fig. 3. The wake of the net is clearly visible and has approximately the same width as the net panel. At $\alpha = 15^\circ$ some fluid is accelerated alongside the net and flows below the panel. As the angle of attack increases, the fluid slows down in front of the net which leads to a decreasing velocity at the net itself. Behind the net, a nearly steady velocity can be observed for all angles of attack. Fig. 4a shows the velocity reduction factor for the different angles of attack and velocities. A very good agreement can be achieved at $\alpha = 45^\circ$ for the whole range of velocities. For $\alpha = 90^\circ$, the numerical model over-predicts the experimental results

with about 50%. In contrast, the model under-predicts the experiment at a small α . The observed offset hints at a good agreement of the chosen distribution of drag forces with respect to Reynolds numbers but a less accurate incorporation of the angle between the fluid and net element. Further research has to clarify this issue. A similar situation can be seen for the force coefficients, shown in Fig. 4b and Fig. 4c. Again, a small over-prediction can be seen for $\alpha = 15^\circ$ and a small under-prediction for $\alpha = 90^\circ$. However, the calculated distributions match well the experimental data with errors less than 20%.

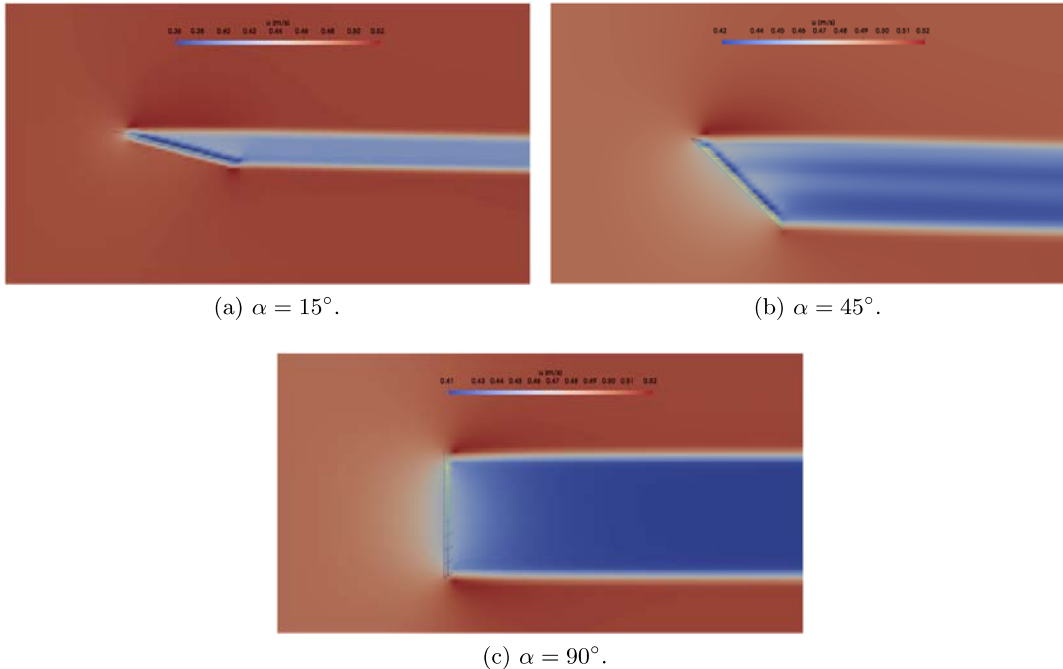


Figure 3: Velocity field for the fixed net panel in steady current flow of $u_\infty = 0.5m/s$.

3.2 Moving net panel in current

The motion of a net panel in steady current shall be analysed next. For this purpose, the experimental setup from [2] for the inflow velocity of $0.226m/s$ is taken as the reference. The net is fixed on the top, and sinker with a weight of $64.5g$ in water is attached to the bottom. It has a size of $0.3m \times 0.3m$ and consists of 225 square meshes. Each twine has a diameter of $2.6mm$ and a length of $20mm$. This results in a solidity of 0.26. Further, the chosen material has a density of $1150kg/m^3$ which leads to small gravity forces in water. In the numerical simulations, the geometry of the net is not changed which prevents eventual scaling effects. The sinker is represented by distributing its weight equally to the bottom knots. The porous resistance coefficients are taken from above, whereas the thickness of the zone is reduced to $20mm$. The three-dimensional computational domain is illustrated in Fig. 5a. The domain has a length of $1.5m$, a width of $0.5m$ and a height of $0.6m$. The numerical grid consists of $0.72Mio$ cells with

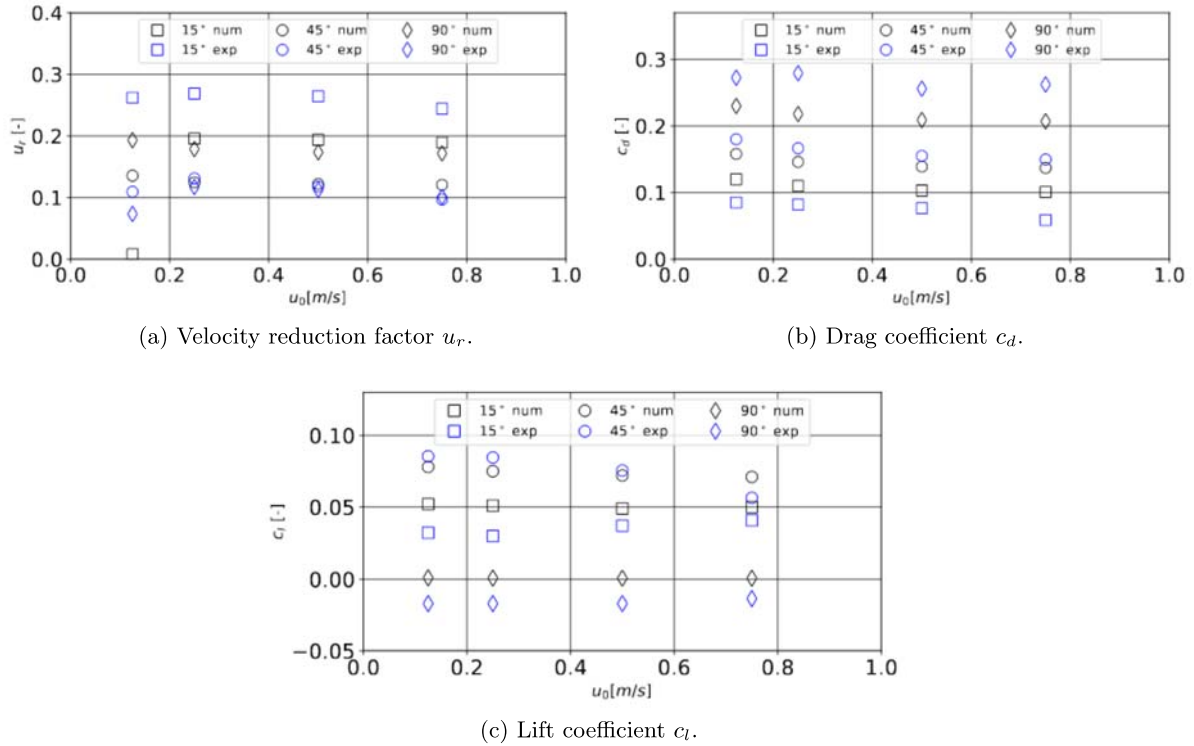
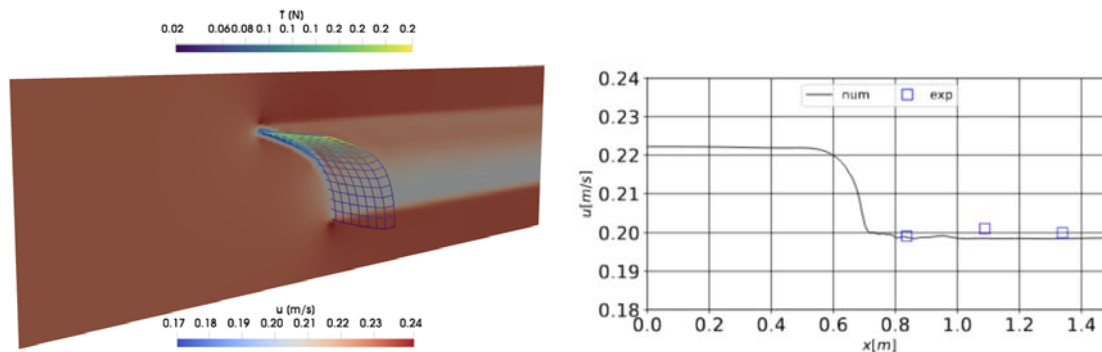


Figure 4: Comparison of numerical and experimental results for the fixed net panel in steady current flow.

gradual refinement around the net. The top bar of the net is fixed in the middle of the tank at $x = 0.5m$ and $z = 0.4m$. In accordance with the experiments, no free surface is taken into account.

The loss of momentum due to the drag of the net is analysed in Fig. 5b. Here, the predicted velocity distribution along the x-axis through the points $(y, z) = (0.25, 0.25)$ is shown. The wake velocity behind the net reproduces the experimental data which indicates properly chosen porous resistance coefficients. The deformation of the net panel is presented in Fig. 6. The displacement of the net bottom is in good agreement with the experiments for the x-direction. In z-direction, the numerical model is 50mm over the experimental results. This is caused by a generally over-prediction of drag and lift forces, which result in a more significant bending of the net geometry.

As a final remark, the tension forces in the net can be seen in Fig. 5a. The highest tension is computed in the upper part of the net where the weight of the net and the sinker is acting in combination with relatively large shear forces due to the small angle between net and fluid. The smallest tension is predicted in the lowest part of the net due to a smaller weight acting on these meshes. In addition, the ideal flexible assumption prevents the eventual occurrence of bending or shear forces in this part.



(a) Velocity distribution and tension forces in deformed net panel. (b) Velocity u over x at $(y, z) = (0.25, 0.25)$. Compared to the experimental results [2]

Figure 5: Results of the simulation of a net panel deformation in steady current.

4 CONCLUSIONS

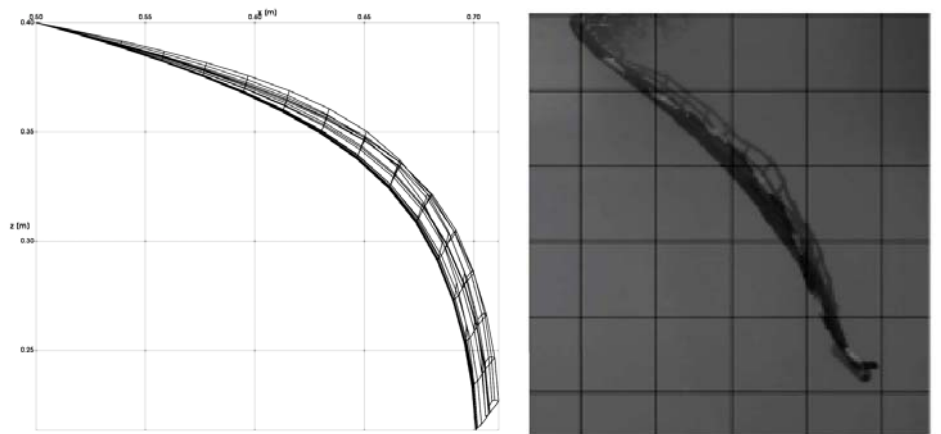
This paper presents a numerical approach for the simulation of the fluid-structure interaction of a net and fluid. The applied tension element method is based on static force equilibria at each knot of the net and additional geometrical constraints to close the system of equations. Hence, a fast and reliable solution procedure for quasi-stationary problems is provided. The coupling between fluid and structural model is achieved by a porous medium introduction into the fluid describing equations. This approach has the advantage of being easy to implement and highly adaptable to various net configurations. The validation of the algorithm indicated the successful implementation but also several discrepancies in comparison to experimental data. Here, the driving factors are the calculation of forces on the net from the surrounding fluid and the porous resistance coefficients which have to be determined from a limited amount of experiments. These indications were also concluded in previous studies, and are especially distinct for more complex structures, such as net cages, and in wave conditions. Therefore, an improvement of these leading factors has to be sought during further research.

5 ACKNOWLEDGMENT

The authors are grateful for the grants provided by the Research Council of Norway under the Havbruk2 project (No. 267981). This research was supported in part with computational resources at NTNU provided by The Norwegian Metacenter for Computational Sciences (NOTUR, <http://www.notur.no>) under project no. NN2620K.

REFERENCES

- [1] Patursson, Ø., 2007. Tow tank measurements of drag- and lift force on a net panel and current reduction behind the net panel. Technical Report NVDRit2007:10, University of the Faroe Islands, Torshavn, Faroe Islands.
- [2] Bi, C.-W., Zhao, Y.-P., Dong, G.-H., Xu, T.-J., and Gui, F.-K., 2014. “Numerical simulation of the interaction between flow and flexible nets”. *J. Fluids Struct.*, **45**, pp. 180–201.



(a) Numerical predicted net deformation.

(b) Experimental result taken from [16] for comparison. Each mesh has a length of 50mm.

Figure 6: Comparison of numerical and experimental deformation of a net in steady current.

- [3] Lader, P. F., and Enerhaug, B., 2005. “Experimental investigation of forces and geometry of a net cage in uniform flow”. *IEEE Journal of Oceanic Engineering*, **30**(1), pp. 79–84.
- [4] Lader, P., Jensen, A., Sveen, J. K., Fredheim, A., Enerhaug, B., and Fredriksson, D., 2007. “Experimental investigation of wave forces on net structures”. *Applied Ocean Research*, **29**(3), pp. 112–127.
- [5] Lader, P. F., Olsen, A., Jensen, A., Sveen, J. K., Fredheim, A., and Enerhaug, B., 2007. “Experimental investigation of the interaction between waves and net structures—Damping mechanism”. *Aquacultural Engineering*, **37**(2), pp. 100–114.
- [6] Kristiansen, T., and Faltinsen, O. M., 2015. “Experimental and numerical study of an aquaculture net cage with floater in waves and current”. *Journal of Fluids and Structures*, **54**, pp. 1–26.
- [7] Tronstad, H., 2000. Nonlinear Hydroelastic Analysis and Design of Cable Net Structures Like Fishing Gear Based on the Finite Element Method. Ph.D. thesis, Norwegian University of Science and Technology, Faculty of Marine Technology.
- [8] Priour, D., 1999. “Calculation of net shapes by the finite element method with triangular elements”. *Commun. Numer. Meth. Engng.*, **15**, pp. 757–765.
- [9] Lader, P. F., and Fredheim, A., 2006. “Dynamic properties of a flexible net sheet in waves and current—A numerical approach”. *Aquacultural Engineering*, **35**(3), pp. 228–238.
- [10] Tsukrov, I., Eroshkin, O., Fredriksson, D., Swift, M. R., and Celikkol, B., 2003. “Finite element modeling of net panels using a consistent net element”. *Ocean Engineering*, **30**, pp. 251–270.

-
- [11] Marichal, D., 2003. Cod-end numerical study. In: 3rd International Conference on Hydroelasticity in Marine Technology, Oxford, UK.
- [12] Martin, T., Schacht, S., Riesen, P., and Paschen, M., 2018. “Efficient implementation of a numerical model for flexible net structures”. *Ocean Engineering*, **150**, pp. 272–279.
- [13] Patursson, Ø., Swift, M. R., Tsukrov, I., Simonsen, K., Baldwin, K., Fredriksson, D., and Celikkol, B., 2010. “Development of a porous media model with application to flow through and around a net panel”. *Ocean Engineering*, **37**, pp. 314–324.
- [14] Zhao, Y.-P., Bi, C.-W., Liu, Y.-X., Dong, G.-H., and Gui, F.-K., 2014. “Numerical Simulation of Interaction Between Waves and Net Panel Using Porous Media Model”. *Engineering Applications of Computational Fluid Mechanics*, **8**(1), pp. 116–126.
- [15] Chen, H., and Christensen, E., 2016. “Investigations on the porous resistance coefficients for fishing net structures”. *J. Fluids Struct.*, **65**, pp. 76–107.
- [16] Chen, H., and Christensen, E., 2017. “Development of a numerical model for fluid-structure interaction analysis of flow through and around an aquaculture net cage”. *Ocean Engineering*, **142**, pp. 597–615.
- [17] Bihs, H., Kamath, A., Chella, M. A., Aggarwal, A., and Arntsen, Ø. A., 2016. “A new level set numerical wave tank with improved density interpolation for complex wave hydrodynamics”. *Computers & Fluids*, **140**, pp. 191–208.
- [18] Kamath, A., Chella, M. A., Bihs, H., and Arntsen, Ø. A., 2017. “Energy transfer due to shoaling and decomposition of breaking and non-breaking waves over a submerged bar”. *Engineering Applications of Computational Fluid Mechanics*, **11**(1), pp. 450–466.
- [19] Kamath, A., Chella, M. A., Bihs, H., and Arntsen, Ø. A., 2015. “Evaluating wave forces on groups of three and nine cylinders using a 3D numerical wave tank”. *Engineering Applications of Computational Fluid Mechanics*, **9**, pp. 343–354.
- [20] Bihs, H., and Kamath, A., 2017. “A combined level set/ghost cell immersed boundary representation for floating body simulations”. *Int. J. Numer. Meth. Fluids*, **83**, pp. 905–916.
- [21] Martin, T., Kamath, A., and Bihs, H., 2018. “Modelling and Simulation of Moored-floating Structures using the Tension-Element-Method”. *ASME 2018 37th International Conference on Ocean, Offshore and Arctic Engineering*, **2**.
- [22] Chorin, A., 1968. “Numerical solution of the Navier-Stokes equations”. *Mathematics of Computation*, **22**, pp. 745–762.
- [23] Shu, C., and Osher, S., 1988. “Efficient implementation of essentially non-oscillatory shock-capturing schemes”. *Journal of Computational Physics*, **77**(2), pp. 439–471.
- [24] Jiang, G., and Shu, C., 1996. “Efficient implementation of weighted ENO schemes”. *Journal of Computational Physics*, **126**(1), pp. 202–228.

- [25] van der Vorst, H., 1992. “BiCGStab: A fast and smoothly converging variant of Bi-CG for the solution of nonsymmetric linear systems”. *SIAM Journal of Scientific Computing*, **13**, pp. 631–644.
- [26] Jensen, B., Jacobsen, N., and Christensen, E., 2014. “Investigations on the porous media equations and resistance coefficients for coastal structures”. *Coastal Engineering*, **84**, pp. 56–72.
- [27] Fredheim, A., 2005. Current Forces on Net Structures. Ph.D. thesis, Norwegian University of Science and Technology, Faculty of Marine Technology.
- [28] Choo, Y., and Casarella, M., 1971. “Hydrodynamics resistance of towed cables”. *Journal of Hydraulics*, **5**, pp. 126–131.

A SENSITIVITY ANALYSIS OF CFD TRANSITION MODELLING IN THE CONTEXT OF VORTEX ROLL-UP PREDICTION

RENS LIEBRAND*, MAARTEN KLAPWIJK^{†,‡}, THOMAS LLOYD*, GUILHERME VAZ*, and RUI LOPES^{‡,◇}

* Faculty of Aerospace Engineering
rensliebrand@gmail.com

† Faculty of Mechanical, Maritime and Material Engineering
Delft University of Technology
Mekelweg 5, 2628 CD Delft, The Netherlands

‡ Maritime Research Institute Netherlands (MARIN) academy, * MARIN
Haagsteeg 2, 6708 PM Wageningen, The Netherlands

◇ Instituto Superior Técnico
University of Lisbon
Av. Rovisco Pais 1, 1049-001 Lisbon, Portugal

Key words: Cavitating tip vortex noise, elliptical wing, transition modelling, ReFRESCO

Abstract. A sensitivity analysis of the transitional flow over a NACA66₂ – 415 foil and the elliptical Arndt wing is carried out. The SST turbulence model is complemented with the $\gamma - \tilde{Re}_\theta$ transition model to determine the effect of varying turbulence intensity and eddy-viscosity ratio on the integral quantities and transition locations. Local grid refinement at the transition location is used to improve convergence. The skin friction drag coefficient is found to be more sensitive to the inflow conditions for 5° angle of attack compared to 9°. The movement of the transition location on the suction side is found to be responsible for this. The transition model captures a laminar separation bubble at the pressure side for both angles of attack, causing the lift coefficient to drop slightly. 3D calculations for the Arndt wing with the same foil section show that applying a transition model can decrease the boundary layer thickness by a factor of three, which is expected to influence the viscous core radius and consequently the minimum pressure in the tip vortex.

1 INTRODUCTION

Motivated by increased awareness of the harmful environmental effects of underwater noise generated by ships, there is a need to better understand the noise-generation mechanisms. An important contributor to ship noise is propeller cavitation [1]. While the numerical prediction of developed sheet cavitation is relatively well-understood [2], knowledge regarding modelling aspects of the inception and dynamics of tip vortex cavitation is still insufficient to obtain reliable numerical results in relation to noise predictions.

A popular approach for studying cavitating vortices is to investigate a tip-loaded finite span lifting surface which induces a tip vortex while avoiding rotational motion. An often-used benchmark is the elliptical wing with NACA66₂ – 415 cross-section as introduced by Arndt et al [3]. Recent experimental

[4] and numerical studies [5, 6, 7] revealed the complexity of the cavitating vortex flow. Figure 1 provides a summary of the numerically as well as experimentally obtained lift coefficients (C_L) for an angle of attack (α) of 9° found in open literature. The spread in the values indicates the high uncertainties and lack of consensus regarding appropriate modelling for this test case.

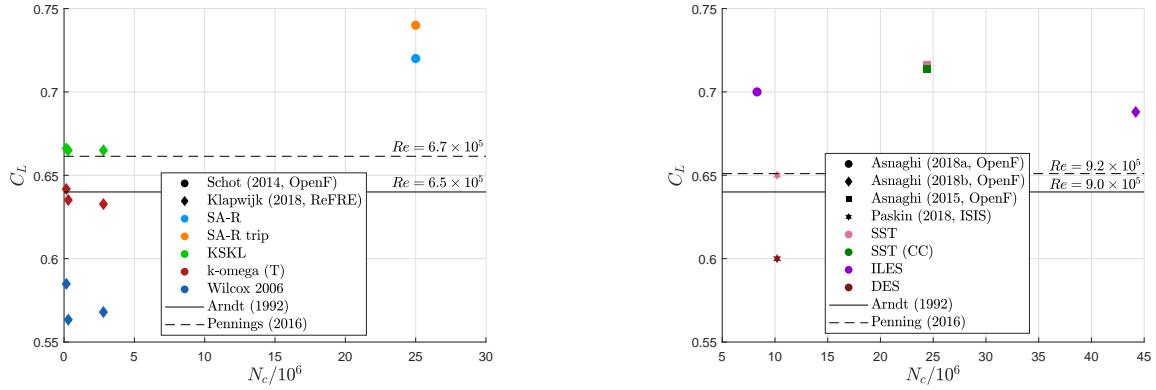


Figure 1: Published lift coefficient data versus number of grid cells (N_c) at $\alpha = 9^\circ$, $Re = 6.8 \times 10^5$ (left) and $Re = 8.95 \times 10^5$ (right). The shape of the data points indicates the reference, the colour stands for the employed turbulence models, and the lines represent experimental results.

Most numerical studies assess the wing at 9° Angle of Attack (AoA) to avoid the presence of a Laminar Separation Bubble (LSB) [5]. Arndt et al [3] show a high dependency of the transition location on the suction side towards the AoA. Flow visualisation for an AoA of 10° at a Reynolds number (Re) of 5.3×10^5 shows natural transition occurring near the leading edge. This is probably due to the foil's geometry, which is designed to be a laminar foil (with a low adverse pressure gradient over the midsection of the foil) and therefore is not supposed to operate at such a high AoA. An AoA of 5° at the same Reynolds number shows laminar flow until $x/c \simeq 0.60$, after which it undergoes separation-induced transition [3]. Here x/c indicates the normalised stream-wise position from the leading edge, where c is the chord.

Although the lift coefficient is directly proportional to the circulation over the wing and thus the strength of the vortex, it does not provide a detailed insight into its structure. In CFD calculations, difficulties in the prediction of the transition location cause errors in the prediction of the Boundary Layer (BL) profile over the wing. Since the BL rolls up in the wake of a lifting surface, it is evident that the structure of the vortex is related to its characteristics. Maines and Arndt [8] observe that “*the vortex mainly interacts with the boundary layer on the suction side of the wing, boundary layer fluid is entrained in the vortex which affects the core radius*”. This observation can be combined with the McCormick hypothesis resulting in the following proportionality,

$$\eta_v \sim \delta_s \sim Re_c^{-h}, \quad (1)$$

with η_v the viscous core radius, δ_s the BL thickness on the suction side, and $Re_c = \frac{U_\infty c}{\nu}$ the chord-based Reynolds number. In this equation U_∞ is the freestream velocity, and ν the kinematic viscosity. The constant h is typically about 0.2 for a turbulent BL and 0.4 for a transitional BL [9].

The flow characteristics within the vortex core play a crucial role in the cavitation inception process as well as the dynamics of the cavity. Bosschers [1] derived a two-dimensional analytical expression for the velocity and pressure distributions within a cavitating vortex. The derivation is based on the Lamb-Oseen vortex which is supplemented by jump relations for the mass transfer and shear stress as boundary

conditions at the vapour-liquid interface. The pressure is supposed to be at its minimum (p_{min}) in the centre of the vortex core ($\eta = 0$). This yields the relation,

$$p(\eta = 0) - p_\infty = p_{min} - p_\infty = -\frac{\rho\Gamma_\infty^2}{(2\pi\eta_v)^2}\zeta\ln(2), \quad (2)$$

where the pressure is denoted by p , the freestream pressure by p_∞ , and the freestream circulation of the vortex by Γ_∞ . The latter is related to the circulation over the wing (Γ_0) through the roll-up process. The constant $\zeta = 1.2564$ is introduced to ensure that the azimuthal velocity is maximum at the viscous core radius.

When employing a transition model, the resulting BL thickness is expected to be predicted more accurately. In most applications, a transition model delays the mixing properties of the BL which yields a laminar profile over a longer distance. This means that the resulting BL is thinner and thus the viscous core length smaller, according to Equation 1. Following Equation 2, this results in a lower minimum pressure and therefore more cavitation. While in prior research [5, 6] the under-predicted vortex cavity length is explained by (i) over-prediction of the eddy-viscosity in the vortex core and (ii) numerical diffusion, it could be that the assumption of a fully turbulent BL also contributes.

Prior to considering the vortex itself to test this hypothesis, it is important to understand the transitional behaviour of the flow over the foil section under different flow conditions. To this end, a 2D sensitivity analysis of the foil at half-span to the turbulent inflow conditions is performed. The effect on the lift coefficient C_l and friction drag coefficient C_{df} is investigated. To draw more general conclusions concerning transition, the 2D simulations were carried out for two AoA: 5° and 9° . Based on these findings, a set of 3D calculations is performed to investigate the effect on the BL itself.

2 NUMERICAL MODELS

Reynolds-Averaged Navier Stokes (RANS) calculations are performed which are by definition not able to capture transitional flows [10]. The 2003 version of the SST [11] turbulence model was complemented with the $\gamma - \tilde{R}e_{\theta_i}$ model [12] to model this process. Downstream of the stagnation point, a turbulent BL starts developing due to the production term P_k in the transport equation for turbulent kinetic energy k .

The $\gamma - \tilde{R}e_{\theta_i}$ model solves a transport equation for the intermittency γ which ranges from 0 (laminar flow) to 1 (turbulent flow). The intermittency is used to adapt the production and destruction term in the k -transport equation,

$$\tilde{P}_k = \gamma_{eff}P_k; \quad \tilde{D}_k = \min[\max(\gamma_{eff}, 0.1), 1.0]D_k, \quad (3)$$

where $\gamma_{eff} = \max(\gamma, \gamma_{sep})$. Here γ_{sep} is a modification to the intermittency for predicting separation induced transition. Using the intermittency to adapt the production and dissipation terms instead of modifying the eddy-viscosity increases the robustness of the model. In this way, γ does not enter the momentum equation directly and therefore does not have to be linearised (which is difficult because of the empirical relations in the source term shown later).

The transport equation for the intermittency reads:

$$\frac{\partial\gamma}{\partial t} + \frac{\partial(u_j\gamma)}{\partial x_j} = P_\gamma - E_\gamma + \frac{\partial}{\partial x_j} \left[\left(\mathbf{v} + \frac{\mathbf{v}_t}{\sigma_f} \right) \frac{\partial\gamma}{\partial x_j} \right], \quad (4)$$

with $P_\gamma = F_{length}c_{a1}S[\gamma F_{onset}]^{0.5}(1 - c_{e1}\gamma)$.

At the start of the BL, $\gamma = 0$ indicates a completely laminar flow. When the BL develops, the intermittency is mainly increased by the production P_γ . This term acts as a source and is designed to be 0

upstream of the transition point and to be active when transition starts, achieved by the limiter F_{onset} . Mathematically the model triggers transition when the vorticity based Reynolds number (Re_V) exceeds the onset criterion. The onset criterion is determined by the *local* transition Reynolds number (\tilde{Re}_{θ_t}) according to the following proportionality,

$$F_{onset} \stackrel{\text{I. limiter}}{\sim} F_{onset2} \stackrel{\text{II. limiter}}{\sim} F_{onset1} \stackrel{\text{III. expression}}{\sim} Re_{\theta_c} \stackrel{\text{IV. empirical relation}}{\sim} \tilde{Re}_{\theta_t} \stackrel{\text{V. diffusion in TE}}{\sim} Re_{\theta_t}. \quad (5)$$

The description of proportionality I-IV can be found in the original paper [12]. The fifth relation is incorporated in the second transport equation:

$$\frac{\partial \tilde{Re}_{\theta_t}}{\partial t} + \frac{\partial (u_j \tilde{Re}_{\theta_t})}{\partial x_j} = P_{\theta_t} + \frac{\partial}{\partial x_j} \left[\sigma_{\theta_t} (\nu + \nu_t) \frac{\partial \tilde{Re}_{\theta_t}}{\partial x_j} \right], \quad (6)$$

$$\text{with } P_{\theta_t} = \frac{c_{\theta_t}}{t} (Re_{\theta_t} - \tilde{Re}_{\theta_t}) (1.0 - F_{\theta_t}). \quad (7)$$

Information from the freestream is passed into the BL by means of the diffusion term. In order to match the local and global variable in the freestream, the production term is employed. The blending factor F_{θ_t} is responsible for deactivating the production inside the BL and activating the term in the freestream. In this blending factor a function F_{wake} ensures that the production term is *not* active in the wake regions.

The behaviour of the model is known to be sensitive to the turbulent inflow quantities, turbulent intensity I and eddy-viscosity ratio $\frac{\nu_t}{\nu}$ [10, 12]. By shifting the transition location, through varying the turbulent inflow conditions, the hypothesis stated in Section 1 can be tested.

3 COMPUTATIONAL SETUP

The computational domain is based on to the cavitation tunnel at Delft University of Technology. The Arndt wing is an elliptical planform with a NACA662 – 415 cross-section over its entire span. In the 2D computations, the wing at half-span ($z/b = 0.5$) is considered. This spanwise location is chosen since least interaction with the tip flow and the side wall is expected there. The chord length at this location is $c = 109.2 \text{ mm}$. The domain extends $6c$ up- and $13c$ downstream of the foil's leading edge. The distance between the leading edge and the top and bottom walls is $1.35c$. Most available 3D reference data is for a *root* chord-based Reynolds number of 8.95×10^5 as shown in Figure 1, corresponding to a Reynolds number at half-span (for 2D computations) of 7.76×10^5 . Using $\nu = 1.002 \times 10^{-6} \text{ m}^2/\text{s}$, this yields an inflow velocity of 0.7783 m/s . Both $\alpha = 5^\circ$ and $\alpha = 9^\circ$ were simulated. The turbulence intensity and the eddy-viscosity ratio were varied between $I = [1, 2, 3]\%$ and $\frac{\nu_t}{\nu} = [1, 2, 3]$. The turbulent quantities are frozen until $0.1c$ upstream of the leading edge of the foil to control the decay in the domain.

A set of four geometrically similar O-grids with a refinement factor of 1.6 between coarsest and finest grid was generated for each AoA. Table 1 displays the details of the grids.

Simulations were performed using ReFRESCO (www.refresco.org), a community based open-usage/open-source CFD code for the Maritime World. It solves multiphase (unsteady) incompressible viscous flows using the Navier-Stokes equations, complemented with turbulence models, cavitation models and volume-fraction transport equations for different phases. The equations are discretised using a finite-volume approach with cell-centred collocated variables, in strong-conservation form, and a pressure-correction equation based on the SIMPLE algorithm is used to ensure mass conservation. The implementation of the $\gamma - \tilde{Re}_{\theta_t}$ model in the solver was tested by [13]. For the convective flux discretisation, the second-order accurate Quadratic Upstream Interpolation for Convective Kinematics (QUICK)

Table 1: 2D grid specifications for $\alpha = 5^\circ$ (left) and $\alpha = 9^\circ$ (right). Normal x_n^+ and tangential x_t^+ wall coordinates are averaged over the surface and obtained by the *SST* simulation. N_s indicates the number of surface cells, N_c the total number of grid cells, and h/h_i the refinement ratio.

| N_s | $N_c/10^5$ | h/h_i | $\overline{x_n^+} \times 10^2$ | $\overline{x_t^+}/10^2$ | N_s | $N_c/10^5$ | h/h_i | $\overline{x_n^+} \times 10^2$ | $\overline{x_t^+}/10^2$ |
|-------|------------|---------|--------------------------------|-------------------------|-------|------------|---------|--------------------------------|-------------------------|
| 600 | 1.00 | 1.60 | 9.23 | 1.41 | 600 | 1.00 | 1.60 | 9.81 | 1.36 |
| 720 | 1.44 | 1.33 | 7.64 | 1.17 | 720 | 1.44 | 1.33 | 8.11 | 1.14 |
| 840 | 1.96 | 1.14 | 6.51 | 1.01 | 840 | 1.96 | 1.14 | 6.92 | 0.97 |
| 960 | 2.56 | 1.00 | 5.68 | 0.88 | 960 | 2.56 | 1.00 | 6.03 | 0.85 |

scheme is employed for the momentum and turbulence equations. A First-Order accurate Upwind (FOU) scheme is used for the transition equations for robustness reasons as elaborated on in Section 5.1. The discretisation of all diffusive terms is second order accurate. Computations are performed steady state since no large separation or vortex shedding was observed by experimentalists [3].

4 ERROR ANALYSIS

In CFD one can distinguish between iterative, discretisation, input, round-off and, for unsteady calculations, statistical errors. The transition model is known to be sensitive to input (parameter) uncertainties, however the assessment of this is not part of this research. Round-off errors can be assumed to be negligible in practical applications [14]. In the 2D sensitivity analysis, the iterative and discretisation error were evaluated.

4.1 Iterative error

To ensure effective use of computational resources, a trade-off between computational costs and iterative error was made. For each AoA, six calculations with different convergence criteria for the maximum residual (L_∞) were performed. The residuals for the transition equations are excluded from these criteria since it was not possible to reach $L_\infty = 10^{-7}$ and $L_\infty = 10^{-8}$ using the FOU scheme for the convective fluxes of γ and $\tilde{R}e_{\theta_i}$. Figure 2 displays the most relevant quantity for transition, C_{df} , versus the convergence criteria. The right axis shows the computational costs to reach the specified L_∞ . Making a trade-off between computational costs and iterative accuracy, a convergence criterion of $(L_\infty)_{\notin \gamma, \tilde{R}e_{\theta_i}} = 10^{-5}$ is considered to be sufficient for both cases. At that level, the iterative errors relative to the 10^{-8} simulation are 0.40% and 0.31% for $\alpha = 5^\circ$ and $\alpha = 9^\circ$ respectively. In order to reduce this error to 0.14% and 0.07% at $(L_\infty)_{\notin \gamma, \tilde{R}e_{\theta_i}} = 10^{-6}$, the computational costs increase by 132% and 111%.

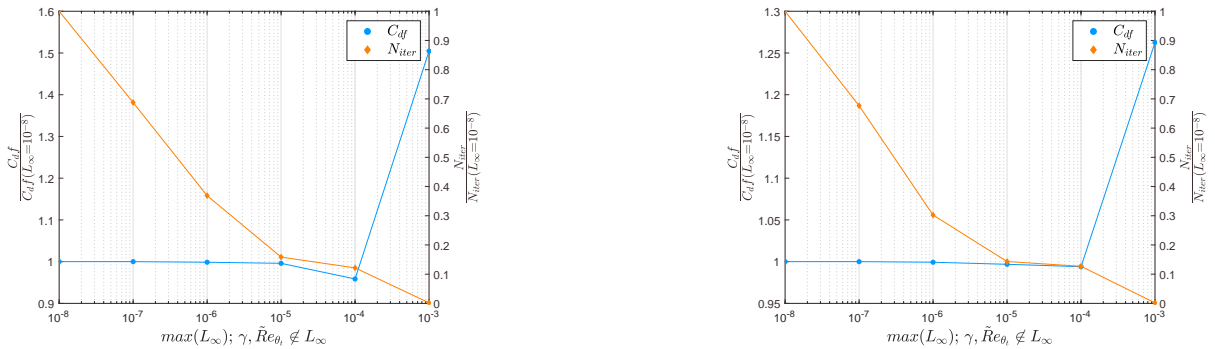


Figure 2: Iterative error analysis for $N_s = 960$ grid, showing the trade-off between numerical accuracy and computational cost for $\alpha = 5^\circ$ (left) and $\alpha = 9^\circ$ (right).

4.2 Discretisation error

The discretisation error was assessed based on the procedure of Eça and Hoekstra [15]. The method relies on (truncated) power series expansions. The basic equation to determine the discretisation error ε for the variable ϕ reads,

$$\varepsilon \simeq \phi_i - \phi_0 = \beta h_i^q, \quad (8)$$

where ϕ_i is any local or integrated flow quantity, ϕ_0 an estimate of the exact solution, β a constant to be determined, h_i the typical cell size and q the observed order of grid convergence. To determine ϕ_0 , β , and q , a set of four geometrically similar structured grids is used, as presented in Table 1. Flux limiters, damping functions and switches in the turbulence model result in noise in the CFD output. This sometimes yields the proposed estimation in Equation 8 to be impossible or unreliable. In that case, either a linear ($q = 1$), quadratic ($q = 2$), or a combination of both ($\beta_1 h_i + \beta_2 h_i^2$) is used.

The resulting uncertainty U_ϕ is determined according to the Grid Convergence Index procedure [14],

$$U_\phi(\phi_i) = F_s \varepsilon(\phi) + \sigma + |\phi_i - \phi_{i_{fit}}|, \quad (9)$$

where the safety factor F_s is set as 1.25 or 3 depending on the quality of the fit, to obtain a 95% confidence interval for U_ϕ . The uncertainties of the integral values (C_l and C_{d_f}) were determined using this approach. These results are visualised by the error bars in Figure 6.

5 RESULTS

5.1 Iterative convergence

A well-known problem of the $\gamma - \tilde{R}e_{\theta_i}$ model is its convergence behaviour, see e.g. [16]. If a FOU scheme for the discretisation of the convection of the transition variables is employed, the simulations converge to the residual criterion ($L_\infty = 10^{-5}$). However, when using the QUICK scheme in all equations the calculation stagnate. Although the residuals are not converged, the forces are observed to be constant over the stagnated part ($N_{iter} > 1.2 \times 10^4$). N_{iter} is the number of iterative loops used to solve the non-linearity in the Navier-Stokes equations.

The stagnating behaviour is related to the transition location continuously switching between two stream-wise cells. If the location moves to the neighbouring cell, the flow-field adapts itself accordingly where-after the transition location moves back to the original location again. This can be explained by the fact that the γ -production is triggered by the limiter $F_{onset} = \max(F_{onset2} - F_{onset3}, 0)$. In the γ -production term, the magnitude of F_{length} is typically large whereby the production increases drastically when F_{onset2} exceeds F_{onset3} . F_{onset3} is relatively constant throughout the simulation since it only depends on k and the specific dissipation rate (ω). The main term responsible for triggering the onset of production is thus F_{onset2} . This term is implicitly related to the strain rate (S_{ij}) in the flow by $F_{onset2} \sim F_{onset1} \sim Re_v \sim S_{ij}$, which causes the observed behaviour. When production of γ starts, P_k , and thus k and ν_t , increase. The resulting higher eddy-viscosity smooths the solution which reduces the magnitude of the gradients. This results in a lower strain rate causing $Re_v \sim F_{onset1} \sim F_{onset2}$ to drop. If this drop is sufficient, the magnitude of

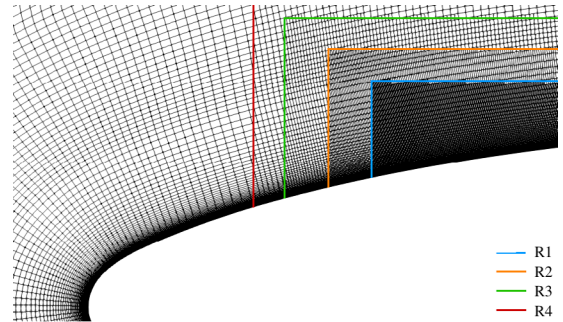


Figure 3: Grid of the suction side at the leading edge, $N_s = 600$. Colours indicate refinements.

F_{onset2} ends up lower than F_{onset3} whereby the limiter cancels the production term again. Although F_{onset3} is introduced to avoid this sort of behaviour [12], it fails to do so in this case.

This reasoning is tested by means of local grid refinement (h-refinement) at the transition location (x_{tr}). The transition location is defined as the point where the derivative of the skin friction changes from negative to positive. If the grid is sufficiently fine in the stream-wise direction (x_t^+), the iterative stagnating behaviour should be absent. The four different refinement levels applied at the suction side (R1-4) are shown in Figure 3. All refinement levels are applied on the baseline grid with $N_s = 600$.

The largest residuals in the original simulation were located at the point of transition on the suction side. *Only* refining at that location does not yield convergence but shifts the maximum residual towards the transition location at the pressure side. Convergence is obtained when the grid around both transition locations is sufficiently refined while controlling the grid diffusion. Table 2 presents all relevant quantities of the refined grids.

Table 2: Grid refinement on the suction side (left) and pressure side (right). Values for x_t^+ at the transition location and x_{tr} given for the corresponding side. x_t^+ on opposite side was 9.1 for simulations *a-d*, and 11.8 for simulations *e-h*.

| Sim. | $N_c/10^5$ | x_t^+ | $\frac{C_l}{(C_l)_{d,h}}$ | $\frac{C_{df}}{(C_{df})_{d,h}}$ | $\frac{x_{tr}}{(x_{tr})_{d,h}}$ | Sim. | $N_c/10^5$ | x_t^+ | $\frac{C_l}{(C_l)_{d,h}}$ | $\frac{C_{df}}{(C_{df})_{d,h}}$ | $\frac{x_{tr}}{(x_{tr})_{d,h}}$ |
|----------|------------|---------|---------------------------|---------------------------------|---------------------------------|----------|------------|---------|---------------------------|---------------------------------|---------------------------------|
| <i>a</i> | 1.35 | 99.1 | 1.0012 | 0.9950 | 1.0308 | <i>e</i> | 1.59 | 71.8 | 1.0008 | 1.0006 | 0.9997 |
| <i>b</i> | 1.43 | 47.3 | 1.0006 | 0.9973 | 1.0301 | <i>f</i> | 1.63 | 36.2 | 1.0003 | 0.9986 | 1.0006 |
| <i>c</i> | 1.58 | 23.7 | 1.0005 | 0.9989 | 1.0240 | <i>g</i> | 1.72 | 18.2 | 1.0003 | 0.9987 | 1.0002 |
| <i>d</i> | 1.89 | 11.8 | 1.0000 | 1.0000 | 1.0000 | <i>h</i> | 1.89 | 9.1 | 1.0000 | 1.0000 | 1.0000 |

When using a QUICK scheme for the transition variables without local grid refinement, the computation typically stagnates with the γ -residual being the largest as shown in Figure 4. Figure 5 displays the residuals of the γ -equation for all refinement levels. In order to obtain convergence, a maximum x_t^+ of ~ 24 and ~ 36 is required on the suction and pressure side respectively. These values are expected to be case specific. Local grid refinement yields small discontinuities in the derivative of the skin friction distribution.

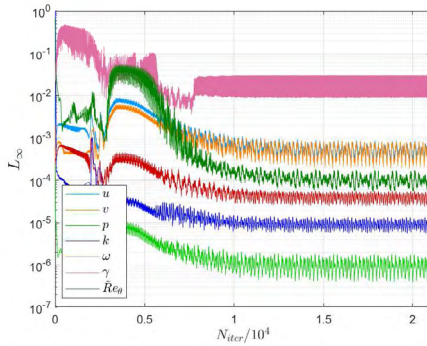


Figure 4: Convergence plot for $\gamma - \tilde{Re}_{\theta_i}$ simulation, $\alpha = 5^\circ$ and $N_s = 600$. QUICK is employed for *all* flux discretisations.

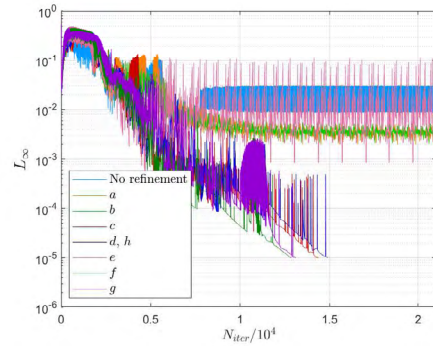


Figure 5: Convergence of γ -residual for all simulations present in Table 2. Stagnated QUICK simulation is also included.

5.2 Sensitivity to inflow conditions

A final simulation was performed using the minimum required x_t^+ values. This converged QUICK simulation only differs 0.65% for C_l , 0.25% for C_{df} , and 0.96% for x_{tr} with respect to a converged FOU simulation without refinement. Considering the increase of computations costs and effort of local grid refinement to obtain convergence if a QUICK scheme is employed in all equations, it was decided to use the FOU settings for the transition variables in this sensitivity analysis.

Figure 6 presents the sensitivity of the integral values towards the inflow conditions. The pure SST result for $I = 1\%$ and $\frac{u_t}{v} = 1$ is also given, in red. All results are normalised by the $\gamma - \tilde{Re}_{\theta_t}$ simulation with $I = 1\%$ and $\frac{u_t}{v} = 1$. Transition predominantly affects the C_{df} since it changes the shape of the BL and thus the velocity derivative at the wall, $C_{df} \sim \tau_w \equiv \mu \left(\frac{\partial u}{\partial y} \right)_{y=0}$. Furthermore, the transition model could influence the pressure distribution and thus the lift coefficient by its ability to capture an LSB or predicting laminar and turbulent separation more accurately.

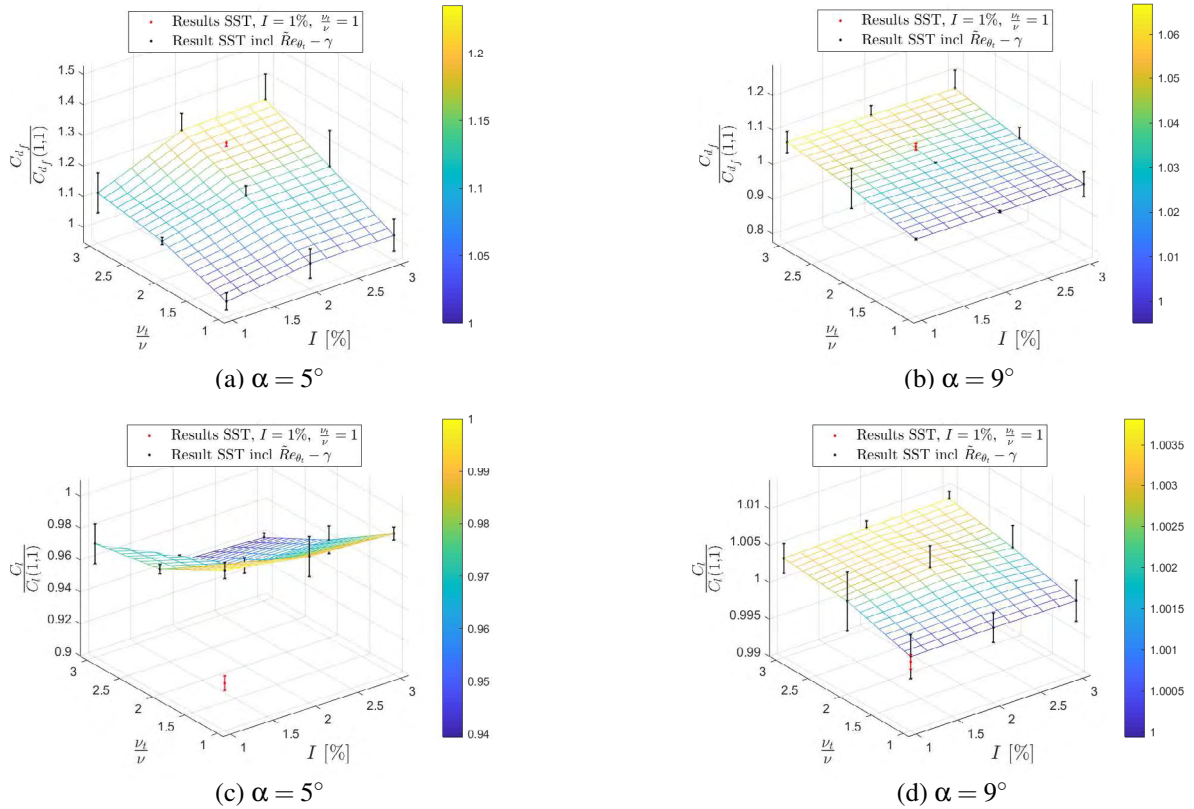


Figure 6: Sensitivity of the integral quantities to the turbulent inflow conditions for both AoA, using a grid with $N_s = 960$. The error bars indicate the discretisation uncertainty.

The skin friction for both AoA is significantly affected by changing the inflow conditions; it increases about 25% for $\alpha = 5^\circ$ and 6% for $\alpha = 9^\circ$. This is due to the up- or downstream movement of the transition location on the suction and pressure side of the foil. It can be observed that C_{df} for $\alpha = 9^\circ$ is less sensitive which is due to the high leading edge curvature at a higher AoA, forcing transition independently of the turbulent state of the inflow. This is confirmed by the skin friction distributions shown in Figure 7 where the high curvature of the leading edge causes the magnitude of the skin friction to be large for $x/c < 0.1$

which triggers transition. For $\alpha = 5^\circ$, transition on the suction side occurs at $x/c \simeq 0.2$ resulting in a completely different distribution.



Figure 7: Skin friction (left) and pressure (right) distributions for both AoA. Both SST and $\gamma - \tilde{R}e_{\theta_t}$, ($[I, \frac{v_t}{v}] = 1$) results are shown.

As expected, the lift coefficient is less sensitive to the turbulent inflow quantities. For $\alpha = 5^\circ$, the change in lift coefficient is at maximum 6%, for $\alpha = 9^\circ$ this reduces to only 0.4%. The fact that the 5° AoA case is influenced more is due to the shift in transition location on the suction side. The location where the flow undergoes transition determines its sensitivity to turbulent separation at the aft of the foil. This can be recognised in the friction and pressure distributions in Figure 7 at the location where C_f is smaller than zero at the trailing edge for the $\alpha = 5^\circ$, $\gamma - \tilde{R}e_{\theta_t}$ simulation. For both AoA, the lift coefficients predicted by the pure SST simulations are lower compared to the $\gamma - \tilde{R}e_{\theta_t}$ simulations. The LSB on the *pressure* side, captured by the $\gamma - \tilde{R}e_{\theta_t}$ model, is partly responsible for this. For both AoA, an LSB is present at $x/c \approx 0.75$ causing a reduced pressure and therefore a slightly lower lift coefficient.

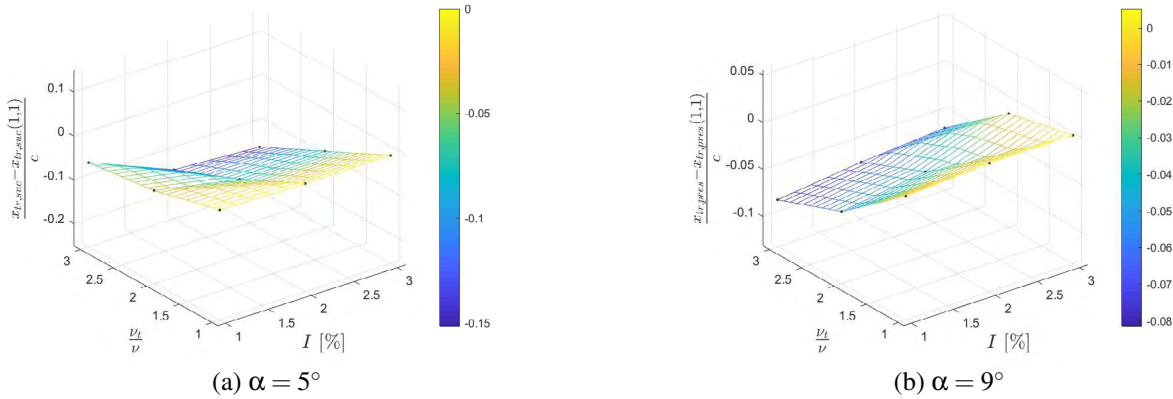


Figure 8: Sensitivity of the transition locations towards the turbulent inflow conditions for both angles of attack on grid with $N_s = 960$.

To further clarify the sensitivities of the integral quantities, Figure 8 presents the sensitivity of the transition locations. All results are reported with respect to the transition location for $I = 1\%$ and $\frac{v_t}{v} = 1$. Only the sensitivity of the transition location on the suction side for $\alpha = 5^\circ$ and the transition location on the pressure side for $\alpha = 9^\circ$ are shown. The other results are almost independent of the inflow conditions ($< 4\%$). The transition location on the suction side for $\alpha = 5^\circ$ moves 15% upstream if both quantities are tripled. This is intuitive since more energetic turbulence upstream should yield earlier transition. In the model, this is incorporated by the empirical relation between I and the *global* Re_{θ_t} . It is interesting to note that the results are insensitive when *only* the turbulence intensity is varied. This is due to the

decay of turbulence in the domain. Increasing the eddy-viscosity ratio accordingly avoids this since a higher $\frac{\nu_t}{\nu}$ reduces the damping. For 9° AoA, the transition location on the suction side is barely changed, a maximum shift of 0.3% is observed.

Transition on the pressure side is triggered at almost the same location for both cases. This location varies more for the 9° AoA case (maximum of $\sim 8\%$) than for the 5° AoA case (maximum of $\sim 4\%$). For both cases, it moves upstream for the reasons previously given. This causes the BL to become turbulent earlier which explains the increased C_{df} as discussed earlier.

5.3 3D wing calculations

Based on the findings in the previous section, 3D calculations were performed. The ultimate goal is to study the effect of transition modelling on the vortex structure itself; here some preliminary work towards this objective is presented. In Section 1, a hypothesis was stated which resulted in, $p_{min} \stackrel{\text{Eq. 2}}{\sim} 1/\eta_v^2 \stackrel{\text{Eq. 1}}{\sim} 1/\delta_s^2$. While this relationship between δ_s , η_v , and p_{min} will be examined in a future study, the current work focuses on the BL thickness.

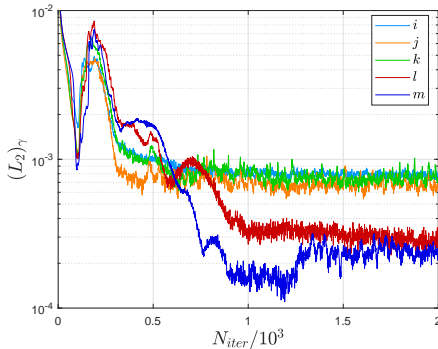


Figure 9: Average γ residuals for locally refined 3D grids. Foil at 5° AoA with $[I, \frac{\nu_t}{\nu}] = 1$.

Calculations are performed on a structured grid with $N_c = 2.61 \times 10^6$. Vortex refinement according to the recommendations of Asnaghi [6] and wake refinement to capture the gradients in the roll-up process more accurately are applied. The average wall coordinates over the surface are 0.147, 343, and 698 for x_n^+ , x_t^+ and x_s^+ respectively. Here x_s^+ indicates the non-dimensional wall unit in spanwise direction.

The same approach as for the 2D results is taken to improve convergence. The grid details are shown in Table 3, refinement is applied in the streamwise and spanwise direction until the requirement of ~ 36 non-dimensional wall units is reached. The residuals for the γ -equation are again observed to be the highest, and they are located at the transition location on the pressure side. Locally refining the grid at the pressure *and* suction sides based on the requirements set in Section 5.1 reduced the average (L_2) residual by a factor of four, as can be seen in Figure 9 (the graph only shows the first $2 \cdot 10^3$ iterations while a total of $2 \cdot 10^4$ iterative loops is performed). However, still small areas with the same value for the maximum residuals remain, i.e. L_∞ remains unaffected. This yields stagnation of the computations even though a FOU scheme is used for the turbulence *and* transition equations. This may be due to the omission of cross-flow instabilities in the $\gamma - \tilde{R}e_\theta$ model and/or the robustness of the model [12].

Further refinement would result in too large grids for a sensitivity analysis, and was therefore not pursued. Forces were observed to be constant over the iterations in the stagnated region. As shown in Table 3, the lift and skin friction drag coefficients only differ with 0.2% and 1.5% respectively. Although

| Sim. | $N_c/10^6$ | $\overline{x_t^+}$ | $\overline{x_s^+}$ | $\frac{C_L}{(C_L)_m}$ | $\frac{C_{Df}}{(C_{Df})_m}$ |
|----------|------------|--------------------|--------------------|-----------------------|-----------------------------|
| <i>i</i> | 2.69 | 289 | 273 | 0.9978 | 0.9852 |
| <i>j</i> | 2.79 | 178 | 198 | 0.9992 | 0.9870 |
| <i>k</i> | 3.13 | 94.9 | 110 | 0.9995 | 0.9956 |
| <i>l</i> | 4.44 | 50.6 | 63.2 | 1.0003 | 0.9920 |
| <i>m</i> | 9.51 | 26.7 | 33.3 | 1.0000 | 1.0000 |

Table 3: 3D simulation details of local grid refinement study. Wall-coordinates at pressure side are shown, they are averaged values at the transition location over the entire span.

the computations stagnate, the high residuals were found to occur very locally, at the transition location on the pressure side. Therefore the flow field on the side of interest (suction side) is not expected to be affected. Furthermore, the maximum and root mean square residuals for all other variables are at least one order of magnitude lower compared to the residuals of the γ equation. For all these reasons it was decided to perform the 3D calculations on the original grid *without* refinement at the transition locations.

Figure 10 visualises the flow over the suction side of the wing. On both sides, a LSB is present. The flow is laminar upstream of the LSB, following which separation induced transition causes the flow to become turbulent. The shape factor, which is defined as the displacement thickness over the momentum thickness, provides more insight in the flow. This number reflects the ‘fullness’ of the profile and is therefore directly related to the state of the BL. Figure 11 shows that transition for the $[I, \frac{\nu_t}{\nu}] = 1$ and $[I, \frac{\nu_t}{\nu}] = 0.5$ cases occurs at $x/c \approx 0.6$ as H reduces from a laminar value (2.6) towards the corresponding value for a turbulent BL (1.4). The fact that $H_{x/c=0.3} > 2.6$ is due to the adverse pressure gradient at that location. H drops below 2.6 between $x/c \simeq 0.3$ and 0.6 due to the favourable pressure gradient. BL details for $x/c > 0.8$ are excluded since turbulent flow separation results in an inaccurate estimation of H .

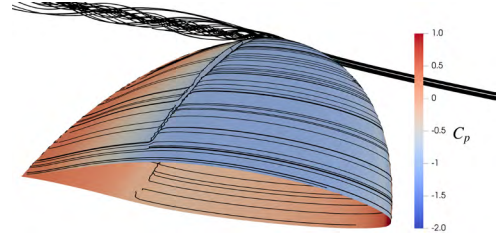


Figure 10: Flow (from right to left) at $\alpha = 5^\circ$. Limiting streamlines and pressure coefficient is visualised on the surface.

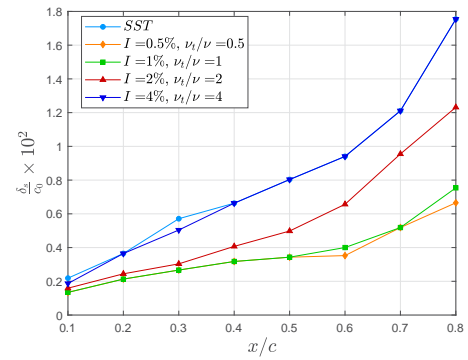
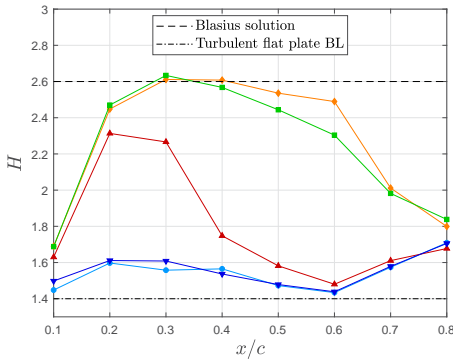


Figure 11: BL characteristics on the suction side over the chord at half-span ($z/b = 0.5$), shape factor (left) and BL thickness (right).

Figure 11 also shows the BL thickness on the suction side which is defined as the point where the magnitude of the velocity is less than 99% of the freestream velocity at that location, i.e. $|U| < 0.99|U_f|$. It can be seen that the δ_s for the *SST* and $[I, \frac{\nu_t}{\nu}] = 4.0$ case almost collapse. This is because for both cases transition occurs near the leading edge. The turbulence quantities are simultaneously decreased to a value of 2, 1 and 0.5. By doing so, transition is delayed which results in a BL almost three times thinner compared to the *SST* result at $x/c = 0.8$. This confirms the first part of the hypothesis: by varying the turbulent inflow conditions, the $\gamma - \tilde{R}e_{\theta}$ model changes the BL thickness at the suction side for $\alpha = 5^\circ$ significantly. This knowledge can now be used to test the effect of transition modelling on the vortex core itself.

6 CONCLUSIONS AND RECOMMENDATIONS

In this study, the effect of modelling transition on the wing’s BL was investigated as a first step towards confirming the hypothesis that links the BL flow and the pressure inside the vortex core. Local

grid refinement around the transition location was found to improve convergence when using the QUICK scheme for the convective flux discretisation in the transport equations of γ and $\tilde{R}e_{\theta}$. Results for C_l , C_{df} and x_{tr} obtained using the QUICK scheme and the FOU scheme are found to be within 1%.

It was observed that C_{df} is much more sensitive to the turbulent inflow conditions for $\alpha = 5^\circ$ than $\alpha = 9^\circ$. The lift coefficient is found to be relatively constant for both AoA. Accounting for transition results in an LSB on the pressure side for both AoA. Furthermore, at $\alpha = 5^\circ$, the sensitivity of the transition location on the suction side to the turbulent inflow conditions influences (turbulent) flow separation at the aft of the foil. Prescribing $I > 2\%$ in combination with $\frac{v_t}{v} > 2$ causes turbulent separation whereby the lift and thus the circulation drop by 6%.

3D calculations showed that δ_s at $x/c = 0.8$ decreases with a factor three when employing the $\gamma - \tilde{R}e_{\theta}$ model. Future work will focus on further evaluation of the hypothesis that this decrease in BL thickness decreases the minimum pressure in the vortex. In the light of this study, it is noted that since transitional effects are not controlled nor quantified in the (experimental) studies presented in Figure 1, it is expected that one should consider the results of these measurements for different AoA with care.

7 ACKNOWLEDGEMENTS

R. Liebrand would like to thank Dr M. Gerritsma and Dr A. van Zuijlen from the faculty of Aerospace Engineering of Delft University of Technology for their support and guidance during his MSc. thesis, part of which is reported in this paper. R. Lopes acknowledges the financial support provided by Fundação para a Ciência e Tecnologia through the Bolsas de Doutorado and Pós-Doutorado 2016 program.

REFERENCES

- [1] Bosschers, J. (2018). *Propeller tip-vortex cavitation and its broadband noise*. PhD thesis, The Netherlands: University of Twente.
- [2] Foeth, E.-J. (2008). *The structure of three-dimensional sheet cavitation*. PhD thesis, The Netherlands: Delft University of Technology.
- [3] Arndt, R., Arakeri, V., and Higuchi, H. (1991). Some observations of tip-vortex cavitation. *Journal of fluid mechanics*, 229:269–289.
- [4] Pennings, P. (2016). *Dynamics of vortex cavitation*. PhD thesis, The Netherlands: Delft University of Technology.
- [5] Schot, J. (2014). *Numerical study of vortex cavitation on the elliptical Arndt foil*. Master's thesis, The Netherlands: Delft University of Technology.
- [6] Asnaghi, A. (2018). *Computational modelling for cavitation and tip vortex flows*. PhD thesis, Sweden: Chalmers University of Technology.
- [7] Paskin, L. (2018). *A numerical assessment of turbulence modelling in tip vortex flows at cavitating conditions*. Master's thesis, France: Ecole Centrale de Nantes.
- [8] Maines, B. H. and Arndt, R. (1997b). Tip vortex formation and cavitation. *Journal of fluids engineering*, 199(2):413-419.
- [9] McCormick, B. (1962). On cavitation produced by a vortex trailing from a lifting surface. *Journal of Basic Engineering*, 84(3):369–378.
- [10] Lopes, R., Eça, L., and Vaz, G. (2018). Assessment of RANS transition models. *Proceedings of the 21st Numerical Towing Tank Symposium (NuTTS'18), Cortina, Italy*.
- [11] Menter, F. R., Kuntz, M., and Langtry, R. (2003). Ten years of industrial experience with the SST turbulence model. *Turbulence, heat and mass transfer*, 4(1):625–632.
- [12] Langtry, R. B. (2006). *A correlation-based transition model using local variables for unstructured parallelized CFD codes*. PhD thesis, Germany: Universität Stuttgart.
- [13] Eça, L., Lopes, R., Vaz, G., Baltazar, J., and Rijpkema, D. (2016). Validation exercises of mathematical models for the prediction of transitional flows. *31st Symposium on Naval Hydrodynamics, 11th-16th September, Berkeley*.
- [14] Roache, P.J. (2009). *Fundamentals of Verification and Validation*, Hermosa Publishers. Albuquerque, New Mexico.
- [15] Eça, L. and Hoekstra, M. (2014). A procedure for the estimation of the numerical uncertainty of CFD calculations based on grid refinement studies. *Journal of Computational Physics*, 262:104–130.
- [16] Baltazar, J., Rijpkema, D., and Falcão de Campos, J.A.C. (2017). On the use of the $\gamma - \tilde{R}e_{\theta}$ transition model for the prediction of the propeller performance at model-scale. *5th international symposium on marine propulsors, June, Finland*.

ANALYSIS OF THE BLADE BOUNDARY-LAYER FLOW OF A MARINE PROPELLER WITH RANSE

JOÃO M. BALTAZAR^{*,†}, DANIELA B. MELO[†] AND DOUWE R.
RIJPKEMA[§]

[†] Marine Environment and Technology Center (MARETEC)-Instituto Superior Técnico
Universidade de Lisboa, Av. Rovisco Pais 1, 1049-001 Lisboa, Portugal
e-mail: joao.baltazar@tecnico.ulisboa.pt; daniela.brito.melo@tecnico.ulisboa.pt
web page: <http://tecnico.ulisboa.pt/>

[§] Maritime Research Institute Netherlands (MARIN)
2 Haagsteeg 6708 PM Wageningen, the Netherlands
e-mail: d.r.rijpkema@marin.nl, web page: <http://www.marin.nl>

Key words: Marine Propeller, Blade Boundary-Layer Flow, RANSE, Transition Modelling

Abstract. In this paper a comparison between RANSE simulations carried out with the $k - \omega$ SST turbulence model and $\gamma - \tilde{R}e_{\theta_t}$ transition model, and experimental measurements for marine propeller P4119 is made. The experiments were conducted at the David Taylor Model Basin and comprehended three-dimensional velocity components measurements of the blade boundary-layer and wake using a LDV system in uniform conditions. The present work includes an estimation of the numerical errors that occur in the simulations, analysis of the propeller blade flow, chordwise and radial components of the boundary-layer velocities and boundary-layer characteristics. From this comparison and depending on the selected turbulence inlet quantities, we conclude that the transition model is able to predict the extent of laminar and turbulent regions observed in the experiments.

1 INTRODUCTION

RANSE (Reynolds-Averaged Navier-Stokes Equations) solvers are becoming a widely used tool for the analysis of marine propellers both in model- and full-scale conditions. For previous applications to marine propellers we refer to [1–3]. This numerical tool offers an alternative for the prediction of the scale-effects, which is traditionally based on simple extrapolation procedures from model-scale experiments carried out in a towing tank or cavitation tunnel. At present, the most common procedure is the 1978 ITTC performance prediction method [4].

The $k - \omega$ SST (Shear Stress Transport) turbulence model [5] is currently one of the most widely used turbulence models for marine propeller applications. However, for an accurate prediction of the performance characteristics at both model- and full-scales, the selected model for turbulence closure must have the ability to simulate different flow regimes including transition,

since a different boundary-layer structure of the flow over the blades arises from the change in Reynolds number. In this sense, the $\gamma - \tilde{R}e_{\theta_t}$ transition model proposed by Langtry and Menter [6] is being used to improve the prediction of the propeller performance at model-scale, see for instance [7].

In a previous study, the $k - \omega$ SST turbulence model and the $\gamma - \tilde{R}e_{\theta_t}$ transition model were combined with a RANSE solver for two marine propellers, for which paint-tests have been conducted and experimental open-water data is available [8]. The analysis of the numerical simulations focussed on a qualitative comparison between the limiting streamlines and paint-tests observations, and propeller force prediction in open-water conditions. From this study, an improvement in the blade boundary-layer flow is obtained with the transition model, whereas the simulations with the turbulence model predict a too large turbulent region on the blade.

Alternatively, the experimental study of the laminar/turbulent flow in the vicinity of a rotating propeller blade conducted by Jessup [9] may be used for a better quantitative comparison and understanding of the blade boundary-layer flow. The experiments were carried out in the David Taylor Model Basin (DTMB) 24 inch water tunnel about marine propeller P4119, where two blades were applied with leading-edge roughness and the remaining was smooth. The experiments comprehended three-dimensional velocity component measurements of the blade boundary-layer and wake using a LDV system in uniform inflow conditions.

From these experimental measurements, a comparison with the numerical results obtained from a RANSE solver using the $k - \omega$ SST turbulence model and $\gamma - \tilde{R}e_{\theta_t}$ transition model is presented in this paper. The present work includes an estimation of the numerical errors involved in the simulations, analysis of the propeller blade flow, chordwise and radial components of the boundary-layer velocities and boundary-layer characteristics. From this study and depending on the selected turbulence inlet quantities, the $\gamma - \tilde{R}e_{\theta_t}$ transition model is able to predict the extent of laminar and turbulent regions observed in the experiments.

This paper is organised as follows: the numerical method including the turbulence and transition models is presented in Section 2; the propeller geometry, grid generation scheme, computational domain and boundary conditions are described in Section 3; the comparison between the numerical results and the experimental measurements are shown in Section 4; in Section 5 the main conclusions are drawn.

2 NUMERICAL METHOD

2.1 RANSE

The RANSE are solved using a so-called absolute formulation. This means that the flow velocity, U_i with $i = 1, 2, 3$, is defined in the absolute or inertial earth-fixed frame of reference, with the equations being solved in the propeller-fixed frame of reference, x_i with $i = 1, 2, 3$, which is rotating with angular velocity Ω . This allows to perform steady simulations for open-water conditions. For the absolute velocity formulation, the RANSE for a steadily rotating frame and using the Boussinesq eddy-viscosity hypothesis may be written in the following form:

$$\begin{aligned} \frac{\partial U_i}{\partial x_i} &= 0, \\ \rho \frac{\partial (V_j U_i)}{\partial x_j} + \rho \varepsilon_{ijk} \Omega_j U_k &= -\frac{\partial P}{\partial x_i} + \frac{\partial}{\partial x_j} \left[(\mu + \mu_t) \left(\frac{\partial U_i}{\partial x_j} + \frac{\partial U_j}{\partial x_i} \right) \right], \end{aligned} \tag{1}$$

where V_i represents the i -th Cartesian component of the velocity vector defined in the propeller-fixed frame of reference, P the modified pressure defined as $P = p + 2/3\rho k$, p the static pressure, k the turbulence kinetic energy, ρ the fluid density, μ and μ_t the molecular and eddy viscosities respectively, and ε the Levi-Civita symbol. In this formulation, the momentum equations contain only one source term $\varepsilon_{ijk}\Omega_j U_k$.

2.2 Turbulence and Transition Models

In the present work, the $k - \omega$ SST turbulence model and the $\gamma - \tilde{\text{Re}}_{\theta_t}$ transition model are chosen for turbulence closure.

The $k - \omega$ SST turbulence model of Menter is a widely used and robust two-equation turbulence model. The variables of the model are the turbulence kinetic energy k and the turbulence dissipation rate ω . This model was originally introduced in 1994 by Menter to deal with the strong sensitivity to the free-stream conditions of the original $k - \omega$ turbulence model and to improve the prediction of the boundary-layer flow with adverse pressure gradients. In the present work, the 2003 version of the $k - \omega$ SST model is used [5].

The $\gamma - \tilde{\text{Re}}_{\theta_t}$ transition model proposed by Langtry and Menter [6] is coupled with the $k - \omega$ SST turbulence model of Menter [5] for the simulation of the flow around the marine propeller at model-scale including transition. This model is based on two transport equations, one for the intermittency γ and one for a transition onset criterion in terms of the momentum-thickness Reynolds number $\tilde{\text{Re}}_{\theta_t}$. It is known that this transition model strongly depends on the turbulence inlet quantities for the prediction of the transition location [8].

2.3 Flow Solver

The RANSE are solved using the ReFRESH code, developed within a cooperation led by MARIN for hydrodynamic applications (www.refresco.org). A finite-volume technique with cell-centred collocated variables is used for solving the equations. For the convective flux terms, a second-order scheme (QUICK) is applied for the momentum equations, and a first-order upwind scheme is applied for the $k - \omega$ SST turbulence model and $\gamma - \tilde{\text{Re}}_{\theta_t}$ transition model. A pressure-correction equation based on the SIMPLE algorithm is used to ensure mass conservation. In this study, ReFRESH version 2.3 is used.

3 PROPELLER GEOMETRY AND NUMERICAL SET-UP

The marine propeller P4119 is considered in the present study. The propeller has three blades, a diameter of 0.305 m and an expanded-area ratio of 0.5. The pitch-diameter ratio and chord-length at 0.7 of the propeller radius are 1.084 and 0.141 m, respectively. The propeller has no skew or rake.

For this propeller six nearly-geometrically similar multi-block structured grids are generated using the commercial grid generation software GridPro (www.gridpro.com). The grids range from 1 to 38 million cells. In Table 1 the number of cells in the volume and on a single blade, and the maximum dimensionless wall distance of the first cell height y^+ are listed for each grid. A fine boundary-layer resolution is obtained, since the maximum y^+ is lower than one for all grids. Therefore, the boundary-layer is fully resolved and no wall functions are used. An overview of the grid with 9.9 million cells is presented in Figure 1.

Table 1: Overview of the grid sizes and number of cell faces on a single blade. Maximum y^+ values refer to the design condition at model-scale.

| Grid | Volume | Blade | y_{\max}^+ |
|------|--------|-------|--------------|
| G1 | 37.6M | 73.9k | 0.20 |
| G2 | 21.0M | 42.3k | 0.24 |
| G3 | 9.9M | 25.6k | 0.31 |
| G4 | 6.1M | 18.6k | 0.39 |
| G5 | 1.9M | 8.6k | 0.51 |
| G6 | 0.9M | 4.9k | 0.66 |

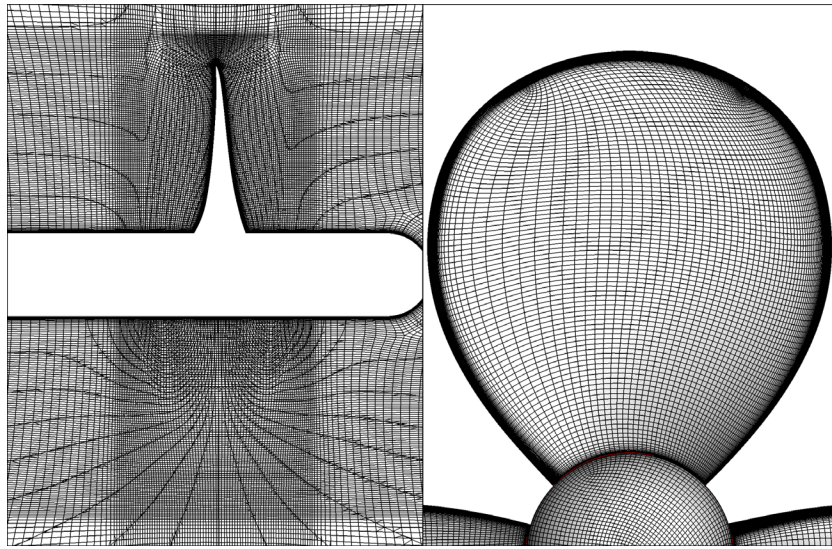


Figure 1: Overview of the grid with 9.9 million cells.

A cylindrical domain is considered, where the inlet, the outlet and the outer boundary are located five propeller diameters from the propeller origin. At the inlet the uniform velocity and the turbulence level depending on the turbulence model are prescribed, at the outlet an outflow condition of zero normal gradient is prescribed for the flow variables, and at the outer boundary a constant pressure is set. For the propeller blades and hub, a no-slip boundary condition is used.

4 RESULTS

The RANSE calculations are compared with LDV measurements of the blade boundary layers that were performed in the DTMB 24 inch water tunnel. The experiments were conducted considering a uniform inflow at a Reynolds number of 9.5×10^5 , based on chord-length and inflow velocity at 0.7 of the propeller radius. Open-water tests were performed earlier in the DTMB towing tank. The propeller open-water characteristics are expressed by the advance

coefficient J , thrust and torque coefficients K_T , K_Q , and the open-water efficiency η_0 as follows:

$$J = \frac{V_A}{nD}, \quad K_T = \frac{T}{\rho n^2 D^4}, \quad K_Q = \frac{Q}{\rho n^2 D^5}, \quad \eta_0 = \frac{J K_T}{2\pi K_Q}, \quad (2)$$

where V_A is the propeller advance speed, $n = \Omega/(2\pi)$ the rotation rate in rps, D the propeller diameter, T the propeller thrust and Q the propeller torque.

4.1 Numerical Errors

In CFD (Computational Fluid Dynamics) methods the three main contributions to the numerical error are: round-off error, iterative error and discretisation error. Since double-precision is used in the present calculations, the round-of error is neglected. Therefore, an analysis of the iterative and discretisation errors involved in the present computations is presented in this section.

First, the iterative error is analysed for the RANSE simulations at $J = 0.883$ with the $k - \omega$ SST turbulence model and $\gamma - \tilde{\text{Re}}_{\theta_t}$ transition model. For the $k - \omega$ SST turbulence model, standard values, i.e. $Tu = 1.0\%$ and $\mu_t/\mu = 1$, are assumed as the initial and inlet turbulence quantities. For the $\gamma - \tilde{\text{Re}}_{\theta_t}$ transition model, the initial and inflow turbulence quantities are set to 1.5% and 500 for the Tu and μ_t/μ , respectively. The L_∞ and L_2 error norms of the Cartesian components of the flow velocity $U_{X,Y,Z}$, modified static pressure P , turbulence kinetic energy k , specific turbulence dissipation rate ω , intermittency γ and local transition onset momentum thickness Reynolds number $\tilde{\text{Re}}_{\theta_t}$ obtained with the grid with 9.9 million cells are plotted in Figure 2 as a function of the number of iterations. The variation of the thrust coefficient K_T and torque coefficient K_Q with the number of iterations is also shown in Figure 2. In this study a convergence criterion of 10^{-6} has been adopted for the L_∞ and L_2 norms of the flow quantities. The analysis of the results obtained with the $k - \omega$ SST turbulence model shows that convergence of the L_∞ and L_2 norms is obtained for all quantities. However, iterative convergence is not achieved for the $\gamma - \tilde{\text{Re}}_{\theta_t}$ transition model. The larger error norms are obtained for the intermittency γ . Nonetheless, a L_2 error norm below 10^{-6} is achieved for the remaining quantities. For the propeller forces convergence is achieved after 5000 iterations, when the error norms of the flow quantities are not yet converged. In this sense, a minor effect of the iterative error is expected on the prediction of the propeller coefficients.

The discretisation error is estimated following the procedure described in Eça and Hoekstra [10]. In this procedure, the discretisation error is estimated based on the truncated power series expansion

$$\phi_i = \phi_0 + \alpha h_i^p, \quad (3)$$

where ϕ_i is a quantity of interest obtained on grid i , ϕ_0 is an estimate of the exact solution, α is a constant, h_i is the typical cell size of grid i and p is the observed order of grid convergence. Since the grids are block-structured and the same coarsening factor is applied on each direction, the typical cell size of grid i is determined from the total number of grid cells N_{cells} by $h_i = (1/N_{\text{cells}})^{1/3}$. The unknown coefficients in Equation (3) are determined from a least-square fit of the numerical solutions for the six grids. The error estimate is then converted into a numerical uncertainty U_{num} that depends on the observed order of accuracy and on the standard deviation of the fit.

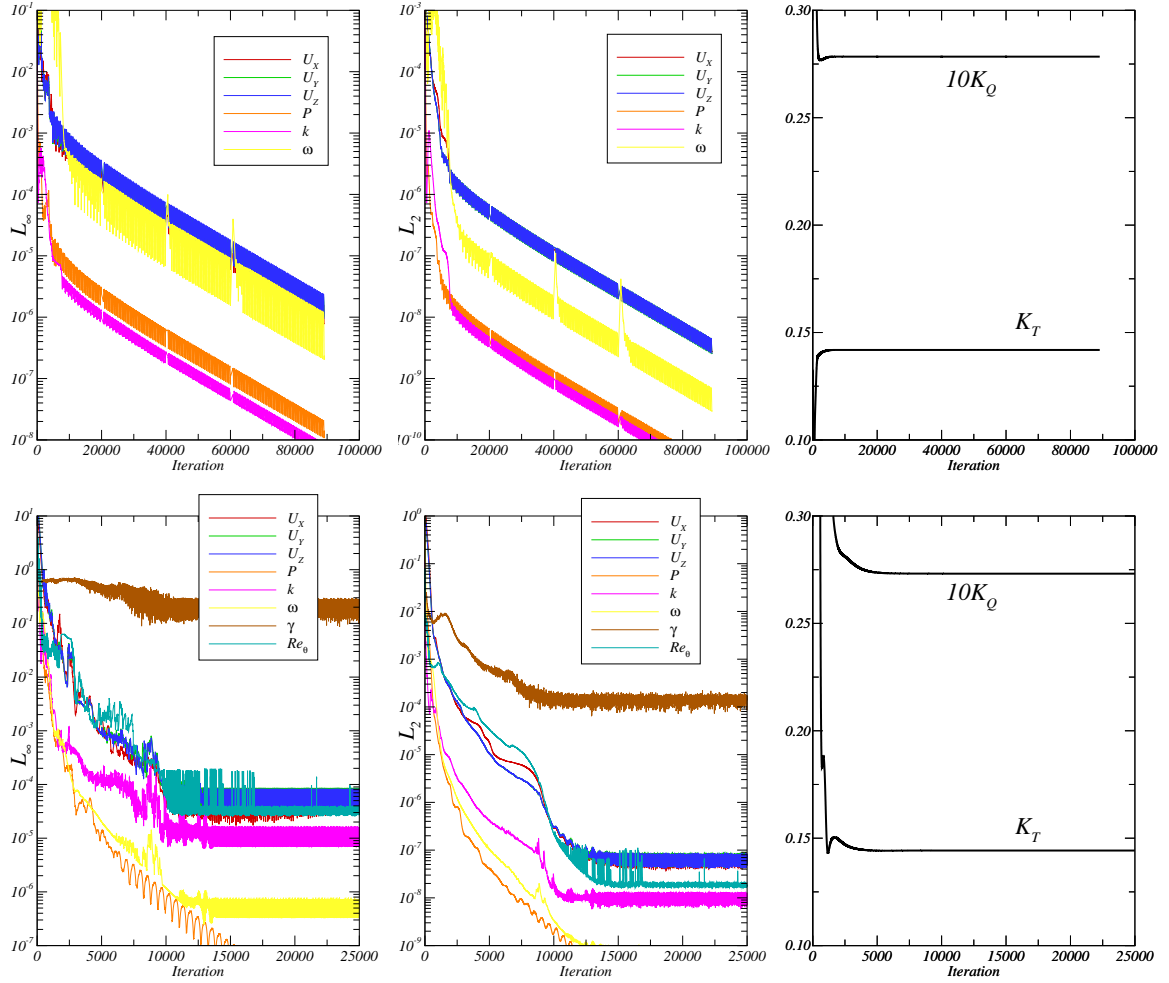


Figure 2: L_∞ (left), L_2 (middle) and propeller force coefficients (right) iterative convergence for $k-\omega$ SST turbulence model (top) and $\gamma-\tilde{Re}_{\theta_t}$ transition model (bottom).

The results of the numerical uncertainty estimation are plotted in Figure 3. The plots include also the fits and the apparent order of convergence. With the exception of the K_T predicted by the $\gamma-\tilde{Re}_{\theta_t}$ transition model, numerical uncertainties lower than 1% are obtained. In these cases, near first-order convergence is obtained for the thrust coefficient, predicted with the $k-\omega$ SST turbulence model, and near second-order convergence is obtained for the torque coefficient. For the K_T predicted by the $\gamma-\tilde{Re}_{\theta_t}$ transition model, the three coarsest grids deviate from the trend and are omitted from the least-square fit. In this case, near first-order convergence is obtained and the uncertainty in the thrust coefficient is 1.03%.

In order to reduce the computational time, the influence of the grid density on the propeller forces and blade boundary-layer velocity profiles is analysed. The variation of the thrust and torque coefficients, and open-water efficiency for each grid compared to the finest grid is listed in Table 2 for both models. Differences lower than 1% are obtained for the grid with 9.9 million cells

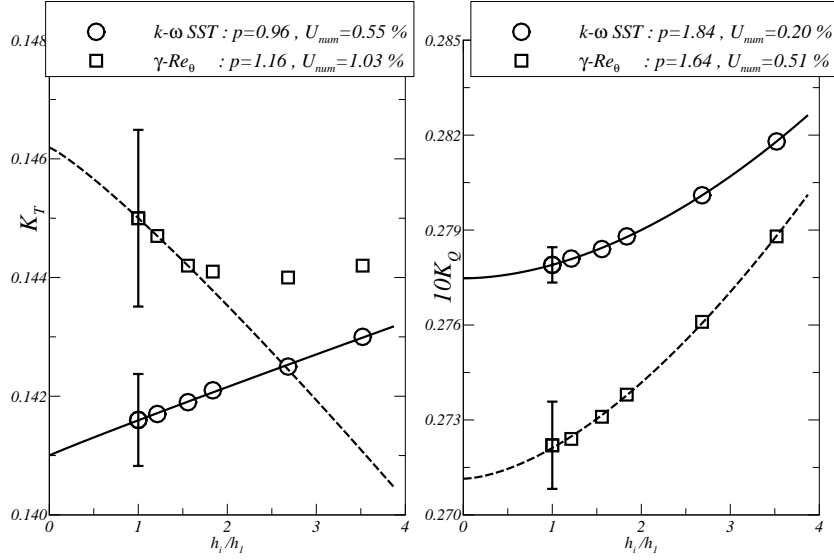


Figure 3: Convergence of K_T (left) and $10K_Q$ (right) with grid refinement ratio h_i/h_1 .

Table 2: Variation of the force coefficients with grid density compared to the finest grid.

| Model | $k - \omega$ SST | | | $\gamma - \tilde{R}e_{\theta_t}$ | | |
|-------|------------------|--------------|-----------------|----------------------------------|--------------|-----------------|
| | ΔK_T | ΔK_Q | $\Delta \eta_0$ | ΔK_T | ΔK_Q | $\Delta \eta_0$ |
| G6 | 1.0% | 1.4% | -0.4% | -0.6% | 2.4% | -2.8% |
| G5 | 0.6% | 0.8% | -0.3% | -0.7% | 1.4% | -2.1% |
| G4 | 0.4% | 0.3% | 0.0% | -0.6% | 0.6% | -1.1% |
| G3 | 0.2% | 0.2% | 0.0% | -0.6% | 0.3% | -0.8% |
| G2 | 0.1% | 0.1% | 0.0% | -0.2% | 0.1% | -0.3% |

(G3). Figure 4 presents the chordwise component V_s of the blade boundary-layer velocity profile on the suction side at 0.2 of the chord-length and 0.7 of the propeller radius. Results obtained for the grids with 9.9 million cells and 37.6 million cells are compared for both models. The velocity profile is presented along the normal direction, where y is the wall distance to blade surface and c the chord-length. The velocity is made non-dimensional by $V_{ref} = \sqrt{V_A^2 + (\Omega 0.7R)^2}$, with R denoting the propeller radius. The comparison shows a minor influence of the grid refinement level on the blade velocity profile. Therefore, the grid with 9.9 million cells (G3) is selected for the comparison with experimental data.

4.2 Propeller Blade Flow

In this section the flow predictions using the turbulence and transition models at $J = 0.833$ are analysed. Due to the strong dependence of the $\gamma - \tilde{R}e_{\theta_t}$ transition model on the turbulence inlet quantities, different turbulence intensities are considered. In this study, $Tu = 1.2\%$ and

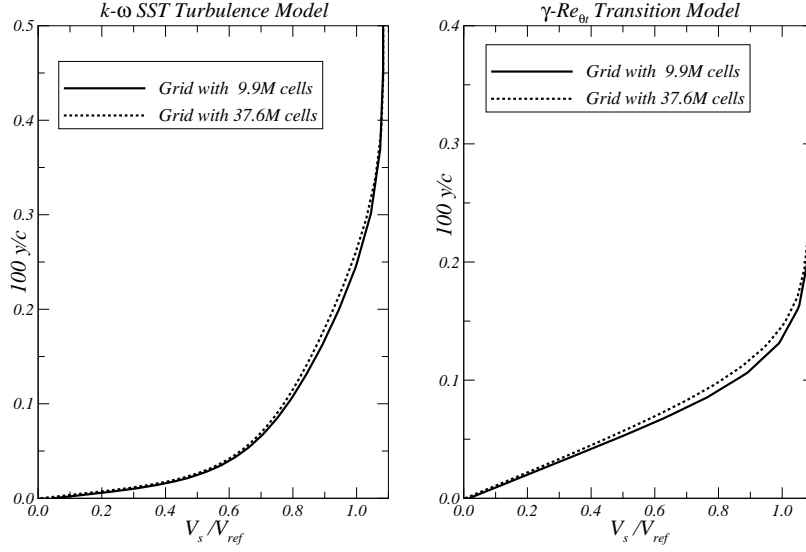


Figure 4: Influence of grid refinement on V_s on the suction side at $s/c = 0.2$ and $r/R = 0.7$. $k - \omega$ SST turbulence model (left) and $\gamma - \tilde{Re}_{\theta_t}$ transition model (right).

Table 3: Pressure (p) and friction (f) contributions to the propeller thrust and torque. Comparison with experimental data.

| Model | Tu | μ_t/μ | K_{T_p} | K_{T_f} | K_T |
|----------------------------------|------|-------------|-------------|-------------|---------|
| $\gamma - \tilde{Re}_{\theta_t}$ | 1.2% | 500 | 0.1498 | -0.002470 | 0.1473 |
| $\gamma - \tilde{Re}_{\theta_t}$ | 1.5% | 500 | 0.1476 | -0.003373 | 0.1442 |
| $k - \omega$ SST | 1.0% | 1 | 0.1463 | -0.004460 | 0.1419 |
| Exp. | – | – | – | – | 0.146 |
| Model | Tu | μ_t/μ | $10K_{Q_p}$ | $10K_{Q_f}$ | $10K_Q$ |
| $\gamma - \tilde{Re}_{\theta_t}$ | 1.2% | 500 | 0.2529 | 0.01771 | 0.2706 |
| $\gamma - \tilde{Re}_{\theta_t}$ | 1.5% | 500 | 0.2489 | 0.02422 | 0.2731 |
| $k - \omega$ SST | 1.0% | 1 | 0.2472 | 0.03117 | 0.2784 |
| Exp. | – | – | – | – | 0.280 |

1.5% and $\mu_t/\mu = 500$ at the inlet boundary are selected. The predicted propeller forces, including the pressure and friction contributions, are compared with the experimental results in Table 3. Due to the growth in the turbulent flow domain, an increase in the magnitude of the friction contribution is observed. At the same time, a decrease in the pressure contribution is observed, which may be explained by a decambering effect due to a thicker boundary-layer. A better agreement with the experimental torque coefficient is obtained with the $k - \omega$ SST turbulence model. For the thrust coefficient, the agreement improves with the use of the $\gamma - \tilde{Re}_{\theta_t}$ transition model. However, the selection of the inlet turbulence quantities at the inlet is currently based on detailed experimental information, which limits the predictive capability of the $\gamma - \tilde{Re}_{\theta_t}$

transition model. For the analysis of the different flow solutions, the limiting streamlines and skin friction coefficient $C_f = \tau_w / (1/2\rho V_A^2)$ on the blade surface are presented in Figure 5, where τ_w is the local wall shear stress. The location where flow transition occurs is identified by the sudden rise of the skin friction distribution and the change in the orientation of the limiting streamlines towards the chordwise direction. For the results obtained with the $\gamma - \tilde{Re}_{\theta_t}$ transition model, the domain of laminar flow reduces with the increase of the turbulence intensity at the inlet. The $k - \omega$ SST turbulence model leads to turbulent flow on the propeller blades.

4.3 Comparison of Velocity Profiles

In this section a comparison of the velocity profiles in the blade boundary-layer between the RANS simulations and the experiments at $J = 0.833$ is made. The measurements comprehended the chordwise V_s and radial V_t components of the flow velocity. In the propeller model, two blades had leading-edges roughened with 60 micron distributed roughness and the other blade was smooth. Figures 6 and 7 show the chordwise and radial velocity profiles at 0.7 of the propeller radius developed on the suction and pressure sides for the smooth and tripped blades at different chordwise locations, respectively. The non-dimensional chordwise location is defined as s/c . The estimated boundary-layer thickness δ is included in the figures, which is obtained from the total pressure loss Δp_t in the rotating frame of reference and is calculated as follows:

$$\Delta p_t = P + 1/2\rho [V_X^2 + V_Y^2 + V_Z^2] - P_{\text{inlet}} - 1/2\rho [V_A^2 + (\Omega 0.7R)^2]. \quad (4)$$

In this work, the boundary-layer thickness is defined by the normal distance to a point where the total pressure loss coefficient $C_{\Delta p_t} = \Delta p_t / (1/2\rho V_{ref}^2)$ is equal to -0.01 . For the smooth blade, the best agreement on the suction side is obtained with $\gamma - \tilde{Re}_{\theta_t}$ transition model using $Tu = 1.2\%$. In this case, an exception is observed for the radial velocity profile at $s/c = 0.6$, since a lower radial velocity due to transition to turbulent flow is predicted by the $\gamma - \tilde{Re}_{\theta_t}$ transition model. On the pressure side, the best agreement is achieved for $\gamma - \tilde{Re}_{\theta_t}$ transition model with $Tu = 1.5\%$, since the results with $Tu = 1.2\%$ predict a too large laminar flow region. The velocity profiles predicted by the $k - \omega$ SST turbulence model approach the measurements on the tripped blade, except at $s/c = 0.2$ and 0.3 . According to Jessup [9], these discrepancies are attributed to the influence of the leading-edge roughness on the propeller flow.

4.4 Boundary-Layer Characteristics

From the predicted profiles, the boundary-layer thickness δ , displacement thickness δ^* and shape factor H are calculated and represented in Figure 8. The estimated displacement thickness and shape factor are also compared with the calculations of Jessup from the measured velocity profiles [9]. The evolution of the boundary-layer thickness along the chordwise direction shows the increase in thickness due to flow transition from laminar-to-turbulent flow regime. For the displacement thickness and shape factor, agreement between the numerical simulations and the experiments is difficult to obtain. In general, the results obtained for the $k - \omega$ SST turbulence model approach the experimental values of the tripped blade. The same trend is observed between $\gamma - \tilde{Re}_{\theta_t}$ transition model and the smooth blade experiments. As expected from the comparison of the velocity profiles, a better agreement is obtained with $Tu = 1.2\%$ on the suction

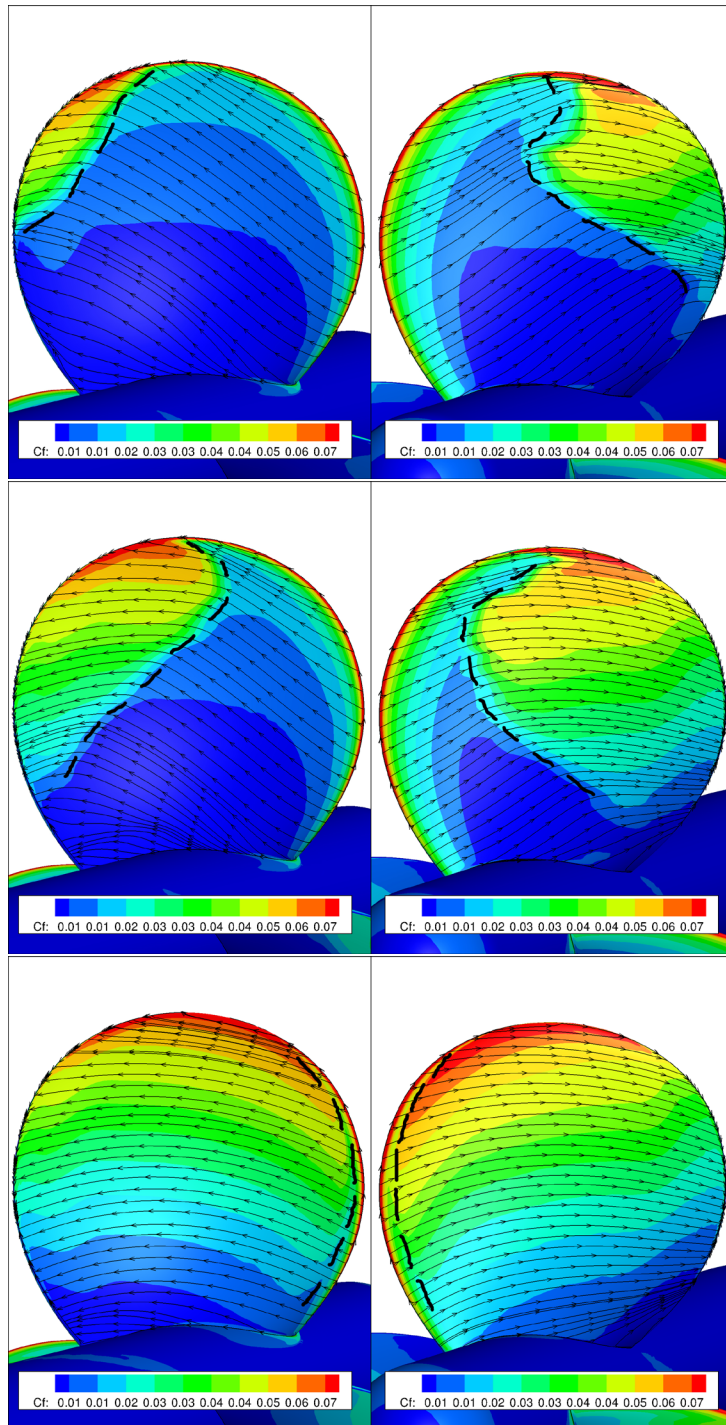


Figure 5: Limiting streamlines and skin friction distribution over the propeller blade using the $\gamma - \tilde{Re}_{\theta_t}$ transition model with $Tu = 1.2\%$ (top) and $Tu = 1.5\%$ (middle) for $\mu_t/\mu = 500$, and $k-\omega$ SST turbulence model with $Tu = 1.0\%$ and $\mu_t/\mu = 1$ (bottom).

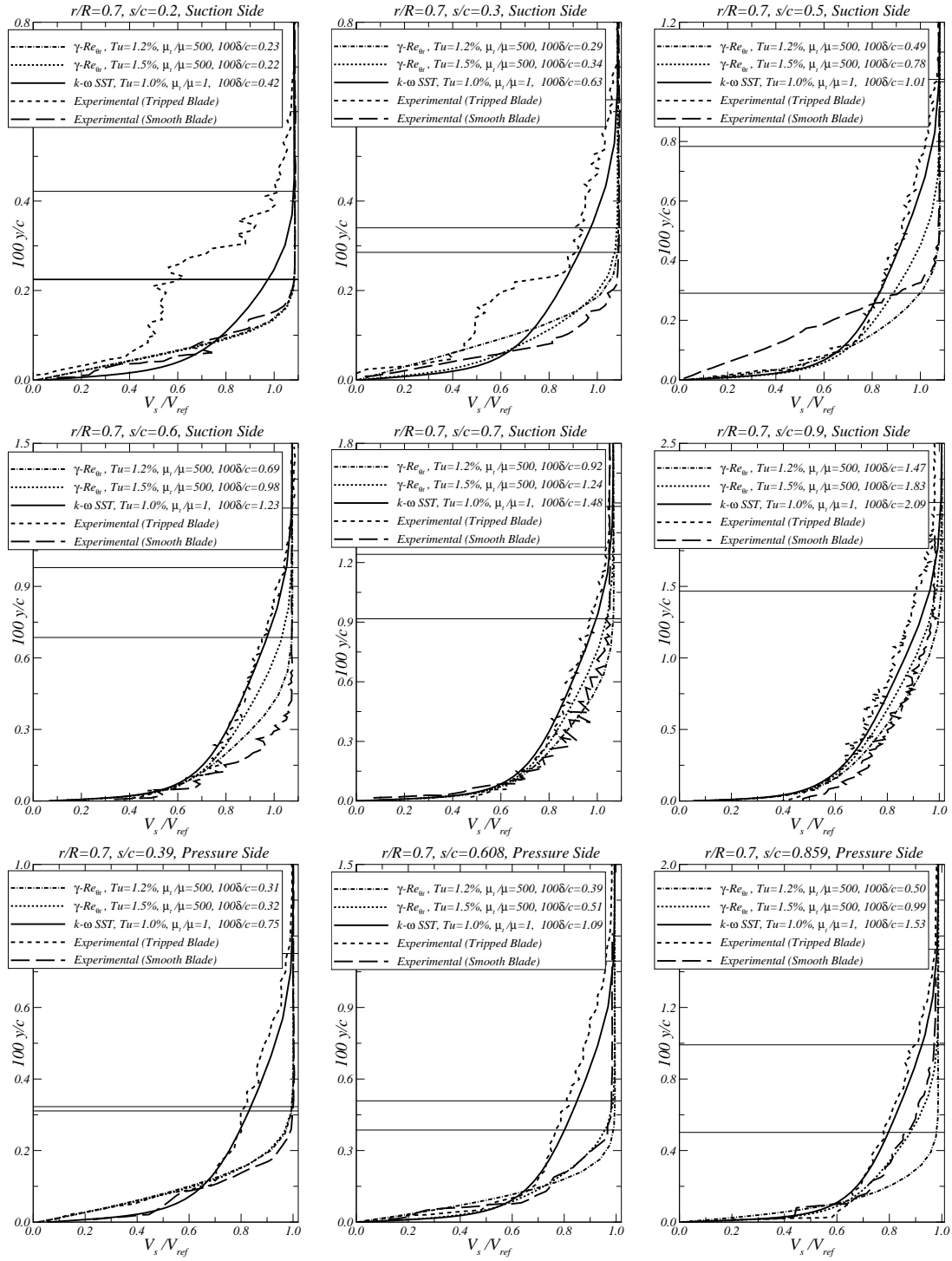


Figure 6: Predicted chordwise component V_s of the flow velocity at $r/R = 0.7$ using the $k-\omega$ SST turbulence model and $\gamma - \tilde{Re}_{\theta_t}$ transition model with different inlet turbulence quantities. Comparison with experimental data [9].

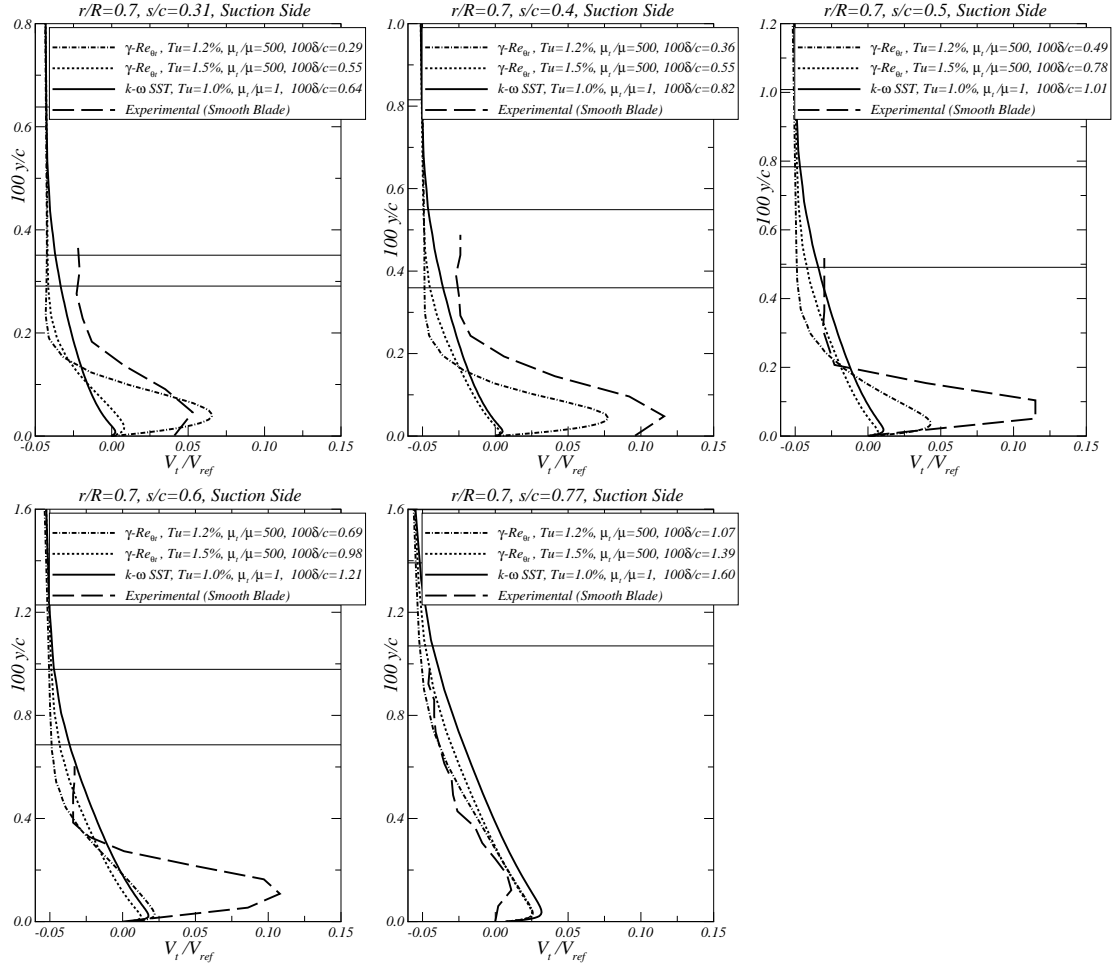


Figure 7: Predicted radial component V_t of the flow velocity at $r/R = 0.7$ using the $k - \omega$ SST turbulence model and $\gamma - \tilde{Re}_{\theta_t}$ transition model with different inlet turbulence quantities. Comparison with experimental data [9].

side, whereas on the pressure side the agreement improves with $Tu = 1.5\%$. The shape factor may be used to determine the nature of the flow. The experimental and numerical shape factors show large values in the laminar flow region, which drop to turbulent profile values around 1.4 typical of two-dimensional flows.

5 CONCLUSIONS

In this paper, a comparison between RANSE calculations and experimental data has been presented. The analysis is carried out for marine propeller P4119, for which three-dimensional velocity component measurements on the blade boundary-layer are available at model-scale. In the propeller model, two blades had rough leading-edges and the other blade was smooth. For the RANS calculations two models are considered: the commonly-used $k - \omega$ SST eddy-viscosity turbulence model, and the $\gamma - \tilde{Re}_{\theta_t}$ transition model. The influence of the iterative

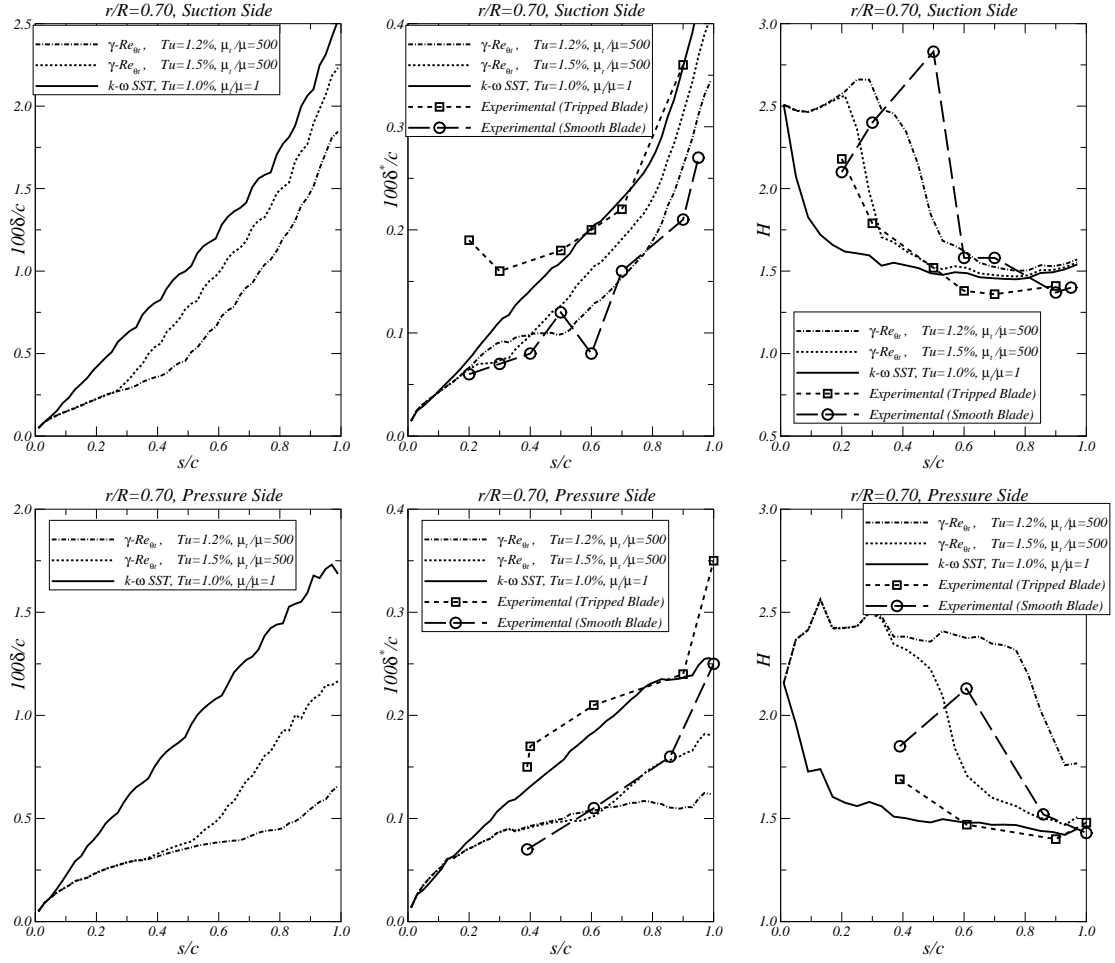


Figure 8: Boundary-layer thickness δ (left), displacement thickness δ^* (middle), and shape factor H (right) at $r/R = 0.7$ using the $k - \omega$ SST turbulence model and $\gamma - \tilde{Re}_{\theta_t}$ transition model with different inlet turbulence quantities. Comparison with experimental data [9].

errors, discretisation errors and boundary conditions on the propeller flow predictions has been analysed. The $\gamma - \tilde{Re}_{\theta_t}$ transition model does not satisfy the iterative convergence criterion. Still, its influence on the propeller forces is assumed to be small due to the fast convergence of the thrust and torque coefficients. The numerical uncertainty of the propeller forces has been determined from an estimation of the discretisation error based on systematically refined grids. Low numerical uncertainties (less than 2%) are obtained for the propeller force coefficients. The numerical predictions of the velocity profiles have been compared with boundary-layer measurements. An agreement is found between the turbulent velocity profile predicted by the $k - \omega$ SST turbulence model and the measured velocities from the tripped blade. For the $\gamma - \tilde{Re}_{\theta_t}$ transition model, the agreement with the smooth blade velocity measurements is highly dependent on the inlet turbulence quantities. In this work, from the selected inlet turbulence quantities, a qualitative agreement is obtained for the blade boundary-layer velocity profiles.

However, this information may not be available, which limits the predictive capabilities of the $\gamma - \tilde{\text{Re}}_{\theta_t}$ transition model at model-scale, specially because the selected inlet values are not realistic from the physical point of view. Finally, boundary-layer integral quantities obtained from the measured and computed velocity profiles have been analysed. The evolution of these quantities along the chordwise direction on the inner part of the blade shows typical laminar and turbulent flow behaviours.

ACKNOWLEDGMENTS

This work was supported by FCT/MCTES (PIDDAC) through project UID/EEA/50009/2019. We are indebted to Luís Eça and Rui Lopes for many fruitful discussions on this topic.

REFERENCES

- [1] Stanier, M. The application of RANS code to investigate propeller scale effects. *Proceedings of the 22th ONR Symposium on Naval Hydrodynamics*, Washington, DC, USA (1998).
- [2] Krasilnikov, V., Sun, J., and Halse, K. CFD investigation in scale effects on propellers with different magnitude of skew in turbulent flow. *Proceedings of the First International Symposium on Marine Propulsors*, Trondheim, Norway (2009).
- [3] Sánchez-Caja, A., González-Adalid, J., Pérez-Sobrino, M. and Sipilä, T. Scale effects on tip loaded propeller performance using a RANSE solver. *Ocean Eng.* (2014) **88**:607–617.
- [4] International Towing Tank Conference *1978 ITTC performance prediction method*, Technical Report ITTC - Recommended Procedures and Guidelines 7.5-02-03-01.4, Revision 07 (2017).
- [5] Menter, F., Kuntz, M. and Langtry, R. Ten years of industrial experience with the SST turbulence model. *Proceedings of the Fourth International Symposium on Turbulence, Heat and Mass Transfer*, **4**:625–632, (2003).
- [6] Langtry, R. and Menter, F. Correlation-based transition modeling for unstructured parallelized computational fluid dynamics codes. *AIAA J.* (2009) **47**:2894–2906.
- [7] Bhattacharyya, A., Krasilnikov, V., and Steen, S. Scale effects on open water characteristics of a controllable pitch propeller working within different duct designs. *Ocean Eng.* (2016) **112**:226–242.
- [8] Baltazar, J., Rijpkema, D. and Falcão de Campos, J.A.C. On the use of the $\gamma - \tilde{\text{Re}}_{\theta_t}$ transition model for the prediction of the propeller performance at model-scale. *Ocean Eng.* (2018) **170**:6–19.
- [9] Jessup, S.D. *An experimental investigation of viscous aspects of propeller blade flow*. Ph.D. Thesis, The Catholic University of America, (1989).
- [10] Eça, L. and Hoekstra, M. A procedure for the estimation of the numerical uncertainty of CFD calculations based on grid refinement studies. *Journal of Computational Physics* (2014) **262**:104–130.

Disequilibrium Wall Function in RANSE Computation applied to flow conditions around ship's hull

MARINE 2019

CARL-UWE BÖTTNER* AND IVAN SHEVCHUK†

* Federal Waterways Engineering and Research Institute (BAW)
Wedeler Landstraße 157, 22559 Hamburg, Germany
email: carl-uwe.boettner@baw.de, www.baw.de

† Hamburg University of Technology (TUHH)
Institute for Fluid Dynamics and Ship Theory
Am Schwarzenberg-Campus 4 (C), 21073 Hamburg, Germany
email: ivan.shevchuk@tuhh.de, www.tuhh.de/fds

Key words: Computational Fluid Dynamics, Boundary Layer, Wall Function, Ship Hydrodynamics

Abstract. Through years of scaled physical model tests to predict ship induced wave loads on rip-rap and bank protection in channels and waterways at Federal Waterways Engineering and Research Institute, a comprehensive collection of squat measurements had grown and became foundation of some principal and systematic conclusions on the squat effect in shallow and restricted waters [1]. There was the observation of a significant increase of the trim angle when water depth to draft ratio is decreased to less than $h/T = 1.3$. A change in the flow regime was suspected to be responsible for this effect [2].

To prove the assumption of different flow regimes the boundary layers in the gap between the hull's bottom and the ground were further investigated. All the investigations so far have been in the scale 1:40 in accordance with Froude's Law. Boundary layers and gap flow conditions heavily depend on the Reynolds' Number and the turbulence degree. Unfortunately it is impossible to satisfy Reynolds' and Froude's Law for this scale and this experimental set-up at the same time. It was decided to bypass this quandary with an extension of the analysis by numerical simulation of the flow around the hull at full scale. In the scaled model tests, the occurrence of a coalescence of the two boundary layers, at the hull and the ground, in the aft third of the hull was observed. In terms of time and computing cost, computational fluid dynamics simulation of flow around a ship's hull at full scale are not reasonably feasible without application of wall functions today. The flow condition in the boundary layer violates the basic assumption of local equilibrium which is common for the regular wall functions implemented in the CFD-Codes solving Reynolds Averaged Navier-Stokes Equations with turbulence models to close the system of equations for solving. To cope with the non-equilibrium condition in the boundary layer at the hull, the "Generalized Wall Functions" [3] were implemented in OpenFOAM [4] and applied to the numerical analysis of the flow conditions around the ship hull.

1 INTRODUCTION

At the Federal Waterways Engineering and Research Institute (BAW) next to civil engineering tasks there has been a long record of experiments in model scale for ship generated waves and load on water buildings as well as ship dynamics in shallow and confined waters. The latter very often aims at proper dimensioning of waterways in terms of depth and width. It has been widely observed that there is a significant change for shallow water behaviour characteristics when water depth to draft ratio (h/T) decreases below 1.3, frequently referred to “very shallow water condition”. As for most of the shallow water effects, like bank effect, squat, increased resistance and power demand to name a few, the squat effect at very shallow water condition is systematically observed in model scale only. There are only few measurement campaigns in the past decades, amongst others in Hamburg [5], Weser [6] or Australia [7], but they can only serve as references for physical model tests since they are more or less snap shots in terms of environmental and hydrodynamic conditions. At these campaigns, there is a small variation of speeds through water, the draft is random and the water depth depends on the actual tide and the time window given to the ship outfitted with sensors to enter the waterway.

While comparing and assembling data of many different systematic investigations from the past decades at BAW, there was clear distinct of shallow water condition to very shallow water condition. But it was not clear at all, what the driving mechanism behind might be. This excited curiosity on the physics behind and an international workshop on the topic was organized [8]. One of the major findings was the general failing of potential flow codes in predicting the dynamic sinkage and trim when the h/T ratio dropped lower than 1.5. This is suspicious of revealing some viscosity influence in the generally regarded Bernoulli-dominated ship hydrodynamic effects [9]. Introducing viscosity driven dynamics in physical model tests in two phase flows with a sharp density jump (air and water surface) can be regarded as a misery. Usually in towing tank tests and wave basins, the model tests are scaled according the Froude’s Law plus the side condition to have a minimum degree of turbulence. This is regarded the case when Reynolds Number is at least higher than 5000. If the viscosity itself is getting a dominant parameter on particular hydrodynamic effect, this assumption very likely is no longer valid.

Therefore a campaign on scale effects in ship hydrodynamics in physical model tests was initiated. In the first attempt a deeper look in the wake flow gained insight in potential flaws when scaling up according to Froude in shallow water conditions. In order to be able to perform the numerical simulations required properly, the introduction of a more general wall function became necessary. When changing to full scale dimensions, the numerical effort increases such, that wall functions are unavoidable for today. Unfortunately the flow conditions at the aft ship are not generally according to an attached boundary layer. Obviously the validity range of the wall functions implemented and generally used to simulate ship hydrodynamics by means of Reynolds Averaged Navier Stokes Equations (RANSE) is violated with this application. To mitigate this and cope with the task properly, a more generalized wall function, introduced by Popovac and Hanjalic in 2007 [3] was implemented.

2 GENERALIZED WALL FUNCTION

The more general applicable wall functions suggested by Popvoac and Hanjalic were implemented supplementary to the already existing ones in the RANSE-solver package OpenFOAM. In the following only the formulas used for implementation are provided, a much deeper description including derivation is given in [3].

The wall functions for two equations turbulence models (in this case the k - ω -SST turbulence model [10] was applied) require the determination of four variables: k , ν_t , ω , P_k . The implementation of the variable k could be used without amendment, since von Neumann boundary condition is applicable at the wall for the generalized wall function as well; the latter three are defined as:

$$P_k = P_{k,vis}e^{-\Gamma} + P_{k,log}e^{-1/\Gamma} = \frac{k}{\omega} \left| \frac{\partial u}{\partial y} \right|^2 e^{-\Gamma} + \frac{C_\mu^{1/2} k}{\ln(Ey^*)} \psi \left| \frac{\partial u}{\partial y} \right| e^{-1/\Gamma} \quad (1)$$

$$\nu_t = \nu(e^{-\Gamma} - 1) + \frac{\kappa C_\mu^{1/4} k^{1/4} y}{\ln(Ey^*)} \psi e^{-1/\Gamma} \quad (2)$$

$$\omega = \omega_{vis}e^{-\Gamma_\epsilon} + \omega_{log}e^{-1/\Gamma_\epsilon} = \frac{6\nu}{\beta_1 y^2} e^{-\Gamma_\epsilon} + \frac{k^{1/2}}{C_\mu \kappa y} e^{-1/\Gamma_\epsilon}. \quad (3)$$

where y^* represents a modified wall coordinated y^+ in which the shear stress velocity u_τ is replaced by u_k to avoid possible singularities. The functions Γ and Γ_ϵ are used to blend the transition between viscous sublayer and logarithmic layer in the boundary layer flow:

$$\Gamma = \frac{0.01y^{*4}}{1 + 5y^*}, \quad \Gamma_\epsilon = \frac{0.001y^{*4}}{1 + y^*} \quad (4)$$

The parameter Ψ in (1) and (2) introduces the sensitivity on non-equilibrium effects in the wall function and modifies the classic logarithmic regime of the boundary layer:

$$\psi = 1 - \frac{C_u y}{\rho u \kappa u_\tau} \quad (5)$$

$$C_u = \rho \frac{\partial u}{\partial t} + \rho u \frac{\partial u}{\partial x} + \rho v \frac{\partial u}{\partial y} + \frac{\partial p}{\partial x}, \quad (6)$$

where x and y refer to the wall-parallel and the wall-orthogonal coordinate, u and v the according component of the velocity close to the wall and p represents the pressure.

For comparison and evaluation the newer extended wall treatment, an implementation of the wall function used in and documented by ANSYS-Fluent®, was applied as well. In the following GWF refers to the generalized wall function by Popovac and Hanjalic, OFWF to the basic OpenFOAM wall function and EWT to the Fluent® wall treatment implementation in OpenFOAM.

2.1 Application of different wall functions at Diffuser Flow

To check proper implementation and prove advantage of the newly implemented approach to the existing ones, several boundary layer flows were simulated and compared. The conditions in diffuser flow revealed the improvements convincingly and satisfactorily. As a benchmark served the experimental data detected in an asymmetric diffuser of Buice and Eaton [11]. This was especially relevant since the flow conditions in the aft ship part and where the wake is generated resembles those in a diffuser. The GWF revealed its strength and superiority over the OFWF became obvious in this for the purpose of this investigation relevant test case.

In Fig 2 a comparison of the results obtained with the three different wall functions applied is given. For values of y^+ in the range of 40 all of the wall functions show satisfying agreement with the experiments. For values smaller ($y^+ = 20$) or bigger ($y^+ = 90$) the range of validity of the basic OpenFOAM-wall-function is obviously violated. The wall treatment EWT performs well and is applicable in the full range of y^+ values investigated here. The newly implemented general wall function shows slightly better agreement with the experimental values than even the EWT.

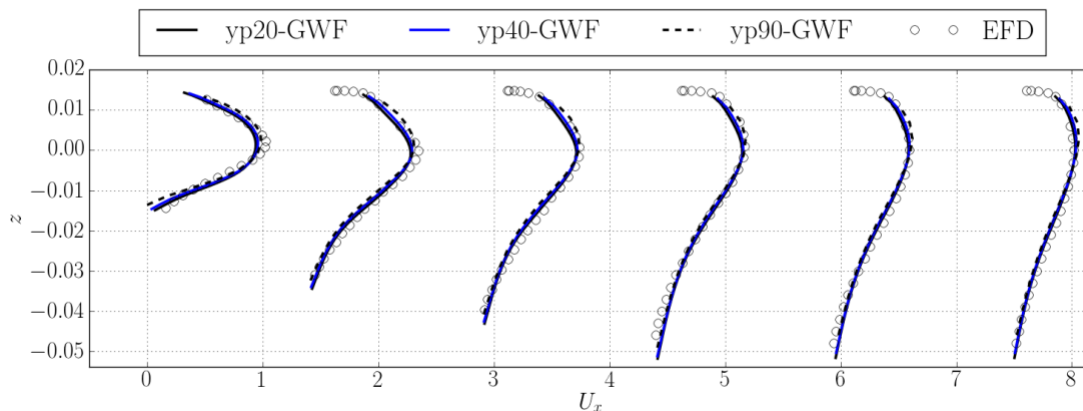


Figure 1: General Wall Function is non-sensitive to Y^+ Values.

As a conclusion the generalized wall function performs satisfactorily and provides independence of the y^+ values in a numerical situation (Figure 1).

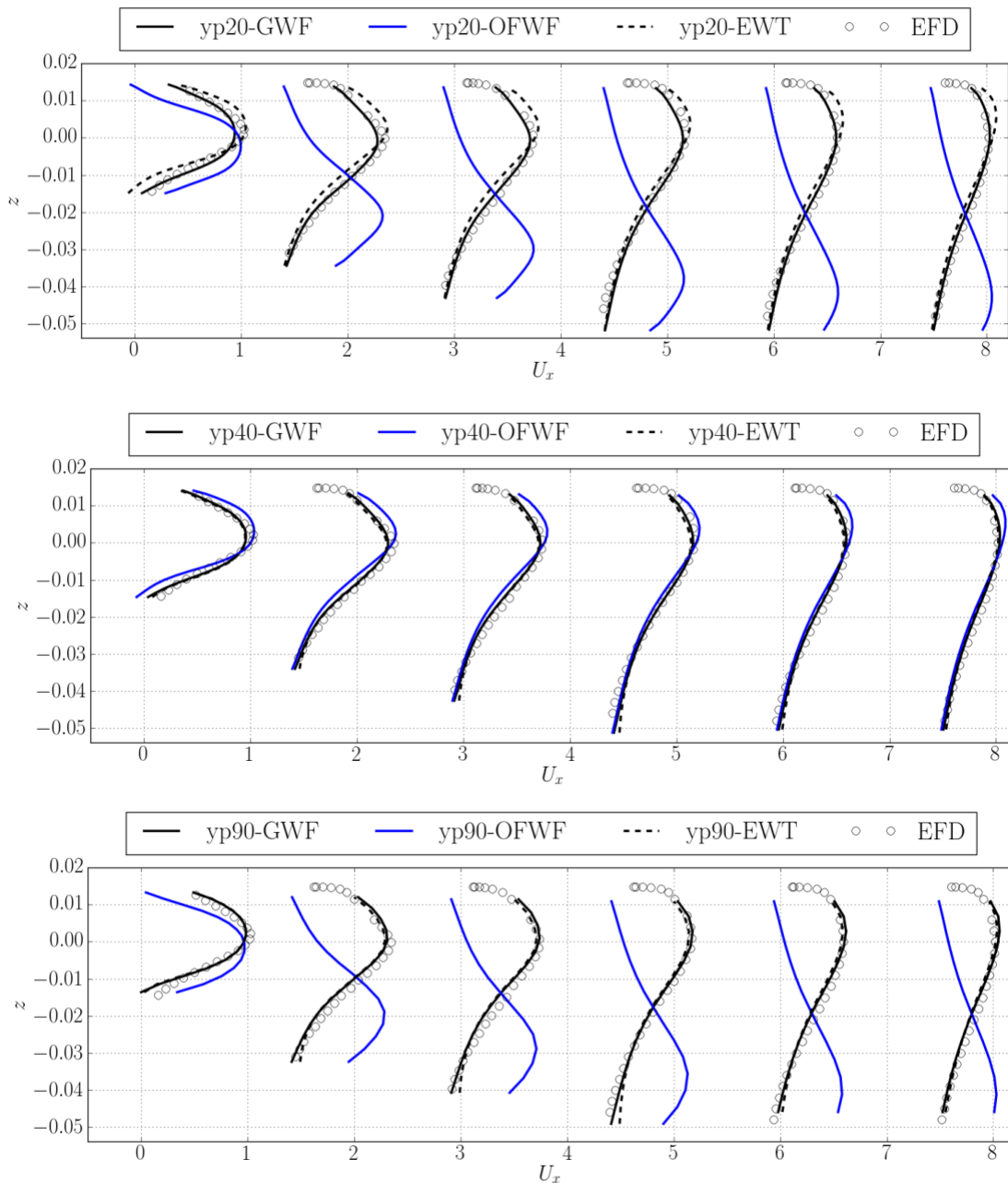


Figure 2: Comparison of different wall function approaches at asymmetric diffuser flow simulation.

3 WAKE FLOW IN MODEL SCALE AND FULL SCALE

Two model ships of similar size but different shapes (Figure 3) were investigated in terms of squat behaviour and wake flow. The models are regularly used at BAW for investigations of ship induced loads on waterways and rip rap and each of their squat-characteristics are well known. This is true for the model scale 1:40, there are no full scale measurements available, since none of them is realized as a ship in service. The squat data detected in wave basin for

the PostPanaMax 55 m breadth (PPM55) accidentally agreed well with field measurements of a slightly smaller container ship on the river Elbe in 2002 [5]. At the time this provided further confidence in the scalability of squat measurements in physical model tests to full scale. Further field measurements and physical models tests revealed a wide variety of squat behaviour and values, heavily depending on the particular hull shape.

Additionally, the case of very shallow water (water depth to ship draft ratio (h/T) smaller 1.3) could not be included in the field measurements campaign; therefore no evidence for negligibility of potential scale effect is available. This is especially misery since the physical model tests render obvious severe changings in the trend of the squat behaviour for small water depth to draft (h/T) ratios.

3.1 Ships

Two Container Carriers were investigated numerically at three different scales (1:40, 1:6 and 1:1). The main dimensions of the ships in full scale are given in Table 1. Of comparable size, the shapes differ remarkably (Figure 3) and lead to different dynamic behaviour in waterways. Additionally, the scale effect on the wakes turned out to be subject of particular hull shape as well.

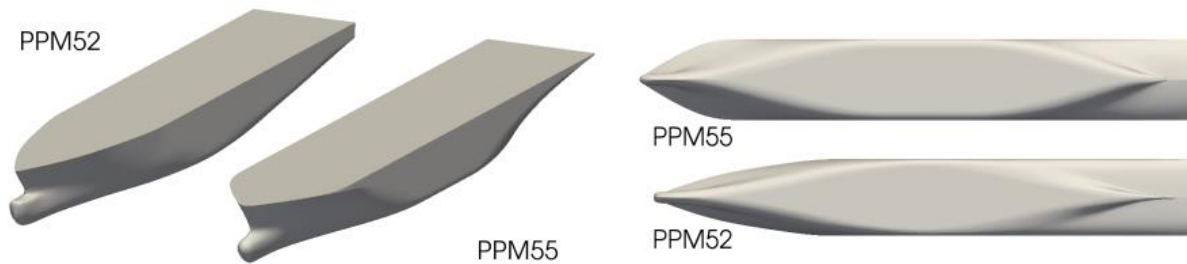


Figure 3: Hull shapes of the two PostPanaMax Container Carriers

Table 1: Particulars of the two Container Carriers

| | PPM 52 | PPM 55 |
|--------------|--------|--------|
| L_{pp} [m] | 347.2 | 355.8 |
| B [m] | 52 | 55 |
| D [m] | 16 | 16 |
| C_B [-] | 0.668 | 0.689 |

The flow around the ships were calculated for centred channel cruise, in a channel of a width of 392m, corresponding to the towing tank width at Duisburg Towing Tank in scale 1:40, where measurements had been performed earlier and the results could serve for validation purposes. Two water depths were chosen, corresponding to h/T -ratio of 1.5 and 2.0. The speeds corresponded to Froude Numbers: $Fn = 0.09, 0.11, 0.12$. Numerical simulations were performed without propeller and with propeller attached and geometrically resolved (Figure 4).

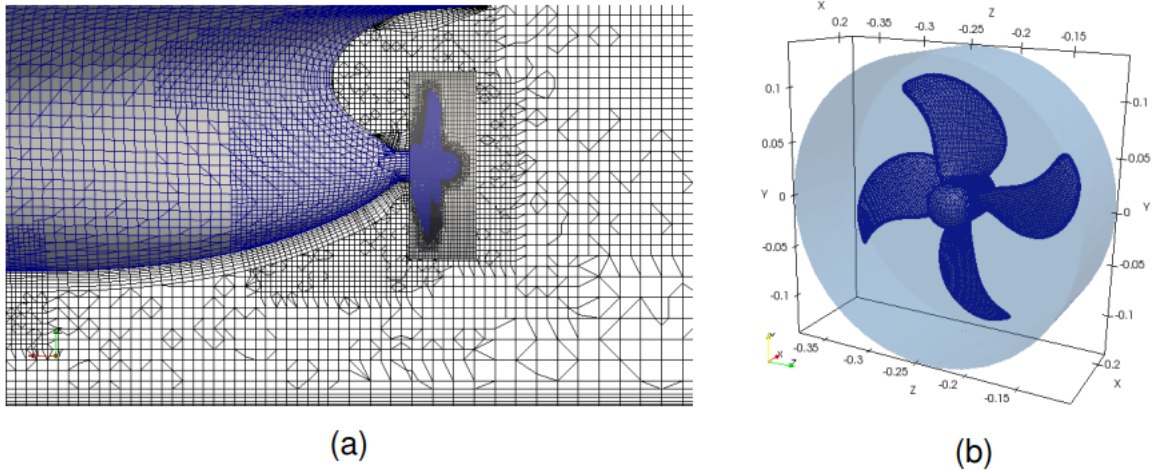


Figure 4: Cut through the numerical grid with the cylindric area of the propeller (a) and the wetted surface of the propeller and blades in the rotating reference frame (b).

3.2 Wake in 1:1, 1:6 and 1:40

Basically the aft ship and the wake were suspicious for causing sale effects, since viscosity and turbulence degree show most effect here. As expected, the wake for the more slender Container ship PPM52 offered clear differences in wake and an obvious dependency on the model scale (Figure 5).

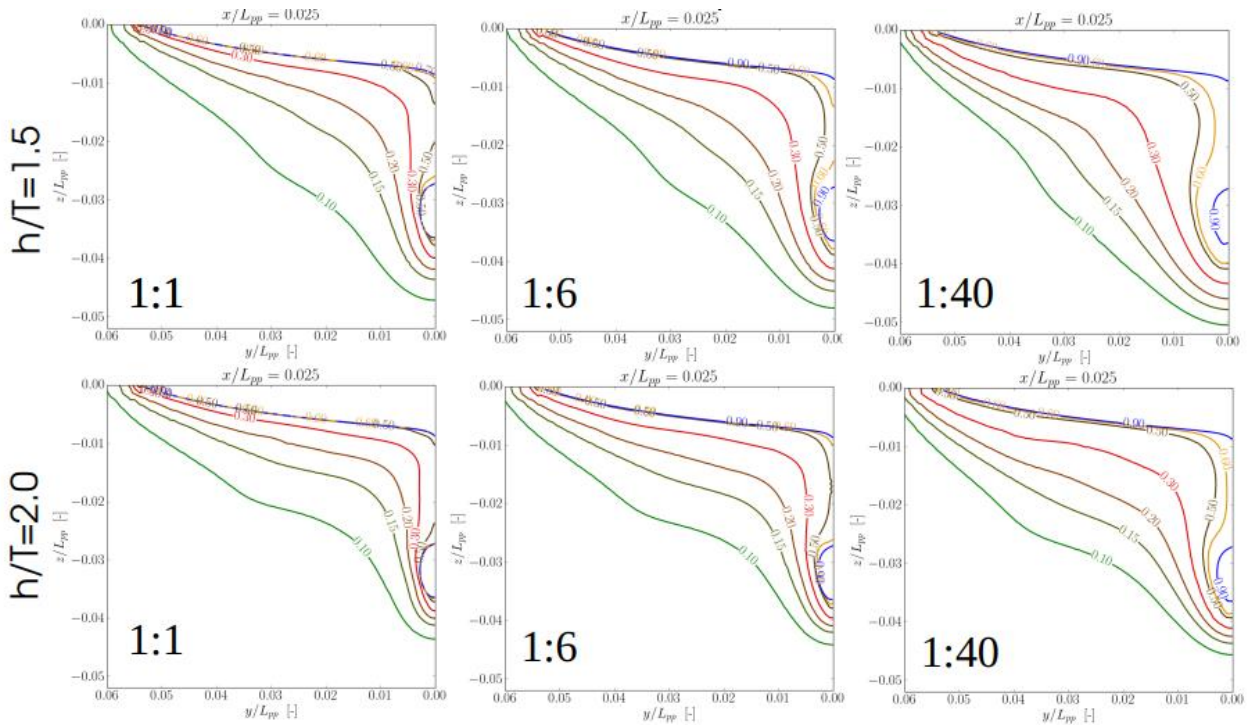


Figure 5: PPM52 Container Ship: wake in three scales without Propeller

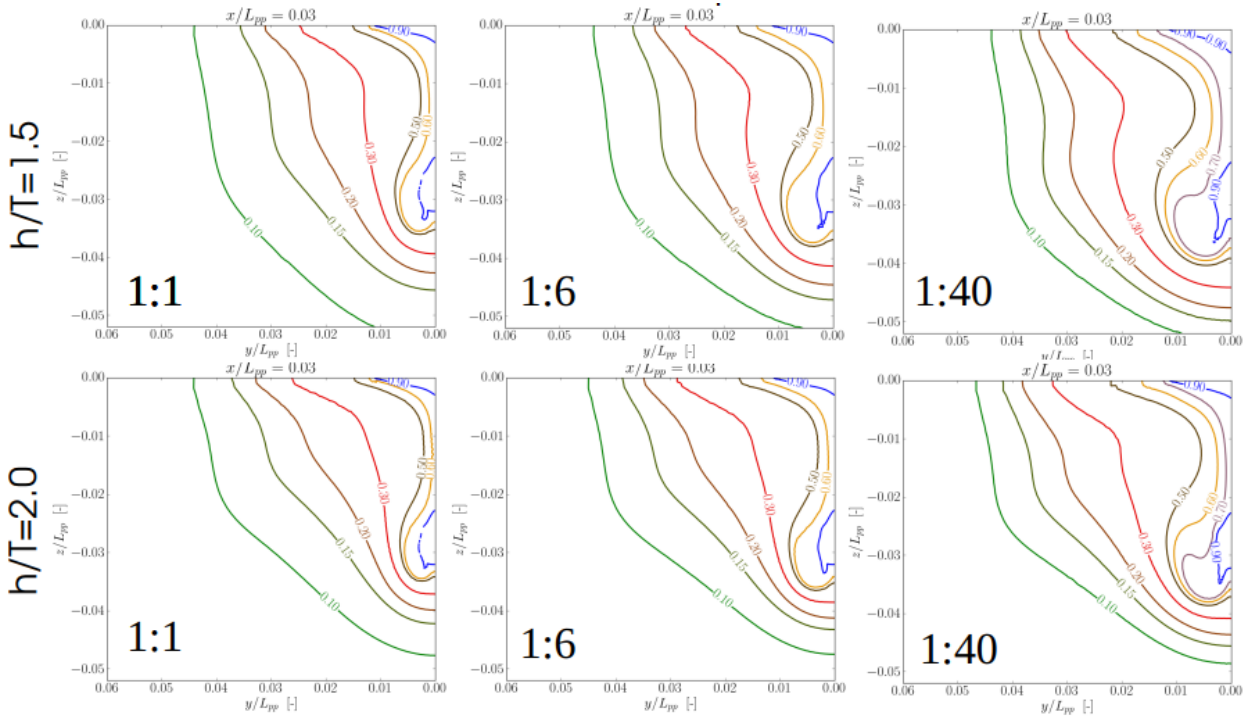


Figure 6: PPM 55 Container Ship: : wake in three scales without Propeller

For the bulkier ship shape of the PPM55 this was true as well, but much less pronounced and prominent (Figure 6). For the full scale sailing ship in the waterway the pure wake alone is not significant, since the interaction with the loaded propeller is always present.

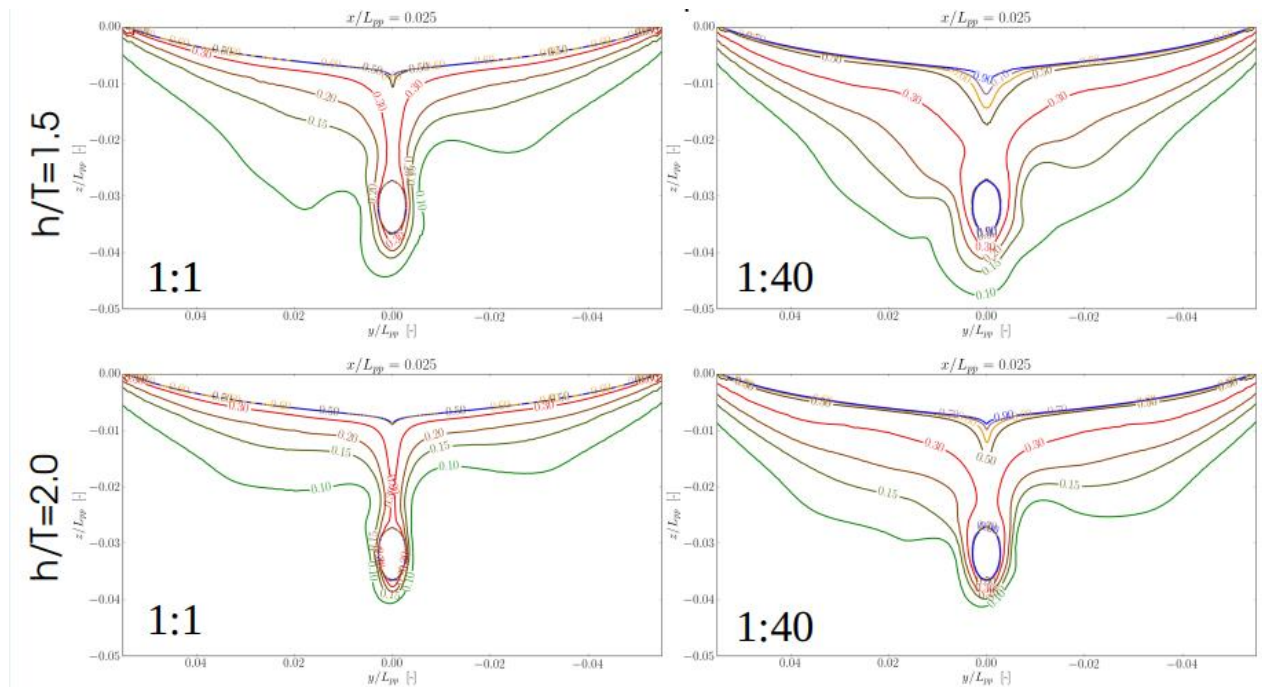


Figure 7: PPM 52: wake with propeller interaction, full scale compared to model scale 1:40

In Figure 7 and 8 the two ships' wake flow are shown with propeller applied. The difference between the ship shapes and their different upscaling characteristics gets even more prominent. Especially for the PPM55 it was quite surprising to find the characteristic unfavourable wake of the physical model almost unmodified in full scale (Figure 8).

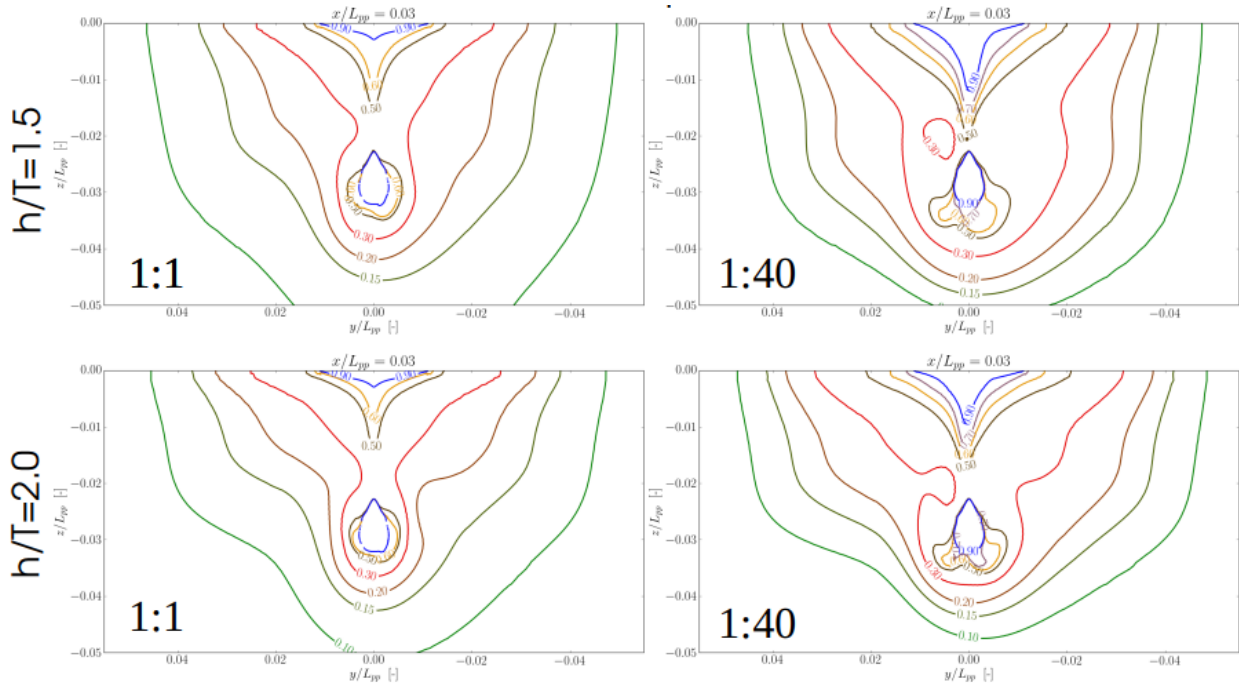


Figure 8: PPM 55: wake with Propeller interaction, full scale compared to model scale 1:40

3.3 Scale Effect on Trim Moment and Vertical Force

The initial question for the investigation was the scale effect on dynamic sinkage and trim. In order to answer this, the preceding work has been performed. The scale effect on the dynamic sinkage and trim finally was gained from comparison of the numerically obtained vertical displacement due to force coefficient in vertical direction and the rotating moment coefficient around the pitch axis. In Figure 9 an outline of the full figure of results is given. The differences from full scale to physical model scale 1:40 are displayed for different Froude numbers, water depths and both container ships investigated. The data of the bulkier PPM55 are in blue, in red the data of the more slender PPM52. Continuous lines represent values for depth to draft ratio (h/T) of 1.5 and dotted those for h/T of 2.0. Basically there is a figure of the very individual scaling effect for each different hull shape observed, comparable to the wake flow in chapter 3.2.

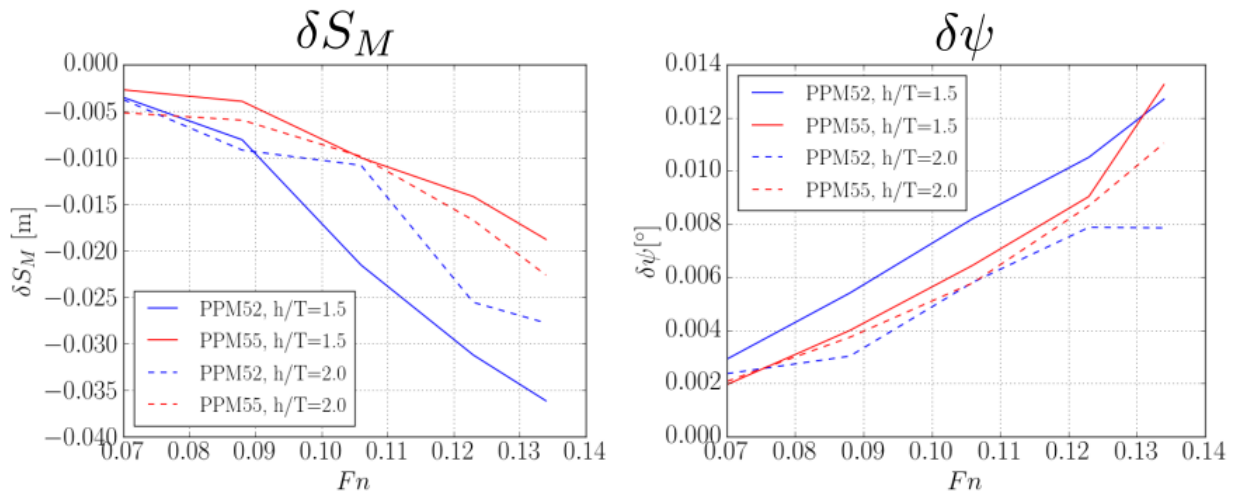


Figure 9: Differences of Sinkage Mean (δS_M) and Trim angle ($\delta \psi$) in Model Scale (1:40) and Full Scale.

The progression of the individual scale effect with increasing speed through water, represented by the Froude Number, can be satisfactorily approximated by a quadratic function, as shown in Figure 10. If this revealed applicable for a wide range of different hull shapes, this approach could be useful to model scale effect on squat in shallow water.

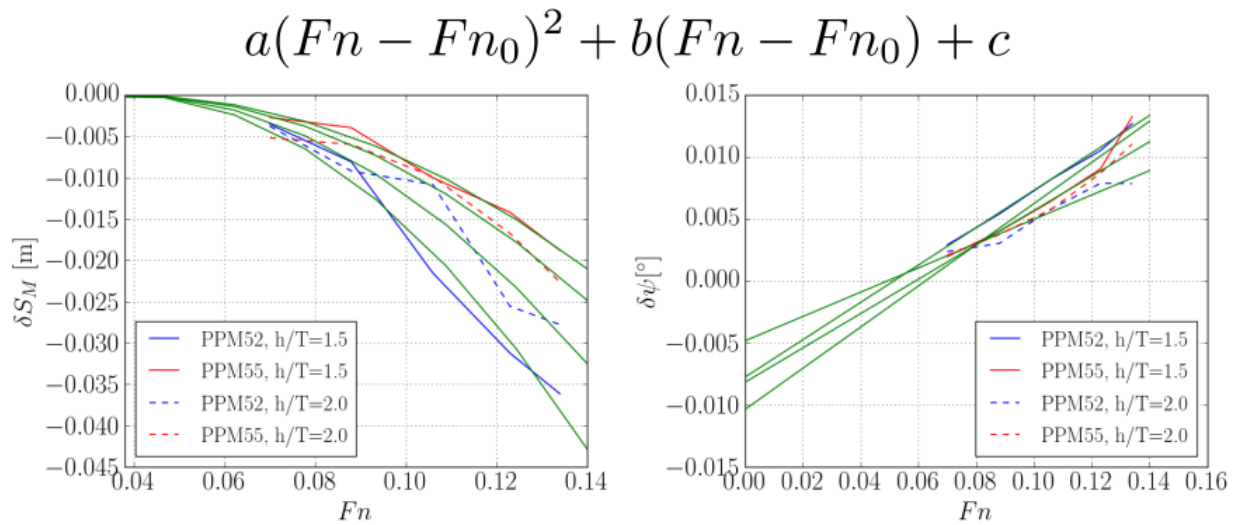


Figure 10: Quadratic approximation of the differences due to scaling from full scale to 1:40.

4 CONCLUSION

Dynamic sinkage and trim are generally regarded as Bernoulli effects, mainly subject of the pressure field generated by the fluid flow around the ship hull. For shallow water conditions this assumption turned out to be no longer true. Viscosity effects got observable with decreasing water depth and under keel clearance.

Since up to now, this was observed and investigated in model scale only, an investigation

was initiated to check for scale effects when upscaling results to full scale. A recently supposed numerical wall treatment was applied to enhance the numerical modelling in this specific case. Two different hull shapes of ships of comparable size and similar purpose were compared and revealed high dependency of scale effect on the particular hull shape. This could be observed for the bare hull and with propeller interaction included.

When evaluating the results it turned out that quadratic fitting was satisfactorily to resemble the scale effect's progression with the speed through water. Further investigation is necessary to confirm validity of this finding for a wider range of different ship types and hull shapes. Provided the quadratic approximation succeeded, this might ease proper model generation of manoeuvring models from scaled physical model tests.

REFERENCES

- [1] Böttner, C.-U., Heimann, J. and Uliczka, K. Numerical prediction of Squat of large Container Carriers on Waterways. *Marine CFD 2011, London, UK* (2011).
- [2] Böttner, C.-U. and Kastens, M. Squat at very shallow water conditions and increased trim: Result of unsteady flow flow and united boundary layers under ship's hull? *MARINE2015, Rome, Italy* (2015).
- [3] Popovac, M. and Hanjalic, K. Compound Wall Treatment for RANS Computation of Complex Turbulent Flows and Heat Transfer. *Flow, Turbulence and Combustion* (2007) **78**(2):177-202.
- [4] Greenshield, C. and Weller, H. *OpenFOAM and the OpenFOAM Foundation* (2019) Available at: <https://openfoam.org>
- [5] Uliczka, K. Kondziella, B. and Flügge, G. Dynamisches Fahrverhalten sehr großer Containerschiffe in seitlich begrenztem Flachwasser. *HANSA* (2004) **141**(1).
- [6] Härting, A. and Reinking, J. SHIPS: A new method for efficient full-scale ship squat determination. *30th PIANC-AIPCN Congress* (2002).
- [7] Gourlay, T.P. Dynamic draught of container ships in shallow water. *Int. J. of Maritime Engng* (2008) **150**(4):43-56.
- [8] Mucha, P., el Moctar, O. and Böttner, C.-U. Technical Note: PreSquat – Workshop on Numerical Prediction of Ship Squat in Restricted Waters. *Ship Technology Research* (2015) **61**(3):162-165.
- [9] Bertram, V. *Practical Ship Hydrodynamics*. Butterworth-Heinemann (2011)
- [10] Menter, F.R. Two Equation Eddy-Viscosity Turbulence Models for Engineering Applications. *AIAA Journal* (1994) **32**(8):1598-1605.
- [11] Buice, C.U. and Eaton, J.K. Experimental Investigation of Flow through an Asymmetric Plane Diffuser, *J. of Fluids Engng*, (2000) **122**:433-435.

IMPROVEMENT OF AN EXISTING SHORELINE EVOLUTION NUMERICAL MODEL

MARINE 2019

LIMA, M.* AND CARLOS, C.*

* Aveiro Research Centre of Risks and Sustainability in Construction (RISCO)
Civil Engineering Department – University of Aveiro
Campus Universitário de Santiago, 3810-193 Aveiro, Portugal
e-mail: marcia.lima@ua.pt, ccoelho@ua.pt - Web page: <http://www.ua.pt>

Key words: LTC, User interface, programming, coastal erosion, coastal interventions

Abstract. The coastal areas are facing serious erosion problems. The increasing urban pressure on coastal areas and the continuous shoreline retreat, lead to the anticipation of significant investments to protect the population living in the littoral. In order to avoid coastal erosion and flooding, and their consequent social, economic and environmental negative impacts, it is essential to accurately characterize the coastal evolution trends. The importance of the numerical modelling in civil engineering has been increasing in the last years, being the coastal engineering a relevant example. Since the 1970s, several types of numerical models have been developed for engineering applications with the purpose of analyze and predict the coastal morphology. One-line models based on the Pelnard-Considère [1] theory are commonly used to simulate the shoreline position variability of sandy beaches. LTC (Long-Term Configuration) is a numerical model developed to support coastal zone planning and management regarding erosion problems [2, 3]. LTC combines a simple classical one-line model with a rule-based model for erosion/accretion volumes distribution along the cross-shore profile. This model was designed for sandy beaches, where the main cause of the coastal dynamics and shoreline evolution is the alongshore sediment transport gradients, depending on the wave climate, water levels, sediment' sources and sinks, sediment's characteristics and boundary conditions. The model inputs are the wave climate, the water level, and the bathymetry and topography of the landward adjacent zones which is changed during calculation. Extensive areas can be analyzed up to 100 years. LTC code was developed in Fortran language and both input and output data were done through notepad files. Therefore, a graphical interface and the improvement of specific aspects on the initial code have been developed, being presented in this work. The knowledge of wave characteristics at the wave breaking depths (output data in the new interface), the representation of the cross-shore active width of the profiles along the coast and along time, and the introduction of new options to read bathymetric data, are some examples of the model updates. The development of the graphical interface is performed in C# language. It was intended that the new interface is resourceful and intuitive, aiming to allow new useful tools for the users. In conclusion, this work presents the new interface of LTC model, highlighting some of the improvements made possible in the numerical model due to the new interface characteristics.

1 INTRODUCTION

A growing trend of erosion problems in coastal areas is being observed worldwide due to important sediment deficit, the increasing urban pressure on coastal areas and the continuous shoreline retreat. LTC (Long-Term Configuration) is a numerical model developed to support coastal zone planning and management regarding erosion problems, by estimating the shoreline evolution in a medium to long-term time horizon, under different coastal intervention scenarios. Using 3D topographic data, which is continuously updated during the simulation, the model assumes that each wave acts during a certain period of time (computational time step) and it is able to distribute erosion or accretion resulting from the longshore sediment transport gradients along the active cross-shore profile, between the depth of closure and the wave run-up limit. The main limitations of the model are inherent to the current knowledge about cross-shore profile evolution under persistent erosion or accretion.

LTC code was developed in Fortran language and both input and output data were done through notepad files. Therefore, this work aimed to develop a graphical interface that allows visualizing the main results of the shoreline evolution when simulating different coastal intervention scenarios. The graphical interface should also allow an easier evaluation of other parameters related to sediment dynamics (breaking wave characteristics, depth of closure, wave run-up limit, longshore sediment transport volumes, etc.), enabling improvements of the performance of the model and supporting the development of associated tools, namely of cost-benefit analysis tools based on shoreline evolution and correspondent accretion or erosion areas, consequence of different coastal intervention scenarios.

To achieve the proposed goals, the next section of this work presents a brief description of one-line model theory to support shoreline evolution simulations, and the following section describes the main assumptions adopted in the LTC numerical model. Then, LTC graphical interface is described in detail and finally some conclusions are presented, related with the potential achievements resulting from the developed graphical interface.

2 NUMERICAL MODELLING OF THE SHORELINE EVOLUTION

The numerical modelling of the shoreline evolution is necessary, not only to understand and predict the coastal systems dynamics, but also to assist an effective decision-making. There are no universal models for the analysis and prediction of the shoreline evolution on a scale of tens of years [4]. The coastal morphology evolution is the result of the interaction of complex physical processes that, in most cases, cannot be numerically represented accurately. Numerical formulations are deterministic, based on known or semi-empirical physical laws obtained from field or laboratory measurements [5]. The analytical models of shoreline evolution are closed solutions of the differential equation of continuity, simplified for the transport of sediments under constant wave climate conditions, in space and time [5]. The first model of this type was introduced by the one-line theory [1], which considers that the cross-shore beach profile, limited to offshore by the depth of closure, beyond which there is no significant changes in the bottoms, moves parallel to itself. Several works [6-10] are examples of other analytical models referred by Rosati et al. [11].

The numerical approach for the simulation of coastal and beaches morphology evolution

are diverse, with varying degrees of complexity, from simple one dimension models, to sophisticated three-dimensional (3D) models. Due to the high computational demands, 3D models can only be used in short-term applications, while the shoreline evolution models can be used for long-term analysis [5]. Coelho et al. [12] classify the coastal morphology evolution in short, medium and long-term temporal scales, according to Table 1.

One of the most used and simple models to predict the shoreline evolution is based on the one-line theory, which, as referred, assumes a constant profile shape that can be moved perpendicular to the coast, as a result of erosion or accretion phenomena. Multiple-line models were developed to describe the contours movement at certain depths, analogous to the one-line models. Despite the additional detail, these models were unsuccessful due to the difficulty of adequately reproduce the cross-shore sediment transport. These models require more calibration and do not represent a significant increase in results quality [4].

Table 1: Numerical models classification, considering the time and spatial scales of the simulation [12].

| | Hours | Years | Decades | > Centuries |
|---------|------------|-------------|-----------|-------------|
| 10 m | Short-term | | | |
| 1 km | | Medium-term | | |
| 5 km | | | | |
| 10 km | | | Long-term | |
| >100 km | | | | |

According to Vicente and Clímaco [13], one-line models used to estimate longshore sediment transport rates and long-term shoreline changes generally assume that the profile is displaced parallel to itself in the cross-shore direction. These models are formulated based on the sediments conservation equation in a control volume or shoreline stretch and on longshore sediment transport equation [11]. It is assumed that there is an offshore depth of closure and an onshore upper end of the active profile, defining the limits where no significant changes happen. A constant profile shape moves in the cross-shore direction between these two limits, implying that sediment transport gradients are uniformly distributed over the active portion of the profile [14]. Following the previous assumptions, and according to Figure 1, sediments volume continuity for an infinitely small length of shoreline can be formulated [15].

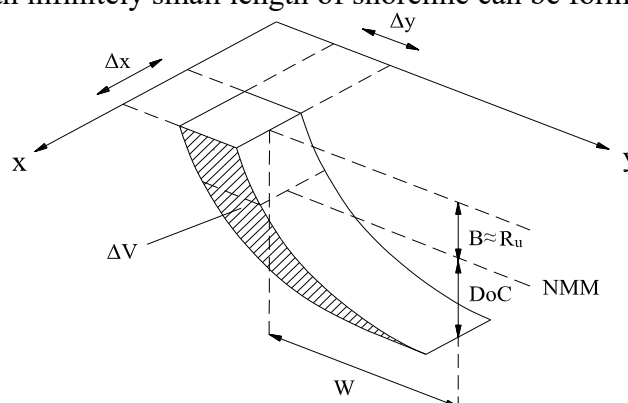


Figure 1: One-line model definition scheme [14].

The continuity equation can be solved for simple boundary conditions and simplified hypothesis, obtaining analytical solutions to the problem of the shoreline evolution [1]. It is important to emphasize that the coastal management and planning primarily work with temporal scales of years or decades, in stretches with tens or hundreds of kilometers. The generality of current models is validated in schematic situations and when applied to real cases, they are calibrated based on specific data. After calibrated, the models are applied differently, in situations of analysis, evaluation of coastal intervention scenarios and prediction of future shoreline conditions [4].

3 NUMERICAL MODEL LTC

LTC (Long-Term Configuration) is a numerical model to simulate the shoreline evolution in a medium to long-term perspective. It was primary developed at Aveiro University, Portugal, version LTC CC2005 [2], and then improved at Faculty of Engineering of Porto University, version LTC-RS2010 [5] and again Aveiro University, in 2012, version LTC-CC2012. LTC was developed to support coastal zone planning and management in relation to coastal erosion problems [16-20]. It was firstly presented at the ICCE 2004 [21] and has been improved and extensively applied since then [20, 22]. LTC combines a simple classical one-line model with a rule-based model for erosion/accretion volumes distribution along the beach profile [17]. This model was designed for sandy beaches, where the main cause of shoreline evolution is the alongshore sediment transport gradients, dependent on the wave climate, water levels, sediment sources and sinks, sediment characteristics and boundary conditions. The model inputs are the wave climate, water level and the bathymetry and topography of the landward adjacent zones (updated during calculation).

The sediment transport volumes are estimated by formulae that consider the shoreline's angle to oncoming breaking waves and the breaking wave height (CERC formula). The sediment volume variation in a coastal stretch is caused by sediment transport gradients between modeled cells where, similar to one-line models, the balance of volumes is defined through the continuity equation. This difference between sediment transport volumes represents a variation in the bottom level of the grid points in the same profile of the modeled domain [17]. LTC assumes a uniform cross-shore distribution of the alongshore sediment transport along the active width of the cross-shore profiles, thus performing a uniform variation of the vertical coordinates of the active profile grid points, adjusting the active profile at the boundaries based on the sediments friction angle defined by the users [18]. This way, the variation of the shoreline position depends, not only, on the sediment volume variation, but also, on the topography and bathymetry associated with each cross-shore profile [2]. With the LTC numerical model, the 3D topo-hydrographic data are continuously updated during simulation, allowing the model to distribute erosion or accretion sediment volumes for each wave action (computational time step). Due to the importance of the boundary conditions in the model simulations, several options can be made: constant sediment volumes going in or out the study area; constant volume variations in the domain border sections; extrapolation from nearby conditions. Moreover, different coastal protection works combinations may be considered with almost no limitation for the number of groins, breakwaters and seawalls, the number of sediment sources/sinks sites, and artificial

nourishments.

The Figure 2 scheme represents the computational structure of the LTC model, developed in Fortran programming code. The topo-hydrography should be provided at the beginning of the simulation, being updated in each time step. The propagation of the waves is carried out on the actual bathymetry, being estimated the wave breaking characteristics. The longshore sediment transport rates are computed alongshore and the sediment transport volumes balance for each coastal stretch is calculated, after which the bottom coordinates are updated, and the new topo-hydrography is calculated. In order to facilitate changes and to promote alternatives in computational methods, the program is composed by small subroutines, increasing the simplicity and comprehension of each of them. The main program uses these subroutines throughout the calculation process [2].

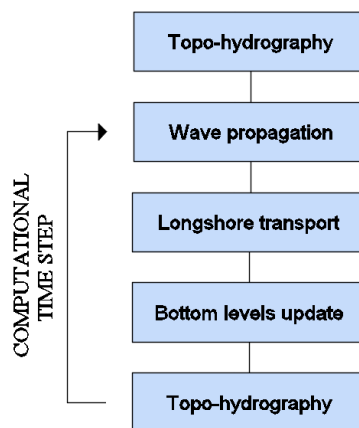


Figure 2: Computational structure of the LTC model [5].

4 LTC GRAPHICAL INTERFACE

The developed graphical interface is described in this section, referring to its use and main potentialities. The main window of the interface can be considered divided into two main zones, allowing visualizing the study area domain, as the remaining input data sections are alternated (Figure 3). After the input data definition, several simulation results can also be visualized in the new developed graphical interface.

4.1 Input data definition

The input of data is divided into six principal groups: 1) spatial domain characteristics definition; 2) wave regime; 3) tidal regime; 4) boundaries conditions; 5) coastal defense interventions; and 6) simulation characteristics and intended outputs. In the "Spatial Domain" window, all the parameters related to the study area are defined, namely the bathymetry/topography. For the immediate determination of the initial shoreline position, the user must also indicate the mean sea water level. Finally, the annual rate of sea level rise due to climate change should be indicated. The user has also the option to import an image with a representation of the spatial domain, which is loaded and is displayed when the user wishes.

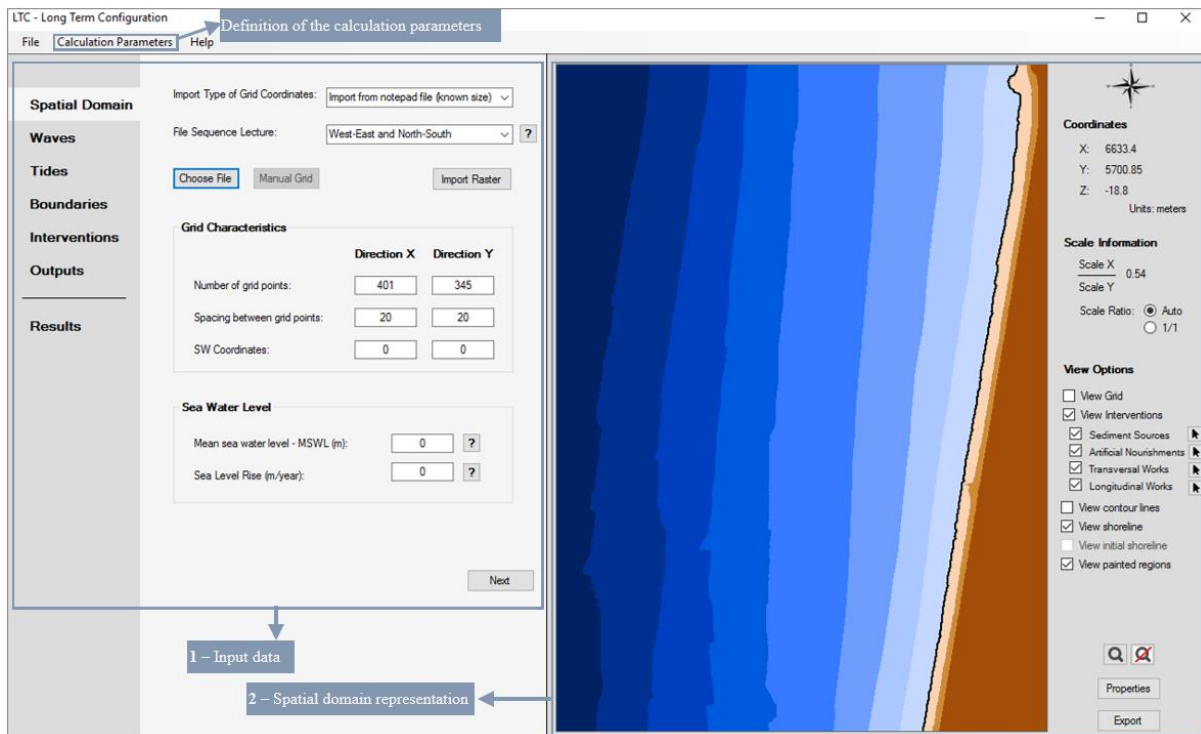


Figure 3: Shoreline evolution model graphic interface main window.

Figure 4 (left) shows an example of the options available for the introduction of wave characteristics. The user can choose one of five available options (in "Wave climate definition"): a fixed wave climate, where the wave height and wave direction will be constant throughout the calculation; generation of a random sequence of waves, based on the occurrence percentages of different wave heights classes, representative of a typical year of wave climate. Based on this option, the user can define a systematically equal wave sequence, maintaining the occurrence percentages, by activating the "Consider the same sequence wave" check box (if this option is not considered, in each simulation the wave classes frequency is the same, but the waves characteristics and its sequence are changed, so the resulting wave climate is different). In the fourth option the user defines a maximum and minimum limit for the wave heights and directions, being these limits automatically represented in the respective graphs and being generated a random wave climate, which respects the defined limits. The last option allows importing a wave data file (Excel@ or text file) with recorded data.

The data for the tidal regime characterization is divided in astronomical and meteorological tides (Figure 4, right). For the astronomical tide, the user may choose to consider that the mean sea level remains fixed (value defined in the "Spatial Domain" window) or that it is variable and must therefore define the maximum amplitude for spring and neap tides. For the definition of the meteorological tide, the user has three options: 1) sea level remains fixed throughout the calculation, and the user just need to define the sea level elevation changes due to high or low meteorological pressures; 2) sea water level varying randomly between two limits, which must be defined by the user; 3) sea water level varying randomly between

previously defined limits, but respecting a correspondence with the wave heights verified at the same time instant.

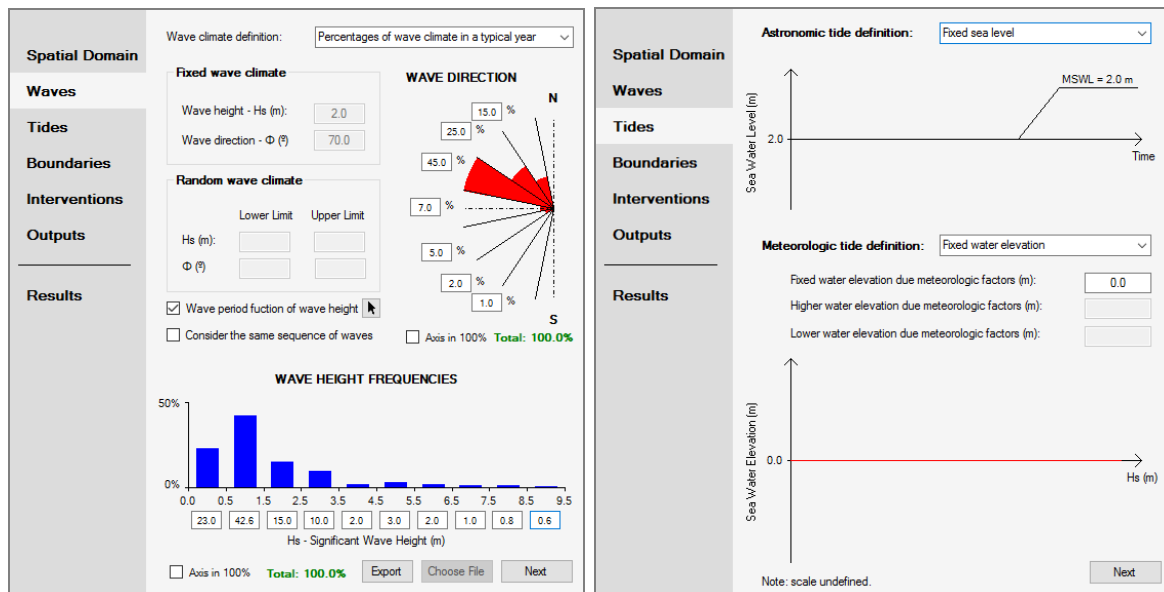


Figure 4: Windows to define the wave and tide climate: left) waves; right) tides.

With respect to boundary conditions, data entry is divided into the definition of sediment volumes at the northern (updrift) and the southern (downdrift) boundaries of the area to be modeled (Figure 5, left). At each border the user can choose one of three options: 1) sediments fixed volume going in or leaving the section that defines the boundary; 2) erosion or accretion fixed rate in the cross-section (the user must define the value of the volume variation, which will be assumed constant throughout the calculation); 3) extrapolation of sediment transport volumes conditions in the vicinity of the border, based on the average of the transport volumes in the adjacent sections (the user may also add/subtract a fixed sediment transport volume to the average of the transport volumes in the adjacent sections).

The LTC model also allows the definition of four different types of coastal defense interventions: punctual alluvial sources, artificial nourishments, defense works perpendicular to the shoreline, like groins or breakwaters, and adherent longitudinal defense works or seawalls (Figure 5, right). In order to add a new coastal defense intervention, the user must click on the "Edit" corresponding to each intervention type, being directed to fill a table with the characteristic of each one of the interventions. After completing the required data, each of the interventions will be automatically represented in the spatial domain window.

The "Outputs" window allows the user to define the characteristics of the simulation and graphic outputs. It is also in this window that the user has the possibility to start the calculation ("Run" button) and where can easily access each of the parameter windows (briefly described in the next section), and check which formulations have been chosen for the calculation. After all data have been entered, the "Run" button will be available. While the simulation is in progress, the program does not allow any change of the data, or the visualization of the windows of the model.

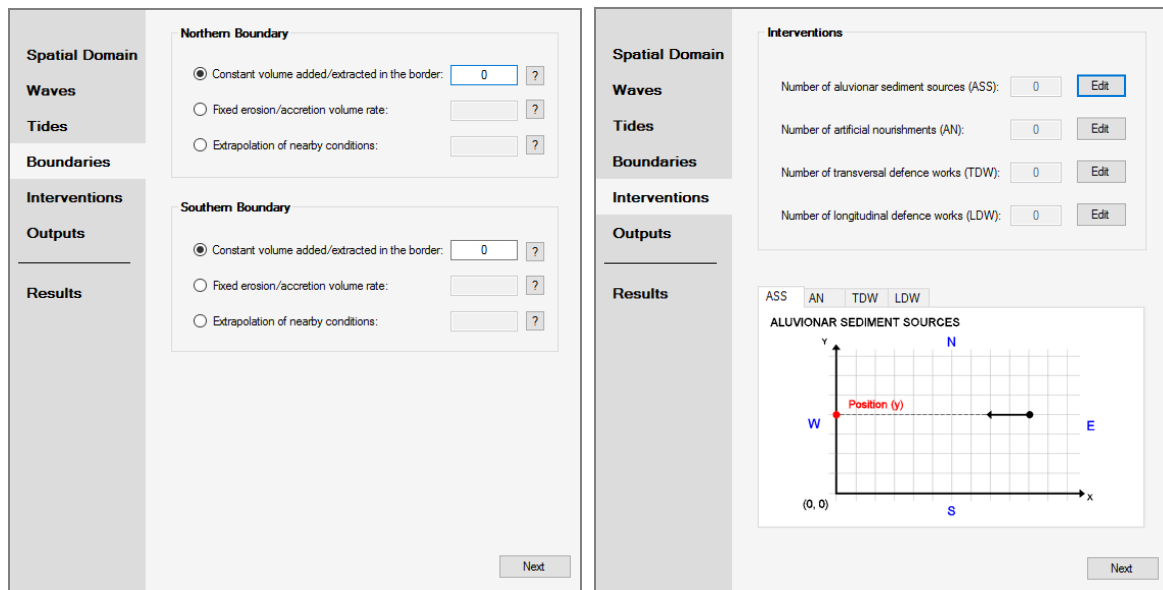


Figure 5: Windows to define domain limits: left) “Boundaries” conditions; right) coastal interventions.

4.2 Calculation parameters

The calculation parameters and formulation choices are complete by default and the user only needs to access their windows if intending to change them. Three windows have been developed. The user can access those three windows through the main window by clicking on "Calculation Parameters": General Parameter's window (water and sediments characteristics); Formulations choice window; and Slope Angles (sediments friction angle).

4.3 Drawing domain

After the user has entered the calculation domain, the shoreline and topo-bathymetric contour lines are automatically represented in the drawing area. The display characteristics can be changed by the user, accessing the "Properties" button. It is possible to change the properties related to the shoreline (initial and final), depth of closure, wave breaking depth line, wave run-up limit and envelope of the active profile width throughout the simulation. It should be notice that, in addition to the shoreline and initial contours, the remaining options are only visible after running the simulation. The user can define the scale in which the domain is displayed. Regarding the spatial domain visualization options, it is possible for the user to view/hide the grid points, the coastal interventions at their locations, topo-bathymetric contours and shoreline. Optionally, the user can view a picture of the spatial domain (Figure 6), which automatically becomes the background of the working area. Finally, in the spatial domain representation area, the "Export" button is also available which allows the user to save the graphical representation of the study zone as an image file.

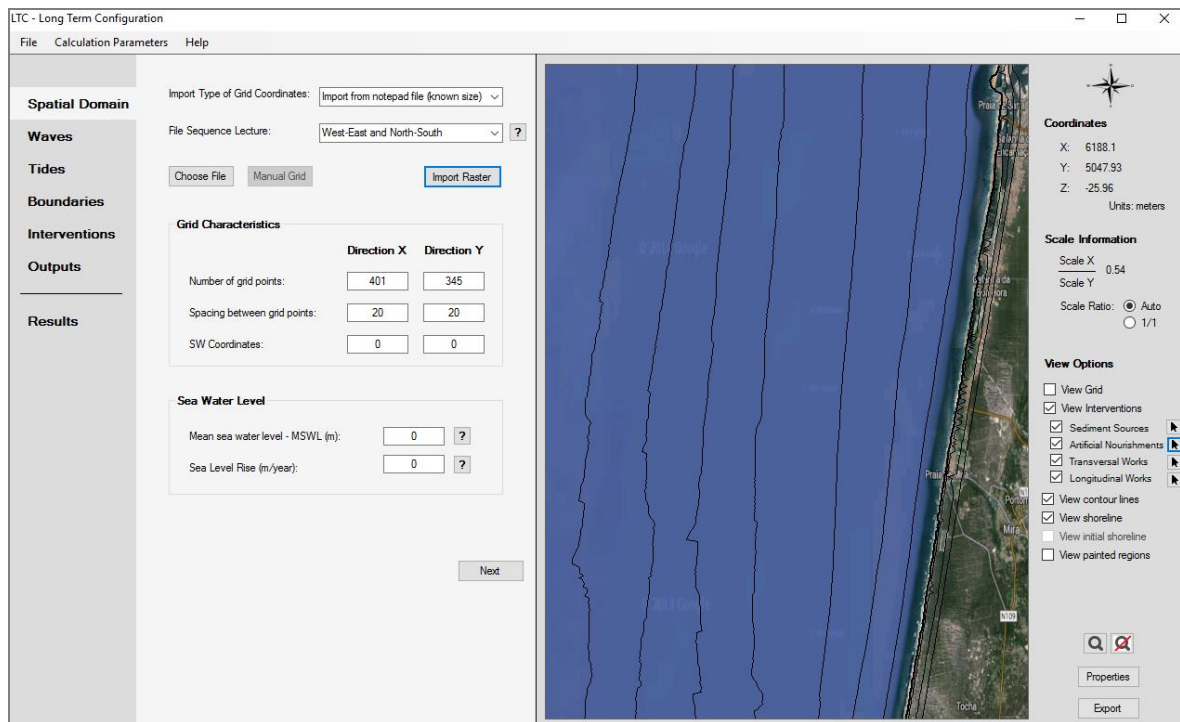


Figure 6: Window with the image of the studied domain.

4.4 Simulation results

After the simulation, a new window is available to visualize the results (Figure 7). This window contains information on the evolution of topo-bathymetry in the spatial domain, shoreline evolution, wave characteristics at breaking, cross-shore profiles and access to AutoCAD® and Excel® files.

In the "Bathymetry and Topography" tab (Figure 7) it is possible to select the time instant corresponding to the result to be displayed. For each of the time instants defined in the data input window "Outputs" (in "Time space between bathymetry/topography") is visible, in the drawing area, the bathymetry and topography of the spatial domain. All of the display options available in the drawing area are active for each of the outputs. The user can also see the envelope of the active profile width along the entire length of the domain, allowing identifying the extreme limits obtained during the simulation for the depth of closure and for the wave run-up. Finally, the user can export to a data file (Excel® or text file) the topo-bathymetry obtained in the represented instants of time. This function enables this file to work as input data to characterize the domain of any future simulation, starting from that time instant. It is also possible to visualize an animation with the shoreline evolution over time.

To evaluate the wave breaking characteristics, the user can visualize the results obtained for the wave height and direction, for each cross-shore profile and time instants defined in the window "Outputs". Through an Excel® file, the user can also access for each profile and instant: the wave height and direction at breaking, breaking depth position, breaking contour orientation, shoreline position, depth of closure and wave run-up positions, width of the cross-shore active profile envelope, potential sediment transport capacity, effective longshore sediment transport volumes, vertical displacement of the grid points of the profile, and

information on the accretion and erosion areas between profiles.

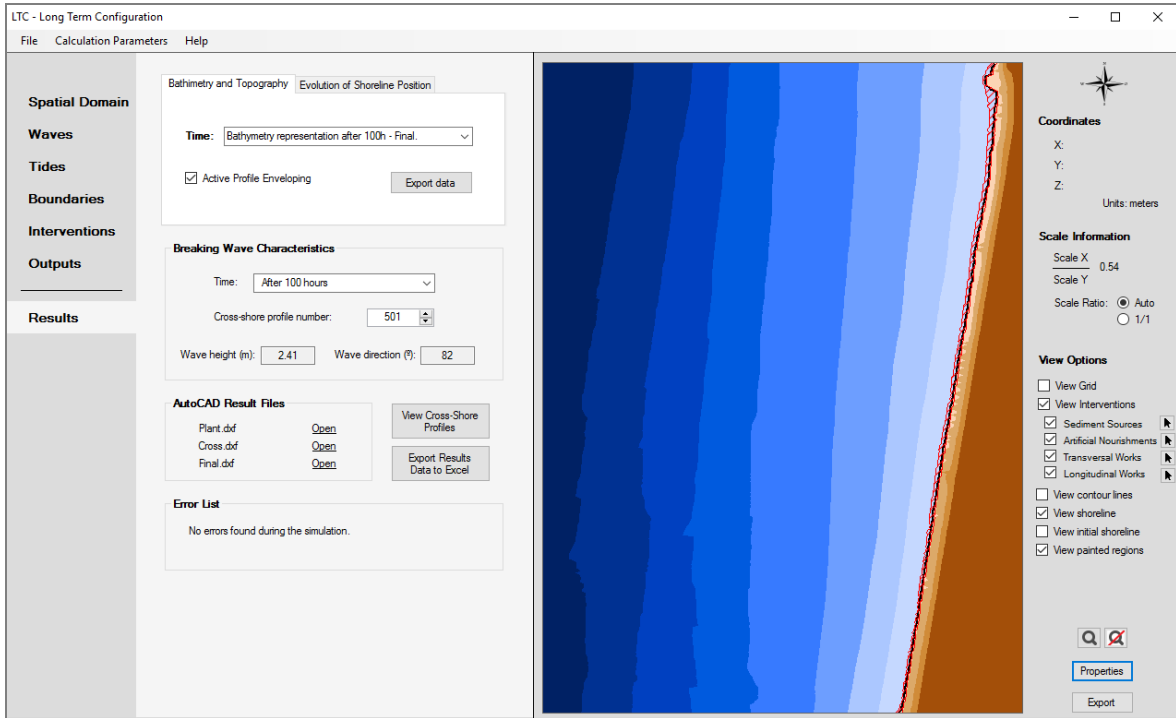


Figure 7: Window with the results of the simulation (“Results”).

The results for the cross-shore profiles are generated in an independent window (Figure 8). For each profile shown, the user can identify the boundaries of the profile, the depth of closure, the wave breaking depth and the wave run-up limit. Depending on the profile and/or time instant chosen, the user can also interactively view an animation with the evolution of the profile over time, or the variation of profiles shape alongshore, at a given time instant.

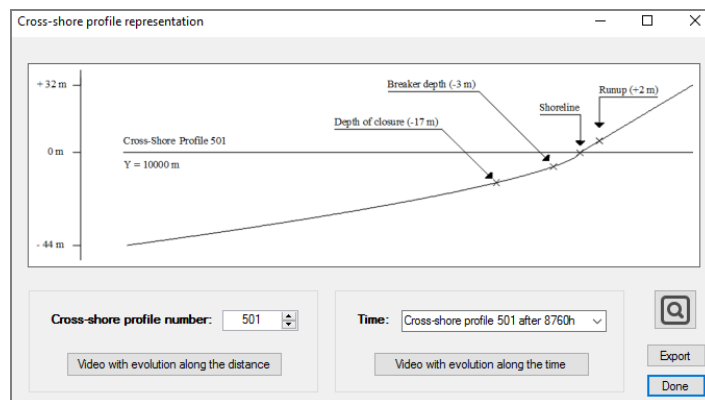


Figure 8: Cross-shore profile results representation.

5 CONCLUSIONS

In spite of extensively applied in the past, LTC was missing a friendly graphical interface, which was a limitation factor to the analysis of all the potential results produced by the model. Thus, efforts were made to facilitate the data introduction by the users, but mainly to make easier the results analysis. The knowledge of wave characteristics at the wave breaking depths (output data in the new interface), the representation of the cross shore active width of the profiles along the coast and along time, and the schematic representation of each cross-shore profile and time instant are some examples of the model updates. The work developed allowed to facilitate the evaluation of important properties in the calculation of the shoreline evolution, namely the characteristics of hydrodynamics (waves at breaking, wave run-up limits) and longshore sediment transport patterns (depth of closure, active profile width and sediment transport rates) during the analyzed time horizon.

It was intended that the new interface is resourceful and intuitive, aiming to allow new useful tools for the users. The results allow anticipating that the LTC model can continue to be developed and may integrate complementary tools, which together with the design of interventions and the analysis of its costs and benefits will facilitate the identification of adequate coastal erosion mitigation scenarios, helping on planning and management of the coastal zones.

REFERENCES

- [1] Pelnard-Considère, R., 1956. Essai de Theorie de l'Evolution des Forms de Rivage en Plage de Sable et de Galets (in French). 4th Journees de l'Hydraulique, Les Energies de la Mer, Question III, Rapport No. 1, pp. 289-298.
- [2] Coelho C., 2005. Riscos de exposição de frentes urbanas para diferentes intervenções de defesa costeira (in Portuguese). Aveiro, Portugal: University of Aveiro, PhD thesis 404p.
- [3] Silva, R., Coelho, C., Taveira-Pinto, F., Veloso-Gomes, F. (2007). Dynamical numerical simulation of medium term coastal evolution of west coast of Portugal. JCR 50, 263-267.
- [4] Hanson, H., Aarninkhof, S., Capobianco, M., Jiménez, J. A., Larson, M., Nicholls, R. J., Plant, N. G., Southgate, H. N., Steetzel, H. J., Stive, M. J. F. e De Vriend, H. J. (2003). Modelling of Coastal Evolution on Yearly to Decadal Time Scales. JCR, 19, 4, pp. 790-811.
- [5] Silva, R. (2010). Avaliação Experimental e Numérica de Parâmetros Associados a Modelos de Evolução da Linha de Costa. Dissertação de Doutoramento, Faculdade de Engenharia da Universidade do Porto, Porto, Portugal, 488 p.
- [6] LeMéhauté, B. e Brebner, A. (1961). An Introduction to Coastal Morphology and Littoral Processes. Report No. 14, Civil Engineering Department, Queens University at Kingston, Ontario, Canada.
- [7] Bakker, W. T. e Edelman, T. (1965). The Coastline of River Deltas. Proceedings of the 9th Coastal Engineering Conference, ASCE, pp. 199-218.
- [8] Bakker, W. T. (1968). The Dynamics of a Coast with a Groyne System. 11th Coastal Engineering Conference, ASCE, pp. 492-517.
- [9] Walton, T. e Chiu, T. (1979). A Review of Analytical Techniques to Solve the Sand Transport Equation and Some Simplified Solutions. Proceedings of Coastal Structures '79,

- American Society of Civil Engineers, pp. 809-837.
- [10] Dean, R. G. (1984). Principles of Beach Nourishment. Chapter 11, CRC Handbook of Coastal Processes and Erosion, P. D. Komar, ed., CRC Press, Inc., Boca Raton, FL, pp. 217-232.
- [11] Rosati, J., Walton, T. e Bodge, K. (2002). Longshore Sediment Transport. In: Walton, T. (editor), Coastal Engineering Manual, Part III, Coastal Sediment Processes, Chapter III-2, Engineer Manual 1110-2-1100, U. S. Army Corps of Engineers, Washington, DC, 119 p.
- [12] Coelho, C., Silva, R., Veloso-Gomes, F. e Taveira-Pinto, F. (2009). Potential Effects of Climate Change on NW Portuguese Coastal Zones. ICES Journal of Marine Science 66, pp. 1497-1507.
- [13] Vicente, C. M. and Clímaco, M. (2003). Evolução de Linhas de Costa. Desenvolvimento e Aplicação de um Modelo Numérico (in Portuguese). Informação Técnica Hidráulica ITH 42, Laboratório Nacional de Engenharia Civil, Lisboa, 167p.
- [14] Gravens, M. B., Kraus, N. C. e Hanson, H. (1991). GENESIS: Generalized Model for Simulating Shoreline Change. Report 2, Workbook and System User's Manual, USACE, 431 p.
- [15] Hanson, H. e Kraus, N. C. (1989). GENESIS: Generalized Model for Simulating Shoreline Change. Report 1, Technical Reference, Technical Report CERC-89-19, U. S. Army Engineer Waterways Experiment Station, Coastal Engineering Research Center, Vicksburg, MS, 185 p.
- [16] Coelho, C., Taveira-Pinto, F., Veloso-Gomes, F. and Pais-Barbosa, J. (2005). Coastal evolution and coastal works in the southern part of Aveiro Lagoon Inlet, Portugal. Proceedings of the Coastal Engineering Conference.
- [17] Coelho, C., Veloso-Gomes, F. and Silva, R. (2007). Shoreline Coastal Evolution Model: Two Portuguese Case Studies. Coastal Engineering 2006: 3430-3441.
- [18] Coelho, C., Lima, M. and Veloso-Gomes, F. (2013). "Relationship Between Cross-Shore Active Profile and One-Line Shoreline Evolution Models Performance." Journal of Coastal Research: 2107-2112.
- [19] Guimarães, A., Lima, M., Coelho, C., Silva, R. and Veloso-Gomes, F. (2016). "Groin impacts on updrift morphology: Physical and numerical study." Coastal Engineering 109: 63-75.
- [20] Lima, M. and Coelho, C. (2017). "LTC shoreline evolution model: Assumptions, evolution, validation and application." Journal of Integrated Coastal Zone Management 17(1): 5-17.
- [21] Coelho, C., Taveira Pinto, F., Veloso Gomes, F. and Pais-Barbosa, J. (2004). Coastal Evolution and Coastal Works in the Southern Part of Aveiro Lagoon Inlet, Portugal. Proceedings of the 29th International Conference on Coastal Engineering, Lisboa, Portugal.
- [22] Lima, M. (2018). Ferramenta numérica de análise do impacto de intervenções de defesa costeira na evolução da linha de costa: custos e benefícios (in Portuguese). PhD Thesis.

IMPROVING THE NUMERICAL ROBUSTNESS OF BUOYANCY MODIFIED $k-\omega$ SST TURBULENCE MODEL

CONG LIU, WEIWEN ZHAO, JIANHUA WANG AND DECHENG WAN*

State Key Laboratory of Ocean Engineering,
School of Naval Architecture, Ocean and Civil Engineering,
Shanghai Jiao Tong University, Shanghai, China

*Corresponding author, E-mail: dewan@sjtu.edu.cn

Key words: Numerical instability, Wave decay, Buoyancy modification, Over-predicted turbulence, OpenFOAM

Abstract. In most previous computational fluid dynamics (CFD) studies involving free surfaces progressive wave with RANS model, they always suffered from over-predicted turbulence near the interface especially for the short wave with high steepness. This over-prediction would lead to severe wave damping and make the results invalid. To overcome this problem, many researchers has modified the RANS model to improve the free surface simulation. The over-prediction is suppressed by: 1) adding a buoyancy term in the turbulent kinetic energy (TKE) equation and 2) redefining the eddy-viscosity to stabilize the model in nearly potential flow region. The new stabilized turbulence model prevents from the exponential growth of the eddy-viscosity and subsequent wave decay exhibited by original model. In this study, the modified models mentioned above are implemented in OpenFOAM. But our practice on modified $k-\omega$ SST model encountered server numerical instability. The numerical instability is caused by the sudden increase of turbulent viscosity. Careful inspection on the results show that this erroneous spikes in the eddy-viscosity is related to the dissipation rate, ω , going to zero in some grid cell near the free surface. To prevent this from happening, a new limiter is simply imposed on the buoyancy term in the TKE equation. This new limiter is validated by conducting 2D wave simulations. The numerical results show good agreement with the experimental measurements for the surface elevations, undertow profiles of the horizontal velocity and turbulent kinetic energy profiles. Meanwhile, the numerical stability is also guaranteed.

1. INTRODUCTION

Among the most common engineering problem related to aquatic environment, free-surface wave has to be reckoned. Usually, these problems include the process of wave propagation, their interaction with structures and wave breaking, which require solving the two-phase flow and turbulence in the same time. Through many years of research and development, volume of fluid (VOF) method has been proved to be reliable to deal with the multiphase problem. The two equation Reynolds-averaged Navier-Stokes (RANS) model has sufficient accuracy to handle most of the turbulence from the view of engineering. Therefore, their combination is widely used by a lot of researchers.[1–3] But one of the most commonly mentioned problems

among these researches is the over-prediction of turbulence and subsequent unavoidable wave decay during its propagation. In the case of breaking wave study using RANS model, there has been a clear tendency to predict turbulence levels that are much higher than have been measured[4][5]. This over-prediction shows itself not only in the surf zone where the wave breaking happened, but also in the region prior to breaking. The over-predicted turbulence both on and beneath the surface wave. On the surface, this over-prediction is induced by the large production of turbulent kinetic energy, k , which is related to the large velocity gradient around the interface between water and air. This issue is suppressed by implementing a buoyancy-modified turbulence model, where an additional sink term is added to the TKE equation[6][7]. The justification of this additional term is given by Van Maele and Merci[8]. For the computation of two-phase flow using VOF, the density is not constant near the air-water interface. But the turbulence model is developed for the incompressible flow. The density variation at the interface has a non-negligible effect on the turbulent nature. For the compressible turbulence flow, the instantaneous density can be expressed as the sum of time average value and a fluctuating term, just like the instantaneous velocity. An extra source term related to the correlation of density-velocity fluctuation will appear in the TKE for compressible turbulence flows, which accounts for the effect of buoyancy on the turbulence. This buoyancy term can be simply calculated using standard gradient diffusion hypothesis (SGDH), which related this density-velocity correlation to the production of density gradient of and turbulence viscosity. This process is similar with the Boussinesq approximation which relates the Reynolds Stress (the correlation of velocity-velocity fluctuation) to the production of mean velocity gradient and turbulence viscosity. Devolder et al. [6][7] developed the buoyancy modified $k-\omega$ and $k-\omega$ SST model and his code is available on the Github[9]. Following this research, the author also modified the code of $k-\omega$ and $k-\omega$ SST turbulence model in OpenFOAM, but the authors' numerical experiments show that the Devolder's $k-\omega$ SST implementation suffers from the numerical instability. This numerical instability is characterized by the sudden increase of turbulent viscosity. Careful inspection on the results show that this erroneous spikes in the eddy-viscosity is related to the dissipation rate, ω , going to zero in some grid cell near the free surface. According to the study of Menter on $k-\omega$ SST model[10], a small disturbances in the source term of TKE can lead to erroneous spikes in the eddy-viscosity. Similarly, our additional buoyancy term in the TKE could also lead to this instability. To prevent this from happening, a limiter is simply added to the buoyancy term in the TKE equation.

Besides, the wave damping crisis still exists beneath the wave surface because of the shear production term in TKE. This issue was originally described by Mayer and Madsen [11] who strictly proved the conditional instability of the $k-\omega$ closure model. Substituting the velocity field from the potential wave theory into the production term of the TKE equation results in a no-zero value by which the k will increase exponentially. They also tried to solve this problem by using the mean rotation instead of the original strain rate in the production terms of k . This alteration greatly suppresses the unphysical growth of the eddy-viscosity and hence improved predictions of the wave breaking point. But the following research by Larsen and Fuhrman [12] proved that there are several fundamental deficiencies with Mayer and Madsen's modification [11]. This modification actually delays the growth of the eddy-viscosity, rather than completely avoids it. And this replacement is a direct violation of the Boussinesq approximation and has a negative effect on performance of model in the shear flow region. To eliminate this anomaly

fundamentally, Larsen and Fuhrman [12] introduced a limiter on turbulent viscosity provided by the ratio of rotation and strain rate. This modification will be activated to restrain the turbulence in the potential flow region while remains passive in sheared flow region. Through this way, the wave decay can be prevented and the capability of turbulence model for shear flow is preserved in the same time. Larsen's code is developed in the frame of OpenFOAM and available on the Github[13] named as stable model.

In this study, k - ω SST model are improved by both adding the buoyancy term and introducing the limiter on turbulent viscosity following the methods mentioned above. The main contribution of the present study is to eliminate the numerical instability caused by the buoyancy term. The present paper is organized as follows: In section 2, the theories of buoyancy modified model and Larsen's stable model will be briefly reviewed and the cause of numerical instability is presented. A new limiter imposed on buoyancy term is proposed to remedy this instability. In section 3, the robust model is validated by conducting two kinds of simulations: simple progressive wave trains and spilling breaking waves. Finally, a brief conclusion is given.

2. MATHEMATICAL AND NUMERICAL MODELLING

2.1 The standard k - ω SST model and production limiter.

The equation of incompressible k - ω SST model [10] originally implemented in OpenFOAM are:

$$\frac{\partial \rho k}{\partial t} + \frac{\partial \rho u_i k}{\partial x_i} = \tilde{P}_k - \beta^* \rho k \omega + \frac{\partial}{\partial x_i} \left[(\mu + \sigma_k \mu_t) \frac{\partial k}{\partial x_i} \right] \quad (1)$$

$$\frac{\partial \rho \omega}{\partial t} + \frac{\partial \rho u_i \omega}{\partial x_i} = \frac{\alpha}{\mu_t} \rho \tilde{P}_k - \beta \rho \omega^2 + \frac{\partial}{\partial x_i} \left[(\mu + \sigma_\omega \mu_t) \frac{\partial \omega}{\partial x_i} \right] + 2(1 - F_1) \rho \sigma_{\omega 2} \frac{1}{\omega} \frac{\partial k}{\partial x_i} \frac{\partial \omega}{\partial x_i} \quad (2)$$

where the turbulent eddy-viscosity is defined as follows:

$$\mu_t = \frac{\alpha_1 k}{\max(\alpha_1 \omega; S \cdot F_2)} \quad (3)$$

The detailed parameters definition can be find in[10]. The only term should be paid attention here is the production term \tilde{P}_k defined as:

$$\tilde{P}_k = \min(P_k, 10 \cdot \beta^* k \omega) \quad \text{where} \quad P_k = \mu_t \frac{\partial U_i}{\partial x_j} \left(\frac{\partial U_i}{\partial x_j} + \frac{\partial U_j}{\partial x_i} \right) \quad (4)$$

From the definition, it is clear that \tilde{P}_k is a production limiter in the SST model. This limiter is used to prevent the erroneous spikes in the eddy-viscosity [10]. In this work, this limiter is extended to limit the buoyancy term which will be introduced in the TKE equation. The justification of this production limiter is given by Menter [10]. Through the experience with two-equation turbulence models, he found that in regions of low values of ω , small disturbances in the shear strain rate can lead to erroneous spikes in the eddy-viscosity in the freestream or near the boundary layer edge. In order to understand the effect, the transport equation for the

eddy-viscosity is derived from the Eqn. 1-3(In this discussion, the production term in Eqn. 1 and 2 should be P_k instead of the production limiter \tilde{P}_k):

$$\frac{D\mu_t}{Dt} = \frac{1}{\omega} \frac{Dk}{Dt} - \frac{k}{\omega^2} \frac{D\omega}{Dt} = (1-\alpha) \frac{P_k}{\omega} + \dots = (1-\alpha) \frac{\mu_t}{\omega} \frac{\partial U_i}{\partial x_j} \left(\frac{\partial U_i}{\partial x_j} + \frac{\partial U_j}{\partial x_i} \right) + \dots \quad (5)$$

If ω goes to zero and μ_t is finite, the production term for the eddy-viscosity goes to infinity for small disturbances in the strain rate. A simple way to prevent this from happening is to limit the production term by the following formula:

$$P_k = \min(P_k, 10D_k) \quad (6)$$

where D_k is dissipation term in Eqn.1 define as $\beta^* \rho k \omega$.

This limiter has been very carefully tested by Menter[14] and it was found that even for complex flows the ratio of P_k/D_k reaches in maximum levels of only about two inside shear layers. This production limiter does not change the solution but only eliminates the occurrence of spikes in the eddy-viscosity due to numerical "wiggles" in the shear-strain tensor.

In our followed study, the buoyancy term will induce the spikes in the eddy-viscosity just like the shear-strain tensor did.

2.2 The buoyancy modification for k - ω SST model and its robustness

According to the Van Maele and Merci [8], a buoyancy term is needed in order to take the varying density around the air-water interface into account. The buoyancy term is only included in the TKE equation based on the SGDH. Following Devolder et al. [6], the buoyancy term is:

$$Gb = -\frac{u_t}{\sigma_t} \frac{\partial \rho}{\partial x_j} g_j \quad (7)$$

where ρ is density, g is gravitational acceleration and σ_t is constant.

Adding this buoyancy term to the right hand side of Eqn. 1, The TKE equation of buoyancy-modified k - ω SST model becomes:

$$\frac{\partial \rho k}{\partial t} + \frac{\partial \rho u_i k}{\partial x_i} = \tilde{P}_k + G_b - \beta^* \rho k \omega + \frac{\partial}{\partial x_i} \left[(\mu + \sigma_k \mu_t) \frac{\partial k}{\partial x_i} \right] \quad (8)$$

which is the same with Eqn. 19 in [7].

But this buoyancy term will induce the numerical instability. To indicate this effect, Eqn .5 is rewritten by Eqn. 8:

$$\frac{D\mu_t}{Dt} = \frac{1}{\omega} \frac{Dk}{Dt} - \frac{k}{\omega^2} \frac{D\omega}{Dt} = \frac{\mu_t}{\omega} \left[(1-\alpha) \frac{\partial U_i}{\partial x_j} \left(\frac{\partial U_i}{\partial x_j} + \frac{\partial U_j}{\partial x_i} \right) - \frac{1}{\sigma_t} \frac{\partial \bar{\rho}}{\partial x_j} \cdot g_j \right] = \frac{\mu_t}{\omega} p_k' \quad (9)$$

Similar to the Eqn.5, if ω goes to zero, eddy-viscosity goes to infinity for small disturbances in the p_k' .

To prevent this from happening, Eqn.6 is modified in this work to limit the production term by the following formula:

$$P_k = \min(P_k - G_b, 10D_k) \quad (10)$$

This new limiter should be further tested and ensure that the ratio of $(P_k - G_b)/10D_k$ is far less than 1.

2.3 Larsen's stabilized k - ω SST model

Simply adding the buoyancy term does not solve the over-prediction of turbulence level fundamentally. Rather, Mayer and Madsen [11] attributed the widespread over-prediction of turbulence in RANS models of surface waves to its unstable when applied to a region of potential flow beneath surface waves. Inspired by this research, Larsen and Fuhrman [12] further proved that k - ω SST model is unconditionally unstable for the conditions of potential flow progressive waves. Inserting velocity given by Stokes first-order wave theory into source term of TKE equation, after period averaging, and depth averaging, the source term is not zero. Subsequently, k and μ_t growing exponentially at certain growth rate. To prevent it from happening, not only the buoyance term should be added in TKE equation, but also the eddy-viscosity should be redefined by:

$$\mu_t = \frac{a_1 k}{\max(a_1 \omega, F_2 \sqrt{p_0}, a_1 \lambda_2 \frac{\beta}{\beta^* \alpha} \frac{p_0}{p_\Omega} \omega)} \quad (11)$$

where $p_0 = 2S_{ij}S_{ij}$, $S_{ij} = \frac{1}{2}(\frac{\partial u_i}{\partial x_j} - \frac{\partial u_j}{\partial x_i})$, $p_\Omega = 2\Omega_{ij}\Omega_{ij}$, $\Omega_{ij} = \frac{1}{2}(\frac{\partial u_i}{\partial x_j} - \frac{\partial u_j}{\partial x_i})$ and $\lambda_2 = 0.05$

Thus, in a region of nearly potential flow where $p_0 \gg p_\Omega$, the new addition to the limiter in (16) will be active. Larsen and Fuhrman [12] suggested that the new closure model will be formally stable as $p_\Omega/p_0 \leq \lambda_2$. Instead, in other more complicated sheared flow regions, p_Ω and p_0 will be the same order of magnitude and the new limiter will remain inactive.

3. NUMERICAL TESTS FOR SURFACE WAVES

In the following two subsections, both Devolder's model and Larsen's model with our new limiter are tested. Two kinds of tests are conducted: a simple progressive wave train and spilling breaking wave. The first simulation is used to demonstrate the stable performance of new model without the sheared flow involved. The latter is to evaluate performance of the new model in a more physically complex situation. In all simulations, the time step has been adjusted such that a maximum Courant number $Co=0.05$ is always guaranteed to ensures accurate velocity kinematics and reduce the numerical dissipation. Our in-house solver naoe-FOAM-SJTU[15][16] is used to solve the governing equations combining with waves2FOAM[2]

toolbox for wave generation and absorption. In our solver, relaxation zones blend the government equation implicitly instead of blending the volume fields explicitly before solving the government equation as suggested by[17]. In our simulations, temporal term is discretized by a second-order backward scheme. Convection terms are discretized using a blend of central difference and upwind schemes. Remaining schemes are second-order accurate central difference schemes.

3.1 Simulation of simple progressive wave train

In this subsection, computed results will be presented for the propagation of surface wave. This is a potential flow dominated case and should ideally be passed by the new models mentioned above. A Stokes first-order wave with wave period $T=1.2s$ and wave height $H=0.12m$ is simulated in 2D grids. Mesh resolution guarantees the horizontal and vertical size $\Delta x=\Delta z=0.01m$.

Layout of the computational domain is showed in Figure 1. Two relaxation zones are set near the inlet and outlet to generate/absorb the wave. To demonstrate the performance of the turbulence closure relative to standard approaches, we will compare computed results from the laminar model, standard $k-\omega$ SST model[10], Devolder's buoyancy modified $k-\omega$ SST model[7] with our new limiter in Eqn. 10, and Larsen's stabilized $k-\omega$ SST model[12] also with our new limiter.

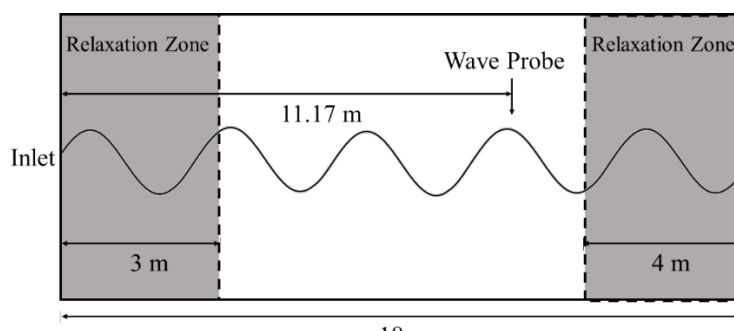


Figure 1 Layout of the computational domain for simulation of simple progressive wave

To demonstrate the necessity of our new limiter in Eqn. 10, this progressive wave simulation is first conducted using Devolder's buoyancy model[17] without our new limiter. This calculation collapsed after around 100 time-steps. At several time-steps before the simulation going divergence, a spike value of turbulent viscosity, μ_t , is presented in one cell as showed in Figure 2. In this cell, the value of ω is very small where a small disturbance of p'_k will leading to a large growth of μ_t according to Eqn. 9. It shows that Devolder's original buoyancy model cannot complete this simulation.

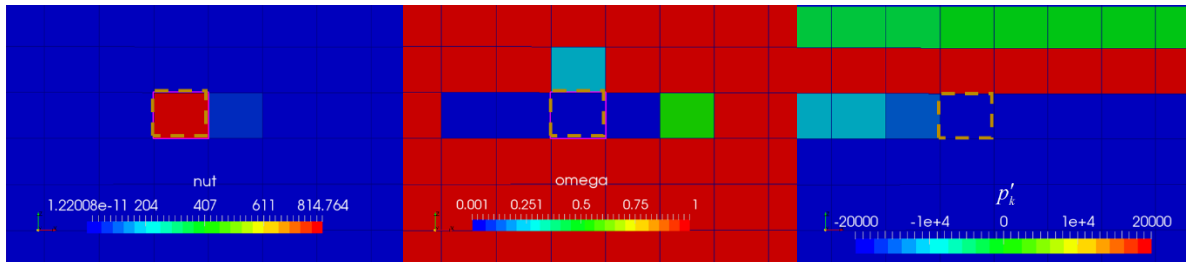


Figure 2 The value of turbulent viscosity μ_t , dissipation rate ω and p'_k

In the following content, both Devolder’s model and Larsen’s model are combined with our new limiter in default. For the sake of brevity, the new limiter will not be mentioned explicitly in the model’s name.

The time history of surface elevation at wave probe is shown in Figure 3. The position of wave probe is 11.17 m away from the inlet boundary as shown in Figure 1. As we can see, the standard $k-\omega$ model has a very different performance from other models. The wave height is terribly decayed when the wave approach to wave probe, while the performance of Devolder’s model and Larsen’s model is almost identical to the laminar model. All improved models maintain a nearly constant wave height. But a close look at the peak values of wave height shows that Devolder’s model causes a slight decay comparing to the Larsen’s model (as shown in the enlarged part of Figure 3). This result is consistent with our expectation since Larsen’s model not only include the buoyancy term, but also stabilize the turbulent viscosity in the potential flow region in waves. The success of this simple wave simulation proves that our new limiter ensures the numerical stability while maintains the performance of the improved turbulence models in potential flow dominated case.

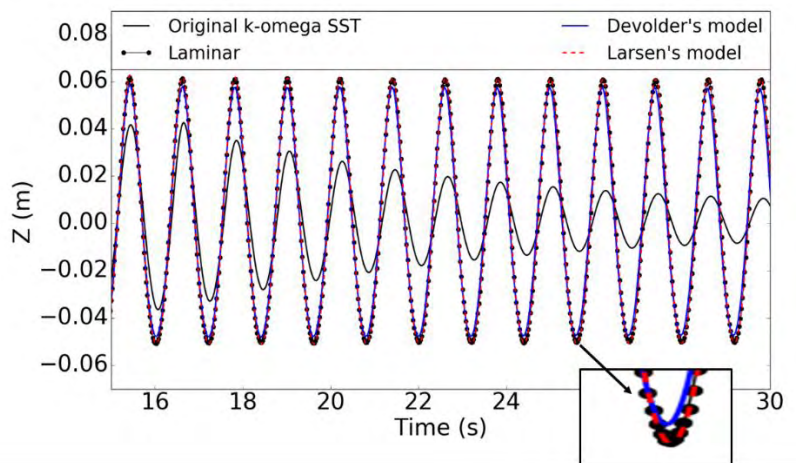


Figure 3 Time histories of surface elevations in the simple progressive wave train simulation using laminar model, $k-\omega$ SST model, Devolder’s model and Larsen’s model

3.2 Simulation of spilling breaking wave

Given that our new limiter passes the simple wave propagation, the new model should be tested for more complex situations in the expectation that our limiter can maintain the numerical

stability and at the same time keep the performance of the improved model. In this subsection, the simulations of the spilling breaking wave experiment[18] is conducted using standard $k-\omega$ SST model and Larsen’s model.

The computational domain for these simulations consists of a flat region with water depth $D=0.4$ m, connected to a 1:35 slope. The waves with wave period $T=2$ s and wave height $H=0.25$ m are generated on the flat region and wave will break as it propagates along the slope. Figure 4 demonstrates the layout of the computational domain. The bottom is modelled as a smooth solid wall on which wall functions are activated. A continuous wall function based on Spalding’s law wall function is implemented for the turbulent viscosity. The initial values for k and ω in the computational domain are set to $2.28e-7$ m^2/s^2 and 2.1 s^{-1} , respectively.

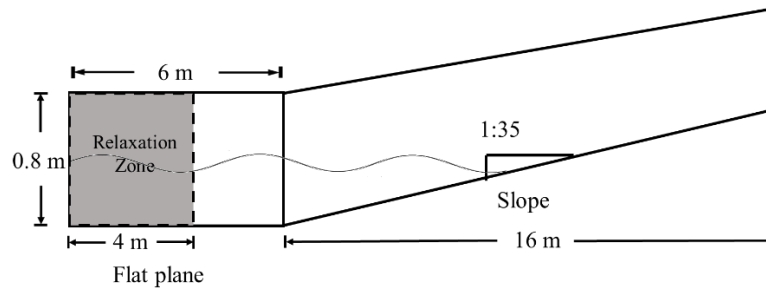


Figure 4: Layout of the computational domain for simulation of the spilling breaking

The numerically obtained surface elevations, undertow profiles and TKE profiles are presented and compared to experimental measurements from Ting and Kirby[18] for spilling breaking. Each numerical simulation ran for 120 wave periods to establish stable conditions in the computational flume. All the results presented in this section are time averaged using the last 20 waves of the 120 waves simulated.

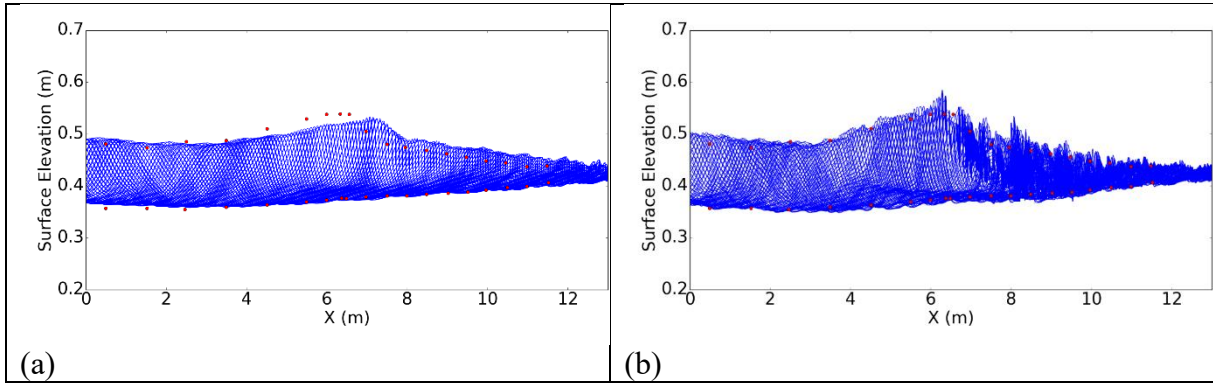


Figure 5: Comparison of modelled (lines) and measured (red dot, from Ting and Kirby[18]) surface elevation envelopes. (a) the standard $k-\omega$ SST model (b) Larsen’s $k-\omega$ SST model

Figure 5 shows the comparison of the computed and experimental surface elevation envelopes as well. It can be seen that the standard model delays the breaking point around $x=6.5$ m and overpredicts the surface elevation in the subsequent surf zone. On the contrary, Larsen’s model better captures the horizontal position of the breaking point and the surface elevation at breaking point and its subsequent decay in the surf zone have a well agreement with experiment.

As a result, the Larsen’s model has better performance in terms of surface elevations for the case of spilling and our new limiter does not have the adverse effect to this advanced model.

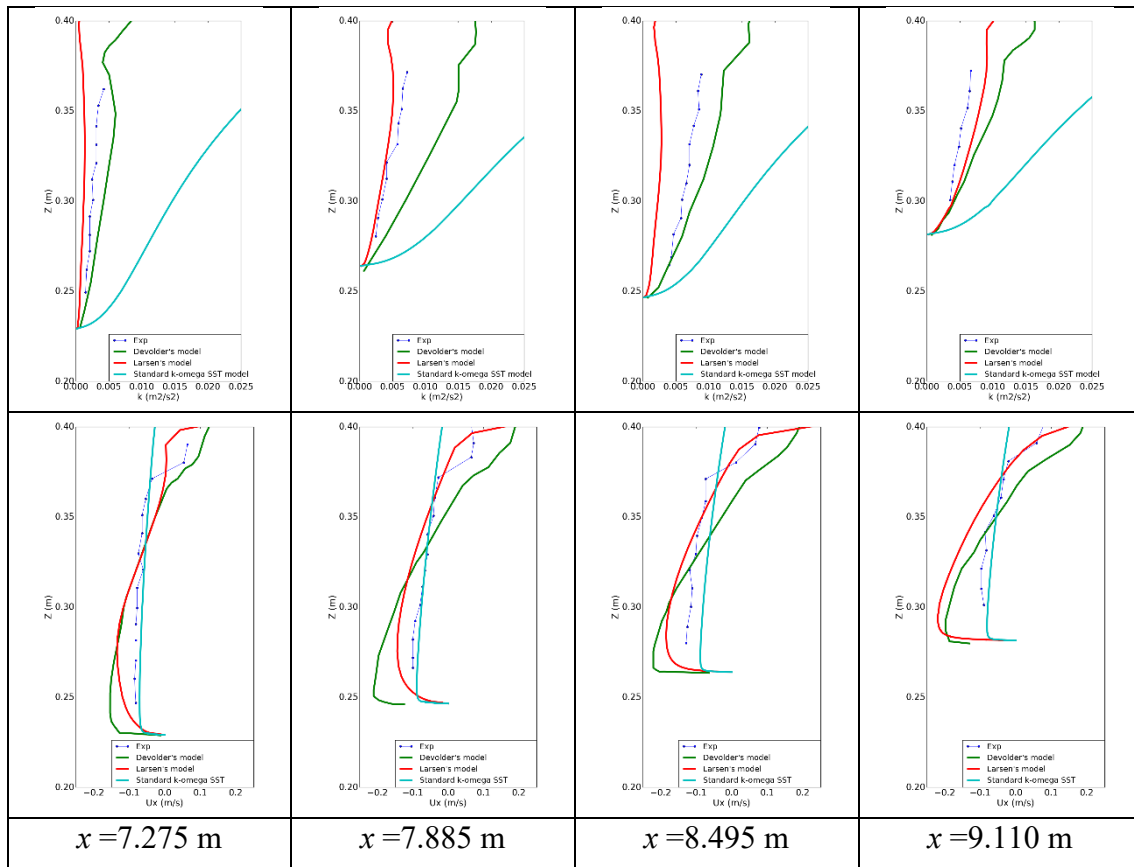


Figure 6: Comparison of modelled (lines) and measured (line with dot) time average turbulent kinetic energy \bar{k} profiles and horizontal velocity \bar{u} at $x = 7.275 \text{ m}$, $x = 7.885 \text{ m}$, $x = 8.495 \text{ m}$, $x = 9.110 \text{ m}$.

Figure 6 presents both measured and simulated undertow profiles at locations $x = 7.225\text{m}$, $x = 7.885 \text{ m}$, $x = 8.495 \text{ m}$ and $x = 9.110 \text{ m}$ (the coordinate positions of these locations are same as the experiment from Ting and Kirby[18]). All these locations locate in the surf zone. Along those vertical profiles, the calculated time averaged horizontal velocity \bar{u} and time averaged turbulent kinetic energy \bar{k} are analyzed. In Figure 6, the results of Devolder’s model are directly from his paper[7]. As might be expected, the standard $k-\omega$ SST models severely over-predict the turbulence. In contrast, Larsen’s model predicts lower turbulent kinetic energy much more in line with the experiments.

In Figure 6, the velocity profiles computed with Larsen’s model remain qualitatively correct in structure, but become exaggerated. In contrast, the standard model actually results in more accurate velocity profiles. This unexpected result is very similar to the calculation obtained from [7] [12] indicating that it is not caused by our new limiter. Larsen and Fuhrman[12] argued that the better performance of standard model on velocity profile should likely be regarded as fortuitous, given that these models did not result in (i) properly spilling waves or (ii) correct turbulence/undertow structure at many positions leading up to the inner surf i.e. a correct qualitative description of the breaking process is lacking with these models. And very similar

exaggerated velocity results were also obtained by Christensen[19] using more accurate LES model.

To further illustrate the difference between the models. The computed snapshots depicting the surface and non-dimensional eddy-viscosity u_t/u in one period are showed in Figure 7. As can be seen, the standard SST model gives over-predicted turbulence model both in the pre-breaking and surf zone. According to the experiment[18], these high values are nonphysical and should not be presented prior to breaking, where nearly potential flow is dominated. These artificial high values will in further contaminate the results of surf zone. Conversely, the results using the Larsen's model surpasses the increase of eddy-viscosity in the nearly protentional region prior to breaking. Meanwhile the eddy-viscosity is rightly predicted in the bottom of boundary layer and surf zone. This demonstrates that Larsen's model with our new limiter give a more reasonable prediction over standard models while the numerical stability is guaranteed.

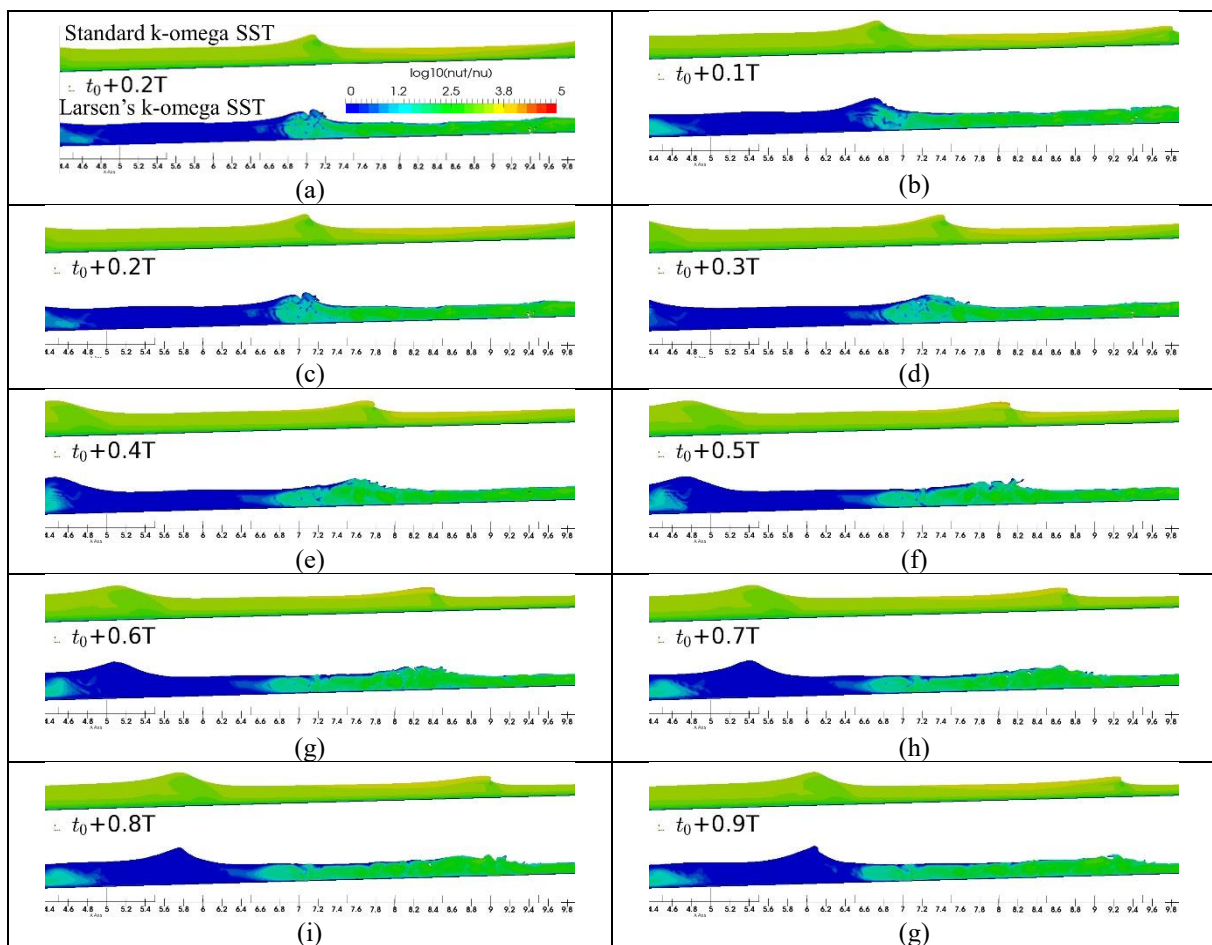


Figure 7: Numerically obtained snapshots around the breaking point of the turbulent kinematic viscosity and free surface at different time phases using the standard $k-\omega$ SST (on the upper side) and Larsen's $k-\omega$ SST model (on the lower side).

4. CONCLUSIONS

In this study, a new source term limiter is proposed to suppress the numerical instability induced by buoyancy term in $k-\omega$ SST model. The reason caused this instability is analyzed by

deriving the transport equation for the eddy-viscosity derivation. It shows that a small disturbances of buoyancy term will induce spike value of eddy-viscosity when the dissipation rate ω goes to zero. To stabilize this instability, the buoyance term compared with the original source term is limited to smaller than the 10 times the dissipation term. The effectiveness of coefficient 10 is validated by two kinds of numerical tests: a simple progressive wave train and spilling breaking wave. The first simulation is used to demonstrate the stable performance of new model without the sheared flow involved. The latter is to evaluate performance of the new model in a more physically complex situation. In summary, our new limiter does not affect the advantage of the buoyance term, and in the meantime eliminates the occurrence of spikes in the eddy-viscosity.

5. REFERENCES

- [1] Xie, Z. (2013) Two-phase flow modelling of spilling and plunging breaking waves. *Applied Mathematical Modelling*. 37 (6), 3698–3713.
- [2] Jacobsen, N.G., Fuhrman, D.R., and Fredsøe, J. (2012) A wave generation toolbox for the open-source CFD library: OpenFoam®. *International Journal for Numerical Methods in Fluids*. 70 (9), 1073–1088.
- [3] Brown, S.A., Greaves, D.M., Magar, V., and Conley, D.C. (2016) Evaluation of turbulence closure models under spilling and plunging breakers in the surf zone. *Coastal Engineering*. 114 177–193.
- [4] Lin, P. and Liu, P.L.-F. (1998) A numerical study of breaking waves in the surf zone. *Journal of Fluid Mechanics*. 359 239–264.
- [5] Bradford Scott F. (2000) Numerical Simulation of Surf Zone Dynamics. *Journal of Waterway, Port, Coastal, and Ocean Engineering*. 126 (1), 1–13.
- [6] Devolder, B., Rauwoens, P., and Troch, P. (2017) Application of a buoyancy-modified k- ω SST turbulence model to simulate wave run-up around a monopile subjected to regular waves using OpenFOAM®. *Coastal Engineering*. 125 81–94.
- [7] Devolder, B., Troch, P., and Rauwoens, P. (2018) Performance of a buoyancy-modified k- ω and k- ω SST turbulence model for simulating wave breaking under regular waves using OpenFOAM®. *Coastal Engineering*. 138 49–65.
- [8] Van Maele, K. and Merci, B. (2006) Application of two buoyancy-modified turbulence models to different types of buoyant plumes. *Fire Safety Journal*. 41 (2), 122–138.
- [9] <https://github.com/BrechtDevolder-UGent-KULeuven/buoyancyModifiedTurbulenceModels>
- [10] Menter, F.R., Kuntz, M., and Langtry, R. (2003) Ten years of industrial experience with the SST turbulence model. *Turbulence, Heat and Mass Transfer*. 4 (1), 625–632.
- [11] Mayer, S. and Madsen, P.A. (2001) Simulation of Breaking Waves in the Surf Zone using a Navier-Stokes Solver. in: *Coast. Eng. 2000*, American Society of Civil Engineers, Sydney, Australia. pp. 928–941.
- [12] Larsen, B.E. and Fuhrman, D.R. (2018) On the over-production of turbulence beneath surface waves in Reynolds-averaged Navier–Stokes models. *Journal of Fluid Mechanics*. 853 419–460.
- [13] https://github.com/BjarkeEltardLarsen/RANS_stableOF50.
- [14] Menter, F. (1993) Zonal two equation kw turbulence models for aerodynamic flows. in: *23rd Fluid Dyn. Plasmadynamics Lasers Conf.*, p. 2906.
- [15] Cao, H. and Wan, D. (2017) Benchmark computations of wave run-up on single cylinder and four cylinders by naoe-FOAM-SJTU solver. *Applied Ocean Research*. 65 327–337.
- [16] Shen, Z., Wan, D., and Carrica, P.M. (2015) Dynamic overset grids in OpenFOAM with application to KCS self-propulsion and maneuvering. *Ocean Engineering*. 108 287–306.
- [17] Jasak, H., Vukčević, V., and Gatin, I. (2015) Numerical simulation of wave loading on static offshore structures. in: *CFD Wind Tidal Offshore Turbines*, Springer, pp. 95–105.
- [18] Ting, F.C.K. and Kirby, J.T. (1994) Observation of undertow and turbulence in a laboratory surf zone. *Coastal Engineering*. 24 (1–2), 51–80.
- [19] Christensen, E.D. (2006) Large eddy simulation of spilling and plunging breakers. *Coastal Engineering*. 53 (5–6), 463–485.

INTERNAL FLOW-INDUCED INSTABILITY ANALYSIS OF CATENARY RISERS

MARINE 2019

KONSTANTINOS N. BAKIS AND NARAKORN SRINIL

Marine, Offshore & Subsea Technology Group, School of Engineering, Newcastle University,
Newcastle upon Tyne, NE1 7RU, United Kingdom

konstantinos.bakis@ncl.ac.uk; narakorn.srinil@ncl.ac.uk; www.muffinsproject.org.uk

Key words: Catenary Riser, Internal Flow, Finite Element Method, Instability Analysis

Abstract.

Offshore production and export risers in deep-water oil and gas applications are highly slender and flexible cylindrical structures subject to complex environmental and operational loading conditions. In particular, catenary risers having variable curvature have been widely considered by industry as a technologically and economically viable solution for deep waters. Nevertheless, the mechanism of dynamic instability of curved bendable pipes transporting flows has not been properly investigated in the literature despite such practical and theoretical importance. In this study, the dynamic response and stability of catenary risers conveying internal flows are investigated by using a linearized finite element-based continuum pipe model. The governing fluid-structure interaction equations are derived using Hamilton's principle and formatted into a generalized eigenvalue form in order to assess its stability for varying internal flow speeds. This procedure elucidates the contribution of the Centrifugal and Coriolis related terms for the onset of divergence and flutter unstable modes. It is shown that the pipe's tension to bending rigidity ratio plays a catalytic role in the occurrence and evolution of intermodal coupling of the flutter modes in post-divergence regime. Theories and numerical strategies present in this study are being extended to the multiphase flow-induced vibration applications.

1 INTRODUCTION

Marine risers are widely used for offshore oil and gas transportation in deep waters and their operability has a direct impact on the life cycle and economics of the field. Because of its inherent flexibility and tight horizontal offset constraints, the riser comprises the most sensitive component within the oil and gas extraction system. It is therefore that the subject of understanding the riser's linear or nonlinear dynamic response has attracted the interest of the scientific community.

A marine riser, transporting crude oil and natural gas is simply supported at normal operation conditions. The dynamics of a pinned-pinned configuration has been extensively studied with regard to external loading and the basic mechanism of vortex induced vibrations (VIVs) is well documented in the literature [1]. In that regard various numerical [2] and computational [3] investigations have been performed in the past two decades. The dynamic response of a flexible riser due to internal single-phase flows has been formulated using

different approaches for planar vibrations, see Semler et al. [4] and Lin et al. [5], while there are also works focusing on the 3D dynamic response behavior [6].

Deep-water ocean exploration expansion constantly demands for longer and slenderer risers, which inherently exhibit new dynamic features [7, 8]. A different modeling methodology is based on elastica theory. The extensible elastica has been well established in previous works [9, 10]. Moreover, the fluid plug flow model has been extended to include the effect of pulsatile flow-induced vibrations [11,12,13,14]. Extensibility effects have been highlighted by Chucheepsakul et al. [15] and Monprappusorn et al. [11].

Dynamic response attributed to internal slug flows in subsea piping systems is quickly becoming an issue of increasing concern due to its role in fatigue related failures. The slug flow regime potentially generates more pronounced structural vibrations due to the fluctuation of density, velocity and pressure of the transported fluid mixture [16]. Patel and Seyed [17] were among the first to formulate the mathematical expressions for the time-varying flow in a flexible riser in the 2-D plane. Their model, however, was a simplified version of internal slug flow excluding a lot of the fluid-structure complexity. It is only recently that the importance of slug flows to the riser dynamics has been appreciated in the academic community [18,19]. So far investigations have demonstrated that slug flows give rise to increased normal and axial responses contributing to higher dynamic tension, curvature and bending stresses. Further experimental and analytical works should be carried out to better understand the dynamic interaction of internal and external flow on a flexible catenary pipe as well as other operational impacts.

The aim of this fundamental work is to make use of a finite element formulation for modeling the effects of single-phase flow on the stability boundaries and dynamic response of deep-water catenary pipes. The current work is the initial stage for incorporating the full 3D nonlinear behavior of a flexible liquid-conveying pipe while subjected to space-time varying external flow excitations. Previous research on the stability limits of pipes [20,21] has focused on simple straight pipe configurations either pinned-pinned or cantilevered. It is believed by the authors that the nature and stability mechanism of a flexible riser with varying curvature has been neglected in the literature. Consequently, this paper will focus on the investigation of different patterns of instability which influence the behavior of the stability limits by formulating the catenary pipe dynamics using a new procedure.

2 MODELING PROCESS

2.1 Static configuration of catenary risers

The riser is considered to be a flexural sagged cable-like elastic structure and its planar configuration only due to the effective self-weight is considered here for convenience. Bending rigidity is neglected for the static analysis but considered for the vibrational response from the equilibrium position. The static profile of an SCR (steel catenary riser) is governed by the catenary configuration given by Equation [1]. This is a plausible simplification because of the pinned connections at the boundaries and due to the fact that SCR curvatures are relatively small [2].

$$\frac{d^2 y}{dx^2} = -\frac{W_E}{H_w} \sqrt{1 + \left(\frac{dy}{dx}\right)^2} \quad (1)$$

W_E is the computed effective weight accounting for the weight of the riser in air, the buoyancy of the riser element, the weight of the internal flow and the added mass effect of the pipe surrounding sea-water. H_w is the horizontal component of the riser tension which is spatially constant. Integrating Equation (1) twice and applying appropriate boundary conditions the static riser shape is obtained. The corresponding riser tension, neglecting the shear component, can also be derived accordingly [22]. Thus, for given W_E , H_w and specified horizontal and vertical pipe projections X_H, Y_H , the total length, catenary geometry and static tension along the pipe is straight forwardly determined. Current flow forces on the pipe are neglected in this work as the focus lies in the internal flow-induced vibrations.

2.2 Fluid-pipe dynamic equations

Consider a straight-pipe element subject to small amplitude vibrations. A generic pipe-fluid element has axial and transverse displacements $\bar{u}(x, t)$ and $\bar{w}(x, t)$, respectively. Let the distance measured along the pipe's local coordinate system be \bar{x} , while the vertical coordinate be \bar{z} . As the fluid flows along the curve described by the centerline, its motion is affected by the vertical acceleration, angular acceleration and changing curvature. An element of fluid being transported along the pipe has constant velocity U tangent to the pipe axis and velocity $\dot{\bar{w}} = \partial \bar{w} / \partial t$ in the vertical direction. For a general pipe planar configuration, the velocity of the center of a fluid element along the curvilinear coordinate s is given by the following expression [20]:

$$\mathbf{V}_f = \left(\frac{\partial}{\partial t} + U \frac{\partial}{\partial s} \right) (x\mathbf{i} + z\mathbf{k}) = \frac{D\mathbf{r}}{Dt} \quad (2)$$

where, \mathbf{r} is the position vector to a point measured from the origin and $\frac{D(\)}{Dt}$ is the material derivative of the fluid element. Assuming that the curvilinear pipe is modeled using inter-connecting straight elements, the kinetic energy of the fluid of a straight segment of length L in the local coordinate system can be written as:

$$\bar{T}_f = \frac{m_f}{2} \int_0^L \left(\frac{\partial \bar{u}}{\partial t} + U \frac{\partial \bar{u}}{\partial \bar{x}} \right)^2 + \left(\frac{\partial \bar{w}}{\partial t} + U \frac{\partial \bar{w}}{\partial \bar{x}} \right)^2 d\bar{x} \quad (3)$$

The kinetic energy of the pipe is simply given by:

$$\bar{T}_p = \frac{m_p}{2} \int_0^L (\dot{\bar{u}}^2 + \dot{\bar{w}}^2) d\bar{x} \quad (4)$$

where, m_f is per unit length mass of the fluid and m_p is the mass density of the pipeline,

respectively. The upper dash denotes the local system in the orientation of the individual straight element. The potential energy of a straight pipe segment because of bending, axial strain and tension is given by the following formula [21]:

$$\bar{U} = \frac{1}{2} \int_0^L EA_p (\boldsymbol{\varepsilon}_T + \boldsymbol{\varepsilon}_x)^2 d\bar{x} + \frac{1}{2} \int_0^L EI_p \bar{w}''^2 d\bar{x} \quad (5)$$

where,

$$\boldsymbol{\varepsilon}_T = \frac{\bar{T}}{EA_p}, \quad \boldsymbol{\varepsilon}_x = \bar{u}' + \frac{1}{2} \bar{u}'^2 \quad (6)$$

The overdot and prime denote the derivatives with respect to time t and local spatial coordinate \bar{x} , respectively. Substituting Equation (6) to (5) and neglecting some higher order terms we get the expression:

$$\bar{U} = \frac{1}{2} \int_0^L \left[\bar{T} [\bar{u}'^2 + 2\bar{u}'] + EA_p \bar{u}'^2 \right] d\bar{x} + \frac{1}{2} \int_0^L EI_p \bar{w}''^2 d\bar{x} \quad (7)$$

A_p, I_p are the second moment of area and the mass density of the pipeline, respectively.

2.3 Effect of cable tension on the system dynamics

In this work the contribution of cable tension on the dynamic equations of motion is considered by referring to Ghaffar's formulation [23] for a uniform section cable under uniform loading. The model stays within linear theory by considering small displacements from the position of the static catenary equilibrium. The analysis restricts its attention to small vibration response in the vertical plane. Let H_w be the horizontal component of cable tension given by the equations of the catenary configuration [22]. $H(t)$ is the cable tension caused by inertia forces. It is assumed that $H(t)$ is small compared to H_w or $H_w + H(t) \approx H_w$. Vibration damping of the structure is neglected at this stage.

As a result of small, free vibrations about the position of static equilibrium, the horizontal component of tension, H_w will change to $H_w + H(t)$ and the differential length of the cable ds will increase to $ds + \Delta ds$. The potential energy of the cable element is then expressed as:

$$dU_t = \left\{ [H_w + H(t)] \frac{ds}{dx} \right\} \cdot \Delta(ds) - W_E w \cdot (ds) \quad (8)$$

where Δds is the pipe stretch of the differential length ds and w is the vertical vibrational displacement in the direction of gravity. The first term in Equation (8) is the strain energy stored in the element ds and is equal to the average force $\left[H_w + \frac{1}{2} H(t) \right] \frac{ds}{dx}$ times the pipe

stretch $\Delta(ds)$. The factor $\frac{1}{2}$ is needed due to the fact that $H(t)$ increases from zero to its

maximum value and $\frac{ds}{dx}$ is the cosine of the inclination angle. The second term represents the gravity energy, i.e., the potential energy loss due to the lowered position of the effective load. Integrating Equation (8) and following several differential calculus manipulations leads to the

following equation:

$$U_r(t) = \frac{1}{2} \left\{ H_w \int_0^{x_H} \left(\frac{\partial w}{\partial t} \right)^2 dx + H(t) \left[\int_0^{x_H} \left(\frac{\partial w}{\partial x} \right) \left(\frac{\partial y}{\partial x} \right) dx + \frac{1}{2} \int_0^{x_H} \left(\frac{\partial w}{\partial x} \right)^2 dx \right] \right\} \quad (9)$$

To bring Equation (9) in a more convenient form, we make use of the cable equation which relates the stretching of the cable element to the geometric displacements which it undergoes [24]:

$$\frac{H(t)L_e}{EA_p} = \int_0^{x_H} \left(\frac{\partial w}{\partial x} \right) \left(\frac{\partial y}{\partial x} \right) dx + \frac{1}{2} \int_0^{x_H} \left(\frac{\partial w}{\partial x} \right)^2 dx \quad (10)$$

$L_e = \int_0^{x_H} \left(\frac{ds}{dx} \right)^3 dx$ is the virtual length of the cable. Equation (9) then becomes:

$$U_r(t) = \frac{1}{2} H_w \int_0^{x_H} \left(\frac{\partial w}{\partial t} \right)^2 dx + \frac{1}{2} \frac{H^2(t)L_e}{EA_p} \quad (11)$$

The second term of the above equation expresses that part of potential energy stored elastically in the cable, i.e. strain energy of the cable. The first term containing the constant H_w represents the potential energy resulting from the elevation of the cable. In this analysis the cable is considered deformable but inextensible.

The differential equations of motion for catenary riser as well as the correct number of boundary conditions can be derived using Hamilton's principle given by the integral form:

$$\int_{t_1}^{t_2} (\delta T - \delta U + \delta W) = 0 \quad (12)$$

The total virtual work δW by the flow induced forces is zero because these have been considered in the terms for the kinetic energy of the fluid. The resulting equations of motion are:

$$EI_p \frac{\partial^4 \bar{w}}{\partial x^4} + m_f U^2 \frac{\partial^2 \bar{w}}{\partial x^2} - H_w \frac{\partial^2 w}{\partial x^2} + \frac{W_E}{H_w} H(t) + 2m_f U \frac{\partial^2 \bar{w}}{\partial x \partial t} + (m_f + m_p) \frac{\partial^2 \bar{w}}{\partial t^2} = 0 \quad (13)$$

where,

$$H(t) = \frac{EA_p}{L_e} \left[\int_0^{x_H} \left(\frac{\partial w}{\partial x} \right) \left(\frac{dy}{dx} \right) dx + \frac{1}{2} \int_0^{x_H} \left(\frac{\partial w}{\partial x} \right)^2 dx \right] \quad (14)$$

and in the axial direction,

$$(EA_p + \bar{T}) \frac{\partial^2 \bar{u}}{\partial x^2} + m_f U^2 \frac{\partial^2 \bar{u}}{\partial x^2} + 2m_f U \frac{\partial^2 \bar{u}}{\partial x \partial t} - (m_p + m_f) \frac{\partial^2 \bar{u}}{\partial t^2} = 0 \quad (15)$$

In Equation (13) the cable tension stiffness contribution is considered in the global w coordinate, while the rest is in the element local coordinate \bar{w} . The above methodology takes into account the static stress as well as the effect of vibrational change of riser tension and consequently the finite element eigenvalue analysis to follow determines more accurately the riser's modal characteristics.

2.3 Finite element formulation

The finite element model is formulated by using directly the potential and kinetic energy expressions presented in the previous sections. The displacement field within the element e is then assumed:

$$\{w(x,t)\}_e = \{\mathbf{N}_w\}_e \{\mathbf{d}(t)\}_e, \quad \{u(x,t)\}_e = \{\mathbf{N}_u\}_e \{\mathbf{d}(t)\}_e \quad (16)$$

where $\{\mathbf{N}_w\}_e$ and $\{\mathbf{N}_u\}_e$ are standard shape function matrices in local vertical and longitudinal direction of the element.

Substitution of Equation (16) to Equations (3), (4), (7) and (11) and appropriate integrations will produce the mass, stiffness and damping related matrices. Following conventional finite element procedure [25] the discretized equation of motion reads:

$$\{\mathbf{M}\} \ddot{\mathbf{d}}(t) + \{\mathbf{C}_{cor}(U)\} \dot{\mathbf{d}}(t) + \{\mathbf{K}_b + \mathbf{K}_T + \mathbf{K}_{Hw} + \mathbf{K}_{Hu} - \mathbf{K}_{cent}(U)\} \mathbf{d}(t) = \{\mathbf{f}_T\} \quad (17)$$

The element mass matrix $\bar{\mathbf{M}}_e$ consists of the terms resulting from the expressions

$$\{\bar{\mathbf{M}}_w\}_e = (m_p + m_f) \int_0^\ell [\mathbf{N}_w]^T [\mathbf{N}_w] d\bar{x} \quad \text{and} \quad \{\bar{\mathbf{M}}_u\}_e = (m_p + m_f) \int_0^\ell [\mathbf{N}_u]^T [\mathbf{N}_u] d\bar{x} \quad \text{in the local}$$

coordinates. The transformation to global coordinates and matrix assembly follows the standard procedure [25]. The bending stiffness matrix is that of typical Euler-Bernoulli beam

$$\text{element consisting of } \{\bar{\mathbf{K}}_{bw}\}_e = \int_0^\ell EI_p [\mathbf{N}_w'']^T [\mathbf{N}_w''] d\bar{x} \quad \text{and} \quad \{\bar{\mathbf{K}}_{bu}\}_e = \int_0^\ell EA_p [\mathbf{N}_u']^T [\mathbf{N}_u'] d\bar{x}.$$

The centrifugal related terms appear as stiffness terms in the discretized equation of motion with the following form:

$$\{\bar{\mathbf{K}}_{cent}\}_e = \begin{bmatrix} \bar{\mathbf{K}}_{cent,u} = m_f U^2 \int_0^\ell \mathbf{N}_u'^T \mathbf{N}_u' d\bar{x} \\ \bar{\mathbf{K}}_{cent,w} = m_f U^2 \int_0^\ell \mathbf{N}_w'^T \mathbf{N}_w' d\bar{x} \end{bmatrix} = \frac{m_f U^2}{30L} \begin{bmatrix} 30 & 0 & 0 & -30 & 0 & 0 \\ 0 & 36 & 3\ell & 0 & -36 & 3\ell \\ 0 & 3L & 4\ell^2 & 0 & -3\ell & -\ell^2 \\ -30 & 0 & 0 & 30 & 0 & 0 \\ 0 & -36 & -3\ell & 0 & 36 & -3\ell \\ 0 & 3L & -\ell^2 & 0 & 3L & 4\ell^2 \end{bmatrix} \quad (18)$$

The Coriolis impact appears in the following damping matrix form:

$$\{\bar{\mathbf{C}}_{cor}\}_e = \begin{bmatrix} \bar{\mathbf{C}}_{cor,u} = 2m_f U \int_0^\ell \mathbf{N}_u^T \mathbf{N}_u' d\bar{x} \\ \bar{\mathbf{C}}_{cor,w} = 2m_f U \int_0^\ell \mathbf{N}_w^T \mathbf{N}_w' d\bar{x} \end{bmatrix} = \frac{m_f U}{30} \begin{bmatrix} -30 & 0 & 0 & -30 & 0 & 0 \\ 0 & -30 & 6\ell & 0 & 30 & -6\ell \\ 0 & -6\ell & 0 & 0 & 6\ell & -\ell^2 \\ 30 & 0 & 0 & 30 & 0 & 0 \\ 0 & -30 & -6\ell & 0 & 30 & 6\ell \\ 0 & 6\ell & \ell^2 & 0 & -6\ell & 0 \end{bmatrix} \quad (19)$$

The gravitational energy related to the constant horizontal riser tension results in:

$$\{\mathbf{K}_{H_w}\}_e = H_w \int_0^{L_x} \mathbf{N}_w'^T \mathbf{N}_w' dx = \frac{H_w}{30L_x} \begin{bmatrix} 0 & 0 & 0 & 0 & 0 & 0 \\ 0 & 36 & 3L_x & 0 & -36 & 3L_x \\ 0 & 3L_x & 4L_x^2 & 0 & -3L_x & -L_x^2 \\ 0 & 0 & 0 & 0 & 0 & 0 \\ 0 & -36 & -3L_x & 0 & 36 & -3L_x \\ 0 & 3L_x & -L_x^2 & 0 & -3L_x & 4L_x^2 \end{bmatrix} \quad (20)$$

where L_x is the element's projection in the horizontal axis. The strain energy of the riser due to additional tension $H(t)$ caused by vibrations reads:

$$U_{H_i}(t) = \frac{1}{2} \frac{H^2(t)L_e}{EA_p} = \frac{1}{2} \frac{L_e}{EA_p} \cdot \left[\frac{EA_p}{L_e} \frac{W_E}{H_w} \int_0^L \sqrt{1 + \left(\frac{dy}{dx}\right)^2} w dx \right]^2 \quad (21)$$

where, the nonlinear second order terms in the cable equation have been neglected. Implementing the displacement model in Equation (21), the latter is written for the summation of N elements.

$$U_{H_i}(t) = \frac{1}{2} \left(\frac{EA_p}{L_e} \right) \{\mathbf{d}\}^T \cdot \left[\sum_{e=1}^N \frac{W_E}{H_w} \int_0^{L_x} \sqrt{1 + \left(\frac{dy}{dx}\right)^2} \mathbf{N}_w'^T dx \right]^T \left[\sum_{e=1}^N \frac{W_E}{H_w} \int_0^{L_x} \sqrt{1 + \left(\frac{dy}{dx}\right)^2} \mathbf{N}_w'^T dx \right] \cdot \{\mathbf{d}\} \quad (22)$$

where, \mathbf{d} is the vector of total degrees of freedom. Using the following notation:

$$\{\hat{f}\}_e = \int_0^{L_x} \mathbf{N}_w'^T dx = \begin{bmatrix} \frac{L_x}{2} & \frac{L_x^2}{12} & \frac{L_x}{2} & -\frac{L_x^2}{12} \end{bmatrix}, \quad \{\hat{f}\}_N = \sum_{e=1}^N \{\hat{f}\}_e \quad (23)$$

The stiffness matrix because of inertial dynamic tension $H(t)$ finally reads:

$$\mathbf{K}_{H_i} = \frac{EA_p}{L_e} \cdot \left[\frac{W_E}{H_w} \sqrt{1 + \left(\frac{dy}{dx}\right)^2} \{\hat{f}\}_N^T \right] \cdot \left[\frac{W_E}{H_w} \sqrt{1 + \left(\frac{dy}{dx}\right)^2} \{\hat{f}\}_N \right] \quad (24)$$

The above matrix is symmetric and partially complete as opposed to banded matrix structures arising from the other elemental matrix structures. The axial tension in the longitudinal direction of the riser is considered from the potential term of Equation (7)

$\bar{U}_1 = \frac{1}{2} \int_0^L \bar{T} \cdot \bar{u}'^2 d\bar{x}$, leading to the elemental stiffness matrix $\{\mathbf{K}_{\bar{T}}\}_e = \bar{T} \int_0^{\ell} \mathbf{N}_u'^T \mathbf{N}_u' d\bar{x}$. The term

$\bar{U}_2 = \frac{1}{2} \int_0^L 2\bar{T} \cdot \bar{u}' d\bar{x}$ leads to the forcing term $\{\bar{f}_T\}_e = -\int_0^{\ell} \bar{T} \mathbf{N}_u'^T d\bar{x}$.

2.4 Stability analysis

In order to assess the stability of the system at different flow velocities U , Equation [17] is conveniently written in the following state space form:

$$\mathbf{E}_c \{\dot{\mathbf{x}}\} = \mathbf{A}_c \{\mathbf{x}\} \quad (25)$$

where, $\{x\} = [d, \dot{d}]$ is the state vector and:

$$E_c = \begin{bmatrix} C_{cor}(U) + C_d & M \\ I & 0 \end{bmatrix}, \quad A_c = \begin{bmatrix} -[K_b + K_T + K_{H_w} + K_{H_i} - K_{cent}(U)] & 0 \\ 0 & I \end{bmatrix} \quad (26)$$

A small amount of structural damping is assumed in the form of a Rayleigh damping matrix $C_d = a_M M + a_K K$. The stability of the system is assessed by plotting the complex eigenvalues of Equation (25) for increasing flow velocities. When the real part of an eigenvalue becomes positive the system loses stability in the linear sense. Two types of instabilities are possible in this case. A divergent type which is reached when the overall stiffness becomes null, and a flutter type instability caused by the coupling of two or more modes at a specific frequency also related to negative damping terms [26, 27].

3 SIMULATION RESULTS

3.1 Application of stability analysis on a long catenary riser

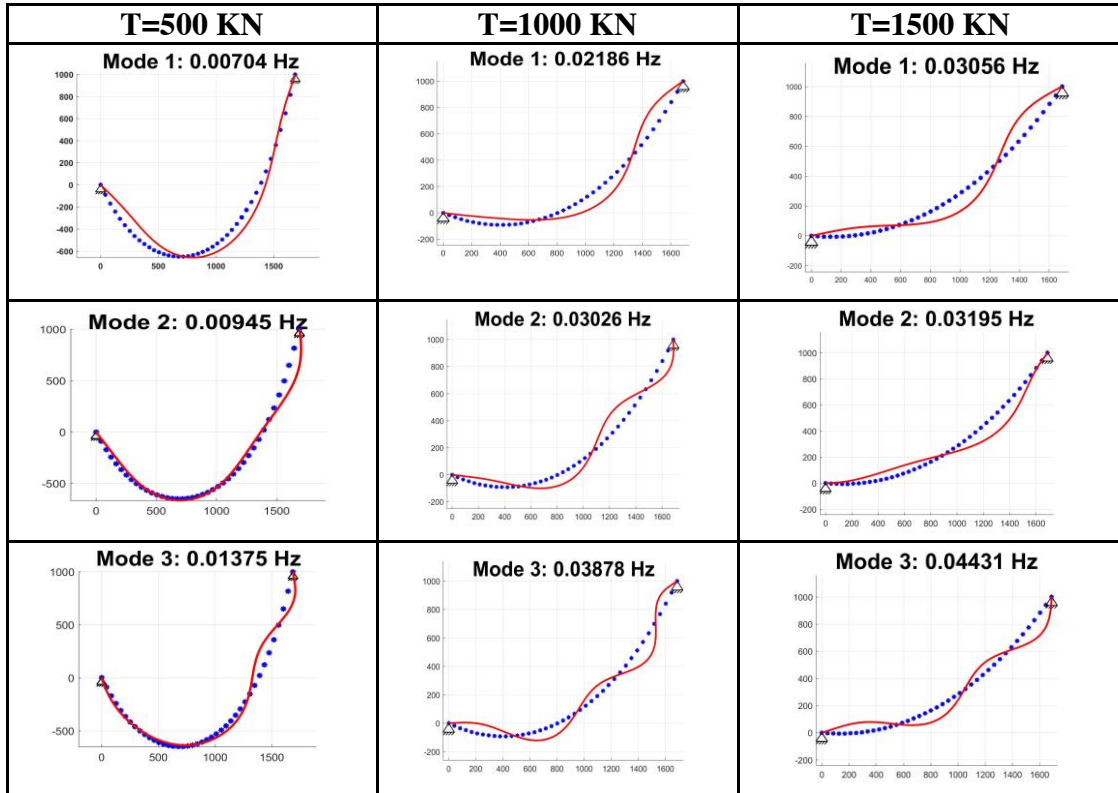


Figure 1: Riser mode shapes for different magnitudes of top tension.

The model developed in the previous section is put to the test by considering catenary risers for different top tensions. Varying top tension leads to a different length and shape for the riser, following Equation (1). The horizontal and vertical riser projections are $X_H = 1688m$ and $Y_H = 1000m$ Chatjigeorgiou [18]. Young's modulus of elasticity is

$E = 207\text{GPa}$ while the inner and outer pipe diameters are $D_i = 0.385\text{m}$ and $D_o = 0.429\text{m}$, respectively. The pipe mass is $m_p = 219.4\text{kg} / \text{m}$ and added mass $m_a = 148.16\text{kg} / \text{m}$ while the submerged weight is $W_E = 699\text{N} / \text{m}$. The elastic stiffness EA_p and flexural rigidity EI_p are equal to $5.83 \times 10^9\text{N}$ and $1.209 \times 10^8\text{Nm}^2$. At static position the pipe is assumed empty. Fig. 1 presents the first three modes for zero internal flow for three different top tension values. The initial static configuration of the catenary is shown in the dotted blue curve.

By solving Equation [25] for increasing flow speed U the system's complex eigenvalues λ are obtained. The dimensionless frequency ω is related to the corresponding eigenvalue by

$$\text{the expressions } \text{Re}(\omega) = \sqrt{\frac{m_p + m_i}{EI_p}} \cdot \text{imag}(\lambda) \cdot X_H^2, \quad \text{Im}(\omega) = -\sqrt{\frac{m_p + m_i}{EI_p}} \cdot \text{Re}(\lambda) \cdot X_H^2 \quad [20].$$

respectively following the example case presented in

The Argand diagram of Fig. 2 depicts the dynamic behavior of the first 5 modes when internal flow velocity is varied between $U = 0 \dots 90\text{m} / \text{s}$ for top tension $T = 500\text{KN}$. In this case the system loses stability in its first mode by divergence via a pitch fork bifurcation at $U = 27\text{m} / \text{s}$. At the divergence limit the frequencies become purely imaginary. The post-divergence dynamic behavior comprises of coupled mode flutter type instabilities as well as higher divergent modes. Fig. 2 shows that for this case of flexible riser the observed flutter instabilities do not follow distinct paths crossing the real axis but appear to oscillate between different modes contributing to the scattered plot arrangement observed. The loci in the plot are symmetric about the real axis but because the modes couple in pairs the mode symbols are exchanged. Fig. 3 presents the first divergence and flutter stability limits for increasing top tension. Obviously higher tension leads to stiffer riser and thus less susceptible to fluid-elastic instabilities put the trend appears not be linear.

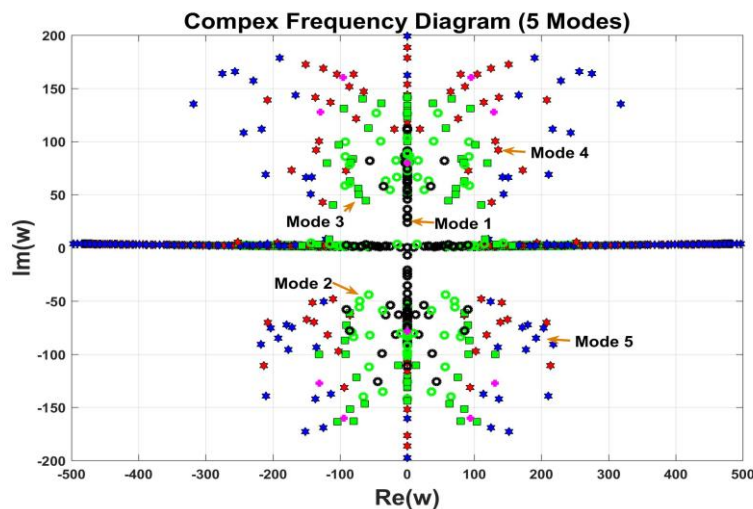


Figure 2: Complex frequency diagrams for a pinned-pinned catenary pipe. First 5 modes are depicted (black circles mode 1, green circles mode 2, green squares mode 3, red hexagons mode 4 and blue hexagons mode 5. Magenta points are the points at final flow speed $U=90\text{m/s}$.)

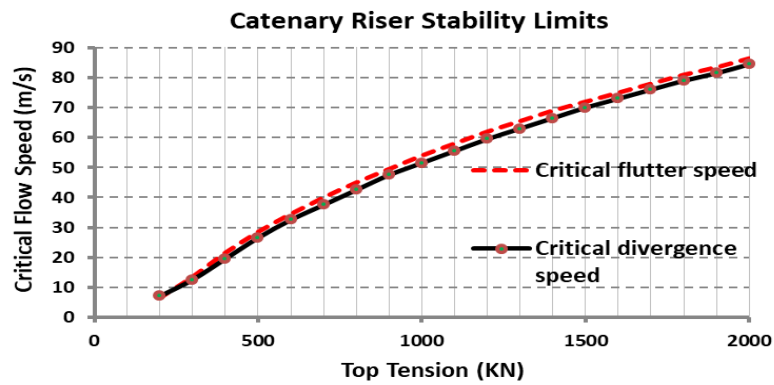


Figure 3: First flutter and divergence critical stability limits for catenary riser subjected to increasing top tension.

3.2 Parameters affecting post-divergence behavior

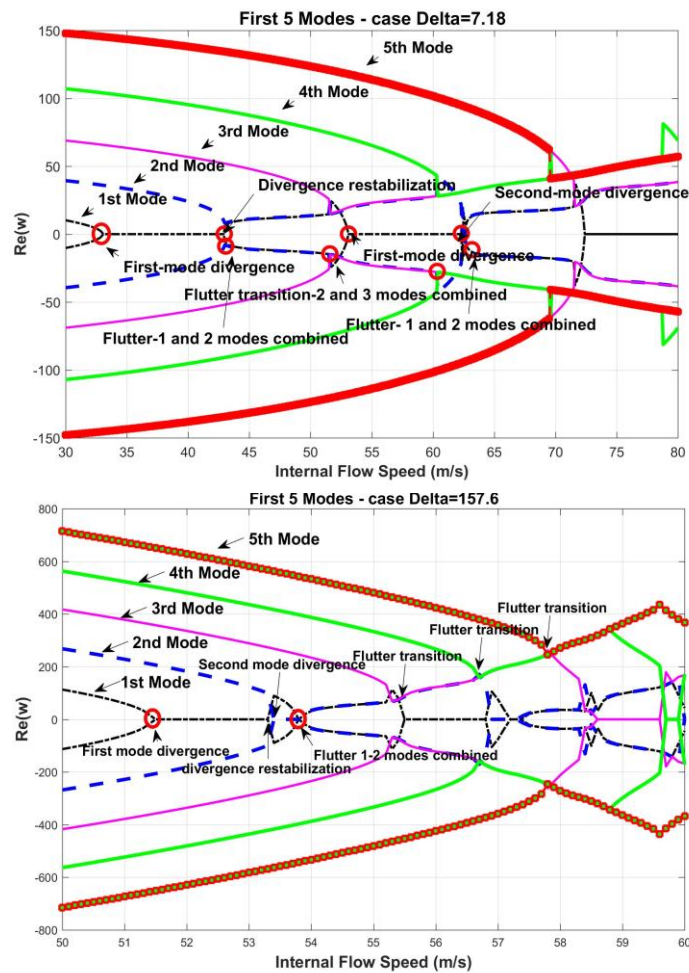


Figure 4: Real component of dimensionless frequency, ω , as a function of internal flow velocity for 2 different catenary cases with Delta parameters (Delta=7.18 and Delta=157.6 respectively).

The post-divergence stability behavior of catenary pipes conveying fluid is quite more complex compared to that of straight pipe configurations, see for example [21]. It has been observed by the authors that the dynamic behavior changes depending whether the pipe works primarily in tension or bending and can be qualitatively described by the parameter [2].

$$\Delta = \sqrt{\frac{H_w}{EI_p}} \Lambda_p \quad (27)$$

where, Λ_p is the total length of the catenary. Fig. 4 presents the evolution of the real component of dimensionless frequency with variable internal flow for two cases. The first case is that of a small catenary having $X_H = 200m$ and $Y_H = 200m$, with top tension $100KN$. The second case is that of a large catenary as depicted in the middle column of Fig. (1). The modal inter-coupling and flutter transition points are much more pronounced for the second case. Apparently, the tension effect results in frequency closeness with increasing flow speed which results in inter-modal coupling in pairs which transits between different modes. Also, there are multiple divergence re-stabilization points and higher divergence modes. Although these results are a product of linear theory, it has been argued that in most cases the buckled case (in this case divergence mode) is not far away from the original stable equilibrium configuration and the linear theory is able to predict the post-divergence dynamics quite well [20].

CONCLUSIONS

A new methodology to model the vibration response and linear instability behavior of catenary riser pipes under different loading and operation conditions has been developed. The pipe's tension contribution to the pipe's modal attributes considers both the static and dynamic inertia contribution. The equations of motion are formatted into a finite element framework and stability limits are assessed by means of a state space approach. The analysis gives insight into the correlation of top tension to divergence and flutter onset as well as the influence of different parameters to the post divergence behavior of the catenary. Pipes mostly working in tension show an irregular flutter coupling behavior.

Acknowledgment: The authors thank the funding support from the Engineering & Physical Sciences Research Council (EPSRC) UK through the MUFFINS project grant EP/P033148/1.

REFERENCES

- [1] Sarpkaya, T. A critical review of the intrinsic nature of vortex-induced vibrations. *J. Num. behaviors Fluid and Structures* (2004) **19**:389-447.
- [2] Srinil, N., Wiercigroch, M., O'Brien P. Reduced-order modeling of vortex-induced vibration of catenary riser. *Ocean Engineering* (2009) **36**:1404-1414.
- [3] Willden, R.H.J., Graham, J.M.R. Multi-modal Vortex-Induced Vibrations of a vertical riser pipe subject to a uniform current profile. *European Journal of Mechanics B/Fluids* (2004) **23**:209-218.
- [4] Semler, C., Xi, G.X., Paidoussis, M.P. The non-linear equations of motion of pipes conveying fluid. *Journal of Sound and Vibration* (1994) **169**(5):577-599.
- [5] Lin, W., Qiao, N., Yuying, H. Dynamical behaviors of a fluid-conveying curved pipe

- subjected to motion constraints and harmonic excitation. *Journal of Sound and Vibration* (2007) **306**:955-967.
- [6] Chatjigeorgiou, I.K. On the effect of internal flow on vibrating catenary risers in three dimensions. *Engineering Structures* (2010) **32**:3313-3329.
- [7] Meng, S., Kajiwara, H., Zhang, W. Internal flow effect on the cross-flow vortex-induced vibration of a cantilevered pipe discharging fluid. *Ocean Engineering* (2017) **137**:120-128.
- [8] Atadan, A.S., Calisal, S.M., Modi, V.J., Guo, Y. Analytical and numerical analysis of the dynamics of a marine riser connected to a floating platform. *Ocean Engineering* (1997) **24**:111-131.
- [9] Antman, S.S. *Nonlinear Problems of Elasticity*. Springer, New York, (1995).
- [10] Kim, H.T., O'Reilly, O.M. Instability of catenary-type flexible risers conveying fluid in subsea environments. *Ocean Engineering* (2019) **173**:98-115.
- [11] Monprapussorn, T., Athisakul, C., Chucheepsakul, S. Nonlinear vibrations of an extensible flexible marine rise carrying pulsatile flow. *Transactions of the ASME* (2007) **74**:754-769.
- [12] Ginsberg, J.H. The dynamic stability of a pipe conveying a pulsatile flow. *Int. J. Eng. Sci.* (1973) **11**:1013-1024.
- [13] Seo, J.S., Jeong, W.B., Jeong, S.H., Oh, J.S., Yoo, W.S. Finite element analysis of forced vibration of a pipe conveying harmonically pulsating fluid. *JSME International Journal* (2005) **48**:688-694.
- [14] Gorman, D.G., Reese, J.M., Zhang, Y.L. Vibration of a flexible pipe conveying viscous pulsating fluid flow. *Journal Sound Vibration* (2010) **230**:379-392.
- [15] Chucheepsakul, T., Monprapussorn, T., Huang, T. Large strain formulations of extensible marine pipes transporting fluid. *Journal Fluid Structures* (2003) **17**:185-224.
- [16] Ma, B., Srinil, N. Dynamic characteristics of deep-water risers carrying multiphase flows. *ASME 2018 37th International Conference on Ocean, Offshore and Arctic Engineering OMAE 2018*, June 17-22, Madrid, Spain.
- [17] Seyed, F.B., Patel, M.H. Mathematics of flexible risers including pressure and internal flow effects. *Marine Structures* (1992) **5**:121-150.
- [18] Chatjigeorgiou, I.K. Hydro-elastic response of marine risers subjected to internal slug-flow. *Applied Ocean Research* (2017) **62**:1-17.
- [19] Ortega, A., Rivera, A., Larsen, C.M. Slug flow and waves induced motions in flexible risers. *Journal of Offshore Mechanics and Arctic Engineering* (2018) **140**:1-9.
- [20] M.P. Paidoussis, *Fluid-Structure Interactions: Slender Structures and Axial Flow. Vol. 1*, Academic Press Limited, London, 1998.
- [21] Lee, U., Park, J. Spectral element modeling and analysis of a pipeline conveying internal unsteady fluid. *Journal of Fluids and Structures* (2006) **22**:273-292.
- [22] Cella, P. Methodology for exact solution of catenary. *Journal of Structural Engineering* (1999) **125**(12):1451-1453.
- [23] Abdel-Ghaffar, A. Free vertical vibrations of suspension bridges. *J. Struct. Div. ASCE* 105(ST10) (1980) 2053-2076.
- [24] Irvine, H.M. *Studies in the statics and dynamics of simple cable systems*. California Institute of Technology, Technical report, 1974.
- [25] J.H. Prevost, S. Bagrianski, *An introduction to matrix structural analysis and finite element methods*. World Scientific Publishing, 2017.
- [26] Bakis, K.N., Massaro, M., Williams M.S., Limebeer, D.J.N. Aeroelastic control of long-span suspension bridges with controllable winglets. *Structural Control and Health Monitoring* (2016) **23**(12):1417-1441.
- [27] Paidoussis, M.P., Issid, N.T. Dynamic stability of pipes conveying fluid. *Journal of Sound and Vibration* (1974) **33**(3):267-294.

MERITS OF THE MAXIMUM ENTROPY MESHLESS METHOD FOR COUPLED ANALYSIS OF OFFSHORE PROBLEMS

MAJIDREZA NAZEM^{*} AND MARK CASSIDY[†]

^{*} Discipline of Civil and Infrastructure, School of Engineering
RMIT University, Melbourne, Victoria 3000, Australia
Email: majidreza.nazem@rmit.edu.au

[†] Melbourne School of Engineering, The University of Melbourne
Parkville, Victoria 3052, Australia
Email: mark.cassidy@unimelb.edu.au

Key words: Computational Methods, Marine Engineering, Consolidation Analysis, Meshless Analysis

Abstract. Despite the recent advances in meshless analysis methods, their application in tackling offshore geotechnical problems is relatively limited. In meshless methods the problem domain is discretised by a set of nodes and, unlike the traditional finite element method, the connectivity between the elements and nodes does not exist. This means that the meshless methods may outperform the finite element method in problems including excessively large deformations, discontinuities or strain localisation. On the other hand, the shape functions in meshless methods are not usually simple polynomial functions which are explicitly evaluated at an arbitrary point. These functions are commonly obtained by solving a complex and relatively time-consuming optimisation problem, significantly affecting the overall computational time. This issue may become even more serious when the shape functions need to be updated during each time step of the analysis. In this study, we attempt to address the efficiency and performance of one of the recently developed meshless methods for solving offshore problems where the solid displacements are coupled with the pore fluid pressures. This method is based on the principle of Maximum-Entropy [1], and its performance is presented by comparing its results with those obtained by the finite element method. This is achieved by studying the consolidation and bearing capacity of soil under an offshore foundation, using various nodal discretisations and boundary conditions. The results indicate that, for the problems considered in this study, the Maximum Entropy Meshless method (1) can provide a stable solution regardless of the domain discretisation density, and (2) outperforms the finite element method by reducing the computational time but achieving the same accuracy.

1 INTRODUCTION

Meshless methods have significantly progressed during past two decades. In these methods only a set of arbitrary distributed nodes (particles) is utilised to discretise the problem domain, without utilising any elements. Consequently, meshless methods can outperform the conventional mesh-based methods, such as the finite element (FE) method, since they do not deal with complex issues such as mesh distortion, mesh generation, and mesh-adaptivity.

Despite their recent advances in solid mechanics, the meshless methods have attracted less attention in geotechnical engineering, particularly in tackling the offshore problems where the continuum usually includes a solid phase as well as a liquid phase. In these problems the displacements of soil particles are coupled with the pore pressure of the liquid. The Element-Free Galerkin (EFG) method [1] has been successful in solving the coupled problems in geomechanics [2][3]. In the EFG method the Moving Least Square shape functions are used to approximate the unknown variables, but these functions do not satisfy the Kronecker delta property, creating additional computational challenge for imposing the boundary conditions. Based on the EFG method, the Maximum Entropy Meshless (MEM) method has been developed [4][5], and its application in solving the single-phase geotechnical problems has been presented in the literature [6][7]. The MEM method takes advantage of the Maximum-Entropy (max-ent) shape functions which satisfy the Kronecker delta property. Recently, this method was extended to the solution of consolidation problems of geomechanics, and some of its advantages were addressed [8]. In this paper, the Maximum-Entropy Meshless method is briefly explained, and then its efficiency and robustness is presented by solving the bearing capacity of soil under a footing, considering a coupled displacement-pore water pressure formulation.

2 MAXIMUM ENTROPY MESHLESS METHOD

In many offshore and geomechanics problems the deformations of solid phase (soil) is coupled with pore water pressure. The global equations describing the behavior of such continuum is obtained by combining the conservation of mass as well as the equilibrium of system through the principle of effective stresses and Darcy's law, and is given by [8]

$$\begin{bmatrix} \mathbf{K} & \mathbf{L} \\ \mathbf{L}^T & \mathbf{0} \end{bmatrix} \begin{Bmatrix} \dot{\mathbf{u}} \\ \dot{\mathbf{p}} \end{Bmatrix} + \begin{bmatrix} \mathbf{0} & \mathbf{0} \\ \mathbf{0} & \mathbf{H} \end{bmatrix} \begin{Bmatrix} \mathbf{u} \\ \mathbf{p} \end{Bmatrix} = \begin{Bmatrix} \dot{\mathbf{F}}^{ext} \\ \dot{\mathbf{Q}}^{ext} \end{Bmatrix} \quad (1)$$

where \mathbf{K} represents the stiffness matrix, \mathbf{L} is the coupling matrix, \mathbf{H} denotes the flow matrix, \mathbf{u} and \mathbf{p} are respectively the vector of displacements and the vector of pore fluid pressures, \mathbf{F}^{ext} is the external force vector and \mathbf{Q}^{ext} represents the fluid supply vector. Note that a superimposed dot represents the derivative of a variable with respect to time.

In the Maximum-Entropy Meshless (MEM) method the problem domain is discretised by a set of nodes, and a uniform background mesh is used for evaluating the matrices in Equation (1). The unknown displacements and pore fluid pressures are approximated by the Maximum-Entropy shape functions according to

$$\begin{aligned} u^h(x) &= \sum_{i=1}^n \Phi_i u_i \\ p^h(x) &= \sum_{i=1}^n \Phi_i p_i \end{aligned} \quad (2)$$

where u^h , p^h , are respectively the approximated values of displacements and pore water pressure of an arbitrary point x , Φ_i represents the matrix of Maximum-Entropy shape functions of field node i , n is the number of field nodes at the support domain of point x , and

u_i and p_i represent the nodal values of displacements and the pore water pressures, respectively. The Maximum-Entropy shape functions are obtained by solving the following optimisation problem [5]

$$\begin{aligned}
 \text{Maximise:} \quad & -\sum_{i=1}^n \Phi_i \ln \left(\frac{\Phi_i}{w_i} \right) \\
 \text{subject to:} \quad & \sum_{i=1}^n \Phi_i = 1, \quad \sum_{i=1}^n \Phi_i x_i = x, \\
 & \sum_{i=1}^n \Phi_i y_i = y, \quad \sum_{i=1}^n \Phi_i z_i = z
 \end{aligned} \tag{3}$$

where w_i represent the weight functions. More details about the MEM method and its generalisation to analysis of consolidation problems can be found in [8].

3 NUMERICAL EXAMPLE

To demonstrate the ability of the MEM method, the bearing capacity of an undrained layer of soil under a strip footing is considered. The problem domain, boundary conditions and material properties are depicted in Figure 1, where E , ν , c , ϕ , ψ , k , and γ_w , respectively, represent the Young's modulus of soil, its Poisson's ratio, cohesion, friction angle, dilation angle, coefficient of permeability and the unit weight of water. A prime superscript represents the drained condition, whereas a 'u' subscript denotes the undrained condition. In this example, the drained parameters are used in the coupled analysis to predict the undrained bearing capacity of soil. According to Small [10], the drained and undrained parameters of a weightless soil are dependent according to

$$\frac{c_u}{c'} = \frac{2\sqrt{N_\phi}}{1+N_\phi}, \quad N_\phi = \frac{1+\sin\phi'}{1-\sin\phi'} \tag{4}$$

where c_u represents the undrained shear strength of soil.

The undrained bearing capacity of soil, q_u , is given by the Pandtl formula

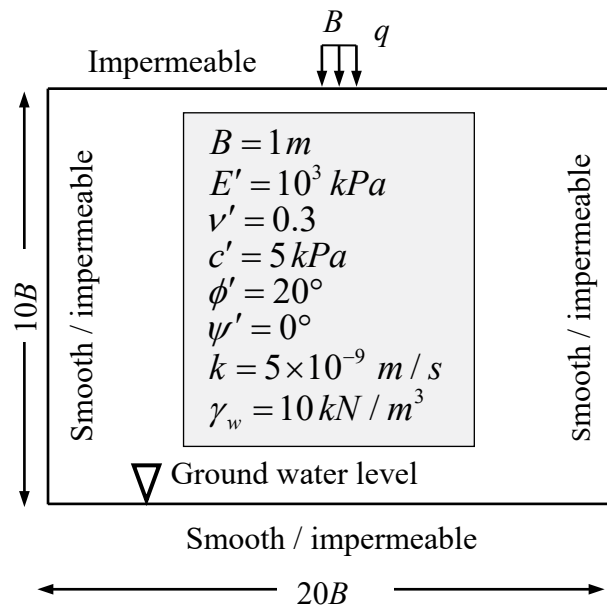


Figure 1. Problem domain, boundary conditions, and material properties.

$$q_u = N_c c_u = (2 + \pi) c_u \quad (5)$$

The undrained bearing capacity can be obtained by conducting a coupled analysis using the drained parameters, provided that the loading rate, ω , is fast enough to simulate the undrained conditions [10]. The loading rate is defined by

$$\omega = \frac{4B^2}{\Delta t c_v} \frac{\Delta q}{c'} \quad (6)$$

where c_v is the coefficient of consolidation. In all analyses presented here, a relatively rapid loading rate of $\omega=150$ is used.

The finite element method (FEM) as well as the MEM method are employed to solve this problem, considering only half of the domain due to symmetry. In the finite element method, the problem domain is discretised by four alternative uniform meshes (A-D), using 8-node rectangular elements. In the 8-node elements, two displacement degrees-of-freedom exist at each node and one pore water pressure degree-of-freedom exists at each corner node. Nine Gauss points are used to integrate the governing equations of each element. The finite element meshes A, B, C, and D, respectively, include 100, 400, 900, and 1600 quadratic elements. In the MEM method, the domain is uniformly discretised by four grids (1-4), as shown in Figure 2. The number of background cells used for integration in grids 1, 2, 3, and 4 are, respectively, 100, 400, 900, and 1600. Each cell includes only four integration points. Table 1 represent the number of nodes, the number of active degrees-of-freedom, the number of integration points, and the number of elements/cells in each discretised domain. It is notable that the source code of the FEM and MEM were written in Fortran and were compiled using same compiler.

Table 1: Comparison between the FEM and the MEM

| Mesh/Grid | Total nodes | Degrees-of-freedom | Elements/Cells | Gauss Points | Predicted N_c | Error (%) | Normalised CPU Time |
|-----------|-------------|--------------------|----------------|--------------|-----------------|-----------|---------------------|
| Mesh A | 341 | 719 | 100 | 900 | 6.44 | 25.3 | 1 |
| Mesh B | 1281 | 2836 | 400 | 3600 | 5.96 | 16.0 | 5 |
| Mesh C | 2821 | 6355 | 900 | 8100 | 5.48 | 6.6 | 16.5 |
| Mesh D | 4961 | 11273 | 1600 | 14400 | 5.29 | 2.9 | 41.5 |
| Grid 1 | 121 | 321 | 100 | 400 | 6.38 | 24.1 | 1.6 |
| Grid 2 | 441 | 1239 | 400 | 1600 | 5.85 | 13.8 | 5.5 |
| Grid 3 | 961 | 2758 | 900 | 3600 | 5.32 | 3.5 | 17.1 |
| Grid 4 | 1681 | 4879 | 1600 | 6400 | 5.23 | 1.8 | 42.3 |

The analysis results, including the predicted N_c value (the exact solution being $N_c=5.14$), the error percentage, and the normalised CPU time (the CPU time of each analysis normalised by the computational time of the fastest analysis) are summarised in Table 1. These results are also plotted in Figures 3.a-c. Figure 3.a plots the error of each analysis versus the number of active degrees-of-freedom. According to this figure the error reduces by increasing the degrees-of-freedom in the MEM and the FE methods; however, it is obvious that the MEM method can achieve the FEM error with a significant lower number of degrees-of-freedom, or less number of nodal points. In Figure 3.b the error is plotted versus the normalised CPU time for each analysis. This figure shows that to achieve the same accuracy, the MEM method

required less computational time compared to the FEM. Finally, the normalised CPU time of each analysis is plotted versus the degrees-of-freedom in Figure 3.c. According to this Figure, the MEM method is normally slower than the FEM, when the active degrees-of-freedom are equal in both methods. This is mainly due to the fact that the max-ent shape functions are implicitly obtained by solving a complex optimisation problem, whereas the finite element shape functions are explicitly evaluated by a quadratic function. On the other hand, and as shown before, the MEM method requires a significant lower number of degrees-of-freedom to achieve the level of accuracy obtained by the FEM.

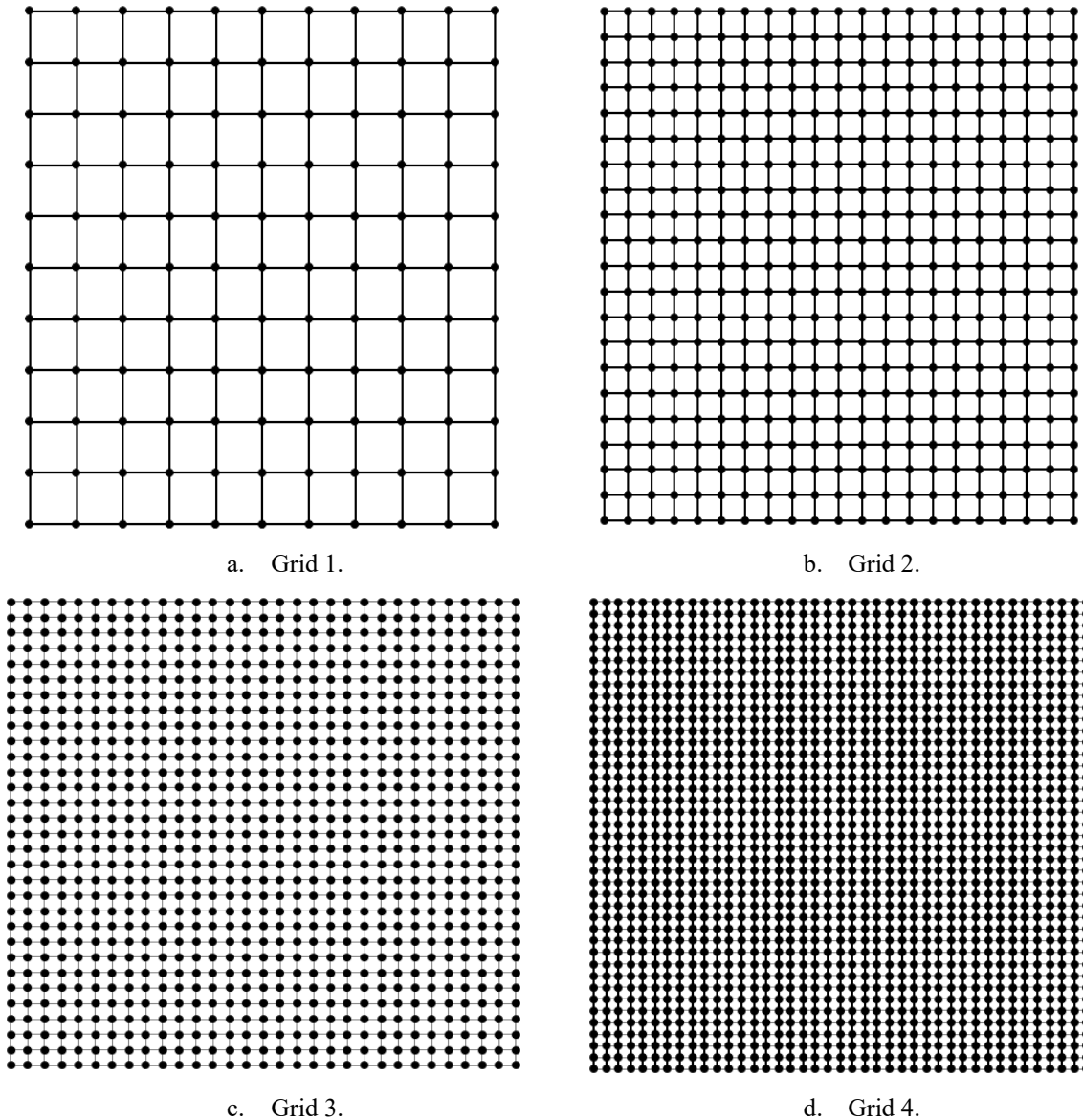
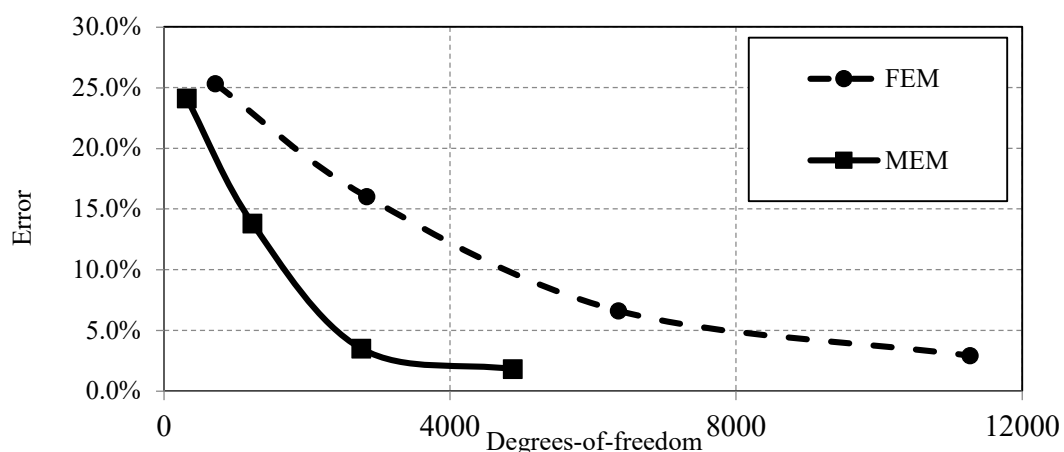
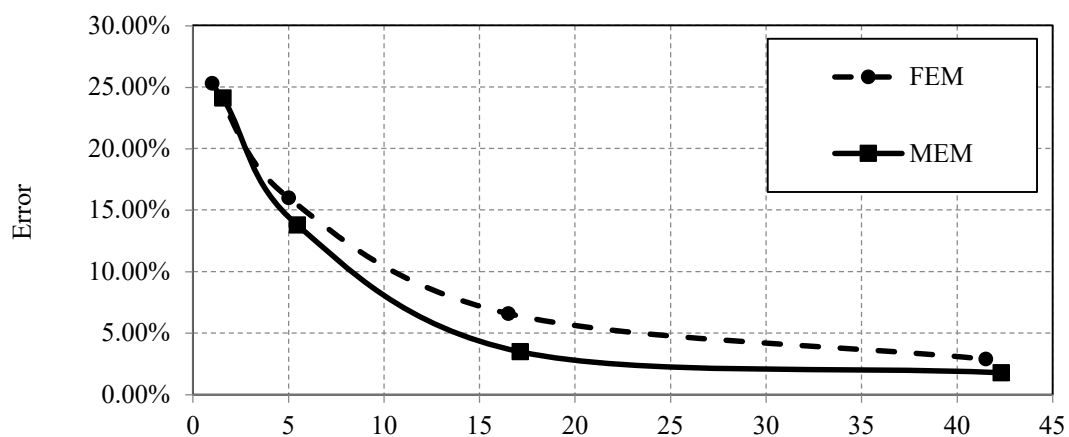


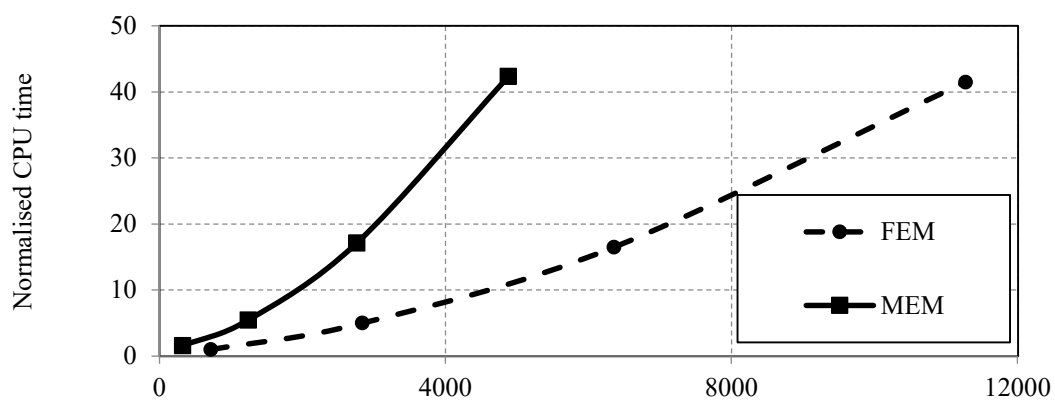
Figure 2. MEM grids used for analysing two-dimensional elasto-plastic consolidation problem.



a. Error versus degrees-of-freedom.



b. Error versus normalised CPU time.



c. Normalised CPU time versus degrees-of-freedom

Figure 3. Performance of the MEM method versus the FE method.

4 CONCLUSIONS

The coupled analysis of geotechnical problems by the Maximum Entropy Meshless (MEM) method was presented in this paper. This method takes advantage of the Maximum Entropy shape functions which satisfy the Kronecker delta property. This method was used here to predict the undrained bearing capacity of a soil layer under a strip footing, assuming the continuum includes a solid phase as well as a liquid phase. The results obtained by this meshless method were compared with their counterparts predicted by the Finite Element Method (FEM). For the problem considered in this paper, it was shown that the MEM method can outperform the FEM.

REFERENCES

- [1] Belytschko, T. Lu, Y.Y. and Gu, L. Element-free Galerkin methods, *Int. J. Num. Meth. Engng* (1994) **3**:229-256.
- [2] Shibata, T., and Murakami, A. A stabilization procedure for soil-water coupled problems using the element-free Galerkin method. *Computers and Geotechnics* (2011), **38**:585-597.
- [3] Wang, J.G., Karim, M.R., and Lin, P.Z. Analysis of seabed instability using element free Galerkin method, *Ocean Engineering* (2007) **34**:247-260.
- [4] Sukumar, N. Construction of polygonal interpolants: a maximum entropy approach, *Int. J. Num. Meth. Engng* (2004) **61**:2159–2181.
- [5] Sukumar, N. and Wright, W.R. Overview and construction of meshfree basis functions: From moving least squares to entropy approximation, *Int. J. Num. Meth. Engng* (2007) **70**:181-205.
- [6] Ullah, Z., Coombs, W.M., and Augarde, C.E. An adaptive finite element/meshless coupled method based on local maximum entropy shape functions for linear and nonlinear problems. *Comput Method Appl M* (2013) **267**:11–132.
- [7] Kardani, O., Nazem, M., Kardani, M. and Sloan, S.W. On the application of the maximum entropy meshfree method for elastoplastic geotechnical analysis. *Comput Geotech* (2017) **84**:68-77.
- [8] Nazem, M., Kardani, M., Bienen, B. and Cassidy, M. A stable Maximum-Entropy Meshless method for analysis of porous media. *Comput Geotech* (2016) **80**:248-260.
- [9] Nazem, M., Sheng, D., Carter, J.P. and Sloan, S.W. Arbitrary-Lagrangian-Eulerian method for large-deformation consolidation problems in geomechanics. *Int. J. Num. Anal Meth. Geom* (2008) **32**:1023-1050.
- [10] Small, J.C. *Elasto-plastic consolidation of soils*. PhD Thesis, University of Sydney, Australia (1977).

A DATA-DRIVEN PROBABILISTIC LEARNING APPROACH FOR THE PREDICTION OF CONTROLLABLE PITCH PROPELLERS PERFORMANCE

STEFANO GAGGERO*, ANTONIO COPPEDE*, DIEGO VILLA*,
GIULIANO VERNENGO* AND LUCA BONFIGLIO†

*DITEN, Polytechnic School
University of Genoa
Via Montallegro 1, 16145, Genoa, Italy
e-mail: stefano.gaggero@unige.it; diego.villa@unige.it; giuliano.vernengo@unige.it;
antonio.coppede@edu.unige.it

† MIT-Sea Grant College Program
Massachusetts Institute of Technology
12 Emily St. NW98-180, Cambridge, MA 02139, USA
e-mail: bonfi@mit.edu

Key words: Controllable Pitch Propeller, Multi-fidelity, Gaussian Process, Uncertainty Quantification

Abstract. The multi-fidelity machine learning framework proposed in this paper leverages a probabilistic approach based on Gaussian Process modeling for the formulation of stochastic response surfaces capable of describing propeller performance for different mission profiles. The proposed multi-fidelity techniques will help coping with the scarcity of high-fidelity measurements by using lower-fidelity numerical predictions. The existing correlation of the multi-fidelity data sets is used to infer high-fidelity measurements from lower fidelity numerical predictions. The probabilistic formulations embedded in Gaussian Process regressions gives the unique opportunity to learn the target functions describing propeller performance at different operating conditions, while quantifying the uncertainty associated to that specific prediction. While the multi-fidelity autoregressive scheme allows to construct high accurate response surfaces using only few experimental data, Uncertainty Quantification (UQ) provides an important metric to assess the quality of the learning process. We demonstrate the capability of the proposed framework to predict the performance of a controllable pitch propeller using few experimental data coming from towing tank experiments and many medium-fidelity predictions obtained using an in-house developed BEM, validated and verified in many previous studies.

1 INTRODUCTION AND MOTIVATION

Controllable Pitch Propellers (CPP) offer a propulsion flexibility that is particularly suitable for marine vehicles designed to operate at different mission profiles. Predicting CPP perfor-

mance in a wide range of operating conditions, therefore, is essential for the characterization of the propulsive features of a vessel. Modern propeller design relies on design by optimization techniques in which propeller performance are predicted using low- or medium-fidelity numerical methods, while design assessment is often performed with high-fidelity computational models [1, 2] or, in case of innovative designs, through open-water experiments at the cavitation tunnels [3]. Once the design process converges towards an optimized shape (as in [4, 5]), it is important to characterize CPP propellers for different operating conditions in order to increase the knowledge of the engineering system, predicting possible pitfalls due to performance loss, increase in fuel oil consumption or other important consequences such as excessive loads on the blade, radiated noise [6] or the occurrence of cavitation that could compromise the structural integrity of the propeller. Considering instead an existing, operating, vessel it would be necessary to measure the performance of the propulsion system in a wide range of operating conditions to have its complete characterization. However, in most cases, this might be technically prohibitive and too expensive to be achieved.

In this study we present a mathematical framework capable of constructing accurate surrogate models using only a few high-fidelity data and many numerical predictions performed with inexpensive, low-fidelity computer codes. In this paper we propose a supervised learning framework in which the labeled data coming from two different outputs are blended together using multi-fidelity Gaussian process regression [7, 8, 9, 10, 11, 12]. Multi-fidelity Gaussian Process Regressions have been successfully applied in the naval engineering field for the hydrodynamic and hydro-structural shape optimization of super-cavitating hydrofoils [13, 14] and hull-forms for both calm water resistance [15] and ship motions reduction [16]. Bonfiglio et al. [17] used numerical predictions and experiments to predict hydrodynamic performance of a conventional super-cavitating hydrofoil in the operating conditions input space by leveraging multi-fidelity Gaussian Process Regressions. More simplified multi-fidelity strategies for surrogate model formulations have been recently proposed in [18, 19]. To the best of our knowledge, this is the first time such tools are applied for the predictions of propeller performance in the operating conditions input space.

2 GAUSSIAN PROCESS REGRESSIONS

The supervised learning framework proposed in this paper is based on the formulation of probabilistic regression models that are capable of combining multiple sets of data coming from different information sources and providing quantities of interest information at different fidelity levels. In particular, we leverage Gaussian Process \mathcal{GP} regressions in order to model a non-linear function describing the CPP performance in terms of thrust (K_T) and torque (K_Q) coefficient at different advance coefficients (J). In the present paper we demonstrate the main advantages of the proposed framework through a study that involves two different information sources, namely experimental data and numerical predictions. The framework can be extended to an arbitrary number of information sources.

2.1 Nonlinear regression with Gaussian processes

The multi-fidelity model proposed in this paper allows to infer high-fidelity predictions by using information mainly provided by lower fidelity models. In this setting, we assume that we

have a data-set comprising of input/output pairs $\mathcal{D} = \{(x_i, y_i)_{i=1}^N\} = \{X, y\}$ where X is a set of given parameters describing the operating conditions of the propeller (e.g. J and P/D) and y is their corresponding performance metric (e.g. K_T or K_Q). The final goal is to infer a latent function f describing each quantity of interest in terms of noisy input data:

$$y = f(X) + \epsilon. \quad (1)$$

Here X is considered to be a matrix in $\mathbb{R}^{N \times D}$ containing the N input points at which we have observed the outputs $y \in \mathbb{R}^{N \times 1}$. Moreover, ϵ is a noise process that may be corrupting our observations of y . For simplicity, here we assume that ϵ is Gaussian and uncorrelated, i.e. $\epsilon \sim \mathcal{N}(0, \sigma_n^2 I)$, where σ_n^2 is an unknown variance parameter that will be learned from the data, 0 is a zero column vector of size N , and I is the $N \times N$ identity matrix.

In this study we will consider, without lack of generality, zero-mean Gaussian process priors on f , i.e., $f(x) \sim \mathcal{GP}(0, k(x, x'; \theta))$, our goal is to first identify the optimal set of kernel hyper-parameters and model parameters, $\Theta = \{\theta, \sigma_n^2\}$, and then use the optimized model to perform predictions at a set of new unobserved locations x^* . A central role in this process is played by the covariance kernel function $k(x, x'; \theta)$ that depends on a set of hyper-parameters θ and encodes any prior belief or domain expertise we may have about the underlying function f . Here, in absence of any domain-specific knowledge we have used the squared exponential covariance kernel.

Model training is performed through minimizing the negative log-marginal likelihood of the Gaussian process model [7]. In our setup, the likelihood is Gaussian and can be computed in a closed analytical form

$$\Theta^* = \arg \min_{\Theta} \mathcal{L}(\Theta) := \frac{1}{2} \log |K + \sigma_n^2 I| + \frac{1}{2} y^T (K + \sigma_n^2 I)^{-1} y + \frac{N}{2} \log(2\pi), \quad (2)$$

where K is a $N \times N$ covariance matrix constructed by evaluating the kernel function $k(\cdot, \cdot; \theta)$ at the locations of the input training data in X . The minimization here is carried out using the quasi-Newton optimizer L-BFGS with random restarts [7]. Finally, once the model has been trained on the available data, we can compute the posterior predictive distribution at a new location x^* , namely $p(y^* | x^*, \mathcal{D}) \sim \mathcal{N}(\mu(x^*), \Sigma(x^*))$, by conditioning on the observed data as

$$\mu(x^*) = k(x^*, X)(K + \sigma_n^2)^{-1} y \quad (3)$$

$$\Sigma(x^*) = k(x^*, x^*) - k(x^*, X)(K + \sigma_n^2)^{-1} k(X, x^*). \quad (4)$$

Here, we must emphasize the use of Gaussian processes as flexible prior distributions for Bayesian regression of deterministic nonlinear functions. It is well known and understood that Gaussian processes offer a flexible class of prior distributions over function spaces, and provide a concrete formulation for Bayesian non-parametric regression [20]. Under the Central Limit Theorem, one can rigorously prove that Gaussian processes can be obtained as the infinite limits of deep neural networks (i.e., neural networks with multiple layers, an infinite number of neurons per layer, and a Gaussian prior on their weights) [21]. Moreover, rigorous statistical consistency estimates can be obtained using approximation theory in Reproducing Kernel Hilbert Spaces [22]. Therefore, our choice of employing a Gaussian process prior for approximating the nonlinear function f in equation 1 is reasonable, as this choice allows us to approximate smooth,

yet arbitrarily complicated functions in high-dimensions. A need for a more complex non-Gaussian prior would only arise in cases where f would have jump discontinuities (leading to a bi-modal distribution of y for a given x), or in cases where our observations are corrupted by a non-Gaussian noise process. Such cases are not relevant to our study as our quantities of interest are smooth functions of their inputs, and our observations y are outputs of deterministic computer simulations. Therefore, the reader should hereby note the difference between modeling stochastic phenomena using Gaussian distributions (which is not relevant to this study) versus approximating smooth deterministic functions using Bayesian non-parametric regression with Gaussian process priors, which is the main building block of this study.

The key motivation for adopting a Bayesian approach to approximate deterministic functions stems from the central role played by the quantification of the uncertainty associated with our surrogate model predictions. This uncertainty can reflect both any bias in the training data as well as the uncertainty inherent to the prior modeling assumptions themselves. Besides offering a quantitative mechanism for assessing model inadequacy, this is key to facilitating the judicious acquisition of new information within an optimization loop (see for instance [17]).

2.2 Multi-fidelity modeling

The aforementioned work-flow can be straightforwardly extended to handle cases involving data that originate from different information sources of variable fidelity [12, 23, 8]. For simplicity, here we outline the process corresponding to two levels of fidelity, although this can be generalized to arbitrarily many levels. In a two-level multi-fidelity setting we observe data $\mathcal{D} = [\{(x_{L_i}, y_{L_i})_{i=1}^{N_L}\}, \{(x_{H_i}, y_{H_i})_{i=1}^{N_H}\}] = \{X, y\}$, where (x_L, y_L) and (x_H, y_H) are input/output pairs generated by a low- and high-fidelity model, respectively, typically with $N_L \gg N_H$. Then, our goal is to set up a multi-variate regression framework that can return accurate high-fidelity predictions while being primarily trained on low-fidelity data. To do so, we consider the following multi-output Gaussian process regression model first put forth by Kennedy and O'Hagan [12]:

$$y_L = f_L(x_L) + \epsilon_L \quad (5)$$

$$y_H = f_H(x_H) + \epsilon_H \quad (6)$$

$$f_H(x) = \rho f_L(x) + \delta(x) \quad (7)$$

$$f_L(x) \sim \mathcal{GP}(0, k_L(x; x'; \theta_L)), \quad \epsilon_L \sim \mathcal{N}(0, \sigma_{n_L}^2 I) \quad (8)$$

$$\delta(x) \sim \mathcal{GP}(0, k_H(x; x'; \theta_H)), \quad \epsilon_H \sim \mathcal{N}(0, \sigma_{n_H}^2 I) \quad (9)$$

Here $f_L(x)$ and $\delta(x)$ are considered to be two independent Gaussian processes, ρ is a scaling parameter that is learned during model training along with the variances $\sigma_{n_L}^2$ and $\sigma_{n_H}^2$ that potentially corrupt the low- and high-fidelity data, respectively. As a consequence of the autoregressive assumption in Eq. 7, the joint distribution of the low- and high-fidelity data inherits the following structure:

$$y = \begin{bmatrix} y_L \\ y_H \end{bmatrix} \sim \mathcal{N} \left(\begin{bmatrix} 0 \\ 0 \end{bmatrix}, \begin{bmatrix} k_L(x_L, x'_L; \theta_L) + \sigma_{n_L}^2 I & \rho k_L(x_L, x'_H; \theta_L) \\ \rho k_L(x_H, x'_L; \theta_L) & \rho^2 k_L(x_H, x'_H; \theta_L) + k_H(x_H, x'_H; \theta_H) + \sigma_{n_H}^2 I \end{bmatrix} \right) \quad (10)$$

Evidently, the covariance of y now has a block structure, where the diagonal blocks model the data in each fidelity level and the off-diagonal blocks model the cross-correlation structure between different levels of fidelity. Model training and posterior predictions can now be performed by using the concatenated low- and high-fidelity data along with this block covariance matrix structure replacing K in Eq. 2- 4. Specifically, the minimization of the log-marginal likelihood in Eq. 2 will return the optimal set of model parameters and hyper-parameters, namely $\Theta = \{\theta_L, \theta_H, \rho, \sigma_{n_L}^2, \sigma_{n_H}^2\}$, which can be subsequently used to perform posterior predictions using Eq. 3, 4.

3 PROPELLER PERFORMANCE DATA SETS

The propeller performance we considered for current analyses are those of the P2772. P2772 is the four-bladed, left-handed controllable pitch propeller of the “Medium Size Tanker” provided in the framework of the European Project AQUO [24]. It has an expanded area ratio of 0.45 and a chord over diameter at $r/R = 0.7$ of 0.29. At the design condition, the pitch over diameter ratio measured at $r/R = 0.7$ is equal to 0.87. Model scale tests are available from SSPA Sweden. Three pitch settings in addition to the design conditions are considered, namely $P/D = 0.9, 0.75$ and 0.6, which correspond to rigid rotations of the propeller blades from $+0.72$ to -6.6° .

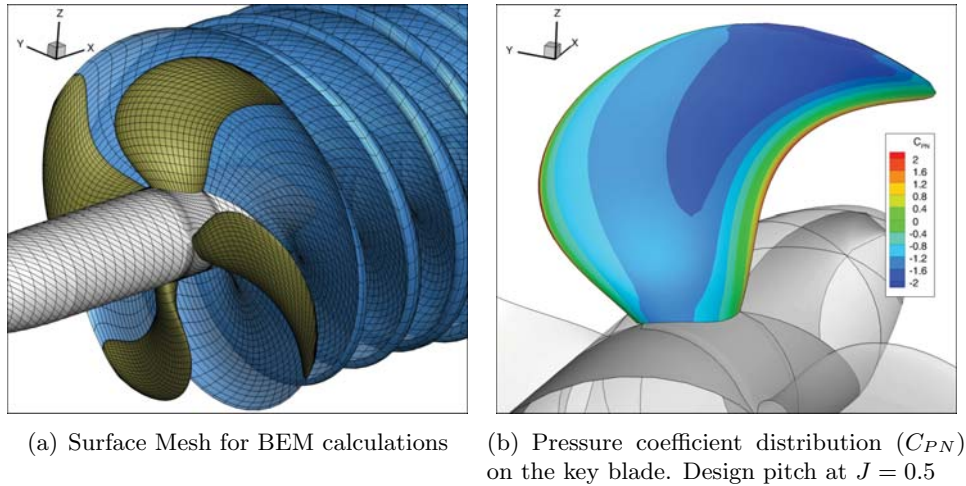


Figure 1: The P2772 propeller.

Numerical calculations were carried out using the Boundary Element Methods developed at the University of Genoa [3, 1]. It makes use of the *key blade* approach (figure 1(b)) to solve steady and unsteady problems also in presence of cavitation. In current analyses, we exploit steady, non-cavitating calculations on a blade surface mesh of 1500 panels (figure 1(a)) to characterize the open water performance of the propeller at the same functioning conditions available from experiments. Bollard-pull functioning, at any pitch settings, were not calculated due to the inherent limitations of BEM in dealing with zero inflow speed. Differences between calculations and measurements are reasonable with an average deviation for thrust and torque of about 2% (both overestimated) when the design pitch is considered. At the reduced pitch, instead, calculations significantly underestimate (18% and 15% on average) propeller performance. Moreover, as

highlighted in figures 3(a) and 3(c), also the slope of the thrust and the torque curves computed by the BEM are significantly different from measurements.

4 STOCHASTIC SURROGATE MODELS PREDICTIONS

We leverage the data set previously described to construct probabilistic surrogate models describing CPP characteristics at different advance coefficients J and different pitch ratios P/D . To demonstrate the capabilities of the multi-fidelity \mathcal{GP} regressions framework proposed in this paper, we first focus on a simplified one-dimensional input space. The input matrix X is defined in $\mathbb{R}^{N_T \times 1}$ where N_T is the number of input points used to train our surrogate models. We have at our disposal $N = 10$ experiments, performed at the SSPA towing tank [24]. The cost of the experimental campaign consists mostly in the construction of the propeller model and set-up of the towing tank, that including the cost of the equipment and the time required for its calibration. Additional experiments at different advance coefficients do not usually cause a significant increase in cost or time. Nevertheless, in this paper we aim at demonstrating the capabilities of the proposed multi-fidelity framework of predicting quantities of interest when high-fidelity measurements are expensive or difficult to obtain. We model our probabilistic surrogates using a zero-mean \mathcal{GP} with a squared exponential covariance function k , which in one dimension is defined as follows:

$$k(x_p, x_q) = \sigma_f^2 \exp\left(-\frac{1}{2\ell}|x_p - x_q|^2\right) + \sigma_n^2 \delta_{pq} \quad (11)$$

The covariance function depends on three hyper-parameters, representing signal variance σ_f , length-scale ℓ and noise-variance σ_n . Here we assume noise-free experiments, hence $\sigma_n=0$. Hyperparameters are discovered using the the available data and minimizing the negative log-likelihood, as described in (2). Once the hyper-parameters describing our data-sets are discovered, posterior mean predictions are obtained from (3) and (4), which for thrust coefficient read as follows:

$$\widehat{K}_T(J^*) = k(J^*, J)(K + \sigma_n^2)^{-1}K_T(J) \quad (12)$$

$$\Sigma(J^*) = k(J^*, J^*) - k(J^*, J)(K + \sigma_n^2)^{-1}k(J, J^*). \quad (13)$$

Here the relative L_2 error between model prediction \widehat{K}_T and experiments K_T is computed (at the location of the measurements) as follows:

$$\frac{\|\widehat{K}_T - K_T\|}{\|K_T\|} = \frac{\sqrt{\sum_{i=1}^{N_V} |\widehat{K}_T(J_i) - K_T(J_i)|^2}}{\sqrt{\sum_{i=1}^{N_V} |K_T(J_i)|^2}} \quad (14)$$

Here N_V is the number of available experiments not including in training ($N_V = N - N_T$).

Figure 2 presents results obtained using $N_T = 3$ (figures 2(a) and 2(b)) and $N_T = 2$ points (figures 2(c) and 2(d)). Each point represent a measurement of thrust and torque obtained an experiment performed at a given advance coefficient J .

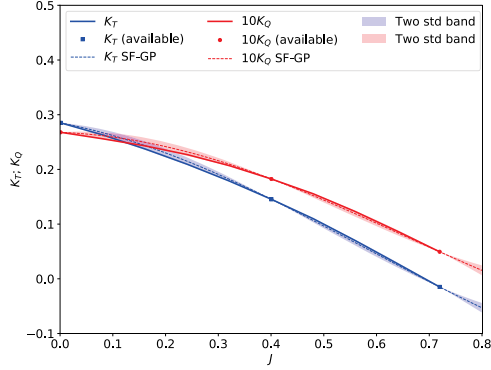
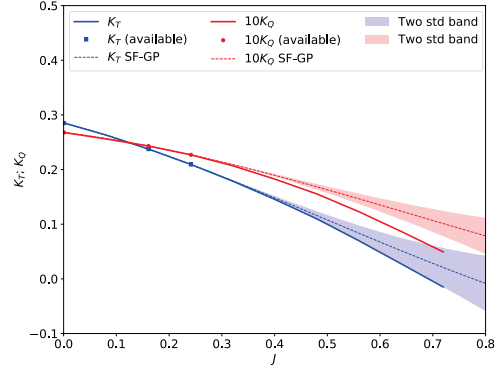
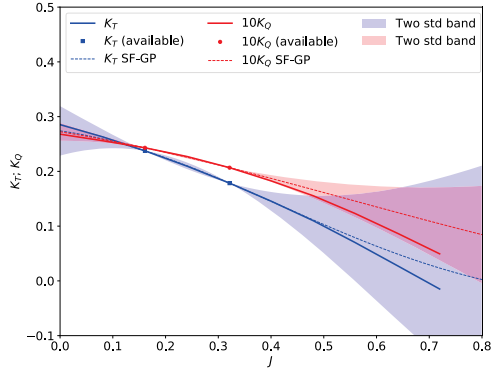
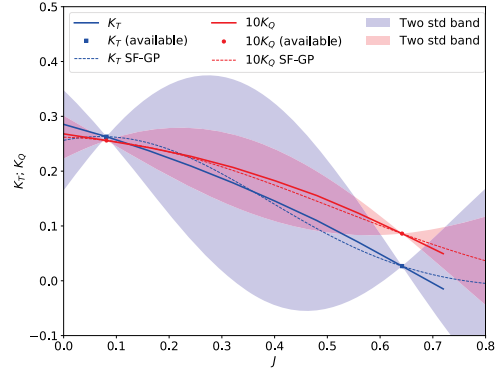

 (a) Three Experiments: $J=0, J=0.4, J=0.72$

 (b) Three Experiments: $J=0, J=0.16, J=0.24$

 (c) Two Experiments: $J=0.16, J=0.321$

 (d) Two Experiments: $J=0.08, J=0.64$

Figure 2: Construction of single-fidelity \mathcal{GP} regressions for thrust (blue) and torque (red) coefficients in the 1-D input space of advance coefficient J . The posterior mean is described by dashed lines, while uncertainty is described by a colored 2σ band. High-fidelity data used in model training are represented by means of circular dots, while high-fidelity measurements are described by green continuous line. Panels show results obtained for different training data sets.

Figure 2 demonstrates how \mathcal{GP} can accurately approximate thrust and torque at different advance coefficients J if surrogate models are trained using $N = 3$ measurements opportunely selected. In figure 2(a) posterior means (dashed lines in figure 2(a)) approximate experiments with a relative L_2 error of 1.96% for K_T and 1.93 for K_Q %. As demonstrated in figure 2(a), the accuracy of model predictions is satisfactory in the whole input range $J \in [0, 0.7]$. The maximum uncertainty is located at $J = 0.17$. This is consistent with the location of the experiments used in training: uncertainty becomes larger far from the data and where the function to discover is characterized by higher gradients. Selecting $N = 3$ experiments at different advance coefficients increases the uncertainty and the relative L_2 error, as presented in figure 2(b), where we trained surrogate models using only experiments performed at the lowest advance coefficients. Also in this case the uncertainty is higher far from the data, as

Table 1: Validation of \mathcal{GP} single-fidelity regressions for different high-fidelity measurements used for model training. Four different cases correspond to different training data sets. Relative L_2 error computed at the locations of high-fidelity measurements that were not included in model training, maximum uncertainty (2σ) and location of maximum uncertainty ($J_{\Sigma_{max}}$) are described for both thrust (K_T) and torque (K_Q) coefficients. High-fidelity inputs are indicated in terms of advance coefficients in square bracket.

| Inputs (J) | K_T | | | K_Q | | |
|-----------------|-------------|------------------------|--------------------|-------------|------------------------|--------------------|
| | L_2 error | $2\sqrt{\Sigma_{max}}$ | $J_{\Sigma_{max}}$ | L_2 error | $2\sqrt{\Sigma_{max}}$ | $J_{\Sigma_{max}}$ |
| [0, 0.40, 0.72] | 1.96% | 0.008 | 0.17 | 1.93 % | 0.008 | 0.17 |
| [0, 0.16, 0.24] | 8.1% | 0.05 | 0.7 | 11.4 % | 0.03 | 0.8 |
| [0.16, 0.321] | 8.2% | 0.15 | 0.7 | 11.7 % | 0.06 | 0.7 |
| [0.08, 0.64] | 8.2% | 0.18 | 0.36 | 3.3% | 0.07 | 0.36 |

demonstrated by the 2σ shaded regions in figure 2(b). When using only $N = 2$ measurements, the quality of model prediction significantly decreases, as showed in figures 2(c) and 2(d). Even if the relative L_2 error does not significantly increase, the trend of both thrust and torque coefficient is not correctly captured and the uncertainty associated to surrogate model prediction highlights these discrepancies. Table 1 summarizes results in figure 2 and demonstrates the importance of a strategic selection of training data when constructing probabilistic surrogate models. In many engineering problems quantities of interest can be inferred using prediction models based on simplified physics, numerical approximations or empirical regressions. This is true also for hydrodynamic objective functions characterizing propeller performance. The following examples demonstrate how numerical models, based on the simplified assumption of potential flow, can significantly improve the predictions of open water propeller performance in a wide range of operating conditions. The situation is well represented in figure 3(a) where we have $N_T = 2$ experiments available and low-fidelity predictions available in the entire range of J . The accuracy of low-fidelity numerical predictions is qualitatively described in figure 3(a). The relative error between predicted and measured thrust coefficient is as high as 20% at $J = 0.1$. We construct multi-fidelity surrogate models as described in section 2(b). In particular, we use a data set $\mathcal{D}_1 = [\{(J_{L_i}, K_{TL_i})_{i=1}^{N_L}\}, \{(J_{H_i}, K_{TH_i})_{i=1}^{N_H}\}] = \{J, K_T\}$ and $\mathcal{D}_2 = [\{(J_{L_i}, K_{QL_i})_{i=1}^{N_L}\}, \{(J_{H_i}, K_{QH_i})_{i=1}^{N_H}\}] = \{J, K_Q\}$ where $N_L = 7$, J_L is a vector of evenly spaced advance coefficients ($J \in [0.1, 0.7]$) and $N_H = 2$ represents the number of high-fidelity measurements collected during the experimental campaign. The covariance selected for modeling both low- and high-fidelity data, as well as the their cross-correlation is a squared exponential function as described in equation (11).

$$k_L(x_{pL}, x_{qL}) = \sigma_{fL}^2 \exp\left(-\frac{1}{2\ell_L}|x_{pL} - x'_{qL}|^2\right) + \sigma_{nL}^2 \delta_{pq} \quad (15)$$

$$k_H(x_{pH}, x_{qH}) = \sigma_{fH}^2 \exp\left(-\frac{1}{2\ell_H}|x_{pH} - x'_{qH}|^2\right) + \sigma_{nH}^2 \delta_{pq} \quad (16)$$

Therefore, a total of 7 hyper-parameters $\Theta = [\sigma_{fL}, \ell_L, \sigma_{nL}, \sigma_{fH}, \ell_H, \sigma_{nH}, \rho]$ will be learned from negative log-likelihood minimization. In the proposed multi-fidelity training, surrogate models are constructed assuming noise-free high-fidelity data and noisy low-fidelity predictions, in which

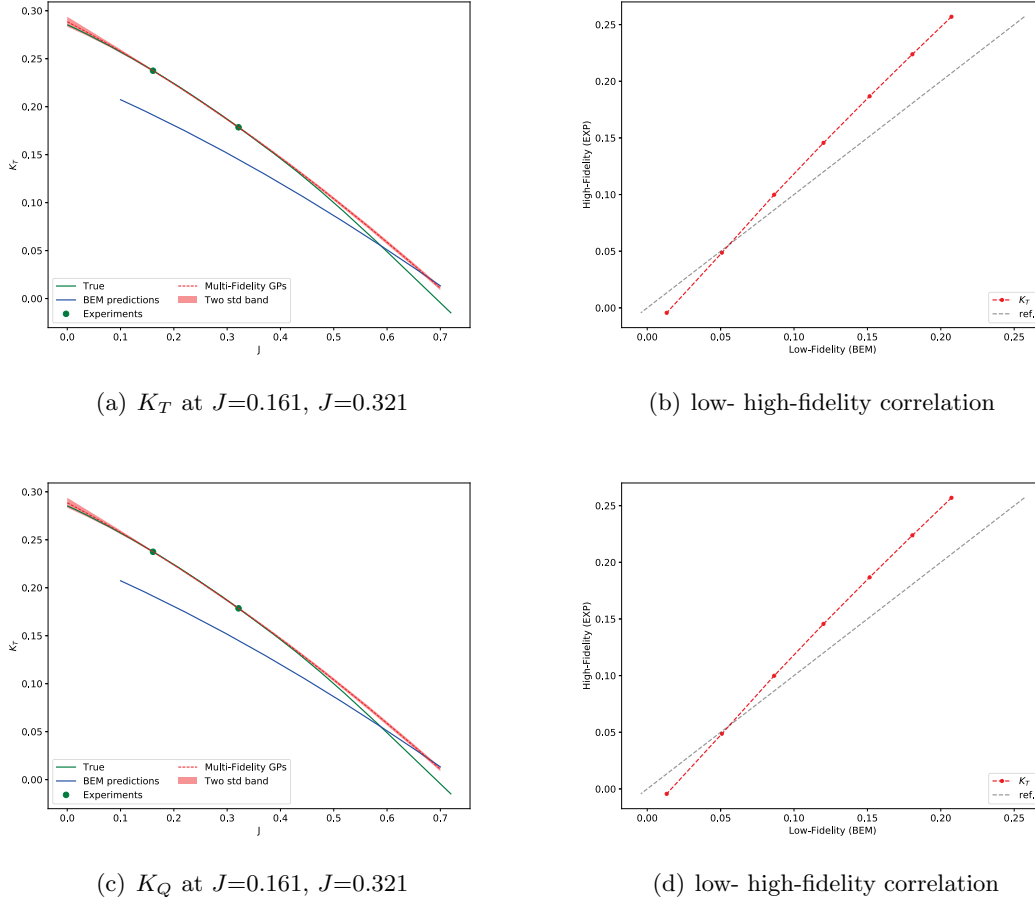


Figure 3: Construction of multi-fidelity \mathcal{GP} regressions for thrust and torque coefficients in the 1-D input space of advance coefficient J . The posterior mean is described by red dashed line, while uncertainty is described by a 2σ band colored in red. Low-fidelity data are evenly distributed in the range of $J \in [0, 0.7]$ and they are described with blue continuous line. High-fidelity data used in model training are represented by means of green circular dots, while high-fidelity measurements are described by green continuous line. For each quantity of interest we indicated the correlation between low- (LF) and high-fidelity (HF) data by means of red dashed curve (figures 3(b) and 3(d)). Grey dashed curve represents the situation for which LF=HF.

the noise σ_{nL} will be learned from data through negative log-likelihood minimization. Figure 3 presents results obtained for thrust coefficient predictions using $N_L = 7$ low-fidelity numerical predictions and $N_H = 2$ high-fidelity towing tank measurements at $J = 0.16$ and $J = 0.32$. Results in figure 3(a) demonstrate the significant improvements obtained by combining high-fidelity experimental measurements with low-fidelity numerical predictions. Even with low-fidelity predictions characterized by high inaccuracies (20% for $J = 0.1$), the linear correlation between low- and high-fidelity data (showed in figure 3(b)), allows to construct multi-fidelity \mathcal{GP} leveraging the autoregressive assumption expressed in (7). Results presented in figure 3(c) in terms of torque coefficient predictions (K_Q) confirms the advantages of the multi-fidelity

Table 2: Validation of \mathcal{GP} regressions for different high-fidelity measurements used for model training. Four different cases correspond to many sets of high-fidelity data. For each high-fidelity data set, multi-fidelity surrogates (HF+LF) are compared to single-fidelity models (HF) in terms of relative L_2 error computed at the locations of high-fidelity measurements that were not included in model training, maximum uncertainty (2σ) and location of maximum uncertainty ($J_{\Sigma_{max}}$). Results are presented for both thrust (K_T) and torque (K_Q) coefficients. High-fidelity inputs are indicated in terms of advance coefficients in square bracket. Low-fidelity inputs are evenly distributed in $J \in [0, 0.7]$.

| Inputs (J) | K_T | | | K_Q | | |
|------------------------|-------------|------------------------|--------------------|-------------|------------------------|--------------------|
| | L_2 error | $2\sqrt{\Sigma_{max}}$ | $J_{\Sigma_{max}}$ | L_2 error | $2\sqrt{\Sigma_{max}}$ | $J_{\Sigma_{max}}$ |
| [0, 0.40, 0.72]HF | 1.96% | 0.008 | 0.17 | 1.93 % | 0.008 | 0.17 |
| [0, 0.40, 0.72]HF + LF | 0.26% | 0.002 | 0.18 | 0.54% | 0.0004 | 0.14 |
| [0, 0.16, 0.24]HF | 8.1% | 0.05 | 0.7 | 11.4 % | 0.03 | 0.8 |
| [0, 0.16, 0.24]HF + LF | 3.95% | 0.001 | 0.8 | 4.36 % | 0.0001 | 0.8 |
| [0.16, 0.321]HF | 8.2% | 0.15 | 0.7 | 11.7 % | 0.06 | 0.7 |
| [0.16, 0.321]HF + LF | 3.9% | 0.0005 | 0 | 2.42 % | 0.0006 | 0 |
| [0.08, 0.64]HF | 8.2% | 0.18 | 0.36 | 3.3% | 0.07 | 0.36 |
| [0.08, 0.64]HF + LF | 2.07% | 0.0004 | 0 | 1.13% | 0.0004 | 0 |

framework. In particular, the good accuracy of the posterior mean obtained using high-fidelity data at low advance coefficients is confirmed also at higher J . Table 2 presents results obtained using the multi-fidelity framework presented in this study and compares them with single-fidelity modeling. For each high-fidelity data set described in table 1 we trained a multi-fidelity surrogate by blending towing tank measurements with low-fidelity predictions obtained using the BEM previously described. Results in table 2 clearly demonstrate the significant advantages of the multi-fidelity framework.

5 CONCLUSIONS

The paper presents a probabilistic approach to predict propeller performance using a diverse pool of data sources. The probabilistic learning framework constructed on the basis of recursive Gaussian Process Regressions is based on a linear autoregressive model. This approach allowed us to seamlessly blend low-fidelity numerical data coming from Boundary Element Method predictions with high-fidelity measurements obtained from cavitation tunnel experiments. In this paper we demonstrate the advantages of the proposed method by constructing surrogate models for open water thrust and torque coefficient of a conventional propeller, for which cavitation tunnel experiments were available at many advance coefficients. However, we validated the proposed framework by considering a limited number of high-fidelity data in the formulation of multi-fidelity \mathcal{GP} models. This demonstrated how the proposed method brings significant advantages if applied to engineering problems characterized by data scarcity such as the performance predictions of full scale propellers on operating vessels.

Acknowledgements

This project has been partially funded by DARPA EQUiPS grant HR0011517798. Authors wish to thank Prof. G.E. Karniadakis at Brown University for his valuable scientific guidance.

References

- [1] S. Gaggero, J. Gonzalez-Adalid, and M. P. Sobrino. Design and analysis of a new generation of CLT propellers. *Applied Ocean Research*, 59:424–450, 2016.
- [2] S. Gaggero, D. Villa, G. Tani, M. Viviani, and D. Bertetta. Design of Ducted Propeller Nozzles through a RANSE-based optimization approach. *Ocean Engineering*, 145:444–463, 2017.
- [3] D. Bertetta, S. Brizzolara, S. Gaggero, M. Viviani, and L. Savio. CPP propeller cavitation and noise optimization at different pitches with panel code and validation by cavitation tunnel measurements. *Ocean engineering*, 53:177–195, 2012.
- [4] S. Gaggero, G. Tani, D. Villa, M. Viviani, P. Ausonio, P. Travi, G. Bizzarri, and F. Serra. Efficient and multi-objective cavitating propeller optimization: An application to a high-speed craft. *Applied Ocean Research*, 64:31–57, 2017.
- [5] G. Tani, D. Villa, S. Gaggero, M. Viviani, P. Ausonio, P. Travi, G. Bizzarri, and F. Serra. Experimental investigation of pressure pulses and radiated noise for two alternative designs of the propeller of a high-speed craft. *Ocean Engineering*, 132:45–69, 2017.
- [6] S. Gaggero, T. Gaggero, E. Rizzuto, G. Tani, D. Villa, M. Viviani, E. Haimov, and J. Hallander. Experimental and numerical investigations for modelling propeller cavitation noise. In Santos T.A. Soares C.G., editor, *Maritime Technology and Engineering - Proceedings of MARTECH 2014: 2nd International Conference on Maritime Technology and Engineering*, pages 695–704. CRC Press/Balkema, 2015.
- [7] C. E. Rasmussen and C. K. Williams. In *Gaussian processes for machine learning*, volume 1, chapter 5. MIT press Cambridge, 2006.
- [8] P. Perdikaris and G. E. Karniadakis. Model inversion via multi-fidelity Bayesian optimization: a new paradigm for parameter estimation in haemodynamics, and beyond. *Journal of The Royal Society Interface*, 13(118):20151107, 2016.
- [9] P. Perdikaris, D. Venturi, J. O. Royset, and G. E. Karniadakis. Multi-fidelity modelling via recursive co-kriging and gaussian-markov random fields. *Proceedings of the Royal Society A: Mathematical, Physical and Engineering Sciences*, 471(2179):20150018, 2015.
- [10] L. Le Gratiet and J. Garnier. Recursive co-kriging model for design of computer experiments with multiple levels of fidelity. *International Journal for Uncertainty Quantification*, 4(5):385–386, 2014.
- [11] A. Forrester and A. Keane. In *Engineering design via surrogate modeling: a practical guide*, chapter 8. John Wiley & Sons, 2008.
- [12] M. C. Kennedy and A. O’Hagan. Predicting the output from a complex computer code when fast approximations are available. *Biometrika*, 87(1):1–13, 2000.

- [13] L. Bonfiglio, P. Perdikaris, S. Brizzolara, and G.E. Karniadakis. Multi-fidelity optimization of super-cavitating hydrofoils. *Computer Methods in Applied Mechanics and Engineering*, 332:63–85, 2018.
- [14] L. Bonfiglio, P. Perdikaris, J. del Águila, and G. E. Karniadakis. A probabilistic framework for multidisciplinary design: Application to the hydrostructural optimization of supercavitating hydrofoils. *International Journal for Numerical Methods in Engineering*, 116(4):246–269, 2018.
- [15] H.C. Raven. Minimising Ship Afterbody Wave Making using Multifidelity Techniques. In *Proceedings of the 32nd Symposium on Naval Hydrodynamics (SNH), August 5-10, 2018, Hamburg, Germany*, 2018.
- [16] L. Bonfiglio, P. Perdikaris, G. Vernengo, J. S. de Medeiros, and G. E. Karniadakis. Improving swath seakeeping performance using multi-fidelity gaussian process and bayesian optimization. *Journal of Ship Research*, 62(4):223–240, 2018.
- [17] L. Bonfiglio, P. Perdikaris, S. Brizzolara, and G. Karniadakis. A multi-fidelity framework for investigating the performance of super-cavitating hydrofoils under uncertain flow conditions. In *19th AIAA Non-Deterministic Approaches Conference*, page 1328, 2017.
- [18] L. Bonfiglio, J. O. Royset, and G. E. Karniadakis. Multi-disciplinary risk-adaptive design of super-cavitating hydrofoil. In *2018 AIAA Non-Deterministic Approaches Conference*, page 1177, 2018.
- [19] J. O. Royset, L. Bonfiglio, G. Vernengo, and S. Brizzolara. Risk-adaptive set-based design and applications to shaping a hydrofoil. *Journal of Mechanical Design*, 139(10):101403, 2017.
- [20] C. E. Rasmussen. Gaussian processes in machine learning. In *Advanced lectures on machine learning*, pages 63–71. Springer, 2004.
- [21] R. M. Neal. Priors for infinite networks. In *Bayesian Learning for Neural Networks*, pages 29–53. Springer, 1996.
- [22] A. Stuart and A. Teckentrup. Posterior consistency for gaussian process approximations of bayesian posterior distributions. *Mathematics of Computation*, 87(310):721–753, 2018.
- [23] P. Perdikaris, D. Venturi, and G. E. Karniadakis. Multifidelity information fusion algorithms for high-dimensional systems and massive data sets. *SIAM Journal on Scientific Computing*, 38(4):B521–B538, 2016.
- [24] AQUO. *Work Package 2: Noise Sources, Task T2.3: Experimental investigations in model scale*. AQUO - Achieve QUIeter Oceans by shipping noise footprint reduction, European Commission within the Call FP7, 7th framework program, Grant Agreement no. 314227, 2015.

Research on Selection of Base for Impact Assessment of Shipborne

Equipment

CHEN JI, CHI ZHANG

Navy Research Academy, Beijing 100161

Keywords: Base; impact assessment; spring mass unit; natural frequency ratio; mass ratio

Abstract: The simulation calculation of the pump shaft shows that the base of the pedestal will impact the impact results in impact assessment. Therefore, the factors affecting the natural frequency of the system are studied by using the spring mass element. Based on the DDAM theory, two variables are calculated by setting control frequency ratio and mass ratio through various working conditions. It is found that the ratio of the natural frequency of the base and the equipment is about 5 is the impact of the base to the impact results, that is, the natural frequency is larger when the ratio is less than 5, and the influence of the base is not changed when the ratio is more than 5. It is also found that the mass ratio is the factor that determines the impact of the pedestal on the final impact. The smaller the mass ratio (the ratio of natural frequency to more than 5), the closer the acceleration response ratio is to 1, that is, the influence of pedestal on impact assessment process can be ignored. Finally, the test and simulation verify that when the natural frequency ratio of the base and equipment is greater than 5, the mass ratio is very small (0.1).

1. INTRODUCTION

Navies all over the world attach great importance to the anti-impact capability of mechanical equipment on warships. After World War II, the U.S. Navy used captured warships to carry out tests, accumulated a large number of test data, and made an important contribution to the research of anti-impact field of U.S. warships^[1]. Germany, the former Soviet Union and other world naval powers have also formulated standards and specifications for ship anti-impact requirements and tests, and formed a relatively mature standard document system for ship anti-impact. In fact, no matter surface ships or submarines, when designing and manufacturing equipment, they all need to have a certain impact resistance ability to meet the requirements of the code, so the key shipborne equipment should carry out impact tests^[2-4].

Overall, the impact of shipborne equipment in foreign countries started earlier, but also carried out a large number of systematic research, from test methods to assessment standards are more detailed. However, the disclosure of public information is rare. Juanito Del Rosario and Steven Murphy briefly introduced the requirements and basic principles of Grade A in ML-S-901D. Steven T Thompson summarized the work of underwater explosion test of class A warship equipment through floating impact platform^[5]. The acceleration and velocity time history curves of some measuring points at Tom Moyer established the finite element model of the extended floating impact platform^[6]. Simple simulation analysis was carried out and

the results were in good agreement with the test results^[7]. Chris Grunau introduced in detail the assessment of medium and heavy equipment in ML-S-901D standard. At the same time, he introduced HI-TEST laboratory in the United States, which can complete the underwater explosion assessment test of standard and medium floating impact platform, and provided beneficial reference for the impact test procedure^[8].

However, in the process of impact assessment of Shipborne equipment, a series of basic but key problems still need to be solved. Among them, the problem of local impact environment and boundary selection of equipment location is particularly prominent. Because most of the equipment components are many and the logic relationship is complex, when they are subjected to strong impact while withstanding working stress, they will produce complex dynamic behavior of motion-impact coupling, which will lead to different degrees of impact or damage caused by local stress concentration of equipment components. As shown in Fig.1, the cabin equipment is installed in the cabin through the base. For non-contact underwater explosion and non-direct hit (for equipment), the cabin equipment is integrated with the whole cabin and even the hull, and its shock response is bound to be related to the cabin structure^[9]. The shock response characteristic of engine room is the basic environment. It is necessary to describe the environment accurately before analyzing the equipment response. Because of the continuity of the structure, it is unrealistic to describe the impact response of the cabin area alone.

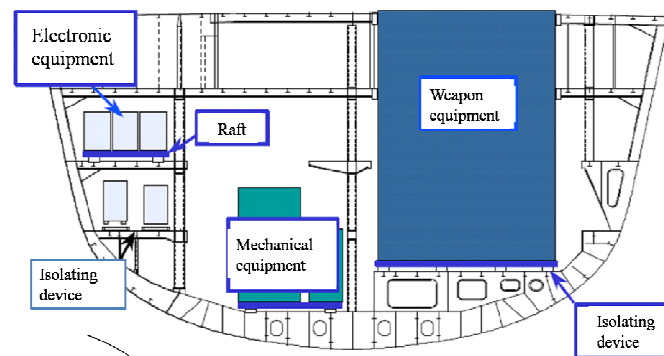


Fig1 Schematic diagram of ship equipment impact damage

Therefore, it is necessary to determine a reasonable technical approach to properly deal with the relationship between external impact environment, intermediate structure and shipborne equipment, especially the selection of installation foundation in the process of impact assessment.

2 SHOCK SPECTRUM THEORY AND DDAM METHOD

2.1 Shock spectrum theory

Shock spectrum has been widely used in the field of shock resistance of Shipborne equipment^[10]. Many literatures have described the concept and classification of shock response spectrum in detail^[11]. SRS-Shock Response Spectrum is also called "Shock Response Spectrum". This concept was proposed by Blot. M. A. in 1963^[12]. It is defined as a series of linear single-degree-of-freedom systems with different frequencies and certain dampers subjected to impact force. The relationship between the maximum response of each single-degree-of-freedom system and its frequency is shown in Fig. 2. Shock response spectrum is usually used to guide the anti-shock design of warships and shipborne equipment^[13].

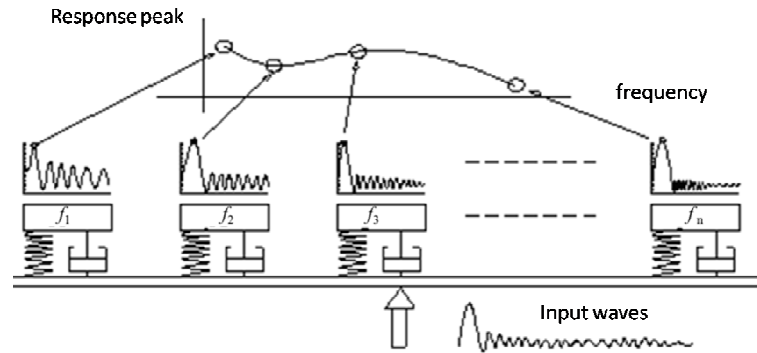


Fig2 Schematic diagram of shock response spectrum definition

The shock spectrum includes four parameters: relative displacement, relative velocity, absolute acceleration and frequency. The velocity spectrum is taken as the ordinate and the frequency as the abscissa, and the coordinate systems of +45 degree and -45 degree with abscissa represent the relative displacement spectrum and the absolute acceleration spectrum, respectively. Figure 3 shows a typical design shock spectrum.

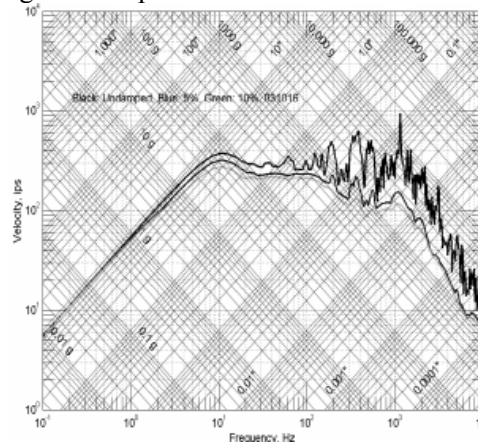


Fig3 Typical ship impact spectrum

By rounding the shock spectrum measured by the test, the shock spectrum can be designed and used as input in the shock resistance analysis of naval equipment. It can be seen from the figure that displacement excitation is the main excitation in the low frequency band, velocity scattering excitation is the main excitation in the middle frequency band and acceleration excitation is the main excitation in the high frequency band. Shock spectrum is the maximum response of a single-degree-of-freedom oscillator with various mounting frequencies on the foundation to describe the impact motion of the foundation. It is convenient for frequency domain calculation.

2.2 Dynamic design analysis method (DDAM)

One dimensional DDAM theory is mainly used in the dynamic analysis method prescribed in the military standard of our country. The basic idea is to obtain the modal frequency and quality of the system through modal analysis, then apply the prescribed impact load spectrum to each modal, then get the response of the modal, and finally get the shock response of the whole equipment by modal synthesis method.

3. ANALYSIS OF BOUNDARY PROBLEM OF INSTALLATION FOUNDATION

3.1 Computing Model

This calculation model is pump shaft equipment, including motor, motor fixture, shaft, shaft support and hull structure at the bottom of the support, etc., as shown in Figure 4.

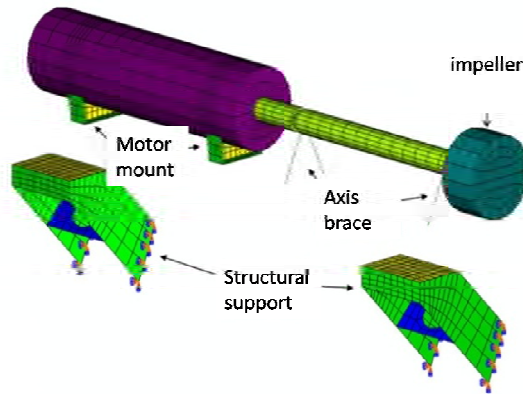


Fig. 4 Assembly sketch of marine pump shaft

Firstly, the dynamic design and analysis of the pump shaft body are carried out, assuming that the hull structure brackets are rigid bodies. Then the analysis model is extended to include the hull structure bracket, and the rationality of the two analysis results is compared.

3.2 Pump Shaft Separate Analysis

The selected research object includes a 7-foot diameter shaft, impeller and two supporting structures, in which the stiffness of bearing 1 is $6.63 \times 10^6 \text{lb/in}$, the axial stiffness of bearing 2 is $2.56 \times 10^6 \text{lb/in}$, and the radial mesh is $6.63 \times 10^6 \text{lb/in}$. The impeller mass is 487.3Lbs and the impeller moment of inertia $I_{11}=I_{22}=65.16 \text{lb-in-sec}^2, I_{33}=93.10 \text{lb-in-sec}^2$. The separate analysis model of the pump shaft is shown in Fig. 5.

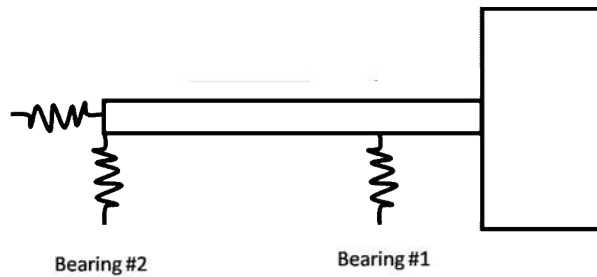


Fig. 5. Simplified diagram and finite element model of pump shaft

The modal analysis of the pump shaft model shown in Fig. 4 is carried out by using ABAQUS simulation software. In the pump shaft model, the first 12 modes reach 80% of the total mass. The main frequencies and input spectra of the model are shown in Table 1.

Tab1 Modes of modal impact load

| The modal number | Frequency (Hz) | Modal mass percentage (%) | Spectral acceleration (g) |
|------------------|----------------|---------------------------|---------------------------|
| 5 | 184.77 | 75.16 | 238.35 |
| 1 | 79.10 | 11.55 | 123.43 |

After determining the load, the displacement and stress response values of each mode of the model under their respective impact loads are calculated in DDAM module, and the peak stress values are synthesized by NRL method. As shown in Fig. 6, the maximum stress response value of the equipment under vertical impact is 370.1 Mpa, which is located near the disc impeller at the bearing 1 support position.

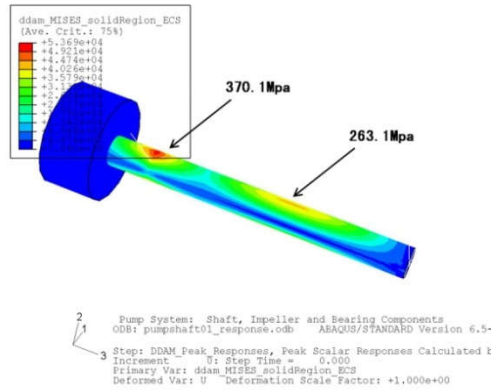


Fig6 Vertical stress response cloud chart of pump shaft

According to the above calculation results, reference is provided for improving the design, such as adjusting the support position or designing the shaft into a variable cross-section beam to make it uniformly stressed, but the analysis results of the pump shaft alone can not determine whether the equipment can withstand the specified impact load. There are two reasons: First, the impact spectrum stipulated by GJB1060.1 is below the equipment base, not the equipment body, so the equipment should be with its base. The DDAM model of the system is established together. The second is that even though the calculation results show that the equipment can withstand the specified impact load, it is also difficult for the equipment to work normally if the base which is not involved in the calculation and verification is damaged under the impact. Therefore, for rigidly mounted equipment on the base, the equipment-base system must be taken as the calculation model.

3.3 Pump Shaft Assembly Overall Response Analysis

Consider the installation infrastructure of pump shaft equipment, including motor fixtures, hull structure brackets, etc., as shown in Figure 7.

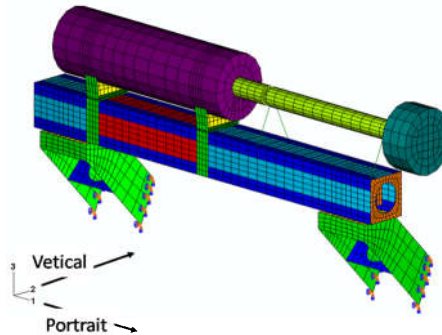


Figure 7 Schematic diagram of pump shaft assembled

The mode shapes and frequencies are changed due to the addition of the pedestal structure. It will take 56 order modes to analyze the modal mass sufficient for 80% of the mass. The final selected modal and input spectral acceleration are shown in Table 2.

Table 2. Modal selection and impact acceleration

| The modal number | Frequency (Hz) | Modal mass percentage (%) | Spectral acceleration (g) |
|------------------|----------------|---------------------------|---------------------------|
| 1 | 20.74 | 70.91 | 31 |
| 11 | 133.6 | 6.65 | 207.83 |
| 7 | 84.44 | 1.63 | 131.78 |
| 2 | 38.04 | 1.5 | 59.37 |
| 10 | 117.84 | 1.41 | 183.93 |
| 17 | 244.09 | 1.22 | 248.41 |
| 16 | 233.65 | 1.14 | 248.49 |
| 8 | 98.28 | 0.45 | 153.5 |
| 3 | 44.49 | 0.36 | 69.48 |

| | | | |
|----|--------|------|--------|
| 12 | 163.17 | 0.14 | 249.46 |
| 13 | 211.68 | 0.11 | 249.49 |

After calculating and synthesizing the impact response of the whole body, the stress and displacement nephogram is drawn as shown in Figure 8. Under the action of vertical impact, due to the interaction between the base structure and the pump shaft equipment, the response of the pump shaft becomes smaller and its position changes than that of the single analysis. The maximum stress occurs in the midspan of bearing 1 and bearing 2, and the maximum value is 160.3 MPa. However, there is no peak stress at the support root where the maximum stress of the model is analyzed separately.

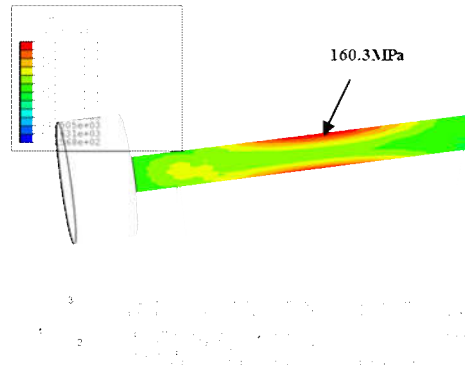


Figure 8 Stress shock response nephogram of pump shaft

According to the above calculation results, it provides a reference for improving the design, such as changing the form of support structure to make the force more uniform, reducing the mass of pump shaft to reduce impact stress, strengthening the size of structural components, etc.

The comparison between the individual analysis and the overall response analysis of the pump shaft shows that the selection of appropriate analysis area is very important for the comprehensiveness and reliability of the calculation results. If the calculation range is incorrect, the result may be misleading to improve the design direction.

4. SIMPLIFIED CALCULATION METHOD

4.1 Research on Spring System

When the bearing equipment of the base can be simplified to a rigid body mass and the support of the equipment in the direction of impact load is symmetrical, the stress of the base structure can be calculated by the simplified calculation method of single degree of freedom^[14]. By single-degree-of-freedom equipment quality M_e The dynamic system model consisting of the stiffness K of the connection between the equipment and the base and the base of the equipment is shown in Fig. 9.

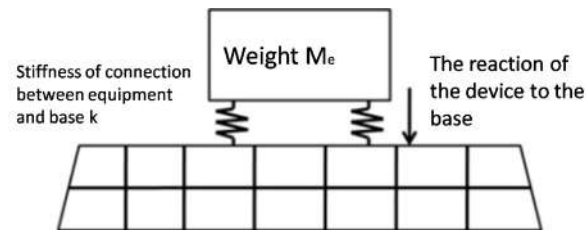


Figure 9 Dynamic system model of single-degree-of-freedom equipment-base

Similarly, there are many random factors in the process of shock calculation of Shipborne equipment^[15]. Therefore, to compare the research of single-degree-of-freedom system, a complex multi-degree-of-freedom system is always considered to be composed of two or more spring mass systems, and some intermediate processes are regarded as spring mass sheets^[16]. As shown in Fig. 10, it is a schematic diagram of two-degree-of-freedom spring mass unit.

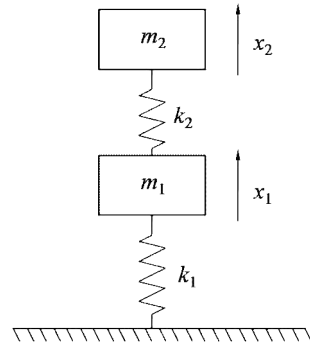


Figure 10. Schematic diagram of 12-DOF spring system

4.2. Research on the Influences of Installation Foundation of Spring System

4.2.1. Working condition setting

In the previous section, we studied the two-degree-of-freedom spring system, but we have not explained the influence rule of the base on the impact results in the process of impact calculation. The loading method of DDAM is different from that of the traditional time-domain bottom loading. So if we use the traditional two-degree-of-freedom spring, we need to fix the bottom completely in the calculation, so the acceleration under the base is 0, which is difficult to be used as comparative data. Therefore, a three-degree-of-freedom spring mass system can be established, as shown in Fig. 11. The upper layer takes the equipment and base as flexible body. The reason for providing a spring mass system with larger stiffness but smaller mass at the bottom as the base is that considering the mode mass as the main parameter of impact input in DDAM method, and the sum of mode mass equals the total mass, the base mass is smaller (100kg) in order not to destroy the whole mass system. It can also be seen that the mode mass (99kg) and frequency (6400Hz) of the third-order modes are basically fixed values. Of course, another consideration of this simplified method is introducing a small mass and large stiffness matrix. While solving this problem, the boundary conditions of type I installation (hull base and bulkhead below main deck) in impact calculation are also simulated. m_1 can be used as the boundary of the first layer. In the problem studied in this paper, it can be expressed as the base under the equipment, where m_1 is the mass of the base and k_1 is the stiffness of the base itself. m_2 is equipment quality, k_2 is equipment stiffness.

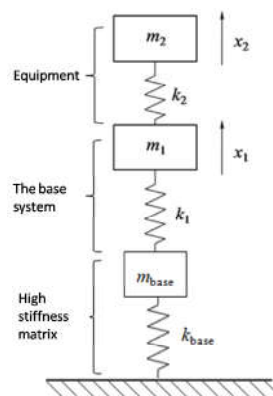


Fig. 11 A schematic diagram of a three-degree-of-freedom spring system

Considering the conclusion that the mass and the natural frequency of single-degree-of-freedom spring have an effect on the calculation results^[17], a number of groups of calculations with natural frequency and mass as variables are set up for comparative study. The natural frequencies of two single-degree-of-freedom systems are taken as variables with the natural frequencies ratio f_1 / f_2 ranging from 0.5 to 8. The quality was also grouped in the form of mass ratio. The mass ratio m_1 / m_2 was divided into six groups: 0.1, 0.4, 0.8, 1, 1.5 and 5.

4.2.2 Analysis of calculation results

Acceleration response (A_d) below the base is extracted and compared with the acceleration response (A_u) above the base. Then the six curves with mass ratio of 0.1-5 are plotted to compare the diagrams shown in Fig. 11 and Fig. 12.

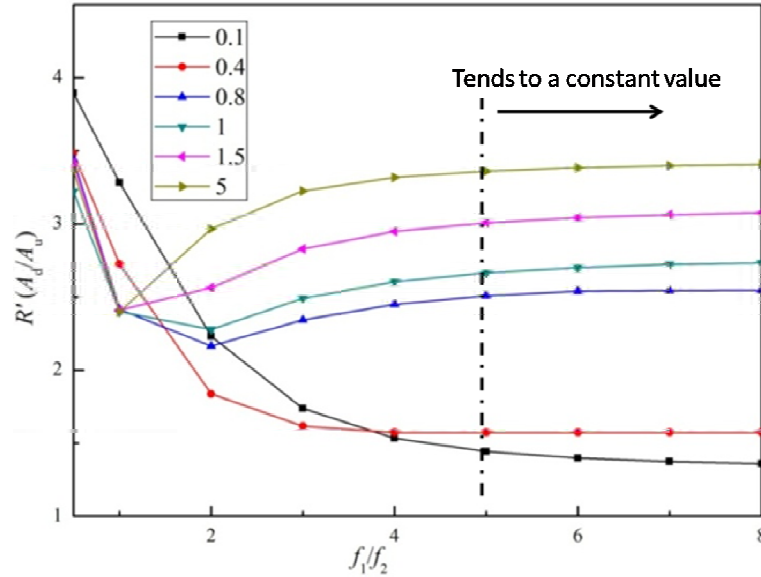


Fig. 11 Acceleration response ratio below and above base

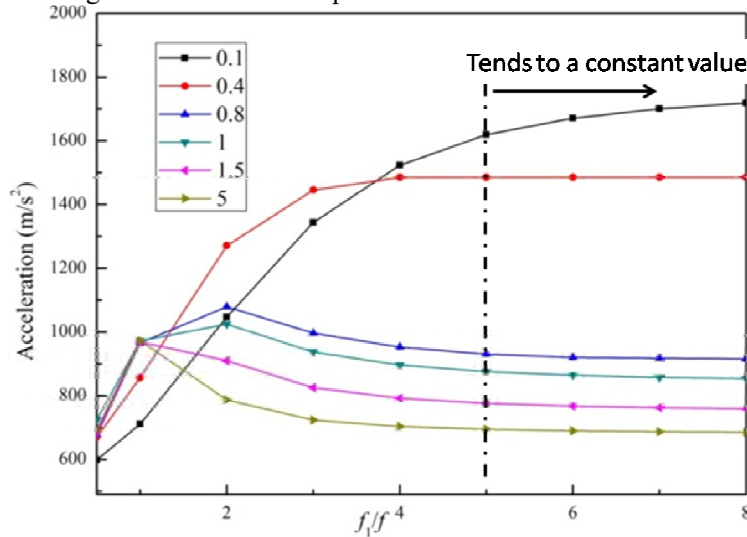


Figure 12. Acceleration response curve above base

Through the two graphs, it can be found that when the ratio of natural frequencies exceeds 5, the influence of the ratio of natural frequencies on the transmission of system response is less. When the ratio is not more than 5, the smaller the mass ratio, the slower it will reach the constant state. In addition, it can be seen from the two charts that after the natural frequency exceeds 5, the mass ratio is the final factor to determine the size of the base. The smaller the mass ratio is, the closer the acceleration response ratio is to 1. This shows that the smaller the influence of the base is, that is, the higher the natural frequency of the base is relative to the equipment, but the lighter the mass of the base has little influence on the results of impact assessment, which is more common in the large-scale equipment installed in the class.

4.3 Simulation and Test Verification

4.3.1 Equipment Base Simulation Analysis

(1) Model introduction

The equipment base structure (finite element model) is shown in Fig. 13. The total mass of the base is 1.5t, the length is 4.6m, the width is 2.0m and the height is 0.4m (0.3m). In the calculation process, the installation frequency and base frequency are considered respectively. In order to simulate the installation of the equipment, the joint on the panel is constrained by coincidence, and the constraint point is the center of gravity of the equipment. Considering the effect of the approximate interaction between the equipment and the base on the results, the upper equipment is replaced by spring mass unit, and the spring stiffness is $3.8 \times 10^7 \text{N/m}$ (set according to the modal analysis results) and the upper mass of the spring is 15t.

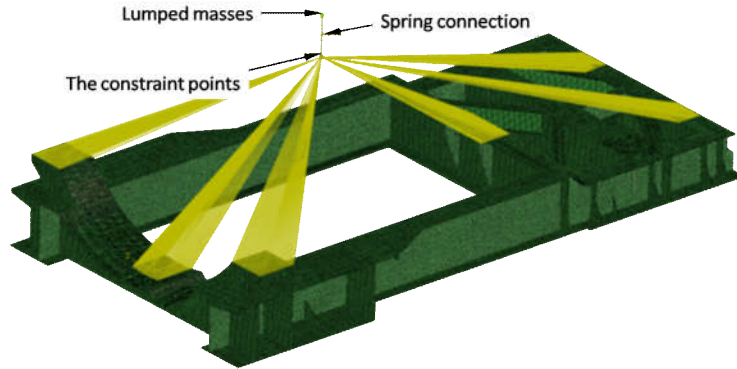


Figure 13. Connection constraints with springs

(2) Modal analysis of equipment

Table 3 shows the frequency and mode shapes of the main constrained modes of Certain equipment. The overall vertical modes are described, while the others are local modes.

Table 3 Global modal calculation results

| Frequency(Hz) | Description of major modes |
|---------------|----------------------------|
| 8.00 | Z swing |
| 14.11 | Z vibration |
| 36.45 | Z vibration |

(3) Modal analysis of base

Firstly, unconstrained modal analysis of the equipment (rigid body displacement has been filtered). Its vertical modal response frequency is shown in Table 4.

Table 4 Modes of each order

| Order number | Frequency | Vibration mode |
|--------------|-----------|----------------|
| 3 | 65 | downwarping |
| 6 | 91 | uprping |

Through modal analysis and calculation, it can be known that the ratio of natural vertical frequency of base and equipment is about 8. The ratio of base mass to equipment mass is 0.1, which meets the requirements of high natural frequency but low quality of base.

4.3.2 simulation results

As shown in Fig. 14, the impact environment above the base after loading shock input is compared with the design spectrum. From the diagram, it can be seen that the impact environment at the bottom of the base almost coincides with the impact environment after passing through the base, and the natural frequency of the coupling system composed of spring-equipment-base changes. It can be seen that the base, especially the base with larger stiffness, has little impact on the impact environment.

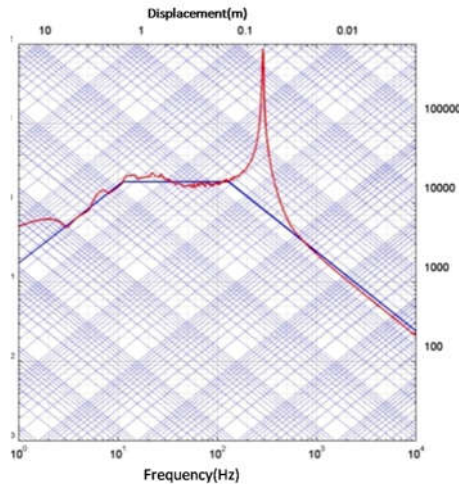


Figure 14 Comparisons of impact environments for spring simulation equipment models

4.4 experimental study

4.4.1 Certain Equipment Impact Test

(1) Equipment and measuring point arrangement

Certain equipment is installed on floating platform on water surface. The base is installed between the Certain equipment and the installation platform. The upper and lower parts of the base are separately set up with measuring points to extract data and draw shock spectra. As shown in Figure 15.

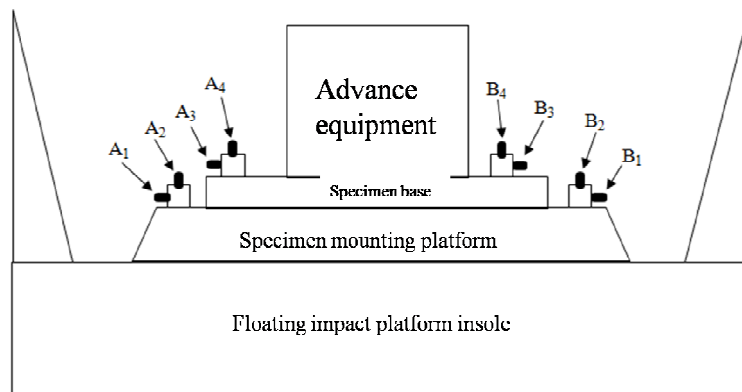


Fig. 15. Schematic diagram of test installation of Certain equipment

(2) Floating test

Platform is used to carry out impact test under working conditions, the underwater non-contact explosion impact test is carried out from far to near.

4.4.2 Test results analysis

In order to increase the reliability of data and retain the features that may be more important, no filtering is carried out in the process of shock harmonic rendering. Fig. 16 is the experimental results. The results of the front-facing test show that the pedestal does amplify the impact environment in the low, middle and high frequency bands, but the amplification is not obvious. The low frequency band of the back-burst has almost no amplification effect, while the acceleration spectrum in the high frequency band has a significant increase. Therefore, it can be found that the base has no effect on the acceleration spectrum in other frequency bands except in the high frequency band.

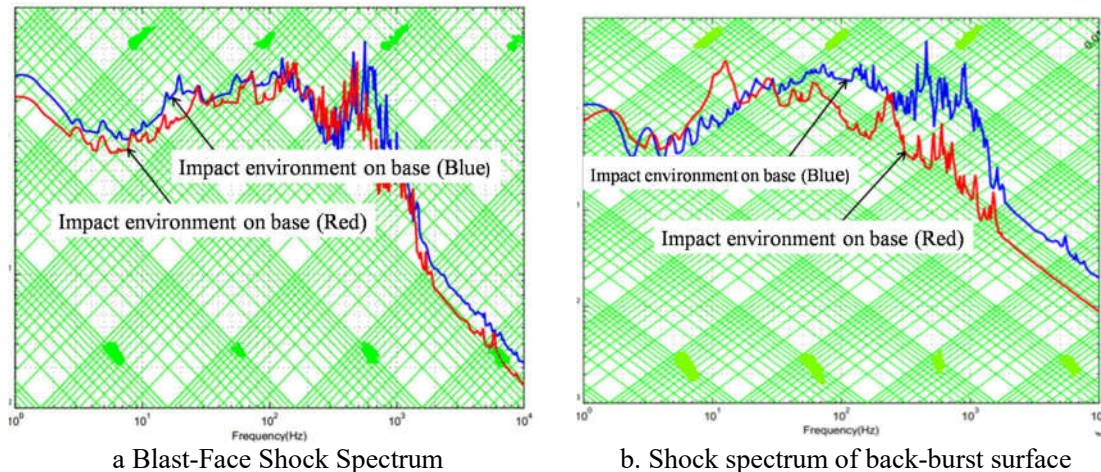


Figure 16 Comparisons of impact environments in case 1

5 CONCLUSION

Through the simulation calculation of the pump shaft, the impact of the installation foundation such as the base on the impact test results is analyzed. Therefore, based on the theory of DDAM and the spring mass element, the selection of the base in the impact assessment of shipborne equipment is studied. It is found that:

The natural frequency ratio of the base to the equipment is about 5, which is the boundary where the base affects the impact results. That is to say, when the ratio is less than 5, the natural frequency has a greater impact, and when the ratio is more than 5, the influence of the base begins to remain unchanged. At the same time, it is found that the mass ratio is the factor that determines the impact of the base on the final impact results. The smaller the mass ratio is, the closer the acceleration response ratio is to 1, that is to say, the influence of base on impact assessment can be neglected.

Finally, experiments and simulations verify that the frequency ratio is greater than 5 and the mass ratio is very small (0.1), which is in line with the research results.

REFERENCE

- [1] LI Zengguang. Impact Resistance Analysis of Ship Propulsion Shafting [D] Wuhan University of Technology, April 2006.
- [2] Zhang A M, Zhou W X, Wang S P, Feng L H. Dynamic response of the non-contact underwater explosions on naval equipment[J]. Marine Structures, 2011, 24(4): 396-411.
- [3] Li J, Rong J L. Experimental and numerical investigation of the dynamic response of structures subjected to underwater explosion[J]. European Journal of Mechanics - B/Fluids, 2012, 32: 59-69.
- [4] Guo Ji. Study on Frequency and Time Domain Characteristics of Ship Impact Environment [D]. Harbin: Harbin Engineering University, 2010.
- [5] Juanito D R, Steven M. OMB No. 0704-0188, Environmental Engineering Grade A Shock Tests[R]. San Diego, California: SPAWAR Systems Center San Diego, SEP, 2003.
- [6] Steven T T. DTI Report NO. 655, Heavyweight high impact (H.I.) shock test report for the argon ship exploration equipment increment E (SSEE-E) system for 901D[R]. Rustburg, Virginia: Dynamic Testing, A Division of DTI Holdings, LLC, July, 2003.

- [7] Chris G. Heavyweight high impact shock testing[R]. Arvonnia, Virginia: HI-TEST Laboratories, Inc., 2007.
- [8] Tom M. Full ship shock test modeling[R]. Washington: Naval Sea Systems Command, April, 2008.
- [9] GeersTL. Doubly asymptotic approximations for transient motions of submerged structures. *J. Acoustic Society of America*, 1978(64): 1500-1508.
- [10] Du Zhipeng, Wang Yu, Yang Yang, Hua Hongxing, Shi Shaohua. Fitting and Application of Shock Signal of Underwater Explosion of Ships [J]. *Vibration and Shock*, 2010,29(3) 182-184.213.
- [11] Parzianello G, Francesconi A, Pavarin D. An estimation method for the Shock Response Spectrum propagating into plates subjected to hypervelocity impact[J]. *Measurement*, 2010, 43: 92-102
- [12] Alexander J E. Shock response spectrum-A primer[J]. *Sound&Vibration*, 2009, 43: 6-14.
- [13] Wang Yu, Hua Hongxing. *Modern Shock Theory and Application of Ships* [M]. Beijing: Science Press, 2005.
- [14] Feng Linhan, Wang Yu, Du Jianye, Jichen. Equivalence study of shock response calculation method for naval equipment [J]. *Shipbuilding Engineering*, 2011, 33 (Sup2): 210-214.
- [15] Feng Linhan, Wang Yu, Zhang Lei. Reliability analysis of shock resistance of naval equipment [J]. *Vibration and shock*, 2013, 32 (1):140-144.
- [16] Jin Chengding, Xia Lijuan. *Ship Vibration* [M]. Shanghai: Shanghai Jiaotong University, Shanghai, 2011.
- [17] Zheng Changyun, Zhao Pengyuan, Hongguang, Song Jingli. Impact Response Analysis of Equipment Buffer Platform under Underwater Explosion Load [J]. *Science and Technology Report*, 2012, 30 (18) 37-40.

DESIGN OF OPEN-WATER AND WAKE-ADAPTED OPTIMUM PROPELLERS BASED ON A VORTEX LATTICE LIFTING-SURFACE MODEL

MARINE 2019

Yong-Sheng Huang, Qi Wang, Xiao-Qian Dong* and Chen-Jun Yang

State Key Laboratory of Ocean Engineering
Collaborative Innovation Center for Advanced Ship and Deep-Sea Exploration
Shanghai Jiao Tong University
No.800,Dongchuan Road, 200240, Shanghai China
*e-mail: xiaoqiandong0330@sjtu.edu.cn

Keywords: Marine propeller, Design, Optimum circulation, Open-water, Wake-adapted, Vortex lattice

Abstract: A new design procedure has been proposed for optimum marine propellers operating in uniform and radially non-uniform inflows based on a vortex lattice lifting-surface model (VLM). The procedure consists of two stages. In the first stage, the optimum circulation distribution along the radius is determined by using a fixed camber line. Assuming that the local inflow is tangent to the camber line at the leading edge, the maximum camber at each radius is expressed as function of the pitch angle. Interactions start from a pitch angle profile that the blade loading is zero. Before the thrust reaches design value, the pitch angle at each radius increases with an increment proportional to the local gradient of efficiency to pitch. In the second stage, the optimum circulation distribution obtained in the first stage is used to design the pitch and camber with a prescribed chordwise loading distribution. For a set of assumed pitch profile and camber surface geometry, the circulation distribution over the camber surface is computed by means of the VLM, and used to update the camber surface geometry by the Newton-Raphson iterative scheme according to the differences between the computed and the prescribed circulation distributions. The proposed method has been applied to the design of a highly skewed propeller in uniform and radially non-uniform inflows.

1 INTRODUCTION

The circulation distribution plays an important role in the performance of marine propellers. In the propeller design, the optimal circulation distribution corresponding to the maximum efficiency of propeller is determined according to the given thrust/torque at first. And then some necessary corrects of circulation are made at the tip and root of the blade to improve the cavitation and vibration performance. Therefore, determining the optimal circulation distribution is the primary work of propeller design.

In 1919, Betz ^[1] determined a criterion for minimum energy loss on the flow downstream of the propeller in ideal fluid, which can be utilized to solve the optimal circulation distribution in open water. Based on the lifting-line model, Lerbs ^[2] established a method for

determining the optimal circulation in non-uniform flow and a propeller design method with the arbitrary circulation. The method was improved by Morgan ^[3] and widely used for decades. Different from the continuous vortex model of Lerbs, in the lifting-line model of Kerwin and Coney ^[4], the horseshoe vortex is represented as discrete vortex elements, and the auxiliary function is used to change the determination of the optimal circulation into the solution of a variational problem, the effect of viscosity can be considered, besides, the model can be applied to traditional propeller and multi-component propeller. Cai ^[5] et al. adopted a particle swarm optimization algorithm based on mutation strategy to determine the optimal circulation, which is applicable for the optimal circulation problem of various propellers including heavy-loading propellers.

The methods based on the lifting-line model were used in a longtime. Recent years the lifting-surface method is adopted to determine the optimum circulation for marine propellers. Olsen ^[6] established a method for determining the optimal circulation based on the VLM. The vortex lattice is arranged on the helical surface that passing through the line connecting the midpoints of the chords. The chordwise distribution of the circulation is specified by the weight function, and the magnitude of the circulation is determined by the variational solution. Lee ^[7] developed Olsen's method, the blade camber surface is represented by a B-spline surface, considering the camber, the least squares minimum of the normal velocity is used to replace the impenetrable condition of the camber surface, so that the circulation optimization and the blade design are performed simultaneously. However, methods developed by Olsen and Lee both involve the complex derivation of partial differential equations.

In this paper, a new design procedure also based on VLM has been established for optimum marine propellers. In the first stage, the optimum circulation is determined based on performance prediction of the propeller and much simple than that used by Olsen and Lee, especially avoids the derivation of partial differential equations. In the second stage, the optimum circulation is used to design blade geometry. To distribute the loading along the chord as prescribed form, the Newton-Raphson iteration is used to design the pitch profile and camber surface geometry. This procedure considers the contraction of the wake vortex and can deal with the highly skewed propeller.

2 DESIGN METHOD

2.1 Method of optimum circulation solution

The current method deals with moderately loaded propellers in accord with the code for propeller performance prediction described later. The parameters of propeller, such as diameter, chord length, trim, skew and thickness are given. The normalized camber profile is selected in advance. The optimum circulation is determined by iteration starting from the state that the blade loading is zero, the distribution of the gradient of the propeller efficiency to the pitch angle is pre-commutated in each iteration, the pitch angle where the gradient is higher increases prior. When the design thrust coefficient is achieved, the optimum circulation is obtained.

2.1.1 Code for propeller performance prediction, SPROP30

The SPROP30 is a performance prediction program based on the vortex lattice

lifting-surface model^[8,9,10]. It is suitable for highly skewed blade geometry, the inflow can be uniform or non-uniform. The code uses quadrilateral lattices to discretize the camber surface. Firstly, the $M+1$ cylindrical surfaces coaxial with the blade are used to cut the camber surface, which is divided into M radial equidistant strips. The radius of the cylindrical surfaces is determined by equation (1):

$$\rho_m = r_H + (D/2 - \Delta r_{in} - r_H) \frac{m-1}{M} \quad (m = 1, 2, \dots, M+1) \quad (1)$$

Where r_H and D represent the hub radius and the blade diameter, respectively, Δr_{in} is the inset of blade tip, here $\Delta r_{in} = 0.01D$. Furthermore, each strip is divided into N quadrilateral with equal arc length along the chordwise direction, then arranging the spanwise vortex element at $1/4$ of the chord length of each lattice. The coordinates of the endpoints of the n -th spanwise vortex element are (ρ_m, s_n) and (ρ_{m+1}, s_n) respectively, where s is the dimensionless chordwise coordinates, $s=0$ at the leading edge, $s=1$ at the trailing edge, s_n is determined by equation (2):

$$s_n = \frac{n-3/4}{N} \quad (n = 1, 2, \dots, N) \quad (2)$$

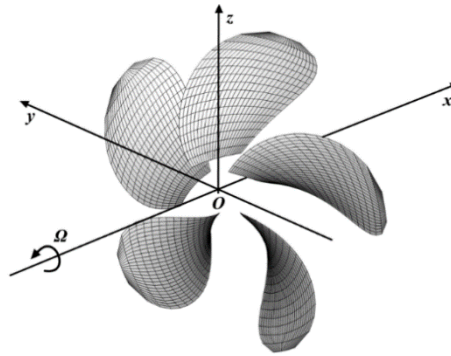


Figure 1: Calculation coordinate system and blade vortex lattice model

Applying the kinematic boundary condition that the flow is tangential to the camber surface of the blade, linear equations for the spanwise vortex intensity are built on the geometric centers of vortex lattices and solved, then hydrodynamic forces acting on the blades are obtained by integrating the forces acting on each vortex elements and source elements. The governing equations, the calculation of thrust and torque, etc., refer to [10]. The calculation in current work does not considerate the influence of hub.

2.1.2 Relationship between maximum camber and pitch under a given camber profile

The assumption is made in current method: on the blade section, the relative velocity V_R , is tangent to the camber line at the leading edge, in which V_R is resultant velocity of axial inflow and circumferential velocity, ignoring the induced velocity. The camber line and velocity at radial position r is as illustrated in Figure 2, V_R is tangent to the camber line at the point O located at the leading edge, $\varphi(r)$, $\beta(r)$ and $\alpha(r)$ are the pitch angle, the advance angle

and the approximate attack angle, respectively. The discrete camber line near the leading edge is illustrated in Figure 3, point O , the local coordinate origin, is the same that shown in Figure 2. The abscissa is dimensionless chordwise coordinate s , and the ordinate is the camber. The point A_1 is the closest vertex of vortex lattice to the leading edge. Seeing also Figure 2, it is obvious that the angle between the camber line and the axis Os in Figure 3 is the approximate attack angle $\alpha(r)$.

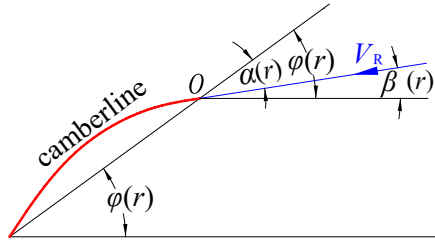


Figure 2: Blade section

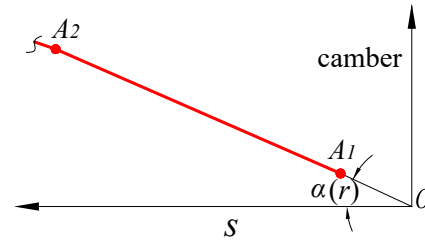


Figure 3: Camber line discrete model

Representing the selected normalized camber line as $f(s)$. At the radius r , the chord length and the maximum camber are denote as $c(r)$ and $f_{\max}(r)$ respectively, then the chordwise coordinate and camber at point A_1 can be expressed as s_1 and $f(s_1) \cdot f_{\max}(r)$ respectively, then:

$$\tan \alpha \approx \frac{f(s_1) \cdot f_{\max}(r)}{s_1 \cdot c(r)} = \frac{f(s_1)}{s_1} \cdot \frac{f_{\max}(r)}{c(r)} = \frac{f(s_1)}{s_1} \cdot \frac{f_{\max}(r)}{c} \quad (3)$$

So when the normalized camber line is selected and the chordwise discretization is determined, angle $\alpha(r)$ depends on the value of $\frac{f_{\max}(r)}{c}$ of the blade section. The relation $\alpha(r) = \varphi(r) - \beta(r)$ is shown in Figure 2, combined with formula (3), the equation can be obtained:

$$\frac{f_{\max}(r)}{c} \approx \frac{s_1}{f(s_1)} \cdot \tan[\varphi(r) - \beta(r)] \quad (4)$$

$$\beta(r) = \tan^{-1} \frac{U_0(1-w)}{\Omega r} \quad (5)$$

Where U_0 , w and Ω are uniform velocity at far upstream, wake fraction, and the rotation speed of propeller. It can be seen from equations (4) and (5) that $\frac{f_{\max}(r)}{c}$ can be expressed as function of $\varphi(r)$, and thus the camber surface is determined by distribution of $\varphi(r)$. In conclusion, with the assumptions above and under given operating conditions, the propeller efficiency depends on the distribution of pitch angle, so the optimum efficiency can be obtained by iteratively adjusting the distribution of pitch angle

2.1.3 Initial pitch angle profile

In the current procedure of determination of optimal circulation, the gradient of efficiency

to pitch angle will be affected by the geometry of the existing camber surface. At the beginning of the pitch angle iterative, the loading on the camber surface needs to be zeroed, that is, the total circulation on each chordwise strip of vortex lattice is require to be zero, and it can be achieved by Newton-Rahpson iteration. The calculation is performed on the control radius r_m determined by equation (6), and vector $\boldsymbol{\varphi}=(\varphi_1, \varphi_2, \dots, \varphi_M)^T$ and $\boldsymbol{\Gamma}=(\Gamma_1, \Gamma_2, \dots, \Gamma_M)^T$ represent the distribution of pitch angle and total circulation on the camber surface respectively.

$$r_m = \frac{\rho_m + \rho_{m+1}}{2} \quad (m = 1, 2, \dots, M) \quad (6)$$

In order to satisfy $\Gamma = 0$, the perturbation, $\Delta\varphi_j=0.05\varphi_j$, is added on to φ_j , calculating the gradient of Γ_i to φ_j according to equation (7):

$$\frac{\partial(\Gamma_i)}{\partial\varphi_j} \approx \frac{\Gamma_i(\varphi_1, \varphi_2, \dots, \varphi_j + \Delta\varphi_j, \dots, \varphi_M) - \Gamma_i(\varphi_1, \varphi_2, \dots, \varphi_j, \dots, \varphi_M)}{\Delta\varphi_j} \quad (7)$$

Take $i, j = 1, 2, \dots, M$, equation (7) constructs an M -order Jacobian matrix \mathbf{J}_0 . According to the Newton-Raphson iterative, the pitch angle is updated according to equation (8), where the superscript with brackets represents the number of iterations.

$$\boldsymbol{\varphi}^{(k+1)} = \boldsymbol{\varphi}^{(k)} - (\mathbf{J}_0^{(k)})^{-1} \cdot \boldsymbol{\varphi}^{(k)} \quad (8)$$

The iteration starts from the pitch angle corresponding to the design advance coefficient J_A , and the maximum camber is determined according to equation (4), so the initial geometry of camber surface and trailing vortex sheet can be established. Then the Jacobian matrix is constructed according to equation (7), and the pitch angle and the camber surface are updated according to equation (8). The calculation is converged when the dimensionless total circulation on each strip is less than 0.01, then the distribution of pitch angle, $\varphi_0(r)$, is to be used as the initial value of the optimal circulation iteration.

2.1.4 Pitch angle iteration – the optimum circulation solution

The propeller efficiency is calculated according to equation (9), Where K_T , K_Q , J_A and \bar{w} are the thrust coefficient, torque coefficient, advance coefficient and area weighted average of the wake fraction in propeller disk, and $\bar{w}=0$ in open water condition.

$$\eta = (1 - \bar{w}) \cdot \frac{K_T}{K_Q} \cdot \frac{J_A}{2\pi} \quad (9)$$

Iteration starts from the initial distribution of pitch angle $\varphi_0(r)$. In each iteration, the distribution of the gradient of efficiency to pitch angle, $\frac{\partial\eta}{\partial\varphi}(r)$, is pre-computed firstly.

Perturbing the $\varphi(r)$ individually as $\varphi(r)=\varphi(r)+\delta_A$ by perturbation, δ_A , and keeping pitch angles at other radial positions unchanged, the performance of propeller is calculated using code SPROP30, then the efficiency increment $\Delta\eta(r)$ caused by perturbation of $\varphi(r)$ can be obtained. Perturbation δ_A is a small angle and kept unchanged in a iteration, then the gradient of

efficiency to $\varphi(r)$ can be written as $\frac{\partial \eta}{\partial \varphi}(r) \approx \frac{\partial \eta}{\delta_A}(r)$. The computation of $\frac{\partial \eta}{\partial \varphi}(r)$ is experienced on the control radius over the blade, then the distribution of $\frac{\partial \eta}{\partial \varphi}(r)$ is obtained.

If the minimum and maximum values of $\frac{\partial \eta}{\partial \varphi}(r)$ are a and b respectively, the increment of $\varphi(r)$, $\delta_B(r)$, in the iteration can be determined according to equation (10):

$$\delta_B(r) = \frac{\frac{\partial \eta}{\partial \varphi}(r) - a}{b - a} \cdot \delta_A \quad (10)$$

The distribution of $\varphi(r)$ is updated from the root to the tip according to equation (11) and the hydrodynamic performance is calculated.

$$\varphi(r)^{(k+1)} = \varphi(r)^{(k)} + \delta_B(r) \quad (11)$$

Above is the computation in an iteration. To achieve the given design thrust coefficient K_{T0} , an initial value of δ_A is taken and the routine is to be carried out as follows:

- 1) Calculating the distribution of $\frac{\partial \eta}{\partial \varphi}(r)$ and updating the distribution of $\varphi(r)$ according to equation (11), the hydrodynamic performance is calculated. If K_T predicted is less than K_{T0} , the K_T is recorded. Keeping the current δ_A unchanged, the iterations go on until $K_T > K_{T0}$;
- 2) If $K_T > K_{T0}$, the K_T will not be recorded, the distribution of $\varphi(r)$ is restored to the last iteration when $K_T < K_{T0}$;
- 3) The current δ_A is halved and go back to step 1) to iterate;
- 4) When $|K_T - K_{T0}| \leq 0.005 K_{T0}$, the iteration exits, then the distribution of optimum circulation is obtained.

The influence of initial value of δ_A on determination of the optimal circulation is investigated by varying the δ_A and computing the optimal circulation. With decrease of δ_A , the results come to convergence, the initial value of δ_A is taken as 1.0° in this paper.

The mesh independence in the approach for determining the optimal circulation is examines for validation by three mesh schemes: the coarse scheme with $M=9$, $N=9$, the moderate scheme with $M=12$, $N=12$ and the refine scheme with $M=15$, $N=15$. The efficiencies of results obtained with equal K_{T0} is 0.6984, 0.6947 and 0.6932 respectively, the relative changes of efficiency of two adjacent schemes are -0.5% and -0.2% respectively. The Figure 4 shows the distributions of dimensionless optimum circulation determined by the three schemes, in which $V_{0.7R}$ is the linear velocity at the 0.7 radius of the blade. It can be seen that the circulation distributions obtained in moderate scheme and refine one are much closer, so the method has good mesh convergence. The following calculations adopt the moderate scheme as balanced tradeoff between time cost and precision of calculation.

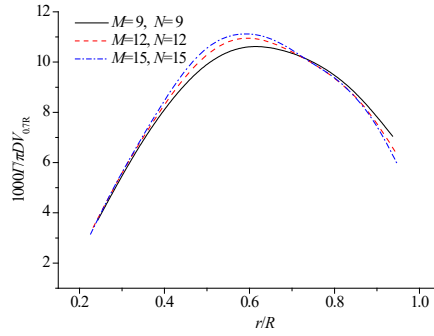


Figure 4: The influence of mesh number on the optimal circulation

2.2 Solution of pitch profile and camber surface geometry by Newton-Raphson method

The chordwise distribution of loading obtained by method in Section 1.1 depends on the geometry of normalized the camber line selected. In most of design cases, the loading is expected to be distributed on the chord as specified form, such as NACA a=0.8. At this point, according to the radial distribution of circulation, $\Gamma(r)$, the spanwise vortex intensity $\gamma_{i_c}^{(0)}$ of each horseshoe vortex on camber surface can be determined according to Greeley and Kerwin's method^[9] and taken as the design target, where $i_c = j + (i-1) \times N = 1, 2, \dots, L$, $i = 1, 2, \dots, M$, $j = 1, 2, \dots, N$, $L = M \times N$. The problem comes down to how to determine the distribution of the pitch and the camber of the blade, so that the distribution of spanwise vortex intensity, γ_{i_c} , is equal to the distribution of $\gamma_{i_c}^{(0)}$ correspondingly.

For the m -th strip in the discrete model shown in Figure 1, the camber, f_{mn} , at the midpoint of each radial edge of quadrilateral inner the blade and the pitch angle, φ_m , at the control radius r_m are taken as design variables. Each strip has $N-1$ cambers to be designed except the points at the leading edge and trailing edge, so there are a total of $M \times N$ design variables on the entire camber surface, which is the same as the number of spanwise vortexes. The design variables are expressed in a single subscript as:

$$\begin{aligned} \chi_{j_c} &= f_{mn} \quad (j_c = n + (m-1) \times N, \quad m = 1, 2, \dots, M, \quad n = 1, 2, \dots, N-1) \\ \chi_{j_c} &= \varphi_m \quad (j_c = m \times N, \quad m = 1, 2, \dots, M) \end{aligned} \quad (12)$$

When χ_{j_c} ($j_c = 1, 2, \dots, L$) is known, the vortex intensity γ_{i_c} can be obtained by performance calculation. Let $\Delta\gamma_{i_c} = \gamma_{i_c} - \gamma_{i_c}^{(0)} = G_{i_c}(\chi_1, \chi_2, \dots, \chi_L)$, the design target is $\Delta\gamma_{i_c} = 0$ ($i_c = 1, 2, \dots, L$), but the form of the function G_{i_c} is unknown. Applying a perturbation $\Delta\chi_{j_c}$ to χ_{j_c} and calculating the performance of propeller, then the change of $\Delta\gamma_{i_c}$ caused by $\Delta\chi_{j_c}$ can be calculated, and the gradient of $\Delta\gamma_{i_c}$ with $\Delta\chi_{j_c}$ can be approximately calculated:

$$\frac{\partial(\Delta\gamma_{i_c})}{\partial\chi_{j_c}} \approx \frac{G_{i_c}(\chi_1, \chi_2, \dots, \chi_{j_c} + \Delta\chi_{j_c}, \dots, \chi_L) - G_{i_c}(\chi_1, \chi_2, \dots, \chi_{j_c}, \dots, \chi_L)}{\Delta\chi_{j_c}} \quad (13)$$

Let $i_c, j_c = 1, 2, \dots, L$, equation (13) constitutes a L -order Jacobian matrix. Solving

$\Delta\gamma_{i_c} = G_{i_c}(\chi_1, \chi_2, \dots, \chi_L) = 0$ by Newton-Raphson method, where $i_c=1, 2, \dots, L$, the iterative calculation formula is:

$$\boldsymbol{\chi}^{(k+1)} = \boldsymbol{\chi}^{(k)} - (\mathbf{J}_I^{(k)})^{-1} \Delta\boldsymbol{\gamma}^{(k)} \quad (14)$$

Perturbation $\Delta\chi_{i_c} = \mu\chi_{i_c}$, in this paper $\mu=0.05$. The iterative calculation begins with the design results in Section 1.1 or other assumed initial geometry. In each iteration, first construct the Jacobian matrix, then calculate the corrections of the camber and the pitch angle according to Equation (14), finally interpolate and update the geometry and position of the camber surface. The calculation is confirmed to be convergent when $|\gamma_{i_c} - \gamma_{i_c}^{(0)}| \leq 10^{-5}$, where γ_{i_c} and $\gamma_{i_c}^{(0)}$ are nondimensionalized by $1000/\pi DV_{0.7R}$.

It should be noted that γ_{i_c} expressed by single subscript also can be expressed as $\gamma(r, s)$, where chordwise coordinate s and radial coordinate r are determined by Equation (2) and Equation (6), respectively.

3 RESULTS AND DISCUSSION

The design procedure is used to redesign DTNSRDC propeller 4382 (P4382) for validation. The thrust coefficient predicted by VLM is taken as the design objective in determination of the optimum circulation. Firstly, the predictions of P4382 are carried out in open water condition at advance coefficient $J_{A0}=0.889$, denoted as model P4382-OW, and in the wake distribution shown as Figure 5 at equivalent advance coefficient $J_{AW}=1.080$, denoted as model P4382-WK, where $J_{AW} = J_{A0}/(1-\bar{w})$. The results of prediction are listed in Table 2, the predicted $K_{T0}=0.2202$ from P4382-OW and $K_{TW}=0.2192$ from P4382-WK is very close.

Then the optimum circulation in open-water is computed as $K_{T0}=0.2202$ the design target. In this stage, the diameter, the profiles of chord length, thickness and skew of P4382 are kept unchanged, so is the original normalized camber line, but the distribution of the pitch and the maximum camber is redesigned to solve the optimum circulation; After that, the optimum circulation obtained is used to design the pitch profile and camber surface geometry with the loading distributed along the chord as the form of NACA $a=0.8$. The design routine in wake condition is similar with that in open-water, only K_{TW} and J_{AW} are taken as the design target and as advance coefficient respectively.

Stage 1 and Stage 2 are used to represent the stage of determining the optimum circulation and the final stage of design with prescribed chordwise distribution of loading respectively; the postfix OW and WK represent the design in open-water and condition and in wake condition respectively. The design results are all shown in Table 2, in which the relative variations of results of Stage 1 and Stage 2 based on the performance of P4382 predicted in corresponding condition are given as percentage.

Figure 6 and Figure 7 shows the dimensionless optimum circulation distribution and the chordwise distributions of dimensionless circulation designed respectively, along with those of P4382 from prediction. It should be noted that the radial distribution of circulation of Stage 1-OW is almost the same as that of Stage 2-OW, similarly, Stage 1-WK and Stage 2-WK also have the same radial distribution of circulation, so Stage 2-OW and Stage 2-WK are not shown in Figure 6. The distributions of P/D and f_{max}/c designed are shown in Figure 8, and the

dimensionless camber line designed on typical blade sections are compared with the uniform dimensionless camber line of P4382 in Figure9.

Table 2: Result of design compared with predicted performance of P4382

| | Model | K_T | | $10 K_Q$ | | η | |
|---------------|------------|---------|-------|----------|-------|--------|------|
| In open-water | P4382-OW | 0.2202 | - | 0.4576 | - | 0.6809 | - |
| | Stage 1-OW | 0.2200 | -0.1% | 0.448 | -2.1% | 0.6947 | 2.0% |
| | Stage 2-OW | 0.2227 | 1.1% | 0.4454 | -2.7% | 0.7074 | 3.9% |
| In wake | P4382-WK | 0.2192 | - | 0.4518 | - | 0.6865 | - |
| | Stage 1-WK | 0.21903 | -0.1% | 0.441 | -2.4% | 0.7027 | 2.4% |
| | Stage 2-WK | 0.2213 | 1.0% | 0.4362 | -3.5% | 0.7178 | 4.6% |

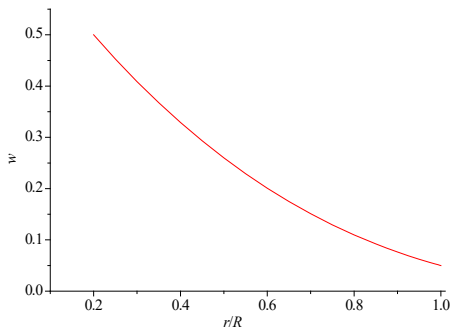


Figure 5: The distribution of wake

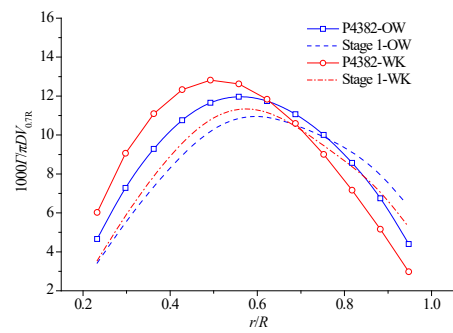
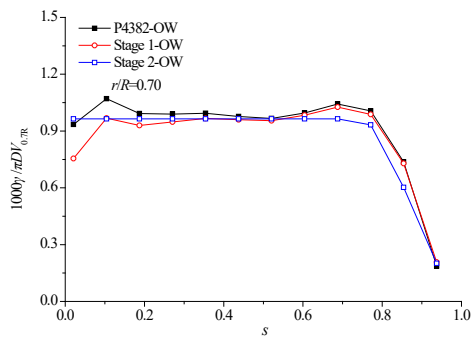
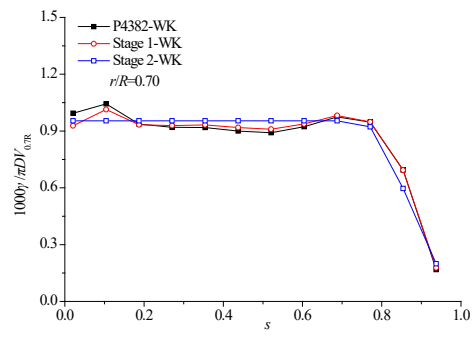


Figure 6: The optimum distributions of circulation



(a) In open-water



(b) In wake condition

Figure 7: Chordwise distributions of circulation on radial position $r/R=0.70$

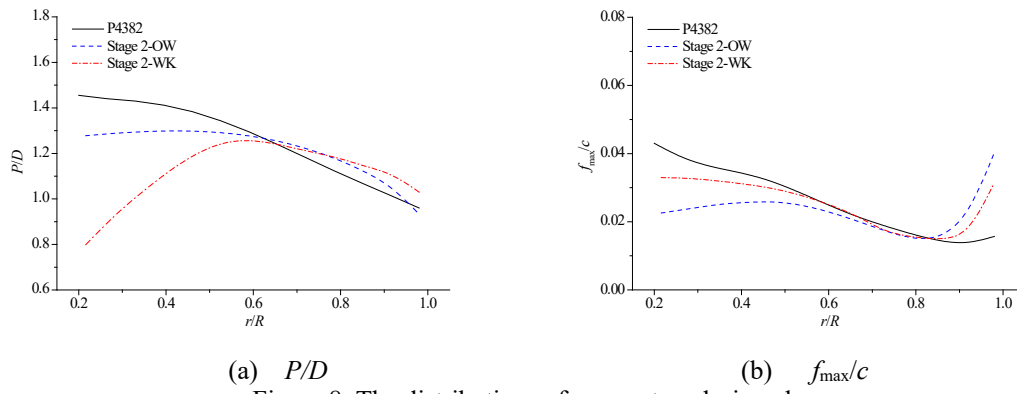


Figure 8: The distributions of parameters designed

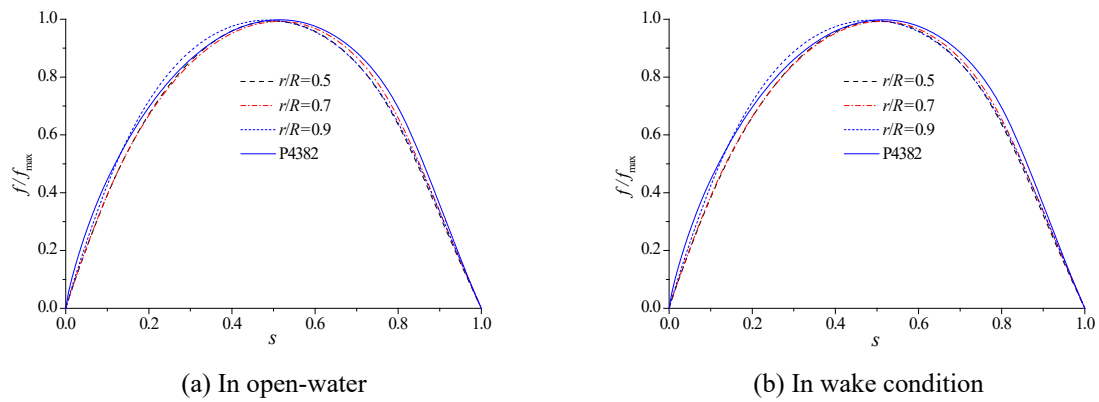


Figure 9: The distributions of camber on typical blade sections

It can be observed in Table 2 that, the thrust coefficients obtained from both Stage 2-OW and Stage 2-WK satisfy the requirements; compared with result from prediction of P4382, the efficiency of model Stage 1-OW is increased by 2.0%, and the efficiency of model Stage 2-OW is further improved, which means the chordwise distribution of loading also affects efficiency in some degree. The similar improvement of efficiency appears in adapted design compared with model P4382-WK.

As can be seen from Figure 6, compared with the predicted radial circulation of P4382, the optimum circulation decreases significantly in the inner radii both in open-water and in wake condition; Compared with Stage 1-OW, the distributions of optimum circulation computed in wake condition move to inner radii, similar for the radial circulation distribution of P4382-OW compared with that of P4382-WK. From the chordwise distribution of the circulations on position $r/R=0.70$ shown in Figure 7, the assumption that the relative velocity is kept tangent to the camber line at the leading edge works well in Stage 1-OW model and Stage 1-WK model, and the circulations at the leading edge are kept at low level as expectation; The circulation of model Stage 2-OW and Stage 2-WK is distributed chordwise as prescribed form of NACA $a=0.8$ on the section where $r/R=0.70$.

The distributions of P/D and f_{\max}/c designed shown in Figure 8 are obviously different from those of P4382, which is caused by the difference of the radial circulation distributions.

With almost the equal rotation speed of propeller and averaged velocity of inflow, the axial velocity within inner radii of model Stage 2-WK is much less than that of model Stage2-OW, namely, the advance angle of the former is much less than that of the latter, meanwhile the real angle of attack is small, so the P/D of the former is much lower than that of the latter within inner radii and the relation reverses in outer radii. As shown in Figure 9, the dimensionless camber lines of model Stage2-OW at various radial position differ from one another to generate circulation distributed as NACA $a=0.8$. Compared with the camber line of P4382, The designed camber line shrink markedly within the chordwise range $s = 0.6\sim 0.8$, which explains the disappearance of humps on chordwise circulation distribution of model P4382-OW and P4382-WE in Figure 7.

4 CONCLUSION

Based on the vortex lattice lifting-surface model, a new design procedure for optimum marine propellers is developed. The first stage of procedure is determining the optimum circulation distribution with selected normalized camber line, and the second stage is design of the pitch profile and camber surface geometry with a prescribed loading distribution along the chord according to the optimum circulation obtained in the first stage. The procedure is used to redesign the distribution of pitch and camber of DTNSRDC P4382 both in open-water and in wake condition. The design results show that:

- 1) The thrust coefficients obtained from result designed in both in open-water and in wake condition satisfy the design objective; Compared with P4382, the efficiencies of optimum propellers redesigned increase 3.9% in open-water and 4.6% in wake condition, respectively;
- 2) Compared with efficiency obtained with fixed normalized camber line, the final efficiency obtained from result of design with chordwise distribution of loading as NACA $a=0.8$ is further improved, which means the chordwise distribution of loading affects the efficiency in some degree.

REFERENCE

- [1] Betz, A. Schraubenpropeller mit geringstem Energieverlust, *Nachrichten der K.Gesellschaft der Wissenschaften zu Gottingen Math-Phys Klass*, 1919.
- [2] Lerbs, H.W. Moderately loaded propellers with a finite number of blades and an arbitrary distribution of circulation, *Transactions of the Society of Naval Architects and Marine Engineers*, 1952, 60:73–123.
- [3] Morgan, W.B. Silovic, V. and Deny, S.B. Propeller lifting surface corrections, *Transactions of the Society of Naval Architects and Marine Engineers*, AD-687670, 1968.
- [4] Kerwin, J. E. Coney, W. B. and Hsin, C. Y. Optimum circulation distributions for single and multi-component propulsors, *Twenty-First American Towing Tank Conference*, National Academy Press, Washington, D.C. 1986:53-62.
- [5] Cai, H.P. Ma, C. Qian, Z.F. Chen, K. and Zhang, H. A method to determine the optimum radial circulation distribution of the marine propeller, *Journal of Ship Mechanics*, 17(11) (2013) 1244-1252. (in Chinese)
- [6] Olsen, A.S. *Optimization of propellers using the vortex lattice method* (Ph.D. thesis),

- Technical University of Denmark, 2001.
- [7] Lee, K. J. Hoshino, T. and Lee, J. H. A lifting surface optimization method for the design of marine propeller blades, *Ocean Engineering*, Vol.88 (2014) 472–479.
 - [8] Kerwin, J. E. and Lee, C.S. Prediction of steady and unsteady marine propeller performance by numerical lifting-surface theory. *Transactions of the Society of Naval Architects and Marine Engineers*, 1978, 86: 218-253.
 - [9] Greeley, D.S. and Kerwin, J. E. Numerical methods for propeller design and analysis in steady flow. *Transactions of the Society of Naval Architects and Marine Engineers*, 1982, 90: 415-453.
 - [10] Yang, C. J. and Tamashima, M. A. Simplified method to predict marine propeller performance including the effect of boss. *Transactions of the West-Japan Society of Naval Architects*, 1990, 80: 23-33.

KINEMATICS AND LOAD CONDITIONS AT THE VOITH-SCHNEIDER-PROPELLER

MARINE 2019

THOMAS ROSENLÖCHER, MAXIMILIAN RÖSNER, BERTHOLD SCHLECHT

Chair of Machine Elements, Institute of Machine Elements and Machine Design
Technische Universität Dresden, 01062 Dresden
e-mail: thomas.rosenloecher@tu-dresden.de, web page: <http://www.tu-dresden.de/me>

Key words: Voith-Schneider-Propeller, Kinematic, Loads, Multibody-System Simulation

Abstract. The Voith-Schneider propeller consists of individual circularly arranged rudder blades which are rotating around the vertical axis. The pitch of the blades can be cyclically adjusted over the rotation by a lever mechanism to define the direction of the propulsion. The kinematic boundary conditions, which define the lengths and joint positions of the lever mechanism and at the same time influence the efficiency of the ship's propulsion, will be presented by an example. Different approaches to finding solutions will be presented and discussed. Based on all determined design parameters, the kinematic of the entire propulsion system were modelled in a multibody-system simulation model and loaded with the position- and angle-dependent water loads on the rudder blades. The simulation of different operating conditions enables the determination of the loads occurring at the blade roots and in the lever system.

1 INTRODUCTION

The design and dimensioning of marine propulsion systems requires a precise knowledge of the existing operating conditions. To ensure maneuverability and the associated safe navigation under all conditions on the water, extremely high demands on the reliability of the propulsion systems exist. The load components to be considered also differ depending on the type of drive which is used.

To drive the vessel, the classic rigid propeller must convert the applied torque into thrust. Rudders are used to change the direction of travel. On ferries, tugs and ships in the oil and gas industry, thruster drives are also used due to their good maneuvering characteristics. In these drives, the function of the drive and rudder is combined in one assembly. The propeller is mounted in a propulsion nacelle under the ship and this nacelle can be arbitrary rotated around the vertical axis. In addition to the torque, bending moments resulting from rudder movements and inflow conditions must also be considered in the design loads. The use of Voith-Schneider propellers provides an even faster possibility for adapting the thrust direction. The drive, consisting of individual circularly arranged rudder blades, rotates around the vertical axis and does not generate any thrust when the blade profiles are guided tangentially through the water. A lever mechanism makes it possible to cyclically adjust the pitch of the blades over the rotation of the drive and thus adjust the direction of the propulsion as required.

This type of combined propulsion and steering enables a very good maneuverability and positioning, which has been used in tugs, ferries, minesweepers and floating cranes since 1927. Figure 1 shows a Voith-Schneider propeller of the type commonly used today. The figure on the right shows a tugboat with two propellers arranged one behind the other. This arrangement makes the tug extremely maneuverable and also allows transverse travel. To protect the blades from ground contact in shallow waters, the propeller is enclosed by a cage.

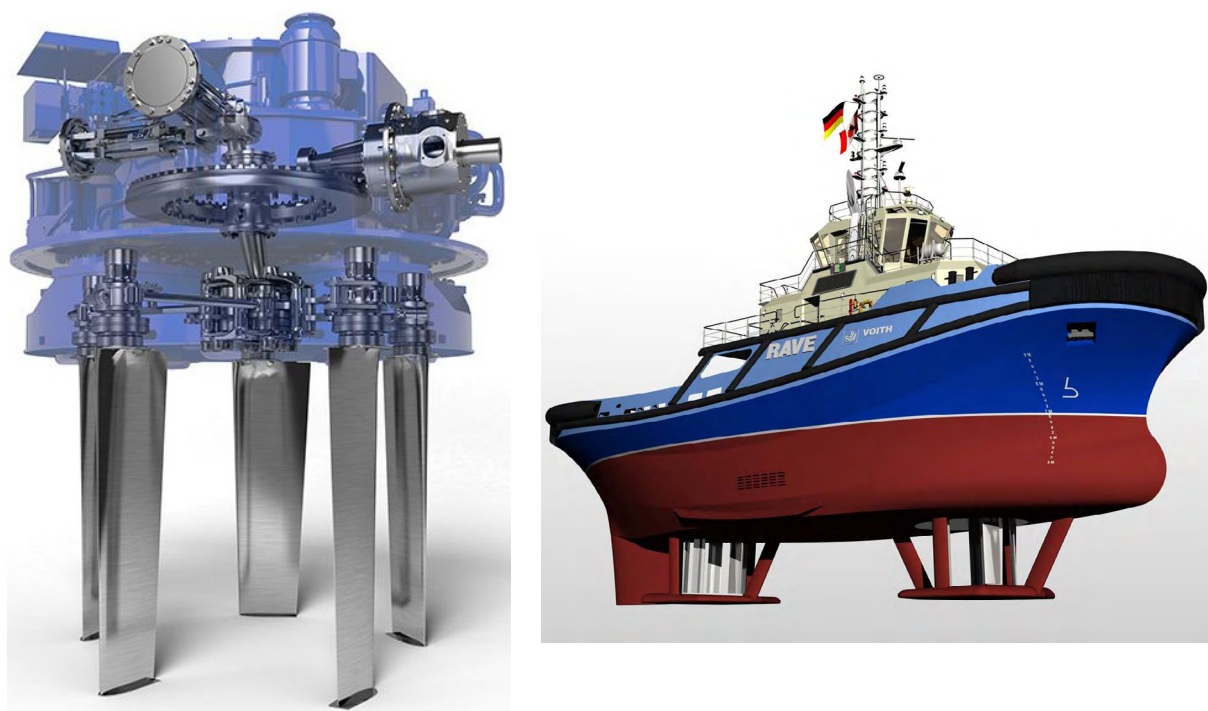


Figure 1: Voith-Schneider-Propeller and tugboat [7]

The name Voith-Schneider-Propeller is derived from the company name of J. M. Voith GmbH and the inventor Ernst Schneider. Ernst Schneider made his invention during his student days mainly through theoretical considerations. Extensive tests were not carried out at this time.

Even before applying for a patent, Schneider contacted J. M. Voith GmbH. In 1925, a meeting was held with representatives of the Voith company, followed by trials at the Schiffsbau technische Versuchsanstalt in Vienna. These tests could not convince the Voith company due to the poor efficiency at that time. On December 7, 1925, Schneider applied for a patent for his invention in Austria and shortly afterwards also in France and Germany. After the patent application, Schneider had the opportunity to test his idea with a small model. Afterwards, he again contacted Voith and was able to convince decision-makers of his drive system with the help of his model. In May 1926, a license agreement is signed between Voith and Ernst Schneider and the basic patent is registered in other countries. In June 1926, the patent is granted in Germany and shortly afterwards also in Austria and France [6]. The first demonstration boat “Torqueo” with a Voith-Schneider propeller powered by a 60 HP gasoline engine was built by Voith in 1929 (figure 2).

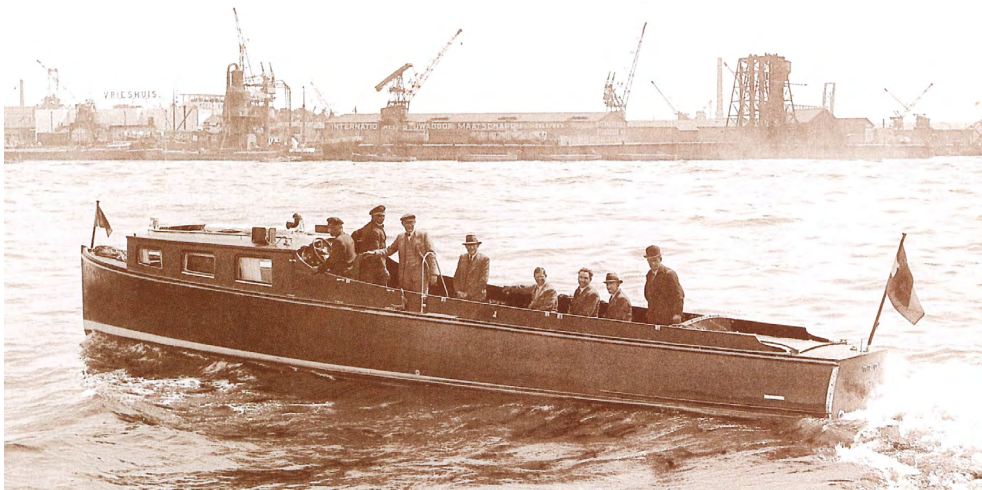


Figure 2: Demonstration boat “Torqueo” in the harbor of Rotterdam [4]

2 OPERATING PRINCIPLE OF THE VOITH-SCHNEIDER-PROPELLER

In comparison to conventional ship propulsion systems, the Voith-Schneider-Propeller is both propulsion and steering unit. The vertically arranged rudder blades rotate around a common axis and can be pitched periodically around their own axis. This rotation generates propulsion and allows to steer the ship at the same time. This makes ships with Voith-Schneider propellers extremely agile and maneuverable. The direction of rotation of the drive does not have to be changed for a change from forward to reverse travel. It is only necessary to steer the propellers in another way. Compared to a classic ship drive it is also not necessary that the rudder is flown with a sufficiently high velocity, so that the steer impulse take effect. The propeller itself provides the necessary inflow. If a ship is equipped with more than one Voith-Schneider propeller and these are arranged one behind the other on the longitudinal axis, the ship can also move sideways. Since a single wing moves through the water on a cycloidal path during operation, the Voith-Schneider propeller is also referred as a cycloidal propeller (see figure 3). The exact mode of operation of the Voith-Schneider-Propeller (VSP) and the basic principle behind it will be discussed in more detail in the next section. [4].

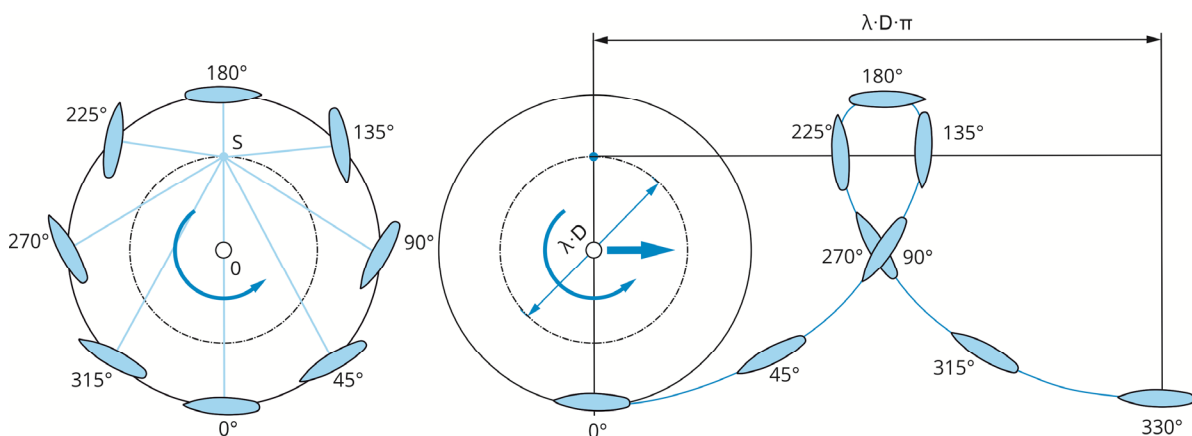


Figure 3: Cycloidal path of the VSP [7]

3 BASIC PRINCIPLE OF A VOITH-SCHNEIDER PROPELLER - NORMAL LAW

Figure 4 shows the basic principle of the Voith-Schneider propeller in plan view. The rotor blades rotate on a circular path around their common axis of rotation. In the left figure, the drive is shown in the neutral position. The rotor blades are tangentially positioned on the circular path described by them at all times. This makes it easy to understand that no force is applied by the rotor blades, regardless of the applied speed. The middle figure shows the theoretical case in which the rudders are deflected at a constant angle to their neutral position. This deflection of the profiles now causes a different inflow of the upper and lower wing surface and thus a pressure difference on both sides. This pressure difference results in a force effect. An analogy can be found in aviation in the functioning of wings. However, the force effect is eliminated in total as a result of the uniform deflection. With an even wing position no feed can be generated.

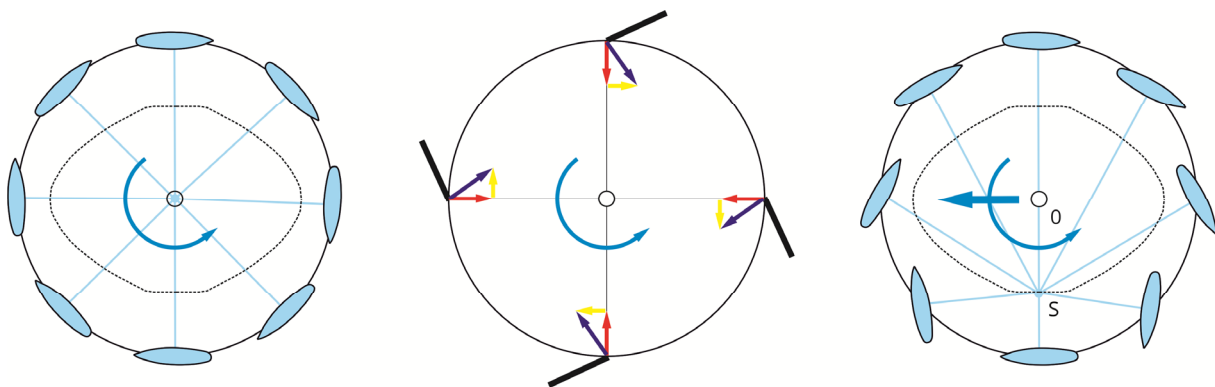


Figure 4: Basic principle of the Voith-Schneider drive with rudders in neutral position (left) [8], an even deflection of the rudders (center) and a periodic deflection of the rudders (right) [8]

The right figure shows that the wings deflected unevenly. To generate a thrust force to the left, it must be ensured that only forces to the left act at all times and that the vertical forces neutralize each other. The mentioned conditions are fulfilled by following the commonly named normal law [4]. This means that the normal of the rudders must meet at a point, the so-called control point S , at all times. If this requirement is met, the resulting force is perpendicular to the distance $0-S$. The direction of the force vector depends on the direction of rotation of the drive and the position of the point S . On the route $0-S$ a line with the origin in 0 shall be drawn for understanding. The angle between line and distance $0-S$ is 90 degrees. This angle should be applied against the direction of rotation of the drive. The force vector points in the direction of this line. In the case shown, the control point is below the axis of rotation and the drive rotates counter clockwise. Thus the vector of the resulting force points to the left. [7]

3 MATHEMATICAL DESCRIPTION OF THE JOINT POSITION POINTS

The mathematical description of the joint position points and the calculation of the necessary angles as a function of the leading point vector (ΔL) and the lengths of the individual levers is the basis for the kinematic description of the drive. Figure 5 shows the necessary geometric definitions schematically and not to scale.

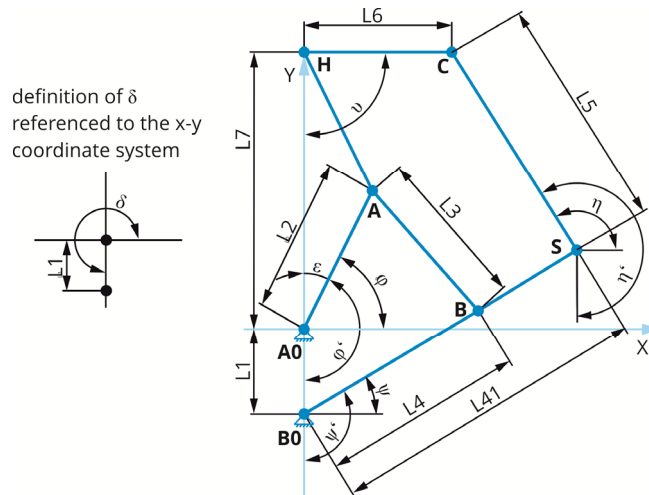


Figure 5: Schematically representation of the Voith-Schneider kinematic

A simple four-joint gearbox (B0-B-A-A0) can be identified in the center of the drive. To describe the four-joint transmission, it is necessary to specify the position from B0 to A0 over the variable length L1 and the variable angle δ by means of a leading point vector (ΔL). In order to simplify the calculation, the rotation angle φ is converted to the respective axis on which the point B0 also lies. The point A0 is fixed. The consequence of this conversion is that the resulting angles must be calculated back to the x-axis in order to determine the respective points. This makes it possible to describe the position of point A as a function of L2 and φ . The position of point B are defined by relations between L4 and ψ as well as L1 and δ . The position of S as an extension of the lever B0-B can also be indicated by L41 and ψ as well as L1 and δ . The position of the joint point H is defined by the length L7 and the angles φ , δ and ϵ . To calculate the position of point C, it is necessary to use the description by means of complex numbers [9]. After solving the equation, the position of the joint point can be described using the relationships between the length L5 and η , L41 and ψ as well as L1 and δ .

In addition to the geometric position of all joints, it is necessary to know the deflection angle of lever 6 in relation to the tangent to the circle in order to describe the forces acting.

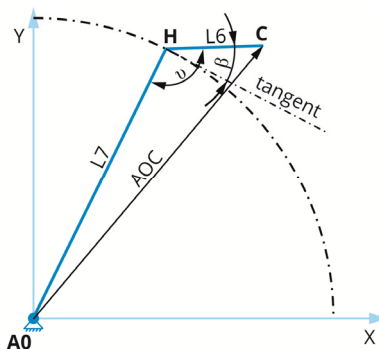


Figure 6: Tangent angle β to the circular tangent of lever 6

The angle included by C, H and A0, ν can be described by the length L6 and L7 as well as with the knowledge of the position of C using the distance A0-C. The angle between the

tangent at point H and the lever 6, β then results from the difference between ν and 90° . The point C thus lies outside the circle if ν is greater than 90° and β is less than 0° , for the inner position there are correspondingly opposite signs.

4 CALCULATION OF THE FORCES ON THE VOITH-SCHNEIDER PROPELLER

In addition to the kinematic conditions of the mechanism, the multibody-system simulation model of the drive should be loaded with the acting flow loads. The overall model can also be used to make statements about the loads acting in the drivetrain. With the assumption that the driving speed is equal to the inflow velocity in the direction of travel, the different speed vectors must be combined. The position of the control point S in figure 7 defines the direction of travel indicated by the arrow.

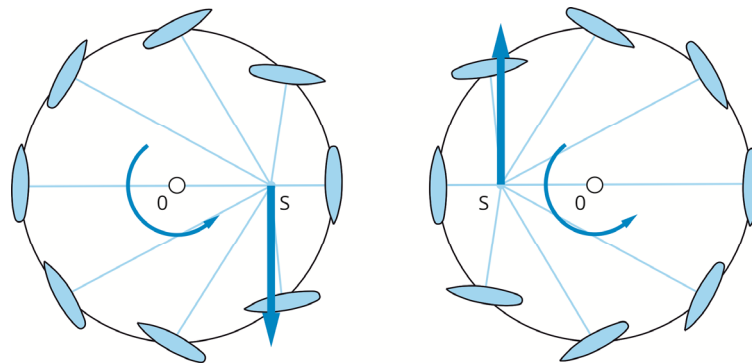


Figure 7: Control point 1; $\delta = 0^\circ$ and control point 2; $\delta = 180^\circ$ [7]

The inflow velocity acts correspondingly against the direction of travel and can be described vectorially using the control point position. However, the resulting velocity which is relevant for the blade profile results from the superposition of the inflow velocity v and the circumferential velocity u (figure 8).

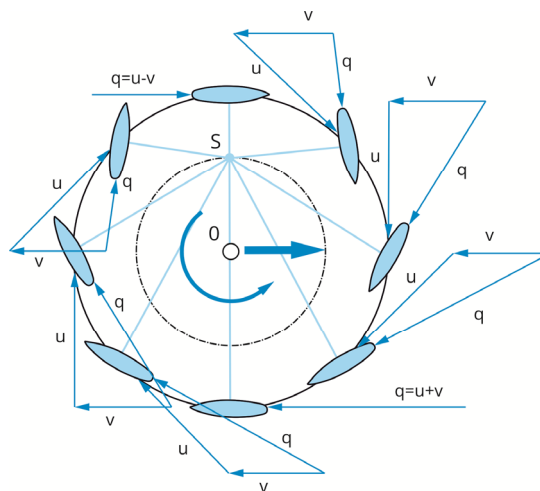


Figure 8: Velocities at the Voith-Schneider-Propeller [7]

The position of both speeds is again dependent on the position at the circumference and

leads to the searched resulting speed q . Maximum and minimum speed q results at a tangential orientation of rudder at 12 and 6 o'clock. With the knowledge of the velocity q and coefficients for the lift and the drag force, which are dependent on the angle of attack and the Reynolds number, a simplified description of the load conditions at the rudders is possible [1], [2].

The forces at the rudder are calculated by means of experimental drag coefficients. Figure 9 shows the resulting lift forces F_L and drag forces F_D in connection with the velocities u , v and q . The resistance force is orientated in the direction of the resulting inflow velocity. The lift force acts at right angles to it and points in the direction of the center or to the outside, depending on which side of the rudder is aligned in the direction of the flow.

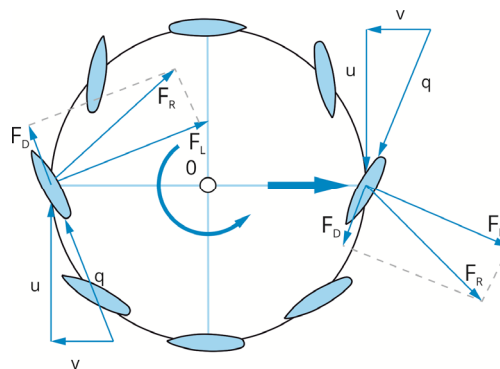


Figure 9: Velocities and forces at the Voith-Schneider-Propeller [7]

5 CONCLUSION

Based on the kinematic description of all joints and lever lengths, it is possible to realize the constructive design in a CAD model (figure 10). Further a multibody-system model is derived with the aim of fulfilling the normal law and to model the forces acting on the rudders.

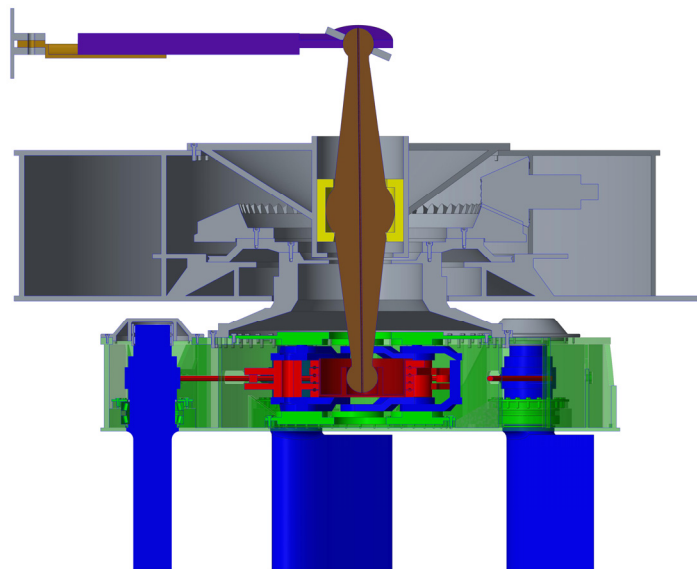


Figure 10: CAD model of the Voith-Schneider drive train

The simulation model is the basis for further investigations on the interactions between the constructive design of the drive, the resulting thrust forces and the occurring loads for the drivetrain components. The complete parameterization of the geometric variables for the simulation model and the corresponding load introduction should make it possible to analyze and compare different configurations of the drive train.

REFERENCES

- [1] Foysi, H., Auftriebs- und Widerstandsmessung an einem Tragflügelprofil, Universität Siegen, Versuchsskript, 2008.
- [2] Hepperle, M., JavaFoil, <https://www.mh-aerotoools.de/airfoils/javafoil.htm>.
- [3] Isay, W., Zur Theorie des Voith-Schneider-Propellers, Institut für Schiffbau, Hamburg, veröffentlicht in: Ingenieur-Archiv, XXXVII. Band, 03.1968.
- [4] Jürgens, B., Fork, W., Faszination Voith-Schneider-Propeller – Geschichte und Technik, Koehlers Verlagsgesellschaft mbH, 2002. ISBN: 3-7822-0854-4.
- [5] Möller, E., Brack, W., 66 Jahre Voith-Schneider-Propeller auf Marineschiffen, In: Einhundert Jahre Dieselmotoren. Koehlers Verlagsgesellschaft, Hamburg, 1998, S. 180-191. ISBN: 978-3813205664.
- [6] Voith, J. M., Schaufelrad mit beweglichen Schaufeln, patentiert ab: 19.08.1927, Deutschland. Patentschrift-500340.
- [7] Voith Turbo GmbH & Co. Kg, Präzise und Sicher Manövrieren. Voith Schneider Propeller, In: VT2070 d Vvkbs 2017-1 (2017).
- [8] Voith GmbH & Co. KGaA, iVSP 2.0, (Interactive Voith Schneider Propeller), 2017.
- [9] Wadewitz, C., Umdruck Mechanismentechnik / Professur für Dynamik und Mechanismentechnik TU Dresden 2005.

NUMERICAL INVESTIGATION OF TIP GEOMETRY ON THE TIP-CLEARANCE FLOW FEATURES OF A PUMP-JET PROPULSOR

Xue-Qin Ji, Xiao-Qian Dong*, Wei Li, Chen-Jun Yang, Francis Noblesse

(State Key Laboratory of Ocean Engineering,
Collaborative Innovation Center for Advanced Ship and Deep-Sea Exploration,
Shanghai Jiao Tong University, Shanghai 200240, China)

*Corresponding author: xiaoqiandong0330@sjtu.edu.cn (X.-Q. D.)

Key words: Pump-jet; Tip-clearance flow; CFD; Uncertainty

Abstract: The numerical simulation for pump-jet propulsors is based on the solution of the Reynolds-Averaged Navier-Stokes (RANS) equations using a two-layer realizable $k-\varepsilon$ model for turbulence closure. The computational domain is discretized into block-structured hexahedral cells. To establish a reliable simulation model, the numerical uncertainties are evaluated according to the procedure recommended by the 28th International Towing Tank Conference (ITTC). Three sets of grids, with a uniform refinement ratio, are generated for a generic pump-jet propulsor at model scale using the grid generator ICEM CFD 17.2, and the flow simulations are carried out using the software package STAR-CCM⁺. The tip-clearance flow features are numerically investigated for varied thickness and rake profiles of the sections close to the rotator tip. It is shown that the tip geometry has significant influence on the tip vortex.

1 INTRODUCTION

The pump-jet propulsor is receiving increased attention for underwater vehicles due to the advantage of low acoustic signature. Lots of experimental and numerical research has been done. Suryanarayana *et al.* [1,2] carried out several experiments in a wind tunnel to evaluate the hydrodynamic performance of a pump-jet propulsor. Ivanell *et al.* [3] used the Computational Fluid Dynamics (CFD) method to simulate the hydrodynamic performance of a torpedo equipped with the pump-jet propulsion system. The numerical results are in good agreement with the experimental data. Cheah *et al.* [4] simulated the complex flow in a centrifugal pump numerically. Pan *et al.* [5] calculated the steady hydrodynamic performance by adopting the RANS method and the $SST k-\omega$ turbulence model. The predicted open water performance indicates that the pump-jet propulsor has a high propulsive efficiency and an ideal balance of performance. Lu *et al.* [6] predicted the unsteady cavitation performance of the pump-jet propulsor for a UUV using Z-G-B cavitation model. The inception and geometry of cavitation were well predicted. Cavitation inception and radiated noise seem to be closely related to the strength of the vortical flow that initiates in the clearance between the rotator tips and the duct. With the development of computer hardware capacity and CFD software technology, the tip-clearance flow can be simulated with higher resolution and fidelity. Lu *et al.* [7] employed the CFD method to investigate the tip-clearance flow characteristics of a pump-jet propulsor and the influence of the tip clearance size on the characteristics of cavitation. The research presents the formation and development of the tip-clearance flow and concludes that the tip-clearance size has a direct influence on the

cavity distribution and the cavitation area enlarges with the increase of the tip-clearance. Qin *et al.* [8] investigated the effect of different tip clearances on the hydrodynamic performance of the pump-jet propulsor numerically. The results show that the low-pressure area gradually moves from the leading edge to the trailing edge and the affected areas of pressure and tip-leakage vortex increase with the increase of the tip clearance, which leads to a reduction in the propulsive efficiency. Gu *et al.* [9] analyzed the impact of the duct camber on a pump-jet propulsor by changing the camber ratio of the duct section. The analysis shows that the propulsive efficiency and the effective work range of the pump-jet propulsor are significantly improved as the camber increases. The research work in wind turbine area [10,11] indicates that the tip vanes. Li *et al.* [12] further investigated the influence of the width and thickness of the tip vanes on the hydrodynamic performance and fluctuating pressure of the pump's shroud. The results show that the fluctuating pressure of the pump's shroud decreases initially but increases afterwards as the widths increase. To the authors' knowledge, there are few studies on the influence of the rotator tip geometry on the tip-clearance flow in a pump-jet propulsor. In this paper, different tip geometries are investigated via viscous flow CFD simulations. The differences in tip-clearance flow and hydrodynamic performance are analyzed by changing the thickness and rake in the tip region.

2 NUMERICAL METHOD

The numerical simulation is based on the solution of the Reynolds-Averaged Navier-Stokes (RANS) equations governing the incompressible single-phase fluid flow. The two-layer realizable k - ε model is employed to simulate the turbulent flow. The two-layer approach proposed by Rodi *et al.* [13] deals with either low-Reynolds-number type grids or wall-function type grids respectively for $y^+ \sim 1$ or $y^+ > 30$. In this paper, we choose to resolve the viscous sub-layer flow by using very thin wall-bounded grid layers to ensure that the body-surface y^+ is in the order of 1. Shih *et al.* [14] found that the realizable k - ε model performs better than the standard k - ε model. The governing equations are discretized with second-order schemes both in space and time and solved by the SIMPLE algorithm. The hydrodynamic interactions of the rotor with the stator and the duct are treated with both steady and unsteady flow models. The RANS simulations are carried out using the CFD software STAR-CCM⁺.

3 NUMERICAL SIMULATION OF PUMP-JET PROPULSOR

3.1 Propulsor geometry

The prototype pump-jet propulsor, named as PJP-1, consists of a five-bladed rotor, a seven-bladed pre-swirl stator and a decelerating duct. Figure 1 shows the geometric model of the pump-jet propulsor. The diameter of the rotor, D_R , is 293.81 mm and the clearance between the rotor blade tips and the duct is 1 mm. The chord length and the maximum thickness of the rotor blade tips are 60.57 mm and 4.14 mm, respectively.

To investigate the influence of blade tip geometry on the tip-clearance flow, another propulsor, named as PJP-2, is designed by changing the thickness and rake profiles of the PJP-1 in the region from $0.95 r_R$ to $1.0 r_R$, where r_R denoted the radius of the tip section at the

rotator blade disk position, $r_R = D_R / 2$. All the other geometric parameters of the two propulsors are kept identical. The amount of changes in section thickness and rake are determined respectively by

$$\Delta t(r) = \Delta t_m \left(20 \frac{r}{r_R} - 19 \right)^2 \quad (0.95 \leq r / r_R \leq 1) \quad (1)$$

and

$$\Delta x(r) = \Delta x_m \left(20 \frac{r}{r_R} - 19 \right)^2 \quad (0.95 \leq r / r_R \leq 1) \quad (2)$$

Where Δt_m and Δx_m denote the maximum amount of changes in section thickness and rake, respectively. For the PJP-2, Δt_m is equal to 20% of t_{tip} , the maximum thickness of PJP-1's tip section, and Δx_m is equal to 0.75% of D_R . Figure 2 and Figure 3 show the changes in thickness and rake at the blade tip, respectively. Figure 4 compares the 3-D geometries of a rotor blade in the tip region before and after the thickness and rake are changed.

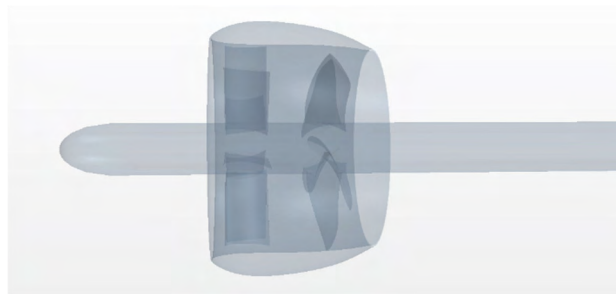


Figure 1: The geometric model of the pump-jet propulsor.

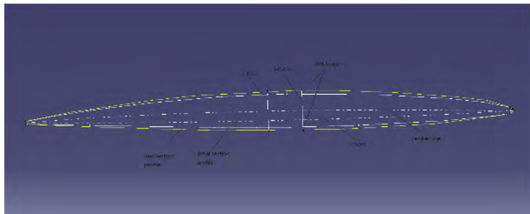


Figure 2: Change in the thickness at the blade tip.

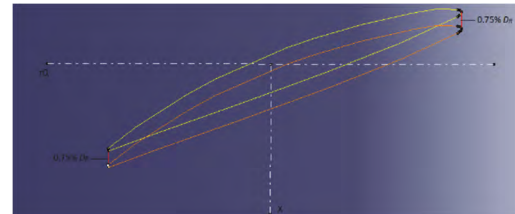


Figure 3: Change in rake at the blade tip.

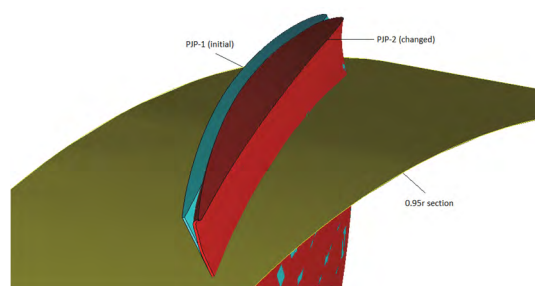
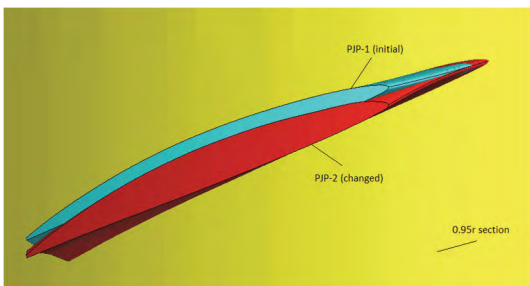


Figure 4: Comparison of the geometries of a rotor blade in the tip region of PJP-1 and PJP-2.

3.2 Computational domain and boundary conditions

Figure 5 shows the computational domain, a cylinder surrounding the pump-jet propulsor which is $15D_R$ in length and $5.9D_R$ in diameter. The velocity inlet is located at $4.7D_R$ upstream of the rotor blade disk, and the pressure outlet is located at $10.3D_R$ downstream of the rotor blade disk. The cylinder surface of the domain is set as the velocity inlet. The computational domain is divided into a static sub-domain and a rotating sub-domain. The coordinate system of the rotating sub-domain is attached to the rotor, while the static sub-domain is earth-fixed. The lateral boundary of the rotating sub-domain is the inner surface of the duct and the length is $0.38D_R$.

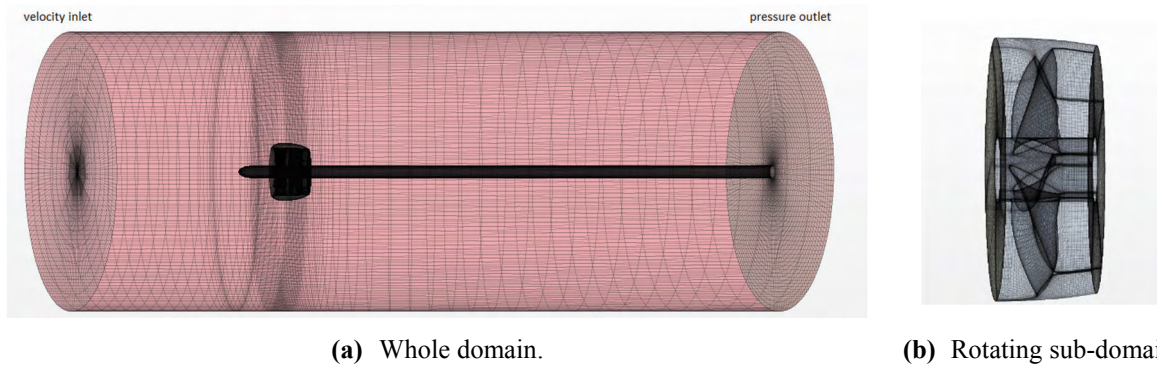


Figure 5: The computational domain.

3.3 Computational grid

The computational domain for the pump-jet propulsor is discretized into block-structured hexahedral cells, using the grid generator ICEM CFD 17.2. The grids are generated for the flow passage containing a single stator blade in the static sub-domain, see Figure 6 (left), and for the flow passage containing a single rotor blade in the rotating sub-domain, see Figure 6 (right). Then the single-passage grid blocks are copied, rotated around the rotor shaft axis, and combined to form the whole flow passage shown in Figure 5. Figure 7 illustrates the grid topology around rotor blade sections and the grids in the tip clearance region. The area around the rotor blade surfaces is discretized with C-type grids and the area between adjacent blades is discretized with L-type grids.

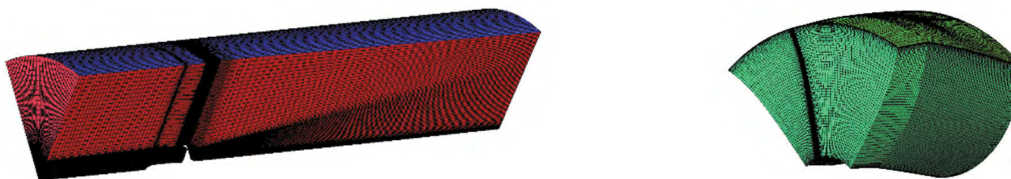


Figure 6: The single-passage grids in the static sub-domain (left) and the rotating sub-domain (right).

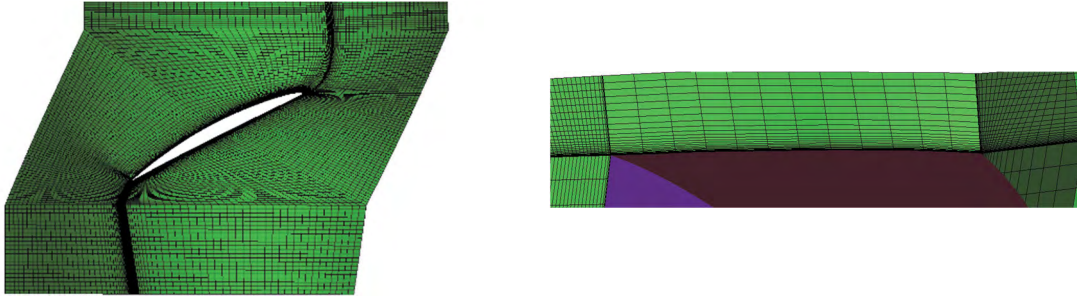


Figure 7: The grid topology around a rotor blade section (left) and the grids structure in the tip clearance at mid-chord (right).

To perform the analysis of numerical simulation uncertainties, three sets of grids are generated with a uniform refinement ratio. The grid refinement ratio, r_G , is defined as

$$r_G = \Delta h_2 / \Delta h_1 = \Delta h_3 / \Delta h_2 = \sqrt{2} \quad (3)$$

where h_1 , h_2 and h_3 denote, respectively, the sizes of fine grid G_1 , medium grid G_2 , and coarse grid G_3 . The grid refinement ratio is set as $\sqrt{2}$ for the three sets of grids.

4 RESULTS AND DISCUSSIONS

To establish a reliable simulation model, the numerical uncertainties are evaluated firstly according to the unsteady flow simulation results of the PJP-1. In addition, steady flow simulations are also carried out to compare the numerical and experimental open water performances. Through the uncertainty analysis and the validation against physical model experiments, the grid parameters suitable for investigating the tip-clearance flow are determined. The tip-clearance flow features and hydrodynamic performance are compared between PJP-1 and PJP-2 to study the influence of tip geometry on the tip-clearance flow.

4.1 Numerical uncertainty analysis for PJP-1

The uncertainty analysis consists of verification and validation based on the procedure recommended by the 28th International Towing Tank Conference (ITTC) [15]. In this paper, the uncorrected approach is adopted to evaluate the numerical uncertainties in the trust coefficient (K_{TR}) and torque coefficient (K_Q) of the rotor, simulated with the unsteady flow model, at the advance coefficient (J) of 0.75 and 0.9.

Verification is the process for estimating the uncertainty in numerical simulations. The numerical uncertainty U_{SN} is expressed as

$$U_{SN}^2 = U_I^2 + U_G^2 + U_T^2 + U_P^2 \quad (4)$$

where U_I , U_G , U_T and U_P , respectively, denote the uncertainties due to iteration, grid size, time step and other parameters. The U_G and U_T can be replaced by a combined uncertainty U_{GT} due to spatial and temporal discretizations (Qiu *et al.* [16]). Then the numerical uncertainty is expressed as

$$U_{SN}^2 = U_I^2 + U_{GT}^2 + U_P^2 \quad (5)$$

The iteration uncertainty U_I is estimated as the difference of the averaged simulation results in the last two revolutions of the rotor.

In this paper, U_P is not investigated and will be neglected.

For the verification based on three solutions, the convergence ratio R is defined as

$$R = \varepsilon_{21} / \varepsilon_{32} = (S_2 - S_1) / (S_3 - S_2) \quad (6)$$

where S_1 , S_2 and S_3 denote the simulation results, respectively, with fine, medium and coarse grid and time step sizes. The convergence is monotonic when $0 < R < 1$.

According to the Richardson Extrapolation (RE) approach, the one-term estimates of the error, δ_{RE}^* and the observed order of accuracy, p , are calculated respectively as

$$\delta_{RE}^* = \frac{\varepsilon_{21}}{r^p - 1} \quad (7)$$

$$p = \frac{\ln(\varepsilon_{32} / \varepsilon_{21})}{\ln(r)} \quad (8)$$

where r denotes the uniform parameter refinement ratio. In this paper, the refinement ratios for grid and time step sizes are both set as $\sqrt{2}$ because the governing equations are discretized with second-order schemes both in space and time, which means $r = r_G = r_T = \sqrt{2}$.

The correction factor, C , is defined as

$$C = \frac{r^p - 1}{r^{p_{est}} - 1} \quad (9)$$

where p_{est} is an estimate for the limiting order of accuracy of the first term as spacing sizes go to zero and the asymptotic range is reached, *i.e.* $C \rightarrow 1$. In this paper, p_{est} is taken as 2.

According to the uncorrected approach, the U_{GT} is estimated as

$$U_{GT} = \begin{cases} [9.6(1-C)^2 + 1.1] |\delta_{RE}^*|, & |1-C| < 0.125 \\ (2|1-C|+1) |\delta_{RE}^*|, & |1-C| \geq 0.125 \end{cases} \quad (10)$$

Validation is the process for assessing simulation modelling uncertainty by using benchmark experimental data. The validation uncertainty U_V is defined as

$$U_V^2 = U_D^2 + U_{SN}^2 \quad (11)$$

where U_D denotes experimental uncertainty. Due to the lack of experimental uncertainty data, the experimental uncertainty U_D is assumed to be 2.5%. The comparison error E , the difference between experimental data D and simulation results S of fine grid, is compared to the validation uncertainty U_V .

Table 1 shows the key parameters of computational grids, where GT1, GT2, and GT3 denote the grid models using fine, medium, and coarse grid and time-step sizes, respectively. The simulation results and comparison errors corresponding to the three grid models are shown in Table 2.

Table 1: Key parameters of the grid models.

| Model ID. | Total number of cells (Million) | Time step size | y^+ ($J=0.75$) | | y^+ ($J=0.9$) | |
|-----------|---------------------------------|----------------|--------------------|------|-------------------|------|
| | | | back | face | back | face |
| GT1 | 37.27 | 0.5° | 0.92 | 0.86 | 0.92 | 0.87 |
| GT2 | 12.53 | 0.707° | 1.28 | 1.18 | 1.29 | 1.19 |
| GT3 | 4.93 | 1° | 1.77 | 1.68 | 1.78 | 1.65 |

Table 2: Simulation results and comparison errors of grid models.

| Model ID. | $J=0.75$ | | | | $J=0.9$ | | | |
|-----------|----------|----------|---------|----------|----------|----------|---------|----------|
| | K_{TR} | E (%D) | $10K_Q$ | E (%D) | K_{TR} | E (%D) | $10K_Q$ | E (%D) |
| GT1 | 0.5321 | -0.34 | 1.0221 | 2.28 | 0.5059 | 2.01 | 0.9897 | 4.27 |
| GT2 | 0.5342 | 0.05 | 1.0254 | 2.61 | 0.5089 | 2.62 | 0.9944 | 4.77 |
| GT3 | 0.5426 | 1.62 | 1.0360 | 3.67 | 0.5183 | 4.51 | 1.0067 | 6.05 |

The iteration uncertainties are all lower than 0.012% and negligibly smaller than U_{GT} , hence $U_{SN} \approx U_{GT}$. The key parameters and uncertainties are presented in Table 3. The validation is successfully achieved at the U_V level of 2.5-2.7%, except for the torque coefficient (K_Q) at $J=0.9$.

Table 3: Results of the uncertainties and comparison errors.

| J | <i>Experiment</i> | R | p | C | U_{SN} (%D) | U_V (%D) | $ E $ (%D) | |
|------|-------------------|--------|------|------|---------------|------------|------------|------|
| 0.75 | K_{TR} | 0.5339 | 0.25 | 4.02 | 3.02 | 0.7 | 2.59 | 0.34 |
| | $10K_Q$ | 0.9993 | 0.30 | 3.45 | 2.31 | 0.5 | 2.55 | 2.28 |
| 0.9 | K_{TR} | 0.4959 | 0.33 | 3.24 | 2.07 | 0.9 | 2.66 | 2.01 |
| | $10K_Q$ | 0.9492 | 0.39 | 2.74 | 1.58 | 0.7 | 2.60 | 4.27 |

4.2 Hydrodynamic performance of PJP-1

Taking computing time into major consideration, GT3 is applied to predict the PJP-1's open water performance by steady and unsteady flow simulation models, although the errors in predicted performance are relatively larger than the other two grid models. Table 4 compares the numerical results with available experimental data, where K_{TR} , K_{TS} , and K_{TD} denote the thrust coefficients of the rotor, the stator, and the duct, respectively. The open-water efficiency, η , of the propulsor is based on K_{TT} , the total thrust coefficient of the propulsor, and K_Q , the torque coefficient of the rotor. The model experiments for the PJP-1 in uniform flows were conducted in the large cavitation tunnel of Shanghai Jiao Tong University in 2018.

Table 4: Comparison of the hydrodynamic coefficients of PJP-1 simulated using GT3 with experimental data.

| J | K_{TR} | | | K_{TD} | | K_{TS} | |
|-------------|----------|----------|--------------|----------|----------|----------|----------|
| | steady | unsteady | experimental | steady | unsteady | steady | unsteady |
| 0.3 | 0.5722 | 0.5815 | 0.6083 | 0.1393 | 0.1319 | -0.0425 | -0.0434 |
| 0.5 | 0.5570 | 0.5736 | 0.5826 | 0.0750 | 0.0696 | -0.0435 | -0.0430 |
| 0.75 | 0.5209 | 0.5426 | 0.5339 | 0.0015 | -0.0057 | -0.0478 | -0.0475 |
| 0.9 | 0.4938 | 0.5183 | 0.4959 | -0.0323 | -0.0433 | -0.0522 | -0.0516 |
| 1.1 | 0.4504 | 0.4779 | 0.4316 | -0.0666 | -0.0805 | -0.0603 | -0.0589 |

| J | K_{TT} | | | $10K_Q$ | | | η | | |
|-------------|----------|----------|--------------|---------|----------|--------------|--------|----------|--------------|
| | steady | unsteady | experimental | steady | unsteady | experimental | steady | unsteady | experimental |
| 0.3 | 0.6690 | 0.6699 | 0.7102 | 1.0565 | 1.0759 | 1.0810 | 0.302 | 0.297 | 0.314 |
| 0.5 | 0.5884 | 0.6002 | 0.6221 | 1.0429 | 1.0722 | 1.0574 | 0.449 | 0.445 | 0.471 |
| 0.75 | 0.4746 | 0.4894 | 0.4993 | 0.9996 | 1.0360 | 0.9993 | 0.567 | 0.564 | 0.593 |
| 0.9 | 0.4093 | 0.4233 | 0.4190 | 0.9654 | 1.0067 | 0.9492 | 0.607 | 0.602 | 0.626 |
| 1.1 | 0.3235 | 0.3385 | 0.2979 | 0.9083 | 0.9547 | 0.8597 | 0.623 | 0.621 | 0.621 |

For $J=0.75$ and 0.9 , simulations are also conducted using finer grid models, GT1 and GT2. Table 5 shows a comparison of rotor thrust and torque yielded from different grid models, where Δ_{su} is the relative difference between steady and unsteady flow simulation results. The open water performance curves are shown in Figure 8.

Table 5: The comparison of steady and unsteady simulations results obtained from different grid models.

| J | Model ID. | K_{TR} | | | $10K_Q$ | | |
|-------------|------------|----------|----------|---------------|---------|----------|---------------|
| | | steady | unsteady | Δ_{su} | steady | unsteady | Δ_{su} |
| 0.75 | GT3 | 0.5209 | 0.5426 | 4.0% | 0.9996 | 1.0360 | 3.5% |
| | GT2 | 0.5160 | 0.5342 | 3.4% | 0.9930 | 1.0254 | 3.2% |
| | GT1 | 0.5148 | 0.5321 | 3.3% | 0.9913 | 1.0221 | 3.0% |
| 0.9 | GT3 | 0.4938 | 0.5183 | 4.7% | 0.9654 | 1.0067 | 4.1% |
| | GT2 | 0.4881 | 0.5089 | 4.1% | 0.9576 | 0.9944 | 3.7% |
| | GT1 | 0.4873 | 0.5059 | 3.7% | 0.9568 | 0.9897 | 3.3% |

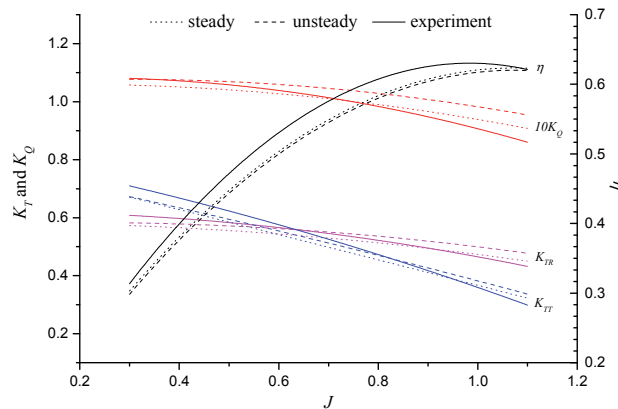


Figure 8: Comparison of RANS-simulated and experimental open water performances.

The results shown in Table 4, Table 5, and Figure 8 indicate that

1) The results of steady and unsteady simulations are generally in agreement with physical model experiments. The simulated thrust and torque coefficients are smaller than experimental data at lower J but higher at larger J . The simulated efficiency is always higher than the experimental values.

2) The results of K_{TR} , K_{TT} and K_Q obtained from unsteady flow simulations are all higher than those of steady flow simulations, although the differences between the two flow models become smaller as the grid and time-step sizes decrease.

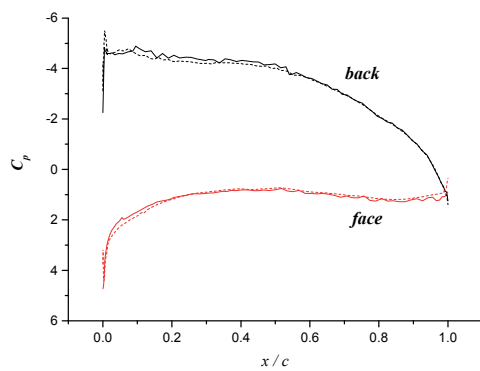
4.3 Influence of tip geometry on tip-clearance flow features

Based on the uncertainty analysis and the validation against physical experiments, the grid model GT2 is chosen for investigating the tip-clearance flow. The tip-clearance flow features, such as streamlines and pressure field, and hydrodynamic performance are numerically investigated and compared between PJP-1 and PJP-2 to study the influence of different tip geometries. The unsteady RANS simulations are carried out at $J=0.75$ and $J=0.9$.

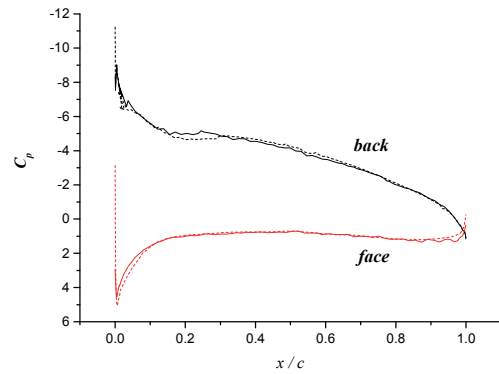
Table 6 compares the simulated rotor thrust and torque, where Δ_{12} is the relative difference between results of PJP-1 and PJP-2. Figure 9 shows the pressure distributions at $r=0.95r_R$ and $r=0.98r_R$. As far as PJP-1 and PJP-2 are concerned, the differences in blade-tip geometry seem to have little influence on the open water performance. The pressure distributions near the tip of PJP-2 are a little smoother than those of PJP-1, but the negative pressure peaks of PJP-2 are higher than those of PJP-1.

Table 6: Comparison of the simulated hydrodynamic performances of PJP-1 and PJP-2.

| J | K_{TR} | | | $10K_Q$ | | |
|-------------|----------|--------|---------------|---------|--------|---------------|
| | PJP-1 | PJP-2 | Δ_{12} | PJP-1 | PJP-2 | Δ_{12} |
| 0.75 | 0.5342 | 0.5351 | 0.17% | 1.0254 | 1.0267 | 0.13% |
| 0.9 | 0.5089 | 0.5099 | 0.18% | 0.9944 | 0.9960 | 0.15% |



(a) $J=0.75$, $r/r_R=0.95$



(b) $J=0.75$, $r/r_R=0.98$

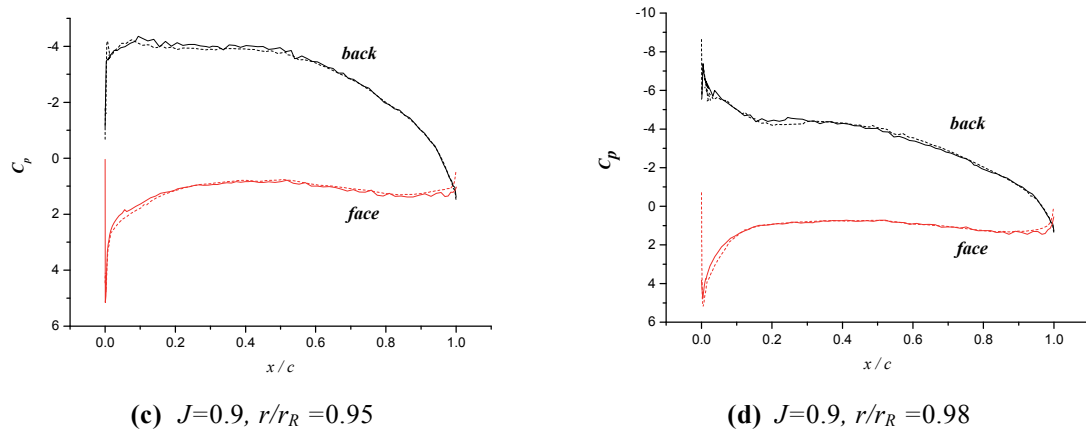


Figure 9: Comparison of simulated pressure distributions near the tips of PJP-1 (solid lines) and PJP-2 (dashed lines).

Figure 10 shows the streamlines in the sections perpendicular to the tip chord. The sections are at the position, respectively, 10%, 30%, 50%, 70% and 90% of the tip chord length from the leading edge. A typical static pressure field around the rotor blade tip and streamlines in one section are shown in Figure 11. Compared to PJP-1, the secondary flow in PJP-2 produces stronger detached vortex near the pressure side but weaker tip leakage vortex behind the suction side. The two vortices travel downstream and form a stable tip vortex. It is notable that in the two conditions ($J=0.75, 0.9$), the tip vortex of PJP-2 is obviously weakened in comparison with PJP-1, especially in the sections close to the leading edge.

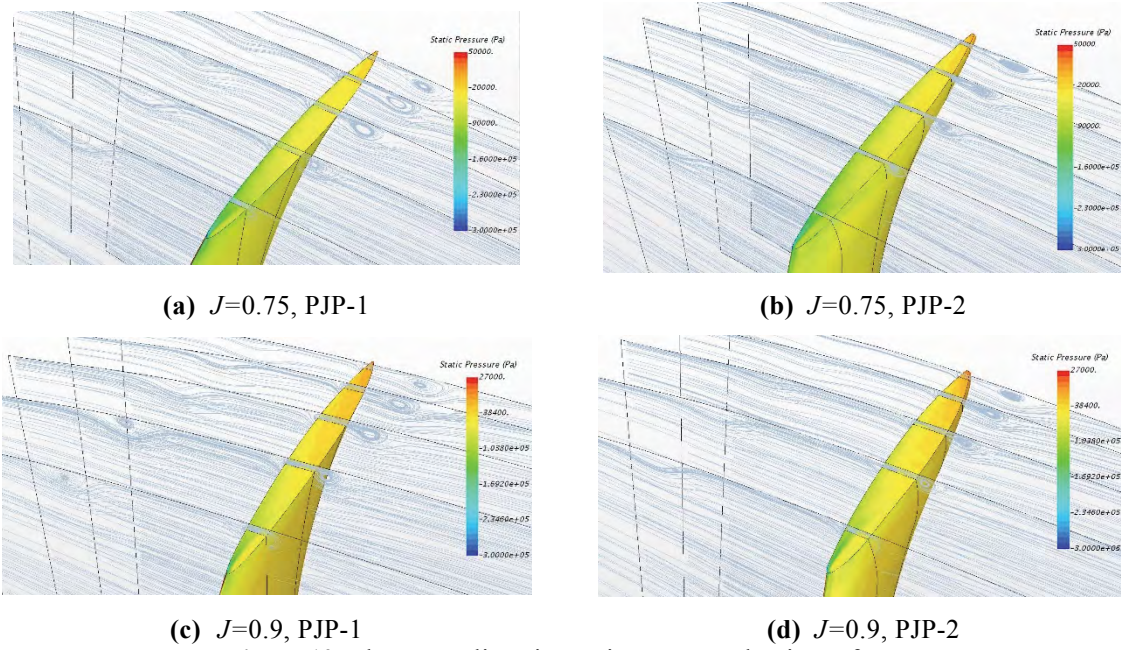


Figure 10: The streamlines in sections across the tip surface.

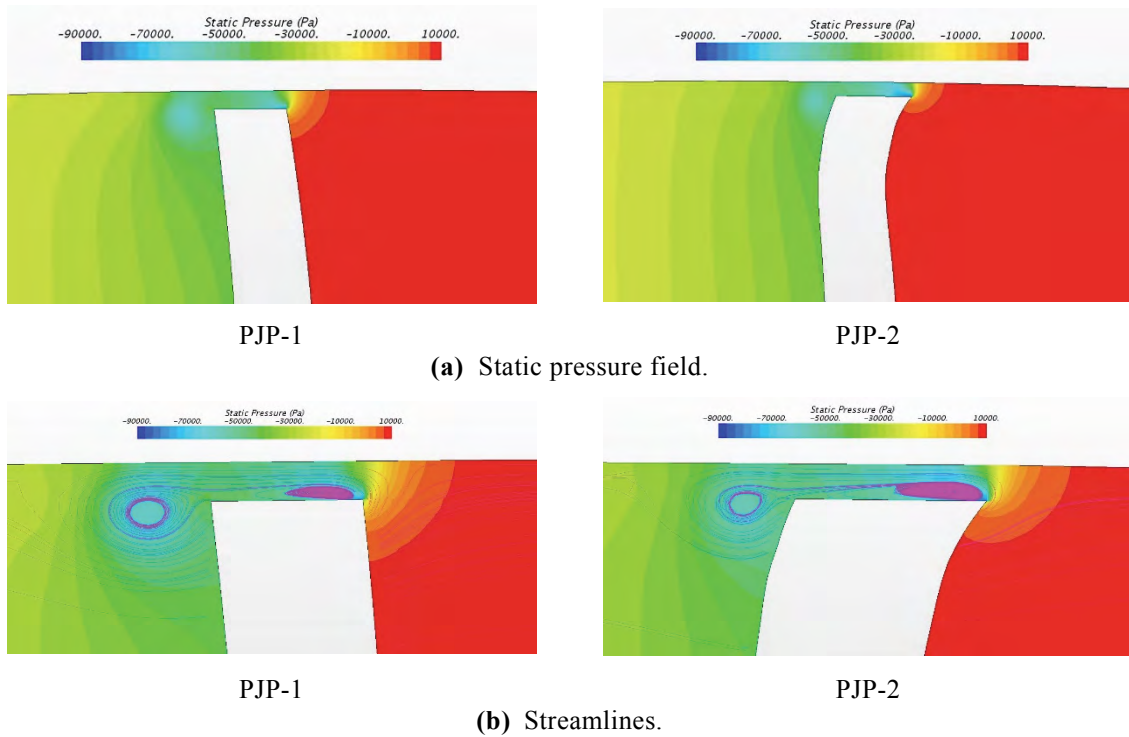


Figure 11: The pressure field and streamlines in the section at 30% tip chord length, $J=0.9$.

5 CONCLUDING REMARKS

In this paper, RANS simulations are carried out to investigate the influence of rotor-tip geometry on the tip-flow features of a pump-jet propulsor. The computational domain is discretized into block-structured hexahedral cells. To evaluate the numerical uncertainties according to the ITTC's recommended procedure, three sets of grids having a uniform refinement ratio are generated, and the unsteady flow simulations are carried out. The validation is generally achieved at the U_V level of 2.5% to 2.7%. The open water performances obtained from steady and unsteady flow simulations are generally in agreement with physical model experiments. The unsteady simulation results of thrust and torque are all higher than those of steady simulation. The differences between steady and unsteady simulations become smaller as the grid size decreases. The tip-clearance flow features are numerically investigated, with medium grids and time step, for varied profiles of section thickness and rake in the tip region. There is no obvious difference in open water performance and pressure coefficient between PJP-1 and PJP-2. The secondary flow in PJP-2 produces stronger detached vortex near the pressure side but weaker tip leakage vortex behind the suction side. The two vortices travel downstream and form a stable tip vortex. It is notable that the tip vortex of PJP-2 is obviously weakened in comparison with PJP-1, especially in the sections close to the leading edge. A more systematic investigation seems to be necessary in the hope of finding a tip geometry capable of weakening the tip-clearance flow.

REFERENCES

- [1] Suryanarayana, Ch. Design development and testing of pump-jet propulsor. *NSTL Report*. Visakhapatnam, No. NSTL/SR/136, (1999).
- [2] Suryanarayana, Ch.; Satyanarayana, B. and Ramji, K. Experimental evaluation of pump-jet propulsor for an axisymmetric body in wind tunnel. *International Journal of Naval Architecture and Ocean Engineering* (2010) **2(1)**: 24-33.
- [3] Ivanell, S. Hydrodynamic simulation of a torpedo with pump jet propulsion system. Master thesis, Royal Institute of Technology, Stockholm, 2001.
- [4] Cheah, K.W.; Lee, T.S.; Winoto, S.H. and Zhao, Z.M. Numerical flow simulation in a centrifugal pump at design and off-design conditions. *Int.J.Rotat*(2007).
- [5] Pan, G.; Hu, B.; Wang, P.; Yang, Z.D. and Wang, Y.Y. Numerical simulation of steady hydrodynamic performance of a pump-jet propulsor. *Journal of Shanghai Jiao Tong University* (2013) **47**:932-937.
- [6] Lu, L. and Pan, G. Numerical simulation analysis of unsteady cavitation performance of a pump-jet propulsor. *Journal of Shanghai Jiao Tong University* (2015) **49**:262-268.
- [7] Lu, L.; Gao, Y.F.; Li, Q.; and Du, L. Numerical investigation of tip flow characteristics of a pump-jet propulsor. *International Journal of Naval Architecture and Ocean Engineering* (2018) **10**:307-317.
- [8] Qin, D.H.; Pan, G.; Huang, Q.G.; Zhang, Z.D. and Ke, J.J. Numerical investigation of different tip clearances effect on the hydrodynamic performance of a pump-jet propulsor. *International Journal of Computational Methods* (2018) **15**.
- [9] Gu, L.; Wang, C. and Hu, J. Hydrodynamic performance prediction of a pump jet and impact analysis of a duct camber. *Journal of Harbin Engineering University* (2018) **39**:1752-1758.
- [10] Shimizu, Y.; Yoshikawa, T. and Matsumuru, S. Power augmentation effects of horizontal axis wind turbine by tip vane. *Trans of JSME* (1990) **56(522)**: 495-507.
- [11] Shimizu, Y.; Yoshikawa, T. and Matsumuru, S. Power augmentation effects of horizontal axis wind turbine with a tip vane part1 : Turbine performance and tip vane configuration. *Fluids Eng.*(1994) **116(2)**: 287-292.
- [12] Li, N.; Zhang, L.G.; Wang, Z.L. and Cai, Y.L. Numerical analysis of influence of tip vane width on pulse pressure of pump's shroud. *Noise and Vibration Control* (2014) **34**:34-37.
- [13] Rodi, W. Experience with two-layer models combining the k-epsilon model with a one-equation model near the wall. In Proceedings of the 29th Aerospace Sciences Meeting, Reno, Nevada, (1991).
- [14] Shih, T.H.; Liou, W.W.; Shabbir, A.; Yang, Z. and Zhu, J. A new k- ϵ eddy viscosity model for high Reynolds number turbulent flows-model development and validation. *Comput. Fluids* (1995) **24**:227-238.
- [15] ITTC. Uncertainty Analysis in CFD, Verification and Validation Methodology and Procedures. *ITTC-Recommended Procedures and Guidelines*, 7.5-03-01-01. In Proceedings of the International Towing Tank Conference, Wuxi, China (2017).
- [16] Qiu, J.T.; Yang, C.J.; Dong, X.Q.; Wang, Z.L.; Li, W. and Noblesse, F. Numerical simulation and uncertainty Analysis of an axial-flow waterjet pump. *J. Mar. Sci. Eng.*(2018).

POSSIBILITIES TO DETERMINE DESIGN LOADS FOR THRUSTERS

MARINE 2019

THOMAS ROSENLÖCHER, MANUEL KOSTIAL AND BERTHOLD SCHLECHT

Chair of Machine Elements, Institute of Machine Elements and Machine Design
Technische Universität Dresden, 01062 Dresden
e-mail: thomas.rosenloecher@tu-dresden.de, web page: <http://www.tu-dresden.de/me>

Key words: Thruster, Load Determination, Multibody-System Simulation, Bevel Gears

Abstract. Drive trains of icebreakers in arctic conditions are subjected to high stress levels. Due to collisions between ice and propeller, overloads and torsional vibrations occur. The main objective of the “Arctic Thruster Ecosystem” (ArTEco) project is to increase the reliability of vessels in arctic conditions. In order to achieve this goal different load scenarios are analyzed with multibody-system (MBS) simulation tools complemented by a test rig facility located in Tuusula (Finland). It is operated by the technical research center of Finland (VTT) and Wärtsilä. On the test rig, various loads can be applied to different azimuth thrusters, which are equipped with diagnostic instruments. For further analysis a simulation model is assembled and verified by several time-based data sets and modal analysis of the test rig. Thereby, overloads and high dynamic loads that are unobtainable at the test rig become accessible in simulations. To reduce torsional vibrations, different damping systems, designed at the department of intelligent hydraulics and automation (IHA) Tampere and the VTT, can be analyzed with the MBS-model. Besides torsional vibrations, one objective is the displacement analysis of the bevel gears. Using simulation-based displacement data and the software BECAL [1], a precise contact pattern can be determined, which allows conclusions regarding the required safety factors.

1 INTRODUCTION

Shipping operation in the sensitive but harsh arctic environment combine the demand for extreme reliable and energy efficient machines with the necessary requirement to prevent pollution of the arctic ecosystem. The main objective of the ArTEco project is an improvement of arctic ship propulsion products, with the target to identify critical areas in ship propulsion design and improve products for this industry. The consortium comprises of skilled research organizations, system integrators, component manufacturers and technology providers. Significant progress in conceptual development is achieved by a new full size thruster test facility established in Finland in 2013. The test facility allows measurements in a way that is not possible when a unit is in operation. A 2 MW thruster can be run with full power at the test rig and the operational loads can be applied to the thruster by hydraulic cylinders. The test rig allows the measurement of bearing loads, gear and shaft displacement and shaft torque. Furthermore, oil temperatures and vibrations are also monitored.

One objective of the research at TU Dresden is to achieve a better understanding of loads

and resulting stresses for thrusters by assembling a simulation model of the Wärtsilä steerable thruster WST14 and the whole test rig, using the software SIMPACK [11]. The assembly of the comprehensive simulation model starts with a torsional vibration system which is stepwise enlarged with more degrees of freedom (DOF) and modally reduced finite element (FE) bodies to a flexible MBS-model with 6-DOF bodies.

The combination of detailed simulation models and full-scale measurements of the corresponding thrusters allows the determination of inaccessible component loads such as bearing and gearing forces. The simulation model of the test rig will be used to determine the forces that have to be introduced by the hydraulic cylinders to emulate the offshore load conditions at the test stand.

As shown in figure 1, the thruster housing is mounted on the structure of the test rig and the drivetrain is connected to an electrical motor and generator. Six hydraulic cylinders can be connected to the loading unit at the end of the propeller shaft, to apply thrust and side forces. The cardan shaft allows an inclination between the thruster and the generator sided gearbox and connects the propeller shaft with the gearbox input shaft. With an electric connection between generator and motor, it is possible to feed only the power losses to the system and use the generator's energy to run the motor.

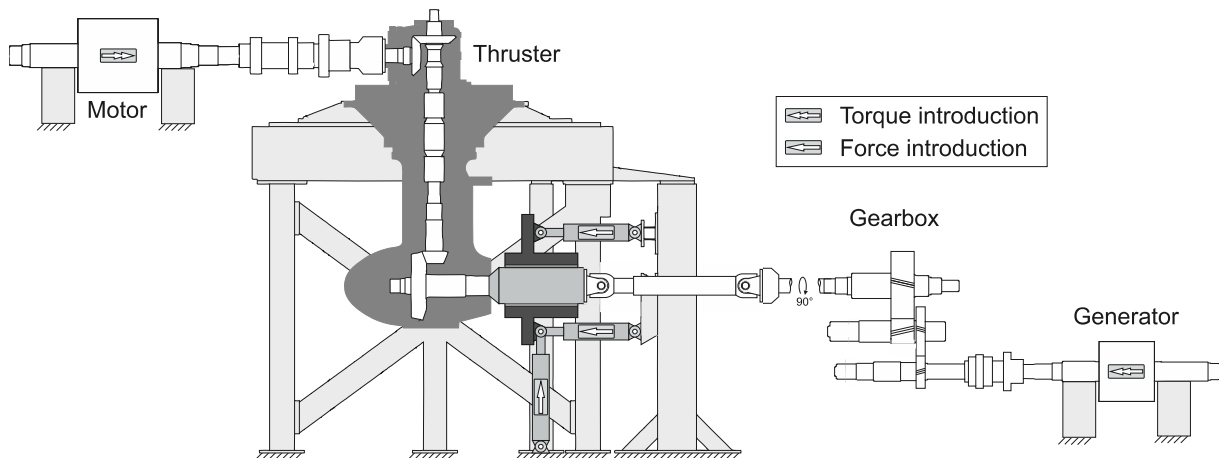


Figure 1: Schematic representation of the test rig

2 TEST RIG AND SIMULATION MODEL

The MBS-simulation allows to determine the dynamic behavior of the mechanical systems, consisting of flexible and rigid bodies. Each body has a mass distribution, allowing storing kinetic energy. With connecting spring damper elements, the energy exchanges and transfers from kinetic to potential energy. Therefore translator or rotatory spring damper elements, rigid connectors or various contacts are used. The mass and stiffness parameters of components given by their geometry, affect the natural frequencies of the system. They represent the frequencies with which the system will response on excitations. Besides the natural frequencies, the model represents the excitation due to the nonlinear characteristics of the gear contacts. The excitation of the gear contact by the variation of the number of teeth in contact and resulting changes in the stiffness are taken into account, according to ISO 6336 [6], [11]. In the MBS, the connection between shaft and housing is realized by spring-damper elements,

which can consider axial, radial and additionally the bearing moments as reactions. Depending on the purpose of the model, a constant stiffness or stiffness characteristics are used [10]. The cooperation partner SKF provides bearing stiffness matrices for each bearing and relevant load cases. The Euler-Bernoulli or Timoshenko beam theory are state of the art for fast calculation of shaft deformations and frequency responses [4]. The Timoshenko approach is used on all shafts of the test rig model, except the lower gearbox shafts. For a high level of accuracy, these shafts are modelled as FE-bodies, to include the flexibility of the bevel gear body. Since MBS-simulation tools compute with a higher resolution in the time domain, only a small number of DOF can be handled. To lower the DOF of FE-bodies, the component mode synthesis (CMS) is widely used in structural mechanics [9]. As shown in figure 2, m load introduction points (master nodes) are defined, which are connected to the nodes of the FE-model by n slave nodes. These multi-point constraints (MPC) are later used to introduce loads in the MBS. In addition to the static stiffness- and mass-matrix between the MPCs, a specified number l of natural frequencies is provided by the CMS. The usage of flexible MBS-models guarantees a more precise representation of the displacement and the excitable natural frequencies of the flexible body with a significantly lower computation time, compared to FE-simulation [2], [5].

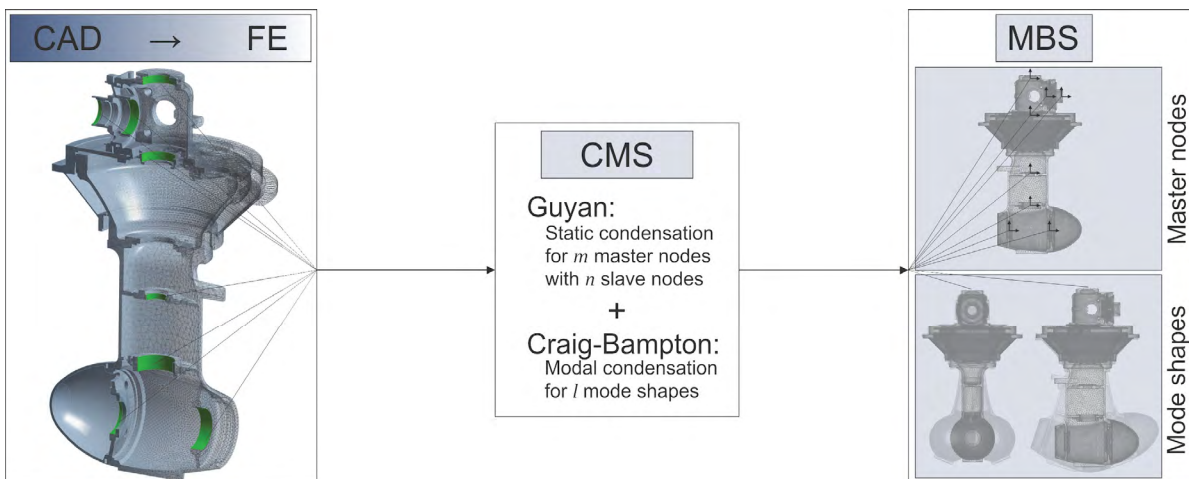


Figure 2: Workflow from CAD part to flexible MBS-body

3 MODEL VALIDATION

The test rig measurement data offer the opportunity to validate the simulation model. The validation is done by using the measurement results from modal analysis and time domain torque and displacement signals.

3.1 Frequency domain

The natural frequencies of the test rig are determined by acceleration sensors during a modal analysis. Besides the torsional frequencies, the longitudinal and transversal frequencies of the thruster housing have a major influence on the system behavior. Using information about inertia and stiffness of the drivetrain components, the torsional natural frequency can be calculated. They correspond well to the measurement results. The comparison of simulated

and measured natural frequencies of the thruster mode shapes in longitudinal, transversal and vertical direction show a good correlation. The natural frequencies of the torsional system, the 6-DOF-MBS-model and measurement results are compared in figure 3.

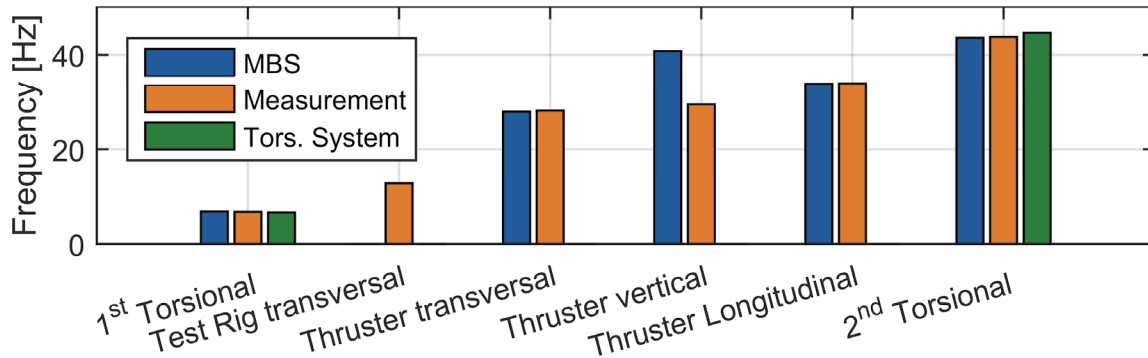


Figure 3: Comparison of natural frequencies of the test rig models

The analysis of the system behavior with a torsional system neglects further excitable frequencies. The test rig and thruster natural frequencies can only be seen in more comprehensive models. The thruster transversal, vertical and longitudinal natural frequencies are in good accordance to the measurement results, due to the considered structure of the flexible thruster housing including the horizontal test rig plate. The four stands of the test rig are not modelled, hence the test rig transversal frequency, which is of minor interest, is not included in the simulation. This rigid behavior, also in vertical direction, affects the thruster vertical mode shape, which does not match to the measurement results. The thruster longitudinal and transversal mode shapes are shown exemplarily in figure 2 (right). The modal analysis was done during stand still and without oil in the thruster housing. The damping and inertia effect of the oil is not included in the MBS-calculation.

3.2 Time domain

The complex control behavior of the motor and generator results in different torque characteristic compared to the simplified PI-control system of the MBS-model. In general, the system behaviors match, but resonance amplitudes do not correspond. Further investigations such as dampening adjustment are needed to achieve a better agreement between measurement and simulation.

To interpret the Hertzian contact stress, a precise determination of the relative bevel gear displacement is required. The use of the CMS reduced thruster housing and shafts is needed for this investigation. The lower gearbox gets loaded by thrust forces and bending moments, so that the stiffness characteristic is of high importance.

Besides the validation by measurement data, a comparison of the displacement results of the MBS-model is done using an analogous FE-model. In addition, the FE-model considers temperature distribution and bearing clearances, which are not included in a fast calculating MBS-model. On a similar level of detail of the models, this approach leads to a convincing accordance of displacement results from MBS and FE near the design torque. A slight deviation occurs at overloads and very low torque.

4 SIMULATION RESULTS

Thrusters running in icy conditions are subject to heavy load peaks. Therefore the "Finnish Swedish travel agency" TRAFI gives load cases, defining the number of amplitudes, magnitude and length of the propeller-ice interaction ([3], [7], [12], [13]). In figure 4 the load case torque characteristics and the simulated propeller shaft torque, as the systems response, is shown.

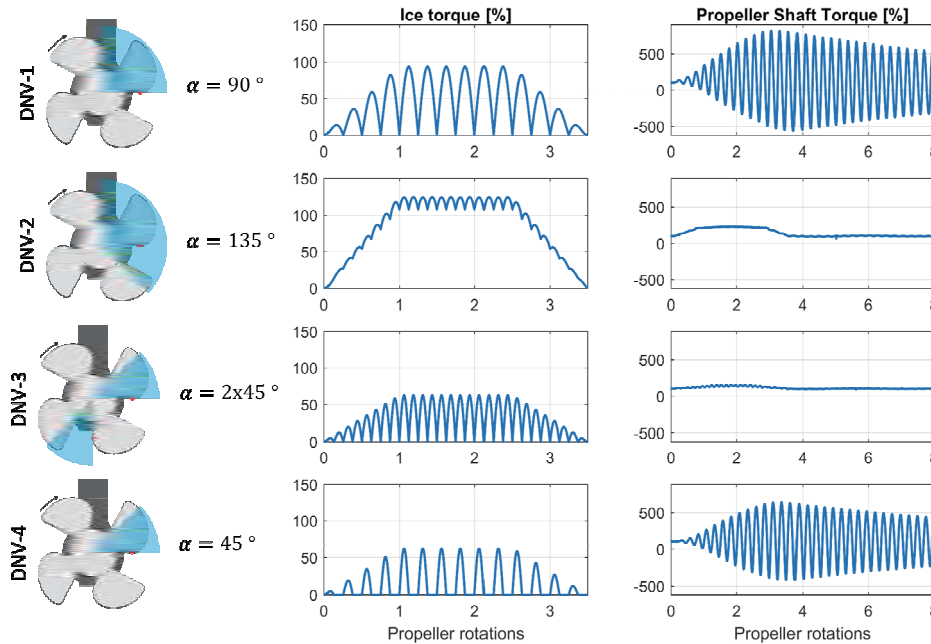


Figure 4: Ice load cases and system response

Thereby must be considered, that the test rig set up leads to torsional natural frequencies of the drive train, which are matching the blade passing frequency represented in the ice load cases. Because of that, high resonances can be seen in the ice load cases 1 and 4, since these load cases have major amplitudes at this frequency. The change of sign of the propeller shaft torque indicates a back flank contact in the lower gear stage.

To get a better understanding when back flank contact occurs, the half-sine ice load characteristic is modified for different amplitudes from 10 kNm to 70 kNm and varying contact length α from 10° to 90° . This results in a matrix of load cases. The minimum circumferential force in the lower gear stage is evaluable to identify critical load cases with back flank contact. In figure 4 the minimum force of the lower gear stage, normalized on the 100 % load case, is shown in relation to the ice torque amplitude and contact length. Besides the current WST14 design (middle), four more simulation results with smaller and bigger propeller inertia and similar loading are shown. The red marked areas represent the ice loads with back flank contact. With different propeller inertias, the 1st torsional natural frequency changes, so that resonances can be avoided and the high system responses are decreasing.

The ice loads, exciting with blade passing frequency, set the WST14 simulation model directly in resonance. This is shown by the high amplitudes seen in figure 4 for the load cases 1 and 4 and in figure 5 (middle).

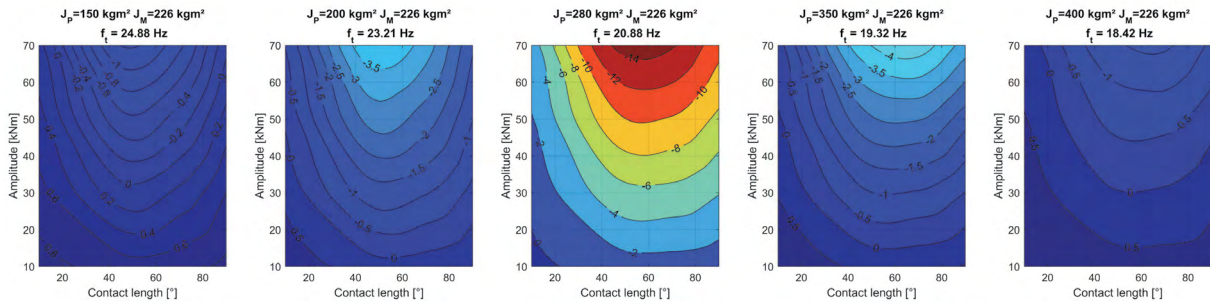


Figure 5: Load variation matrix for different propeller inertias

Besides torsional vibration the effect of bending moments on the propeller affect the gear contact. For the given thruster no information about the propeller are given, so that bending moments resulting from oblique inflow cannot be determined. With a general investigation to bending moments acting on the propeller in the range of the nominal torque, this topic is being investigated. Therefor the model is loaded with torque and different combinations of vertical and horizontal moments on the propeller. In figure 6 the definition of bending moment and resulting Hertzian contact stresses are given. The displacement of the gears is determined with the SIMPACK simulation model. Following the displacements are used to compute the contact stress with the software BECAL. The contact stress is nominated to the 100 % load case. The changes are relatively small compared to resulting stress changes due to torsional overloads.

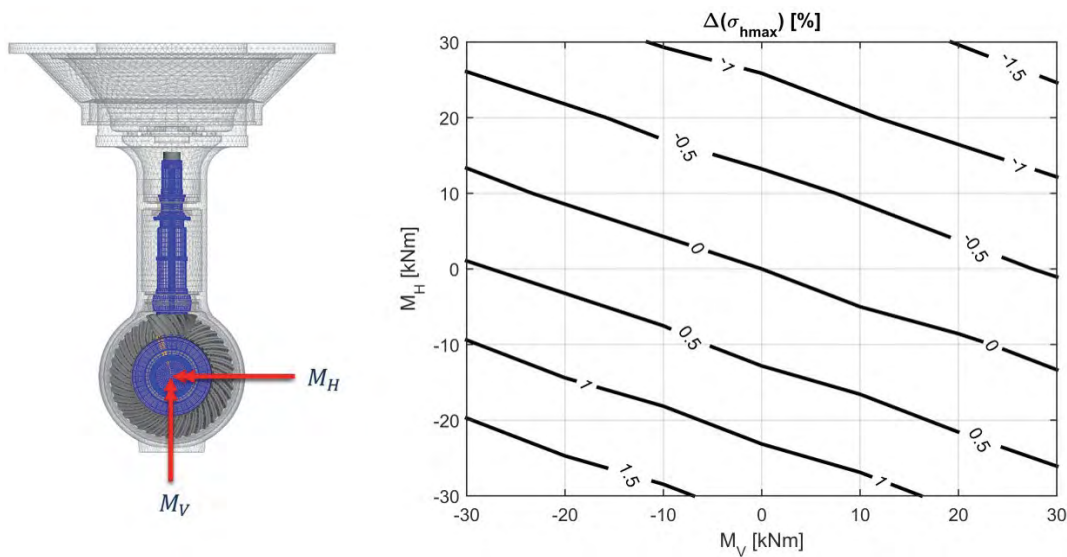


Figure 6: Hertzian contact depending on propeller bending

The Hertzian contact stress is more influenced by the horizontal moment than by the vertical moment. The contact pattern is shifted more to the heel or toe, resulting in different curvature of the flank and different lever to transmit the torque. This effect is seen within a range of +/- 1.5 % of the nominal contact stress. The small deviation of the pressure is the result of the relatively high lead crowning.

5 CONCLUSION

The test rig established by the VTT and Wärtsilä provides the opportunity to analyze the systems behavior, which cannot be done during operation of a vessel. Comprehensive overload tests were performed using different bevel gears. The resulting knowledge gives all partners a better understanding of the complex behavior of azimuth thrusters.

The flexible 6-DOF-MBS-model allows the determination of complex dynamic system behavior under consideration of flexible structures and their excitable mode shapes. The lower bevel gear stage and the flexible housing cross connect the torsional degree of freedom with the transversal thruster housing mode shape. This results in a more flexible torsional drivetrain, then determined with a simple torsional model. As a result, the determined torsional frequency drops and can be shifted in the working point, causing resonances.

The determination of relative gear displacement with SIMPACK shows good accordance to the comprehensive FE-model. A higher accuracy for overload situations is achieved with FE-simulation, when the contact pattern moves to the toe or the heel. Without the knowledge of the actual gear geometry and FE-mesh strategies, the SIMPACK model gives reliable relative displacement results and takes less computational time.

REFERENCES

- [1] BECAL, AK Kegelräder: BECAL –Berechnung an Kegel- und Hypoidgetrieben (Version 4.1.0). FVA Forschungsvorhaben Nr. 223 X, Heft 1037, (2012).
- [2] Craig R.R., Bampton M.C., AIAA Journal, Vol. 6, No. 7 – Coupling of Substructures for Dynamic Analyses, (1968).
- [3] DNV, DNVGL-CG-0041: Ice strengthening of propulsion machinery, Høvik (2016).
- [4] Dresig H., Fidlin A., Schwingungen mechanischer Antriebssysteme – Modellbildung, Berechnung, Analyse, Synthese, (2006).
- [5] Guyan R.J., AIAA Journal, Vol. 3, No. 2-Reduction of Stiffness and Mass Matrices, (1965).
- [6] ISO 6336-1, Calculation of load capacity of spur and helical gears – Part 1, (2006).
- [7] Jones S., Soininen H., Jussila M., Koskinen P., Propeller ice interaction, SNAME Transactions, Vol. 105, 1997, pp. 399-425 (1997)
- [8] Klingenberg J., Kegelräder – Grundlagen, Anwendung, (2008).
- [9] Koutsovasilis P., Model Order Reduction in Structural Mechanics - Coupling the Rigid and Elastic Multi Body Dynamics, Dissertation, (2009).
- [10] Rosenlöcher T., Systematisierung des Modellierungsprozesses zur Erstellung elastischer Mehrkörpersystem-Modelle und dynamische Untersuchung von Großantrieben, Dissertation, (2012).
- [11] SIMPACK GmbH, SIMPACK Documentation, (2016).
- [12] Transport Safety Agency, Finnish-swedish ice class rules 2010, (2010).
- [13] VTT (Technical Research Center Finland Ltd) Kinnunen A., Kurkela J., Juuti P., Azimuthing thruster ice load calculation and simplified ice contact load formulation, (2014).

ACKNOWLEDGEMENT

This work was carried out under the Maritime Technologies II Research program in the framework of the ERA-NET MARTEC II project CA 266111 Ar-TEco ‘Arctic Thruster Ecosystem’.

Gefördert durch:



Bundesministerium
für Wirtschaft
und Energie

aufgrund eines Beschlusses
des Deutschen Bundestages

VISCOUS EFFECTS ON THE HYDRODYNAMIC PERFORMANCE OF SEMI-ACTIVE FLAPPING PROPULSOR

NONTHIPAT THAWEEWAT*, SURASAK PHOEMSAPTHAWEE AND SIRIRAT JUNGRUNGRUENGTAWORN

Department of Maritime Engineering
Faculty of International Maritime Studies, Kasetsart University
199 Moo 6, Sukhumvit Rd, Sriracha, Chonburi 20230, Thailand
*e-mail: nonthipat.t@ku.th

Key words: Flapping foil, Biomimetics, Propulsion

Abstract. A numerical tool based on Lattice Boltzmann Method is used to investigate viscous effects on the hydrodynamic performance of a semi-active flapping propulsor. The obtained viscous results are compared with potential flow results previously presented in literature. It is found that both numerical tools give a qualitatively good trend agreement of the open water performance at high equivalent advance numbers. The results obtained using the viscous solver are slightly lower than that of potential flow in the region where flow separation is not observed. However, in case of small equivalent advance numbers, serious flow separation occurs due to high angle of attack, and hence the viscous results yield significantly lower efficiency. In spite of the mentioned deviation in the performance predictions, the LBM results confirm that the semi-active flapping propulsor is efficient over a wide range of operating conditions. This shows a possibility to practically use such self-pitching foil as a propulsion system.

1 INTRODUCTION

A fully-active flapping foil is the propulsion system where the foil heave and pitch kinematics are directly prescribed [1]. This system generally requires two actuators in order to drive both motions separately. Otherwise, a complex mechanism is required to simultaneously drive the two motions with one actuator. A numerical study based on inviscid model, i.e. Boundary Element Method (BEM), has shown that the fully-active flapping propulsor has high propulsive efficiency [2]. The prescribed pitch amplitude has been found to play a significant role in the range of operation bandwidth. For high pitch amplitude, the propulsor efficiently generates thrust for a relatively narrow range of equivalent advance numbers. A decrease in pitch amplitude tends to give a wider operation range.

In order to simplify the mechanical drive system, the use of spring-loaded oscillating foil, or in other name semi-active flapping propulsor, has been suggested [3, 4]. This system possesses only one actuator driving the foil heave motion while the foil pitch motion is passively adjusted

by interactions between hydrodynamic forces and a torsional spring attached to the foil hinge. Since this semi-active propulsor is a flow-induced vibration system, the spring stiffness as well as both foil and added inertias should influence the propulsive performance. In our previous study [5], the effects of inertia ratio and resonance on the open water characteristics of a semi-active flapping foil have been investigated using a BEM. The inviscid results show that the semi-active flapping propulsor performs efficiently over wide ranges of mechanical and kinematic conditions. The foil can efficiently generate thrust within the considered parametric range including the region where the instantaneous angle of attack is noticeably higher than the foil static stall angle [4].

Although the BEM has been mentioned as a useful approach to predict the unsteady forces generated by flapping foil [6], it should be pointed out that the BEM can sometimes lead to completely different results than the unsteady viscous solver. The disagreement between the both methods is due to a lack of boundary layer model in the potential flow approach. As a result, the inviscid solver may give an unreliable result at a certain range of operating conditions where serious flow separation occurs, e.g. high flapping frequency zone.

In an effort to investigate the effects of viscosity on the performance of fully-active flapping propulsor, different numerical tools have been used [7]. It has been reported that the BEM accurately predict hydrodynamic forces at high equivalent advance numbers due to its capability to model unsteady attached flows. However, in spite of similar trends in open water characteristics, simulations using a viscous solver result in lower efficiency than that of the potential flow code. As for the semi-active flapping propulsor, such viscous investigation has not been yet performed. In the present study, the inviscid results from our previous report concerning semi-active propulsor [5] will be compared to that of viscous approach.

2 SEMI-ACTIVE FLAPPING PROPULSOR

A semi-active flapping propulsor is a heaving foil attached to a torsional spring at its pivot point as schematically illustrated in Figure 1. The foil of span b and chord c is subjected to travel horizontally with a constant advance velocity U and to heave vertically with a sinusoidal motion at its hinge $h(t) = h_0 \sin(2\pi ft)$. The spring provides restoring moment toward static

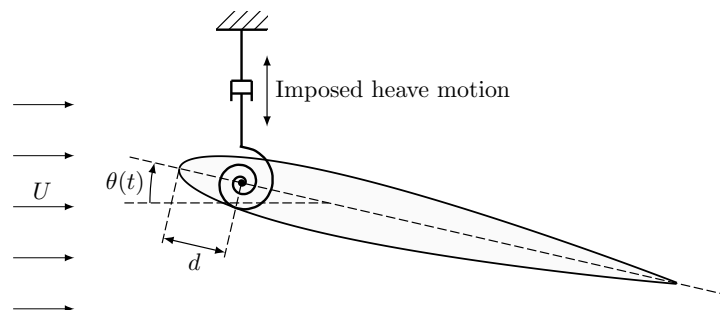


Figure 1: Schematic illustration of the semi-active flapping foil with imposed heave motion $h(t) = h_0 \sin(2\pi ft)$. The pitch angle $\theta(t)$ is passively determined by hydrodynamic and spring forces.

equilibrium in which the foil lies horizontally and also parallelly to the advance velocity. The open water performance such as the propulsive efficiency η is characterized by dimensionless parameters:

$$\eta = \hat{\phi}(h^*, \Lambda, d^*, I^*, J_{\text{eq}}, r) \quad (1)$$

where $h^* = h_0/c$ is the dimensionless heave amplitude, $\Lambda = b/c$ is the wing aspect ratio, $d^* = d/c$ is the dimensionless pivot location, $I^* = I/I_w$ is the inertia ratio, I is foil moment of inertia, and I_w is moment of inertia of fluid volume displaced by the foil around the pitching axis. Note that the foil centre of mass is located at the pivot point.

The propulsive performance of flapping propulsor is traditionally presented as functions of reduced frequency $k = \pi fc/U$ or alternatively Strouhal number St . However, in the present study, the open water characteristics of the foil is expressed in functions of advance ratio $J = U/nD$ similarly to that of conventional marine propeller in order to be able to fairly compare both systems. This can be done by introducing an equivalent diameter for the flapping kinematics on the basis of similar swept area: $D_{\text{eq}} = \sqrt{8h_0b/\pi}$. The equivalent advance number can therefore be defined as $J_{\text{eq}} = U/fD_{\text{eq}}$ which can be considered as another form of invert Strouhal number.

The last parameter in Eq. 1 is the frequency ratio representing the effects of spring stiffness and foil inertia:

$$r = \frac{f}{f_n} = 2\pi\sqrt{\frac{If^2}{K}} \quad (2)$$

where r is the structural frequency ratio, f_n is the natural frequency calculated based on the foil inertia I , and K is the torsional spring stiffness. It should be noted that the added inertia is not taken into account in the calculation of frequency ratio r . The effect of the added inertia has already been discussed in our previous study [5]. In order to investigate the influence of advance number as well as frequency ratio on the propulsive performance, the foil parameters are defined as shown in Table 1.

Table 1: Mechanical and kinematic parameters.

| | | |
|-------------------------------|-----------------|-----------|
| Dimensionless heave amplitude | h^* | 2.0 |
| Wing aspect ratio | Λ | 5.0 |
| Dimensionless pivot location | d^* | 0.0 |
| Inertia ratio | I^* | 10.0 |
| Equivalent advance number | J_{eq} | 1.5 - 6.0 |
| Frequency ratio | r | 0.1 - 1.8 |

3 NUMERICAL TOOL

In the present study, the Lattice Boltzmann Method (LBM) approach provided by a commercial CFD solver XFlow 2018 of Dassault Systèmes is used to simulate the flow around the semi-active flapping propulsor. The implementation can be summarized as follow. This unsteady viscous solver uses distribution functions in order to describe the collective behaviour of several mesoscopic particles. The governing equation is the discrete Boltzmann equation:

$$f_i(x + c_i\delta t, t + \delta t) = f_i(x, t) + \Omega_i(x, t) \quad (3)$$

where f_i is the particle distribution function for discrete direction i , c_i is the corresponding discrete velocity, Ω_i is the collision operator. Macroscopic parameters of density and momentum are calculated using the equilibrium distribution function by:

$$\rho = \sum_{i=0}^{b-1} f_i \quad (4)$$

and

$$\rho u = \sum_{i=0}^{b-1} f_i c_i \quad (5)$$

respectively, where b is the number of discrete directions of particle velocities. The solver uses D3Q27 model with twenty seven velocities for three-dimensional flow.

Viscous effects are taken into account via a relaxation time parameter in the collision operator. In order to improve numerical stability and accuracy, a collision model based on multiple relaxation time (MRT) scheme is utilized [8]. This alternative meshless approach has characteristics of wall-adapting local eddy (WALE) which is applied for turbulence closure and near-wall treatment.

The flow around the semi-active flapping propulsor is simulated in a three-dimensional domain with the length, width and height of $40c$, $30c$ and $30c$ respectively, where c is the chord length. The computational domain is considerably large so that the wall effect is negligible on the basis of a small blockage ratio. An adaptive refinement is applied in the vicinity of both foil and wake giving lattice node size of $c/32$ as suggested by [7]. A time step size of $dt = T/400$ is utilized in the LBM simulations which is considered sufficient to capture the flow physics. It has been found that the smaller time step provides the nearly coincident thrust production with the $T/400$ case, whilst the larger time step gives a slight deviation.

4 RESULTS

The simulations have been performed for at least 5 flapping periods or until periodic solutions have been observed. The results presented in this section are obtained from the last 2 periods of simulations in which the solutions are periodic. The propulsive performance η of semi-active flapping propulsor are presented in the range of the equivalent advance number of $1.5 \leq J_{eq} \leq 6.0$ and the frequency ratio of $0.1 \leq r \leq 1.8$.

4.1 Performance prediction

Contours of the simulated propulsive efficiency (—) along with lines of maximum angle of attack (- -) on the (J_{eq}, r) parametric space for different numerical tools are presented in Figure 2. The results show a similar trend in maximum angle of attack within the considered range of the parametric space. This consequently means that both inviscid and viscous solvers give nearly identical response in pitch motion. However, there is a deviation in the predicted propulsive efficiencies especially in high angle of attack regimes. For the LBM simulations, the extreme incidence angle together with the high frequency ratio leads to a drastic decrease in propulsive efficiency. In the zone of high frequency ratio and low advance number, a cycle-averaged drag can be observed for the LBM simulations, whereas thrust is still found for the BEM simulations.

Moreover, the LBM yields a slightly lower optimal efficiency ($\eta \approx 82.0\%$) compared to that obtained by BEM ($\eta \approx 87.4\%$). Nevertheless, the peaks approximately take place at the same location for both frequency ratio ($r \approx 0.51$) and advance number ($J_{eq} \approx 2.85$) as indicated by the markers \times in Figure 2(a) and 2(b).

In spite of the mentioned deviation in the performance predictions, the LBM results confirm that the semi-active flapping propulsor is efficient over a wide range of operating conditions.

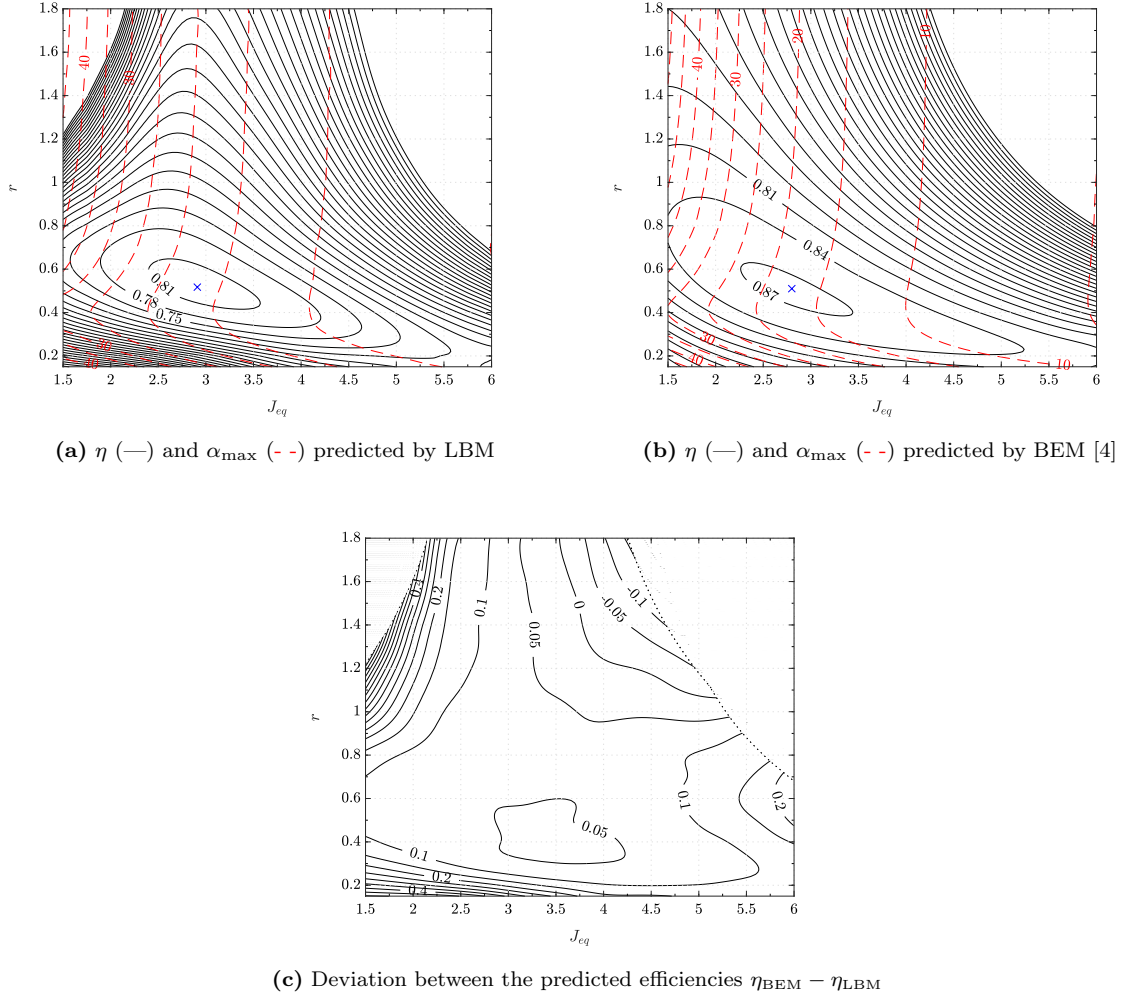


Figure 2: Performance of semi-active flapping foil as a function of equivalent advance number J_{eq} and frequency ratio r : (a) and (b) propulsive efficiency η along with the maximum angle of attack α_{\max} predicted by LBM and BEM [4] respectively, (c) deviation of efficiency between BEM and LBM. The markers \times indicate the peak locations.

4.2 Deviation in efficiency prediction

When the propulsor operates at very low advance numbers, the kinematic conditions could momentarily give an angle of attack higher than the static stall angle, especially for very low and high frequency ratios, as shown in Figure 2(a) and 2(b). This is because the value of frequency ratio represents the spring stiffness as indicated by Eq. 2. The rigid spring (small frequency ratio) resists the foil from pitching, while the more elastic spring (high frequency ratio) leads to undesired pitching direction at the beginning of a new stroke. Both mechanisms together with high flapping frequency, i.e. small advance numbers, result in an effective angle of attack

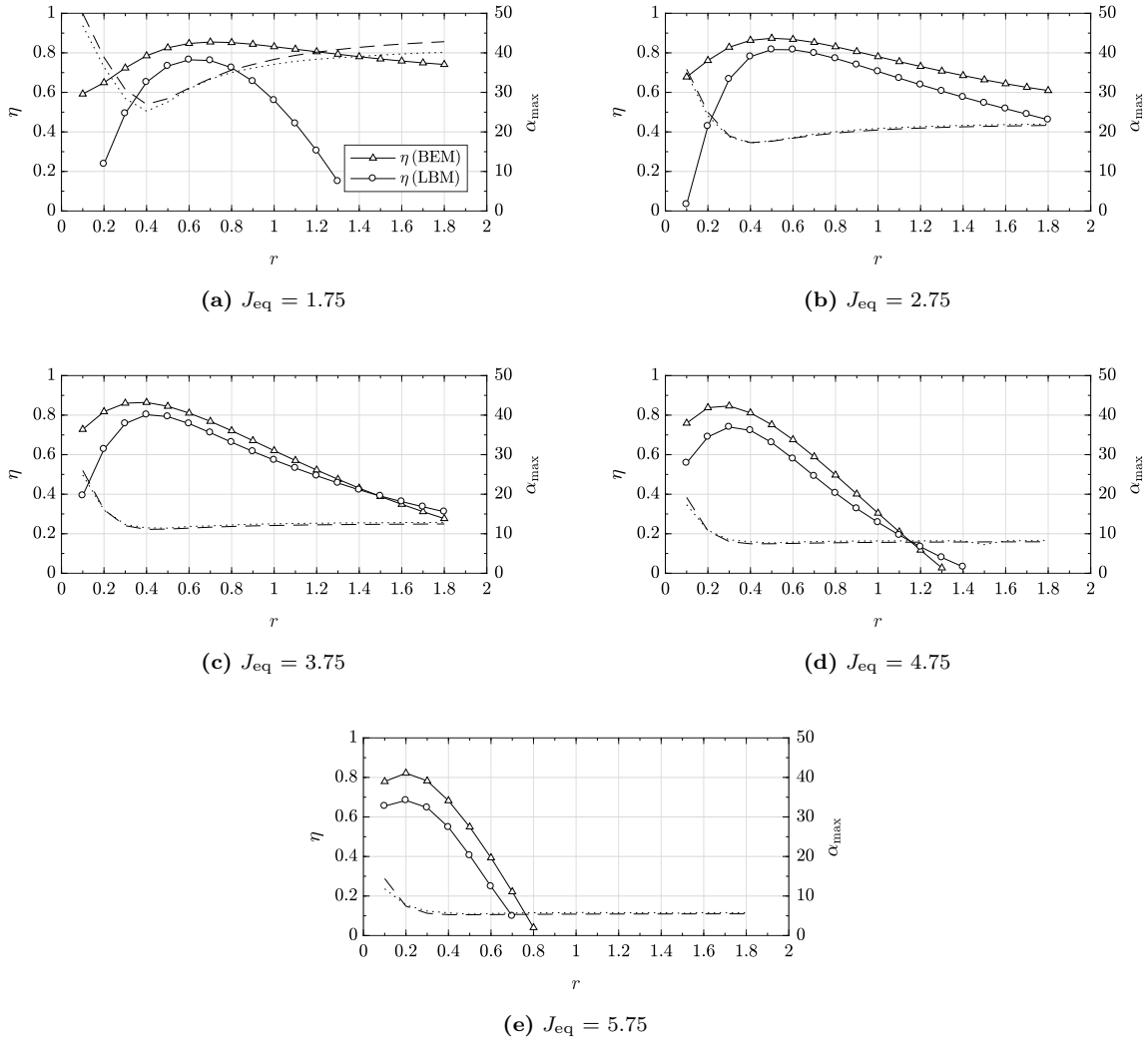


Figure 3: Propulsive efficiencies (solid lines with markers) as functions of frequency ratio for different equivalent advance numbers along with the maximum angle of attack α_{\max} predicted by BEM (- -) and LBM (\cdots) over a flapping period.

considerably greater than the foil static stall angle. In these extreme incidence angle cases, there is a noticeable deviation between the LBM and the BEM predictions (Figure 2(c)) as a result of flow separation.

The fully separation flow occurs and subsequently leads to a reduction in thrust and a rapid increase in required heave force. The force generation at this operating condition is therefore characterized by significant viscous effect which is not appropriately modeled using potential flow approach. Consequently, the deviation between BEM and LBM becomes obviously noticeable especially for both low and high frequency ratios, as seen in Figure 3(a). However, an appropriate range of frequency ratio ($0.4 \leq r \leq 0.7$) could prevent the extreme incidence angle. The results of both numerical approaches become close to each other. Note that the efficiency in Figure 3 is calculated only in the case of thrusting mode.

For low to intermediate advance numbers, the instantaneous angle of attack becomes moderately higher than static stall angle, seemingly affect the reliability of the BEM results. However, it has been shown that the rapid change in angle of attack of the foil could delay the flow separation to higher incidences compared to its normal static stall case. The stall could be temporarily delayed to angle of attack approximately 20° to 25° depending on foil kinematics [9]. The thrust and propulsive efficiency predicted by LBM simulations are therefore enhanced by this delayed stall mechanism. On the other hand, the enhancement in the BEM case is a result of naturally attached flow of the potential approach. For these moderate advance numbers, e.g. Figure 3(b), the LBM results agree well with the BEM results despite different performance enhancement mechanisms. Nevertheless, the deviation becomes significant at small frequency ratio due to extreme angle of attack.

The angle of attack, when it is small or equivalent to the foil static stall angle, does not remarkably influence the predictive capability of the BEM. In case of large equivalent advance number, i.e. low flapping frequency and hence small angle of attack, the potential approach seemingly appears to simulate the semi-active propulsor with acceptable agreement despite a slight deviation between the open water characteristics as shown in Figure 3(c), 3(d) and 3(e). The deviation between the two approaches is likely due to viscous effects. However, the trend remains unchanged.

5 CONCLUSIONS

The open water characteristics of a semi-active flapping propulsor is numerically studied using LBM. The investigation shows satisfactory trend agreement between viscous and inviscid solvers when the angle of attack is small or moderate in spite of a slight deviation which seemingly results from viscous effects. In the cases where the angle of attack is considerably high, the BEM inaccurately predicts the hydrodynamic forces and performance of the semi-active propulsor due mainly to flow separation. The LBM results also confirm that the propulsive performance of such biomimetic foil is efficient over a wide range of operating conditions.

ACKNOWLEDGEMENTS

The authors would like to acknowledge Phatcharak Buatee, Pongsit Payaptiva and Prawut Booranariththithawee for their contribution and generous supply of simulation results.

REFERENCES

- [1] Thaweewat, N., Bos, F.M., van Oudheusden, B.W., Bijl, H. Numerical study of vortex-wake interactions and performance of a two-dimensional flapping foil. *In: 47th AIAA Aerospace Sciences Meeting, Orlando* (2009) **791**.
- [2] Floc'h, F., Phoemsapthawee, S., Laurens, J.M., Leroux, J.B. Porpoising foil as a propulsion system. *Ocean Engineering* (2012) **39**:53–61.
- [3] Bøckmann, E., Steen, S. Experiments with actively pitch-controlled and spring-loaded oscillating foils. *Applied Ocean Research* (2014) **48**:227–235.
- [4] Thaweewat, N., Phoemsapthawee, S. and Juntasaro, V. Semi-active flapping foil for marine propulsion. *Ocean Engineering* (2018) **147**:556–564.
- [5] Phoemsapthawee, S., Thaweewat, N. and Juntasaro, V. Influence of resonance on the performance of semi-active flapping propulsor. *Ship Technology Research* (2019) (Article in Press).
- [6] Mantia, M.L., Dabnichki, P. Effect of the wing shape on the thrust of flapping wing. *Applied Mathematical Modelling* (2011) **35**(10):4979–4990.
- [7] Posri, A., Phoemsapthawee, S., Thaweewat, N. Viscous investigation of a flapping foil propulsor. *IOP Conference Series: Materials Science and Engineering* (2018) **297** 012012.
- [8] Lallemand, P., Luo, L.S. Theory of the lattice Boltzmann method: Dispersion, dissipation, isotropy, Galilean invariance, and stability. *Physical Review E* (2000) **61**(6):6546.
- [9] Akbari, M.H., Price, S.J., Simulation of dynamic stall for a NACA 0012 airfoil using a vortex method. *Journal of Fluids and Structures* (2003) **17**(6):855–874.

EFFICIENCY IMPROVEMENT EFFECT AND WATER NOISE REDUCTION BY ENERGY SAVING DEVICES

**Takuya Tachikawa*, Yoshihisa Okada*, Kenta Katayama*, Akinori Okazaki*
Masafumi Okazaki*, Kenichi Fukuda*, Yosuke Kobayashi*, Toshie Kajino***

* Propeller &ESD design department, NAKASHIMA PROPELLER Co., Ltd.
688-1 Joto-Kitagata, Higashi-ku Okayama 709-0625, Japan
e-mail: t-tachikawa@nakashima.co.jp
web page: <https://www.nakashima.co.jp/eng>

Key words: Energy Saving Device, Synergistic Effect, Underwater Radiated Noise

Abstract. In recent years, the Energy Efficiency Design Index (EEDI) regulations for global GreenHouse Gas (GHG) reduction has been strictly updated. From these back ground, environmentally friendly operation and propulsion systems are expected.

In the view of propulsion system design, GHG reduction by improving propulsion efficiency and comfortable habitability by noise reduction are focused. Consequently, many ship designers and manufactures developed a variety of energy saving devices such as the propeller cap with fins, rudder bulb and duct to improve propulsion efficiency.

In general, the improvement effects of each energy saving devices are estimated by ship designers or manufactures. Therefore, when several energy saving devices is installed with the ship, several energy saving devices, the actual degree of propulsion efficiency from synergistic effects are sometimes unknown at the design stage.

In this paper, in order to evaluate synergistic effects of energy saving devices, the authors designed ECO-Cap[1], Ultimate Rudder Bulb[2] and Neighbor Duct[3] for 82kBC by using CFD and then conducted the model tests of each devices. Furthermore, the combinations tests of such devices were carried out in model tests.

This paper summarizes the synergistic effects of energy saving devices on the basis of the model tests. In addition, noise reduction effects by energy saving devices are also described for informative reference.

1 INTRODUCTION

There are many energy saving devices available in market of merchant vessel. For example, a propeller cap with fins, rudder bulb and duct are popular products for improvement of fuel oil consumption. However, there are few available research results for combination of their individual effects.

Firstly, the propeller cap with fins is well-known product for energy saving because of easy installation and inexpensive. In particular, Propeller Boss Cap Fins (PBCF) is very famous product for this kind of device [4]. Another product called as ECO-Cap is recently released to the market (See Figure 1(a)). ECO-Cap has small seven fins for diffusing of negative pressure at the propeller cap end. Furthermore, the thickness of such fins can thin

because of Fiber Reinforced Plastics (FRP) made, and this leads to reduce the drag. In previous study, the efficiency increased by ECO-Cap was abt.1.2% in the model test [5]. However, ITTC referred the model test results and the results of full scale analyses, and mentioned that the full scale improvement rate of propulsion efficiency can be 2 to 3 times greater than the model scale prediction in their guidance [6]. Furthermore, the full scale improvement rate of propulsion efficiency by ECO-Cap was changed by propeller particulars, and it was observed 1.5 to 3.2 times greater than the model scale [7]. In addition to the efficiency improvement effect, the noise reduction effect was reported by preventing the generation of hub vortex cavitation [8]. ECO-Cap prevents the generation of hub vortex cavitation by effect of small seven fins (See Figure 1(b)). Therefore, ECO-Cap can be expected the noise reduction effect.

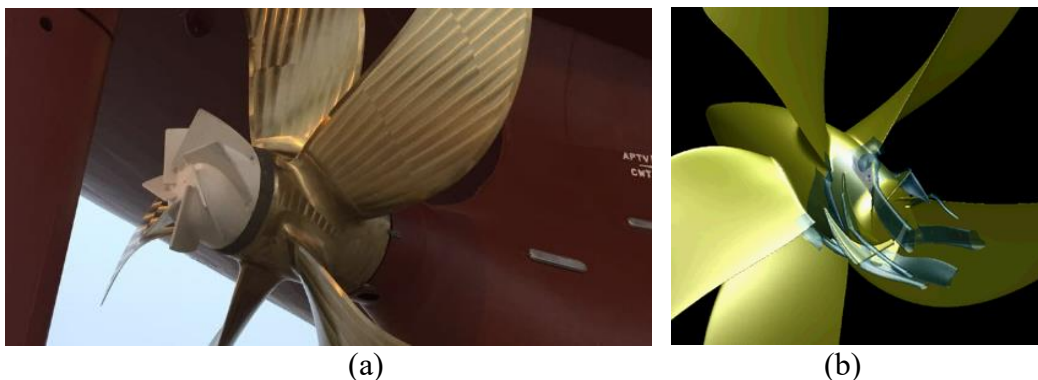


Figure 1: (a) ECO-Cap, (b) Isosurface of the absolute value of rotational flow

Secondly, the rudder bulb is also a popular energy saving device and has a long history for the delivery. The rudder bulb was developed by Costa in 1952 and the efficiency increased by rudder bulb for container vessel was 1% on average [9]. Mitsui Engineering and Shipbuilding developed “MIPB (Mitsui Integrated Propeller Boss)” as advanced rudder bulb [10]. The feature of MIPB was streamlined profile, which were smooth from a propeller cap to rudder. According to the paper about MIPB, the efficiency increased by installing MIPB was 2-4%. The reason of the efficiency improvement of the rudder bulb is wake gain and the recovery of energy loss caused by disappearance of hub vortex. Therefore, the bulb position that is close to the propeller plane is more preferable. In the case of MIPB, the bulb position was closer than general rudder bulb by installation of divergent propeller cap and the efficiency was increased. Thereafter, some manufactures installed the divergent propeller cap for their own rudder bulb. If the propeller cap become to rounded profile, then the efficiency will increase by upgrading of wake gain. Propeller cap for Ultimate Rudder Bulb was developed the rounded profile (see Figure 2(a)). Okada et al. (2015) optimized profile of Ultimate Rudder Bulb by CFD and confirmed efficiency increase by abt.5-6% in the self-propulsion test (see Figure 2(b)). In addition, the noise reduction effect of Ultimate Rudder Bulb can be expected same as ECO-Cap.

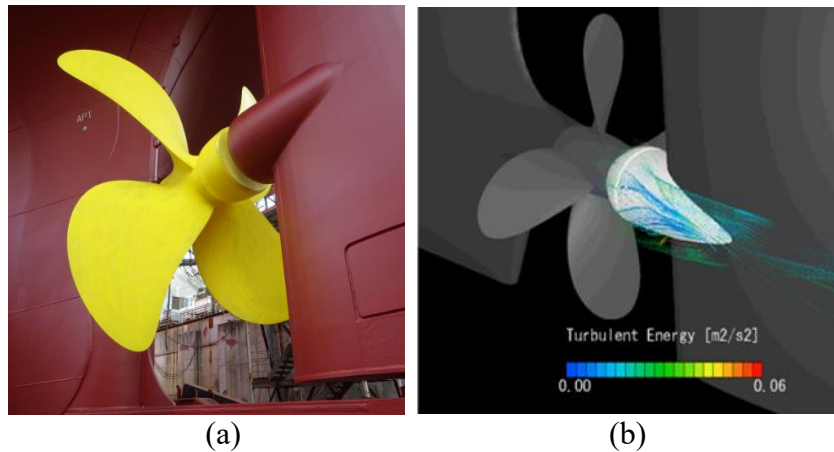


Figure 2: (a) Ultimate Rudder Bulb, (b) Turbulent Energy

Thirdly, the duct is thought to be one of the most effective energy saving devices. There are many similar ducts in maritime industry. Weather Adapted Duct (WAD) was developed by National Maritime Research Institute (NMRI). The feature of WAD is small size and the harmful cavitation on the propeller blades is hardly occurred. The effect of power reduction by WAD is 3-7% [11].

Another duct called as Neighbor Duct developed by authors (see Figure 3(a)), gains the improvement of thrust deduction fraction $(1-t)$ (see Figure 3(b)). This duct is vertically long elliptical profile and there is little influence on wake fraction $(1-w)$. The improvement of propulsion efficiency was 4.7% in the model test.

As described above, each saving devices has the increase of the efficiency and integrated optimal design of those devices should be considered for the market of merchant vessel. The authors carried out a model test to clarify the combined the effect from those three energy saving devices.

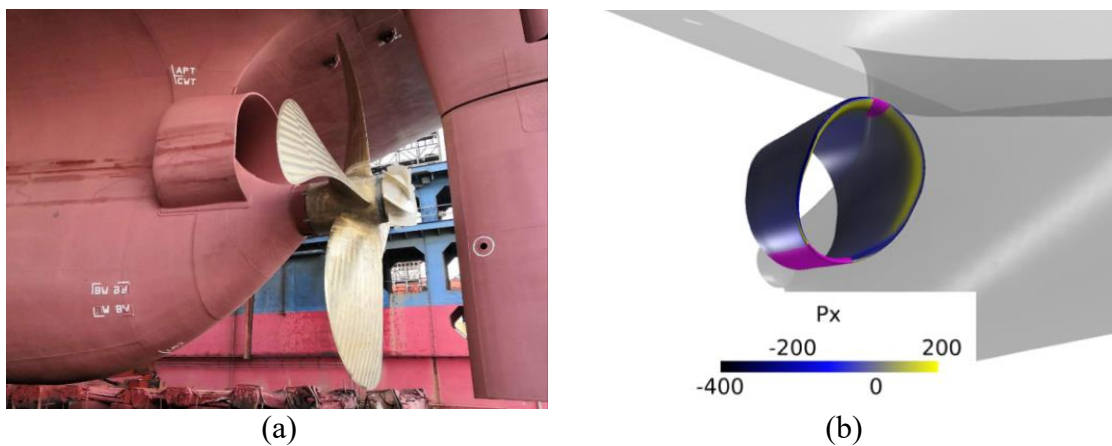


Figure 3: (a) Neighbor Duct, (b) Thrust distribution

2 EFFICIENCY IMPROVEMENT EFFECT

2.1 TEST CONDITIONS

The self-propulsion tests were conducted at 400m long towing tank in NMRI. In the model test, 82kBC developed by NMRI was used. Principal the hull particulars of 82kBC are shown in Table 1 and the propeller particulars are shown in Table 2.

ECO-Cap, Ultimate Rudder Bulb and Neighbor Duct for 82kBC were designed by using CFD in this study. Figure 4 shows the image of Ultimate Rudder Bulb and ECO-Cap for 82kBC. In addition, the model tests in each device and combined condition with each device were conducted.

Table 1: Principal particulars of hull

| NMRI 82Pana_Max Bulk Carrier | | |
|------------------------------------|---------------|-------|
| Condition | Designed Full | |
| Principal Dimension | Model | |
| Length Between Perpendiculars | [m] | 7.631 |
| Length on Designed Load Water Line | [m] | 7.734 |
| Breadth | [m] | 1.109 |
| Depth | [m] | 0.653 |
| Design Draft | [m] | 0.419 |
| Block Coefficient | 0.87 | |

Table 2: Principal particulars of propeller

| Principal Dimension | Model | |
|--------------------------|-------|--------|
| Diameter | [m] | 0.22 |
| Pitch Ratio | 0.65 | |
| Boss Ratio | 0.16 | |
| Expanded Area Ratio | 0.55 | |
| Chord Length at 0.7R | [m] | 0.0696 |
| Number of Blades | 4 | |
| Shaft Center Line Height | [m] | 0.1203 |

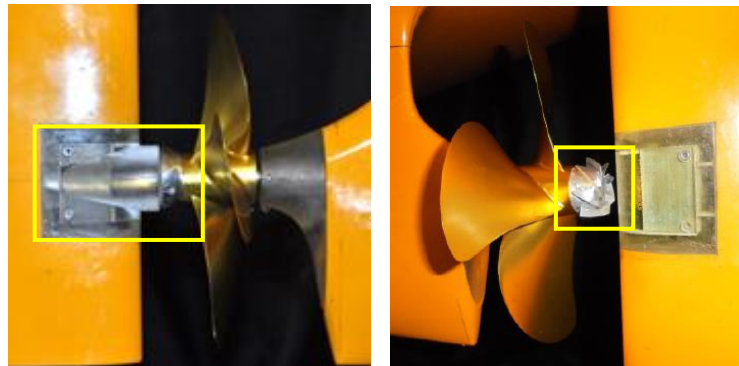


Figure 4: Ultimate Rudder Bulb and ECO-Cap

2.2 TEST RESULTS OF EACH DEVICE

Figure 5 shows the model test results with each device. Vertical axis in Figure 5 indicates the ratio of “with” and “without” each device in the self-propulsion factors. All energy saving devices showed effective for improvement of efficiency.

In the results, Neighbor Duct was the most effective and $\Delta\eta$ (energy saving index) was 4.7%, while that index of Ultimate Rudder Bulb and ECO-Cap was 3.9% and 2.9%, respectively. The definition of each item is described below.

$$\eta = (1-t)/(1-w) \eta_o \eta_R \quad (1)$$

$$\Delta\eta = \eta_{with} / \eta_{without} \quad (2)$$

| | |
|-----------------------------------|--|
| η : Propulsive efficiency | η_o : Propeller open water efficiency |
| $1-t$: Thrust deduction fraction | η_R : Relative rotative efficiency |
| $1-w$: Wake fraction | |

The results of $1-w$ and $1-t$ for three energy saving devices indicated the better trend in terms of efficiency. $1-w$ showed negative trend while $1-t$ showed positive trend. This leads to improve the efficiency with each device.

It was confirmed that Neighbor Duct and Ultimate Rudder Bulb had a better improvement effect because the degree of the absolute ratio for $1-t$ is large compared with that for $1-w$. The tendency of the improvement of Neighbor Duct was similar compared with Ultimate Rudder Bulb. On the other hand, ECO-Cap was effective in terms of the improvement of η_R .

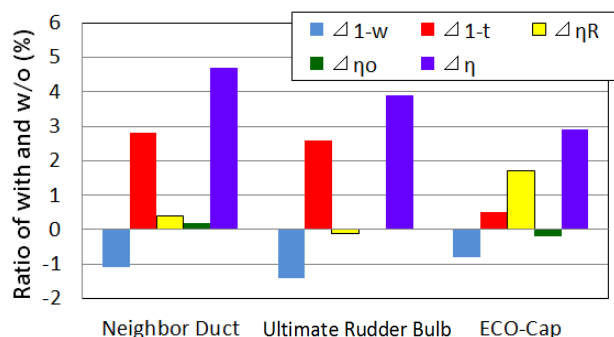


Figure 5: Model test results of each device

2.3 TEST RESULTS OF COMBINED DEVICE

The combination of energy saving devices was selected and the most effective combination was investigated. Figure 6 shows the combination test results for Neighbor Duct and ECO-Cap. The energy saving index of combination of Neighbor Duct and ECO-Cap was 6.2%.

The improvement of $1-t$ was almost same between condition of only Neighbor Duct and combination condition. Also, The improvement of η_R was almost same between condition of only ECO-Cap and combination condition. Therefore this model test results shown that the

improvement effect by different items such as $1-t$ and η_R is not canceled.

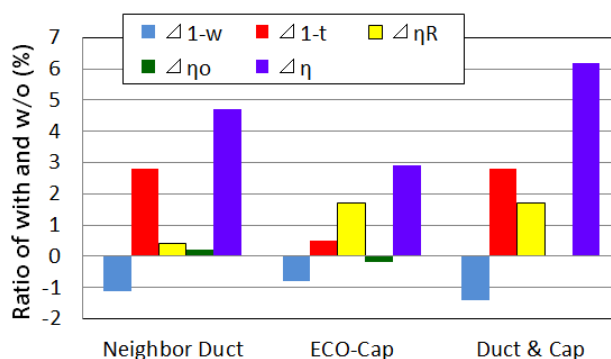


Figure 6: Model test results of combined condition

Figure 7 shows the combination test results for Neighbor Duct and Ultimate Rudder Bulb. The energy saving index of combination of Neighbor Duct and Ultimate Rudder Bulb was 8.7%. The improvement tendency of self-propulsion factors from both Neighbor Duct and Ultimate Rudder Bulb showed similar. The highest improvement effect was obtained from the combination of Neighbor Duct and Ultimate Rudder Bulb. This is because that the increase of $1-t$ was highest in all energy saving effects examined.

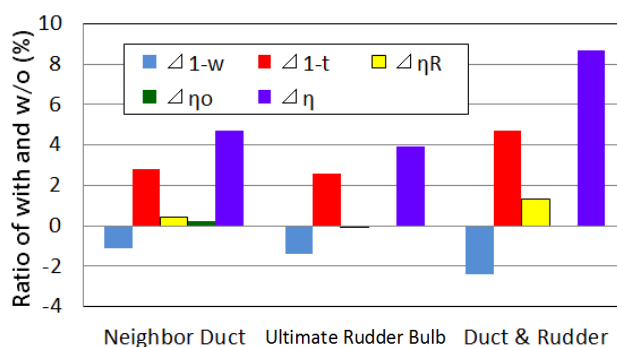


Figure 7: Model test results of combined condition

3 UNDERWATER RADIATED NOISE

3.1 TEST CONDITIONS

The model test for cavitation noise measurement was conducted in large cavitation tunnel of NMRI. The propeller model was used same as propeller model which was used for the self-propulsion tests. The test conditions are shown in Table 3.

Table 3: The test conditions for cavitation noise measurement

| | |
|------------|------------|
| J | 0.484 |
| K_T | 0.150 |
| σ_n | 2.25 |
| n | [rps] 35.0 |

$$J = V/nD \quad (3)$$

$$K_T = Thrust / \rho n^2 D^4 \quad (4)$$

$$\sigma_n = P_{atm} + \rho g I - P_v / (1/2 \rho n^2 D^2) \quad (5)$$

| | |
|---------------------------------|----------------------------------|
| J : Advance coefficient | V : Velocity of the flow |
| D : propeller diameter | n : propeller shaft speed |
| K_T : Thrust coefficient | ρ : Density of water |
| σ_n : Cavitation number | P_{atm} : Atmospheric pressure |
| g : Gravity Acceleration | I : Immersion |
| P_v : Vapor pressure of water | |

Figure 8 shows arrangement of cavitation noise measurement. The underwater radiated noise is measured by using the hydrophone attached with the rudder.



Figure 8: The arrangement of cavitation noise measurement

3.2 TEST RESULTS

Figure 9 shows the comparison of hub vortex cavitation behavior with and without energy saving devices (ECO-Cap and Ultimate Rudder Bulb). In Figure 9 (a), the hub vortex cavitation caused by the negative pressure at the propeller cap end was observed. On the other hand, in Figure 9 (b) and (c), hub vortex cavitation was not observed with ECO-Cap and Ultimate Rudder Bulb.

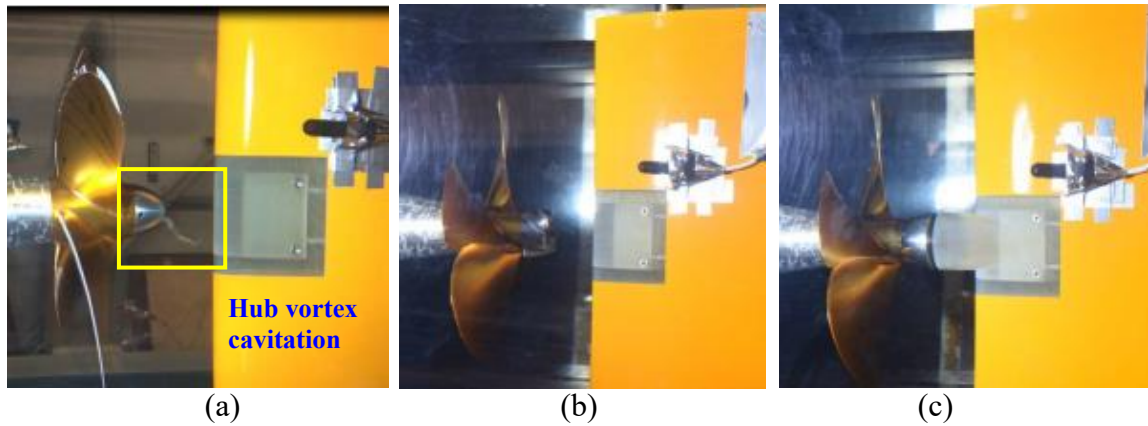


Figure 9: Comparison of hub vortex cavitation behavior (a) w/o energy saving devices, (b) with ECO-Cap, (c) with Ultimate Rudder Bulb

Figure 10 shows comparison of the Sound Pressure Level (SPL) between condition without and with ECO-Cap. In the over range of 100Hz, it was confirmed that the underwater radiated noise reduction effect of ECO-Cap is around 6dB.

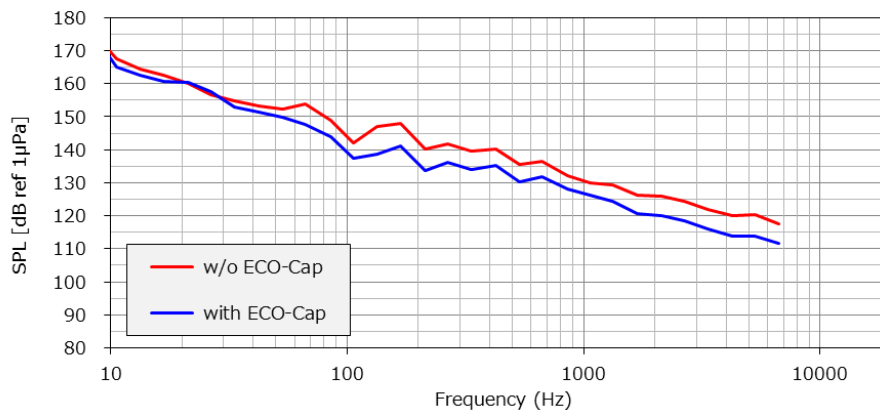


Figure10: Reduction effect of ECO-Cap for underwater radiated noise

Figure 11 shows comparison of SPL between condition without and with Ultimate Rudder Bulb. As is the case with ECO-Cap, in the over range of 100Hz, it was confirmed that the underwater radiated noise reduction effect of Ultimate Rudder Bulb is around 7dB. As a result, it was confirmed that ECO-Cap and Ultimate Rudder Bulb are effective devices to reduce the underwater radiation noise.

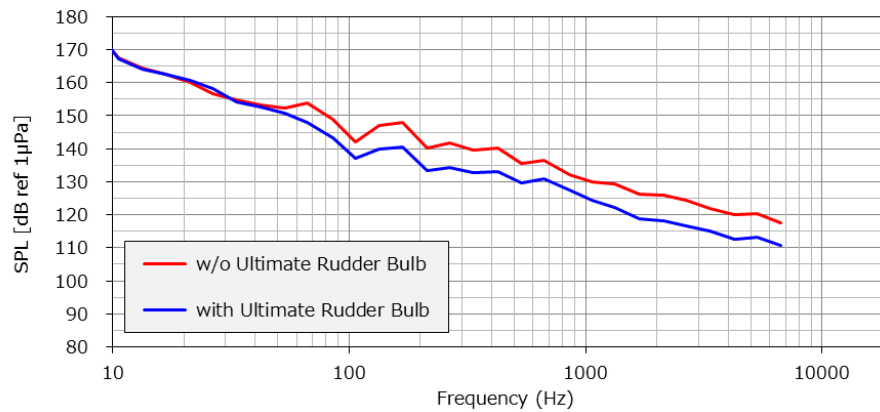


Figure11: Reduction effect of Ultimate Rudder Bulb for underwater radiated noise

4 CONCLUSIONS

The authors confirmed the following contents from the model test and CFD analysis by energy saving devices.

1) From the model test results for 82kBC, ECO-Cap, Ultimate Rudder Bulb and Neighbor Duct were effective for energy saving. In terms of the amount of energy saving index, ECO-Cap was 2.9%, Ultimate Rudder Bulb was 3.9% and Neighbor Duct was 4.7%. ECO-Cap improved η_R , while Neighbor Duct and Ultimate Rudder Bulb improved especially 1-t.

2) In combined results from the model test, it was confirmed that the combinations of each energy saving devices were effective. The energy saving index from combination of Neighbor Duct and ECO-Cap was 6.2%, while the combination of Neighbor Duct and Ultimate Rudder Bulb was 8.7%.

3) In the noise measurement results from model test, the underwater radiated noise reduction effect of ECO-Cap and Ultimate Rudder Bulb was confirmed. The underwater radiated noise reduction effect of ECO-Cap was 6dB, while that of Ultimate Rudder Bulb was 7dB.

REFERENCES

- [1] Okada, Y., Okazaki, A., and Katayama, K., “Numerical Analysis of the Propeller with Economical Cap by CFD”, Proceedings of 16th Numerical Towing Tank Symposium, Mulheim, Germany, (2013).
- [2] Okada, Y., Okazaki, A., Katayama, K., Kawasaki, M., Fukuda, K., and Okazaki, M., ‘The development of “Ultimate Rudder” for EEDI’, Proceedings of MARINE 2015, Rome, Italy, (2015).
- [3] Katayama, K., Okada, Y., Ichinose, Y., and Fukasawa, R., ‘Propulsion Performance Optimization of “Neighbor Duct” by CFD’, Proceedings of MARINE 2017, Nantes, France, (2017).
- [4] Kawamura, T., Ouchi, K., and Takeuchi, S., “Model and full scale CFD analysis of

- propeller boss cap fins”, Proceedings of smp’13, Launceston, Australia, (2013).
- [5] Katayama, K., Okada, Y., and Okazaki, A., “Optimization of the Propeller with ECO-Cap by CFD”. Proceedings of smp’15, Austin, Texas, USA, (2015).
- [6] Bose, N., Billet, M., Andersen, P., Atlar, M., Dugué, C., Ferrando, M., Qian, W., and Shen, Y., “Final Report and Recommendations to the 22nd ITTC”. The specialist Committee on Unconventional Propulsors, (1999).
- [7] Okazaki, M., Kajihama, T., Katayama, and K., Okada, Y., “Propeller Particulars and Scale Effect Analysis of ECO-Cap by CFD”, Proceedings of 18th Numerical Towing Tank Symposium, Cortona, Italy, (2015).
- [8] Ouchi, K., Tamashima, M., and Arai, K., “Reduction of Propeller Cavitation Noise by PBCF (Propeller Boss Cap Fins)”, Journal of the Kansai Society of Naval Architects, Japan No.216, (1991).
- [9] Mewis, F., and Deichmann, F., “Power and Cost-Savings for Container Vessels by Hydrodynamic Energy Saving Devices”, International Conference on Ship Efficiency by STG, Hamburg, Germany, (2013).
- [10] Fujii, A., “New Energy Saving System -Mitsui Integrated Propeller Boss-”, Proceedings of ISME Yokohama’95, Yokohama, Japan, (1995).
- [11] Kawashima, H., Kume, K., and Sakamoto, N., “Study of Weather Adapted Duct (WAD)”, NMRI Report Vol.14, No.2, (2014).

A LINEARIZED FREE-SURFACE RANS METHOD FOR SHIP MANEUVERING

MARINE 2019

PAOLO GEREMIA*, KEVIN J. MAKI† AND PAVLOS ALEXIAS†*

* ENGYS S.R.L.

Strada per Vienna, 9
34151 Trieste, Italy

Email: p.geremia@engys.com - Web page: <http://www.engys.com>

† University of Michigan

Ann Arbor, Michigan, USA

Email: kjmaki@umich.edu - Web page: <http://cshl.engin.umich.edu/>

†* ENGYS Ltd

Studio 20 - Royal Victoria Patriotic Building, John Archer Way,
London SW18 3SX, United Kingdom

Email: p.alexias@engys.com - Web page: <http://www.engys.com>

Key words: CFD, free-surface, maneuvering, PMM, self-propulsion

Abstract. Proper prediction of ship maneuvering – together with powering and seakeeping – is considered essential these days to help naval architects design optimal ship hulls. In this context, traditional finite-volume Computational Fluid Dynamics (CFD) methods offer a well-proven simulation platform to realize such predictions with a high degree of certainty. In this work, a novel transient CFD method based on a linearized free-surface RANS solver is presented to assess maneuvering actions of both captive and free-running ship performance on a series of selected test cases. The performance of the proposed solver is considerably better in terms of solution speed than other traditional CFD methods employed for this type of analysis, especially when applied to transient solutions requiring long simulation times.

1 INTRODUCTION

CFD solvers employed in the study of ship hull hydrodynamics are usually based on either Volume-Of-Fluid (VOF) [1] or level-set methods [2], both implemented as part of the Reynolds Averaged Navier Stokes (RANS) equations in a finite-volume framework. Albeit these methods have proven to deliver highly accurate predictions for hull resistance and other important performance parameters, they often require very long computational times which are incompatible with the time available at the early stages of the design process. During the ship design process, different design candidates must be evaluated by the designers and, ideally, fast turnaround times are required to quickly screen multiple layouts to find an optimal solution for the hull.

In order to overcome the high computational costs associated to traditional VOF and level-set methods, a new RANS based Linearized Free-Surface (LFS) solver with viscous effects was successfully implemented and employed to perform fast hull-form optimization using a steady-state formulation [3], which allowed for faster predictions of hull resistance and other parameters without compromising the overall accuracy of the results.

In this paper, the original steady-state LFS solver described in [3] has been extended to enable time-dependent solutions using an unsteady RANS (uRANS) formulation. The new unsteady solver has also been modified to incorporate a full 6 Degrees-of-Freedom (DoF) rigid body motion framework in order to simulate a variety of hull motions, including calm-water resistance, seakeeping, maneuvering and self-propulsion.

The use of the uRANS approach is of significant importance to accurately predict both the pressure and viscous forces acting on the hull, including the interaction with the propeller and the rudder components. In this context, the application of the LFS solver allows for a more efficient solution in terms of computational time, hence allowing the designer to investigate the effects of multiple hull motions in shorter times.

The current implementation of the new unsteady LFS solver is limited for now to in-plane motions only (namely: surge, sway and yaw) due to the nature of the rigid-body 6DoF library employed. Therefore, all model tests and validations presented herein are focused on Planar Motion Mechanism (PMM) and free-running 3DoF maneuvering tests, assuming negligible roll and pitch angles at low running speeds.

2 DESCRIPTION OF FLOW SOLVER

The proposed uRANS LFS flow solver is based on the linearized unsteady Neumann-Kelvin ship wave boundary-value problem. The ship generated wave is assumed to be of small wave amplitude and steepness, and the fully-nonlinear free-surface boundary condition can be satisfied in linearized form on the calm-water plane. This allows for a double-body discretization to be used together with a single-phase flow solver.

In the present work, the unsteady kinematic condition is coupled to the unsteady uRANS equations via the dynamic free-surface condition that is applied to the free-surface boundary of the domain. The mathematical details and extensive validation of the formulation can be found in [6, 9].

One improvement, unique to this solver, is the way in which the 3DoF dynamic mesh motion and the Multiple Reference Frame (MRF) are applied. In this case, the entire domain translates and rotates with the geometry while the reference frame remains earth-fixed [4]. This improves the accuracy when solving the non-linear equations, the ability to simulate wave patterns and the solver's robustness.

The 3DoF motion capabilities make this model applicable to a wide range of problems, including the free-fall of a body that impacts the air-water interface, the seakeeping response of a surface vessel or submarine, or the maneuvering response of a ship.

3 CAPTIVE TEST CASES

The first application considered in this paper is a series of PMM captive tests performed on the KRISO Container Ship (KCS) model [5]. The characteristics of the hull are summarized in Table 1.

Table 1: KCS Geometry and conditions for PMM tests

| | |
|---------|--------|
| Scale | 52.667 |
| Lpp [m] | 4.3671 |
| Bwl [m] | 0.6114 |
| T [m] | 0.2051 |
| U [m/s] | 1.701 |
| Fn [-] | 0.26 |

The maneuvering simulation tests are performed in even keel conditions with dynamic sinkage and trim suppressed to mimic the results obtained in the towing tank experiments when using the PMM system. In the uRANS method employed for all the captive tests described in this work, the two equations k - ω SST turbulence model was used due to its accurate prediction of pressure forces when applied to ship hydrodynamics.

To assess the convergence of the rigid-body motion library applied to the LFS solver, a preliminary mesh convergence study was carried out in preparation for the subsequent captive test simulations performed [6].

3.1 Static Drift

The first test performed as part of this study was a static drift maneuver of the KCS model with a yaw amplitude $\xi_6 = 5deg$ simulation, travelling at a constant speed at $Fn = 0.26$ in calm-water conditions, with a 2.5s ramp applied in which the body is accelerated until it reaches the target nominal speed.

The main objective of this task was to carry out a grid convergence study and determine a convergence criterion for both the sway force and the yaw moment calculated on the hull on a coarse, medium and fine grid with 321K, 843K and 2.8M cells, respectively. The mesh layout and the resulting free-surface elevation for the fine mesh case are shown in Figure 1.

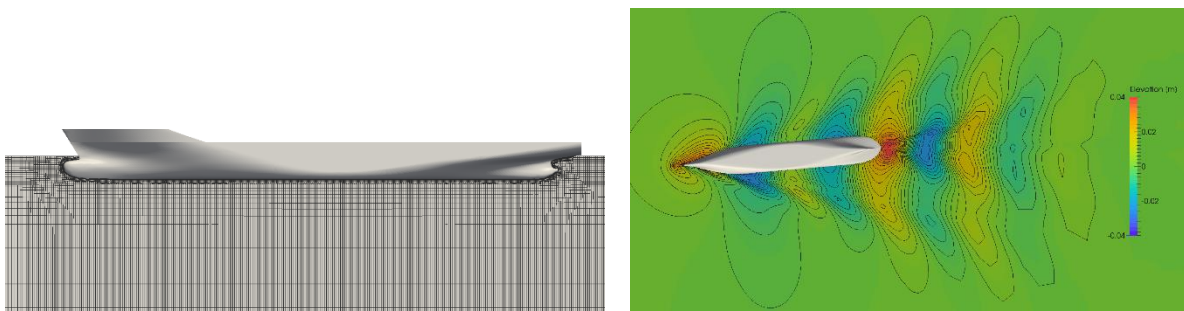


Figure 1: Static Drift: fine mesh overview (left) and free-surface elevation (right)

To check the convergence of the solver against the grid size, the sway force and yaw moment output responses were considered. Assuming h_i as the reference size of the i -th grid, where h_1 is the fine mesh reference cell size, the Richardson extrapolated exact solution ϕ_0 was defined starting from the ϕ_1 , ϕ_2 and ϕ_3 measured responses for the fine, medium and coarse grids respectively, according to the following formula:

$$\phi_0 = \phi_1 + \frac{\phi_1 - \phi_2}{r^p - 1} \quad (1)$$

where p is the order of the interpolation defined as follows:

$$p = \frac{\ln[(\phi_3 - \phi_2)/(\phi_2 - \phi_1)]}{\ln(r)} \quad (2)$$

And $r = h_{i+1}/h_i$ is the constant ratio of refinement between the grids. The extrapolated solution ϕ_0 as well the mesh extrapolation curves are shown in Figure 2 for both the sway force and the yaw moment.

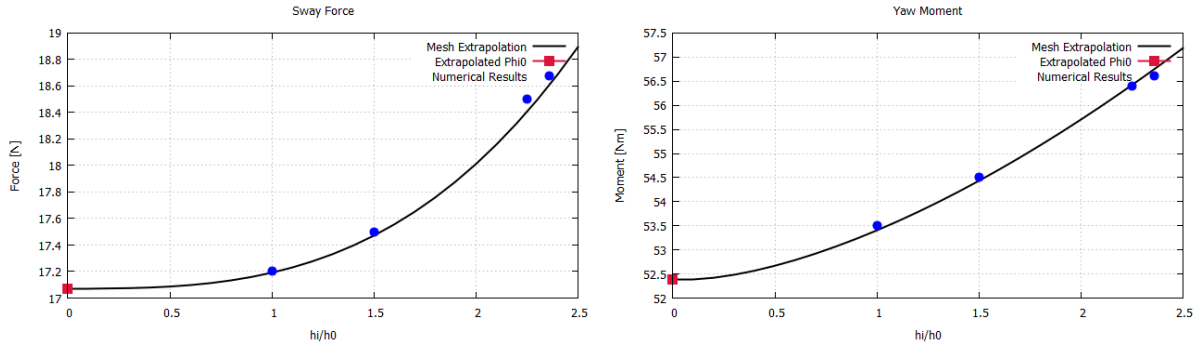


Figure 2: Mesh extrapolation: sway force (left) and yaw moment (right)

It can be noticed that a monotone convergence is achieved for both the forces considered in Figure 2. The same can be also seen if the Grid Convergence Index (GCI) is defined as follows:

$$GCI = 1.25 \frac{|\phi_{i+1} - \phi_i|}{\phi_i} \frac{1}{r^p - 1} \quad (3)$$

In fact, an asymptotic range of convergence is obtained for both sway force and yaw moment, as follows:

$$\begin{aligned} \left(\frac{GCI_2}{r^p GCI_1} \right)_{Surge\ Force} &= 0.984 \approx 1 \\ \left(\frac{GCI_2}{r^p GCI_1} \right)_{Yaw\ Moment} &= 0.980 \approx 1 \end{aligned} \quad (4)$$

The same grid and numerical setup employed for the static drift run was thus used for running two additional captive tests, namely: a pure sway and a pure yaw PMM maneuvers, as detailed in the following sections.

3.2 Pure Sway

A pure sway maneuver was carried out with a sway amplitude of $\xi_2 = 0.127\text{m}$ and a PMM period of 13.33s. For this purpose, a total of 34CPU hours (defined as number of processors multiplied by the clock time for each PMM period) was required.

The results in terms of sway force and yaw moment were compared against the experimental measurements provided by FORCE Technology and made available for the SIMMAN 2014

workshop [7].

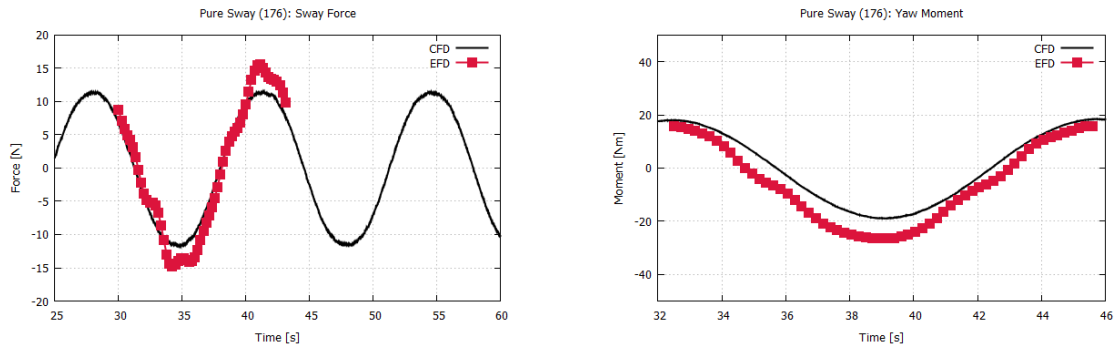


Figure 3: Pure sway forces: CFD vs. experiments

Figure 3 shows the comparison between CFD and experiments for the hydrodynamic forces as a function of time. It can be clearly noticed that the new uRANS LFS solver predicts correctly both the amplitude and the frequency of the time series compared to the experiments, with just a few asymmetries in the forces noticed in the experiments which cannot be reproduced in the CFD simulation.

3.3 Pure Yaw

The pure yaw forced motion was performed using a sway amplitude of $\xi_2 = 0.297\text{m}$, a yaw amplitude $\xi_6 = 4.7\text{deg}$ and a PMM period of 13.33s. The time series of the forces predicted with the uRANS LFS solver are compared to the experiments in Figure 4.

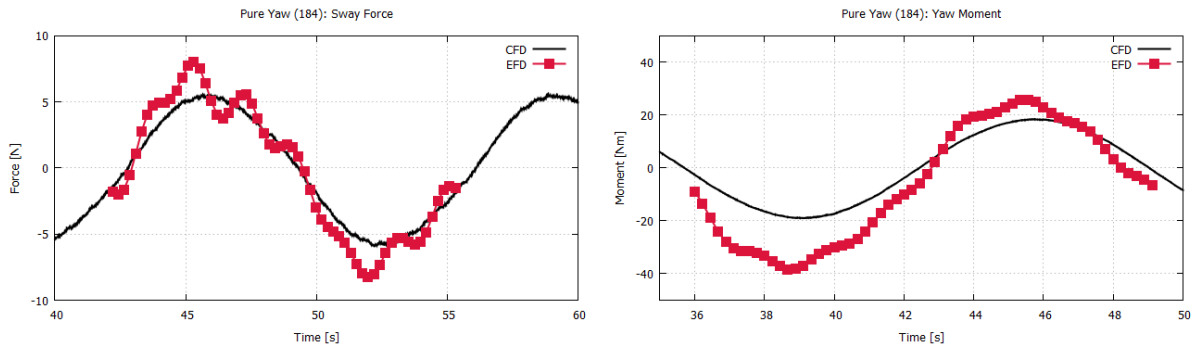


Figure 4: Pure yaw forces: CFD vs. experiments

In this case, high-frequency components in the experiments not visible in the CFD results for the sway force can be identified. The yaw moment instead, shows that the maximum value of the moment is correctly predicted, whereas the minimum is underpredicted and this again is due to an asymmetry in the experimental results. For the pure yaw case the total CPU time per PMM period was set to 34.8 CPU hours, which was quite in line with the turnaround times required for the pure sway case.

4 SELF-PROPULSION TESTS

The new uRANS LFS solver was also employed on a series of free-running tests, including

self-propulsion, turning circle and zig-zag maneuvers. In the work detailed here though, only the results of the self-propulsion tests are presented.

The test case considered for the self-propulsion simulation is the KCS hull form according to the Gothenburg 2010 Case 2.3a workshop specifications [8]. The aim of this test was to evaluate the accuracy of the uRANS LFS solver to predict maneuvering operations, which require the inclusion of the propulsion system modelling. Typically, this type of simulations entails considerable computational efforts when employing traditional fully non-linear uRANS methods, such as VOF based solvers. The KCS model test conditions are outlined in Table 2.

Table 2: KCS Geometry and conditions for the self-propulsion test

| | |
|---------------------|--------|
| Scale | 31.600 |
| L _{pp} [m] | 7.2785 |
| B _{wl} [m] | 1.019 |
| T [m] | 0.3418 |
| U [m/s] | 2.196 |
| Fn [-] | 0.26 |
| S/L ² | 0.1781 |

The self-propulsion test was carried out at the ship point in calm-water conditions to reproduce the test setup. A fixed rotational speed was applied to the propeller in order to determine the towing force measured during the experiments and defined as $(R_r - T)$, where R_r is the hull resistance force and T is the propeller thrust.

In order to assess the accuracy and the performance of the uRANS LFS solver, the results obtained with this solver were compared to results obtained using a VOF type solver. In both cases, the same rigid-body motion self-propulsion framework was employed, assuming an initial 10s time ramp to accelerate both the body motion and the propeller speed to match the nominal target conditions. Also in both cases, the $k-\omega$ SST turbulence model was applied and a transient sliding mesh approach was employed to model the propeller rotation using Arbitrary Mesh Interface (AMI). No rudder was considered in the models.

4.1 Model Setup

Two computational grids were created, one for the VOF case and another one for the uRANS LFS solver case. The background block mesh employed to create both grids used the same anisotropic refinements near the free-surface to ensure a correct prediction of the wave-making resistance, as well as high-aspect ratio cells in the far field to reduce the total cell count. Near-wall layers with an overall y^+ of 60 were defined on the hull body walls, and the same surface and volume refinement levels were applied to both grids to ensure a fair and consistent comparison between both methods.

The total cell count achieved using this approach was 3.44M for the VOF grid and 2.7M cells for uRANS LFS grid, with the latter mesh having less cells only because the air domain is ignored in favor of the first-order free-surface boundary condition applied at the free-surface. The resulting grids are both shown in Figure 5.

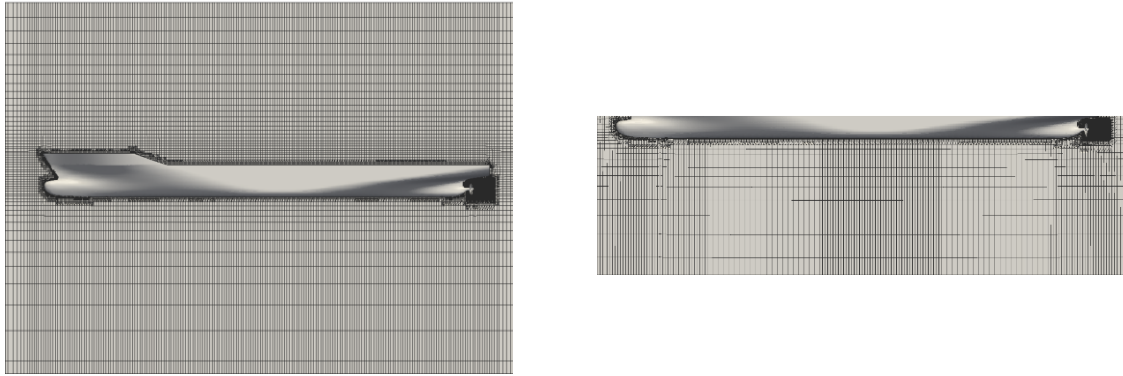


Figure 5: Computational grid for VOF (left) and uRANS LFS (right) solver cases

In terms of solver settings, the same discretization schemes were employed in both cases for time (first-order Euler) and advection (second-order). In the VOF model, 3 outer correctors without relaxation were employed, whereas only 2 outer correctors were required for the uRANS LFS solver. All the degrees of freedom were enforced in both solvers.

Furthermore, a maximum CFL of 10 was set for the initial phase of the VOF simulation to reach converged conditions. Similarly, in the uRANS LFS solver case, the initial phase was completed using a maximum CFL of 100. In both simulations, a finer time step was employed after completing the initial phase of the runs to model a 1deg-span of the propeller revolution to correctly predict the thrust and torque forces.

4.2 Self-propulsion Results

The free-surface elevation field and the vorticity near the propeller are shown in Figure 6 for the uRANS LFS solver. This solution was achieved in 295 CPU hours, as opposed to the 4,980 CPU hours it took to reach the same level of convergence using the VOF solver.

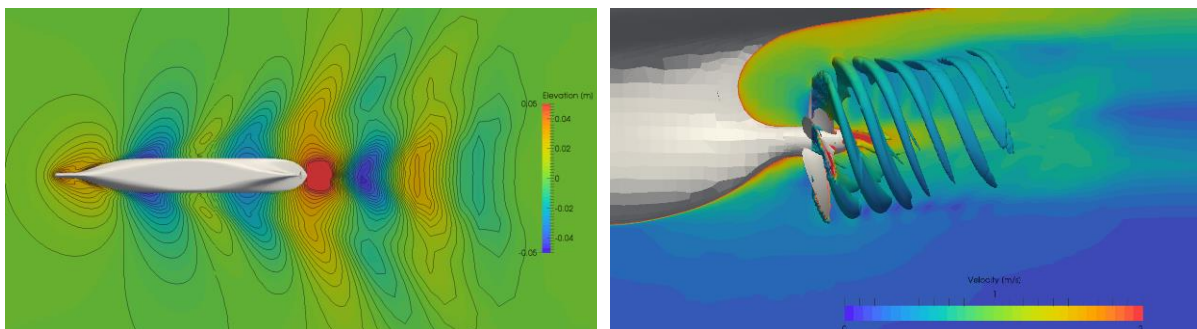


Figure 6: Free-surface elevation (left) and vorticity field (right) for the LFS case

Table 3 compares the experimental data (EFD) and simulation results for the forces obtained using the VOF and uRANS LFS solvers.

Table 3: Self-propulsion simulation results

| Solver Type | CFD | | | | EFD | | | |
|-------------|----------|--------------|-------|--------|-------|----------|-------|-------|
| | Ct | Rt(SP)-T [N] | Kt | Kq | Ct | Rt(SP)-T | Kt | Kq |
| VOF | 0.003891 | 28.7 | 0.170 | 0.0311 | -1.9% | -5.1% | -0.1% | 8.1% |
| LFS | 0.004005 | 33.4 | 0.164 | 0.0318 | 1.0% | 10.4% | -3.8% | 10.5% |

The results obtained with the uRANS LFS solver show a good agreement with the experiments for both the propeller and hull forces. It can be observed that the uRANS LFS solver tends to underpredict the propeller thrust and overpredict the torque forces with respect to the VOF solver and experimental measurements. This is expected due to the approximate nature of the LFS method against the fully non-linear uRANS equations used in the VOF solver.

Figure 7 shows the axial velocity contours downstream of propeller plane at $x/L_{pp}=0.9911$ from the experiments, VOF and uRANS LFS solver simulations. Although the CFD results presented are instantaneous values of the axial velocity, it can be seen that the wake behavior is consistent between the VOF and LFS cases, and that both simulations are in a good agreement with the averaged results available from the experiments.

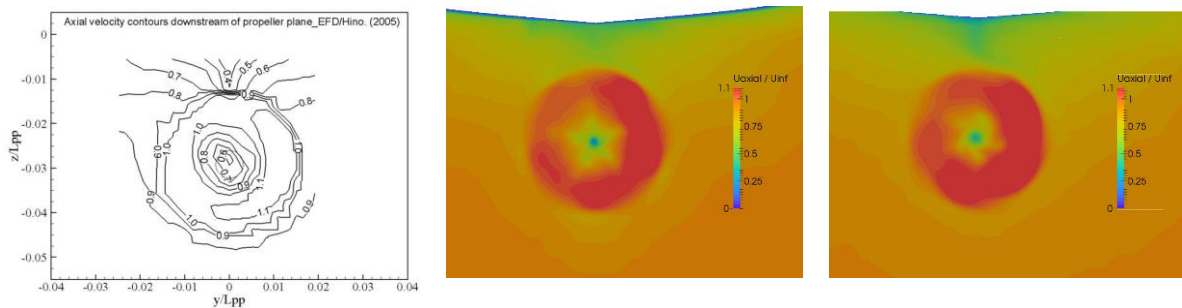


Figure 7: Axial velocity contours at $x/L_{pp}=0.9911$: EFD (left), VOF (center) and LFS (right)

Finally, Figure 8 shows the velocity components downstream of the propeller plane for both simulation cases. The results show good agreement between the VOF and uRANS LFS solvers in terms of axial and transverse velocities. However, the comparison with the experiments are clearly better for axial velocity than transverse velocities in both cases.

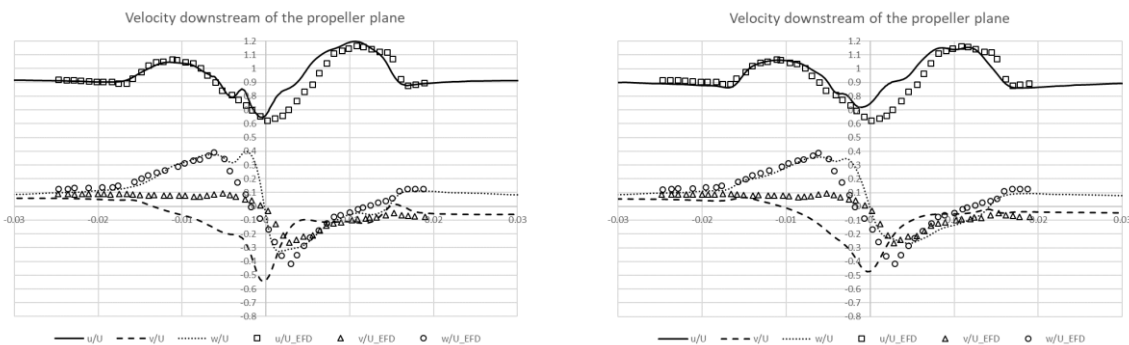


Figure 8: Velocity at $x/L_{pp}=0.9911$ and $z/L_{pp}=-0.03$: CFD vs. EFD for the VOF (left) and LFS (right) solvers

5 CONCLUSIONS

In this work, an innovative unsteady CFD solver based on the Linearized Free-Surface (LFS) approach has been presented as a novel approach to simulate ship hull maneuvering. The proposed LFS solver was validated against a series of well-known test-cases. The results achieved with the new solver for both captive and free-running tests showed that it provides a viable and more cost-effective alternative than traditional VOF methods without compromising in accuracy. The LFS solver can also run with CFL numbers 10 times higher than the equivalent VOF methods to deliver faster solutions for the correct prediction of ship behavior in the early stages of the design process. Further work is being carried out at present to validate the linearized free-surface solver framework for more complex free-running maneuvers, such as turning circle and zig-zag tests. Results of these additional test will be presented by the same authors in future works.

REFERENCES

- [1] W. Xu, G. Filip, and K.J. Maki "A Method for the Prediction of Extreme Ship Responses using Design-Event Theory and Computational Fluid Dynamics", *Journal of Ship Research*, under review.
- [2] A. Di Mascio, R. Broglia, and R. Muscari "On the Application of the Single-Phase Level-Set Method to Naval Hydrodynamic Flows", *Computers and Fluids*, **36**(2007), 868-886.
- [3] W. J. Rosemurgy, D. O. Edmund, K. J. Maki, and R. F. Beck "A Method for Resistance Prediction in the Design Environment", *11th International Conference on Fast Sea Transportation*, 2011.
- [4] Maki, K. and Piro, D. "Whipping response of a box barge in oblique seas". *28th International Workshop on Water Waves and Floating Bodies*, 2013.
- [5] W.J. Kim, S.H. Van, D.H. Kim. "Measurements of Flows around modern commercial ship models". In: *Experiments in Fluids*, **31**(2001), 567-578.
- [6] M. O. Woolliscroft, "A Linearized Free-Surface Method for Prediction of Unsteady Ship Maneuvering", *PhD Thesis*, University of Michigan, USA, 2015.
- [7] J.F. Otzen, C.D. Simonsen editors, *Proceedings SIMMAN 2014 Workshop*, Copenhagen, Denmark, 2014.
- [8] L. Larsson, F. Stern, M. Visonneau editors, *Gothenburg 2010 A Workshop on Numerical Ship Hydrodynamics - Proceedings, Volume II*, Gothenburg, Sweden, 2010.
- [9] Woolliscroft, M. O., and K. J. Maki. "A fast-running CFD formulation for unsteady ship maneuvering performance prediction." *Ocean Engineering* **117**(2016), 154-162.

NUMERICAL INVESTIGATION OF A LARGE DIAMETER PROPELLER EMERGENCE RISK FOR A VESSEL IN WAVES

MOHSEN IRANNEZHAD, ARASH ESLAMDOOST AND RICKARD E.
BENSOW

Division of Marine Technology
Department of Mechanics and Maritime Sciences
Chalmers University of Technology, Gothenburg, Sweden
e-mail: mohsen.irannezhad@chalmers.se

Key words: Large Diameter Propeller, Propeller Emergence, Reynolds-Averaged Navier-Stokes, Potential Flow, Ship Motions, Regular Head Waves.

Abstract. Although a Large Diameter Propeller (LDP) has a significant potential to improve a vessel propulsive efficiency, it may have a higher risk of propeller emergence and thus thrust reduction relative to a conventional propeller. The instantaneous propeller submergence can be considered as the main factor in the inception of the propeller emergence when the interaction between a running propeller and free-surface are disregarded. Therefore, accurate prediction of the ship motions and the hull wake in the vicinity of the propeller play a significant role in the propeller emergence risk assessment. In an earlier investigation, the authors of the current paper have carried out a comprehensive study on the seakeeping performance of the LDP vessel employing a Fully Non-linear Unsteady Potential Flow Panel Code in which a selected number of critical operating conditions with respect to the risk of propeller emergence have been identified. The objective of this paper is to further investigate the selected critical operating conditions by a higher fidelity approach which also takes the viscous effects into account. To this end, an Unsteady Reynolds-Averaged Navier-Stokes (URANS) solver is used for studying the seakeeping performance of the LDP vessel. The propeller is not modeled in the simulations. A good agreement is seen between the computed motions and resistance in regular head waves and the measurements data. Also, the results are compared to those from the potential flow simulations.

1 INTRODUCTION

Shipping is the most efficient and cost-effective mode of cargo transportation. Increasing environmental concerns and consequently growing demands for diminishing the shipping emissions and its environmental impacts drive marine industry towards further energy efficiency improvements. Numerical and experimental investigations carried out in STREAMLINE^[1] revealed a significant potential to improve a vessel propulsive efficiency by transforming its conventional-sized propeller to a Large Diameter Propeller (LDP). This concept is further developed in

LeanShips^[2] for a general cargo vessel incorporating an LDP in a conventional position but with much reduced propeller/hull clearance as well as a 'tunnel-shaped' aft design. One possible drawback of using such a large propeller is a greater risk of propeller ventilation/emergence which may affect the vessel propulsive efficiency. Propeller ventilation/emergence may cause a sudden change in propeller thrust and torque which may consequently lead to propeller racing, noise and vibrations.

Several experimental and numerical attempts have been carried out in order to investigate the propeller ventilation phenomenon and its adverse effects on propulsive efficiency, such as the investigations by Faltinsen et al.^[3], Califano et al.^[4] and Yvin et al.^[5], for propellers in open water conditions. In open water conditions, the interaction between ship and propeller is not taken into consideration, hence the dynamics of the propeller working behind the ship are not fully reproduced. A more realistic scenario of propeller ventilation happens when the propeller approaches free-surface and emerges out of water as a results of ship motions and the local water surface elevation behind the hull.

Generally, high propeller loading and limited submergence are the dominating factors in the initialization of the propeller ventilation, also mentioned by Yvin et al.^[5] and Kozłowska et al.^[6]. Ventilation of a highly-loaded and fully-submerged propeller mostly starts by formation of a tip vortex, which ingests air from the free-surface and transports it in the direction of the propeller rotation, Kozłowska et al.^[7]. However, considering the operating propeller behind a ship, the existence of the hull partly blocks the access of the propeller to free-surface. In case of the LDP vessel, the tunnel-shaped aft design configuration significantly reduces the air ingestion into the propeller which makes the propeller submergence a more crucial factor in the occurrence of propeller ventilation. The vertical ship motions (caused by heave, pitch and roll) significantly affect the instantaneous submergence of the propeller. Although the importance of the vessel motions in the occurrence of propeller ventilation/emergence has been emphasized in literature, for instance by Koushan^[8], the risk assessment for propeller emergence is not fully understood based on the actual position of the water surface due to ship motion responses in the wake behind a hull.

In an earlier investigation (unpublished), the authors of the current paper have carried out a comprehensive study on the seakeeping performance of the LDP vessel employing SHIPFLOW Motions (Fully Non-linear Unsteady Potential Flow Panel Code^[9]) in which a selected number of critical operating conditions with respect to the risk of propeller emergence have been identified. The objective of this paper is to further investigate the selected critical operating conditions by a higher fidelity approach which also takes the viscous effects into account. To this end, an Unsteady Reynolds-Averaged Navier-Stokes (URANS) solver, STAR-CCM+ 13.06.011, is used for studying the seakeeping performance of the LDP vessel. The current paper is mostly concerned with the methodology and the results of the CFD solver, while the results of the potential flow code are also provided for comparison. The propeller is not modeled in the simulations and its interaction with free-surface is assumed to be insignificant in comparison to the contribution from the propeller submergence governed by the ship motions and the hull wake. The relative distance between the free-surface and the conceptual propeller is then studied based on monitoring the ship motions and the pressure at the conceptual propeller tip clearance.

2 VESSEL GEOMETRY AND CONDITIONS

An overview of the LDP vessel geometry is shown in Figure 1 together with the ship-fixed coordinate system at the vessel Center Of Gravity (COG). A simple shaft connects the vessel bare hull to an appended asymmetric rudder. Although the LDP is not modeled in the simulations, its conceptual geometry is represented in Figure 1. A point probe at the position of the LDP blade tip near the propeller/hull clearance is specified in order to characterize the propeller emergence in the absence of propeller in the simulations. The LDP vessel main particulars in model-scale, its speed as well as the corresponding Froude number are listed in Table 1.



Figure 1: LDP vessel geometry, point probe and ship-fixed coordinate system at COG.

Table 1: The model-scale LDP vessel main particulars and conditions (scale factor = 27).

| Particular | \approx Value | Unit | Denotation |
|------------|-----------------|---------------|-------------------------------|
| L_{pp} | 7.95 | [m] | Length Between Perpendiculars |
| LOS | 8.11 | [m] | Length Overall Submerged |
| B | 0.88 | [m] | Breadth at mid-ship |
| T_A | 0.296 | [m] | Draft at Aft Perpendicular |
| T_F | 0.296 | [m] | Draft at Fore Perpendicular |
| Δ | 1740 | [kg] | Mass Displacement |
| V | 0.89 | $\frac{m}{s}$ | Model Speed |
| Fr | 0.10 | [-] | Froude Number |
| Re | 7.1E6 | [-] | Reynolds Number |

The model-scale LDP vessel appended with a rudder and a shaft, free to heave and pitch is used within the numerical investigations. On the other hand, the LDP vessel model-tests were conducted in free-running self-propulsion mode (later specified by SP EFD within results and plots) by Maritime Research Institute Netherlands (MARIN) where the time-series of the motion responses and thrust measurements were provided.

All simulations in SHIPFLOW and STAR-CCM+ are performed in model-scale in fresh water with the density of $\rho = 998.3 \frac{kg}{m^3}$. The simulations are performed employing the 5th order Stokes regular head waves ($\mu = 180^\circ$) in deep water. In all of the simulations the wave height of $H \approx 0.22$ m is considered. The simulations are performed for three different wave lengths, as listed in Table 2, each identified by their case numbers. Moreover, the wave encounter frequency (ω_e)

is computed based on Equation 1 in which ω is the wave frequency and g is the gravitational acceleration.

Table 2: Wave characteristics of the studied cases.

| Case no. | $\approx \lambda$ [m] | $\approx \frac{\lambda}{LOS}$ [-] | $\approx \text{Steepness} = \frac{H}{\lambda}$ [-] | $\approx \omega_e$ [$\frac{rad}{s}$] |
|----------|-----------------------|-----------------------------------|--|--|
| 1 | 5.57 | 0.68 | 0.039 | 4.33 |
| 2 | 7.27 | 0.89 | 0.030 | 3.68 |
| 3 | 9.90 | 1.22 | 0.022 | 3.06 |

$$\omega_e = \omega - \frac{\omega^2 \times V}{g} \cos(\mu). \quad (1)$$

Fast Fourier Transform (FFT) analysis is used in order to post-process the experimental and numerical data. The vessel periodic response signal r to regular waves in the time domain is approximated by a three component Fourier analysis, see Equation 2, where the 0^{th} component is the mean value and the 1^{st} , the 2^{nd} and the 3^{rd} components are three harmonic amplitudes. Moreover, $\varphi^{1^{st}}$, $\varphi^{2^{nd}}$ and $\varphi^{3^{rd}}$ are the phase components in the Fourier analysis of the response signal,

$$r(t) = r^{0^{th}} + r^{1^{st}} \cos(\omega_e t + \varphi^{1^{st}}) + r^{2^{nd}} \cos(2\omega_e t + \varphi^{2^{nd}}) + r^{3^{rd}} \cos(3\omega_e t + \varphi^{3^{rd}}). \quad (2)$$

The results of the Fourier analysis of the SP EFD time-series are very sensitive to the extracted window (the time period that is cut from the experimental data in the time domain) due to the complex seakeeping performance of the vessel, motion couplings in the free-running mode and vessel response during the emergence period. In the lack of a proper systematic procedure, the post-processed results of SP EFD in the following are based on bias FFT windows chosen by the authors.

An earth-fixed coordinate system at at the initial mean free-surface (positive Z upwards and positive X pointing the direction of the ship forward speed) is considered. The total resistance in SHIPFLOW is computed based on the summation of the wave making resistance (integration of the pressure over the instantaneous wetted surface area of the hull) and the viscous resistance (in which the frictional resistance coefficient is computed by Grigson^[10] formula, together with the experimentally derived form factor of $1 + k = 1.167$). The STAR-CCM+ computed total resistance is the mean drag force (the 0^{th} harmonic component in the Fourier analysis of the longitudinal force in the earth-fixed coordinate system) on the hull surface during the response of the hull to waves. The total resistance R_T in SP EFD is estimated based on the mean measured thrust \bar{T} (the 0^{th} harmonic amplitude of the measured thrust in the chosen FFT window) and the given calm water thrust deduction factor of $t_d = 0.159$ at Froude number 0.10, see Equation 3. It is assumed that the thrust deduction factor in waves is equal to that of calm water, t_d .

$$R_T = (1 - t_d) \times \bar{T}. \quad (3)$$

Different factors are affecting the occurrence of the LDP emergence, such as the harmonic amplitudes and phases of motions responses as well as the instantaneous position of the water surface in the vicinity of the propeller. However, based on the previous study in SHIPFLOW, three cases, given in Table 2, are chosen. Case 1 represents the conditions where the wave encounter frequency is close to the vessel natural heave and pitch frequencies ($\omega_{N_{heave}} \approx 4.25 \frac{rad}{s}$ and $\omega_{N_{pitch}} \approx 4.50 \frac{rad}{s}$), in order to study near resonance conditions. Case 2 represents the conditions in which the first harmonic phase difference between heave and pitch motions is close to $-\pi$ rad, hence large relative motions are expected. Case 3 represents the conditions in which the pitch excitation moment is near its maximum value, hence large amplitude pitch responses are expected.

3 NUMERICAL MODELING

The CFD simulations are performed using an URANS approach. A finite volume method together with a segregated approach for coupling velocity and pressure fields are used for solving the conservation equations for mass, momentum as well as turbulence quantities. A second order spacial discretization scheme is used.

In order to simulate the vessel motions, the Dynamic Fluid Body Interaction (DFBI) module is used. The DFBI Rotation and Translation model is used in order to enable the RANS solver to compute the vessel motions from the exciting fluid forces and moments as well as the gravity force. The Planar Motion Carriage mechanism is used within the DFBI Rotation and Translation model, in order to simulate the hull free to heave and pitch (2 degrees of freedom) while it is translating with a prescribed constant speed (ship forward speed V) in the longitudinal direction in the earth-fixed coordinate system. In order to achieve a robust simulation setup for wave propagation in STAR-CCM+, the best practice provided by Peric^[11] is complied. The aim is to minimize the wave propagation simulation issues, such as amplitude reduction and period change during propagation, disturbances (wiggles) on the free-surface and reflection at boundaries.

The Volume of Fluid (VOF) multiphase model is used as the free-surface capturing technique. The High-Resolution Interface Capturing (HRIC)^[12] scheme is used in VOF simulations to maintain a sharp interface between the incompressible fluid phases (water and air).

Mesh generation was performed using the automatic mesh generation tool in STAR-CCM+. The trimmed hexahedral meshes with local refinements near the free-surface as well as near the hull together with prism layers along the hull surface are used. Overset method consisting a moving overset region and a stationary background region with specific treatment of cell sizes near the overlapping region is used to discretize the computational domain. The dimensions of different regions of the computational domain are depicted in Figure 2. An overview of the background mesh is shown in Figure 3 in which the applied boundary conditions is also given. Due to the asymmetric geometry of the rudder, no symmetry plane is considered and both side boundaries are given as velocity inlets. The wave forcing capability is applied with the forcing coefficient of $\frac{20\omega}{2\pi}$ to all of the vertical boundaries in order to force the solution of the discretized Navier-Stokes equations towards the theoretical 5th order Stokes wave solution over a distance equal to Length Overall Submerged (LOS) from the boundaries.

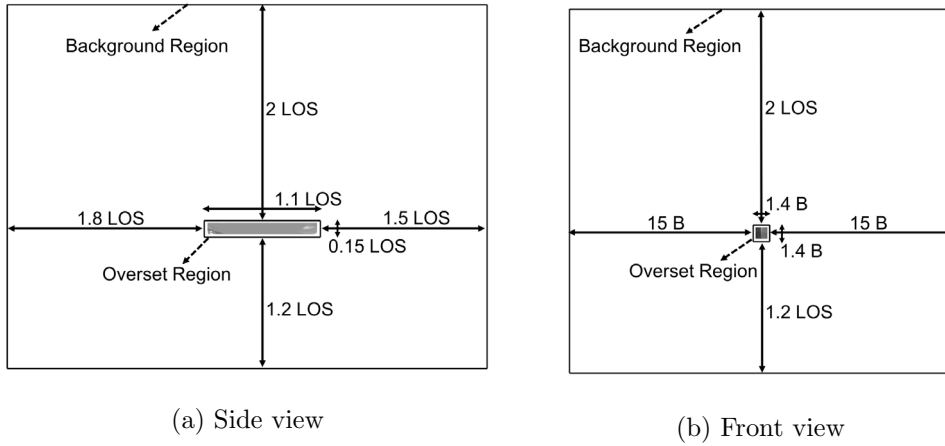


Figure 2: The dimensions of the computational domain, background region and overset region.

The prism layers are placed in such a way that the non-dimensional wall distance y^+ remains above 30 over the major part of the hull surface during the simulation, hence wall functions utilization. The mesh refinements at the overlapping region of the overset mesh and background mesh is done in such a way that the cell sizes in both regions remain approximately similar while the overset region is moving based on the heave and pitch motions of the hull, see Figure 4.

The mesh within the free-surface is refined in such a way that approximately 16 cells are used per wave height. The aspect ratio of the cell sizes in the direction of propagation (X) is assumed to be twice of the cell sizes in wave height direction (Z). Therefore, for Case 1, Case 2 and Case 3 the total number of cells per wave length are approximately 200, 260 and 350, respectively. The number of cells at each region are given in Table 3. In the phase interaction modeling, the interface artificial viscosity of 1.0 is introduced in order to reduce wiggles on the free-surface. The Interface Momentum Dissipation (IMD) model adds extra momentum dissipation in the proximity of the free-surface to dissipate parasitic currents.

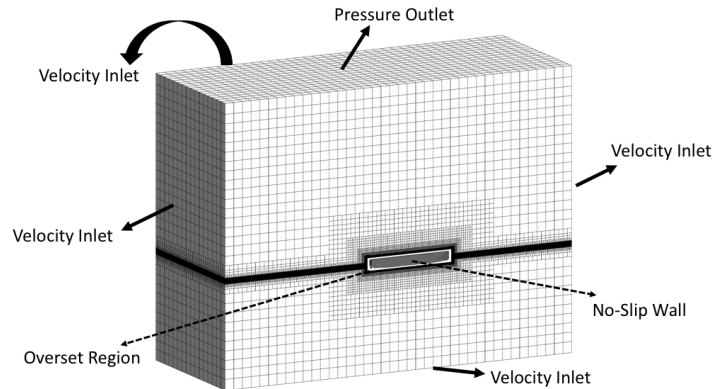


Figure 3: An overview of the background mesh and the applied boundary conditions.

Table 3: Number of cells in each region.

| Region | Background | Overset | Total |
|---------------------------|------------|---------|--------|
| \approx Number of Cells | 13.5 M | 4.1 M | 17.6 M |

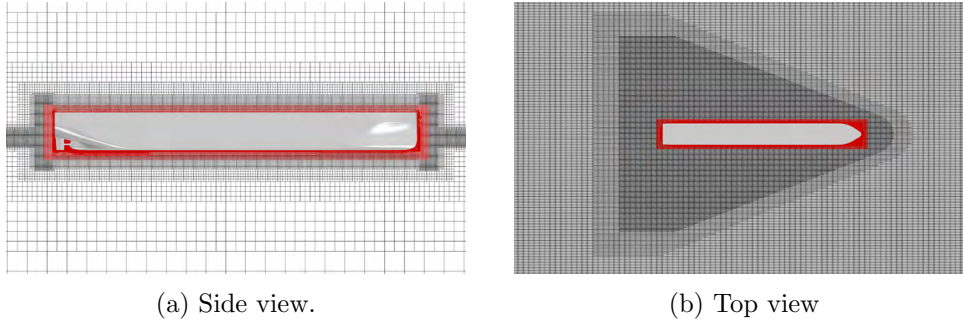


Figure 4: The mesh refinement in the vicinity of the overset and background overlapping region.

The Standard Low-Re $k - \varepsilon$ turbulence model with all y^+ wall treatment is used with the initial and boundary conditions of turbulent kinetic energy $k = 1.0E - 6 \frac{J}{kg}$ and turbulent dissipation rate $\varepsilon = 1.0E - 5 \frac{m^2}{s^3}$, in order to diminish the growth of turbulent viscosity in the free-surface zone. An implicit unsteady solver with a second order temporal discretizational scheme and the time-step of 0.003 s is used in order to keep the courant number less than 0.3 during the wave propagation. The chosen time-step also fulfills the ITTC^[13] recommended criteria of at least 100 time-steps per encountered wave period. Last but not least, ten maximum number of inner iterations for each unsteady time-step is considered.

4 RESULTS AND DISCUSSIONS

4.1 Wave propagation verification

It is necessary to ensure that the wave propagation issues are diminished with the current simulation setups in STAR-CCM+, hence the hull is subjected to a wave as similar as possible to the introduced Stokes wave at the boundaries. Therefore, a wave propagation simulation for the Case 1 (steepest wave) is performed for an empty domain in the absence of the hull without the implementation of the overset approach. The simulated wave profile at the middle of the domain ($Y = 0$ in the earth-fixed coordinate system) after 20 encountered wave periods of propagation is comparable to the theory, see Figure 5.

Moreover, the Fourier analysis of the monitored vertical position of the free-surface (wave elevation) during the last 10 encountered wave periods (FFT window) at a location within the empty domain representing the fore perpendicular of the vessel gives the 1st harmonic amplitude of 0.106 m and the 2nd harmonic amplitude of 0.0068 m. The 1st and the 2nd harmonic amplitudes are under-predicted by approximately 3% and 6% respectively, which was found to be acceptable for the current cell size and time-step and was sufficiently reasonable for the verification of wave propagation by the current CFD model.

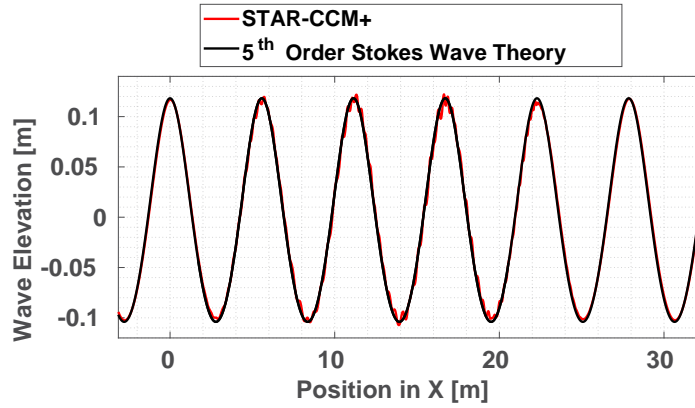


Figure 5: The 5th order Stokes wave cut after 20 propagated wave periods.

4.2 Resistance and motions validation

In this section, the LDP vessel resistance, heave and pitch motions results are shown and validated against the experimental data for the vessel in regular head waves. The 0th harmonic amplitudes of motions in different cases are approximately similar and relatively small. The 1st harmonic amplitudes of heave and pitch motions, shown in Figure 6, are the dominating components while higher order components are close to zero.

Both SHIPFLOW and STAR-CCM+ heave and pitch motion response predictions are comparable to the SP EFD data. However, more accurate ship motions predictions are derived from STAR-CCM+ simulations. One interesting point is the lower value of the heave 1st harmonic amplitudes at Case 2 in comparison to the shorter wave (Case 1) and the longer wave (Case 3). The large amplitude heave response in Case 1 might be due to the near heave resonance conditions. Furthermore, large pitch motion responses are seen for Case 3 with a wave length close to the wave length representing the maximum pitch excitation moments. The first harmonic phase difference between heave and pitch motions are quite similar from both SHIPFLOW and STAR-CCM+ computations for different cases. The phase difference is predicted to be roughly close to $\frac{\pi}{2}$ rad for Case 3 and $-\pi$ rad for Case 1 as well as Case 2. The total resistance responses, computed based on the methods explained in Section 2, are compared in Figure 6.

It is worth mentioning that the results of the SP EFD data are derived from the bias Fourier analysis window selection by the authors. This in return introduces a high level of uncertainty to the experimental data. The deviation errors of the 1st harmonic amplitudes of motions and the 0th harmonic amplitudes of resistance from the experimental data are presented on top of each bar in Figure 6. Although large deviations are computed with respect to the experimental data, the numerical methods exhibit a better agreement with each other. The overall discrepancies between the computed harmonic amplitudes of resistance, heave and pitch motions obtained from the potential flow and the viscous flow simulations are about 6.6 %, 6.6 % and 10.3 %, respectively. The trend of the results within the RANS solver for the studied cases is comparable to that of potential flow solver as well as experimental data. Therefore, a comparative propeller emergence risk assessment can be carried out between the studied cases.

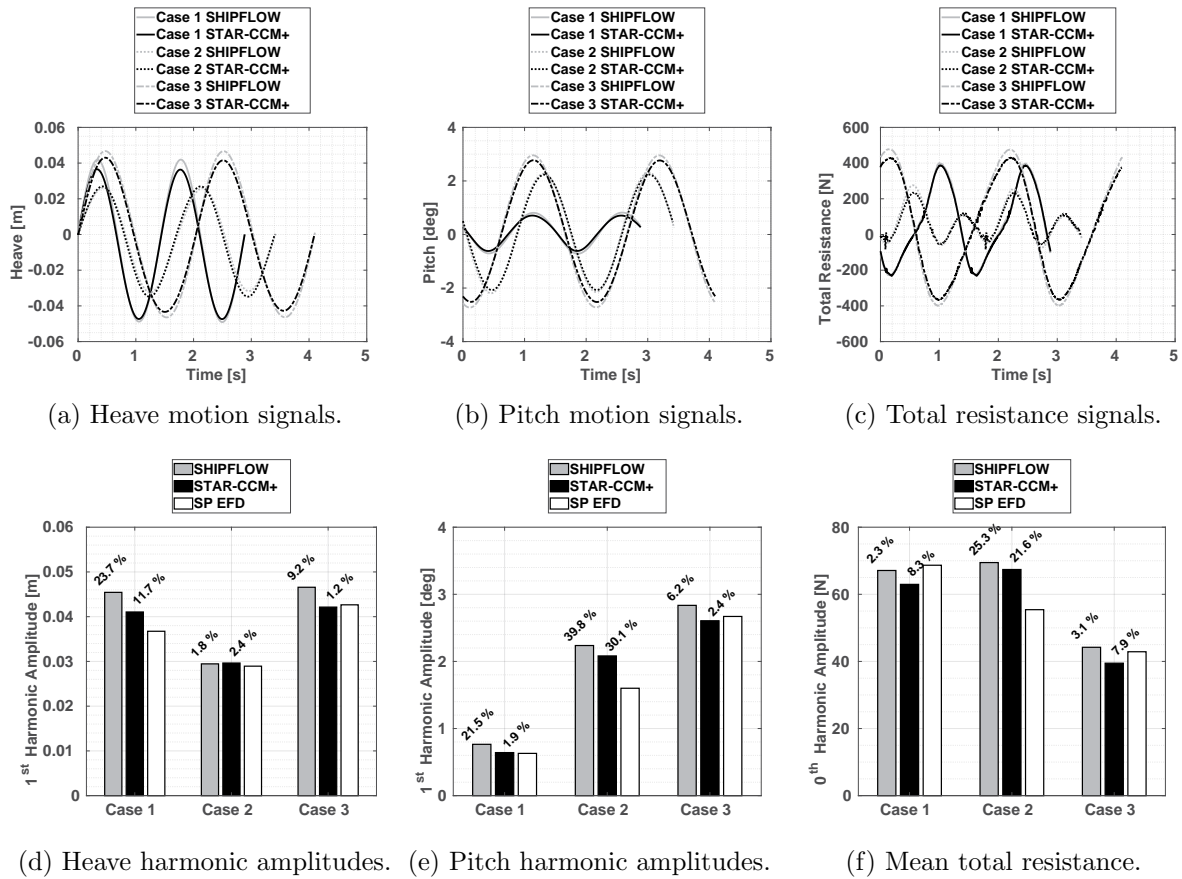


Figure 6: The LDP vessel responses comparison during two encountered wave periods.

4.3 LDP emergence risk assessment

In order to investigate the risk of propeller emergence for the LDP vessel, different assessment methods are examined for the point probe at the propeller/hull clearance. The vertical position of the probe in the earth-fixed coordinate system, the volume fraction of water as well as the static pressure are monitored during the response of the vessel, see Figure 7. The monitored vertical position of the probe during the response period indicates the occurrence of the largest vertical displacement of the probe for Case 3 as well as a relatively larger displacement for Case 2 in comparison to Case 1, see Figure 7a. The large vertical displacements for Case 3 and Case 2 might be originated from the large pitch motions and their corresponding vertical motions at the vessel stern. This might declare a relatively higher risk of propeller emergence for Case 3 and Case 2 in comparison to Case 1; however, due to the missing information about the actual position of the water surface in the vicinity of the propeller, a solid risk assessment can not be established.

The monitored probe volume fraction confirms the propeller emergence occurrence for Case 2 and Case 3 (sudden change in volume fraction), where the emergence for Case 3 is more intense; meaning that the probe is out of water for a longer period of time. However, through

monitoring probe volume fraction, the risk of propeller emergence can not be sorted to high and low levels for the cases where the propeller emergence is not occurring. For instance, the probe volume fraction for Case 1 remains 1 during the whole period of response but it is not possible to evaluate how close the probe comes to the water surface through the monitored volume fraction.

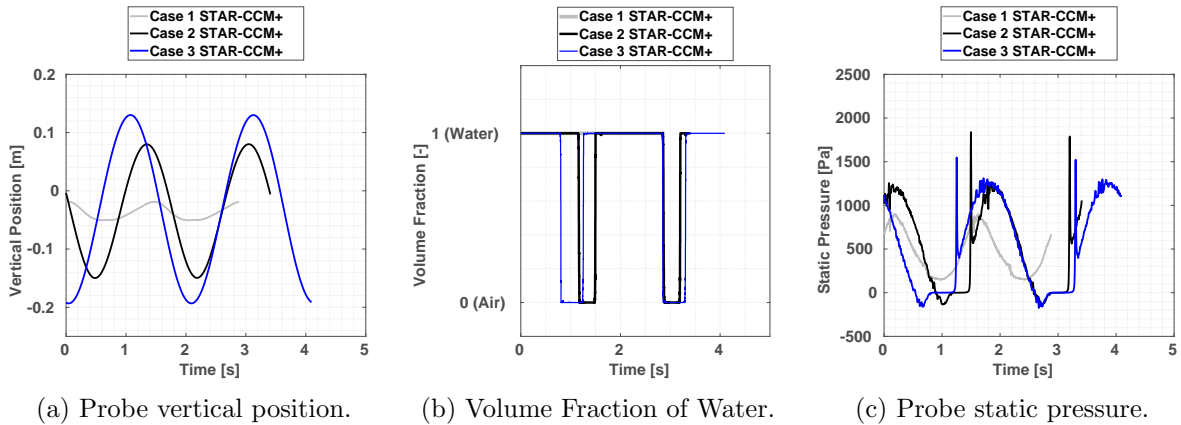


Figure 7: Propeller emergence assessment based on the monitored data during the response.

Therefore, another measure for the risk assessment is introduced by monitoring the static pressure of the probe during the response of the vessel. When the static pressure at the probe is approximately zero, the probe is emerged, see Case 2 and Case 3 in Figure 7c. Contrary to the monitored probe volume fraction, the emergence risk assessment can be performed for the conditions where the probe marches towards the free-surface but it does not emerge out of water. For instance, Case 1 does not emerge but based on the instantaneous submergence of the propeller interpreted from the monitored pressure, the propeller emergence is close to occur, hence more investigations of propeller ventilation/emergence risk assessment for Case 1 is encouraged for the hull with a running propeller. The negative static pressure values are originated from the fact that the reference of the hydrostatic pressure is set to be at the initial mean free-surface level. When the probe is positioned above this level, the hydrostatic pressure attains negative values which in turn may result in negative values of static pressure at this point. An unexpected behaviour of the static pressure, in form of a high amplitude spike, is seen at the monitored probe immediately after occurrence of a full emergence cycle, which is probably caused by stern slamming when the hull aft tunnel hits the waves. This is investigated by studying the hydrodynamic pressure at the probe as well as on the hull surface at the moment of slamming. The hull stern is just about to move downwards while an incoming wave crest reaches the aft part of the hull. At this point, The flow gets trapped between the rudder and the hull bottom in this region and consequently, the local pressure increases abruptly. The hydrodynamic pressure at the probe is approximately 2400 Pa for Case 2 which is comparable to the hydrodynamic pressure values on hull surface at that moment shown in Figure 8. Despite the large peak in the pressure, the ship motions are not affected and the motion acceleration curves are quite smooth. However, the consequences of such a large local pressure on the ship structure in the aft needs further investigation.

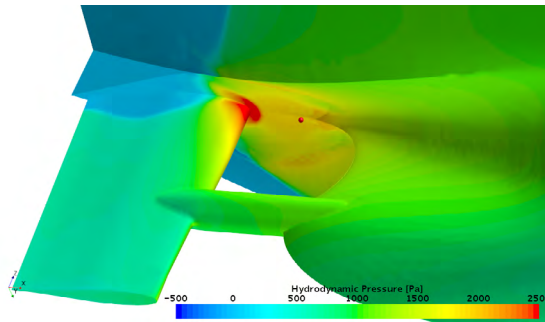


Figure 8: Hydrodynamic pressure on the hull surface at the slamming moment for Case 2.

5 CONCLUSIONS

The propeller emergence risk has been assessed for a vessel incorporating a conceptual Large Diameter Propeller in three critical operating conditions which are identified from a series of potential flow computations. An Unsteady Reynolds-Averaged Navier-Stokes solver has been employed for further investigation of the aforementioned cases. First, a simulation for the wave propagation of the steepest wave has been carried out in the absence of the hull in order to evaluate the computational set-up. The 1st and the 2nd harmonic amplitudes of the wave elevation during a period within the wave propagation simulation are under-predicted by 3 % and 6 %, respectively, which are considered acceptable for performing the seakeeping simulations. Despite the high uncertainty level of the experimental data and occasionally large deviation of the computed results from the measured motions and resistance, an approximately similar trend between different study cases in each methods is seen. The comparison between the numerical methods shows that the overall discrepancies between the potential flow and the viscous flow computations of the harmonic amplitudes of resistance, heave and pitch motions are approximately 6.6 %, 6.6 % and 10.3 %, respectively. The simulation time in terms of core-hours for the viscous flow solver is roughly between 20000 to 25000, while for the potential flow solver it is substantially lower, about 150 to 200 core-hours. A comparative propeller emergence risk assessment has been carried out for the studied cases based on monitoring the variation of static pressure at a probe placed in the vicinity of the propeller/hull clearance. The propeller emergence is more likely to occur for the intermediate wave length and the longer wave length whereas an intenser emergence is expected for the longer wave length due to a longer period of time in which the static pressure remains zero in each emergence cycle. An unexpected behaviour of the static pressure, in form of a high amplitude spikes, is seen at the monitored probe immediately after occurrence of a full emergence cycle. Sudden increase of hydrodynamic pressure due to stern slamming, which is also confirmed by monitoring hydrodynamic pressure on the hull surface during the simulation, is found to be the main cause of the high amplitude spikes of the static pressure.

ACKNOWLEDGEMENTS

This research is funded by LeanShips^[2] project through the European Unions Horizon 2020 research and innovation programme (Contract No.: 636146). The simulations were performed

on resources at Chalmers Centre for Computational Science and Engineering (C3SE) as well as National Supercomputer Center at Linköping University (NSC) provided by the Swedish National Infrastructure for Computing (SNIC). The Maritime Research Institute Netherlands (MARIN) is acknowledged for providing the experimental data.

REFERENCES

- [1] STREAMLINE (STrategic REsearch for innovAtive Marine propuLsioN concEpts), EU-funded project, (2010–2014).
- [2] LeanShips (Low Energy And Near to zero emissions Ships), EU-funded project, (2015–2019).
- [3] Faltinsen, O.M., Minsaas, K.J., Liapis N. and Skjördal S.O. Prediction of Resistance and Propulsion of a Ship in a Seaway. *Proceedings of 13th Symposium on Naval Hydrodynamics*. pp. 505–529. The Shipbuilding Research Association of Japan, Tokyo, Japan, (1981).
- [4] Califano, A. and Steen, S. Numerical Simulations of a Fully Submerged Propeller Subject to Ventilation. *Journal of Ocean Engineering*, Vol. **67**, pp. 1582–1599, (2011).
- [5] Yvin, C., Muller, P. and Koushan, K. Numerical Study of Propeller Ventilation. *Fifth International Symposium on Marine Propulsors*, Espoo, Finland, (2017).
- [6] Kozłowska, A.M. and Steen, S. Experimental Analysis on the Risk of Vortex Ventilation and the free surface Ventilation of Marine Propellers. *Journal of Applied Ocean Research*, Vol. **67**, pp. 201–212, (2017).
- [7] Kozłowska, A.M., Wöker, K., Steen, S., Rung, T., Koushan, K. and Spence, S.J.B. Numerical and Experimental Study of Propeller Ventilation. *Second International Symposium on Marine Propulsors*, Hamburg, Germany, (2011).
- [8] Koushan K. Dynamics of Propeller Blade and Duct Loading on Ventilated Thrusters in Dynamic Positioning Mode. *Dynamic Positioning Conference*, Houston, USA, (2007).
- [9] Kjellberg M. Fully Nonlinear Unsteady Three-dimensional Boundary Element Method for Ship Motions in Waves. *PhD Thesis*, Chalmers University of Technology, Gothenburg, Sweden, (2013).
- [10] Watson, D.G.M. *Practical Ship Design*. Elsevier, Vol 1, pp. 195–198 (1998).
- [11] Peric’ M. Best Practices for Simulations With Waves. *Presentation at STAR Global Conference*, Berlin, Germany, (2017).
- [12] Muzaferija, S and Peric’, M. Computation of free surface flows using interface-tracking and interface-capturing methods. *In Nonlinear water wave interaction*, pp. 59–100, Southampton: WIP Press, (1999).
- [13] International Towing Tank Conference (ITTC). Practical Guidelines for Ship CFD Applications. In: *Proceedings of the 26th ITTC*, (2011).

PREDICTION OF PARAMETRIC ROLLING FOR A CONTAINER SHIP IN REGULAR AND IRREGULAR WAVES USING A FULLY NONLINEAR TIME DOMAIN POTENTIAL FLOW METHOD

Francesco Coslovich*, Martin Kjellberg[†] and Carl-Erik Janson[‡]

* Chalmers University of Technology
Department of Mechanics and Maritime Sciences
Hörselgången 4, Gothenburg, Sweden
e-mail: francesco.coslovich@chalmers.se/

[†] SSPA Sweden AB
Chalmers Tvärgata 10, Gothenburg, Sweden
e-mail: martin.kjellberg@sspa.se/

[‡]Chalmers University of Technology
Department of Mechanics and Maritime Sciences
Hörselgången 4, Gothenburg, Sweden
e-mail: carl-erik.janson@chalmers.se/

Key words: Parametric Rolling, Potential Flow, BEM

Abstract. In this paper numerical simulations of parametric rolling have been performed. SAFEDOR, an EU funded benchmark study on the capability of different methods to predict such motion, was replicated here, in order to assess the quality of SHIPFLOW MOTIONS for the evaluation of this phenomenon. The code is a fully nonlinear 3D unsteady potential flow method. Since viscosity is not implicitly accounted for by a potential flow method, two different techniques are used here to introduce viscous damping coefficients in the roll motion equation. The results obtained with this method are aligned with the results from the best performing methods analyzed in the benchmark, showing a satisfactory match with experimental results.

1 Introduction

Although studies on parametric roll have been carried out since the middle of the last century, they have mainly been focusing on fishing vessels and small coastal cargo carriers in following seas. After an accident in the late nineties where a large container ship suffered significant cargo loss and structural damaged while sailing in head sea, see [1],

parametric rolling has increased the attention of researchers and international authorities. In fact, even relatively small amplitude waves can trigger this phenomenon which can lead to severe roll amplitudes.

Parametric roll is induced by a periodic change in the transverse stability. This change is due to large variations of the water plane area in head and following seas and can be significant for ships with bow flare and overhanging stern. In the last twenty years, especially concerning container ships and ferries, which can be characterized by these kinds of stern and bow features, parametric roll has become an important aspect considered thoroughly in the design phase. Numerical methods that allow for a correct prediction of parametric roll have become important tools.

In this paper, the 3-D fully nonlinear time domain potential flow method SHIPFLOW MOTIONS has been used as a basis for the study. The method has shown to give accurate predictions of ship motions in head sea, see for instance [2]. Its capability is extended and has been used here to simulate parametric roll in head and following waves. The method employs the fully nonlinear boundary conditions on the body and free surface, as well as fully coupled rigid body motions. The evolution in time is performed with fourth-order Adam-Bashforth-Moulton method. The forces acting on the ship are obtained by integrating the fluid pressure on the instantaneous wetted surface. Since roll motion is usually heavily influenced by viscosity and roll damping has a primary role in the phenomena of parametric rolling, damping coefficients are added in the roll motion equation. There are various techniques available to predict these coefficients, see for example [3]. For this paper, two formulations have been followed. One proposed by Watanabe and Inoue, presented in [3], has been used to estimate roll damping starting from geometrical and inertial characteristics and a parameter identification technique to obtain these coefficients from roll-decay model tests has been applied to a partial set of simulations, where model tests were available.

The numerical simulations presented here reproduce a benchmark study (SAFEDOR, see [4]) for a container ship, where solutions from different numerical methods were compared with model test results. Semi-captive tests were carried out in head and following seas, for monochromatic and three-component regular waves as well as for irregular waves. The benchmark study had two objectives: the first was to assess the capability of the different codes to simulate the resonance occurrence of parametric roll and the second was to evaluate the quality of the predictions in terms amplitude of the roll motion.

2 Mathematical Model and Numerical Approach

The method used in this study is based on potential flow theory. This means that the fluid is assumed to be homogeneous, inviscid, incompressible and irrotational. Under this hypothesis there exists a scalar quantity referred to as velocity potential ϕ , representing the velocity field of the fluid and which satisfies Laplace's equation:

$$\nabla^2\phi = 0 \tag{1}$$

On the free surface, the fully nonlinear kinematic and dynamic boundary conditions are applied:

$$\frac{D\mathbf{x}}{Dt} = \nabla\phi \quad (2)$$

where $\mathbf{x} = (x, y, z)$ is the position of a fluid particle on the free surface and

$$\frac{D\phi}{Dt} = -gz + \frac{1}{2}\nabla\phi \cdot \nabla\phi - \frac{p_a}{\rho} \quad (3)$$

where g is the gravitational acceleration, p_a is the atmospheric pressure and ρ is the fluid density. The material derivative is defined as

$$\frac{D}{Dt} \equiv \frac{\partial}{\partial t} + \nabla\phi \cdot \nabla \quad (4)$$

On the rigid body surface a Neumann type impermeability condition is given, taking into account body motion:

$$\frac{\partial\phi}{\partial n} = \mathbf{n} \cdot (\mathbf{u} + \boldsymbol{\omega} \times \mathbf{r}) \quad (5)$$

where \mathbf{u} and $\boldsymbol{\omega}$ are the translational and angular velocities, \mathbf{r} is the position of the point where the condition is applied with respect to the center of rotation and \mathbf{n} is the unit normal vector pointing into the fluid domain. A Neumann type impermeability condition is applied also on the bottom surface of the domain:

$$\frac{\partial\phi}{\partial n} = 0 \quad (6)$$

The boundary value problem, defined by Equation (1) and by the boundary conditions, Equations (2), (3), (5) and (6), is solved by means of a boundary element method, placing constant strength sources on quadrilateral panels both on the hull and free surface, see [5]. The evolution of the free surface is obtained through a *Mixed Euler-Lagrangian* (MEL) method, as described in [6]. The time stepping is performed with a fourth order Adam-Bashforth-Moulton method.

On the boundaries of the numerical domain a blending zone is introduced. The purpose of this zone is twofold: it dampens out the perturbed solution obtained in the inner part of the domain with respect to the undisturbed solution of the outer part, where the velocity potential is known *a priori*, while at the same time functions as a wave generator.

Once the solution of the boundary value problem is obtained at each time step, *i.e.* the velocity potential is evaluated on all the panels and the fluid velocity on the hull is known. Knowing the velocity potential and the fluid velocity, is possible to obtain compute the pressure using the unsteady Bernoulli equation. Integrating the pressure on the instantaneous wetted surface, forces and moments acting on the hull are known and

it is thus possible to solve ship motions equations. Considering the uncoupled equations for sake of simplicity, even though they are included in the method, we have:

$$m\ddot{\mathbf{x}} = \mathbf{F} = - \iint_{S_b} p\mathbf{n} dS \quad (7)$$

$$I\ddot{\boldsymbol{\gamma}} = \mathbf{M} = - \iint_{S_b} p(\mathbf{r} \times \mathbf{n}) dS \quad (8)$$

being $\ddot{\mathbf{x}}$ the acceleration of the center of gravity along the axis, $\ddot{\boldsymbol{\gamma}}$ the angular accelerations and \mathbf{n} the normals to each panel on the hull.

Since the method is based on the hypothesis of potential flow, viscosity is not included in the calculations. The error introduced by such approximation can usually be neglected for motions such as heave and pitch. On the other hand, roll motion is generally heavily influenced by viscous effects. The term that is more affected by viscosity in the roll motion equation is the damping term. It is therefore necessary to account for viscosity in some way. The most common way to account for such effects is through damping coefficients, $B(\dot{\varphi})$, that are included in the roll motion equation. If we consider the equation for *One Degree of Freedom* (1DOF), without the coupling terms with other motions, we have:

$$I_{xx}\ddot{\varphi} = - \iint_{S_b} p(\mathbf{r} \times \mathbf{n}) \cdot \mathbf{i} dS - B(\dot{\varphi}) \quad (9)$$

It is possible to find in literature many ways to express the damping model, see for instance [7]; the most common are:

$$B(\dot{\varphi}) = B_l\dot{\varphi} + B_q|\dot{\varphi}|\dot{\varphi} + B_c\dot{\varphi}^3 \quad (10)$$

$$B(\dot{\varphi}) = B_l\dot{\varphi} + B_q|\dot{\varphi}|\dot{\varphi} \quad (11)$$

$$B(\dot{\varphi}) = B_l\dot{\varphi} + B_c\dot{\varphi}^3 \quad (12)$$

and the choice of one model instead of another can be justified by different considerations on the physics and mathematical details. In order to perform the simulations, it is necessary to evaluate such coefficients, once that a model is chosen. In the present paper, two methodologies, each one based on different models from the above, are used to evaluate damping coefficients. The first one follows a different form of Equation (11), where only the quadratic term is considered. It is based on regression analysis and was proposed by Watanabe and Inoue (W-I), see [3]. This method uses geometrical and inertial characteristics of a ship to estimate the quadratic term B_q :

$$B_q = h\left[1.42\frac{C_{BT}}{L} + 0.01\right]f(Fn, \Lambda) \quad (13)$$

where h is a function that depends on the forms and mass distribution of the ship, Fn is the Froude number and Λ is the tuning ratio, between the encounter frequency of the

incoming waves and the natural roll frequency. The other method used here, a *Parameter Identification Technique* (PIT), to obtain damping coefficients analyzes model test results, using either time series of roll decay or frequency domain curve of beam sea. Given some input values φ , the equation of motion, written as a sum of components, is numerically solved. Damping and restoring coefficients in this equation are systematically varied to minimize the square error:

$$\chi^2(\mathbf{p}) = \sum_{i=1}^{N_{data}} (\varphi(i) - \hat{\varphi}(i, \mathbf{p}))^2 \quad (14)$$

In this way it is possible to find the best set of parameters \mathbf{p} that gives the best fit between the input values φ and the numerically evaluated values $\hat{\varphi}(\mathbf{p})$. It is possible to choose the damping model from Equations (10), (11) or (12) which best suits the specific need. Here, a linear plus cubic model was chosen, as the one of Equation (12). For a deeper insight of this method, see [8]. Since the PIT evaluates the damping coefficients starting from model test results, and thus these values are tailored for each ship, we can expect a better evaluation of such terms, compared with the more generic one proposed by Watanabe and Inoue.

3 Numerical Simulations

Numerical simulations have been performed here to replicate the EU funded project SAFEDOR, an international benchmark study aimed to assess the performance of different numerical codes for the prediction of parametric roll. The ship tested is a container ship and model experiments were carried out in two different model basins. In order to have a better control over the parameters that characterize and affect parametric roll, semi-captive tests were performed. This makes it easier to benchmark numerical simulations against experimental tests since uncertainties and bias are reduced. The whole set of tested cases is given in Table 1, where H and T are wave height and period. Ship properties are given in Table 2. Note that cases 1 and 12 are roll decay tests and irregular waves are obtained with a JONSWAP spectrum with an overshoot parameter $\gamma = 3.3$.

In order to properly replicate the benchmark study, the same input information was used. The only inputs given were the test matrix of Table 1 and the roll decay time series. In the same way as almost half the participants did during the study, the time series of roll decay were used to tune the roll inertial properties. Unfortunately, for this paper only the time series of roll decay from the first half of tests were available, *i.e.* only the case with $GM = 1.38 m$. Since the roll radius of inertia in the benchmark report is the same between the two sets of simulations, the error expected from this lack of information is negligible. On the other hand, the PIT uses model test results to obtain the damping coefficients: the coefficients are tuned on the roll decay curve and then used to simulate the parametric roll cases. This means that damping coefficients have been evaluated with the Watanabe-Inoue formulation for both sets, while with the PIT for the first set only.

Table 1: Experimental tests

| Test | GM | Heading | Fn | H ₁ | T ₁ | H ₂ | T ₂ | H ₃ | T ₃ | Description |
|------|------|---------|------|----------------|----------------|----------------|----------------|----------------|----------------|-------------|
| 01 | 1.38 | - | 0.00 | - | - | - | - | - | - | Roll Decay |
| 02 | 1.38 | 180° | 0.08 | 3.6 | 10.63 | - | - | - | - | 1 Harmonic |
| 03 | 1.38 | 180° | 0.08 | 5.7 | 10.63 | - | - | - | - | 1 Harmonic |
| 04 | 1.38 | 180° | 0.12 | 3.6 | 10.63 | - | - | - | - | 1 Harmonic |
| 05 | 1.38 | 180° | 0.12 | 5.7 | 10.63 | - | - | - | - | 1 Harmonic |
| 06 | 1.38 | 180° | 0.12 | 2.4 | 10.63 | 2.4 | 9.66 | 2.4 | 11.55 | 3 Harmonics |
| 07 | 1.38 | 180° | 0.12 | 4.0 | 10.63 | 1.0 | 9.66 | 1.0 | 11.55 | 3 Harmonics |
| 08 | 1.38 | 180° | 0.12 | 5.0 | 10.63 | - | - | - | - | Irregular |
| 09 | 1.38 | 160° | 0.12 | 3.6 | 10.63 | - | - | - | - | 1 Harmonic |
| 10 | 1.38 | 160° | 0.12 | 5.7 | 10.63 | - | - | - | - | 1 Harmonic |
| 11 | 1.38 | 160° | 0.12 | 4.0 | 10.63 | 1.0 | 9.66 | 1.0 | 11.55 | 3 Harmonics |
| 12 | 1.00 | - | 0.00 | - | - | - | - | - | - | Roll Decay |
| 13 | 1.00 | 0° | 0.08 | 3.6 | 8.00 | - | - | - | - | 1 Harmonic |
| 14 | 1.00 | 0° | 0.08 | 6.0 | 8.00 | - | - | - | - | 1 Harmonic |
| 15 | 1.00 | 0° | 0.04 | 3.6 | 8.00 | - | - | - | - | 1 Harmonic |
| 16 | 1.00 | 0° | 0.04 | 6.0 | 8.00 | - | - | - | - | 1 Harmonic |
| 17 | 1.00 | 0° | 0.04 | 2.4 | 8.00 | 2.4 | 7.11 | 2.4 | 8.89 | 3 Harmonics |
| 18 | 1.00 | 0° | 0.08 | 2.4 | 8.00 | 2.4 | 7.11 | 2.4 | 8.89 | 3 Harmonics |
| 19 | 1.00 | 0° | 0.08 | 5.0 | 8.00 | - | - | - | - | Irregular |
| 20 | 1.00 | 180° | 0.08 | 5.0 | 12.12 | - | - | - | - | 1 Harmonic |
| 21 | 1.00 | 180° | 0.12 | 5.0 | 12.12 | - | - | - | - | 1 Harmonic |
| 22 | 1.00 | 180° | 0.08 | 4.0 | 12.12 | 1.0 | 10.77 | 1.0 | 13.47 | 3 Harmonics |

Table 2: Ship Particulars

| | |
|--------------------|---------|
| L_{pp} | 150.0 m |
| B | 27.2 m |
| T | 8.5 m |
| C_b | 0.667 |
| C_p | 0.678 |
| GM tests 1 ÷ 11 | 1.38 m |
| GM tests 12 ÷ 22 | 1.00 m |
| k_{xx} | 9.96 m |

Given the wide range covered by the test matrix, different type of responses were expected, as shown in [4]. Since the aim of the study presented here was to compare the current method with the methods evaluated in the benchmark, the same way to analyze the results was followed. In the case of a reached steady state, the mean value of roll amplitude for the stationary response had been taken. This is typically the case for one harmonic waves. When the simulations were performed for group waves, a sort of stationary responses were obtained but without steady state. Finally, for the irregular waves, the responses were chaotic. In the two latter cases, the amplitudes of the whole simulation record were averaged, excluding the transient part where the motion was not fully developed. Comparing the values of roll amplitude obtained in this way with model test results, it is possible to compare the quality of the predicted amplitude. To have some terms of comparison, the standard deviation σ and the correlation coefficient r were used in the benchmark study. Being x_i the mean amplitude of the i -th case, \bar{x}_i the corresponding amplitude of the model test and $\hat{x}_i = x_i - \bar{x}_i$, standard deviation and correlation coefficient are evaluated with:

$$\sigma = \sqrt{\frac{\sum_{i=1}^n (\hat{x}_i - \hat{x}_m)^2}{n-1}} \quad (15)$$

$$r = \frac{cov(x, \bar{x})}{\sigma_x \sigma_{\bar{x}}} \quad (16)$$

where \hat{x}_m is the difference between the mean value of the amplitudes of numerical results and model tests. Standard deviation and correlation coefficient were evaluated for each method, allowing to rank them and to find the best performing ones. The main aim of the study, however, was to verify whether or not the different methods were able to predict the occurrence of parametric rolling, regardless of the value of the amplitude simulated. In order to evaluate the successful detection of parametric rolling, a critical roll amplitude was introduced in the study. An event is marked as successful when numerical and model test results coincide with respect of the critical roll amplitude. Choosing a critical roll amplitude equal to $x_{cr} = 0.5^\circ, 1.0^\circ, 1.5^\circ, 2.0^\circ$, a success rate was evaluated for each method and for each critical value:

$$P = \frac{1}{n} \sum_{i=1}^n q_i \quad (17)$$

where:

$$q_i = \begin{cases} 1 & \text{if } (x_i - x_{cr})(\bar{x}_i - x_{cr}) \geq 0 \\ 0 & \text{if } (x_i - x_{cr})(\bar{x}_i - x_{cr}) < 0 \end{cases} \quad (18)$$

Once the success rate was evaluated for each critical value, the mean was taken to define the best performing methods. For a deeper insight on the ranking of the methods and on data processing, see [4].

4 Numerical Results

In this section numerical results are presented. Before running the tests for the evaluation of parametric rolling, roll decay tests were simulated. Time series of roll decay can be seen in Figure 1. Both approaches to obtain damping coefficients were used and compared. As can be noticed, since the PIT uses the model test results to get the damping coefficients, the simulations performed with such coefficients are more accurate. Nevertheless, there is a good agreement between model test and numerical simulations with both methods. Since model test for roll decay were also used to tune inertia properties of the ship, there is an almost perfect match between simulated and tested roll frequencies.

In Figures 2 and 3 the mean roll amplitudes, evaluated as described in the previous section, are shown. As said, for the set of tests with $\overline{GM} = 1.0m$ the computations were done using only the damping coefficients obtained with the Watanabe and Inoue formulation, since the roll decay test was not available and thus it was not possible to get the coefficients using the parameter identification technique. Since it is not easy to see a trend from these figures, standard deviation and correlation coefficient are used to assess the quality of the predicted amplitudes. In Table 3 it is possible to compare the correlation coefficient r and standard deviation σ obtained using the current method. These values are evaluated for each set of tests using both the techniques to get the damping coefficients and they can be compared with the values from the benchmark: both the mean values for the overall benchmark study and for the four best performing methods are shown. It is important to stress that the values obtained for the simulations where the PIT was used to evaluate the damping coefficients are referred only to first set of simulations. As can be seen, the method used here is aligned with the best performing methods in the benchmark study.

In Table 4 the success rate P is presented and compared with the overall and with the results of the best performing methods in order to assess the efficiency of the method when it comes to the prediction of the occurrence of parametric rolling. Values are shown for each critical roll amplitude and the mean of these values, P_m , is presented as well. In the table are also shown the values of P for the overall benchmark and for the four best performing methods, expressed only through the mean value since data for each point were not available. Again, the values obtained from the numerical simulations using the PIT to get the damping coefficients are referred only to the first set of tests. Results obtained with the current method are at the same level of the best performing methods from the benchmark.

5 Discussion

The current fully nonlinear potential flow method is used to replicate a benchmark study on parametric roll. In the benchmark study, the best performing methods both in terms of occurrence and amplitude prediction are identified. Numerical simulations presented here show a general good agreement with model test results. In terms of the

Table 3: Correlation coefficient and standard deviation.

| | σ | r |
|-------------------|----------|------|
| PIT tests 2 ÷ 11 | 4.64° | 0.74 |
| W-I tests 2 ÷ 11 | 4.71° | 0.74 |
| W-I tests 13 ÷ 22 | 6.63° | 0.67 |
| W-I tests 2 ÷ 22 | 6.13° | 0.62 |
| Overall | 10.5° | 0.37 |
| Best Performing | 6.4° | 0.64 |

Table 4: Success rate as a function of the critical rolling angle.

| | $P _{x_{cr}=0.5^\circ}$ | $P _{x_{cr}=1.0^\circ}$ | $P _{x_{cr}=1.5^\circ}$ | $P _{x_{cr}=2.0^\circ}$ | P_m |
|-------------------|-------------------------|-------------------------|-------------------------|-------------------------|-------|
| PIT tests 2 ÷ 11 | 1.0 | 1.0 | 0.7 | 0.7 | 0.85 |
| W-I tests 2 ÷ 11 | 1.0 | 1.0 | 0.7 | 0.7 | 0.85 |
| W-I tests 13 ÷ 22 | 0.7 | 0.8 | 0.8 | 0.8 | 0.78 |
| W-I tests 2 ÷ 22 | 0.85 | 0.9 | 0.75 | 0.75 | 0.81 |
| Overall | <i>na</i> | <i>na</i> | <i>na</i> | <i>na</i> | 0.62 |
| Best Performing | <i>na</i> | <i>na</i> | <i>na</i> | <i>na</i> | 0.78 |

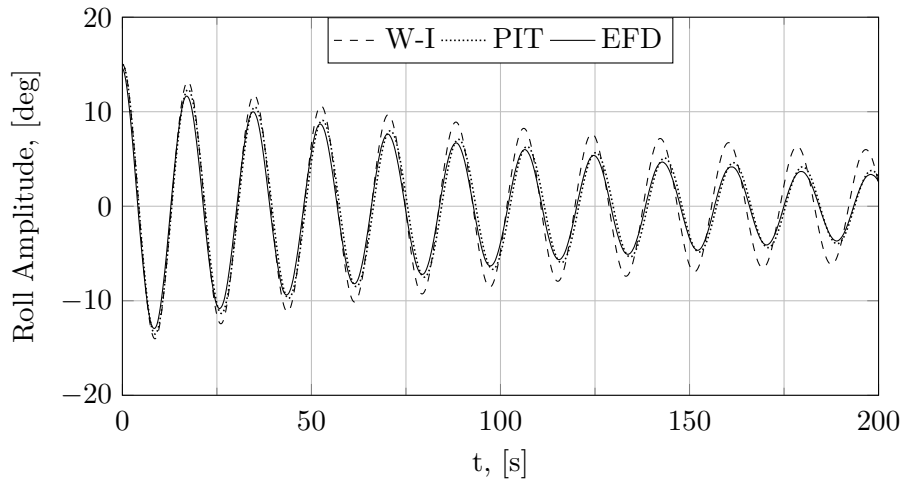


Figure 1: Roll decay for the case with $\overline{GM} = 1.38 m$.

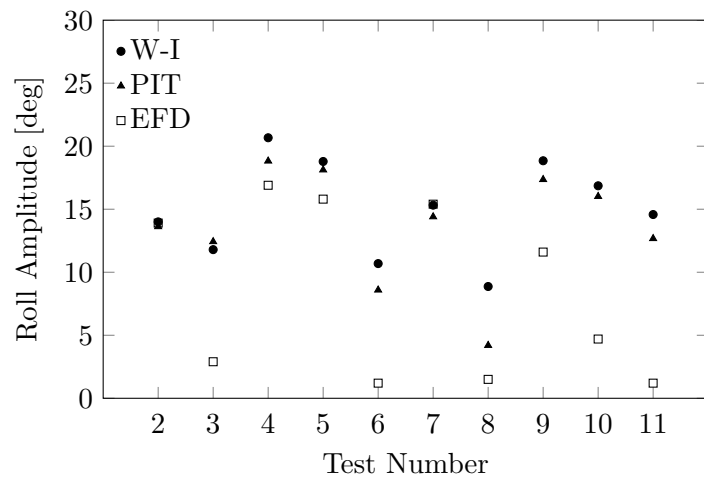


Figure 2: Mean roll amplitudes for set of tests with $\overline{GM} = 1.38 m$.

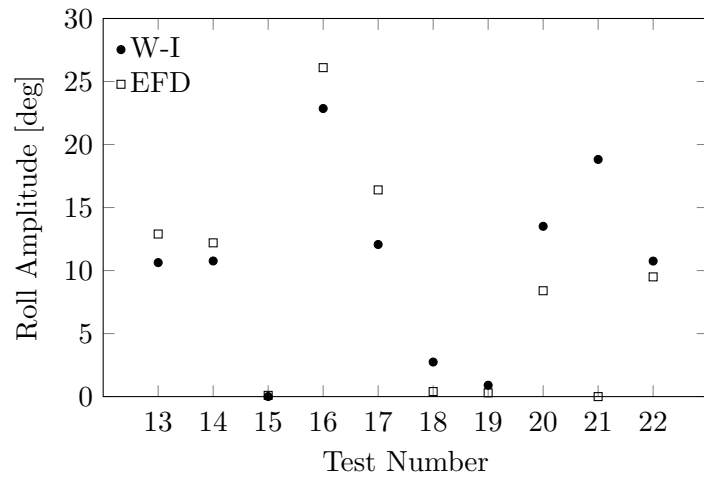


Figure 3: Mean roll amplitudes for set of tests with $\overline{GM} = 1.0 m$.

ability of the method to replicate the resonance occurrence of parametric roll, results are aligned with the mean value of the best performing methods. The success rate represents the accuracy in the predictability of the phenomenon and the results presented show that we can expect a correct detection of parametric roll eight times out of ten. Furthermore, the difference between the two sets of simulations is rather small, suggesting that the accuracy of the prediction does not depend on loading condition and waves. Not only, results are similar in terms of predictability also between simulations performed with different damping coefficients. Regarding the quality of the amplitude of the simulated conditions, measured with standard deviation and correlation coefficient, results show a satisfactory match with model tests, being aligned again with the best performing methods. The difference between the values obtained using different methods for the evaluation of damping coefficients is small as well. The discrepancy between σ and r for the tests $2 \div 11$ and $13 \div 22$ is due to the big difference in amplitude in the test number 21, where no roll motion was experienced in the basin and the simulated condition has an amplitude around $\phi \cong 19^\circ$. However, the ratio between encounter and natural roll frequencies is $\omega_e/\omega_\phi = 2.13$. One of the conditions that triggers parametric rolling is that such ratio has to be in the following range: $\omega_e/\omega_\phi \cong 2/n$ with n integer. It can be said then that this case lays on the edge of possible parametric rolling. From a design point of view though, the current method is on the safe side since it would show a possible danger situation when conditions are on the borderline.

To sum up, the current method employed in this paper has proved to be a reliable tool for the prediction of parametric roll and to be aligned with the best performing methods in the benchmark. It is worth mentioning that even with simple methods such as the one proposed by the Watanabe and Inoue for the evaluation of damping coefficients, good results are reached. Furthermore, for a correct prediction of this phenomenon, restoring force characteristics must be evaluated properly. Since forces are evaluated on the instantaneous wetted surface in the method used here with a fully nonlinear approach, a good prediction can generally be expected.

REFERENCES

- [1] France, W. N. and al. An investigation of head-sea parametric rolling and its influence on container lashing systems. *Marine Technology*, Vol. **40**, No. 1, pp. 1–19, (2003).
- [2] Kjellberg, M. Fully nonlinear potential unsteady three-dimensional boundary element method for ship motions in waves. *Chalmers University of Technology, Ph.D. Thesis*, (2013).
- [3] Himeno, Y. Prediction of ship roll damping - State of the art. *University of Michigan, Report*, (1981).

- [4] Papanikolaou, A. and Spanos, D. SAFEDOR International benchmark study on numerical simulation methods for the prediction of parametric rolling of ships in waves. *NTUA-SDL Report*, (2009).
- [5] Hess J. and Smith A. Calculation of potential flow about arbitrary bodies. *Progress in Aerospace Science*, (1967).
- [6] Longuet-Higgins M. S. and Cokelet E. D. The deformation of steep surface waves on water. I. A numerical method of computation. *Proceedings of the Royal Society A: Mathematical, Physical and Engineering Sciences*, (1976).
- [7] Bass, D.W. and Haddara, M.R. Nonlinear models of ship roll damping. *International Shipbuilding Progress* 35, (1988).
- [8] Francescutto A. and Contento G. Bifurcation in ship rolling: experimental results and parameter identification technique. *Ocean Engineering* 26, (1999).

TO EVALUATE THE INFLUENCE OF DOF ON MANOEUVRING PREDICTIONS BY DIRECT CFD ZIG-ZAG SIMULATIONS

XIN GAO^{*} AND GANBO DENG[†]

^{*} Dynamics of Maritime Systems (DMS)
Technical University of Berlin
SG 17, Salzufer 17-19, 10587 Berlin, Germany
e-mail: x.gao@campus.tu-berlin.de, www.dms.tu-berlin.de

[†] Laboratoire de recherche en Hydrodynamique, Énergétique et Environnement Atmosphérique (LHEEA)
Ecole Centrale de Nantes
1 Rue de la Noë, B.P. 92101, 44321 Nantes Cedex 3, France
email: ganbo.deng@ec-nantes.fr, lhea.ec-nantes.fr

Key words: DOF, Manoeuvring Predictions, Zig-Zag, CFD, Direct Manoeuvring Simulations

Abstract: *In this paper, direct CFD zig-zag simulations of 10°/10° and 20°/20° are performed in deep water condition under the consideration of different degrees of freedom, namely 3 DOF, 4 DOF, and 6 DOF, to evaluate their influence on manoeuvring predictions. A modern container ship KCS with a slightly simplified semi-balanced rudder is chosen as the benchmark model. All simulations are conducted in the numerical environment FINETM/Marine with the ISIS-CFD code as the flow solver. It solves incompressible unsteady RANS equations in full hexahedral unstructured meshes and implicitly couples the flow field with motion equations of a rigid body in 6 DOF. Current direct manoeuvring simulations are achieved by means of the overlapping grid technique. To reduce the computational effort, propeller effect is modelled by a simple prescribed body force model. Trajectories are straightforward recorded without any further treatment to extract hydrodynamic derivatives. The prediction accuracy is evaluated by comparing derived parameters, i.e. overshoot angles and times, peak yaw rates, drift angles, etc. against experimental data. In conclusion, 4 DOF and 6 DOF concept present similar results for current ship type. The tiny changes in pitch and heave motion indicate they can be neglectable to simplify the complex mesh strategy. In addition, the large roll angle over zig-zag manoeuvres implies that 4 DOF concept should be more reasonable for container ships to obtain roll-motion-related data. Meanwhile, 3 DOF concept underestimates all overshoot angles in each simulation. This also highlights the reasonability of 4 DOF concept.*

1 INTRODUCTION

Recently, major liner companies are speeding up to place orders of Mega Container Ships (MCS) with the capacity over 20,000 TEUs so as to provide a more competitive freight rate. For instance, CMA CGM has ordered a group of nine container carriers with each capacity of 22,000 TEUs^[16]. However, this type of vessel is usually characterised by 400 metres long and 60 metres wide, which in turn can challenge ship manoeuvrability, especially in the heavy

traffic areas. Conventional CFD manoeuvring predictions are subjected to 3 DOF or 4 DOF considering the complexity of mesh strategy during ship motion and the possibility of introducing numerical error. Whether full 6 DOF can contribute to increasing the prediction accuracy for container ships is still rarely studied. This paper is proposed to evaluate this influence to obtain the accurate results at the lowest expense in the future.

With the development of computer performance and the advance in numerical technique, CFD approach is widely adopted in marine hydrodynamics. For cases like resistance and propulsion, high-fidelity simulations have been achieved without any problems. And, above all, more local flow information can be captured for anytime and anywhere in simulations, which is not available or costly in physical experiments. Considering these advantages, CFD approach is employed in the framework of this paper. As in real experiments, two possible kinds of manoeuvring tests are achievable in use of numerical environment, namely virtual captive model tests (VCMT) and virtual free-running model tests (VFRMT). According to the conclusions of successive SIMMAN workshops (2008 and 2014), VCMT has been a suitable alternative to model experiments to perform manoeuvring predictions^[10]. Presentative work includes^[3, 5, 9, 13, 14]. However, large numbers of simulations and post-processing to extract hydrodynamic derivatives are still inevitable. Combing these derivatives with mathematical models, trajectories can only be predicted. In contrast, the trajectories can be directly recorded to calculate the derived kinematic parameters in VFRMT, as used in the current study. In general, appropriate treatment of propeller and movable rudder are two key points to perform VFRMT. In case of simulating real propeller, time consumption still cannot be affordable for industrial applications, since temporal discretisation must be small enough to solve the propeller rotation. In contrast, propeller effect can be modelled by a body force model to reduce computation effort. On the other hand, the movement of rudder can be realised by different mesh strategies depending on rudder configurations. For highly complex semi-balanced rudder, overlapping grid technique is the only solution for now. Worldwide, several research groups have carried out this type of simulation. Jensen, Klemt, & Xing-Kaeding achieved the turning circle tests using commercial code COMET^[7]. The deflection of a simple spade rudder was realised by the sliding mesh technique and the propeller effect is modelled by a body force model. Direct manoeuvring simulations of turning circle tests show reasonable results for yaw rate, tactical diameter, and heel angle. Carrica, Ismail, Hyman, Bhushan, & Stern presented direct free-running manoeuvres for a surface combatant at both model and full scale using in-house code CFD Ship-Iowa V4 packaged with overset grid capability^[2]. Dynamic rudder deflection is coupled with ship 6 DOF motion. The results demonstrated the feasibility of VFRMT using overset grid technique, although inaccurate body force model caused some discrepancies. Furthermore, Dubbioso, Durante, & Broglia simulated zig-zag manoeuvres of a tanker-like vessel by means of a global second order accurate finite volume solver Xnavis implemented with overlapping grids on block-structured meshes^[4]. Numerical results of zig-zag manoeuvres taking into account different propeller models were compared with the data of free-running model tests. The effect of rudder rate was also investigated. It is concluded that the improvement of a simplified propeller model would be necessary. In another study, by implementing dynamic overset grids into the open source code OpenFOAM, Shen, Wan, & Carrica achieved direct simulations of standard zigzag 10°/10° and modified 15°/1° manoeuvres using the HSVA KCS model^[12]. This implementation relied on the library Suggar++ to compute the domain connectivity information (DCI) dynamically at run time. Although numerical results agreed

well with experimental results, each simulation was still subject to months of computation time.

2 NUMERICAL FRAMEWORK

Numerical simulations are performed in the FINETM/Marine environment, which includes all necessary CFD tools to solve maritime dedicated applications. Non-conformal body-fitted full hexahedral unstructured meshes can be generated by the mesh generation tool HEXPRESSTM on any complex arbitrary geometries. Its flow solver is built on the widespread ISIS-CFD code developed by METHRIC group of ECN. The code solves incompressible unsteady Reynolds-averaged Navier Stokes equations and is also in couple with the motion equations of rigid body. The spatial discretization of transport equations is based on the finite volume method. The velocity field is calculated from the momentum conservation equations, while the pressure field is obtained from the pressure equation (Poisson equation). To solve turbulent flow, several sophisticated turbulence models such as one-equation model (Spalart-Allmaras), two-equation model (Wilcox or Menter), and etc. are available to choose. The turbulence variables can be solved in a form similar to that of the momentum equations. This solution concept also applies to the calculation of each volume fraction of fluid in case of simulating multiphase flow. A detailed numerical implementation of ISIS-CFD code can be found in ^[11].

3 TEST DISCRIPTION

3.1 Ship model

The ship model selected for the current study is a modern container ship with the name of Korean Container Ship (KCS). Figure 1 shows a 3D overview of this model. It is one of three benchmark ship types used in the SIMMAN 2008 and 2014 workshop. Free-running model tests are newly repeated for SIMMAN 2014 in MARIN. These experimental data with the model scale of 37.89 are used to validate current numerical simulations ^[8]. In Table 1, necessary main characteristics of ship, rudder, and propeller are listed in model scale as reference ^[1]. Since the real geometry of ship model in the experiment is not known before current simulations, the head box is retained as the ship model used in SIMMAN 2008 for free-running model tests. The ship is configured with a complicated semi-balanced rudder. Its turning rate is 14.3 deg/s. Since the propeller effect is modelled by an actuator disk, only several geometric parameters are needed. To reproduce original physical experiments, direct manoeuvring simulations are restarted from previous self-propulsion computations at a constant advancing speed of 2.005 m/s.

3.2 Computational mesh

As we know, a high-quality mesh is the basis of accurate numerical simulations. For the current study, there are mainly two challenges. The first one is how to solve the large amplitude roll motion during zig-zag manoeuvres, since almost 17 degrees of roll angle were observed in physical tests. Considering possible numerical errors, the mesh should have the ability to handle the roll angle of at least 20 degrees. According to the state of the art, three mesh strategies are available to deal with this large amplitude roll motion, namely mesh

morphing, sliding mesh and overset grid. However, mesh morphing can lead to a number of negative-volume meshes at around the moment of maximal roll angle, while sliding mesh can capture at most 5 DOF motions without pitch. In view of the possibility to expand to all 6 DOF motions, the overset grid strategy is a suitable selection to further study. Usually, three domains are necessary to implement this strategy, namely background domain, ship domain, and rudder domain. The dimensions of each domain in current study are illustrated in Figure 2, whereby L_{PP} and L_R are the ship length between perpendiculars and the maximal chord line of rudder profile. Ship domain has 4.6 million cells, while background domain and rudder domain have 0.9 million cells and 1.8 million cells, respectively. Totally, 7.4 million cells are used for medium mesh. A comprehensive convergence study including grid size and time step can be found in [6].



Figure 1: 3D overview of KCS model

Table 1: Main characteristics of ship and its appendages

| Ship | Model Scale | Ship | Model Scale |
|------------------------------|--------------------|--------------------------------|--------------------|
| L_{PP} [m] | 6.0702 | I_{XX}/B [-] | 0.4000 |
| B_{WL} [m] | 0.8498 | I_{ZZ}/L_{PP} [-] | 0.2500 |
| T [m] | 0.2850 | Rudder | |
| S_{Ship} [m ²] | 6.6381 | S_{Rudder} [m ²] | 0.0801 |
| LCG [m] | 2.9450 | Propeller | |
| KG [m] | 0.3785 | $D_{Propeller}$ [m] | 0.2080 |
| GM_T [m] | 0.0160 | $D_{Hub}/D_{Propeller}$ [-] | 0.1860 |

The second challenge is how to guarantee enough overlapping meshes across the 2mm gap between the moveable rudder blade and the fixed rudder horn. Based on the experience, at least 8 cells in three coordinate directions from each overlapping domain should be generated

to fill this gap to avoid orphan cells. In addition, to ensure a smooth transformation of fluid information, mesh sizes across overset interfaces from different domains should be kept consistent. To reduce the total number of cells and keep the effective rudder force unchanged. The original gap is enlarged twice the size by reducing the area of the rudder horn, while the rudder blade remains unchanged. In Figure 3, a mesh configuration near the rudder using medium mesh is demonstrated. A prescribed refinement box within the range of rudder execution is proposed to guarantee a successful overset interpolation, however, with many more cells. An alternative to achieve accurate overset interpolation is by adaptive grid refinement (AGR), which can automatically refine the mesh during the computation and meanwhile smooth out the transition in cell sizes across overset interfaces between domains. Some applications can be found in [15].

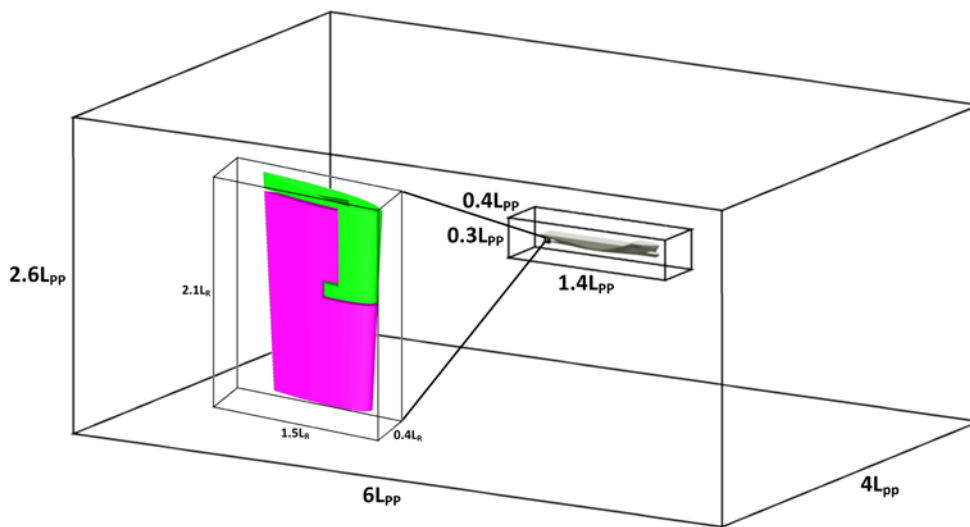


Figure 2: Dimensions of three-domains configuration

3.3 Computational settings

The final zig-zag simulation is set as an unsteady simulation. Robust turbulence model $k-\omega$ SST is used to close RANS equations. Free surface is solved by means of VOF method with a high-resolution scheme BRICS. It cannot only guarantee a sharp interface between two fluids but also can avoid the limit of courant number. The boundary conditions are illustrated in Figure 4. For inlet, outlet and side patches, far field condition is used. A Dirichlet or a Neuman condition can be alternately applied depending on the local flow direction. Prescribed pressure condition (Dirichlet condition) is adopted for top and bottom patches, on which the pressure value can be updated according to the free surface position. On the ship hull and the rudder surface, wall function is used to solve the flow near the solid patches without extremely fine mesh. Furthermore, slip wall condition is set on deck because we are not interested in it. The external patches of ship domain and rudder domain are defined as overset boundary condition, on which the flow solver allows the information exchange across different domains.

Direct manoeuvring simulation is restarted from a previous converged self-propulsion test at a constant advancing speed. For 3 DOF and 4 DOF concept, pitch and heave motion in the self-propulsion test are blocked, while they are free to be solved for 6 DOF concept. In the 3 DOF manoeuvring simulation, only planar DOFs (namely surge, sway, and yaw motions) are free. The additional free motion in the 4 DOF simulation is the roll motion, while all motions are free in the 6 DOF simulation. The rudder motion is controlled by a compiled FORTRAN library, which can be edited according different steering pre-settings. During the unsteady manoeuvring motion, background domain has only planar motion, in contrast, body fitted overset grid is extended to perform roll, pitch, and heave motion. The propeller effect is

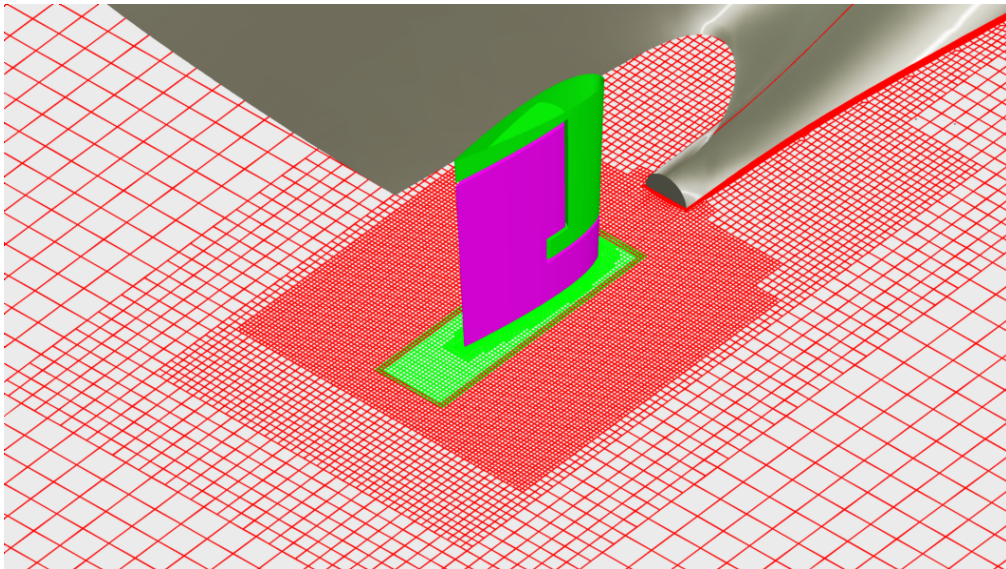


Figure 3: Medium mesh configuration near the rudder

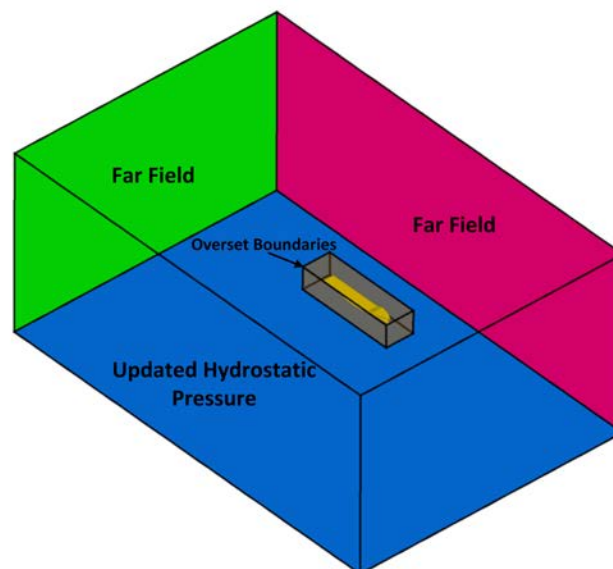


Figure 4: Boundary conditions in the framework of current study

modelled by an actuator disk. It updates the thrust in accordance with a given KCS open water curve measured in Korea Research Institute of Ships and Ocean Engineering (KRISO) for current study. To ensure a precise propeller force, the update procedure is called at each time step. The convection term of the transport equation to solve volume fraction is discretized by BRICS scheme, while AVLSMART scheme is employed for the discretization of convection terms of other transport equations. 10 non-linear iterations are given to proceed the outer loop of iterative algorithm. A pre-conditioned biconjugate gradient stabilized method named PCGSTAB_MB is adopted to solve equation systems. According to the convergence study of time step, 0.02 second is a trade-off value between accuracy and efficiency^[6]. Trajectories are recorded in inertial system, whose origin corresponds to the middle point of L_{PP} at the initial time. The details of discretisation scheme and solution algorithm are also explained in^[11]

4 RESULTS AND DISCUSSIONS

Direct manoeuvring simulations are performed on three nodes in the cluster of the department of dynamic systems at the technical university of Berlin. Totally, 64 processors are used for each simulation. With the help of the efficient actuator disk, a 4 DOF zig-zag simulation in deep water condition with 7.4 million cells took only 3 days. Taking into of a previous self-propulsion simulation, 4 days are still acceptable. For 3 DOF and 4 DOF concepts, the model self-propulsion point (MSPP) is equal to 11.3 rps, which is only 2.1% lower than the experimental value of 11.50 rps provided by MARIN. For 6 DOF concept, this value stays almost the same as the revolution rate in the experiment. In Figure 5 and Figure 6, numerical results for cases of zig-zag $10^\circ/10^\circ$ and $20^\circ/20^\circ$ to starboard using different DOF concepts are compared with the experimental data published in SIMMAN 2014. To ensure the credibility of numerical simulations, validation and verification procedures are conducted for 3 DOF and 4 DOF concept under the consideration of grid size and time step. Space constraints permit only the comparison of kinematic parameters in different DOFs to be discussed. Interested readers can refer to^[6].

Since the International Maritime Organization (IMO) has only specified the criteria to evaluate ship yaw-checking ability up to the second overshoot angle, all current simulations are shut down shortly after the second peak heading to save computational time. The kinematic parameters to be discussed in Figure 5 and 6 include heading Ψ , rudder angle δ , drift angle β , roll angle ϕ , resultant velocity V , pitch angle θ , vertical displacement ζ , and dimensionless yaw rate r' and roll rate p' . As can be seen in Figure 5, the results of 4 DOF concept are almost in accordance with that of 6 DOF concept, e.g. yaw angle, yaw rate, drift angle, etc. Additionally, the results for each concept agree very well with experiment data before the second rudder execution. And except for roll-motion-related parameters, 3 DOF concept can also have a good agreement with experimental values as illustrated from Figure 5.1 to Figure 5.4. Especially, the difference of the first overshoot angle between the numerical result and the experimental value is only 2 degrees, while these values are 3.3 degrees and 3.2 degrees for 4 DOF and 6 DOF concept. The value of the difference of the second overshoot angle for 3 DOF concept remains the same with 4 DOF (or 6 DOF) concept, however, in opposite signs. Despite of this good agreement, 3 DOF concept cannot provide roll-motion related information, which can be important for mega container ships. Figure 5.5 and 5.6 provide these interesting data regarding roll angle and roll rate for 4 DOF and 6 DOF concept

and experimental data. The numerical results show the similar trends to change as the data of the experiment. The first peak roll angle is well predicted, while the second numerical roll angle is 2 degrees and 1 degree larger than experimental value for 4 DOF and 6 DOF concept. The roll rate also agrees well with experimental data for 4 DOF and 6 DOF concept. However, after the third rudder execution there is a phase shift. Because of the limited experimental data, no pitch and heave relevant data are available for now. Therefore, only numerical results are exhibited here. In fact, the pitch and heave motion in Figure 5.7 and 5.8 have a tiny change over manoeuvring motions. The pitch amplitude is only 0.2 degree and the heave amplitude is merely 0.007m. This means they can be neglected for current situation. Concerning the resultant velocity in Figure 5.4, the value rises at the beginning of the zig-zag motion in the experiment (see thick red line), which is impossible with the setup used in the CFD. This phenomenon may due to the procedure employed in the experiment. In current simulation, the computation before the zig-zag motion is a captive motion with zero rudder angle and yaw angle, while in the experiment, a counter ruder must be given because of the asymmetric inflow to the rudder. Hence, there may be some experiment uncertainties with respect to the first overshoot angle.

Figure 6 depicts the results of zig-zag 20°/20° simulations and corresponding experimental data. It is similar to zig-zag 10°/10° simulations, all variables for 6 DOF concept have the same changing trends as for 4 DOF concept. The agreements of kinematic variables between the 3 DOF concept and the experiment shown from Figure 6.1 to Figure 6.4 are still quite good. Nevertheless, the disadvantage of 3 DOF concept to predict roll motion highlights the necessity to increase the number of DOF. Furthermore, in zig-zag 20°/20° simulations 3 DOF concept underestimates both overshoot angles with 6.5 degrees and 5.5 degrees. While 4 DOF and 6 DOF have the same discrepancy of the first overshoot angle for 2.1 degrees, the discrepancy of the second overshoot angle for 6 DOF concept is only 1.2 degrees, which is better than 4 DOF concept for 4.7 degrees. In Figure 6.4, 3 DOF and 6 DOF concept can give identically accurate speed loss, but 4 DOF concept shows a large discrepancy of the lowest speed loss for about 0.1 m/s compared with the experimental value. In terms of roll angle and roll rate, 6 DOF concept presents a better prediction than 4 DOF concept. The peak roll angles for 6 DOF concept keep the same value with the experimental values despite of time shift for the second peak value. 6 DOF concept is also apparently better than 4 DOF concept for roll rate, especially after the third rudder execution 4 DOF concept underestimates the dimensionless roll rate for 0.1. Besides, the time shift still exists. The pitch and heave motion in this case are still quite tiny. The amplitude of pitch and heave motion is 0.36 degree and 0.012 m, respectively, which also means these two degrees of freedom can be neglectable for current simulation condition.

As can be seen from Figure 5.5 and 6.5, the object ship suffers from a significant roll motion during manoeuvres. Comparing Figure 5.5 with 5.1 or Figure 6.5 with 6.1, it is clear that the time of peak roll angle does not correspond with the time of peak yaw angle, but with the rudder execution. The maximal roll angle happens when or shortly after the rudder reaches the counter target angle. As an example, Figure 7 illustrates the contours of midship plotted by axial vorticity ω_x at the moment of two peak roll angles for zig-zag 10°/10° in 4 DOF. When the ship is subjected to the peak roll angle inwards, the flow around outward bilge has an obvious separation. This vortex structure caused by the roll motion can change the distribution of hydrodynamic forces, which can then influence the ship manoeuvrability.

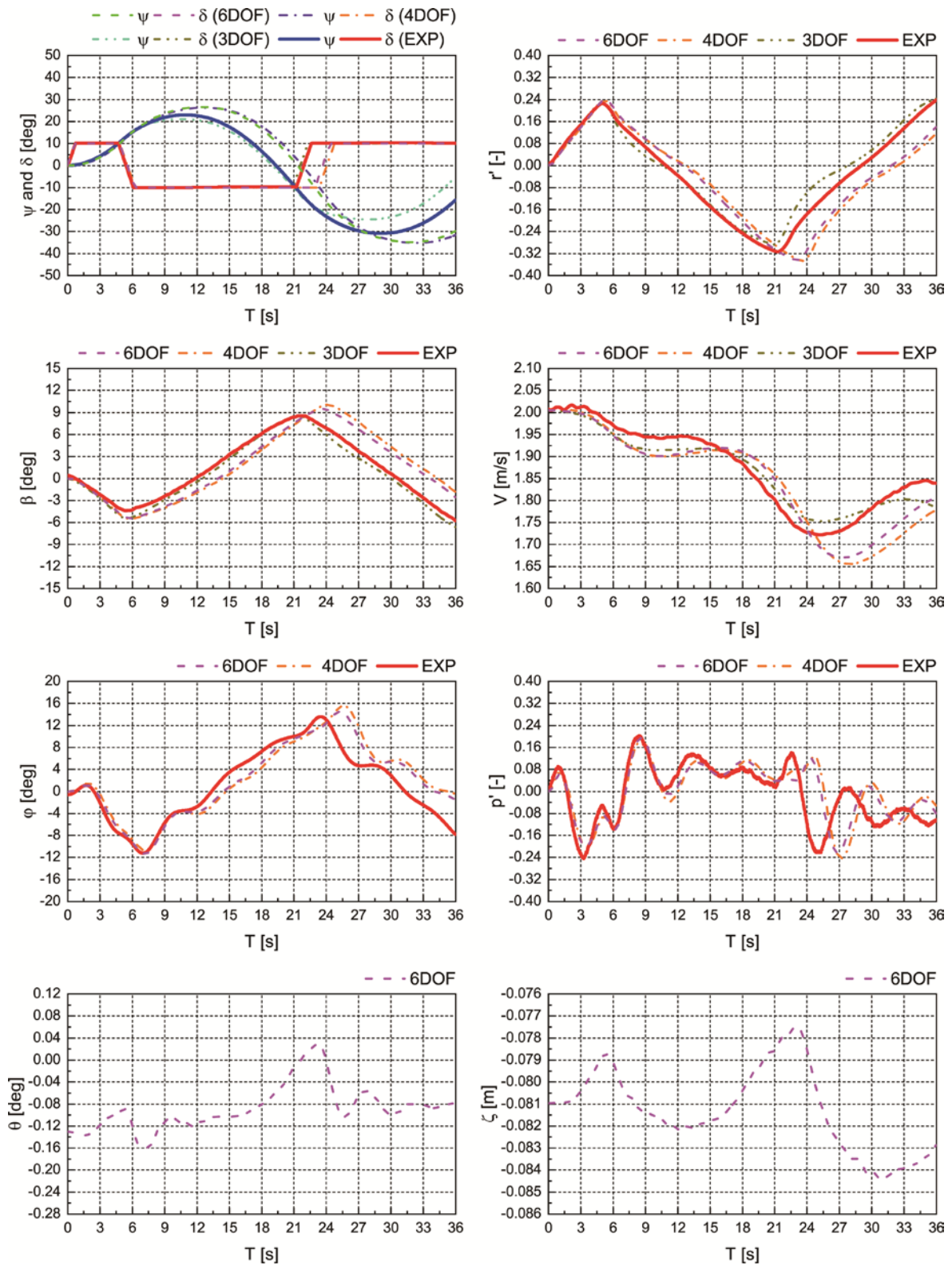


Figure 5: Comparison of kinematic parameters for zig-zag $10^\circ/10^\circ$ to starboard in different DOF concepts (Top left: 5.1, Top right: 5.2, Bottom left: 5.7, Bottom right: 5.8)

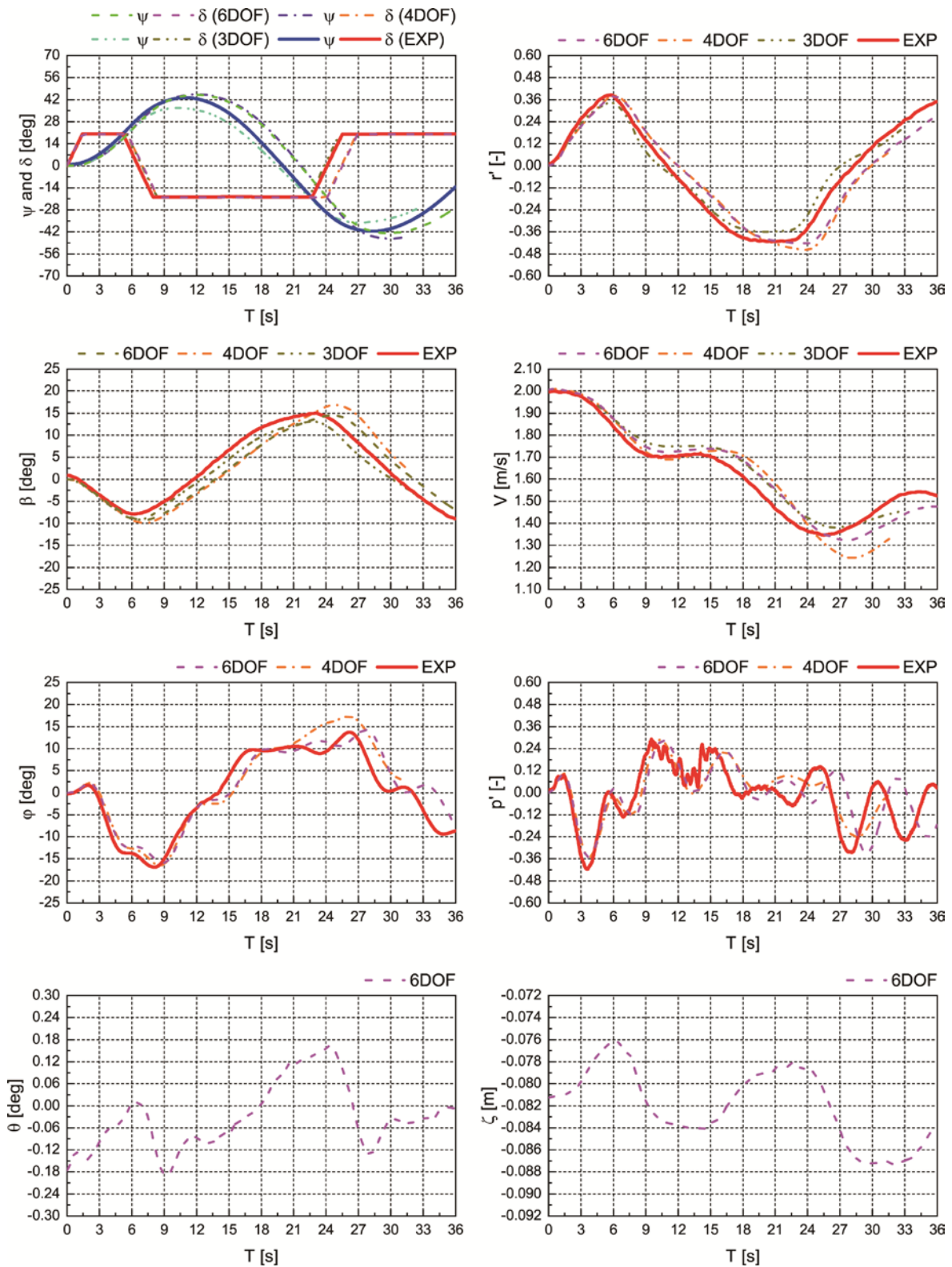


Figure 6: Comparison of kinematic parameters for zig-zag 20°/20° to starboard in different DOF concepts (Top left: 6.1, Top right: 6.2, Bottom left: 6.7, Bottom right: 6.8)

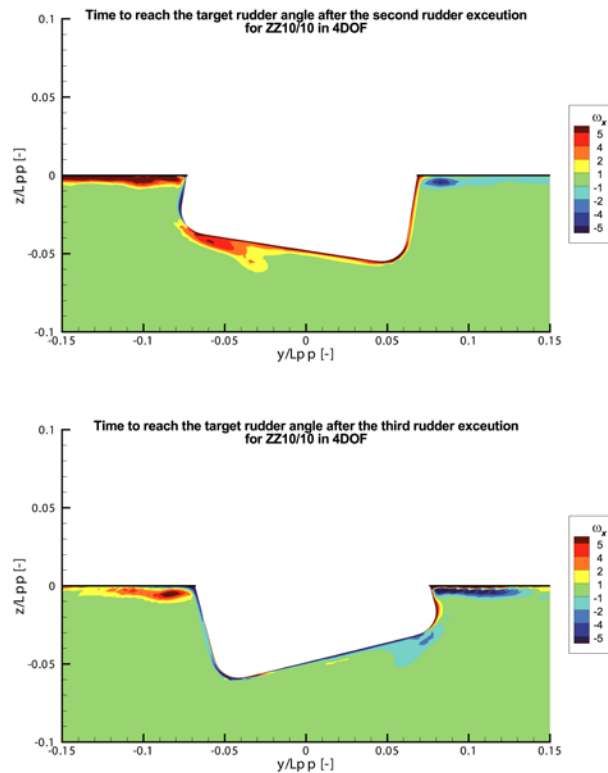


Figure 7: Contours of vortex structure amidships for zig-zag $10^\circ/10^\circ$ in 4 DOF (See from bow to aft)

5 CONCLUSIONS

From the simulations that have been performed, it is possible to conclude that 4 DOF concept can be more reasonable than 6 DOF concept for current ship type since the tiny pitch and heave motion observed in the simulations can be neglected. As a result, mesh strategy can be simplified using 4 DOF concept. Additionally, large roll angle during manoeuvring motions implies that 4 DOF concept should be preferred to the container ships which may have severe roll motion in service. Compared with 4 DOF and 6 DOF concept, 3 DOF concept underestimates all overshoot angles of each simulation. The reason for above mentioned behaviour can be explained by the change of the side projected area under the waterplane in different DOFs, which indirectly affects the distribution of hydrodynamic forces and moments.

6 ACKNOWLEDGEMENTS

The authors would like to thank the engineering office of NUMECA in Germany for its license and also the technical staff in the department of DMS for HPC resource to implement the study. Additionally, fruitful discussions over simulations with Professor Cura Hochbaum and Dr. Uharek are gratefully acknowledged. At last, the authors would like to extend their thanks to MARIN for providing the experimental data, especially to Mr. Quadvlieg and Mr. Tonelli. Part of this work was granted access to the HPC resources of [CINES/IDRIS] under the allocation 2018-A0052A01308 made by GENCI.

REFERENCES

- [1] Carrica, P. M., Ismail, F., Hyman, M., Bhushan, S., & Stern, F. (2008). *Turn and zigzag maneuvers of a surface combatant using a URANS approach with dynamic overset grids*. Paper presented at the SIMMAN 2008, Copenhagen, Denmark.
- [2] Cura Hochbaum, A. (1998). *Computation of the turbulent flow around a ship model in steady turn and in steady oblique motion*. Paper presented at the 22nd Symposium on Naval Hydrodynamics, Washington, D.C., United States.
- [3] Dubbioso, G., Durante, D., & Brogna, R. (2013). *Zig-zag maneuver simulation by CFD for tanker like vessel*. Paper presented at the 5th International Conference on Computational Methods in Marine Engineering, Hamburg, Germany.
- [4] El Moctar, O. M. (2001). Numerical computations of flow forces in ship manoeuvring. *Ship Technology Research*, 48(3), 98-123.
- [5] Gao, X. (2019). *Analysis of the influence of bilge keels on manoeuvring by means of virtual zigzag tests*. (M.Sc.), Technical University of Berlin,
- [6] Jensen, G., Klemm, M., & Xing-Kaeding, Y. (2004). *On the way to the numerical basin for seakeeping and manoeuvring*. Paper presented at the 9th Symposium on Practical Design of Ship and Other Floating Structures, Luebeck Travemuende, Germany.
- [7] MARIN. (2010). Manoeuvring tests on KCS. *MARIN Report: 23991-1-SMB*.
- [8] Ohmori, T., & Miyata, H. (1993). Oblique Tow Simulation by a Finite-Volume Method. *Journal of the Society of Naval Architects of Japan*, 1993(173), 27-34.
- [9] Quadvlieg, F., Stern, F., Simonsen, C. D., & Otzen, J. F. (2014). *Proceedings of SIMMAN 2014*, Copenhagen, Denmark.
- [10] Queutey, P., & Visonneau, M. (2007). An interface capturing method for free-surface hydrodynamic flows. *Computers & fluids*, 36(9), 1481-1510.
- [11] Shen, Z. R., Wan, D. C., & Carrica, P. M. (2015). Dynamic overset grids in OpenFOAM with application to KCS self-propulsion and maneuvering. *Ocean Engineering*, 108, 287-306.
- [12] SIMMAN 2014. (2014). Retrieved from <https://simman2014.dk>
- [13] Simonsen, C. D., & Stern, F. (2005). RANS maneuvering simulation of Esso Osaka with rudder and a body-force propeller. *Journal of Ship Research*, 49(2), 98-120.
- [14] Toxopeus, S. L. (2011). *Practical application of viscous-flow calculations for the simulation of manoeuvring ships*. (Ph.D.), Delft University of Technology,
- [15] Wackers, J., Deng, G., Leroyer, A., Queutey, P., & Visonneau, M. (2012). Adaptive grid refinement for hydrodynamic flows. *Computers & fluids*, 55, 85-100.
- [16] World Maritime News Staff. (2018). Steel Cut for CMA CGM' s 22,000 TEU Behemoths, World' s Largest Boxships. Retrieved from <https://worldmaritimeneews.com/archives/257983/steel-cut-for-cmacgms-22000-teu-behemoths-worlds-largest-boxships>

VALIDATION OF A ROLL DECAY TEST OF AN OFFSHORE INSTALLATION VESSEL USING OPENFOAM

MARINE 2019

BRECHT DEVOLDER^{*}, FLORIAN STEMPINSKI[†], ARJAN MOL[†] AND PIETER
RAUWOENS^{*}

^{*} Department of Civil Engineering, Construction Technology Cluster
KU Leuven, campus Bruges
Sporwegstraat 12, 8200 Brugge, Belgium
e-mail: brecht.devolder@kuleuven.be, pieter.rauwoens@kuleuven.be

[†] DEME group
Haven 1025, Scheldedijk 30, 2070 Zwijndrecht, Belgium
Email: stempinski.florian@deme-group.com, mol.arjan@deme-group.com

Key words: Numerical modelling; CFD; OpenFOAM; Floating structures

Abstract. In this work, the offshore heavy lift DP2 jack-up vessel Innovation from the DEME group is studied using the Computational Fluid Dynamics (CFD) toolbox OpenFOAM. The two-phase Navier-Stokes fluid solver is coupled with a motion solver using a partitioned fluid-structure interaction algorithm. Firstly, two dimensional numerical simulations of a cross-section of the hull are performed using two different mesh motion techniques: a mesh morphing method and an overset mesh method. Subsequently, the addition of a bilge keel pair on the hull is studied numerically by performing a two dimensional roll decay simulation. Finally, a three dimensional simulation is performed for a roll decay test and validated by using experimental data measured in the MARIN seakeeping and manoeuvring basin. As a first result, the coupled CFD–motion solver proves to be a promising toolbox for the study of fluid-structure interaction problems of realistic marine structures such as an offshore installation vessel.

1 INTRODUCTION

Floating structures are prominently present in coastal and offshore regions, e.g. ships, pontoons, barges and pipelines. In the future, it is expected that innovative floating structures such as wave energy converters and wind turbines will be installed for renewable energy production. These structures need special installation vessels such as a heavy lift jack-up vessel or a heavy lift floating installation vessel. The workability of these vessels depends on the wave, current and wind loading. Not only the forcing is of large importance for the installation of structures but also the response to the environmental loads needs an accurate quantification.

Nowadays, simplified radiation-diffraction models such as linear potential flow solvers based on boundary element methods (BEM) are used to simulate vessel motions in waves [1,2]. These models are not capable in resolving nonlinear, viscous and turbulent effects and complex free surface deformations such as waves breaking on a vessel. Computational Fluid Dynamics (CFD) is selected to overcome these shortcomings. For example, the roll damping of a vessel

with forward speed is governed by viscous effects. By using a CFD model, the contribution of viscous effects to the roll damping is resolved without any simplification to the underlying physics. As a result, the roll damping coefficient of a vessel can be obtained accurately and can be used as input for simplified models such as BEM to perform a large and wide variety of numerical simulations.

CFD models have been successfully applied and validated for numerous studies related to marine applications such as wave generation [3–5], wave-current generation [6], wave breaking [7,8], wave-structure interaction [9–12] and seakeeping simulations [13–15]. In general for CFD models, a balance has to be sought between numerical accuracy and numerical efficiency to obtain accurate results in an acceptable time window.

In this work, the offshore heavy lift DP2 jack-up vessel Innovation from the DEME group is studied, see Figure 1. The vessel has a length of 147.50 m, a beam of 42 m and a depth of 11 m. It is mainly used for the installation of offshore structures such as offshore wind turbine foundations.

The paper is structured as follows. In section 2, the experimental tests are briefly presented. Section 3 reports the numerical framework used for the simulations presented in section 4. An outlook to further research is listed in section 5 and the conclusions are given in section 6.



Figure 1: The offshore heavy lift DP2 jack-up vessel Innovation (DEME group).

2 EXPERIMENTAL SETUP

The experimental tests used in this work are performed in the seakeeping and manoeuvring basin in MARIN (The Netherlands). The basin measures 170 x 40 x 5 metres in length, width and water depth respectively. The wave generation system comprises of 331 individual flaps of 0.6 m width. At the opposite side, a beach is absorbing the incoming waves. A scale model of the Innovation was built to a geometric scale ratio of 1 to 30, see Figure 2. The key geometrical properties of the vessel are listed in Table 1. The underwater part of the scale model is equipped with four azimuthing stern thrusters, three bow tunnel trusters, four lattice jack-up legs with spudcans, a central skeg and a bilge keel pair. Note that the four lattice legs are not physically present during the model tests but their mass and inertia have been taken into account for the weight distribution by using equivalent masses.

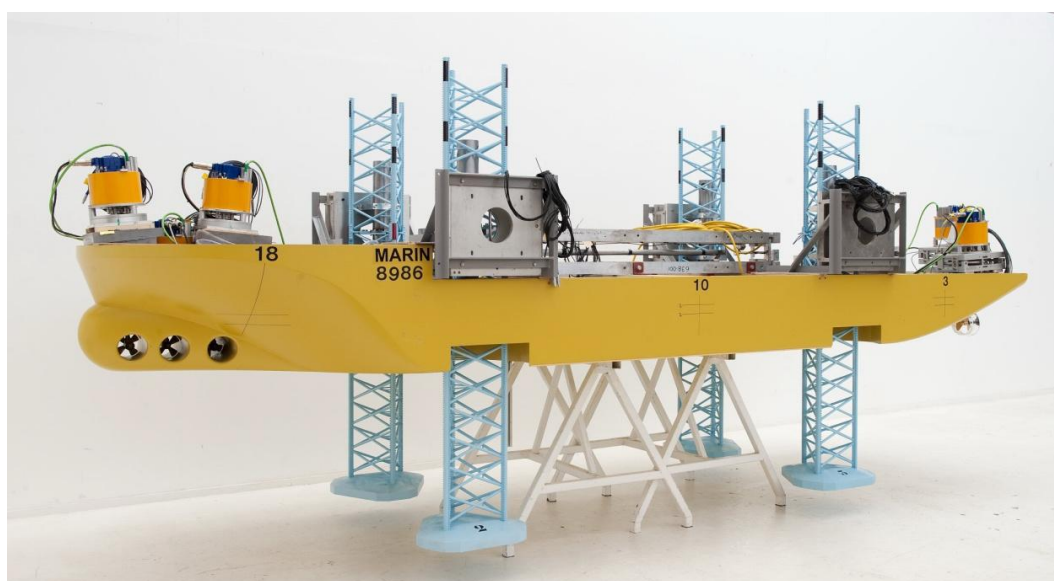


Figure 2: Scale model of the Innovation used for the experimental measurements (scale 1 to 30).

Table 1: Geometrical properties of the Innovation, both for prototype and model scale (1:30).

| Parameter | Units | Prototype | Model |
|--|-------|------------|-----------|
| Length | m | 147.500 | 4.916 |
| Breadth | m | 42.000 | 1.400 |
| Depth | m | 11.000 | 0.367 |
| Mass * | kg | 28 135 800 | 1 016.650 |
| Draft | m | 5.959 | 0.199 |
| Mass radius of gyration around X-axis | m | 21.700 | 0.723 |
| Mass radius of gyration around Y-axis | m | 42.300 | 1.410 |
| Centre of gravity (X) from aft | m | 73.095 | 2.437 |
| Centre of gravity (Y) from centre line | m | 0.000 | 0.000 |
| Centre of gravity (Z) from keel (KG) | m | 17.665 | 0.589 |

* Salt water (1025 kg/m³) is assumed in prototype while fresh water (1000 kg/m³) was used for the experiments.

3 NUMERICAL FRAMEWORK

Numerical modelling is performed for the study of a floating offshore installation vessel. The two-phase flow solver with dynamic mesh handling is available in OpenFOAM-v1812 [16,17] to perform transient simulations of a floating structure in a numerical basin. In order to simulate the fluid-structure interaction (FSI) problem, a partitioned approach is used in which a CFD fluid solver (section 3.1) and a motion solver (section 3.2) are called consecutively by a coupling algorithm (section 3.3). Details regarding the mesh motion and boundary conditions are given in sections 3.4 and 3.5 respectively.

3.1 CFD fluid solver

Simulations of the two-phase flow field are performed by solving the incompressible RANS equations and a conservation equation for the Volume of Fluid (VoF) [18] using a finite volume method [19]. Turbulent effects are taken into account by applying a buoyancy-modified $k-\omega$ SST turbulence model [7,20]. This model is developed to obtain a stable wave propagation model without wave damping due to RANS turbulence modelling. It also predicts the turbulence level inside the flow field more accurately during wave breaking. In particular, a buoyancy-modified turbulence model significantly reduces the overestimation of turbulent kinetic energy in the two-phase flow field, commonly presented in literature for wave simulations using a CFD fluid solver.

For all simulations the following settings are used: first order, bounded, implicit time discretisation; a maximum Courant number of 0.30; upwind discretisation for the turbulent divergence operators; central discretisation for the pressure gradient, the diffusion terms and all the other divergence operators.

3.2 Motion solver

The kinematic motion of a rigid structure is calculated by a six degrees of freedom motion solver. Three translations (surge, sway, heave) and three rotations (roll, pitch and yaw) are allowed. The motion of the structure is based on the overall force F and the torque τ acting on all boundary faces calculated by the fluid solver:

$$\sum F = ma \quad (1)$$

$$\sum \tau = I\alpha \quad (2)$$

in which m is the mass, I is the moment of inertia tensor and a and α the linear and angular acceleration vector. Subsequently, a first order implicit integration scheme is used to obtain the velocity, position, angular velocity and orientation of the rigid structure during every time step of the transient simulation.

3.3 Coupling algorithm

This section presents the coupling algorithm between a CFD fluid solver (section 3.1) and a motion solver (section 3.2). The coupling algorithm is an extension of the developments reported in previous work of the main author [21] based on the IQN-ILS algorithm from [22]. This coupling algorithm results in stable simulations for the case of significant added mass

effects. It will also reduce the number of sub iterations to reach convergence between the flow field around and the motion of the floating structure during every time step of the transient simulation, increasing the computational efficiency. The numerical implementation of the accelerated coupling algorithm is documented in Algorithm 1. \mathcal{M} represents the motion solver, \mathcal{F} the CFD fluid solver and $\mathcal{F} \circ \mathcal{M}$ means that the output of \mathcal{M} is given as input to \mathcal{F} . At the start of a FSI simulation, all the variables are initialised, such as the pressure, velocity, volume fraction and turbulent quantities. For each time step, there are $i + 1$ sub iterations needed to reach convergence between the fluid and the motion solver. Note that the algorithm is formulated in terms of a generalised vector x , which is in our case the linear acceleration a as well as the rotational acceleration α (i.e. the algorithm is called twice during every sub iteration). The relative residual has to be smaller than a value ε which is equal to 0.01 for the simulations presented. The relaxation factor ω must be between 0 and 1 and is equal to 0.5 in this paper.

Algorithm 1: Accelerated coupling algorithm used for fluid-structure interaction problems.

```

1:   $i = 0$ 
2:   $\tilde{x}^0 = \mathcal{F} \circ \mathcal{M}(x^0)$ 
3:   $r^0 = \tilde{x}^0 - x^0$ 
4:  while  $|r^i|/\tilde{x}^i > \varepsilon$  do
5:      if  $i = 0$  then
6:           $x^{i+1} = x^i$ 
7:      if  $i = 1$  then
8:           $x^{i+1} = x^i + \omega r^i$ 
9:      else
10:          $x^{i+1} = x^i + \left[ \frac{(\tilde{x}^i - \tilde{x}^{i-1})(r^i - r^{i-1})^T}{(r^i - r^{i-1})^T (r^i - r^{i-1})} - I \right] (-r^i)$ 
           in which  $I$  is the unity tensor
11:     end if
12:      $\tilde{x}^{i+1} = \mathcal{F} \circ \mathcal{M}(x^{i+1})$ 
13:      $r^{i+1} = \tilde{x}^{i+1} - x^{i+1}$ 
14:      $i++$ 
15: end while

```

3.4 Mesh motion

In this work, two different mesh motion methods are applied: mesh morphing and overset. The mesh morphing method used within this study is based on spherical linear interpolation (SLERP). The motion of the computational cells is a function of the distance to the moving boundary. The method enforces smoothness and the distance function has a cosine profile to preserve shape of cells close to the moving surface [23]. More recently, the overset method is implemented in the OpenFOAM toolbox to avoid mesh morphing [24]. As a result, undesirable mesh deformation (i.e. high non-orthogonality and skewness of the grid cells) around the air-water interface is absent, reducing the discretisation error for the applied finite volume method. On the other hand, the overset method is interpolating between a background mesh and one or more overset meshes which leads to interpolation errors.

3.5 Boundary conditions

All the simulations presented are performed in a numerical basin which represents the physical basin as good as possible. However, some simplifications are made in order to obtain economical simulation times. For example, the depth of the numerical basin is limited to 1 m instead of 5 m in the experimental facility. Also a reduction of length in the longitudinal direction is made. All these simplifications will however not affect significantly the numerical results presented in this paper.

Each boundary of the computational domain needs specific boundary conditions. The bottom and the four side walls of the basin are set to a no-slip condition and behaves as a fully reflective structure: a Dirichlet boundary condition is set for the velocity (0 m/s in all directions) while the pressure and volume fraction are set to a Neumann condition. The atmospheric conditions at the top of the numerical domain are set to a mixed Dirichlet-Neumann boundary condition for the velocity, pressure and volume fraction. In order to have convergence between the fluid and motion solver, the following kinematic condition needs to be fulfilled at the interface between the fluid and the body:

$$u_{fluid} = u_{body} \quad (3)$$

in which u_{fluid} and u_{body} are the vertical fluid velocity and the vertical body's velocity, respectively. As such, this velocity is used in the moving wall boundary condition at the body's interface.

Wall functions are activated for k and ω on the boundary faces of the floating structure. A continuous wall function based on Spalding's law [25] switching between low- and high-Reynolds numbers is implemented for the turbulent viscosity ν_t . The initial values for k and ω in the computational domain are set to $10^{-10} \text{ m}^2/\text{s}^2$ and 1.0 s^{-1} respectively.

4 RESULTS AND DISCUSSION

Firstly, two dimensional (2D) numerical simulations for a roll decay test are performed using two different mesh motion techniques: mesh morphing and overset. Subsequently, the addition of a bilge keel pair is also studied by a 2D roll decay test. Lastly, a full three dimensional (3D) simulation is performed for a roll decay test and validated by using experimental data measured in the MARIN seakeeping and manoeuvring basin. During the roll decay tests presented, the vessel is inclined to an initial roll angle of 2 degrees and is then released. The vessel begins a roll oscillation with a decaying amplitude until all the hydrodynamic forces on the vessel are again in equilibrium with the weight of the vessel. For all the simulations, *snappyHexMesh* has been used for mesh generation.

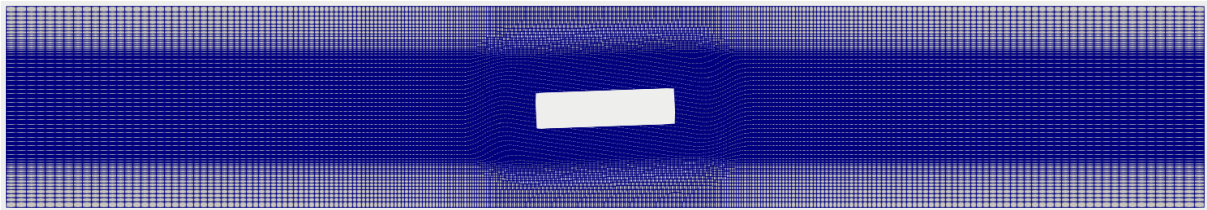
4.1 2D roll decay test without a bilge keel pair

For the 2D simulations, the midship cross-section of the Innovation is used without the presence of a bilge keel pair. After discretisation, the size of a cell around the hull in Y -direction and Z -direction is equal to 0.02 m and 0.01 m respectively. The cells are gradually becoming larger towards the boundaries of the computational domain. This will reduce the number of cells and will speed up the simulations without losing accuracy of the roll decay test. In total six simulations for each mesh motion technique (mesh morphing and overset) are performed: without and with boundary layer, and additional local refinements in Y - and Z -directions around

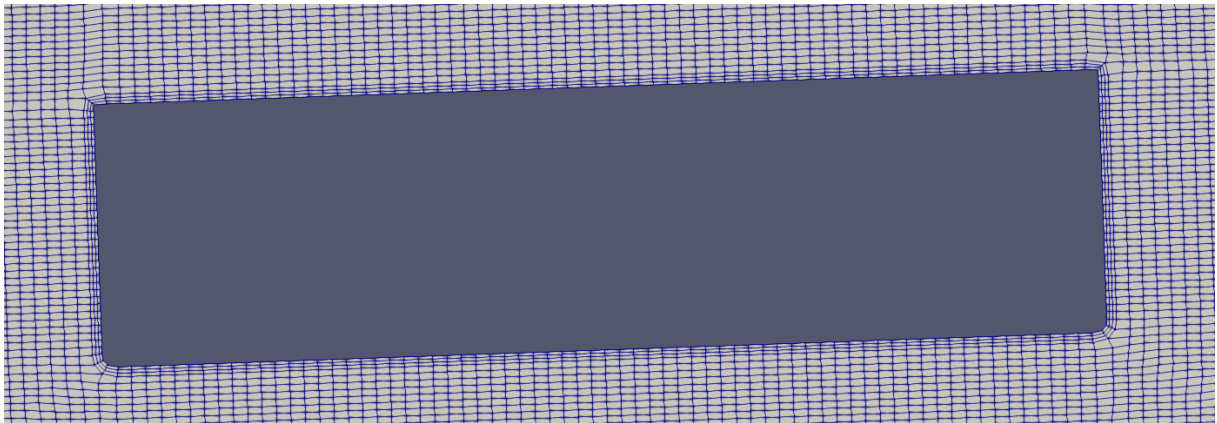
the hull, see Table 2. An overview of the computational domain is depicted in Figure 3a for the mesh morphing method (case1-SLERP). Figure 3b shows a detail around the cross-section with boundary layer (case1-SLERP+BL).

Table 2: An overview of the 2D roll decay test simulations.

| Simulation | Boundary layer | Δy [m] | Δz [m] | # cells | Simulation time [s] | Roll angle [°] |
|------------------|----------------|----------------|----------------|---------|---------------------|----------------|
| case1-SLERP | ✗ | 0.02 | 0.01 | 39 410 | 715 | 1.069 |
| case1-overset | ✗ | 0.02 | 0.01 | 49 410 | 2 721 | 1.331 |
| case2-SLERP | ✗ | 0.01 | 0.005 | 53 242 | 2 099 | 1.264 |
| case2-overset | ✗ | 0.01 | 0.005 | 84 840 | 7 820 | 1.440 |
| case3-SLERP | ✗ | 0.005 | 0.0025 | 80 328 | 15 113 | 1.331 |
| case3-overset | ✗ | 0.005 | 0.0025 | 168 960 | 83 062 | 1.500 |
| case1-SLERP+BL | ✓ | 0.02 | 0.01 | 40 052 | 812 | 1.164 |
| case1-overset+BL | ✓ | 0.02 | 0.01 | 50 052 | 3174 | 1.369 |
| case2-SLERP+BL | ✓ | 0.01 | 0.005 | 54 520 | 2 391 | 1.275 |
| case2-overset+BL | ✓ | 0.01 | 0.005 | 87 408 | 10 495 | 1.478 |
| case3-SLERP+BL | ✓ | 0.005 | 0.0025 | 82 872 | 16 392 | 1.339 |
| case3-overset+BL | ✓ | 0.005 | 0.0025 | 177 126 | 149 759 | 1.511 |



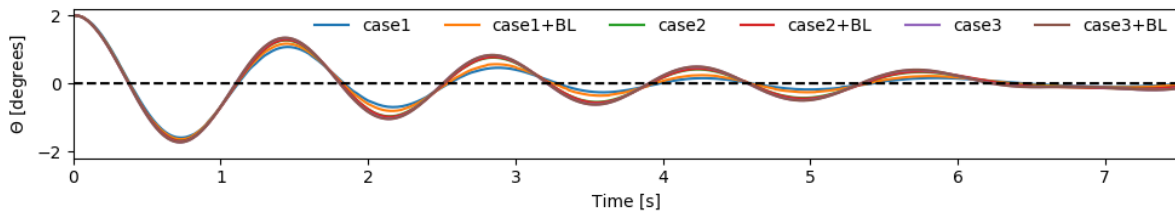
(a)



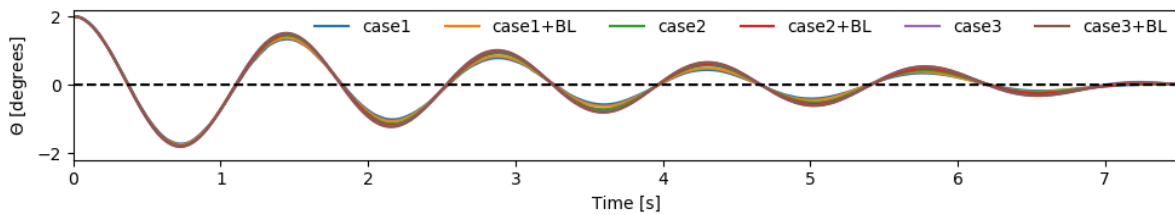
(b)

Figure 3: Computational domain in 2D, (a) full domain, (b) boundary layer around the hull.

The numerical results of the roll decay test with an initial roll angle of 2 degrees are presented in Figure 4a and Figure 4b using the SLERP and overset approach respectively. The roll angle is given as a function of time. After 7 seconds, the roll motion is almost fully damped out. The value of the roll angle at the first peak around 1.5 seconds is also reported in the last column of Table 2. The solutions are converging monotonically for each additional local refinement, both without and with boundary layer. The presence of a boundary layer near the hull is not influencing the results significantly, both for the SLERP and overset approach. Between two levels of refinement, the difference in roll angle around 1.5 seconds is smaller for the overset method than for the SLERP approach. In addition, the difference between SLERP and overset is decreasing for an increase in the number of cells due to local refinements. It is very important to stress that the overset method requires a significantly larger amount of computational time, see Table 2. This is not only related to the larger number of computational cells but also due to the implementation of the overset interpolation operation.



(a)



(b)

Figure 4: Roll angle as a function of time during a roll decay test: (a) SLERP (b) overset.

4.2 2D roll decay test with a bilge keel pair

In this section a bilge keel pair is added to the hull of the vessel. During the 3D model tests, a bilge keel pair was installed in order to enhance the roll stability of the vessel. Local refinement of the computational cells (case1-SLERP) is required to create a proper mesh around the bilge keel, see Figure 5. The numerical results are presented in Figure 6 for a simulation without and with bilge keel. It is demonstrated that the addition of a bilge keel pair only leads to a small increase of the roll damping. Also the natural roll period is slightly increasing if a bilge keel pair is modelled. Figure 7 shows the velocity field around the cross-section. By adding a bilge keel pair, the local velocity magnitude of the water increases significantly which affects slightly the roll motion as well. Interestingly, the simulation without bilge keel pair was completed in 1 360 seconds while with a bilge keel pair 2 388 seconds were needed. This increase is originating from the limiting Courant number and smaller cells near the bilge keels.

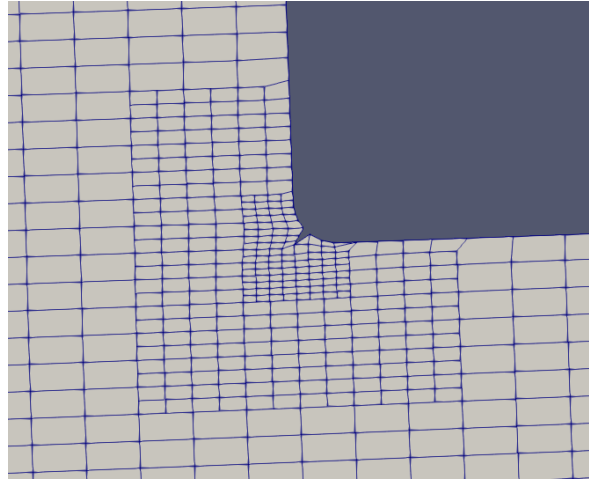


Figure 5: Detail of the computational domain (2D) around the cross-section of the hull with a bilge keel pair.

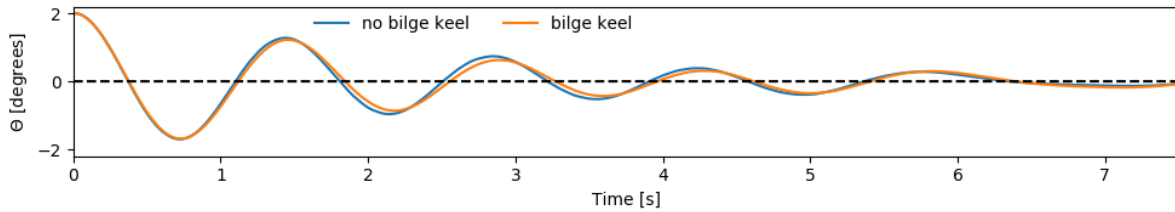


Figure 6: Roll angle as a function of time during a roll decay test: without and with bilge keel pair.

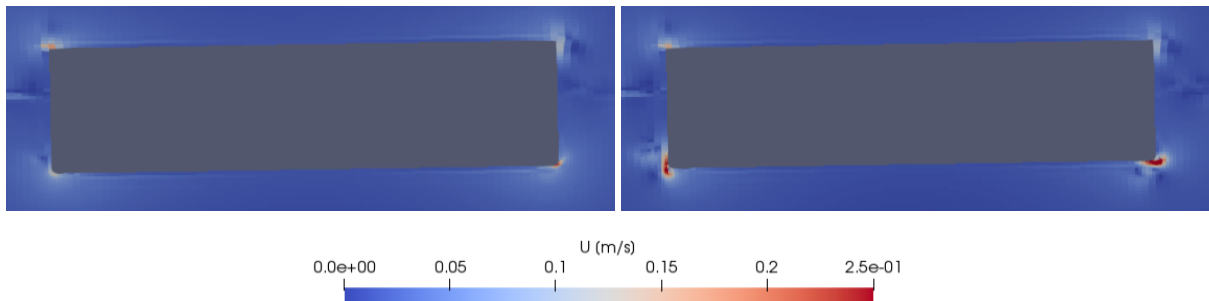


Figure 7: Velocity field around the hull: (left) without bilge keel pair, (right) with bilge keel pair.

4.3 3D roll decay test

In this section, a 3D simulation of a roll decay test with zero forward speed is performed and validated with the experimental measurements introduced in section 2. The computational domain around the hull is depicted in Figure 8. Local refinements are made around the hull and the free water surface where the mesh motion is happening (SLERP interpolation). The overset method is not chosen due to the larger computational overhead (see section 4.1 for the 2D simulations). In addition, the bilge keel is not considered in a first instance due to the limiting effect and large increase in computational time (see section 4.2). The final mesh consists of 672 316 cells and has a resolution of 0.40 m in the far field down to 0.05 m near the hull.

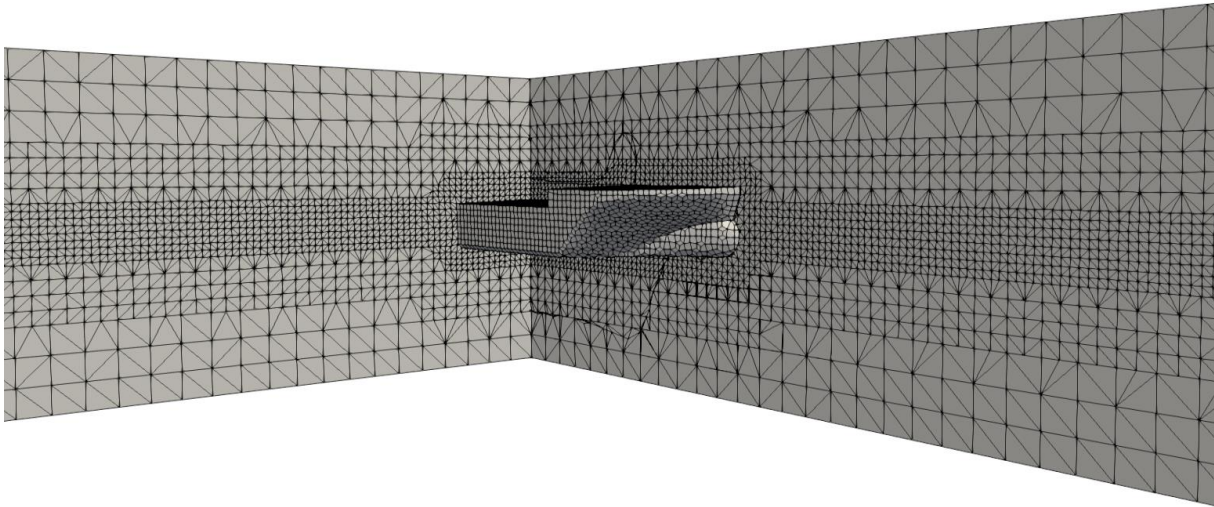


Figure 8: Computational domain around the hull of the Innovation. Two vertical cross-sections are shown to indicate the discretisation in the numerical basin.

The numerical and experimental results of the roll decay test are given as time series in Figure 9. In general, the roll damping motion predicted by the numerical model is in a very good agreement with the experimental measurements. However after 10 seconds, the observed roll damping is slightly bigger for the experimental result signal compared to the numerical result. These differences are addressed to the simplifications made to the geometry used for the numerical simulations. For example, during the experimental propulsion tests, the spudcans were not fully hidden inside their garages increasing the resistance. This might also add damping during the experimental roll decay tests compared to the numerical simulations in which the spudcans are not considered at all on the geometry. Also the propellers installed on the ship model are excluded on the numerical geometry. As reported by [26], the eddy damping and wave radiation damping have a significant contribution to the total roll damping for a vessel with zero forward speed. Both of them depend on the position of the centre of gravity and the shape of the hull.

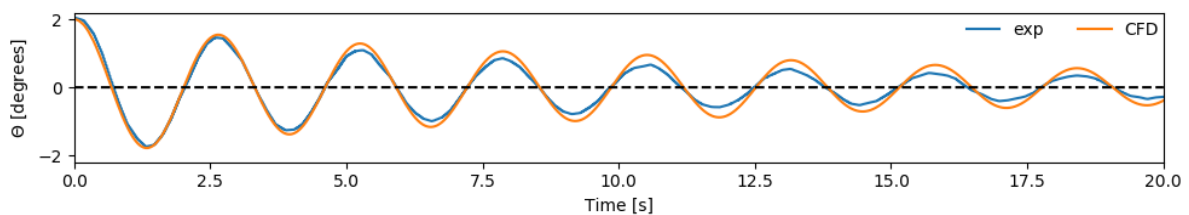


Figure 9: Roll angle as a function of time during a roll decay test of an offshore installation vessel: numerical CFD result and experimental measurement.

5. RESEARCH TOPICS UNDER INVESTIGATION

The topics listed below will be investigated in the near future:

- Validation of roll damping simulations of a vessel with a forward speed;
- Overset mesh method for seakeeping simulations;
- Roll damping tests of the Innovation on which spudcan shoes are installed;
- Validation of a freely floating vessel in regular waves.

6 CONCLUSIONS

We have presented numerical simulations of a vessel during a roll decay test. Two mesh motion techniques have been compared using 2D simulations: SLERP and overset. In addition, the addition of a bilge keel pair is studied which has only a small influence on the roll damping motion. A 3D simulation of an offshore installation vessel, the Innovation from the DEME group, during a roll decay test with zero forward speed is validated by using experimental data. Discrepancies have been observed, discussed and further research is proposed to fully understand the hydrodynamics around the vessel during seakeeping simulations.

7 ACKNOWLEDGEMENTS

The first author is postdoctoral researcher at the department of civil engineering at KU Leuven, campus Bruges. The project is a collaboration between KU Leuven and DEME and is funded by the agency Flanders Innovation & Entrepreneurship (VLAIO) and DEME.

REFERENCES

- [1] Babarit A, Delhommeau G. Theoretical and numerical aspects of the open source BEM solver NEMOH. Proc. 11th Eur. Wave Tidal Energy Conf., 2015.
- [2] ANSYS. ANSYS Aqwa n.d.
- [3] Jacobsen NG, Fuhrman DR, Fredsøe J. A wave generation toolbox for the open-source CFD library: OpenFoam®. *Int J Numer Methods Fluids* 2012;70:1073–88. doi:10.1002/flid.2726.
- [4] Higuera P, Lara JL, Losada IJ. Realistic wave generation and active wave absorption for Navier-Stokes models. Application to OpenFOAM. *Coast Eng* 2013;71:102–18. doi:10.1016/j.coastaleng.2012.07.002.
- [5] Windt C, Davidson J, Schmitt P, Ringwood J V., Windt C, Davidson J, et al. On the Assessment of Numerical Wave Makers in CFD Simulations. *J Mar Sci Eng* 2019, Vol 7, Page 47 2019;7:47. doi:10.3390/JMSE7020047.
- [6] Lara JL, Barajas G, Maza M, Losada IJ. Wave-current generation with OpenFOAM. Application to coastal and offshore structures. 4th OpenFOAM User Conf., Cologne, Germany: 2016.
- [7] Devolder B, Troch P, Rauwoens P. Performance of a buoyancy-modified $k-\omega$ and $k-\omega$ SST turbulence model for simulating wave breaking under regular waves using OpenFOAM®. *Coast Eng* 2018;138:49–65. doi:10.1016/j.coastaleng.2018.04.011.
- [8] Larsen BE, Fuhrman DR. On the over-production of turbulence beneath surface waves in Reynolds-averaged Navier–Stokes models. *J Fluid Mech* 2018;853:419–60. doi:10.1017/jfm.2018.577.

- [9] Devolder B, Stratigaki V, Troch P, Rauwoens P. CFD Simulations of Floating Point Absorber Wave Energy Converter Arrays Subjected to Regular Waves. *Energies* 2018;11:641. doi:10.3390/en11030641.
- [10] Higuera P, Liu PL-F, Lin C, Wong W-Y, Kao M-J. Laboratory-scale swash flows generated by a non-breaking solitary wave on a steep slope. *J Fluid Mech* 2018;847:186–227. doi:10.1017/jfm.2018.321.
- [11] Windt C, Davidson J, Akram B, Ringwood J V. Performance assessment of the overset grid method for numerical wave tank experiments in the OpenFOAM environment. *Proc. ASME 2018 37th Int. Conf. Ocean. Offshore Arct. Eng.*, 2018, p. 1–10.
- [12] Di Paolo B, Lara JL, Barajas G, Paci A, Losada IJ. Numerical Analysis of Wave and Current Interaction With Moored Floating Bodies Using Overset Method. *Proc. ASME 2018 37th Int. Conf. Ocean. Offshore Arct. Eng.*, ASME; 2018, p. 1–10. doi:10.1115/OMAE2018-77284.
- [13] Piehl HP. *Ship Roll Damping Analysis*. University of Duisburg-Essen, 2016.
- [14] Gatin I, Vukčević V, Jasak H, Rusche H. Enhanced coupling of solid body motion and fluid flow in finite volume framework. *Ocean Eng* 2017;143:295–304. doi:10.1016/j.oceaneng.2017.08.009.
- [15] Gatin I, Vukčević V, Jasak H, Seo J, Rhee SH. CFD verification and validation of green sea loads. *Ocean Eng* 2018;148:500–15. doi:10.1016/j.oceaneng.2017.10.026.
- [16] Weller HG, Tabor G, Jasak H, Fureby C. A tensorial approach to computational continuum mechanics using object-oriented techniques. *Comput Phys* 1998;12:620. doi:10.1063/1.168744.
- [17] OpenCFD. OpenFOAM 2018. <https://www.openfoam.com/>.
- [18] Berberović E, van Hinsberg NP, Jakirlić S, Roisman I V., Tropea C. Drop impact onto a liquid layer of finite thickness: Dynamics of the cavity evolution. *Phys Rev E* 2009;79:036306. doi:10.1103/PhysRevE.79.036306.
- [19] Versteeg HK, Malalasekera W. *An Introduction to Computational Fluid Dynamics - The Finite Volume Method*. Pearson Education; 2007. doi:10.2514/1.22547.
- [20] Devolder B, Rauwoens P, Troch P. Application of a buoyancy-modified $k-\omega$ SST turbulence model to simulate wave run-up around a monopile subjected to regular waves using OpenFOAM®. *Coast Eng* 2017;125:81–94. doi:10.1016/j.coastaleng.2017.04.004.
- [21] Devolder B, Troch P, Rauwoens P. Accelerated numerical simulations of a heaving floating body by coupling a motion solver with a two-phase fluid solver. *Comput Math with Appl* 2018. doi:10.1016/j.camwa.2018.08.064.
- [22] Degroote J. Partitioned Simulation of Fluid-Structure Interaction. *Arch Comput Methods Eng* 2013;20:185–238. doi:10.1007/s11831-013-9085-5.
- [23] OpenFOAM Foundation. OpenFOAM 2018. <https://openfoam.org/>.
- [24] Janssens M. Native overset meshes in OpenFOAM. 4th OpenFOAM User Conf. 2016, Cologne, Germany: 2016.
- [25] Spalding DB. A Single Formula for the “Law of the Wall.” *J Appl Mech* 1961;28:455. doi:10.1115/1.3641728.
- [26] Himeno Y. Prediction of Ship Roll Damping - State of the Art. *Rep Dep Nav Archit Mar Eng Univ Michigan* 1981;239.

Effects of Section Geometry on the Energy-saving Rate of PBCF and Model/full-scale Correlation - A CFD Study

Heng Zhang, Xiao-Qian Dong*, Wei Li*, Chen-Jun Yang, Francis Noblesse

(State Key Laboratory of Ocean Engineering,
Collaborative Innovation Center for Advanced Ship and Deep-Sea Exploration
Shanghai Jiao Tong University, Shanghai 200240, China)
E-mail: xiaoqiandong0330@sjtu.edu.cn (X.-Q. D.); wli@sjtu.edu.cn (W.L.)

Key words: PBCF, Section geometry, Scale effect, RANS, CFD

Abstract. The steady flows and hydrodynamic performances of a propeller without and with the Propeller Boss Cap Fins (PBCFs) are simulated by solving the Reynolds-averaged Navier-Stokes (RANS) equations using the software package STAR-CCM⁺. To determine a suitable grid setting, a grid convergence study is carried out first by changing the grid sizes separately in the sub-domains enclosing the propeller blades and the PBCFs. The CFD investigation into the energy-saving rate of the PBCFs with systematically varied section profiles at model-scale shows the PBCFs with modified ‘NACA M7’ section geometry performs better than the flat plate in energy-saving effect. Full-scale simulations are also carried out using typical PBCF geometries investigated at model scale, and the results are compared with model-scale ones to evaluate the Reynolds scale effects on the energy-saving rate. The hydrodynamic forces acting on the propeller blades, the PBCFs, and the boss cap are compared to explore the mechanism behind the scale effects on the PBCFs. The study indicates that the scale effect positively influences the energy-saving effect of all the PBCFs investigated, while the flat-plate PBCFs benefit more from the scale effect.

1 INTRODUCTION

As the global warming problem becomes more serious and the energy consumption increases sharply, countries worldwide are paying more attention to the energy problem of shipping industry. In 2011, IMO enacted the Energy Efficiency Design Index (EEDI), which has been enforced since 2013 ^[1]. Moreover, the recent rise in oil price has also made Energy Saving Devices (ESDs) become a research focus. One of the popular ESDs which has been widely used in vessels is the Propeller Boss Cap Fins (PBCFs) due to its low cost and easy installation. The research of the PBCFs was first introduced by Ouchi *et al.* ^[2] in 1988. Based on the model tests, they verified that the hub vortex is weakened and the efficiency increases with the installation of the PBCFs. In the tests, the model propeller was located at the downstream of the dynamometer so that the hub vortex can be observed. The test was called the reverse propeller open water test (RPOT) and it has been widely adopted in later studies of the PBCFs.

In the last decade, with the rapid development of computer hardware capability and software technology, Computational Fluid Dynamics (CFD) has become increasingly preferred to evaluate the energy efficiency of ESDs, as it can provide more details of the viscous flow than potential flow methods.

Kai *et al.* [3] divided the propeller and the PBCFs into several parts and analyzed them respectively based on CFD technology. Li *et al.* [4] put forward a design method for the PBCFs based on viscous flow analysis and the lifting line theory. Mizzi *et al.* [5], Seo *et al.* [6] and Lim *et al.* [7] investigated and optimized the influence of design parameter variations for the PBCFs via viscous flow CFD simulations. However, among many of the parameters for PBCFs, the effects of section geometry have hardly been studied in existing studies, and most of the PBCFs take the shape of a flat plate for the convenience and cost-saving of manufacture. As the Computerized Numerical Control technology is widely adopted in propeller manufacture nowadays, machining the PBCFs with a complex geometry becomes relatively easy and inexpensive, which makes it possible to further improve the design of the PBCFs.

It is indicated that the energy saving effect of PBCFs is mostly better at full scale than at model scale [8,9]. Kawamura *et al.* [10] investigated the energy-saving rate of the PBCFs at model and full scale Reynolds numbers with two different inflow conditions by means of CFD analyses. The numerical result showed that the energy-saving rate of the PBCFs at high Reynolds number and non-uniform inflow is larger than that at low Reynolds number and uniform inflow which explains some of the reasons for the higher energy saving effects of PBCFs at full-scale.

This paper presents a CFD study on the energy-saving rate of the PBCFs with systematically varied section profiles, based on the RANS simulations using the software package STAR-CCM⁺. Firstly, a grid convergence study is carried out by changing the grid sizes separately in the sub-domains enclosing the propeller blades and the PBCFs. Then the RANS simulations are conducted at model scale in steady flows and the hydrodynamic forces are evaluated for different thickness ratios and camber line geometries of the PBCF sections. Furthermore, full-scale simulations are carried out using typical PBCF geometries investigated at model scale. Based on the numerical results, effects of section geometry on the energy-saving rate of PBCFs and model/full-scale correlation are discussed.

2 CFD MODELING APPROACH

2.1 Governing equations

The steady flows and hydrodynamic performances of a propeller without and with the PBCFs were simulated by solving the Reynolds-averaged Navier-Stokes (RANS) equations using the software package STAR-CCM⁺ version 12.02. The SST $k-\omega$ model is employed for turbulence closure, which seems to be mostly used for practical engineering calculations [11]. In all the governing equations, the convection terms are discretized with a second-order upwind scheme and the dissipative terms with a second-order central difference scheme. The overall solution process is based on the SIMPLE algorithm and the gradients are calculated by Green-Gauss techniques.

2.2 Setup of the computational model

The propeller investigated in this paper is DTMB 4381, a five-bladed propeller without skew, presented by Kerwin *et al.* [12]. Table 1 shows the geometric particulars as well as operating conditions of the propeller at model- and full-scale. The square-shaped PBCFs are

adopted in this paper, as illustrated in Figure 1, where the chord length of a fin, c , is 30mm and the height of a fin, d , varies with the radius of the fin. The fins can move relative to the local coordinate system $x'o'y'$ to change its particulars. In order to study the effects of section geometry on the energy-saving rate of PBCFs, the remaining parameters of PBCFs should be consistent. Based on our previous work on the parametric study of the PBCFs, the optimal collection of the PBCFs' design parameters has been found, as listed in Table 2, where the axial distance denotes distance at root between the trailing edge of propeller blade and the leading edge of fin, and the shifting angle denotes the angle between the reference lines of a propeller blade and a fin. In addition, as shown in Figure 2, an S-shaped airfoil profile 'NACA M7' chosen from software Profili Pro is used as the profile of the PBCFs in the grid convergence study presented in Section 2.3.

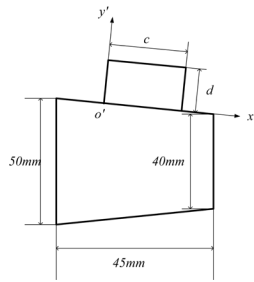


Figure 1: Schematic of the PBCF geometric model.



Figure 2: Geometry of the NACA M7 profile.

Table 1: Particulars of propeller DTMB 4381 at model- and full-scale.

| | Model-scale | Full-scale |
|----------------------------|-------------------|-------------------|
| Scale ratio | 20 | 1 |
| Number of blades | | 5 |
| Diameter (m) | 0.25 | 5.0 |
| Boss/diameter ratio | | 0.2 |
| Blade area ratio A_E/A_0 | | 0.725 |
| Rotation | | Right-handed |
| Velocity of inflow (m/s) | 4.445 | 12.86 |
| Re at $0.75R, J=0.889$ | 4.2×10^5 | 2.1×10^7 |

Table 2: Geometric particulars of the model-scale PBCFs.

| | |
|-----------------|--------------|
| Pitch angle | 53° |
| Hub ratio | 0.316 |
| Axial distance | 15.0 mm |
| Shifting angle | 36° |
| Skew angle | 0° |
| Profile of fins | Varied |
| Number of fins | 5 |
| Rotation | Right-handed |

The computational domain is divided into far, blade and PBCF sub-domains. The inlet and outlet boundaries of the far sub-domain are $5D$ upstream and $10D$ downstream of the blade, where D is the propeller diameter. Numerical simulation of the propeller and the PBCFs is based on the multi reference frame (MRF) method, where the far sub-domain is fixed, while

the blade and PBCF sub-domains are rotating. Interfaces are defined between adjacent domains, as shown in Figure 3. The inlet is set as the uniform inflow; the rotating sub-domains are set at a fixed rotation speed, which makes the advance ratio $J=0.889$ (design condition of DTMB 4381); and the outlet is set as the pressure outlet.

Grids of the three sub-domains are generated separately. The fixed sub-domain is discretized with trimmed grids, and the rotating sub-domains are discretized with polyhedral unstructured grids. Prism layer grids are generated over blade and fin surfaces. The meshing strategy is meant to reduce numerical uncertainties. When changing the geometry of PBCFs, only the grids in the PBCF sub-domain need to be modified while the grids in the remaining sub-domains can be kept unchanged. Grids in the PBCF sub-domain are further refined to make detailed investigation of the flow behind the boss cap. Grids around the tip, trailing edge and leading edge of blades and fins, and the hub surface are all refined since the grid size plays an important role in the CFD simulation of PBCFs. Figure 4 shows the computational meshes in a longitudinal cross section of the computational domain, and on blade and fin surfaces at model-scale. For full-scale simulations, the computational grids, except for those in the prism layers, are scaled up from the model-scale grids. By using the SST $k-\omega$ turbulence model, the boundary layer flow is resolved down to the viscous sub-layer at model-scale, while the wall-function approach is employed at full-scale^[13]. Therefore, the y^+ on the body surfaces has to be kept within a certain range by using proper prism layer heights. The average values of the y^+ over blade and fin surfaces at mode-scale are approximately equal to 1 and 0.8 respectively, while those at full-scale are approximately equal to 60 and 45 respectively.

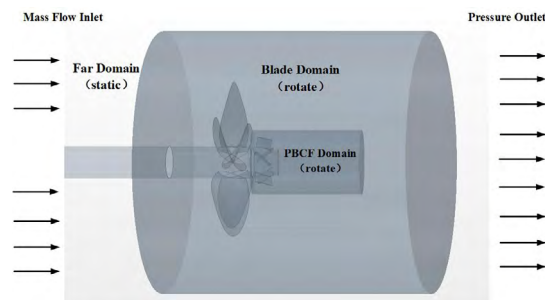


Figure 3: Sub-domains for the propeller and PBCFs.

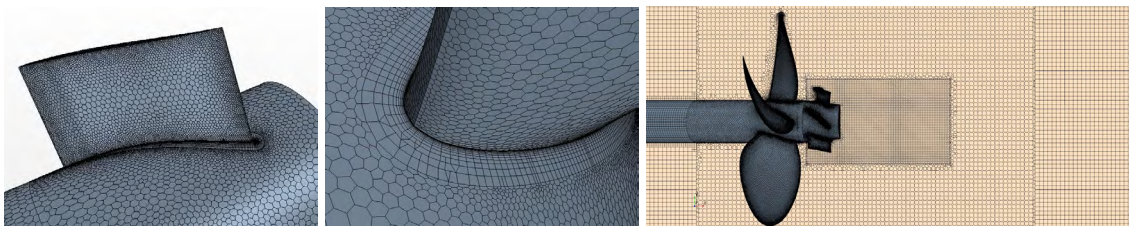


Figure 4: Grids on fin (left) and blade (middle) surfaces, and refined grids in PBCF sub-domain (right).

2.3 Grid convergence study

A grid convergence study is carried out by changing the grid sizes in different sub-domains separately. The convergence properties are investigated for the grids in far and propeller sub-domains firstly. Four sets of grids are generated for the propeller without PBCFs with a

uniform grid refinement ratio of $\sqrt{2}$, except for the prism layer heights which are kept the same to make the y^+ averaged over the body surfaces almost the same for all the grid sets. Table 3 shows the total number of cells in each grid set and the relative changes in K_T and K_Q of the propeller between different grid sets, where $i=1$ denotes the finest grid set, and $i=4$ the coarsest grid set. As the grids are refined, the differences in simulated K_T and K_Q become smaller between the successively refined grid sets; in fact, the differences are less than 0.1% between the finest ($i=1$) and the second finest ($i=2$) grid sets. To save computer resources, the second finest ($i=2$) grid set is chosen for far and propeller sub-domains in the following simulations.

Then the grid convergence study is performed for the PBCF sub-domain with four sets of successively refined grids having a uniform grid refinement ratio of $\sqrt{2}$, using the second finest grid set for the far and propeller sub-domains. Table 4 shows the number of cells in the PBCF sub-domain and the relative changes in K_T and K_Q of the fins between different grid sets. Again, it is obvious that the thrust and torque on the PBCFs converge as the grids are refined, and the differences are less than 0.1% between the finest ($i=1$) and the second finest ($i=2$) grid sets. Similarly, the second finest grid set ($i=2$) is chosen for the PBCF sub-domain in the following simulations.

Table 3: Convergence of propeller thrust and torque with the grid size in far and propeller sub-domains.

| i | Number of cells (Million) | K_T | $\frac{(K_T)_i}{(K_T)_{i-1}} - 1$ | $10K_Q$ | $\frac{(K_Q)_i}{(K_Q)_{i-1}} - 1$ | η | $\frac{\eta_i}{\eta_{i-1}} - 1$ |
|-----|---------------------------|--------|-----------------------------------|---------|-----------------------------------|--------|---------------------------------|
| 1 | 11.93 | 0.1972 | | 0.4137 | | 0.6745 | |
| 2 | 5.70 | 0.1973 | 0.07% | 0.4140 | 0.08% | 0.6744 | -0.01% |
| 3 | 3.26 | 0.1976 | 0.13% | 0.4150 | 0.24% | 0.6737 | -0.10% |
| 4 | 1.86 | 0.1979 | 0.16% | 0.4161 | 0.27% | 0.6730 | -0.11% |

Table 4: Convergence of fin thrust and torque with the grid size in PBCF sub-domain.

| i | Number of cells (Million) | K_T | $\frac{(K_T)_i}{(K_T)_{i-1}} - 1$ | $10K_Q$ | $\frac{(K_Q)_i}{(K_Q)_{i-1}} - 1$ |
|-----|---------------------------|-----------|-----------------------------------|-----------|-----------------------------------|
| 1 | 2.53 | -0.005078 | | -0.007638 | |
| 2 | 1.34 | -0.005074 | -0.08% | -0.007633 | -0.06% |
| 3 | 0.73 | -0.005090 | 0.32% | -0.007648 | 0.20% |
| 4 | 0.46 | -0.005123 | 0.64% | -0.007691 | 0.57% |

3 EFFECTS OF SECTION GEOMETRY AT MODEL-SCALE

3.1 Selection of section geometry and analytical method

To investigate the effect of section geometry on the energy-saving rate of the PBCFs, systematically varied section profiles are adopted for the PBCFs. In this paper, we choose the S-shaped airfoil profile ‘NACA M7’ (abbreviated as ‘M7’ hereinafter) as the baseline of the fins, of which the maximum camber ratio, f_{max}/c , is -0.05 and the maximum camber ratio, t_{max}/c , is 0.0619. It is noted that the fins are cambered towards the face side, as they experience a negative angle of attack. Three camber lines, named respectively as ‘mod1’,

‘mod2’, and ‘mod3’, are generated using based on the baseline ‘M7’. When the camber line is normalized with the maximum camber, they have the same camber distribution. The f_{max}/c of ‘mod1’, ‘mod2’ and ‘mod3’ is 0.025, 0.035, and 0.08 respectively. The camber line ‘mod4’ has the same f_{max}/c as the baseline (which is 0.05), while its S-shaped tail is more curved. The camber line ‘flat’ denotes the flat plate. Figure 5 illustrates the above-mentioned camber lines, where the y coordinate has been magnified tenfold. Two types of thickness distributions are adopted including that of the baseline and the flat plate, named as ‘M7’ and ‘flat’ respectively. The maximum thickness of the fins is 1.5mm. According to different combinations of camber lines and thickness distributions, twelve types of the PBCFs are generated, named by A-B, where ‘A’ denotes the camber line type and ‘B’ denotes the thickness distribution. The edges and corners of the PBCFs with thickness distributions of ‘flat’ are rounded.

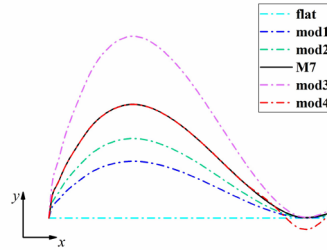


Figure 5: Schematic of systematically varied camber lines.

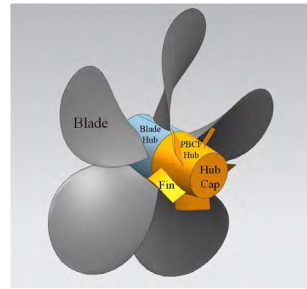


Figure 6: Definition of each part of the propeller and PBCFs.

To investigate the interactions between the propeller, the boss, and the PBCFs in detail, the hydrodynamic forces on the various parts as marked out in Figure 6 are analyzed. The thrust and torque coefficients are decomposed as

$$\left. \begin{aligned} K_T &= K_T^B + K_T^F + K_T^{BH} + K_T^{FH} + K_T^C \\ K_Q &= K_Q^B + K_Q^F \end{aligned} \right\} \quad (1)$$

where superscript B , F , BH , FH and C denote the blade, fin, blade hub, fin hub and hub cap, respectively. The relative changes in thrust and torque coefficients are defined as

$$\left. \begin{aligned} \Delta K_T &= \frac{K'_T - K_T}{K_T} \\ \Delta K_Q &= \frac{K'_Q - K_Q}{K_Q} \end{aligned} \right\} \quad (2)$$

where K'_T and K'_Q denote the thrust and torque coefficients of the propeller with PBCFs, and

K_T and K_Q denote the thrust and torque coefficients of the propeller without PBCFs.

The energy-saving rate is defined as

$$\Delta\eta = \frac{\eta' - \eta}{\eta} \quad (3)$$

where η' denotes the efficiency of the propeller with PBCFs and η denotes the efficiency of the propeller without PBCFs.

3.2 Analysis of PBCF's energy-saving mechanism

Table 5 and Table 6 show the model-scale CFD simulation results of the gains in K_T , K_Q and η for the DTMB 4381 propeller fitted with the PBCFs having different section geometries. The differences in $\Delta\eta$ between Table 5 and Table 6 indicate that thickness distribution of 'M7' performs better in energy-saving effect than the 'flat' thickness distribution. As seen in Figure 7, flow separation occurs near the leading edge of the PBCF with 'flat-flat' camber and thickness distributions, but it does not occur in the case of 'mod1-M7'. Consequently, the fin drags ΔK_T^F with the 'flat' thickness distribution in Table 6 are all larger than those with the 'M7' thickness in Table 5. Comparing the $\Delta\eta$ with different fin section geometries, it is found that appropriate camber lines for both 'M7' and 'flat' thickness distributions can further improve the energy-saving rate. The camber ratios 0.025 and 0.035 are the most suitable for the S-shaped camber line while larger camber ratio 0.08 has relatively poor performance on the energy-saving rate. The larger camber ratio generates higher lift and drag, so that both thrust and torque of the PBCFs increase. Because the thrust in 'mod4-M7' case occupies larger proportion than torque, the energy saving performance of the PBCF in that case is not so good. And compared with 'M7-M7' and 'mod4-M7' PBCFs, the modification of S-shaped tail has no obvious influence on the energy-saving rate.

In order to analyze the flow fields with different PBCFs, circumferentially averaged velocity profiles at different axial stations are shown in Figure 8, where V_a and V_t denote respectively the axial and tangential flow velocities, and V denotes the advance speed. As seen in Figure 8(a), the axial flow slows down a little due to the blockage effect of PBCFs, which results in the increases in K_T^B and K_Q^B . A significant decrease in the tangential induced velocity and a slight decrease in the axial velocity within range of the fin and hub cap can be seen in Figure 8(b). The decrease in tangential velocity in the wake means the hub vortex behind the hub cap is greatly eliminated, as seen in Figure 9. Because of the elimination of hub vortex, the pressure resistance on the hub cap is reduced, as K_T^C greatly increases. However, the energy-saving rate of 'mod3-M7' case is the lowest, although the induced velocities in that case are lower than in other cases, which seems to suggest that the energy-saving effect cannot be evaluated only by the reduction in the tangential induced velocities in the slipstream.

Table 5: CFD results of PBCFs with thickness distributions of ‘M7’ for the propeller at model-scale.

| Relative value (%) | flat-M7 | mod1-M7 | mod2-M7 | M7-M7 | mod3-M7 | mod4-M7 |
|--------------------|---------|---------|---------|-------|---------|---------|
| ΔK_T^B | 0.61 | 0.61 | 0.61 | 0.63 | 0.72 | 0.62 |
| ΔK_T^F | -2.43 | -2.46 | -2.53 | -2.65 | -3.10 | -2.58 |
| ΔK_T^{BH} | 0.01 | 0.01 | 0.01 | 0.01 | 0.01 | 0.01 |
| ΔK_T^{FH} | 0.19 | 0.22 | 0.23 | 0.24 | 0.25 | 0.24 |
| ΔK_T^C | 2.75 | 2.78 | 2.80 | 2.80 | 2.84 | 2.81 |
| ΔK_T | 1.13 | 1.16 | 1.13 | 1.03 | 0.71 | 1.09 |
| ΔK_Q^B | 0.27 | 0.26 | 0.25 | 0.25 | 0.30 | 0.25 |
| ΔK_Q^F | -1.72 | -1.80 | -1.82 | -1.84 | -1.94 | -1.78 |
| ΔK_Q | -1.45 | -1.54 | -1.57 | -1.59 | -1.64 | -1.53 |
| $\Delta \eta$ | 2.62 | 2.75 | 2.74 | 2.66 | 2.39 | 2.66 |

Table 6: CFD results of PBCFs with thickness distributions of ‘flat’ for the propeller at model-scale.

| Relative value (%) | flat-flat | mod1-flat | mod2-flat | M7-flat | mod3-flat | mod4-flat |
|--------------------|-----------|-----------|-----------|---------|-----------|-----------|
| ΔK_T^B | 0.64 | 0.65 | 0.66 | 0.70 | 0.75 | 0.71 |
| ΔK_T^F | -2.63 | -2.74 | -2.79 | -2.90 | -3.25 | -3.00 |
| ΔK_T^{BH} | 0.01 | 0.01 | 0.01 | 0.01 | 0.01 | 0.01 |
| ΔK_T^{FH} | 0.19 | 0.21 | 0.22 | 0.23 | 0.25 | 0.24 |
| ΔK_T^C | 2.77 | 2.79 | 2.79 | 2.84 | 2.85 | 2.83 |
| ΔK_T | 0.97 | 0.91 | 0.88 | 0.88 | 0.61 | 0.78 |
| ΔK_Q^B | 0.27 | 0.27 | 0.27 | 0.30 | 0.31 | 0.29 |
| ΔK_Q^F | -1.63 | -1.76 | -1.78 | -1.84 | -1.90 | -1.86 |
| ΔK_Q | -1.35 | -1.49 | -1.51 | -1.54 | -1.59 | -1.57 |
| $\Delta \eta$ | 2.36 | 2.44 | 2.43 | 2.46 | 2.24 | 2.38 |

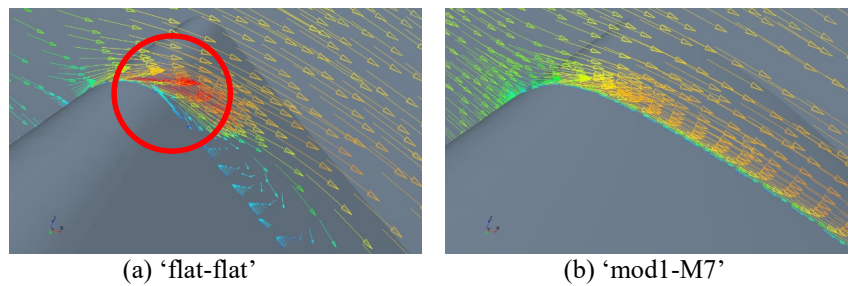
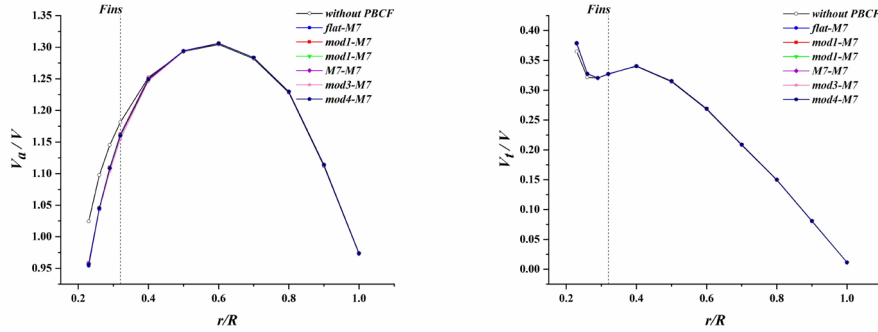
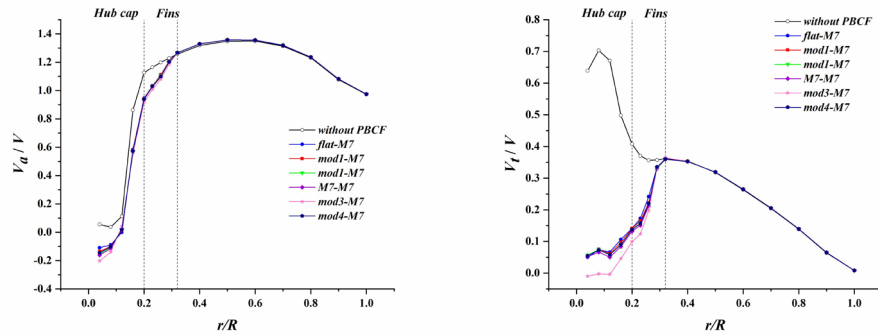


Figure 7: Relative flow velocities around the mid-span section of the PBCFs at model scale.



(a) At the station in the middle of propeller and PBCF,



(b) $0.02D$ downstream from the end of the hub cap,

Figure 8: Radial distributions of circumferentially averaged velocities, axial component (left) and tangential component (right).

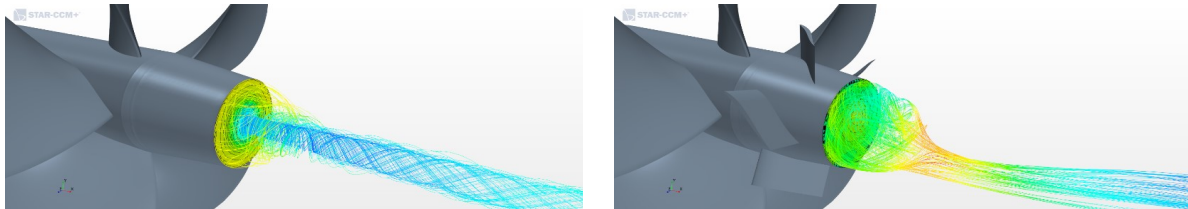


Figure 9: Streamlines behind the hub cap without PBCF and with ‘mod1-M7’ PBCF.

4 SCALE EFFECT

Tables 7 and 8 show the CFD simulation results of the components of PBCFs with different section geometries at full scale. Comparing the model- and full-scale open water performances of the propeller and PBCFs in Tables 5 through 8, the full-scale $\Delta\eta$ for all the PBCFs at the design point are 0.13%~0.35% higher than corresponding model-scale results. The conclusion about geometry effect drawn at model-scale also applies to full-scale, the appropriate camber ratio can improve the performance of PBCF and camber line ‘mod1’ is the most effective. In addition, different section profile has different scale effect, where the energy-saving rate with the thickness distribution of ‘flat’ has a higher increase than ‘M7’ at full-scale. As it can be seen, the energy-saving rate of PBCFs with ‘flat-flat’ and ‘flat-M7’ are almost equal at full-scale. The negative thrust of PBCFs with thickness distribution of ‘flat’

increase not as much as ‘M7’, because the flow separation in ‘flat’ cases at model-scale disappear at full-scale due to fully developed turbulent flow, as seen in Figure 10. The distinctions of the scale effects are mainly in hydrodynamic performance of the fins. Both thrust and torque of the fins increase at full-scale, while torque contributes more to the efficiency improvement. To better understand scale effects in Reynolds number, the open water performances of the propeller and typical PBCFs are divided into pressure and viscous components in Table 9. The scale effect on both thrust and torque of fins can mainly attribute to pressure components partly as a result of reduced boundary layer thickness on full-scale fin surfaces ^[13].

Table 7: CFD results of PBCFs with thickness distributions of ‘M7’ for the propeller at full-scale.

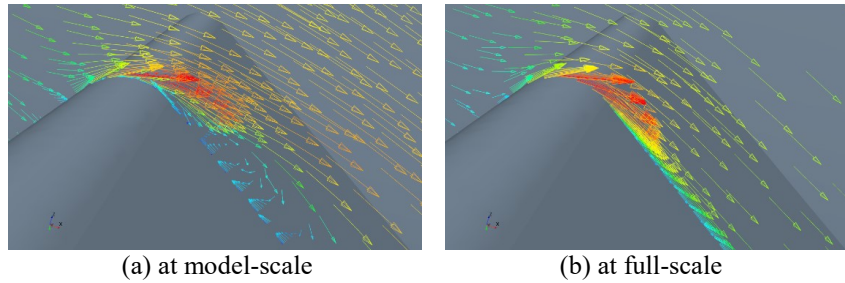
| Relative value (%) | flat-M7 | mod1-M7 | mod2-M7 | M7-M7 | mod3-M7 | mod4-M7 |
|--------------------|---------|---------|---------|-------|---------|---------|
| ΔK_T^B | 0.70 | 0.68 | 0.68 | 0.73 | 0.79 | 0.69 |
| ΔK_T^F | -2.66 | -2.69 | -2.76 | -2.86 | -2.29 | -2.68 |
| ΔK_T^{BH} | 0.00 | 0.00 | 0.00 | 0.00 | 0.00 | 0.00 |
| ΔK_T^{FH} | 0.22 | 0.25 | 0.25 | 0.26 | 0.28 | 0.26 |
| ΔK_T^C | 2.67 | 2.71 | 2.70 | 2.71 | 2.76 | 2.71 |
| ΔK_T | 0.93 | 0.95 | 0.87 | 0.84 | 0.64 | 0.98 |
| ΔK_Q^B | 0.34 | 0.31 | 0.31 | 0.35 | 0.37 | 0.32 |
| ΔK_Q^F | -2.11 | -2.22 | -2.26 | -2.27 | -2.26 | -2.13 |
| ΔK_Q | -1.77 | -1.91 | -1.95 | -1.92 | -1.89 | -1.81 |
| $\Delta \eta$ | 2.75 | 2.92 | 2.88 | 2.82 | 2.57 | 2.84 |

Table 8: CFD results of PBCFs with thickness distributions of ‘flat’ for the propeller at full-scale.

| Relative value (%) | flat-flat | mod1-flat | mod2-flat | M7-flat | mod3-flat | mod4-flat |
|--------------------|-----------|-----------|-----------|---------|-----------|-----------|
| ΔK_T^B | 0.64 | 0.70 | 0.71 | 0.76 | 0.78 | 0.72 |
| ΔK_T^F | -2.49 | -2.70 | -2.79 | -2.86 | -3.13 | -2.83 |
| ΔK_T^{BH} | 0.00 | 0.00 | 0.00 | 0.00 | 0.00 | 0.00 |
| ΔK_T^{FH} | 0.23 | 0.24 | 0.25 | 0.27 | 0.28 | 0.26 |
| ΔK_T^C | 2.66 | 2.69 | 2.69 | 2.77 | 2.79 | 2.71 |
| ΔK_T | 1.04 | 0.93 | 0.87 | 0.93 | 0.73 | 0.85 |
| ΔK_Q^B | 0.30 | 0.33 | 0.33 | 0.36 | 0.36 | 0.33 |
| ΔK_Q^F | -1.92 | -2.04 | -2.10 | -2.13 | -2.17 | -2.05 |
| ΔK_Q | -1.62 | -1.71 | -1.76 | -1.77 | -1.81 | -1.71 |
| $\Delta \eta$ | 2.71 | 2.69 | 2.68 | 2.75 | 2.58 | 2.61 |

Table 9: Pressure and viscous components of the effect of PBCFs for the propeller.

| Relative value (%) | Model-scale | | | | Full-scale | | | |
|--------------------|-------------|---------|----------|---------|------------|---------|----------|---------|
| | flat-flat | | mod1-M7 | | flat-flat | | mod1-M7 | |
| | pressure | viscous | pressure | viscous | pressure | viscous | pressure | viscous |
| ΔK_T^B | 0.63 | 0.01 | 0.60 | 0.01 | 0.64 | 0.00 | 0.67 | 0.00 |
| ΔK_T^F | -2.54 | -0.10 | -2.35 | -0.11 | -2.44 | -0.05 | -2.64 | -0.05 |
| ΔK_T^{BH} | 0.00 | 0.01 | 0.00 | 0.01 | 0.00 | 0.00 | 0.00 | 0.00 |
| ΔK_T^{FH} | 0.17 | 0.02 | 0.20 | 0.02 | 0.22 | 0.01 | 0.24 | 0.01 |
| ΔK_T^C | 2.77 | 0.00 | 2.78 | 0.00 | 2.66 | 0.00 | 2.71 | 0.00 |
| ΔK_Q^B | 0.28 | -0.01 | 0.27 | -0.01 | 0.30 | 0.00 | 0.31 | 0.00 |
| ΔK_Q^F | -1.68 | 0.03 | -1.87 | 0.04 | -1.94 | 0.02 | -2.24 | 0.02 |


Figure 10: Relative velocity vectors on the 0.5d section of the 'flat-flat' PBCF

5 CONCLUSIONS

Based on the RANS simulations, the effects of section geometry and model/full scale correlation of the PBCF have been numerically studied. A grid convergence study was carried out first by changing the grid sizes separately enclosing the propeller and PBCFs to determine appropriate grid sizes. By analyzing the hydrodynamic performances of each part of the propeller and PBCFs with different section profiles at model-scale, the PBCFs with modified 'NACA M7' section geometry showed a better energy-saving performance than the flat plate section. It is found that the S-shaped camber line with an appropriate camber ratio could further improve the energy-saving rate. The flow field characteristic of PBCFs also inferred that the energy saving effect cannot be evaluated only by the velocity reduction in the wake field.

The hydrodynamic performances at model- and full-scale were investigated using typical PBCF geometries. High Reynolds number had the positive influence on the energy-saving effect for all the PBCFs. The section geometry effect at model-scale also agreed with that at full-scale. From the viscous CFD results, PBCFs with different section geometries had different scale effects, which suggests that the design of ESDs should be carried out at full-scale condition when it is possible. Future studies will take the presence of the wake of the hull into consideration at full-scale and more effective section geometry for the PBCFs will be exploited.

REFERENCES

- [1] MEPC. The Marine Environment Protection Committee Resolution. (2011).
- [2] Ouchi, K.; Ogura, M.; Kono, Y.; Orito, H.; Shiotsu, T.; Tamashima, M. and Koizuka, H. A research and development of PBCF (propeller boss cap fins). *Journal of the Society of Naval Architects of Japan* (1988) **163**:66-78.
- [3] Kai, H.; Bito, S. and Miura, Y. Study on clarification of hydrodynamic mechanisms of PBCF by CFD. *Journal of the Japan Society of Naval Architects and Ocean Engineers* (2009) **12(10)**:37-47.
- [4] Li, P.C.; Zhou, W.X. and Dong S.T. A design method of propeller boss cap fins (PBCF). *China Shipbuilding* (2014) **55(01)**:19-27.
- [5] Mizzi, K.; Demirel, Y.K.; Banks, C.; Turan, O.; Kaklis, P. and Atlar, M. Design optimisation of propeller boss cap fins for enhanced propeller performance. *Applied Ocean Research* (2017) **62**:210-222.
- [6] Seo, J.; Lee, S.J.; Han, B. and Rhee, S.H. Influence of design parameter variations for Propeller-Boss-Cap-Fins on hub vortex reduction. *Journal of Ship Research* (2016) **60(4)**:203-218.
- [7] Lim, S.S.; Kim, T.W.; Lee, D.M.; Kang, C.G. and Kim, S.Y. Parametric study of propeller boss cap fins for container ships. *International Journal of Naval Architecture and Ocean Engineering* (2014) **6(2)**:187-205.
- [8] Nojiri, T.; Ishii, N. and Kai, H. Energy saving technology of propeller boss cap fins (PBCF) and its evolution. *J JIME* (2011) **46(3)**:350-358.
- [9] Hansen, H.R.; Dinham-Peren, T. and Nojiri, T. Model and full scale evaluation of a 'propeller boss cap fins' device fitted to an Aframax tanker. In Second International Symposium on Marine Propulsors, smp'11, Hamburg, Germany (2011)
- [10] Kawamura, T.; Ouchi, K. and Nojiri, T. Model and full scale CFD analysis of propeller boss cap fins (PBCF). *Journal of marine science and technology* (2012) **17(4)**: 469-480.
- [11] Morgut, M. and Nobile, E. Influence of grid type and turbulence model on the numerical prediction of the flow around marine propellers working in uniform inflow. *Ocean Engineering* (2012) **42**:26-34.
- [12] Kerwin, J.E. and Lee, C.S. Prediction of steady and unsteady marine propeller performance by numerical lifting-surface theory. *Sname Transactions* (1978) **86**:1-30.
- [13] Dong, X.Q.; Li, W.; Yang, C.J. and Noblesse, F. RANSE-based Simulation and Analysis of Scale Effects on Open-Water Performance of the PPTC-II Benchmark Propeller. *Journal of Ocean Engineering and Science* (2018) **3(3)**:186-204.

NUMERICAL FRICTION LINES FOR CFD BASED FORM FACTOR DETERMINATION

Kadir B. Korkmaz^{*†}, Sofia Werner[†] and Rickard Bensow^{*}

^{*} Department of Mechanics and Maritime Sciences
Chalmers University of Technology
Chalmersplatsen 4, 412 96 Göteborg, Sweden
e-mail: korkmaz@chalmers.se
e-mail: rickard.bensow@chalmers.se

[†] SSPA Sweden AB
Chalmers Tvärgata 10, 412 58 Göteborg, Sweden
email: sofia.werner@sspa.se - Web page: www.sspa.se

Key words: Friction resistance coefficient, form factor, numerical uncertainty, flat plate

Abstract. In this study, frictional resistance coefficients of an infinitely thin 2D plate have been computed at 14 Reynolds numbers (between $\log_{10}(Rn) = 6.25$ to 9.5) in sets of five geometrically similar structured grids in order to perform reliable grid dependence studies. Additional grid dependency studies have been performed by using 5 sets of grids which have the same number of cells in all directions but varying first cell sizes normal to the flat plate at $\log_{10}(Rn) = 6.25$. Average y^+ values for each grid set for the finest grid varies between 0.0075 and 0.5 (from set 1 to 5 respectively) while none of the simulations exceeded average y^+ value of 1. All simulations were performed with the direct application of the no-slip condition at walls. Therefore, no wall functions were used. Two turbulence models have been used for the investigations: $k - \omega$ SST and EASM. Extensive grid dependence studies have been performed with two different CFD codes SHIPFLOW and FINETM/MARINE, using the same grids. Special attention was paid to the transition from laminar to turbulent flow at the lowest Reynolds number since laminar part can cover a significant part of the plate. At $\log_{10}(Rn) = 6.25$ for both CFD codes, laminar flow and transition to turbulent flow was distinctive even though no transition models were applied. Significant dependency on y^+ has been observed with FINETM/MARINE on friction resistance coefficient. On the other hand, SHIPFLOW exhibited less sensitivity to the first cell size variation, hence, revealed smaller numerical uncertainties in general. To ensure a numerical uncertainty of frictional resistance component below 1%, average $y^+ < 0.016$ have been used for generating the data points of friction line with SHIPFLOW for each turbulence model. Data points of 14 Reynolds number have been transformed into numerical friction lines by applying curve fits. Obtained friction lines are compared with ITTC57 line, Schoenherr, Hughes, Toki, Katsui, Grigson lines and two numerical friction lines.

1 INTRODUCTION

The friction line, i.e. the dependency of flat plate frictional resistance coefficients on Reynolds number, is used in the 1978 ITTC method for scaling of ship resistance measured in a towing tank. The 1978 ITTC method adopted the form factor concept as described by Hughes

in [1], where the viscous resistance is expressed in relation to the “ITTC 57 model-ship correlation line” as shown in the following equation:

$$C_V = (1 + k)C_F \quad (1)$$

where k is the form factor and C_F is the friction resistance coefficient. The form factor concept, as well as the determination method proposed by Prohaska [2] has been questioned and investigated for many decades. The scale effects on form factor has been well demonstrated by García-Gómez [3], Toki [4] and Van et al. [5] using geosim test data analysis. In addition to the re-analysis of the geosim test data, CFD studies by Raven et al. [6] and Wang et al. [7] supported the existence of substantial scale effects on form factor and the main cause of the scale effects have been found to be the “ITTC 57 model-ship correlation line” rather than the original hypothesis of Hughes which suggested the form factor is independent of the Reynolds number. Additionally, when the growing disposition to leave the Prohaska’s method of form factor determination and growing confidence in numerical resistance calculations are considered, CFD might be able to provide a new method of form factor determination, which can increase the accuracy of the full-scale resistance predictions.

In this study, numerical friction lines have been investigated and two numerical friction lines have been derived with k - ω SST and EASM turbulence models. Grid dependency studies have been performed with SHIPFLOW and FINE™/MARINE codes in order to highlight the aspects that influence the skin friction coefficient, such as the effect of non-dimensional wall distance (y^+), turbulence intensity and transition from laminar to turbulent flow. The study is part of a larger research scope with the goal of recommending suitable procedures for using CFD to derive the form factor and the full scale ship resistance based on towing tank test.

2 FLOW SOLVERS, COMPUTATIONAL DOMAIN, BOUNDARY CONDITIONS AND GRIDS

2.1 Flow Solvers

Two CFD codes have been used for this study: SHIPFLOW 6.3 and FINE™/MARINE 7.2. Starting with the former, XCHAP is the solver of SHIPFLOW which solves the Reynolds averaged Navier-Stokes (RANS) equations with a finite volume method. EASM, as described in [8], and k - ω SST, of [9], turbulence models are available. The convective terms are discretized with a Roe scheme which is first order accurate. Therefore, in order to increase the accuracy a flux correction is applied explicitly. The equations are solved with Krylov solver (adopted from PETSc) which implements the Generalized Minimal Residual method (KSPGMRES). Note that results from SHIPFLOW will be referred as “SF” in the plots in order to save space.

ISIS-CFD is the flow solver of FINE™/MARINE. The solver is based on Finite volume method and incompressible unsteady Reynolds-averaged Navier Stokes equations are solved. There is no specific requirements on the topology of cells since the face-based method is used. The discretisation of the convective fluxes in both the momentum equations and the equations for turbulence modelling have been performed with AVLSMART scheme for this study. Among many turbulence models available in FINE™/MARINE, EASM, described in [8], and k - ω SST, of [9], turbulence models have been selected. Note that results from FINE™/MARINE will be referred as “FM” in the plots.

2.2 Computational Domain

The computational domain size is based on the requirements of XCHAP and ISIS-CFD solvers. The domain is shaped as a rectangular prism since a 3D domain is required by the solvers. Size of the domain has been determined by the preliminary computations carried out at $\log_{10}(Rn) = 6.25$ with two alternative domains. The flat plate have a length of L . The first domain has the inlet located $0.25L$ upstream of the leading edge, the outlet is placed $0.25L$ downstream of the trailing edge, side boundary located $0.25L$ away from the flat plate in the normal direction. The second domain (Dm2) has been designed with double the distance of the inlet, outlet and side boundaries ($0.5L$). The height of the domain is $1L$ for both domains since the flow is 2D and height has no effect on the results.

Table 1 Comparison of influence of domain size on the computed prediction of the friction resistance

| | EASM | | EASM | | $k - \omega$ SST | | $k - \omega$ SST | |
|------------------|------------|------|------------------------------|------|------------------|------|------------------------------|------|
| | (SHIPFLOW) | | (FINE TM /MARINE) | | (SHIPFLOW) | | (FINE TM /MARINE) | |
| | g1 | g5 | g1 | g5 | g1 | g5 | g1 | g5 |
| $\Delta C_F(\%)$ | -0.6 | -0.6 | -0.6 | -0.7 | -0.6 | -0.6 | -0.6 | -0.6 |
| $U(C_F)(\%)$ | | | | | | | | |
| Dm1 | 0.08 | 0.29 | 0.13 | 0.37 | 0.18 | 0.69 | 0.09 | 0.32 |
| Dm2 | 0.08 | 0.28 | 0.10 | 0.36 | 0.17 | 0.63 | 0.10 | 0.35 |

The differences between the frictional resistance coefficients for the two domain sizes, $\Delta C_F(\%) = 100 \times (C_F(Dm2) - C_F(Dm1))/C_F(D1)$, together with obtained numerical uncertainties, $U(C_F)$, for the finest grid are presented in Table 1. The differences in C_F between the two domains are larger than the numerical uncertainties (presented in Section 3), opposed to what was observed by Eça and Hoekstra [10]. The investigations have indicated that the difference might originate from the dissipated turbulent kinetic energy between the inlet boundary and the flat plate. As it will be more thoroughly discussed in the Section 2.4, larger domain (Dm2) seems to act as a flow with lower turbulence intensity which results in slightly delayed transition from laminar to turbulent flow and lower friction resistance in the turbulent region. In order to confirm this argument, additional simulations have been performed with Dm2 domain at $\log_{10}(Rn) = 8.00$. The difference of C_F has been reduced to the numerical uncertainty levels as at such high Reynolds numbers turbulence intensity is not expected to have substantial impact. In the light of these findings the initial domain, Dm1, has been chosen for the further computations.

2.3 Boundary Conditions

The inlet boundary conditions are fixed uniform velocity (U_∞) and specific turbulent dissipation rate, ω , at the inlet is calculated by $(\omega)_{inlet} = \lambda U_\infty/L$. The default values of the factor of proportionality, λ , are set to $\lambda = 1$ for FINETM/MARINE and $\lambda = 10$ for SHIPFLOW. The turbulent kinetic energy at the inlet is defined as $(k)_{inlet} = \mu \omega_{inlet} C_i / \rho$ where μ and ρ are dynamic viscosity and density respectively. FINETM/MARINE assumes the value of the constant $C_i = 1 \times 10^{-3}$ while SHIPFLOW adopted $C_i = 1 \times 10^{-4}$. As a result, both codes have the same turbulence intensity at the inlet. The outlet boundary condition of both codes consists of Neumann boundary condition that sets the gradient of velocity, k and pressure to zero,

normal to the outflow plane. Slip condition simulates a symmetry condition by setting the normal velocity and normal gradient of other variables to zero. Noslip condition specifies the velocities components, k and normal pressure component as zero at the wall. ω on the wall is specified differently by both codes. For FINE™/MARINE, $\omega_w = 10 \times (6\mu/0.075\rho d^2)$ where d is the distance of the first cell away from the wall. SHIPFLOW defines the wall value of ω of a smooth surface as $\omega_w = (u_\tau^2/\nu) \times (50/4.3y^{+0.85})^2$ as introduced in [11] where u_τ is the frictional resistance and ν is the kinematic viscosity. All simulations have been performed with the direct application of the no-slip condition at walls. Therefore, no wall functions were used.

2.4 Local skin friction coefficient and transition from laminar to turbulent flow

Local skin friction coefficients have been investigated in order to assess the behaviour of turbulence models in transition from laminar to turbulent flow. The local skin friction coefficient has been defined as:

$$C_f = \frac{\mu \left(\frac{\partial u_x}{\partial y} \right)_{y=0}}{\frac{1}{2} \rho U_\infty L} \quad (2)$$

At the typical Rn that towing tank model tests are normally performed, transition is considered to be important. As indicated by Eça et al. [10], the natural transition in the boundary layer of a flat plate occurs approximately at $Re_x = 10^6$. However, the transition can occur earlier if the turbulence intensity is increased. In this study, no transition models have been used as the aim is to determine the behaviour of the regular turbulence models readily available in both SHIPFLOW and FINE™/MARINE.

The calculated skin friction coefficients from SHIPFLOW and FINE™/MARINE at $\log_{10}(Rn) = 6.25$ are presented in Figure 1 together with the ERCOFTAC Classic Database [12] where flat plate experiments with three different free-stream turbulence intensity ($0.009U_\infty^2$, $0.03U_\infty^2$ and $0.06U_\infty^2$) were performed. The turbulence intensity at the inlet boundary with SHIPFLOW and FINE™/MARINE are the same, $k_\infty \cong 5.6 \times 10^{-10}U_\infty^2$ for $\log_{10}(Rn) = 6.25$. The first significant observation is the laminar flow region where C_f of both turbulence models and CFD codes follow Blasius line until the transition to turbulent flow occurs. If laminar flow covers a significant part of the plate, the calculated skin friction coefficient will be smaller than a fully turbulent flow. However, both turbulence models and CFD solvers predicted the transition location approximately where the turbulence stimulators are usually fitted to towing tank ship models (5% of L_{pp} from fore perpendicular). The position of the transition is similar to ERCOFTAC experiments with 3% and 6% even though turbulence intensity in the computations are extremely smaller than the experiments. It is also significant that the transition shows qualitatively similar behaviour to the experiments with both $k - \omega$ SST and EASM turbulence models with both solvers. The laminar flow can be observed even at Rn numbers as high as $\log_{10}(Rn) = 9.5$ as presented in Figure 1 even though only a fraction of the flat plate ($\sim 0.003\%$) is covered with laminar flow. As can be seen from the Figure 1 (on the right), simulations at different Reynolds numbers show consistency in skin friction coefficient not only at the laminar region but also at the turbulent region. It should be noted that, the vertical lines occurs due to local increase of C_f at the trailing edge of the flat plate.

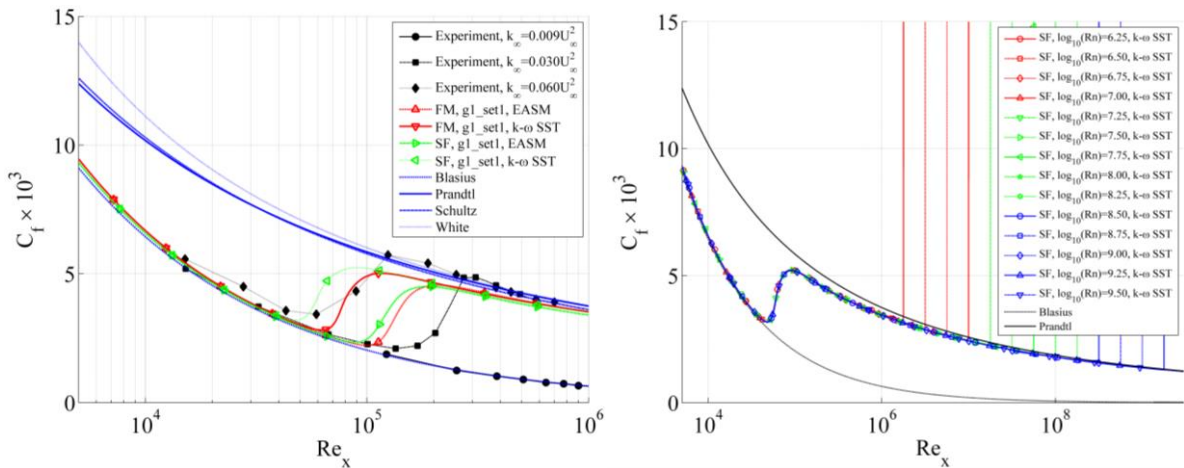


Figure 1 Skin friction coefficient C_f along the flat plate at $\log_{10}(Rn) = 6.25$ (on the left) and C_f along the flat plate at $\log_{10}(Rn) = 6.25$ to 9.5

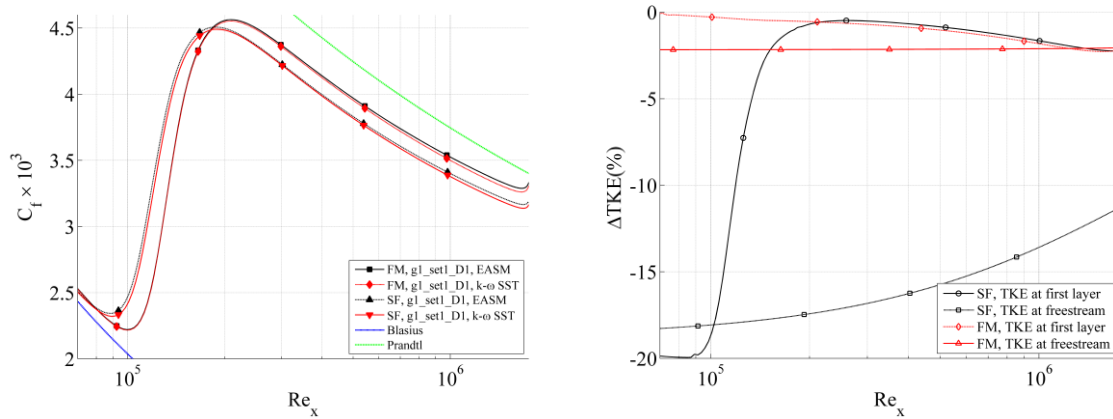


Figure 2 Influence of domain size on TKE and on the skin friction coefficient along the flat plate at $\log_{10}(Rn) = 6.25$. $\Delta TKE(\%) = 100 \times (TKE(Dm2) - TKE(Dm1))/TKE(Dm1)$

As mentioned previously, the increase of the domain size resulted in a reduction of C_f approximately 0.6% which is significantly larger than the numerical error for both codes. The investigations have shown that with a larger domain size (Dm2), the turbulent kinetic energy (TKE) dissipates more than with the smaller domain (Dm1). The difference of TKE between the domains has been calculated as $\Delta TKE(\%) = 100 \times (TKE(Dm2) - TKE(Dm1))/TKE(Dm1)$. As shown in Figure 2 (on the right), the freestream TKE levels are approximately -18.8% and -2.1% lower in Dm2 compared to Dm1 domain at the alignment in x-direction of the leading edge of the plate for SHIPFLOW and FINE™/MARINE respectively. The reason of such difference in TKE dissipation levels is explained by the different boundary condition of $(\omega)_{inlet}$ which is ten times larger in SHIPFLOW than FINE™/MARINE. TKE at the first layer away from the plate with Dm2 are also lower than Dm1 all over the Re_x range. As shown in Figure 2, the transition has been slightly delayed in SHIPFLOW simulation and the C_f values are lower with an increasing rate from the transition location (where TKE levels are similar in both domains around $Re_x = 2 \times 10^5$) to the trailing edge where C_f is approximately 0.8% lower in Dm2 than Dm1 case for both codes. This means that the domain size has an effect on the TKE that gives a non-negligible impact on the total skin friction.

2.5 Grid Sets

The discretization of the computational domain has been done by five sets (sets 1 to 5) of orthogonal stretched grids. Each set consists of five geometrically similar grids. Grid sets have the same number of cells along the x-direction and y-direction but differing in the first cell size perpendicular to the flat plate for the corresponding Reynolds number. The smallest first cell sizes in y-direction (yielding lowest y^+ values) are denoted as set1 and first cell sizes are gradually increased from set1 to set5 having the largest y^+ values. In all the grids, the number of cells along the plate makes $4/6$ of all the cells in x-direction, leaving $1/6$ of cells for upstream and downstream of the plate. The cells in the normal direction has been stretched with a one sided stretching function. The leading edge and trailing edges are also stretched in a similar fashion. The five geometrically similar grids of each set have been refined with grid refinement ratio of $h_i/h_1 = \sqrt{N_{cells_1}/N_{cells_i}}$. The number of cells corresponding to each grid and flow speed are presented in Table 2. In order to assure growth rate of the cells in y-direction (normal to the plate) remain in similar levels throughout the Rn range, three different mesh density have been used.

Table 2 Number of cells in each direction

| lo10Rn | g1 | | g2 | | g3 | | g4 | | g5 | |
|-----------|------|-----|------|-----|------|-----|------|-----|------|-----|
| | Nx | Ny | Nx | Ny | Nx | Ny | Nx | Ny | Nx | Ny |
| 6.25-7.0 | 1440 | 240 | 1260 | 210 | 1080 | 180 | 900 | 150 | 720 | 120 |
| 7.25-8.25 | 2160 | 360 | 1890 | 315 | 1620 | 270 | 1350 | 225 | 1080 | 180 |
| 8.5-9.5 | 2880 | 480 | 2520 | 420 | 2160 | 360 | 1800 | 300 | 1440 | 240 |

Table 3 Calculated $(y^+)_{mean}$ and $(y^+)_{max}$ values from SHIPFLOW at the first layer away from the flat plate for EASM turbulence model at $\log_{10}(Rn) = 6.25$

| | $(y^+)_{mean}$ | | | | | $(y^+)_{max}$ | | | | |
|----|----------------|-------|-------|-------|-------|---------------|------|------|------|------|
| | set1 | set2 | set3 | set4 | set5 | set1 | set2 | set3 | set4 | set5 |
| g1 | 0.008 | 0.057 | 0.105 | 0.238 | 0.448 | 0.09 | 0.53 | 0.90 | 1.73 | 2.66 |
| g2 | 0.009 | 0.065 | 0.120 | 0.272 | 0.512 | 0.10 | 0.59 | 1.00 | 1.88 | 2.88 |
| g3 | 0.010 | 0.076 | 0.140 | 0.318 | 0.598 | 0.11 | 0.66 | 1.12 | 2.08 | 3.15 |
| g4 | 0.012 | 0.091 | 0.167 | 0.381 | 0.719 | 0.13 | 0.76 | 1.27 | 2.33 | 3.50 |
| g5 | 0.016 | 0.113 | 0.209 | 0.477 | 0.900 | 0.15 | 0.90 | 1.48 | 2.66 | 3.96 |

The first layer cell size is varied with the same ratio (h_i/h_1) for each grid set. In Table 3, mean and maximum y^+ values for computations from SHIPFLOW at $\log_{10}(Rn) = 6.25$ have been presented. The y^+ values from FINETM/MARINE were almost identical to Table 3. All simulations have been performed with $(y^+)_{mean} < 1$ which is the widespread rule of thumb. The $(y^+)_{max}$ values exceeds the non-dimensional height of $y^+ = 1$ for set3 to set5, however, it is observed only at the very ends of leading and trailing edges of the plate. For a given Reynolds number (the speeds other than $\log_{10}(Rn) = 6.25$), first cells sizes has been adjusted so that similar $(y^+)_{mean}$ values are obtained as presented in Table 3.

It is important to note that SHIPFLOW solver does not have 2D flow option therefore 3 cells are added in the z-direction which is the only way they differ from the meshes used for FINETM/MARINE. To ensure FINETM/MARINE solver provides the same results for 2D and

3D meshes, several computations have been performed and no significant difference has been found. Therefore, 2D grids have been calculated with ISIS-CFD solver in order to save time and reduce the computational demand.

3 GRID DEPENDENCE STUDY

In order to assess the numerical uncertainty, grid dependence studies have been performed. All computations have been performed in double precision in order to eliminate the round-off errors. Additionally, iterative uncertainties have been predicted from the standard deviation of the force in percent of the average force over the last 10% iterations. Iterative uncertainty was kept below 0.01% for all simulations. Simulations at $\log_{10}(Rn) < 8$ exhibited even lower standard deviations of force (typically lower than 1×10^{-4}). Therefore, both iterative errors and round-off errors are assumed to be small enough to be neglected and numerical errors are dominated by the discretization errors. The procedure proposed in [13] have been adopted to predict the numerical uncertainties.

Table 4 Observed order of accuracy, p , for the flat plate at $\log_{10}(Rn) = 6.25$

| | SHIPFLOW | | | | | FINE™/MARINE | | | | |
|------------------|----------|------|------|------|------|--------------|------|------|------|------|
| | set1 | set2 | set3 | set4 | set5 | set1 | set2 | set3 | set4 | set5 |
| EASM | 1.9 | 1.9 | 1.6 | 1.1 | 1.5 | 1.5 | 1.4 | 1.2 | 0.9 | 0.6 |
| $k - \omega$ SST | 2 | 2 | 1.8 | 1.1 | 0.9 | 1.8 | 1.4 | 1.1 | 0.8 | 0.5 |

Table 5 Predicted numerical uncertainties, $U(C_F)$, for EASM turbulence model, in percentage

| | SHIPFLOW | | | | | FINE™/MARINE | | | | | |
|----|----------|------|------|------|------|--------------|------|------|------|------|------|
| | set1 | set2 | set3 | set4 | set5 | set1 | set2 | set3 | set4 | set5 | |
| g1 | 0.08 | 0.10 | 0.18 | 0.55 | 0.62 | g1 | 0.13 | 0.41 | 0.86 | 2.48 | 6.15 |
| g2 | 0.10 | 0.13 | 0.22 | 0.64 | 0.76 | g2 | 0.16 | 0.50 | 1.01 | 2.79 | 6.65 |
| g3 | 0.14 | 0.17 | 0.29 | 0.76 | 0.94 | g3 | 0.20 | 0.62 | 1.21 | 3.19 | 7.28 |
| g4 | 0.19 | 0.24 | 0.39 | 0.93 | 1.24 | g4 | 0.26 | 0.79 | 1.50 | 3.74 | 8.12 |
| g5 | 0.29 | 0.36 | 0.55 | 1.19 | 1.71 | g5 | 0.37 | 1.08 | 1.95 | 4.55 | 9.26 |

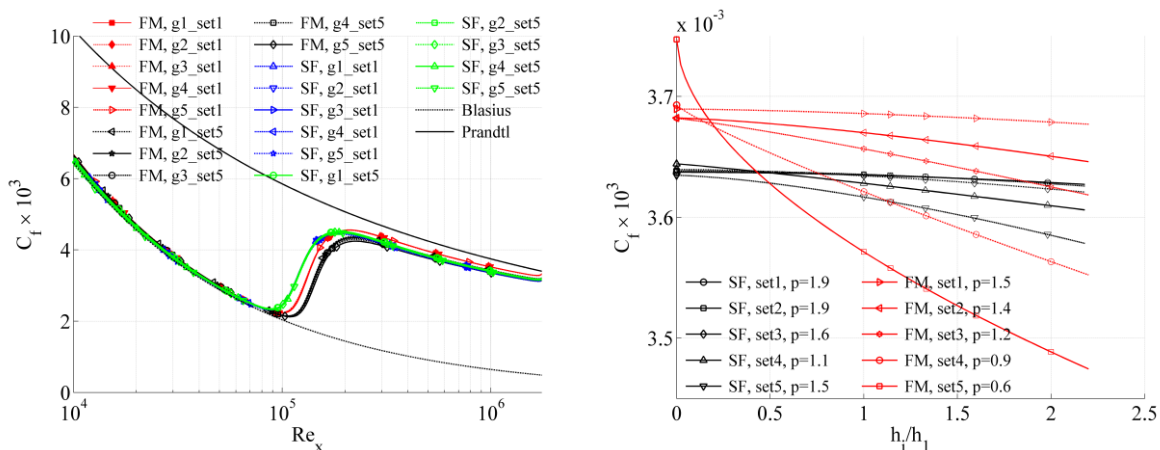


Figure 3 Influence of first cell size (set1 and set5) on the skin friction coefficient along the flat plate and convergence of friction coefficient C_F for SHIPFLOW and FINE™/MARINE at $\log_{10}(Rn) = 6.25$

The observed order of accuracies and numerical uncertainties for SHIPFLOW and FINETM/MARINE are presented in Table 4 and Table 5. The numerical uncertainties from $k-\omega$ SST model is slightly higher than EASM for all grid sets with FINETM/MARINE. However, predicted uncertainties on set 1 and set2 with $k-\omega$ SST are almost two times higher with SHIPFLOW. The ISIS-CFD solver have been found to be sensitive to near wall cell height compared to XCHAP solver since numerical uncertainties on the skin friction coefficient can be as high as 9% with $(y^+)_{\text{mean}}$ values around 0.9.

In order to explain the difference of $U(C_F)$ between the two solvers, the skin friction coefficient along the flat plate has been investigated. As presented in Figure 3, the grids belong to set1 and set5 has been plotted for SHIPFLOW and FINETM/MARINE. It is important to notice that C_f values from SHIPFLOW are consistent in set1 and set5 grids in the laminar region and transition location but differing marginally in the turbulent region. However, for FINETM/MARINE the C_f values are consistent in the laminar region but differing significantly between set1 and set 5 for the transition location also in the fully turbulent region (up to 5% difference in C_f). Sensitivity to y^+ can also be observed with convergence of C_f with the grid refinement presented for EASM model for both solvers in Figure 3. It is worth to recall that the number of cells corresponding to each h_i/h_1 value ($h_i/h_1 = 1$ being the finest grid) are identical. Considering the numerical uncertainties presented, it can be concluded that $(y^+)_{\text{mean}} \cong 1$ is not acceptable for any of the solvers and in order to attain $U(C_F)$ lower than 1%, $y^+ \cong 0.1$ should be used for $k-\omega$ SST and EASM turbulence models, as also concluded by Eça et al. [14].

Considering the outcomes of the grid dependence study performed at $\log_{10}(Rn) = 6.25$, the rest of the simulations have been performed with 5 geometrically similar grids per speed with y^+ values similar to the set1 presented in Table 3. Observed order of accuracies and predicted numerical uncertainties for the finest grids are presented in Table 6 and Table 7.

Table 6 Observed order of accuracy, p , of the friction resistance for SHIPFLOW

| | $\log_{10}(Rn)$ | | | | | | | | | | | | | |
|----------------|-----------------|-----|------|-----|------|-----|------|-----|------|-----|------|-----|------|-----|
| | 6.25 | 6.5 | 6.75 | 7 | 7.25 | 7.5 | 7.75 | 8 | 8.25 | 8.5 | 8.75 | 9 | 9.25 | 9.5 |
| EASM | 1.9 | 1.8 | 1.7 | 1.7 | 1.8 | 1.9 | 1.8 | 1.7 | 1.7 | 2 | 1.8 | 1.7 | | |
| $k-\omega$ SST | 2 | 2 | 2 | 2 | 2 | 2 | 1.2 | 2 | 2 | 2 | 2 | 2 | 2 | 2 |

Table 7 Predicted numerical uncertainties of the finest grids (g_1), of the friction resistance, $U(C_F)$, for SHIPFLOW, in percentage

| | $\log_{10}(Rn)$ | | | | | | | | | | | | | |
|----------------|-----------------|------|------|------|------|------|------|------|------|------|------|------|------|------|
| | 6.25 | 6.5 | 6.75 | 7 | 7.25 | 7.5 | 7.75 | 8 | 8.25 | 8.5 | 8.75 | 9 | 9.25 | 9.5 |
| EASM | 0.08 | 0.10 | 0.12 | 0.13 | 0.06 | 0.06 | 0.07 | 0.09 | 0.08 | 0.04 | 0.05 | 0.05 | | |
| $k-\omega$ SST | 0.18 | 0.21 | 0.25 | 0.29 | 0.10 | 0.11 | 0.14 | 0.14 | 0.15 | 0.04 | 0.09 | 0.08 | 0.08 | 0.05 |

4 NUMERICAL FRICTION LINE

The friction resistance coefficient C_F is obtained from the integration of the C_f along the flat plate. As explained earlier, C_F of 5 geometrically similar grids for 14 Reynolds number has been calculated with $k-\omega$ SST and EASM turbulence models with SHIPFLOW. The last two

speeds with EASM are omitted due to difficulties with convergence issues. As a result of performing the grid dependence study as explained by Eça and Hoekstra [13], the exact numerical solution of friction resistance coefficient at each Reynolds number have been calculated. The exact solutions or in other words grid independent results, are then used for the generation of numerical friction lines. Curve fits have been applied to data generated using the two alternative formulations. The first alternative is based on the ITTC 57 analytical formula

$$C_F^a = \frac{a_1^a}{(\log_{10}(Rn) - a_2^a)a_3^a} \quad (3)$$

The second alternative as adopted from [10] assumes that C_F can be expressed as a cubic polynomial in logarithmic scales

$$\log(C_F^c) = \log(a_1^c) + a_2^c \log(Rn) + a_3^c (\log Rn)^2 + a_4^c (\log Rn)^3 \quad (4)$$

Eq. 4 can be re-formulated as the following

$$C_F^c = a_1^c (Rn)^{(a_2^c + a_3^c \log(Rn) + a_4^c (\log Rn)^2)} \quad (5)$$

The three constants a_1^a , a_2^a and a_3^a of Eq. 3 and the four constants a_1^c , a_2^c , a_3^c and a_4^c of Eq. 5 have been determined with a non-linear least squares approach. In order to assess the quality of the fit, root-mean-square error (denoted as S) has been calculated by determining the degree of freedom by the difference between the number of data points and number of constraints. The constants and the standard deviations of the two equations have been presented in Table 8.

Table 8 Constants of the curve fits for of Eq. 3 and Eq. 5 to the friction coefficients of EASM and $k-\omega$ SST turbulence models

| | C_F^a | | | | C_F^c | | | | |
|------------------|---------|---------|---------|-------------------|---------------------|---------------------|---------------------|---------------------|-------------------|
| | a_1^a | a_2^a | a_3^a | $S^a \times 10^6$ | $a_1^c \times 10^2$ | $a_2^c \times 10^2$ | $a_3^c \times 10^3$ | $a_4^c \times 10^5$ | $S^c \times 10^6$ |
| EASM | 11.300 | -3.617 | 3.512 | 5.329 | 1.792 | -2.400 | -9.40 | 23.40 | 2.796 |
| $k - \omega$ SST | 0.612 | -0.592 | 2.638 | 2.383 | 10.810 | -30.75 | 5.81 | -3.96 | 1.627 |

The curve fits of Eq.3 and Eq.5 shows both very good agreement with the data. The differences between the two fits are graphically hard to assess since they are almost coinciding throughout the Rn range. However, the root-mean-square error indicates that Eq.5 is the better fit for both turbulence models. Therefore, Eq. 5 is adopted and compared to the other friction lines. Obtained numerical frictional lines for $k-\omega$ SST and EASM turbulence models have been compared with ITTC57 line [15], Schoenherr [16], Hughes [1], Toki [4], Katsui [17], Grigson [18] and two numerical friction lines proposed by Eça et al. [10] and Wang et al. [7]. Figure 4 presents the friction lines in a relative way because the visual judgement over the friction lines is difficult when presented many lines at a time. The differences between the friction lines are presented with respect to numerical friction derived from $k-\omega$ SST model of SHIPFLOW and calculated, i.e. $\Delta C_F(ITTC57) (\%) = 100 \times (C_F(ITTC57) - C_F(k - \omega SST)) / C_F(k - \omega SST)$. As can be seen from Figure 4, $k-\omega$ SST lines of Eça et al. [10] and Wang et al. [7] are very similar to $k-\omega$ SST line derived by SHIPFLOW in all Reynolds numbers. The spread among the numerical friction lines is much smaller than analytical friction lines in general. All numerical friction lines lead to lower C_F values than the analytical correlations (except Hughes line) at the lower Rn range but the gap is reduced around $\log_{10}(Rn) = 8.0$ and onwards. Existence of

laminar flow in the lowest Reynolds numbers for the numerical friction lines can be responsible for such behavior which should be investigated further.

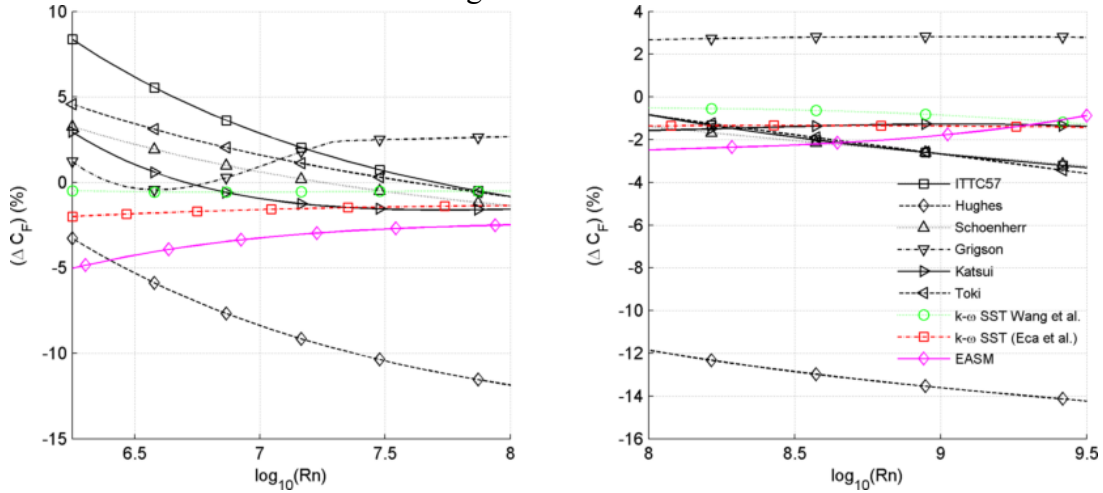


Figure 4 Friction lines in comparison to SHIPFLOW $k - \omega$ SST, in percentage

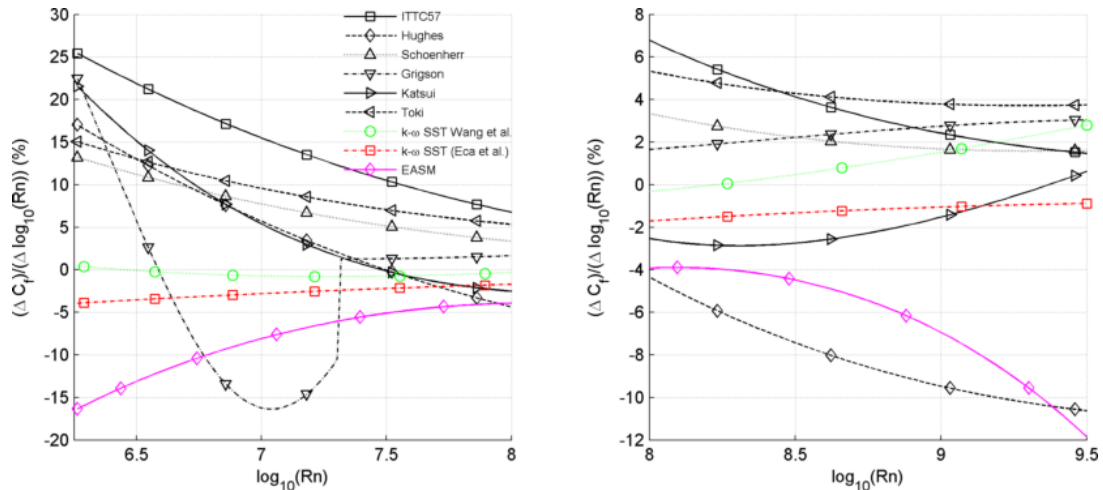


Figure 5 Derivative of the friction lines in comparison to SHIPFLOW $k - \omega$ SST, in percentage

The slope of the friction line is more important than the absolute values for the purpose of extrapolation. Therefore, the derivatives of the lines have been calculated and presented in Figure 5, again with respect to $k-\omega$ SST line of SHIPFLOW. The similarity of $k-\omega$ SST lines of Eça and Hoekstra [10] and Wang et al. [7] to the $k-\omega$ SST line derived from SHIPFLOW is remarkable. All numerical friction lines possess significantly lower slope at the lower range of Reynolds numbers, but this difference is reduced significantly at $Rn < 10^8$ except Hughes lines and the friction line derived from EASM turbulence model. The slope obtained with EASM is distinctively smaller at the both ends of the Reynolds numbers.

5 CONCLUSIONS

This paper presents a study on the numerically calculated friction resistance coefficient of an infinitely-thin flat plate as a function Reynolds number in the range of $6.25 < \log_{10}(Rn) < 9.5$. EASM and $k-\omega$ SST turbulence models have been used and investigated. Comprehensive

grid dependence studies have been performed with SHIPFLOW and FINE™/MARINE codes. Two numerical friction lines are derived from the SHIPFLOW and compared to the lines available in open literature.

The grid dependence studies at $\log_{10}(Rn) = 6.25$ indicated that numerical uncertainty on the friction resistance coefficient is highly dependent on the first cell size. In order to achieve numerical uncertainty of frictional resistance coefficients below 1%, SHIPFLOW requires approximately $y^+ \leq 0.4$ for both EASM and $k-\omega$ SST models. However, the requirement to achieve numerical uncertainties below 1% for FINE™/MARINE is $y^+ \leq 0.1$ for both EASM and $k-\omega$ SST models which was also the conclusion of [14] for the latter turbulence model.

Two main modelling errors have been investigated: transition of flow from laminar to turbulent and turbulence models. Laminar to turbulent transition has been observed in both turbulence models and CFD solvers. Even though, transition location was predicted differently by the two CFD codes, transition behavior was qualitatively correct compared to ERCOFTAC experiments. Comparing the turbulence intensity levels at ERCOFTAC experiments to the very low turbulence intensity levels in CFD, transition occurs at too low Reynolds numbers with CFD. When the location of the transition is analyzed, only around 5% of the plate featuring the laminar flow at the lowest Rn . Considering that the turbulence stimulators in model testing are usually placed at 5% of L_{pp} from the fore perpendicular, amount of wetted surface covered by laminar flow in a model test is comparable to the numerical conditions.

The numerical calculations with two different domain sizes indicated that the effect of turbulence intensity at the leading edge affects the calculated friction resistance. Obviously, the slope of the friction line at the lower Reynolds number will change depending on which turbulence intensity have been chosen. Its implications are not investigated within the context of this study.

Numerical friction lines have been obtained for EASM and $k-\omega$ SST turbulence models using SHIPFLOW. The expression based on cubic polynomial in the logarithmic scales (Eq.5) provided the best fit for both turbulence models. The derived numerical friction lines were compared to the friction lines available in open literature. The slope of the line derived from $k-\omega$ SST is similar to other the numerical friction lines of Eça and Hoekstra [10] and Wang et al. [7] of the same turbulence model. EASM line exhibits significantly less slope at the both ends of the Rn range and differing from all other friction lines in the high Rn range except the Hughes line to some extent.

When using a numerical friction line for ship resistance extrapolation it should be considered that the result could be highly dependent on several factors: non-dimensional wall distance (y^+), choice of turbulence model, boundary conditions such as turbulence intensity and the CFD code. Since numerical approaches differ for each code, the effect of these factors can be different as well. Hence, it may not be advisable to use a general friction line for CFD based form factor determination method. The next step in our research is to study the previously mentioned factors that may affect the ship resistance extrapolation.

REFERENCES

- [1] G. Hughes, "Friction and Form Resistance in Turbulent Flow, and a Proposed Formulation for Use in Model and Ship Correlation". *Trans. RINA*, Vol. 96, (1954) p.314-376
- [2] C. W. Prohaska, "A Simple Method for the Evaluation of the Form Factor and Low Speed

- Wave Resistance”, *Proceeding of 11th ITTC*, (1966).
- [3] A. García-Gómez, “On the Form Factor Scale Effect”, *Ocean Engineering*, Vol 26, (2000) pp.97-109.
- [4] N. Toki, “Investigation on Correlation Lines through the Analyses of Geosim Model Test Results”, *Journal of the Japan Society of Naval Architects and Ocean Engineers*, Vol 8, (2008). pp.71-79
- [5] S.-H. Van, H. Ahn, Y.-Y. Lee, C. Kim, Hwang, S. Hwang, J. Kim, K.-S. Kim, I.-R. Park, “Resistance Characteristics and Form Factor Evaluation for Geosim Models of KVLCC2 and KCS”, *Advanced Model Measurement Technology for EU Maritime Industry*, (2011) pp.282-293.
- [6] H. C. Raven, A. van der Ploeg, A.R. Starke, L. Eça, “Towards a CFD-based prediction of ship performance --- progress in predicting full-scale resistance and scale effects”, *International Journal of Maritime Engineering*, Vol. 135, (2009).
- [7] Z.-z. Wang, Y. Xiong, L.-p. Shi, Z.-h. Liu, “A Numerical Flat Plate Friction Line and Its Application”, *Journal of Hydrodynamics*, Vol 23 (3), (2015) pp.383-393.
- [8] G. B. Deng and M. Visonneau, “Evaluation of eddy- viscosity and second- moment turbulence closures for steady flows around ships,”, *21st ONR Symposium on Naval Hydrodynamics*, (1996) pp. 453–469.
- [9] F. Menter, “Two-equation Eddy-viscosity turbulence models for engineering applications”, *AIAA Journal* Vol.32 no. 8 (1994) pp.1598-1605
- [10] L. Eça and M. Hoekstra, “The numerical friction line”, *Journal of Marine Science and Technology*, Vol 13, (2008) pp. 328-345.
- [11] A. Hellsten Some improvements in Menter’s k-omega SST turbulence model, *29th AIAA, Fluid Dynamics Conference*, Fluid Dynamics and Co-located Conferences, (1998)
- [12] ECOFTAC Classic Collection Database -<http://cfd.mace.manchester.ac.uk/ercoftac>
- [13] L. Eça and M. Hoekstra, “A Procedure for the Estimation of the Numerical Uncertainty of CFD Calculations Based on Grid Refinement Studies”, *Journal of Computational Physics*, Vol 262, (2014) pp. 104-130.
- [14] L. Eça, F.S. Pereira, G. Vaz, “Viscous flow simulations at high Reynolds numbers without wall functions: Is $y^+ \cong 1$ enough for the near-wall cells?”, *Computers and Fluids*, Vol. 170, (2018) pp.157-175
- [15] Proceedings of the 8th ITTC, Madrid, 1957
- [16] Karl E. Schoenherr, “Resistance of flat plate surfaces”, *Trans. SNAME* (1932) 40:279-313
- [17] T. Katsui, H. Asai, Y. Himeno, Y. Tahara, “The Proposal of a New Friction Line” *Fifth Osaka Colloquium on Advanced CFD Applications to Ship Flow and Hull Form Design*, Osaka, Japan, (2005).
- [18] C.W.B. Grigson, “A planar algorithm and its use in analysing hull resistance”. *Trans. RINA*, Vol 142, (1999) pp. 76-115.

NUMERICAL STUDY OF ROUGHNESS MODEL EFFECT AT ACTUAL SHIP SCALE

KUNIHIDE OHASHI*

*National Maritime Research Institute
6-38-1 Shinkawa, Mitaka, Tokyo, Japan
e-mail: k-ohashi@nmri.go.jp

Key words: Surface Roughness, Actual Ship Scale

Abstract. Numerical study of roughness effects at an actual ship scale is performed. The roughness models which are based on the two equation turbulence model are employed. First, the roughness models are examined on the 2D flat plate case at the Reynolds numbers 1.0×10^8 and 1.0×10^9 . The resistance coefficient increases with the roughness height, and the uncertainty analysis about the resistance coefficient is performed. Additionally, the distributions of the non-dimensional velocities u^+ based on the non-dimensional heights y^+ are compared with changing the roughness height. Next, the roughness models are applied to the flows around a ship in the actual scale. The velocity contours are compared with the measured results on the actual ship. The results with the roughness models show the good agreement comparing with the smooth surface condition.

1 INTRODUCTION

Numerical study about the roughness effect at the actual ship scale is performed. The roughness models on the two equation turbulence model are employed. Computations of flows around a flat plate corresponding to an actual ship scale are selected as the fundamental test case, and detailed analysis is carried out. Next, the present method is applied to the flows around the ship which has the measured data on the actual sea test. The roughness effect is revealed through the comparisons on the case with/without the roughness model and the measured data.

2 COMPUTATIONAL METHOD

2.1 Base solver

An in-house structured CFD solver [1] is employed. The governing equation is 3D RANS equation for incompressible flows. Artificial compressibility approach is used for the velocity-pressure coupling. Spatial discretization is based on a finite-volume method. A cell centered layout is adopted in which flow variables are defined at the centroid of each cell and a control volume is a cell itself. Inviscid fluxes are evaluated by the third-order upwind scheme based on the flux-difference splitting of Roe. The evaluation of viscous fluxes is second-order accurate.

The first order Euler implicit scheme is employed for the temporal step. The linear equation system is solved by the symmetric Gauss-Seidel (SGS) method.

For free surface treatment, an interface capturing method with a single phase level set approach is employed. The propeller effects are accounted for according to the body forces derived from the propeller model[1], which is based on the potential theory.

2.2 Overset-grid method

The weight values for the overset-grid interpolation are determined by an in-house system[2]. The detail of the system can be found on [2], the summary is described.

1. The priority of the computational grid is set.
2. The cells of a lower priority grid and inside a body is identified (called as in-wall cell in here).
3. Receptors cells which the flow variables have to be interpolated from donor cells are defined. Two cells on a higher priority grid and facing to the outer boundary are set as receptor cells to satisfy the third order discretization of NS solver. Additionally, two cells neighborhood of in-wall cells, the cells of a lower priority grid and inside the domain of a higher priority grid are also set as the receptor cell.
4. The weight values for the overset interpolation are determined by solving the inverse problem based on Ferguson spline interpolation.

Flow variables of the receptor cell are updated when the boundary condition is set. The forces and moments are integrated on the higher priority grid to eliminate the lapped region on body surfaces. At first, the cell face of the lower priority grid is divided into small pieces. Secondly, the small piece is projected to the cell face of the higher priority grid by using the normal vector of the higher priority face. Then the 2D solid angle is computed and the small piece is decided in or out of the higher priority face. Once the small piece is in the higher priority face, the area ratio of the piece is set to zero. Finally, the area ratio is integrated on the lower priority face, then we have the ratio to integrate the forces and moments on lower priority face.

2.3 Roughness model

Roughness effects are taken into account by the roughness models based on the two models. The model which is proposed by Wilcox [3][4] is named as Model1, and the model which is proposed by Hellsten [5] is named as Model2 in hereafter. Non-dimensionalized roughness height is defined by using frictional velocity u_τ and roughness height h_r as follows:

$$h_r^+ = \frac{u_\tau h_r}{\nu} \quad (1)$$

Non-dimensionalized form of Eq.(1) is given as follows:

$$h_r^+ = u_\tau h_r R \quad (2)$$

Non-dimensionalized roughness height is limited $h_r^+ < 400$ in Model1 and the function S_R is introduced.

$$S_R = \begin{cases} \left(\frac{200}{\max(h_R^+, h_{min}^+)} \right)^2 & h_R^+ \leq 5 \\ \frac{100}{h_R^+} + \left[\left(\frac{200}{h_R^+} \right)^2 - \frac{100}{h_R^+} \right] e^{5-h_R^+} & h_R^+ > 5 \end{cases} \quad (3)$$

where the new variable h_{min}^+ is employed above equation based on the Model2 which is proposed by Hellsten to ensure the function to the smooth surface condition, and h_{min}^+ is defined as $h_{min}^+ = 9.6y_1^{+0.85}$ which is based on the first computational cell adjacent to the wall surface and non-dimensionalized height y_1^+ .

The function S_R is introduced by the Model2 as follows:

$$S_R = \begin{cases} \left(\frac{50}{\max(h_R^+, h_{min}^+)} \right)^2 & h_R^+ < 25 \\ \frac{100}{h_R^+} & h_R^+ \geq 25 \end{cases} \quad (4)$$

where $h_{min}^+ = 2.4y_1^{+0.85}$ is applied.

The boundary condition of ω on a wall surface is given as follows:

$$\omega = \frac{u_\tau^2}{\nu} S_R \quad (5)$$

Non-dimensionalized form of Eq.(5) is given as follows:

$$\omega = u_\tau^2 S_R R \quad (6)$$

The reference velocity profile which is proposed by Apsley[6] is used in the present study.

$$u^+ = y_{v0}^+ + \frac{1}{\kappa} \ln \left(\frac{1 + \kappa(y^+ - y_v^+)}{1 + \kappa(y_{v0}^+ - y_v^+)} \right) \quad (7)$$

$$y_v^+ = \begin{cases} C - \frac{1}{\kappa} \ln(\kappa) & C - \frac{1}{\kappa} \ln(\kappa) \geq 0 \\ \frac{1}{\kappa} (1 - e^{-\kappa(C - \frac{1}{\kappa} \ln(\kappa))}) & C - \frac{1}{\kappa} \ln(\kappa) < 0 \end{cases} \quad (8)$$

$$C = 8 - \frac{1}{\kappa} \ln(h_R^+ + 3.152) \quad (9)$$

$$y_{v0}^+ = \max(y_v^+, 0) \quad (10)$$

where κ is assumed as 0.41.

2.4 Uncertainty analysis

Uncertainty analysis based on the Richardson extrapolation method with the FS method[7] is performed. The grid discretization uncertainty is evaluated due the steady condition on the present study, and the three systematic grids with the uniform refinement ratio $r_G = \sqrt{2}$ are utilized. Once, the solutions S_3 , S_2 , S_1 relevant from the coarse grid to fine grid are obtained, the solution changes are defined as $\epsilon_{12} = S_2 - S_1$, $\epsilon_{23} = S_3 - S_2$. The convergence ratio R is $\epsilon_{12}/\epsilon_{23}$, and R takes the monotonic convergence with $0 < \epsilon_{12}/\epsilon_{23} < 1$. The order of accuracy p and the error δ_{RE} are defined as follows:

$$p = \frac{\ln(\epsilon_{23}/\epsilon_{12})}{\ln(r_G)}, \quad \delta_{RE} = S_1 - S_0 = \frac{\epsilon_{12}}{r_G^p - 1} \quad (11)$$

The uncertainty is estimated by the following equation using the variable $P = p/p_{th}$. Theoretical accuracy p_{th} is assumed $p_{th} = 2$.

$$U_{SN} = \begin{cases} (2.45 - 0.85P)|\delta_{RE}|, & 0 < P \leq 1 \\ (16.4P - 14.8)|\delta_{RE}|, & P > 1 \end{cases} \quad (12)$$

3 COMPUTED RESULTS

3.1 2D Flat plate case

A 2D flat plate case is selected as the fundamental test case. The Reynolds number is set 1.0×10^8 and 1.0×10^9 based on the plate length L as the reference length. Table 1 shows the computational grids with the three resolutions. The space between the first cell center and wall surface satisfies $y^+ \leq 1$. Fig.1 shows the computational grid of the medium grid, the boundary conditions and the definitions of directions of the divisions. The distance between the wall surface and the top boundary is $0.1L$.

Table 1: Division number of computational grid

| Grid | IM×JM |
|-----------------|---------|
| Coarse(G_3) | 137×81 |
| Medium(G_2) | 193×113 |
| Fine(G_1) | 273×161 |

The value which is estimated by the empirical formula [8] utilized for the reference.

$$C_D = \left(2.635 + 0.618 \ln \frac{L}{h_r} \right)^{-2.57} \quad (13)$$

Table 2 shows the comparison of the resistance coefficients of model1 with changing the roughness height from $h_r = 1 \times 10^{-6}$ to $h_r = 7.5 \times 10^{-6}$ and the grid resolutions at the Reynolds number $R = 1.0 \times 10^8$. The roughness height is non-dimensionalized by the plate length L , and the roughness height is selected in the range where the resistance coefficient becomes larger than

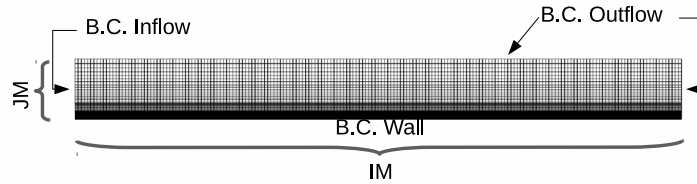


Figure 1: Computational grid(Medium grid)

the value of the smooth surface. The uncertainty is resulted in the range from 1% to 3% of the solution of the fine grid, thus, the uncertainty takes small value using the present computational grids. Although the computed results are slightly higher than the value of the empirical formula, the resistance coefficient increase with the roughness height. Table 2 shows similar results with the model2. The uncertainty is about 1% to 3% of the solution of the fine grid. Comparing between the results of model1 and model2, the resistance coefficient of model2 becomes larger than the value of model1 at $h_r = 1 \times 10^{-6}$, and the values of model2 takes smaller value than the results of model1 at 2.5×10^{-6} and 5×10^{-6} . The results of model1 and model2 are same at 7.5×10^{-6} .

Figure 2 shows the comparisons of the non-dimensionalized velocity u^+ and non-dimensionalized distance y^+ of model2 at the positions $x/L = 0.5$ and $x/L = 0.9$. The results of model1 are the same as the results of model2, then, the results of model1 are omitted. For the reference, the correlations based on the smooth surface condition and Eq.(7) with the roughness $h_r = 7.5 \times 10^{-6}$ are also shown in Figure 2. The velocity distributions change and become slower in the logarithmic region with the roughness height. The difference due to the roughness height seems small in the viscous sublayer region. The velocities at $x/L = 0.5$ and $x/L = 0.9$ take the same distribution in the logarithmic region, and the difference can be found in the outer region.

Table 2: Resistance coefficient (Model1, $R = 1.0 \times 10^8$)

| Grid | Smooth | 1×10^{-6} | 2.5×10^{-6} | 5×10^{-6} | 7.5×10^{-6} |
|---------------|--------|--------------------|----------------------|--------------------|----------------------|
| Coarse | 2.062 | 2.074 | 2.307 | 2.618 | 2.734 |
| Medium | 2.096 | 2.119 | 2.374 | 2.686 | 2.808 |
| Fine | 2.108 | 2.130 | 2.382 | 2.696 | 2.818 |
| $U_{SN}\%G_1$ | 3.06 | 3.10 | 1.62 | 1.95 | 1.81 |
| Emp. | — | 2.024 | 2.313 | 2.572 | 2.742 |

Table 4 shows the results of model1 at $R = 1.0 \times 10^9$ with changing the non-dimensionalized roughness height from $h_r = 1 \times 10^{-7}$ to $h_r = 7.5 \times 10^{-7}$. The roughness height is selected in the range where the resistance coefficient becomes larger than the value of the smooth surface. The uncertainty becomes smaller than the values of the Reynolds number $R = 1.0 \times 10^8$, and the resistance coefficient takes similar value of the empirical formula. Table 5 shows the results of model2. The resistance coefficient of model2 takes larger value than the results of model1 in the range until $h_r = 2.5 \times 10^{-7}$, then, the relation shows the opposite trend.

Table 3: Resistance coefficient (Model2, $R = 1.0 \times 10^8$)

| Grid | Smooth | 1×10^{-6} | 2.5×10^{-6} | 5×10^{-6} | 7.5×10^{-6} |
|---------------|--------|--------------------|----------------------|--------------------|----------------------|
| Coarse | 2.062 | 2.149 | 2.286 | 2.526 | 2.734 |
| Medium | 2.096 | 2.197 | 2.342 | 2.597 | 2.808 |
| Fine | 2.108 | 2.208 | 2.352 | 2.606 | 2.818 |
| $U_{SN}\%G_1$ | 3.06 | 2.97 | 2.40 | 1.71 | 1.81 |
| Emp. | — | 2.024 | 2.313 | 2.572 | 2.742 |

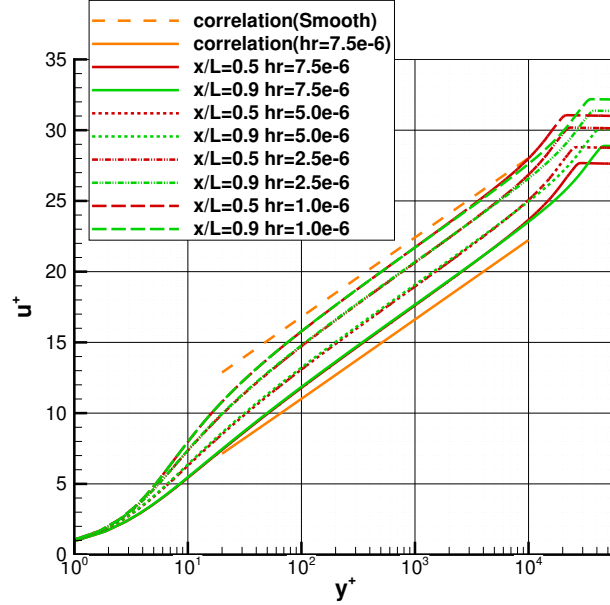
**Figure 2:** Comparison of y^+ and u^+ at $R = 1.0 \times 10^8$ (Model2)

Figure 3 shows the distributions based on u^+ and y^+ . For the reference, the correlation based on Eq.(7) at $h_r = 7.5 \times 10^{-7}$ is shown. The computed results show the similar distribution with the case $R = 1.0 \times 10^8$ excepting the logarithmic region becomes wider than the results of $R = 1.0 \times 10^8$.

Figure 4 shows the distribution of h_r^+ on the flat plate at the condition with $h_r = 7.5 \times 10^{-7}$. h_r^+ takes larger value near the front end of the flat plate, then, the value becomes almost constant value with $h_r^+ = 25$, and the value is within the model limitation $h_r^+ < 400$.

3.2 Actual ship scale

The numerical study with/without the roughness effect is performed on the case with the tanker hull[9] which has the flow measurement data on the actual ship. The computations are carried out on the propulsive condition with the free surface effect. The Reynolds number based

Table 4: Resistance coefficient (Model1, $R = 1.0 \times 10^9$)

| Grid | Smooth | 1×10^{-7} | 2.5×10^{-7} | 5×10^{-7} | 7.5×10^{-7} |
|---------------|--------|--------------------|----------------------|--------------------|----------------------|
| Coarse | 1.538 | 1.553 | 1.635 | 1.878 | 1.952 |
| Medium | 1.565 | 1.580 | 1.669 | 1.917 | 1.994 |
| Fine | 1.571 | 1.586 | 1.673 | 1.922 | 1.998 |
| $U_{SN}\%G_1$ | 0.17 | 2.25 | 1.14 | 1.29 | 0.86 |
| Emp. | — | 1.487 | 1.673 | 1.837 | 1.944 |

Table 5: Resistance coefficient (Model2, $R = 1.0 \times 10^9$)

| Grid | Smooth | 1×10^{-7} | 2.5×10^{-7} | 5×10^{-7} | 7.5×10^{-7} |
|---------------|--------|--------------------|----------------------|--------------------|----------------------|
| Coarse | 1.538 | 1.593 | 1.672 | 1.802 | 1.936 |
| Medium | 1.565 | 1.621 | 1.704 | 1.840 | 1.980 |
| Fine | 1.571 | 1.627 | 1.709 | 1.845 | 1.984 |
| $U_{SN}\%G_1$ | 0.17 | 2.18 | 1.58 | 1.36 | 0.85 |
| Emp. | — | 1.487 | 1.673 | 1.837 | 1.944 |

on the ship length L is $R = 2.43 \times 10^9$, and the Froude number is $Fn = 0.153$. Propulsive condition is achieved by using the propeller model[1]. The propeller rotational speed and thrust is adjusted to be equal to the resistance of the ship. The roughness value is set $150 \times 10^{-6}m$ based on the ITTC recommended procedure[10].

Table 6 shows the division number of computational grids in each direction. The grids are arranged with the priority of the overset interpolation. The computational grid is consisted from the hull grid, the rudder grid and two rectangular grids including the refinement grid near the aft part of the ship hull and the grid covering the whole domain. The division numbers of the hull and rudder grids are altered to examine the effect of the grid resolution with reference to the 2D flat plate case.

Figure 5 shows the global view of the computational grids with the boundary conditions and the grids near the aft part of the ship. The space between the first cell center and wall surface also satisfies $y^+ \leq 1$.

Table 6: Division number of computational grid

| Grid | Coarse | Medium | Fine |
|---------------|------------|------------|-------------|
| | IM×JM×KM | IM×JM×KM | IM×JM×KM |
| Rudder | 45×69×35 | 61×97×49 | 85×137×69 |
| Refined Rect. | 45×33×45 | 45×33×45 | 45×33×45 |
| Hull | 141×145×65 | 197×209×89 | 277×305×125 |
| Rect. | 337×89×57 | 337×89×57 | 337×89×57 |

Figure 6 shows the axial velocity contour with/without the roughness effect at the propeller plane on the towing condition. The results based on the three grid are also shown. The region which the axial velocity is lower than 0.3 spreads corresponding to the grid resolution. The axial

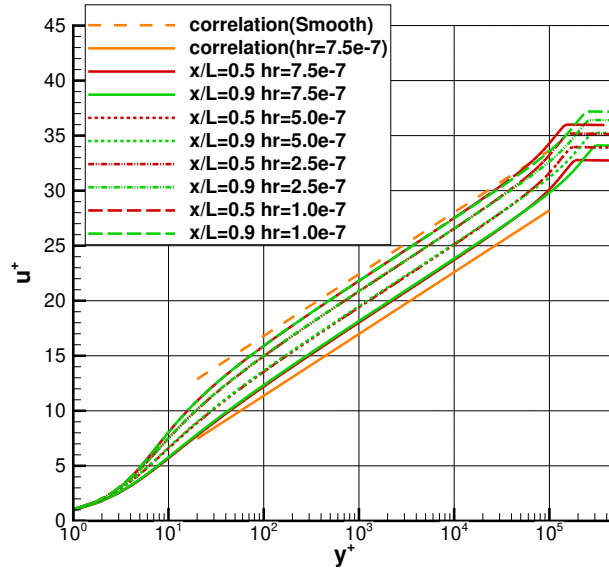


Figure 3: Comparison of y^+ and u^+ at $R = 1.0 \times 10^9$ (Model2)

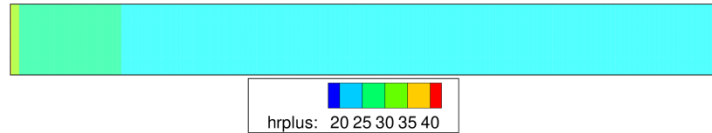


Figure 4: Non-dimensional roughness on the plate at $R = 1.0 \times 10^9$ (Model2)

velocity with the roughness effect becomes lower than the value of the smooth surface condition, and the difference between the roughness models is slightly small.

Figure 7 shows the comparisons with the measured data at the actual ship. The position is $x/L=0.98533$ from the fore perpendicular position. The results with the roughness effect show agreement with the measured data, especially, the range $u/U = 0.5 - 0.7$. The differences between the result of the grid resolutions are slightly small, and the differences between the result of model1 and model2 can be negligible.

Figure 8 shows the distribution of the non-dimensionalized roughness height h_r^+ on the body surfaces. h_r^+ takes small value near the fore and stern end, and h_r^+ is distributed on the body surface with the value near 40. The difference between the port and starboard sides is slightly small. The non-dimensionalized roughness height on the rudder surface which is positioned behind the propeller takes higher value than h_r^+ on the hull surface. The difference between the port and starboard sides on the rudder surface can be observed which is affected by the propeller rotational flow. The velocities of the two models have the identical lines.

Finally, the distribution of the non-dimensional velocity u^+ at the bottom of the hull and midship $x/L = 0$ and center line $y/L = 0$ is shown in Figure 9. The correlation based on Eq.(7) is also shown in Figure 9. The non-dimensional velocities with the roughness models decreases

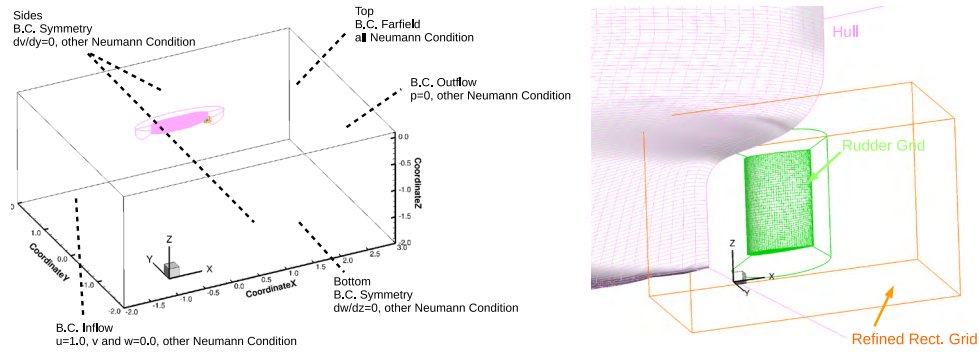


Figure 5: Computational grids(left:global view, right:near aft part of hull)

comparing with the velocity of the smooth surface condition. The non-dimensional velocities with the roughness are decreased by the rise of frictional velocity due the roughness effect. The difference between the roughness models is negligible.

4 CONCLUSIONS

- The two roughness models based on $k - \omega SST$ model are introduced to examined the roughness effect on the actual ship scale.
- The 2D flat plate case is selected as the fundamental test case, and the comparisons of the resistance coefficient and uncertainty analysis are performed.
- The effect of the roughness model is examined at the case with the tanker hull which has the the flow measurement data on the actual ship, and the axial flows behind the ship hull are decelerated by the roughness effect.
- The computed results with the roughness effect show good agreement with the measured data on the actual ship.

REFERENCES

- [1] K. Ohashi et al., Development of a structured overset Navier-Stokes solver including a moving grid with a full multigrid method, *J. Mar. Sci. Tech.*, 2018.
- [2] H. Kobayashi and Y. Kodama, Developing Spline Based Overset Grid Assembling Approach and Application to Unsteady Flow Around a Moving Body, *Journal of Mathematics and System Science* 6, pp.339-347, 2016
- [3] D.C. Wilcox, *Turbulence modeling for CFD*, Third Edition, DCW Industries, 2006.
- [4] L. Eça, M. Hoekstra, Numerical aspects of including wall roughness effects in the SST $k - \omega$ eddy-viscosity turbulence model, *Comp. and Fluids*, Vol.40, pp.299-314, 2011.
- [5] A. Hellsten., Some improvements in Menter's $k - \omega$ SST AIAA-98-2554, 1997.

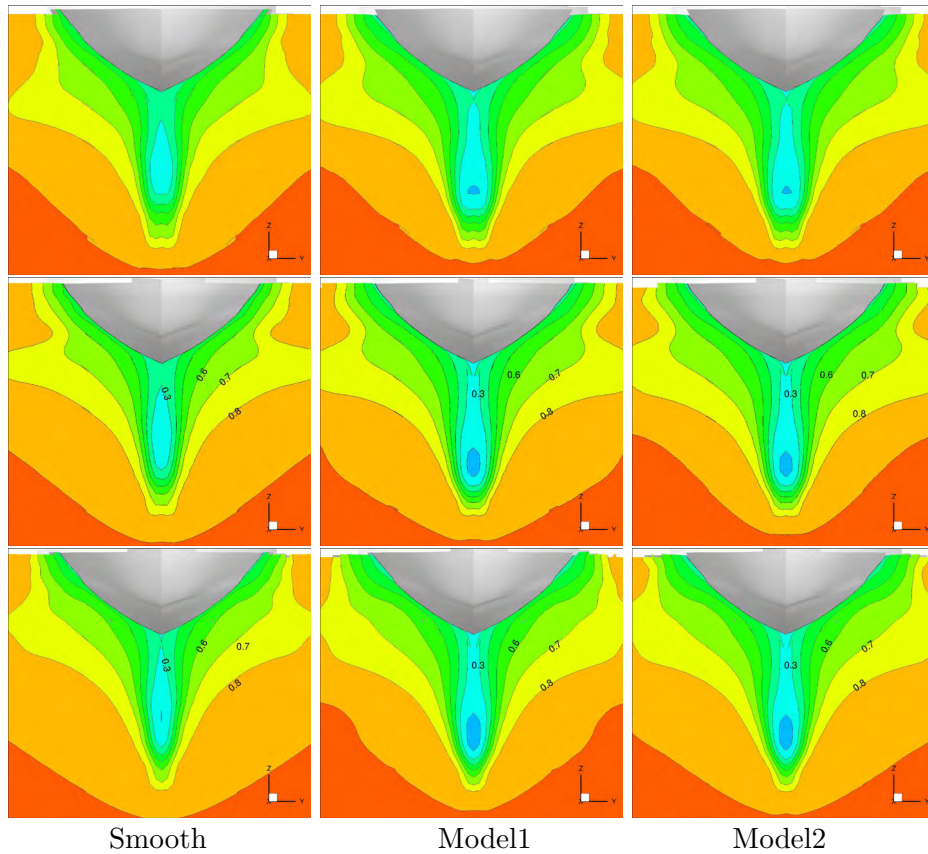


Figure 6: Axial velocity contour(Top:Coarse grid, Mid:Medium grid, Bottom:Fine grid)

- [6] D. Apsley, CFD calculation turbulent flow with arbitrary wall roughness, *Flow Turb. Comb.*, Vol.78, pp.153-175, 2007.
- [7] T. Xing, , F. Stern, Factors of safety for Richardson extrapolation, *J. Fluids Eng.*, Vol.132(6), 2010.
- [8] A. Mills, X. Hang, On the skin friction coefficient for a fully rough flat plate, *Trans. ASME, J. Fluids Eng.*, Vol.105, pp.364-365, 1983.
- [9] Proc. of CFD Workshop Tokyo 1994
- [10] ITTC recommended procedures and Guidelines 7.5-02-03-01.4, 1978 ITTC Performance Prediction Method.

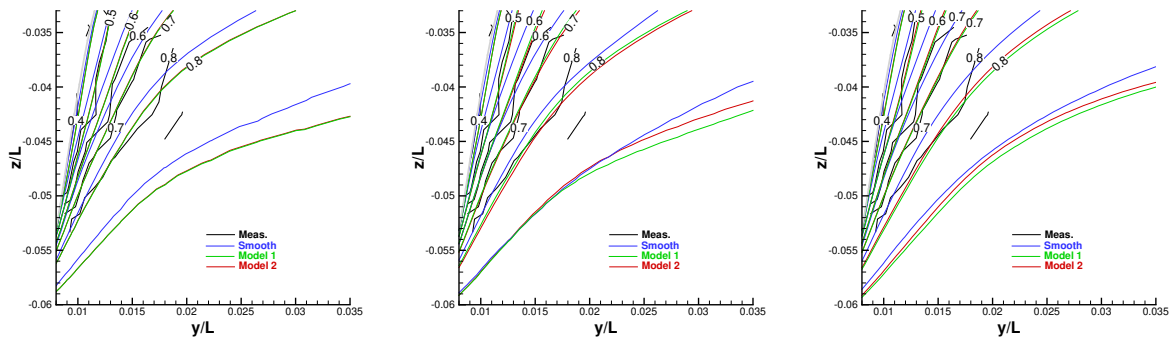


Figure 7: Comparison of velocity contours with measured results (Top:Coarse grid, Mid:Medium grid, Bottom:Fine grid)

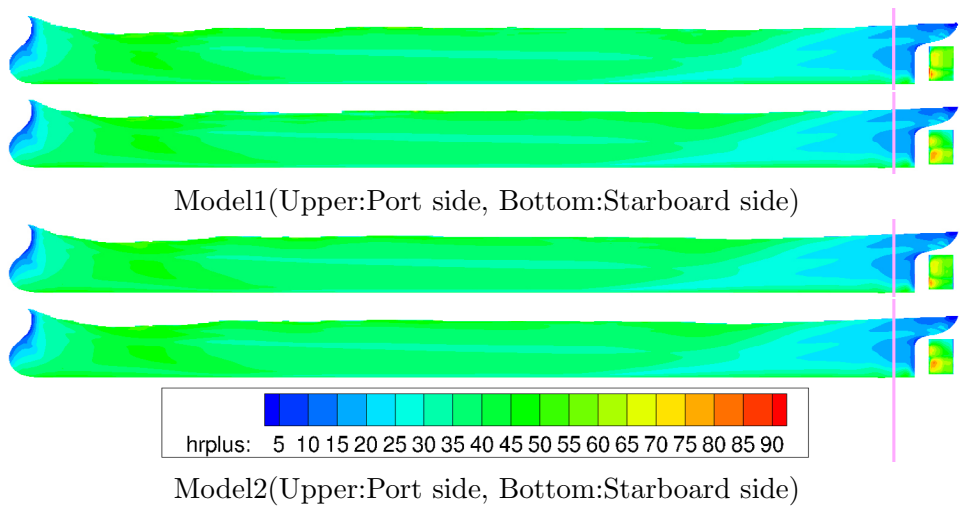


Figure 8: Non-dimensional roughness on the hull and rudder surfaces

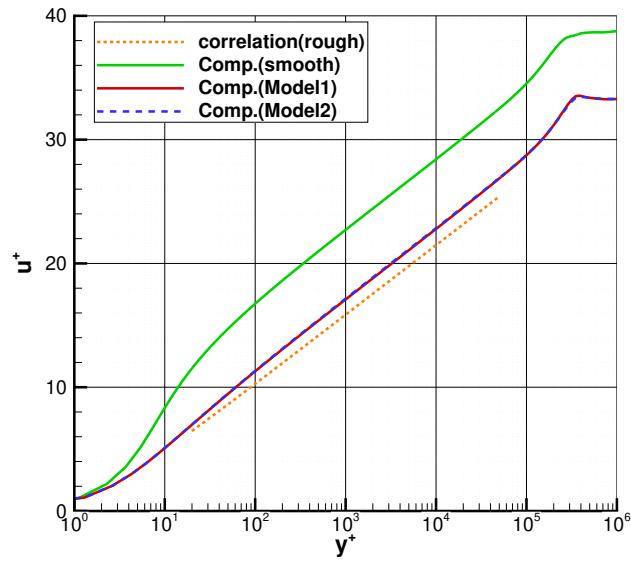


Figure 9: Comparison of y^+ and u^+ at $x/L = 0$ and $y/L = 0$

PREDICTION OF SHIP RESISTANCE WITH THE USE OF FULL-SCALE CFD SIMULATIONS

MARINE 2019

KAROL NIKLAS^{*}, HANNA PRUSZKO^{*}

^{*} Faculty of Ocean Engineering and Ship Technology
Gdansk University of Technology

Narutowicza 11/12, 80233 Gdansk, Poland

e-mail: karol.niklas@pg.edu.pl, www.oio.pg.edu.pl/about

Key words: Computational Methods, Marine Engineering, CFD, Ship Resistance

Abstract. In recent years, the IMO has introduced new regulations to reduce the negative impact of ships on the natural environment. A particularly important step forcing technological innovations is the increasing requirement of ship energy efficiency. It is expressed by the Energy Efficiency Design Index (EEDI). Another important step towards green shipping is raising the required quality of fuel used for propulsion, the so-called Tier limits. Higher demand of Low Sulfur Fuel Oil resulted in its price rising up by 200% in the past two years. All these aspects increase the importance of ship fuel economy. As a result, the hull resistance reduction plays a significant role in the design process of new vessels. For vessels operating at sites with moderate and rough waves, the shape of the hull and, in particular, the bow section plays an important role. The paper presents results of some of the research carried out as a part of the "Smart Propulsion System" research project. The presented stage of the work includes a full-scale CFD simulation for a case study ship redesigned from an as-built V-shaped bulbous bow to three different innovative variants. Changes in the hull form were made in such a way that the redesigned hull versions preserved the main dimensions and hydrostatic parameters of the original design. The paper presents ship resistance analysis on calm water as a part of seakeeping analysis. The scope of the work was full-scale CFD simulations of four innovative hull forms in order to determine total resistance, dynamic trim and sinkage. The influence of bow and stern shape, wetted surface area and waterplane area on total resistance was investigated. Main conclusions were formulated for the novel hull forms being analysed. The scope of further work was formulated, and it included assessment of the combined influence of the ship's speed and waving conditions on the performance at a specific operational site. To reduce fuel consumption, the optimal design and operation of the ship are equally important and can be supported by full-scale CFD simulations.

1 INTRODUCTION

Accurate and reliable determination of ship resistance by CFD simulations is of great importance. The methodology is described by the ITTC recommended practice [1], [2] and quite often used by different researchers for hydrodynamic analyses. The wave pattern, wake and resistance of a fully appended ship were studied numerically in [3]. In paper [4], numerical simulations as a powerful tool to compute viscous flows and a way to improve prediction of

full-scale resistance were presented. In [5], simulations of calm water resistance and seakeeping performance were presented. Numerous papers address the potential of hull form optimization using numerical methods. In [6], slender body approximation was used to compute wave resistance and find optimum shape among series of eight hull forms. Parametric modelling of hull shape was also presented in [7]. The possible application of RANSE was discussed, as well as robustness and efficiency of numerical simulations. Different optimization techniques can be applied. The one studied in [8] was an evolutionary technique used for hull resistance optimization taking as a starting point the Wigley hull form. The Boundary Element Method was used in [9] for optimisation of the parametric model of hull forms that were created based on T-splines. Shape of the bow was also of great interest. For example, [10] created the generation of bulbous bows with a goal of drag reduction. New forms were analysed numerically and experimentally. CFD simulations were also used as a tool to investigate more sophisticated methods of ship resistance analysis. The effect of coating and biofouling was studied in [11]. Drag reduction of superhydrophobic surfaces was investigated in [12]. In the articles [13], [14], [15], the CFD simulation of a full-scale ship with self-propulsion was presented. Simulations of ship maneuverability were presented in [16]. The method was applied also in unusual offshore applications, i.e. [17], [18], [19].

2 AIM AND SCOPE

The aim of the study was to investigate the influence of the hull form of the case study vessel on calm water performance. The selected hull forms represent the most recognised examples of concepts recently developed by different design offices.

The scope of the work included full-scale simulations of four variants of hull shape. The compared concepts were similar to: V-shaped bulbous bow, X-bow, X-bow-X-aft, and B-bow. The X-bow [20] and X-aft concepts were developed by the Ulstein company. The concept denoted as B-bow was developed by the Havyard company. The total resistance and its components (frictional and pressure resistance), dynamic trim and sinkage were analysed. The paper presents a part of the research on the application of full-scale CFD simulations into ship design and operation for increasing energy efficiency, comfort and safety of ships.

In Section 3, the case study vessels were described. In Section 4, the setup of numerical simulations was presented. In Section 5, results were analysed. In Section 6, conclusions and recommendations for further study were described.

3 THE CASE STUDY VESSEL AND HULL FORM VARIANTS

For the purpose of research, the case study vessel Navigator XXI (IMO: 9161247) was selected. She is a training and research vessel operating mainly on the Baltic Sea. The hull form characteristics are transom stern, full midship section and V-shaped bulbous bow with a flare. The ship in the as-built version was denoted as CSV1. The hull form was redesigned according to selected innovative variants in such a way to preserve the main dimensions and hydrostatic parameters. The body forms were denoted from CSV2 to CSV4. The main particulars are presented in Table 1. The side views of CSV1–CSV4 are presented in Fig. 1.

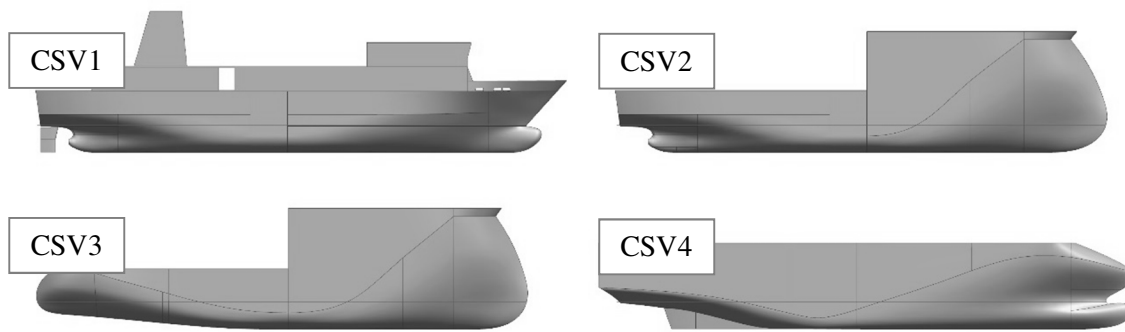


Figure 1: Hull forms of the case study vessel: CSV1 – V-shaped bulbous bow and transom stern; CSV2 – X-bow and transom stern; CSV3 – X-bow and X-aft (cruiser stern); CSV4 – B-bow and V-shaped transom stern

Table 1: Main particulars of CSV1–CSV4 hull forms

| Name | unit | CSV1 | CSV2 | CSV3 | CSV4 |
|--|---------------|-------|-------|-------|-------|
| Waterline length L_{WL} | (m) | 55.68 | 55.15 | 55.50 | 55.24 |
| Breadth B | (m) | 10.50 | 10.50 | 10.50 | 10.50 |
| Drought T | (m) | 3.14 | 3.14 | 3.14 | 3.14 |
| Displacement D | (m^3) | 1110 | 1109 | 1110 | 1110 |
| Wetted surface area S_w | (m^2) | 677.3 | 652.6 | 648.4 | 690.9 |
| Waterplane area S_{WP} | (m^2) | 473.3 | 456.4 | 468.3 | 447.6 |
| Longitudinal centre of buoyancy L_{CB} | (% L_{WL}) | 46.70 | 47.94 | 48.69 | 51.90 |
| Vertical position of centre of gravity Z_G | (m) | 4.16 | 4.16 | 4.16 | 4.16 |
| Gyradius k_{YY} | [-] | 0.219 | 0.219 | 0.219 | 0.219 |

4 FULL-SCALE CFD SIMULATION FOR THE DETERMINATION OF CALM WATER RESISTANCE

Numerical methods allow us to solve the discretised governing equations of mass, momentum and energy conservation that are commonly known as the Navier–Stokes equations. Depending on the problem complexity, different simplifications might be applied. For naval applications, where fluid is assumed to be incompressible, only mass and momentum continuity are considered. However, the great complexity of the flow around a ship’s hull does not allow for solving equations analytically, and numerical methods need to be applied.

To run CFD calculations, the commercial code STAR CCM+ was used. The solver uses a finite volume method that discretises the whole computational domain and iteratively solves the integral version of the transport equations. The flow was solved as three-dimensional, turbulent, viscous, incompressible and multiphase. In order to capture the interface between phases, a surface-capturing VOF (Volume of Fluid) model was applied. The turbulent flow was modelled using the RANS approach. This method is based on the assumption that instantaneous velocity can be represented by the sum of mean and fluctuating components. Those values are then averaged and inserted into the N-S equations. The averaging process involves introducing additional terms that increase the number of unknown values in the RANS equations. To solve the closure problem, the turbulence model needs to be applied [21]. The $k-\epsilon$ model with all $y+$

treatment was applied for simulations. This model offers a good compromise between robustness and accuracy. The model is also a frequent choice when using STAR CCM+ software [22], [23]. For spatial discretisation, a second-order upwind numerical scheme was used for the convection term, and a first-order implicit scheme was used for temporal discretisation. The time step of the numerical simulations varied according to the vessel's speed in order to satisfy the Courant–Friedrichs–Lewy condition, defined by Equation 1. In the formula, Δt stands for a time step, Δx is a grid size in the direction of a flow velocity vector, u is velocity, and C is a constant. For naval applications, it is recommended that C is equal to 0.5–0.7 for a free surface and 5–10 for a hull surface [21].

$$\frac{u \cdot \Delta t}{\Delta x} \leq C \quad (1)$$

To compute the motions of a ship as a response to fluid forces, the DFBI model (Dynamic Fluid Body Interaction) was applied. This module allows to integrate the pressure and shear forces over the surface of a body. Acting forces and moments are used to find, in an iterative way, the new position of an object after translational motion and angular rotation of a body's centre of mass [24]. Four degrees of freedom were restrained, and the model was allowed to sink and trim.

The size of the domain and ship position were specified in order to capture the Kelvin wave pattern and also to avoid reflection from the side and downstream boundary. For the same reason, numerical wave damping was applied on these boundaries. The computational domain is presented in Figure 2. The setup of the numerical domain is presented in Table 2.

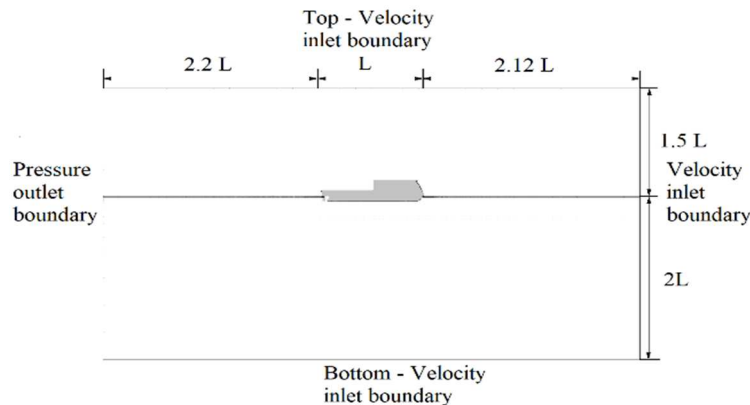


Figure 2: Computational domain and boundary conditions

Table 2: Boundary conditions

| Boundary | Position | Boundary Condition |
|----------|----------------------------------|--------------------|
| Inlet | $2.12 L_{pp}$ in front of a ship | Velocity inlet |
| Outlet | $2.2 L_{pp}$ behind a ship | Pressure outlet |
| Symmetry | Symmetry plane of a ship | Symmetry |
| Side | $2.2 L_{pp}$ from symmetry plane | Velocity inlet |
| Top | $1.5 L_{pp}$ above free surface | Velocity inlet |
| Bottom | $2 L_{pp}$ below free surface | Velocity inlet |

The discretisation of the volume was performed according to a recent state-of-art method. Grid refinements were applied in a way to make it possible to capture the most important features of the flow. This included increasing the mesh resolution in the free surface, wake and closest proximity to the hull surface where prism layers were used in the region of the boundary layer — see Figure 3. The mesh resolution in the region of the ship’s boundary layer resulted in a value of y^+ within a range of 30–50. The approach with a symmetry plane of a ship was used, and the total number of volumetric cells was equal to 2.1 million for the CSV1. To allow for objective comparison between hulls, all four meshes were designed in the same way, resulting in the same grid resolution in the region of the boundary layer and refinements in the region around the hulls. However, due to features of the hull shape such as bulbous bow or propeller shaft tube the total number of cells was slightly different for each mesh. The total number of cells for each variant is presented in Table 3.

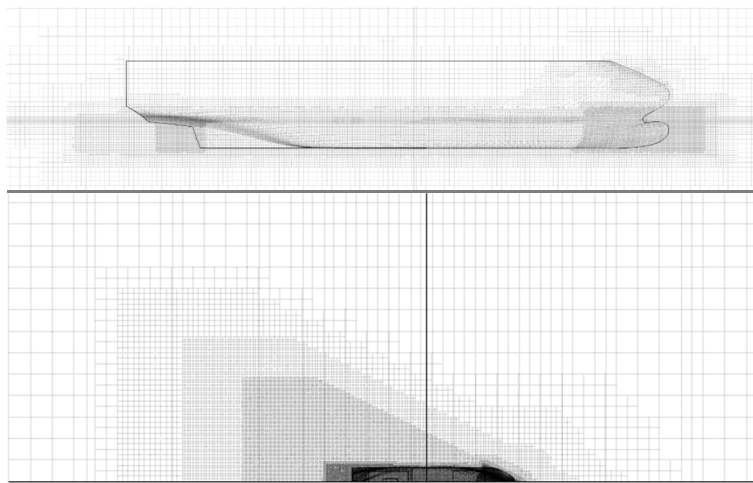


Figure 3: Computational mesh – side and top view

Table 3: Number of cells for hull variants CSV1–CSV4

| | CSV1 | CSV2 | CSV3 | CSV4 |
|--------------|-------|-------|------|-------|
| No. of cells | 2.1 M | 2.1 M | 2.2M | 2.2 M |

Computations were performed for a range of speed from 5 to 13 knots with 1 knot increment in range from 7 to 13 knots. This corresponds to a Froude number F_N from 0.11 to 0.29.

In order to assess the accuracy of the numerical solution, a verification study was performed. The verification study was carried out for CSV1 for two coarser meshes with total cell number equal to 1 M and 0.5 M cells for vessel speed of 10 knots. This follows the ITTC procedure for verification and validation of CFD computations [25]. The results are presented in Table 4. The simulations were characterised by monotonic convergence with grid size error equal to 0.8% and corrected grid size uncertainty equal to 0.22%.

Table 4: Results of the verification study

| Ship velocity [knots] | F_N [-] | Grid refinement ratio R_G [-] | Correction factor C_G [-] | Grid size uncertainty U_G [%S] | Grid size error δ_G^* [%S] | Corrected grid uncertainty U_{Gc} [%S] |
|-----------------------|-----------|---------------------------------|-----------------------------|----------------------------------|-----------------------------------|--|
| 10 | 0.22 | 0.44 | 0.74 | 0.86% | 0.80% | 0.22 |

4 RESULTS

The results of total resistance for all analysed hull form variants are presented in Table 5. The calculated speed range was from 5 to 13 knots (F_N from 0.11 to 0.29). For each speed, the lowest values of resistance are marked in **bold**, whereas the highest values of resistance are marked in *italics*.

Table 5: Results of total resistance R_T for hull variants CSV1–CSV4

| Speed [knots] | F_N [-] | CSV1 R_T [kN] | CSV2 R_T [kN] | CSV3 R_T [kN] | CSV4 R_T [kN] |
|---------------|-----------|-----------------|-----------------|-----------------|-----------------|
| 5 | 0.11 | 7.47 | 6.59 | 5.47 | 6.29 |
| 7 | 0.15 | 14.84 | 13.10 | 10.81 | 11.67 |
| 8 | 0.18 | 20.04 | 17.71 | 14.52 | 15.26 |
| 9 | 0.20 | 25.4 | 23.54 | 19.64 | 19.50 |
| 10 | 0.22 | 33.52 | 31.42 | 26.33 | 29.1 |
| 11 | 0.24 | 43.63 | 41.20 | 35.88 | 38.42 |
| 12 | 0.26 | 56.62 | 61.99 | 51.18 | 53.42 |
| 13 | 0.29 | 81.98 | 106.55 | 84.97 | 95.85 |

For the speed corresponding to Froude number of $F_N \leq 0.24$, the vessel in the as-built variant (CSV1) had the highest resistance. For higher speed, the CSV2 had the highest total resistance. In the range of Froude number from 0.11 to 0.26 (5–12 knots), excluding $F_N = 0.2$ (9 knots), the CSV3 had the lowest resistance. It was the variant with a cruiser stern instead of a transom stern. For $F_N = 0.2$, the CSV4 had the lowest resistance. For the highest analysed speed of $F_N = 0.29$ (13 knots), the CSV1 had the lowest value of resistance. The hull form of CSV4 had relatively low resistance for the entire range of speed.

The results of the calculated total resistance coefficient are presented in Figure 4. For $F_N \leq 0.26$ (12 knots), the relative differences for the analysed variants of hull form were significant. For higher speeds, the difference in resistance performance increased much more rapidly. The comparison between variants CSV1 and CSV2 assessed the influence of the X-bow type bow shape. The comparison between CSV2 and CSV3 assessed the influence of a cruiser-type stern shape (X-aft). The comparison between CSV1, CSV3 and CSV4 assessed the influence of the hull form concept on the resistance performance.

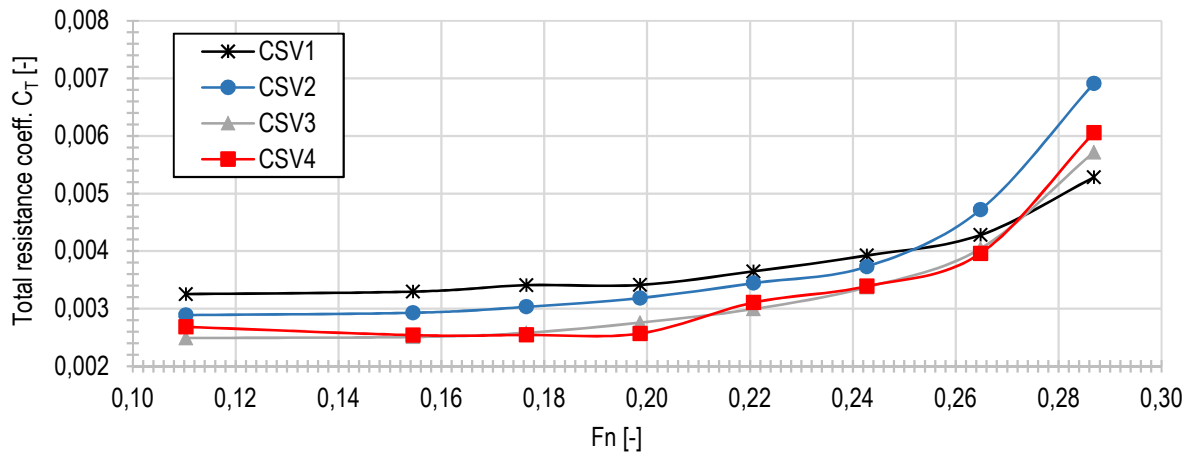


Figure 4: Total resistance coefficient for hull variants CSV1–CSV4

Vessels CSV1 and CSV2 had different bow forms. The replacement of the typical V-shaped bulbous bow by the X-bow form can be studied. For small Froude numbers, the CSV2 was characterised by lower resistance. For $F_N = 0,25$, the resistance curves intersected. For higher speed, the variant with bulbous bow was highly beneficial, and differences between total resistance coefficients increased with speed. This was a result of the reduction of pressure resistance by the bulbous bow. The comparison between variants CSV2 and CSV3 allowed to assess the influence of X-aft. It can be noticed that the resistance curves for CSV2 and CSV3 were almost parallel, and the variant with cruiser stern had lower resistance for the entire speed range. Transom sterns are applied on semi-planing and planing crafts and are beneficial for higher values of Froude number. The case study vessel operates in a displacement speed regime, thus the cruiser stern is supposed to be beneficial. The obtained results confirmed that expectation. Unlike the CSV3, for the CSV2 a hollow on the resistance curve for $F_N = 0,24$ (11 knots) and a hump for $F_N = 0,29$ (13 knots) occurred. Both hulls were subjected to significant increase of total resistance for speed above $F_N = 0,26$ (12 knots). The CSV4 has an atypically inclined stern that is supposed to damp transverse waves with a sharp waterline ending. This variant has an elongated and narrow bulbous bow with a conical flare. This bow form resembles the letter B. The CSV4 had reduced resistance in comparison to the CSV1 for $F_N < 0,27$. Despite the very different hull forms, the CSV3 and CSV4 had the most similar resistance for the entire speed range. The relative differences of resistance were equal 15%, 8%, 5%, -0.7%, 11%, 7%, 4%, 13% for F_N of 0,11, 0,15, 0,18, 0,20, 0,22, 0,24, 0,26, 0,28, accordingly. In Figure 5, the relative difference of the total resistance between the modified variants of the study vessel and the as-built (CSV1) version are shown. For F_N up to 0,24, the redesigned versions had significant reduction of hull resistance from -6% to -28%. For the design speed of $F_N = 0,22$ (10 knots), the reductions of total resistance for CSV2, CSV3, CSV4 were equal to -6%, -21%, -13%, accordingly. The resistance reduction for CSV2 varies between 6% and 12%, for CSV3 between 18% and 28%, and for CSV4 between 12% and 24%. For $F_N = 0,26$, the CSV2 had 9% higher resistance, and the remaining two vessels has 10% and 6% lower resistance. For $F_N = 0,29$, the CSV2–CSV4 had higher resistance than the CSV1 had, with up to 30% increase for CSV2.

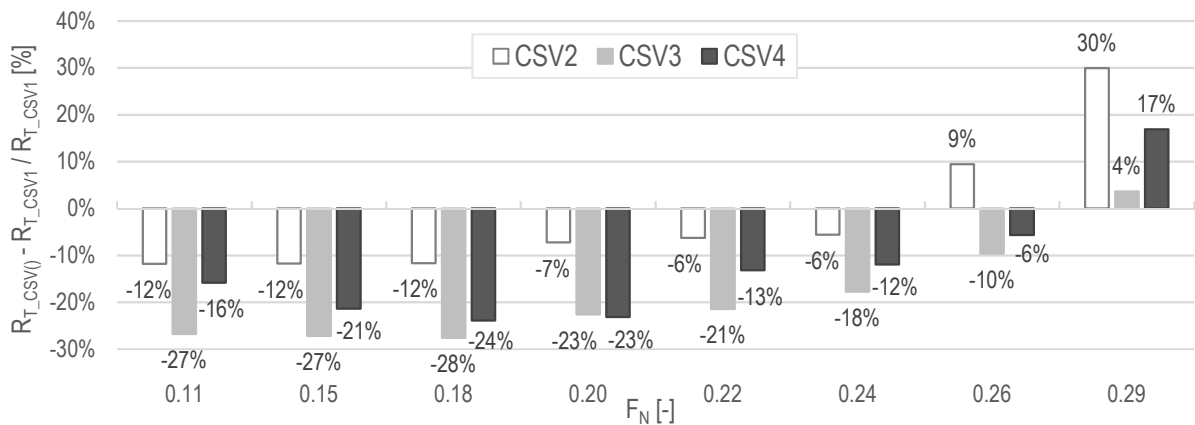


Figure 5: Relative change of total resistance caused by redesigning the hull CSV1 (as-built) to CSV2–CSV4

In Figure 6, pressure and frictional resistance coefficients are presented. The frictional resistance coefficient for all hull variants of the case study vessel were similar. This resulted from similar values of wetted surface area. For CSV1 and CSV4, the differences between values of frictional resistance for $F_N = 0.15, 0.26$ and 0.29 were less than 0.5%. For F_N between 0.25 and 0.26, pressure resistance became a bigger contributor to total resistance for all vessels, and its value started to increase rapidly. The humps and hollows of pressure resistance curves are visible. The CSV1 with a bulbous bow had much smaller pressure resistance for F_N above 0.27. For the entire range of speed, the CSV3 had the lowest frictional resistance due to the smallest wetted surface area.

Results of sinkage and dynamic trim are presented in Figure 7. It can be noticed that the smaller the area of waterplane, the higher the value of sinkage. The CSV1 was the only vessel that had negative value of dynamic trim, with bow up varying from -0.48 to -0.34 degrees. Other variants had dynamic trim with bow down. The highest value of running trim was equal to 0.6 degrees corresponding to $F_N = 0.29$ for CSV4. The CSV2 and the CSV3 had similar values of running trim, ranging between 0.1 and 0.31 degrees. For the CSV1–CSV2 hull forms and $F_N = 0.26$, the maximum value of running trim occurred.

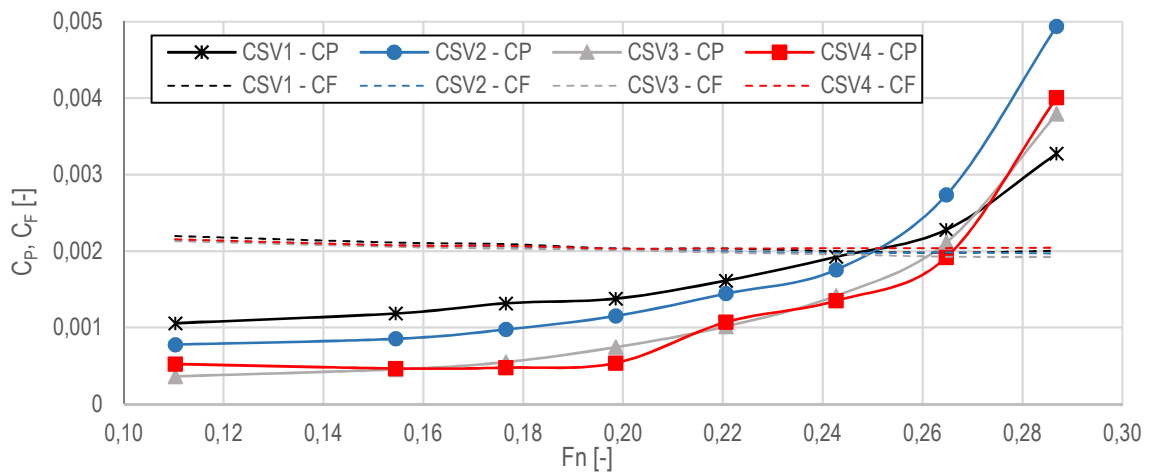


Figure 6: Pressure resistance coefficient C_P and frictional resistance coefficient C_F

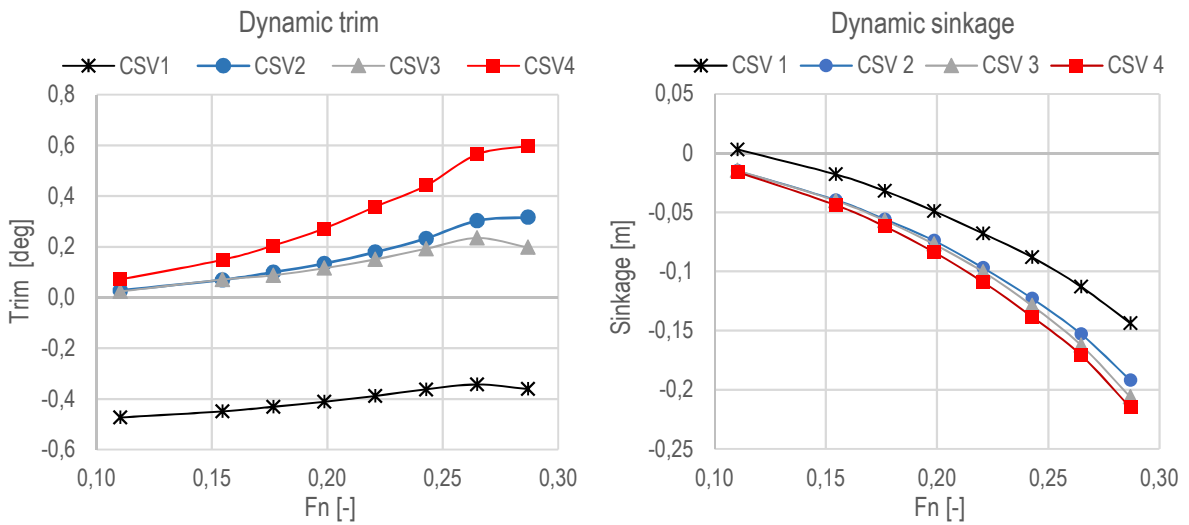


Figure 7: Dynamic trim and sinkage

In Figure 8, the relations between speed, wetted surface area S_w , waterplane area S_{WP} , and total resistance coefficient C_T are presented. On the left plot, hull variants are ranked from the one with the smallest wetted surface area, which in this case was the CSV3, to the one with the greatest — CSV4. The conclusion was that the wetted surface area for the analysed hull variants had minor impact on the value of total resistance. The difference of total resistance coefficient between CSV3 and CSV4 was slight. Furthermore, the CSV2 and CSV3, despite their moderate values of wetted surface area, had higher resistance than the CSV4 had. On the right plot, hull variants were ranked from CSV4 with the lowest waterplane area to CSV1 with the highest waterplane area. The conclusion was that the differences of waterplane area for the analysed hull variants had minor impact on the value of total resistance.

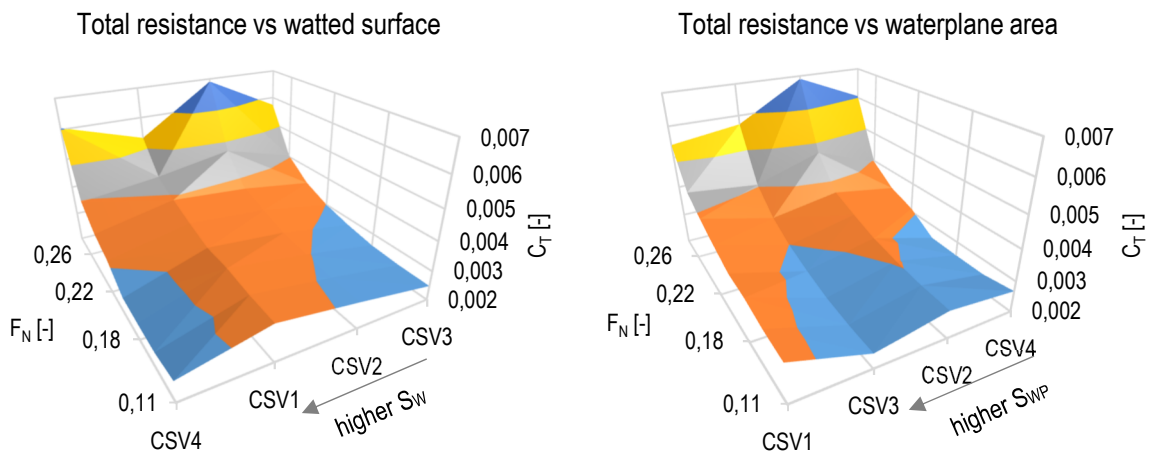


Figure 8: Influence of wetted surface area S_w and waterplane area S_{WP} on total resistance coefficient C_T

5 CONCLUSIONS

In upcoming years, due to new IMO regulations, the fuel economy of ships needs to be improved. Thus, the reduction of hull resistance will be increasingly important. The ship's design process can be significantly supported by full-scale CFD simulations giving a great possibility of proper hull form selection analysis. This paper demonstrated full-scale CFD simulations of calm water performance executed for four variants of a hull form. These four variants represent the innovative concepts of hull forms available on the commercial market. Namely, the V-shaped bulbous bow, X-bow, X-aft and B-bow. Analysis of the influence of hull form on calm water resistance was performed with the use of a case study vessel. The redesigned hull variants preserved the main hull dimensions and hydrostatic data, as well as the mass distribution. The following conclusions were formulated:

1. Full-scale CFD simulation can be used as a reliable and effective tool for resistance performance. The method takes advantage of directly modelling the ship's full scale. Thus, there is no need for extrapolation from a model scale to a full scale. This is important, especially for innovative and atypical hull forms with unknown form factor. Because of that, the determination of hull resistance with the use of towing tank testing has high uncertainty. The full-scale CFD simulations overcome this issue and can deliver the advantage of analysing many different hull forms evaluated both by an evolutionary and revolutionary approach.
2. The redesigned variants of the case study vessel, namely CSV2–CSV4, had significantly reduced resistance in a speed range from $F_N = 0.11$ (5 knots) to $F_N = 0.25$ (11.5 knots). For the operational speed corresponding to $F_N = 0.22$ (10 knots), the reduction of total resistance for CSV2, CSV3, CSV4 was equal 6%, 21%, 13%, accordingly. For lower speeds, the reduction was from 7% to 28%. For $F_N = 0.26$ (12 knots), the CSV3 and CSV4 had reduction of total resistance by 10% and 6%, accordingly. For the speed corresponding to $F_N = 0.29$ (13 knots), the CSV2–CSV4 had increased resistance in comparison with the original CSV1 hull form by 30%, 4%, and 17%, accordingly. This resulted from increased pressure forces acting on the hull starting to exceed frictional forces. As a consequence, a significant wave pattern developed around the hull. For the speed of $F_N = 0.29$ (13 knots), the original hull form benefited from the bulbous bow which greatly reduced the pressure component of resistance.
3. Reduction of resistance due to change of the stern shape from transom to X-aft (cruiser-type stern) was almost constant in a range of F_N from 0.11 to 0.24. The relative average difference between CSV2 and CSV3 was equal to 16%. For higher Froude numbers of $F_N = 0.26$ and $F_N = 0.29$, the reductions of resistance were equal to 17% and 20%, accordingly. The stern similar to the X-aft concept was better than the transom stern of the CSV1. For the displacement speed regime, a cruiser stern type should always be beneficial from the hydrodynamic point of view. Despite that, transom sterns are most frequently applied on merchant displacement ships. The reason for this can be much easier manufacturing. The transom stern is generally expected to provide better performance for speeds $F_N > 0.4$.

4. The redesigned hull variants CSV2–CSV4 had higher values of dynamic trim and sinkage than the original hull form CSV1 had. The CSV1 was the only vessel with initial trim bow up, varying from 0.34 degrees for $F_N = 0.26$ to 0.48 degrees for $F_N = 0.11$. The remaining hull variants had dynamic trim with bow down. The greatest trim angle was in the CSV4 for the maximum value of 0.6 degrees for $F_N = 0.29$. The CSV2 and CSV3 had very similar values of trim angle, varying from 0.1 to 0.32 degrees. For CSV3, the maximum trim angle was equal to 0.24 degrees and occurred for $F_N = 0.26$, and CSV2 reached maximum trim angle equal to 0.32 degrees for $F_N = 0.29$. The highest sinkage was equal to 0.21 m and occurred for the maximum speed of CSV4. This vessel was characterised by the smallest waterplane area. The CSV1 had the lowest sinkage, and for the maximum speed it was equal 0.14 m.
5. Analysis of the waterplane area and wetted surface area influence allows to draw conclusions that both particulars had minor influence on the resistance of the analysed hull variants.
6. This article presented the crucial step of overall analysis as calm water resistance is necessary to assess the added resistance. A subsequent paper will investigate the influence of hull form on the seakeeping performance, especially on the added resistance and ship motions.

Acknowledgements

The research was supported by the National Centre for Research and Development (NCRD) and the SmartPS project No. MARTECII/SmartPS/4/2016. The research was supported by the Academic Computer Centre in Gdansk (CI TASK). All the support is highly appreciated by the authors.

REFERENCES

- [1] ITTC, “ITTC – Recommended Procedures and Guidelines - Practical guidelines for ship CFD applications. 7.5-03-02-03 (Revision 01),” in *ITTC – Recommended Procedures and Guidelines*, 2014, p. 19.
- [2] ITTC, “Practical Guidelines for Ship Resistance CFD - 7.5-03-02-04,” in *ITTC – Recommended Procedures and Guidelines*, 2014, pp. 1–9.
- [3] Z.-R. Zhang, H. Liu, S.-P. Zhu, and F. Zhao, “Application of CFD in ship engineering design practice and ship hydrodynamics,” *J. Hydrodyn.*, vol. 18, iss. 3, suppl., pp. 315–322, 2006.
- [4] H. C. Raven, A. van der Ploeg, A. R. Starke, and L. Eça, “Towards a CFD-based prediction of ship performance — Progress in predicting full-scale resistance and scale effects,” *Trans. R. Inst. Nav. Archit. Part A Int. J. Marit. Eng.*, 2008.
- [5] R. Broglia, B. Bouscasse, B. Jacob, A. Olivieri, S. Zaghi, and F. Stern, “Calm water and seakeeping investigation for a fast catamaran,” *FAST 2011 11th Int. Conf. Fast Sea Transp.*, 2011.
- [6] S. Percival, D. Hendrix, and F. Noblesse, “Hydrodynamic optimization of ship hull forms,” *Appl. Ocean Res.*, 2001.
- [7] J. J. Maisonneuve, S. Harries, J. Marzi, H. C. Raven, U. Viviani, and H. Piippo,

- “Towards Optimal Design of Ship Hull Shapes,” *8th Int. Mar. Des. Conf.*, 2003.
- [8] H. Zakerdoost, H. Ghassemi, and M. Ghiassi, “An evolutionary optimization technique applied to resistance reduction of the ship hull form,” *J. Nav. Archit. Mar. Eng.*, 2013.
- [9] K. V. Kostas, A. I. Ginnis, C. G. Politis, and P. D. Kaklis, “Ship-hull shape optimization with a T-spline based BEM-isogeometric solver,” *Comput. Methods Appl. Mech. Eng.*, 2015.
- [10] F. Huang and C. Yang, “Hull form optimization of a cargo ship for reduced drag,” *J. Hydrodyn.*, vol. 28, no. 2, pp. 173–183, 2016.
- [11] Y. K. Demirel, O. Turan, and A. Incecik, “Predicting the effect of biofouling on ship resistance using CFD,” *Appl. Ocean Res.*, 2017.
- [12] Y. Li, K. Alame, and K. Mahesh, “Feature-resolved computational and analytical study of laminar drag reduction by superhydrophobic surfaces,” *Phys. Rev. Fluids*, 2017.
- [13] D. Ponkratov and C. Zegos, “Validation of ship scale CFD self-propulsion simulation by the direct comparison with sea trials results,” in *4th Int. Symp. Marine Propulsors*, 2015.
- [14] S. Bhushan, T. Xing, P. Carrica, and F. Stern, “Model- and full-scale URANS simulations of Athena resistance, powering, seakeeping, and 5415 maneuvering,” *J. Sh. Res.*, vol. 53, no. 4, pp. 179–198, 2009.
- [15] P. M. Carrica, H. Fu, and F. Stern, “Computations of self-propulsion free to sink and trim and of motions in head waves of the KRISO Container Ship (KCS) model,” *Appl. Ocean Res.*, 2011.
- [16] A. Mofidi and P. M. Carrica, “Simulations of zigzag maneuvers for a container ship with direct moving rudder and propeller,” *Comput. Fluids*, vol. 96, pp. 191–203, 2014.
- [17] A. Elhanafi, “Prediction of regular wave loads on a fixed offshore oscillating water column-wave energy converter using CFD,” *J. Ocean Eng. Sci.*, vol. 1, no. 4, pp. 268–283, 2016.
- [18] K. Niklas, “Strength analysis of a large-size supporting structure for an offshore wind turbine,” *Polish Marit. Res.*, vol. 24, no. s1, Jan. 2017.
- [19] A. Elhanafi, G. Macfarlane, and D. Ning, “Hydrodynamic performance of single-chamber and dual-chamber offshore-stationary Oscillating Water Column devices using CFD,” *Appl. Energy*, vol. 228, no. March, pp. 82–96, 2018.
- [20] Ulstein Design AS, “A foreship arrangement for a vessel of the displacement type,” WO 2006/096066 A1, 2006.
- [21] J. H. Ferziger and M. Peric, *Computational Methods for Fluid Dynamics*. Springer, 2002.
- [22] Y. C. Kim, K. S. Kim, J. Kim, Y. Kim, I. R. Park, and Y. H. Jang, “Analysis of added resistance and seakeeping responses in head sea conditions for low-speed full ships using URANS approach,” *Int. J. Nav. Archit. Ocean Eng.*, vol. 9, no. 6, pp. 641–654, 2017.
- [23] T. Tezdogan, Y. K. Demirel, P. Kellett, M. Khorasanchi, A. Incecik, and O. Turan, “Full-scale unsteady RANS CFD simulations of ship behaviour and performance in head seas due to slow steaming,” *Ocean Eng.*, vol. 97, pp. 186–206, 2015.
- [24] Siemens PLM Software, “User Guide Star CCM+ v12.04,” 2017.
- [25] ITTC, “ITTC Quality System Manual Recommended Procedures and Guidelines Preparation , Conduct and Analysis of Speed / Power Trials 7.5-04-01-01.1,” 2017.

SHIP SCALE VALIDATION OF CFD MODEL OF SELF-PROPELLED SHIP

HENRIK MIKKELSEN*, MADS L. STEFFENSEN*, COSMIN CIORTAN†
AND JENS H. WALTHER*‡

*Technical University of Denmark (DTU)
Department of Mechanical Engineering
Nils Koppels Allé, Building 404, 2700 Kgs. Lyngby, Denmark.
e-mail: jhw@mek.dtu.dk, web page: <http://www.mek.dtu.dk/>

† DNV-GL
Section for Hydrodynamic and Stability
Veritasveien 1, 1363 Høvik, Norway

‡ Swiss Federal Institute of Technology Zurich
Computational Science & Engineering Laboratory
Clausiusstrasse 33, CH-8092 Switzerland

Key words: Computational fluid dynamics, Ship scale ship propulsion, Sea trial validation, Self-propulsion simulation

Abstract. This paper presents a comparison of towing tank testing, ship scale computational fluid dynamics (CFD) simulations, sea trial measurements and in-service performance. The study includes extensive convergence tests and validation of both resistance, open-water and self-propulsion CFD simulations in both model and ship scale. The self-propulsion CFD simulations are conducted using a novel method. This method includes calculating the wave-making resistance separately, in order to reduce the computational cost.

The results of the ship scale self-propulsion CFD show an average overestimation of delivered power of 2% compared to the sea trial results, where the predicted delivered power using the towing tank approach shows an average overestimation of delivered power of 6%. Both predictions are within the uncertainty of the speed trial measurements. The study shows that both the towing tank approach and ship scale CFD can make reasonable and similar estimations of the ship scale performance of a ship. Furthermore, we find that for the present ship, CFD is able to predict performance as accurately as towing tank procedures, indicating that ship scale CFD is a mature tool for use in future ship designs.

1 INTRODUCTION

Traditionally, the performance of a ship design is estimated by conducting towing tank tests on a downscaled version of the ship (model scale). The results from these towing tank tests

are then extrapolated to the scale of the actual ship (ship scale). An alternative to testing in a towing tank is to simulate the flow around the ship using computational fluid dynamics (CFD). CFD simulations can be performed in ship scale, which eliminates scale effects and the need for extrapolation. A disadvantage of using CFD is modelling errors which occur due to simplification of the flow physics (e.g. turbulence).

Extensive validation of CFD simulations in model scale has been conducted by e.g [7], which showed good agreement with experimental results of the research ship Kriso Container Ship (KCS). Furthermore, validation workshops have been hosted, where the participants blindly submit CFD results to be compared with towing tank results [9, 8].

With the increased confidence in model scale, the next step is ship scale CFD, which has been studied by e.g. [1]. However, in ship scale publicly accessible validation data is extremely rare. The largest contribution so far on ship scale validation, is the Lloyd’s Register workshop from 2016 [11]. A comparison between ship scale CFD and sea trial measurements of a car carrier has been conducted by [6] showing accurate correspondence.

The present paper includes a comparison between sea trial measurements, ship scale CFD, model tank experiments and in-service performance. It is the first published study, where all these elements are compared. The conducted self-propulsion CFD simulations in the present study calculate the wave-making resistance in a different way than e.g. [13, 6] since the wave-making resistance is calculated separately. This results in a significantly reduced computational cost.

The key to a useful comparison is highly accurate sea trial data. Sea trial data generally has significant uncertainties because of the lack of control in the experimental environment. There is a focus in the industry on obtaining increasingly accurate sea trial results, as seen with introduction of the new sea trial procedure ISO 15016:2015 cf. [4]. Besides the difficulties in conducting experiments at such a large scale, it is also important to remember that there are many stakeholders in a sea trial, each with different interests.

2 THE STUDIED VESSEL AND MEASUREMENTS

The ship considered in the present study is a $L_{PP} = 196$ m bulk carrier built by a Japanese shipyard.

2.1 Hull

The hull has been provided as a 3D geometry by the Japanese shipyard. The hull and water lines of the design and sea trial conditions are shown in Figure 1. The displacement of the ship in sea trial condition is 40.2% of the displacement in the design condition. The vessel is at design speed sailing at a Reynolds number $Re = \frac{V_{Design} L_{PP}}{\nu} \approx 1.1 \times 10^9$ and a Froude number $Fr = \frac{V_{Design}}{\sqrt{g L_{PP}}} \approx 0.2$.

2.2 Propeller

The data of the actual and the stock propeller can be seen in Table 1. Due to confidentiality it has not been possible for the propeller manufacturer to provide the 3D geometry of the actual propeller. Therefore, the stock propeller has been used for all CFD simulations.

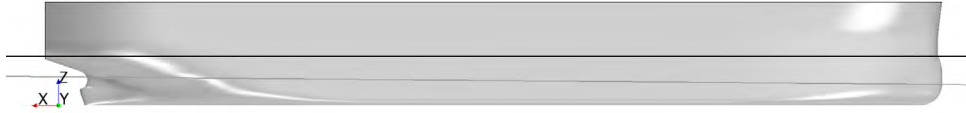


Figure 1: Hull geometry. The upper horizontal line is the water line of the design condition, and the lower horizontal line is the water line of the sea trial condition. Seen from starboard side.

| Parameter | Actual | Stock |
|------------------------|--------|--------|
| Ship scale diameter | 6.00 m | 6.00 m |
| Boss ratio | 0.1417 | 0.18 |
| Pitch ratio ($0.7r$) | 0.7284 | 0.76 |
| Expanded area ratio | 0.48 | 0.58 |
| Number of blades | 4 | 4 |

Table 1: Data of the actual and the stock propeller.

2.3 Appendages

The actual ship is mounted with a rudder, a number of upstream stator fins and bilge keels. The "to-be-built" 2D-drawings of the stator fins and rudder including rudder bulb have been provided by the Japanese shipyard. Based on these drawings, the stator fins and rudder geometry have been recreated in 3D.

The stator fins are a retrofitted energy saving device and are mounted upstream of the propeller to produce pre-swirl.

Bilge keels are not included in the CFD simulations since they are not mounted on the model ship in the towing tank test. They are instead accounted for in the towing tank and CFD simulations by using the standard International Towing Tank Committee (ITTC) method [5].

2.4 Towing tank testing

Towing tank tests of the vessel are conducted by the National Maritime Research Institute in Tokyo, Japan. The tests conducted by the towing tank are resistance tests, open water tests and self-propulsion tests. The results from the towing tank have been extrapolated using the standard ITTC extrapolation procedure [5].

2.5 Sea trial

Four sister vessels of the same design have been built in total. Speed trials have been conducted for each of the four sister ships. In 2015, the International Maritime Organisation (IMO) and ITTC released ISO15016:2015 [4], an updated version of the ISO 15016:2002 standard procedure for carrying out and correcting speed trials. The speed trials of the fourth ship have been conducted mostly as described in [4]. The speed trials of the three other ships have been conducted prior to the release of that procedure, but is assumed to have been conducted using similar procedures. The Japanese shipyard has provided the results of these speed trials for all four ships. The main measurements in the speed trial are speed, propeller rate of rotation, and the engine power. After the speed trial, the measurements are corrected for the environment

forces.

2.5.1 Speed measurement and corrections

The speed of the ship during the speed trial is measured using a Differential-GPS (DGPS). The temporary DGPS is installed on top of the bridge and is connected to a laptop. From the DGPS data, the ship speed over ground is calculated by assuming no lateral drift. The ship speed is recorded during each speed run, with a sampling frequency of about 1 Hz. From the recorded data, a mean ship speed is calculated.

The speed over ground signal is visually inspected, showing only minor fluctuation. Based on observations, it is concluded that the speed signal is reliable and that the mean is an accurate measurement of the actual speed over ground of the ship. To obtain the speed through water, the speed measurement has to be corrected for current. The measured speed is corrected for the tidal current by using double runs: one in the direction against the current and one with the current.

2.5.2 Power measurement and correction

The power of the engine is calculated from the engine rate of rotation and the the fuel index (FI), which is indicating the amount of fuel injected ranging from 0 to 100, using the following formula provided by the engine manufacturer:

$$P = C_{cyl} C_{eng} n p_{me} \quad (1)$$

$$C_{eng} = \frac{60}{2\pi} 100.7355 \times 10^{-3} \quad (2)$$

$$p_{me} = 19375 FI - 105938 \quad (3)$$

Here P denotes the engine power in Watts, C_{cyl} and C_{eng} are cylinder coefficient provided by the engine manufacturer, n is the rate of revolutions per second, p_{me} is the mean effective pressure in Pascals. The mean effective pressure (p_{me}) is calculated from the fuel index cf. Equation (3) as provided by the engine manufacturer:

Both the rate of rotation and the fuel index are sampled directly from the engine control system. The revolutions per minute of the engine is measured directly on the shaft, and there is no gear box.

ISO15016:2015 [4] states that the power has to be measured using a torque meter mounted directly on a shaft. Such a device is also installed, but the measurements are not used in the speed trial results.

The measured power is corrected for the difference between the planned and the actual displacement of the ship [4]. The planned displacement of the ship in sea trial condition is calculated before conducting the sea trial, and the actual displacement is measured at the beginning of the sea trial. The correction is conducted by the shipyard. The difference in displacements is less than 1 %.

The performance of the ship is corrected for the added wind resistance [4, Annex C]. The wind correction is based on an estimated drag coefficient, an estimated projected front area and

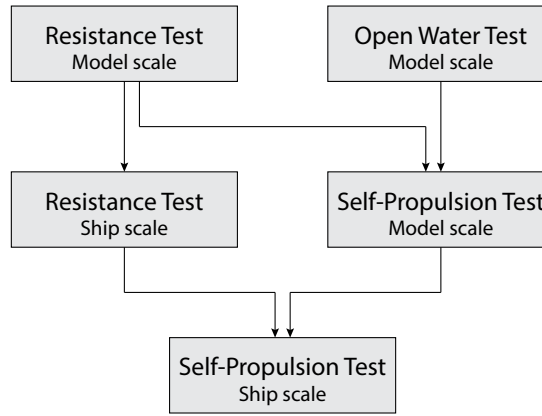


Figure 2: The five CFD setups. The arrows indicate the direction of the work flow.

a relative wind speed. The absolute wind speed is measured using a wind anemometer placed above the bridge.

The results used in the present study are corrected for waves as described in [4]. The method requires significant wave height and direction of the waves. These two parameters were not recorded during any of the sea trials of the four sister ships. Instead, the parameters have been estimated using Atmospheric Reanalysis (ERA)-Interim data from satellite weather data and a meteorological model.

3 COMPUTATIONAL FLUID DYNAMICS

This section briefly describes the CFD setups developed and used in this study. More details can be found in [10]. All the CFD simulations are performed by discretizing the domain by hexahedral cells in the commercial CFD-code STAR-CCM+ v.10.04.011 from CD-Adapco, now SIEMENS [2]. STAR-CCM+ discretizes the governing equations using an unstructured finite-volume method. The code is widely used in the marine industry and is well-known for its capabilities within marine applications.

In total five CFD setups are developed: model scale resistance setup, ship scale resistance setup, model scale open water setup, model scale self-propulsion setup, and ship scale self-propulsion setup. The five CFD setups are illustrated Figure 2.

3.1 Governing equations and CFD output

The governing equations of an incompressible Newtonian fluid are the continuity and Navier-Stokes equations:

$$\frac{\partial u_i}{\partial x_i} = 0 \quad (4)$$

$$\rho \frac{\partial u_i}{\partial t} + \rho u_j \frac{\partial u_i}{\partial x_j} = -\frac{\partial p}{\partial x_i} + \frac{\partial}{\partial x_j} \left(2\mu S_{ij} - \overline{\rho u'_j u'_i} \right) \quad (5)$$

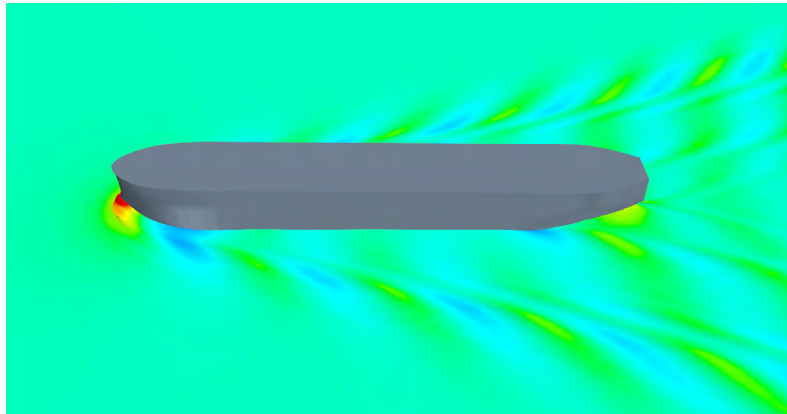


Figure 3: Wave elevation from model scale resistance simulation.

where u_i is the velocity vector, t is time, p is pressure, μ is dynamic viscosity, $S_{ij} = \frac{1}{2} \left(\frac{\partial u_i}{\partial x_j} + \frac{\partial u_j}{\partial x_i} \right)$ is the mean strain rate and u' is the fluctuating part of the velocity.

The calm free surface in the resistance and self-propulsion simulations is resolved using the volume of fluid (VOF) method in STAR-CCM+ [2, 3]. The turbulence is modelled using the realisable k - ϵ turbulence model [2, 12].

One output from the CFD simulations is the total ship resistance, which is calculated by integrating the shear and pressure force on the entire ship hull excluding the propeller.

The propeller thrust T is calculated by integrating all shear and pressure forces on the propeller parallel to the shaft axis.

The propeller torque Q is calculated by integrating all moment contribution from both the shear and pressure forces on the propeller around the shaft axis.

3.2 CFD resistance test

The calm water resistance calculation is first created in model scale and validated by comparing results with the towing tank results. The validated model scale setup is then scaled up to a ship scale setup. Convergence studies are conducted in both the model and ship scale setup. Results of the ship scale CFD setup are compared with the extrapolated resistance data from the towing tank data. More details on the CFD resistance setup, can be found in [10].

All resistance simulations are performed in the sea trial condition similarly to the towing tank test and sea trial. The initial CFD setup used to estimate the calm water resistance is an automated CFD setup developed by OSK-ShipTech A/S. An illustration of the wave elevation in a resistance simulation is shown in Figure 3.

The CFD resistance setup uses a number of different physics models to describe the flow around the ship. Free surface waves are modelled using volume of fluid [2, 3]. The hull is allowed dynamic pitch and heave motions. The simulations are solved using a 1st order implicit unsteady solver.

After demonstrating good agreement with the towing tank results, the ship scale resistance setup is created by scaling up the model scale resistance setup with the scaling factor. The prism layers is changed so the wall y^+ is still mostly in the range of 50–100.

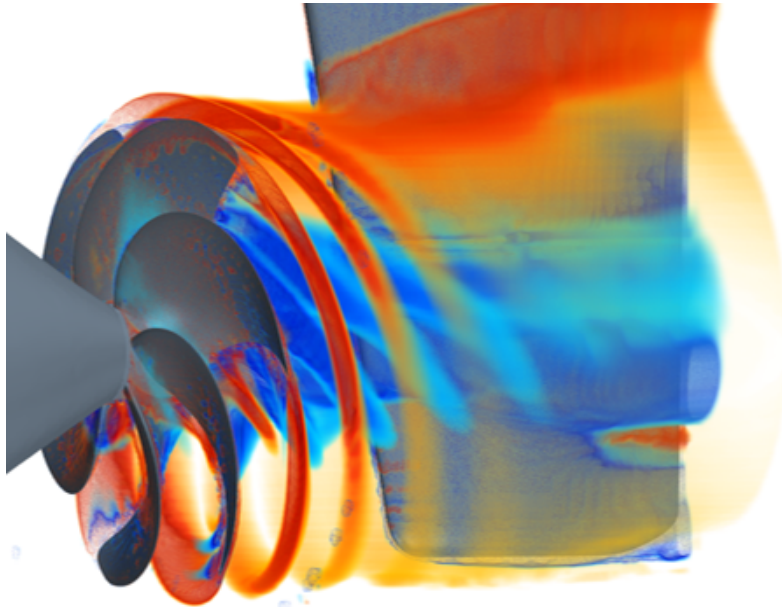


Figure 4: Vorticity downstream of propeller in self-propulsion simulation.

3.3 CFD open water

Modelling the open water test using CFD is less complex than modelling the self-propulsion test because the hull-propeller interaction is not included in the open water setup. The idea is that a separately validated resistance and open water setup can be combined to a self-propulsion setup by using the validated mesh and time step settings. This self-propulsion setup can then be validated in model scale by comparing it with self-propulsion results from towing tank tests.

The single phase open-water CFD setup is fully resolving the boundary layer with wall y^+ values approximately equal to one.

The open water setup uses two domains: A stationary domain and a rotating domain. The two domains are connected by an interface. The shape of the stationary domain is a rectangular cuboid. The shape of the rotating domain is a cylinder which is located inside the static domain and around the propeller. In order to better resolve the flow around the propeller, two refinement zones are used to refine the mesh in the volume around the propeller.

The propeller movement can be modelled using two methods: the moving reference frame (MRF) method or the sliding mesh (SM) method. For the open-water simulation, MRF is used.

3.4 CFD self-propulsion

The self-propulsion CFD setup is created by combining the model scale resistance CFD setup with the propeller and the open water CFD setup. As in the open water setup, the self-propulsion setup uses two domains; a large static domain, with a small rotating domain inside. The shape of the static domain is a rectangular cuboid, and the shape of the rotating domain is a cylinder. The resolved flow around propeller is illustrated in Figure 4.

In order to minimize computational cost, the free surface is not included directly in the self-

propulsion simulation. This is conducted by replacing the free surface with a slip wall. The method is originally developed and validated at DNV-GL. Instead of modelling the dynamic pitch and heave using the DFBI model, the dynamic pitch and heave of the resistance simulations are prescribed to the self-propulsion simulations before they are simulated. Removing the free surface waves from the simulations gives rise to another problem. In reality, a stern wave is created by the ship. The stern wave increases the water height above the propeller, which affects the flow. In order to resolve this, the symmetry plane is raised to a highest point of the stern wave obtained in the resistance simulation. In the present case, the symmetry plane is elevated 3% of the draft in the sea trial condition. The decision not to model the free surface waves and to raise the calm water surface decreases the measured resistance on the ship. In order to compensate for this change, a free surface correction is performed on the results of the self-propulsion simulations. The correction is performed in two steps. The first step is to correct for not modelling the free surface waves, which reduces the hull resistance by removing the wave making resistance. The wave making resistance is quantified by simulating the resistance setup both with and without the free surface waves. The difference between those two results is the wave making resistance:

$$R_W = R_T - R_V \quad (6)$$

where R_W is the wave making resistance, R_T is the total resistance and R_V is the total resistance without free surface waves, also referred to as the viscous resistance. In the present study the wave making resistance is approximately 25% of the total resistance.

The second step is to correct for the raised free surface which increases the resistance on the hull, because a larger surface area is submerged. The increase in resistance is quantified by simulating the resistance both with the initial and the raised surface heights without modelling the free surface. The difference between those two results is the added resistance due to the raised surface ΔR_{SH} , which in the present study is approximately 7% of the total resistance, is given by:

$$\Delta R_{SH} = R_{V,SH} - R_V \quad (7)$$

where $R_{V,SH}$ is the viscous resistance with the raised surface height. The resistance of the self-propulsion simulations can then be corrected for wave making resistance and added resistance due to the raised surface height:

$$R_{Tm} = R_{Vm,SH} + R_{Wm} - \Delta R_{SHm} \quad (8)$$

where the subscript 'm' refers to model scale.

For the self-propulsion simulations a combination of the two methods is used for increased computational efficiency. The modelling of the propeller rotation is initialized by using the MRF method, followed by the SM method. The SM uses a time step corresponding to two degrees of propeller rotation. These steps with different methods and time steps are used to minimize the computational cost. One advantage of using the method with the separate calculation of the wave-making resistance is that the MRF step can be solved with a steady-state solver. Furthermore, it is not necessary to solve the volume fraction transport equation or to refine

| Simulation type | Parameter | Discrepancy from model tank test |
|-----------------|--------------------|----------------------------------|
| Resistance | Total resistance | $\approx 0\text{--}2\%$ |
| Open water | Thrust coefficient | $\approx 1\text{--}3\%$ |
| | Torque coefficient | $\approx 3\text{--}5\%$ |
| | Efficiency | $\approx 2\text{--}7\%$ |
| Self-propulsion | Thrust coefficient | $\approx 3\text{--}7\%$ |
| | Torque coefficient | $\approx 6\text{--}7\%$ |
| | Rotation rate | $\approx 2\text{--}6\%$ |

Table 2: Discrepancy of model scale CFD results from model tank test [10].

the mesh near the free surface. This significantly decreases the computational cost. The self-propulsion simulation has more than double as many cells as the resistance simulation and a time step in the SM step, which is approximately a factor of 30 smaller cf. [10]. However, the computational cost of the self-propulsion simulation, using the present approach, is only approximately 20% higher than a resistance simulation.

The CFD self-propulsion setup is carried out by changing the rate of revolution of the propeller until a force equilibrium is obtained in the sailing direction within a reasonable small tolerance.

The ship scale self-propulsion setup is created by scaling up the model scale self-propulsion setup according to the scaling factor. The prism layers is changed so the wall y^+ is still mostly in the range of 30–100 on the hull and propeller.

The free surface correction method is changed slightly from model scale to ship scale in order to account for the roughness resistance, air resistance and bilge keel resistance which are only relevant for the ship scale simulations. The wave making resistance and the added resistance of the increased surface height are calculated similarly to Equations (6) and (7).

The ship scale resistance is then calculated using:

$$R_{Ts} = \frac{S + S_{BK}}{S} (R_{Vs,SH} + \Delta R_F) + R_{Ws} + R_{AAS} - \Delta R_{SHs} \quad (9)$$

where the subscript 's' refers to ship scale, S is the wetted surface without the bilge keels, S_{BK} is the wetted surface including the bilge keels, ΔR_F is the roughness resistance, and R_{AAS} is the air resistance. The correlation allowance C_A cf. [5] is not included in the total resistance because its purpose is to correct for systematic errors in the towing tank extrapolation procedure.

4 RESULTS AND DISCUSSION

4.1 Validation of the CFD simulations

It is essential to ensure the accuracy of the CFD setup before conclusions are based on the results of the setup.

Convergence studies have been conducted for both the spatial and temporal discretization for all five setups. The discrepancy of the model scale CFD results from the model tank test are shown in Table 2. More details can be found in [10].

Based on the convergence studies and comparisons to the towing tank tests, the results of the model scale self-propulsion setup are reasonable. The ship scale set-up has been built up in

the same way as the model scale CFD set-up. All convergence tests and comparisons in ship scale have shown satisfactory results cf. [10].

4.2 Comparison of sea trial and in-service performance data

The results provided by the shipyard are the measured values corrected for wind and current. The procedures of the sea trial and corrections are briefly described in Section 2.5.

The results from the sea trials seen in Figure 5 show high correlation between speed and power, and low scatter of the data points. This indicates that the accuracy of the speed trial data is high. However, systematic errors can not be determined solely from the data provided for this study.

The correction for wind, waves and current is a possible sources for systematic errors. As mentioned, the ISO 15016:2015 procedure [4] defines strict standards for conducting sea trials and ensures accurate measurements and corrections. The power measurements based on engine formulas are another possible source for systematic errors.

A way to validate the results from the sea trial is by comparing the results with performance measurements on the ship after the delivery while it is in service. The ship owner has provided in-service performance data in sea trial condition corrected for wind and waves by the ship owner. The data is the mean performance of all four sister ships in the first 3-9 months of operation. The power is based on torque measurements directly on the shaft and not the engine manufacturer formula as in case of the sea trial measurements. The ship owner has estimated the uncertainty to be approximately $\pm 3.5\%$ maximum continuous rating (MCR). Uncertainties in the performance data includes e.g. uncertainties in the raw torque measurement, the correction for wind and waves and the averaging of the data from the four sister ships.

The results of the sea trial are compared to the in-service performance data in Figure 5. The comparison shows that the ships use more power in-service than during sea trial. On average, the sea trial data shows 8% less power than the in-service performance data. This is expected since the ships are in excellent condition at the sea trial with minimal fouling on the ship hull. Even though both the sea trial data and the in-service performance data have uncertainties, the relatively low offset in power shows that the sea trial data and the in-service performance data measures delivered power in the same range. Furthermore, there is only a small scatter of the sea trial data, which indicates good consistency in the measurements.

4.3 Comparison of sea trial, CFD and towing tank test

The sea trial results presented in Section 4.2 are compared to the extrapolated self-propulsion results from the towing tank test and ship scale CFD in Figure 5. In this comparison, it is assumed that there is no loss in the shaft, which is a reasonable assumption, since there is no gear.

The extrapolated towing tank results are overestimating the power by approximately 3–9% with an average of 6% compared to the sea trial results. Considering that towing tank tests are conducted at a much lower Reynolds number and extrapolated, the observed discrepancies are satisfactory.

Is it important to remember that the extrapolation of the towing tank results are performed by the authors using the standard ITTC procedure [5]. Based on the authors' experience, many

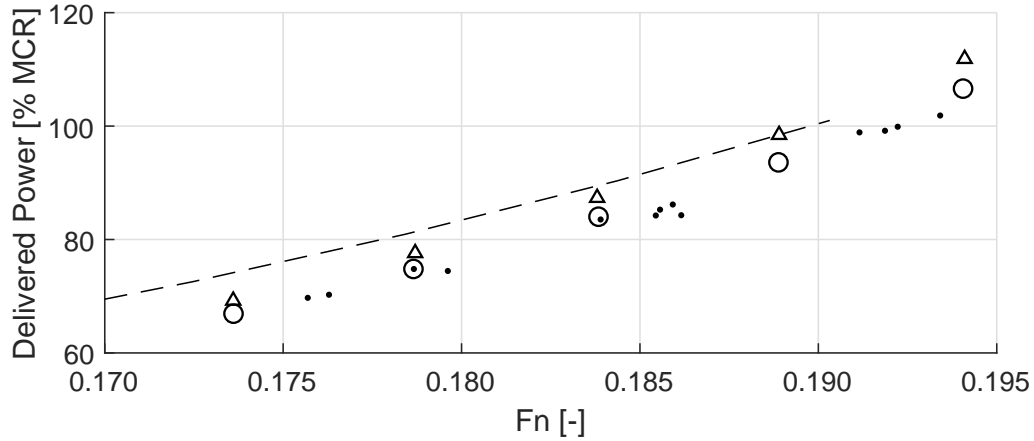


Figure 5: Comparison of the corrected speed trial results (dot), the extrapolated self-propulsion results (triangle) from the towing tank and the ship scale CFD self-propulsion results (circle). Delivered power P_{D_s} as a function of Froude number F_n .

towing tanks use slightly different coefficients and corrections than the standard ITTC procedure recommends. These changes to the standard procedure are based on experience, tradition, studies of systematic errors and validation studies of each tank. It has not been possible to have the exact extrapolation procedure that the towing tank uses in the present study. Therefore, the extrapolation procedure used in this study is the standard ITTC procedure.

Furthermore, it can be seen in Figure 5 that the CFD overestimates the delivered power by approximately 0–5% with an average of 2%. It is important to remember that the CFD simulations are performed using the stock propeller and not the actual propeller.

5 CONCLUSION

A ship scale self-propulsion CFD setup using a new method developed by DNV-GL has been built and validated. The results of the CFD simulations showed an overestimation of the delivered power by approximately 2% on average compared to the sea trial results. Raw experimental towing tank test results have been extrapolated to ship scale using the ITTC procedure. It was found that this prediction overestimated the delivered power with 6% in average compared to the sea trial results. Both predictions are within the uncertainty of the speed trial measurements.

6 ACKNOWLEDGEMENT

The research was supported by The Danish Maritime Fund under grant 2015-103 and 2018-11, whose support is greatly appreciated.

Furthermore, we would like to express our sincere gratitude to the Japanese shipyard and European ship-owner for inviting us to the sea trial and providing unique and rarely shared data.

REFERENCES

- [1] A. M. Castro, P. M. Carrica, and F. Stern. Full scale self-propulsion computations using discretized propeller for the KRISO container ship KCS. *Comput. Fluids*, 51(1):35–47, 2011.
- [2] CD-Adapco. STAR-CCM+ Documentation, Version 10.04, 2015.
- [3] C. Hirt and B. Nichols. Volume of fluid (VOF) method for the dynamics of free boundaries. *J. Comput. Phys.*, 39(1):201–225, 1981.
- [4] IMO. ISO 15016:2015. *MEPC 68/INF.14*, 2015.
- [5] ITTC. Recommended Procedures and Guidelines, 1978 ITTC Performance Prediction Method, 2005.
- [6] H. Jasak, V. Vukčević, I. Gatin, and I. Lalović. CFD validation and grid sensitivity studies of full scale ship self propulsion. *Int. J. Nav. Archit. Ocean Eng.*, 2018.
- [7] J. Kim, I.-R. Park, K.-S. Kim, and S.-H. Van. Numerical Simulation of Turbulent Free Surface Flow around a Self-Propelled Ship. In *Proc. Fifteenth Int. Offshore Polar Eng. Conf.*, pages 180–186, Seoul, Korea, 2005.
- [8] L. Larsson, F. Stern, M. Visonneau, T. Hino, N. Hirata, and J. Kim. *PROCEEDINGS, TOKYO 2015 WORKSHOP ON CFD IN SHIP HYDRODYNAMICS*. 2015.
- [9] L. Larsson, F. Stern, and M. Visonneau. Gothenburg 2010 A Workshop on Numerical Ship Hydrodynamics Editors. II(1652), 2010.
- [10] H. Mikkelsen and M. L. Steffensen. *Full Scale Validation of CFD Model of Self-Propelled Ship*. Master’s thesis, Technical University of Denmark, <https://doi.org/10.13140/RG.2.2.25689.21607>, 2016.
- [11] D. Ponkratov. 2016 Workshop on Ship Scale Hydrodynamic Computer Simulation. Lloyd’s Register, 2017.
- [12] T.-H. Shih, W. W. Liou, A. Shabbir, Z. Yang, and J. Zhu. A new k- ϵ eddy viscosity model for high Reynolds number turbulent flows. *Comput. Fluids*, 24(3):227–238, 1995.
- [13] C. Zegos and D. Ponkratov. Ship scale CFD free sink, trim & surge self-propulsion simulation and direct comparison to sea trials. *Rina, R. Inst. Nav. Archit. - Int. Conf. Comput. Appl. Shipbuild.*, 2:49–57, 2015.

HOMOGENIZED AND NON-CLASSICAL BEAM THEORIES IN SHIP STRUCTURAL DESIGN – CHALLENGES AND OPPORTUNITIES

JANI ROMANOFF*, ANSSI KARTTUNEN*[†], BRUNO REINALDO GONCALVES* AND JN
REDDY[†]

* Marine Technology, Department of Mechanical Engineering,
School of Engineering, Aalto University
Puumiehenkuja 5 A, 00076 Aalto, Finland
e-mail: jani.romanoff@aalto.fi, webpage: <https://people.aalto.fi/jani.romanoff>

[†] Advanced Computational Mechanics Laboratory
Texas A&M University
180 Spence Street, College Station, TX 77843, USA
webpage: <https://mechanics.tamu.edu>

Key words: Computational mechanics, Non-classical continuum mechanics, Marine Engineering, Beam theory, Homogenization

Abstract. The paper gives an overview of the recent developments on the application of homogenized, non-classical beam theories used to predict the micro- and macrostructural stresses in the design of marine structures. These theories become important when ultra-lightweight marine structures are developed and one needs to explore the regions where the length scales of beam openings are in the range of the characteristic lengths of the beams or when lattice/frame-type beams are used to reduce the weight of ship structures. The homogenized beam models are based on non-classical continuum mechanics that allow local bending inside the beams. This added feature allows the treatment of size effects with great accuracy. The resulting analytical and finite element models have special features in terms of shape functions and iterative solutions in non-linear problems. Non-classical beam models enable localization processes that recover the microstructural effects from homogenized solutions accurately and the models are able to handle limit states of serviceability and ultimate strength. The non-classical models are validated by experiments and 3D FE simulations of periodic beams and plates. The non-classical beam theories converge to the physically correct solutions for wider range of beam parameters than the classical beam theories do.

1 INTRODUCTION

Thin-walled structures form the basis of transportation of people and goods as they are widely used in different length-scales in vehicles, containers and tanks, in packaging and they are used even in the microelectronics to control vehicles' operation; see Figure 1. The thin-walled structures contribute significantly to the overall weight of a vehicle itself and to the payload. Structural performance is measured by the ratio between the payload and the structural weight. We aim to build increasingly lighter vehicles, to diminish the environmental impact of transportation. However, the limits to which we can push the structural performance ratio are defined by safety and further by the probability of failure of the transportation system, of the vehicles, and of their structures all the way to the materials.

The probability of failure is defined by the relation between the demand (load) and the capacity (strength) of the structure. Demand results from operations in random environments,

whereas capacity stems from structural design, manufacturing, materials and operations. Since both of them have a statistical nature, the definition of uncertainty and the acceptable levels for the probability of failure are to a great extent affected by computational modelling. Due to global warming, the random environments are proven more aggressive which increases the loads and further the probability of failure. Simultaneously, new ultra-lightweight materials and lattice structures are introduced to small length-scales via advanced manufacturing methods such as additive manufacturing and laser-welding, see Figure 1 and Ref. [1].

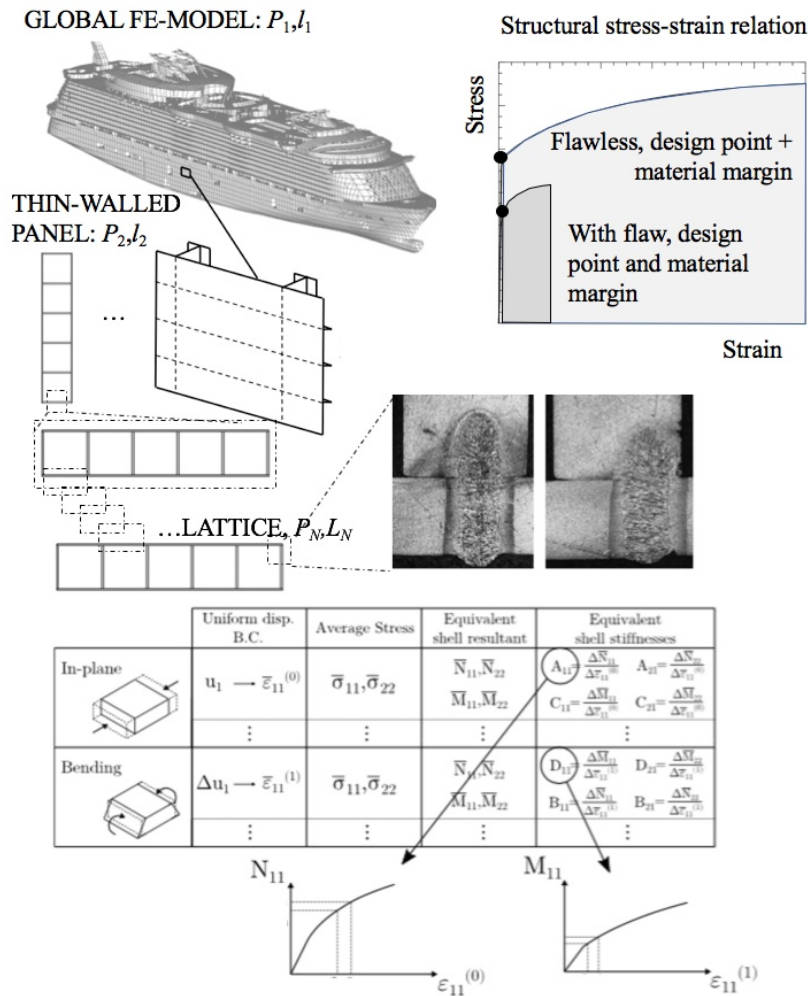


Figure 1: Lightweight design of marine structures through hierarchical structures with finite scale separation based multi-scale modelling. Classical length-scales range from ship hull girder (primary response) to bulkheads (secondary response) and further to stiffened panels (tertiary response). Modern manufacturing and materials technology is enabling additional length-scales with geometrical and material non-linearity.

The ultra-lightweight features are obtained by applying to ever smaller scales the ideas of civil engineers (e.g. Eiffel tower), bridge-builders (e.g. Viereendeel frames), off-shore engineers and naval architects (e.g. 3D-truss-structures, side shells with balcony openings), and aeronautical engineers (e.g. wing-spars) who have over long time found these feasible solutions to very complex problems where different length-scales interact. The ultra-lightweight

materials and structures have relative densities, ρ_{mat}/ρ_{bulk} , often as low as 0.1-0.2, but stiffness-to-strength values are not reduced as much. However, the material reserve in terms of plastic capacity with respect to the elastic limit (design point) is significantly reduced especially when the material contains flaws or perforations, see Figure 1. This forces designers to impose larger safety factors for these ultra-lightweight builds. Thus, even though we gain better performance in the material scale, we tend to suffer larger overall uncertainty in structural scale as the integration into structural systems contains increasing complexity and layers of advanced structures. This uncertainty originates partly from production challenges, such as the positioning of laser-welds, initial imperfections and residual stresses, but more importantly from the limitations of the current strength-assessment methods which need to evaluate response and strength at all relevant length-scales simultaneously.

This paper gives an overview of the recent developments on the application of homogenized beam theories based on non-classical continuum mechanics used to predict the micro- and macrostructural stresses in the design of marine structures. The paper is organized so that we first present the main assumptions introduced by homogenization and localization and discuss their relevancy in terms of marine structures. Then we move to the resulting differential equations and discuss their analytical and numerical solutions in linear elastic problems, eigenvalue vibration and buckling problems and in a problem where geometrical non-linearity is faced in micro and macroscales. In order to demonstrate the gains and remaining challenges we present case studies where comparison to experiments and high-fidelity finite element simulations are performed.

2 HOMOGENIZATION AND LOCALIZATION

In the assessment of structural performance, the response is needed to ensure that the load-carrying mechanism is correct within a complex structure and strength is needed to ensure capacity. In terms of solid mechanics, the response is effectively determined by using homogenized continuum models, while strength requires localization and understanding of how damage spreads in the structure in a realistic manner. The challenge between the two approaches is the scale-transition so that the energy, stresses and strains are all kept in balance between the continuum model and the sub-model where localization and strength are defined. This difference between the two approaches is presented here by an example of periodic, linear elastic web-core sandwich beam for which the accurate solution can be derived by assuming that the faces and webs bend locally as Euler-Bernoulli beams; we consider this here as *Assumption 0* for the reason that more advanced local deformation models can be developed easily by more advanced beam models or superelements. The beam deflection by using discontinuity functions [2] is given as:

$$w^{face}(x) = w^{l,bend}(x) + w^{g,bend} \quad (1a)$$

$$w^{l,bend}(x) = w_0^l + \theta_0^l x + \frac{1}{D_i} \left[\sum_{i=1}^I \frac{H(x - a_i^M) M_i (x - a_i^M)^2}{2!} + \sum_{j=1}^J \frac{H(x - a_j^F) F_j (x - a_j^F)^3}{3!} + \sum_{k=1}^K \frac{H(x - a_k^q) q_k (x - a_k^q)^3}{4!} \right] \quad (1b)$$

$$w^{g,bend}(x) = w_0^g + \theta_0^g x - \frac{1}{D_g} \left[\sum_{l=1}^L \frac{(M_l^t + M_l^b) H(x - a_l^{M_i})(x - a_l^{M_i})^2}{2!} \right] \quad (1c)$$

where $w^{l,bend}$ is the local deflection of the face due to point forces and moments and distributed external and internal loads applied directly to the face and $w^{g,bend}$ is the global deflection caused by elongation of the faces to opposite directions. w_0 and θ_0 are the local and global transverse displacement and rotation boundary conditions, respectively. Symbols a indicate the locations of the point moments (superscript M), forces (superscript F) and uniform distributed loads (superscript q). H is the Heaviside function with first and second derivative being Dirac's delta and unit doublet functions respectively.

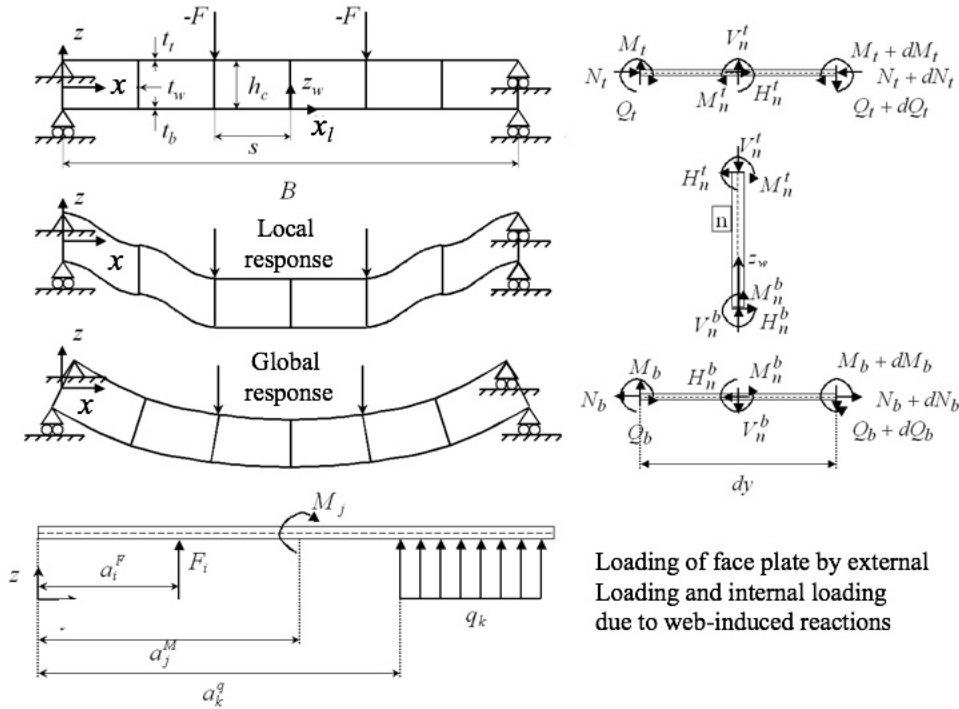


Figure 2: Two-scale modeling of web-core beam with discontinuity functions and an assumption of microstructural Euler-Bernoulli beam behavior.

This solution is accurate, but needs to be solved for each location of flexible core members (including joint rigidity) along x -axis resulting in $3L+4$ equations, where L is the number of web-plates in the beam [1]. The solution can be simplified towards a homogenized solution by neglecting distributed loads and moving all loads to the locations of webs; this is *Assumption 1* that currently limits the use of continuum models to the cases of finite length-scale ratio. The result is:

$$w^{face}(x) = w_0^l + \theta_0^l x + w_0^g + \theta_0^g x + \sum_{l=1}^L \frac{H(x - a_l)(x - a_l)^2}{2!} \left[\frac{1}{D_l} \left(M_l + \frac{F_l(x - a_l)}{3} \right) - \frac{1}{D_g} (M_l^t + M_l^b) \right] \quad (2)$$

When in **localization** the peak response at the location of high gradients must be assessed,

we can use Taylor-series expansion around point a as

$$w(x) = w^0(a) + \frac{w^1(a)}{1!}(x-a) + \frac{w^2(a)}{2!}(x-a)^2 + \dots \quad (3)$$

The comparison of Eqs. (1)-(3) reveals that the $(x-a)^n$ -terms are maintained to various degrees and the accuracy around the point of interest can be maintained by including enough terms in the Taylor series to compensate for the neglect of the Heaviside operator. In the case of an entire beam, we end up with the same number of terms as in the accurate solution given by Eq. (1). Thus, this expansion is useful, but should be only performed locally. In order to approximate the response in smooth, periodic, fields of deformation away from high gradients, the **homogenization** theory can be used, where the two length-scale asymptotic expansion is used instead to give:

$$w^k(x) = w^0(x, y) + k^1 w^1(x, y) + k^2 w^2(x, y) + \dots \quad (4)$$

$$k = \frac{l_{micro}}{l_{macro}} \ll 1 \quad (5)$$

$$w^k(x, y) = w^k(x, y + l_{micro}) \quad (6)$$

where the microlevel coordinate $y=x/k$ is the local coordinate which is assumed to be infinitely small in comparison to x . In Eq. (4), the $(x-a)^n$ -terms are approximated with x^n -terms multiplied by powers of the length-scale ratio, k , Eq. (5). The microscale responses are assumed to be fully periodic, Eq. (6) and these should be recoverable from the macroscale responses. Thus, the actual positioning of the unit cell along the beam is not considered and the continuity conditions on deflection and its derivatives at the edges of unit cell are used to secure that microscale responses do not transfer through unit cell edges, except through macro-scale phenomena; this is *Assumption 2* that limits the use of continuum theories.

The *Assumption 3* that the length-scale ratio is infinitely small is never true. Especially when applied to ultra-lightweight structures, the geometrical and physical characteristic lengths of the vehicles themselves (e.g. hull girder of the ship, $l_1 \sim 300\text{m}$), the secondary structures (e.g. bulkheads and decks, $l_2 \sim 30\text{m}$) and the tertiary structures (e.g. stiffened or corrugated sandwich panels, $l_3 \sim 3\text{m}$) can be close. The approximation can be improved when more terms are included in the asymptotic expansion especially close to the locations of high gradients. These additional terms, however, increase the computational costs. These different approaches have very similar form. While the asymptotic expansion with increasing terms aims to model with continuum the discrete structure, the Taylor series aims to do this from the discrete structure towards continuum. When and how these two approaches meet for finite length scale ratio is a grand-challenge. Analytical solutions exist for the simplest of cases. However, these solutions have very little practical relevance. An alternative is to use the fine mesh finite element method, but this is not a sustainable solution in the long run, since we expect new emerging length scales in future structures developed with novel manufacturing technologies and materials, see Figure 1. In these FEM models, the element size is defined by the smallest detail that affects strength. For the limit state of fatigue, the size of such detail can be 10^{-6}m , which calls for a mesh size at least 5-10 times smaller. This scale difference of 10^9m in ship structures results in enormous computational models beyond current and near future computational capabilities. Therefore, the natural choice of computational approach is the extended non-classical continuum description. Here we focus on two sub-classes of namely those based on strain-gradient/couple stress and micropolar models; extensive review of different models is given by Srinivasa and Reddy [3].

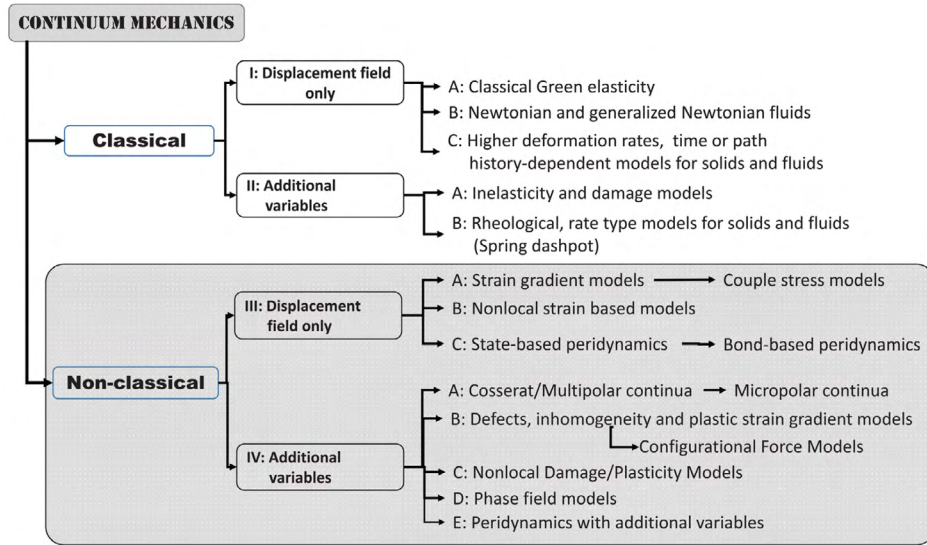


Figure 3: Taxonomy of continuum mechanics as described by Srinivasa and Reddy [3].

3 DIFFERENTIAL EQUATIONS AND THEIR SOLUTIONS

3.1 Beam formulations based on micropolar and couple-stress models

The displacements for a micropolar Timoshenko beam can be written as [4-7]

$$u(x, y) = u_x(x) + y\theta(x), w(x, y) = w(x), \Psi(x, y) = \varphi(x) \tag{7}$$

where the classical displacements u and w and rotation θ are complemented by a non-classical microrotation φ . In the micropolar formulation the microrotation enters the beam through strain formulation as [4-5]

$$\varepsilon_x = \frac{\partial u}{\partial x}, \varepsilon_{xy} = \frac{\partial w}{\partial x} - \Psi, \varepsilon_{yx} = \frac{\partial u}{\partial y} + \Psi, \kappa_{xz} = \frac{\partial \Psi}{\partial x} \tag{7}$$

which ultimately means that the shear strain will consist of symmetric and antisymmetric parts and there is an additional curvature κ_{xz} that can be used to describe local bending. In a couple stress based approach the strains read [6-7]

$$\varepsilon_x = \frac{\partial u}{\partial x}, \gamma = \theta - \frac{\partial w}{\partial x}, \chi_{xy} = \frac{1}{4} \left(\frac{\partial \theta}{\partial x} - \frac{\partial^2 w}{\partial x^2} \right) \tag{7}$$

Thus, instead of formulating shear into antisymmetric and symmetric parts, average shear strain is used and non-classical, local bending features are introduced through curvature χ_{xy} . By employing a constitutive model and variational principles, one obtains the governing equations for the micropolar and couple stress beam models.

3.2 Analytical and Finite Element Solutions

The fact that the beam strains include microrotations or gradients of local rotations increases the total differential order of the governing beam differential equations. This means that the analytical solutions will include higher-order terms that appear as exponential or hyperbolic functions. Such terms are significant in the vicinity of strain gradients and in structures where internal stiffness of the microstructure is significant in comparison to macroscale strain gradients. In analytical solutions this effect is of course directly included to the solution and

does not require special attention. However, in finite element approximations it creates a need to include higher-order polynomials to shape function approximations. Karttunen et al. [8] derived also exact shape functions which do not suffer from convergence issues due to numerical procedures. However, these elements have been tested only for linear elastic cases.

3.3 Scale Interaction

The scale transition is needed between micro- and macroscale analyses, see Figure 4 (couple stress approach). Up-scaling results in homogenized stiffness properties for which in addition to classical in-plane, bending, membrane-bending and shear stiffness, the local unit cell stiffness in terms of strain gradients are needed. This process can be linear or non-linear in terms of geometry. The inverse-process of homogenization, i.e. down-scaling/localization instead results periodic stresses that can be used to assess the stress peaks inside microstructure. This improves to a great extent the strength predictions essential in marine structures.

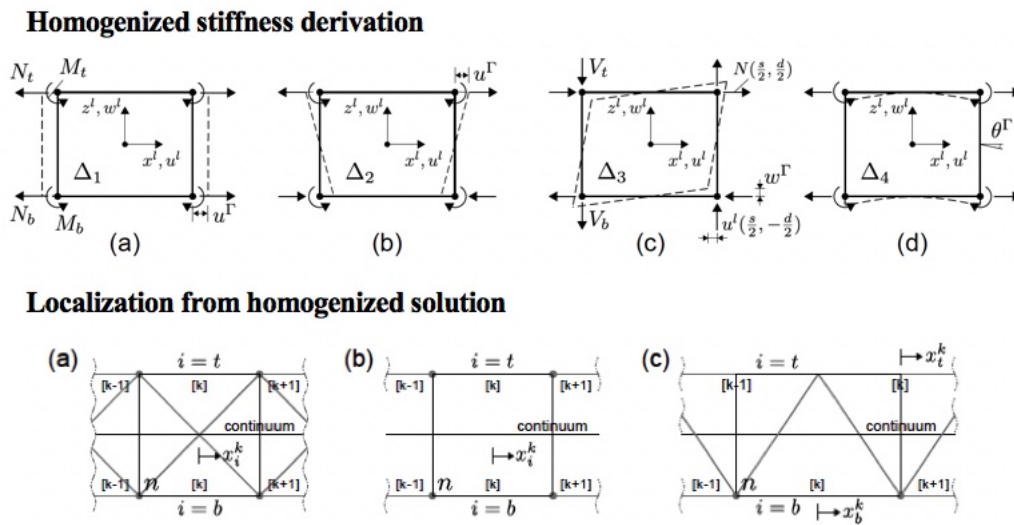


Figure 4: Top. Derivation of homogenized stiffness properties for in-plane, bending, shear and couple stresses. Localization of microstresses from homogenized solution. [6].

4 LIMIT STATES

4.1 General

In the following examples we demonstrate the different aspects of non-local beam theories in terms of gains in accuracy and remaining challenges. These have been collected from various sources and presented here to give insight to the current state of the art. The limit states selected are those categorized as by International Ships and Offshore Structures Congress (ISSC); serviceability, ultimate, fatigue and accidental.

4.2 Serviceability

The functionality of a ship structure is crucial in terms fulfilling the mission needs. This means that the deformation/stress levels, stiffness and vibratory (e.g. comfort) need to be within the design limits. Figure 5 shows examples from Refs. [4, 9], that demonstrate clearly the main benefits of the non-classical formulations and the challenges faced due to homogenization for

the linear-elastic, static case. Figure 6 presents this for the eigenvalue vibratory responses. In this example the homogenous core sandwich panels with thick-faces and the discrete web-core sandwich panels are considered both with couple stress and micropolar frameworks respectively.

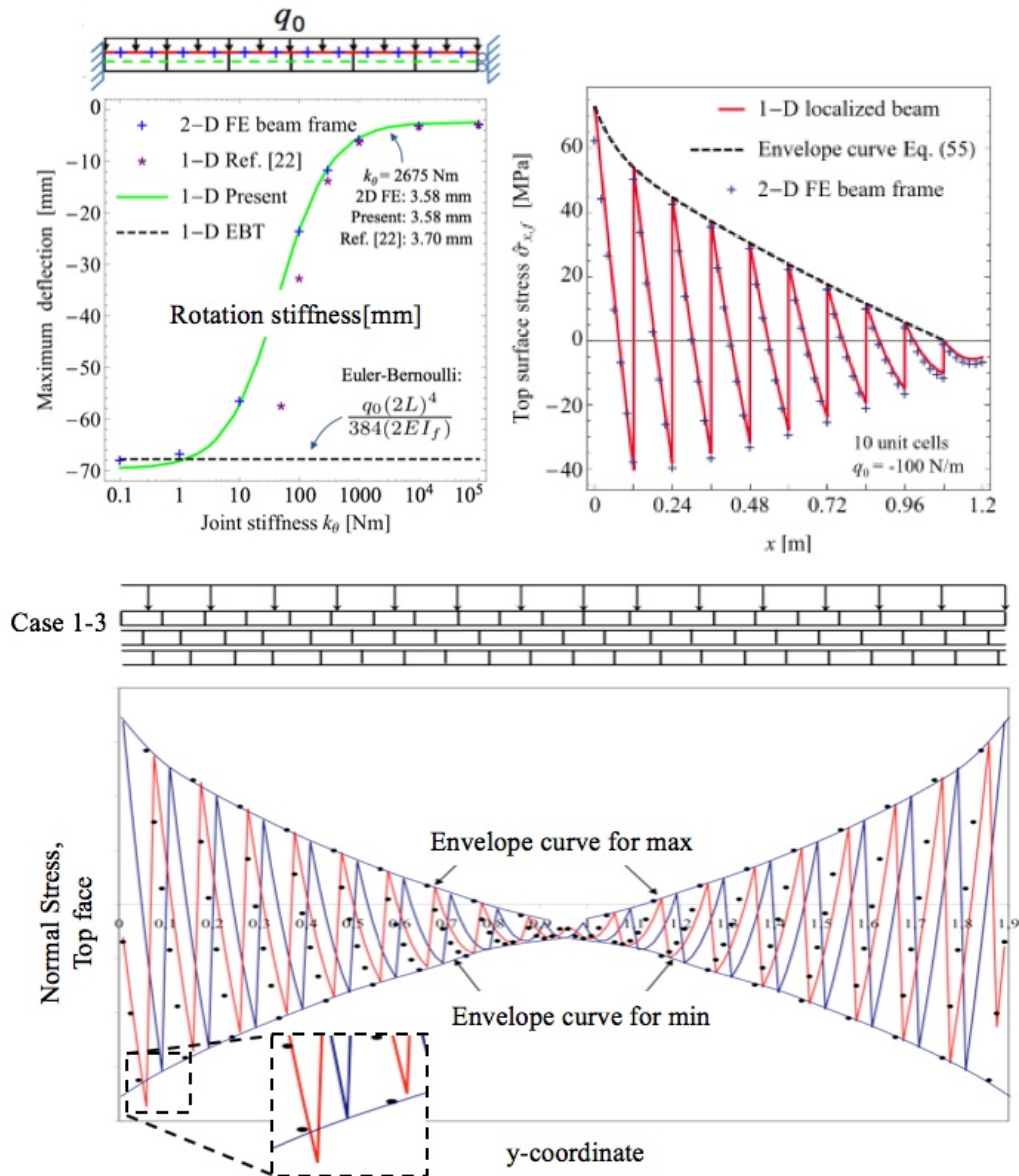


Figure 5: Top. Comparison between developed micropolar method [4] and high-fidelity FEA with the envelope curves for maximum stress from localization. Bottom. Effect of different unit cell positioning on observed discrete and envelope curve stress distributions [9].

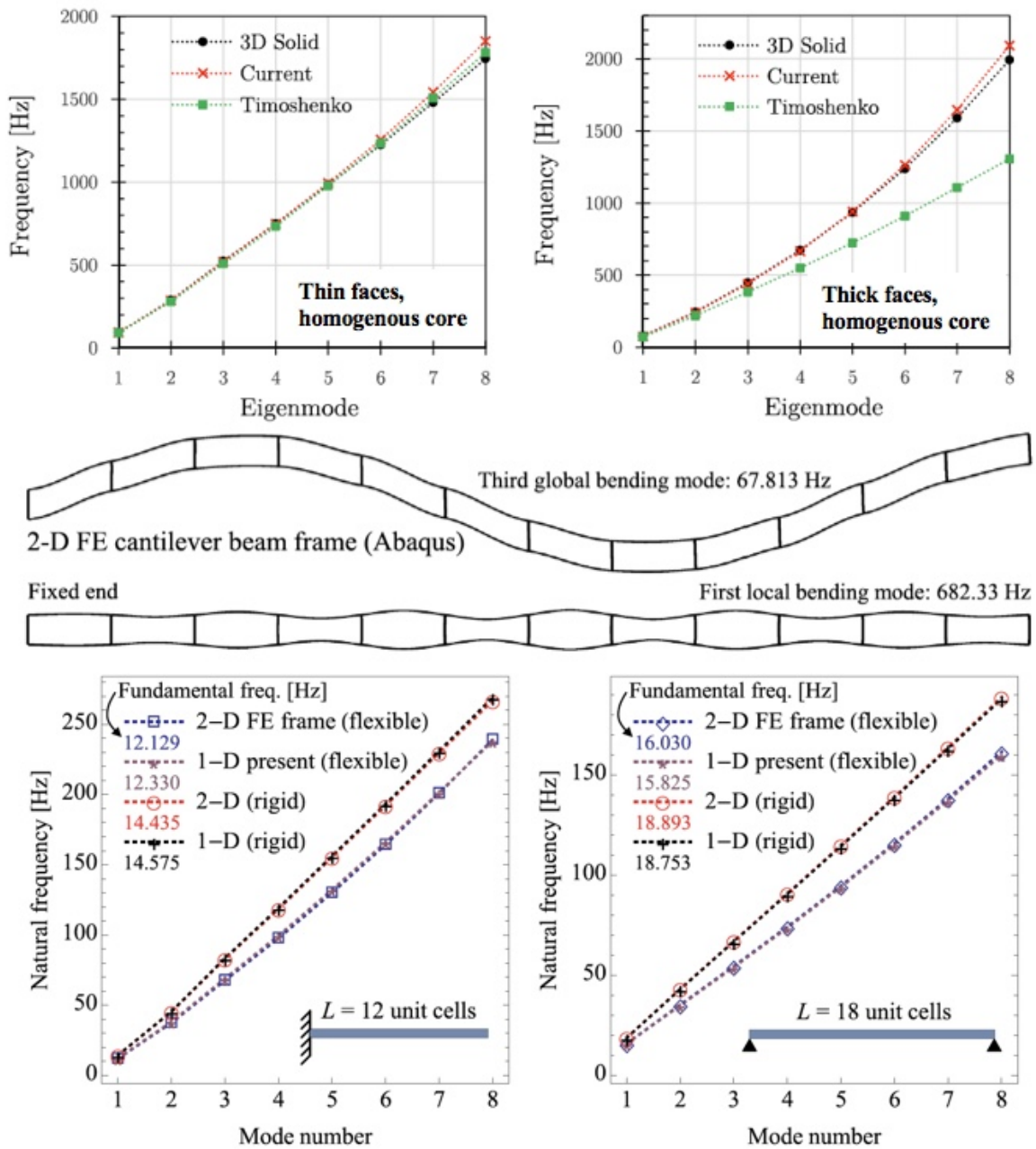


Figure 6: Comparison of beam solutions for eigenfrequency analysis. Top: 1-D Couple stress, Middle: 2-D FE frame example Bottom: 1-D Micropolar. [6,7].

Figure 5 shows that for beams with length-scale aspect ratio of $l_{micro}/l_{macro}=1/12$ the deflection can be obtained very accurately with the micropolar model. It is shown that the agreement between the high-fidelity Finite Element Analysis is perfect for various joint rotation stiffness values between the face and web-plates. In the case of classical Timoshenko theory, the results are in agreement with FEA in the cases of high rotation stiffness, but start to deviate as the rotation stiffness approaches zero. This means that micropolar model is able to converge

to physically correct behavior for the entire rotation stiffness range as long as the microstructure is periodically regular over beam span. The accuracy of the method is further highlighted in the top surface normal stress comparison. The surface stress is very important when for example fatigue strength is assessed. It is also shown that the strain/stress localization can be approached with envelope curve capturing the maximum stresses from each unit cell. This results in a continuous curve far above the floating unit cell average, indicating that in these structures with high length-scale aspect ratio, stress localization is more important design criterion than stiffness. It is also seen that the unit cell positioning with respect to beam boundaries has significant effect on single stress peaks near the boundaries. In these cases, the application of the Taylor series would become important to consider in localization process, i.e. Assumption 1 should be relaxed.

Figure 6 shows that the influence of non-classical continuum mechanics become important when the faces of sandwich panels have significant local bending stiffness in relation to bending and shear deformations. The fact that these non-classical solutions are considering the finite curvature of microstructure stiffens the structure and it can be seen that the agreement with 3D-FEA is excellent. As the formulation is continuum-based, the local vibrations at the unit cell level cannot be properly assessed. In terms of beam theories based on classical continuum corrections have been proposed for this issue recently, thus there is possibilities to correct this also in non-classical setting.

4.3 Ultimate, Accidental and Fatigue Strength

Ultimate, accidental and fatigue strength are important strength criteria for design of marine structures as they define the maximum stresses that the structure can tolerate. Figure 7 presents results of ultimate strength assessment based on classical one-scale and non-classical two-scale geometrical nonlinearity and the influence of rotation stiffness to the linear elastic response used to assess the fatigue strength.

Figure 7 shows clearly that conducting a two-scale geometric non-linear analysis coupled with a non-classical model is very important in predicting the non-linear buckling load of sandwich beams regardless of the core type. The microscale effect is larger in stretch-dominated cores, where a rapid decrease of the beam stiffness properties occurs after local buckling and the macroscale load carrying mechanism changes. In case of bending-dominated cores such as web-core panels, the geometric non-linearity is only relevant at the macroscale and described through the *von Kármán* term. Differences between the classical and non-classical solutions are due to the incorporation of an additional scale in stretch-dominated cores, whereas in bending-dominated cores the effect is similar to the one observed in the linear case. Figure 7 also shows that as rotation stiffness of the joint connecting the core and face plates changes, the dominating deformation modes change rapidly. The rotation stiffness can change for example through plasticity induced by high-level monotonic loading or by propagating fatigue cracks through the laser-welds. Here it should be recognized that the beam theories based on classical continuum mechanics fail to predict the response accurately on the low rotation stiffness values due to lack of inclusion of the finite curvature condition to the beam formulation. When the couple stress or micropolar formulations are used, the responses are accurately captured. The reason is better illustrated through spectral analysis of the deformation wave-lengths which reveals that the deformation amplitude is dominated by the response at the level of characteristic length of the beam, while the second most important average length corresponds to that of the unit cell. The spectral analysis also reveals that there is significant characteristic length amplitude between

these two wave lengths which is associated with the strain gradient. The amplitudes of these different characteristic wave lengths are related to the T-joint rotation stiffness. This means that in principle it should be possible to extract damage from the panels by analysis the deformation mode changes in the structure over the lifetime. However, in this case it should be recognized that the continuum assumption cannot handle the variation of beam stiffness properties along beam length. This influence is especially important that the closeness of boundaries where for example shear response can be very different between consecutive unit cells due to variation of laser-weld positioning.

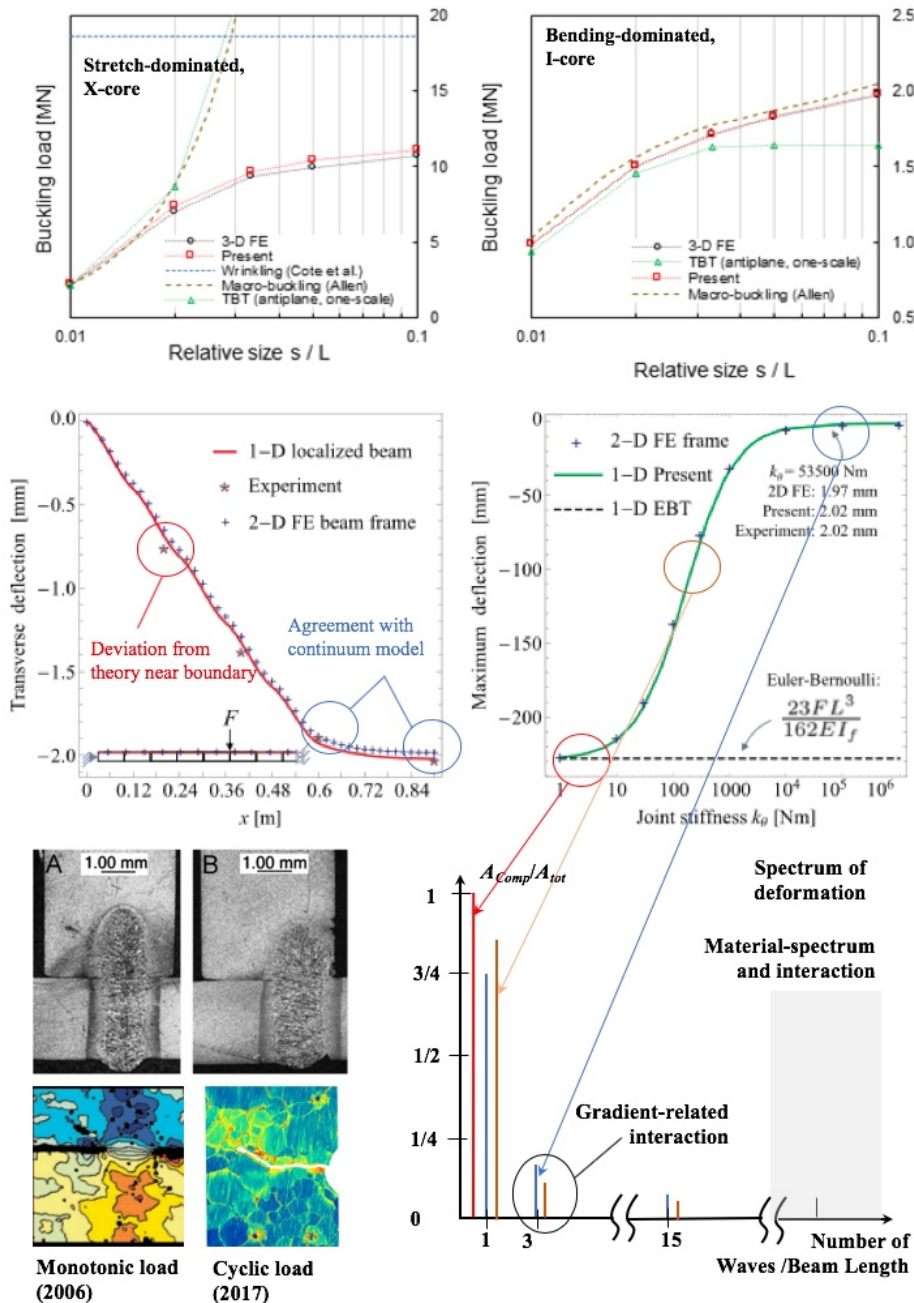


Figure 7: Beam solutions ultimate strength.

5 CONCLUSIONS

The paper gave an overview of the recent developments on the application of homogenized, non-classical beam theories used to predict the micro- and macrostructural stresses in the design of marine structures. These theories are important when ultra-lightweight marine structures are developed and one needs to explore the regions where the length scales of beam openings are in the range of the characteristic lengths of the beams or when lattice/frame-type beams are used to reduce the weight of ship structures. The homogenized beam models are based on non-classical continuum mechanics that allow local bending inside the beams. This added feature allows the treatment of size effects with great accuracy. The resulting analytical and finite element models have special features in terms of shape functions and iterative solutions in non-linear problems.

The non-classical beam theories converge to the physically correct solutions for wider range of beam parameters than the classical beam theories do. The investigations show that the localization of stresses is accurate for cases where the periodic continuum type of boundary conditions for the unit cells are valid. The theories should be developed that allow random positioning in order to satisfy the needs of maritime solutions. For the vibratory response the eigenfrequencies and -modes are predicted with much better accuracy than for classical models. However, the coupling between local and global modes should be developed and analyses should be extended to allow assessment of forced vibrations. In ultimate strength analysis 2-way coupling accounting geometrical non-linearity have been developed and it shows excellent agreement with 3D high fidelity FEA. These successes should be extended to cover material non-linearity and formulations for plates and shells.

REFERENCES

- [1] Fleck, N.A., Deshpande, V.S. and Ashby, M.F., “*Micro-architecture materials: past, present and future*”, *Proceedings of Royal Society, A*, Vol. **466**, pp. 2495-2516 (2010)
- [2] Romanoff, J. and Varsta, P., “*Bending response of web-core sandwich beams*”, *Composite Structures*, Vol. **73**, pp. 478-487, (2006).
- [3] Srinivasa, A.R. and Reddy, J.N., “*An overview of theories of continuum mechanics with nonlocal elastic response and a general framework for conservative and dissipative systems*”. *Applied Mechanics Reviews*, Vol. **69**(3), pp. 030802-1-17, (2019).
- [4] Karttunen, A., Reddy, JN and Romanoff, J., “*Two-scale constitutive modeling of a lattice core sandwich beam*”, *Composites - Part B Engineering*, Vol. **160**, pp. 66-75, (2019).
- [5] Nampally, P., Karttunen, A. and Reddy, JN, “*Nonlinear finite element analysis of lattice core sandwich beams*”, *European Journal of mechanics, / A Solids*, Vol. **74**, pp. 431-439 (2019)
- [6] Reinaldo Goncalves, B., Karttunen, A. and Romanoff, J., “*A nonlinear couple stress model for periodic sandwich beams*”, *Composite Structures*, Vol. **212**, pp. 586-597, (2019).
- [7] Reinaldo Goncalves, B., Karttunen, A., Romanoff, J. and Reddy, JN, “*Buckling and free vibration of shear-flexible sandwich beams using a couple-stress-based finite element*”, *Composite Structures*, Vol. **165**, pp. 233-241, (2017).
- [8] Karttunen, A., Romanoff, J., and Reddy, JN, “*Exact microstructure-dependent Timoshenko beam element*”, *International Journal of Mechanical Sciences*, Vol. **111-112**, pp. 35-42, (2016).
- [9] Romanoff, J., “*Optimization of web-core steel sandwich decks at concept design stage using envelope surface for stress assessment*”, *Engineering Structures*, Vol. **66**, pp. 1-9, (2014).

STRUCTURE DESIGN OF THE SHIP PEDESTAL BASED ON TOPOLOGY OPTIMIZATION

CHUNHUI ZHANG, ZECUI ZENG, CHEN JI

Naval Research Academy, Beijing100000, China
e-mail: 502773429@qq.com

Key words: Topology Optimization; Pedestal; Lightweight; Anti-shock

Abstract. The optimization study of the ship pedestal structure is of great significance to the lightweight and the anti-shock performance of the ship. Therefore, the TOSCA software is used to design the ship pedestal in topology optimization. of a ship's pedestal. By setting the load, determining the objective function, selecting the constraints, and selecting the optimization region, the topology-optimized pedestal structure is obtained. Then, the structure was redesigned to determine the final structure of the pedestal. Finally, compared with the traditional pedestal for modal and anti-shock performance, it is verified that the designed pedestal in this paper has improved performance over the traditional one.

1 INTRODUCTION

The ship pedestal is a kind of structure specially designed for installing the equipment on the hull. Generally, the ship equipment must be connected to the hull structure through the pedestal to prevent the equipment from damage caused by shocking and vibration.

When engineering technicians actually design the pedestal, they often rely on existing experience to design the structure and size of the pedestal, making the actual pedestal used to be excessively conservative and bulky. In order to reduce the weight of the pedestal and improve the performance of it, scholars in various countries generally consider both material and structure. In order to improve the performance of the ship pedestal, various materials are used in it. Zhang Xiangwen^[1] used the good energy absorption characteristics of Woven bee materials to design two kinds of honeycomb pedestals with macroscopic negative and positive Poisson ratio effects, and compared their stiffness, strength, vibration isolation and shocking isolation performance. The results show that the honeycomb pedestal has excellent anti-vibration and anti-shocking performance. Luo Zhong and Mao Liang^[2-3] used the sandwich composite materials to propose a sandwich pedestal. Research has shown that the sandwich pedestal has a lighter weight and impedance damping designing.

It can be seen that the pedestal made of new materials is light in weight and excellent in performance, but most of them are still in the theoretical research stage. Moreover, the threshold of new materials is relatively high, and the preparation and welding processes are not mature enough to be widely used. Therefore, many people start with structural aspects and adopt the new structures to improve the performance of the pedestal. Cheng Huanbo^[4] carried out topological optimization analysis on the pedestal of the concrete conveying arm, and designed a new pedestal according to the optimization results. The results show that when the new pedestal meets the strength and natural frequency, the base weight is reduced by 18.3kg. Sun Yumei^[5] carried out sensitivity analysis and size optimization for a naval gun pedestal, which reduced the weight of the pedestal by 13.2%, achieving the goal of lightweight. Huang Haiyan^[6] took the weight of the host pedestal structure as the objective function, and used stability, allowable stress, and fatigue strength as constraint conditions. Optimized the structure of the host pedestal using the annealing algorithm. San Xiaogang^[7] topologically optimized the design of a large-scale theodolite pedestal. According to the relative density cloud map of the material obtained, the new pedestal was rebuilt with the hollow square tube. Under the requirements of strength and stiffness, the weight of the pedestal was reduced by 27.8%.

The optimization of the pedestal structure is of great significance for ship lightweight and anti-shock performance^[8]. Therefore, with the help of TOSCA software, the topology optimization design of a ship pedestal will be carried out. In the period of conceptual design, we should jump out of the original thinking formula for the pedestal design to find a structure style with lighter weight and better performance.

2 TOPOLOGY OPTIMIZATION METHOD BASED ON MINIMUM FLEXIBILITY

2.1 Model Establishment

The Full Paper must be written in English within a printing box of 16cm*21cm, centered in

the page. The Full Paper including figures, tables and references must have a minimum length of 6 pages and must not exceed 12 pages. Maximum file size is 4 MB.

The variable density method based on minimum flexibility is the foundation of other topological optimization methods with the global volume as a constraint. In this paper, the material difference model based on SIMP is used to solve the problem. The mathematical model is as follows:

$$\begin{cases} \text{Min} : C = F^T U \\ \text{s.t.} : V < \varepsilon V_0 \\ F = KU \\ 0 < \rho_{\min} \leq \rho_i \leq 1, (i = 1, 2, 3 \dots n) \end{cases} \quad (1)$$

Where C is the structural flexibility (the deformation energy generated by the structure under external force, the smaller the deformation, the smaller the flexibility and the greater the stiffness); F is the external force matrix of the structure; U is the total displacement matrix of the structure; K is the total stiffness matrix of the structure.

2.2 Structure Discretization

For the sake of narrative convenience, the density ρ is represented by the variable x , then in the discrete finite element structure

$$V = \sum_{i=1}^n x_i v_i \quad (2)$$

Where n is the number of elements; v_i is the volume of element i .

At the same time, assuming that the element stiffness and element elastic modulus before and after optimization are the same, they are also an exponential relationship with the density. That is:

$$k_i = (x_i)^p k_0 \quad (3)$$

Where k_i is stiffness of the i -th element after optimization; k_0 is stiffness of the i -th element before optimization.

Since the total stiffness of the structure

$$K = \sum_{i=1}^n k_i \quad (4)$$

The total flexibility of the structure

$$C = F^T U = U^T K U = \sum_{i=1}^n u_i^T k_i u_i = \sum_{i=1}^n (x_i)^p u_i^T k_0 u_i \quad (5)$$

Where U_i is the displacement of the i -th element.

Therefore, from Equation (3) to Equation (8), we can know that under the constraint of volume fraction, with the maximum stiffness as the objective function, the mathematical model of the variable density method based on the SIMP method can be written as

$$\left\{ \begin{array}{l} \text{Min: } C = \sum_{i=1}^n (x_i)^p u_i^T k_0 u_i \\ \text{s.t.: } \sum_{i=1}^n x_i v_i - \varepsilon V_0 \leq 0 \\ ku = f \\ 0 < x_{\min} \leq x_i \leq 1, (i = 1, 2, 3 \dots n) \end{array} \right. \quad (6)$$

Where x is the design variable (unit relative density) and $x_i (i=1,2,3\dots n)$ is the unit design variable. To avoid the singularity phenomenon in the stiffness matrix when calculating the finite element, x_{\min} is usually taken as 0.001 and X_i is between x_{\min} and 1.

2.3 Sensitivity analysis

In order to get the optimization direction of the design variables, the structural response needs to be partial derivative of the element relative density, that is the sensitivity analysis. Then the relative density of the element is calculated by the displacement u to obtain the finite element equilibrium equation:

$$ku = f \quad (7)$$

Derivatives for x_i on both sides:

$$\frac{\partial k}{\partial x_i} u + k \frac{\partial u}{\partial x_i} = \frac{\partial f}{\partial x_i} \quad (8)$$

The load f is an external force and is independent of the element relative density.

$$\frac{\partial f}{\partial x_i} = 0 \quad (9)$$

Bring equation (9) into equation (8), and it will get

$$\frac{\partial k}{\partial x_i} u = -k \frac{\partial u}{\partial x_i} \quad (10)$$

Find the partial derivative of the relative density for the volume V to the element. Because of:

$$V = \sum_{i=1}^n x_i v_i \quad (11)$$

So that:

$$\frac{\partial V}{\partial x_i} = v_i \quad (12)$$

The flexibility C finds partial derivatives of the element relative densities. The expression of element flexibility is:

$$\frac{\partial C}{\partial x_i} = \frac{\partial U^T}{\partial x_i} KU + U^T K \frac{\partial U}{\partial x_i} + U^T \frac{\partial K}{\partial x_i} U \quad (13)$$

By the balance equation $KU = F$, we get:

$$\frac{\partial K}{\partial x_i} U + K \frac{\partial U}{\partial x_i} = 0 \quad (14)$$

With the simultaneous expressions (13) and (14), the sensitivity of the objective function can be obtained:

$$\frac{\partial C}{\partial x_i} = -U^T \frac{\partial K}{\partial x_i} U = -\sum_{i=1}^n u_i^T \frac{\partial k_i}{\partial x_i} u_i \quad (15)$$

Equations (6) and (15) are the mathematical model and sensitivity of the minimum flexibility optimization problem respectively. It can be seen that the sensitivity of volume and flexibility is a local variable and only relates to the element. Theoretically, a mathematical model similar to the above equation can be given with any objective function and constraints, and the corresponding sensitivity can be obtained. In fact, some responses are difficult to define, and sensitivity is difficult to deduce. The type of optimization that can be used in engineering practice is very limited. Most of the problems are focused on the optimization of structures subjected to static loads and the optimization of improving the first-order natural frequencies of structures^[9-10].

3 OPTIMIZATION DESIGN OF A SHIP PEDESTAL

The topology optimization method based on the minimum flexibility is described above. Based on the above theoretical methods, the TOSCA software is used to optimized design the topology of a ship pedestal with the maximum stiffness as the objective function and the volume fraction as the constraint condition. Based on the optimization results, the influence of structural parameters such as support form and panel shape on the performance of the pedestal is discussed, and the pedestal is redesigned. Finally, Abaqus software was used to compare the modal and anti-shock performance of the two pedestals. The optimized design flow chart of the base is shown in Fig. 1.

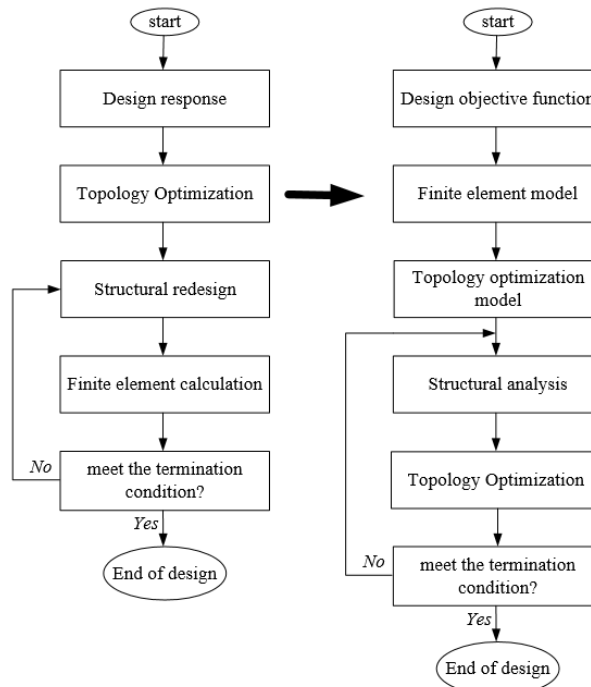


Figure 1: Flow chart of pedestal topology optimization design

3.1 Traditional pedestal model

The title should be written centered, in 14pt, boldface Roman, all capital letters. It should be single spaced if the title is more than one line long.

Select a device pedestal on the inner bottom of a frigate for topology optimization. The pedestal is a typical "box shaped" pedestal that is welded directly to the inner bottom. The device is rigidly connected to the pedestal plate by bolts. The base is 800mm in length, 670mm in width, 150mm in height, 10mm in a panel thickness, 8mm in thickness of abdominal plate and elbow plate, and 46.8kg in weight, as shown in Fig. 2 in detail. The pedestal material is 907A steel with a density of $7.8 \times 10^{-9} \text{t/mm}^3$, an elastic modulus of 2.06e5MPa, a Poisson Ratio of 0.3, and a yield limit of 380MPa.

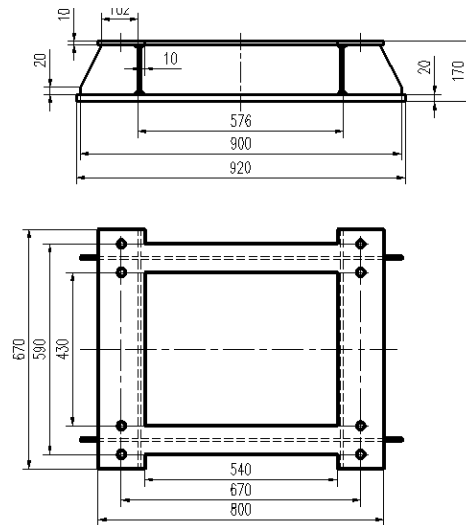


Figure 2: An engineering drawing of a pedestal

3.2 The optimal setting of the pedestal

1) Shocking load setting of the pedestal

When the pedestal is subjected to a three-phase shocking, the vertical shocking is the most dangerous situation. When undergoing topology optimization, the vertical shocking is the input load. The topology optimization of the pedestal in this paper is rigidly installed on the inner bottom, which belongs to the hull installation, and the equipment it carries is Class A equipment. The input value of shocking load is designed according to the standard GJB1060.1-91^[11]. The pedestal weighs 46.8kg and the equipment weighs 240kg. When calculating, 80% of the total mass is taken as the effective mass. It was calculated that: the equal acceleration spectrum is $A_s=2203\text{m/s}^2$; the equal speed spectrum is $V_s=2.92\text{m/s}$; and the equal displacement spectrum is $D_s=0.045\text{m}$.

2) Objective Function

The pedestal is rigidly connected to the device. When subjected to shocking loads, the pedestal is not allowed to deform in order to ensure the accuracy of the equipment it carries. The objective function for optimization is the maximum stiffness of the pedestal, which is set to the minimum in the TOSCA software for structural flexibility (ie strain energy).

3) Constraints

Spatial aspects: Ship equipment not only has high weight requirements, but also has strict requirements on the volume. To ensure that the equipment environment does not require much adjustment, the size of the space occupied by the structure must not change much. That is, the variable area does not exceed the cube area formed by the original structure of length, width and height.

In terms of connection: The pedestal serves as a "bridge" between the equipment and the hull, and is connected to the equipment through bolts. In order to ensure the reliability and convenience of connection with the equipment before and after optimization, the position and size of the screw hole can not be changed.

In terms of process: the geometric structure of the pedestal and the load it bears are all symmetrical about the horizontal and vertical planes passing through the gravity center of the pedestal, so there is a symmetry constraint in the topology optimization. In order to eliminate the small transmission path in the optimization result and make the topology optimization structure more regular, the size of the smallest member of the structure is required to be constrained. The optimization result requires that the smallest member size of the structure is $\geq 10\text{mm}$. The pedestal is welded through the plate. If the plate is too thin, it will burn easily, or it will cause large deformation due to uneven heat. Therefore, the thickness of the plate should be $\geq 5\text{mm}$.

4) Setting the Optimization Zone

On the one hand, the pedestal limits the space occupied. On the other hand, the number, position and specification of the bolts remain unchanged. Therefore, an optimization model is designed to constrain different volume fractions and to research the effect of different structural parameters on the topology results. A cubic block is constructed based on the length, width and height of the original pedestal, and the bolt holes are excavated in the middle. The remaining area is used as the optimization area, as shown in Fig. 3.

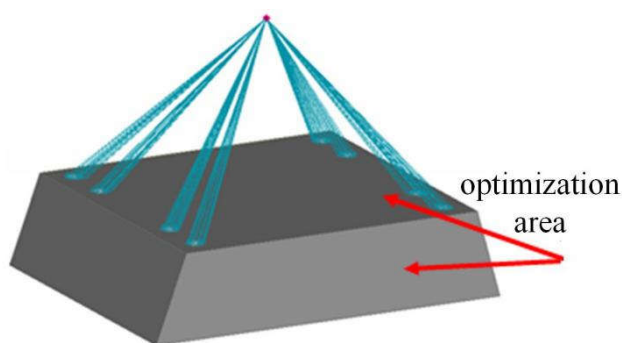


Figure 3: Optimization model

The general process of topology optimization is designing-optimization-redesigning. This optimization aims to find the best force transmission path through topological optimization under constraint conditions, and retain the most efficient materials. Through the analysis of the topology optimization results, valuable conclusions are obtained, and used for the guidance of anti-shock designing of the pedestal, so as to design a new pedestal and compare the modal and anti-shocking performance of the old and new pedestals.

3.3 Analysis of Optimization Results

With TOSCA software, topology optimization was performed on two pedestal structure models under different volume constraints. After many iterations, the pedestal quality and the stiffness gradually decreases as shown in Fig. 4. Both the constraints and the objective function converge very quickly. The objective function tends to stabilize after the 5th iterations, and the volume fraction reaches the setting value 0.4 after the 15th iterations.

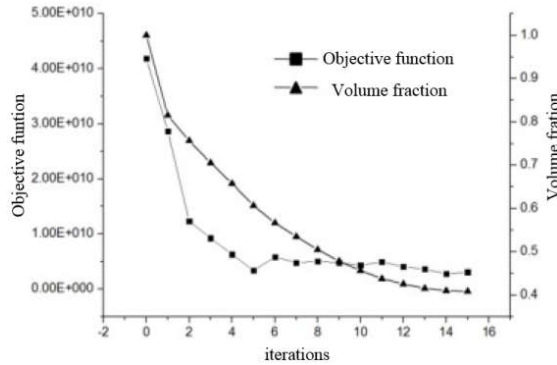


Figure 4: Constraint conditions and objective function iteration curves with volume fraction of 0.4.

Fig. 5 shows the pedestal structure after the topology optimization of Model 2 at a volume fraction of 0.4. It can be seen that many elements have been removed. Through the processing of the Smooth module in the TOSCA software, a relatively smooth structure is obtained, and several formats commonly used in CAD software can be output to facilitate the redesign of the pedestal.

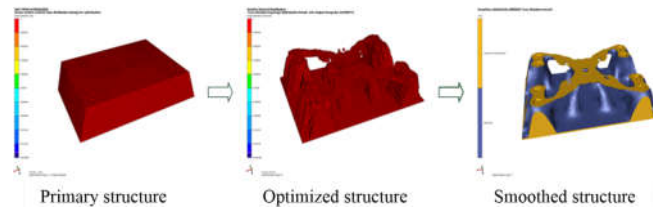


Figure 5: Optimization results when the volume fraction is 0.4

3.4 The parameters discussion of the pedestal structure

Although the structural topology optimization results can indicate the optimal material allocation of the structure, the optimization results tend to produce some ambiguous structures locally. Extract the concept of wireframe and panel for the optimization result. Restore the structure concept as realistically as possible, and try to make the similar endpoints reach one point.

1) Support Form

From the previous analysis, it can be found that the pillar below the bolt is the most important force transmission structure. It exists when the volume fraction and retention quality are low, so the support structure of the panel is the most important structural parameter.

Ensure that the pedestal quality is almost constant. All the panel thickness of the pedestal is 10mm, and the truss sections are all 12×12 rectangles. The material is 907A steel. By comparing the shocking responses of different supporting structures such as trusses, plates, '⊥' shaped beams and 'box' shaped beams, the changing regular that the anti-shocking performance of the pedestal changes with the structure is studied.

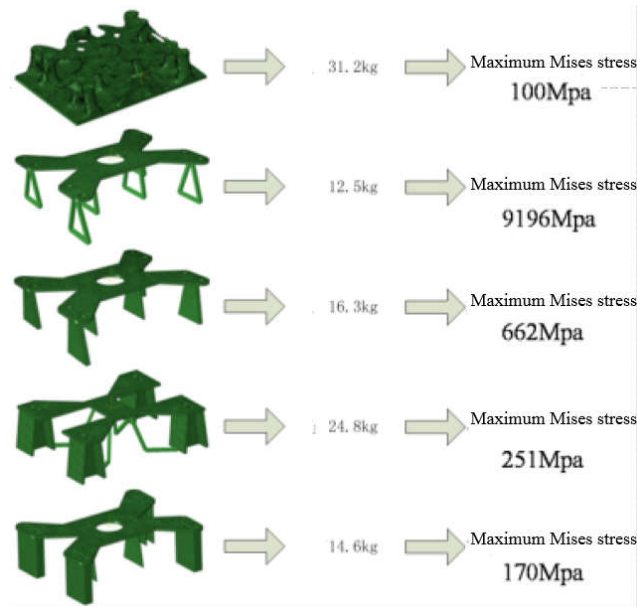


Figure 6: The shocking response of the pedestal in different supporting forms

Fig. 6 shows the maximum Mises stress corresponding to the pedestal under different cross-sectional shapes. It can be seen that using the box beam supports the least stress and best results. The "box" shaped beam supporting structure was used as the research object for force analysis, and the panel was considered as a fixed constraint. The other end of the "box" shaped beam is subjected to bending moment M and pressure F . The force diagram is shown in Fig. 7.

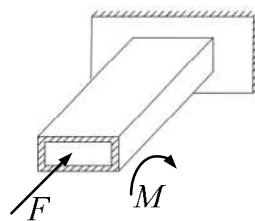


Figure 7: Force diagram of "box" beam support structure

From the knowledge of material mechanics, it can be known that for cantilever beams, the maximum stress is at the fixed support, ie at the panel. The stress size is

$$\sigma = \frac{F}{A} + \frac{M}{W} \tag{16}$$

Where, F and M are the axial pressure and bending moment of the cantilever beams respectively; A and W are the sectional area and the section modulus of the cross-section respectively.

Therefore, increasing the contact area between the support structure and the panel can reduce the stress of the pedestal. When the Sectional area does not change significantly, the higher the section modulus, the smaller the stress of the pedestal. Under different supporting forms, the maximum stress of the pedestal is ranked from large to small as truss > plate > ‘ \perp ’ shaped beams > ‘box’ shaped beam.

2) Plate Shape

In the process of topology optimization, the shape of the plate is also changing. According to the optimization results of the pedestal under different volume fraction constraints, the plate shape can be divided into four cases as shown in Fig. 8 .

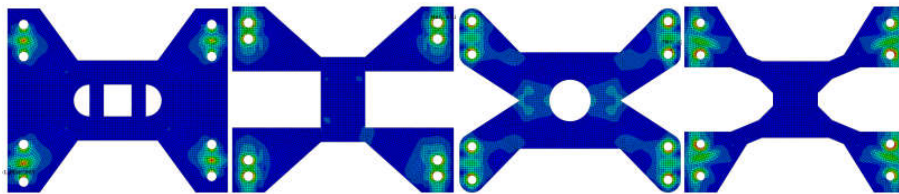


Figure 8: Different shapes of the pedestal plate

Ensure that the support of the pedestal is unchanged and compare the maximum Mises stress in the structure. This type of support is all supported by ‘ \perp ’ shaped beams, and the pedestal have approximately the same mass and are subject to the same shocking load.

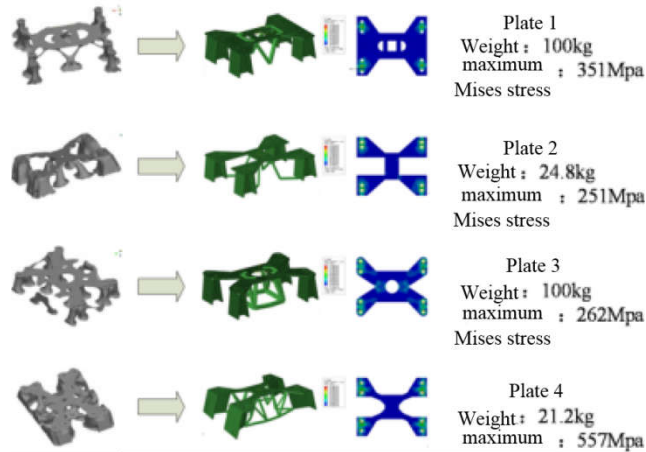


Figure 9: Shocking response of the pedestal with different plate shapes

Fig. 9 shows the maximum Mises stress in the pedestals of different plates under the same shocking load. It can be seen that these four plates shape do not have much influence on the shocking response; the difference in stress is largely determined by the form of support and the form of the structure. In view of the process and the structural durability, the plates corresponding to cases 2 and 4 are thinner at the four corners and the middle connection, and they are not as safe as the plates corresponding to cases 1 and 3.

3) Redesign of the Pedestal

Based on the optimized results and parameter analysis of the pedestal, it can be seen that it is more suitable to use a “box” shaped beam and the shape of the panel corresponding to Case 1 or Case 3. However, during the actual manufacturing process, it was found that the screw used to secure the equipment bolts on the panel would penetrate deep into the “box” beam, resulting in the inability to install the nuts. For this purpose, change the section shape to "E" which is as shown in Fig. 10. At the same time, in order to avoid structural damage caused by stress concentration, the structural boundary should be as smooth as possible. For this reason, a slight improvement is made on the basis of the plate 3. The length, width and height of the final optimized designing pedestal are basically the same as those of the original pedestal, and the positions of the bolts do not change. The plate thickness is 10mm which is supported by four brackets. The cross-section of the bracket is in an "E" shape and the thickness of it is 6mm. The pedestal is supported by equilateral angle steel truss in the middle and its weight is 36.2kg (22.6% of weight has been reduced). The finite element model of the optimized pedestal is shown in Figure 11, and its engineering drawings are shown in Fig. 12.

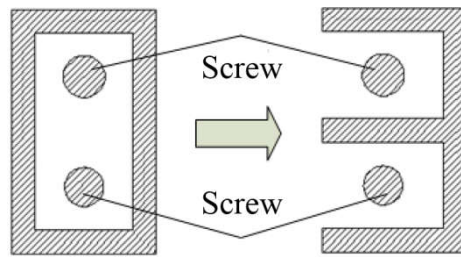


Figure 10: Ideal and actual sections

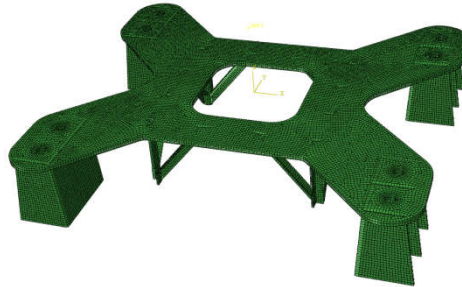


Figure 11: The final optimized pedestal finite element model

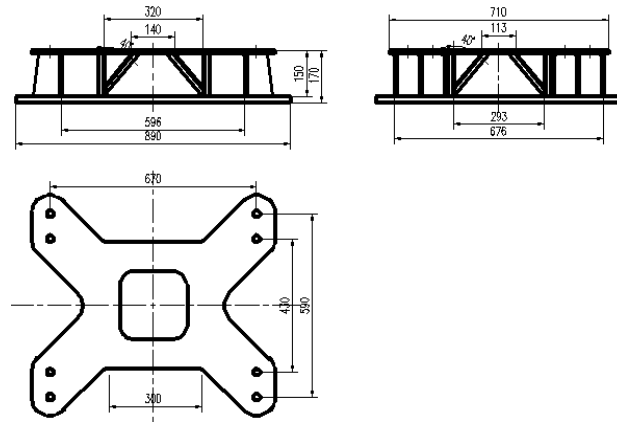


Figure 12: Engineering drawings for the optimized pedestal

4 COMPARISON OF PEDESTAL PERFORMANCE

4.1 Modal comparison

The main headings should be written left aligned, in 12pt, boldface and all capital Roman letters. There should be a 12pt space before and 6pt after the main headings.

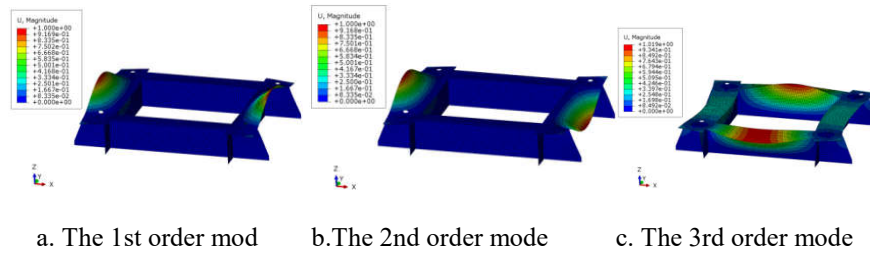
This paper considered the actual working environment of the pedestal and separately constrained the six degrees freedom of the original pedestal and the optimized pedestal in contact with the insole. In the Abaqus software, the six modes were calculated separately. The vertical participation quality of each mode was shown in Tab. 1.

Table 1: The first 6 modes of the pedestal

| Modal order | Traditional pedestal | | Optimized pedestal | |
|-------------|----------------------|-----------|--------------------|-----------|
| | f_1 (Hz) | p_1 (t) | f_2 (Hz) | p_2 (t) |
| 1 | 306.82 | 3.1E-03 | 430.82 | 2.9E-04 |
| 2 | 331.15 | 2.6E-08 | 764.35 | 1.1E-10 |
| 3 | 448.70 | 2.2E-14 | 825.59 | 3.4E-03 |
| 4 | 448.76 | 1.3E-12 | 885.15 | 2.5E-10 |
| 5 | 554.66 | 5.8E-07 | 943.05 | 1.9E-14 |
| 6 | 592.96 | 6.1E-16 | 999.27 | 4.1E-10 |

In this table, f_1 is traditional pedestal frequency, p_1 is traditional pedestal participation quality, f_2 is optimized pedestal frequency, p_1 is optimized pedestal participation quality.

The first six vibration modes of the two pedestals are shown in Figs. 13 and 14, and it can be seen that the first vibration modes of the two pedestals are mainly vertical vibrations.



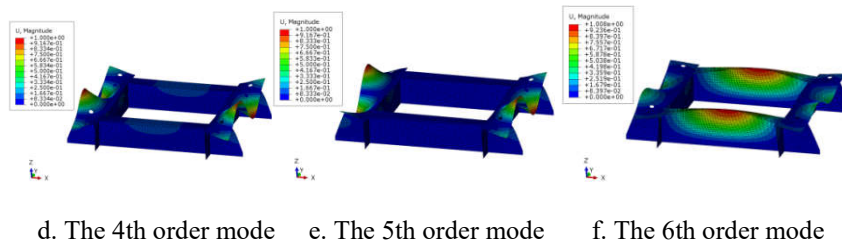


Figure 13: The first six-order modes of the traditional pedestal

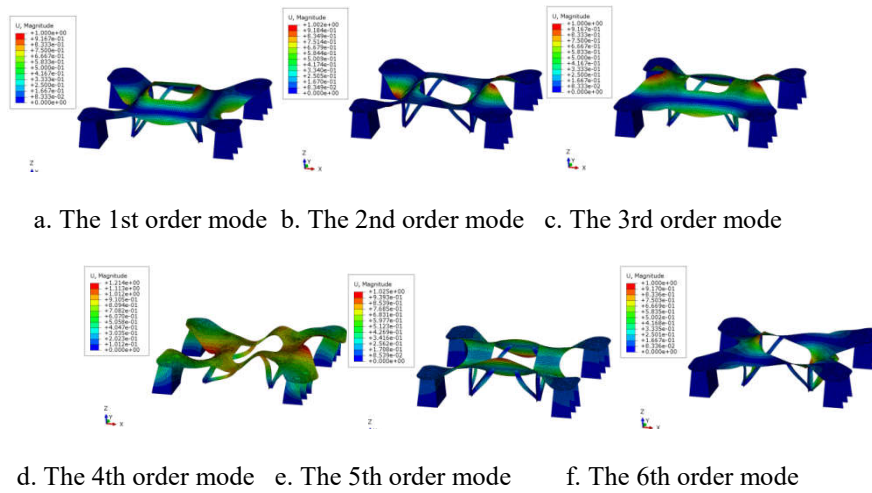


Figure 14: The first six-order modes of the optimized pedestal

It can be seen that the vibration modes of the first two stages of the two pedestals are similar. The vertical minimum resonant frequency of the traditional pedestal is 306.82 Hz; the vertical minimum resonant frequency of the optimized pedestal is 430.82 Hz. After the pedestal is optimized, its vertical stiffness is increased.

4.2 Shocking Comparison

Secondary headings should be written left aligned, 12 pt, boldface Roman, with an initial capital for first word only. There should be a 12pt space before and 6pt after the secondary headings.

According to the method specified in GJB 1060.1-91, the shocking load of the traditional pedestal and the optimized pedestal is designed, and it is converted to a dual-triangular acceleration time-domain curve according to the German specification BV430/85 as the input load for shocking calculation^[12]. The vertical, lateral and vertical directions of the two pedestals were checked for anti-shocking. According to formula (15), the input value of the shocking load can be obtained, as shown in Tab. 2. It can be seen that the spectral value calculated according to the specification is related to the weight. When the mass of the optimized pedestal is small, the input load obtained will be slightly larger.

Table 2: Input loads in different shocking directions

| Direction | Value | Model pedestal | Topology pedestal |
|--------------|-------------------|----------------|-------------------|
| Vertical | A_s (m/s^2) | 2203 | 2213 |
| | V_s (m/s) | 2.92 | 2.93 |
| | D_s (m) | 0.045 | 0.045 |
| Lateral | A_s (m/s^2) | 881 | 885 |
| | V_s (m/s) | 1.17 | 1.17 |
| | D_s (m) | 0.045 | 0.045 |
| Longitudinal | A_s (m/s^2) | 441 | 443 |
| | V_s (m/s) | 0.58 | 0.59 |
| | D_s (m) | 0.045 | 0.045 |

In this table, A_s = Acceleration spectrum, V_s = Speed spectrum, D_s = Displacement spectrum.

1) Response curve of the device acceleration

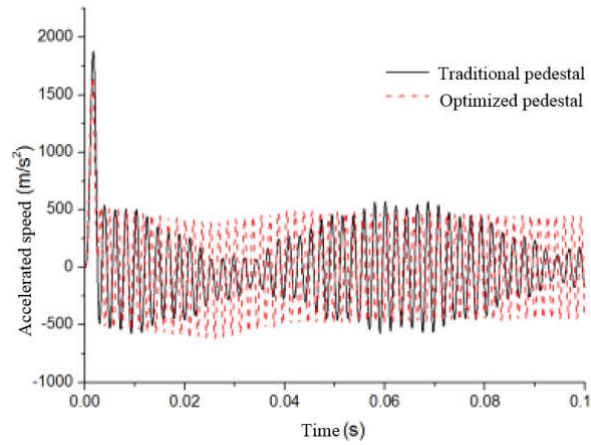


Figure 15: Vertical acceleration response of the device

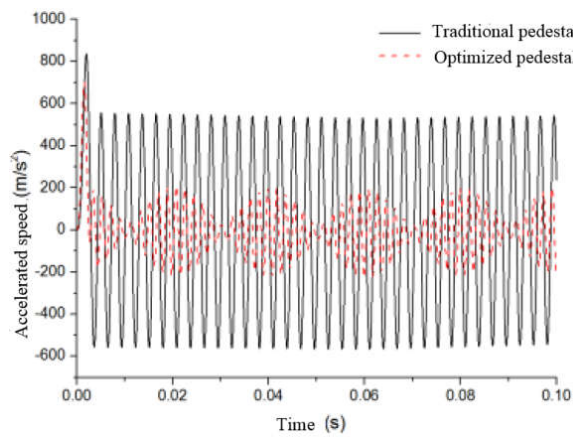


Figure 16: Lateral acceleration response of the device

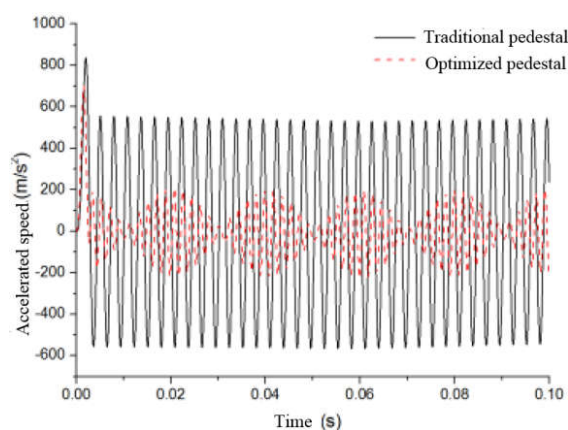


Figure 17: Longitudinal acceleration response of device

Figs. 15 to 17 are the vertical, lateral and vertical acceleration curves of the traditional spectral and the optimized spectral. It can be seen that the device acceleration curve shapes of the two bases in the three directions are very similar. Under the action of the shocking, the acceleration value increases rapidly and basically reaches the maximum value at the same moment, and then decays rapidly. Since no damping is set, the acceleration of the equipment will continue to oscillate after the shocking load ends. It can also be seen that despite the rigid connections, the isolation performance is limited. However, in both the vertical and lateral directions where the shocking loads are larger, the input value of the optimized pedestal is slightly larger than that of the traditional pedestal, but the maximum acceleration at the gravity center of the device is smaller than that of the traditional pedestal. From this point of view, the anti-shocking performance of the optimized pedestal is slightly better than that of the traditional pedestal.

2) Response of pedestal stress

Figs. 18 to 20 are Mises stress cloud figures for the maximum stress in vertical, lateral, and longitudinal directions of the traditional pedestal and the optimized pedestal. The bolt connection is simulated using the MPC-Beam method, and the calculated stress at the nodes near the bolts will be larger. The three level units near the bolt have been hidden in the figure. It can be seen that when the pedestal is subjected to a vertical shocking, the stress value is the highest, which is the most dangerous condition of the pedestal. The shapes of stress cloud figures for the two bases are similar. The maximum stress appears near the plate bolts, and the maximum stress value of the traditional pedestal is 616 MPa, which is beyond the requirements of the Chinese military standard GJB1060.1-91 (The stress is not exceeded the material's static yield strength of 390 MPa). The maximum Mises stress of the optimized pedestal is only 272 MPa, which is reduced by 55.8% and meets the requirements of GJB 1060.1-91. Under the lateral and vertical shocking loads, the maximum Mises stress of the traditional pedestal is low. They are 97.6 MPa and 71.2 MPa respectively, which are far less than the static yield limit of the material. The maximum Mises stress at the optimized pedestal was increased compared to the traditional pedestal. They are 237 MPa and 116 MPa respectively, but they are still smaller than the static yield limit of the material and the pedestal was in a safe state

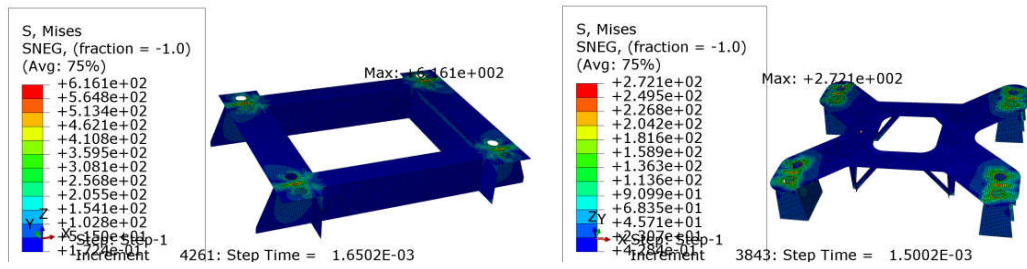


Figure 18: Pedestal stress cloud figure at vertical shocking

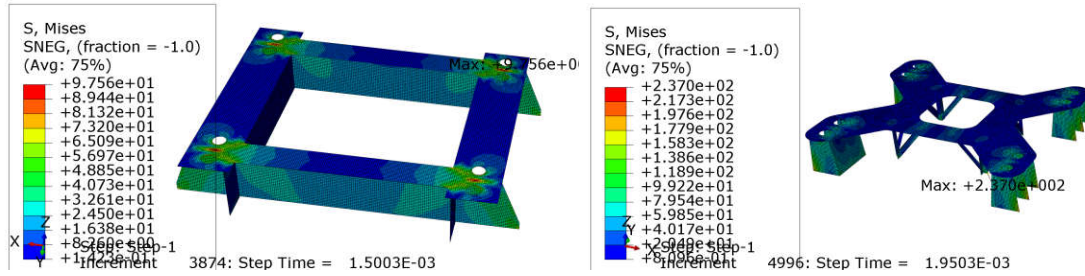


Figure 19: Pedestal stress cloud figure at lateral shocking

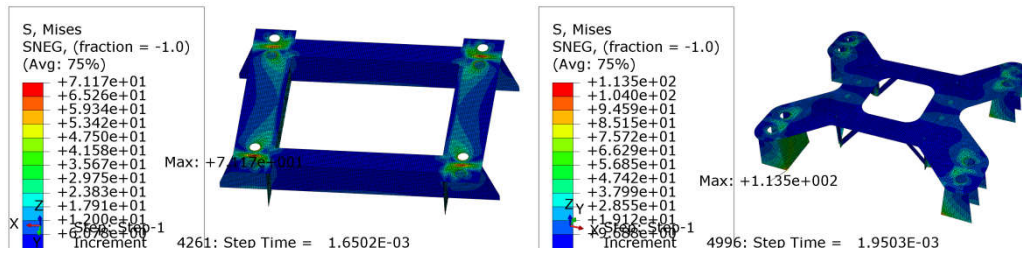


Figure 20: Pedestal stress cloud figure at longitudinal shocking

5 CONCLUSION

This paper mainly used TOSCA software to optimize the designing of a ship pedestal, and designed a new structure of the pedestal. Firstly, established a finite element model of a pedestal, and set the shocking load of the pedestal according to the national military standard of GJB1060.1-91. Then, the topology optimization of the two pedestals is designed. The maximum stiffness is used as the objective function, and the volume fraction is the constraint condition. A series of pedestals with different structural forms are set up based on the optimization results, and the effecting of the support form and the plate on the pedestal anti-shocking performance is studied. Finally, considering the stress concentration effect, the constraints of the actual processing technology, and the convenience of equipment installation, the shape of the support frame was changed from the most ideal "box" shaped to the "E" shaped and the edges and corners of the panel were smoothed. The pedestal designed in this paper was finally obtained. Compared with the traditional pedestal, the weight was reduced by 22.6%, the vertical minimum resonance frequency is increased from 306.82Hz to 430.82Hz, the vertical and horizontal anti-shocking performance are slightly improved, and the anti-

shocking performance is greatly improved. When the shocking strength of the pedestal was checked in the form of “box” support, the maximum Mises stress of the pedestal was reduced from 616 MPa to 272 MPa, which was a drop of 55.8% under the vertical shocking load.

REFERENCES

- [1] Zhang Xiangwen, Yang Deqing. A novel marine impact resistance and vibration isolation cellular mounting[J]. *Journal of Vibration and Shock*,2015, 34(10): 40-45.
- [2] Luo Zhong,Zhu Xi, Jian Lin'an. Isolation of vibration by the impedance and damping of a composite sandwich base[J].*Journal of Harbin Engineering University*,2009,(09):980-985.
- [3] Mao Liang,Mei Zhiyuan,Luo Zhong. Structure design and strength analysis of foundation structure of sandwich composite[J].*Journal of Naval University of Engineering*, 2008, 20(1):98-102.
- [4] Cheng Huanbo,Liu Zhifeng,Yuan He. Study of lightweight design method for the concrete pump base[J]. *Mechanical Science and Technology for Aerospace Engineering*, 2015, 34(1):23-26.
- [5] Sun Yumei,Zhang Long,Zhu Chuanchao. Lightweight design and sensitivity analysis for a naval gun seat[J].*Machinery & Electronics*,2016, 34(1):35-38.
- [6] Huang Haiyan,Liu Xiaowei,Jiang Shuwei. Optimization of main engine foundation based on fatigue strength[J].*Shipbuilding of China*,2010, 51(3):101-107.
- [7] San Xiaogang,Wang Ying,Xue Yu. Based on the continuum topology optimization of the large based lightweight design[J].*Journal of Changchun University of Science and Technology(Nature Science Edition)*,2012, 35(3):4-7.
- [8] Wu Guangming,Mei Yongjuan,Zhu Xinjin. Analysis of Shock Resistance of Diesel Engine Mounting. *Chinese Journal of Ship Research*, 2006, 1(4): 41-43,61.
- [9] Man Hongliang. Theory research and application on topology optimization of engineering structure [D]. Ji Lin University, 2007.
- [10] Li Xiang. Research on structural dynamic response topology optimization based on variable density method[D].Fu Dan University,2011.
- [11] GJB1060. 1-91.*Ship Environmental Requirements - Mechanical Environment*[S].

EFFICIENT TIME DOMAIN SIMULATION OF WAVES

OLOV LUNDBÄCK*

* SSPA Sweden AB
P O Box 24001
SE-400 22, Göteborg, Sweden
e-mail: olov.lundback@sspa.se, <https://www.sspa.se>

Key words: Numerical Methods, Waves, Simulations, Time Domain

Abstract. The current paper investigates different methods for time domain realization of irregular seastates. The paper also proposes and discuss quality measures to ensure that the right amount of frequency components is used for different applications. The current paper also studies different approaches to select discrete frequencies to minimise the number of frequencies required to achieve a good, time domain, representation of a wave spectrum. Increased interest in simulating manoeuvring, marine operations, tug boat operations etc in waves with several ships involved is one of the drivers for the current work. The current method investigation plays a central role in providing such simulations of missions and operations without demand for excessive computational resources. Efficient wave simulations are also an enabler for providing simulations in the form of software as a service, which require centralised core computations and distributed graphics.

1 INTRODUCTION

Most often metocean data are presented either in the frequency domain or as scatter matrices with frequency of occurrence versus wave period and significant wave height. As a result, seastates for time domain simulations are most often obtained from frequency domain data. Normally the transformation from frequency domain to time domain is carried out by inverse Fourier transformation or similar procedure. Currently, methods are available with good quality of much of the statistical properties, presented in e.g. ref. [1] and widely spread in standards and recommended practices such as [3]. However, commonly used methods require a large number of frequency components to obtain waves that does not repeat in relatively short periods. For many applications this results in computationally intensive simulations. The current work is targeted towards providing ship motion simulations with efficient time domain realization of seastates, enabling e.g. simulations of complex scenarios in waves with several ships, tug boats etc. involved. In addition, more efficient wave simulations are also put forward to enhance ship motion simulations distributed in the form of software as a service.

Currently this approach of providing simulations is demonstrated by SSPA Sweden's SEAMAN ONLINE service [2], which can be run in the end users own web browser. Figure 1 display a scenario with a port arrival, utilising this service, for education of ship officers.



Figure 1: Example of a scenario with a port arrival from ref. [2]

2 INVESTIGATED METHODS FOR TIME DOMAIN REALISATION OF WAVES

Fundamentals of the different methods utilized in the current work for time domain realization, of wave surface elevation - $\zeta(t)$, from a wave spectrum are shown by eq. (1)-(4) below:

$$\zeta(t) = \sum_{n=1}^N A_n \cdot \cos(\omega_n \cdot t + \varphi_n) \quad (1)$$

$$\zeta(t) = \sum_{n=1}^N A_n \cdot \cos((\omega_n + \delta\omega_n) \cdot t + \varphi_n) \quad (2)$$

, ω_n are equidistant distributed over the frequency interval and φ_n is a random sample of a uniform distribution over the interval from 0 to 2π for each frequency. A_n is the deterministic amplitude for each frequency, determined by the wave spectrum. In in eq. (2) the term $\delta\omega_n$ is added as a random sample of a uniform distribution over the frequency increment for each frequency.

$$\zeta(t) = \sum_{n=1}^N A_n \cdot \cos(\omega_n \cdot t + \varphi_n) \quad (3)$$

In eq. (3) A_n is Rayleigh distributed amplitude for each frequency, with $E(A_n)$ determined by the wave spectrum.

$$\zeta(t) = \sum_{n=1}^N A_n \cdot \cos\left(\frac{2 \cdot \pi}{T_n} \cdot t + \varphi_n\right) \quad (4)$$

, T_n are equidistant distributed over the period interval and φ_n are random samples of a uniform distribution over the interval from 0 to 2π . A_n is the amplitude for each frequency, determined by the wave spectrum.

Eq. 1 describe a widely spread method for summing discrete spectrum components to generate a time domain realization of an irregular seastate. However, in several applications, flaws of this method have been noted as described in e.g. [1], where shortcomings on statistical properties are pointed out. In [5] potential improvements regarding both statistical properties and computational efficiency are noted and proposed.

Eq. 2 have been put forward to improve statistical properties and have been detailed as a recommended practice in [6].

Time domain realisations of eq. (3) are presented as results in the frequency domain in [1]. Here it was noted that the random amplitudes of eq. 3 resulted in less faithful representation of the original spectrum. A filtering procedure to mitigate this was proposed but noted to be computationally intensive. Hence this filtering procedure have not been considered for the present work.

3 RESULTS

Time domain realizations of a Pierson-Moskowitz spectrum with significant wave height 1m and $T_p=6s$ have been carried out utilizing the methods described by eq. (1)-(4). All realizations cover a three-hour seastate.

The number of components has been varied to study how the number of components affect statistical properties of the time series generated. 20, 60 and 500 components have been used. Table 1 describe which results in Figure 2-Figure 10 that are related to which equation.

Table 1: Description of denomination of the different methods and results

| Method | Described by eqn. | Identifier in Figure 2-Figure 10 |
|---------------|--------------------------|--|
| 1 | (1) | random φ_n |
| 2 | (2) | random φ_n and $\Delta\omega$ |
| 3 | (3) | random A_n |
| 4 | (4) | constant ΔT , random φ_n |

3.1 Comparison between input spectrum and spectrum of time series generated

The graphs in this subsection show a comparison between input spectrum and fft of generated time series. The fft of the time series have been processed with Welch's method to provide better means for comparing input spectrum and the discrete frequencies captured by an fft on the time domain realization. An overlap of 90% have been used for Figure 2-Figure 4 and a lag number of 2048 have been utilized for Figure 2 and Figure 3 and 800 for Figure 4. The frequency domain data of the time series in Figure 4 have also been processed through a running average filter with averaging on 3 samples (in the frequency domain) to provide a possibility to compare with the input spectrum.

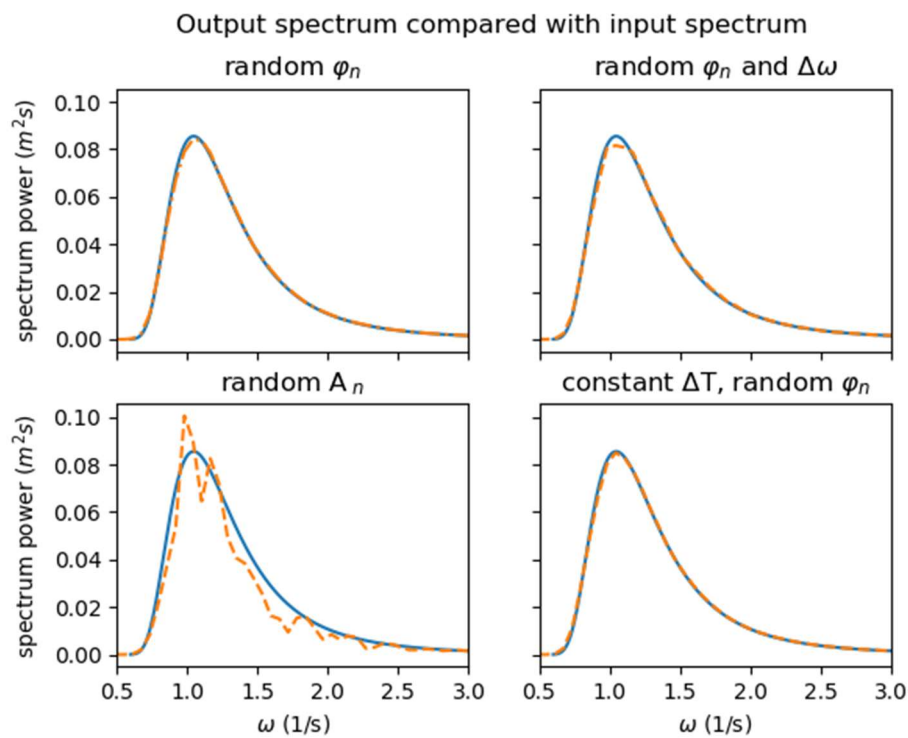


Figure 2: Comparison between input spectrum and fft of time domain realization with 500 frequency components

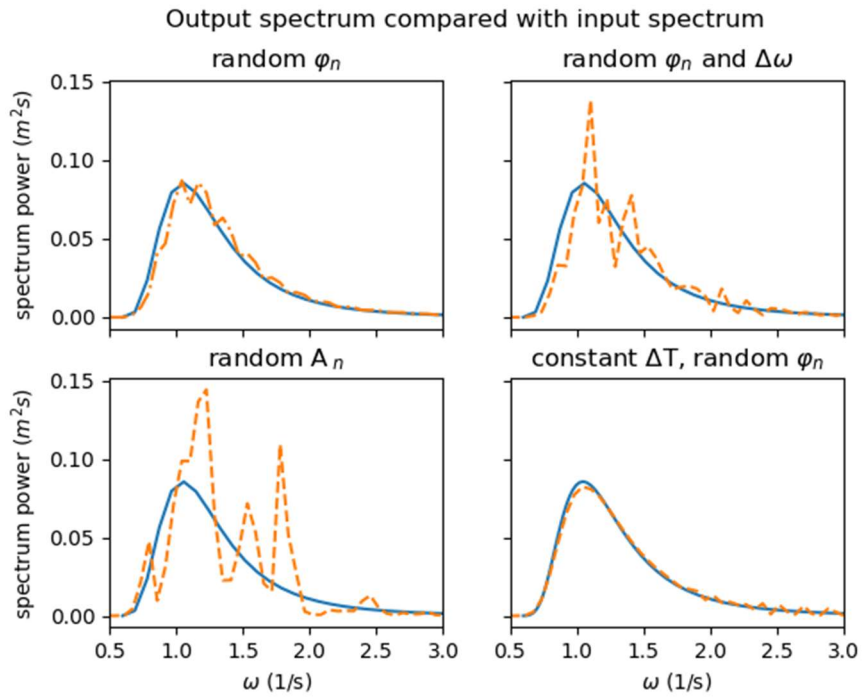


Figure 3: Comparison between input spectrum and fft of time domain realization with 60 frequency components

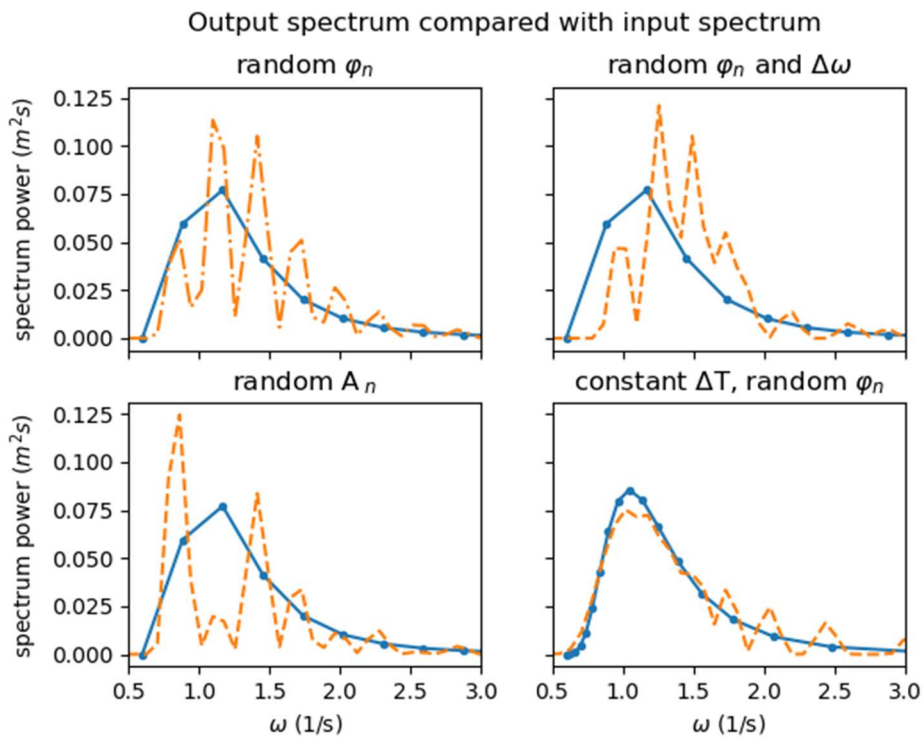


Figure 4: Comparison between input spectrum and fft of time domain realization with 20 frequency components

3.2 Distribution of wave elevation

The vertical position of the water surface can be represented as narrow banded Gaussian noise, which have been noted in e.g. [1] and [5]. Figure 5-Figure 7 show how well time domain realization with the methods described by eq. (1)-(4) resemble a Gaussian function with a mean value of 0 and standard deviation of 0.25.

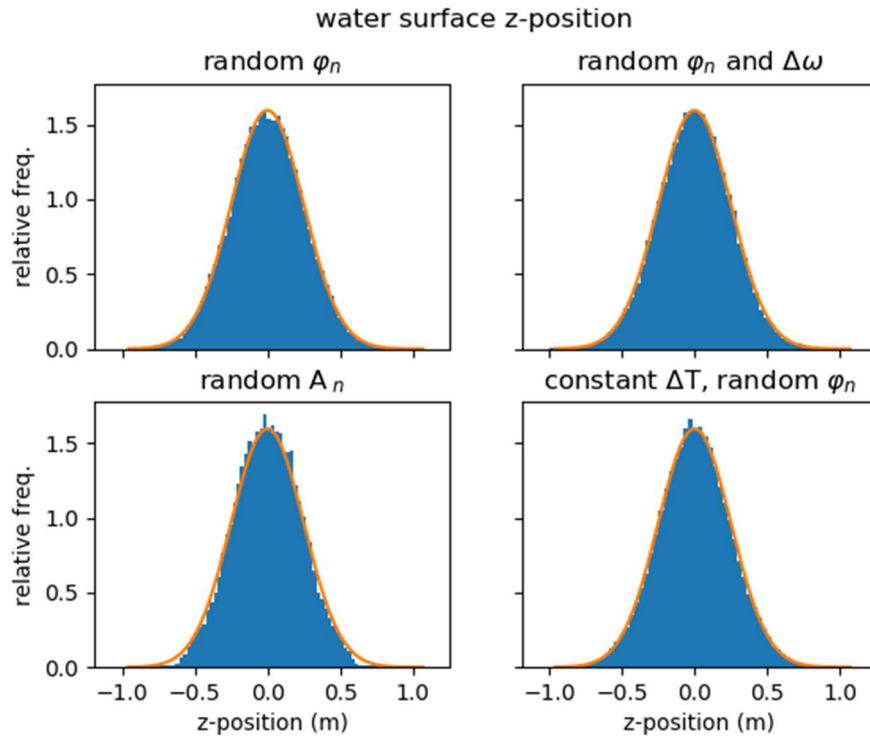


Figure 5: Comparison between a time domain realisation and Gaussian representation for the four different methods described by eq. (1)-(4). 500 frequency components have been utilized.

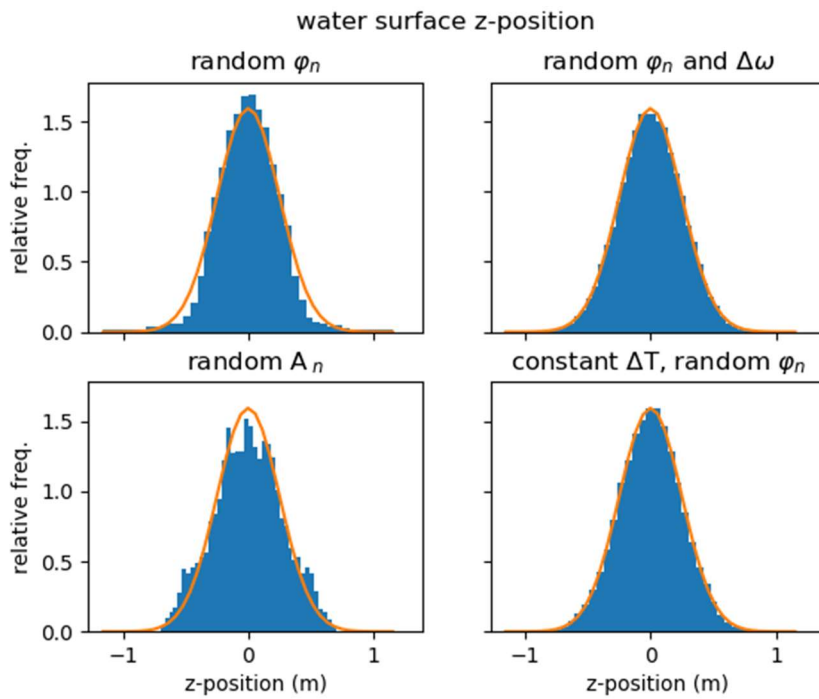


Figure 6: Comparison between a time domain realisation and Gaussian representation for the four different methods described by eq. (1)-(4). 60 frequency components have been utilized.

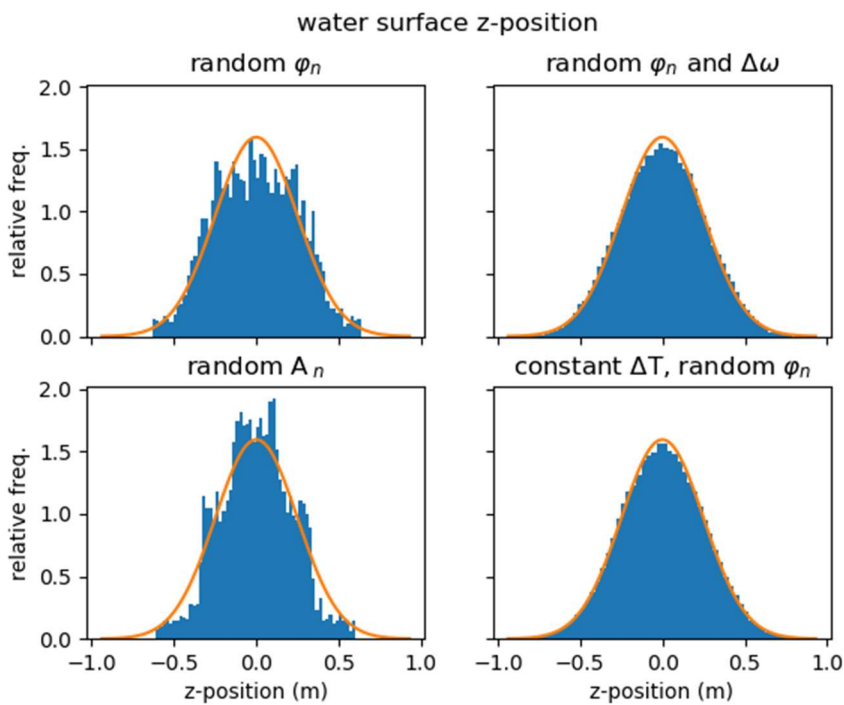


Figure 7: Comparison between a time domain realisation and Gaussian representation for the four different methods described by eq. (1)-(4). 20 frequency components have been utilized.

3.3 Autocorrelation

Figure 8-Figure 10 display auto correlation for the four methods, which can be used as an indication of the degree of repetitive patterns occurring in the different time domain realizations. All the time series used as input have a length of 3h with a sample frequency of 10Hz.

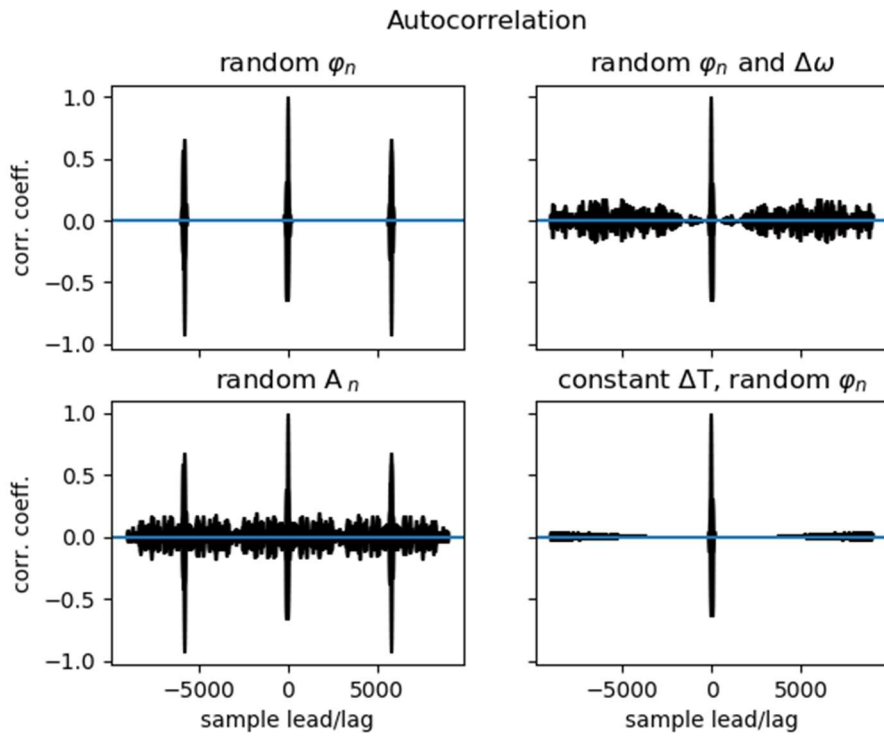


Figure 8: Comparison of autocorrelation of four methods for time domain realization of waves utilizing 500 components.

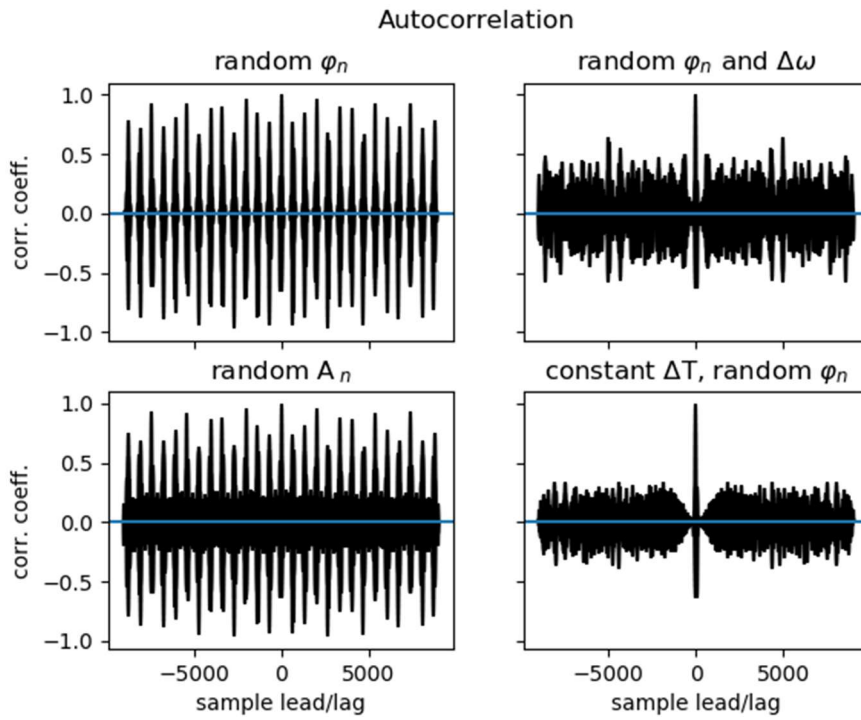


Figure 9: Comparison of autocorrelation of four methods for time domain realization of waves utilizing 60 components.

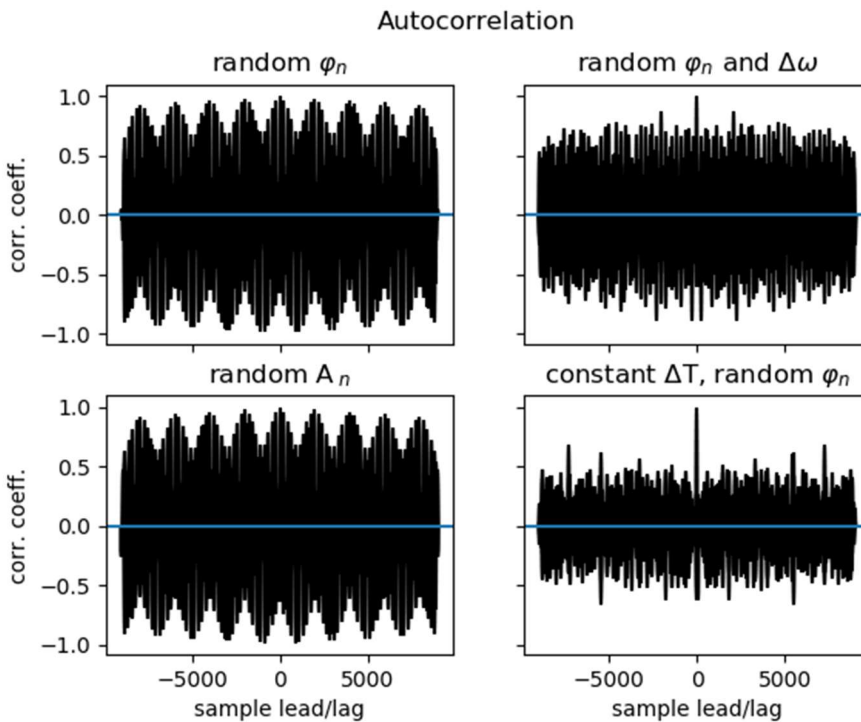


Figure 10: Comparison of autocorrelation of four methods for time domain realization of waves utilizing 20 components.

4 COMPUTATIONAL EFFICIENCY, QUALITY MEASURES AND DISCUSSION

For testing purposes, the four methods as described by eq. (1)-(4) have been implemented as similar, to each other, as possible in Python for the current investigation. The difference in computational time between the different methods show very small differences for the same number of components.

For many applications, it seems likely to be sufficient that the generated elevation of the wave surface is close to a Gaussian distribution with mean value and standard deviation close to the input spectrum. For such cases both method 2 and 4 could be run with only 20 components, which is indicated by Figure 5 - Figure 7. For cases where spectrum of time series need to show relatively close resemblance to input spectrum, in addition to the above quality measure, only method 4 can be considered for use with merely 20 components.

Increasing the number of components from 20 to 60, give significant improvements for all four investigated methods. For applications where extreme values are important, there should be a low degree of repeating wave patterns. Figure 8-Figure 10 show the degree of repetitiveness for the different methods with different number of components applied. Again method 4 show characteristics often sought for, i.e. small degree of repeating patterns and indicated long return periods even for small number of frequency components. Method 2 show low degree of repetitiveness for intermediate to high number of components, while method 1 and 3 require a large number of components to reach a lower extent of repeating patterns.

However, for some special cases, e.g. model tests with short testing time. Short and tailor-made return periods may be beneficial.

Table 2: Relative computational time for the investigated methods with different number of components

| Case | Method | Average (% of case 1) | St dev (% of average of case 1) |
|-----------------------|---------------|----------------------------------|--|
| <i>500 Components</i> | | | |
| 1 | 1 | 100.0 | 3.1 |
| 2 | 2 | 100.5 | 3.6 |
| 3 | 3 | 100.0 | 3.5 |
| 4 | 4 | 99.7 | 3.4 |
| <i>60 Components</i> | | | |
| 5 | 1 | 11.8 | 0.1 |
| 6 | 2 | 11.8 | 0.1 |
| 7 | 3 | 11.9 | 0.0 |
| 8 | 4 | 11.5 | 0.1 |
| <i>20 Components</i> | | | |
| 9 | 1 | 4.3 | 0.1 |
| 10 | 2 | 4.3 | 0.5 |
| 11 | 3 | 4.1 | 0.4 |
| 12 | 4 | 4.3 | 0.8 |

Table 3: Proposal for a way to recommend minimum number of components

| Accuracy requirement | | | |
|-----------------------------|------------|---------------|-------------|
| Method | Low | Medium | High |
| 1 | 60 | 500 | 500 |
| 2 | 20 | 60 | 500 |
| 3 | 60 | 500 | 500 |
| 4 | 20 | 20 | 60 |

Table 4: Relative computational time (in % of case 1) for the cases of Table 2

| Accuracy requirement | | | |
|-----------------------------|------------|---------------|-------------|
| Method | Low | Medium | High |
| 1 | 11.8 | 100.0 | 100.0 |
| 2 | 4.3 | 11.8 | 100.5 |
| 3 | 11.8 | 100.0 | 100.0 |
| 4 | 4.3 | 4.3 | 11.8 |

Table 3 give an outline on one way to recommend minimum number of components. The figures in Table 3 are based on judgement by inspection of Figure 2-Figure 10. The need for a more objective way of quantifying statistical properties of generated time series is also identified but outside of the scope for the current work. A set of recommendations may also need more detailed and specific targeted requirements directed to e.g. extreme value analysis, parametric roll, et.c. For extreme value analysis, the repetitiveness characteristics are important. For parametric roll, the “groupiness” is crucial, which is determined, among others, by how samples of the water surface resemble Gaussian curve, as displayed by Figure 5-Figure 7. Table 4 give relative computational time when the number of components from

Table 3 are applied. For such a case it is indicated that potential saving in computational time is up to 20 times by choosing a method for time domain realization of waves that fit the application. This is in the same order of magnitude as the reduction of number of components. For a simulation program that utilize wave elevation, its first and second derivative to compute forces in six degrees of freedom, a considerable amount of total computational work is related to time domain realization of wave surface and its derivatives.

5 CONCLUSIONS

Four different methods for generating time domain realizations of waves have been investigated. Large difference in statistical properties are noted. Quality measures are outlined and discussed. Computational time at given accuracy levels are assessed, where it was indicated that choosing a suitable method for time domain realization of waves may give time savings up to 20 times for the wave generation.

REFERENCES

- [1] Tucker M.J. “Numerical simulation of a random sea: a common error and its effect upon wave group statistics”, Applied Ocean Research, Volume 6, Issue 2, April 1984, Pages 118-122
- [2] <https://seaman.sspa.se>
- [3] DNV GL RP-C 205, “Environmental-Conditions-and-Environmental Loads”, Edition August 2017.
- [4] Forristall, G., (2000), “Wave crest distributions: observations and second-order theory”, Journal of Physical Oceanography, 30, pp. 1931-1943 (2000).
- [5] Huss M., “Notes on the modeling of irregular seas in time simulations”, http://www.mhuss.se/documents/Downloads/101129mh_Notes_IrrSea_R2.pdf
- [6] Det Norske Veritas, Recommended Practice, “Environmental Conditions and Environmental Loads”, DNV-RP-C205, OCTOBER 2010.

SIMULATION OF IRREGULAR WAVE MOTION USING A FLAP-TYPE WAVEMAKER

S. RAMEZANZADEH ^{1,†}, M. OZBULUT ² AND M. YILDIZ ^{1,†}

¹ Faculty of Engineering and Natural Sciences, Sabanci University, Istanbul 34956, Turkey
Email: ramezanzadeh@sabanciuniv.edu - Web page: <http://www.sabanciuniv.edu>

² Faculty of Engineering, Piri Reis University, Istanbul 34940, Turkey
Email: mozbulut@pirireis.edu - Web page: <http://www.pirireis.edu.tr>

[†] Integrated Manufacturing Technologies Research and Application Center, Sabanci University, Tuzla, Istanbul 34956, Turkey

Keywords: SPH Method, Numerical Wave Tank, Irregular Wave, Wave Energy Spectrum

Abstract. The main objective of the present study is to propose a numerical scheme to model irregular wave systems through a Lagrangian, particle-based numerical method, namely, Smoothed Particle Hydrodynamics (SPH). A numerical wave generator tank, which can generate desired irregular waves is modeled by the SPH method. The fluid motion is governed by continuity and Navier-Stokes equations where Weakly Compressible SPH (WCSPH) approximation is employed for the numerical discretization of the problem domain. To generate the irregular wave spectrum, a flap-type wave generator is adopted into the computational domain which yields to the modeling of moving boundary conditions on the problem domain. As benchmark studies, JONSWAP and Pierson-Moskowitz wave spectrums are simulated to validate the obtained wave characteristics with the theoretical results. The performances of the wave maker are tested under different peak wave frequency values. Fast Fourier Transformation (FFT) analysis is conducted to scrutinize the distribution of wave energy spectrum in the frequency domain. In the light of sufficiently long-term simulation results, it can be said that a good agreement is obtained between the numerical and theoretical results, which indicates that the presented SPH scheme can be utilized in further free-surface hydrodynamics studies related to the irregular wave regimes.

1 INTRODUCTION

Ocean surface waves generally produce periodic pressure loads on floating or fixed marine structures; therefore, the problem of determining the motion of objects under the influence of oceanic waves and determining hydrodynamic forces on these objects is an area which gets a lot of interest among free-surface water scientists. Further research on wave mechanics is required in today's engineering applications, namely, marine sciences, coastal engineering, port management, the design of any offshore structures like ships, and wave energy systems.

Regular waves do not represent the real state of the sea because the nature of oceanic waves is mostly random or irregular. Indeed, these waves can be considered as the summation of many regular waves, each with its own amplitude, period or frequency, length, and propagation direction [1]. Fast Fourier transformation (FFT) can be used to transfer random sea surface into the summation of linear waves. A wave spectrum describes the distribution of wave energy

over a frequency range for a given sea or ocean region [2]. There are several wave spectra available in the literature and JONSWAP and Pierson-Moskowitz which are modeled in this study are one of the most common irregular wave systems [2-4].

As a natural consequence of the development of new generation technology on experimental opportunities, today, scientific studies on the investigation of free-surface flows can get more realistic and accurate results. Numerous experimental researches have been carried out to investigate the spread of irregular waves and their interaction with the offshore structures [5-7]. On the other hand, although experimental studies capture and reveal the physical background of such problems in a more realistic way, they are generally an expensive tool for the specific industrial applications. Alternatively, compared to experimental testing, a relatively reliable and cheaper technique is the computational modeling and analysis of the wave conditions in a numerical wave tank.

Along this line, this work aims to utilize one of the popular computational technique on the modeling of free surface problems, a Lagrangian, particle-based method named as Smoothed Particle Hydrodynamics (SPH). The SPH method has been used in modeling of free-surface water flow problems since the mid-90s [8]. The application of the SPH method to study coastal engineering problems has increased during the last few years [9-13]. Due to its intrinsic advantages on the modeling of highly nonlinear violent free-surface problems, the SPH method has been widely used in numerical calculations to capture high free-surface deformations which may occur in the problem domain. The method defines the physical behavior of the fluid through an interpolation process using a weight function that varies in proportion to the position of the particles distributed within the problem area. The physical properties (density, pressure, velocity, etc.) of each particle are updated at each time step so that the time-varying physical properties of each particle can be tracked instantaneously.

In this study, a numerical wave tank which generates desired irregular waves is modeled. The fluid motion is governed by continuity and Navier-Stokes equations, and Weakly Compressible SPH (WCSPH) approximation is employed for the numerical discretization of the problem domain. To generate the irregular wave spectrum in a more realistic manner, a flap-type wave generator is adopted into the computational domain which yields to the modeling of moving boundary conditions on the problem domain.

The rest of the paper is organized as follows: In the second section, the governing equations and the discretization methodology of these equations together with the corrective treatments are stated. Following the mathematical background of the irregular wave systems utilized in this work, the physical parameters of the problem and obtained numerical results are presented in the third section. Finally, the concluding remarks are emphasized in the last part.

2 MATHEMATICAL FORMULATIONS

2.1 Governing equations

In the present study, the fluid is assumed to be weakly compressible. The continuity equation and Navier-Stokes equations are employed to describe the fluid motion and can be written as:

$$\frac{d\rho}{dt} = -\rho\nabla \cdot \vec{u} \quad (1)$$

$$\frac{d\vec{u}}{dt} = -\frac{1}{\rho}\nabla p + \nu\nabla^2\vec{u} + \vec{g} \quad (2)$$

The displacement of fluid particles is provided by the following equation:

$$\frac{d\vec{r}}{dt} = \vec{u} \quad (3)$$

Where \vec{u} is the velocity vector, p is the pressure, ν is the kinematic viscosity, ρ is the density, \vec{r} is the particle positions and \vec{g} denotes gravitational acceleration vector. The governing equations are discretized utilizing WSPH method [8]. In this approach, the pressure term is determined by the implementation of the artificial equation of state, which couples pressure and density variations through a coefficient commonly known as the speed of sound. In the present study, the equation of state proposed by Monaghan [14] is used:

$$p = \frac{\rho_0 c_0^2}{\gamma} \left[\left(\frac{\rho}{\rho_0} \right)^\gamma - 1 \right] \quad (4)$$

Where c_0 is the reference speed of sound taken as 30 [m/s], ρ_0 is the reference density equal to 1000 [kg/m³], and γ is the specific heat ratio of water (considered to be 7). The reference speed of sound is determined by dimensionless Mach number (M), which represents the ratio of fluid to sound velocities. The amount of M lower than 0.1 guarantees the density fluctuations less than the 1% of the reference density [14].

2.2 SPH scheme and numerical discretization of the governing equations

The SPH method is based on the interpolation process. According to this approach, any field function is expressed by means of the interaction of neighboring particles using an analytic function called the weight function. The weight function, $W(r_{ij}, h)$, is defined as a function, equivalent to Delta Dirac (δ) when h , interpolation length, is zero. Mathematically, any continuous function (scalar, vectorial, or tensor) can be written as follows:

$$A(\vec{r}_i) = \int_{\Omega} A(\vec{r}_j) \delta(\vec{r}_i - \vec{r}_j) d^3\vec{r}_{ij} \quad (5)$$

$$\int_{\Omega} \delta(\vec{r}_i - \vec{r}_j) d^3\vec{r}_{ij} = \begin{cases} 1, & \vec{r}_i = \vec{r}_j \\ 0, & \vec{r}_i \neq \vec{r}_j \end{cases} \quad (6)$$

Where $A(\vec{r}_i)$ is the continuous function, $\vec{r}_{ij} = \vec{r}_i - \vec{r}_j$ represents the distance vector between the particle of interest i and its neighboring particle j , and \vec{r}_i and \vec{r}_j represents the position vectors for the i and j particles, respectively. Value of any continuous function, $A(\vec{r}_i)$, is expressed in the SPH method as follows:

$$A_i \cong \langle A(\vec{r}_i) \rangle \equiv \int_{\Omega} A(\vec{r}_j) W(r_{ij}, h) d^3\vec{r}_{ij} \quad (7)$$

In the above formulation, the angle bracket $\langle \rangle$ defines the kernel approximation and $d^3\vec{r}_{ij}$ denotes the infinitesimally small volume of the particle which equals to the mass, m_j , divided

by the density of the particle, ρ_j , and Ω represents the total bounded volume of the domain. A_i function represents any hydrodynamic properties such as velocity, pressure, density, and viscosity. In the SPH method, the derivative of any arbitrary function can be easily calculated by taking the derivative from the weight function:

$$\left\langle \frac{\partial A(\vec{r}_i)}{\partial x_i^k} \right\rangle \equiv - \int_{\Omega} A(\vec{r}_j) \frac{\partial W(r_{ij}, h)}{\partial x_i^k} d^3 \vec{r}_{ij} \quad (8)$$

There are various kinds of kernel functions in the literature [15, 16]. In this study, the quintic kernel function is utilized due to its high accuracy and stability [17]:

$$W(R, h) = \alpha_d \begin{cases} (3 - R)^5 - 6(2 - R)^5 + 15(1 - R)^5, & 0 \leq R < 1 \\ (3 - R)^5 - 6(2 - R)^5, & 1 \leq R < 2 \\ (3 - R)^5, & 2 \leq R < 3 \\ 0, & R \geq 3 \end{cases} \quad (9)$$

In Eq. (9), $R = |\vec{r}_{ij}|/h$, h is the smoothing length, and α_d is a coefficient dependent on the dimension of the problem. In two dimensions, α_d is equal to $7/(478\pi h^2)$. As a result, the numerical discretization of the the continuity and momentum equations of fluid motion can be expressed respectively by the following relations [14, 18]:

$$\frac{d\rho_i}{dt} = \rho_i \sum_{j=1}^N (\vec{u}_i - \vec{u}_j) \cdot \nabla_i W_{ij} V_j \quad (10)$$

$$\rho_i \frac{d\vec{u}_i}{dt} = - \sum_{j=1}^N \left(\frac{p_i}{\rho_i^2} + \frac{p_j}{\rho_j^2} \right) \nabla_i W_{ij} V_j + K\nu \sum_{j=1}^N \Pi_{ij} \nabla_i W_{ij} V_j + \vec{g} \quad (11)$$

Here, N is the number of neighbor particles for particle i , ∇_i is the gradient operator taken with respect to the position of particle i , $K=2(n+2)$ where n is the dimension of the problem domain, V_j indicates the volume of particles which is calculated by $V_j = \sum_{i=1}^N 1/W_{ij}$ and Π_{ij} is the viscosity term which is defined as [19]:

$$\Pi_{ij} = \frac{(\vec{u}_j - \vec{u}_i) \cdot (\vec{r}_j - \vec{r}_i)}{\|\vec{r}_j - \vec{r}_i\|^2} \quad (12)$$

Kinematic viscosity (ν) is taken as 10^{-6} (m²/s) for water.

2.3 Corrective numerical algorithms

In this section, we will briefly mention the correction terms added into the numerical scheme to increase the stability and robustness of the method.

2.3.1 Kernel gradient correction

In this study, in order to increase the accuracy of the evaluation of any linear velocity field and conservation of angular momentum, the derivatives of the kernel function given by Eq. (9) is renormalized by multiplying with the following local $L(\vec{r}_i)$ matrix [20, 21]:

$$\nabla^c W_{\vec{r}_i} = L(\vec{r}_i) \nabla_i W_{ij} \quad (13)$$

$$L(\vec{r}_i) = \left[\sum_j \begin{pmatrix} x_{ji} \frac{\partial W_{ij}}{\partial x_i} & y_{ji} \frac{\partial W_{ij}}{\partial x_i} \\ x_{ji} \frac{\partial W_{ij}}{\partial y_i} & y_{ji} \frac{\partial W_{ij}}{\partial y_i} \end{pmatrix} V_j \right]^{-1} \quad (14)$$

2.3.2 Density correction

In the weakly compressible SPH approach, the precise calculation of the density field is crucial because the pressure values are coupled to the density values in the equation of state (see Eq. 4) and small density disturbances can lead to high oscillations in the pressure field, and in turn, cause a decline in numerical accuracy and stability [22]. In order to eliminate this problem, density correction algorithms are frequently used in SPH literature [19, 23]. In this study, The density correction algorithm is applied through:

$$\hat{\rho}_i = \rho_i - \frac{\sum_{j=1}^N (\rho_i - \rho_j) W_{ij}}{\sum_{j=1}^N W_{ij}} \quad (15)$$

Here, $\hat{\rho}_i$ is the corrected density.

2.3.3 Hybrid free-surface and artificial particle displacement algorithm

Velocity variance-based free-surface algorithm (VFS) is a numerical correction treatment which is applied to only free-surface particles and help the particles on the free-surface to stay away from excessive scattering by providing a numerical surface tension on the free surface. The particles which have neighbor particle amount less than 65% of the average neighbor particle number in the problem domain are marked as free-surface articles along this line, the applied free-surface treatment is given below [22, 24]:

$$\delta \vec{u}_i = \frac{\sum_{j=1}^N (\vec{u}_i - \vec{u}_j) W_{ij}}{\sum_{j=1}^N W_{ij}}, \quad \vec{u}_i = \vec{u}_i - \varepsilon \delta \vec{u}_i \quad (16)$$

where \vec{u}_i is the corrected particle velocity, and ε is a constant which is sufficient to assign a value between 0.05 and 0.1 times the initial particle spacing (dx). On the other hand, Artificial Particle Displacement (APD) algorithm which is applied to the fully populated regions of the fluid domain provides a homogeneous particle distribution during the evolution of the flow which significantly enhances the accuracy of the interpolation processes of the SPH method. The formulation of the APD algorithm is as follows [22, 24]:

$$\delta \vec{r}_i = \sum_{j=1}^N \frac{\vec{r}_{ij}}{r_{ij}^3} r_0^2 u_{c_{ff}} \Delta t \quad (17)$$

$$r_0 = \frac{1}{N} \sum_{j=1}^N r_{ij}, \quad u_{cff} = |\delta \vec{u}_i|$$

2.4 Irregular wave generation

The procedure for the generation of these irregular waves starts from dividing the wave density spectrum into n equal parts ($n > 50$) in a frequency domain which separates spectrum into n equal monochromatic waves each with their own wave characteristics like amplitude, frequency, and wavelength [25]. Angular frequencies and amplitudes of all wave components are calculated as follows:

$$\omega_i = 2\pi f_i \quad (18)$$

$$a_i = \sqrt{2S_\eta(f_i)\Delta f} = \frac{H_i}{2} \quad (19)$$

Where f_i indicates the frequency of each wave, H_i denotes the corresponding wave heights, $S_\eta(f_i)$ represents the wave energy spectrum of each wave frequency, ω_i is the angular frequency, and a_i is the amplitude. The time series of wave amplitudes are converted into the flap movement by means of the Biesel transfer function [26]:

$$\frac{H_i}{S_{0,i}} = 4 \left(\frac{\sinh k_i d}{k_i d} \right) \frac{k_i d \sinh k_i d - \cosh k_i d + 1}{\sinh 2k_i d + 2k_i d} \quad (20)$$

where d is the water depth, k_i is the wave number (calculated by $k_i = \omega_i^2/g$), and δ_i is the initial phase which is a random number between 0 and 2π . All wave components obtained by Eq. 20 are combined in the flap displacement time series equation:

$$e(t) = \sum_{i=1}^n \frac{S_{0,i}}{2} \sin(\omega_i t + \delta_i) \quad (21)$$

The present study aims to model two standard wave spectra to generate irregular wave trains, namely, JONSWAP (Joint North Sea Wave Project) and Pierson-Moskowitz spectra.

2.4.1 JONSWAP wave spectrum

Various wave energy spectra are found in literature and used for ocean engineering problems [2], JONSWAP is one of the most common spectrum among them, which is an experimental relationship that describes the distribution of energy with a frequency in the ocean. JONSWAP was developed by Hasselmann from 1968 to 1969 [3] after analyzing and measuring data collected during the Joint North Sea Wave Study Project. The following equation of JONSWAP wave spectrum is recommended by the 23th ITTC in 2002 for limited fetch conditions [2]:

$$S(f) = \alpha g^2 (2\pi)^{-4} f^{-5} \exp \left[-\frac{5}{4} \left(\frac{f}{f_p} \right)^{-4} \right] \gamma \exp \left[-\frac{(f-f_p)^2}{2\tau^2 f_p^2} \right] \quad (22)$$

$$\tau = 0.07 \quad , f \leq f_p$$

$$\tau = 0.09 \quad , f > f_p$$

$$\alpha = 0.0081$$

Where g is the gravity acceleration, f_p is the wave peak frequency in Hertz, and γ is the wave peak enhancement factor taken as 3.3.

2.4.2 Pierson-Moskowitz wave spectrum

The Pierson-Moskowitz spectrum is based on measurements taken in the North Atlantic Ocean [4]. This spectrum is proper for fully developed wind sea studies:

$$S(f) = \frac{A}{f^5} \exp\left(-\frac{B}{f^4}\right) \quad (23)$$

$$A = \alpha g^2 (2\pi)^{-4}$$

$$B = (5/4)f_p^4$$

where A is the scaling parameter and α is the intensity of the spectrum that relates to the wind speed and fetch length. In this study, α is taken as 8.1×10^{-3} .

3 PROBLEM DEFINITION AND NUMERICAL RESULTS

3.1 Problem definition

The geometrical scheme of the two-dimensional numerical wave tank is shown in Fig.1. The flap-type wavemaker in the left-hand side of the tank generates the required irregular waves. The still water level and the channel horizontal length were taken $d = 1$ [m] and $L = 5$ [m], respectively. The initial interparticle distance equals to $dx = 0.01$ [m], which leads to the employment of 66,840 fluid particles in all of the simulations. In order to physically dampen the produced waves without using any numerical damping algorithm, a linearly increasing beach with an angle of $\beta = 21.8^\circ$ is placed at the end of the tank. The wave heights are recorded at $x_{rec} = 2.5$ [m] from the flap, and the obtained wave heights time series are compared with theoretical solutions.

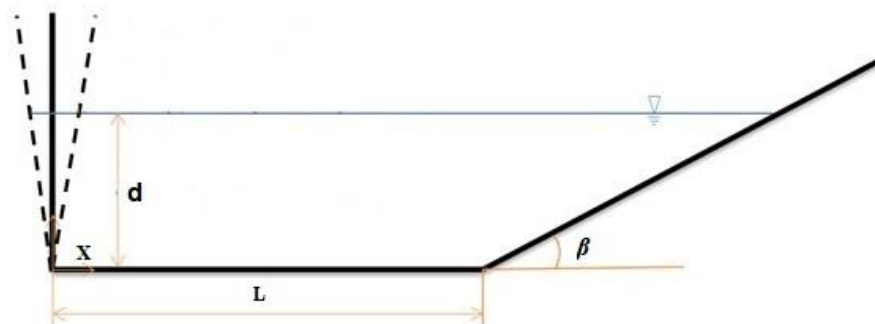


Figure 1: Numerical wave tank setup

3.2 Numerical results

Irregular wave simulations of two different wave spectra and three peak frequencies for each spectrum are performed with the SPH solution scheme described in Chapter 2. The summary of the simulation cases in the present study is provided in Table 1.

Table 1: Spectrum type, frequency range and peak frequencies of the simulated test cases

| Case No | Spectrum Type | Frequency Range | Peak Frequency |
|---------|-------------------|-----------------|----------------|
| 1 | JONSWAP | 0.3-2.5 Hz | 0.6 Hz |
| 2 | JONSWAP | 0.3-2.5 Hz | 0.7 Hz |
| 3 | JONSWAP | 0.5-2.5 Hz | 0.8 Hz |
| 4 | Pierson-Moskowitz | 0.3-3.0 Hz | 0.6 Hz |
| 5 | Pierson-Moskowitz | 0.3-3.0 Hz | 0.7 Hz |
| 6 | Pierson-Moskowitz | 0.3-3.0 Hz | 0.8 Hz |

Fig.2 and Fig.3 depict the time series of both wave spectrum types obtained by calculated wave elevations from still water level at point $x = x_{rec}$. It can be said that the obtained SPH results are consistent with the theoretical wave height of the irregular waves especially while the peak frequency value is increasing in both wave spectra. The main reason for the discrepancies between the obtained free surface elevations and the theoretical solution can be attributed to the presence of the relatively low number of wave components which have higher wavelengths causing reflection from the damping beach at the end of the tank. To overcome this physical problem, a longer wave tank is required which leads to the utilization of a higher amount of particles hence causing a dramatical increase in terms of computational costs.

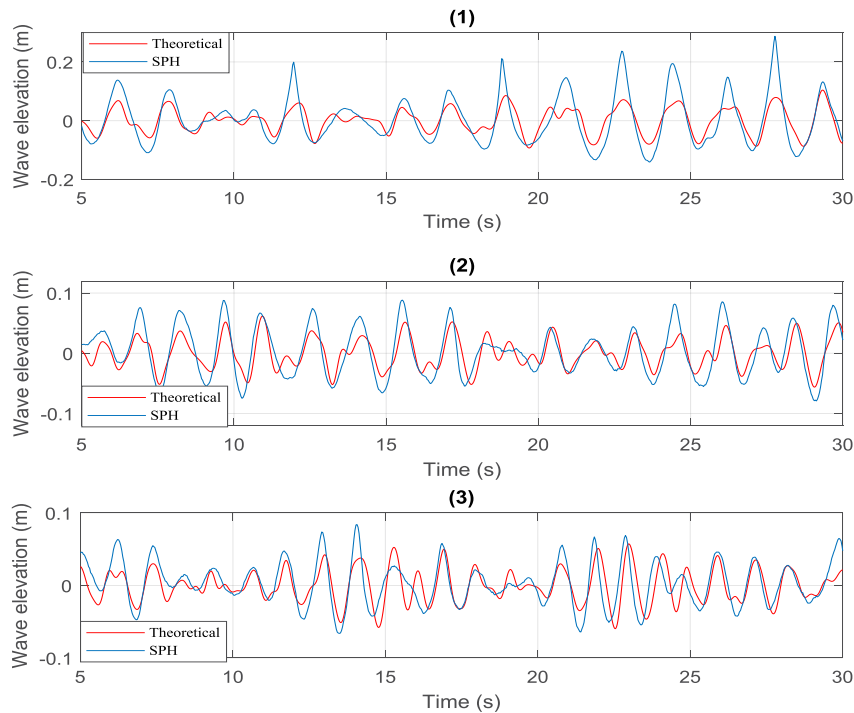


Figure 2: Comparison between theoretical and SPH wave amplitudes for JONSWAP wave spectrum test cases.

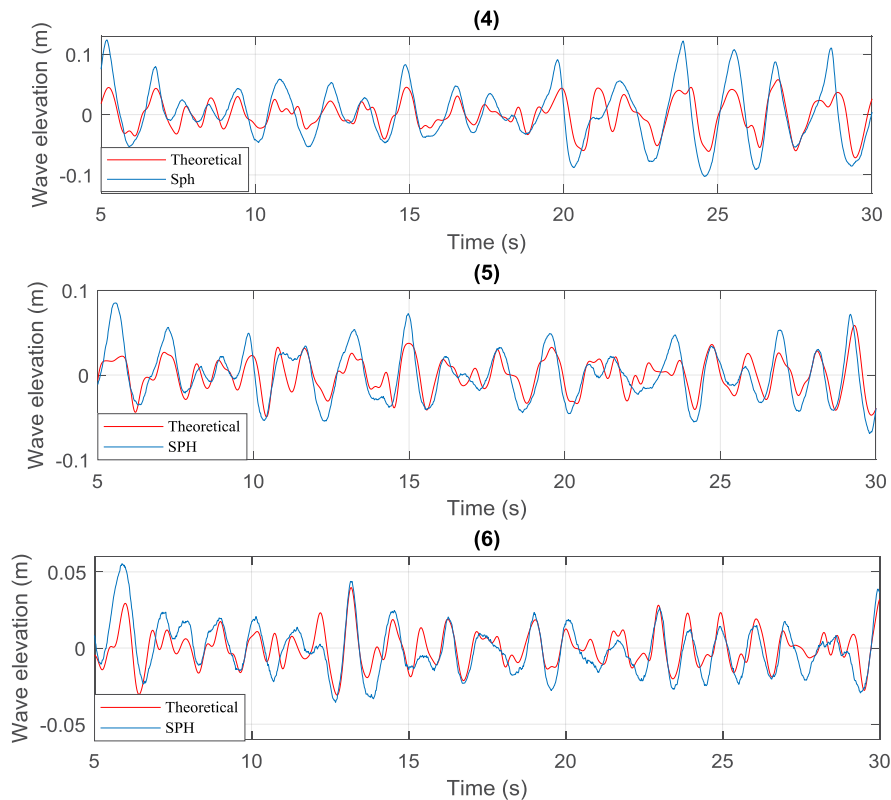


Figure 3: Comparison between theoretical and SPH numerical wave amplitudes for Pierson-Moskowitz wave spectrum test cases.

Fig.4 displays the wave energy spectrum of the SPH numerical results and expected theoretical energy density distribution for all test cases. In JONSWAP simulations, a reasonable agreement is achieved in terms of spectrum form, energy peak values, and the peak frequencies. As for the Pierson-Moskowitz wave spectrum simulations, the energy levels at higher frequency bands are consistent with the expected theoretical results however there occurs a wide peak-frequency zone in SPH results with high noise levels in energy results. The main source of the difference in energy levels of Pierson-Moskowitz simulations can arise due to the necessity of longer simulation times to mimic the fully developed and unlimited fetch sea conditions nature of the spectrum.

4 CONCLUDING REMARKS AND FUTURE WORK

This study aims to model a wave tank that can generate irregular waves which is highly required in research and development stages of many engineering fields such as shipbuilding, marine sciences, and coastal engineering. To provide a unique contribution to the solution of the engineering problems mentioned in this scope, the particle-based SPH algorithm is proposed together with the numerical correction treatments. The results obtained from the simulations compared with the theoretically calculated wave characteristics and energy densities. In the shed of the simulation results, it can be stated that quite promising agreement is achieved with the theoretical results in terms of wave characteristics and wave energy densities while long-

term simulations for the Pierson-Moskowitz wave spectrum is still required to represent the whole characteristics of the wave train. As a concluding remark one can argue that the presented SPH-based numerical solution scheme can be assumed as a practical tool to investigate the problems regarding irregular wave generation systems.

In the next steps of this study, a piston-type wave generator will be adopted into the computational domain for generating the regular and irregular wave spectrums. As benchmark studies, JONSWAP and Pierson-Moskowitz wave spectrums will be simulated to validate the obtained wave characteristics with the theoretical results. Finally, a more challenging problem, namely, the dynamic behaviors of floating bodies under the effect of generated random waves will be investigated.

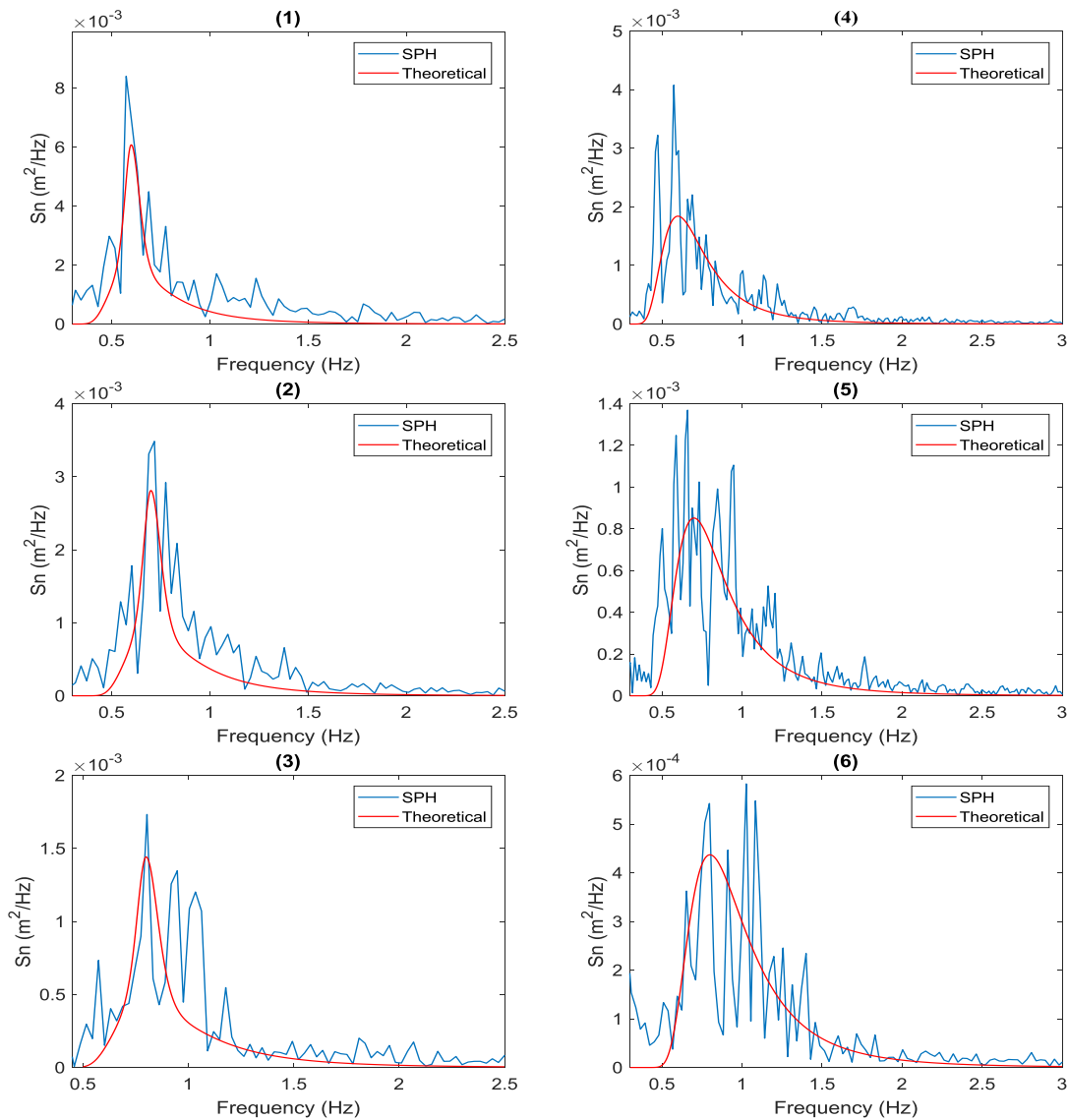


Figure 4: Comparison of theoretical and numerical spectral density for irregular waves.

5 ACKNOWLEDGEMENT

The authors gratefully acknowledge financial support provided by the Scientific and Technological Research Council of Turkey (TUBITAK) for project number 117M091.

REFERENCES

- [1] Pierson, W. and M. St Denis, *On the motion of ships in confused seas*. Transactions SNAME, 1953. **61**: p. 280-354.
- [2] Stansberg, C., et al., *The specialist committee on waves final report and recommendations to the 23rd ITTC*. Proceedings of the 23rd ITTC, 2002. **2**: p. 505-551.
- [3] Hasselmann, K., et al., *Measurements of wind-wave growth and swell decay during the Joint North Sea Wave Project (JONSWAP)*. Ergänzungsheft 8-12, 1973.
- [4] Pierson Jr., W.J. and L. Moskowitz, *A proposed spectral form for fully developed wind seas based on the similarity theory of S. A. Kitaigorodskii*. Journal of Geophysical Research (1896-1977), 1964. **69**(24): p. 5181-5190.
- [5] Boccotti, P., et al., *Field experiment on random wave forces acting on vertical cylinders*. Probabilistic Engineering Mechanics, 2012. **28**: p. 39-51.
- [6] Boo, S., *Measurements of higher harmonic wave forces on a vertical truncated circular cylinder*. Ocean engineering, 2006. **33**(2): p. 219-233.
- [7] Kim, C. and Z. Wangv, *Horizontal force of vertical truncated column in Stokes 5th-order waves*. International Journal of Offshore and Polar Engineering, 1999. **9**(03).
- [8] Monaghan, J.J., *Simulating free surface flows with SPH*. Journal of computational physics, 1994. **110**(2): p. 399-406.
- [9] Barreiro, A., et al., *Smoothed particle hydrodynamics for coastal engineering problems*. Computers & Structures, 2013. **120**: p. 96-106.
- [10] Vanneste, D.F., et al., *Comparison of numerical models for wave overtopping and impact on a sea wall*. Coastal Engineering Proceedings, 2014. **1**(34): p. 5.
- [11] Shadloo, M.S., et al., *Numerical simulation of long wave runup for breaking and nonbreaking waves*. International Journal of Offshore and Polar Engineering, 2015. **25**(01): p. 1-7.
- [12] Liu, X., P. Lin, and S. Shao, *ISPH wave simulation by using an internal wave maker*. Coastal Engineering, 2015. **95**: p. 160-170.
- [13] Altomare, C., et al., *Applicability of smoothed particle hydrodynamics for estimation of sea wave impact on coastal structures*. Coastal Engineering, 2015. **96**: p. 1-12.
- [14] Monaghan, J. and A. Kos, *Solitary waves on a Cretan beach*. Journal of waterway, port, coastal, and ocean engineering, 1999. **125**(3): p. 145-155.
- [15] Liu, G.-R., *Meshfree methods: moving beyond the finite element method*. 2009: CRC press.
- [16] Müller, M., D. Charypar, and M. Gross. *Particle-based fluid simulation for interactive applications*. in *Proceedings of the 2003 ACM SIGGRAPH/Eurographics symposium on Computer animation*. 2003. Eurographics Association.
- [17] Liu, M. and G. Liu, *Smoothed particle hydrodynamics (SPH): an overview and recent developments*. Archives of computational methods in engineering, 2010. **17**(1): p. 25-76.

- [18] Monaghan, J.J., *Smoothed particle hydrodynamics*. Reports on progress in physics, 2005. **68**(8): p. 1703.
- [19] Antuono, M., A. Colagrossi, and S. Marrone, *Numerical diffusive terms in weakly-compressible SPH schemes*. Computer Physics Communications, 2012. **183**(12): p. 2570-2580.
- [20] Randles, P. and L. Libersky, *Smoothed particle hydrodynamics: some recent improvements and applications*. Computer methods in applied mechanics and engineering, 1996. **139**(1-4): p. 375-408.
- [21] Khayyer, A., H. Gotoh, and S. Shao, *Corrected incompressible SPH method for accurate water-surface tracking in breaking waves*. Coastal Engineering, 2008. **55**(3): p. 236-250.
- [22] Ozbulut, M., et al., *Investigation of wave characteristics in oscillatory motion of partially filled rectangular tanks*. Journal of Fluids Engineering, 2018. **140**(4): p. 041204.
- [23] Meringolo, D.D., F. Aristodemo, and P. Veltri, *SPH numerical modeling of wave-perforated breakwater interaction*. Coastal Engineering, 2015. **101**: p. 48-68.
- [24] Ozbulut, M., M. Yildiz, and O. Goren, *A numerical investigation into the correction algorithms for SPH method in modeling violent free surface flows*. International Journal of Mechanical Sciences, 2014. **79**: p. 56-65.
- [25] Liu, Z. and P. Frigaard, *Generation and analysis of random waves*. 1999.
- [26] Dean, R.G. and R.A. Dalrymple, *Water wave mechanics for engineers and scientists*. Vol. 2. 1991: World Scientific Publishing Company.

A FIRST ASSESSMENT OF THE INTERDEPENDENCY OF MESH MOTION AND FREE SURFACE MODELS IN OPENFOAM REGARDING WAVE-STRUCTURE INTERACTION

GRIET DECORTE, GEERT LOMBAERT AND JAAK MONBALIU

KU Leuven, Department of Civil Engineering
Kasteelpark Arenberg 40, B-3001 Leuven, Belgium
e-mail: griet.decorte@kuleuven.be, web page: <http://bwk.kuleuven.be/hydr>

Key words: OpenFOAM, wave-structure interaction, mesh motion, free surface models

Summary. Mesh motion is of key importance in assuring adequate CFD modelling of wave-structure interaction problems, such as wave impact on floating offshore wind turbines and seakeeping of ships. Wave forcing often leads to large displacements of floating structures. As a consequence, the fluid domain boundaries need to move in order to accommodate for these wave-induced displacements. The mesh quality needs to be preserved at all times to guarantee accurate and stable results for the rigid body displacements as well as for the fluid variables. Mesh deformation techniques, in particular algebraic mesh motion methods, have been widely used within the OpenFOAM framework during the last decade. Unfortunately, stability is easily jeopardized in case of large displacements. Large mesh deformation gives rise to computationally demanding and unstable results. Sliding meshes have been used to address this issue, but they are cumbersome for multi-degree of freedom motion. Therefore, overset methods have been implemented in recent versions of OpenFOAM. Especially, the newly implemented overset methods in the OpenFOAM branch `foam-extend`, have shown to give good results for an acceptable runtime.

Simultaneously, considerable progress has been made on the development of alternatives for algebraic volume-of-fluid methods for free surface modelling, which notoriously suffer from smearing effects. Although it seems reasonable to expect that the choice in free surface model combined with a certain mesh motion technique will have an influence on the overall result, the interdependency between mesh motion techniques and free surface modelling has not been studied yet. This paper aims at taking the first steps towards a better understanding of this mesh motion-free surface interdependency and, as such, facilitate an informed choice.

1 INTRODUCTION

Currently, the design of floating offshore structures strongly relies on the well-established experience from the oil and gas industry. In order to model the hydrodynamic behaviour of oil and gas rigs and related structures, the use of a potential flow approach combined with a

boundary element method is common practice in modelling flow and wave loads. Well-known examples of such hydrodynamics software packages are WAMIT and Ansys AQWA.

In the light of the world-wide energy crisis and the ocean's great renewable energy potential, the behaviour of innovative floating structures, such as floating offshore wind turbines and wave energy converters, needs to be thoroughly assessed. Due to their specific design, smaller submerged volumes and slender members, effects due to viscosity and higher-order wave loads need to be considered. Potential flow-based models are not able to include higher-order nonlinearities, generally not above second-order, and viscosity is only taken along empirically.

As computational power grows, Computational Fluid Dynamics (CFD) software, which solves the Navier-Stokes equations, presents a promising alternative for the previously mentioned potential flow-based packages. Because these codes account for both viscosity and higher-order nonlinear wave loads, they overcome the main shortcomings of the potential flow approach. One of the most promising of them is the open-source code OpenFOAM to which research groups worldwide contribute and of which different branches exist as shown in Figure 1 [1, 2]. In addition to the foam-extend branch, an extension package, **Naval Hydro Pack**, has been developed. **Naval Hydro Pack** is especially suited for simulating the viscous, two-phase, large-scale flows which naval structures frequently encounter, and the interactions involved [3].

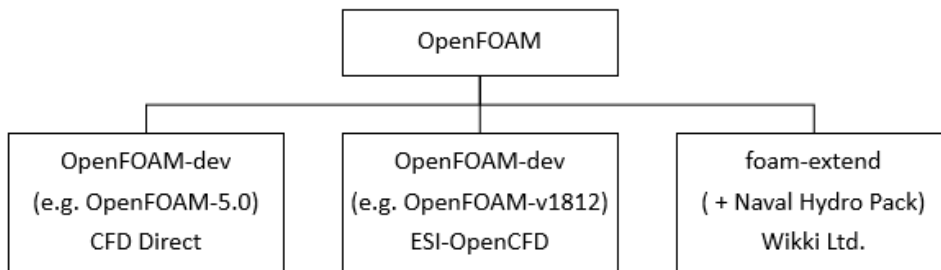


Figure 1: OpenFOAM branches.

In order for OpenFOAM to model wave-structure interaction, two strongly grid dependent challenges have to be overcome. On the one hand, the desired wave conditions can only be obtained if the free surface is accurately described. On the other hand, the resulting floater motion needs to be adequately accommodated for by the mesh guaranteeing a stable and reliable outcome. Recent research has made considerable progress on both aspects compared to the original two-phase fluid solver **interFOAM** [1, 4, 5].

Concerning the free surface modelling, two main categories of volume-of-fluid (VOF) methods are traditionally used. Within the original **interFOAM** solver, an algebraic VOF solver, **MULES**, is implemented. The algebraic VOF solver describes the fluid interface by computing the water fraction in each cell. The free surface is therefore smeared over several cells. The **MULES** solver tries to limit this smearing by adopting a (non-physical) compression term. Due to this smearing effect, an accurate solution for the algebraic VOF solver can only be found through small spatial and temporal resolutions, rendering computations costly [1, 6]. In a bid to overcome the computational limits posed by the algebraic VOF method and to arrive at a sharper surface, the geometric VOF method, **isoAdvector**, has been proposed [5]. Notwithstanding the improved

water surface modelling, this method appears not to honour its original promise in allowing accurate results at higher Courant numbers (Co) and, hence, in reducing computational cost. This is attributed to the coupling of `isoAdvector` with the pressure-velocity coupling step (PISO loop) in the `interFOAM` solver [7].

As wave forcing often leads to large displacements of floating structures, the fluid domain boundaries need to accommodate for these wave-induced displacements. Moreover, the mesh quality needs to be preserved at all times to guarantee accurate and stable results for the solid body displacements as well as the fluid variables. The fluid domain mesh thus needs to adapt to its deforming boundaries. Because these displacements of the fluid-structure interfaces are, especially in the case of six-degrees-of-freedom (6-DOF) rigid body motion, a priori unknown and as such the result of the solution itself, this mesh motion is ideally done automatically.

Although several of the currently available automatic mesh motion techniques have shown to do to a proper job for a variety of naval applications [8, 9], the interdependency between these mesh motion techniques and the free surface description adopted has not been formally identified. This paper wants to take the first steps towards a better understanding of this interdependency of mesh motion technique and free surface description, and their combined effects on the overall model result, to facilitate an informed choice.

The paper is structured as follows. First, an overview of the mesh motion techniques implemented in OpenFOAM is given. Next, the research method is explained and, subsequently, the results are presented and discussed. Finally, conclusions concerning performance and further work are drawn.

2 OVERVIEW OF THE MESH MOTION TECHNIQUES IN OPENFOAM

In the literature, an exhaustive body of knowledge concerning (automatic) mesh handling techniques already exists. Because this paper attempts to merely assess the performance of only two of these, the algebraic mesh motion and the overset method, we will only give a brief overview of the methods currently implemented within the OpenFOAM framework. In OpenFOAM, the mesh motion techniques can be roughly divided into four main categories; algebraic mesh motion techniques, topological changes, immersed boundary methods and overset methods. An overview is shown in Figure 2.

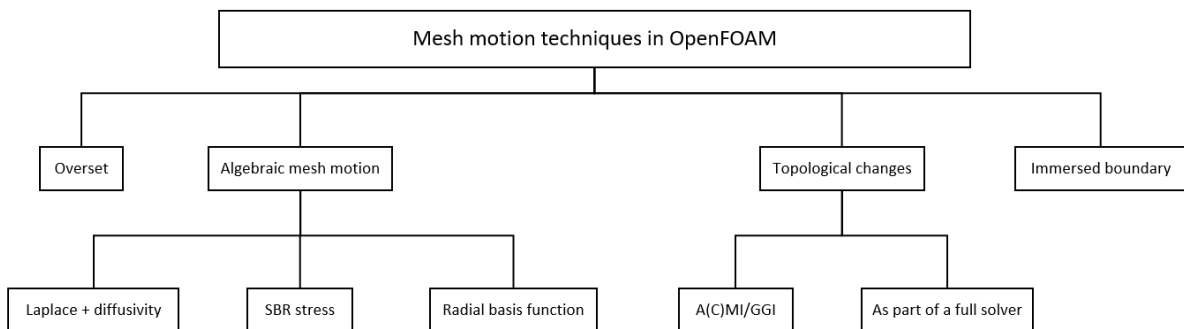


Figure 2: Overview of mesh motion techniques in OpenFOAM.

The algebraic mesh motion techniques adopt an Arbitrary Lagrangian-Eulerian (ALE) form of the conservation equations combined with a Space Conservation Law which prevents from creating an extra source term and thus from generating large errors [10, 11]. ALE necessitates that an automatic mesh displacement prescription algorithm be supplied to adapt the (fluid) grid velocities to the problem under consideration. Ideally, this is done through potential type equations or interpolations. Often, a Laplacian is solved with a certain diffusivity, allowing to distribute the mesh deformation over a certain distance from the moving boundary. Because of its high accuracy and its discretisation error being comparable to static meshes, this method is the preferred option for small displacements. Unfortunately, in case of large boundary deformation, the mesh deteriorates, giving rise to stability problems and loss of accuracy [12]. Two of the most promising ways to tackle this are the radial basis function technique (RBF) which allows for larger displacements but ultimately leads to distorted meshes as well [13], and topological changes.

Topological changes are used to change the mesh resolution and connectivity, using sliding interfaces, cell layering and similar techniques. They involve data mapping, which gives rise to distribution and conservation errors [12]. Ideally these operations are bundled. Examples of topological changes can be found in [9, 14]. Because applying topological changes for 6-DOF rigid body motion becomes quite tedious, the immersed boundary method and the overset methods might be a more viable candidates to accommodate the large displacements.

In the immersed boundary methods, a Dirac delta function is introduced as a body force in the conservation equations. This body force only differs from one at the fluid-structure interface. Because the immersed boundary method does not allow for mesh refinement close to the structure and, thus, does not allow for accurate boundary layer simulation, it is often not well-suited for the naval applications and will therefore be disregarded in the following [15]. However, it is worth to note that this method has been included in the `Naval Hydro Pack` [4].

Overset methods are by far the most versatile and computationally efficient techniques when confronted with large mesh motion. In this method, two meshes are created initially. A fixed mesh is used for the background, while the overset mesh which is allowed to move relatively to the background mesh, is connected to the moving object. Two fundamentally different implementations of overset are currently available within the OpenFOAM framework. One in the OpenFOAM-dev line, from version v1706 on, and another one in the foam-extend branch, starting from version 4.1. The main differences between both implementations are related to their position and role within the PIMPLE algorithm, which solves the momentum equations while accommodating for mass conservation in the pressure-velocity coupling step (PISO), and the amount of interpolations involved. Before reading on, the reader not familiar with the `interFoam` solver lay-out is referred to Figure 8 in Appendix A.

In `OpenFOAM-v1712`, at the beginning of each iteration, the motion of the structure is determined based on the pressure field computed on the overset mesh in the previous iteration. Subsequently, the overset mesh is moved accordingly and the hole cells, which are the background cells overlapped by the moving object which are excluded from the computations, the interpolated cells, which are the cells of the background overlapped by the overset mesh, and the calculated cells, which are the remaining background cells, are determined (see Figure 3a). Next, the water fraction and the velocity field are computed on both meshes and the velocity field is interpolated onto the border of the overset mesh. Finally, the velocity field is corrected

for both meshes in the PISO loop and the resulting pressure field is computed, before starting a new round of fluid-structure interaction computations in the next iteration [1]. Although this implementation has certainly merits, the interpolation is not well parallelized and therefore highly time-consuming. Inadequate interpolation may introduce large mapping errors into the computations necessitating high spatial resolution and therefore an even larger computational cost.

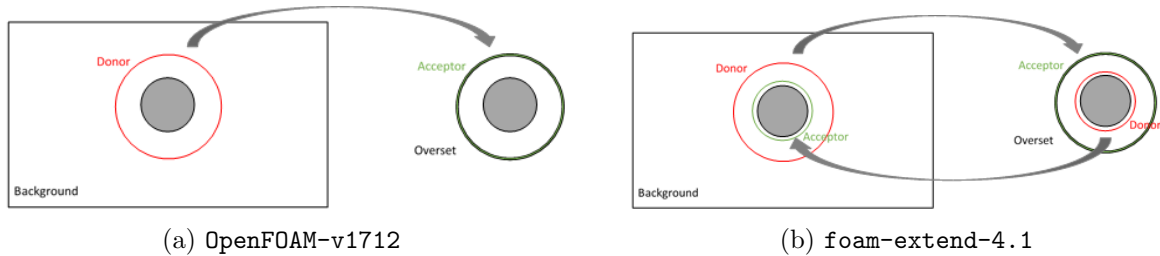


Figure 3: Donor-acceptor assembly for `OpenFOAM-v1712` and `foam-extend-4.1`.

Contrary to the `OpenFOAM-v1712` implementation, `foam-extend-4.1` adopts a two-way coupling between the background and the overset mesh as shown in Figure 3b. At the beginning of each PIMPLE iteration, the motion of the structure is updated based on the pressure field computed during the previous iteration. Next, the fringe layers, i.e. donor-acceptor pairs, are created, either manually or through adaptive overlap, and the hole cells are determined. Subsequently, the water fraction is calculated and interpolated in the fringe layers, and a velocity estimate is computed. In the PISO loop, the interpolated velocity field is then used as “boundary condition” to correct the velocity fields and compute the pressure field on both meshes. The velocity field as well as the pressure field is interpolated and the next iteration starts [8]. This two-way coupling presents the main difference between the `OpenFOAM-v1712` and the `foam-extend-4.1` implementation. In addition, the overset method in `foam-extend-4.1` is well parallelized, which means substantial computational time can be saved.

3 METHODOLOGY

Because the choice of a mesh motion technique for a specific application depends to some extent on the chosen free surface model, the consequences of such combinations need to be known. Therefore, in the following, the two most commonly used mesh motion techniques, algebraic mesh motion and overset, will be both combined with the traditional algebraic VOF method, `MULES`, and the innovative geometric VOF method, `isoAdvect`. For each combination, visual assessment will be done through comparison with a reference case, the freely heaving cylinder case documented by Ito (1977). In these experimental tests, a rigid horizontal cylinder with a diameter of 0.1524m (0.5 ft.) is released from an initial height of 0.0254m (1 in.) above a calm water surface and left to freely decay its heave motion. The depth of the wave flume is 1.22m (4 ft.) and its original length is 27m (90 ft.) [16].

As algebraic mesh motion eliminates the influence of any inadequate coupling between meshes, it is used to assess grid convergence and is therefore treated first. A set-up with `MULES` and

`isoAdvector` is run for three mesh sizes each chosen relative to the cylinder diameter D , notably $D/10$, $D/20$ and $D/40$. As the `interDyMFoam` solver, an `interFoam` solver allowing for dynamic mesh motion, is quite similar in `OpenFOAM-v1712` and `foam-extend-4.1/Naval Hydro Pack` and `isoAdvector` has already been added to the `interDyMFoam` solver in `Naval Hydro Pack`, `navalFoam`, a loosely coupled 6-DOF rigid body motion solver in `navalFoam` is adopted. Even though `OpenFOAM-v1712` and `foam-extend-4.1` both offer a lot of freedom through the availability of different solvers for solving the motion equations of the floater, only the extension package for `foam-extend-4.1` offers anything besides loosely coupled fluid-structure interaction, for instance Aitken relaxation and multiple loops enabling strongly coupled fluid-structure computations [4]. In the following, only Aitken relaxation is used. As both free surface modelling approaches have shown to give best results for Co smaller than 0.1, an adaptive time step based on a maximum Co of 0.1 is used [6, 7].

Next, the reference case presented above is computed for the overset approach. Due to the significantly different implementation of the overset methods in `OpenFOAM-v1712` and `foam-extend-4.1/Naval Hydro Pack`, the interdependency between the two free surface models and the overset approach are studied for both branches. As the 6-DOF rigid body motion is currently not implemented in the overset solver of the publicly released `foam-extend-4.1`, the `navalOversetFoam` solver in `Naval Hydro Pack` is used for the `foam-extend-4.1` case and compared to its counterpart, `overInterDyMFoam`, in `OpenFOAM-v1712`. Both cases are run with `inverseDistance` interpolation for the donor-acceptor pairs. For `navalOversetFoam`, implicit overset is used to guarantee strong coupling between the meshes and prevent using many corrector loops to reach a sufficiently strong coupling as would be the case if explicit overset mesh had been chosen. For a thorough overview of the overset mesh coupling and interpolations strategies in `foam-extend-4.1/Naval Hydro Pack`, the reader is referred to the existing literature [4, 8]. In choosing time and spatial resolution, a trade-off needs to be made between accuracy and computational cost. This is done based on the algebraic mesh motion cases.

Although in the `Naval Hydro Pack` `isoAdvector` has been added to the `navalFoam` solver, which allows algebraic mesh motion to be applied in combination with `isoAdvector`, none of this has been done yet in `OpenFOAM-v1712`, nor for the `navalOversetFoam` solver in `Naval Hydro Pack`. Therefore, we have extended the overset solvers in `OpenFOAM-v1712` and `Naval Hydro Pack` to allow for `isoAdvector` free surface modelling. However, it has to be noted that this coupling was only done as a first assessment. As will be shown in the next section, in most cases, enhancements should be made in order to arrive at a robust solver.

4 RESULTS AND DISCUSSION

To provide a first assessment of the interdependency between the two most commonly used mesh motion techniques, algebraic mesh motion and overset, and the free surface model, each mesh motion technique has been run with both the MULES approach and the `isoAdvector` method. In the following, first, the interdependency between the algebraic mesh motion and the free surface model, is discussed. Next, the same is done for the overset approach.

4.1 Algebraic mesh motion

As shown in Figure 4a, the **MULES** approach models the free decay well. The solution converges and, even for coarse meshes, the results collide well with the reference solution by Ito(1977). However, when **isoAdvect** is used to model the free surface, only the first time steps are modelled well. As can be seen in Figure 4b, the floating cylinder performs an oscillation with a frequency close to its eigenfrequency, but it does not execute a regular decay.

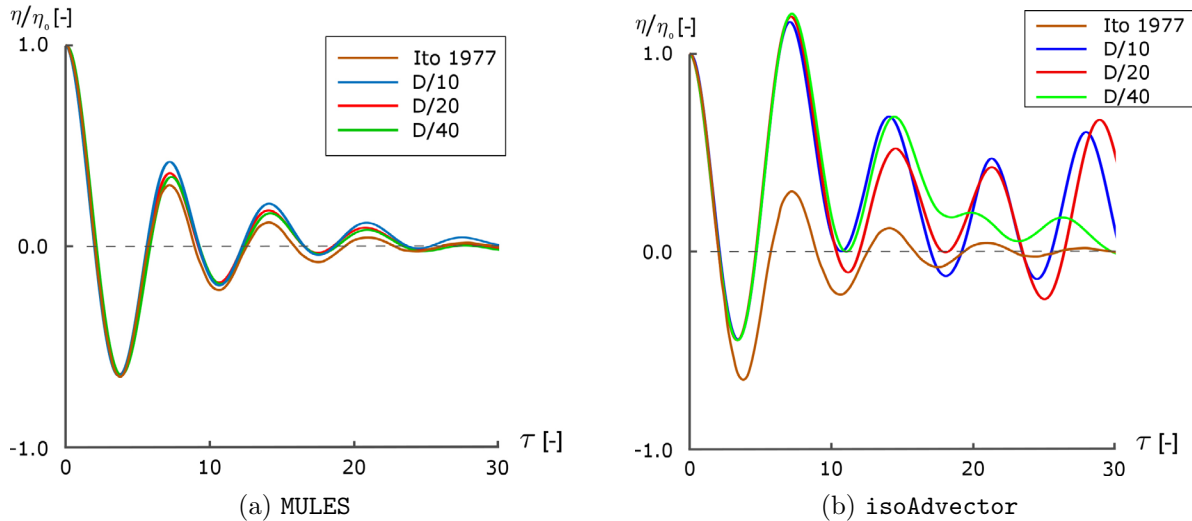


Figure 4: Non-dimensional free decay heave motion η/η_0 , with η the absolute heave and η_0 the initial displacement from rest, vs. non-dimensional time $\tau = t\sqrt{g/(D/2)}$, with g the gravitational acceleration, for algebraic mesh motion combined with (a) **MULES** and (b) **isoAdvect** free surface modelling for three grid resolutions.

When analysing the water phase of the **isoAdvect** solution in Figure 5, it becomes clear that the free surface modelling may be at the origin of the unsatisfactory free decay simulation. Small volumes of low water fraction appear (Figure 5a), which subsequently lead to non-physical air bubbles in the water volume. Due to their lower density, these bubbles rise to disturb the free surface and as such the free decay motion (Figure 5b). The reason for this most probably lies in the way **isoAdvect** is currently implemented within the **navalFoam** solver.

Starting from the first time step, the mesh is deformed and subsequently the mass flux and the velocity fields are updated. However, although the volume and the shape of the cells have changed, the water fraction scalar field remains the one calculated in the previous **PIMPLE** iteration. In calculating the water fraction field in the **isoAdvect**, first, the change in volume over each cell-to-cell face is determined. To do so, the updated fluxes are multiplied by the water fraction field from the previous iteration. As the cell volumes have now changed due to the mesh deformation, the resulting change in volume over each cell-to-cell face is incorrect. For each fully immersed cell, the new water fraction is subsequently determined by subtracting from the water fraction, from the previous iteration, the total change in volume integrated over its

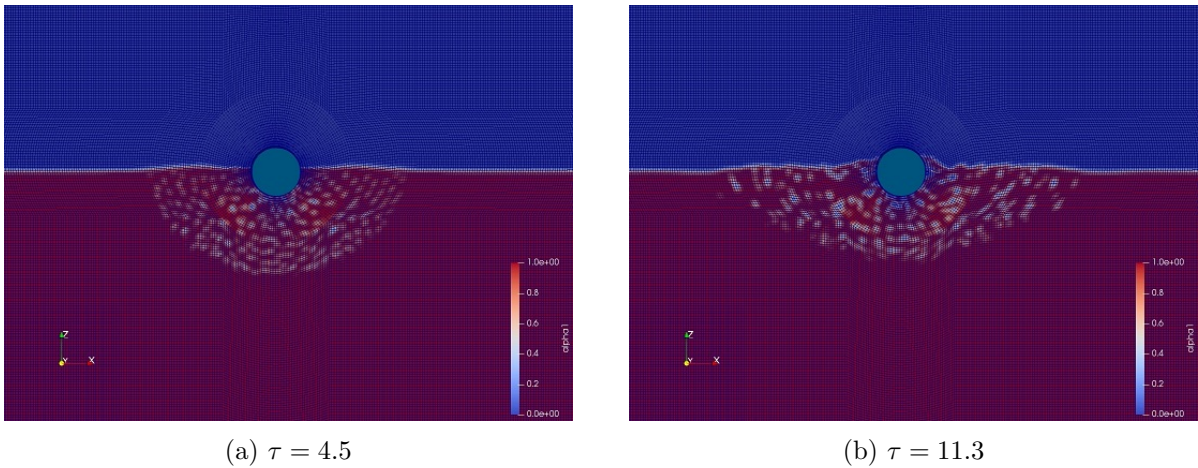


Figure 5: Water fractions for the algebraic mesh motion with `isoAdvector` at non-dimensionalized times $\tau = 4.5$ (left) and $\tau = 11.3$ (right).

faces and divided by the new volume of that cell. This introduces an additional error into the resulting water fraction. When progressing further in time, this error will accumulate and, at some point, the erroneously computed water fractions of the fully immersed cells will reach the threshold for `isoAdvector` to consider them as partly filled with air. This leads then to the formation of non-physical air bubbles, which is clearly seen in Figure 5. For full details on the `isoAdvector` algorithm, the reader is kindly referred to the literature [5].

It has to be noted that `MULES` suffers slightly from this issue as well. In the water volume where the mesh deforms, smaller water fractions could also be observed. However, this was easily resolved by increasing the iterations over the `MULES` computation. The same reasoning was used in trying to eliminate the air bubbles for the `isoAdvector` algorithm. Although, their severity diminished, it did not seem possible to fully resolve the air bubbles by increasing the number of iterations, i.e. the correctors, in the `PIMPLE` loop.

4.2 Overset mesh motion

Based on the results for the algebraic mesh motion in Figure 4, a trade-off was made between accuracy and computational cost to determine time and spatial resolutions for the overset models. A grid resolution of $D/20$ and an adaptive time step according to a Co of 0.2 was chosen. In the following, first, the overset method in `OpenFOAM-v1712` is discussed and, next, its version in `foam-extend`.

As can be noticed in Figure 7, `MULES` aligns reasonably well with the experimental result. On the contrary, the `isoAdvector` solution decays, but at a frequency smaller than its eigenfrequency. In addition, when released from rest, the cylinder starts its decay, but does not reach the expected depth. This can most probably be attributed to one of the main shortcomings of the current overset implementation in `OpenFOAM-v1712` and seems as such not to be related to the overset mesh coupling.

`OpenFOAM-v1712` computes its water fraction (and pressure) for the hole cells, i.e. the cells

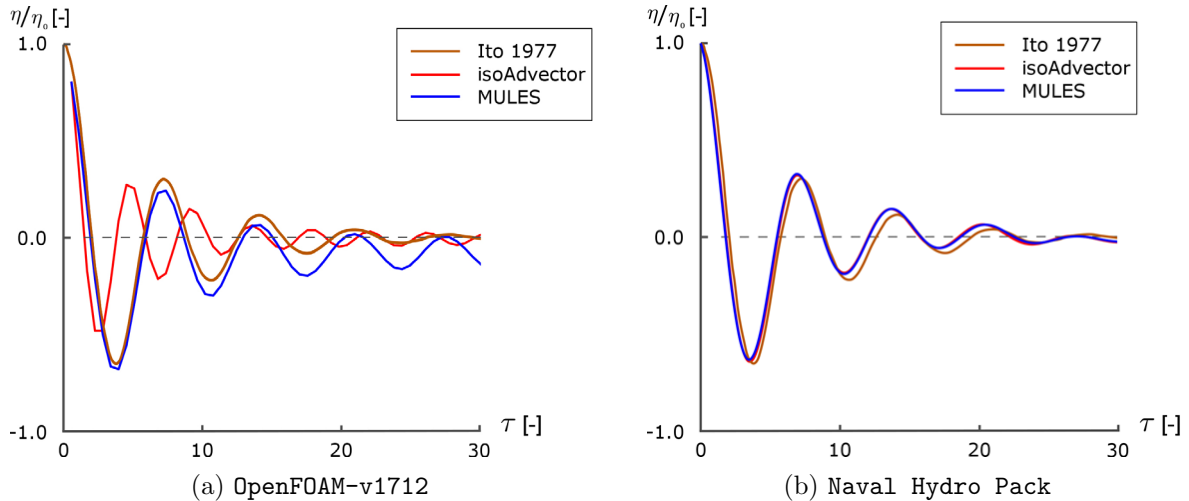


Figure 6: Non-dimensional free decay heave motion η/η_0 , with η the absolute heave and η_0 the initial displacement from rest, vs. non-dimensional time $\tau = t\sqrt{g/(D/2)}$, with g the gravitational acceleration, for the overset method combined with MULES and isoAdvector for (a) OpenFOAM-v1712 and (b) Naval Hydro Pack (foam-extend-4.1).

covered by the cylinder on the background grid, and assumes as such that there is water where there is in fact not. Due to the diffusive nature of MULES, no real air phase is formed in the hole as shown in Figure 7a, which lead to moderate negative pressures on the inside of the cylinder and can explain the relatively small error at first. However, in the case where isoAdvector is used in Figure 7b, a separate air phase and water phase arise inside the cylinder. This reduces the buoyancy and as such the eigenfrequency in heave. Additionally, as the air phase is enclosed under the water, suction seems to arise as the cylinder moves down. This results in a higher upward force on the cylinder, which might be the reason for the reduced depth.

On the opposite, as can be noticed in 6b, the `navalOverFoam` solver seems to perform equally well for both the MULES and the isoAdvector approach. When setting up a case in `foam-extend-4.1/Naval Hydro Pack`, the initial field values for the hole are set to zero and the hole cells are fully excluded from further computations. This effectively prevents the separate water volume from arising in the cylinder.

5 CONCLUSIONS

The aim of this paper was to take the first steps towards a better understanding of the interdependency of mesh motion methods and free surface models and, as such, facilitate an informed choice. Therefore, the two most commonly used mesh motion techniques, algebraic mesh motion and overset, were both combined with the traditional algebraic VOF method, MULES, and the innovative geometric VOF method, isoAdvector. For each combination, a visual assessment was done through comparison with a freely heaving cylinder reference case.

Concerning algebraic mesh motion, the solution for MULES converged towards the reference solution, while, in case of isoAdvector, the cylinder heaves in an unorganized way. The air bubbles

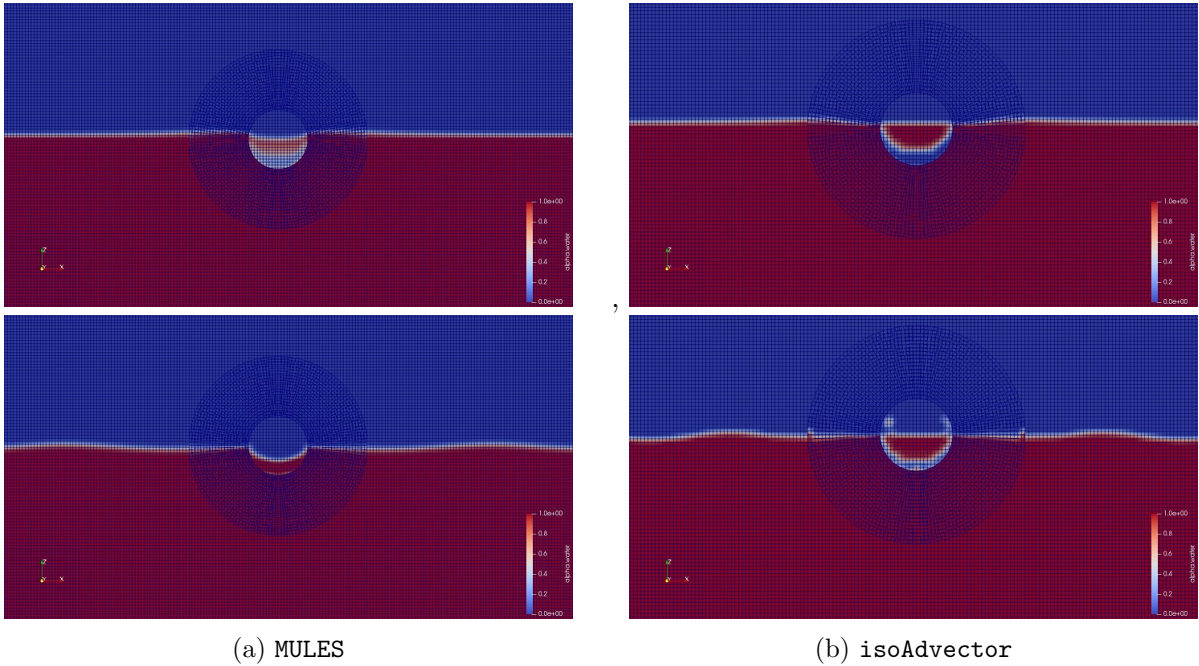


Figure 7: Water fractions for the overset method in OpenFOAM-v1712 at $\tau = 3$ (up) and $\tau = 14$ (down). Left: MULES. Right: isoAdvector.

arising in the water volume and eventually disturbing the free surface are the most probable culprits. They arise due to the fact that `isoAdvector` uses the water fraction from the previous iteration, i.e. before the mesh was deformed. In order to overcome this issue, two ways forward seem practical. On the one hand, the water fraction could be corrected after mesh deformation. On the other hand, a conditional statement could be used to prevent these air bubbles from arising in the water volume.

Furthermore, the overset method in `foam-extend-4.1/Naval Hydro Pack` appeared to perform well for both the MULES and `isoAdvector` simulation. On the contrary, no similar observations could be made for the OpenFOAM-v1712 implementation. Although the overset in OpenFOAM-v1712 seemed to perform reasonably well for the MULES case, this appears not to be so for the `isoAdvector` simulation. This may have been caused by the lingering issue of the hole cells being included in most of the OpenFOAM-v1712 overset solver's fluid computations. Future releases of OpenFOAM need to tackle this issue in order to allow for robust overset mesh simulations.

Overall, all mesh motion solvers perform well with MULES. In addition, the overset methods show the most potential when combined with `isoAdvector`, while significant adaptations are needed to the algebraic mesh motion solvers in order for them to be combined with the `isoAdvector` free surface modelling.

ACKNOWLEDGEMENTS

The first author is Ph.D. fellow of the Research Foundation Flanders (FWO), Belgium (Ph.D. fellowship 11A1217N). Furthermore, the authors gratefully acknowledge the collaboration with the research group of prof. Hrvoje Jasak at UniZagreb and the chance to use their extension package for `foam-extend-4.1`, `Naval Hydro Pack`, in their research.

A General overview of the `interDyMFoam` and `overInterDyMFoam` solvers in OpenFOAM.

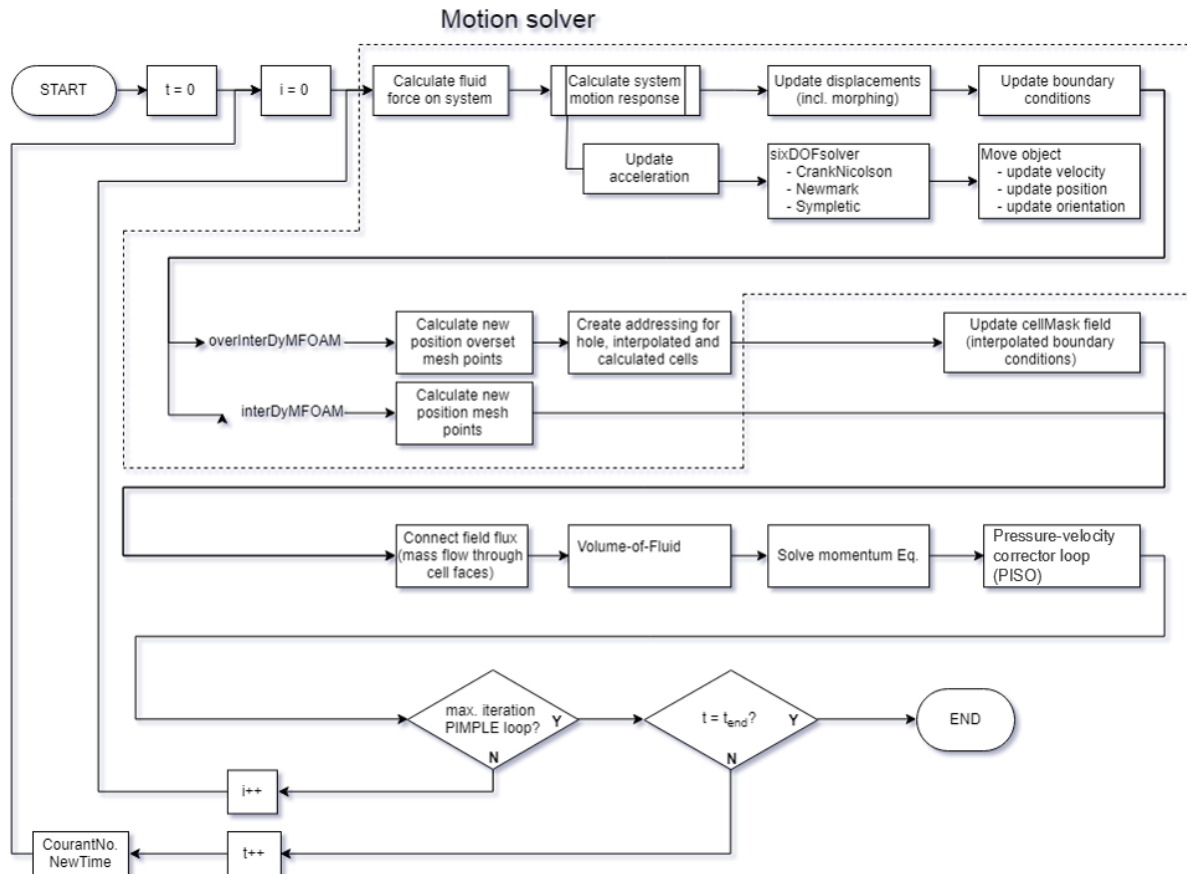


Figure 8: The program structure of the two-phase fluid-structure motion solvers, `interDyMFoam` (includes algebraic mesh motion and topological changes) and `overInterDyMFoam` (includes overset mesh motion).

REFERENCES

- [1] OpenCFD. *OpenFOAM user guide*. (2008) <http://www.openfoam.org>.

- [2] Weller, H., Tabor, G., Jasak, H. and Fureby, C. A tensorial approach to computational continuum mechanics using object-oriented techniques. *Computers in Physics*. (1998) **12**:620-631.
- [3] Jasak, H. OpenFOAM: open source CFD in research and industry. *International Journal of Naval Architecture and Ocean Engineering*. (2009) **1**(2):89-94.
- [4] Vukčević, V., Gatin, I. and Jasak, H. The Naval Hydro Pack: current status and challenges. *In: 13th OpenFOAM Workshop*. (2018)
- [5] Røenby, J., Bredmose, H. and Jasak, H. A computational method for sharp interface advection. *Open Science*. (2016) **3**(11).
- [6] Larsen, B.E., Fuhrman, D.R., and Røenby, J. Performance of interFoam on the simulation of progressive waves. Preprint, ArXiv:1804.01158. (2018).
- [7] Røenby, J., Larsen, B.E., Bredmose, H. and Jasak, H. A new Volume-Of-Fluid Method in OpenFOAM. *In: MARINE 2017 Computational Methods in Marine Engineering VII*. (2017) pp. 266-278.
- [8] Vukčević, V. and Jasak, H. Overset Mesh Library in Foam-Extend [Powerpoint slides]. (2018) Retrieved from <https://foam-extend.fsb.hr/wp-content/uploads/2018/07/OversetTrainingSlides.pdf>.
- [9] Devolder, B. and Stratigaki, V. and Troch, P. and Rauwoens, P. CFD Simulations of Floating Point Absorber Wave Energy Converter Arrays Subjected to Regular Waves. *Energies*. (2018) **11**(3):641.
- [10] Demirdžić, I. and Perić, M. Space conservation law in finite volume calculations of fluid flow. *International Journal of Numerical Methods in Fluids*. (1988) **8**(9):1037-1050.
- [11] Demirdžić, I. and Perić, M. Finite volume method for prediction of fluid flow in arbitrarily shaped domains with moving boundaries. *International Journal of Numerical Methods in Fluids*. (1990) **10**(7):771-790.
- [12] Jasak, H. Dynamic mesh handling in openfoam. *In: 47th AIAA Aerospace Sciences*. (2009) pp. 341-350.
- [13] Bos, F.M. *Numerical simulations of flapping foil and wing aerodynamics*. PhD Thesis, TU Delft (2009).
- [14] Liu, Y., Xiao, Q., Incecik, A., Peyrard, C. and Wan, D. Establishing a fully coupled CFD analysis tool for floating offshore wind turbines. *Renewable Energy*. (2017) **112**: 280-301.
- [15] Dooms, D. *Fluid-structure interaction applied to flexible silo constructions*. PhD Thesis, KU Leuven (2009).
- [16] Ito, S. *Study of the transient heave oscillation of a floating cylinder*. MSc Thesis, Massachusetts Institute of Technology (1977).

NUMERICAL AND EXPERIMENTAL INVESTIGATION OF FLOATING STRUCTURES IN REGULAR WAVES

Leon-Carlos Dempwolff*, Tobias Martin[†], Arun Kamath[†] AND Hans Bihs[†]

*Ludwig-Franzius-Institute for Hydraulic, Estuarine and Coastal Engineering
Leibniz Universität Hannover
Nienburger Str. 4, 30167 Hannover, Germany
e-mail: c.dempwolff.cd@gmail.com

[†] Department of Civil and Environmental Engineering
Norwegian University of Science and Technology
Høgskoleringen 7a, 7491 Trondheim, Norway
e-mail: tobias.martin@ntnu.no

Key words: Computational fluid dynamics, Fluid structure interaction, Floating, Mooring

Abstract. In this paper, an experimental and numerical study of a floating object is presented. The incorporation of both experimental and numerical tools for the investigation of a simple floating object provides the opportunity to validate the proposed numerical model in detail. The experiments are performed in the wave flume of the Leibniz Universität Hannover, Germany. The flume is capable of generating high-fidelity waves with a wide range of parameters. The study consists of a free-floating box which is placed in the middle of the flume. A soft mooring line system is attached to the box in order to prevent motion perpendicular to the incoming wave direction. Heave and pitch motion are measured for different wave heights and periods. Additionally, measurements under consideration of mooring are presented. For this purpose, different rope mooring systems are attached to the box, and the motion of the moored-floating body in different wave conditions is analysed. In a second step, numerical simulations of the same setup are presented. The applied numerical tool is the open-source CFD model REEF3D.

1 INTRODUCTION

For applications in the field of marine engineering coupled fluid structure interaction is of major importance. To account for this, several attempts are proposed on basis of the Navier-Stokes-equations. First attempts proposed by Ramaswamy et al. (1986) made it necessary to constantly adapt the grid to fit it to the floating body, with possible drawbacks to stability and accuracy. To avoid constant remeshing, dynamic overset-meshes were developed (Borazjani et al. (2013)). For referencing the points of the body's overset mesh in relation to the Eulerian grid, a stable scheme as given in Carrica et al. (2007) has to be introduced.

Another approach is a direct forcing immersed boundary method presented in Yang and Stern (2012). Here, the interaction is included as an additional term in the NS-equations, instead of

introducing a second grid. An important aspect is the field extension method avoiding unphysical values by describing the change from solid in fluid cells and vice versa (Yang and Balaras (2006)).

In Calderer et al. (2014) an extension of the local directional immersed boundary method is applied in use of the field extension method. No additional terms are added but the closest distance to body is added to the interpolation stencils. This was further simplified by Berthelsen and Faltinsen (2008) for fixed bodies using the distances in the principal directions. This makes the interpolations straightforward evaluations of Lagrangian polynomials. A ghost cell-immersed boundary method for floating bodies by Bihs et al. (2016) derived from this is the main model used here. Its successful application can be seen in Martin et al. (2018a), Martin et al. (2018b) and Martin et al. (2019).

To show the accuracy of the capabilities of this algorithm benchmark cases from experimental results are needed. A typical application for floating bodies are floating wave-breakers, that are used to protect coastal structures against ocean-coming waves in a more cost-efficient way than fixed bottom structures. In the past years they have been studied extensively, using both numerical and experimental methods. A focus was put on the design of the floating bodies and not on the use of the mooring line parameters. Experiments showed how pneumatic chambers can alter the behaviour of the floating structures and reduce waves on the leeward side He et al. (2012). Several different set-ups of floating bodies, including mesh elements, porous parts and cylindrical shapes were experimentally tested in Ji et al. (2016) and showed a difference performance in wave-reduction, motion responses and mooring forces. A comparison of numerical and experimental results for two different breakwater shapes is given in Ji et al. (2017), showing an overall good match of the data. In Christensen et al. (2018) the influence of horizontal plates under wave-breakers are examined, both with experimental and numerical methods, showing a reduction of the motion depending on the wave-frequency and the Eigen-frequency. Sannasiraj et al. (1998) examined the influence of different attachment-points in a series of experiments, showing dominance of mooring-forces in lower frequencies.

The complexity of the floating bodies studied in the work make the implementation in the numerical tool unnecessarily complex. In addition not all the parameters influencing the movement in the experimental test are known (e.g the mooring lines), so that the set-up cannot directly be transferred to the numerical model. Therefore a set of benchmark-data is generated to precisely validate the numerical tool presented in subsection 2.2.

Especially in large movements the mooring lines have a significant impact on the behaviour of a floating body. Various ways of implementing this in a numerical tool is shown in Davidson and Ringwood (2017). To account for different configurations of mooring lines, they have been included in the benchmark data generation, and the general influence of elasticity is discussed. In further research this will be used to validate the mooring models of REEF3D.

The experimental set up is given in subsection 2.1, before the solver is briefly explained in subsection 2.2 and the set up of the numerical reproduction is introduced in section 3. The influence on different parameters on the experimental results is discussed in subsection 4.1 followed by the comparison between the numerical and experimental results. Finally concluding remarks are given in section 6 and prospects for further research are shown.

2 Methods

2.1 Experimental methods

The tests were performed at the wave flume of the Ludwig-Franzius-Institute in Hanover. The flume has a width of 2.2m and the waterdepth was chosen to 0.85m. It is equipped with a piston-type wave maker. A wooden box of the dimensions $0.6m \cdot 0.3m \cdot 0.15m$ with a weight of 18.35 kg, was placed in the flume and moored with a soft-mooring system and a traditional one.

The soft-mooring system consisted of a set of soft springs in horizontal plane, keeping the barge in place at 39.5 m behind the wavemaker, but allowing for unhindered movement in heave and pitch direction. These test were performed within the framework of Meyer (2018).

The traditional mooring system was composed of two ropes on each side perpendicular to the wave direction, connected to the flume's floor via a set of springs, keeping the barge in place 15m behind the wavemaker.

To measure the movement of the barge an 'Opti-Track' motion tracking system of four infrared cameras was used, referencing active markers attached on the box. The waves were measured between the wavemaker and the gauge and at the position of the barge using ultrasonic wave gauges. On the traditional mooring-system force sensors on the floor of the flume were used, to measure the forces exceeded on the mooring-lines. All instruments were connected to HBM-Quantum Amplifiers, and triggered to ensure synchronization of the data.

Decay-Tests for both heave and Pitch motions are performed for all the configurations, and the free floating body without any mooring-system. Afterwards each configuration is tested under waves ranging from 2cm to 4cm in height and 0.8s and 2.4s in period.

2.2 Numerical Model

2.2.1 Fluid solver

Reef3D (Bihs et al. (2016)) is a numerical solver based on the finite differences approach. The governing equations are the RANS-equations:

$$\frac{\partial u_i}{\partial x_i} = 0 \quad (1)$$

$$\frac{\partial u_i}{\partial t} + u_j \frac{\partial u_i}{\partial x_j} = -\frac{1}{\rho} \frac{\partial p}{\partial x_i} + \frac{\partial}{\partial x_j} \left[\nu \left(\frac{\partial u_i}{\partial x_j} + \frac{\partial u_j}{\partial x_i} \right) \right] + g_i \quad (2)$$

Where u are the velocity components in the coordinate directions, ρ is the fluid density, p is the pressure, ν is the kinematic viscosity and g_i is the gravity acceleration vector.

For spatial discretization the fifth order WENO-scheme according to Jiang and Shu (1996) is used. A staggered grid is used to enhance stability.

For the discretization in time, the third order TVD Runge-Kutta scheme (Shu and Osher (1988)) is employed. To control the CFL number, adaptive time-stepping is applied, taking into account the influences from diffusion, velocity and a source term, such as gravity.

The free surface is represented, by a signed-distance function, giving the closest distance to the free surface Osher and Sethian (1988). The two phases are distinguished by the change of sign, resulting in:

$$\phi(\vec{x}, t) \begin{cases} > 0 & \text{if } \vec{x} \in \text{phase1} \\ = 0 & \text{if } \vec{x} \in \Gamma \\ < 0 & \text{if } \vec{x} \in \text{phase2} \end{cases} \quad (3)$$

The pressure term is solved iteratively making use of Chorin's projection method Chorin (1968).

2.2.2 6 DOF- algorithm

Details on the implementation are given in Bihs and Kamath (2017). The body gets defined using a surface mesh that can be defined in STL-format by most CAD-tools. To calculate the interface between it and the cartesian grid a Ray-Tracing algorithm is applied, providing inside-outside information and the shortest distance to a triangle from a given coordinate Yang and Stern (2013). The forces in each coordinate- direction on the floating body are defined with the help of the pressure p and the viscous stress tensor τ :

$$F_{i,e} = \int_{\omega} (-n_i p + n_i * \tau) d\omega \quad (4)$$

To describe any point relating to the floating body the position vector:

$$x = (x_1, x_2, x_3, x_4, x_5, x_6)^T \quad (5)$$

is introduced, defining the body's center of gravity and the orientation of the inertial coordinate system in Euler angles ϕ , θ and ψ . By applying coordinate transformation, including several time derivatives of moments can be avoided. This leads to the following vector for the rotation components of the body's principal coordinate system:

$$\xi = (\xi_1, \xi_2, \xi_3)^T \quad (6)$$

The inertia tensor is reduced to

$$I = \begin{bmatrix} I_x & 0 & 0 \\ 0 & I_y & 0 \\ 0 & 0 & I_z \end{bmatrix} = \begin{bmatrix} mr_x^2 & 0 & 0 \\ 0 & mr_y^2 & 0 \\ 0 & 0 & mr_z^2 \end{bmatrix}, \quad (7)$$

assuming that the body's principal axes are known. m is the mass of the body and r_i are distances to the center of gravity.

That leads to the description of the rigid body using three equations for the translational movement in the inertial system:

$$\begin{pmatrix} \ddot{x}_1 \\ \ddot{x}_2 \\ \ddot{x}_3 \end{pmatrix} = \frac{1}{m} * \begin{pmatrix} F_{x_1,x} \\ F_{x_2,x} \\ F_{x_3,x} \end{pmatrix} \quad (8)$$

For the rotational movements the three Euler-equations in the non inertial system are used:

$$\begin{aligned}
 I_x \ddot{\xi}_1 + \dot{\xi}_2 \dot{\xi}_3 * (I_z - I_y) &= M_{1,\xi} \\
 I_y \ddot{\xi}_2 + \dot{\xi}_1 \dot{\xi}_3 * (I_x - I_z) &= M_{2,\xi} \\
 I_z \ddot{\xi}_3 + \dot{\xi}_1 \dot{\xi}_2 * (I_y - I_x) &= M_{3,\xi}
 \end{aligned} \tag{9}$$

The position of the body is calculated analytically, integrating Equation 9 twice, while its orientation is calculated numerically Fossen (1994). (9) is solved explicitly in use of the second-order accurate Adam-Bashforth scheme.

The Euler angles in the non-inertial system need to be transformed back to the inertial one. Fluid structure coupling is arranged in a weak form. That is the calculation of the acting forces from the fluid first and afterwards updating it to the new time level.

3 Numerical set-up

For the numerical modeling REEF3D's numerical wave tank is used. A 12m long flume is used with a wave generation zone of the wave length and a damping zone of twice the length for the decay-tests, while the flume used for the regular wave tests is 20m long, due to the longer time modelled. The height of the model is 1.5 m with the waterlevel at 0.85 m. Due to the incident wave direction and in order to reduce the computational cost, the set-up is reduced to a two-dimensional model. So only one grid layer is modelled in y-direction. The gridsize is chosen to be 0.5 cm.

At first the decay-tests are reproduced, by defining the initial position different from the balanced one. In heave direction the offset is 0.75cm, while the initial angle for the pitch decay-test is 5.8°

For the wave-induced modelling 2nd-order Stokes wave theory showed a good reproduction of the experimental tests. To keep the barge in place a set of springs is introduced, the same way as in the experimental tests but with a scaled stiffness.

4 Results

4.1 Experimental Results

While the movement is measured in all six degrees of freedom it is in the following just given for pitch and heave-movements, since the others are negligible due to the incident wave direction. All movements are normalized with the water-depth, and the wave number for a 1.2s 3cm wave, and the period of the same wave.

Comparing the soft-mooring system with the traditional one with a spring constraint of 0.209N/mm shows almost no influence on the heave-motions, but an impact on the pitch motion. The similarity for the heave-motion extends to the amplitude and the period. The timeseries are matched by implementing a phase shift in the one for the traditional mooring. Applying the same shift to the pitch motion shows a small lag in the movement. The periods for this degree of freedom match, but the pitch-amplitude is significantly higher than for the soft-moored system.

For a given wave of 3cm with a period of 1.2s the comparison of the three springs examined shows only little differences in heave direction. The amplitude of the movement of F2 is a little smaller than for the other set-ups, that are almost identical, but the difference is only

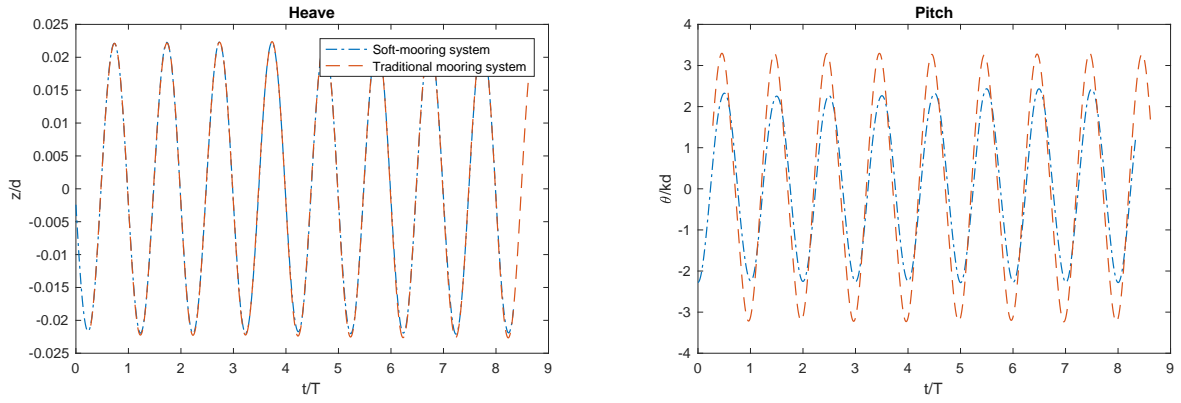


Figure 1: Comparison of the soft-moored system with the traditional one for a 1.2s wave with a height of 3cm

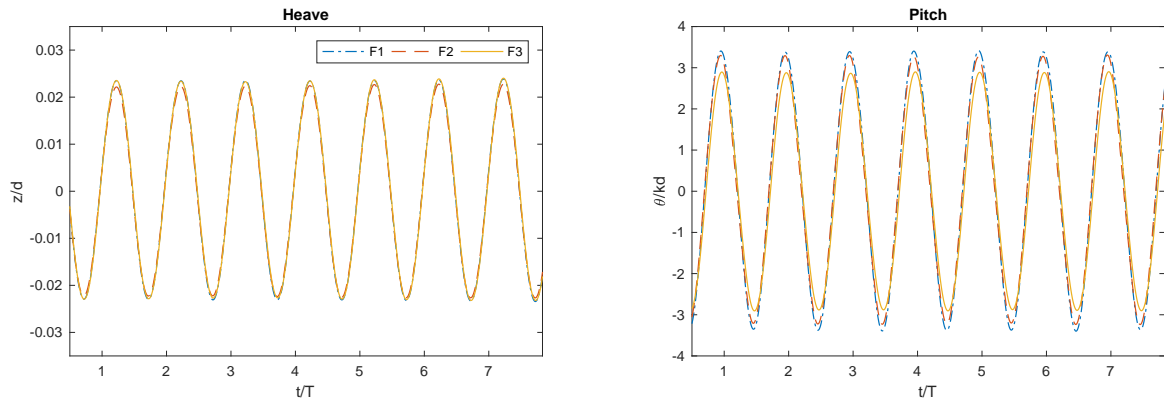


Figure 2: Comparison of the three different spring constraints for a 1.2s wave with a height of 3cm

marginal. For the-pitch motion the amplitudes are higher the stiffer the spring gets, with a maximal difference between the set-ups of about 0.5. No phase lag can be observed.

The comparison of three different wave-periods for a given set-up with spring 2 shows some differences in the amplitudes. In heave-direction the movement is highest for a period of 1.2s, followed by 1.6s and lowest for 0.8s. Movements are symmetric to both sides of the water level. In pitch-direction, the movements are not symmetric for periods 0.8s and 1.6s. While the values for 1.6s are higher in negative orientation, the ones for 0.8s are higher for the positively oriented angle. The highest amplitudes can again be observed for the period 1.2s, followed by 0.8s for the positive values. The values for the negative values equal each other for the periods 0.8s and 1.6s. Inaccuracy in the model-set up is not an explanation for this behaviour, since it wasn't changed in between the experiments.

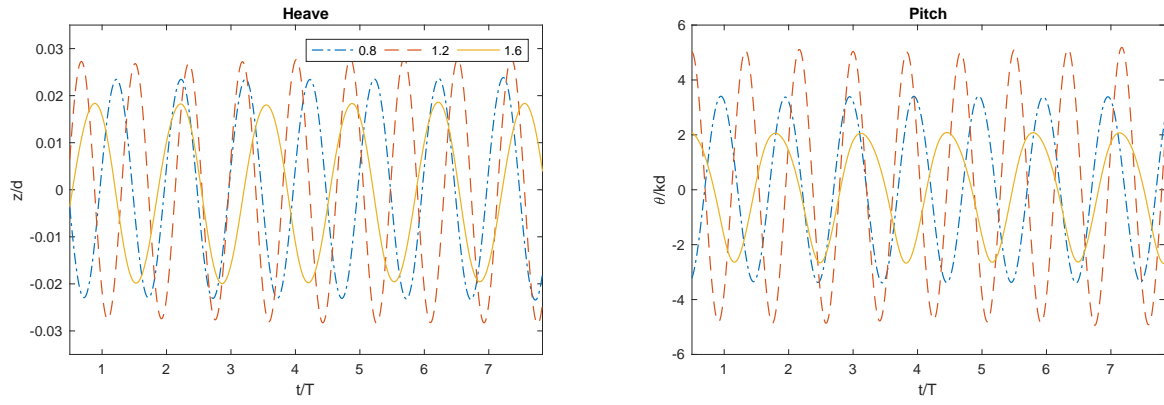


Figure 3: Comparison of the intermediate stiff spring F2 under 3cm waves with three different wave periods

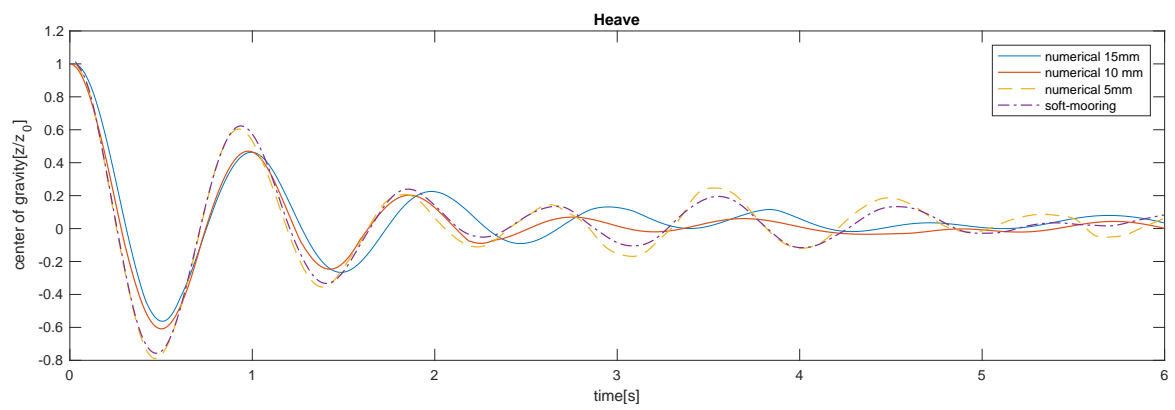


Figure 4: Convergence of the Heave-Decay-Test

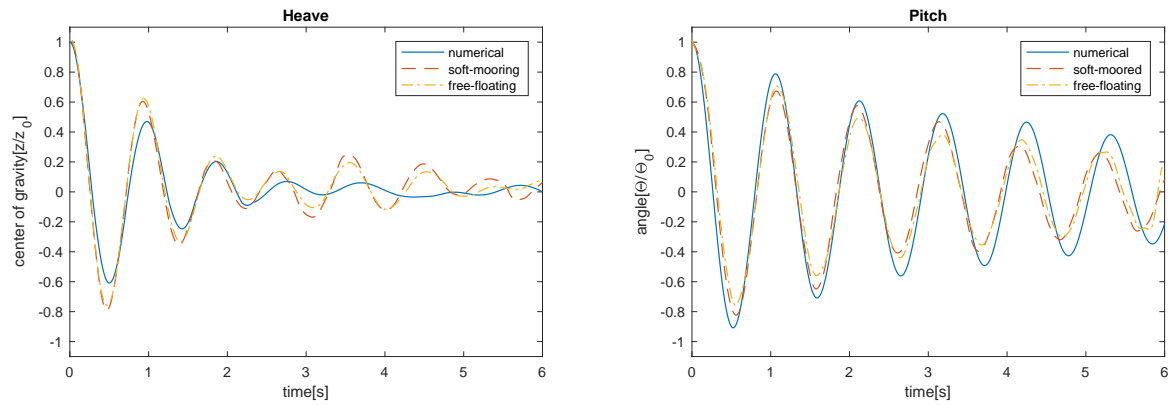


Figure 5: Comparison of the numerical and experimental decay-tests

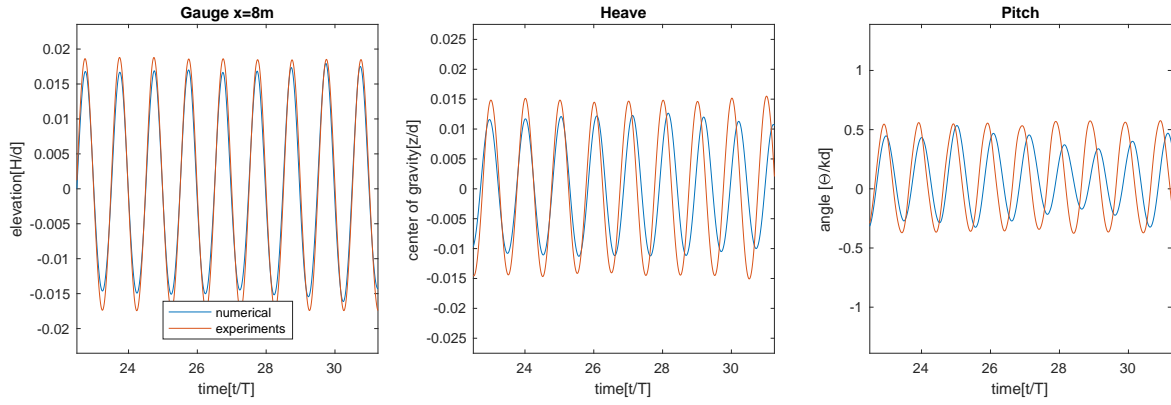


Figure 6: The movement of the soft-moored barge in waves with a period of 0.8s

5 Comparison of the numerical and experimental results

5.1 Decay-Tests

For the resolutions of 10mm and 5mm the results are similar, but especially for the third period the results for the higher resolved grid are closer to the experimental ones. Therefore it is chosen for further numerical models. For even finer grids the model shows to be unstable.

The overall reproduction of the decay-tests is not of a high quality. Due to the manual adjustment of the initial displacement, there is a little difference in between the two experimental set ups. To overcome this the values are normalized with the initial displacement.

In the heave decay-tests the first two periods are well reproduced concerning the wavelength, afterwards there is a large lag to be seen. The amplitudes of the numerical simulation are significantly smaller than in the experimental tests. The reduction is about one fourth within the first two periods.

The values of the pitch-decay test are in general better reproduced. The first three periods of the movement are well reproduced, afterwards the period of the simulation is a little longer than in the experiments. The amplitude of the simulation is about a tenth higher than in the experiments.

5.2 The soft-moored-body in regular Waves

The movement of the barge in the regular waves is generally well reproduced. Since it takes some time for the body to start a regular movement, a window after the initialization period is shown.

Worst results are obtained for a wave period of 0.8s. The period of the simulated movement is a little longer for both movements, than in the experiments. The amplitudes are about one fifth smaller than in the experiments. Regardless of the springs the model drifts about 30 cm. This could be a reason of the prolonged period. As mentioned before the pitch movement shows asymmetries which is captured by the numerical model.

For a wave with a period of 1.2s (Figure 5.2) the heave movement matches almost exactly. The numerical pitch-movement is a little underestimated, but the difference is only small. The

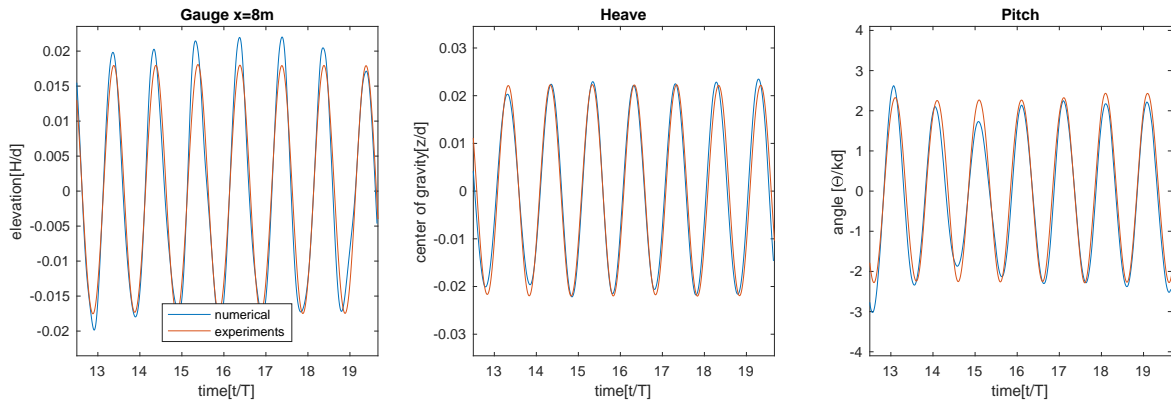


Figure 7: The movement of the soft-moored barge in waves with a period of 1.2s

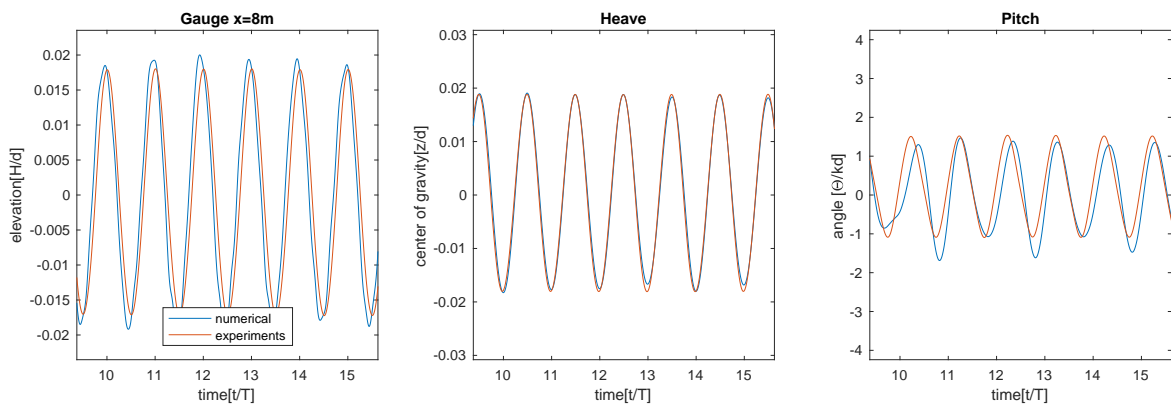


Figure 8: The movement of the soft-moored barge in waves with a period of 1.6s

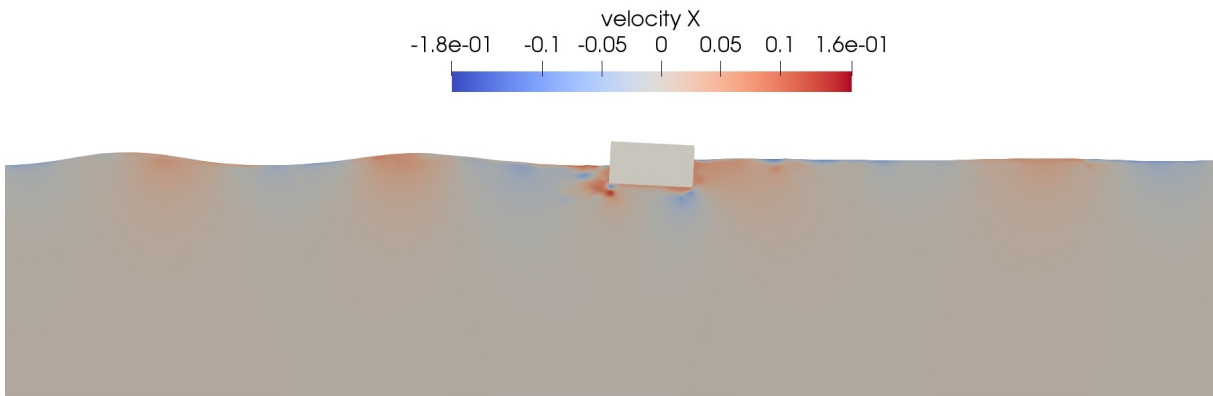


Figure 9: The barge and the velocity in x-direction waves with a period of 0.8s

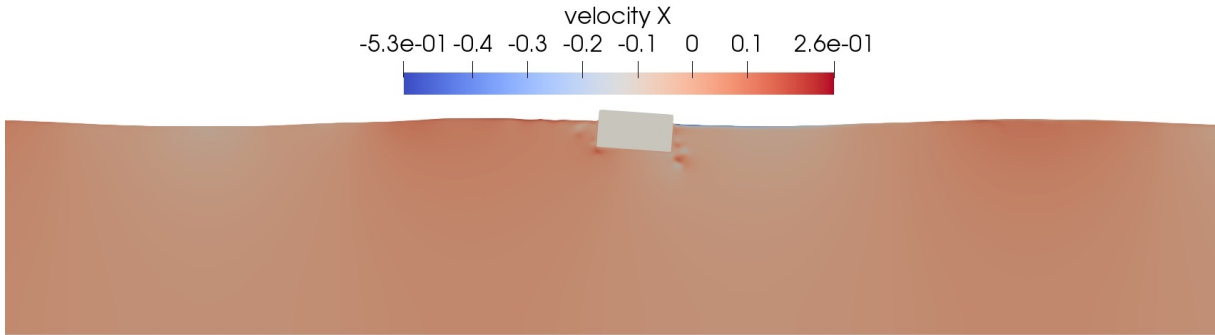


Figure 10: The barge and the velocity in x-direction waves with a period of 1.2s

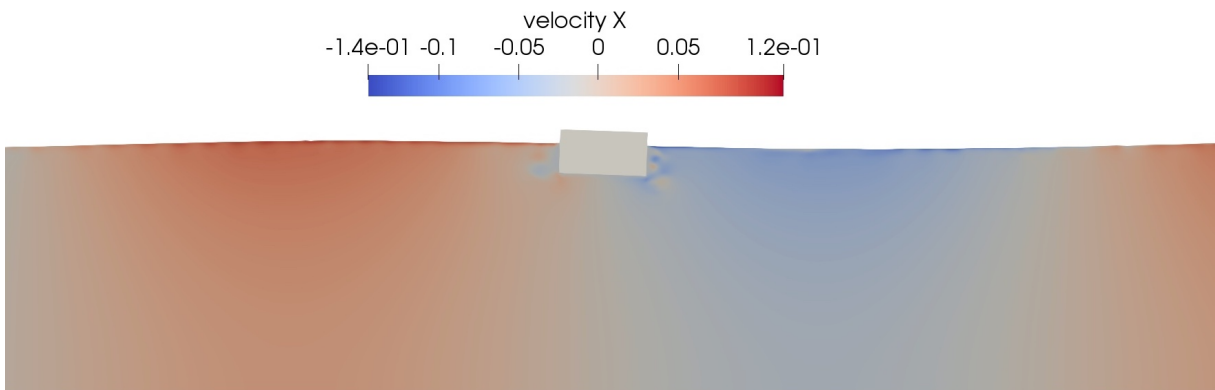


Figure 11: The barge and the velocity in x-direction waves with a period of 1.6s

wave amplitudes in the middle of the flume in y-direction are slightly overestimated by the numerical tool. It can be observed that the waves are asymmetrical with positive values larger than the negative ones.

For a period of 1.6s the simulations match the experiments well. The periods for heave and pitch motion are matched well. The amplitudes in heave direction are also matched very well, while for the pitch motion every second minimum shows larger angles, which is not the case in the experimental data. Apart from that the data is matched well. The gaugedata is also well reproduced, exceeding the experimental data only a little.

6 Conclusions

The experiments show a large influence of the traditional mooring-system on the pitch-movement of a barge. The barge shows a larger amplitude for the traditional mooring system compared to the soft-moored one. On the traditional mooring system a reduced stiffness leads to higher amplitudes. The influence on the heave motion is marginal. Different wave periods have an influence on the heave and pitch motion of the moored system, with largest amplitudes for a waveperiod of 1.2s, for both movements.

The numerical reproduction has to be improved for the decay test. In heave direction the motion is damped while it overestimates the motion in pitch direction. The motion in regular waves is well predicted for the more gentle waves, with periods of 1.2s and 1.6s. For steeper waves with a period of 0.8s the movement is not accurate, which may be connected to the large surge offset for these waves.

The solver is able to qualitatively predict the motion of a floating barge, compared to experimental results, but has deficits in quantities for some models. This is clearly a topic adressed by further research. One possibility to overcome this is adding springs to prevent the surge motions from getting to large. In addition to that the experimental set-up including a traditional mooring-system will be simulated, comparing different mooring models implemented in REEF3D with the generated data-set.

References

- Berthelsen, P.A. and Faltinsen, O.M. (2008). A local directional ghost cell approach for incompressible viscous flow problems with irregular boundaries. *Journal of Computational Physics*, **227**(9), 4354 – 4397. ISSN 0021-9991. doi:<https://doi.org/10.1016/j.jcp.2007.12.022>.
- Bihs, H. and Kamath, A. (2017). A combined level set/ghost cell immersed boundary representation for floating body simulations. *International Journal for Numerical Methods in Fluids*, **83**(12), 905–916. doi:[doi:10.1002/flid.4333](https://doi.org/10.1002/flid.4333).
- Bihs, H., Kamath, A., Chella, M.A., Aggarwal, A. and Arntsen, Ø.A. (2016). A new level set numerical wave tank with improved density interpolation for complex wave hydrodynamics. *Computers Fluids*, **140**, 191 – 208. ISSN 0045-7930. doi:<https://doi.org/10.1016/j.compfluid.2016.09.012>.
- Borazjani, I., Ge, L., Le, T. and Sotiropoulos, F. (2013). A parallel overset-curvilinear-immersed

- boundary framework for simulating complex 3d incompressible flows. *Computers Fluids*, **77**, 76 – 96. ISSN 0045-7930. doi:<https://doi.org/10.1016/j.compfluid.2013.02.017>.
- Calderer, A., Kang, S. and Sotiropoulos, F. (2014). Level set immersed boundary method for coupled simulation of air/water interaction with complex floating structures. *Journal of Computational Physics*, **277**, 201 – 227. ISSN 0021-9991. doi:<https://doi.org/10.1016/j.jcp.2014.08.010>.
- Carrica, P.M., Wilson, R.V., Noack, R.W. and Stern, F. (2007). Ship motions using single-phase level set with dynamic overset grids. *Computers Fluids*, **36**(9), 1415 – 1433. ISSN 0045-7930. doi:<https://doi.org/10.1016/j.compfluid.2007.01.007>.
- Chorin, A.J. (1968). Numerical solution of the navier-stokes equations. *Mathematics of Computation*, **22**(104), 745–762. ISSN 00255718, 10886842.
- Christensen, E.D., Bingham, H.B., Friis, A.P.S., Larsen, A.K. and Jensen, K.L. (2018). An experimental and numerical study of floating breakwaters. *Coastal Engineering*, **137**, 43 – 58. ISSN 0378-3839. doi:<https://doi.org/10.1016/j.coastaleng.2018.03.002>.
- Davidson, J. and Ringwood, J. (2017). Mathematical modelling of mooring systems for wave energy converters-a review. *Energies*, **10**. doi:10.3390/en10050666.
- Fossen, T.I. (1994). *Guidance and control of ocean vehicles*. John Wiley & Sons Inc.
- He, F., Huang, Z. and Law, A.W.K. (2012). Hydrodynamic performance of a rectangular floating breakwater with and without pneumatic chambers: An experimental study. *Ocean Engineering*, **51**, 16 – 27. ISSN 0029-8018. doi:<https://doi.org/10.1016/j.oceaneng.2012.05.008>.
- Ji, C., Cheng, Y., Yang, K. and Oleg, G. (2017). Numerical and experimental investigation of hydrodynamic performance of a cylindrical dual pontoon-net floating breakwater. *Coastal Engineering*, **129**, 1 – 16. ISSN 0378-3839. doi:<https://doi.org/10.1016/j.coastaleng.2017.08.013>.
- Ji, C.Y., Chen, X., Cui, J., Gaidai, O. and Incecik, A. (2016). Experimental study on configuration optimization of floating breakwaters. *Ocean Engineering*, **117**, 302 – 310. ISSN 0029-8018. doi:<https://doi.org/10.1016/j.oceaneng.2016.03.002>.
- Jiang, G.S. and Shu, C.W. (1996). Efficient implementation of weighted eno schemes. *Journal of Computational Physics*, **126**(1), 202 – 228. ISSN 0021-9991. doi:<https://doi.org/10.1006/jcph.1996.0130>.
- Martin, T., Bihs, H., Kamath, A. and Arntsen, Ø.A. (2019). Simulation of floating bodies in waves and mooring in a 3d numerical wave tank using reef3d. In: K. Murali, V. Sriram, A. Samad and N. Saha (Editors), *Proceedings of the Fourth International Conference in Ocean Engineering (ICOE2018)*, 673–683. Springer Singapore, Singapore. ISBN 978-981-13-3119-0.
- Martin, T., Kamath, A. and Bihs, H. (2018a). *Modelling and Simulation of Moored-floating Structures using the Tension-Element-Method*, volume 2. ASME 2018 37th International Conference on Ocean, Offshore and Arctic Engineering.

- Martin, T., Kamath, A. and Bihs, H. (2018*b*). Numerical simulation of interactions between water waves and a moored-floating breakwater. *Coastal Engineering Proceedings*, **1**(36), 105. ISSN 2156-1028. doi:10.9753/icce.v36.papers.105.
- Meyer, J. (2018). Physical and numerical simulation of floating bodies. In: *Master thesis - Leibniz Universität Hannover*.
- Osher, S. and Sethian, J.A. (1988). Fronts propagating with curvature-dependent speed: Algorithms based on hamilton-jacobi formulations. *Journal of Computational Physics*, **79**(1), 12 – 49. ISSN 0021-9991. doi:https://doi.org/10.1016/0021-9991(88)90002-2.
- Ramaswamy, B., Kawahara, M. and Nakayama, T. (1986). Lagrangian finite element method for the analysis of two-dimensional sloshing problems. *International Journal for Numerical Methods in Fluids*, **6**(9), 659–670. doi:doi:10.1002/fld.1650060907.
- Sannasiraj, S., Sundar, V. and Sundaravadivelu, R. (1998). Mooring forces and motion responses of pontoon-type floating breakwaters. *Ocean Engineering*, **25**(1), 27 – 48. ISSN 0029-8018. doi:https://doi.org/10.1016/S0029-8018(96)00044-3.
- Shu, C.W. and Osher, S. (1988). Efficient implementation of essentially non-oscillatory shock-capturing schemes. *Journal of Computational Physics*, **77**(2), 439 – 471. ISSN 0021-9991. doi:https://doi.org/10.1016/0021-9991(88)90177-5.
- Yang, J. and Balaras, E. (2006). An embedded-boundary formulation for large-eddy simulation of turbulent flows interacting with moving boundaries. *Journal of Computational Physics*, **215**(1), 12 – 40. ISSN 0021-9991. doi:https://doi.org/10.1016/j.jcp.2005.10.035.
- Yang, J. and Stern, F. (2012). A simple and efficient direct forcing immersed boundary framework for fluid–structure interactions. *Journal of Computational Physics*, **231**(15), 5029 – 5061. ISSN 0021-9991. doi:https://doi.org/10.1016/j.jcp.2012.04.012.
- Yang, J. and Stern, F. (2013). Robust and efficient setup procedure for complex triangulations in immersed boundary simulations. *Journal of Fluids Engineering*, **135**, 101107 0098–2202.

THE COMMOTION PROJECT: COMPUTATIONAL METHODS FOR MOVING AND DEFORMING OBJECTS IN EXTREME WAVES

ARTHUR E.P. VELDMAN^{1*}, PETER VAN DER PLAS^{1,3}, HENK SEUBERS¹, S. MATIN HOSSEINI ZAHRAEI², XING CHANG², PETER R. WELLENS² AND JOOP HELDER³

¹ Bernoulli Institute for Mathematics, Computer Science and Artificial Intelligence, University of Groningen, PO Box 407, 9700AK Groningen, The Netherlands
e-mail: {a.e.p.veldman, h.seubers}@rug.nl

² Department of Maritime and Transportation Technology, Delft University of Technology, Mekelweg 2, 2628 CD Delft, The Netherlands
e-mail: {s.hosseinizahraei, x.chang, p.r.wellens}@tudelft.nl

³ MARIN, PO Box 28, 6700AA Wageningen, The Netherlands
e-mail: {p.v.d.plas, j.helder}@marin.nl

Key words: Extreme waves, fluid–solid body interaction, CFD, local grid refinement, experimental validation.

Abstract. Extreme waves and their impact on (fixed and floating) offshore structures have long been subjects that could only be studied with experimental methods; sufficiently accurate existing numerical methods (CFD) are only recently emerging. Phenomena like green water loading and slamming are highly dependent on the relative motion of a ship versus the on-coming wave crests, as influenced by the preceding wave groups. Thus, accurate prediction of the hydrodynamic forces requires methods that can reliably predict the interaction between extreme waves and body dynamics. Over the years, the ComFLOW simulation method has been developed to cover this CFD niche. A novel ingredient developed in the ComMotion project is an unsteady coupling algorithm that is numerically stable under all circumstances (such as ratio of body mass versus added mass). Also, a new class of absorbing boundary conditions has been extended to include the effects of current. Several applications will be presented, including experimental validation.

1 INTRODUCTION

Under extreme weather conditions, waves and currents can induce large forces and stresses on sea-going ships and offshore constructions (production and offloading platforms, mooring systems, wind turbine farms) [1]. For example, in heavy storms solid amounts of seawater,

called ‘green water’, flow over the deck, thus threatening the safety and operability of the ship. The amount of shipped water obviously depends on the phase between ship and wave motion, and hence on the preceding wave group and its interaction with the ship dynamics. The same holds for slamming impacts against a ship’s bow. As a special case, free fall lifeboats (Fig. 1) face these challenges when a ship or platform needs to be evacuated.

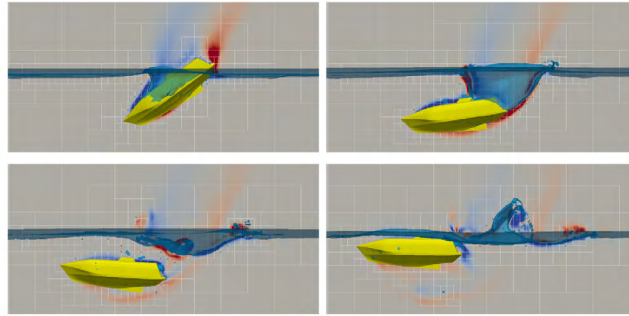


Figure 1: Simulated snapshots of a free-fall life boat.

Until recently, these violent flow phenomena were mainly studied experimentally, but there is a growing need for a numerical simulation tool capable of predicting in detail the hydrodynamic loads due to slamming and green water; see, e.g., [2–4]. However, the tools currently available are based on e.g. linear potential flow theory or shallow-water theory; see e.g. [5]. These tools based on simple models are hardly capable of predicting such events to an acceptable level of accuracy. The physical phenomena accompanying extreme events are both highly non-linear and highly dispersive due to the occurring wave steepness, and require new methods as a basis for the prediction of the water flow and its induced hydrodynamic loads.

It is only recently that the Navier–Stokes equations can be solved for large-scale complex free-surface flow problems, thanks to novel numerical algorithms and the increase in computer power [6–8]. For an overview of basic Navier–Stokes methods for free-surface flow we refer to [9], with some offshore applications in [10–12].

In this paper we will present the main physical and numerical ingredients of the ComMotion project:

- Interactively moving bodies.
- Hydroelasticity.
- Absorbing boundary conditions incorporating current.
- Experimental validation.

For reliable load predictions in these examples, it is necessary to determine the position and dynamics of the objects as part of the flow simulation. The ComMotion project makes this major step by extending the ComFLOW simulation method to interactively moving and deforming objects in extreme waves. Also, attention is paid to numerical absorbing outflow boundary conditions in the presence of current. The new developments will be illustrated with a number of maritime applications.

2 MODELLING

2.1 Flow model

Incompressible, turbulent fluid flow can be modelled by means of the Navier–Stokes equations.

$$M\mathbf{u} = 0, \quad \frac{\partial \mathbf{u}}{\partial t} + C(\mathbf{u})\mathbf{u} + Gp - V\mathbf{u} = \mathbf{f}. \quad (1)$$

The divergence operator is denoted $M \equiv \nabla \cdot$, the convection operator $C(\mathbf{u})\mathbf{v} \equiv \nabla \cdot (\mathbf{u} \otimes \mathbf{v})$, the pressure gradient operator $G = \nabla$, the viscous diffusion operator $V(\mathbf{u}) \equiv \nabla \cdot \nu \nabla \mathbf{u}$ and \mathbf{f} a forcing term. The kinematic viscosity is denoted by ν . Turbulence is modelled by means of large-eddy simulation (LES) using a state-of-the-art low-dissipation QR/AMD-model [13–16]. For its use in maritime applications, see [17, 18].

The evolution of the free water surface is described by an adapted and improved version of the Volume-of-Fluid method (VOF) introduced in [6] and [19]. The free surface is reconstructed by Youngs’ PLIC method [20, 21] and advanced by a local height function [21, 22]. Specifically, use will be made of the ComFLOW simulation method, developed at the University of Groningen in cooperation with the Technical University of Delft and MARIN. It is described in full detail in a handful of PhD theses [18, 21–27].

Bodies can move and deform through the fixed Cartesian grid, with their position described in a cut-cell fashion by edge and volume apertures, as is done for non-moving objects [28] (see also [29, 30]). Local grid refinement [31] can be applied in ‘interesting’ regions.

The Navier–Stokes equations (1) are discretized on a staggered computational grid [32]. The second-order finite-volume discretization of the continuity equation at the ‘new’ time level $^{n+1}$ is given by

$$M_0 \mathbf{u}^{n+1} = -M_\Gamma \mathbf{u}_\Gamma^{n+1}, \quad (2)$$

where M_0 acts on the interior of the domain and M_Γ acts on the boundaries. The discretization keeps convection $C(\mathbf{u}_n)$ skew symmetric and diffusion V symmetric. In this exposition, for simplicity reasons the first-order forward Euler time integration will be used. In the actual calculations, a second-order Adams–Bashforth method for convection and a fully implicit method for diffusion is applied.

The discrete momentum equation can be formulated as

$$\mathbf{u}^{n+1} = \tilde{\mathbf{u}} - \delta t \Omega^{-1} G \mathbf{p}^{n+1}, \quad \text{where} \quad \tilde{\mathbf{u}} = \mathbf{u}^n + \delta t \Omega^{-1} [-C(\mathbf{u}^n) \mathbf{u}^n + V \mathbf{u}^n + \mathbf{f}]. \quad (3)$$

Here, the diagonal matrix Ω contains the geometric size of the control volumes. This discretization does not produce artificial diffusion and convectively preserves the energy of the flow [15, 33]. The discrete gradient operator and the divergence operator are each other’s negative transpose, i.e. $G = -M_0^T$ mimicking the analytic symmetry $\nabla = -(\nabla \cdot)^T$, such that the work done by the pressure vanishes discretely.

Imposing discrete mass conservation (2) at the new time level, substitution of (3) results in a discrete Poisson equation for the pressure:

$$\delta t M_0 \Omega^{-1} G \mathbf{p}^{n+1} = M_0 \tilde{\mathbf{u}} + M_\Gamma \mathbf{u}_\Gamma^{n+1}. \quad (4)$$

Here Γ is the boundary of the fluid domain where boundary conditions involving the velocity are prescribed; it includes the fluid-solid interface Γ_{FS} .

For future reference, the fluid dynamic problem will be formally abbreviated as

$$\mathbf{M}_{\text{ad}} \ddot{\mathbf{d}}_{\Gamma_{\text{FS}}} = -\mathbf{f}_{\Gamma_{\text{FS}}}. \quad (5)$$

Here, \mathbf{M}_{ad} is the so-called fluid added-mass operator, which governs the relation between the motion of an immersed body and the reactive forces exerted by the fluid. Further, \mathbf{d} is the displacement of the fluid-solid interface.

2.2 Structural model

For simplicity in this study, the structure is selected to be a one dimensional Euler–Bernoulli beam. Assuming a constant cross section $A = TW$ for the beam (thickness T and width W), its equation of motion is

$$\rho_s A \frac{\partial^2 d}{\partial t^2} + EI \frac{\partial^4 d}{\partial s^4} = f, \quad (6)$$

with appropriate initial and boundary conditions. Here, s denotes a coordinate along the beam, d the beam deformation, ρ_s the beam density, E Young’s modulus, I the second moment of inertia and f the load per unit length of the beam.

The structural response is modeled with a finite element method. Omitting the technical details, the resulting discrete set of equations can be written in the form

$$\mathbf{M}_{\text{eb}} \ddot{\mathbf{d}} + \mathbf{K}_{\text{eb}} \mathbf{d} = \mathbf{f}_{\Gamma_{\text{FS}}}, \quad (7)$$

where \mathbf{M}_{eb} is the discrete mass operator and \mathbf{K}_{eb} the discrete stiffness operator. The temporal integration of the structure equations is performed by means of the generalized- α method [34].

2.3 Fluid-solid coupling conditions

The coupling relations along the fluid-solid interface Γ_{FS} consist of two relations. The kinematic condition states that the motion of the interface on both sides matches, whereas the dynamic condition ensures equilibrium of stresses:

$$\text{kinematic} \quad \mathbf{u} = \frac{\partial \mathbf{d}}{\partial t} \mathbf{n}; \quad \text{dynamic} \quad \bar{\bar{\sigma}}_f \cdot \mathbf{n} = \bar{\bar{\sigma}}_s \cdot \mathbf{n}. \quad (8)$$

3 NUMERICAL COUPLING METHODS

3.1 Numerical coupling with a solid body

Traditional weak (hierarchical) coupling methods, with information exchange once per time step, are only numerically stable within a restricted range of added-mass ratios. If the application covers a larger range, one has to resort to strong (simultaneous) coupling [35]. Usually, some form of subcycling within each time step is applied, where information is exchanged at the ‘hearts’ of the numerical algorithms (like in a monolithic code). For two-way coupled problems, a monolithic procedure of the subdomains would be most powerful. However, such a simultaneous approach is not always possible, e.g. when ‘black-box’ commercial codes are being used, as the

subdomain solvers have to be coupled at a deep iterative level. In this section we will describe an approach that tries to combine the simplicity of a hierarchical coupling approach with the iterative power of a monolithic approach.

Segregated coupling The stability of the two-way coupled system can be investigated in an abstract setting. On both sides of the fluid-body interface Γ_{FS} physical properties need to be continuous, as expressed in the kinematic and dynamic conditions (8). Thus the coupling problem can be formulated in terms of interface variables only: the velocity along the interface \mathbf{u}_Γ and the local or total load exerted by the fluid to the structure \mathbf{f}_Γ (for an elastic body found from the local stresses, for a solid body found from their integration along the interface).

The solid body reacts by accelerating due to the exerted force from the fluid. For a solid body a six degrees of freedom (DOF) mass operator (\mathbf{M}_{sb}) containing inertial properties of the body rules its dynamic response. The fluid, on the other hand, reacts to the accelerated solid body with a new pressure field. The so-called added-mass operator (\mathbf{M}_{ad}) describes the fluid's response. Thus we can formulate the coupled problem in abstract notation as

$$\text{solid body dynamics } \mathbf{M}_{sb}\ddot{\mathbf{d}}_\Gamma^{k+1} = \mathbf{f}_\Gamma^k; \quad \text{fluid dynamics } \mathbf{f}_\Gamma^{k+1} = -\mathbf{M}_{ad}\ddot{\mathbf{d}}_\Gamma^{k+1}. \quad (9)$$

We have already indicated the usual iterative process which is used to solve this set of, basically, 2 equations in 2 unknowns. Its formal amplification operator follows as

$$\mathbf{f}_\Gamma^{k+1} = -\mathbf{M}_{ad}\mathbf{M}_{sb}^{-1}\mathbf{f}_\Gamma^k, \quad \text{which is stable if and only if } \rho(\mathbf{M}_{ad}\mathbf{M}_{sb}^{-1}) < 1. \quad (10)$$

In other terms, the ratio of the added mass to the solid body mass for each DOF, more precisely all eigenvalues, should be less than one. If the problem violates this requirement, methods like the under-relaxation method, can only keep this value below unity at the cost of (severely) increasing computational effort.

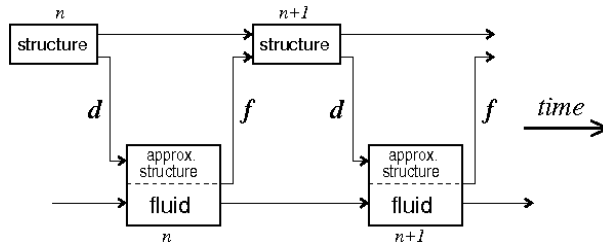


Figure 2: Coupling strategy for simulating the interaction between a solid-body/structure and a fluid. To improve the numerical stability, an interaction law is used consisting of an approximate model for the solid-body/structure dynamics.

Quasi-simultaneous coupling It is not necessary to perform a *fully* simultaneous coupling. A good approximation of one of the two submodels is sufficient to be fully intertwined with the other submodel. The difference between the approximation and the original submodel can be dealt with in the traditional, weak fashion. Such a coupling is called *quasi-simultaneous*, and

was introduced in a steady, aerodynamic context in the late 1970s [36,37]. Recently, the method has been re-discovered in the FSI community [11, 38].

In time-integration terms, the bulk of the interaction is treated implicitly, the remaining part explicitly. Numerical stability of this approach requires that, roughly spoken, the implicit part contains at least ‘half of the physics’, which is a very weak requirement. An essential step is that the equations approximating the other submodel, such as an elastic wall model, are considered boundary conditions for the fluid flow equations. In particular, they will show up as a boundary condition in the pressure Poisson equation.

In this quasi-simultaneous method an approximation of the body dynamics is solved simultaneously with the fluid. This *interaction law* anticipates the body response in advance of the actual solid dynamics computation. As such, the interaction law is an approximation $\widetilde{\mathbf{M}}_{\text{sb}}^{-1}$ to the inverse mass operator $\mathbf{M}_{\text{sb}}^{-1}$ of the solid body dynamics (9a). In the iterative process within each time step, the interaction law is exploited as

$$\text{solid body} \quad \ddot{\mathbf{d}}_{\Gamma}^{k+1} = \mathbf{M}_{\text{sb}}^{-1} \mathbf{f}_{\Gamma}^k, \quad (11)$$

$$\text{interaction law} \quad \dot{\mathbf{u}}_{\Gamma} - \widetilde{\mathbf{M}}_{\text{sb}}^{-1} \mathbf{f}_{\Gamma}^{k+1} = \ddot{\mathbf{d}}_{\Gamma}^{k+1} - \widetilde{\mathbf{M}}_{\text{sb}}^{-1} \mathbf{f}_{\Gamma}^k, \quad (12)$$

$$\text{fluid} \quad \mathbf{f}_{\Gamma}^{k+1} + \mathbf{M}_{\text{ad}} \dot{\mathbf{u}}_{\Gamma} = 0. \quad (13)$$

Eliminating $\ddot{\mathbf{u}}_{\Gamma}$ leads to the following iterative process, which can be compared to (10):

$$\left(\mathbf{I} + \mathbf{M}_{\text{ad}} \widetilde{\mathbf{M}}_{\text{sb}}^{-1} \right) \mathbf{f}_{\Gamma}^{k+1} = -\mathbf{M}_{\text{ad}} \left(\mathbf{M}_{\text{sb}}^{-1} - \widetilde{\mathbf{M}}_{\text{sb}}^{-1} \right) \mathbf{f}_{\Gamma}^k, \quad (14)$$

where \mathbf{I} is the unit operator. In mathematical terms, the interaction law should neutralize the most cumbersome eigenvalues of the iteration matrix.

This relation simplifies to (10) if the interaction law is zero, or in other words not employed, which breaks down if \mathbf{M}_{ad} is large. Similar to the segregated method, the iterative procedure is stable if and only if the spectral radius of the amplification matrix is less than one, i.e. $\rho\left(\left(\mathbf{M}_{\text{ad}}^{-1} + \widetilde{\mathbf{M}}_{\text{sb}}^{-1}\right)^{-1} \left(\mathbf{M}_{\text{sb}}^{-1} - \widetilde{\mathbf{M}}_{\text{sb}}^{-1}\right)\right) < 1$. When $\left(\mathbf{M}_{\text{sb}}^{-1} - \widetilde{\mathbf{M}}_{\text{sb}}^{-1}\right)$ is sufficiently small, this process will converge, in spite of a possibly large \mathbf{M}_{ad} .

3.2 Numerical coupling with an elastic body

Because the structural equation (7) contains both $\ddot{\mathbf{d}}$ and \mathbf{d} , first a discrete time integration is carried out. Thereafter, an analysis similar to the above can be carried out. Then the discrete version of the hierarchically coupled problem at the new time level can be denoted as

$$\text{elastic body} \quad \left(\frac{\mathbf{M}_{\text{eb}}}{\delta t^2} + \mathbf{K}_{\text{eb}} \right) \mathbf{d}_{\Gamma}^{k+1} = \mathbf{f}_{\Gamma}^k + \dots, \quad (15)$$

$$\text{fluid} \quad \mathbf{f}_{\Gamma}^{k+1} = -\frac{\mathbf{M}_{\text{ad}}}{\delta t^2} \mathbf{d}_{\Gamma}^{k+1}. \quad (16)$$

Here, \mathbf{M}_{eb} denotes the discrete elastic body mass operator, while \mathbf{K}_{eb} is the discrete elastic body stiffness operator; compare (7). The contribution from the previous time steps is omitted in view of clarity; it is just an inhomogeneous term in the right-hand side, which is not relevant for the convergence of the subiterations per time step.

Matrices M_{eb} and K_{eb} can be simultaneously diagonalized as $Q^T M_{\text{eb}} Q = I$ and $Q^T K_{\text{eb}} Q = \Lambda$, where Q contains the normalized elastic body eigenvectors with eigenvalues Λ . In this way, the elastic body dynamics (15) can be rewritten as

$$\text{elastic body} \quad Q^{-T} \left(\frac{1}{\delta t^2} + \Lambda \right) Q^{-1} \mathbf{d}_{\Gamma}^{k+1} = \mathbf{f}_{\Gamma}^k. \quad (17)$$

The displacement \mathbf{d}^{k+1} can be eliminated from the system of equations (16) and (17), after which the iterative process can be written as

$$\mathbf{f}^{k+1} = -M_{\text{ad}} Q (I + \delta t^2 \Lambda)^{-1} Q^T \mathbf{f}^k. \quad (18)$$

For small enough δt , the amplification factor simplifies to $M_{\text{ad}} Q Q^T$. For a solid body with 6 DOF, $Q Q^T$ can be replaced by the inverse solid-body mass M_{sb}^{-1} .

It can be shown [39] that the lower modes are most delicate, as they correspond with the largest fluid added mass. Therefore we take care that these modes are treated more simultaneous. Thus we construct an approximation of the full elastic equations, built from the lowest elastic modes of the structure.

4 EXAMPLES

4.1 Tank with membrane bottom

In order to assess the performance of the quasi-simultaneous approach for different mass ratios, a test case has been designed in which this ratio can be varied. Also, the physical contents of the interaction law has been varied.

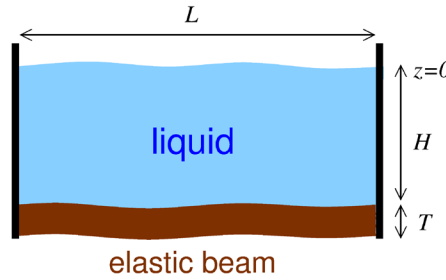


Figure 3: Schematic of the first test case; the domain with free-surface flow on top and flexible beam at the bottom.

At the bottom of a rectangular container ($1.0 \times 0.1 \times 0.5 \text{ m}^3$) filled with 50 kg of water, a flexible beam is placed, as illustrated in Fig. 3. The mass of the beam is varied between 1 kg and 50 kg; its module of elasticity is 1 MPa. The interaction law is made out of truncated structural modes; the number of modes dictates its accuracy.

Cases with mass ratio 1 and 50 are presented, where the number of included modes is increased in order of relevance. Figure 4 shows the convergence history during the first time step. The effect of the number of modes in the interaction law can be inferred. For a small added-mass ratio one mode suffices, but for the more difficult mass ratio 50 it is profitable to include more modes in the interaction law. This behaviour is perfectly in line with the theoretical stability analysis in [39].

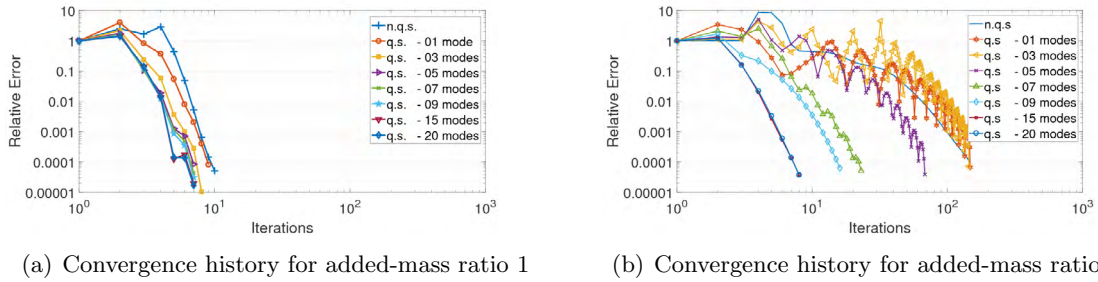


Figure 4: Convergence history of the quasi-simultaneous method for the first time step for an increasing number of included modes.

4.2 Free-fall life boat

The second example concerns a simulation of a free-fall life boat (Fig. 1). During the penetration of the free water surface the added mass can become quite large with added-mass ratios upto 40. Hence it is a perfect test case to evaluate the performance of the quasi-simultaneous modes coupling method. The main finding is summarized in Fig. 5(right). It shows the amount of floating-point operations to solve the pressure Poisson equation including the FSI-iterations that are required per time step to converge the coupling with the moving solid body. In particular, the dependence of this computational effort with the added-mass ratio is shown. The graph shows that at larger added-mass ratios the quasi-simultaneous coupling method is much more efficient than the ‘classical’ segregated coupling; it is even more efficient at small added-mass ratios.



Figure 5: Free-fall life boat being launched (left). The computational effort required per time step for the FSI coupling (right).

4.3 CALM buoy

The third case is a validation against model tests of a CALM buoy (Fig. 6) in a shallow water basin at MARIN [40]. These tests include the freely decaying motion of the buoy after being released from a given position into calm water. This allows us to compare the simulated and measured natural periods as well as the amount of hydrodynamic damping. The buoy in its default configuration has been modelled as a cylinder with a diameter of 12 m and a height of 6.5 m.

The simulation has been performed at different grids, with approximately 6, 10 and 18 cells



Figure 6: Model of the CALM buoy in the shallow water basin at MARIN (left) and the geometrical representation in the simulations (right).

per cylinder diameter. The results for heave motion are shown in Fig. 7. Using the approach of Eca et al. [41], the numerical uncertainty has been assessed from these three grids and is also indicated. The resulting uncertainty was found quite small, whereas it is understandable that for later times in the simulation the uncertainty increases. The validation of the simulations was monitored by a comparison with the experiments at MARIN and also indicated in Fig. 7. The period as well as damping of the heave motion are found well-predicted.

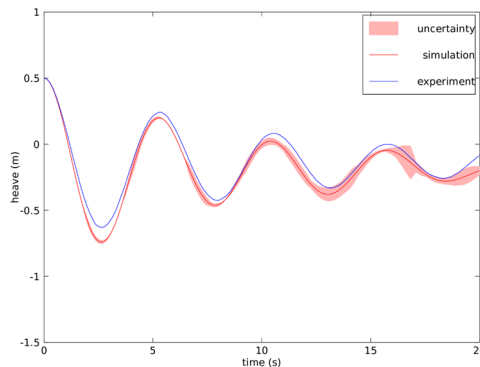


Figure 7: Heave motions of a free-floating CALM buoy in simulation and experiment.

5 ABSORBING BOUNDARY CONDITIONS

In the CALM-buoy simulations, the computational domain has to be restricted to a finite region; one has to take care that no numerical reflections from these artificial domain boundaries enter the physical region of interest. To minimize these reflections a new type of absorbing boundary conditions (ABC) has been developed, which can adapt itself to the passing waves [21, 42]. Also, the effect of current (in arbitrary direction) has been included. In 2D, Peregrine [43] already studied the effect of current on the dispersion relation. In 3D the dispersion relation involving current \mathbf{U} reads, using the abbreviation $k = |\mathbf{k}|$,

$$\omega_{\pm} = \frac{\mathbf{U} \cdot \mathbf{k}}{k} + c_{k0} \quad \text{with} \quad c_{k0} = \sqrt{gh} \sqrt{\frac{\tanh(kh)}{kh}}. \quad (19)$$

The ABC is basically of Sommerfeld type, which in 3D reads as

$$\left[\cos \alpha \left(\frac{\partial}{\partial t} + \mathbf{U} \cdot \nabla \right) + c_{k0} \frac{\partial}{\partial n} \right] \phi_w = 0, \quad (20)$$

where α is the angle between the wave \mathbf{k} and the normal \mathbf{n} . This new condition lets waves with wave number \mathbf{k} pass freely; it is not unique. Further, ϕ_w is the wave component of the potential, which is reformulated in terms of pressure p and velocity \mathbf{u} , using the unsteady Bernoulli equation. This results in a relation between p and \mathbf{u} which is used as a boundary condition to the pressure Poisson equation, similar to the interaction law for fluid-structure interaction that we discussed above. The phase speed c_{k0} is replaced by a Padé approximation, with the unknown wave number \mathbf{k} found from the local solution [21,42].

Figure 8 shows a simulation of an oscillating sphere, with prescribed motion, which generates outgoing waves. A current is present, running in diagonal direction through the domain. The current makes the radiating circles no longer concentric. The domain has been kept rather small, in order to study reflections at the boundaries. The figure clearly shows no visible irregularities near the domain boundaries, demonstrating the potential of the new ABC.

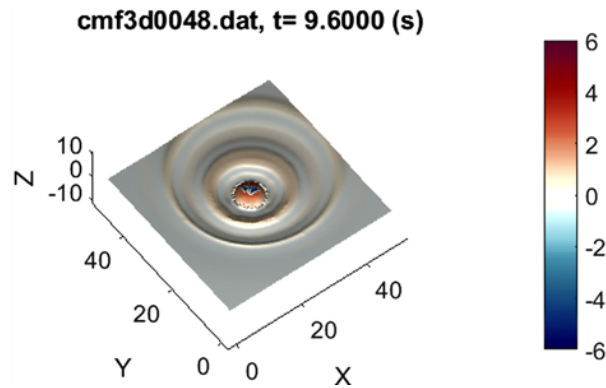


Figure 8: Oscillating buoy in a current, generating non-concentric waves. Observe the regularity of the results at the boundary of the computational domain.

6 CONCLUSION

Several of the newly-developed ingredients of the ComFLOW simulation method have been sketched. Firstly, a quasi-simultaneous numerical coupling method has been presented. It can handle large added-mass ratios efficiently and can also be extended to cover the coupling with elastically-deforming objects. The lower elastic modes are found the most 'tricky' and can be 'tamed' by including them in the interaction law. Secondly, ComFLOW's absorbing boundary condition which adjusts itself to the oncoming waves has been extended to cover the influence of current. Several examples of verification and validation have been included.

ACKNOWLEDGMENTS

This work is part of the research programme Maritime2013 with project number 13267 which is (partly) financed by the Netherlands Organisation for Scientific Research (NWO).

REFERENCES

- [1] S. Haver. Evidences of the existence of freak waves. In Ifremer, editor, *Rogue Waves 2000, Proc. of Int. Workshop*, pages 129–140, Brest (France), 29-30 November, 2000.
- [2] O. M. Faltinsen. *Sea Loads on Ships and Offshore Structures*. Cambridge University Press, 1999.
- [3] B. Buchner. *Green water on ship-type offshore structures*. PhD Thesis, University of Delft, Delft, The Netherlands, November 2002.
- [4] B. Molin and J. Ferziger. Hydrodynamique des structures offshore. *Appl. Mech. Rev.*, 56:B29, 2003.
- [5] W. Tsai and D. K. P. Yue. Computation of nonlinear free-surface flows. *Ann. Rev. Fluid Mech.*, 28:249–278, 1996.
- [6] C. W. Hirt and B. D. Nichols. Volume of fluid (VOF) method for the dynamics of free boundaries. *J. Comput. Phys.*, 39:201–25, 1981.
- [7] W. J. Rider and D. B. Kothe. Reconstructing volume tracking. *J. Comput. Phys.*, 141:112–152, 1998.
- [8] T. Yabe, F. Xiao, and T. Utsumi. The constrained interpolation profile method for multiphase analysis. *J. Comput. Phys.*, 169:556–593, 2001.
- [9] S. J. Osher and G. Tryggvason (eds.). Special issue on ‘Computational Methods for Multiphase Flows’. *J. Comput. Phys.*, 169:249–759, 2001.
- [10] Mathieu Durand, Alban Leroyer, Corentin Lothodé, Frédéric Hauville, Michel Visonneau, Ronan Floch, and Laurent Guillaume. Fsi investigation on stability of downwind sails with an automatic dynamic trimming. *Ocean Engineering*, 90:129–139, 2014.
- [11] David Gross. New quasi-monolithic method to solve dynamic fluid-structure interaction problems on membranes. In *Textiles composites and inflatable structures VII: proc. VII Int. Conf. on Textile Composites and Inflatable Structures, Barcelona, Spain. 19-21 October, 2015*, pages 344–355. CIMNE, 2015.
- [12] Daniel Oliveira, Aldina Santiago, and Constança Rigueiro. Fluid structure interaction in offshore environment. In J.F. Silva Gomes and S.A. Meguid, editors, *Proc. 5th Int. Conf. on Integrity-Reliability-Failure*, Porto (Portugal), July 24-28 2016. Paper ref: 6258.
- [13] R. Verstappen. When does eddy viscosity damp subfilter scales sufficiently? *J. Sci. Comput.*, 49(1):94–110, 2011.
- [14] W. Rozema. *Low-dissipation methods and models for the simulation of turbulent subsonic flow*. PhD thesis, University of Groningen, 2015.
- [15] Wybe Rozema, Roel W. C. P. Verstappen, Johan C. Kok, and Arthur E. P. Veldman. Low-dissipation simulation methods and models for turbulent subsonic flow. *Arch. Comput. Meth. Eng.*, 2019. DOI: 10.1007/s11831-018-09307-7.
- [16] Mahdi Abkar, Hyun J. Bae, and Parviz Moin. Minimum-dissipation scalar transport model for large-eddy simulation of turbulent flows. *Physical Review Fluids*, 1(4):041701, 2016.
- [17] A. E. P. Veldman, R. Luppés, P. van der Plas, H. J. L. van der Heiden, J. Helder, and T. Bunnik. Turbulence modeling for locally-refined free-surface flow simulations in offshore applications. In *Proc. Int. Symp. Offshore Polar Eng. ISOPE2015, Kona (Hawaii, USA), 23-27 June 2015*. paper ISOPE2015-TPC-0282.
- [18] H.J.L. van der Heiden. *Modelling viscous effects in offshore flow problems - a numerical study*. PhD thesis, University of Groningen, 2019.
- [19] K. M. T. Kleefsman, G. Fekken, A. E. P. Veldman, B. Iwanowski, and B. Buchner. A Volume-of-Fluid based simulation method for wave impact problems. *J. Comput. Phys.*, 206:363–393, 2005.
- [20] D. L. Youngs. An interface tracking method for a 3d Eulerian hydrodynamics code. Technical Report AWRE/44/92/35, Atomic Weapons Research Establishment, 1987.
- [21] B. Düz. *Wave generation, propagation and absorption in CFD simulations of free surface flows*. PhD thesis, Technical University Delft, 2015.
- [22] J. Gerrits. *Dynamics of Liquid-Filled Spacecraft*. PhD thesis, University of Groningen, The Netherlands, 2001.

-
- [23] G. Fekken. *Numerical simulation of free-surface flow with moving objects*. PhD Thesis, University of Groningen, The Netherlands, 2004.
- [24] K. M. T. Kleefsman. *Water impact loading on offshore structures - a numerical study*. PhD thesis, University of Groningen, The Netherlands, 2005.
- [25] R. Wemmenhove. *Numerical simulation of two-phase flow in offshore environments*. PhD Thesis, University of Groningen, The Netherlands, 2008.
- [26] P. R. Wellens. *Wave simulation in truncated domains for offshore applications*. PhD Thesis, Technical University Delft, The Netherlands, 2012.
- [27] P. van der Plas. *Local grid refinement for free-surface flow simulations*. PhD thesis, University of Groningen, 2017.
- [28] M. Dröge and R. Verstappen. A new symmetry-preserving Cartesian-grid method for computing flow past arbitrarily shaped objects. *Int. J. Numer. Meth. Fluids*, 47:979–985, 2005.
- [29] Y. Cheny and O. Botella. The LS-STAG method; a new immersed boundary/level-set method for the computation of incompressible viscous flows in complex moving geometries with good conservation properties. *J. Comput. Phys.*, 229:1043–1076, 2010.
- [30] H. B. Gu, D. M. Causon, C. G. Mingham, and L. Qian. Development of a free surface flow solver for the simulation of wave/body interactions. *Eur. J. Mech. B/Fluids*, 38:1–17, 2013.
- [31] A. E. P. Veldman, P. van der Plas, H. Seubers, J. Helder, and K.-W. Lam. Adaptive grid refinement for two-phase offshore applications. In *Proc. 37th Int. Conf. Ocean, Offshore Arctic Eng. OMAE2018*, Madrid (Spain), 17-22 June 2018. paper OMAE2018-77309.
- [32] F. H. Harlow and J. E. Welch. Numerical calculation of time-dependent viscous incompressible flow of fluid with free surface. *Phys. Fluids*, 8:2182–2189, 1965.
- [33] R. W. C. P. Verstappen and A. E. P. Veldman. Symmetry-preserving discretization of turbulent flow. *J. Comput. Phys.*, 187:343–368, 2003.
- [34] J. Chung and G. M. Hulbert. A time integration algorithm for structural dynamics with improved numerical dissipation: the generalized- α method. *J. Appl. Mech.*, 60(2):371–375, August 1992.
- [35] P. Causin, J. F. Gerbau, and F. Nobile. Added-mass effect in the design of partitioned algorithms for fluid-structure problems. *Comput. Methods Appl. Mech. Engr.*, 194:4506–4527, 2005.
- [36] A. E. P. Veldman. New, quasi-simultaneous method to calculate interacting boundary layers. *AIAA J.*, 19:79–85, 1981.
- [37] A. E. P. Veldman. A simple interaction law for viscous-inviscid interaction. *J. Eng. Math.*, 65:367–383, 2009.
- [38] Mathieu Durand. *Interaction fluide-structure souple et l egere, application aux voiliers*. PhD thesis, Ecole Centrale de Nantes (ECN), 2012.
- [39] Arthur E. P. Veldman, Peter van der Plas, Henk Seubers, Matin Hosseini Zahraei, Xing Chang, Peter R. Wellens, and Joop Helder. Overview of fluid-structure coupling in ansys-cfx. In *Proc. 38th Int. Conf. Offshore Mech. Arctic Eng.*, pages OMAE2019–96321, Glasgow (Scotland), June 9-14 2019.
- [40] T. H. J. Bunnik and A. G. van Doeveren. CALM buoy model tests. Technical Report report 18378-3-BT, MARIN, 2008.
- [41] Luis Eça and Martin Hoekstra. Discretization uncertainty estimation based on a least squares version of the grid convergence index. In *Proc. 2nd Workshop on CFD Uncertainty Analysis, Instituto Superior Tecnico, Lisbon*, 2006.
- [42] B. Düz, M. J. A. Borsboom, P. R. Wellens, A. E. P. Veldman, and R. H. M. Huijsmans. An absorbing boundary condition for free-surface water waves. *Comput. Fluids*, 156:562–578, 2017.
- [43] D. H. Peregrine. Interaction of water waves and currents. *Advances in Applied Mechanics.*, 16:9–117, 1976.

AUTHORS INDEX

| | | | |
|-----------------------|---------------|-----------------------------|----------|
| Albaina, I. | 134 | Ficini, S. | 334 |
| Alexias, P. | 625 | Fornberg, B. | 213 |
| Antognoli, L. | 334 | Fukuda, K. | 615 |
| Ascic, B. | 321 | Gadalla, M. | 201 |
| Asnaghi, A. | 383 | Gaggero, S. | 296, 544 |
| Bakis, K.N. | 525 | Galera, L. | 134 |
| Baltazar, J.M. | 477 | Gao, X. | 658 |
| Bardera, R. | 405 | Garcia-Magariño, A. | 405 |
| Bensow, R. | 634, 383, 694 | Gerber, A. G. | 223 |
| Bergqvist, B. | 441 | Geremia, P. | 625 |
| Berstad, A.J. | 259 | Grassi, D. | 201 |
| Bibuli, M. | 334 | Grassi, D. | 296 |
| Bihs, H. | 807, 453 | Gustafsson, R. | 383 |
| Blanco, J.M. | 134 | Hallander, J. | 441 |
| Bonfiglio, L. | 428, 544 | Heimstad, L.F. | 259 |
| Brizzolara, S. | 428, 346 | Helder, J. | 820 |
| Brogli, R. | 177 | Hosseini Zahraei, M. | 820 |
| Böttner, C.-U. | 491 | Ianniello, S. | 99 |
| Cassidy, M. | 537 | Irannezhad, M. | 634 |
| Celik, E. | 321 | Izquierdo, U. | 134 |
| Chandar, D. | 145 | Janson, C-E. | 646 |
| Chang, X. | 820 | Ji, C. | 556, 754 |
| Chen, H.-C. | 223 | Ji, X.-Q. | 588 |
| Chen, J. | 556 | Jungrungruentaworn, S. | 607 |
| Chen-Jun, Y. | 568 | Kajino, T. | 615 |
| Chi, Z. | 556 | Kamath, A. | 807, 453 |
| Ciortan, C. | 730 | Karttunen, A. | 742 |
| Coelho, C. | 502 | Katayama, K. | 615 |
| Conti, F. | 296 | Kjellberg, M. | 646 |
| Coppedè, A. | 544 | Klajj, C. M. | 223 |
| Coslovich, F. | 646 | Klapwijk, M. | 465, 48 |
| Damkilde, L. | 213 | Knight, J. | 169 |
| Dashtimanesh, A. | 417 | Kobayashi, Y. | 615 |
| Davidson, J. | 145 | Kofoed, J. P. | 157 |
| de Baar, J.H.S. | 321 | Korkmaz, K.B. | 694 |
| De Carlini, M. | 417 | Kornev, N. | 60 |
| de Jong, J.S. | 321 | Kostial, M. | 600 |
| Decorte, G. | 795 | Koushan, K. | 35 |
| Degroote, J. | 235 | Kring, D. | 169 |
| Demeester, T. | 235 | Kristiansen, D. | 271 |
| Demo, N. | 111, 122 | LeBlanc, B. E. | 223 |
| Dempwolff, L.-C. | 807 | Li, J. | 428 |
| Deng, G. | 658 | Li, R. | 71 |
| Devolder, B. | 670 | Li, W. | 588, 682 |
| Diez, M. | 177, 334 | Liebrand, R. | 465 |
| Dong, X.-Q. | 588, 682, 371 | Lima, M. | 502 |
| Durante, D. | 334 | Liu, C. | 514 |
| Eskilsson, C. | 157 | Lloyd, T. | 48, 465 |
| Eslamdoost, A. | 634 | Lombaert, G. | 795 |
| Esteban, G.A. | 134 | Lopes, R. | 465 |

| | | | |
|-----------------------------|---------------|--------------------------|---------------|
| Lundbäck, O. | 771 | Seubers, H. | 820 |
| Maki, K.J. | 625, 359 | Shevchuk, I. | 491 |
| Mancini, S. | 417 | Shi, G. | 71 |
| Marrone, S. | 334 | Shiri, A. | 441 |
| Martin, T. | 807, 453 | Skoda, R. | 83 |
| Matias, J. C. | 405 | Smith, T.A. | 393 |
| Melo, D.B. | 477 | Srinil, N. | 525 |
| Mesa, J.D. | 359 | Steffensen, M. L. | 730 |
| Mieth, F. | 600 | Stempinski, F. | 670 |
| Mikkelsen, H. | 730 | Svennberg, U. | 383 |
| Mol, A. | 670 | Tachikawa, T. | 615 |
| Mola, A. | 201, 111 | Tavakoli, S. | 417 |
| Monbaliu, J. | 795 | Testa, C. | 99 |
| Mottyll, S. | 83 | Tezzele, M. | 111, 201, 122 |
| Moura Paredes, G. | 157 | Thaweewat, N. | 607 |
| Nazem, M. | 537 | Tsarau, A. | 271 |
| Niazmand Bilandi, R. | 417 | Vaccaro, C. | 296 |
| Nielsen, M. E. | 213 | Valdenazzi, F. | 201, 296 |
| Niklas, K. | 718 | van Brummelen, E.H. | 235 |
| Noblesse, F. | 588, 682 | Van der Plas, P. | 820 |
| Odetti, A. | 334 | van Straten, O.F.A. | 321 |
| Ohashi, K. | 706 | van Terwisga, T. | 48 |
| Okada, Y. | 615 | Vaz, G. | 465, 48 |
| Okazaki, A. | 615 | Veldman, A.E.P. | 820, 247 |
| Okazaki, M. | 615 | Ventikos, Y. | 393 |
| Ozbulut, M. | 783 | Vernengo, G. | 544 |
| Padovan, R. | 201 | Villa, D. | 296, 544 |
| Pellegrini, R. | 177 | Visonneau, M. | 177 |
| Phoemsaphawee, S. | 607 | Wackers, J. | 177 |
| Pruszek, H. | 718 | Walther, J. H. | 730 |
| Qi, W. | 568 | Wan, D. | 23, 285, 514 |
| Ramezanzadeh, S. | 783 | Wang, J. | 23, 514 |
| Rauwoens, P. | 670 | Wang, Q. | 371 |
| Raven, H.C. | 189 | Wellens, P.R. | 820 |
| Reddy, J.N. | 742 | Werner, S. | 694 |
| Reinaldo Goncalves, B. | 742 | Windt, C. | 145 |
| Remmerswaal, R. | 247 | Wyman, J. | 169 |
| Rijpkema, D.R. | 477 | Xiao, Q. | 71 |
| Ringwood, J.V. | 145 | Xiao-Qian, D. | 568 |
| Romanoff, J. | 742 | Yang, C.-J. | 588, 371 |
| Rosenlöcher, T. | 580, 600 | Yang, Ch.-J. | 682 |
| Rozza, G. | 111, 122, 201 | Yildiz, M. | 783 |
| Rösner, M. | 580 | Yong-sheng, H. | 568 |
| Samarbakhsh, S. | 60 | Zeng, Z. | 754 |
| Santic, I. | 334 | Zhang, C. | 556, 754 |
| Savio, L. | 35 | Zhang, H. | 682 |
| Schlecht, B. | 600, 580 | Zhang, X. | 285 |
| Scholcz, T.P. | 189, 309 | Zhao, W. | 514 |
| Schreiner, F. | 83 | | |
| Serani, A. | 177, 334 | | |

This volume contains the full papers of the VIII International Conference on Computational Methods in Marine Engineering (MARINE 2019) held in Gothenburg, Sweden on May 13-15, 2019.

